



*pharmaceuticals*

# Anticancer Drugs 2021

---

Edited by  
Mary J. Meegan and Niamh M O'Boyle  
Printed Edition of the Special Issue Published in *Pharmaceuticals*

# **Anticancer Drugs 2021**



# Anticancer Drugs 2021

Editors

**Mary J. Meegan**

**Niamh M O'Boyle**

MDPI • Basel • Beijing • Wuhan • Barcelona • Belgrade • Manchester • Tokyo • Cluj • Tianjin



*Editors*

Mary J. Meegan  
School of Pharmacy and  
Pharmaceutical Sciences  
Trinity College Dublin  
Dublin  
Ireland

Niamh M O'Boyle  
School of Pharmacy and  
Pharmaceutical Sciences  
Trinity College Dublin  
Dublin  
Ireland

*Editorial Office*

MDPI  
St. Alban-Anlage 66  
4052 Basel, Switzerland

This is a reprint of articles from the Special Issue published online in the open access journal *Pharmaceuticals* (ISSN 1424-8247) (available at: [www.mdpi.com/journal/pharmaceuticals/special\\_issues/Anticancer\\_Drugs\\_2](http://www.mdpi.com/journal/pharmaceuticals/special_issues/Anticancer_Drugs_2)).

For citation purposes, cite each article independently as indicated on the article page online and as indicated below:

LastName, A.A.; LastName, B.B.; LastName, C.C. Article Title. <i>Journal Name</i> <b>Year</b> , <i>Volume Number</i> , Page Range.
--

**ISBN 978-3-0365-4348-2 (Hbk)**

**ISBN 978-3-0365-4347-5 (PDF)**

© 2022 by the authors. Articles in this book are Open Access and distributed under the Creative Commons Attribution (CC BY) license, which allows users to download, copy and build upon published articles, as long as the author and publisher are properly credited, which ensures maximum dissemination and a wider impact of our publications.

The book as a whole is distributed by MDPI under the terms and conditions of the Creative Commons license CC BY-NC-ND.

# Contents

<b>About the Editors</b> . . . . .	<b>ix</b>
<b>Preface to "Anticancer Drugs 2021"</b> . . . . .	<b>xi</b>
<b>Mary J. Meegan and Niamh M. O'Boyle</b> Special Issue "Anticancer Drugs 2021" Reprinted from: <i>Pharmaceuticals</i> <b>2022</b> , <i>15</i> , 479, doi:10.3390/ph15040479 . . . . .	<b>1</b>
<b>Mohd. Imran, Syed Mohammed Basheeruddin Asdaq, Shah Alam Khan, Dhanalekshmi Unnikrishnan Meenakshi, Abdulhakeem S. Alamri and Walaa F. Alsanie et al.</b> Innovations and Patent Trends in the Development of USFDA Approved Protein Kinase Inhibitors in the Last Two Decades Reprinted from: <i>Pharmaceuticals</i> <b>2021</b> , <i>14</i> , 710, doi:10.3390/ph14080710 . . . . .	<b>7</b>
<b>Sun-Young Han</b> TRK Inhibitors: Tissue-Agnostic Anti-Cancer Drugs Reprinted from: <i>Pharmaceuticals</i> <b>2021</b> , <i>14</i> , 632, doi:10.3390/ph14070632 . . . . .	<b>67</b>
<b>Karishma K. Mashelkar, Woong Sub Byun, Hyejin Ko, Kisu Sung, Sushil K. Tripathi and Seungchan An et al.</b> Discovery of a Novel Template, 7-Substituted 7-Deaza-4'-Thioadenosine Derivatives as Multi-Kinase Inhibitors Reprinted from: <i>Pharmaceuticals</i> <b>2021</b> , <i>14</i> , 1290, doi:10.3390/ph14121290 . . . . .	<b>79</b>
<b>Viola Previtali, Helene B. Mihigo, Rebecca Amet, Anthony M. McElligott, Daniela M. Zisterer and Isabel Rozas</b> Exploring the Anti-Cancer Mechanism of Novel 3,4'-Substituted Diaryl Guanidinium Derivatives Reprinted from: <i>Pharmaceuticals</i> <b>2020</b> , <i>13</i> , 485, doi:10.3390/ph13120485 . . . . .	<b>103</b>
<b>Ranza Elrayess, Yasmine M. Abdel Aziz, Mohamed Saleh Elgawish, Marwa Elewa, Asmaa S. A. Yassen and Sameh S. Elhady et al.</b> Discovery of Potent Dual EGFR/HER2 Inhibitors Based on Thiophene Scaffold Targeting H1299 Lung Cancer Cell Line Reprinted from: <i>Pharmaceuticals</i> <b>2020</b> , <i>14</i> , 9, doi:10.3390/ph14010009 . . . . .	<b>127</b>
<b>Tarek S. Ibrahim, Azizah M. Malebari and Mamdouh F. A. Mohamed</b> Design, Synthesis, In Vitro Anticancer Evaluation and Molecular Modelling Studies of 3,4,5-Trimethoxyphenyl-Based Derivatives as Dual EGFR/HDAC Hybrid Inhibitors Reprinted from: <i>Pharmaceuticals</i> <b>2021</b> , <i>14</i> , 1177, doi:10.3390/ph14111177 . . . . .	<b>149</b>
<b>Irving Balbuena-Rebolledo, Itzia Irene Padilla-Martínez, Martha Cecilia Rosales-Hernández and Martiniano Bello</b> Repurposing FDA Drug Compounds against Breast Cancer by Targeting EGFR/HER2 Reprinted from: <i>Pharmaceuticals</i> <b>2021</b> , <i>14</i> , 791, doi:10.3390/ph14080791 . . . . .	<b>171</b>
<b>Warit Ruanglertboon, Michael J. Sorich, Ashley M. Hopkins and Andrew Rowland</b> Mechanistic Modelling Identifies and Addresses the Risks of Empiric Concentration-Guided Sorafenib Dosing Reprinted from: <i>Pharmaceuticals</i> <b>2021</b> , <i>14</i> , 389, doi:10.3390/ph14050389 . . . . .	<b>191</b>

<b>Manar I. Nagy, Khaled M. Darwish, Safaa M. Kishk, Mohamed A. Tantawy, Ali M. Nasr and Mona Qushawy et al.</b> Design, Synthesis, Anticancer Activity, and Solid Lipid Nanoparticle Formulation of Indole- and Benzimidazole-Based Compounds as Pro-Apoptotic Agents Targeting Bcl-2 Protein Reprinted from: <i>Pharmaceuticals</i> <b>2021</b> , <i>14</i> , 113, doi:10.3390/ph14020113 . . . . .	<b>203</b>
<b>Margarida Espadinha, Valentina Barcherini, Lídia M. Gonçalves, Elies Molins, Alexandra M. M. Antunes and Maria M. M. Santos</b> Tryptophanol-Derived Oxazolopyrrolidone Lactams as Potential Anticancer Agents against Gastric Adenocarcinoma Reprinted from: <i>Pharmaceuticals</i> <b>2021</b> , <i>14</i> , 208, doi:10.3390/ph14030208 . . . . .	<b>241</b>
<b>Camelia Elena Stecoza, George Mihai Nitulescu, Constantin Draghici, Miron Teodor Caproiu, Octavian Tudorel Olaru and Marinela Bostan et al.</b> Synthesis and Anticancer Evaluation of New 1,3,4-Oxadiazole Derivatives Reprinted from: <i>Pharmaceuticals</i> <b>2021</b> , <i>14</i> , 438, doi:10.3390/ph14050438 . . . . .	<b>261</b>
<b>Marta Gargantilla, José López-Fernández, Maria-Jose Camarasa, Leentje Persoons, Dirk Daelemans and Eva-Maria Priego et al.</b> Inhibition of XPO-1 Mediated Nuclear Export through the Michael-Acceptor Character of Chalcones Reprinted from: <i>Pharmaceuticals</i> <b>2021</b> , <i>14</i> , 1131, doi:10.3390/ph14111131 . . . . .	<b>277</b>
<b>Mohammad Mahboob Alam, Abdulraheem SA Almalki, Thikryat Neamatallah, Nada M. Ali, Azizah M. Malebari and Syed Nazreen</b> Synthesis of New 1, 3, 4-Oxadiazole-Incorporated 1, 2, 3-Triazole Moieties as Potential Anticancer Agents Targeting Thymidylate Synthase and Their Docking Studies Reprinted from: <i>Pharmaceuticals</i> <b>2020</b> , <i>13</i> , 390, doi:10.3390/ph13110390 . . . . .	<b>297</b>
<b>Kseniya Kovaleva, Olga Yarovaya, Konstantin Ponomarev, Sergey Cheresiz, Amirhossein Azimirad and Irina Chernyshova et al.</b> Design, Synthesis, and Molecular Docking Study of New Tyrosyl-DNA Phosphodiesterase 1 (TDP1) Inhibitors Combining Resin Acids and Adamantane Moieties Reprinted from: <i>Pharmaceuticals</i> <b>2021</b> , <i>14</i> , 422, doi:10.3390/ph14050422 . . . . .	<b>313</b>
<b>Dong-Hee Lee, Seunghyun Choi, Yoon Park and Hyung-seung Jin</b> Mucin1 and Mucin16: Therapeutic Targets for Cancer Therapy Reprinted from: <i>Pharmaceuticals</i> <b>2021</b> , <i>14</i> , 1053, doi:10.3390/ph14101053 . . . . .	<b>331</b>
<b>Gloria Ana, Patrick M. Kelly, Azizah M. Malebari, Sara Noorani, Seema M. Nathwani and Brendan Twamley et al.</b> Synthesis and Biological Evaluation of 1-(Diarylmethyl)-1 <i>H</i> -1,2,4-triazoles and 1-(Diarylmethyl)-1 <i>H</i> -imidazoles as a Novel Class of Anti-Mitotic Agent for Activity in Breast Cancer Reprinted from: <i>Pharmaceuticals</i> <b>2021</b> , <i>14</i> , 169, doi:10.3390/ph14020169 . . . . .	<b>357</b>
<b>Jaime Pérez-Villanueva, Félix Matadamas-Martínez, Lilián Yépez-Mulia, Vadim Pérez-Koldenkova, Martha Leyte-Lugo and Karen Rodríguez-Villar et al.</b> Synthesis and Cytotoxic Activity of Combretastatin A-4 and 2,3-Diphenyl-2 <i>H</i> -indazole Hybrids Reprinted from: <i>Pharmaceuticals</i> <b>2021</b> , <i>14</i> , 815, doi:10.3390/ph14080815 . . . . .	<b>411</b>
<b>Benas Balandis, Vytautas Mickevičius and Vilma Petrikaitė</b> Exploration of Benzenesulfonamide-Bearing Imidazole Derivatives Activity in Triple-Negative Breast Cancer and Melanoma 2D and 3D Cell Cultures Reprinted from: <i>Pharmaceuticals</i> <b>2021</b> , <i>14</i> , 1158, doi:10.3390/ph14111158 . . . . .	<b>429</b>

<b>Paulina Strzyga-Łach, Alicja Chrzanowska, Katarzyna Podsadni and Anna Bielenica</b> Investigation of the Mechanisms of Cytotoxic Activity of 1,3-Disubstituted Thiourea Derivatives Reprinted from: <i>Pharmaceuticals</i> <b>2021</b> , <i>14</i> , 1097, doi:10.3390/ph14111097 . . . . .	<b>443</b>
<b>Yehezkiel Steven Kurniawan, Krisfian Tata Aneka Priyanga, Jumina, Harno Dwi Pranowo, Eti Nurwening Sholikhah and Abdul Karim Zulkarnain et al.</b> An Update on the Anticancer Activity of Xanthone Derivatives: A Review Reprinted from: <i>Pharmaceuticals</i> <b>2021</b> , <i>14</i> , 1144, doi:10.3390/ph14111144 . . . . .	<b>461</b>
<b>Ana Reis-Mendes, José Luís Dores-Sousa, Ana Isabel Padrão, Margarida Duarte-Araújo, José Alberto Duarte and Vítor Seabra et al.</b> Inflammation as a Possible Trigger for Mitoxantrone-Induced Cardiotoxicity: An In Vivo Study in Adult and Infant Mice Reprinted from: <i>Pharmaceuticals</i> <b>2021</b> , <i>14</i> , 510, doi:10.3390/ph14060510 . . . . .	<b>501</b>
<b>Anna Merwid-Lad, Dorota Ksiadzyna, Agnieszka Hałoń, Danuta Szkudlarek, Małgorzata Trocha and Marta Szandruk-Bender et al.</b> Morin-5'-Sulfonic Acid Sodium Salt (NaMSA) Attenuates Cyclophosphamide-Induced Histological Changes in Genitourinary Tract in Rats—Short Report Reprinted from: <i>Pharmaceuticals</i> <b>2021</b> , <i>14</i> , 192, doi:10.3390/ph14030192 . . . . .	<b>529</b>
<b>Anna Merwid-Lad, Piotr Ziólkowski, Marta Szandruk-Bender, Agnieszka Matuszewska, Adam Szelag and Małgorzata Trocha</b> Effect of a Low Dose of Carvedilol on Cyclophosphamide-Induced Urinary Toxicity in Rats—A Comparison with Mesna Reprinted from: <i>Pharmaceuticals</i> <b>2021</b> , <i>14</i> , 1237, doi:10.3390/ph14121237 . . . . .	<b>541</b>
<b>Anunay J. Pulukuri, Anthony J. Burt, Larissa K. Opp, Colin M. McDowell, Maryam Davaritouchaee and Amy E. Nielsen et al.</b> Acquired Drug Resistance Enhances Imidazoquinoline Efflux by P-Glycoprotein Reprinted from: <i>Pharmaceuticals</i> <b>2021</b> , <i>14</i> , 1292, doi:10.3390/ph14121292 . . . . .	<b>565</b>





# About the Editors

## Mary J. Meegan

Professor Mary J Meegan completed her PhD degree in University College Dublin under the direction of Professor Dervilla Donnelly in the area of natural product chemistry and subsequently carried out postdoctoral research at the University Chemical Laboratory, Cambridge University, in the research group of Professor Alan Battersby in the area of porphyrin synthesis and biosynthesis. Following further research periods at University College Dublin and CNRS Gif-sur-Yvette, she was appointed as a lecturer in Pharmaceutical Chemistry at the School of Pharmacy and Pharmaceutical Sciences in Trinity College Dublin. Her research experience is in the general area of pharmaceutical and medicinal chemistry, with over 100 peer-reviewed scientific papers covering topics such as: (i) novel ligands for nuclear receptors (ER&AR), HSP90 and tubulin; (ii) the synthesis of small-molecule inhibitors of the enzymes involved in the metastasis of breast tumors; (iii) the design and evaluation of dual targeting agents for tubulin and aromatase; and (iv) the design of drugs which target the proliferation of chronic lymphocytic leukaemia (CLL), Burkitt lymphoma and related malignancies. Research collaborations are established within Trinity College with Dr. Niamh O'Boyle (School of Pharmacy and Pharmaceutical Sciences), Dr D Zisterer, Dr D Fayne in the School of Biochemistry and Immunology and also with many European research centers. She is a member of the Royal Society of Chemistry and the Irish and European Associations for Cancer Research.

## Niamh M O'Boyle

Dr. Niamh O'Boyle is an Assistant Professor in Pharmaceutical Chemistry in Trinity College Dublin. She received her BSc (Pharm) (1st class) and PhD degrees from Trinity College Dublin, working with Prof. Mary J. Meegan. She subsequently completed postdoctoral fellowships at the University of Gothenburg (Sweden) with Prof. Ann-Therese Karlberg and the School of Biochemistry and Immunology (TCD), working with Prof. Daniela Zisterer. Niamh is fascinated by the interaction of chemicals, both drugs and toxins, with the body. This inspires her research in the development of novel drugs for hard-to-treat cancers and in discovering the underlying mechanisms of skin allergy. Drug targets of interest include the protein tubulin, the estrogen and progesterone receptors, and the role of reactive oxygen species.

Niamh is a member of the Pharmaceutical Society of Ireland, the Royal Society of Chemistry and the Irish and European Associations for Cancer Research. She is the early career representative on the Royal Society of Chemistry Ireland Regional Steering Group (2020–2023) and is a committee member of the international GP2A medicinal chemistry group. She has been appointed to the Physical, Chemical & Mathematical Sciences multidisciplinary committee of the Royal Irish Academy (2022-2026). She is involved in the CRYSTAL3 EU MSCA-Rise project and the COST action CA17104 STRATAGEM “New diagnostic and therapeutic tools against multidrug resistant tumours”.



## Preface to "Anticancer Drugs 2021"

The research presented in this Special Issue, "Anticancer Drugs 2021", of *Pharmaceuticals* provides a broad selection of results that were achieved in the field of anticancer drug development in 2021. The collection contains contributions which are focused on cancer drug discovery and newly approved anticancer drugs together with important reviews in specific areas of cancer therapeutics. The development of new anticancer drugs for clinical use is extremely challenging, because of the emergence of resistance to many chemotherapeutic agents. The investigations reported in this Special Issue on anticancer drugs cover a wide area of research and include the design and synthesis of new molecular entities, molecular modelling, computational techniques and the development of molecular and biochemical tests. The discovery of compounds targeting kinases, tubulin, thymidylate synthase, histone deacetylase, HER2 and apoptosis-related proteins, together with studies on cancer drug toxicity and resistance mechanisms, are included. Both the current direction and future potential for research in these areas are outlined.

This Special Issue highlights both the opportunities and challenges which are identified in the discovery of novel small-molecule cancer drugs, and also demonstrates the applications of innovative cancer therapies. Contemporary drug design offers exciting opportunities for the discovery of new anticancer therapeutics and provides a direction for future research in this area. Recent trends in the design, synthesis, therapeutic applications and regulatory approvals of anticancer drugs are presented in this collection which demonstrate the relevance of medicinal chemistry in cancer research.

**Mary J. Meegan and Niamh M O'Boyle**  
*Editors*



Editorial

# Special Issue “Anticancer Drugs 2021”

Mary J. Meegan\* and Niamh M. O’Boyle\* 

School of Pharmacy and Pharmaceutical Sciences, Trinity Biomedical Sciences Institute, Trinity College Dublin, 152-160 Pearse Street, 2 DO2R590 Dublin, Ireland

\* Correspondence: mmeegan@tcd.ie (M.J.M.); nioboyle@tcd.ie (N.M.O.)

This Special Issue of *Pharmaceuticals* is devoted to significant advances achieved in the field of Anticancer Drugs in 2021. Recent findings and trends in the design, synthesis and mechanism of action and therapeutic applications of anticancer drugs are presented. These research studies demonstrate the relevance of medicinal chemistry and the pharmaceutical sciences in cancer research. The research illustrates the exciting opportunities that contemporary drug design offers for the discovery of new therapies and diagnostics for cancer and offers perspectives on the future directions of anticancer therapeutics. Resistance to anticancer drugs has become a major threat to the success of chemotherapeutic agents, and therefore the discovery and development of new anticancer drugs for clinical use is extremely challenging. Investigations into anticancer drugs covers a vast area of research and includes natural products, design and synthesis of new molecular entities, molecular modelling, computational techniques and development of molecular and biochemical tests. Heterocycles are well represented in this collection with the inclusion of novel compounds targeting kinases, tubulin, thymidylate synthase, histone deacetylase, HER2 and apoptosis-related proteins. Original research into amelioration of toxicity associated with current chemotherapeutics and resistance is also featured.

In 2020, the FDA approved 18 new cancer drugs, including the HER2-directed margetuximab, sacituzumab govitecan [a TROP2-targeted antibody–drug conjugate (ADC) for triple-negative breast cancer] and the BCMA-targeted ADC belantamab mafodotin for multiple myeloma. Among the kinase inhibitors approved were the HER2 kinase inhibitor tucatinib, together with the RET kinase inhibitors selpercatinib and pralsetinib with indication for RET fusion-positive NSCLC. Lurbinectedin, approved for multiple myeloma, covalently binds to the DNA minor groove. Despite the continued impact of COVID-19, 15 new cancer drugs were approved by the FDA in 2021. The allosteric inhibitor sotorasib targets KRAS-G12C mutated NSCLC, while the novel allosteric HIF-2 $\alpha$  inhibitor belzutivan targets von Hippel-Lindau tumours. Dostarlimab, a PD1/PDL1-targeted antibody for endometrial cancer was approved, together with the ADCs loncastuximab teserine, a CD19-targeted ADC for B-cell lymphomas, and tisotumab vedotin, a tissue targeted ADC approved for cervical cancer. The bispecific antibody amivantamab targeting EGFR and MET gained approval for small molecule-resistant NSCLC, the kinase inhibitor mobocertinib selectively inhibits EGFR in NSCLC and the kinase inhibitor asciminib was approved for Philadelphia chromosome-positive CML. Several BCMA-targeted CAR-T cell therapies were also approved in 2021.

Protein kinase inhibitors (PKIs) are clinically significant drugs in the treatment of cancer and inflammatory diseases, with over 535 reported PKs and over 70 PKIs approved by the FDA. Imran et al. have reviewed the USFDA PKI patent approvals for the period 2001 to 31 May 2021 and have provided a comprehensive timeline depicting the PKI approvals, molecular structures, primary targets and approved indications [1]. Availability of generic PKI drugs in the USA market is also discussed together with the development of PKIs with structurally varied scaffolds, chemotypes and pharmacophores. The development of larotrectinib and entrectinib as tissue-agnostic anti-cancer tropomyosin receptor kinase

**Citation:** Meegan, M.J.; O’Boyle, N.M. Special Issue “Anticancer Drugs 2021”. *Pharmaceuticals* **2022**, *15*, 479. <https://doi.org/10.3390/ph15040479>

Received: 31 March 2022

Accepted: 8 April 2022

Published: 14 April 2022

**Publisher’s Note:** MDPI stays neutral with regard to jurisdictional claims in published maps and institutional affiliations.



**Copyright:** © 2022 by the authors. Licensee MDPI, Basel, Switzerland. This article is an open access article distributed under the terms and conditions of the Creative Commons Attribution (CC BY) license (<https://creativecommons.org/licenses/by/4.0/>).

(Trk) inhibitors is reviewed by Han [2]. In clinical trials with larotrectinib and entrectinib in patients with a wide range of tumour types with various types of Trk fusion, clinical benefits were observed indicating tumour-agnostic activity. It is concluded that the adoption of the tissue-agnostic approach has accelerated the clinical development of Trk inhibitors.

The simultaneous inhibition of multiple protein kinases targets involved in cancer progression is a possible route to increasing potency and overcoming resistance. Many multi-kinase inhibitors occupy only the hinge and hydrophobic region in the ATP binding site. Mashelkar et al. designed multi-kinase inhibitors that occupy the ribose pocket, along with the hinge and hydrophobic region [3] and identified a novel 4'-thionucleoside with potent anticancer activity and marked inhibition of TRKA, CK1 $\delta$ , and DYRK1A/1B kinases, with potential for developing anti-cancer drugs. Previtali et al. reported the anti-cancer mechanism of a novel 3,4'-substituted diaryl guanidinium compound that inhibits BRAF through a hypothetical type-III allosteric mechanism [4]. Following a docking study using an active triphosphate-containing BRAF protein, a variety of structural modifications were evaluated in leukaemia, breast, cervical and colorectal carcinoma cell lines with pro-apoptotic effects. A divergent effect on inhibition of MAPK/ERK signalling pathway was demonstrated, confirming that diaryl guanidinium compounds are excellent hit molecules for new anticancer therapies. Elrayess et al. reported a series of thieno[2,3-d][1,2,3]triazine and acetamide derivatives as dual epidermal growth factor receptor (EGFR) and human EGFR-related receptor 2 (HER2) inhibitors targeting non-small cell lung cancer (NSCLC) [5]. The lead compound was cytotoxic at nanomolar levels in the H1299 cell line, with activity against EGFR and HER2 comparable to imatinib and was identified as a promising agent for NSCLC.

Ibrahim et al. investigated the design and synthesis of a series of dual targeting hybrid molecules by combining histone deacetylase (HDAC) inhibition with epidermal growth factor receptor (EGFR-TK) inhibition [6]. The novel hydroxamic acid hybrids were cytotoxic in cancer cell lines, proapoptotic, showed increased expression of caspases 3/8 and Bax and down-regulation in Bcl-2 and inhibition of both EGFR and HDAC1 enzymes. Balbuena-Rebolledo identified several FDA-approved drugs as potential inhibitors of the intracellular domain of epidermal growth factor receptor 1 (EGFR) and human epidermal receptor 2 (HER2) which are important targets for cancer drugs [7]. FDA-approved drugs with similar structures to lapatinib and gefitinib were identified in the DrugBank. Docking and molecular dynamics simulations on the selected compounds identified interactions with the ligand-binding sites of EGFR and HER2, without interaction with residues involved in drug resistance; cytotoxicity was confirmed in breast cancer cell lines. These repurposed compounds may offer possible new anticancer treatments by targeting HER2 and EGFR.

Sorafenib is an orally administered kinase inhibitor used to treat advanced hepatocellular and renal cell cancer. Inconsistencies in treatment efficacy and tolerability may be attributed to variability in sorafenib exposure over time. Ruanglertboon et al. developed a concentration-guided sorafenib dosing protocol to increase the proportion of patients that achieve a sorafenib  $C_{max}$  within the required range by using a model to simulate sorafenib exposure [8].

Nagy et al. investigated the inhibition of Bcl-2 as a promising strategy for cancer treatment [9]. Benzimidazole and indole-containing analogues of the Bcl-2 inhibitor obatoclax were designed by introduction of alkylamine or carboxyhydrazine methylene linkers to facilitate improved hydrophobic Bcl-2 binding. Anti-cancer activity was confirmed in MDA-MB-231 (breast cancer) and A549 (lung adenocarcinoma) cells with significantly upregulated expression of pro-apoptotic Bax and caspase-3, -8 and -9, and downregulation of anti-apoptotic Bcl-2. Espadinha et al. reported indole-based tryptophanol-derived polycyclic compounds as activators of the tumour suppressor protein p53, a therapeutic target in many cancers [10]. A novel series of enantiomerically pure tryptophanol-derived small molecules was optimised, and absolute configuration established by X-ray analysis. These compounds target human gastric adenocarcinoma (AGS) cells while mediating apoptosis via increase in caspase 3/7 activity. In vitro stability and metabolic studies identified

potent lead compounds for further studies. Stecoza et al. have developed a series of new 2,5-diaryl/heteroaryl-1,3,4-oxadiazoles as novel chemotherapeutic agents [11]. Following evaluation in human colon and breast cancer cell lines, STAT3 and miR-21 are suggested as the most probable targets for these compounds suggesting future studies to improve the anticancer profile and to reduce the toxicological risks.

The nuclear export receptor exportin-1 (XPO1, CRM1) is a relevant target in haematological malignancies. The XPO1 inhibitor leptomyacin B interacts with XPO1 by covalent interaction with Cys528. Gargantilla et al. synthesised a series of chalcones designed to react with XPO1 thiol groups via hetero-Michael addition reactions [12]. Reactions of selected chalcones with GSH demonstrated potential reversible covalent interaction with XPO1 thiols. Good correlation was observed in antiproliferative assays with cancer cell lines and as XPO1 inhibitors. Thymidylate synthase (TS) is an established target in cancer treatment, as it is directly involved in DNA synthesis. Alam et al. developed potential chemotherapeutic hybrid compounds containing 1,2,3-triazole and 1,3,4-oxadiazole heterocycles [13]. Evaluation for inhibition of breast and human colorectal carcinoma demonstrated superior activity to tamoxifen and 5-fluorouracil, with inhibition of thymidylate synthase enzyme superior to pemetrexed. The DNA repair enzyme tyrosyl-DNA-phosphodiesterase 1 (TDP1) acts by removal of TOP1-DNA adducts stabilized by TOP1 inhibitors. The combination of a terpene resin acid backbone with an adamantane fragment as a DNA repair inhibitor was reported by Kolaleva et al. [14]. The linker type and length, diterpene and adamantane moieties were optimised. The synthesised compounds were effective inhibitors of TDP1 while molecular modelling indicated that the TDP1 intermediate (covalent complex of TDP1 with DNA) may be stabilised as observed for topoisomerase–DNA covalent complexes by camptothecins. The highly glycosylated transmembrane mucin (MUC) proteins are over-expressed in different types of cancers and are both promising cancer therapeutic targets and also biomarkers for human cancer. Current efforts to develop MUC1- and MUC16-targeted cancer therapies include antibody-based therapeutics, small molecule inhibitors, vaccines and cell therapies. Lee et al. have comprehensively reviewed the various therapeutic agents targeting mucins which are under different stages of clinical trial for several cancers [15].

The synthesis and biochemical evaluation of novel hybrids of the microtubule targeting benzophenone phenstatin and the aromatase triazole inhibitor letrozole are reported by Ana et al. [16]. The compounds demonstrated potency in MCF-7 and MDA-MB-231 breast cancer cells, together with significant G<sub>2</sub>/M phase cell cycle arrest, induction of apoptosis, inhibition of tubulin polymerisation and selective inhibition of aromatase. These hybrids are promising candidates for development as antiproliferative, aromatase inhibitory and microtubule-disrupting agents for breast cancer. The antitumour activity of hybrid compounds based on the structure of combretastatin A-4 and 2,3-diphenyl-2*H*-indazole has been evaluated by Perez-Villanueva et al [17]. Selected hybrid compounds possess significant cytotoxic activity superior to cisplatin against HeLa and SK-LU-1 cells, with similar potency to imatinib against K562 cells, inhibited tubulin polymerisation and induced G<sub>2</sub>/M arrest. Balandis et al. synthesized a series of new imidazole derivatives incorporating a novel benzenesulfonamide moiety [18]. Evaluation against MDA-MB-231 breast cancer and human malignant melanoma (IGR39) cell identified the optimal aryl and imidazole substitution required. A core pharmacophore for the design of anticancer compounds against aggressive and invasive cancers such as malignant melanoma and triple-negative breast cancer was identified. 1,3-Disubstituted derivatives of urea and thiourea are reported to possess antiproliferative properties against various solid and leukaemia tumour cell lines. Strzyga-Lach et al. have developed a series of selective 3-(trifluoromethyl)phenylthiourea analogues with selective cytotoxic effects against human colon, prostate and leukaemia cell lines [19]. The most potent compounds showed pro-apoptotic activity and inhibited release of the cytokine IL-6 in the colon SW480 and SW620 cells lines. The anticancer effects of xanthenes may be attributed to caspase activation, DNA cross-linking, inhibition of kinases and topoisomerase. Recent advances in the discovery of xanthone derivatives with



anticancer activity, both isolated from natural sources and synthetic examples are reviewed by Kurniawan et al., together with potential further developments of active, selective and efficient anticancer drugs based on xanthone derivatives [20].

Toxicity and drug resistance remains a challenging issue in cancer drug development. The type II topoisomerase inhibitor mitoxantrone (MTX) is used in to treat several cancers and refractory multiple sclerosis. Reis-Mendes et al. investigated the cardiotoxicity of MTX to determine if inflammation or oxidative stress-related pathways are involved [21]. Histopathology results indicated that MTX caused cardiotoxicity while inflammation may be an important trigger to MTX-induced cardiotoxicity in adult mice, with increased expression of NF- $\kappa$ B p65, NF- $\kappa$ B p52 and TNF- $\alpha$  with decrease in IL-6. The widely used DNA alkylating agent cyclophosphamide (CPX) causes toxic effects in the urogenital system. Merwid-Lad examined the effect of morin-5'-sulfonic acid sodium salt (NaMSA) on CPX-induced urogenital toxicity in rats by histological evaluation, morphological changes and relative decrease in sperm count [22]. Co-administration of NaMSA reversed most of the morphological changes and may attenuate CPX-induced histological changes in the urogenital tract. The nephroprotective effects of the beta-adrenergic antagonist carvedilol on CPX-induced urotoxicity was also examined [23]. When co-administered with mesna, carvedilol improved kidney function and reversed histological abnormalities in bladders, presumably via antioxidant and anti-inflammatory effects. Multidrug-Resistant (MDR) cancers modulate chemotherapeutic efficacy through drug efflux. Pulukuri et al. investigated P-glycoprotein 1 mediated efflux of Toll-Like Receptor (TLR 7/8) agonist immunotherapies [24]. The imidazoquinoline TLR agonists imiquimod, resiquimod and gardiquimod are P-gp substrates. Imidazoquinoline efflux occurs through P-gp and is enhanced for imiquimod due to acquired drug resistance. This enhancement could be beneficial for modulating the activity of tumour-infiltrating immune cells in local proximity to cancer cells

The research presented in this Special Issue contains contributions which are focussed on cancer drug discovery together with important reviews in specific areas of cancer therapeutics. This Special Issue highlights both the challenges and opportunities in the discovery and development of both novel small-molecule cancer drugs and applications of innovative cancer therapies and demonstrates the direction and potential for future research in these areas.

**Author Contributions:** M.J.M. and N.M.O. compiled the editorial manuscript and M.J.M. submitted the manuscript. All authors have read and agreed to the published version of the manuscript.

**Funding:** This research received no external funding.

**Institutional Review Board Statement:** Not applicable.

**Informed Consent Statement:** Not applicable.

**Data Availability Statement:** Data is contained in the article.

**Acknowledgments:** We thank the authors for their hard work to produce an up-to-date and comprehensive Issue on anticancer drugs.

**Conflicts of Interest:** The authors declare no conflict of interest.

## References

1. Imran, M.; Asdaq, S.M.B.; Khan, S.A.; Unnikrishnan Meenakshi, D.; Alamri, A.S.; Alsanie, W.F.; Alhomrani, M.; Mohzari, Y.; Alrashed, A.; AlMotairi, M.; et al. Innovations and patent trends in the development of usfda approved protein kinase inhibitors in the last two decades. *Pharmaceuticals* **2021**, *14*, 710. [CrossRef] [PubMed]
2. Han, S.Y. Trk inhibitors: Tissue-agnostic anti-cancer drugs. *Pharmaceuticals* **2021**, *14*, 632. [CrossRef]
3. Mashelkar, K.K.; Byun, W.S.; Ko, H.; Sung, K.; Tripathi, S.K.; An, S.; Yum, Y.A.; Kwon, J.Y.; Kim, M.; Kim, G.; et al. Discovery of a novel template, 7-substituted 7-deaza-4'-thioadenosine derivatives as multi-kinase inhibitors. *Pharmaceuticals* **2021**, *14*, 1290. [CrossRef] [PubMed]
4. Previtali, V.; Mihigo, H.B.; Amet, R.; McElligott, A.M.; Zisterer, D.M.; Rozas, I. Exploring the anti-cancer mechanism of novel 3,4'-substituted diaryl guanidinium derivatives. *Pharmaceuticals* **2020**, *13*, 485. [CrossRef] [PubMed]

5. Elrayess, R.; Abdel Aziz, Y.M.; Elgawish, M.S.; Elewa, M.; Yassen, A.S.A.; Elhady, S.S.; Elshihawy, H.A.; Said, M.M. Discovery of potent dual EGFR/HER2 inhibitors based on thiophene scaffold targeting H1299 lung cancer cell line. *Pharmaceuticals* **2020**, *14*, 9. [CrossRef]
6. Ibrahim, T.S.; Malebari, A.M.; Mohamed, M.F.A. Design, synthesis, in vitro anticancer evaluation and molecular modelling studies of 3,4,5-trimethoxyphenyl-based derivatives as dual EGFR/HDAC hybrid inhibitors. *Pharmaceuticals* **2021**, *14*, 1177. [CrossRef]
7. Balbuena-Rebolledo, I.; Padilla, M., II; Rosales-Hernandez, M.C.; Bello, M. Repurposing FDA drug compounds against breast cancer by targeting EGFR/HER2. *Pharmaceuticals* **2021**, *14*, 791. [CrossRef]
8. Ruanglertboon, W.; Sorich, M.J.; Hopkins, A.M.; Rowland, A. Mechanistic modelling identifies and addresses the risks of empiric concentration-guided sorafenib dosing. *Pharmaceuticals* **2021**, *14*, 389. [CrossRef]
9. Nagy, M.I.; Darwish, K.M.; Kishk, S.M.; Tantawy, M.A.; Nasr, A.M.; Qushawy, M.; Swidan, S.A.; Mostafa, S.M.; Salama, I. Design, synthesis, anticancer activity, and solid lipid nanoparticle formulation of indole- and benzimidazole-based compounds as pro-apoptotic agents targeting bcl-2 protein. *Pharmaceuticals* **2021**, *14*, 113. [CrossRef]
10. Espadinha, M.; Barcherini, V.; Goncalves, L.M.; Molins, E.; Antunes, A.M.M.; Santos, M.M.M. Tryptophan-derived oxazolopyrrolidone lactams as potential anticancer agents against gastric adenocarcinoma. *Pharmaceuticals* **2021**, *14*, 208. [CrossRef]
11. Stecoza, C.E.; Nitulescu, G.M.; Draghici, C.; Caproiu, M.T.; Olaru, O.T.; Bostan, M.; Mihaila, M. Synthesis and anticancer evaluation of new 1,3,4-oxadiazole derivatives. *Pharmaceuticals* **2021**, *14*, 438. [CrossRef] [PubMed]
12. Gargantilla, M.; Lopez-Fernandez, J.; Camarasa, M.J.; Persoons, L.; Daelemans, D.; Priego, E.M.; Perez-Perez, M.J. Inhibition of XPO-1 mediated nuclear export through the michael-acceptor character of chalcones. *Pharmaceuticals* **2021**, *14*, 1131. [CrossRef] [PubMed]
13. Alam, M.M.; Almalki, A.S.; Neamatallah, T.; Ali, N.M.; Malebari, A.M.; Nazreen, S. Synthesis of new 1, 3, 4-oxadiazole-incorporated 1, 2, 3-triazole moieties as potential anticancer agents targeting thymidylate synthase and their docking studies. *Pharmaceuticals* **2020**, *13*, 390. [CrossRef]
14. Kovaleva, K.; Yarovaya, O.; Ponomarev, K.; Cheresiz, S.; Azimirad, A.; Chernyshova, I.; Zakharenko, A.; Konev, V.; Khlebnikova, T.; Mozhaytsev, E.; et al. Design, synthesis, and molecular docking study of new tyrosyl-DNA phosphodiesterase 1 (TDP1) inhibitors combining resin acids and adamantane moieties. *Pharmaceuticals* **2021**, *14*, 422. [CrossRef] [PubMed]
15. Lee, D.H.; Choi, S.; Park, Y.; Jin, H.S. Mucin1 and mucin16: Therapeutic targets for cancer therapy. *Pharmaceuticals* **2021**, *14*, 1053. [CrossRef]
16. Ana, G.; Kelly, P.M.; Malebari, A.M.; Noorani, S.; Nathwani, S.M.; Twamley, B.; Fayne, D.; O'Boyle, N.M.; Zisterer, D.M.; Pimentel, E.F.; et al. Synthesis and biological evaluation of 1-(diarylmethyl)-1H-1,2,4-triazoles and 1-(diarylmethyl)-1H-imidazoles as a novel class of anti-mitotic agent for activity in breast cancer. *Pharmaceuticals* **2021**, *14*, 169. [CrossRef]
17. Perez-Villanueva, J.; Matadamas-Martinez, F.; Yopez-Mulia, L.; Perez-Koldenkova, V.; Leyte-Lugo, M.; Rodriguez-Villar, K.; Cortes-Benitez, F.; Macias-Jimenez, A.P.; Gonzalez-Sanchez, I.; Romero-Velasquez, A.; et al. Synthesis and cytotoxic activity of combretastatin a-4 and 2,3-diphenyl-2H-indazole hybrids. *Pharmaceuticals* **2021**, *14*, 815. [CrossRef]
18. Balandis, B.; Micevicius, V.; Petrikaite, V. Exploration of benzenesulfonamide-bearing imidazole derivatives activity in triple-negative breast cancer and melanoma 2D and 3D cell cultures. *Pharmaceuticals* **2021**, *14*, 1158. [CrossRef]
19. Strzyga-Lach, P.; Chrzanowska, A.; Podsadni, K.; Bielenica, A. Investigation of the mechanisms of cytotoxic activity of 1,3-disubstituted thiourea derivatives. *Pharmaceuticals* **2021**, *14*, 1097. [CrossRef]
20. Kurniawan, Y.S.; Priyanga, K.T.A.; Jumina; Pranowo, H.D.; Sholikhah, E.N.; Zulkarnain, A.K.; Fatimi, H.A.; Julianus, J. An update on the anticancer activity of xanthone derivatives: A review. *Pharmaceuticals* **2021**, *14*, 1144. [CrossRef]
21. Reis-Mendes, A.; Dores-Sousa, J.L.; Padrao, A.I.; Duarte-Araujo, M.; Duarte, J.A.; Seabra, V.; Goncalves-Monteiro, S.; Remiao, F.; Carvalho, F.; Sousa, E.; et al. Inflammation as a possible trigger for mitoxantrone-induced cardiotoxicity: An in vivo study in adult and infant mice. *Pharmaceuticals* **2021**, *14*, 510. [CrossRef] [PubMed]
22. Merwid-Lad, A.; Ksiadzyna, D.; Halon, A.; Szkudlarek, D.; Trocha, M.; Szandruk-Bender, M.; Matuszewska, A.; Nowak, B.; Sozanski, T.; Kuzniar, A.; et al. Morin-5'-sulfonic acid sodium salt (namsa) attenuates cyclophosphamide-induced histological changes in genitourinary tract in rats-short report. *Pharmaceuticals* **2021**, *14*, 192. [CrossRef] [PubMed]
23. Merwid-Lad, A.; Ziolkowski, P.; Szandruk-Bender, M.; Matuszewska, A.; Szelag, A.; Trocha, M. Effect of a low dose of carvedilol on cyclophosphamide-induced urinary toxicity in rats-a comparison with mesna. *Pharmaceuticals* **2021**, *14*, 1237. [CrossRef] [PubMed]
24. Pulukuri, A.J.; Burt, A.J.; Opp, L.K.; McDowell, C.M.; Davaritouchaee, M.; Nielsen, A.E.; Mancini, R.J. Acquired drug resistance enhances imidazoquinoline efflux by P-glycoprotein. *Pharmaceuticals* **2021**, *14*, 1292. [CrossRef]





Review

# Innovations and Patent Trends in the Development of USFDA Approved Protein Kinase Inhibitors in the Last Two Decades

Mohd. Imran <sup>1,\*</sup>, Syed Mohammed Basheeruddin Asdaq <sup>2,\*</sup>, Shah Alam Khan <sup>3</sup>,  
Dhanalekshmi Unnikrishnan Meenakshi <sup>3</sup>, Abdulhakeem S. Alamri <sup>4,5</sup>, Walaa F. Alsanie <sup>4,5</sup>,  
Majid Alhomrani <sup>4,5</sup>, Yahya Mohzari <sup>6</sup>, Ahmed Alrashed <sup>7</sup>, Mohammed AlMotairi <sup>8</sup>, Eman H. Alkhalidi <sup>9</sup>,  
Abeer K. Alorabi <sup>10</sup>, Ahmed Subeh Alshrari <sup>11</sup>, Mohammad Tauseef <sup>12</sup>, Abida <sup>1</sup>, Saleh I. Alaql <sup>1</sup>, Ozair Alam <sup>13</sup>  
and Md. Afroz Bakht <sup>14</sup>

- <sup>1</sup> Department of Pharmaceutical Chemistry, Faculty of Pharmacy, Northern Border University, Arar 91911, Saudi Arabia; aqua\_abkhan@yahoo.com (A.); saleh\_alagel@hotmail.com (S.I.A.)
  - <sup>2</sup> Department of Pharmacy Practice, College of Pharmacy, AlMaarefa University, Dariyah, Riyadh 13713, Saudi Arabia
  - <sup>3</sup> College of Pharmacy, National University of Science and Technology, Muscat 130, Oman; shahalam@nu.edu.om (S.A.K.); dhanalekshmi@nu.edu.om (D.U.M.)
  - <sup>4</sup> Department of Clinical Laboratory Sciences, The Faculty of Applied Medical Sciences, Taif University, Taif 21944, Saudi Arabia; a.alamri@tu.edu.sa (A.S.A.); w.alsanie@tu.edu.sa (W.F.A.); m.alhomrani@tu.edu.sa (M.A.)
  - <sup>5</sup> Centre of Biomedical Sciences Research (CBSR), Deanship of Scientific Research, Taif University, Taif 21944, Saudi Arabia
  - <sup>6</sup> Clinical Pharmacy Department, King Saud Medical City, Riyadh 12746, Saudi Arabia; Yali2016@hotmail.com
  - <sup>7</sup> Pharmaceutical Services Administration, Inpatient Department, Main Hospital, King Fahad Medical City, Riyadh 11564, Saudi Arabia; emadasdaq@gmail.com
  - <sup>8</sup> Department of Clinical Pharmacy, King Fahad Medical City, Riyadh 11564, Saudi Arabia; mhospital1920@gmail.com
  - <sup>9</sup> Pharmaceutical Care Services, King Saud Medical City, Riyadh 12746, Saudi Arabia; emanalka62@gmail.com
  - <sup>10</sup> Pharmaceutical Care Services, King Salman Specialist Hospital, Hail 55471, Saudi Arabia; Akalorabi@moh.gov.sa
  - <sup>11</sup> Department of Biological Sciences, Faculty of Science, Northern Border University, Arar 91431, Saudi Arabia; alshrari@live.com
  - <sup>12</sup> Department of Pharmaceutical Sciences, College of Pharmacy, Chicago States University, Chicago, IL 60607, USA; mtauseef@csu.edu
  - <sup>13</sup> Medicinal Chemistry and Molecular Modelling Lab., Department of Pharmaceutical Chemistry, School of Pharmaceutical Education and Research, Jamia Hamdard, New Delhi 110062, India; dr.ozairalam@gmail.com
  - <sup>14</sup> Department of Chemistry, College of Science and Humanities, Prince Sattam Bin Abdulaziz University, Al-Kharj 11942, Saudi Arabia; bakhtpharm@gmail.com
- \* Correspondence: imran.pchem@gmail.com (M.I.); sasdaq@gmail.com or sasdaq@mcst.edu.sa (S.M.B.A.); Tel.: +966-599577945 (M.I.); +966-1-403555-3399 (S.M.B.A.)

**Citation:** Imran, M.; Asdaq, S.M.B.; Khan, S.A.; Unnikrishnan Meenakshi, D.; Alamri, A.S.; Alsanie, W.F.; Alhomrani, M.; Mohzari, Y.; Alrashed, A.; AlMotairi, M.; et al. Innovations and Patent Trends in the Development of USFDA Approved Protein Kinase Inhibitors in the Last Two Decades. *Pharmaceuticals* **2021**, *14*, 710. <https://doi.org/10.3390/ph14080710>

Academic Editors: Mary J. Meegan and Niamh M O'Boyle

Received: 17 June 2021

Accepted: 19 July 2021

Published: 22 July 2021

**Publisher's Note:** MDPI stays neutral with regard to jurisdictional claims in published maps and institutional affiliations.



**Copyright:** © 2021 by the authors. Licensee MDPI, Basel, Switzerland. This article is an open access article distributed under the terms and conditions of the Creative Commons Attribution (CC BY) license (<https://creativecommons.org/licenses/by/4.0/>).

**Abstract:** Protein kinase inhibitors (PKIs) are important therapeutic agents. As of 31 May 2021, the United States Food and Drug Administration (USFDA) has approved 70 PKIs. Most of the PKIs are employed to treat cancer and inflammatory diseases. Imatinib was the first PKI approved by USFDA in 2001. This review summarizes the compound patents and the essential polymorph patents of the PKIs approved by the USFDA from 2001 to 31 May 2021. The dates on the generic drug availability of the PKIs in the USA market have also been forecasted. It is expected that 19 and 48 PKIs will be genericized by 2025 and 2030, respectively, due to their compound patent expiry. This may reduce the financial toxicity associated with the existing PKIs. There are nearly 535 reported PKs. However, the USFDA approved PKIs target only about 10–15% of the total said PKs. As a result, there are still a large number of unexplored PKs. As the field advances during the next 20 years, one can anticipate that PKIs with many scaffolds, chemotypes, and pharmacophores will be developed.

**Keywords:** protein kinase inhibitors; USFDA; cancer; inflammation; patent review; generic product

## 1. Introduction

Protein kinases (PKs) are ubiquitous intracellular and cell surface enzymatic proteins that selectively catalyze phosphate group's relocation from ATP, GTP, and other phosphate donors to protein substrates [1]. The PKs mainly catalyze the relocation of a  $\gamma$ -phosphatase group of ATP to the oxygen atom of the -OH group of threonine, serine, and tyrosine residues in peptides/polypeptides, thereby making a conformational variation from an inactive to an active form [1,2]. They constitute an extensive family of structurally related enzymes that are known to be implicated in almost all the signal transduction activities, frequently with cascades of phosphorylation proceedings taking place within the cell [3]. The signal transduction involves the reversible phosphorylation of proteins that helps to regulate mature proteins by altering their structure and function [4,5]. To date, nearly 535 human PKs have been identified [6], wherein more than 478 belong to a superfamily whose catalytic domains are sequentially interrelated. These PKs are additionally categorized into groups, families, and subfamilies established on their biochemical activities. The main two classifications are Serine/threonine PKs and Tyrosine-specific PKs [5]. The seven significant groups with the description of families, subfamilies, and functions are listed in Table 1.

TKs form a distinct group, which phosphorylates proteins on tyrosine, whereas others phosphorylate serine and threonine residues. In addition to this category, there are atypical kinases, which are not related to any sequence resemblance to characteristic kinases but are well recognized for their enzymatic activity similar to specific kinases. Some kinases are believed to lack the catalytic domain for effective phosphorylation and are called pseudokinases. Still, they are distributed across all kinase families, indicating that an absence of catalysis is not a formal barricade to the evolution of unique or irreplaceable biological functions [7].

**Table 1.** Families and subfamilies of PKs.

S. No.	Kinase	Families	Subfamilies	Functions
Serine/Threonine-Specific Protein Kinases				
1	AGC	PKA, PKG, PKC, DMPK, NDR, AKT, SGK, RSK, PKN, GRK, PDK1, RSKR, RSKL, MAST	DMPK: GEK, ROCK, CRK PKC: Alpha, Delta, Gamma, Epsilon RSK: MSK, P70 RSKL: RSKL1, RSKL2 MAST: MAST1, MAST 2, MAST3, MAST4, MASTL	They are implicated in various cellular activities and are prospective targets to treat cancer, inflammation, viral infections, obesity, diabetes, and neurological disorders [8]
2	CAMK	Calcium/calmodulin-dependent protein kinase-CAMK1, Unique VACAMKL, PSK, DAPK, MLCK, TRIO, CASK, CAMK2, PHK, DCAMKL, MAPKAPK, CAMKL, TSK, PIM, TRB1, Unique STK33, PKD, RAD53	MAPKAPK: MNK, MAPKAPK1, MAPKAPK2, MAPKAPK3, JNK CAMKL: AMPK, BRSK, MELK, MARK, QIK, NUA, NIMI, SNRK, PASK, CHK1, LKB1, HUNK	They are implicated in the phosphorylation of transcription factors and the control of gene expression. They also control the life cycle of the cell [9]
3	CK1	Casein kinase 1, TTBK, VRK	-	They are involved in the phosphorylation of significant governing molecules in cellular translation/transcription, cell-cell adhesion, and receptor coupled signal transduction. They control main signaling trails, particularly in cancer evolution [10]

Table 1. Cont.

S. No.	Kinase	Families	Subfamilies	Functions
4	CMGC	CDK, MAPK, GSK3, CLK families, CDKL, CLK, RCK, DYRK	-	Critical role in cell cycle regulation and intracellular signal transduction [11]
5	STE	Homologs of yeast Sterile 7/MAP3K, Sterile 11/MAP2K, Sterile 20/MAP4K	MAP4K: FRAY, STLK, PAKA, PAKB, MST, YSK, TAO, MSN, NINAC, KHS, SLK	Crucial role in MAP kinase pathways, which require a sequential PK reaction to activate the next kinase in the pathway, especially in cascade process [12]
Tyrosine-Specific Protein Kinases				
6	TK	Tyrosine kinase	Receptor Tyrosine Kinases (RTKs): EGFR, EPH, SEV, ALK, TRK, INSR, CCK4, AXL, VEGFR, FGFR, MUSK, LMR, DDR, ROR, TIE, SEF, PDGFR, RET, MET, RYK	They play a vital role in controlling cellular differentiation, cell division, and morphogenesis. They primarily act as growth factor receptors and in downstream signaling [13]
			Non-Receptor Tyrosine Kinases (nRTKs): CSK, JAK, SRC (SFKs, BCR), BTK, ACK, SYK, FER, TEC, ABL, FAK	They are involved in signaling cascades, particularly those implicated in growth hormone and cytokine signaling. Some of them are involved in synaptic transmission, myelination, axon guidance, and oligodendrocyte formation [13]
7	TKL	Tyrosine kinase-like	IRAK, MLKL, LIMK, TESK, LRRK, ALK, ACTR, TGFR, MISR, BMPR, RAF, KSR, TAK, ILK, DLK, LZK, MLK, ZAK, RIPK, ANKRP, SGK, RIPK	They control apoptosis, cell differentiation/growth, angiogenesis, vascular development, and the protective response against pathogens [5,14]

PKs perform a significant function in signal transduction and control of most cellular processes, including cell growth, differentiation, proliferation, angiogenesis, apoptosis, cytoskeletal arrangement, regulation of metabolic reactions, membrane transport, and motility, etc. [6]. Non-catalytic functions of PKs are also essential and include the allosteric effect, subcellular targeting, the scaffolding of protein complexes, competition for protein interactions, and DNA binding [15]. Because PKs regulate most fundamental biological processes, any dysregulation, genetic alteration, and abrupt change in kinase function are typically linked with pathological conditions such as cancer, immunologic, neurological, cardiovascular, and metabolic disorders [3,5]. Hence, manipulation of PKs signaling pathway, regulation, and inhibition constitutes important clinical targets for pharmacological intervention and thus for the identification and development of Protein Kinase Inhibitors (PKIs) to manage and treat several chronic diseases [4,6,16]. Over the past two decades, approximately 1/5th-1/3rd drug discovery programs worldwide have targeted PKs for the drug development of various illnesses.

Kinase mutation frequency is much less, and thus targeting kinases could be helpful in life-saving therapies especially for cancer. A well-known example is receptor tyrosine kinase ALK where gene fusion between EML4 and ALK occurs only in 5% of NSCLC patients and therefore many patients responded to the kinome therapy effectively. Identification of additional effective kinome targets will therefore represent an Achilles heel in a subset of cancer. The use of bioinformatics tools in predicting the likelihood that a given mutation will alter the function of a kinase will be essential in pinpointing cancer-associated kinases [17].

There are about 175 kinase drugs under clinical trials and newer targets are also under evaluation including AKT, Aurora kinases, CHEK1, and CDK1. However, most of the drugs

under investigation are well known for targeting EGFR, VEGFR, PI3K, and mTOR [18]. Even though CAMK, CK1, or AGC kinases groups are well-known and evidenced as the primary targets for cancer, there are no investigational drugs that target these kinases are enrolled. So far only 8% of the entire kinome has been effectively “drugged” and a quarter of human kinases are vastly understudied [19]. A wide-ranging scoring system to rank and prioritize clinically relevant kinase targets of different solid tumor cancers from The Cancer Genome Atlas (TCGA) has been developed [19].

Successful applications and deep insights into the ever-diversifying therapeutic space occupied by kinase targets are also explored. For effective target validation and to avoid complicating off-target mediated response it is essential to achieve the desired selectivity while targeting kinases, though it is still an ongoing challenge. The application of large-scale omics data has been modernized to combine multiple parameters to evaluate the protein’s potential as a drug target or biomarker [19].

In recent years, intricately selective kinase chemical probes have been generated by the exploitation of unique pockets using molecular modeling and bioinformatics, prioritizing the ligand-efficient leads and novel chemotypes and the extensive use of kinome-wide profiling [20].

Chemical proteomics and broad kinome profiling of compound libraries have been implemented as an efficient method to lead to discovery, analyzing targets, and optimization [21]. Results revealed that unknown targets for established drugs presented a viewpoint on the “druggable” kinome, emphasized non-kinase off-targets, and recommended for potential therapeutic applications. A database of the cellular targets of 243 clinical kinase inhibitors has been made available using kinobead technology [21].

The ongoing research will undoubtedly pave the way for a better understanding of molecular pathways that will further unravel the role of PKs in pathogenesis. As of now, the majority of the USFDA-approved PKIs are Protein Tyrosine Kinase inhibitors (PTKIs) followed by protein-serine/threonine PKIs. Most of these drugs are clinically used to treat solid (breast, lung, colon) and non-solid tumors (leukemia). Some PKIs are also effective in treating non-malignant diseases, including myelofibrosis, rheumatoid arthritis, glaucoma, ulcerative colitis, pulmonary fibrosis, etc. [22,23].

## 2. USFDA Approved Protein Kinase Inhibitors

In 2001, the USFDA approved the marketing of the first clinical PKI, imatinib. Since then, the USFDA has approved about 70 PKIs for clinical use (Table 2) (Figure 1). The data provided in Table 2 have been obtained from USFDA’s Orange Book website (<https://www.accessdata.fda.gov/scripts/cder/ob/index.cfm?resetfields=1> (accessed on 31 May 2021) using the drug’s name.

**Table 2.** The Orange Book data of the USFDA approved PKIs.

Marketed Active Ingredient (Proprietary Name, Applicant)	Approved Dosage Form (Strength)	Approval Date (Marketing Status)	Primary Target #	Approved Indication
Imatinib mesylate (Gleevec, Novartis Pharmaceuticals)	Tablet (100 and 400 mg of imatinib free base)	18 April 2003 (Prescription)	BCR-Ab1	Many cancer types, including CML, Ph <sup>+</sup> -ALL, CEL, and GISTs
	Capsule (50 and 100 mg of imatinib free base)	10 May 2001 (Discontinued)		
Gefitinib (Iressa, AstraZeneca Pharmaceuticals)	Tablet (250 mg)	13 July 2015 (Prescription)	EGFR	NSCLC
	Tablet (250 mg)	5 May 2003 (Discontinued)		
Erlotinib hydrochloride (Tarceva, OSI Pharmaceuticals)	Tablet (25, 100, and 150 mg of erlotinib free base)	18 November 2004 (Prescription)	EGFR	Metastatic NSCLC and pancreatic cancer
Sorafenib tosylate (Nexavar, Bayer Healthcare Pharmaceuticals)	Tablet (200 mg of sorafenib free base)	20 December 2005 (Prescription)	VEGFR/BRAF	HCC, RCC, and DTC
Sunitinib malate (Sutent, CP Pharmaceuticals International)	Capsule (12.5, 25, 37.5, and 50 mg of sunitinib free base)	26 January 2006 (Prescription, 12.5, 25, and 50 mg) 31 March 2009 (Prescription, 37.5 mg)	VEGFR/PDGFR	GIST, RCC, and pNET
Dasatinib (Sprycel, Bristol Myers Squibb)	Tablet (20, 50, 70, 80, 100, and 140 mg)	28 June 2006 (Prescription)	BCR-Ab1/ABL2	Ph <sup>+</sup> -CML
Lapatinib ditosylate (Tykerb, Novartis Pharmaceuticals)	Tablet (250 mg of lapatinib free base)	13 March 2007 (Prescription)	HER-1/HER-2/EGFR	Breast cancer
Temsirolimus (Torisel, PF Prism CV)	IV Solution (25 mg/mL)	30 May 2007 (Prescription)	FKBP12/mTOR	ARCC



Table 2. Cont.

Marketed Active Ingredient (Proprietary Name, Applicant)	Approved Dosage Form (Strength)	Approval Date (Marketing Status)	Primary Target #	Approved Indication
Everolimus (Afinitor, Zortress, AfinitorDisperz, Novartis Pharmaceutical)	Tablet (2.5 mg, 5 mg, 7.5 mg, and 10 mg)	30 March 2009 (5 mg and 10 mg) 9 July 2010 (2.5 mg) 30 March 2012 (5 mg) (All are prescription products)	FKBP12/mTOR	pNET and RCC
	Tablet (0.25 mg, 0.5 mg, 0.75 mg, and 1 mg)	20 April 2010 (0.25, 0.5, and 0.75 mg) 10 August 2018 (1 mg) (All are prescription products)		
	Tablet for suspension (2 mg, 3 mg, and 5 mg)	29 August 2012 (Prescription)		
Nilotinib hydrochloride (Tasigna, Novartis Pharmaceuticals)	Capsule (50, 150, and 200 mg of nilotinib base)	29 October 2007 (200 mg Tablet) 17 June 2010 (150 mg Tablet) 22 March 2018 (50 mg Tablet) (All are prescription products)	BCR-Abl	Ph <sup>+</sup> -CML
Pazopanib hydrochloride (Votrient, Novartis Pharmaceuticals)	Tablet (200, and 400 mg of pazopanib base)	19 October 2009 (200 mg tablet, Prescription) (400 mg tablet has been discontinued)	VEGFR/PDGFR	RCC and STS
	Tablet (100 mg and 300 mg)	6 April 2011 (Prescription)		
Vemurafenib (Zelboraf, Hoffmann La Roche)	Tablet (240 mg)	17 August 2011 (Prescription)	B-Raf	Melanoma with BRAF V600E mutation
	Capsule (200 mg and 250 mg)	26 August 2011 (Prescription)		
Ruxolitinib phosphate (Jakafi, Incyte Corp)	Tablet (5 mg, 10 mg, 15 mg, 20 mg, and 25 mg of ruxolitinib free base)	16 November 2011 (Prescription)	JAK1/2/3 and Tyk2	Myelofibrosis and polycythemia vera
Axitinib (Inlyta, PF Prism CV)	Tablet (1 mg and 5 mg)	27 January 2012 (Prescription)	VEGFR/PDGFR	RCC

Table 2. Cont.

Marketed Active Ingredient (Proprietary Name, Applicant)	Approved Dosage Form (Strength)	Approval Date (Marketing Status)	Primary Target #	Approved Indication
Bosutinib monohydrate (Bosulif, PF Prism CV)	Tablet (100 mg, 400 mg, and 500 mg of bosutinib free base)	4 September 2012 (100 and 500 mg) 27 October 2017 (400 mg) (All are prescription products)	BCR-Abi	Ph <sup>+</sup> -CML
Regorafenib (Shivarga, Bayer Healthcare Pharmaceuticals)	Tablet (40 mg)  Solution (1 mg/mL of tofacitinib free base)	27 September 2012 (Prescription)  25 September 2020 (Prescription)	VEGFR/TIE	Colorectal cancer, GIST, HCC, RCC and STS
Tofacitinib citrate (Xeljanz, Pfizer)	Tablet (5 mg and 10 mg of tofacitinib free base)  Extended-release tablet (11 mg and 22 mg of tofacitinib free base)	6 November 2012 (5 mg) 30 May 2018 (10 mg) (All are prescription products)  23 February 2016 (11 mg) 12 December 2019 (22 mg) (All are prescription products)	JAK1/2/3 and Tyk2	Rheumatoid arthritis, psoriatic arthritis, ulcerative colitis, and juvenile idiopathic arthritis
Cabozantinib S-malate (Cometriq and Cabometyx, Exelixis)	Capsule (20 mg and 80 mg of cabozantinib free base)  Tablet (20 mg, 40 mg and 80 mg of cabozantinib free base)	29 November 2012 (Prescription)  25 April 2016 (Prescription)	RET	MTC, RCC, and HCC
Ponatinib hydrochloride (Iclusig, Ariad Pharmaceuticals)	Tablet (10 mg, 15 mg, 30 mg, and 45 mg of ponatinib free base)	18 December 2020 (10 mg) 14 December 2012 (15 mg and 45 mg) 23 April 2015 (30 mg) (All are prescription products)	BCR-Abi	CML, Ph <sup>+</sup> -ALL, T315I-positive CML or Ph <sup>+</sup> -ALL
Trametinib dimethyl sulfoxide (Mekinist, Novartis Pharmaceuticals)	Tablet (0.5 mg, 1 mg and 2 mg)	29 May 2013 (Prescription) (The 1 mg tablet has been discontinued)	MEK1/2	Metastatic melanoma, NSCLC, and ATC

Table 2. Cont.

Marketed Active Ingredient (Proprietary Name, Applicant)	Approved Dosage Form (Strength)	Approval Date (Marketing Status)	Primary Target #	Approved Indication
Dabrafenib mesylate (Tafinlar, Novartis Pharmaceuticals)	Capsule (50 mg and 75 mg of dabrafenib free base)	29 May 2013 (Prescription)	B-Raf	Metastatic melanoma, NSCLC, and ATC
Afatinib dimaleate (Gilotrif, Boehringer Ingelheim)	Tablet (20 mg, 30 mg, and 40 mg of afatinib free base)	12 July 2013 (Prescription)	EGFR/HER2/HER4	NSCLC
Ibrutinib (Imbruvica, Pharmacyclics)	Capsule (70 mg and 140 mg)  Tablet (140 mg, 280 mg, 420 mg, and 560 mg)	13 November 2013 (140 mg) 20 December 2017 (70 mg)  16 February 2018	BTK	MCL, CLL, SLL, and MZL
Ceritinib (Zykadia, Novartis Pharmaceuticals)	Tablet (150 mg)  Capsule (150 mg)	18 March 2019 (Prescription)  29 April 2014 (Discontinued)	ALK	NSCLC
Idelalisib (Zydelig, Gilead Sciences)	Tablet (100 mg and 150 mg)	23 July 2014 (Prescription)	PI3K $\delta$	CLL, FL, and SLL
Nintedanib esylate (Ofev, Boehringer Ingelheim Pharmaceuticals)	Capsule (100 mg and 150 mg of nintedanib free base)	15 October 2014 (Prescription)	PDGFR/FGFR/VEGFR	IPF, ILDs, and SSC-ILD
Palbociclib (Ibrance, Pfizer)	Capsule (75 mg, 100 mg, and 125 mg)  Tablet (75 mg, 100 mg, and 125 mg)	3 February 2015 (Prescription)  1 November 2019 (Prescription)	CDK4/6	Breast cancer
Lenvatinib mesylate (Lenvima, Eisai)	Capsule (4 mg and 10 mg of lenvatinib free base)	13 February 2015 (Prescription)	VEGFR/RET	Thyroid cancer, RCC, HCC, and endometrial carcinoma
Cobimetinib fumarate (Cotellic, Genentech)	Tablet (20 mg of cobimetinib free base)	10 November 2015 (Prescription)	MEK1/2	Melanoma
Osimertinib mesylate (Tagrisso, AstraZeneca Pharmaceuticals)	Tablet (40 mg and 80 mg of osimertinib free base)	13 November 2015 (Prescription)	EGFR	NSCLC

Table 2. Cont.

Marketed Active Ingredient (Proprietary Name, Applicant)	Approved Dosage Form (Strength)	Approval Date (Marketing Status)	Primary Target #	Approved Indication
Alectinib hydrochloride (Alecensa, Hoffmann-La Roche)	Capsule (150 mg of alectinib free base)	11 December 2015 (Prescription)	ALK/RET	NSCLC
Ribociclib succinate (Kisqali, Novartis Pharmaceuticals)	Tablet (200 mg of ribociclib free base)	13 March 2017 (Prescription)	CDK4/6	Breast cancer
Brigatinib (Alunbrig, Ariad Pharmaceuticals)	Tablet (30 mg, 90 mg, and 180 mg)	28 April 2017 (30 mg, and 90 mg) 2 October 2017 (180 mg) (All are prescription products)	ALK	NSCLC
Midostaurin (Rydapt, Novartis Pharmaceuticals)	Capsule (25 mg)	28 April 2017 (Prescription)	FLT3	AML, MCL, and systemic mastocytosis
Neratinib maleate (Nerlynx, Puma Biotechnology)	Tablet (40 mg of neratinib free base)	17 July 2017 (Prescription)	EGFR/HER2	Breast cancer
Copanlisib dihydrochloride (Alicopa, Bayer Healthcare Pharmaceuticals)	Powder (60 mg/vial)	14 September 2017 (Prescription)	PI3K- $\alpha$ / $\beta$ / $\delta$	FL and Non-Hodgkin Lymphoma
Abemaciclib (Verzenio, Eli Lilly)	Tablet (50 mg, 100 mg, 150 mg, and 200 mg)	28 September 2017 (Prescription)	CDK4/6	Breast cancer
Acalabrutinib (Calquence, AstraZeneca)	Capsule (100 mg)	31 October 2017 (Prescription)	BTK	MCL, CLL, SLL, and urothelial carcinoma
Netarsudil mesylate (Rhopressa, Aerie Pharmaceuticals)	Solution/Drops (0.02% of netarsudil free base)	18 December 2017 (Prescription)	ROCK1/2	Open-angle glaucoma or ocular hypertension
Baricitinib (Olumiant, Eli Lilly)	Tablet (1 mg and 2 mg)	8 October 2019 (1 mg) 31 May 2018 (2 mg) (All are prescription products)	JAK1/2/3 and Tyk	Rheumatoid arthritis
Binimetinib (Mektovi, Array Biopharma)	Tablet (15 mg)	27 June 2018 (Prescription)	MEK1/2	Melanoma with a BRAF V600 mutation
Dacomitinib (Vizimpro, Pfizer)	Tablet (15 mg, 30 mg, and 45 mg)	27 September 2018 (Prescription)	EGFR/HER1	NSCLC
Encorafenib (Braftovi, Array Biopharma)	Capsule (50 mg, and 75 mg)	27 June 2018 (Prescription) (50 mg capsules have been discontinued)	B-Raf	Melanoma

Table 2. Cont.

Marketed Active Ingredient (Proprietary Name, Applicant)	Approved Dosage Form (Strength)	Approval Date (Marketing Status)	Primary Target #	Approved Indication
Fostamatinib disodium (Tubeless, Rigel Pharmaceuticals)	Tablet (100 mg, and 150 mg of fostamatinib free base)	17 April 2018 (Prescription)	Syk	ITP
Duvelisib (Copiktra, Secura Bio)	Capsule (15 mg, and 25 mg)	24 September 2018 (Prescription)	PI3K- $\delta$ /PI3K- $\gamma$	CLL, SLL, FL, and hematological malignancies
Gilteritinib fumarate (Xospata, Astellas Pharma)	Tablet (40 mg of gilteritinib free base)	28 November 2018 (Prescription)	FLT3	AML
Larotrectinib sulfate (Vitrakvi, Bayer Healthcare Pharmaceuticals)	Capsule (25 mg, and 100 mg of larotrectinib free base) Solution (20 mg of larotrectinib free base per ml)	26 November 2018 (Prescription)	TRK	Solid tumors
Lorlatinib (Lorbrena, Pfizer)	Tablet (25 mg, and 100 mg)	2 November 2018 (Prescription)	ALK	NSCLC
Entrectinib (Rozlytrek, Genentech)	Capsule (100 mg and 200 mg)	15 August 2019 (Prescription)	TRK-A, TRK-B, and TRK-C	NSCLC and solid tumors
Upadacitinib (Rinvoq, Abbvie)	Extended-release tablet (15 mg)	16 August 2019 (Prescription)	JAK	Rheumatoid arthritis
Alpelisib (Piqray, Novartis Pharmaceuticals)	Tablet (50 mg, 100 mg, and 200 mg)	24 May 2019 (Prescription)	PI3K	Breast cancer
Erdafitinib (Balversa, Janssen Biotech)	Tablet (3 mg, 4 mg, and 5 mg)	12 April 2019 (Prescription)	FGFR1/2/3/4	Metastatic urothelial carcinoma (mUC)
Pexidartinib hydrochloride (Turalio, Daiichi Sankyo)	Capsule (200 mg of pexidartinib free base)	2 August 2019 (Prescription)	CSF1R/KIT/FLT3	TGCT
Fedratinib hydrochloride (Inrebic, Impact Biomedicines)	Capsule (100 mg of fedratinib free base)	16 August 2019 (Prescription)	JAK2	Myelofibrosis
Zanubrutinib (Brukinsa, Beigene)	Capsule (80 mg)	14 November 2019 (Prescription)	BTK	MCL, CLL, WM, and SLL
Avapritinib (Ayyakit, Blueprint Medicines)	Tablet (100 mg, 200 mg, and 300 mg)	9 January 2020 (Prescription)	PDGFRA/KIT	GIST
Selumetinib sulfate (Koselugo, AstraZeneca Pharmaceuticals)	Capsule (10 mg and 25 mg of selumetinib free base)	10 April 2020 (Prescription)	MAPK/MEK 1,2	Neurofibromatosis type 1 (NF1)

Table 2. Cont.

Marketed Active Ingredient (Proprietary Name, Applicant)	Approved Dosage Form (Strength)	Approval Date (Marketing Status)	Primary Target #	Approved Indication
Pemigatinib (Pemazyre, Incyte)	Tablet (4.5 mg, 9 mg, and 135 mg)	17 April 2020 (Prescription)	FGFR1-3	Cholangiocarcinoma
Tucatinib (Tukysa, Seagen)	Tablet (50 mg and 150 mg)	17 April 2020 (Prescription)	HER2	Breast cancer
Capmatinib hydrochloride (Tabrecta, Novartis Pharmaceutical)	Tablet (150 mg and 200 mg of capmatinib free base)	6 May 2020 (Prescription)	MET	NSCLC
Selpercatinib (Retevmo, Loxo Oncology)	Capsule (40 mg and 80 mg)	8 May 2020 (Prescription)	RET/VEGFR	NSCLC, and MTC
Ripretinib (Qinlock, Deciphera Pharmaceuticals)	Tablet (50 mg)	15 May 2020 (Prescription)	PDGFRA/KIT	GIST
Pralsetinib (Gavreto, Blueprint Medicines)	Capsule (100 mg)	4 September 2020 (Prescription)	RET	NSCLC, and MTC
Trilaciclib dihydrochloride (Cosela; GI Therapeutics Inc.,)	Powder for IV injection (300 mg of Trilaciclib free base per vial)	12 February 2021 (Prescription)	CDK4	ES-SCLC
Tepotinib hydrochloride monohydrate (Tepmetko; EMD Serono Inc.,)	Tablet (225 mg of Tepotinib free base)	3 February 2021 (Prescription)	MET	NSCLC
Umbralisib tosylate (Ukoniq; TG Therapeutics)	Tablet (200 mg of Umbralisib free base)	5 February 2021 (Prescription)	PI3K $\delta$ and CK1 $\epsilon$	MZL, and FL
Tivozanib hydrochloride monohydrate (Fotivda; Aveo Pharmaceuticals)	Capsule (0.89 mg and 1.34 mg of tivozanib free base)	10 March 2021 (Prescription)	VEGFR/PDGFR	RCC
Infigratinib (Truseltiq; QED Therapeutics)	Capsule (25 and 100 mg)	28 May 2021 (Prescription)	FGFR	Cholangiocarcinoma

# Some drugs are multikinase inhibitors.

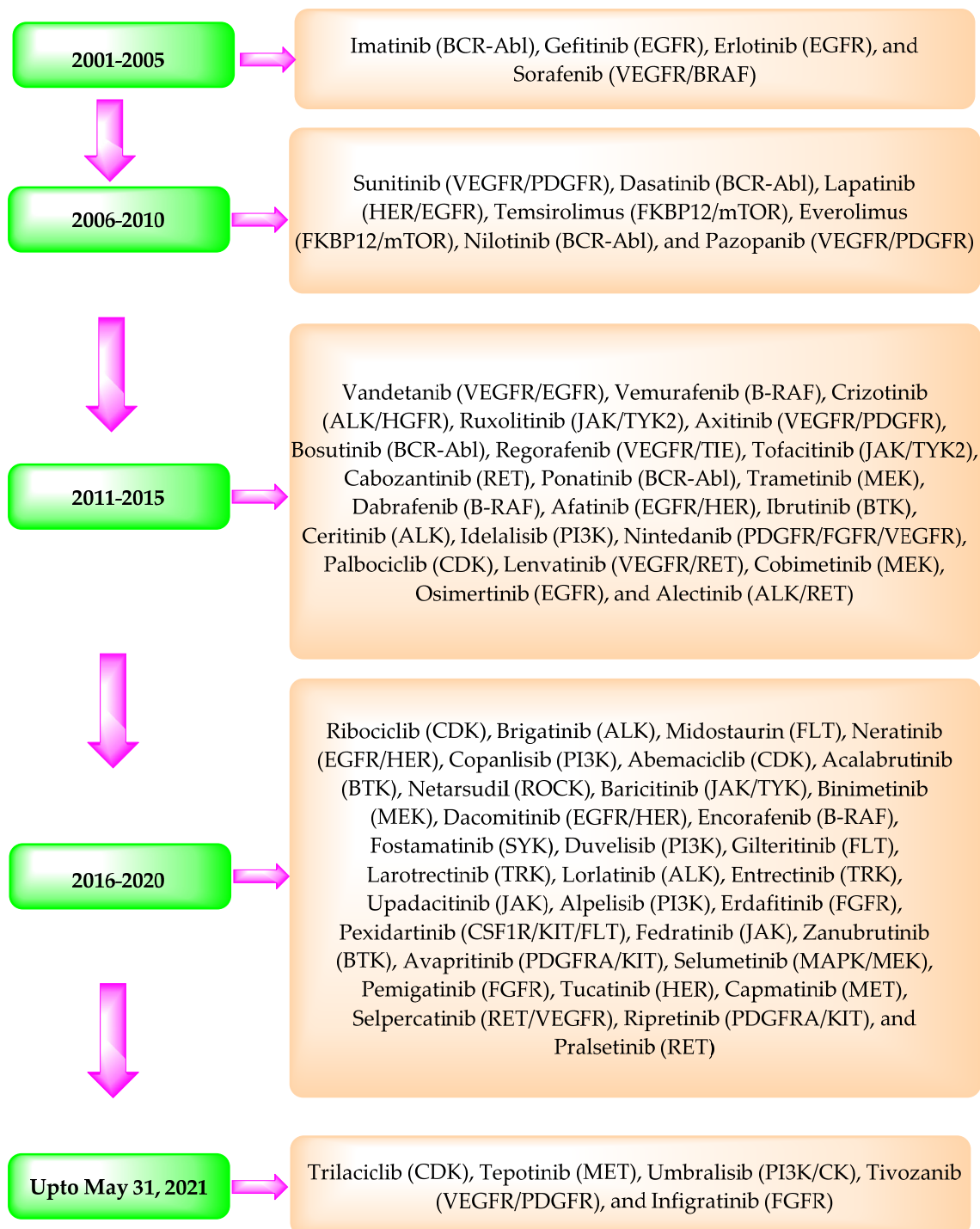


Figure 1. Timeline depicting the approval of the PKIs by the USFDA and their primary targets in brackets.

### 3. Patent Searching

The patent searching was performed using the Sci-finder database (CAS Number search, and the exact structure search of each TKI), USFDA’s Orange Book website (mentioned above), and the Drugbank’s website (<https://go.drugbank.com/> (accessed on 31 May 2021)) using the drug’s name. The patents disclosing the specific TKI, its marketed active pharmaceutical ingredient, and important polymorphs from the innovative com-

pany for the first time were identified and included in this review. The patents of each TKI that claim its treatment methods, dosage forms, formulations, drug combinations, particle size, impurity, preparation process, intermediates, etc., have been excluded from this review. The expiry dates of the selected patents were calculated (20 years from the patent application filing date comprising patent term extension, if any). Sometimes, the drug's patent term is extended up to five years based on the USPTO's laws. Accordingly, the expiry dates of the selected patents were also verified from the USPTO's website. It was also observed that some TKIs were disclosed in different patents of the same patent family and had other expiry dates. In such cases, the patent that had a more extended expiry date was selected for this review because the generic launch of the drug is based on the expiry date of the drug's patent. The legal status of the patents cited herein was obtained from the website of USPTO (<https://portal.uspto.gov/pair/PublicPair> (accessed on 31 May 2021)).

#### 4. Summary of the Patents

The proprietary name, approved dosage form, approval date, and marketing status of each marketed PKIs are mentioned in Table 2. The patent number, applicant/assignee, expiry date, and legal status of the cited patents of each PKI are provided in Table 3. A brief description of the PKIs and their important patents are provided below.

**Table 3.** Patent number, applicant/assignee, expiry date, and legal status of the cited patents.

S. No.	Drug's Name	Patent Number	Applicant/Assignee	Expiry Date	Legal Status	Expected Date of Generic Availability in the USA *
1	Imatinib	US5521184A	Ciba Geigy	4 July 2015	Expired	Generic is available
		USRE43932E	Novartis	16 July 2019	Expired	
2	Gefitinib	US5457105A	Zeneca	19 January 2013	Expired	July 2022 due to the Orphan Drug Exclusivity
		US5770599A	Zeneca	5 May 2017	Expired	
3	Erlotinib	USRE41065E	OSI Pharmaceuticals	8 May 2019	Expired	Generic is available
		US6900221B1	OSI Pharmaceuticals	9 May 2021	Litigation	
4	Sorafenib	US7235576B1	Bayer Pharmaceuticals	12 January 2020	Expired	Generic is available
		US8877933B2	Bayer IP	24 December 2027	Patented	
5	Sunitinib	US7125905B2	Sugen Incorporation	15 August 2021	Patented	August 2021
		US6573293B2	Sugen Incorporation	15 August 2021	Patented	
6	Dasatinib	US6596746B1	Bristol-Myers Squibb	28 December 2020	Expired	Generic is available
		US7491725B2	Bristol-Myers Squibb	28 September 2026	Patented	
7	Lapatinib	US8513262B2	Glaxo Group	8 January 2019	Expired	Generic is available
		US7157466B2	Smithkline Beecham	19 November 2021	Patented	
8	Temsirolimus	USRE44768E	Wyeth	15 August 2019	Expired	Generic is available
9	Everolimus	US5665772A	Sandoz	9 March 2020	Expired	Generic is available
10	Nilotinib	US7169791B2	Novartis	4 January 2024	Patented	February 2029
		US8163904B2	Novartis	23 February 2029	Patented	
		US8415363B2	Novartis	18 January 2027	Patented	
11	Pazopanib	US7105530B2	Smithkline Beecham	19 October 2023	Patented	October 2023
		US8114885B2	Glaxosmithkline	19 December 2021	Patented	
12	Vandetanib	USRE42353E	Astrazeneca	27 June 2022	Patented	June 2022



Table 3. Cont.

S. No.	Drug's Name	Patent Number	Applicant/Assignee	Expiry Date	Legal Status	Expected Date of Generic Availability in the USA *
13	Vemurafenib	US8143271B2	Plexxikon Incorporation	21 June 2026	Patented	June 2026
14	Crizotinib	US7858643B2	Agouron Pharmaceuticals	8 October 2029	Patented	October 2029
		US8217057B2	Pfizer	6 November 2029	Patented	
15	Ruxolitinib	US7598257B2	Incyte Corporation	24 December 2027	Patented	June 2028
		US8722693B2	Incyte Corporation	12 June 2028	Patented	
16	Axitinib	US6534524B1	Agouron Pharmaceuticals	29 April 2025	Patented	April 2025
		US8791140B2	Pfizer	14 December 2030	Patented	
17	Bosutinib	USRE42376E	Wyeth	13 April 2024	Patented	April 2024
		US7767678B2	Wyeth	23 November 2026	Patented	
18	Regorafenib	US8637553B2	Bayer Healthcare	16 February 2031	Patented	July 2032
		US9957232B2	Bayer Healthcare	9 July 2032	Patented	
19	Tofacitinib	USRE41783E	Pfizer	8 December 2025	Patented	December 2025
		US6965027B2	Pfizer	25 March 2023	Patented	
20	Cabozantinib	US7579473B2	Exelixis	14 August 2026	Patented	August 2026
		US8877776B2	Exelixis	8 October 2030	Patented	
21	Ponatinib	US8114874B2	Ariad Pharmaceuticals	24 January 2027	Patented	January 2027
		US9493470B2	Ariad Pharmaceuticals	12 December 2033	Patented	
22	Trametinib	US7378423B2	Japan Tobacco	29 May 2027	Patented	May 2027
23	Dabrafenib	US7994185B2	Glaxo Smith Kline	20 January 2030	Patented	January 2030
24	Afatinib	USRE43431E	Boehringer Ingelheim	13 January 2026	Patented	January 2026
		US8426586B2	Boehringer Ingelheim	10 October 2029	Patented	
25	Ibrutinib	US8735403B2	Pharmacyclics	28 December 2026	Patented	December 2026
		US9296753B2	Pharmacyclics	30 October 2033	Patented	
26	Ceritinib	US8039479B2	IRM	29 June 2030	Patented	June 2030
		US9309229B2	Novartis	18 January 2032	Patented	
27	Idelalisib	USRE44638E	ICOS Corporation	5 August 2025	Patented	August 2025
		US9469643B2	Gilead	2 September 2033	Patented	
28	Nintedanib	US6762180B1	Boehringer Ingelheim	1 October 2025	Patented	October 2025
		US7119093B2	Boehringer Ingelheim	21 February 2024	Patented	
29	Palbociclib	USRE47739E	Warner Lambert	5 March 2027	Patented	5 March 2027
		US10723730B2	Pfizer	8 February 2034	Patented	
30	Lenvatinib	US7253286B2	Eisai	19 October 2021	Patented	October 2021
		US7612208B2	Eisai	19 September 2026	Patented	
31	Cobimetinib	US7803839B2	Exelixis	10 November 2029	Patented	November 2029
		US10590102B2	Exelixis	30 June 2036	Patented	
32	Osimertinib	US8946235B2	Astrazeneca	8 August 2032	Patented	August 2032

Table 3. Cont.

S. No.	Drug's Name	Patent Number	Applicant/Assignee	Expiry Date	Legal Status	Expected Date of Generic Availability in the USA *
33	Alectinib	US9126931B2	Chugai Pharmaceutical	29 May 2031	Patented	May 2031
34	Ribociclib	US8415355B2	Astex Therapeutics	19 February 2031	Patented	19 February 2031
		US9193732B2	Astex Therapeutics	9 November 2031	Patented	
35	Brigatinib	US9012462B2	Ariad Pharmaceuticals	31 July 2030	Patented	July 2030
		US10385078B2	Ariad Pharmaceuticals	10 November 2035	Patented	
36	Midostaurin	US5093330A	Ciba Geigy	21 July 2009	Expired	October 2024
		US7973031B2	Novartis	17 October 2024	Patented	
37	Neratinib	US7399865B2	Wyeth	29 December 2025	Patented	December 2025
38	Copanlisib	USRE46856E	Bayer	22 October 2029	Patented	March 2032
		US10383876B2	Bayer	29 March 2032	Patented	
39	Abemaciclib	US7855211B2	Eli Lilly	15 December 2029	Patented	December 2029
40	Acalabrutinib	US9290504B2	Merck	11 July 2032	Patented	July 2032
		US9796721B2	Acerta Pharma	1 July 2036	Patented	
41	Netarsudil	US8394826B2	Aerie Pharmaceuticals	10 November 2030	Patented	March 2034
		US9415043B2	Aerie Pharmaceuticals	14 March 2034	Patented	
42	Baricitinib	US8158616B2	Incyte Corporation	8 June 2030	Patented	June 2030
43	Binimetinib	US7777050B2	Array Biopharma	13 March 2023	Patented	June 2025 based on ODE
		US9562016B2	Array Biopharma	18 October 2033	Patented	
44	Dacomitinib	US7772243B2	Warner Lambert	26 August 2028	Patented	August 2028
45	Encorafenib	US8501758B2	IRM	4 March 2031	Patented	March 2031
46	Fostamatinib	US7449458B2	Rigel Pharmaceuticals	4 September 2026	Patented	4 September 2026
		US8163902B2	Rigel Pharmaceuticals	17 June 2026	Patented	
47	Duvelisib	US8193182B2	Intellikine	13 February 2030	Patented	February 2030
		USRE46621E	Infinity Pharmaceuticals	17 May 2032	Patented	
48	Gilteritinib	US8969336B2	Astellas Pharma	27 January 2031	Patented	January 2031
49	Larotrectinib	US9127013B2	Array Biopharma	21 October 2029	Patented	October 2029
		US10172861B2	Array Biopharma	16 November 2035	Patented	
50	Lorlatinib	US8680111B2	Pfizer	5 March 2033	Patented	March 2033
		US10420749B2	Pfizer	27 July 2036	Patented	
51	Entrectinib	US8299057B2	Nerviano Medical Sciences	1 March 2029	Patented	March 2029
		US10738037B2	Nerviano Medical Sciences	18 May 2037	Patented	
52	Upadacitinib	USRE47221E	Abbvie	1 December 2030	Patented	December 2030
		US9951080B2	Abbvie	17 October 2036	Patented	
53	Alpelisib	US8227462B2	Novartis	28 September 2030	Patented	September 2030
54	Erdafitinib	US8895601B2	Astex Therapeutics	22 May 2031	Patented	May 2031
55	Pexidartinib	US9169250B2	Plexxikon	21 November 2027	Patented	November 2027
		US9802932B2	Plexxikon	5 May 2036	Patented	

Table 3. Cont.

S. No.	Drug's Name	Patent Number	Applicant/Assignee	Expiry Date	Legal Status	Expected Date of Generic Availability in the USA *
56	Fedratinib	US7528143B2	Targegen	16 December 2026	Patented	December 2026
57	Zanubrutinib	US9447106B2	Beigene	22 April 2034	Patented	April 2034
58	Avapritinib	US9944651B2	Blueprint Medicines Corporation	15 October 2034	Patented	October 2034
59	Selumetinib	US7425637B2	Array Biopharma	11 April 2024	Patented	April 2027 based on ODE
		US9156795B2	Array Biopharma	12 December 2026	Patented	
60	Pemigatinib	US9611267B2	Incyte Corporation	30 January 2035	Patented	January 2035
61	Tucatinib	US8648087B2	Array Biopharma	12 April 2031	Patented	April 2031
62	Capmatinib	US7767675B2	Incyte Corporation	19 November 2027	Patented	June 2031
		US8420645B2	Incyte Corporation	5 June 2031	Patented	
63	Selpercatinib	US10112942B2	Array Biopharma	10 October 2037	Patented	October 2037
		US10584124B2	Array Biopharma	10 October 2038	Patented	
64	Ripretinib	US8461179B1	Deciphera Pharmaceuticals	7 June 2032	Patented	June 2032
65	Pralsetinib	US10030005B2	Blueprint Medicines Corporation	1 November 2036	Patented	November 2036
66	Trilaciclib	US8598186B2	G1 Therapeutics	25 October 2031	Patented	October 2031
67	Tepotinib	US8580781B2	Merck	19 March 2030	Patented	March 2030
		US8329692B2	Merck	30 October 2029	Patented	
68	Umbralisib	US10570142B2	Rhizen Pharmaceuticals	2 July 2033	Patented	July 2033
		US10414773B2	Rhizen Pharmaceuticals	26 May 2035	Patented	
69	Tivozanib	US6821987B2	Kirin Beer Kabushiki Kaisha	26 April 2022	Patented	10 March 2026, based on NCE (Patent term extension is possible)
		US7211587B2	Kirin Beer Kabushiki Kaisha	26 April 2022	Patented	
		US7166722B2	Kirin Beer Kabushiki Kaisha	21 October 2023	Patented	
70	Infigratinib	US8552002B2	Novartis	13 December 2025	Patented	25 May 2026, based on NCE (Patent term extension is possible)
		US9067896B2	Novartis	24 February 2031	Patented	

\* Based on the patent expiry date.

#### 4.1. Imatinib Mesylate

Imatinib mesylate (Figure 2) is a pyridine-pyrimidine based piperazine derivative (MF:  $C_{29}H_{31}N_7O \cdot CH_4SO_3$ ; MW: 589.7; CAS Number: 220127-57-1) [24]. **US5521184A** claims *N*-phenyl-2-pyrimidine-amine compounds, including imatinib and its pharmaceutically acceptable salts, as antitumor drugs [25]. **USRE43932E** (Re-issue of US7544799B2) claims the  $\beta$ -crystal form of imatinib mesylate as having favorable thermodynamic stability, flow properties, and low hygroscopicity that makes it a suitable active pharmaceutical ingredient (API) to be used in the tablet/capsule dosage forms [26].

#### 4.2. Gefitinib

Gefitinib (Figure 3) is a morpholine based quinazolinamine derivative (MF:  $C_{22}H_{24}ClFN_4O_3$ ; MW: 446.9; CAS Number: 184475-35-2) [27]. **US5457105A** unveils quinazoline derivatives and their salts to treat neoplastic disease. This patent claims gefitinib generically [28]. **US5770599A** also covers quinazoline derivatives as anticancer agents. This patent claims gefitinib specifically, along with its pharmaceutically acceptable acid-addition salts [29].

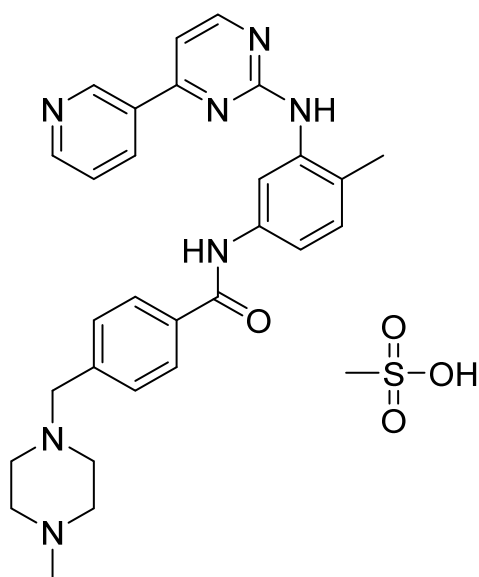


**Figure 2.** Imatinib mesylate (4-[(4-Methyl-1-piperazinyl)methyl]-N-[4-methyl-3-[[4-(3-pyridinyl)-2-pyrimidinyl]amino]phenyl]benzamide methanesulfonate).

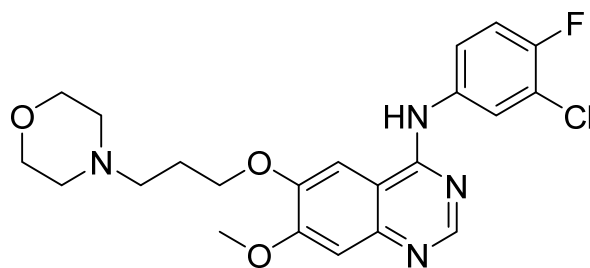


**Figure 3.** Gefitinib (*N*-(3-chloro-4-fluorophenyl)-7-methoxy-6-[3-(4-morpholinyl)propoxy]-4-quinazolinamine).

#### 4.3. Erlotinib Hydrochloride

Erlotinib hydrochloride (Figure 4) is a quinazolinamine derivative (MF:  $C_{22}H_{23}N_3O_4 \cdot HCl$ ; MW: 429.90; CAS Number: 183319-69-9) [30]. **USRE41065E** (Reissue patent of US5747498) discloses 4-(substituted phenylamino)quinazolinamine derivatives, which are useful in treating cancers. It also claims erlotinib hydrochloride specifically [31]. **US6900221B1** provides polymorphs of erlotinib hydrochloride and processes for their selective production. It claims homogeneous thermodynamically stable crystalline polymorph of erlotinib hydrochloride (Form B), suitable for making tablet dosage forms [32].

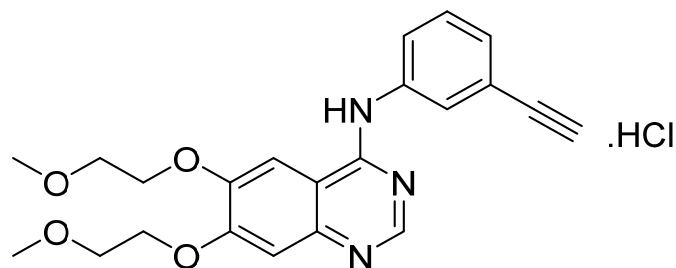


**Figure 4.** Erlotinib hydrochloride (*N*-(3-ethynylphenyl)-6,7-bis(2-methoxyethoxy)-4-quinazolinamine hydrochloride).

#### 4.4. Sorafenib Tosylate

Sorafenib tosylate (Figure 5) is a urea-pyridine based diaryl ether derivative (MF:  $C_{21}H_{16}ClF_3N_4O_3 \cdot C_7H_8O_3S$ ; MW: 637.0; CAS Number: 475207-59-1) [33]. **US7235576B1** provides aryl urea derivatives for treating RAF-mediated diseases like cancer and their pharmaceutical compositions. It claims sorafenib tosylate specifically [34]. **US8877933B2** discloses novel polymorphs of sorafenib tosylate, processes for its synthesis, and compositions comprising it. It claims thermodynamically stable polymorph (Form I) of sorafenib tosylate, which can provide quality dosage form concerning bioavailability and patient safety [35].

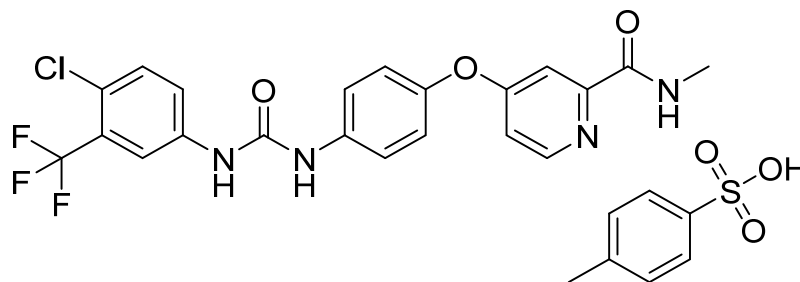


**Figure 5.** Sorafenib tosylate (4-[4-([4-chloro-3-(trifluoromethyl)phenyl]carbamoyl)amino]phenoxy]-N-methylpyridine-2-carboxamide 4-methylbenzenesulfonate).

#### 4.5. Sunitinib Malate

Sunitinib malate (Figure 6) is an indole based pyrrole-3-carboxamide derivative (MF:  $C_{22}H_{27}FN_4O_2 \cdot C_4H_6O_5$ ; MW: 532.6; CAS Number: 341031-54-7) [36]. **US7125905B2** covers 3-pyrrole substituted 2-indolinone compounds as PK activity modulators for treating disorders related to abnormal PK activity. It claims sunitinib malate specifically [37]. The sunitinib malate is also claimed in **US6573293B2** [38].

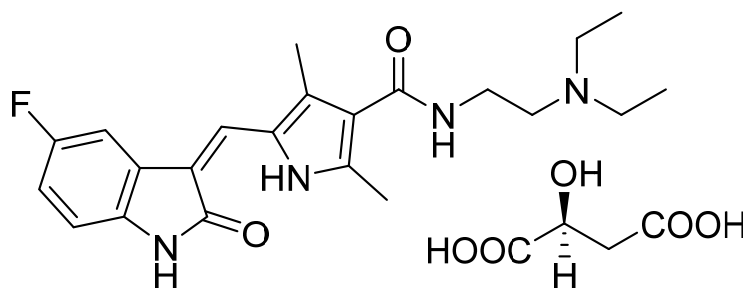


**Figure 6.** Sunitinib malate (*N*-[2-(diethylamino)ethyl]-5-[(*Z*)-(5-fluoro-1,2-dihydro-2-oxo-3H-indol-3-ylidene)methyl]-2,4-dimethyl-1H-pyrrole-3-carboxamide (2*S*)-2-hydroxybutanedioic acid).

#### 4.6. Dasatinib Monohydrate

Dasatinib monohydrate (Figure 7) is a piperazine-pyrimidine-thiazole based anilide (MF:  $C_{22}H_{26}ClN_7O_2S \cdot H_2O$ ; MW: 506.02; CAS Number: 863127-77-9) [39]. **US6596746B1** provides cyclic compounds for use as PKIs to treat cancer. It claims dasatinib specifically [40]. **US7491725B2** claims crystalline monohydrate of dasatinib and process for its preparation [41].

#### 4.7. Lapatinib Ditosylate Monohydrate

Lapatinib ditosylate monohydrate (Figure 8) is a furan based quinazolinamine derivative (MF:  $C_{29}H_{26}ClFN_4O_4S \cdot (C_7H_8O_3S)_2 \cdot H_2O$ ; MW: 943.5; CAS Number: 388082-78-8) [42]. **US8513262B2** discloses substituted heteroaromatic compounds, their synthesis, compositions, and their use in medicine as PTKIs. It claims lapatinib specifically [43]. **US7157466B2** relates to quinazolinone compounds, anhydrate and hydrate ditosylate salts thereof, and the

process for their preparation. It claims lapatinib ditosylate monohydrate specifically. The claimed lapatinib ditosylate possesses physical stability and moisture sorption properties superior to di-HCl salt, making it suitable for developing tablet formulations [44].

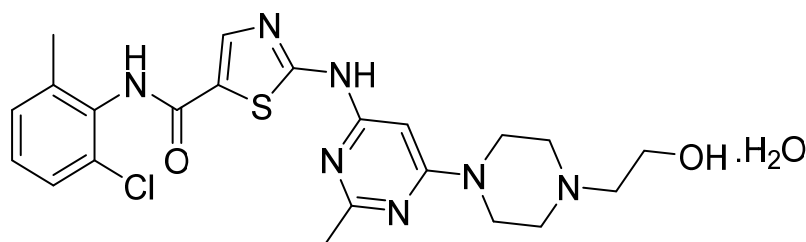


**Figure 7.** Dasatinib monohydrate (*N*-(2-chloro-6-methylphenyl)-2-[[6-[4-(2-hydroxyethyl)-1-piperazinyl]-2-methyl-4-pyrimidinyl]amino]-5-thiazole carboxamide monohydrate).

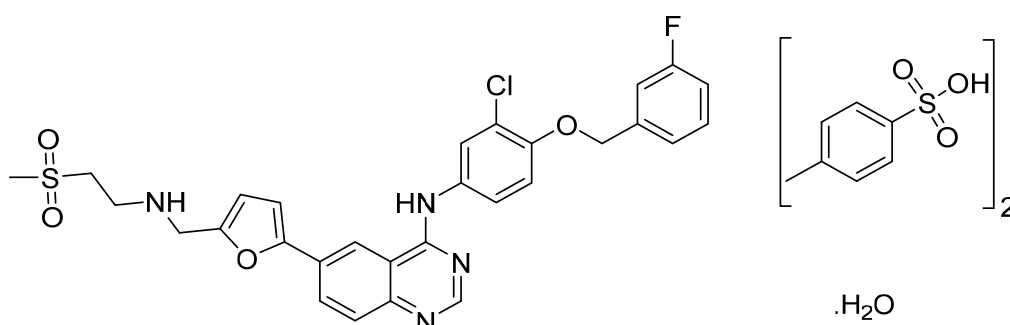


**Figure 8.** Lapatinib ditosylate monohydrate (*N*-(3-chloro-4-((3-fluorophenyl)methyl)oxy)phenyl)-6-[5-((2-(methylsulfonyl)ethyl)amino)methyl)-2-furanyl]-4-quinazolinamine bis(4-methylbenzenesulfonate) monohydrate).

#### 4.8. Temsirolimus

Temsirolimus (Figure 9) is a piperidine-tetrahydropyran based macrolide lactams (MF: C<sub>56</sub>H<sub>87</sub>NO<sub>16</sub>; MW: 1030.30; CAS Number: 162635-04-3) [45]. **USRE44768E** (Reissue of US5362718) relates to hydroxy esters of rapamycin for treating T-cell leukemia/lymphoma, solid tumors, and hyperproliferative vascular disorders. It claims temsirolimus specifically [46].

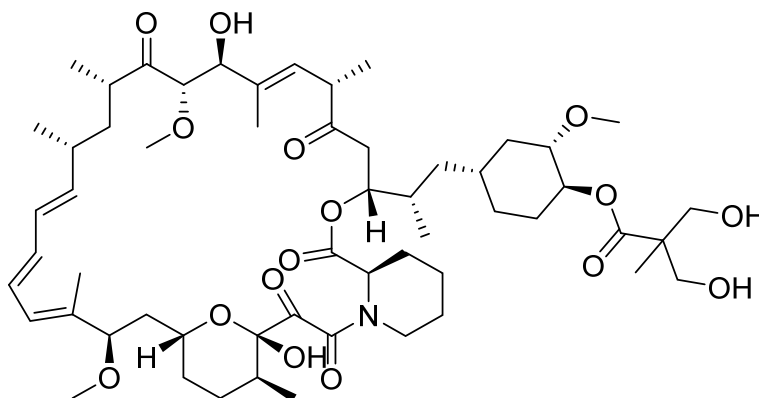


**Figure 9.** Temsirolimus ((3*S*,6*R*,7*E*,9*R*,10*R*,12*R*,14*S*,15*E*,17*E*,19*E*,21*S*,23*S*,26*R*,27*R*,34*aS*)-9,10,12,13,14,21,22,23,24,25,26,27,32,33,34,34*a*-Hexadecahydro-9,27-dihydroxy-3-[(1*R*)-2-[(1*S*,3*R*,4*R*)-4-hydroxy-3-methoxycyclohexyl]-1-methylethyl]-10,21-dimethoxy-6,8,12,14,20,26-hexamethyl-23,27-epoxy-3*H*-pyrido[2,1-*c*][1,4]oxaazacyclohentacontine-1,5,11,28,29(4*H*,6*H*,31*H*)-pentone 4'-[2,2-bis(hydroxymethyl)propionate]).

#### 4.9. Everolimus

Everolimus (Figure 10) is a piperidine-tetrahydropyran based macrolide lactam (MF:  $C_{53}H_{83}NO_{14}$ ; MW: 958.25; CAS Number: 159351-69-6) [47]. **US5665772A** provides alkylated derivatives of rapamycin as immunosuppressants. It claims everolimus specifically [48].

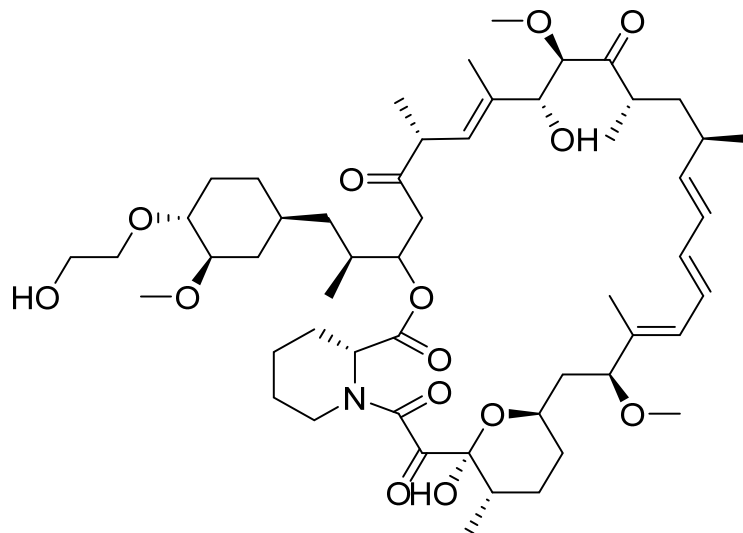


**Figure 10.** Everolimus ((1R,9S,12S,15R,16E,18R,19R,21R,23S,24E,26E,28E,30S,32S,35R)-1,18-dihydroxy-12-((1R)-2-[(1S,3R,4R)-4-(2-hydroxyethoxy)-3-methoxycyclohexyl]-1-methylethyl)-19,30-dimethoxy-15,17,21,23,29,35-hexamethyl-11,36-dioxo-4-aza-tricyclo[30.3.1.04,9]hexatriaconta-16,24,26,28-tetraene-2,3,10,14,20-pentaone).

#### 4.10. Nilotinib Hydrochloride Monohydrate

Nilotinib hydrochloride monohydrate (Figure 11) is a pyridine-pyrimidine-imidazole-based benzanilide derivative (MF:  $C_{28}H_{22}F_3N_7O \cdot HCl \cdot H_2O$ ; MW: 584; CAS Number: 923288-90-8) [49]. **US7169791B2** covers substituted pyrimidinyl aminobenzamides, methods of synthesis, and their compositions to treat neoplastic diseases like leukemia. It claims nilotinib and its salts [50]. **US8163904B2** claims nilotinib hydrochloride monohydrate as having physicochemical properties required to develop a good dosage form [51]. **US8415363B2** claims crystalline form B of nilotinib hydrochloride monohydrate having superior crystallinity and physical stability over other polymorphs [52].

#### 4.11. Pazopanib Hydrochloride

Pazopanib hydrochloride (Figure 12) is a benzenesulfonamide bearing benzimidazole-pyrimidinyl compound (MF:  $C_{21}H_{23}N_7O_2S \cdot HCl$ ; MW: 473.99; CAS Number: 635702-64-6) [53]. **US7105530B2** reports pyrimidine derivatives as inhibitors of VEGFR-2 to treat disorders, including cancer, associated with inappropriate angiogenesis. It claims pazopanib and its salts [54]. **US8114885B2** claims pazopanib hydrochloride precisely [55]. The claimed hydrochloride salt possesses advantageous properties like stability and solubility to develop quality dosage forms.

#### 4.12. Vandetanib

Vandetanib (Figure 13) is a piperidine based 4-aminoquinazolinamine derivative (MF:  $C_{22}H_{24}BrFN_4O_2$ ; MW: 475.36; CAS Number: 443913-73-3) [56]. **USRE42353E** (Reissue of US6414148B1) provides quinazoline derivatives, synthesis, and compositions to treat illness linked with angiogenesis and amplified vascular permeability. It claims vandetanib precisely [57].

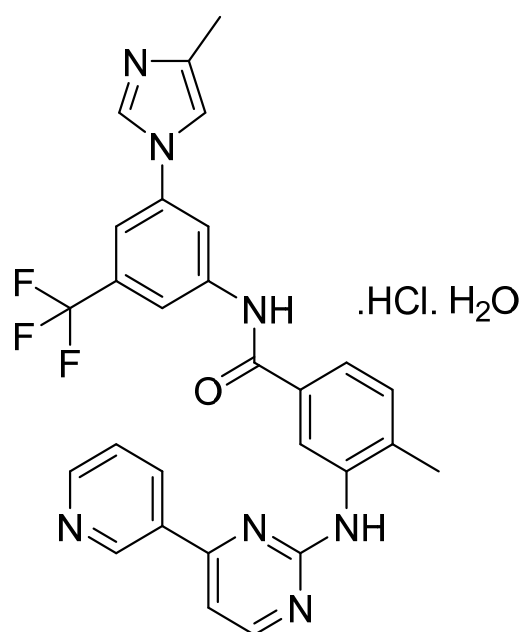


**Figure 11.** Nilotinib hydrochloride monohydrate (4-methyl-*N*-[3-(4-methyl-1H-imidazol-1-yl)-5-(trifluoromethyl)phenyl]-3-[[4-(3-pyridinyl)-2-pyrimidinyl]amino]-benzamide monohydrochloride monohydrate).

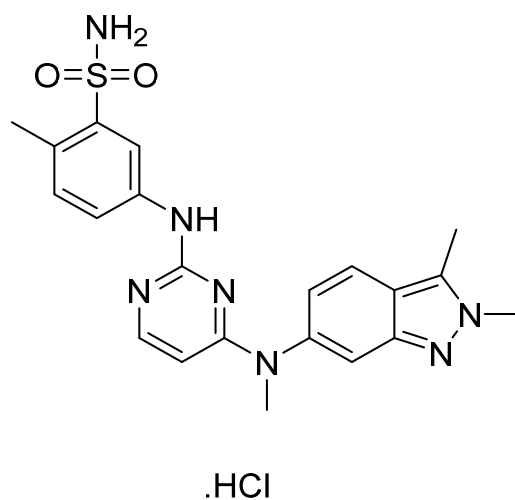


**Figure 12.** Pazopanib hydrochloride (5-[[4-[(2,3-dimethyl-2H-indazol-6-yl)methylamino]-2-pyrimidinyl]amino]-2-methylbenzenesulfonamide monohydrochloride).

#### 4.13. Vemurafenib

Vemurafenib (Figure 14) is a phenylketone based pyrrolopyridine (MF:  $C_{23}H_{18}ClF_2N_3O_3S$ ; MW: 489.9; CAS Number: 918504-65-1) [58]. **US8143271B2** describes pyrrolopyridine based compounds as PTKIs to treat diseases and conditions associated with aberrant activity of PTKs. It claims vemurafenib specifically [59].

#### 4.14. Crizotinib

Crizotinib (Figure 15) is a piperidine based pyrazolopyridine derivative (MF:  $C_{21}H_{22}Cl_2F N_5O$ ; MW: 450.34; CAS Number: 877399-52-5) [60]. **US7858643B2** describes aminopyridines and aminopyrazines having PTKI activity, methods of synthesizing and using these compounds as anticancer agents. It claims crizotinib and its salts [61]. **US8217057B2** claims a crystalline form of a free base of crizotinib with improved solubility, stability, and physicochemical properties to develop solid dosage forms, such as capsules [62].



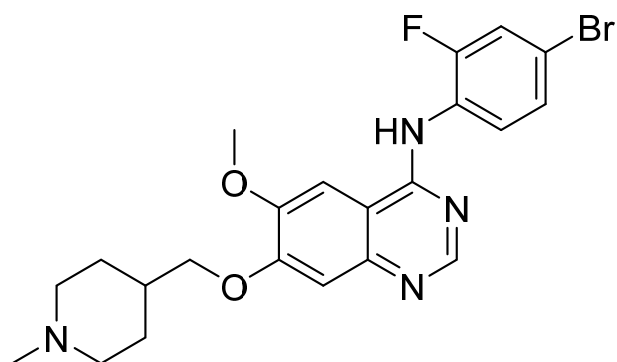


**Figure 13.** Vandetanib (*N*-(4-bromo-2-fluorophenyl)-6-methoxy-7-[(1-methylpiperidin-4-yl)methoxy]quinazolin-4-amine).

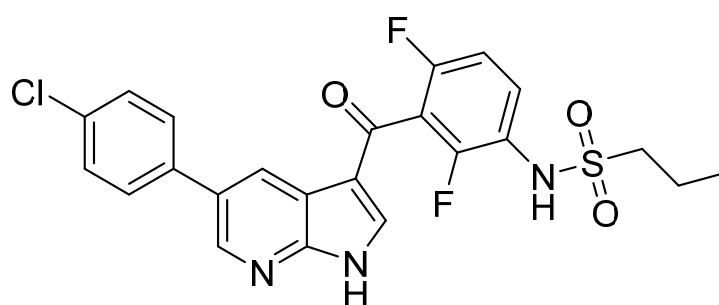


**Figure 14.** Vemurafenib (Propane-1-sulfonic acid {3-[5-(4-chlorophenyl)-1H-pyrrolo[2,3-*b*]pyridine-3-carbonyl]-2,4-difluoro-phenyl}-amide).

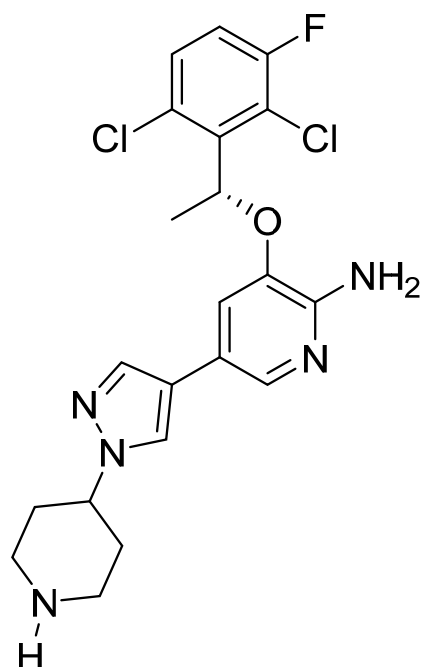


**Figure 15.** Crizotinib ((*R*)-3-[1-(2,6-Dichloro-3-fluorophenyl)ethoxy]-5-[1-(piperidin-4-yl)-1H-pyrazol-4-yl]pyridin-2-amine).

#### 4.15. Ruxolitinib Phosphate

Ruxolitinib phosphate (Figure 16) is a pyrrolo[2,3-*d*]pyrimidine based pyrazole derivative (MF: C<sub>17</sub>H<sub>21</sub>N<sub>6</sub>O<sub>4</sub>P; MW: 404.36; CAS Number: 1092939-17-7) [63]. **US7598257B2**

provides pyrrolo[2,3-*b*]pyridines as JAK modulators, which are beneficial to treat immune-related disorders, skin diseases, myeloid proliferative ailments, and cancer. It claims ruxolitinib and its salts [64]. **US8722693B2** claims ruxolitinib phosphate, which has improved water solubility, dissolution rate, chemical stability, long shelf life, excipients, and reproducibility compared to the free base [65].

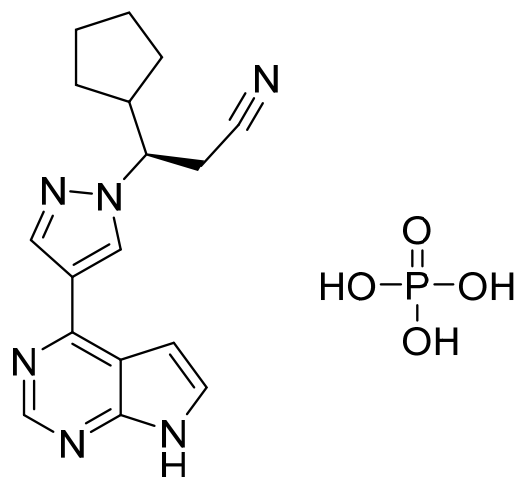


**Figure 16.** Ruxolitinib phosphate ((*R*)-3-(4-(7H-pyrrolo[2,3-*d*]pyrimidin-4-yl)-1H-pyrazol-1-yl)-3-cyclopentylpropanenitrile phosphate).

#### 4.16. Axitinib

Axitinib (Figure 17) is a pyridine based indazolylphenyl thioether (MF: C<sub>22</sub>H<sub>18</sub>N<sub>4</sub>OS; MW: 386.47; CAS Number: 319460-85-0) [66]. **US6534524B1** relates to indazole compounds as PTKIs and their pharmaceutical compositions to treat diseases linked with undesirable angiogenesis and cellular proliferation. It claims axitinib specifically [67]. **US8791140B2** claims crystalline forms of axitinib that have advantages in bioavailability, stability, manufacture ability, and suitability for bulk preparation [68].

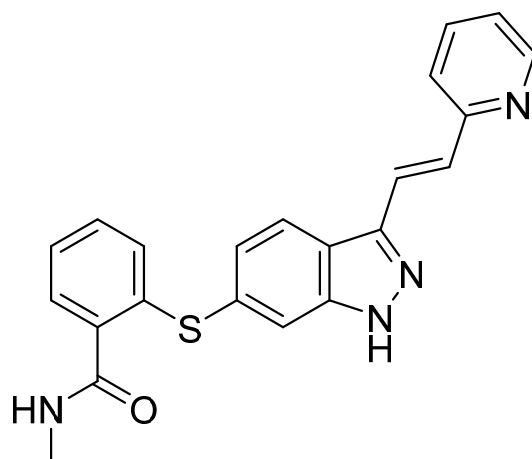


**Figure 17.** Axitinib (*N*-methyl-2-[3-((*E*)-2-pyridin-2-yl-vinyl)-1H-indazol-6-ylsulfanyl]-benzamide).

#### 4.17. Bosutinib Monohydrate

Bosutinib monohydrate (Figure 18) is a piperazine based 3-quinolinecarbonitrile derivative (MF: C<sub>26</sub>H<sub>29</sub>Cl<sub>2</sub>N<sub>5</sub>O<sub>3</sub>·H<sub>2</sub>O; MW: 548.46; CAS Number: 918639-08-4) [69]. **USRE42376E** (Reissue of US6297258B1) describes substituted 3-cyano quinoline compounds as PTKIs to treat diseases resulting from deregulation of PTKs, for example, cancer and polycystic kidney disease. It claims bosutinib [70]. **US7767678B2** claims non-hygroscopic and stable

crystalline bosutinib monohydrate (Form I) having good solubility that can be used to prepare different solid dosage forms [71].

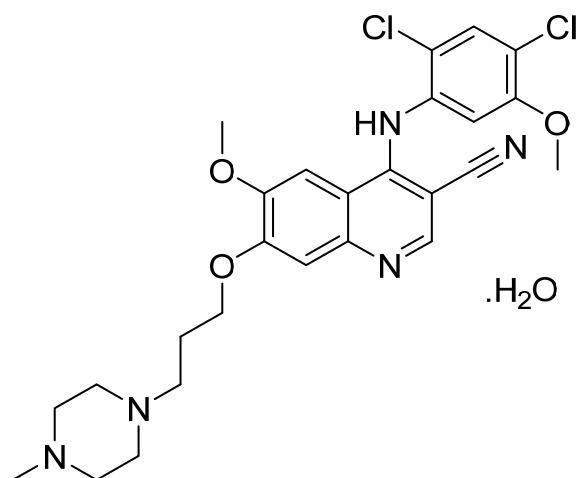


**Figure 18.** Bosutinib monohydrate (4-[(2,4-dichloro-5-methoxyphenyl)amino]-6-methoxy-7-[3-(4-methylpiperazin-1-yl)propoxy]quinoline-3-carbonitrile monohydrate).

#### 4.18. Regorafenib Monohydrate

Regorafenib monohydrate (Figure 19) is pyridinylphenyl urea derivative (MF:  $C_{21}H_{15}ClF_4N_4O_3 \cdot H_2O$ ; MW: 500.83; CAS Number: 1019206-88-2) [72]. **US8637553B2** discloses omega-carboxaryl diphenyl urea derivatives as potent inhibitors of PDGFR, VEGFR, RAF, and p38 kinase to treat cancer, inflammatory diseases, and osteoporosis. It claims regorafenib and its salts [73]. **US9957232B2** claims regorafenib monohydrate with high stability and good physicochemical features to manufacture pharmaceutical compositions [74].

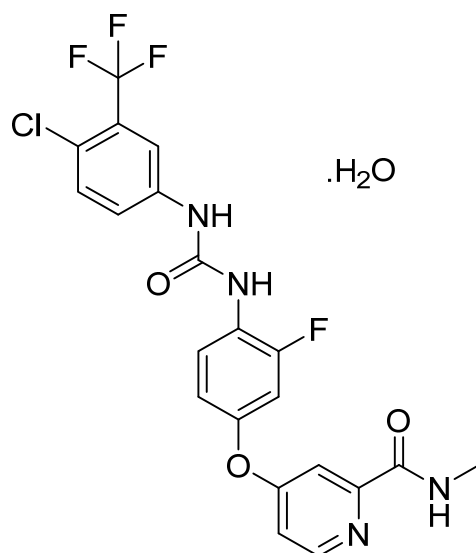


**Figure 19.** Regorafenib monohydrate (4-[4-([4-chloro-3-(trifluoromethyl)phenyl] carbamoyl)amino]-3-fluorophenoxy]-N-methylpyridine-2-carboxamide monohydrate).

#### 4.19. Tofacitinib Citrate

Tofacitinib citrate (Figure 20) is an pyrrolo[2,3-*d*]pyrimidine based piperidine derivative (MF:  $C_{16}H_{20}N_6O \cdot C_6H_8O_7$ ; MW: 504.5; CAS Number: 540737-29-9) [75]. **USRE41783E** (Reissue of US6627754B2) provides pyrrolo[2,3-*d*]pyrimidines as JAK3 inhibitors to treat rheumatoid arthritis, psoriasis, cancer, and leukemia. It claims tofacitinib and its salt [76].

**US6965027B2** claims a crystalline form of tofacitinib mono citrate salt with solid-state properties (solubility, stability, compressibility, etc.), which are acceptable to support tablet development [77].

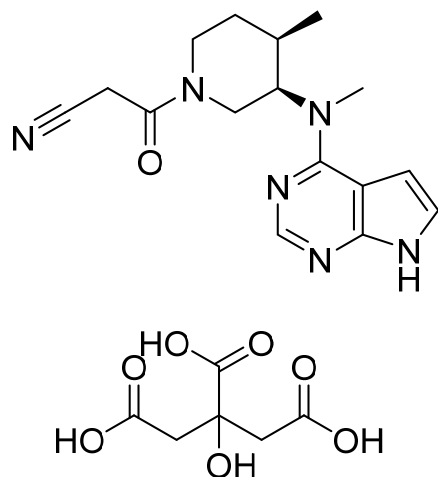


**Figure 20.** Tofacitinib citrate ((3R,4R)-4-methyl-3-(methyl-7H-pyrrolo[2,3-d]pyrimidin-4-ylamino)- $\beta$ -oxo-1-piperidinepropanenitrile 2-hydroxy-1,2,3-propanetricarboxylate (1:1)).

#### 4.20. Cabozantinib S-Malate

Cabozantinib S-malate (Figure 21) is a quinolinylphenyl ether derivative (MF:  $C_{28}H_{24}FN_3O_5 \cdot C_4H_6O_5$ ; MW: 635.6; CAS Number: 1140909-48-3) [78]. **US7579473B2** relates to quinazolines and quinolines as TKIs, and their pharmaceutical compositions to treat psoriasis, multiple sclerosis, and rheumatoid arthritis. It claims cabozantinib and its salts [79]. **US8877776B2** claims cabozantinib (L)-malate salt having desirable solubility and chemical/physical stability to develop a tablet/capsule dosage forms for intended use [80].

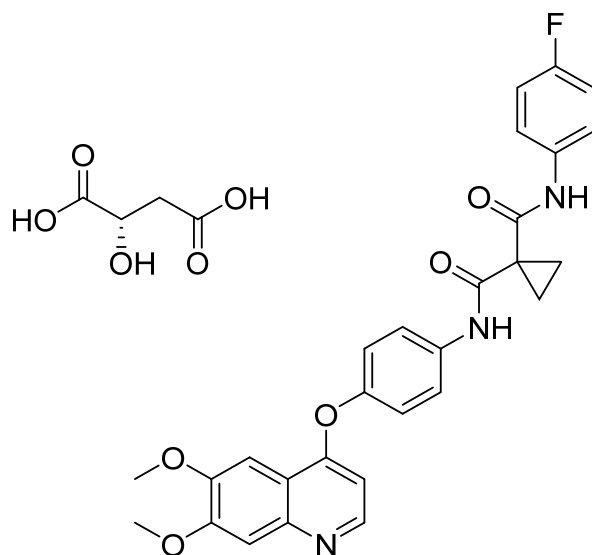


**Figure 21.** Cabozantinib (S)-malate (*N*-(4-(6,7-dimethoxyquinolin-4-yloxy)phenyl)-*N'*-(4-fluorophenyl)cyclopropane-1,1-dicarboxamid (2S)-hydroxybutanedioate).

#### 4.21. Ponatinib Hydrochloride

Ponatinib hydrochloride (Figure 22) is an imidazo[1,2-*b*]pyridazine based piperazine derivative (MF:  $C_{29}H_{28}ClF_3N_6O$ ; MW: 569.02; CAS Number: 1114544-31-8) [81]. **US8114874B2** describes imidazo[1,2-*b*]pyridazines as PTKIs and their pharmaceutical compositions to treat cancer and other diseases mediated by PTKs. It claims ponatinib hydrochloride specifically [82]. **US9493470B2** claims stable crystalline form A of ponatinib hydrochloride that is

advantageous for the commercial preparation of solid dosage forms because of its physico-chemical stability compared to amorphous ponatinib hydrochloride [83].

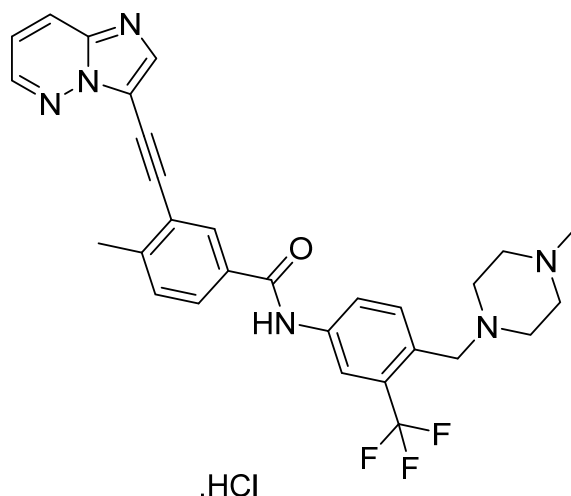


**Figure 22.** Ponatinib hydrochloride (3-(imidazo[1,2-*b*]pyridazin-3-ylethynyl)-4-methyl-*N*-{4-[(4-methylpiperazin-1-yl)methyl]-3-(trifluoromethyl)phenyl}benzamide hydrochloride).

#### 4.22. Trametinib Dimethyl Sulfoxide

Trametinib dimethyl sulfoxide (Figure 23) is a pyridopyrimidine derivative (MF:  $C_{26}H_{23}FIN_5O_4 \cdot C_2H_6OS$ ; MW: 693.53; CAS Number: 1187431-43-1) [84]. **US7378423B2** unveils pyrimidine compounds, their salts, synthetic procedures, and compositions to treat ailments caused by unwanted cell proliferation, for example, cancer. It claims trametinib dimethyl sulfoxide specifically [85].

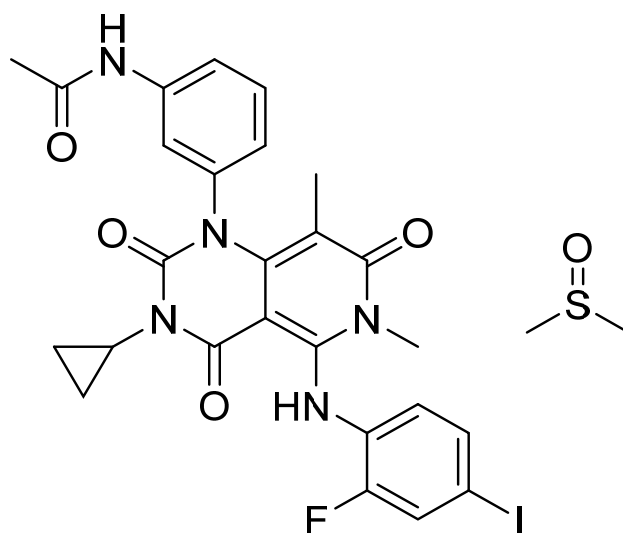


**Figure 23.** Trametinib dimethyl sulfoxide (*N*-(3-(3-cyclopropyl-5-[(2-fluoro-4-iodophenyl)amino]-6,8-dimethyl-2,4,7-trioxo-1*H*,2*H*,3*H*,4*H*,6*H*,7*H*-pyrido[4,3-*d*]pyrimidin-1-yl)phenyl)acetamide dimethyl sulfoxide).

#### 4.23. Dabrafenib Mesylate

Dabrafenib mesylate (Figure 24) is a pyrimidine-thiazole based diphenyl sulfonamide derivative (MF:  $C_{23}H_{20}F_3N_5O_2S_2 \cdot CH_4O_3S$ ; MW: 615.68; CAS Number: 1195768-06-9) [86]. **US7994185B2** provides benzene sulfonamide thiazole and oxazole compounds, their pharmaceutical compositions, processes for their preparation, and methods of using these

compounds and compositions for treating cancer and melanoma. It claims dabrafenib mesylate specifically [87].

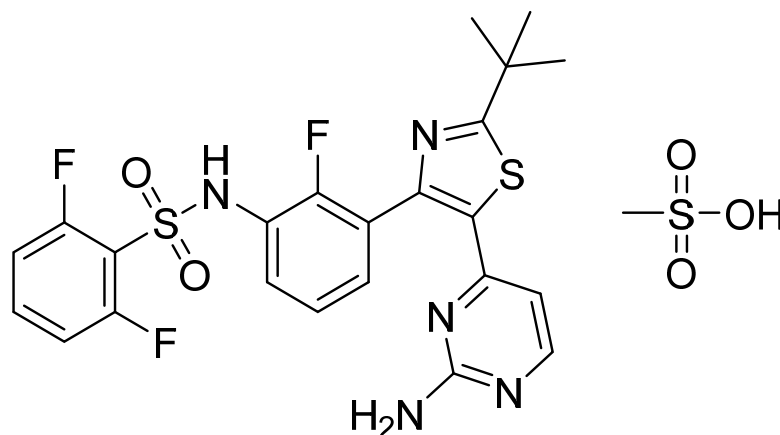


**Figure 24.** Dabrafenib mesylate (*N*-{3-[5-(2-amino-4-pyrimidinyl)-2-(1,1-dimethylethyl)-1,3-thiazol-4-yl]-2-fluorophenyl}-2,6-difluorobenzene sulfonamide mesylate).

#### 4.24. Afatinib Dimaleate

Afatinib dimaleate (Figure 25) is a tetrahydrofuran based quinazolinamine derivative (MF:  $C_{32}H_{33}ClFN_5O_{11}$ ; MW: 718.1; CAS Number: 850140-73-7) [88]. **USRE43431E** (Reissue of US7019012B2) unveils quinazoline derivatives and their physiologically acceptable salts possessing an inhibitory effect on signal transduction mediated by PTKs to treat tumoral diseases, diseases of the lungs, and respiratory tract. It claims afatinib dimaleate precisely [89]. **US8426586B2** claims crystalline afatinib dimaleate, synthesis, and its compositions. The claimed crystalline form is stable and has advantageous properties to develop quality dosage forms [90].

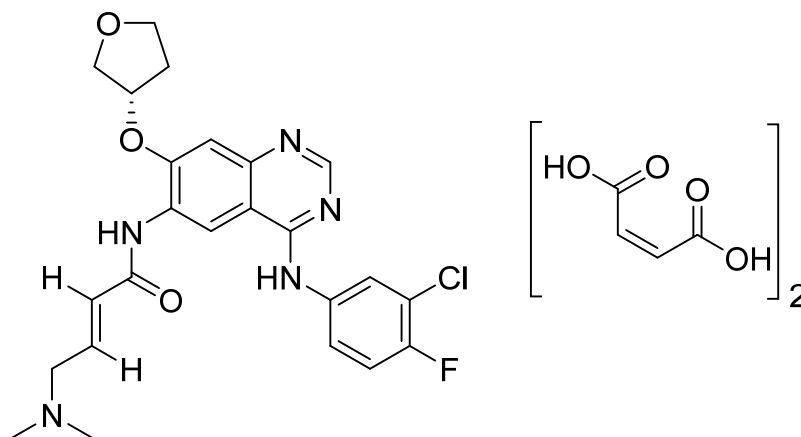


**Figure 25.** Afatinib dimaleate (*N*-[4-[(3-chloro-4-fluorophenyl)amino]-7-[[3(3S)-tetrahydro-3-furanyl]oxy]-6-quinazolinyl]-4-(dimethylamino)but-2-enamide dimaleate).

#### 4.25. Ibrutinib

Ibrutinib (Figure 26) is a piperidine based pyrazolo[3,4-*d*]pyrimidine (MF:  $C_{25}H_{24}N_6O_2$ ; MW: 440.50; CAS Number: 936563-96-1) [91]. **US8735403B2** describes pyrazolo[3,4-*d*]pyrimidine based inhibitors of BTK, their synthesis, and compositions to treat diseases, wherein inhibition of BTK delivers therapeutic advantage to the diseased person. It claims ibrutinib specifically [92]. **US9296753B2** claims stable, water-soluble, and non-hygroscopic crystalline ibrutinib that can be used to manufacture quality dosage forms [93].

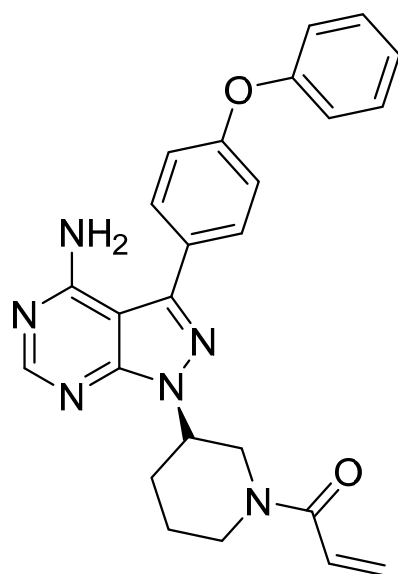


**Figure 26.** Ibrutinib (1-[(3R)-3-[4-amino-3-(4-phenoxyphenyl)-1H-pyrazolo[3,4-*d*]pyrimidin-1-yl]-1-piperidinyl]-2-propen-1-one).

#### 4.26. Ceritinib

Ceritinib (Figure 27) is a pyrimidine based phenylpiperidine derivative (MF: C<sub>28</sub>H<sub>36</sub>N<sub>5</sub>O<sub>3</sub>ClS; MW: 558.14; CAS Number: 1032900-25-6) [94]. **US8039479B2** reveals pyrimidine and pyridine derivatives and their pharmaceutical compositions to treat a condition that responds to inhibition of ALK, FAK, ZAP-70, IGF-1R, or a combination thereof. It claims ceritinib specifically [95]. **US9309229B2** claims a pure and stable crystalline form of ceritinib with desirable physicochemical properties to provide good dosage forms [96].

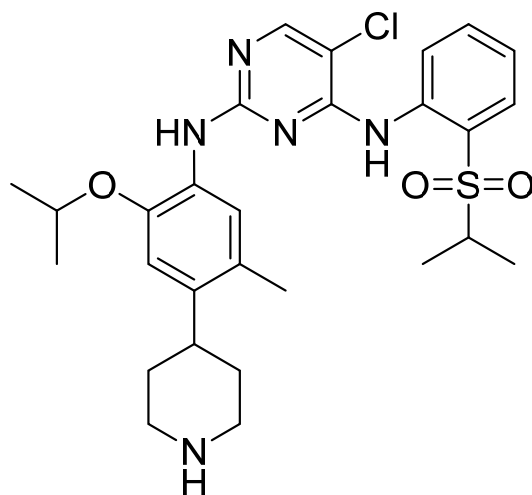


**Figure 27.** Ceritinib (5-Chloro-*N*4-[2-[(1-methylethyl)sulfonyl]phenyl]-*N*2-[5-methyl-2-(1-methylethoxy)-4-(4-piperidinyl)phenyl]-2,4-pyrimidinediamine).

#### 4.27. Idelalisib

Idelalisib (Figure 28) is a purine based quinazolinone derivative (MF: C<sub>22</sub>H<sub>18</sub>FN<sub>7</sub>O; MW: 415.42; CAS Number: 870281-82-6) [97]. **USRE44638E** (Reissue of US7932260B2) reports substituted quinazolinone compounds as PI3K<sub>δ</sub> inhibitors to treat diseases like bone-resorption disorders, hematopoietic cancers, lymphomas, multiple myelomas, and leukemia. It claims idelalisib and its salts [98]. **US9469643B2** claims a water-soluble

bioavailable and stable polymorph of idelalisib (Form II) that can be used to provide quality dosage forms [99].

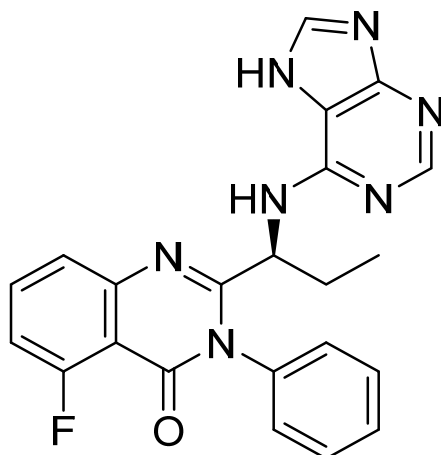


**Figure 28.** Idelalisib (5-fluoro-3-phenyl-2-[(1S)-1-(9H-purin-6-ylamino)propyl]quinazolin-4(3H)-one).

#### 4.28. Nintedanib Esylate

Nintedanib esylate (Figure 29) is a piperazine based indole carboxylic acid derivative (MF:  $C_{31}H_{33}N_5O_4 \cdot C_2H_6O_3S$ ; MW: 649.76; CAS Number: 656247-18-6) [100]. **US6762180B1** states indolinone derivatives as PTKIs, synthesis, and compositions to treat proliferative sicknesses. It claims nintedanib and its salts [101]. **US7119093B2** claims a stable nintedanib esylate salt specifically characterized by good crystallinity and low amorphization during grinding and compression. This salt is claimed to have good physicochemical characteristics to support quality dosage forms [102].

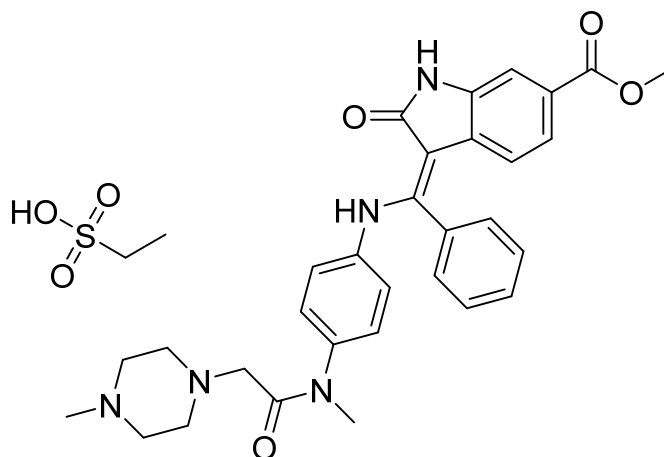


**Figure 29.** Nintedanib esylate (methyl (3Z)-3-[(4-[N-methyl-2-(4-methylpiperazin-1-yl)acetamido]phenyl)amino](phenyl)methylidene]-2-oxo-2,3-dihydro-1H-indole-6-carboxylate esylate).

#### 4.29. Palbociclib

Palbociclib (Figure 30) is a pyrido[2,3-*d*]pyrimidine based pyridinylpiperazine derivative (MF:  $C_{24}H_{29}N_7O_2$ ; MW: 447.54; CAS: 571190-30-2) [103]. **USRE47739E** (Reissue of US7208489B2) delivers substituted 2-amino pyridines as potent inhibitors of CDK 4, useful for treating inflammation and proliferative cell diseases such as cancer and restenosis. It claims palbociclib and its salts [104]. **US10723730B2** claims a stable crystalline free base of palbociclib with larger primary particle size, reduced specific surface area, lower surface energy measurements, and physicochemical properties to formulate a good dosage form [105].



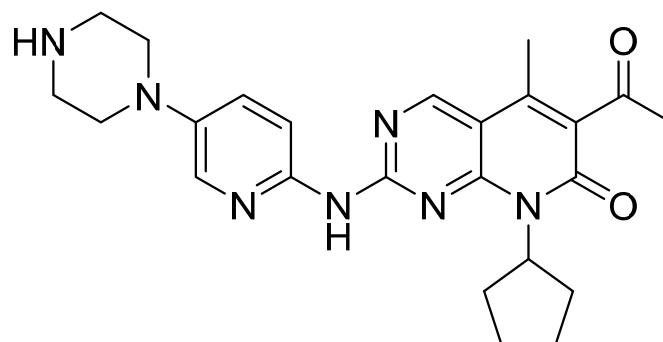


**Figure 30.** Palbociclib (6-acetyl-8-cyclopentyl-5-methyl-2-[[5-(piperazin-1-yl)pyridin-2-yl]amino]pyrido[2,3-*d*]pyrimidin-7(8H)-one).

#### 4.30. Lenvatinib Mesylate

Lenvatinib mesylate (Figure 31) is a quinoline carboxamide derivative (MF: C<sub>21</sub>H<sub>19</sub>ClN<sub>4</sub>O<sub>4</sub>.CH<sub>4</sub>O<sub>3</sub>S; MW: 522.96; CAS Number: 857890-39-2) [106]. **US7253286B2** reports nitrogen-containing aromatic derivatives and salts or hydrates thereof to treat various diseases associated with abnormal angiogenesis. It claims lenvatinib and its pharmacologically active salts [107]. **US7612208B2** claims a crystalline form of lenvatinib mesylate with improved features (physical/pharmacokinetics) compared to the free-form [108].

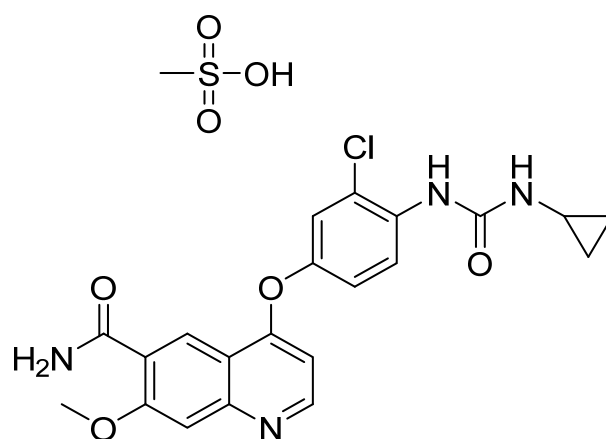


**Figure 31.** Lenvatinib mesylate (4-[3-chloro-4-(*N'*-cyclopropylureido)phenoxy]-7-methoxyquinoline-6-carboxamide methanesulfonate).

#### 4.31. Cobimetinib Fumarate

Cobimetinib fumarate (Figure 32) is a piperidine-azetidine based anthranilamide derivative (MF: C<sub>46</sub>H<sub>46</sub>F<sub>6</sub>I<sub>2</sub>N<sub>6</sub>O<sub>8</sub> (2C<sub>21</sub>H<sub>21</sub>F<sub>3</sub>IN<sub>3</sub>O<sub>2</sub>.C<sub>4</sub>H<sub>4</sub>O<sub>4</sub>); MW: 1178.71; CAS Number: 1369665-02-0) [109]. **US7803839B2** provides azetidin-1-yl(2-(2-fluorophenylamino)cyclic)methanone derivatives as inhibitors of MEK that are useful in cancer treatment. It claims cobimetinib and its salts [110]. **US10590102B2** claims a thermodynamically stable and non-hygroscopic crystalline fumarate salt (Form A) of cobimetinib with suitable properties for use in a pharmaceutical composition [111].

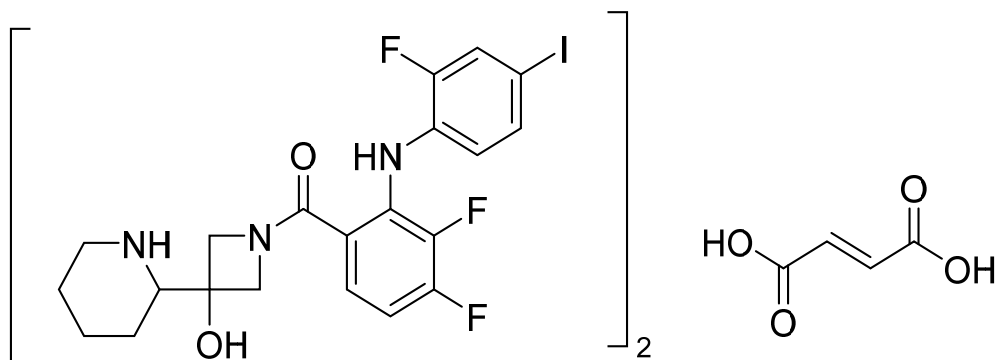


**Figure 32.** Cobimetinib fumarate ((S)-[3,4-difluoro-2-(2-fluoro-4-iodophenylamino)phenyl][3-hydroxy-3-(piperidin-2-yl)azetidin-1-yl]methanone hemifumarate).

#### 4.32. Osimertinib Mesylate

Osimertinib mesylate (Figure 33) is a pyrimidine based indole derivative (MF:  $C_{28}H_{33}N_7O_2 \cdot CH_4O_3S$ ; MW: 596; CAS Number: 1421373-66-1) [112]. **US8946235B2** states 2-(2,4,5-substituted-anilino)pyrimidines, useful in treating a disease mediated by EGFR, for example, cancer. It claims osimertinib mesylate specifically [113].

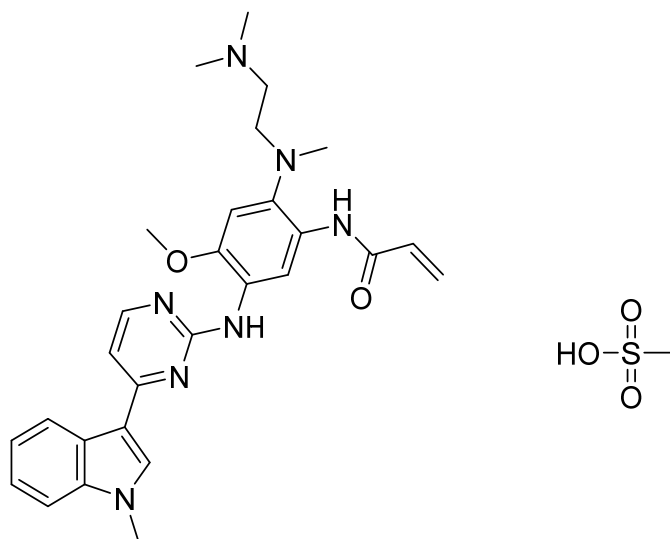


**Figure 33.** Osimertinib mesylate (*N*-(2-[2-dimethylaminoethyl-methylamino]-4-methoxy-5-[[4-(1-methylindol-3-yl)pyrimidin-2-yl]amino]phenyl)prop-2-enamide mesylate).

#### 4.33. Alectinib Hydrochloride

Alectinib hydrochloride (Figure 34) is a morpholine-piperidine based carbazole derivatives (MF:  $C_{30}H_{34}N_4O_2 \cdot HCl$ ; MW: 519.08; CAS Number: 1256589-74-8) [114]. **US9126931B2** relates to tetracyclic compounds as ALK inhibitors for treating a disease accompanied by an abnormality in ALK, for example, cancer, depression, and cognitive function disorder. It claims alectinib and its salts [115].

#### 4.34. Ribociclib Succinate

Ribociclib succinate (Figure 35) is a pyridine-piperazine based pyrrolo[2,3-*d*]pyrimidine derivative (MF:  $C_{23}H_{30}N_8O \cdot C_4H_6O_4$ ; MW: 552.64; CAS Number: 1374639-75-4) [116]. **US8415355B2** discloses pyrrolopyrimidine compounds, the process for their preparation, and their pharmaceutical compositions to treat a disease linked with CDK 4 inhibition. It claims ribociclib and its salts [117]. **US9193732B2** claims succinate salt of ribociclib that

has good stability, non-hygroscopicity, and good solubility. These features make this salt a suitable salt to develop the desired formulation [118].

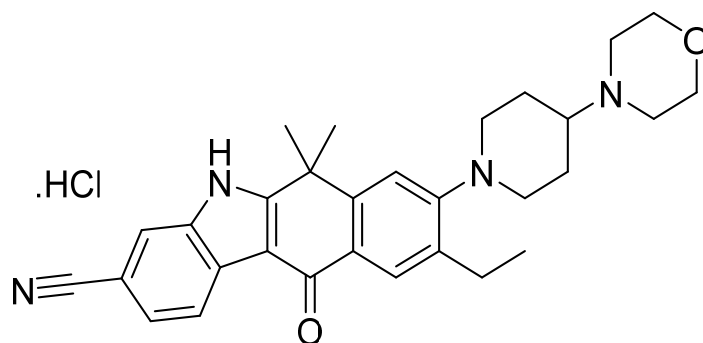


**Figure 34.** Alectinib hydrochloride (9-Ethyl-6,6-dimethyl-8-[4-(morpholin-4-yl)piperidin-1-yl]-11-oxo-6,11-dihydro-5H-benzo[b]carbazole-3-carbonitrile hydrochloride).

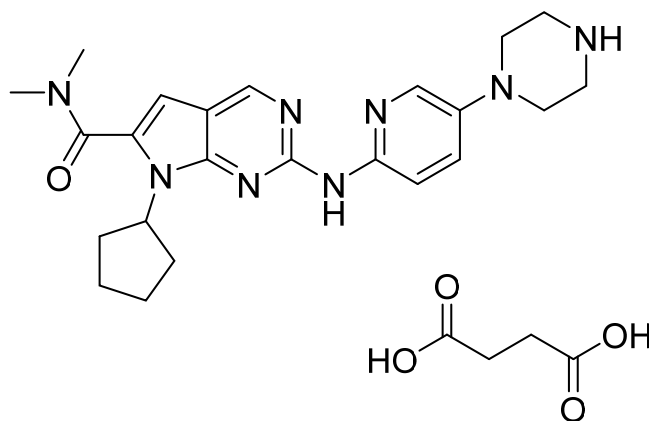


**Figure 35.** Ribociclib succinate (7-cyclopentyl-*N,N*-dimethyl-2-[[5-(piperazin-1-yl)pyridin-2-yl]amino]-7H-pyrrolo[2,3-*d*]pyrimidine-6-carboxamide succinate).

#### 4.35. Brigatinib

Brigatinib (Figure 36) is a piperazine-piperidine based pyrimidine derivative (MF:  $C_{29}H_{39}ClN_7O_2P$ ; MW: 584.10; CAS Number: 1197953-54-0) [119]. **US9012462B2** narrates phosphorous compounds as PTKIs and their use in treating cancers. It claims brigatinib and its salts [120]. **US10385078B2** claims a stable and non-hygroscopic anhydrous crystalline form A of brigatinib suitable for pharmaceutical formulation development [121].

#### 4.36. Midostaurin

Midostaurin (Figure 37) is an indolocarbazole derivative (MF:  $C_{35}H_{30}N_4O_4$ ; MW: 570.65; CAS Number: 120685-11-2) [122]. **US5093330A** relates to staurosporine derivatives, their salts, synthesis, and compositions encompassing them to treat cancer and inflammation. It discloses midostaurin [123]. **US7973031B2** claims a method for treating AML using a dosage form (a microemulsion, soft gel, or solid dispersion) of midostaurin, wherein the AML is characterized by deregulated FLT3 receptor tyrosine kinase activity [124].

#### 4.37. Neratinib Maleate

Neratinib maleate (Figure 38) is a pyridine based 4-aminoquinoline derivative (MF:  $C_{30}H_{29}ClN_6O_3 \cdot C_4H_4O_4$ ; MW: 673.11; CAS Number: 915942-22-2) [125]. **US7399865B2** reports substituted 3-cyanoquinoline compounds and their salts as inhibitors of HER-2 and EGFR to treat cancer. It claims neratinib and its salts [126].

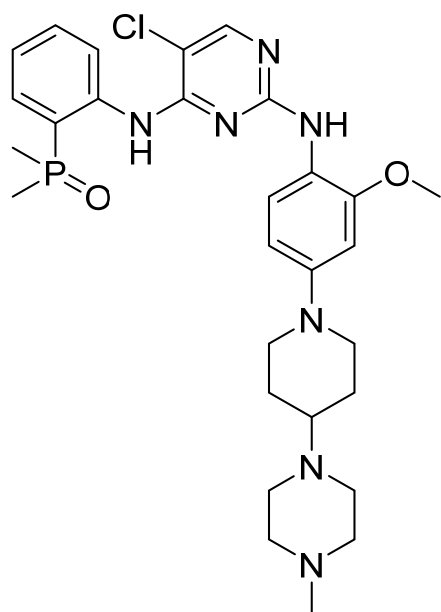


**Figure 36.** Brigatinib (5-chloro-*N*4-[2-(dimethylphosphoryl)phenyl]-*N*2-[2-methoxy-4[4-(4-methylpiperidin-1-yl)piperidin-1-yl]phenyl]pyrimidine-2,4-diamine).

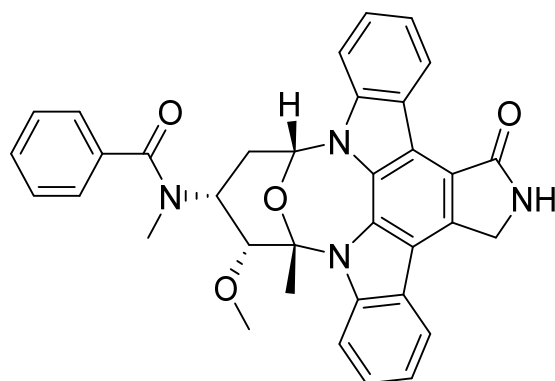


**Figure 37.** Midostaurin (*N*-[(2*S*,3*R*,4*R*,6*R*)-3-Methoxy-2-methyl-16-oxo-29-oxa-1,7,17-triazaocyclo[12.12.2.12,6.07,28.08,13.015,19.020,27.021,26]nonacosa-8,10,12,14,19,21,23,25,27-nonaen-4-yl]-*N*-methylbenzamide).

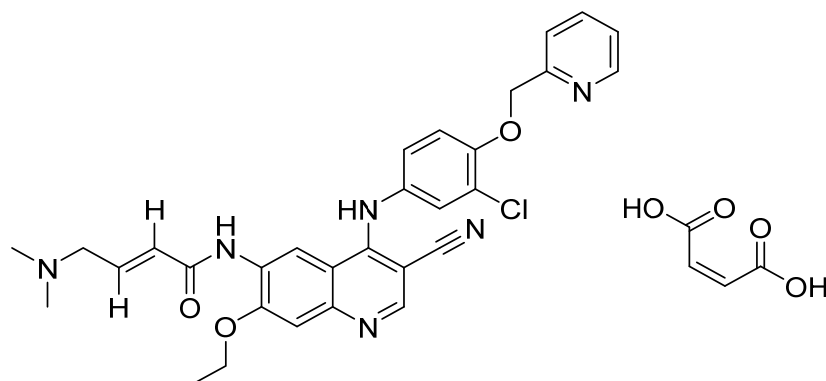


**Figure 38.** Neratinib maleate ((*E*)-*N*-{4-[3-chloro-4-(pyridin-2-ylmethoxy)anilino]-3-cyano-7-ethoxyquinolin-6-yl}-4-(dimethylamino)but-2-enamide maleate).

#### 4.38. Copanlisib Dihydrochloride

Copanlisib dihydrochloride (Figure 39) is a morpholine-pyrimidine based 2,3-dihydroimidazo[1,2-*c*]quinazoline derivative (MF: C<sub>23</sub>H<sub>28</sub>N<sub>8</sub>O<sub>4</sub>·2HCl; MW: 553.45; CAS Number: 1402152-13-9) [127]. **USRE46856E** (Reissue of US8466283B2) unveils 2,3-dihydroimidazo[1,2-*c*]quinazoline derivatives, pharmaceutical compositions comprising them, and the use of these compounds for treating hyperproliferative and angiogenesis disorders. It claims copanlisib and its salts [128]. **US10383876B2** claims copanlisib dihydrochloride salt that possesses technically advantageous properties (stability, solubility, hygroscopicity, etc.) to develop a quality pharmaceutical composition [129].

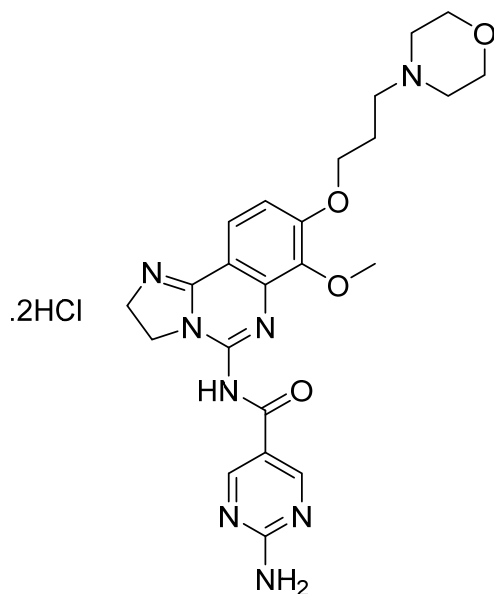


**Figure 39.** Copanlisib dihydrochloride (2-amino-*N*-[7-methoxy-8-[3-(morpholin-4-yl)propoxy]-2,3-dihydroimidazo[1,2-*c*]quinazolin-5-yl]pyrimidine-5-carboxamide dihydrochloride).

#### 4.39. Abemaciclib

Abemaciclib (Figure 40) is a piperazine-pyridine-pyrimidine based benzimidazole derivative (MF: C<sub>27</sub>H<sub>32</sub>F<sub>2</sub>N<sub>8</sub>; MW: 506.59; CAS Number: 1231929-97-7) [130]. **US7855211B2** reports piperazine-pyridine-pyrimidine based benzimidazole derivatives and salts thereof, a pharmaceutical formulation comprising them to treat cancers selected from the group colorectal cancer, breast cancer, NSCLC, prostate cancer, glioblastoma, MCL, CML, and AML. It claims abemaciclib and its salts [131].

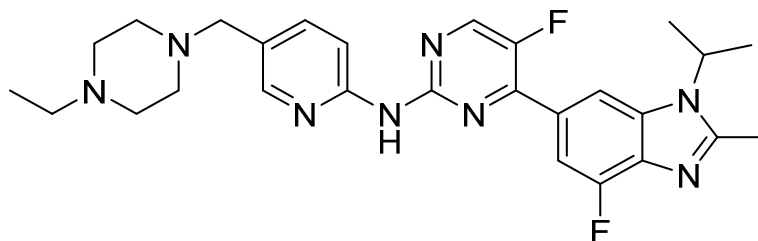


**Figure 40.** Abemaciclib (*N*-[5-[(4-ethyl-1-piperazinyl)methyl]-2-pyridinyl]-5-fluoro-4-[4-fluoro-2-methyl-1-(1-methylethyl)-1H-benzimidazol-6-yl]pyrimidin-2-amine).

#### 4.40. Acalabrutinib

Acalabrutinib (Figure 41) is a pyrrolidine-pyridine based imidazo[1,5-*a*]pyrazine derivative (MF: C<sub>26</sub>H<sub>23</sub>N<sub>7</sub>O<sub>2</sub>; MW: 465.51; CAS Number: 1420477-60-6) [132]. **US9290504B2** provides 4-imidazopyridazin-1-yl-benzamides for the treatment of BTK mediated disorders.

It claims acalabrutinib and its salts [133]. **US9796721B2** claims a stable and non-hygroscopic anhydrate crystal form of acalabrutinib as having advantageous parameters for making quality pharmaceutical compositions [134].

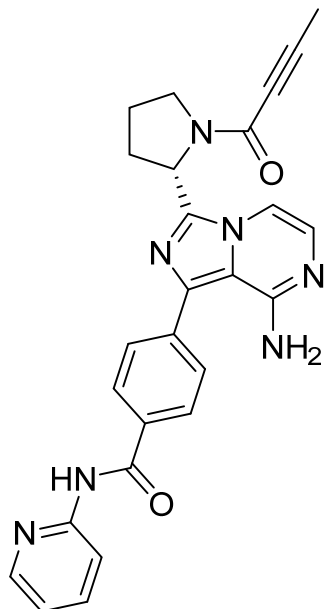


**Figure 41.** Acalabrutinib (4-{8-amino-3-[(2S)-1-(but-2-ynoyl)pyrrolidin-2-yl]imidazo[1,5-*a*]pyrazin-1-yl}-*N*-(pyridin-2-yl)benzamide).

#### 4.41. Netarsudil Dimesylate

Netarsudil dimesylate (Figure 42) is an isoquinoline based beta-amino acid derivative (MF:  $C_{30}H_{35}N_3O_9S_2$ ; MW: 645.74; CAS Number: 1422144-42-0) [135]. **US8394826B2** relates to isoquinoline amide and benzamide based compounds as dual inhibitors of Rho kinase and a monoamine transporter (MAT), useful in treating diseases like glaucoma and cancer. It claims netarsudil [136]. **US9415043B2** claims a chemically stable and water-soluble dimesylate salt of netarsudil that can provide a quality ophthalmic solution [137].

#### 4.42. Baricitinib

Baricitinib (Figure 43) is a pyrazole-azetidine based pyrrolo[2,3-*d*]pyrimidine derivative (MF:  $C_{16}H_{17}N_7O_2S$ ; MW: 371.42; CAS Number: 1187594-09-7) [138]. **US8158616B2** provides azetidine derivatives as JAK inhibitors, synthetic methods, and compositions encompassing them to treat inflammatory and autoimmune disorders, along with cancer. It claims baricitinib and its salts [139].

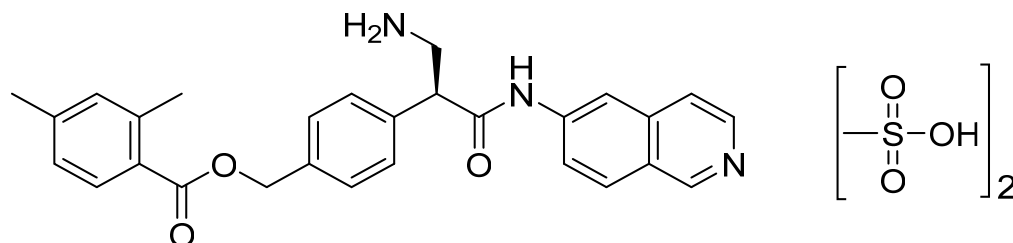


**Figure 42.** Netarsudil dimesylate ((*S*)-4-(3-amino-1-(isoquinolin-6-ylamino)-1-oxopropan-2-yl)benzyl-2,4-dimethylbenzoate dimesylate).

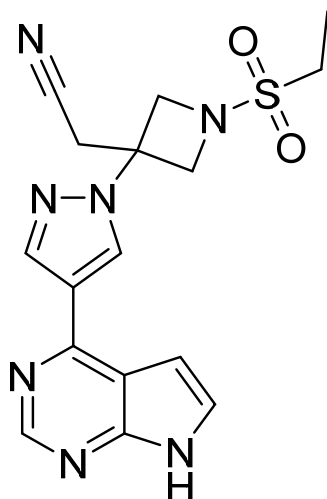


**Figure 43.** Baricitinib ((1-(ethylsulfonyl)-3-[4-(7H-pyrrolo[2,3-d]pyrimidin-4-yl)-1H-pyrazol-1-yl]azetidin-3-yl}acetonitrile).

#### 4.43. Binimetinib

Binimetinib (Figure 44) is a benzimidazole derivative (MF:  $C_{17}H_{15}BrF_2N_4O_3$ ; MW: 441.2; CAS Number: 606143-89-9) [140]. **US7777050B2** states alkylated (1H-Benzoimidazol-5-yl)-(4-substituted-phenyl)-amine derivatives, helpful in managing sicknesses like cancer. It claims binimetinib and pharmaceutically acceptable salts thereof [141]. **US9562016B2** claims a crystallized form of binimetinib with better purity and an enhanced physical characteristic, beneficial in pharmaceutical dosage form preparation [142].

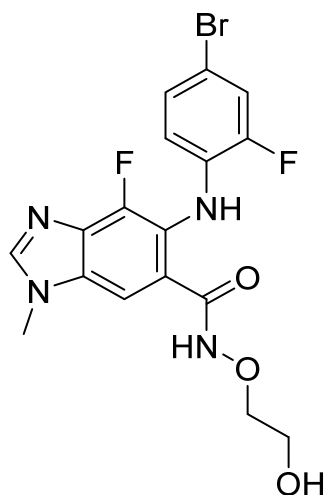


**Figure 44.** Binimetinib (5-[(4-bromo-2-fluorophenyl)amino]-4-fluoro-N-(2-hydroxyethoxy)-1-methyl-1H-benzimidazole-6-carboxamide).

#### 4.44. Dacomitinib Monohydrate

Dacomitinib monohydrate (Figure 45) is a piperidine based quinazolinamine derivatives (MF:  $C_{24}H_{25}ClFN_5O_2 \cdot H_2O$ ; MW: 487.95; CAS Number: 1042385-75-0) [143]. **US7772243B2** unveils 4-anilino-6-substituted alkenoylamino-quinazoline compounds as TKIs to treat proliferative diseases, including cancer and restenosis endometriosis and psoriasis. It claims dacomitinib and its salts [144].

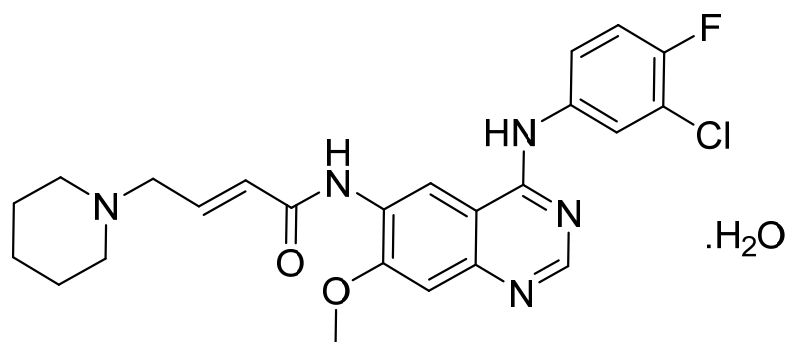


**Figure 45.** Dacomitinib monohydrate ((*2E*)-*N*-[4-[(3-Chloro-4-fluorophenyl)amino]-7-methoxyquinazolin-6-yl]-4-(piperidin-1-yl)but-2-enamide monohydrate).

#### 4.45. Encorafenib

Encorafenib (Figure 46) is a pyrazole based pyrimidine derivative (MF: C<sub>22</sub>H<sub>27</sub>ClFN<sub>7</sub>O<sub>4</sub>S; MW: 540; CAS Number: 1269440-17-6) [145]. **US8501758B2** provides pyrazole based pyrimidine and pharmaceutical compositions comprising them to treat disorders associated with the deregulated activity of B-Raf. It claims encorafenib and its salts [146].

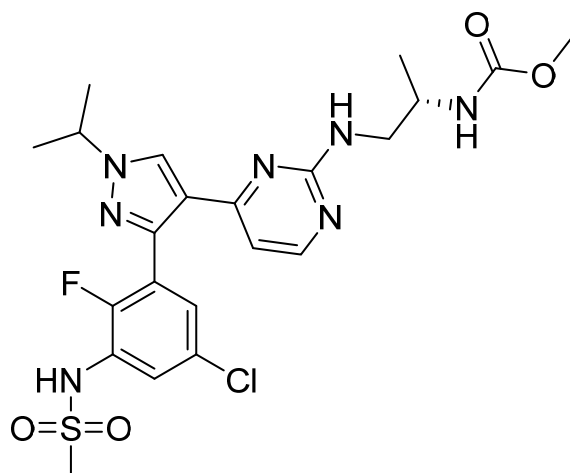


**Figure 46.** Encorafenib (*N*-{(2*S*)-1-[(4-{3-[5-chloro-2-fluoro-3-(methanesulfonamido)phenyl]-1-(propan-2-yl)-1*H*-pyrazol-4-yl}pyrimidin-2-yl)amino]propan-2-yl}carbamate).

#### 4.46. Fostamatinib Disodium Hexahydrate

Fostamatinib disodium hexahydrate (Figure 47), a phosphate prodrug of tiamatinib, is a pyrimidine based pyrido[3,2-*b*][1,4]oxazine derivative (MF: C<sub>23</sub>H<sub>24</sub>FN<sub>6</sub>Na<sub>2</sub>O<sub>9</sub>P·6H<sub>2</sub>O; MW: 732.52; CAS Number: 914295-16-2) [147]. **US7449458B2** reports prodrugs of pharmacologically active 2,4-pyrimidinediamine derivatives, intermediates thereof, the process of manufacturing them, and pharmaceutical compositions comprising them to treat diseases mediated by the activation of PTKs. It claims fostamatinib disodium hexahydrate, which has increased solubility concerning the parent phosphate prodrug [148]. **US8163902B2** claims a thermodynamically stable crystalline form of fostamatinib disodium hexahydrate that is stable over a wide range of relative humidity and requires substantial heating to lose its water molecules. This property makes it a suitable API to develop the desired dosage form [149].



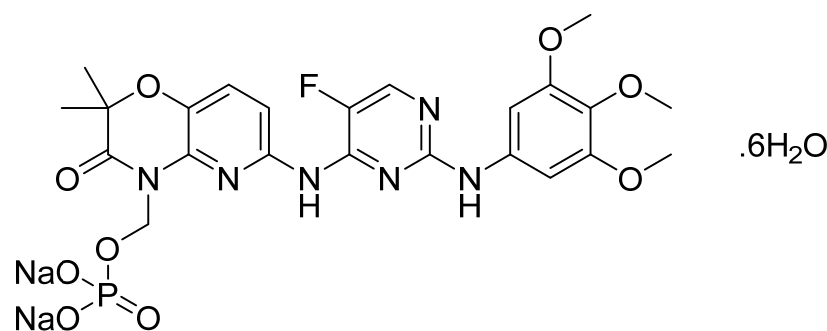


**Figure 47.** Fostamatinib disodium hexahydrate (Disodium (6-[[5-fluoro-2-(3,4,5-trimethoxyanilino)pyrimidin-4-yl]amino]-2,2-dimethyl-3-oxo-pyrido[3,2-*b*][1,4]oxazin-4-yl)methyl phosphate hexahydrate).

#### 4.47. Duvelisib Hydrate

Duvelisib hydrate (Figure 48) is a purine based isoquinolone derivative (MF:  $C_{22}H_{17}ClN_6O \cdot H_2O$ ; MW: 434.88; CAS Number: 1201438-56-3) [150]. **US8193182B2** provides isoquinolin-1(2H)-one derivatives as modulators of PI3 kinase activity and pharmaceutical compositions comprising them to treat diseases associated with P13 kinase activity. It claims duvelisib and its salts [151]. **USRE46621E** (Reissue of US8809349B2) claims physically and chemically stable polymorphs of duvelisib, salt, solvate, or hydrate that do not readily decompose or change in chemical makeup or physical state for more than 60 months and are suitable to develop the desired dosage forms of the API [152].

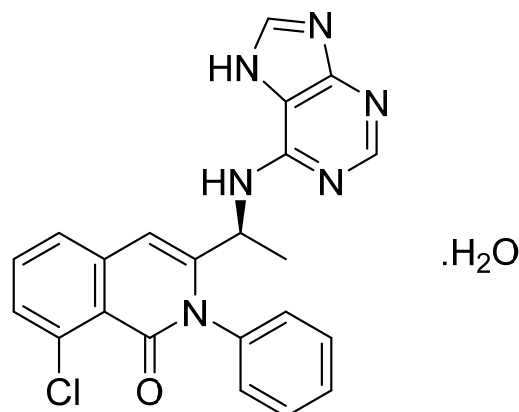


**Figure 48.** Duvelisib hydrate ((*S*)-3-(1-(9H-purin-6-ylamino)ethyl)-8-chloro-2-phenylisoquinolin-1(2H)-one hydrate).

#### 4.48. Gilteritinib Fumarate

Gilteritinib fumarate (Figure 49) piperazine-piperidine based pyrazine carboxamide derivative (MF:  $(C_{29}H_{44}N_8O_3)_2 \cdot C_4H_4O_4$ ; MW: 1221.50; CAS Number: 1254053-84-3) [153]. **US8969336B2** states diamino heterocyclic carboxamide derivatives as having outstanding inhibitory activity against EML4-ALK fusion proteins for use in cancer therapy. It claims gilteritinib and its salts [154]. The gilteritinib fumarate salt is stable in heat, humidity, and storage conditions.

#### 4.49. Larotrectinib Sulfate

Larotrectinib sulfate (Figure 50) is a pyrrolidine based pyrazolo[1,5-*a*]pyrimidine derivative (MF:  $C_{21}H_{24}F_2N_6O_6S$ ; MW: 526.51; CAS Number: 1223405-08-0) [155]. **US9127013B2** relates to pyrazolo[1,5-*a*] pyrimidine derivatives as TRK family PTKIs that are useful to treat cancer, inflammation, and certain infectious diseases. It claims larotrectinib sulfate

specifically [156]. **US10172861B2** claims crystalline larotrectinib sulfate having stable physicochemical properties, which can be used to develop quality dosage forms [157].

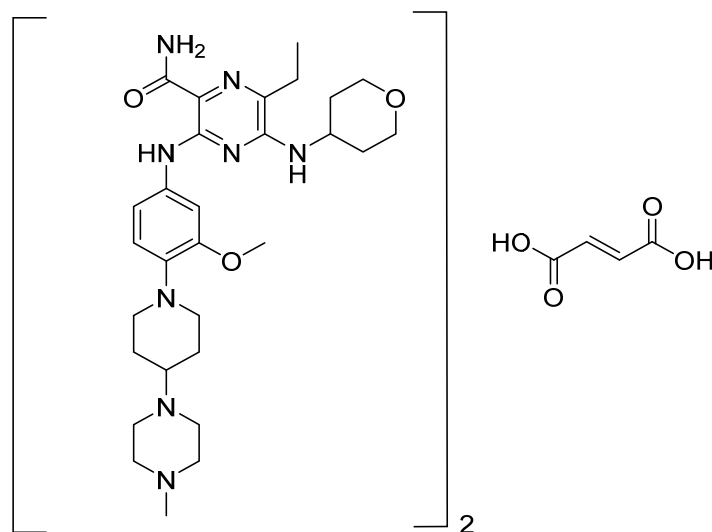


**Figure 49.** Gilteritinib fumarate (2-Pyrazinecarboxamide 6-ethyl-3-[[3-methoxy-4-[4-(4-methyl-1-piperazinyl)-1-piperidinyl]phenyl]amino]-5-[(tetrahydro-2H-pyran-4-yl)amino]-, (2E)-2-butenedioate (2:1)).

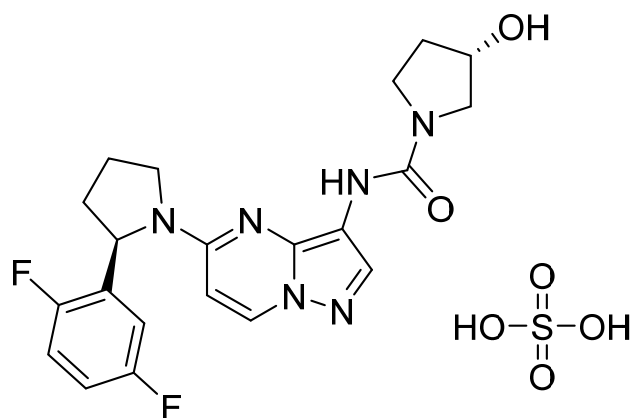


**Figure 50.** Larotrectinib sulfate ((3S)-N-[5-[(2R)-2-(2,5-difluorophenyl)-1-pyrrolidinyl]pyrazolo[1,5-a]pyrimidin-3-yl]-3-hydroxy-1-pyrrolidinecarboxamide sulfate).

#### 4.50. Lorlatinib

Lorlatinib (Figure 51) is a pyrazole-pyridine based benzoxadiazacyclotetradecine derivative (MF:  $C_{21}H_{19}FN_6O_2$ ; MW: 406.41; CAS Number: 1223403-58-4) [158]. **US8680111B2** discloses macrocyclic compounds as inhibitors of ALK and/or EML4-ALK and their pharmaceutical composition to treat illnesses linked with the deregulation of ALK and EML4-ALK. It claims lorlatinib and its salts [159]. **US10420749B2** claims crystalline polymorphs of lorlatinib having high crystallinity and purity, low hygroscopicity, and favorable dissolution and mechanical properties to develop quality pharmaceutical formulations [160].

#### 4.51. Entrectinib

Entrectinib (Figure 52) is a tetrahydropyran-piperazine based indazole derivative (MF:  $C_{31}H_{34}F_2N_6O_2$ ; MW: 560.64; CAS Number: 1108743-60-7) [161]. **US8299057B2** discloses indazole derivatives as potent PKIs that are useful in anticancer therapy. It claims entrectinib and its salts [162]. **US10738037B2** claims a crystalline Form 4 of entrectinib that exhibits greater thermodynamic stability at a temperature of about 40 °C than other known polymorphs and offers advantages in preparing dosage forms [163].

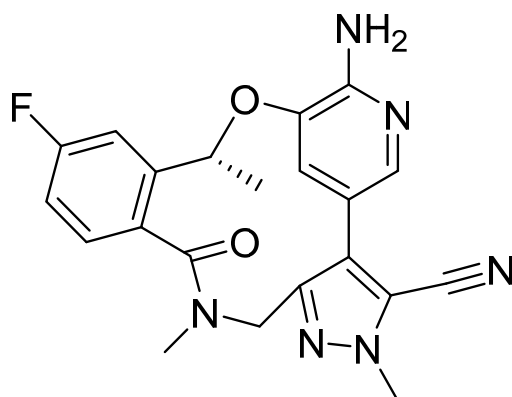


**Figure 51.** Lorlatinib ((10R)-7-amino-12-fluoro-2,10,16-trimethyl-15-oxo-10,15,16,17-tetrahydro-2H-4,8-methenopyrazolo[4,3-H][2,5,11]benzoxadiazacyclotetradecine-3-carbonitrile).

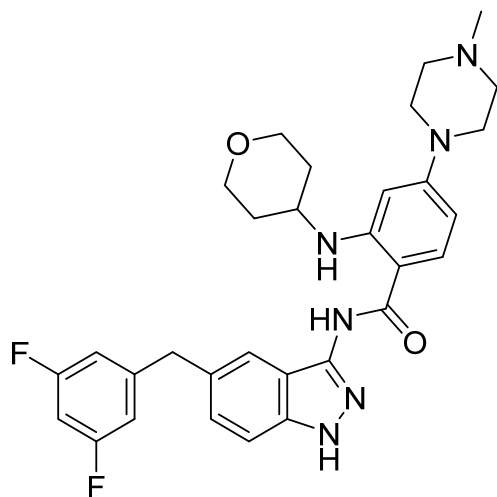


**Figure 52.** Entrectinib (*N*-[5-(3,5-difluorobenzyl)-1H-indazol-3-yl]-4-(4-methylpiperazin-1-yl)-2-(tetrahydro-2H-pyran-4-ylamino)benzamide).

#### 4.52. Upadacitinib Hemihydrate

Upadacitinib hemihydrate (Figure 53) is an imidazo[1,2-*a*]pyrrolo[2,3-*e*]pyrazine based pyrrolidine derivative (MF: C<sub>17</sub>H<sub>19</sub>F<sub>3</sub>N<sub>6</sub>O·1/2 H<sub>2</sub>O; MW: 389.38; CAS Number: 1310726-60-3) [164]. **USRE47221E** (Reissue of US8426411B2) describes tricyclic compounds that inhibit JAK family kinase activity for treating diseases, including rheumatoid arthritis, multiple sclerosis, and psoriasis. It claims upadacitinib [165]. **US9951080B2** claims physicochemically stable crystalline hemihydrate of upadacitinib having solid-state properties to develop quality pharmaceutical dosage forms [166].

#### 4.53. Alpelisib

Alpelisib (Figure 54) is a pyridine-thiazole based pyrrolidine derivative (MF: C<sub>19</sub>H<sub>22</sub>F<sub>3</sub>N<sub>5</sub>O<sub>2</sub>S; MW: 441.47; CAS Number: 1217486-61-7) [167]. **US8227462B2** unveils pyrrolidine-1,2-dicarboxamide derivatives for the treatment of illnesses ameliorated by inhibition of PI3Ks. It claims alpelisib in a free form and its salts [168].

#### 4.54. Erdafitinib

Erdafitinib (Figure 55) is a pyrazole based quinoxaline derivative (MF: C<sub>25</sub>H<sub>30</sub>N<sub>6</sub>O<sub>2</sub>; MW: 446.56; CAS Number: 1346242-81-6) [169]. **US8895601B2** relates to pyrazole based quinoxaline derivatives and their pharmaceutical compositions to treat diseases like cancer. It claims erdafitinib and its salts [170].

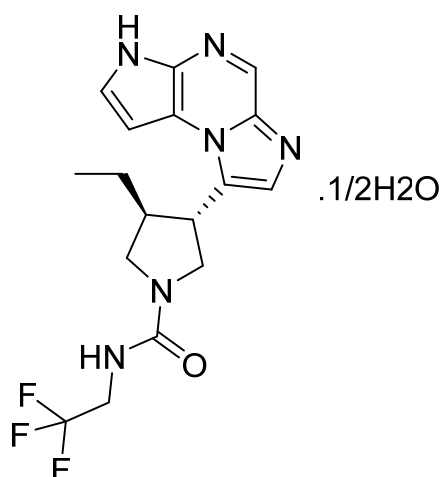


**Figure 53.** Upadacitinib hemihydrate ((3*S*,4*R*)-3-Ethyl-4-(3*H*-imidazo[1,2-*a*]pyrrolo[2,3-*e*]pyrazin-8-yl)-*N*-(2,2,2-trifluoroethyl)pyrrolidine-1-carboxamide hydrate (2:1)).

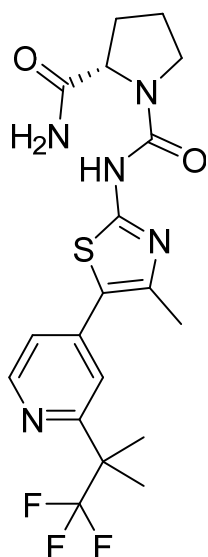


**Figure 54.** Alpelisib ((2*S*)-*N*1-[4-Methyl-5-[2-(2,2,2-trifluoro-1,1-dimethylethyl)-4-pyridinyl]-2-thiazolyl]-1,2-pyrrolidine dicarboxamide).

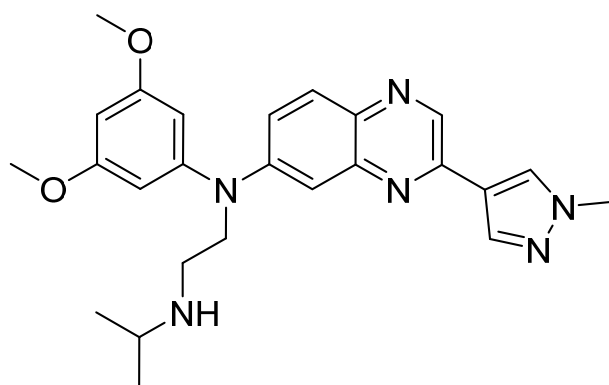


**Figure 55.** Erdafitinib (*N*-(3,5-dimethoxyphenyl)-3-(1-methyl-1*H*-pyrazol-4-yl)-*N*-{2-[(propan-2-yl)amino]ethyl}quinoxalin-6-amine).

#### 4.55. Pexidartinib Hydrochloride

Pexidartinib hydrochloride (Figure 56) is a pyrrolo[2,3-*b*]pyridine based pyridine derivative (MF: C<sub>20</sub>H<sub>15</sub>ClF<sub>3</sub>N<sub>5</sub>·HCl; MW: 454.28; CAS Number: 1029044-16-3) [171]. **US9169250B2** provides fused azacyclic compounds as dual inhibitors of c-FMS and c-KIT to treat diseases that arise due to deregulation of c-FMS and c-KIT. It claims pexidartinib hydrochloride [172]. **US9802932B2** claims a stable crystalline form of pexidartinib hydrochloride having attributes for developing a quality pharmaceutical composition [173].

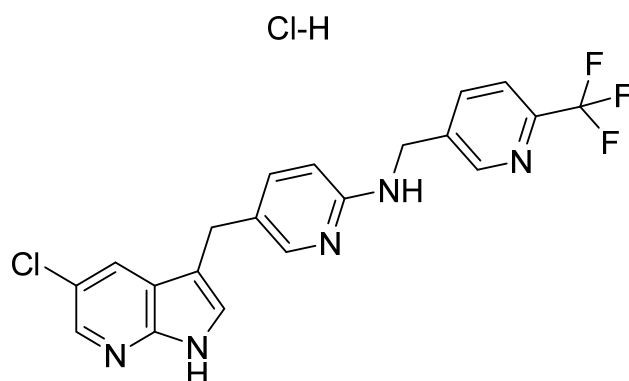


**Figure 56.** Pexidartinib hydrochloride (5-[(5-Chloro-1H-pyrrolo[2,3-*b*]pyridin-3-yl)methyl]-N-[[6-(trifluoromethyl)pyridin-3-yl]methyl]pyridin-2-amine monohydrochloride).

#### 4.56. Fedratinib Dihydrochloride Monohydrate

Fedratinib dihydrochloride monohydrate (Figure 57) is a pyrrolidine-pyrimidine based benzenesulfonamide derivative (MF: C<sub>27</sub>H<sub>36</sub>N<sub>6</sub>O<sub>3</sub>S·2HCl·H<sub>2</sub>O; MW: 615.62; CAS Number: 1374744-69-0) [174]. **US7528143B2** unveils biaryl m-pyrimidine compounds as an inhibitor of the JAK family and their pharmaceutical compositions to treat diseases mediated by modulation of JAK activity. It claims fedratinib and its salts [175].

#### 4.57. Zanubrutinib

Zanubrutinib (Figure 58) is a piperidine based pyrazolo[1,5-*a*]pyrimidine derivative (MF: C<sub>27</sub>H<sub>29</sub>N<sub>5</sub>O<sub>3</sub>; MW: 471.56; CAS Number: 1691249-45-2) [176]. **US9447106B2** states substituted pyrazolo[1,5-*a*]pyrimidines as BTK modulators and used these compounds to treat diseases intervened by BTK. It claims zanubrutinibas and its salts [177].

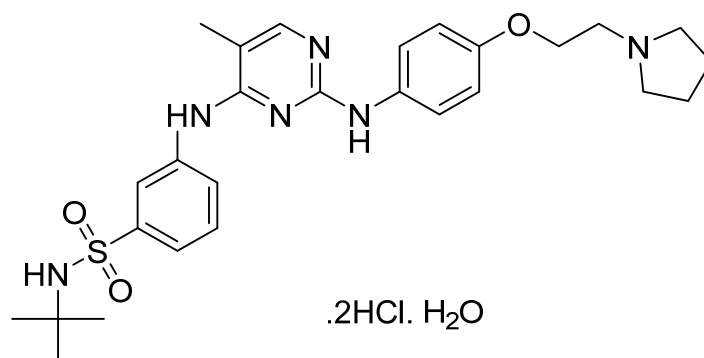


**Figure 57.** Fedratinib dihydrochloride monohydrate (*N*-tert-butyl-3-[[5-methyl-2-[(4-[2-(pyrrolidin-1-yl)ethoxy]phenyl)amino]pyrimidin-4-yl]amino]benzene-1-sulfonamide dihydrochloride monohydrate).

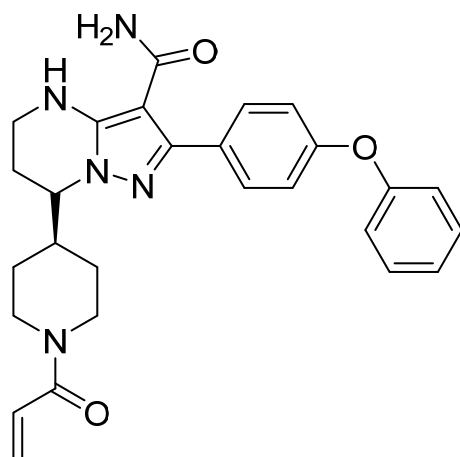


**Figure 58.** Zanutrutinib ((S)-7-(1-Acryloylpiperidin-4-yl)-2-(4-phenoxyphenyl)-4,5,6,7-tetrahydropyrazolo[1,5-*a*]pyrimidine-3-carboxamide).

#### 4.58. Avapritinib

Avapritinib (Figure 59) is a pyrazole-piperazine-pyrimidine based pyrrolo[2,1-*f*][1,2,4]triazine derivative (MF: C<sub>26</sub>H<sub>27</sub>FN<sub>10</sub>; MW: 498.57; CAS Number: 1703793-34-3) [178]. **US9944651B2** refers to piperazine-based pyrrolo[2,1-*f*][1,2,4]triazine derivatives for treating conditions like mastocytosis and mast cell diseases by modifying the activity of KIT. It claims avapritinib and its salts [179].

#### 4.59. Selumetinib Sulfate

Selumetinib sulfate (Figure 60) is a benzimidazole derivative (MF: C<sub>17</sub>H<sub>17</sub>BrClFN<sub>4</sub>O<sub>7</sub>S; MW: 555.76; CAS Number: 943332-08-9) [180]. **US7425637B2** reports *N*3-alkylated benzimidazole compounds that inhibit MEK and are helpful to treat cancer and inflammation. It claims selumetinib and its salts [181]. **US9156795B2** claims a stable crystalline hydrogen sulfate salt of selumetinib with enhanced solubility and bioavailability, making it a suitable API to develop desired pharmaceutical dosage forms [182].

#### 4.60. Pemigatinib

Pemigatinib (Figure 61) is a morpholine based pyrrolo[3',2':5,6]pyrido[4,3-*d*]pyrimidine derivative (MF: C<sub>24</sub>H<sub>27</sub>F<sub>2</sub>N<sub>5</sub>O<sub>4</sub>; MW: 487.5; CAS Number: 1513857-77-6) [183]. **US9611267B2** relates to tricyclic compounds as inhibitors of FGFR, useful in ailments facilitated by FGFR malfunctioning like cancer. It claims pemigatinib and its salts [184].

#### 4.61. Tucatinib

Tucatinib (Figure 62) is a quinazoline-oxazoline based triazolo[1,5-*a*]pyridine derivative (MF: C<sub>26</sub>H<sub>24</sub>N<sub>8</sub>O<sub>2</sub>; MW: 480.52; CAS Number: 937263-43-9) [185]. **US8648087B2** discloses *N*4-phenyl-quinazoline-4-amine derivatives as TKIs to treat cancer and inflammation. It claims tucatinib [186].

#### 4.62. Capmatinib Dihydrochloride Monohydrate

Capmatinib dihydrochloride monohydrate (Figure 63) is an imidazo[1,2-*b*][1,2,4]triazine based quinoline derivative (MF: C<sub>23</sub>H<sub>21</sub>Cl<sub>2</sub>FN<sub>6</sub>O<sub>2</sub>; MW: 503.36; CAS Number: 1865733-40-9) [187]. **US7767675B2** reveals imidazotriazines and imidazopyrimidines as MET inhibitors and their pharmaceutical compositions useful in cancer treatment. It claims capmatinib and its salts [188]. **US8420645B2** claims a stable capmatinib dihydrochloride monohydrate with pharmaceutical attributes to manufacture quality pharmaceutical formulations [189].

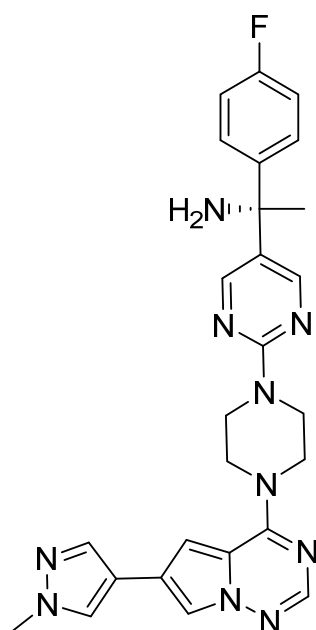


**Figure 59.** Avapritinib ((S)-1-(4-fluorophenyl)-1-(2-(4-(6-(1-methyl-1H-pyrazol-4-yl)pyrrolo[2,1-f][1,2,4]triazin-4-yl)piperazin-yl)pyrimidin-5-yl)ethan-1-amine).

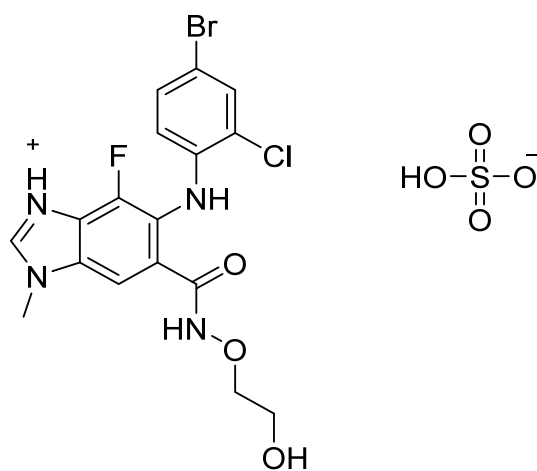


**Figure 60.** Selumetinib sulfate (5-[(4-bromo-2-chlorophenyl)amino]-4-fluoro-6-[(2-hydroxyethoxy) carbonyl]-1-methyl-1H-benzimidazol-3-ium hydrogen sulfate).

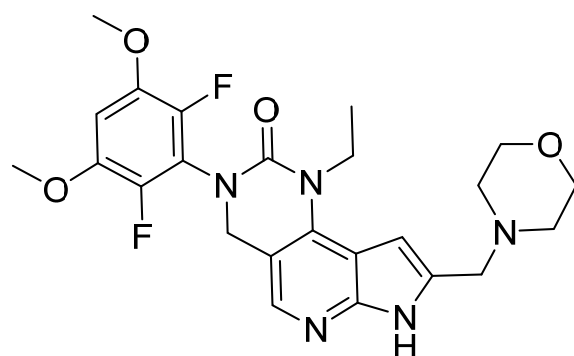


**Figure 61.** Pemigatinib (3-(2,6-difluoro-3,5-dimethoxyphenyl)-1-ethyl-8-(morpholin-4-ylmethyl)-1,3,4,7-tetrahydro-2H-pyrrolo[3',2':5,6]pyrido[4,3-d]pyrimidin-2-one).

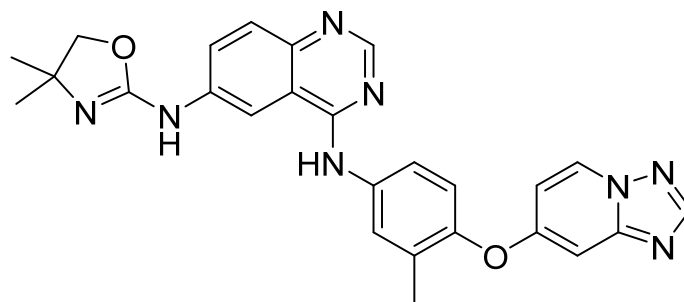


**Figure 62.** Tucatinib (*N*6-(4,4-dimethyl-4,5-dihydro-1,3-oxazol-2-yl)-*N*4-(3-methyl-4-[[1,2,4]triazolo[1,5-*a*]pyridin-7-yloxy]phenyl)quinazoline-4,6-diamine).

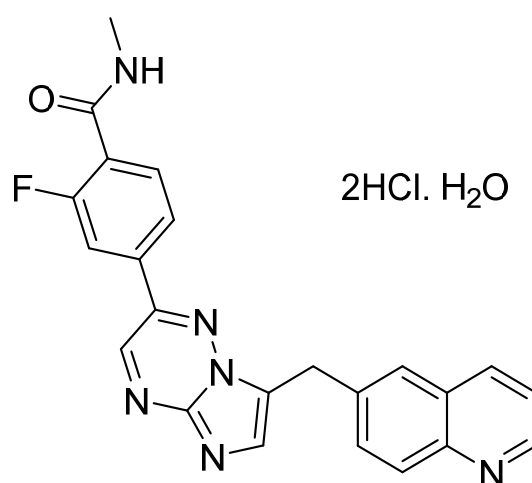


**Figure 63.** Capmatinib dihydrochloride monohydrate (2-fluoro-*N*-methyl-4-(7-[(quinolin-6-yl)methyl]imidazo[1,2-*b*][1,2,4]triazin-2-yl)benzamide dihydrochloride monohydrate).

#### 4.63. Selpercatinib

Selpercatinib (Figure 64) is a pyridine-diazabicycloheptane based pyrazolo[1,5-*a*]pyridine derivative (MF: C<sub>29</sub>H<sub>31</sub>N<sub>7</sub>O<sub>3</sub>; MW: 525.61; CAS Number: 2152628-33-4) [190]. **US10112942B2** uncovers pyrazolo[1,5-*a*]pyridines as RET inhibitors, useful to treat RET-associated diseases. It claims selpercatinib and its salts [191]. **US10584124B2** claims a stable crystalline polymorph of selpercatinib that is useful for developing pharmaceutical formulations [192].

#### 4.64. Ripretinib

Ripretinib (Figure 65) is a naphthyridine based phenylurea derivative (MF: C<sub>24</sub>H<sub>21</sub>BrFN<sub>5</sub>O<sub>2</sub>; MW: 510.36; CAS Number: 1442472-39-0) [193]. **US8461179B1** uncovers dihydronaphthyridine derivatives that inhibit c-KIT and that have utility to treat GIST, mast cell leukemia, or mastocytosis. It claims ripretinib and its salts [194].

#### 4.65. Pralsetinib

Pralsetinib (Figure 66) is a pyridine-pyrimidine based pyrazole derivative (MF: C<sub>27</sub>H<sub>32</sub>FN<sub>9</sub>O<sub>2</sub>; MW: 533.61; CAS Number: 2097132-94-8) [195]. **US10030005B2** discloses pyrazole based RET inhibitors and their pharmaceutical compositions to treat a condition mediated by aberrant RET activity, e.g., cancer. It claims pralsetinib [196].

#### 4.66. Trilaciclib Dihydrochloride

Trilaciclib dihydrochloride (Figure 67) is a piperazine-pyridine based pyrazino[1',2':1,5]pyrrole derivative (MF: C<sub>24</sub>H<sub>30</sub>N<sub>8</sub>O·2HCl; MW: 519.48; CAS Number: 1977495-97-8) [197]. **US8598186B2** reveals tricyclic compounds as CDK inhibitors, which have utility in the



treatment of disorders intervened by CDK malfunction like cancer. It claims trilaciclib and its salts [198].

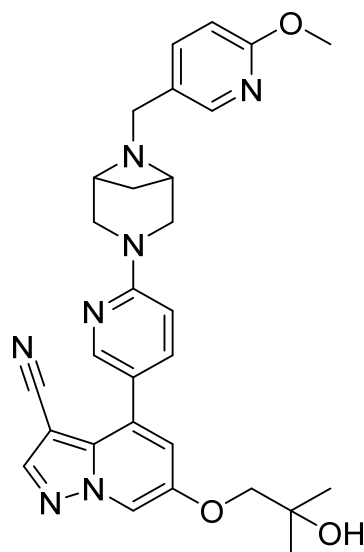


**Figure 64.** Selpercatinib (6-(2-hydroxy-2-methylpropoxy)-4-(6-(6-((6-methoxypyridin-3-yl)methyl)-3,6-diazabicyclo[3.1.1]heptan-3-yl)pyridin-3-yl)pyrazolo[1,5-*a*]pyridine-3-carbonitrile).

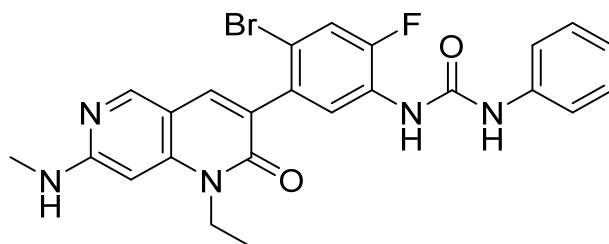


**Figure 65.** Ripretinib (1-(4-bromo-5-[1-ethyl-7-(methylamino)-2-oxo-1,2-dihydro-1,6-naphthyridin-3-yl]-2-fluorophenyl)-3-phenylurea).

#### 4.67. Tepotinib Hydrochloride Monohydrate

Tepotinib hydrochloride monohydrate (Figure 68) is a piperidine-pyrimidine based dihydropyridazine derivative (MF:  $C_{29}H_{28}N_6O_2 \cdot HCl \cdot H_2O$ ; MW: 547.05; CAS Number: 1946826-82-9) [199]. **US8580781B2** reveals certain pyridazinones as MET inhibitors to treat tumors. It claims tepotinibor and its salts [200]. Tepotinib hydrochloride hydrate is claimed explicitly in **US8329692B2** [201].

#### 4.68. Umbralisib Tosylate

Umbralisibtosylate (Figure 69) is a chromen-4-one based pyrazolo[3,4-*d*]pyrimidine derivative (MF:  $C_{38}H_{32}F_3N_5O_6S$ ; 743.75; 1532533-72-4) [202]. **US10570142B2** provides pyrazolo[3,4-*d*]pyrimidines as inhibitors of PI3K $_{\delta}$  and their pharmaceutical compositions to treat PI3K $_{\delta}$  mediated disorders. It claims umbralisib tosylate having at least 95% enantiomeric excess [203]. **US10414773B2** unveils a stable crystalline form of umbralisib tosylate possessing specified particle sizes with enhanced solubility and improved pharmacokinetics. This property makes it suitable to prepare a quality oral dosage form [204].

#### 4.69. Tivozanib Hydrochloride Monohydrate

Tivozanib hydrochloride monohydrate (Figure 70) is an isoxazole base quinoline derivative (MF:  $C_{22}H_{19}ClN_4O_5 \cdot HCl \cdot H_2O$ ; MW: 509.34; CAS Number: 682745-41-1) [205]. **US6821987B2** and **US7211587B2** unveil quinoline derivatives having azolyl group, useful

for treating tumors, chronic rheumatism, psoriasis, and Kaposi's sarcoma. These patents claim tivozanib and its salts [206,207]. **US7166722B2** claims a physically stable crystalline form of tivozanib hydrochloride monohydrate stable under high temperature and humidity. This form is suitable for developing quality dosage forms [208].

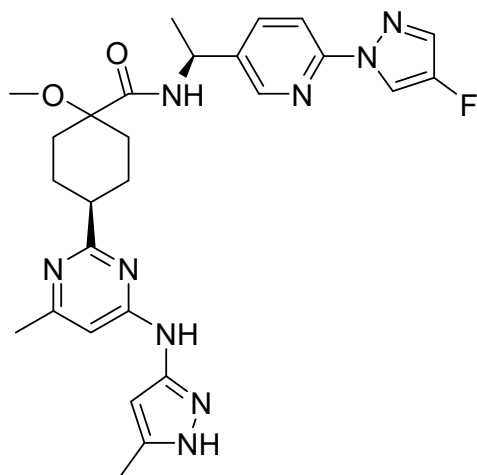


**Figure 66.** Pralsetinib ((Cis)-N-((S)-1-(6-(4-fluoro-1H-pyrazol-1-yl)pyridin-3-yl)ethyl)-1-methoxy-4-(4-methyl-6-(5-methyl-1H-pyrazol-3-ylamino)pyrimidin-2-yl)cyclohexane carboxamide).

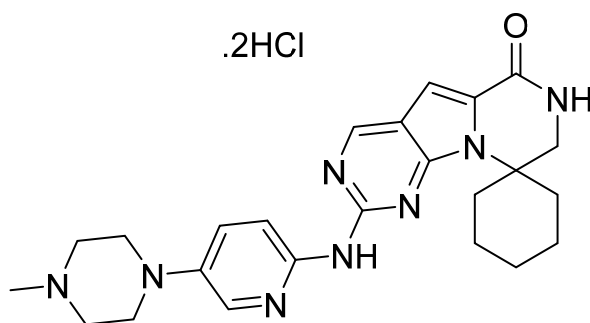


**Figure 67.** Trilaciclib dihydrochloride (2'--[5-(4-methylpiperazin-1-yl)pyridin-2-yl]amino)-7',8'-dihydro-6'H-spiro[cyclohexane-1,9'-pyrazino[1',2':1,5]pyrrolo[2,3-d]pyrimidin]-6'-one).

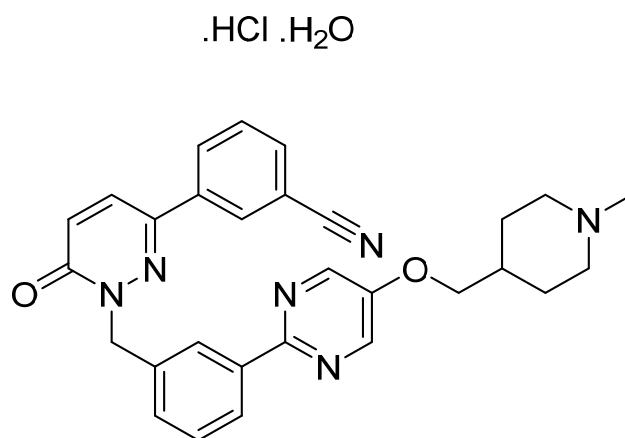


**Figure 68.** Tepotinib hydrochloride monohydrate (3-[1-[(3-[5-[(1-methylpiperidin-4-yl)methoxy]pyrimidin-2-yl]phenyl)methyl]-6-oxo-1,6-dihydropyridazin-3-yl]benzonitrile hydrochloride monohydrate).

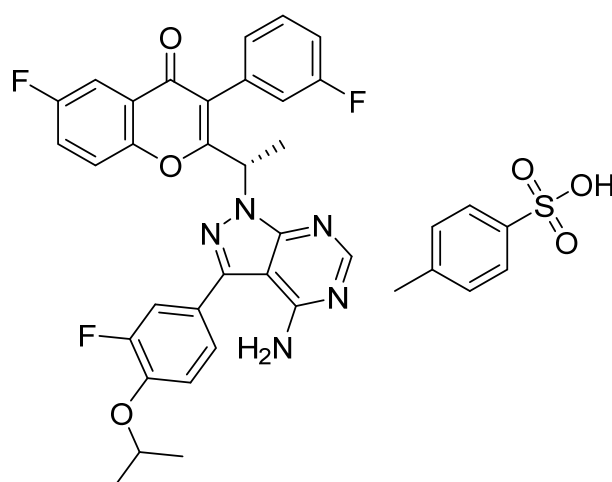


**Figure 69.** Umbralisib tosylate ((S)-2-(1-(4-amino-3-(3-fluoro-4-isopropoxyphenyl)-1H-pyrazolo[3,4-d]pyrimidin-1-yl)-ethyl)-6-fluoro-3-(3-fluorophenyl)-4H-chromen-4-one tosylate)).

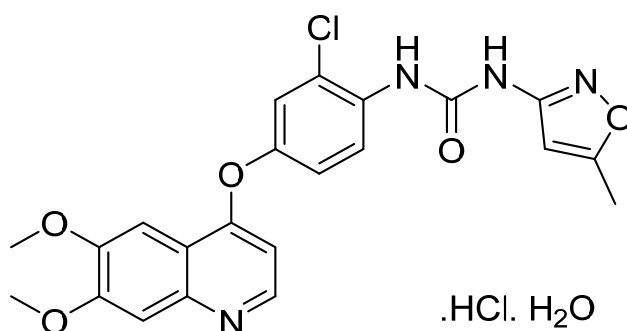


**Figure 70.** Tivozanib hydrochloride monohydrate (1-[2-chloro-4-[(6,7-dimethoxyquinolin-4-yl)oxy]phenyl]-3-(5-methylisoxazol-3-yl)urea hydrochloride monohydrate).

#### 4.70. Infigratinib Phosphate

Infigratinib (Figure 71) is a piperazine based pyrimidine derivative (MF: C<sub>26</sub>H<sub>31</sub>Cl<sub>2</sub>N<sub>7</sub>O<sub>3</sub>·H<sub>3</sub>PO<sub>4</sub>; MW: 658.47; CAS Number: 1310746-10-1) [209]. **US8552002B2** claims infigratinib and its salts [210]. **US9067896B2** claims a monophosphoric acid salt of infigratinib as well as its anhydrous crystalline polymorph (Form A) and amorphous polymorph. The stability and physicochemical parameters of the crystalline Form A were better than other disclosed polymorphs [211].

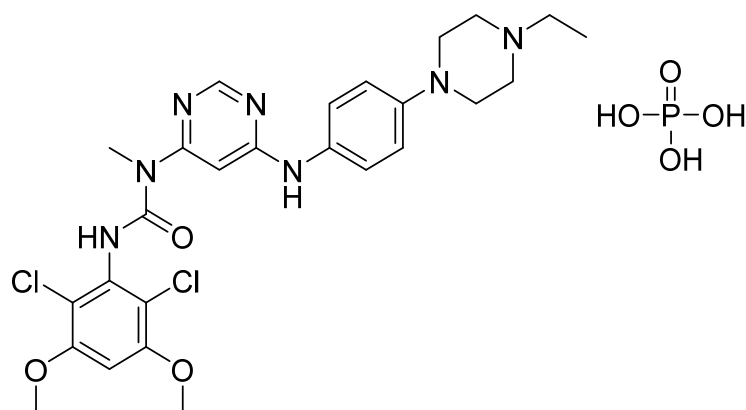


**Figure 71.** Infigratinib phosphate (3-(2,6-dichloro-3,5-dimethoxyphenyl)-1-[6-[4-(4-ethylpiperazin-1-yl)phenylamino]pyrimidin-4-yl]-1-methylurea phosphate).

## 5. Expert Opinion

In 2001, USFDA approved the marketing of the first clinical PKI, imatinib. From 2001 to 31 May 2021, about 70 PKIs have been approved by the USFDA (Table 2). The USFDA has also approved antibodies as PKIs such as trastuzumab and bevacizumab. A few antibodies are also in the clinical trial (amivantamab and patritumab). This review is limited to small molecules as PKIs. Accordingly, USFDA approved antibodies such as PKIs have not been discussed here. The physicochemical properties of about 55 USFDA approved PKIs from 2001 to 2020 have been described in the literature [22,23]. However, these reports are silent about the patent data of the PKIs reported therein.

According to the patent literature, and the data presented in Tables 2 and 3, the major players that developed the marketed PKIs include Novartis (imatinib, lapatinib, everolimus, nilotinib, pazopanib, trametinib, dabrafenib, ceritinib, ribociclib, midostaurin, alpelisib, capmatinib, and infigratinib), Pfizer (tofacitinib, palbociclib, dacomitinib, and lorlatinib), Astrazeneca (gefitinib, osimertinib, acalabrutinib, and selumetinib), Bayers (sorafenib, regorafenib, copanlisib, and larotrectinib), and PF Prism (temsirolimus, crizotinib, axitinib, and bosutinib). Nearly 535 PKs have been reported [6]. However, the major primary target of the approved PKIs includes ALK, BCR-Abel, B-RAF, BTK, CDK, EGFR, JAK, MEK, PDGFR, PI3K, RET, and VEGFR (Table 2). Accordingly, there remains a large number of unexplored PKs. Some PKs have specificity for multiple kinases and are called multikinase inhibitors (MKIs), such as sunitinib, regorafenib, imatinib, sorafenib, axitinib, lenvatinib, cabozantinib, vandetanib, and pazopanib. The MKIs are supposed to reduce the chances of developing resistance. However, they are also linked to causing adverse effects in patients, for example, hypertension, gastric upset, and dermatological reactions [212]. The development of the covalent PKIs (ibrutinib, dacomitinib, osimertinib, afatinib, and neratinib) had been an unwilling strategy because they can bind to certain proteins and cause toxicity. Furthermore, the allosteric PKIs (trametinib, asciminib, and selumetinib) are considered better than covalent inhibitors as they are not supposed to bind with other proteins. However, many new kinases have been identified possessing cysteine residues at their active sites. Therefore, the design of potent and selective covalent inhibitors may be useful against such kinases [213,214]. The pharmaceutical industries are trying to develop more potent and safer PKIs that can be used to treat many more PKs associated disorders with fewer adverse events [23]. Some example of PKIs, which are under development and/or waiting for the USFDA approval, include abrocitinib, belumosudil, dovitinib, sitravatinib, abivertinib, enzastaurin, rivoceranib (apatinib), asciminib, ensartinib, mobocertinib, momelotinib, pacritinib, quizartinib, vorolanib, GLPG3970, CA-4948, BAY1834845, BAY1830839, and PF-06650833 [213,214].

The PKIs contain one or more heterocyclic moieties in their structure that can explain the difference in their binding to the target and thus the spectrum of activity. The primary heterocyclic moieties include quinazoline, quinoline, isoquinoline, pyridine, pyrimidine, pyrazole, benzimidazole, indazole, imidazole, indole, carbazole, or their fused structures. This observation suggests that many clinical PKIs have been developed by the chemical modification of a formerly approved drug, and PKs are promiscuous targets. Further, most of the PKIs are marketed as acid-addition salts (hydrochloride, mesylate, tosylate, phosphate, malate, citrate, esylate, fumarate, succinate, and sulfate). This observation indicates the basic nature of the chemical nucleus of the PKIs.

The majority of the PKIs are approved to treat cancer and inflammatory disorders. Some of the PKIs have shown efficacy towards autoimmune diseases, Alzheimer's disease (neflamapimod, tideglusib, and saracitinib), and Parkinson's disease (DNL201). It is also expected that PKIs of PKC/WNK that control the activity of ion transporters may be developed to treat hypertension [214].

The malignant cells have genomic instability, which may cause the development of resistance to PKIs. This phenomenon is the reason for developing 2nd, 3rd, and later generations of PKIs targeting the equivalent PKs and their related disorders [212]. To combat resistance development, scientists are exploring different chemical templates and

pharmacophores to develop novel PKIs [22]. Besides, inflammatory conditions do not exhibit genomic instability. Therefore, the PKIs, which are approved to treat inflammatory disorders, seldom demonstrate the development of resistance [22,23].

The main marketed dosage form of about 66 USFDA approved PKIs is either a tablet or capsule (Table 2). These are solid dosage forms. The quality of the formulation of a solid dosage form depends upon the solid-state properties (stability, solubility, compressibility, etc.) of the drug [215]. Therefore, many patents related to salts and polymorphs (mostly crystalline forms) of the USFDA approved PKIs have been obtained by the innovator companies. The innovator companies have done this to capture the market for a longer time.

The development of the PKIs is considered a medical breakthrough. However, the prices of these therapeutics cause financial toxicity. The financial burden can make the patients non-compliant with the treatment instructions as they may take lower doses than the prescribed doses. This causes failure of the treatment [216,217]. One way to avoid financial toxicity is to develop the generic version of a drug [218]. Currently, seven PKIs have been genericized (imatinib, erlotinib, sorafenib, dasatinib, lapatinib, temsirolimus, and everolimus) (Table 3). These generic versions must have lower prices than the innovator products. The data given in Table 3 also suggest that twelve more PKIs (gefitinib, sunitinib, pazopanib, vandetanib, axitinib, bosutinib, tofacitinib, idelalisib, nintedanib, lenvatinib, midostaurin, and neratinib) may be genericized by 2025 due to basic/compound/governing patent expiry or expiry of the drug exclusivity. It means by the end of 2025, 19 PKIs will have their generic version in the USA market. Besides, it is also expected that the generic version of about 48 PKIs will be available in the USA market by the end of 2030. Thus, it is hoped that the generic availability of these PKIs will reduce the financial toxicity on a patient.

Although great strides have been made in developing small molecule such as PKIs during the past 20 years, this field is still in its infancy. PKs are ubiquitous, and hence specificity has always been an issue regarding the design of new therapies targeting them. The major disadvantage of the existing PKIs is that they target a minor portion of the kinome, with countless clinically significant kinases missing validated inhibitors [22,23]. There are essential kinases without any inhibitors, and this is a critical area for further research. As the field advances during the next 20 years, one can anticipate that PKIs with many scaffolds, chemotypes, and pharmacophores will be developed. Other innovative strategies are also expected soon. A summary of the PKIs is provided in Figure 72.

In conclusion, there is a huge scope for discovering PKIs, and it will dominate other cancer discovery strategies for decades. The rate of discovery of better and selective PKIs having less propensity for resistance development will be faster than the last two decades because of the better understanding of the molecular and structural aspects of the human kinases. The development of PKIs to treat hypertension, Alzheimer's disease, and Parkinson's disease are foreseeable.

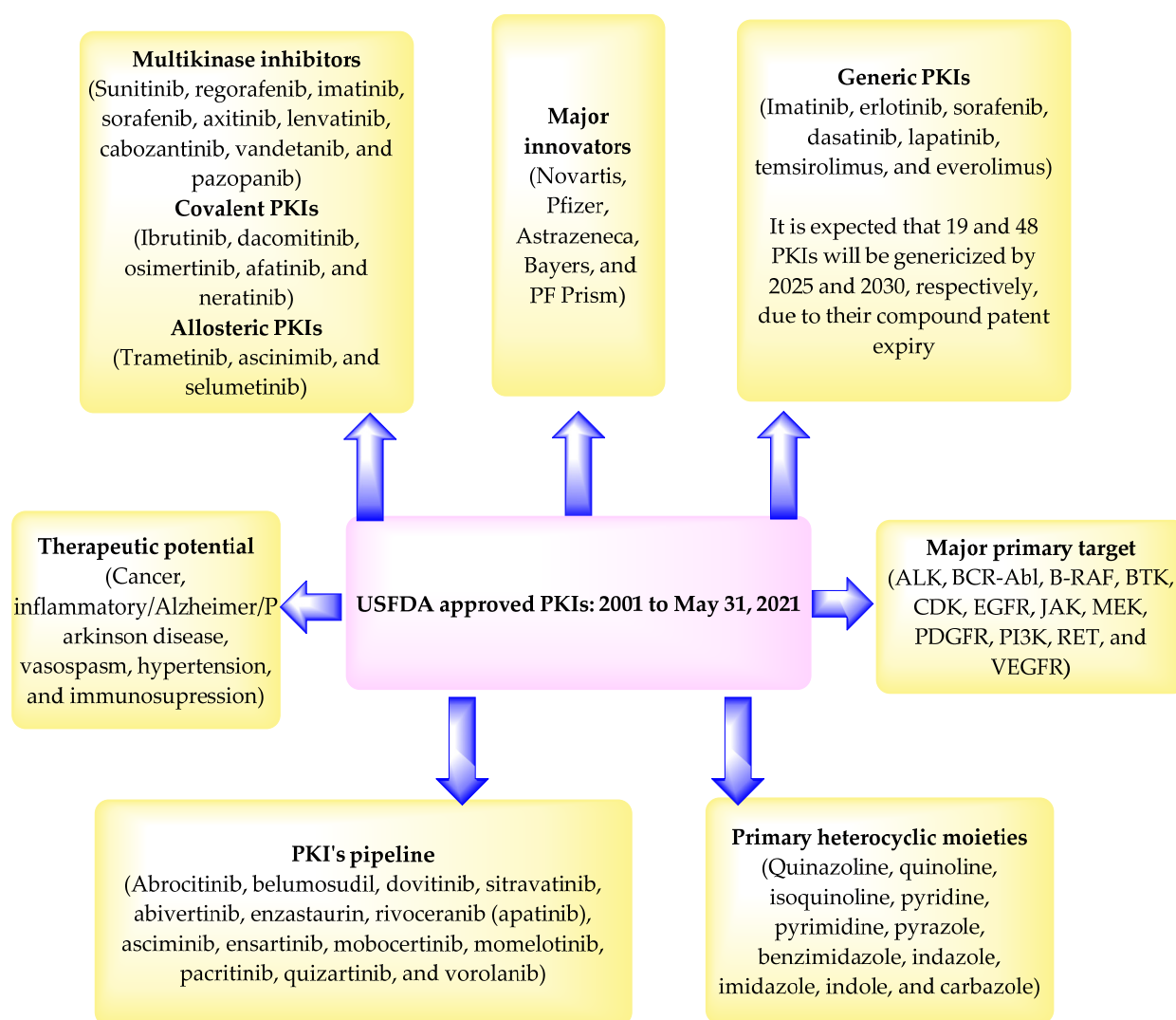


**Figure 72.** Summary of the USFDA approved PKIs.

**Author Contributions:** Conceptualization, M.I. and S.A.K.; methodology, S.M.B.A. and M.A. (Majid Alhomrani); validation, D.U.M. and E.H.A.; formal analysis, A.S.A. (Abdulhakeem S. Alamri), M.T., A., S.I.A., M.A.B. and A.K.A.; resources, W.F.A. and O.A.; data curation, M.A. (Mohammed AlMotairi) and A.S.A. (Ahmed Subeh Alshrari); writing—original draft preparation, M.I.; writing—review and editing, S.A.K., D.U.M., M.T., A.; visualization, S.I.A. and M.A.B.; supervision, M.I. and S.A.K.; project administration, Y.M.; funding acquisition, A.A. All authors have read and agreed to the published version of the manuscript.

**Funding:** This research received no external funding.

**Institutional Review Board Statement:** Not applicable.

**Informed Consent Statement:** Not applicable.

**Data Availability Statement:** Data sharing not applicable.

**Acknowledgments:** The authors are thankful to AlMaarefa University, Riyadh for providing support to write this review article.

**Conflicts of Interest:** The authors declare no conflict of interest.

## Abbreviations

ALK: Anaplastic lymphoma kinase; ALL: Acute lymphoblastic leukemia; AML: Acute myelogenous leukemia; API: Active pharmaceutical ingredient; ARCC: Advanced renal cell carcinoma; ATC: Anaplastic thyroid cancer; ATP: Adenosine triphosphate; BCR-Abl: Breakpoint cluster region/abl oncogene; BRAF/B-raf: Murine sarcoma viral oncogene homolog; BTK: Bruton's tyrosine kinase; CDK: Cyclin-dependent protein kinase; CLL: Chronic lymphocytic leukemia; CML: Chronic myeloid leukemia; CSF1R: Colony stimulating factor 1 receptor; DTC: Differentiated thyroid cancer; EGFR: Epidermal growth factor receptor; FKBP12/mTOR: FK Binding Protein-12/mammalian target of rapamycin; FL: Follicular lymphoma; Flt3: fms-like tyrosine kinase 3; GISTs: Gastrointestinal stromal tumors; GTP: Guanosine triphosphate; HCC: Hepatocellular carcinoma; HER-1/HER-2: Human epidermal growth factor receptor 1/2; HGFR: Hepatocyte growth factor receptor; ILDs: Interstitial lung disease; IPF: Idiopathic pulmonary fibrosis; ITP: Immune thrombocytopenic purpura; JAK: Janus kinase; MAPK/MEK1/2: Mitogen-activated protein kinase kinase; MAT: Monoamine transporter; MCL: Mantle cell lymphoma; MTC: Medullary thyroid cancer; mUC: Metastatic urothelial carcinoma); MZL: Marginal zone lymphoma; NF1: Neurofibromatosis type 1; NSCLC: Non-small cell lung cancer; PDGFR: Platelet-derived growth factor receptor; Ph<sup>+</sup>-ALL: Philadelphia chromosome-Positive Acute lymphoblastic leukemia; Ph<sup>+</sup>-CML: Philadelphia chromosome-positive chronic myeloid leukemia; PI3K: Phosphatidylinositol 3-kinase; PKIs: Protein kinase inhibitors; PKs: Protein kinases; pNET: Primitive neuroectodermal tumor; RCC: Renal cell carcinoma; SLL: Small lymphocytic lymphoma; SSc: Systemic sclerosis; STS: Soft-tissue sarcomas; TKI: Tyrosine Kinase inhibitors; Tyk2: Tyrosine kinase; USFDA: United States Food and Drug Administration; VEGFR: Vascular endothelial growth factor receptor.

## References

1. Keohane, E.M.; Otto, C.N.; Walenga, J.M. *Rodak's Hematology-E-Book: Clinical Principles and Applications*; Elsevier Health Sciences: Amsterdam, The Netherlands, 2019.
2. Prescott, J.C.; Braisted, A. Identification of Kinase Inhibitors. PCT Patent Application Publication Number WO2005034840A2, 21 April 2005.
3. Charrier, J.D.; Durrant, S. Protein Kinase Inhibitors. U.S. Patent Application Publication Number US20120028966A1, 2 February 2012.
4. Liu, C.; Ke, P.; Zhang, J.; Zhang, X.; Chen, X. Protein kinase inhibitor peptide as a tool to specifically inhibit protein kinase A. *Front. Physiol.* **2020**, *11*, 574030. [CrossRef] [PubMed]
5. Plowman, G.; Whyte, D.; Manning, G.; Sudarsanam, S.; Martinez, R. Novel human protein kinases and protein kinase-like enzymes. U.S. Patent Application Publication Number US20040048310A1, 11 March 2004.
6. Buljan, M.; Ciuffa, R.; van Drogen, A.; Vichalkovski, A.; Mehnert, M.; Rosenberger, G.; Lee, S.; Varjosalo, M.; Pernas, L.E.; Spegg, V.; et al. Kinase interaction network expands functional and disease roles of human kinases. *Mol. Cell* **2020**, *79*, 504–520.e9. [CrossRef] [PubMed]
7. Wilson, L.J.; Linley, A.; Hammond, D.E.; Hood, F.E.; Coulson, J.M.; MacEwan, D.J.; Ross, S.J.; Slupsky, J.R.; Smith, P.D.; Evers, P.A.; et al. New perspectives, opportunities, and challenges in exploring the human protein kinome. *Cancer Res.* **2018**, *78*, 15–29. [CrossRef] [PubMed]
8. Arencibia, J.M.; Pastor-Flores, D.; Bauer, A.F.; Schulze, J.O.; Biondi, R.M. AGC protein kinases: From structural mechanism of regulation to allosteric drug development for the treatment of human diseases. *Biochim. Biophys. Acta* **2013**, *1834*, 1302–1321. [CrossRef]
9. Junho, C.V.C.; Caio-Silva, W.; Trentin-Sonoda, M.; Carneiro-Ramos, M.S. An overview of the role of calcium/calmodulin-dependent protein kinase in cardiorenal syndrome. *Front. Physiol.* **2020**, *11*, 735. [CrossRef]
10. Schitteck, B.; Sinnberg, T. Biological functions of casein kinase 1 isoforms and putative roles in tumorigenesis. *Mol. Cancer* **2014**, *13*, 231. [CrossRef]
11. Strang, B.L. RO0504985 is an inhibitor of CMGC kinase proteins and has anti-human cytomegalovirus activity. *Antivir. Res.* **2017**, *144*, 21–26. [CrossRef]
12. Sawa, M.; Masai, H. Drug design with Cdc7 kinase: A potential novel cancer therapy target. *Drug Des. Devel. Ther.* **2009**, *2*, 255–264. [CrossRef]
13. Matrone, C.; Petrillo, F.; Nasso, R.; Ferretti, G. Fyn tyrosine kinase as harmonizing factor in neuronal functions and dysfunctions. *Int. J. Mol. Sci.* **2020**, *21*, 4444. [CrossRef]
14. Petrie, E.J.; Hildebrand, J.M.; Murphy, J.M. Insane in the membrane: A structural perspective of MLKL function in necroptosis. *Immunol. Cell Biol.* **2017**, *95*, 152–159. [CrossRef]

15. Rauch, J.; Volinsky, N.; Romano, D.; Kolch, W. The secret life of kinases: Functions beyond catalysis. *Cell Commun. Signal.* **2011**, *9*, 23. [CrossRef]
16. Ochoa, D.; Bradley, D.; Beltrao, P. Evolution, dynamics and dysregulation of kinase signalling. *Curr. Opin. Struct. Biol.* **2018**, *48*, 133–140. [CrossRef]
17. Brognard, J.; Hunter, T. Protein kinase signaling networks in cancer. *Curr. Opin. Genet. Dev.* **2011**, *21*, 4–11. [CrossRef]
18. Oprea, T.I.; Bologa, C.G.; Brunak, S.; Campbell, A.; Gan, G.N.; Gaulton, A.; Gomez, S.M.; Guha, R.; Hersey, A.; Holmes, J.; et al. Unexplored therapeutic opportunities in the human genome. *Nat. Rev. Drug Discov.* **2018**, *17*, 317–332. [CrossRef]
19. Essegian, D.; Khurana, R.; Stathias, V.; Schürer, S.C. The clinical kinase index A method to prioritize understudied kinases as drug targets for the treatment of cancer. *Cell Rep. Med.* **2020**, *1*, 100128. [CrossRef]
20. Ferguson, F.M.; Gray, N.S. Kinase inhibitors: The road ahead. *Nat. Rev. Drug Discov.* **2018**, *17*, 353–377. [CrossRef]
21. Klaeger, S.; Heinzlmeier, S.; Wilhelm, M.; Polzer, H.; Vick, B.; Koenig, P.A.; Reinecke, M.; Ruprecht, B.; Petzoldt, S.; Meng, C.; et al. The target landscape of clinical kinase drugs. *Science* **2017**, *358*, eaan4368. [CrossRef]
22. Roskoski, R., Jr. Properties of FDA-approved small molecule protein kinase inhibitors. *Pharmacol. Res.* **2019**, *144*, 19–50. [CrossRef]
23. Roskoski, R., Jr. Properties of FDA-approved small molecule protein kinase inhibitors: A 2021 update. *Pharmacol. Res.* **2021**, *165*, 105463. [CrossRef]
24. Iqbal, N.; Iqbal, N. Imatinib: A breakthrough of targeted therapy in cancer. *Chemother. Res. Pract.* **2014**, *2014*, 357027. [CrossRef]
25. Zimmermann, J. Pyrimidine Derivatives and Processes for the Preparation Thereof. U.S. Patent Number US5521184A, 28 May 1996.
26. Zimmermann, J.; Sutter, B.; Buerger, H.M. Crystal Modification of a *N*-Phenyl-2-Pyrimidineamine Derivative, Processes for its Manufacture and Its Use. U.S. Patent Number USRE43932E1, 15 January 2013.
27. Sim, E.H.; Yang, I.A.; Wood-Baker, R.; Bowman, R.V.; Fong, K.M. Gefitinib for advanced non-small cell lung cancer. *Cochrane Database Syst. Rev.* **2018**, *1*, CD006847. [CrossRef]
28. Barker, A.J. Quinazoline Derivatives Useful for Treatment of Neoplastic Disease. U.S. Patent Number US5457105A, 10 October 1995.
29. Gibson, K.H. Quinazoline Derivatives. U.S. Patent Number US5770599A, 23 June 1998.
30. Steins, M.; Thomas, M.; Geibler, M. Erlotinib. *Recent Results Cancer Res.* **2018**, *211*, 1–17. [CrossRef]
31. Schnur, R.C.; Arnold, L.D. Alkynyl and Azido-Substituted 4-Anilinoquinazolines. U.S. Patent Number USRE41065E1, 29 December 2009.
32. Norris, T.; Raggon, J.W.; Connell, R.D.; Moyer, J.D.; Morin, M.J.; Kajiji, S.M.; Foster, B.A.; Ferrante, K.J.; Silberman, S.L. Stable Polymorph on *N*-(3-ethynylphenyl)-6,7-Bis (2methoxyethoxy)-4-Quinazolinamine Hydrochloride, Methods of Production, and Pharmaceutical Uses Thereof. U.S. Patent Number US6900221B1, 31 May 2005.
33. Chen, F.; Fang, Y.; Zhao, R.; Le, J.; Zhang, B.; Huang, R.; Chen, Z.; Shao, J. Evolution in medicinal chemistry of sorafenib derivatives for hepatocellular carcinoma. *Eur. J. Med. Chem.* **2019**, *179*, 916–935. [CrossRef]
34. Riedl, B.; Dumas, J.; Khire, U.; Lowinger, T.B.; Scott, W.J.; Smith, R.A.; Wood, J.E.; Monahan, M.K.; Natero, R.; Renick, J.; et al. Omega-Carboxyaryl Substituted Diphenyl Ureas as Raf Kinase Inhibitors. U.S. Patent Number US7235576B1, 26 June 2007.
35. Alfons, T.G.; Jana, L. Hermodynamically Stable Form of a Tosylate Salt. U.S. Patent Number US8877933B2, 27 August 2009.
36. Carlisle, B.; Demko, N.; Freeman, G.; Hakala, A.; MacKinnon, N.; Ramsay, T.; Hey, S.; London, A.J.; Kimmelman, J. Benefit, Risk, and Outcomes in Drug Development: A Systematic Review of Sunitinib. *J. Natl. Cancer Inst.* **2015**, *108*, djv292. [CrossRef]
37. Tang, P.C.; Miller, T.A.; Li, X.; Sun, L.; Wei, C.C.; Shirazian, S.; Liang, C.; Vojtkovsky, T.; Nematalla, A.S.; Hawley, M. Pyrrole Substituted 2-Indolinone Protein Kinase Inhibitors. U.S. Patent Number US7125905B2, 11 August 2005.
38. Tang, P.C.; Miller, T.A.; Li, X.; Sun, L.; Wei, C.C.; Shirazian, S.; Liang, C.; Vojtkovsky, T.; Nematalla, A.S.; Hawley, M. Pyrrole Substituted 2-Indolinone Protein Kinase Inhibitors. U.S. Patent Number US6573293B2, 24 October 2002.
39. Korashy, H.M.; Rahman, A.F.; Kassem, M.G. Dasatinib. *Profiles Drug Subst. Excip. Relat. Methodol.* **2014**, *39*, 205–237. [CrossRef]
40. Das, J.; Padmanabha, R.; Chen, P.; Norris, D.J.; Doweiko, A.M.P.; Barrish, J.C.; Wityak, J. Cyclic Protein Tyrosine Kinase Inhibitors. U.S. Patent Number US6596746B1, 22 July 2003.
41. Lajeunesse, J.; Dimarco, J.D.; Galella, M.; Chidambaram, R. Process for Preparing 2-Aminothiazole-5-Aromatic Carboxamides as Kinase Inhibitors. U.S. Patent Number US7491725B2, 17 February 2009.
42. Gross-Goupil, M.; Bernhard, J.C.; Ravaud, A. Lapatinib and renal cell carcinoma. *Expert Opin. Investig. Drugs* **2012**, *21*, 1727–1732. [CrossRef]
43. Carter, M.C.; Cockerill, G.S.; Lackey, K.E. Bicyclic Heteroaromatic Compounds as Protein Tyrosine Kinase Inhibitors. U.S. Patent Number US8513262B2, 20 September 2013.
44. McClure, M.S.; Osterhout, M.H.; Roschangar, F.; Sacchetti, M.J. Quinazoline Ditosylate Salt Compounds. U.S. Patent Number US7157466B2, 2 January 2007.
45. Bukowski, R.M. Temsirolimus: A safety and efficacy review. *Expert Opin. Drug Saf.* **2012**, *11*, 861–879. [CrossRef]
46. Skotnicki, J.S.; Leone, C.L.; Schiehsler, G.A. Rapamycin Hydroxyesters. U.S. Patent Number USRE44768E1, 18 February 2014.
47. Guarini, A.; Minoia, C.; Giannoccaro, M.; Rana, A.; Iacobazzi, A.; Lapietra, A.; Raimondi, A.; Silvestris, N.; Gadaleta, C.D.; Ranieri, G. mTOR as a target of everolimus in refractory/relapsed Hodgkin lymphoma. *Curr. Med. Chem.* **2012**, *19*, 945–954. [CrossRef]
48. Cottens, S.; Sedrani, R. O-alkylated Rapamycin Derivatives and Their Use, Particularly as Immunosuppressants. U.S. Patent Number US5665772A, 9 September 1997.



49. Vaid, A. Nilotinib as first-line therapy for chronic myeloid leukemia. *Indian J. Cancer* **2011**, *48*, 438–445. [CrossRef]
50. Breitenstein, W.; Furet, P.; Jacob, S.; Manley, P.W. Inhibitors of Tyrosine Kinases. U.S. Patent Number US7169791B2, 30 January 2007.
51. Manley, P.W.; Shieh, W.C.; Sutton, P.A.; Karpinski, P.P.H.; Wu, R.R.; Monnier, S.M.; Brozio, J. Salts of 4-methyl-*N*-[3-(4-methyl-imidazol-1-yl)-5-trifluoromethyl-phenyl]-3-(4-pyridin-3-yl-pyrimidin-2-ylamino)-benzamide. U.S. Patent Number US8163904B2, 24 April 2012.
52. Manley, P.W.; Shieh, W.C.; Sutton, P.A.; Karpinski, P.P.H.; Wu, R.R.; Monnier, S.M.; Brozio, J. Crystalline Forms of 4-methyl-*N*-[3-(4-methyl-imidazol-1-yl)-5-trifluoromethyl-phenyl]-3-(4-pyridin-3-yl-pyrimidin-2-ylamino)-benzamide. U.S. Patent Number US8415363B2, 9 April 2013.
53. Schutz, F.A.; Choueiri, T.K.; Sternberg, C.N. Pazopanib: Clinical development of a potent anti-angiogenic drug. *Crit. Rev. Oncol. Hematol.* **2011**, *77*, 163–171. [CrossRef] [PubMed]
54. Bloor, A.; Cheung, M.; Davis, R.; Harris, P.A.; Hinkle, K.; Mook, R.A., Jr.; Stafford, J.A.; Veal, J.M. Pyrimidineamines as Angiogenesis Modulators. U.S. Patent Number US7105530B2, 12 September 2006.
55. Bloor, A.; Cheung, M.; Hinkle, K.; Hinkle, K.; Veal, J.M.; Harris, P.A.; Mook, R.A., Jr.; Stafford, J.A. Chemical Compounds. U.S. Patent Number US8114885B2, 12 September 2012.
56. Sim, M.W.; Cohen, M.S. The discovery and development of vandetanib for the treatment of thyroid cancer. *Expert Opin. Drug Discov.* **2014**, *9*, 105–114. [CrossRef] [PubMed]
57. Thomas, A.P.; Johnstone, C.; Clayton, E.; Stokes, E.S.E.; Lohmann, J.J.M.; Hennequin, L.F.A. Quinazoline Derivatives and Pharmaceutical Compositions Containing Them. U.S. Patent Number USRE42353E1, 10 May 2011.
58. Kim, A.; Cohen, M.S. The discovery of vemurafenib for the treatment of BRAF-mutated metastatic melanoma. *Expert Opin. Drug Discov.* **2016**, *11*, 907–916. [CrossRef] [PubMed]
59. Artis, D.R.; Bollag, G.; Bremer, R.; Cho, H.; Hirth, K.P.; Ibrahim, P.N.; Tsai, J.; Zhang, C.; Zhang, J. Compounds and Methods for Kinase Modulation, and Indications Therefor. U.S. Patent Number US8143271B2, 27 March 2012.
60. Roskoski, R., Jr. The preclinical profile of crizotinib for the treatment of non-small-cell lung cancer and other neoplastic disorders. *Expert Opin. Drug Discov.* **2013**, *8*, 1165–1179. [CrossRef] [PubMed]
61. Ia, L.; Kung, P.P.; Shen, H.; Tran, D.M.; Cui, J.J.; Funk, L.A.; Meng, J.J.; Nambu, M.D.; Pairish, M.A. Enantiomerically Pure Aminoheteroaryl Compounds as Protein Kinase Inhibitors. U.S. Patent Number US7858643B2, 28 December 2010.
62. Cui, J.J.; Tran, D.M.B. Polymorphs of a c-MET/HGFR Inhibitor. U.S. Patent Number US8217057B2, 10 July 2012.
63. Naqvi, K.; Verstovsek, S.; Kantarjian, H.; Ravandi, F. A potential role of ruxolitinib in leukemia. *Expert Opin. Investig. Drugs* **2011**, *20*, 1159–1166. [CrossRef]
64. Rodgers, J.D.; Shepard, S. Heteroaryl Substituted pyrrolo[2,3-*b*]pyridines and pyrrolo[2,3-*b*]pyrimidines as Janus Kinase Inhibitors. U.S. Patent Number US7598257B2, 6 October 2009.
65. Li, H.Y.; Rodgers, J.D. Salts of the Janus kinase Inhibitor (R)-3-(4-(7H-pyrrolo[2,3-*d*]pyrimidin-4-yl)-1H-pyrazol-1-yl)-3-cyclopentylpropanenitrile. U.S. Patent Number US8722693B2, 13 May 2014.
66. Zakharia, Y.; Zakharia, K.; Rixe, O. Axitinib: From preclinical development to future clinical perspectives in renal cell carcinoma. *Expert Opin. Drug Discov.* **2015**, *10*, 925–935. [CrossRef]
67. Bender, S.L.; Borchardt, A.J.; Collins, M.R.; Hua, Y.; Johnson, M.D.; Johnson, T.O., Jr.; Luu, H.T.; Palmer, C.L.; Reich, S.H.; Tempczyk-Russell, A.M.; et al. Indazole Compounds and Pharmaceutical Compositions for Inhibiting Protein Kinases, and Methods for Their Use. U.S. Patent Number US6534524B1, 18 March 2003.
68. Campeta, A.M.; Chekal, B.P.; Singer, R.A. Crystalline Forms of 6-[2-(methylcarbamoyl) phenylsulfanyl]-3-*E*-[2-(pyridin-2-yl)ethenyondazole Suitable for the Treatment of Abnormal Cell Growth in Mammals. U.S. Patent Number US8791140B2, 29 July 2014.
69. Quintás-Cardama, A.; Kantarjian, H.; Cortes, J. Bosutinib for the treatment of chronic myeloid leukemia in chronic phase. *Drugs Today (Barc)*. **2012**, *48*, 177–188. [CrossRef]
70. Berger, D.M.; Floyd, M.B.; Frost, P.; Hamann, P.R.; Tsou, H.R.; Wissner, A.; Zhang, N. Substituted 3-cyanoquinolines. U.S. Patent Number USRE42376E, 17 May 2011.
71. Feigelson, G.; Strong, H.; Wen, H.; Tesconi, M.S. Crystalline Forms of 4-[(2,4-dichloro-5-methoxyphenyl)amino]-6-methoxy-7-[3-(4-methyl-1-piperazinyl)propoxy]-3 Quinolinecarbonitrile and Methods of Preparing the Same. U.S. Patent Number US7767678B2, 3 August 2010.
72. Miura, K.; Satoh, M.; Kinouchi, M.; Yamamoto, K.; Hasegawa, Y.; Philchenkov, A.; Kakugawa, Y.; Fujiya, T. The preclinical development of regorafenib for the treatment of colorectal cancer. *Expert Opin. Drug Discov.* **2014**, *9*, 1087–1101. [CrossRef]
73. Boyer, S.; Dumas, J.; Riedl, B.; Wilhelm, S. Fluoro Substituted omega-carboxyaryl Diphenyl Urea for the Treatment and Prevention of Diseases and Conditions. U.S. Patent Number US8637553B2, 28 January 2014.
74. Grunenberg, A.; Keil, B.; Stiehl, J.; Tenbrieg, K. 4-[4-([4-chloro-3-(trifluoromethyl) phenyl] carbamoyl) amino]-3-fluorophenoxy]-*N*-methylpyridine-2-carboxamide Monohydrate. U.S. Patent Number US9957232B2, 1 May 2018.
75. Kaur, K.; Kalra, S.; Kaushal, S. Systematic review of tofacitinib: A new drug for the management of rheumatoid arthritis. *Clin. Ther.* **2014**, *36*, 1074–1086. [CrossRef]
76. Blumenkopf, T.A.; Flanagan, M.E.; Munchhof, M.J. Pyrrolo [2,3-*d*]pyrimidine Compounds. U.S. Patent Number USRE41783E, 28 September 2010.

77. Flanagan, M.E.; Li, Z.J. Crystalline 3-[4-methyl-3-[methyl-(7H-pyrrolo [2,3-*d*]pyrimidin-4-yl)-amino]-piperidin-1-yl]-3-oxo-propionitrile Citrate. U.S. Patent Number US6965027B2, 15 November 2005.
78. Grassi, P.; Verzoni, E.; Ratta, R.; Mennitto, A.; de Braud, F.; Procopio, G. Cabozantinib in the treatment of advanced renal cell carcinoma: Design, development, and potential place in the therapy. *Drug Des. Devel. Ther.* **2016**, *10*, 2167–2172. [CrossRef]
79. Chan, D.S.M.; Forsyth, T.P.; Khoury, R.G.; Leahy, J.W.; Mann, L.W.; Nuss, J.M.; Parks, J.J.; Wang, Y.; Xu, W.; Bannen, L.C.; et al. c-Met Modulators and Methods of Use. U.S. Patent Number US7579473B2, 28 May 2009.
80. Brown, A.S.C.; Gallagher, W.P.; Lamb, P. (L)-malate Salt of *N*-(4-[[6,7-bis (methoxy) quinolin-4-yl] oxy] phenyl)-*N'*-(4-fluorophenyl) cyclopropane-1, 1-dicarboxamide. U.S. Patent Number US8877776B2, 4 November 2014.
81. Tan, F.H.; Putoczki, T.L.; Stylli, S.S.; Luwor, R.B. Ponatinib: A novel multi-tyrosine kinase inhibitor against human malignancies. *Oncol. Targets Ther.* **2019**, *12*, 635–645. [CrossRef]
82. Dalgarno, D.C.; Huang, W.S.; Qi, J.; Sawyer, T.K.; Shakespeare, W.C.; Sundaramoorthi, R.; Wang, Y.; Zhu, X.; Zou, D.; Metcalf, C.A., III; et al. Substituted Acetylenic imidazo[1,2-*b*]pyridazine Compounds as Kinase Inhibitors. U.S. Patent Number US8114874B2, 14 February 2012.
83. Chaber, J.J.; Murray, C.K.; Rozamus, L.W.; Sharma, P. Crystalline Forms of 3-(imidazo[1,2-*b*] pyridazin-3-ylethynyl)-4-methyl-*N*-{4-[(4-methylpiperazin-1-yl) methyl]-3-(trifluoromethyl)phenyl}benzamide and Its Mono Hydrochloride Salt. U.S. Patent Number US9493470B2, 15 November 2016.
84. Jeanson, A.; Boyer, A.; Greillier, L.; Tomasini, P.; Barlesi, F. Therapeutic potential of trametinib to inhibit the mutagenesis by inactivating the protein kinase pathway in non-small cell lung cancer. *Expert Rev. Anticancer Ther.* **2019**, *19*, 11–17. [CrossRef]
85. Abe, H.; Hayakawa, K.; Hori, Y.; Iida, T.; Kawasaki, H.; Kikuchi, S.; Kurachi, H.; Nanayama, T.; Sakai, T.; Takahashi, M.; et al. Pyrimidine Compound and Medical Use Thereof. U.S. Patent Number US7378423B2, 17 May 2008.
86. Knispel, S.; Zimmer, L.; Kanaki, T.; Ugurel, S.; Schadendorf, D.; Livingstone, E. The safety and efficacy of dabrafenib and trametinib for the treatment of melanoma. *Expert Opin. Drug Saf.* **2018**, *17*, 73–87. [CrossRef]
87. Rheault, T.R. Benzene Sulfonamide Thiazole and Oxazole Compounds. U.S. Patent Number US7994185B2, 9 August 2011.
88. Brückl, W.; Tufman, A.; Huber, R.M. Advanced non-small cell lung cancer (NSCLC) with activating EGFR mutations: First-line treatment with afatinib and other EGFR TKIs. *Expert Rev. Anticancer Ther.* **2017**, *17*, 143–155. [CrossRef]
89. Himmelsbach, F.; Blech, S.; Langkopf, E.; Jung, B.; Baum, A.; Solca, F. Quinazoline Derivatives and Pharmaceutical Compositions Containing Them. U.S. Patent Number USRE43431E1, 29 May 2012.
90. Kulinna, C.; Rall, W.; Schnaubelt, J.; Sieger, P.; Soyka, R. Process for Preparing Amino Crotonyl Compounds. U.S. Patent Number US8426586B2, 23 April 2013.
91. Liu, L.; Shi, B.; Wang, X.; Xiang, H. Strategies to overcome resistance mutations of Bruton's tyrosine kinase inhibitor ibrutinib. *Future Med. Chem.* **2018**, *10*, 343–356. [CrossRef]
92. Honigberg, L.; Pan, Z.; Verner, E. Inhibitors of Bruton's Tyrosine Kinase. U.S. Patent Number US8735403B2, 27 May 2014.
93. Goldman, E.; Purro, N.; Smyth, M.; Wirth, D.D. Crystalline Forms of a Bruton's Tyrosine Kinase Inhibitor. U.S. Patent Number US9296753B2, 29 March 2016.
94. De Pas, T.; Pala, L.; Catania, C.; Conforti, F. Molecular and clinical features of second-generation anaplastic lymphoma kinase inhibitors: Ceritinib. *Future Oncol.* **2017**, *13*, 2629–2644. [CrossRef]
95. Michellys, P.Y.; Pei, W.; Marsilje, T.H.; Chen, B.; Uno, T. Compounds and Compositions as Protein Kinase Inhibitors. U.S. Patent Number US8039479B2, 18 October 2011.
96. Feng, L.; Gong, B.; Karpinski, P.H.; Waykole, L.M. Crystalline Forms of 5-chloro-*N*2-(2-isopropoxy-5-methyl-4-piperidin-4-yl-phenyl)-*N*4-[2-(propane-2-sulfonyl)-phenyl]-pyrimidine-2, 4-diamine. U.S. Patent Number US9309229B2, 12 April 2016.
97. Zirlík, K.; Veelken, H. Idelalisib. *Recent Results Cancer Res.* **2018**, *212*, 243–264. [CrossRef]
98. Fowler, K.W.; Huang, D.; Kesicki, E.A.; Oliver, A.; Ooi, H.C.; Puri, K.D.; Ruan, F.; Treiberg, J. Quinazolinones as Inhibitors of Human Phosphatidylinositol 3-kinase Delta. U.S. Patent Number USRE44638E, 10 December 2013.
99. Carra, E.; Everts, J.B.; Gerber, M.; Shi, B.; Sujino, K.; Tran, D.; Wang, F. Polymorphic Forms of (S)-2-(1-(9H-purin-6-ylamino)propyl)-5-fluoro-3-phenylquinazolin-4(3H)-one. U.S. Patent Number US9469643B2, 18 October 2016.
100. Khalique, S.; Banerjee, S. Nintedanib in ovarian cancer. *Expert Opin. Investig. Drugs* **2017**, *26*, 1073–1081. [CrossRef]
101. Heckel, A.; Hilberg, F.; Redemann, N.; Roth, G.J.; Spevak, W.; Tontsch, G.U.; Van, M.J.; Walter, R. Substituted Indolines which Inhibit Receptor Tyrosine Kinases. U.S. Patent Number US6762180B1, 13 July 2004.
102. Bock, T.; Hilberg, F.; Linz, G.; Rall, W.; Roth, G.J.; Sieger, P. 3-*Z*-[1-(4-(*N*-((4-Methyl-piperazin-1-yl)-methylcarbonyl)-*N*-methyl-amino)-anilino)-1-phenyl-methylene]-6-methoxycarbonyl-2-indolinone-monoethanesulphonate and the Use Thereof as a Pharmaceutical Composition. U.S. Patent Number US7119093B2, 10 October 2006.
103. de Dueñas, E.M.; Gavila-Gregori, J.; Olmos-Antón, S.; Santaballa-Bertrán, A.; Lluch-Hernández, A.; Espinal-Domínguez, E.J.; Rivero-Silva, M.; Llombart-Cussac, A. Preclinical and clinical development of palbociclib and future perspectives. *Clin. Transl. Oncol.* **2018**, *20*, 1136–1144. [CrossRef]
104. Barvian, M.; Booth, R.J.; Quinn, J., III; Repine, J.T.; Sheehan, D.J.; Toogood, P.L.; Vanderwel, S.N.; Zhou, H. 2-(pyridin-2-ylamino)-pyrido[2,3-*d*]pyrimidin-7-ones. U.S. Patent Number USRE47739E, 26 November 2019.
105. Chekal, B.P.; Ide, N.D. Solid Forms of a Selective CDK4/6 Inhibitor. U.S. Patent Number US10723730B2, 28 July 2020.

106. Capozzi, M.; De Divitiis, C.; Ottaiano, A.; von Arx, C.; Scala, S.; Tatangelo, F.; Delrio, P.; Tafuto, S. Lenvatinib, a molecule with versatile application: From preclinical evidence to future development in anti-cancer treatment. *Cancer Manag. Res.* **2019**, *11*, 3847–3860. [CrossRef]
107. Arimoto, I.; Fukuda, Y.; Funahashi, Y.; Haneda, T.; Kamat, J.; Matsui, J.; Matsui, K.; Matsukura, M.; Matsushima, T.; Mimura, F.; et al. Nitrogen-Containing Aromatic Derivatives. U.S. Patent Number US7253286B2, 7 August 2007.
108. Matsushima, T.; Arimoto, I.; Ayata, Y.; Gotoda, M.; Kamada, A.; Nakamura, T.; Sakaguchi, T.; Suzuki, N.; Yoshizawa, K. Crystalline Form of the Salt of 4-(3-chloro-4-(cyclopropylaminocarbonyl)aminophenoxy)-7-methoxy-6-quinolinecarboxamide or the Solvate of the Salt and a Process for Preparing the Same. U.S. Patent Number US7612208B2, 3 November 2009.
109. Eagles, J.R.; Jimeno, A. Cobimetinib: Inhibiting MEK1/2 in BRAF V600-mutant melanoma. *Drugs Today (Barc)* **2016**, *52*, 593–605. [CrossRef]
110. Aay, N.; Anand, N.K.; Blazey, C.M.; Bowles, O.J.; Bussenius, J.; Costanzo, S.; Curtis, J.K.; Defina, S.C.; Dubenko, L.; Joshi, A.A.; et al. Azetidines as MEK Inhibitors for the Treatment of Proliferative Diseases. U.S. Patent Number US7803839B2, 28 September 2010.
111. Brown, A.C. Crystalline Fumarate Salt of (S)-[3,4-difluoro-2-(2-fluoro-4-iodophenylamino)phenyl] [3-hydroxy-3-(piperidin-2-yl)azetidin-1-yl]methanone. U.S. Patent Number US10590102B2, 17 March 2020.
112. Santarpia, M.; Liguori, A.; Karachaliou, N.; Gonzalez-Cao, M.; Daffinà, M.G.; D’Aveni, A.; Marabello, G.; Altavilla, G.; Rosell, R. Osimertinib in the treatment of non-small-cell lung cancer: Design, development and place in therapy. *Lung Cancer (Auckl)* **2017**, *8*, 109–125. [CrossRef]
113. Butterworth, S.; Finlay, M.R.V.; Redfearn, H.M.; Ward, R.A. 2-(2,4,5-substituted-anilino) pyrimidine Compounds. U.S. Patent Number US8946235B2, 3 February 2015.
114. Srinivasamaharaj, S.; Salame, B.K.; Rios-Perez, J.; Kloecker, G.; Perez, C.A. The role of alectinib in the treatment of advanced ALK-rearranged non-small-cell lung cancer. *Expert Rev. Anticancer Ther.* **2016**, *16*, 1227–1233. [CrossRef]
115. Asoh, K.; Emura, T.; Furuichi, N.; Hong, W.; Ishii, N.; Ito, T.; Kawada, H.; Kinoshita, K.; Morikami, K.; Oikawa, N.; et al. Tetracyclic Compound. U.S. Patent Number US9126931B2, 8 September 2015.
116. Curigliano, G.; Criscitiello, C.; Esposito, A.; Intra, M.; Minucci, S. Pharmacokinetic drug evaluation of ribociclib for the treatment of metastatic, hormone-positive breast cancer. *Expert Opin. Drug Metab. Toxicol.* **2017**, *13*, 575–581. [CrossRef]
117. Brain, C.T.; Sung, M.J.E.; Lagu, B. Pyrrolopyrimidine Compounds and Their Uses. U.S. Patent Number US8415355B2, 9 April 2013.
118. Calienni, J.V.; Chen, G.P.; Gong, B.; Kapa, P.K.; Saxena, V. Salt(s) of 7-cyclopentyl-2-(5-piperazin-1-yl-pyridin-2-ylamino)-7H-pyrrolo[2,3-*d*]pyrimidine-6-carboxylic Acid Dimethylamide and Processes of Making Thereof. U.S. Patent Number US9193732B2, 24 November 2015.
119. Ali, R.; Arshad, J.; Palacio, S.; Mudad, R. Brigatinib for ALK-positive metastatic non-small-cell lung cancer: Design, development and place in therapy. *Drug Des. Devel. Ther.* **2019**, *13*, 569–580. [CrossRef]
120. Dalgarno, D.C.; Huang, W.S.; Li, F.; Liu, S.; Qi, J.; Romero, J.A.C.; Shakespeare, W.C.; Thomas, R.M.; Wang, Y.; Zhu, X.; et al. Phosphorous Derivatives as Kinase Inhibitors. U.S. Patent Number US9012462B2, 21 April 2015.
121. Rozamus, L.W.; Sharma, P. Crystalline Forms of 5-chloro-N4-[2 (dimethylphosphoryl)phenyl]-N2-[2-methoxy-4-[4-(4-methylpiperazin-1-yl) piperidin-1-yl]phenyl]pyrimidine-2,4-diamine. U.S. Patent Number US10385078B2, 20 August 2019.
122. Kim, E.S. Midostaurin: First Global Approval. *Drugs* **2017**, *77*, 1251–1259. [CrossRef]
123. Caravatti, G.; Fredenhagen, A. Staurosporine Derivatives Substituted at Methylamino Nitrogen. U.S. Patent Number US5093330A, 3 March 1992.
124. Griffin, J.D.; Manley, P.W. Staurosporine Derivatives as Inhibitors of FLT3 Receptor Tyrosine Kinase Activity. U.S. Patent Number US7973031B2, 5 July 2011.
125. Deeks, E.D. Neratinib: First Global Approval. *Drugs* **2017**, *77*, 1695–1704. [CrossRef]
126. Rabindran, S.K.; Tsou, H.R.; Wissner, A. Protein Tyrosine Kinase Enzyme Inhibitors. U.S. Patent Number US7399865B2, 15 July 2008.
127. Markham, A. Copanlisib: First Global Approval. *Drugs* **2017**, *77*, 2057–2062. [CrossRef] [PubMed]
128. Bullion, A.M.; Campbell, A.M.; Hentemann, M.; Michels, M.; Redman, A.; Rowley, B.R.; Scott, W.; Wood, J. Substituted 2,3-dihydroimidazo[1,2-*c*]quinazoline Derivatives Useful for Treating Hyper-Proliferative Disorders and Diseases Associated with Angiogenesis. U.S. Patent Number USRE46856E, 22 May 2018.
129. Militzer, H.C.; Müller, H.; Peters, J.G. Substituted 2,3-dihydroimidazo[1,2-*c*]quinazoline Salts. U.S. Patent Number US10383876B2, 20 August 2019.
130. Kim, E.S. Abemaciclib: First Global Approval. *Drugs* **2017**, *77*, 2063–2070. [CrossRef] [PubMed]
131. De Dios, M.A.; De Prado, G.A.; Filadelfa, D.P.C.M.; Garcia, P.M.C.; Gelbert, L.M.; Knobloch, J.M.; Martin, D.L.N.E.M.; Martin, O.F.M.D.; Martinez, P.J.A. Protein Kinase Inhibitors. U.S. Patent Number US7855211B2, 21 December 2010.
132. Markham, A.; Dhillion, S. Acalabrutinib: First Global Approval. *Drugs* **2018**, *78*, 139–145. [CrossRef] [PubMed]
133. Barf, T.A.; Man, P.A.D.A.; Oubrie, A.A.; Rewinkel, J.B.M.; Sterrenburg, J.G.; Jans, C.G.J.M.; Raaijmakers, H. 4-imidazopyridazin-1-yl-benzamides and 4-imidazotriazin-1-yl-benzamides as Btk Inhibitors. U.S. Patent Number US9290504B2, 22 March 2016.
134. Aret, E.; Barf, T.; Blatter, F.; Evarts, J.; Ingallinera, T.; Krejsa, C. Crystal forms of (S)-4-(8-amino-3-(1-(but-2-ynoyl) pyrrolidin-2-yl)imidazo[1,5-*a*]pyrazin-1-yl)-N-(pyridin-2-yl)benzamide. U.S. Patent Number US9796721B2, 24 October 2017.

135. Lin, C.W.; Sherman, B.; Moore, L.A.; Laethem, C.L.; Lu, D.W.; Pattabiraman, P.P.; Rao, P.V.; deLong, M.A.; Kopczynski, C.C. Discovery and preclinical development of netarsudil, a novel ocular hypotensive agent for the treatment of glaucoma. *J. Ocul. Pharmacol. Ther.* **2018**, *34*, 40–51. [CrossRef] [PubMed]
136. Elong, M.A.; Royalty, S.M.; Sturdivant, J.M. Dual Mechanism Inhibitors for the Treatment of Disease. U.S. Patent Number US8394826B2, 12 March 2013.
137. Kopczynski, C.; Lin, C.W.; Sturdivant, J.M.; deLong, M.A. Combination Therapy. U.S. Patent Number US9415043B2, 16 August 2016.
138. Markham, A. Baricitinib: First Global Approval. *Drugs* **2017**, *77*, 697–704. [CrossRef]
139. Rodgers, J.D.; Shepard, S. Azetidine and Cyclobutane Derivatives as JAK Inhibitors. U.S. Patent Number US8158616B2, 17 April 2012.
140. Tran, B.; Cohen, M.S. The discovery and development of binimetinib for the treatment of melanoma. *Expert Opin. Drug Discov.* **2020**, *15*, 745–754. [CrossRef]
141. Wallace, E.M.; Lyssikatos, J.P.; Marlow, A.L.; Hurley, T.B. N3 Alkylated Benzimidazole Derivatives as MEK Inhibitors. U.S. Patent Number US7777050B2, 17 August 2010.
142. Rell, C.M.; Liu, W.; Misun, M.; Nichols, P.; Niederer, D.A.; Pachinger, W.H.; Stengel, P.J.; Wolf, M.C.; Zimmermann, D. Preparation of and Formulation Comprising a MEK Inhibitor. U.S. Patent Number US9562016B2, 7 February 2017.
143. Shirley, M. Dacomitinib: First Global Approval. *Drugs* **2018**, *78*, 1947–1953. [CrossRef]
144. Fakhoury, S.A.; Lee, H.T.; Reed, J.E.; Schlosser, K.M.; Sexton, K.E.; Teclé, H.; Winters, R.T. 4-phenylamino-quinazolin-6-yl-amides. U.S. Patent Number US7772243B2, 10 August 2010.
145. Koelblinger, P.; Thuerigen, O.; Dummer, R. Development of encorafenib for BRAF-mutated advanced melanoma. *Curr. Opin. Oncol.* **2018**, *30*, 125–133. [CrossRef]
146. Huang, S.; Jin, X.; Liu, Z.; Poon, D.; Tellew, J.; Wan, Y.; Wang, X.; Xie, Y. Compounds and Compositions as Protein Kinase Inhibitors. U.S. Patent Number US8501758B2, 6 August 2013.
147. Markham, A. Fostamatinib: First Global Approval. *Drugs* **2018**, *78*, 959–963. [CrossRef]
148. Bhamidipati, S.; Singh, R.; Stella, V.J.; Sun, T. Prodrugs of 2,4-pyrimidinediamine Compounds and Their Uses. U.S. Patent Number US7449458B2, 11 November 2008.
149. Bhamidipati, S.; Masuda, E.; Singh, R.; Sun, T. Prodrugs of 2,4-pyrimidinediamine Compounds and Their Uses. U.S. Patent Number US8163902B2, 24 April 2012.
150. Blair, H.A. Duvelisib: First Global Approval. *Drugs* **2018**, *78*, 1847–1853. [CrossRef]
151. Chan, K.; Li, L.; Liu, Y.; Ren, P.; Rommel, C.; Wilson, T.E. Substituted Isoquinolin-1(2H)-ones, and Methods of Use Thereof. U.S. Patent Number US8193182B2, 5 June 2012.
152. Isbester, P.; Kropp, J.; Lane, B.S.; Michael, M.; Pingda, R. Processes for Preparing Isoquinolinones and Solid Forms of Isoquinolinones. U.S. Patent Number USRE46621E, 5 December 2017.
153. Dhillon, S. Gilteritinib: First Global Approval. *Drugs* **2019**, *79*, 331–339. [CrossRef]
154. Kazuhiko, I.; Yoshinori, I.; Akio, K.; Yutaka, K.; Kazuo, K.; Takahiro, M.; Itsuro, S.; Hiroshi, T. Diamino Heterocyclic Carboxamide Compound. U.S. Patent Number US8969336B2, 3 March 2015.
155. Scott, L.J. Larotrectinib: First Global Approval. *Drugs* **2019**, *79*, 201–206. [CrossRef]
156. Andrews, S.W.; Haas, J.; Jiang, Y.; Zhang, G. Method of treatment using substituted pyrazolo[1,5-*a*] pyrimidine compounds. U.S. Patent Number US9127013B2, 8 September 2015.
157. Alisha, B.; Juengst, D.; Shah, K. Crystalline Form of (S)-N-(5-((R)-2-(2,5-difluorophenyl)-pyrrolidin-1-yl)-pyrazolo[1,5-*a*]pyrimidin-3-yl)-3-hydroxypyrrolidine-1-carboxamide Hydrogen Sulfate. U.S. Patent Number US10172861B2, 8 January 2019.
158. Syed, Y.Y. Lorlatinib: First Global Approval. *Drugs* **2019**, *79*, 93–98. [CrossRef]
159. Bailey, S.; Burke, B.J.; Collins, M.R.; Cui, J.J.; Deal, J.G.; Hoffman, R.L.; Huang, Q.; Johnson, T.W.; Kania, R.S.; Kath, J.C. Macrocyclic Derivatives for the Treatment of Diseases. U.S. Patent Number US8680111B2, 25 March 2014.
160. Birch, M.J.; Pencheva, K.D. Crystalline Form of Lorlatinib Free Base. U.S. Patent Number US10420749B2, 24 September 2019.
161. Al-Salama, Z.T.; Keam, S.J. Entrectinib: First Global Approval. *Drugs* **2019**, *79*, 1477–1483. [CrossRef]
162. Lombardi, B.A.; Marchionni, C.; Menichincheri, M.; Nesi, M.; Orsini, P.; Panzeri, A.; Perrone, E.; Vanotti, E. Substituted Indazole Derivatives Active as Kinase Inhibitors. U.S. Patent Number US8299057B2, 30 October 2012.
163. Candiani, I.; Ottaiano, G.; Tomasi, A. Crystalline Form of N-[5-(3,5-difluoro-benzyl)-1H-indazol-3-yl]-4-(4-methyl-piperazin-1-yl)-2-(tetrahydro-pyran-4-ylamino)-benzamide. U.S. Patent Number US10738037B2, 11 August 2020.
164. Duggan, S.; Keam, S.J. Upadacitinib: First Approval. *Drugs* **2019**, *79*, 1819–1828. [CrossRef]
165. Frank, K.E.; Friedman, M.; George, D.M.; Stewart, K.D.; Wallace, G.A.; Wishart, N. Tricyclic Compounds. U.S. Patent Number USRE47221E, 5 February 2019.
166. Allian, A. Processes for the Preparation of (3S,4R)-3-ethyl-4-(3H-imidazo[1,2- $\alpha$ ]pyrrolo[2,3-*e*]-pyrazin-8-yl)-N-(2,2,2-trifluoroethyl)pyrrolidine-1-carboxamide and Solid State Forms Thereof. U.S. Patent Number US9951080B2, 24 April 2018.
167. Markham, A. Alpelisib: First Global Approval. *Drugs* **2019**, *79*, 1249–1253. [CrossRef]
168. Caravatti, G.; Fairhurst, R.A.; Furet, P.; Guagnano, V.; Imbach, P. Pyrrolidine-1,2-dicarboxamide Derivatives. U.S. Patent Number US8227462B2, 24 July 2012.
169. Hanna, K.S. Erdafitinib to treat urothelial carcinoma. *Drugs Today (Barc.)* **2019**, *55*, 495–501. [CrossRef]

170. Akkari, R.; Berdini, V.; Besong, G.E.; Embrechts, W.C.J.; Freyne, E.J.E.; Gilissen, R.A.H.J.; Hamlett, C.C.F.; Johnson, C.N.; Lacrampe, J.F.A.; Meerpoel, L.; et al. Pyrazolyl Quinoxaline Kinase Inhibitors. U.S. Patent Number US8895601B2, 25 November 2014.
171. Monestime, S.; Lazaridis, D. Pexidartinib (TURALIO™): The first FDA-indicated systemic treatment for Tenosynovial Giant Cell Tumor. *Drugs R D* **2020**, *20*, 189–195. [CrossRef]
172. Bremer, R.; Ibrahim, P.N.; Zhang, J. Compounds Modulating c-fms and/or c-kit Activity and Uses Therefor. U.S. Patent Number US9169250B2, 27 October 2015.
173. Ibrahim, P.N.; Visor, G.C. Solid Forms of a Compound Modulating Kinases. *U.S. Patent* **2017**.
174. Blair, H.A. Fedratinib: First Approval. *Drugs* **2019**, *79*, 1719–1725. [CrossRef]
175. Cao, J.; Hood, J.D.; Lohse, D.L.; Mcpherson, A.; Noronha, G.; Pathak, V.P.; Renick, J.; Soll, R.M.; Zeng, B.; Mak, C.C. Bi-aryl meta-pyrimidine Inhibitors of Kinases. U.S. Patent Number US7528143B2, 5 May 2009.
176. Syed, Y.Y. Zanubrutinib: First Approval. *Drugs* **2020**, *80*, 91–97. [CrossRef] [PubMed]
177. Guo, Y.; Wang, Z. Substituted pyrazolo[1,5-*a*]pyrimidines as Bruton's Tyrosine Kinase Modulators. U.S. Patent Number US9447106B2, 20 September 2016.
178. Dhillon, S. Avapritinib: First Approval. *Drugs* **2020**, *80*, 433–439. [CrossRef] [PubMed]
179. Hodous, B.L.; Kim, J.L.; Wilson, D.; Wilson, K.J.; Zhang, Y. Compositions Useful for Treating Disorders Related to Kit. U.S. Patent Number US9944651B2, 17 April 2018.
180. Markham, A.; Keam, S.J. Selumetinib: First Approval. *Drugs* **2020**, *80*, 931–937. [CrossRef] [PubMed]
181. Wallace, E.M.; Lyssikatos, J.P.; Marlow, A.L.; Hurley, T.B. N3 Alkylated Benzimidazole Derivatives as MEK Inhibitors. U.S. Patent Number US7425637B2, 16 September 2008.
182. Chuang, T.H.; Demattei, J.; Dickinson, P.A.; Ford, J.G.; Pervez, M.; Roberts, R.J.; Sharma, S.G.; Squire, C.J.; Storey, R.A. Hydrogen Sulfate Salt. U.S. Patent Number US9156795B2, 13 October 2015.
183. Hoy, S.M. Pemigatinib: First Approval. *Drugs* **2020**, *80*, 923–929. [CrossRef]
184. He, C.; Lu, L.; Wu, L.; Yao, W.; Zhang, C. Substituted Tricyclic Compounds as FGFR Inhibitors. U.S. Patent Number US9611267B2, 4 April 2017.
185. Lee, A. Tucatinib: First Approval. *Drugs* **2020**, *80*, 1033–1038. [CrossRef]
186. Greschuk, J.M.; Hennings, D.D.; Liu, W.; Lyssikatos, J.P.; Marmsaeter, F.P.; Zhao, Q. N4-phenyl-quinazoline-4-amine Derivatives and Related Compounds as ErbB type I Receptor Tyrosine Kinase Inhibitors for the Treatment of Hyperproliferative Diseases. U.S. Patent Number US8648087B2, 11 February 2014.
187. Dhillon, S. Capmatinib: First Approval. *Drugs* **2020**, *80*, 1125–1131. [CrossRef]
188. He, C.; Metcalf, B.; Qian, D.Q.; Xu, M.; Yao, W.; Zhang, C.; Zhuo, J. Imidazotriazines and Imidazopyrimidines as Kinase Inhibitors. U.S. Patent Number US7767675B2, 3 August 2010.
189. Liu, P.; Pan, Y.; Qiao, L.; Weng, L.; Zhou, J. Salts of 2-fluoro-N-methyl-4-[7-(quinolin-6-yl-methyl)-imidazo[1,2-*b*][1,2,4]triazin-2-yl]benzamide and Processes Related to Preparing the Same. U.S. Patent Number US8420645B2, 16 April 2013.
190. Markham, A. Selpercatinib: First Approval. *Drugs* **2020**, *80*, 1119–1124. [CrossRef]
191. Andrews, S.W.; Aronow, S.; Blake, J.F.; Brandhuber, B.J.; Cook, A.; Haas, J.; Jiang, Y.; Kolakowski, G.R.; McFaddin, E.A.; McKenney, M.L.; et al. Substituted Pyrazolo[1,5-*a*]pyridine Compounds as RET Kinase Inhibitors. U.S. Patent Number US10112942B2, 30 October 2018.
192. Metcalf, A.T.; Fry, D.; McFaddin, E.A.; Kolakowski, G.R.; Haas, J.; Tang, T.P.; Jiang, Y. Crystalline Forms. U.S. Patent Number US10584124B2, 10 March 2020.
193. Dhillon, S. Ripretinib: First Approval. *Drugs* **2020**, *80*, 1133–1138. [CrossRef]
194. Flynn, D.L.; Kaufman, M.D.; Petillo, P.A. Dihydronaphthyridines and Related Compounds Useful as Kinase Inhibitors for the Treatment of Proliferative Diseases. U.S. Patent Number US8461179B1, 11 June 2013.
195. Markham, A. Pralsetinib: First Approval. *Drugs* **2020**, *80*, 1865–1870. [CrossRef]
196. Brubaker, J.D.; DiPietro, L.V.; Kim, J.L.; Wilson, D.W.; Wilson, K.J. Inhibitors of RET. U.S. Patent Number US10030005B2, 24 July 2018.
197. Dhillon, S. Trilaciclib: First Approval. *Drugs* **2021**, *81*, 867–874. [CrossRef]
198. Strum, J.C.; Tavares, F.X. CDK Inhibitors. U.S. Patent Number US8598186B2, 3 December 2013.
199. Markham, A. Tepotinib: First Approval. *Drugs* **2020**, *80*, 829–833. [CrossRef]
200. Dorsch, D.; Steiber, F.; Schadt, O.; Blaukat, A. Pyridazinone Derivatives. U.S. Patent Number US8580781B2, 12 November 2013.
201. Schadt, O.; Dorsch, D.; Steiber, F.; Blaukat, A. Pyrimidinyl Pyridazinone Derivatives. U.S. Patent Number US8329692B2, 11 December 2012.
202. Dhillon, S.; Keam, S.J. Umbralisib: First Approval. *Drugs* **2021**, *81*, 857–866. [CrossRef]
203. Muthuppalaniappan, M.; Nagarathnam, D.; Vakkalanka, S.K. Selective PI3K Delta Inhibitors. *U.S. Patent* **2020**.
204. Vakkalanka, S.K. Forms of a PI3K Delta Selective Inhibitor for Use in Pharmaceutical Formulations. *U.S. Patent* **2019**.
205. Tivozanib Hydrochloride. *Am. J. Health Syst. Pharm.* **2021**, zxab199. [CrossRef]
206. Kubo, K.; Sakai, T.; Nagao, R.; Fujiwara, Y.; Isoe, T.; Hasegawa, K. Quinoline Derivatives and Quinazoline Derivatives Having Azolyl Group. U.S. Patent Number US6821987B2, 23 November 2004.
207. Kubo, K.; Sakai, T.; Nagao, R.; Fujiwara, Y.; Isoe, T.; Hasegawa, K. Quinoline Derivatives and Quinazoline Derivatives Having Azolyl Group. U.S. Patent Number US7211587B2, 1 May 2007.

208. Matsunaga, N.; Yoshida, S.; Yoshino, A.; Nakajima, T. *N*-{2-chloro-4-[(6,7-dimethoxy-4-quinolyl)oxy]phenyl}-*N'*-(5-methyl-3-isoxazolyl)urea Salt in Crystalline Form. U.S. Patent Number US7166722B2, 23 January 2007.
209. Botrus, G.; Raman, P.; Oliver, T.; Bekaii-Saab, T. Infigratinib (BGJ398): An investigational agent for the treatment of FGFR-altered intrahepatic cholangiocarcinoma. *Expert Opin. Investig. Drugs* **2021**, *30*, 309–316. [CrossRef]
210. Ding, Q.; Gray, N.S.; Li, B.; Liu, Y.; Sim, T.; Uno, T.; Zhang, G.; Soldermann, C.P.; Breitenstein, W.; Bold, G.; et al. Compounds and Compositions as Protein Kinase Inhibitors. U.S. Patent Number US8552002B2, 8 October 2013.
211. Berghausen, J.; Kapa, P.K.; McKenna, J.; Slade, J.; Wu, R.; Du, Z.; Stowasswer, F. Crystalline Forms of 3-(2,6-dichloro-3,5-dimethoxy-phenyl)-1-[6-[4-(4-ethyl-piperazin-1-yl)-phenylamino]-pyrimidin-4-yl]-1-methyl-urea and Salts Thereof. U.S. Patent Number US9067896B2, 30 June 2015.
212. Kanev, G.K.; de Graaf, C.; de Esch, I.J.P.; Leurs, R.; Würdinger, T.; Westerman, B.A.; Kooistra, A.J. The Landscape of Atypical and Eukaryotic Protein Kinases. *Trends Pharmacol. Sci.* **2019**, *40*, 818–832. [CrossRef]
213. 2020 Medicines in Development—Cancer. Available online: [https://www.phrma.org/-/media/Project/PhRMA/PhRMA-Org/PhRMA-Org/PDF/MID-Reports/MID-Cancer2020\\_Product-List\\_FINAL.pdf](https://www.phrma.org/-/media/Project/PhRMA/PhRMA-Org/PhRMA-Org/PDF/MID-Reports/MID-Cancer2020_Product-List_FINAL.pdf) (accessed on 31 May 2021).
214. Cohen, P.; Cross, D.; Jänne, P.A. Kinase drug discovery 20 years after imatinib: Progress and future directions. *Nat. Rev. Drug Discov.* **2021**, 1–19. [CrossRef]
215. Couillaud, B.M.; Espeau, P.; Mignet, N.; Corvis, Y. State of the art of pharmaceutical solid forms: From crystal property issues to nanocrystals formulation. *Chem. Med. Chem.* **2019**, *14*, 8–23. [CrossRef]
216. Smalley, K.S.M. Pharmacological research and cancer: A call to arms. *Pharmacol. Res.* **2019**, *146*, 104291. [CrossRef]
217. Kantarjian, H.M.; Fojo, T.; Mathisen, M.; Zwellling, L.A. Cancer drugs in the United States: Justum Pretium—the just price. *J. Clin. Oncol.* **2013**, *31*, 3600–3604. [CrossRef]
218. Mishuk, A.U.; Fasina, I.; Qian, J. Impact of U.S. federal and state generic drug policies on drug use, spending, and patient outcomes: A systematic review. *Res. Soc. Adm. Pharm.* **2020**, *16*, 736–745. [CrossRef]



Review

# TRK Inhibitors: Tissue-Agnostic Anti-Cancer Drugs

Sun-Young Han 

Research Institute of Pharmaceutical Sciences and College of Pharmacy,  
Gyeongsang National University, Jinju-si 52828, Korea; syhan@gnu.ac.kr

**Abstract:** Recently, two tropomyosin receptor kinase (Trk) inhibitors, larotrectinib and entrectinib, have been approved for Trk fusion-positive cancer patients. Clinical trials for larotrectinib and entrectinib were performed with patients selected based on the presence of Trk fusion, regardless of cancer type. This unique approach, called tissue-agnostic development, expedited the process of Trk inhibitor development. In the present review, the development processes of larotrectinib and entrectinib have been described, along with discussion on other Trk inhibitors currently in clinical trials. The on-target effects of Trk inhibitors in Trk signaling exhibit adverse effects on the central nervous system, such as withdrawal pain, weight gain, and dizziness. A next generation sequencing-based method has been approved for companion diagnostics of larotrectinib, which can detect various types of Trk fusions in tumor samples. With the adoption of the tissue-agnostic approach, the development of Trk inhibitors has been accelerated.

**Keywords:** Trk; NTRK; tissue-agnostic; larotrectinib; entrectinib; Trk fusion

**Citation:** Han, S.-Y. TRK Inhibitors: Tissue-Agnostic Anti-Cancer Drugs. *Pharmaceuticals* **2021**, *14*, 632. <https://doi.org/10.3390/ph14070632>

Academic Editors: Mary J. Meegan, Niamh M. O'Boyle and Jean Jacques Vanden Eynde

Received: 18 May 2021

Accepted: 25 June 2021

Published: 29 June 2021

**Publisher's Note:** MDPI stays neutral with regard to jurisdictional claims in published maps and institutional affiliations.



**Copyright:** © 2021 by the author. Licensee MDPI, Basel, Switzerland. This article is an open access article distributed under the terms and conditions of the Creative Commons Attribution (CC BY) license (<https://creativecommons.org/licenses/by/4.0/>).

## 1. Introduction

Tropomyosin receptor kinases (Trk) are tyrosine kinases encoded by neurotrophic tyrosine/tropomyosin receptor kinase (NTRK) genes [1]. Chromosomal rearrangement of NTRK genes is found in cancer tissues [2]. The resulting fusion proteins containing part of the Trk protein have a constitutively active form of kinase that transduces deregulating signals. There is active progress in the development of small molecule inhibitors against Trk kinases in the field of cancer therapeutics [1]. Currently, larotrectinib and entrectinib are two approved drugs for Trk fusion-positive cancers in the market [3,4]. The timeline for the clinical development of the two Trk inhibitors is shown in Figure 1.

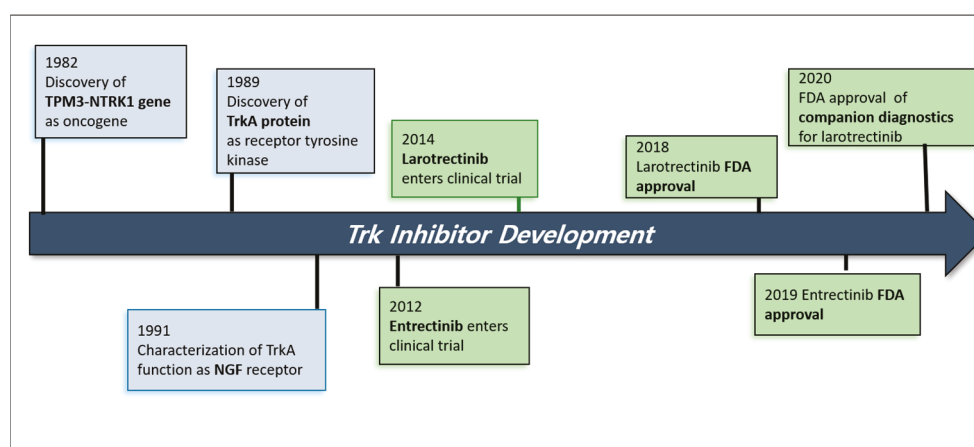


**Figure 1.** Timeline for the clinical development of larotrectinib and entrectinib. TPM3, tropomyosin 3; NTRK1, neurotrophic tyrosine receptor kinase 1; TrkA, tropomyosin receptor kinase A; NGF, nerve growth factor; FDA, US Food and Drug Administration.



A unique process of drug development, known as tissue-agnostic development, was employed for larotrectinib and entrectinib approval. Patients for tissue-agnostic clinical trials were selected based on the presence of NTRK gene rearrangement, independent of tumor type [5,6]. Trk fusion-positive tumors of several cancer types were tested for Trk inhibitors, and excellent efficacy of these drugs was shown in tissue-agnostic trials.

In this review, the development process and pharmacological efficacy of current Trk inhibitors in the market will be described, along with some discussion on the Trk inhibitors currently in clinical development. In addition, we will review the development process of tissue-agnostic drugs. Finally, we aim to provide perspectives learned from the pioneering approach of tissue-agnostic therapy for Trk inhibitors.

## 2. Tissue-Agnostic Drug Development

Targeted cancer therapies that act on specific molecules have become mainstream strategies for anti-cancer drug development. There are two milestones for targeted cancer drug development: trastuzumab and imatinib. Trastuzumab is a monoclonal antibody specific to the human epidermal growth factor receptor 2 (HER2) protein [7]. The US Food and Drug Administration (FDA) approval for trastuzumab was obtained in 1998 for metastatic breast cancer overexpressing HER2 protein [8]. Imatinib is a small-molecule drug targeting the fusion protein BCR-ABL. The fusion protein is generated by chromosomal rearrangement in chronic myeloid leukemia cells. The remarkable efficacy of these two drugs paved the way for the era of targeted cancer therapy, and this made kinase family proteins major targets for cancer therapy [9].

The concept of targeted therapy expanded to the term precision medicine, personalized medicine, or stratified medicine, meaning “targeting drugs for each genetic profile” [7]. In contrast to the traditional “one-size-fits-all” approach, individualizing pharmacotherapy was emphasized upon due to the factors of disease heterogeneity and genetic variability [10]. Biomarkers that can predict therapeutic responses are important elements in precision medicine. Therefore, the diagnosis of biomarkers has become an important step in precision medicine, generating new terms such as companion diagnostics (CDx) or drug-diagnostic co-development [7]. With the adoption of CDx, it was possible to enroll only selected patients who were likely to respond to drug therapy. Clinical research involving a relatively small number of patients, enabled by screening out of non-responders, is called enrichment trial [11]. Trastuzumab was the first drug developed using a CDx approach. A diagnostic assay (HercepTest), which tests the expression of HER2 in breast tumors was developed and approved together with the drug [12]. Another representative example of CDx and enrichment trials is crizotinib, an anaplastic lymphoma kinase (ALK) inhibitor for non-small cell lung cancer (NSCLC) patients [13]. ALK fusion proteins caused by chromosomal rearrangement are found in approximately 4% of NSCLC patients, and these ALK fusion proteins have been reported to induce tumorigenesis. Enrichment clinical trials were conducted for crizotinib development in ALK fusion-positive NSCLC patients, and the number of patients in phase I trials was only 143. Diagnostic tests for ALK gene rearrangement were developed in conjunction with crizotinib development, and the approval of drugs and diagnostic tests were linked and included in the drug labeling.

Before the concept of tissue-agnostic drug was introduced, the development process of precision medicine included only one type of tumor. In the case of crizotinib, only NSCLC patients were included in the clinical trials, even though ALK gene fusion was originally found in anaplastic large cell lymphoma (ALCL) as well [14]. ALK translocation has also been discovered in rare tumors called inflammatory myofibroblastic tumors (IMTs) [15]. Clinical trials of crizotinib for patients with ALCL are ongoing. If clinical research was implemented regardless of tumor type, crizotinib could be used in ALCL and IMT patients as well as in subsets of NSCLC patients. In this way, clinical research with patient selection based on molecular features would have benefitted more cancer patients.

Therefore, a biomarker-guided drug development process has been proposed and successfully applied to three FDA-approved drugs. The immune checkpoint inhibitor,

pembrolizumab, and two Trk inhibitors, larotrectinib and entrectinib, underwent tissue-agnostic development. Tissue-agnostic drugs target specific genetic molecular features regardless of tumor sites [16]. Terms such as histology-agnostic, tumor-agnostic, site-agnostic, pan-tumor therapies are used, depending on the literature [17]. If specific genetic aberrations are found across several tumor types, tissue-agnostic drug development can be utilized. Select ongoing tumor-agnostic developments with several cancer targets are listed in Table 1.

**Table 1.** Select tissue-agnostic developments in clinical trials.

Drug Name	Target	Development Phase	Reference
Repotrectinib (TPX-0005)	Trk/ALK, ROS1	II	[18,19]
Selitrectinib (LOXO-195)	Trk	II	[20]
Taletrectinib (DS-6051b)	Trk/ROS1	I	[21]
TPX-0046	RET/SRC	II	[22]
Debio1347	FGFR	II	[23]
Dubermatinib (TP-0903)	AXL	I	[24]
PLX8394	BRAF	II	[25]
Tislelizumab (BGB-A317)	PD-1	II	[26]

ALK, anaplastic lymphoma kinase; ROS1, c-ros proto-oncogene 1; RET, ret proto-oncogene; SRC, src proto-oncogene; FGFR, fibroblast growth factor receptor; BRAF, B rapidly accelerated fibrosarcoma; PD-1, programmed cell death protein 1.

As a type of clinical research, encompassing different tumor types with the same molecular features is called a basket trial. Unlike enrichment trial, which generally consists of patients with a single tumor type, in basket trials, patients are selected based on their molecular characteristics, regardless of tumor histology. Sometimes, basket trials are viewed as a set of sub-trials [27]. Hypothetically, if crizotinib is developed using a basket trial, the basket trial would be composed of sub-trial 1 with NSCLC, sub-trial 2 with ALCL, and sub-trial 3 with IMT, all with ALK fusion-positive tumors. The results will be analyzed either by tumor type within the sub-trials or altogether.

Traditional clinical trials are based on randomization in new treatment vs. standard of care to avoid selection bias. With the introduction of targeted therapy, molecular segmentation of cancer resulted in a small patient population. And this became a challenge for conducting clinical trials [28]. In crizotinib phase 3 clinical trials in Europe, for example, there was a patient selection process from NSCLC patients. A total of 4967 NSCLC patients were screened, and 347 ALK fusion-positive patients were selected and randomized. The clinical benefit of crizotinib over chemotherapy was shown with overall response rates (65% vs. 20%) and a median PFS (7.7 months vs. 3 months) [29]. Given the large number of patients to be screened and the high overall response rate, the requirement of randomization was called into question. With the introduction of drug development in a tissue-agnostic way, FDA approval could be granted based on the nonrandomized trials. Pembrolizumab obtained FDA approval based on the clinical trials with 149 patients [30], larotrectinib with 55 patients [3], and entrectinib with 54 patients [4]. Given the extremely low prevalence of NTRK fusion (0.31%) [31], it would take a much more extended period to recruit patients for randomized clinical trials.

Tumor-agnostic approach cannot be adopted for all oncogenic alterations [6,16]. The B rapidly accelerated fibrosarcoma (BRAF) inhibitor vemurafenib is very effective in melanoma and NSCLC patients with the BRAF V600 mutation, an activating mutation of BRAF. However, only 5% of colorectal cancers harboring the BRAF V600 mutation respond to vemurafenib therapy [32]. Several clinical studies have been conducted on trastuzumab for tumors with HER2 mutations or amplification; the clinical benefits differed depending on the tumor type. A subset of colorectal cancer with HER2 amplification (5%) showed an overall response rate (ORR) of 30% only for lapatinib plus trastuzumab therapy [33]. Despite the 20 years of clinical research on various tumor types with HER2 aberration, the indications for trastuzumab are only breast cancer and gastroesophageal cancer. These

studies clearly show that not all biomarkers can be developed in a tissue-agnostic manner. Besides Trk and PD-1 inhibitors already approved by the FDA, the targets for potential tissue-agnostic drugs in clinical development are ret proto-oncogene (RET), ALK, fibroblast growth factor receptor (FGFR), Axl, ros proto-oncogene 1 (ROS1), and BRAF (Table 1) [17]. It is interesting to note that oncogenic alterations caused by chromosomal rearrangements, RET, ALK, FGFR, and ROS1 fusion proteins account for the majority of cancer targets in tissue-agnostic therapy.

Besides regulatory reasons, there are several factors why drug development processes have been restricted to one cancer type before pembrolizumab. There are different available therapies and unmet medical needs for each tumor type, factors that are considered substantially for development decisions and drug approval. In addition, the endpoints of drug efficacy for each tumor type are different. As some drug discovery experts term as 'low hanging fruit', generally a tumor type with no known therapy and urgent unmet medical need is first taken up for clinical research, subsequently followed by development in another tumor type.

With the introduction of tissue-agnostic drug development approaches, several tumor types can be subjected to clinical trials at the same time. Tissue-agnostic drug development is also good news for rare cancer patients. Due to the small number of patients, it is not easy to conduct clinical trials for cancers with low incidence. Tissue-agnostic drug development enables the participation of rare cancer patients in clinical trials; therefore, rare cancer patients can benefit from this new paradigm of drug approval process [28].

### 3. Trk Inhibitors

#### 3.1. Trk and Cancer

The Trk family is comprised of three isoforms, TrkA, TrkB, and TrkC, encoded by NTRK1, NTRK2, and NTRK3, respectively. The Trk family is abundantly expressed in the nervous system. Ligands for Trk cell surface receptor tyrosine kinase are nerve growth factor (NGF) for TrkA, brain-derived neurotrophic factor or neurotrophin 4 for TrkB, and neurotrophin 3 for TrkC [1]. Downstream signaling for Trk receptor kinases is primarily mediated by the phospholipase C $\gamma$ , mitogen-activated protein kinase, and phosphoinositol-3 kinase pathways.

As implicated by the expression pattern and cognate ligands, neuronal development and differentiation have been reported as major functions of Trk pathways. The importance of TrkA in neuronal development is shown in case of genetic diseases with loss-of-function NTRK genes. Hereditary disorder called congenital insensitivity to pain (CIPA) is reported to have NTRK1 gene mutations [34]. The absence of TrkA during fetal development results in the loss of pain sensing in TrkA-deficient mice [35,36], suggesting the crucial role of TrkA signaling in nociceptive reception [37]. In case of TrkB, impairment of TrkB signaling causes hyperphagia and consequent obesity [38].

Various mechanisms of Trk activation exist in cancer, including somatic mutations, activating splice variants, Trk overexpression, and NTRK fusion [1]. The most common mechanism of Trk activation in cancer is fusion involving NTRK1, NTRK2, and NTRK3. Trk fusion proteins are generated by chromosomal rearrangements between NTRK genes, including the kinase domain, with different partner genes. The resulting fusion proteins are chimeras with a constitutively activated Trk kinase, independent of ligand binding [39].

The first identified NTRK fusion was tropomyosin 3 (TPM3)-NTRK1, which was found in patients with colorectal cancer [40]. Subsequently, Trk fusion proteins with different partners have been identified in a variety of cancer types. The NTRK fusions include translocated promoter region (TPR)-NTRK1 in thyroid cancer [41], tripartite motif containing 24 (TRIM24)-NTRK2 [42] and ETS variant transcription factor 6 (ETV6)-NTRK3 in fibrosarcoma [43].

### 3.2. Larotrectinib

Larotrectinib, also known as ARRY-470, LOXO-101, and Vitakvi<sup>®</sup>, is the first FDA-approved Trk inhibitor with high potency and selectivity. Larotrectinib inhibits the *in vitro* kinase activity of TrkA by blocking ATP-binding sites with an half maximal inhibitory concentration (IC<sub>50</sub>) of 10 nM [44]. Kinase selectivity analyses with 226 kinases indicated that larotrectinib is highly selective for TrkA, TrkB, and TrkC. Except for one kinase, TNK2, inhibition of no other notable kinases was observed. Larotrectinib potently suppressed the growth of cancer cells harboring TrkA and TrkB fusion proteins *in vitro* and *in vivo* [45].

Based on the impressive preclinical efficacy, clinical trials of larotrectinib started in 2014. Approval of larotrectinib is based on three clinical studies: an adult phase 1 trial (NCT02122913; LOXO-TRK-14001), a pediatric phase 1/2 trial called SCOUT (NCT02637687; LOXO-TRK-15003), and an adult/adolescent phase 2 basket trial called NAVIGATE (NCT02576431; LOXO-TRK-15002). Five journal articles have been published to date on these clinical trials. Deobele et al. described a case of a patient with soft-tissue sarcoma treated with larotrectinib in the LOXO-TRK-14001 trial [45]. Cases of five patients in the SCOUT clinical trial were discussed in the paper by Dubois et al. [46], and the overall phase 1 study results of the SCOUT trial with 24 pediatric solid tumor patients were published by Laetsch et al. [47]. The combined analyses of the three clinical trials stated above (LOXO-TRK-14001, SCOUT, and NAVIGATE) were published for 55 patients from 2015 to 2017 (data cut-off), and larotrectinib was approved on the basis of these results [48]. Clinical research continued, and data from 2014 to 2019 with 159 patients were analyzed and reported in 2020 by Hong et al. [49].

According to a recent report by Hong et al. [49], 159 patients with Trk fusion-positive cancers were treated with larotrectinib, with ages ranging from less than 1 month to 84 years. There were 153 evaluable patients, and the ORR was 79% (121 patients), consisting of complete response in 16% (24 patients) and partial response in 63% (97 patients). More than 16 tumor types were included in the clinical research, and clinical benefits were observed in a wide range of tumor types indicating tumor-agnostic activity. Trk fusions for NTRK1, NTRK2, and NTRK3 were included with 29 distinct fusion partners. The response rate was independent of the Trk subtype and upstream fusion partners. The adverse events of larotrectinib treatment were predominantly grade 1 and 2, indicating that long-term administration is feasible.

### 3.3. Entrectinib

Entrectinib, also called RXDX-101, NMS-E628, and Rozlyreck<sup>®</sup>, is an orally available inhibitor of TrkA/B/C, ROS1, and ALK [4]. Potent *in vitro* kinase activity for TrkA/B/C, ROS1, and ALK exhibited IC<sub>50</sub> values between 1 nM and 12 nM [50]. The growth of cancer cell lines addicted to these kinases was suppressed upon entrectinib treatment *in vitro* and *in vivo*. Entrectinib was designed to have intracranial activity; thus, penetration into the central nervous system (CNS) has been demonstrated in preclinical models. The brain/plasma ratio of entrectinib in mice was 0.43 [50].

Three representative clinical trials of entrectinib are ALKA-372-001 (EudraCT 2012-000148-88), STARTRK-1 (NCT02097810), and STARTRK-2 (NCT02568267). ALKA-372-001 and STARTRK-1 are phase 1 dose-escalation studies, while STARTRK-2 is a phase 2 basket trial. The interim results of ALKA-372-001 and STARTRK-1 in 119 patients were published in 2017 [51]. Integrated analyses of the three clinical trials were reported in 2020 [52]. Another key trial is STARTRK-NG (NCT02650401), which is a phase 1/1b multicenter, dose-escalation study in patients aged 2–21 years with recurrent or refractory solid tumors and primary CNS tumors [4]. The STARTRK-1, -2, and -NG trials are ongoing.

Pooled analyses of ALKA-372-001, STARTRK-1, and STARTRK-2 with a data cut-off date in May 2018 were performed [52]. Efficacy-evaluable patients included 54 adults with NTRK fusion-positive solid tumors. Ten different types of tumor types were included, with the predominant types being sarcoma (13 (24%) patients) and NSCLC (10 (19%)). Among the 54 patients, 12 (22%) had baseline CNS disease and 31 (57%) had an objective response,

comprising of 4 (7%) complete responses and 27 (50%) partial responses. 9 patients (17%) showed stable disease. The median response duration was 10 months. Among the 11 patients with brain metastases at baseline, six patients had measurable disease for intracranial response: four with complete response or partial response, one with stable disease, and one with progressive disease. The overall safety-evaluable population was 355 patients, and the most common grade 3 or 4 adverse events were weight gain and anemia. The most serious adverse events were nervous system disorders, reported in 10 (3%) of the 355 patients. Overall, entrectinib achieved anti-tumor activity against tumors harboring NTRK1, NTRK2, and NTRK3 fusions, including CNS activity.

#### 3.4. Trk Inhibitors in Clinical Development

Other Trk inhibitors have been developed to overcome resistance mutations. Selitrectinib (LOXO-195, BAY 2731954) and repotrectinib (TPX-0005) are next-generation Trk inhibitors with efficacy against Trk with acquired resistance. Resistance mutations in the amino acid substitution of the Trk kinase domain have been reported in clinical cases [53]. The most common mutations are “solvent-front” mutations, termed after the hydrophilic solvent-exposed portion of the kinase domain ATP-binding site. TrkA G595R and TrkC G623R are solvent-front mutations, and TrkB mutations have not been reported to date [1]. In addition, gatekeeper mutations (TrkA F589L) and xDFG (Aspartate-Phenylalanine-Glycine) site mutations of TrkA (G667S) and TrkC (G696A) were identified in patients.

Selitrectinib has been developed in parallel with clinical trials to prepare for the emergence of resistance to larotrectinib [54]. Selitrectinib showed potent activity against TrkA/C solvent-front- and xDFG site-mutated forms as well as TrkA/C wild-type in *in vitro* and *in vivo* xenograft experiments. Kinase profiling of selitrectinib showed that it is highly selective for Trk kinase. A Phase 1/2 clinical trial for selitrectinib is ongoing (NCT03215511), and interim results have been reported [20]. Patient selection was based on presence of tumor with TRK fusion and tumor progression or intolerance to prior Trk inhibitors. A total of 31 patients were analyzed and an ORR of 34% was reported. Trk mutations were identified in 20 patients, including 14 solvent-front, 4 gatekeeper, and 2 xDFG mutations, and a complete or partial response was observed in 9 patients.

Repotrectinib is a next-generation TKI inhibitor designed to inhibit the solvent-front mutations of Trk, ROS1, and ALK. In addition to TrkA G595R and TrkC G623R, repotrectinib is also active against solvent-front mutations of ROS1 and ALK *in vitro* and *in vivo* [18]. A phase 1/2 clinical trial of repotrectinib (TRIDENT-1, NCT03093116) is ongoing for TKI-refractory patients.

#### 3.5. Adverse Effects of Trk Inhibitors on the Central Nervous System

Given the physiological roles of Trk signaling in the neuronal system, the effects of Trk inhibitors in the CNS are expected. It is reasonable to expect and prepare for the adverse effects of Trk inhibitors on the CNS. As described above, congenital insensitivity to pain is caused by NTRK1 mutation [34]. Based on the role of NTRK1 in pain sensing, NGF/TrkA is a target for analgesics, and several small molecules and antibodies modulating the NGF/TrkA pathway are under development [55].

Trk signaling is known to play a role in nerve growth during the fetal period, while NGF function is reported to induce pain in adulthood [55]. From the beginning of Trk inhibitor development, there was a concern for adverse CNS effects, and thus, adverse events were closely observed and characterized [56]. Representative adverse events related to neurological systems include withdrawal pain, weight gain, and dizziness [48,52].

Patients who discontinued Trk inhibitor therapy experienced symptoms of pain. Full-body ache, muscle pain, allodynia, and concurrent flares of pre-existing pain are described as withdrawal symptoms [56]. The mechanisms of withdrawal pain are not clear, but it is presumed to be caused by increased expression of transient receptor potential vanilloid I, a nociceptive mediator [57]. Weight gain was observed in more than 50% of patients, as expected from the role of the brain-derived neurotrophic factor (BDNF)-

TrkB pathway in appetite centers [38,58,59]. Hyperphagia and consequent obesity were observed upon BDNF-TrkB axis impairment in both mice and humans. Dizziness was caused upon TrkB and TrkC inhibition. Mutant mice with low levels of BDNF in the cerebellum developed ataxia [60]. Mice with NTRK3 gene knockout exhibited abnormal movement and posture [61]. These adverse events in the CNS caused by on-target inhibition of Trk inhibitors should be monitored carefully.

### 3.6. Identification of NTRK Fusions

Obviously, the diagnostic identification of NTRK fusion genes is an important process in tissue-agnostic Trk inhibitor development. Patient selection with NTRK fusion-positive cancers is a key point in screening responders and non-responders. NTRK fusions can be evaluated using immunohistochemistry (IHC), fluorescence in situ hybridization (FISH), reverse transcriptase polymerase chain reaction (RT-PCR), and next-generation sequencing (NGS) [2].

IHC using antibodies against Trk proteins can be utilized for identification of NTRK fusion, as Trk proteins are poorly expressed in normal adult tissues [62]. Positive staining in the IHC test can be interpreted as the presence of NTRK fusions. Information about cellular localization of fused proteins can also be obtained from IHC results. The localization of fusion proteins depends on the normal localization of the fusion partner [62]. For example, LMNA-NTRK1 fusion result in nuclear membrane staining due to the nuclear membrane protein lamin A/C encoded by the LMNA gene, while ETV6-NTRK3 fusions exhibit nuclear staining due to the ETV6-encoding protein located in the nucleus. IHC can be used for diagnosis in conjunction with other diagnostic methods.

FISH is a highly sensitive and specific tool for the detection of fused genes generated from chromosomal rearrangements, such as ALK, ROS1, and RET. In general, FISH has many advantages, such as high sensitivity and quick turn-around time. In case of NTRK1, 2, and 3 fusions, three separate assays are required for each gene. When chromosomal rearrangements involve non-canonical sites or intra-chromosomal rearrangements, FISH can lead to false negative results [63].

RT-PCR uses primers recognizing the 5'-fusion partner and NTRK kinase domain. Since there are numerous fusion partners, RT-PCR has limitations in clinical applications. Furthermore, fused genes with novel fusion partners cannot be detected using RT-PCR [64].

NGS offers the advantage of simultaneous assessment of multiple oncogenes. NGS is a highly sensitive and specific assay via which unknown NTRK fusions can be identified. DNA- and RNA-based NGS assays are currently available. Sometimes DNA-based NGS can fail to detect NTRK fusions because of the large intronic regions. RNA-based NGS assays can overcome this disadvantage of DNA-based NGS, as the results are not affected by intron size. However, the unstable nature of RNA is a major limitation of this assay. Currently, NGS assay sequencing of mature mRNA is considered the gold standard for NTRK fusion detection [64].

In 1998, the FDA approved the first CDx for drug-diagnostic co-development, HercepTest for trastuzumab therapy [65]. According to the regulatory guidance issued by the FDA in 2014, CDx testing is mandatory and must be performed before the use of the corresponding therapeutic product [66]. The FDA has approved an NGS-based CDx test for larotrectinib (Foundation Medicine Inc., F1CDx) [65]. It is a DNA-based NGS assay and was approved based on the retrospective testing of available tumor samples from patients in the three clinical trials of larotrectinib described above. Currently, there is no FDA-approved CDx for entrectinib.

## 4. Conclusions

Novel Trk inhibitors, larotrectinib and entrectinib, exhibit impressive clinical activity in cancer patients with Trk fusions. The tissue-agnostic drug development approach made it possible for a relatively efficient clinical development process. Although the tissue-agnostic approach cannot be applied to all cancer targets, these processes can expedite some of

the drug development projects with unique biomarkers that enable patient selection. The adoption of the tissue-agnostic approach is expected to increase, resulting in an accelerated development process and the possibility of developing therapy for rare cancers.

**Funding:** This research was funded by the National Research Foundation, Government of Korea (grant number 2021R1A2C1007790).

**Institutional Review Board Statement:** Not applicable.

**Informed Consent Statement:** Not applicable.

**Data Availability Statement:** Data sharing not applicable.

**Conflicts of Interest:** The authors declare no conflict of interest.

## Abbreviations

ABL	abl proto-oncogene
ALCL	anaplastic large cell lymphoma
ALK	anaplastic lymphoma kinase
BCR	breakpoint cluster region
BDNF	brain-derived neurotrophic factor
BRAF	B rapidly accelerated fibrosarcoma
CDx	companion diagnostics
CIPA	congenital insensitivity to pain with anhidrosis
CNS	central nervous system
ETV6	ETS variant transcription factor 6
FDA	food and drug administration
FGFR	fibroblast growth factor receptor
FISH	fluorescence in situ hybridization
HER2	human epidermal growth factor receptor 2
IC <sub>50</sub>	half maximal inhibitory concentration
IHC	immunohistochemistry
IMT	inflammatory myofibroblastic tumor
LMNA	lamin A/C
NGF	nerve growth factor
NGS	next-generation sequencing
NSCLC	non-small cell lung cancer
NTRK	neurotrophic tyrosine receptor kinase
ORR	overall response rate
PD-1	programmed cell death protein 1
RET	ret proto-oncogene
ROS1	c-ros proto-oncogene
RT-PCR	reverse transcriptase polymerase chain reaction
SRC	src proto-oncogene
TNK2	tyrosine kinase non receptor 2
TPM3	tropomyosin 3
TPR	translocated promoter region
TRIM24	tripartite motif containing 24
Trk	tropomyosin receptor kinase
xDFG	Aspartate-Phenylalanine-Glycine

## References

1. Cocco, E.; Scaltriti, M.; Drilon, A. NTRK fusion-positive cancers and TRK inhibitor therapy. *Nat. Rev. Clin. Oncol.* **2018**, *15*, 731–747. [CrossRef]
2. Hsiao, S.J.; Zehir, A.; Sireci, A.N.; Aisner, D.L. Detection of Tumor NTRK Gene Fusions to Identify Patients Who May Benefit from Tyrosine Kinase (TRK) Inhibitor Therapy. *J. Mol. Diagn.* **2019**, *21*, 553–571. [CrossRef]
3. Scott, L.J. Larotrectinib: First Global Approval. *Drugs* **2019**, *79*, 201–206. [CrossRef] [PubMed]
4. Al-Salama, Z.T.; Keam, S.J. Entrectinib: First Global Approval. *Drugs* **2019**, *79*, 1477–1483. [CrossRef]

5. Hierro, C.; Matos, I.; Martin-Liberal, J.; De Olza, M.O.; Garralda, E. Agnostic-Histology Approval of New Drugs in Oncology: Are We Already There? *Clin. Cancer Res.* **2019**, *25*, 3210–3219. [CrossRef] [PubMed]
6. Adashek, J.J.; Subbiah, V.; Kurzrock, R. From Tissue-Agnostic to N-of-One Therapies: (R)Evolution of the Precision Paradigm. *Trends Cancer* **2021**, *7*, 15–28. [CrossRef] [PubMed]
7. Jørgensen, J.T. Twenty Years with Personalized Medicine: Past, Present, and Future of Individualized Pharmacotherapy. *Oncologist* **2019**, *24*, e432–e440. [CrossRef]
8. Nahta, R.; Esteva, F.J. Trastuzumab: Triumphs and tribulations. *Oncogene* **2007**, *26*, 3637–3643. [CrossRef]
9. Cohen, P.; Cross, D.; Jänne, P.A. Kinase drug discovery 20 years after imatinib: Progress and future directions. *Nat. Rev. Drug Discov.* **2021**, 1–19. [CrossRef]
10. Langreth, B.R.; Waldholz, M. New era of personalized medicine: Targeting drugs for each unique genetic profile. *Oncologist* **1999**, *4*, 426–427. [CrossRef] [PubMed]
11. Dienstmann, R.; Rodon, J.; Tabernero, J. Drug Development in the Era of Personalized Oncology: From Population-Based Trials to Enrichment and Prescreening Strategies. *Am. Soc. Clin. Oncol. Educ. Book* **2012**, 168–172. [CrossRef] [PubMed]
12. Hayes, D.F. HER2 and Breast Cancer—A Phenomenal Success Story. *N. Engl. J. Med.* **2019**, *381*, 1284–1286. [CrossRef]
13. Shaw, A.T.; Engelman, J.A. Alk in Lung Cancer: Past, Present, and Future. *J. Clin. Oncol.* **2013**, *31*, 1105–1111. [CrossRef]
14. Morris, S.W.; Kirstein, M.N.; Valentine, M.B.; Dittmer, K.G.; Shapiro, D.N.; Saltman, D.L.; Look, A.T. Fusion of a Kinase Gene, Alk, to a Nucleolar Protein Gene, Npm, in Non-Hodgkin's Lymphoma. *Science* **1994**, *263*, 1281–1284. [CrossRef] [PubMed]
15. Lawrence, B.; Perez-Atayde, A.; Hibbard, M.K.; Rubin, B.P.; Cin, P.D.; Pinkus, J.L.; Pinkus, G.S.; Xiao, S.; Yi, E.S.; Fletcher, C.D.; et al. TPM3-ALK and TPM4-ALK Oncogenes in Inflammatory Myofibroblastic Tumors. *Am. J. Pathol.* **2000**, *157*, 377–384. [CrossRef]
16. Lemery, S.; Keegan, P.; Pazdur, R. First FDA Approval Agnostic of Cancer Site—When a Biomarker Defines the Indication. *N. Engl. J. Med.* **2017**, *377*, 1409–1412. [CrossRef]
17. Jørgensen, J.T. Site-agnostic biomarker-guided oncology drug development. *Expert Rev. Mol. Diagn.* **2020**, *20*, 583–592. [CrossRef] [PubMed]
18. Drilon, A.; Ou, S.-H.I.; Cho, B.C.; Kim, D.-W.; Lee, J.; Lin, J.J.; Zhu, V.W.; Ahn, M.-J.; Camidge, D.R.; Nguyen, J.; et al. Repotrectinib (TPX-0005) Is a Next-Generation ROS1/TRK/ALK Inhibitor That Potently Inhibits ROS1/TRK/ALK Solvent-Front Mutations. *Cancer Discov.* **2018**, *8*, 1227–1236. [CrossRef] [PubMed]
19. Turning Point Therapeutics Granted Fast-Track Designation for Repotrectinib in Ntrk-Positive Tki-Pretreated Advanced Solid Tumors. *Turning Point Therapeutics*, 24 August 2020.
20. Hyman, D.; Kummar, S.; Farago, A.; Georger, B.; Mau-Sorensen, M.; Taylor, M.; Garralda, E.; Nagasubramanian, R.; Natheson, M.; Song, L.; et al. Abstract CT127: Phase I and expanded access experience of LOXO-195 (BAY 2731954), a selective next-generation TRK inhibitor (TRKi). *Clin. Trials* **2019**, *79*, 127. [CrossRef]
21. Papadopoulos, K.P.; Borazanci, E.; Shaw, A.T.; Katayama, R.; Shimizu, Y.; Zhu, V.W.; Sun, T.Y.; Wakelee, H.A.; Madison, R.; Schrock, A.B.; et al. U.S. Phase I First-in-human Study of Taletrectinib (DS-6051b/AB-106), a ROS1/TRK Inhibitor, in Patients with Advanced Solid Tumors. *Clin. Cancer Res.* **2020**, *26*, 4785–4794. [CrossRef]
22. Turning Point Therapeutics Announces Initial Clinical Data from Phase 1/2 Sword-1 Study of Ret Inhibitor Tpx-0046. *Turning Point Therapeutics*, 5 April 2021.
23. Voss, M.H.; Hierro, C.; Heist, R.S.; Cleary, J.M.; Meric-Bernstam, F.; Tabernero, J.; Janku, F.; Gandhi, L.; Iafrate, A.J.; Borger, D.R.; et al. A Phase I, Open-Label, Multicenter, Dose-Escalation Study of the Oral Selective Fgfr Inhibitor Debio 1347 in Patients with Advanced Solid Tumors Harboring Fgfr Gene Alterations. *Clin. Cancer Res.* **2019**, *25*, 2699–2707. [CrossRef] [PubMed]
24. Sumitomo Dainippon Pharma Oncology Announces First Patient Dosed in the Dubermatinib Arm of the Leukemia & Lymphoma Society's Beat Aml Master Clinical Trial in Patients with Acute Myeloid Leukemia. 2020. Available online: [www.sdponcology.com/news-media/20201023/](http://www.sdponcology.com/news-media/20201023/) (accessed on 18 June 2021).
25. Janku, F.; Sherman, E.J.; Parikh, A.R.; Feun, L.G.; Tsai, F.; Allen, E.; Zhang, C.; Severson, P.; Inokuchi, K.; Walling, J.; et al. Interim Results from a Phase 1/2 Precision Medicine Study of Plx8394—A Next Generation Braf Inhibitor. *Eur. J. Cancer* **2020**, *138*, S2–S3. [CrossRef]
26. Shen, L.; Guo, J.; Zhang, Q.; Pan, H.; Yuan, Y.; Bai, Y.; Liu, T.; Zhou, Q.; Zhao, J.; Shu, Y.; et al. Tislelizumab in Chinese Patients with Advanced Solid Tumors: An Open-Label, Non-Comparative, Phase 1/2 Study. *J. Immunother. Cancer* **2020**, *8*, e000437. [CrossRef]
27. Cunanán, K.M.; Gonen, M.; Shen, R.; Hyman, D.M.; Riely, G.J.; Begg, C.B.; Iasonos, A. Basket Trials in Oncology: A Trade-Off Between Complexity and Efficiency. *J. Clin. Oncol.* **2017**, *35*, 271–273. [CrossRef] [PubMed]
28. Du Rusquec, P.; Le Tourneau, C. Drug Development in Tissue-Agnostic Indications. *Cancers* **2021**, *13*, 2758. [CrossRef]
29. Shaw, A.T.; Kim, D.-W.; Nakagawa, K.; Seto, T.; Crinó, L.; Ahn, M.-J.; De Pas, T.; Besse, B.; Solomon, B.J.; Blackhall, F.; et al. Crizotinib versus Chemotherapy in Advanced ALK-Positive Lung Cancer. *N. Engl. J. Med.* **2013**, *368*, 2385–2394. [CrossRef] [PubMed]
30. First Tissue-Agnostic Drug Approval Issued. *Cancer Discov.* **2017**, *7*, 656.
31. Okamura, R.; Boichard, A.; Kato, S.; Sicklick, J.K.; Bazhenova, L.; Kurzrock, R. Analysis of NTRK Alterations in Pan-Cancer Adult and Pediatric Malignancies: Implications for NTRK-Targeted Therapeutics. *JCO Precis. Oncol.* **2018**, *2*, 1–20. [CrossRef]



32. Kopetz, S.; Desai, J.; Chan, E.; Hecht, J.R.; O'Dwyer, P.J.; Maru, D.M.; Morris, V.; Janku, F.; Dasari, A.; Chung, W.; et al. Phase II Pilot Study of Vemurafenib in Patients with Metastatic BRAF-Mutated Colorectal Cancer. *J. Clin. Oncol.* **2015**, *33*, 4032–4038. [CrossRef]
33. Sartore-Bianchi, A.; Trusolino, L.; Martino, C.; Bencardino, K.; Lonardi, S.; Bergamo, F.; Zagonel, V.; Leone, F.; Depetris, I.; Martinelli, E.; et al. Dual-Targeted Therapy with Trastuzumab and Lapatinib in Treatment-Refractory, Kras Codon 12/13 Wild-Type, Her2-Positive Metastatic Colorectal Cancer (Heracles): A Proof-of-Concept, Multicentre, Open-Label, Phase 2 Trial. *Lancet Oncol.* **2016**, *17*, 738–746. [CrossRef]
34. Indo, Y.; Tsuruta, M.; Hayashida, Y.; Karim, M.A.; Ohta, K.; Kawano, T.; Mitsubuchi, H.; Tonoki, H.; Awaya, Y.; Matsuda, I. Mutations in the TRKA/NGF receptor gene in patients with congenital insensitivity to pain with anhidrosis. *Nat. Genet.* **1996**, *13*, 485–488. [CrossRef]
35. Smeyne, R.; Klein, R.; Schnapp, A.; Long, L.K.; Bryant, S.; Lewin, A.; Lira, S.A.; Barbacid, M. Severe sensory and sympathetic neuropathies in mice carrying a disrupted Trk/NGF receptor gene. *Nature* **1994**, *368*, 246–249. [CrossRef]
36. Crowley, C.; Spencer, S.D.; Nishimura, M.C.; Chen, K.S.; Pitts-Meek, S.; Armanin, M.P.; Ling, L.H.; McMahon, S.; Shelton, D.L.; Levinson, A.D.; et al. Mice lacking nerve growth factor display perinatal loss of sensory and sympathetic neurons yet develop basal forebrain cholinergic neurons. *Cell* **1994**, *76*, 1001–1011. [CrossRef]
37. Indo, Y. Molecular basis of congenital insensitivity to pain with anhidrosis (CIPA): Mutations and polymorphisms in TRKA (NTRK1) gene encoding the receptor tyrosine kinase for nerve growth factor. *Hum. Mutat.* **2001**, *18*, 462–471. [CrossRef]
38. Yeo, G.S.H.; Hung, C.-C.C.; Rochford, J.; Keogh, J.; Gray, J.; Sivaramakrishnan, S.; O'Rahilly, S.; Farooqi, S. A de novo mutation affecting human TrkB associated with severe obesity and developmental delay. *Nat. Neurosci.* **2004**, *7*, 1187–1189. [CrossRef]
39. Vaishnavi, A.; Le, A.T.; Doebele, R.C. TRKking Down an Old Oncogene in a New Era of Targeted Therapy. *Cancer Discov.* **2014**, *5*, 25–34. [CrossRef]
40. Martin-Zanca, D.; Hughes, S.H.; Barbacid, M. A human oncogene formed by the fusion of truncated tropomyosin and protein tyrosine kinase sequences. *Nature* **1986**, *319*, 743–748. [CrossRef] [PubMed]
41. Greco, A.; Pierotti, M.A.; Bongarzone, I.; Pagliardini, S.; Lanzi, C.; Della Porta, G. TRK-T1 is a novel oncogene formed by the fusion of TPR and TRK genes in human papillary thyroid carcinomas. *Oncogene* **1992**, *7*, 237–242. [PubMed]
42. Stransky, N.; Cerami, E.; Schalm, S.; Kim, J.L.; Lengauer, C. The landscape of kinase fusions in cancer. *Nat. Commun.* **2014**, *5*, 4846. [CrossRef]
43. Knezevich, S.R.; McFadden, D.; Tao, W.; Lim, J.F.; Sorensen, P.H. A novel ETV6-NTRK3 gene fusion in congenital fibrosarcoma. *Nat. Genet.* **1998**, *18*, 184–187. [CrossRef] [PubMed]
44. Chung, H.J.; Park, K.R.; Lee, H.J.; Lee, J.; Kim, J.-H.; Kim, Y.-C.; Han, S.-Y. Effects of KRC-108 on the Aurora A activity and growth of colorectal cancer cells. *Biochem. Biophys. Res. Commun.* **2015**, *461*, 605–611. [CrossRef] [PubMed]
45. Doebele, R.C.; Davis, L.E.; Vaishnavi, A.; Le, A.T.; Estrada-Bernal, A.; Keysar, S.B.; Jimeno, A.; Varella-Garcia, M.; Aisner, D.L.; Li, Y.; et al. An Oncogenic NTRK Fusion in a Patient with Soft-Tissue Sarcoma with Response to the Tropomyosin-Related Kinase Inhibitor LOXO-101. *Cancer Discov.* **2015**, *5*, 1049–1057. [CrossRef]
46. Dubois, S.G.; Laetsch, T.W.; Federman, N.; Turpin, B.K.; Albert, C.M.; Nagasubramanian, R.; Anderson, M.E.; Davis, J.L.; Qamoos, H.E.; Reynolds, M.E.; et al. The use of neoadjuvant larotrectinib in the management of children with locally advanced TRK fusion sarcomas. *Cancer* **2018**, *124*, 4241–4247. [CrossRef] [PubMed]
47. Laetsch, T.W.; DuBois, S.G.; Mascarenhas, L.; Turpin, B.; Federman, N.; Albert, C.M.; Nagasubramanian, R.; Davis, J.L.; Rudzinski, E.; Feraco, A.M.; et al. Larotrectinib for Paediatric Solid Tumours Harbouring Ntrk Gene Fusions: Phase 1 Results from a Multicentre, Open-Label, Phase 1/2 Study. *Lancet Oncol.* **2018**, *19*, 705–714. [CrossRef]
48. Drilon, A.; Laetsch, T.W.; Kummar, S.; DuBois, S.G.; Lassen, U.N.; Demetri, G.D.; Nathanson, M.; Doebele, R.C.; Farago, A.F.; Pappo, A.S.; et al. Efficacy of Larotrectinib in Trk Fusion-Positive Cancers in Adults and Children. *N. Engl. J. Med.* **2018**, *378*, 731–739. [CrossRef]
49. Hong, D.S.; DuBois, S.G.; Kummar, S.; Farago, A.F.; Albert, C.M.; Rohrberg, K.S.; van Tilburg, C.M.; Nagasubramanian, R.; Berlin, J.D.; Federman, N.; et al. Larotrectinib in Patients with Trk Fusion-Positive Solid Tumours: A Pooled Analysis of Three Phase 1/2 Clinical Trials. *Lancet Oncol.* **2020**, *21*, 531–540. [CrossRef]
50. Menichincheri, M.; Ardini, E.; Magnaghi, P.; Avanzi, N.; Banfi, P.; Bossi, R.; Buffa, L.; Canevari, G.; Ceriani, L.; Colombo, M.; et al. Discovery of Entrectinib: A New 3-Aminoindazole as a Potent Anaplastic Lymphoma Kinase (ALK), c-ros Oncogene 1 Kinase (ROS1), and Pan-Tropomyosin Receptor Kinases (Pan-TRKs) inhibitor. *J. Med. Chem.* **2016**, *59*, 3392–3408. [CrossRef]
51. Drilon, A.; Siena, S.; Ou, S.-H.I.; Patel, M.; Ahn, M.J.; Lee, J.; Bauer, T.M.; Farago, A.F.; Wheler, J.J.; Liu, S.V.; et al. Safety and Antitumor Activity of the Multitargeted Pan-TRK, ROS1, and ALK Inhibitor Entrectinib: Combined Results from Two Phase I Trials (ALKA-372-001 and STARTRK-1). *Cancer Discov.* **2017**, *7*, 400–409. [CrossRef]
52. Doebele, R.C.; Drilon, A.; Paz-Ares, L.; Siena, S.; Shaw, A.T.; Farago, A.F.; Blakely, C.M.; Seto, T.; Cho, B.C.; Tosi, D.; et al. Entrectinib in patients with advanced or metastatic NTRK fusion-positive solid tumours: Integrated analysis of three phase 1–2 trials. *Lancet Oncol.* **2020**, *21*, 271–282. [CrossRef]
53. Russo, M.; Misale, S.; Wei, G.; Siravegna, G.; Crisafulli, G.; Lazzari, L.; Corti, G.; Rospo, G.; Novara, L.; Mussolin, B.; et al. Acquired Resistance to the TRK Inhibitor Entrectinib in Colorectal Cancer. *Cancer Discov.* **2016**, *6*, 36–44. [CrossRef]

54. Drilon, A.; Nagasubramanian, R.; Blake, J.F.; Ku, N.; Tuch, B.B.; Ebata, K.; Smith, S.; Lauriault, V.; Kolakowski, G.R.; Brandhuber, B.J.; et al. A Next-Generation TRK Kinase Inhibitor Overcomes Acquired Resistance to Prior TRK Kinase Inhibition in Patients with TRK Fusion-Positive Solid Tumors. *Cancer Discov.* **2017**, *7*, 963–972. [CrossRef]
55. Hirose, M.; Kuroda, Y.; Murata, E. NGF/TrkA Signaling as a Therapeutic Target for Pain. *Pain Pract.* **2015**, *16*, 175–182. [CrossRef]
56. Liu, D.; Flory, J.; Lin, A.; Offin, M.; Falcon, C.; Murciano-Goroff, Y.; Rosen, E.; Guo, R.; Basu, E.; Li, B.; et al. Characterization of on-target adverse events caused by TRK inhibitor therapy. *Ann. Oncol.* **2020**, *31*, 1207–1215. [CrossRef] [PubMed]
57. Zhang, X.; Huang, J.; McNaughton, P. NGF rapidly increases membrane expression of TRPV1 heat-gated ion channels. *EMBO J.* **2005**, *24*, 4211–4223. [CrossRef]
58. Lin, J.C.; Tsao, D.; Barras, P.; Bastarrachea, R.A.; Boyd, B.; Chou, J.; Rosete, R.; Long, H.; Forgie, A.; Abdiche, Y.; et al. Appetite Enhancement and Weight Gain by Peripheral Administration of TrkB Agonists in Non-Human Primates. *PLoS ONE* **2008**, *3*, e1900. [CrossRef] [PubMed]
59. Rios, M.; Fan, G.; Fekete, C.; Kelly, J.; Bates, B.; Kuehn, R.; Lechan, R.M.; Jaenisch, R. Conditional Deletion of Brain-Derived Neurotrophic Factor in the Postnatal Brain Leads to Obesity and Hyperactivity. *Mol. Endocrinol.* **2001**, *15*, 1748–1757. [CrossRef]
60. Richardson, C.A.; Leitch, B. Phenotype of cerebellar glutamatergic neurons is altered in stargazer mutant mice lacking brain-derived neurotrophic factor mRNA expression. *J. Comp. Neurol.* **2004**, *481*, 145–159. [CrossRef] [PubMed]
61. Klein, R.; Silos-Santiago, I.; Smeyne, R.; Lira, S.A.; Brambilla, R.; Bryant, S.; Zhang, L.; Snider, W.D.; Barbacid, M. Disruption of the neurotrophin-3 receptor gene *trkC* eliminates la muscle afferents and results in abnormal movements. *Nature* **1994**, *368*, 249–251. [CrossRef] [PubMed]
62. Hechtman, J.F.; Benayed, R.; Hyman, D.M.; Drilon, A.; Zehir, A.; Frosina, D.; Arcila, M.E.; Dogan, S.; Klimstra, D.S.; Ladanyi, M.; et al. Pan-Trk Immunohistochemistry Is an Efficient and Reliable Screen for the Detection of NTRK Fusions. *Am. J. Surg. Pathol.* **2017**, *41*, 1547–1551. [CrossRef]
63. Penault-Llorca, F.; Rudzinski, E.R.; Sepulveda, A.R. Testing algorithm for identification of patients with TRK fusion cancer. *J. Clin. Pathol.* **2019**, *72*, 460–467. [CrossRef]
64. Beadling, C.; Wald, A.I.; Warrick, A.; Neff, T.L.; Zhong, S.; Nikiforov, Y.E.; Corless, C.L.; Nikiforova, M.N. A Multiplexed Amplicon Approach for Detecting Gene Fusions by Next-Generation Sequencing. *J. Mol. Diagn.* **2016**, *18*, 165–175. [CrossRef] [PubMed]
65. Jørgensen, J.T. The current landscape of the FDA approved companion diagnostics. *Transl. Oncol.* **2021**, *14*, 101063. [CrossRef] [PubMed]
66. FDA. List of Cleared or Approved Companion Diagnostic Devices (In Vitro and Imaging Tools). Available online: <https://www.fda.gov/medical-devices/in-vitro-diagnostics/list-cleared-or-approved-companion-diagnostic-devices-in-vitro-and-imaging-tools> (accessed on 16 June 2021).





## Article

# Discovery of a Novel Template, 7-Substituted 7-Deaza-4'-Thioadenosine Derivatives as Multi-Kinase Inhibitors

Karishma K. Mashelkar <sup>1</sup>, Woong Sub Byun <sup>1</sup>, Hyejin Ko <sup>1</sup>, Kisu Sung <sup>1</sup>, Sushil K. Tripathi <sup>1</sup>,  
Seungchan An <sup>1</sup>, Yun A Yum <sup>1</sup>, Jee Youn Kwon <sup>1</sup>, Minjae Kim <sup>1</sup>, Gibae Kim <sup>1</sup>, Eun-Ji Kwon <sup>1</sup>,  
Hyuk Woo Lee <sup>2</sup>, Minsoo Noh <sup>1</sup>, Sang Kook Lee <sup>1</sup> and Lak Shin Jeong <sup>1,\*</sup>

<sup>1</sup> Research Institute of Pharmaceutical Sciences, College of Pharmacy, Seoul National University, Seoul 08826, Korea; karimashelkar@gmail.com (K.K.M.); sky\_magic@naver.com (W.S.B.); hyejinko@snu.ac.kr (H.K.); stkiss@snu.ac.kr (K.S.); bipinsu.5@gmail.com (S.K.T.); ann081993@snu.ac.kr (S.A.); dua010@snu.ac.kr (Y.A.Y.); wldus5116@snu.ac.kr (J.Y.K.); mingae93@naver.com (M.K.); kgb\_not\_beer@naver.com (G.K.); Ejkwon226@gmail.com (E.-J.K.); minsoonoh@snu.ac.kr (M.N.); sklee61@snu.ac.kr (S.K.L.)

<sup>2</sup> Future Medicine Co., Ltd., Seongnam 13449, Korea; hwlee@futuremedicine.co.kr

\* Correspondence: lakjeong@snu.ac.kr

**Citation:** Mashelkar, K.K.; Byun, W.S.; Ko, H.; Sung, K.; Tripathi, S.K.; An, S.; Yum, Y.A.; Kwon, J.Y.; Kim, M.; Kim, G.; et al. Discovery of a Novel Template, 7-Substituted 7-Deaza-4'-Thioadenosine Derivatives as Multi-Kinase Inhibitors. *Pharmaceuticals* **2021**, *14*, 1290. <https://doi.org/10.3390/ph14121290>

Academic Editors: Mary J. Meegan and Niamh M O'Boyle

Received: 12 October 2021

Accepted: 8 December 2021

Published: 10 December 2021

**Publisher's Note:** MDPI stays neutral with regard to jurisdictional claims in published maps and institutional affiliations.



**Copyright:** © 2021 by the authors. Licensee MDPI, Basel, Switzerland. This article is an open access article distributed under the terms and conditions of the Creative Commons Attribution (CC BY) license (<https://creativecommons.org/licenses/by/4.0/>).

**Abstract:** The development of anticancer drugs remains challenging owing to the potential for drug resistance. The simultaneous inhibition of multiple targets involved in cancer could overcome resistance, and these agents would exhibit higher potency than single-target inhibitors. Protein kinases represent a promising target for the development of anticancer agents. As most multi-kinase inhibitors are heterocycles occupying only the hinge and hydrophobic region in the ATP binding site, we aimed to design multi-kinase inhibitors that would occupy the ribose pocket, along with the hinge and hydrophobic region, based on ATP-kinase interactions. Herein, we report the discovery of a novel 4'-thionucleoside template as a multi-kinase inhibitor with potent anticancer activity. The *in vitro* evaluation revealed a lead **1g** (7-acetylene-7-deaza-4'-thioadenosine) with potent anticancer activity, and marked inhibition of TRKA, CK1δ, and DYRK1A/1B kinases in the kinome scan assay. We believe that these findings will pave the way for developing anticancer drugs.

**Keywords:** 7-deaza-4'-thioadenosine derivatives; multi-kinase inhibitor; anticancer; nucleoside

## 1. Introduction

Although cancer has been extensively investigated, drug resistance remains a major challenge in the clinical progress of anticancer drugs [1]. It is frequently responsible for treatment failure in patients with cancer undergoing monotherapy. Under these circumstances, a polypharmacological strategy may overcome the drug resistance crisis. The question then arises: How would it work? Cancer cells are dependent not only on a single oncogene but also on cells enclosing it. Therefore, inhibition of a single target produces mutations that promote cancer cell survival, in advanced cancers [2]. Rationally designed multi-target inhibitors that could hit more than one oncogenic target may surpass the effect mediated by single-target inhibitors, as they would obstruct cancer cell proliferation and, secondly, block the microenvironment that facilitates oncogenesis [3]. This would more comprehensively inhibit the pathway involved, simultaneously reducing the negative impact on tumor cells to acquire a resistance mutation. Accordingly, the synergistic effect of inhibiting multiple targets would induce less resistance and greater efficacy [3]. As cancer is a polygenic disease, it is worth noting that a single drug acting synchronously on multiple targets is advantageous over the combined use of individual single-target drugs [3]. Accordingly, smaller doses are required for simultaneous targets to produce desired effects as the molecule will be concurrently present in tissues (at the site of action).

On the other hand, combination therapy complicates the dosing schedule, increases the risk of toxicity arising from drug-drug interactions, and negatively impacts patient adherence, contrary to multi-target drugs [4,5]. These well-established facts motivate our interest in the current study. Polypharmacology has become more appealing in recent years and is currently a hot topic in this field [6–8].

One main factor underlying cancer growth is the presence of kinase mutations. Protein kinases play a crucial role in cellular functions by mediating protein phosphorylation. These enzymes transfer the terminal phosphoryl group of adenosine triphosphate (ATP) to a protein substrate, ultimately resulting in processes, such as signal transduction, gene regulation, and metabolism. Therefore, dysregulation of kinases is often associated with several diseases, including cancer [9]. The protein kinase domain is the most common domain encoded by cancer genes [10] and is linked to cancer onset and progression [10,11]. Several multi-kinase inhibitors are currently in clinical use, indicating growing attention for multi-kinase inhibitors [12]; for example, multi-targeted receptor tyrosine kinase inhibitors, such as sorafenib—approved for the treatment of renal cell carcinoma (RCC) and hepatocellular carcinoma, and sunitinib—approved for the treatment of RCC and imatinib-resistant gastrointestinal stromal tumor have been developed [3,13,14]. Recently, the multi-target kinase inhibitor, entrectinib was approved by the Food and Drug Administration for the treatment of ROS1 (c-ros oncogene 1)-positive, metastatic non-small cell lung cancer and solid tumors with neurotrophic receptor tyrosine kinase (NTRK) fusions [15,16].

The majority of the kinase inhibitors are heterocycles, which are ATP-competitive [17–19], i.e., they act by competing with ATP to bind to the ATP-binding site of kinases, and therefore, block the phosphorylation process. The ATP binding site of protein kinases is illustrated in Figure 1A. The catalytic domain of all protein kinases encompasses two lobes, linked by a flexible hinge region. ATP binds to the cleft, between the two lobes, a highly conserved catalytic structure in protein kinases [20], where the transfer of  $\gamma$ -phosphate of ATP to protein substrate is catalyzed by kinases in their active DFG-in conformation. The adenine ring from ATP forms two hydrogen bonds with the amino acids in the hinge region [21]. The ATP pocket also contains the unoccupied hydrophobic pockets and a hydrophilic ribose region. Most of the ATP-competitive inhibitors known, commonly occupy the hinge and hydrophobic regions I, II [22,23] but rarely the ribose pocket. Nevertheless, it is worthy to note that, occupying the ribose region results in improved binding towards kinases as demonstrated by Gandin et al. [23]. Since ATP binding site is conserved in protein kinases, it could be a challenging task to design selective multi-kinase inhibitors [24] as it can often lead to off-target interactions [22,25]. It may be advantageous in treating polygenic diseases like cancer, where polypharmacological agents are more effective [3]. However, to maintain the safety profile of a multi-kinase inhibitor, only specific kinases should be targeted [22]. It would be of great importance to find out the combination of kinases whose inhibition would result in therapeutic benefits without unwanted side effects [26,27]. The state-of-the-art of kinase inhibitors in human trials have been provided by Klaeger et al. [28].

In the present study, we aimed to design multi-kinase inhibitors that would interact with the hinge region, hydrophobic pocket I, also known as buried region adjacent to the hinge region and ribose pocket at the same time. The interactions with the hydrophobic pocket have frequently been utilized to achieve inhibitor selectivity over kinases [23]. On this basis, we attempted to design novel kinase inhibitors with a nucleoside skeleton as it's an ATP-mimic by modifying the hydrophobic residue (R), based on ATP-kinase interactions, as illustrated in Figure 1B. These compounds are expected to simultaneously inhibit several kinases, given the sequence and structural homology among the ATP binding sites of kinases [20]. Nevertheless, we wanted to determine the most suitable substituent for the hydrophobic pocket which is not occupied by ATP, whether acting as a pharmacophore for selective kinase inhibition. To achieve this goal, we selected a 7-deazaadenine scaffold, as it serves as a good template for functionalization at the 7-position to occupy the adjacent hydrophobic pocket, thereby enhancing the interactions with the kinase. It is interesting to note how a subtle structural variation in the nucleobase

of adenosine exerts cytotoxic biological properties, as demonstrated by a natural product tubercidin (7-deazaadenosine) [29,30]. The 7-substituted-tubercidin analogs also showed very interesting anti-cancer activity [31]. The sugar pocket is predominantly hydrophilic and conserved in most protein kinases. It is well known that the bioisosteric replacement of oxygen with sulfur on furanose imparts chemotherapeutic properties to its respective sulfur analog [32–35] with metabolic stability [36]. Like the ribose ring in ATP, the hydrophilic polar hydroxyl group of the 4-thiosugar moiety will form a hydrogen bond with the sugar region enabling the molecule to fit in it, resulting in enhanced binding [23].

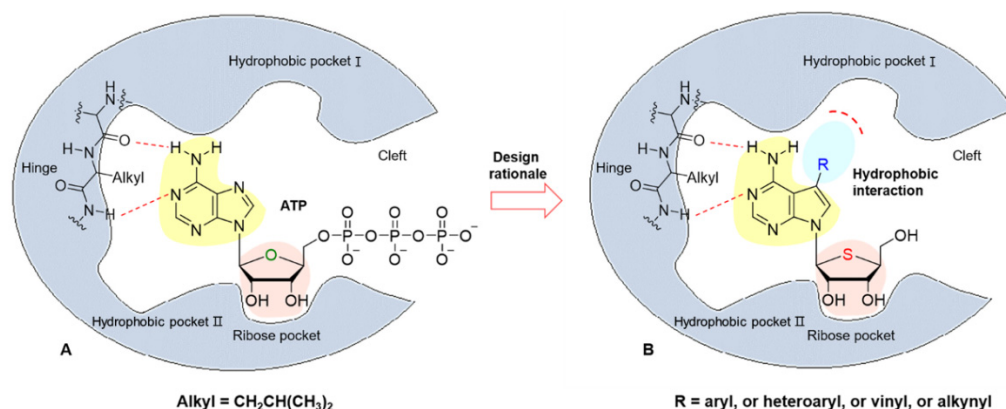


**Figure 1.** The rationale for the design of multi-kinase inhibitors with a nucleoside skeleton. (A) Schematic representation displaying catalytic domain of typical protein kinases binding ATP. Important interactions are highlighted with either colored or dashed lines, indicating hydrophobic interaction/hydrogen bonding. (B) Rational design of kinase inhibitors based on ATP-kinase interactions.

All the synthesized compounds were evaluated for their anticancer activity by employing a sulforhodamine B (SRB) colorimetric assay and the most potent compound **1g** (7-acetylene-7-deaza-4'-thioadenosine) was screened for kinase panel assay. Accordingly, compound **1g** was found to inhibit TRKA (neurotrophic tyrosine receptor kinase 1, NTRK1), DYRK1A/1B (dual specificity tyrosine-phosphorylation-regulated kinase 1A and 1B), and CK1 $\delta$  (casein kinase 1 delta, CSNK1D) kinases, reportedly associated with overexpression in cancer cells [11,37–39]. To the best of our knowledge, we report for the first time the design and synthesis of 7-substituted 7-deaza-4'-thionucleoside analogs that are supposed to simultaneously occupy hinge, hydrophobic, and ribose regions and their structure-activity relationship as a multi-kinase inhibitor against TRKA, DYRK1A, DYRK1B, and CK1 $\delta$  with potent anticancer activity.

## 2. Results and Discussion

### 2.1. Chemistry

The structures of synthesized compounds are represented in Figure 2.

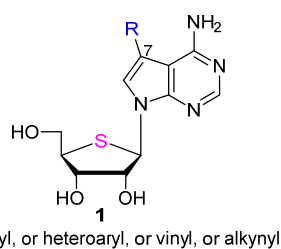
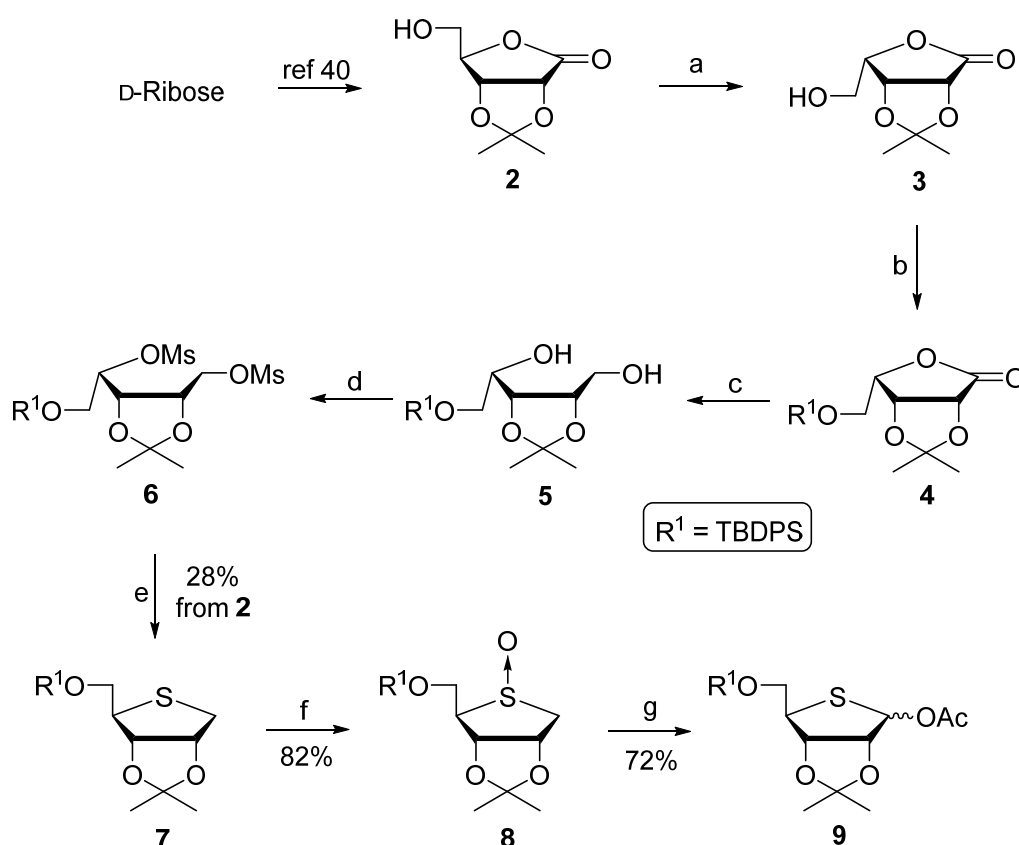


**Figure 2.** The structures of target nucleoside analogs were modified at the C7 position.

As shown in Scheme 1, to synthesize the final nucleoside **1**, we first synthesized the glycosyl donor **9** from commercially available D-ribose.

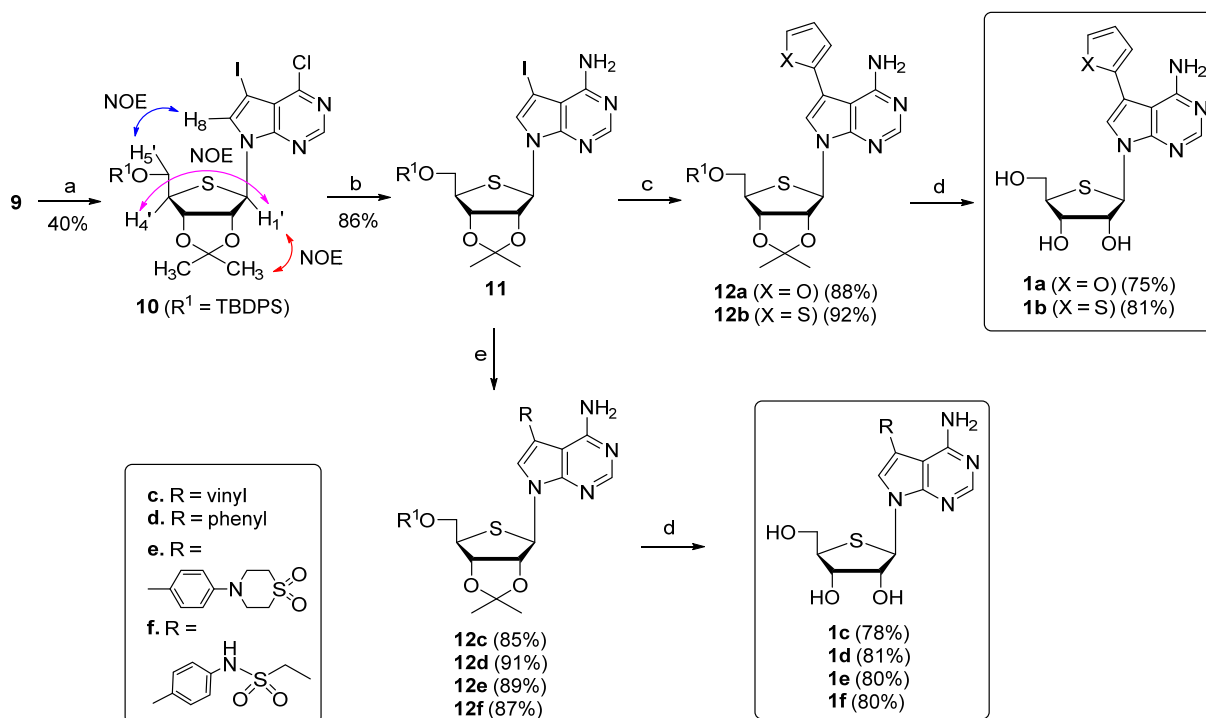


**Scheme 1.** Synthesis of glycosyl donor **9** from D-ribose. Reagents and conditions: (a) (i) MsCl, pyridine, 0 °C, 4 h; (ii) KOH, H<sub>2</sub>O, rt, 12 h; (b) TBDPSCl, imidazole, DMAP, CH<sub>2</sub>Cl<sub>2</sub>, 0 °C to rt, 12 h; (c) NaBH<sub>4</sub>, THF/MeOH, 0 °C to rt, 2 h; (d) MsCl, Et<sub>3</sub>N, CH<sub>2</sub>Cl<sub>2</sub>, 0 °C to rt, 2 h; (e) Na<sub>2</sub>S·9H<sub>2</sub>O, DMF, 90 °C, 15 h; (f) *m*CPBA, CH<sub>2</sub>Cl<sub>2</sub>, −78 °C, 45 min; (g) acetic anhydride, 110 °C, 4 h.

D-Ribose was converted to 2,3-O-isopropylidene-D-ribonic  $\gamma$ -lactone (**2**) using the two steps protocol as described previously [40]. First, D-ribose was converted to D-ribonolactone using bromine/water in the presence of potassium carbonate and later treated with acetone in the presence of a catalytic amount of concentrated sulfuric acid at room temperature to afford **2**. Following the reported general protocol [41] for thiosugar **7**, the inversion of configuration at the C4 chiral center of D-ribonolactone was achieved by treating **2** initially with mesyl chloride and subjecting it to base hydrolysis using aqueous potassium hydroxide solution to give **3** with inverted stereochemistry. Protection of the C5-hydroxyl of **3** with *tert*-butyldiphenylsilyl (TBDPS), followed by reduction of the resulting compound **4** with NaBH<sub>4</sub>, afforded diol **5**. Sulfur heterocyclization was performed by converting **5** to dimesylate **6**, immediately reacted with sodium sulfide nonahydrate at 90 °C to give **7** at a 28% overall yield from **2**. Compound **7** was subjected to *m*CPBA oxidation at −78 °C to give sulfoxide **8** (82% yield). Pummerer rearrangement of **8** occurred upon heating with acetic anhydride to afford glycosyl donor **9** as a 1:1.6  $\alpha/\beta$  anomeric mixture.

The glycosyl donor **9** was then condensed with silylated 7-deaza-7-iodo-6-chloropurine under heating at 80 °C for 1 h in the presence of a Lewis acid, TMSOTf, to afford the desired  $\beta$ -stereoisomer **10** as a single stereoisomer (40% yield; Scheme 2); however, the same reaction at room temperature failed to afford the desired product. The  $\beta$  configuration of condensed nucleoside **10** was easily determined by 2D NOESY experiments. The NOESY spectrum revealed a correlation between 1'-H and 4'-H, as well as between 1'-H and one of the two methyl groups of the acetonide group. A correlation between 5'-H and H-8 was also observed, confirming the presence of the  $\beta$ -D-anomer (see the Supporting Information). Ammonolysis of **10** in *tert*-butanolic ammonia at 90 °C produced key intermediate

**11**, which was ready for functionalization with hydrophobic groups at the C7 position via palladium-catalyzed cross-coupling reactions. Pd-catalyzed Stille coupling of 7-iodo derivative **11** with 2-tributylstannylfuran and 2-tributylstannylthiophene in the presence of  $\text{PdCl}_2(\text{PPh}_3)_2$  yielded 7-furanyl and 7-thiofuranyl derivatives **12a** and **12b**, respectively. Removal of acetonides of **12a** and **12b** with 50% aqueous trifluoroacetic acid (TFA) afforded the final nucleosides, **1a**, and **1b**, respectively.

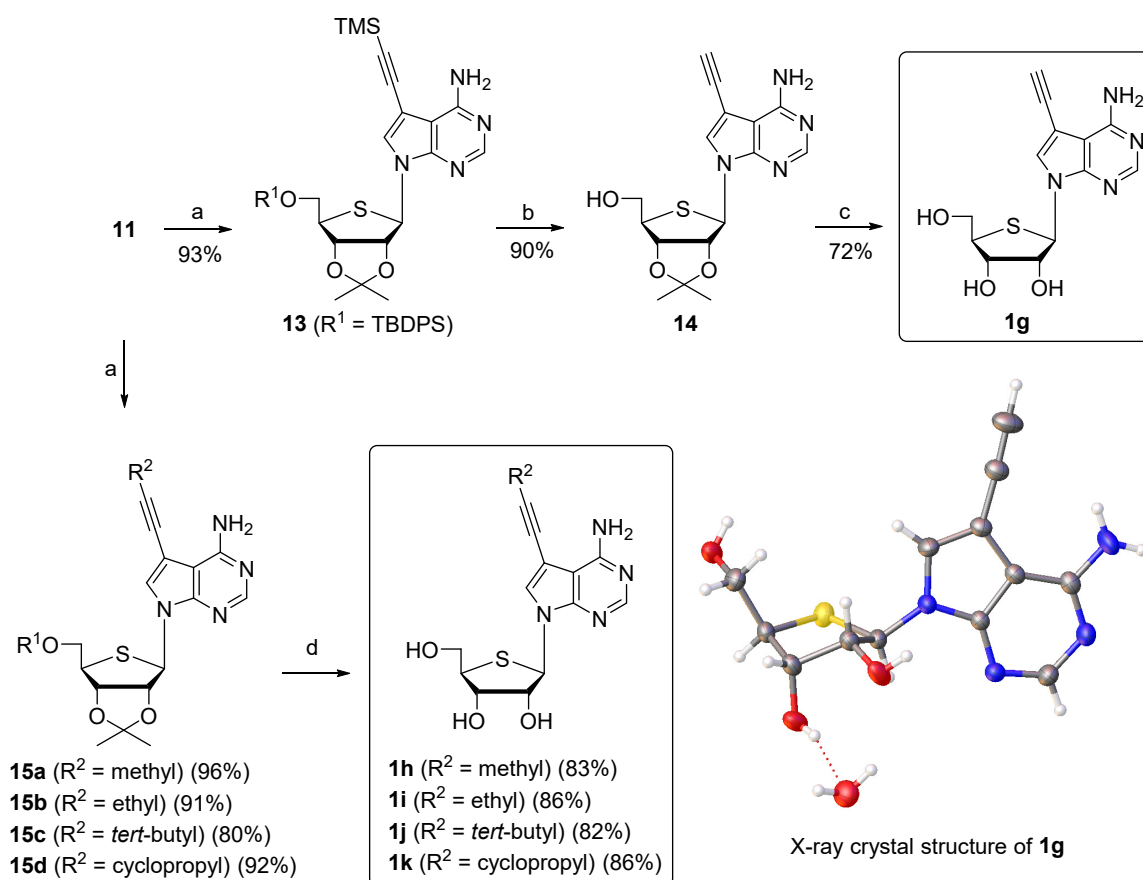


**Scheme 2.** Synthesis of 7-substituted 7-deaza-4'-thioadenosine derivatives **1a–f**. Reagents and conditions: (a) 7-Deaza-7-iodo-6-chloropurine, BSA, TMSOTf,  $\text{CH}_3\text{CN}$ , rt to  $80^\circ\text{C}$ , 1 h; (b)  $\text{NH}_3$ /*tert*-BuOH,  $90^\circ\text{C}$ , 12 h; (c) corresponding 2-tributylstannylheteroaryl,  $\text{PdCl}_2(\text{PPh}_3)_2$ , THF, MW,  $70^\circ\text{C}$ , 1 h; (d) 50% TFA/ $\text{H}_2\text{O}$ , THF, rt, 12 h; (e) corresponding boronic ester,  $\text{PdCl}_2(\text{PPh}_3)_2$ ,  $\text{Na}_2\text{CO}_3$ , DMF/ $\text{H}_2\text{O}$ , MW,  $70^\circ\text{C}$ , 1 h.

Further Suzuki coupling reactions were performed to introduce other hydrophobic groups, such as vinyl, phenyl, and 4-substituted-phenyl to **11**. Coupling of **11** with vinyl boronic ester in the presence of  $\text{PdCl}_2(\text{PPh}_3)_2$  in DMF/ $\text{H}_2\text{O}$  gave **12c** in 85% yield. In this Suzuki coupling reaction, water was used as a co-solvent to avoid side reactions, resulting from Heck coupling [42]. The desired Suzuki coupled product was obtained as a single product. Similar Suzuki reactions of **11** with phenyl and 4-substituted phenyl boronic esters afforded 7-phenyl and 7-(4-substituted)phenyl derivatives, **12d–f**. Treatment of **12c–f** with 50% aqueous TFA yielded the final nucleosides **1c–f**, respectively.

Next, to introduce other linear hydrophobic groups, such as acetylene, Sonogashira coupling was employed, as shown in Scheme 3. Treatment of **11** with trimethylsilyl acetylene in the presence of a palladium catalyst and copper iodide afforded **13** (93% yield). Removal of the silyl groups of **13** with 1 M TBAF solution in THF afforded **14**, which was treated with 2 N HCl to yield the 7-acetylene derivative **1g**. The molecular structure of **1g** was confirmed by a single X-ray crystal analysis (CCDC 1575257); further evidence supporting the  $\beta$ -configuration is provided in the Supporting Information [43]. Several 2-substituted acetylene analogs **15a–d** were also synthesized from **11** by employing the same Sonogashira coupling conditions. The final propylene, butylene, *tert*-butyl acetylene, and cyclopropyl acetylene analogs **1h–k** were obtained by treating **15a–d** with 50% aqueous TFA at room temperature.



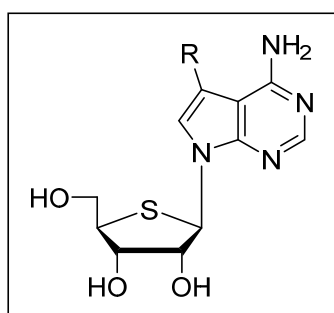


**Scheme 3.** Synthesis of 7-substituted 7-deaza-4'-thioadenosine derivatives **1g–k**. Reagents and conditions: (a) corresponding alkyne,  $\text{PdCl}_2(\text{PPh}_3)_2$ ,  $\text{CuI}$ ,  $\text{Et}_3\text{N}$ , DMF, MW,  $50^\circ\text{C}$ , 1 h; (b) 1 M TBAF, THF, rt, 40 min; (c) 2 N HCl, THF, rt, 15 h; (d) 50% TFA/ $\text{H}_2\text{O}$ , THF, rt, 12 h.

## 2.2. Biological Evaluation

### 2.2.1. Antiproliferative Activity

All synthesized compounds **1a–k** were evaluated for their antiproliferative activity against six different cancer cell lines, including human lung (A549), colon (HCT116), breast (MDA-MB-231), liver (SK-HEP-1), stomach (SNU638), and prostate (PC-3) cancer cells, using SRB colorimetric assay [44,45]. As demonstrated in Table 1, compounds **1a** and **1b** possessing furanyl and thiofuranyl moieties at the 7-position, respectively, exhibited moderate antiproliferative activity. Compound **1c**, with a vinyl substituent at the 7-position, displayed potent anticancer activity, whereas bulky groups, such as phenyl (**1d**) and substituted phenyls (**1e** and **1f**) showed low to no anticancer activity. In contrast, the linear acetylene moiety (**1g**) at the 7-position exhibited excellent anticancer activity in the nanomolar range. Surprisingly, 2-substituted acetylene derivatives **1h–k** abolished antiproliferative activity. This result demonstrates that a small and linear hydrophobic group, such as acetylene is necessary for potent anticancer activity. Since compound **1g** exhibited the most potent antiproliferative activity against cancer cells ( $\text{IC}_{50} = 0.004\text{--}0.06 \mu\text{M}$ ), the antiproliferative activity of **1g** against normal cells was additionally evaluated in primary dermal fibroblast cells. Compound **1g** also showed considerable growth inhibition in cultured human normal dermal fibroblast cells ( $\text{IC}_{50} = 0.15 \mu\text{M}$ ). Although rather toxic, compound **1g** seems to be more potent in the antiproliferative activity of cancer cells than normal cells.

**Table 1.** Anticancer activity of the final 7-substituted 7-deaza-4'-thionucleosides **1a–k** against several human cancer cell lines.

- 1a** (R = 2-furanyl)  
**1b** (R = 2-thiofuranyl)  
**1c** (R = vinyl)  
**1d** (R = phenyl)  
**1e** (R = 4-phenylthiomorpholine 1,1-dioxide)  
**1f** (R = *N*-phenylethanesulfonamide)  
**1g** (R = acetylene)  
**1h** (R = propylene)  
**1i** (R = butylene)  
**1j** (R = *tert*-butyl acetylene)  
**1k** (R = cyclopropyl acetylene)

Compound No.	IC <sub>50</sub> (μM) <sup>a</sup>					
	A549 <sup>b</sup>	HCT116 <sup>c</sup>	MDA-MB-231 <sup>d</sup>	SK-HEP-1 <sup>e</sup>	SNU638 <sup>f</sup>	PC-3 <sup>g</sup>
<b>1a</b>	1.02	2.16	3.31	3.38	1.95	2.46
<b>1b</b>	1.65	1.74	2.72	1.38	2.41	2.48
<b>1c</b>	0.97	0.56	0.31	0.22	0.47	0.2
<b>1d</b>	7.57	6.35	8.83	7.81	6.32	9.21
<b>1e</b>	>50	>50	>50	>50	>50	>50
<b>1f</b>	41.6	30.6	30.1	10.3	27.5	15.4
<b>1g</b>	0.06	0.03	0.05	0.05	0.03	0.004
<b>1h</b>	>50	>50	45.5	6.05	>50	>50
<b>1i</b>	>50	>50	>50	>50	>50	>50
<b>1j</b>	>50	>50	29.6	>50	>50	>50
<b>1k</b>	>50	>50	30.6	8.31	>50	>50
Etoposide <sup>h</sup>	0.36	1.11	4.9	0.91	0.41	23.4
Gemcitabine <sup>i</sup>	0.3	0.2	1.1	0.2	0.1	3.6

<sup>a</sup> Measured using SRB assay. <sup>b</sup> Human lung cancer cells. <sup>c</sup> Human colon cancer cells. <sup>d</sup> Human breast cancer cells. <sup>e</sup> Human liver cancer cells. <sup>f</sup> Human stomach cancer cell. <sup>g</sup> Human prostate cancer cells. <sup>h</sup> Etoposide was used as positive control. <sup>i</sup> Gemcitabine was used as positive control [44].

### 2.2.2. Kinome Scan Profile

To characterize the kinase inhibition profile of the most potent compound **1g**, it was profiled against a panel of 96 kinases at a concentration of 1 μM (Figure 3). The results revealed that compound **1g** exhibited strong inhibitory activities against four kinases at 1 μM (<20% activity remaining), i.e., TRKA (NTRK1), DYRK1B, and CK1δ (CSNK1D) among the panel (see the Supporting Information for tabular representation of kinome scan data, Table S1). Since compound **1g** showed strong inhibition of DYRK1B, it was evaluated for its isoform, DYRK1A inhibition. Compound **1g** displayed potent inhibition of DYRK1A (IC<sub>50</sub> = 43 nM, see the Supporting information, Table S2). These kinases are reportedly involved in cancer initiation and progression [11,37–39] and represent promising targets for cancer therapy. Based on this result, it could be inferred that the hydrophobic pocket in the ATP binding site of these four kinases could accommodate only small and linear hydrophobic groups such as acetylene for kinase inhibition. Next, the concentration-dependent inhibitory activities of compounds **1a–k** were investigated and the half-maximal inhibitory concentration (IC<sub>50</sub>) was determined against four kinases, TRKA, DYRK1A, DYRK1B, and CK1δ (see the Supporting information, Table S2). The kinase inhibition trend observed for **1a–k** was almost similar to that of their antiproliferative activity. In general, compounds **1a**, **1b**, and **1g** exhibited excellent kinase inhibition activities, whereas compounds **1c** and **1d** exhibited moderate kinase inhibition. Among compounds tested, compounds **1a** and **1b** with 7-furanyl and 7-thiofuranyl substituents, respectively showed excellent kinase inhibition activity against NTRK1, whereas compounds **1a** and **1g** with 7-furanyl and 7-acetylene substituents, respectively showed excellent kinase inhibition activity against DYRK1A and DYRK1B. Compounds **1b** and **1d** with 7-thiofuranyl and 7-phenyl substituents, respectively showed excellent inhibition against CSNK1D. However,

sterically demanding compounds **1e** and **1f** and the 2-substituted acetylene derivatives **1h–k** demonstrated weak to no inhibitory activity. Compound **1g** showed the best antiproliferative activity, but compound **1a** was discovered as the best inhibitory compound against the above-mentioned four kinases, indicating that the anti-cancer effect of **1g** might occur by unexpected mode of action.

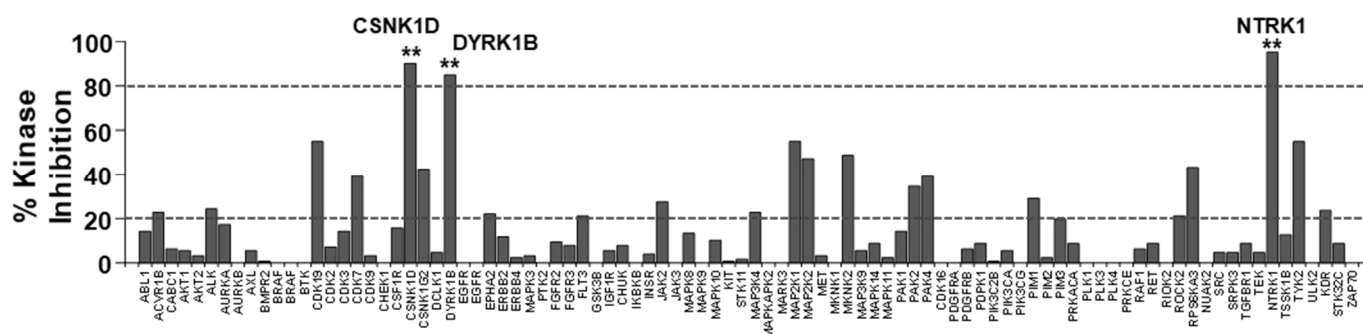


**Figure 3.** Kinase inhibition profile of compound **1g**. Kinome scan assays were performed for compound **1g** (1  $\mu$ M) against 96 kinases. \*\*—strong inhibition of target kinases (<20% activity remaining).

### 2.2.3. Antiproliferative Activity against KM12 and ACHN Cell Lines

The effect of **1g** on cell growth was also determined in KM12, a colon cancer cell line that highly expresses NTRK1/2/3 and DYRK3. Compared to doxorubicin ( $IC_{50} = 0.12 \mu$ M), compound **1g** ( $IC_{50} = 0.07 \mu$ M) showed marked activity against the cell growth of KM12. Likewise,  $IC_{50}$  of **1g** on cell growth of ACHN, a renal cancer cell line, expressing CK1 $\delta$  and DYRK2 was approximately  $0.04 \mu$ M, when compared with  $0.04 \mu$ M of doxorubicin, suggesting the highly effective and selective anti-proliferative activity of **1g** in cancer cell lines expressing NTRK, DYRK2 or CK1 $\delta$ ; However, we can't exclude the possibility that anti-cancer phenotype might be driven through some other mechanism.

### 2.2.4. Metabolic Stability and CYP Inhibition

Based on anticancer and kinase inhibition data, compound **1g** was examined for its microsomal stability and CYP isozyme inhibition in vitro (Table 2). Compound **1g** was metabolically stable in human liver microsomes. Moreover, it showed no CYP isozyme inhibition against the five major drug-metabolizing cytochrome P450 isozymes.

**Table 2.** Human liver microsomal stability and CYP isozyme inhibition activity of **1g**.

Compound No.	Metabolic Stability (%) <sup>a</sup>	CYP Inhibition, $IC_{50}$ ( $\mu$ M) <sup>b</sup>				
		CYP1A2	CYP2C9	CYP2C19	CYP2D6	CYP3A4
<b>1g</b>	82.3	>20	>20	>20	>20	>20
Verapamil	15.3	-	-	-	-	-
Ketoconazole <sup>d</sup>	-	95.7 <sup>c</sup>	93.6 <sup>c</sup>	93.6 <sup>c</sup>	96.0 <sup>c</sup>	27.2 <sup>c</sup>

<sup>a</sup> % Remaining during 30 min. <sup>b</sup>  $IC_{50} < 1 \mu$ M—potent inhibition;  $1 \mu$ M <  $IC_{50} < 10 \mu$ M—moderate inhibition;  $IC_{50} > 10 \mu$ M—no or weak inhibition. <sup>c</sup> Percentage of enzyme remaining after inhibition. <sup>d</sup> CYP3A4 inhibitor (0.1  $\mu$ M).

### 2.3. Docking Analysis

Next, to justify the rationale of this design strategy, the ligand-bound DYRK1A (PDB ID: 7A51) [46] and TRKA (PDB ID: 5JFV) [47] crystal structures were used for the molecular docking study (Figure 4). The docked pose of compound **1g** into the ATP binding site of DYRK1A and TRKA, as depicted in Figure 4A and 4B respectively, revealed that the purine ring formed two key hydrogen bonds with hinge residue Leu 241, and Glu 239 of DYRK1A, whereas in the case of TRKA the purine ring of **1g** formed hydrogen bonding with Met 592 and Glu 590, in a manner comparable with that of ATP. Furthermore, hydrogen bonding interaction was seen between 5'-OH of **1g** and Glu 291 of DYRK1A (Figure 4C). Similarly, hydrogen bonding interaction between 5'-OH of **1g** and Glu 518 of TRKA was

observed. In addition, the acetylene moiety occupied the hydrophobic pocket as supposed and displayed hydrophobic interactions with gatekeeper residue, Phe 238 and Val 306 of DYRK1A (Figure 4C). While, in the TRKA: **1g** docked pose acetylene was found to form hydrophobic interactions with the gatekeeper residue, Phe 589 and Phe 669 (Figure 4D). Additionally, a hydrophobic interaction of 4-thio of the sugar moiety with Val 173 and Val 524 of DYRK1A and TRKA, respectively was observed. Thus, it can be concluded that compound **1g** fits markedly well in the ATP binding sites of DYRK1A and TRKA, thus providing a new scaffold that inhibits the activity of these enzymes.

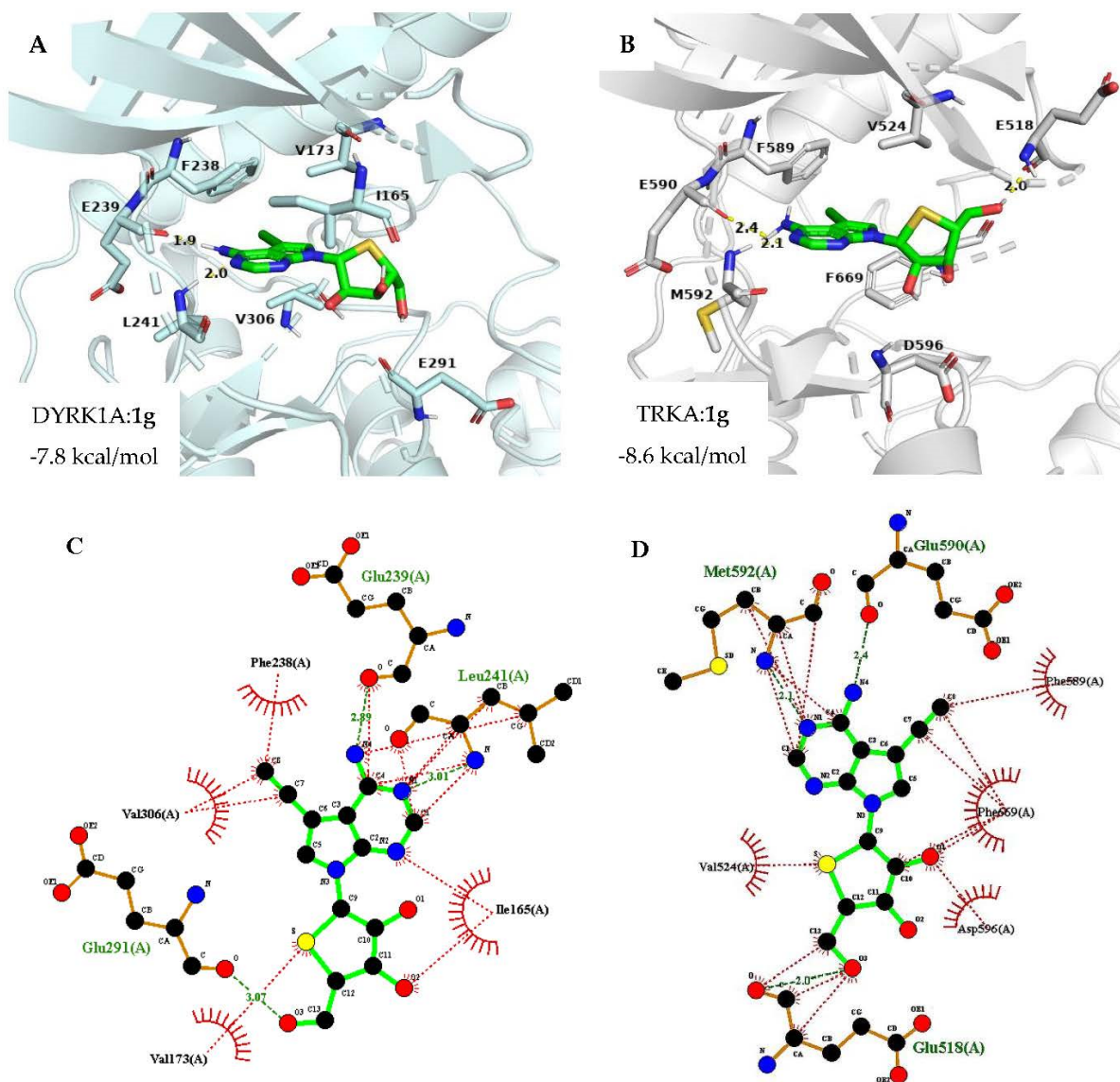


**Figure 4.** (A) Proposed binding mode of **1g** (represented in green) in the ATP binding site of (A) DYRK1A (represented in pale cyan; PDB ID: 7A51). (B) TRKA (represented in gray; PDB ID: 5JFV). Hydrogen bonding is represented as yellow dashed lines. Non-polar hydrogen atoms are omitted. (B) 2D interaction diagram of **1g** (represented in green) with (C) DYRK1A amino acid residues. (D) TRKA amino acid residues.

### 3. Materials and Methods

#### 3.1. General Methods

Proton ( $^1\text{H}$ ) and carbon ( $^{13}\text{C}$ ) NMR spectra were recorded on a JEOL JNM-GCX (400/100 MHz), Bruker AMX-500 (500/125 MHz), or JEOL JNM-ECA 600 (600/150 MHz) spectrometer. Chemical shifts are given in parts per million ( $\delta$ ), calibrated to the solvent peak, and coupling constants ( $J$ ) in hertz (Hz). High-resolution mass (HRMS) measure-

ments were recorded on a Thermo LCQ XP instrument. UV spectra were recorded in methanol on a U-3000 made by Hitachi. Optical rotations were measured on Jasco III in an appropriate solvent and  $[\alpha]_D^{25}$  values are given in  $10^{-1}$  deg  $\text{cm}^2 \text{g}^{-1}$ . Melting points were determined on a Barnstead electrothermal 9100 instrument and are uncorrected. Microwave-assisted reactions were conducted in Biotage Initiator+ US/JPN (part no. 356007) microwave reactor. The TLC spots were examined under ultraviolet light at 254 nm and further visualized by *p*-anisaldehyde or phosphomolybdic acid stain solution. Column chromatography was performed using silica gel (Kieselgel 60, 70–230 mesh, Merck). The purity of all tested compounds was determined by high-performance liquid chromatography (HPLC) analysis, confirming  $\geq 95\%$  purity.

### 3.2. Chemical Synthesis

#### 3.2.1. (3aR,6S,6aR)-6-(Hydroxymethyl)-2,2-dimethyldihydrofuro[3,4-d][1,3]dioxol-4(3aH)-one (3)

To an ice-cooled solution of **2** (50 g, 0.265 mol) in pyridine (330 mL), methanesulfonyl chloride (52.34 g, 0.45 mol) was dropwise added under a nitrogen atmosphere and the solution was stirred at room temperature for 4 h. The reaction was quenched with slow addition of saturated aqueous  $\text{NaHCO}_3$  (520 mL) with stirring until no effervescence and extracted with dichloromethane (2 L). The combined organic layer was washed successively with water and brine, dried ( $\text{MgSO}_4$ ), and concentrated in vacuo below  $25^\circ\text{C}$  to give the crude product. To this crude mesylate, a solution of potassium hydroxide (36.74 g, 0.65 mol) in water (250 mL) was added using a dropping funnel, maintaining the temperature below  $30^\circ\text{C}$ . This reaction mixture was stirred at room temperature for 12 h and then adjusted to pH 3.0 to 4.0 by adding 3 M hydrochloric acid (260 mL). The acidic solution was concentrated under reduced pressure to afford a solid mass. The solid mass was triturated with acetone (2 L) and heated to  $50^\circ\text{C}$  for 30 min. The acetone was decanted, dried over anhydrous  $\text{MgSO}_4$ , and filtered. The filtrate was concentrated to obtain crude **3** ( $R_f = 0.45$ , TLC eluent =  $\text{CH}_2\text{Cl}_2/\text{MeOH}$ , 19:1).

#### 3.2.2. (3aR,6S,6aR)-6-(((*tert*-butyldiphenylsilyl)oxy)methyl)-2,2-dimethyldihydrofuro[3,4-d][1,3]dioxol-4(3aH)-one (4)

To a solution of **3** in methylene chloride (240 mL), imidazole (8.78 g, 129 mmol) was added, followed by dropwise addition of *tert*-butyldiphenylsilyl chloride (26 g, 94.26 mmol) at  $0^\circ\text{C}$ . After being stirred at room temperature for 12 h, the reaction mixture was partitioned between methylene chloride ( $3 \times 600$  mL) and water (760 mL). The layers were separated and the combined organic layer was dried ( $\text{MgSO}_4$ ), filtered, and evaporated to give crude **4** ( $R_f = 0.50$ , TLC eluent = hexane/ethyl acetate, 4:1).

#### 3.2.3. (S)-2-(((*tert*-butyldiphenylsilyl)oxy)-1-((4S,5R)-5-(hydroxymethyl)-2,2-dimethyl-1,3-dioxolan-4-yl)ethan-1-ol (5)

The crude **4** was dissolved in THF-MeOH (285 mL-54 mL) and to this, sodium borohydride (14.64 g, 387.07 mmol) was added portion wise at  $0^\circ\text{C}$ . After stirring for 2 h at room temperature, the reaction mixture was quenched with glacial acetic acid (26 mL) and evaporated. The residue was diluted with 20% aqueous potassium sodium tartrate (500 mL) and the aqueous layer was extracted with ethyl acetate ( $3 \times 600$  mL). The organic layer was washed with brine, dried over  $\text{MgSO}_4$ , and evaporated to obtain crude **5** ( $R_f = 0.50$ , TLC eluent = hexane/ethyl acetate, 3:2).

#### 3.2.4. (S)-2-(((*tert*-butyldiphenylsilyl)oxy)-1-((4R,5R)-2,2-dimethyl-5-((methylsulfonyl)oxy)methyl)-1,3-dioxolan-4-yl)ethyl Methanesulfonate (6)

To a solution of **5** in methylene chloride (277 mL), 4-dimethylaminopyridine (0.36 g, 2.96 mmol) and triethylamine (106.40 g, 1051.53 mmol) were added and the solution was cooled to  $0^\circ\text{C}$ . To this methanesulfonyl chloride (59.11 g, 516.09 mmol) was added dropwise and the reaction mixture was stirred at room temperature for 2 h. The reac-

tion was quenched with saturated aqueous NaHCO<sub>3</sub> (300 mL) until no effervescence and extracted with methylene chloride (3 × 520 mL). The combined organic layer was washed with brine (150 mL), dried (MgSO<sub>4</sub>), and passed through silica to remove any inorganic impurities and evaporated below 25 °C to give crude di-*O*-mesylate **6** (*R*<sub>f</sub> = 0.55, TLC eluent = hexane/ethyl acetate, 3:2).

### 3.2.5. *tert*-Butyl(((3*aS*,4*R*,6*aR*)-2,2-dimethyltetrahydrothieno[3,4-*d*][1,3]dioxol-4-yl)methoxy)diphenylsilane (**7**)

To a stirred solution of **6** in DMF (1.5 L) crushed Na<sub>2</sub>S·9H<sub>2</sub>O (43.37g, 180.60 mmol) was added and the reaction mixture was transferred to a preheated bath at 90 °C. After being stirred for 15 h, the reaction mixture was cooled to room temperature and quenched with water (1 L). The aqueous layer was extracted with *n*-hexane (3 × 1 L). The organic layer was combined, washed with brine, dried over anhydrous MgSO<sub>4</sub>, and concentrated. The residue was purified by column chromatography (silica gel, hexane/ethyl acetate, 19:1) to afford **7** (31.6 g, 28% in 5 steps) as pale yellow syrup; [α]<sub>D</sub><sup>25</sup> 45.17 (*c* 14.5, CH<sub>3</sub>OH); UV (CH<sub>3</sub>OH) λ<sub>max</sub> 264.94 nm; <sup>1</sup>H NMR (CDCl<sub>3</sub>, 500 MHz): δ 7.67–7.63 (m, 4H), 7.42–7.35 (m, 6H), 4.79 (d, *J* = 1.7 Hz, 2H), 3.76 (dd, *J* = 10.6, 4.9 Hz, 1H), 3.60 (dd, *J* = 10.6, 6.8 Hz, 1H), 3.38–3.35 (m, 1H), 3.13–3.10 (m, 1H), 2.82 (merged dd, *J*<sub>1</sub> = *J*<sub>2</sub> = 12.6 Hz, 1H), 1.50 (s, 3H), 1.30 (s, 3H), 1.04 (s, 9H); <sup>13</sup>C NMR (CDCl<sub>3</sub>, 125 MHz): δ 135.56, 135.55, 133.0, 132.9, 129.8, 129.7, 127.7, 110.6, 85.9, 83.7, 65.9, 55.4, 38.3, 26.8, 26.4, 24.5, 19.1; HRMS (ESI-Q-TOF) *m/z* [M + NH<sub>4</sub>]<sup>+</sup> for C<sub>24</sub>H<sub>36</sub>NO<sub>3</sub>SSi calculated 446.218, found 446.2175.

### 3.2.6. (3*aS*,4*R*,5*S*,6*aR*)-4-(((*tert*-butyldiphenylsilyl)oxy)methyl)-2,2-dimethyltetrahydrothieno[3,4-*d*][1,3]dioxole 5-oxide (**8**)

A solution of 3-chloroperbenzoic acid (5.56 g, 32.25 mmol) in methylene chloride (110 mL) was added dropwise to a stirred solution of **7** (27.65 g, 64.50 mmol) in methylene chloride (110 mL) at −78 °C under a nitrogen atmosphere and stirred at the same temperature for 45 min. The reaction mixture was quenched with saturated NaHCO<sub>3</sub> solution and extracted with methylene chloride (3 × 650 mL). The combined organic layer was washed with brine, dried over MgSO<sub>4</sub>, evaporated, and the residue was purified by silica gel column chromatography (hexane/ethyl acetate, 2:3) to afford **8** (23 g, 82%) as a colorless syrup; [α]<sub>D</sub><sup>25</sup> 17.87 (*c* 3.75, CH<sub>3</sub>OH); UV (CH<sub>3</sub>OH) λ<sub>max</sub> 264.94 nm; <sup>1</sup>H NMR (CDCl<sub>3</sub>, 500 MHz): δ 7.59–7.54 (m, 4H), 7.46–7.43 (m, 2H), 7.40–7.37 (m, 4H), 5.21 (t, *J* = 5.5 Hz, 1H), 4.97 (d, *J* = 5.3 Hz, 1H), 4.09 (dd, *J* = 11.2, 2.5 Hz, 1H), 3.82 (dd, *J* = 11.2, 3.3 Hz, 1H), 3.58 (s, 1H), 3.39 (merged dd, *J*<sub>1</sub> = *J*<sub>2</sub> = 14.8 Hz, 1H), 3.25 (dd, *J* = 14.8, 6.0 Hz, 1H), 1.56 (s, 3H), 1.33 (s, 3H), 1.01 (s, 9H); <sup>13</sup>C NMR (CDCl<sub>3</sub>, 125 MHz): δ 135.4, 135.3, 131.7, 131.6, 130.1, 130.0, 127.9, 127.8, 112.2, 86.3, 84.7, 74.7, 61.7, 58.3, 26.7, 26.6, 24.3, 18.9; HRMS (ESI-Q-TOF) *m/z* [M + H]<sup>+</sup> for C<sub>24</sub>H<sub>33</sub>O<sub>4</sub>SSi calculated 445.1863, found 445.1862.

### 3.2.7. (3*aR*,6*R*,6*aS*)-6-(((*tert*-butyldiphenylsilyl)oxy)methyl)-2,2-dimethyltetrahydrothieno[3,4-*d*][1,3]dioxol-4-yl acetate (**9**)

A solution of **8** (16 g, 35.98 mmol) in acetic anhydride (142 mL) was transferred to a preheated bath at 110 °C and stirred at the same temperature for 4 h. After concentration under reduced pressure, the residue was neutralized with aqueous sat. NaHCO<sub>3</sub> until pH 7.0 and stirred for 15 min. To the solution brine was added and extracted with ethyl acetate (3 × 600 mL). The organic layer was combined and washed with brine, dried (MgSO<sub>4</sub>), filtered, and evaporated under reduced pressure. The crude residue obtained was purified by silica gel column chromatography (hexane/ethyl acetate, 19:1) to give **9** (12.6 g, 72%) as a colorless syrup: 1:1.6 α/β mixture of anomers; UV (CH<sub>3</sub>OH) λ<sub>max</sub> 259.85 nm; <sup>1</sup>H NMR (CDCl<sub>3</sub>, 500 MHz): δ 7.70–7.62 (m, 6H), 7.43–7.40 (m, 3H), 7.39–7.36 (m, 7H), 6.09 (d, *J* = 5.3 Hz, 0.4H), 5.90 (s, 1H), 4.99 (d, *J* = 5.4 Hz, 1H), 4.82–4.80 (m, 0.6H), 4.64–4.61 (m, 1.5H), 3.82–3.80 (m, 1H), 3.77–3.72 (m, 1.6H), 3.60–3.52 (m, 2H), 2.13 (s, 1.4H), 1.81 (s, 3H), 1.53 (s, 1.9H), 1.48 (s, 3H), 1.30 (s, 1.6H), 1.28 (s, 3H), 1.06 (s, 9H), 1.04 (s, 5H); HRMS (ESI-Q-TOF) *m/z* [M + Na]<sup>+</sup> for C<sub>26</sub>H<sub>34</sub>NaO<sub>5</sub>SSi calculated 509.1788, found 509.1791.

3.2.8. 7-((3aR,4R,6R,6aS)-6-(((*tert*-butyldiphenylsilyl)oxy)methyl)-2,2-dimethyltetrahydrothieno[3,4-d][1,3]dioxol-4-yl)-4-chloro-5-iodo-7H-pyrrolo[2,3-d]pyrimidine (**10**)

*N,O*-Bis(trimethylsilyl)acetamide (BSA, 2.5 mL, 10.27 mmol) was added to a stirred suspension of 4-chloro-5-iodo-7H-pyrrolo[2,3-d]pyrimidine (2.6 g, 9.33 mmol) in anhydrous acetonitrile (67 mL) under nitrogen atmosphere. The resulting suspension was stirred at room temperature for 10 min until a homogeneous solution was obtained. To this clear solution a solution of **9** (5 g, 10.27 mmol) in anhydrous acetonitrile (50 mL) were added followed by dropwise addition of trimethylsilyl trifluoromethanesulfonate (1.5 mL, 8.40 mmol). The reaction mixture was stirred at room temperature for 15 min before transferring it to a preheated bath at 80 °C. After stirring at the same temperature for 1 h, the reaction mixture was cooled to room temperature and diluted with ethyl acetate (700 mL). The organic layer was washed with aqueous sat. NaHCO<sub>3</sub> (3 × 250 mL) and brine (100 mL), dried over MgSO<sub>4</sub>, filtered, and concentrated. The residue was purified by column chromatography (silica gel, hexane/ethyl acetate, 50:3) to give **10** (2.9 g, 40%) as a pale yellow sticky mass;  $[\alpha]_D^{25} -7.03$  (c 0.6, CH<sub>3</sub>OH); UV (CH<sub>3</sub>OH)  $\lambda_{\max}$  310.78 nm; <sup>1</sup>H NMR (CD<sub>3</sub>OD, 500 MHz):  $\delta$  8.46 (s, 1H), 7.87 (s, 1H), 7.64–7.58 (m, 4H), 7.40–7.33 (m, 4H), 7.31–7.28 (m, 2H), 6.24 (d, *J* = 2.2 Hz, 1H), 5.10 (dd, *J* = 5.5, 2.2 Hz, 1H), 4.96 (dd, *J* = 5.5, 2.1 Hz, 1H), 3.88 (dd, *J* = 10.4, 7.2 Hz, 1H), 3.81 (dd, *J* = 10.4, 7.3 Hz, 1H), 3.75 (td, *J* = 7.2, 2.1 Hz, 1H), 1.55 (s, 3H), 1.28 (s, 3H), 1.04 (s, 9H); <sup>13</sup>C NMR (CD<sub>3</sub>OD, 100 MHz):  $\delta$  154.2, 152.5, 152.3, 137.5, 137.4, 136.2, 135.0, 134.7, 131.9, 131.8, 129.7, 129.6, 119.9, 114.0, 90.9, 87.0, 70.1, 67.7, 58.9, 53.5, 28.3, 28.1, 26.1, 20.8; HRMS (ESI-Q-TOF) *m/z* [M + H]<sup>+</sup> for C<sub>30</sub>H<sub>34</sub>ClIN<sub>3</sub>O<sub>3</sub>SSi calculated 706.0818, found 706.0798.

3.2.9. 7-((3aR,4R,6R,6aS)-6-(((*tert*-butyldiphenylsilyl)oxy)methyl)-2,2-dimethyltetrahydrothieno[3,4-d][1,3]dioxol-4-yl)-5-iodo-7H-pyrrolo[2,3-d]pyrimidin-4-amine (**11**)

A solution of **10** (2.9 g, 4.11 mmol) in saturated solution of NH<sub>3</sub>/*t*-BuOH (30 mL) contained in a stainless steel bomb reactor was transferred to a preheated bath at 90 °C and stirred at the same temperature for 24 h. The steel bomb containing reaction mixture was cooled to room temperature and solvent was evaporated under reduced pressure. The residue was purified by silica gel column chromatography (hexane/ethyl acetate, 13:7) to obtain **11** (2.42 g, 86%) as a sticky mass;  $[\alpha]_D^{25} -45.49$  (c 2.4, CH<sub>3</sub>OH); UV (CH<sub>3</sub>OH)  $\lambda_{\max}$  286.04 nm; <sup>1</sup>H NMR (CDCl<sub>3</sub>, 500 MHz):  $\delta$  8.22 (s, 1H), 7.64–7.62 (m, 4H), 7.43–7.40 (m, 2H), 7.37–7.33 (m, 5H), 6.21 (d, *J* = 2.7 Hz, 1H), 5.88 (br s, 2H), 4.88 (dd, *J* = 5.6, 2.8 Hz, 1H), 4.78 (dd, *J* = 5.6, 2.8 Hz, 1H), 3.86–3.79 (m, 2H), 3.77–3.75 (m, 1H), 1.58 (s, 3H), 1.27 (s, 3H), 1.07 (s, 9H); <sup>13</sup>C NMR (CDCl<sub>3</sub>, 125 MHz):  $\delta$  156.7, 151.9, 150.1, 135.5, 135.5, 132.9, 132.8, 129.9, 129.8, 127.8, 127.0, 112.4, 104.5, 89.0, 84.0, 66.3, 65.1, 55.7, 50.5, 27.3, 26.8, 25.1, 19.2; HRMS (ESI-Q-TOF) *m/z* [M + H]<sup>+</sup> for C<sub>30</sub>H<sub>36</sub>IN<sub>4</sub>O<sub>3</sub>SSi calculated 687.1317, found 687.1301.

General Procedure of Stille Coupling for the Synthesis of **12a** and **12b**. To the compound **11** (1 equiv) in a microwave vial equipped with a septum, catalyst PdCl<sub>2</sub>(PPh<sub>3</sub>)<sub>2</sub> (15 mol %) was added and degassed THF (2.8 mL/mmol) under nitrogen atmosphere. The resulting solution was degassed for 5 min and a corresponding 2-(tributylstannyl)hetaryl (2.5 equiv) was added. After stirring the reaction mixture in a microwave for 1 h at 70 °C, it was quenched by adding water and brine. The aqueous layer was extracted with ethyl acetate thrice and organics were concentrated. The residue was purified by column chromatography.

3.2.10. 7-((3aR,4R,6R,6aS)-6-(((*tert*-butyldiphenylsilyl)oxy)methyl)-2,2-dimethyltetrahydrothieno[3,4-d][1,3]dioxol-4-yl)-5-(furan-2-yl)-7H-pyrrolo[2,3-d]pyrimidin-4-amine (**12a**)

Compound **12a** (0.16 g, 88%) was obtained from **11** (0.2 g, 0.29 mmol) as a pale yellow sticky mass; silica gel column chromatography (hexane/ethyl acetate, 3:2);  $[\alpha]_D^{25} -31.0$  (c 0.2, CH<sub>3</sub>OH); UV (CH<sub>3</sub>OH)  $\lambda_{\max}$  291.76 nm; <sup>1</sup>H NMR (CDCl<sub>3</sub>, 400 MHz):  $\delta$  8.27 (s, 1H),

7.64–7.61 (m, 4H), 7.47–7.46 (m, 1H), 7.39–7.36 (m, 3H), 7.33–7.29 (m, 4H), 6.45–6.44 (m, 1H), 6.28–6.27 (m, 2H), 5.98 (br s, 2H), 4.95 (dd,  $J = 5.9, 3.2$  Hz, 1H), 4.82 (dd,  $J = 5.9, 3.2$  Hz, 1H), 3.92–3.82 (m, 2H), 3.79–3.75 (m, 1H), 1.59 (s, 3H), 1.28 (s, 3H), 1.05 (s, 9H);  $^{13}\text{C}$  NMR ( $\text{CDCl}_3$ , 100 MHz):  $\delta$  157.2, 152.9, 151.2, 149.0, 141.3, 135.77, 135.74, 133.17, 133.11, 130.1, 130.0, 127.9, 120.0, 112.7, 112.1, 107.3, 105.6, 100.9, 89.2, 84.2, 66.3, 65.3, 55.8, 27.6, 27.0, 25.4, 19.5; HRMS (ESI-Q-TOF)  $m/z$   $[\text{M} + \text{H}]^+$  for  $\text{C}_{34}\text{H}_{39}\text{N}_4\text{O}_4\text{SSi}$  calculated 627.2456, found 627.2463.

3.2.11. 7-((3aR,4R,6R,6aS)-6-(((*tert*-butyldiphenylsilyloxy)methyl)-2,2-dimethyltetrahydrothieno[3,4-d][1,3]dioxol-4-yl)-5-(thiophen-2-yl)-7H-pyrrolo[2,3-d]pyrimidin-4-amine (**12b**)

Compound **12b** (0.21 g) was afforded from **11** (0.25 g, 0.36 mmol) in 92% yield as colorless sticky mass; silica gel column chromatography (hexane/ethyl acetate, 3:2);  $[\alpha]_D^{25} -51.36$  (c 0.31,  $\text{CH}_3\text{OH}$ ); UV ( $\text{CH}_3\text{OH}$ )  $\lambda_{\text{max}}$  287.13 nm;  $^1\text{H}$  NMR ( $\text{CDCl}_3$ , 400 MHz):  $\delta$  8.28 (s, 1H), 7.62–7.59 (m, 4H), 7.37–7.34 (m, 3H), 7.32–7.27 (m, 4H), 7.23 (s, 1H), 7.10–7.07 (m, 1H), 7.00–6.99 (m, 1H), 6.28 (d,  $J = 2.7$  Hz, 1H), 5.41 (br s, 2H), 4.94 (dd,  $J = 5.5, 3.2$  Hz, 1H), 4.81 (dd,  $J = 5.9, 3.2$  Hz, 1H), 3.91–3.82 (m, 2H), 3.79–3.74 (m, 1H), 1.59 (s, 3H), 1.28 (s, 3H), 1.03 (s, 9H);  $^{13}\text{C}$  NMR ( $\text{CDCl}_3$ , 100 MHz):  $\delta$  156.7, 152.1, 150.7, 135.68, 135.63, 129.97, 129.94, 128.0, 127.8, 126.5, 125.8, 121.9, 112.6, 109.4, 102.1, 89.0, 84.1, 66.2, 65.3, 55.6, 27.5, 26.9, 25.3, 19.3; HRMS (ESI-Q-TOF)  $m/z$   $[\text{M} + \text{H}]^+$  for  $\text{C}_{34}\text{H}_{39}\text{N}_4\text{O}_3\text{S}_2\text{Si}$  calculated 643.2227, found 643.2218.

General Procedure for the Synthesis of **1a** and **1b**. To an ice-cooled solution of **12a** and **12b** (1 equiv) in THF (3 mL/mmol) 50% aqueous trifluoroacetic acid (19.5 mL/mmol) was dropwise added and the resulting mixture was stirred at room temperature for 12 h. Acidic solution was basified using a weakly basic anion-exchange resin (Dowex<sup>®</sup> 66 free base) and stirred for an additional 3 h, filtered, and concentrated under vacuum. The residue was purified by silica gel column chromatography ( $\text{CH}_2\text{Cl}_2/\text{MeOH}$ , 47:3) to give **1a** and **1b** respectively.

3.2.12. (2R,3R,4S,5R)-2-(4-Amino-5-(furan-2-yl)-7H-pyrrolo[2,3-d]pyrimidin-7-yl)-5-(hydroxymethyl)tetrahydrothiophene-3,4-diol (**1a**)

It was obtained in 75% yield as white solid; mp 197–199 °C;  $[\alpha]_D^{25} -21.14$  (c 0.05,  $\text{CH}_3\text{OH}$ ); UV ( $\text{CH}_3\text{OH}$ )  $\lambda_{\text{max}}$  290.77 nm;  $^1\text{H}$  NMR ( $\text{DMSO}-d_6$ , 500 MHz):  $\delta$  8.13 (s, 1H), 7.95 (s, 1H), 7.78 (s, 1H), 6.90 (br s, 2H,  $\text{D}_2\text{O}$  exchange), 6.72 (d,  $J = 3.0$  Hz, 1H), 6.62–6.61 (m, 1H), 6.17 (d,  $J = 7.0$  Hz, 1H), 5.43 (d,  $J = 6.4$  Hz, 1H,  $\text{D}_2\text{O}$  exchange), 5.27 (d,  $J = 4.4$  Hz, 1H,  $\text{D}_2\text{O}$  exchange), 5.18 (t,  $J = 5.5$  Hz, 1H,  $\text{D}_2\text{O}$  exchange), 4.48–4.45 (m, 1H), 4.19–4.18 (m, 1H), 3.78–3.75 (m, 1H), 3.63–3.58 (m, 1H), 3.29–3.28 (m, 1H);  $^{13}\text{C}$  NMR ( $\text{DMSO}-d_6$ , 100 MHz):  $\delta$  157.6, 152.5, 151.6, 149.1, 142.3, 120.7, 112.3, 106.8, 105.6, 99.4, 77.7, 73.6, 63.9, 61.3, 53.4; HRMS (ESI-Q-TOF)  $m/z$   $[\text{M} + \text{H}]^+$  for  $\text{C}_{15}\text{H}_{17}\text{N}_4\text{O}_4\text{S}$  calculated 349.0965, found 349.0974; purity  $\geq 95\%$ .

3.2.13. (2R,3R,4S,5R)-2-(4-Amino-5-(thiophen-2-yl)-7H-pyrrolo[2,3-d]pyrimidin-7-yl)-5-(hydroxymethyl)tetrahydrothiophene-3,4-diol (**1b**)

It was afforded in 81% yield as white solid; mp 166–172 °C;  $[\alpha]_D^{25} -23.93$  (c 0.09,  $\text{CH}_3\text{OH}$ ); UV ( $\text{CH}_3\text{OH}$ )  $\lambda_{\text{max}}$  286.41 nm;  $^1\text{H}$  NMR ( $\text{CD}_3\text{OD}$ , 500 MHz):  $\delta$  8.13 (s, 1H), 7.66 (s, 1H), 7.42 (d,  $J = 5.0$  Hz, 1H), 7.14–7.11 (m, 2H), 6.22 (d,  $J = 5.9$  Hz, 1H), 4.52 (dd,  $J = 5.7, 3.7$  Hz, 1H), 4.29 (merged dd,  $J_1 = J_2 = 3.8$  Hz, 1H), 3.88–3.80 (m, 2H), 3.48 (dd,  $J = 9.4, 4.8$  Hz, 1H);  $^{13}\text{C}$  NMR ( $\text{CD}_3\text{OD}$ , 125 MHz):  $\delta$  159.5, 153.5, 152.6, 137.5, 129.8, 128.5, 127.6, 124.5, 111.6, 103.5, 80.8, 76.3, 65.1, 64.5, 54.8; HRMS (ESI-Q-TOF)  $m/z$   $[\text{M} + \text{H}]^+$  for  $\text{C}_{15}\text{H}_{17}\text{N}_4\text{O}_3\text{S}_2$  calculated 365.0737, found 365.0749; purity  $\geq 95\%$ .

General Procedure of Suzuki Coupling for the Synthesis of **12c–f**. A degassed mixture of DMF/ $\text{H}_2\text{O}$  (6.9 mL/2.7 mL/mmol) was added to a microwave vial containing compound **11** (1 equiv), corresponding boronic ester (1.2 equiv),  $\text{PdCl}_2(\text{PPh}_3)_2$  (6 mol %), and sodium carbonate (2 equiv). The resulting reaction mixture was heated in a microwave at 70 °C for 1 h. After quenching with water, the reaction mixture was extracted with ethyl



acetate thrice. The organic layers were combined, washed with brine, dried over  $\text{MgSO}_4$ , filtered, and evaporated. The residue obtained was purified by column chromatography.

3.2.14. 7-((3aR,4R,6R,6aS)-6-(((*tert*-butyldiphenylsilyl)oxy)methyl)-2,2-dimethyltetrahydrothieno[3,4-d][1,3]dioxol-4-yl)-5-vinyl-7H-pyrrolo[2,3-d]pyrimidin-4-amine (**12c**)

Compound **12c** was obtained in 85% yield as yellow sticky mass; silica gel column chromatography (hexane/ethyl acetate, 13:7);  $[\alpha]_D^{25} -38.33$  (c 1.1,  $\text{CH}_3\text{OH}$ ); UV ( $\text{CH}_3\text{OH}$ )  $\lambda_{\text{max}}$  288.95 nm;  $^1\text{H}$  NMR ( $\text{CD}_3\text{OD}$ , 400 MHz):  $\delta$  8.03 (s, 1H), 7.64 (t,  $J = 9.2$  Hz, 4H), 7.42–7.39 (m, 3H), 7.37–7.31 (m, 4H), 6.91 (dd,  $J = 17.2, 10.8$  Hz, 1H), 6.21 (s, 1H), 5.44 (d,  $J = 17.6$  Hz, 1H), 5.20 (d,  $J = 10.8$  Hz, 1H), 5.07–5.05 (m, 1H), 4.96–4.95 (m, 1H), 3.93–3.89 (m, 1H), 3.86–3.81 (m, 1H), 3.73–3.69 (m, 1H), 1.55 (s, 3H), 1.29 (s, 3H), 1.04 (s, 9H);  $^{13}\text{C}$  NMR ( $\text{CD}_3\text{OD}$ , 100 MHz):  $\delta$  157.8, 151.1, 150.1, 135.37, 135.35, 133.0, 132.7, 129.74, 129.71, 128.1, 127.58, 127.54, 119.4, 115.8, 114.4, 112.0, 101.4, 88.4, 84.5, 66.0, 65.5, 55.7, 26.3, 26.0, 24.0, 18.7; HRMS (ESI-Q-TOF)  $m/z$   $[\text{M} + \text{H}]^+$  for  $\text{C}_{32}\text{H}_{39}\text{N}_4\text{O}_3\text{SSi}$  calculated 587.2507, found 587.2506.

3.2.15. 7-((3aR,4R,6R,6aS)-6-(((*tert*-butyldiphenylsilyl)oxy)methyl)-2,2-dimethyltetrahydrothieno[3,4-d][1,3]dioxol-4-yl)-5-phenyl-7H-pyrrolo[2,3-d]pyrimidin-4-amine (**12d**)

It was obtained in 91% yield as colorless sticky mass; silica gel column chromatography (hexane/ethyl acetate, 1:1);  $[\alpha]_D^{25} -46.89$  (c 0.14,  $\text{CH}_3\text{OH}$ ); UV ( $\text{CH}_3\text{OH}$ )  $\lambda_{\text{max}}$  283.50 nm;  $^1\text{H}$  NMR ( $\text{CD}_3\text{OD}$ , 400 MHz):  $\delta$  8.11 (s, 1H), 7.62–7.59 (m, 4H), 7.43–7.41 (m, 3H), 7.39–7.33 (m, 4H), 7.29–7.26 (m, 4H), 7.23 (s, 1H), 6.27 (d,  $J = 2.7$  Hz, 1H), 5.09 (dd,  $J = 5.4, 2.7$  Hz, 1H), 4.96 (dd,  $J = 5.5, 2.3$  Hz, 1H), 3.92–3.82 (m, 2H), 3.75–3.71 (m, 1H), 1.57 (s, 3H), 1.30 (s, 3H), 1.01 (s, 9H);  $^{13}\text{C}$  NMR ( $\text{CD}_3\text{OD}$ , 100 MHz):  $\delta$  157.4, 151.2, 150.1, 135.38, 135.34, 134.1, 132.9, 132.7, 129.7, 128.7, 128.6, 127.55, 127.50, 127.1, 120.7, 117.9, 111.9, 101.3, 88.6, 84.7, 66.5, 65.6, 56.0, 26.2, 25.9, 24.0, 18.6; HRMS (ESI-Q-TOF)  $m/z$   $[\text{M} + \text{H}]^+$  for  $\text{C}_{36}\text{H}_{41}\text{N}_4\text{O}_3\text{SSi}$  calculated 637.2663, found 637.2646.

3.2.16. 4-(4-(4-Amino-7-((3aR,4R,6R,6aS)-6-(((*tert*-butyldiphenylsilyl)oxy)methyl)-2,2-dimethyltetrahydrothieno[3,4-d][1,3]dioxol-4-yl)-7H-pyrrolo[2,3-d]pyrimidin-5-yl)phenyl)thiomorpholine 1,1-dioxide (**12e**)

It was afforded in 89% yield as colorless sticky mass; silica gel column chromatography (hexane/ethyl acetate, 11:9);  $[\alpha]_D^{25} -28.78$  (c 0.38,  $\text{CH}_3\text{OH}$ ); UV ( $\text{CH}_3\text{OH}$ )  $\lambda_{\text{max}}$  270.04 nm;  $^1\text{H}$  NMR ( $\text{CDCl}_3$ , 400 MHz):  $\delta$  8.27 (s, 1H), 7.61–7.59 (m, 4H), 7.40–7.34 (m, 4H), 7.32–7.27 (m, 4H), 7.14 (s, 1H), 6.94–6.92 (m, 2H), 6.31 (d,  $J = 3.6$  Hz, 1H), 5.28 (br s, 2H), 4.99 (dd,  $J = 5.9, 3.2$  Hz, 1H), 4.82 (dd,  $J = 5.9, 2.7$  Hz, 1H), 3.93–3.86 (m, 4H), 3.84–3.82 (m, 2H), 3.79–3.75 (m, 1H), 3.13–3.11 (m, 4H), 1.60 (s, 3H), 1.29 (s, 3H), 1.03 (s, 9H);  $^{13}\text{C}$  NMR ( $\text{CDCl}_3$ , 100 MHz):  $\delta$  156.6, 151.5, 150.7, 146.9, 135.66, 135.62, 133.0, 130.3, 129.96, 129.92, 127.8, 126.5, 120.6, 116.8, 116.6, 112.7, 101.9, 88.9, 84.0, 66.0, 65.2, 55.5, 50.5, 47.6, 27.5, 26.9, 25.3, 19.3; HRMS (ESI-Q-TOF)  $m/z$   $[\text{M} + \text{H}]^+$  for  $\text{C}_{40}\text{H}_{48}\text{N}_5\text{O}_5\text{S}_2\text{Si}$  calculated 770.2861, found 770.2865.

3.2.17. N-(4-(4-Amino-7-((3aR,4R,6R,6aS)-6-(((*tert*-butyldiphenylsilyl)oxy)methyl)-2,2-dimethyltetrahydrothieno[3,4-d][1,3]dioxol-4-yl)-7H-pyrrolo[2,3-d]pyrimidin-5-yl)phenyl)ethanesulfonamide (**12f**)

Compound **12f** was obtained in 87% yield as colorless sticky mass; silica gel column chromatography (hexane/ethyl acetate, 2:3);  $[\alpha]_D^{25} -48.16$  (c 0.09,  $\text{CH}_3\text{OH}$ ); UV ( $\text{CH}_3\text{OH}$ )  $\lambda_{\text{max}}$  286.04 nm;  $^1\text{H}$  NMR ( $\text{CDCl}_3$ , 500 MHz):  $\delta$  8.29 (s, 1H), 7.60–7.59 (m, 4H), 7.39–7.34 (m, 2H), 7.32–7.30 (m, 4H), 7.28–7.27 (m, 2H), 7.25–7.24 (m, 2H), 7.20 (s, 1H), 6.66 (br s, 1H), 6.30 (d,  $J = 2.9$  Hz, 1H), 5.37 (br s, 2H), 4.97 (dd,  $J = 5.6, 3.0$  Hz, 1H), 4.82 (dd,  $J = 5.6, 2.7$  Hz, 1H), 3.90–3.82 (m, 2H), 3.80–3.78 (m, 1H), 3.15 (q,  $J = 7.3$  Hz, 2H), 1.60 (s, 3H), 1.39 (t,  $J = 7.3$  Hz, 3H), 1.29 (s, 3H), 1.02 (s, 9H);  $^{13}\text{C}$  NMR ( $\text{CDCl}_3$ , 100 MHz):  $\delta$  156.3, 151.1, 150.7, 136.4, 135.63, 135.60, 132.8, 130.9, 130.0, 127.8, 121.3, 120.9, 116.4, 112.6, 101.7, 89.1,

84.1, 66.4, 65.2, 55.6, 46.3, 27.5, 26.9, 25.3, 19.3, 8.4; HRMS (ESI-Q-TOF)  $m/z$   $[M + H]^+$  for  $C_{38}H_{46}N_5O_5S_2Si$  calculated 744.2704, found 744.2698.

3.2.18. (2R,3R,4S,5R)-2-(4-Amino-5-vinyl-7H-pyrrolo[2,3-d]pyrimidin-7-yl)-5-(hydroxymethyl)tetrahydrothiophene-3,4-diol (**1c**)

Compound **12c** (0.12 g, 0.20 mmol) was converted to **1c** as described for **1a**, affording white solid (47.5 mg, 78%); silica gel column chromatography ( $CH_2Cl_2/MeOH$ , 19:1); mp 110–112 °C;  $[\alpha]_D^{25} -41.86$  (c 0.20,  $CH_3OH$ ); UV ( $CH_3OH$ )  $\lambda_{max}$  288.50 nm;  $^1H$  NMR ( $DMSO-d_6$ , 500 MHz):  $\delta$  8.04 (s, 1H), 7.77 (s, 1H), 7.10 (dd,  $J = 17.2, 10.9$  Hz, 1H), 6.70 (br s, 2H,  $D_2O$  exchange), 6.12 (d,  $J = 7.0$  Hz, 1H), 5.59 (d,  $J = 17.1$  Hz, 1H), 5.38 (d,  $J = 6.4$  Hz, 1H,  $D_2O$  exchange), 5.25 (d,  $J = 4.4$  Hz, 1H,  $D_2O$  exchange), 5.17 (t,  $J = 5.5$  Hz, 1H,  $D_2O$  exchange), 5.11 (d,  $J = 11.0$  Hz, 1H), 4.46–4.41 (m, 1H), 4.18–4.14 (m, 1H), 3.77–3.72 (m, 1H), 3.61–3.55 (m, 1H), 3.27–3.24 (m, 1H);  $^{13}C$  NMR ( $CD_3OD$ , 100 MHz):  $\delta$  157.8, 150.9, 150.6, 128.3, 119.9, 115.3, 113.9, 78.6, 74.1, 63.0, 62.2, 52.6; HRMS (ESI-Q-TOF)  $m/z$   $[M + H]^+$  for  $C_{13}H_{17}N_4O_3S$  calculated 309.1016, found 309.1018; purity  $\geq 95\%$ .

3.2.19. (2R,3R,4S,5R)-2-(4-Amino-5-phenyl-7H-pyrrolo[2,3-d]pyrimidin-7-yl)-5-(hydroxymethyl)tetrahydrothiophene-3,4-diol (**1d**)

Compound **1d** was prepared from **12d** (0.16 g, 0.25 mmol) as described for **1a**, affording white solid (72.5 mg, 81%); silica gel column chromatography ( $CH_2Cl_2/MeOH$ , 19:1); mp 102–104 °C;  $[\alpha]_D^{25} -46.30$  (c 0.06,  $CH_3OH$ ); UV ( $CH_3OH$ )  $\lambda_{max}$  280.95 nm;  $^1H$  NMR ( $DMSO-d_6$ , 500 MHz):  $\delta$  8.14 (s, 1H), 7.66 (s, 1H), 7.50–7.46 (m, 4H), 7.38–7.34 (m, 1H), 6.18 (d,  $J = 6.9$  Hz, 1H), 5.42 (d,  $J = 6.4$  Hz, 1H), 5.28 (d,  $J = 4.5$  Hz, 1H), 5.16 (t,  $J = 5.5$  Hz, 1H), 4.51–4.47 (m, 1H), 4.19–4.16 (m, 1H), 3.77–3.71 (m, 1H), 3.61–3.56 (m, 1H), 3.29–3.25 (m, 1H);  $^{13}C$  NMR ( $CD_3OD$ , 125 MHz):  $\delta$  159.5, 153.1, 152.8, 136.6, 130.9, 130.7, 129.2, 123.4, 119.7, 103.2, 80.9, 76.4, 65.2, 64.5, 54.8; HRMS (ESI-Q-TOF)  $m/z$   $[M + H]^+$  for  $C_{17}H_{19}N_4O_3S$  calculated 359.1172, found 359.1177; purity  $\geq 95\%$ .

3.2.20. 4-(4-(4-Amino-7-(3,4-dihydroxy-5-(hydroxymethyl)tetrahydrothiophen-2-yl)-7H-pyrrolo[2,3-d]pyrimidin-5-yl)phenyl)thiomorpholine 1,1-dioxide (**1e**)

It was obtained from **12e** (0.1 g, 0.12 mmol) as described for **1a**, as white solid (47.1 mg, 80%); silica gel column chromatography ( $CH_2Cl_2/MeOH$ , 93:7); mp 188–192 °C;  $[\alpha]_D^{25} -24.29$  (c 0.05,  $CH_3OH$ ); UV ( $CH_3OH$ )  $\lambda_{max}$  270.04 nm;  $^1H$  NMR ( $DMSO-d_6$ , 500 MHz):  $\delta$  8.13 (s, 1H), 7.54 (s, 1H), 7.35 (merged dd,  $J_1 = J_2 = 8.4$  Hz, 2H), 7.13 (merged dd,  $J_1 = J_2 = 8.5$  Hz, 2H), 6.18 (d,  $J = 6.9$  Hz, 1H), 5.40 (d,  $J = 6.4$  Hz, 1H), 5.26 (d,  $J = 4.3$  Hz, 1H), 5.16 (t,  $J = 5.4$  Hz, 1H), 4.49–4.47 (m, 1H), 4.18–4.17 (m, 1H), 3.87–3.82 (m, 4H), 3.75–3.72 (m, 1H), 3.60–3.57 (m, 1H), 3.29–3.27 (m, 1H), 3.17–3.12 (m, 4H);  $^{13}C$  NMR ( $DMSO-d_6$ , 125 MHz):  $\delta$  157.2, 151.6, 151.0, 146.2, 129.4, 125.1, 120.1, 116.2, 116.0, 100.3, 77.3, 73.3, 63.3, 60.9, 52.8, 49.7, 46.5; HRMS (ESI-Q-TOF)  $m/z$   $[M + H]^+$  for  $C_{21}H_{26}N_5O_5S_2$  calculated 492.137, found 492.1388; purity  $\geq 95\%$ .

3.2.21. N-(4-(4-Amino-7-(3,4-dihydroxy-5-(hydroxymethyl)tetrahydrothiophen-2-yl)-7H-pyrrolo[2,3-d]pyrimidin-5-yl)phenyl)ethanesulfonamide (**1f**)

It was afforded from **12f** (90 mg, 0.12 mmol) as described for **1a**, as white solid (44.6 mg, 80%); silica gel column chromatography ( $CH_2Cl_2/MeOH$ , 91:9); mp 127–132 °C;  $[\alpha]_D^{25} -35.60$  (c 0.05,  $CH_3OH$ ); UV ( $CH_3OH$ )  $\lambda_{max}$  283.86 nm;  $^1H$  NMR ( $DMSO-d_6$ , 500 MHz):  $\delta$  9.87 (s, 1H), 8.14 (s, 1H), 7.60 (s, 1H), 7.42 (merged dd,  $J_1 = J_2 = 8.2$  Hz, 2H), 7.31 (merged dd,  $J_1 = J_2 = 8.1$  Hz, 2H), 6.18 (d,  $J = 6.9$  Hz, 1H), 5.40 (d,  $J = 6.4$  Hz, 1H), 5.26 (d,  $J = 4.3$  Hz, 1H), 5.15 (t,  $J = 5.4$  Hz, 1H), 4.49–4.46 (m, 1H), 4.19–4.17 (m, 1H), 3.76–3.72 (m, 1H), 3.61–3.57 (m, 1H), 3.29–3.27 (m, 1H), 3.13 (q,  $J = 7.2$  Hz, 2H), 1.22 (t,  $J = 7.2$  Hz, 3H);  $^{13}C$  NMR ( $DMSO-d_6$ , 125 MHz):  $\delta$  157.2, 151.6, 151.1, 137.1, 129.7, 129.2, 120.7, 119.8, 115.9, 100.1, 77.3, 73.3, 63.3, 60.9, 52.8, 45.0, 8.02; HRMS (ESI-Q-TOF)  $m/z$   $[M + H]^+$  for  $C_{19}H_{24}N_5O_5S_2$  calculated 466.1213, found 466.1225; purity  $\geq 95\%$ .

General Procedure of Sonogashira Coupling for the Synthesis of **13**. To a microwave vial equipped with a septum, containing **11** (1 equiv), CuI (25 mol %), and PdCl<sub>2</sub>(PPh<sub>3</sub>)<sub>2</sub> (10 mol %) a degassed mixture of DMF-Et<sub>3</sub>N (6.1 mL/mmol, 4:1) was added. The resulting reaction mixture was degassed with nitrogen for 5 min before adding corresponding alkyne (1.1 equiv) and heated in a microwave at 50 °C for 1 h. The reaction mixture was partitioned between ethyl acetate and water. The combined organic layer was dried over MgSO<sub>4</sub>, filtered, and evaporated. The resulting residue was purified by silica gel chromatography to afford the respective compounds.

3.2.22. 7-((3aR,4R,6R,6aS)-6-(((*tert*-butyldiphenylsilyl)oxy)methyl)-2,2-dimethyltetrahydrothieno[3,4-d][1,3]dioxol-4-yl)-5-((trimethylsilyl)ethynyl)-7H-pyrrolo[2,3-d]pyrimidin-4-amine (**13**)

The desired compound **13** was obtained from **11** (1.67 g, 2.43 mmol) in 93% yield as sticky mass; silica gel column chromatography (hexane/ethyl acetate, 4:1); [α]<sup>25</sup><sub>D</sub> −74.11 (*c* 0.65, CH<sub>3</sub>OH); UV (CH<sub>3</sub>OH) λ<sub>max</sub> 284.59 nm; <sup>1</sup>H NMR (CDCl<sub>3</sub>, 500 MHz): δ 8.24 (s, 1H), 7.65–7.62 (m, 4H), 7.42–7.39 (m, 3H), 7.37–7.34 (m, 4H), 6.19 (d, *J* = 2.6 Hz, 1H), 5.73 (br s, 2H), 4.89 (dd, *J* = 5.6, 2.6 Hz, 1H), 4.78 (dd, *J* = 5.6, 2.3 Hz, 1H), 3.87–3.84 (m, 1H), 3.79–3.73 (m, 2H), 1.57 (s, 3H), 1.27 (s, 3H), 1.07 (s, 9H), 0.24 (s, 9H); <sup>13</sup>C NMR (CDCl<sub>3</sub>, 100 MHz): δ 157.3, 153.0, 149.7, 135.7, 135.6, 133.0, 132.9, 130.0, 127.9, 126.9, 112.5, 104.0, 98.4, 97.7, 96.2, 89.3, 84.2, 66.5, 65.2, 56.0, 27.4, 26.9, 25.2, 19.3, 0.01; HRMS (ESI-Q-TOF) *m/z* [M + H]<sup>+</sup> for C<sub>35</sub>H<sub>45</sub>N<sub>4</sub>O<sub>3</sub>Si<sub>2</sub> calculated 657.2745, found 657.2739.

3.2.23. ((3aS,4R,6R,6aR)-6-(4-Amino-5-ethynyl-7H-pyrrolo[2,3-d]pyrimidin-7-yl)-2,2-dimethyltetrahydrothieno[3,4-d][1,3]dioxol-4-yl)methanol (**14**)

To the stirred solution of **13** (0.58 g, 0.88 mmol) in anhydrous THF (5.8 mL) a solution of 1 M TBAF in THF (2.64 mL, 2.64 mmol) was added under nitrogen atmosphere and the resulting reaction mixture was stirred at room temperature for 40 min. The reaction was quenched with saturated aqueous NH<sub>4</sub>Cl solution (5 mL) and extracted with ethyl acetate (3 × 150 mL). The combined organic layer was washed with brine (100 mL), dried over MgSO<sub>4</sub>, filtered, and concentrated to give the residue. Upon silica gel column chromatography (methylene chloride/methanol, 97:3), compound **14** (0.27 g, 90%) was obtained as pale yellow syrup; [α]<sup>25</sup><sub>D</sub> −51.62 (*c* 1.15, CH<sub>3</sub>OH); UV (CH<sub>3</sub>OH) λ<sub>max</sub> 280.95 nm; <sup>1</sup>H NMR (CD<sub>3</sub>OD, 500 MHz): δ 8.12 (s, 1H), 7.78 (s, 1H), 6.27 (d, *J* = 3.0 Hz, 1H), 5.14 (dd, *J* = 5.3, 3.1 Hz, 1H), 4.97 (dd, *J* = 5.4, 2.2 Hz, 1H), 3.79–3.74 (m, 2H), 3.73 (s, 1H), 3.71–3.68 (m, 1H), 1.58 (s, 3H), 1.32 (s, 3H); <sup>13</sup>C NMR (CD<sub>3</sub>OD, 125 MHz): δ 159.9, 154.4, 151.2, 129.7, 114.1, 105.2, 97.7, 91.1, 87.4, 77.9, 68.7, 65.8, 57.7, 28.6, 26.2; HRMS (ESI-Q-TOF) *m/z* [M + H]<sup>+</sup> for C<sub>16</sub>H<sub>19</sub>N<sub>4</sub>O<sub>3</sub>S calculated 347.1172, found 347.1168.

3.2.24. (2R,3R,4S,5R)-2-(4-Amino-5-ethynyl-7H-pyrrolo[2,3-d]pyrimidin-7-yl)-5-(hydroxymethyl)tetrahydrothiophene-3,4-diol (**1g**)

To a solution of **14** (0.21 g, 0.60 mmol) in THF (6 mL) 2 N HCl solution (6 mL) was added dropwise at 0 °C and the reaction mixture was stirred at room temperature for 15 h. A weakly basic anion-exchange resin (Dowex<sup>®</sup> 66 free base) was added to the resulting solution to neutralize HCl and stirred for additional 3 h. The solution was filtered, evaporated, and the residue was purified by silica gel column chromatography (methylene chloride/methanol, 47:3) to afford **1g** (0.13 g, 72%) as white solid; mp 235–237 °C; [α]<sup>25</sup><sub>D</sub> −47.30 (*c* 0.05, CH<sub>3</sub>OH); UV (CH<sub>3</sub>OH) λ<sub>max</sub> 280.59 nm; <sup>1</sup>H NMR (DMSO-*d*<sub>6</sub>, 500 MHz): δ 8.12 (s, 1H), 7.93 (s, 1H), 6.06 (d, *J* = 6.9 Hz, 1H), 5.43 (d, *J* = 6.3 Hz, 1H), 5.27 (d, *J* = 4.3 Hz, 1H), 5.17 (t, *J* = 5.3 Hz, 1H), 4.45–4.42 (m, 1H), 4.28 (s, 1H), 4.16–4.14 (m, 1H), 3.76–3.71 (m, 1H), 3.61–3.57 (m, 1H), 3.28–3.25 (m, 1H); <sup>13</sup>C NMR (DMSO-*d*<sub>6</sub>, 150 MHz): δ 157.3, 152.6, 149.8, 127.6, 102.2, 94.0, 83.0, 77.34, 77.30, 73.2, 63.1, 61.1, 53.0; HRMS (ESI-Q-TOF) *m/z* [M + H]<sup>+</sup> for C<sub>13</sub>H<sub>15</sub>N<sub>4</sub>O<sub>3</sub>S calculated 307.0859, found 307.0863; purity ≥95%.

3.2.25. 7-((3aR,4R,6R,6aS)-6-(((*tert*-butyldiphenylsilyl)oxy)methyl)-2,2-dimethyltetrahydrothieno[3,4-d][1,3]dioxol-4-yl)-5-(prop-1-yn-1-yl)-7H-pyrrolo[2,3-d]pyrimidin-4-amine (**15a**)

Following the procedure described to synthesize **13**, compound **11** (200 mg, 0.29 mmol) afforded **15a** (164 mg, 96%) as sticky mass; silica gel column chromatography (hexane/ethyl acetate, 3:1);  $[\alpha]_D^{25}$   $-63.53$  (c 0.195, CH<sub>3</sub>OH); UV (CH<sub>3</sub>OH)  $\lambda_{\max}$  282.77 nm; <sup>1</sup>H NMR (CDCl<sub>3</sub>, 400 MHz):  $\delta$  8.22 (s, 1H), 7.66–7.63 (m, 4H), 7.41–7.40 (m, 2H), 7.38–7.34 (m, 4H), 7.30 (s, 1H), 6.20 (d,  $J = 2.8$  Hz, 1H), 5.74 (br s, 2H), 4.90 (dd,  $J = 5.6, 2.8$  Hz, 1H), 4.80 (dd,  $J = 6.0, 5.8$  Hz, 1H), 3.88 (dd,  $J = 10, 6.8$  Hz, 1H), 3.82–3.75 (m, 2H), 2.07 (s, 3H), 1.58 (s, 3H), 1.28 (s, 3H), 1.08 (s, 9H); <sup>13</sup>C NMR (CDCl<sub>3</sub>, 100 MHz):  $\delta$  157.0, 152.3, 149.4, 135.7, 135.6, 133.0, 132.9, 129.9, 127.8, 125.8, 112.6, 103.8, 97.0, 89.1, 88.4, 84.1, 72.5, 66.3, 65.2, 55.9, 27.4, 26.9, 25.2, 19.3, 4.6; HRMS (ESI-Q-TOF)  $m/z$   $[M + H]^+$  for C<sub>33</sub>H<sub>39</sub>N<sub>4</sub>O<sub>3</sub>SSi calculated 599.2507, found 599.2512.

3.2.26. 5-(But-1-yn-1-yl)-7-((3aR,4R,6R,6aS)-6-(((*tert*-butyldiphenylsilyl)oxy)methyl)-2,2-dimethyltetrahydrothieno[3,4-d][1,3]dioxol-4-yl)-7H-pyrrolo[2,3-d]pyrimidin-4-amine (**15b**)

It was obtained from **11** (234 mg, 0.34 mmol) as described for **13**, as sticky mass (189 mg, 91%); silica gel column chromatography (hexane/ethyl acetate, 7:3);  $[\alpha]_D^{25}$   $-71.76$  (c 0.06, CH<sub>3</sub>OH); UV (CH<sub>3</sub>OH)  $\lambda_{\max}$  283.50 nm; <sup>1</sup>H NMR (CDCl<sub>3</sub>, 500 MHz):  $\delta$  8.22 (s, 1H), 7.65–7.62 (m, 4H), 7.42–7.39 (m, 2H), 7.37–7.34 (m, 4H), 7.30 (s, 1H), 6.19 (d,  $J = 2.7$  Hz, 1H), 5.68 (br s, 2H), 4.89 (dd,  $J = 5.7, 2.8$  Hz, 1H), 4.79 (dd,  $J = 5.6, 2.8$  Hz, 1H), 3.87–3.85 (m, 1H), 3.80–3.77 (m, 1H), 3.76–3.74 (m, 1H), 2.43 (q,  $J = 14.9, 7.5$  Hz, 2H), 1.57 (s, 3H), 1.27 (s, 3H), 1.23 (t,  $J = 7.5$  Hz, 3H), 1.06 (s, 9H); <sup>13</sup>C NMR (CDCl<sub>3</sub>, 100 MHz):  $\delta$  157.0, 152.4, 149.4, 135.6, 135.5, 132.99, 132.9, 129.8, 127.8, 127.7, 125.6, 112.5, 103.8, 96.8, 94.1, 89.0, 84.0, 72.7, 66.1, 65.1, 55.8, 27.3, 26.8, 25.1, 19.2, 13.9, 13.2; HRMS (ESI-Q-TOF)  $m/z$   $[M + H]^+$  for C<sub>34</sub>H<sub>41</sub>N<sub>4</sub>O<sub>3</sub>SSi calculated 613.2663, found 613.2669.

3.2.27. 7-((3aR,4R,6R,6aS)-6-(((*tert*-butyldiphenylsilyl)oxy)methyl)-2,2-dimethyltetrahydrothieno[3,4-d][1,3]dioxol-4-yl)-5-(3,3-dimethylbut-1-yn-1-yl)-7H-pyrrolo[2,3-d]pyrimidin-4-amine (**15c**)

For the synthesis of **15c**, compound **11** (300 mg, 0.43 mmol) was treated as described for **13**, yielding sticky mass (224 mg, 80%); silica gel column chromatography, hexane/ethyl acetate, 13:7;  $[\alpha]_D^{25}$   $-67.09$  (c 0.265, CH<sub>3</sub>OH); UV (CH<sub>3</sub>OH)  $\lambda_{\max}$  283.86 nm; <sup>1</sup>H NMR (CDCl<sub>3</sub>, 500 MHz):  $\delta$  8.21 (s, 1H), 7.64 (t,  $J = 6.4$  Hz, 4H), 7.42–7.40 (m, 2H), 7.38–7.34 (m, 4H), 7.32 (s, 1H), 6.20 (d,  $J = 2.6$  Hz, 1H), 5.83 (br s, 2H), 4.88 (dd,  $J = 5.6, 2.7$  Hz, 1H), 4.77 (dd,  $J = 5.5, 2.5$  Hz, 1H), 3.87 (dd,  $J = 9.7, 6.2$  Hz, 1H), 3.79–3.73 (m, 2H), 1.57 (s, 3H), 1.31 (s, 9H), 1.26 (s, 3H), 1.07 (s, 9H); <sup>13</sup>C NMR (CDCl<sub>3</sub>, 100 MHz):  $\delta$  157.2, 152.6, 149.6, 135.7, 135.6, 133.0, 132.9, 129.9, 127.9, 125.3, 112.5, 103.9, 101.1, 96.9, 89.2, 84.1, 72.1, 66.2, 65.2, 55.9, 31.0, 28.3, 27.4, 26.9, 25.2, 19.3; HRMS (ESI-Q-TOF)  $m/z$   $[M + H]^+$  for C<sub>36</sub>H<sub>45</sub>N<sub>4</sub>O<sub>3</sub>SSi calculated 641.2976, found 641.2991.

3.2.28. 7-((3aR,4R,6R,6aS)-6-(((*tert*-butyldiphenylsilyl)oxy)methyl)-2,2-dimethyltetrahydrothieno[3,4-d][1,3]dioxol-4-yl)-5-(cyclopropylethynyl)-7H-pyrrolo[2,3-d]pyrimidin-4-amine (**15d**)

It was obtained from **11** (214 mg, 0.31 mmol) as described for **13**, as sticky mass (180 mg, 92%); silica gel column chromatography, hexane/ethyl acetate, 13:7;  $[\alpha]_D^{25}$   $-70.38$  (c 0.10, CH<sub>3</sub>OH); UV (CH<sub>3</sub>OH)  $\lambda_{\max}$  284.50 nm; <sup>1</sup>H NMR (CDCl<sub>3</sub>, 400 MHz):  $\delta$  8.21 (s, 1H), 7.66–7.63 (m, 4H), 7.44–7.40 (m, 2H), 7.39–7.34 (m, 4H), 7.31 (s, 1H), 6.19 (d,  $J = 3.2$  Hz, 1H), 5.93 (br s, 2H), 4.88 (dd,  $J = 5.9, 3.2$  Hz, 1H), 4.79 (dd,  $J = 5.9, 2.7$  Hz, 1H), 3.89–3.85 (m, 1H), 3.82–3.73 (m, 2H), 1.58 (s, 3H), 1.49–1.44 (m, 1H), 1.27 (s, 3H), 1.07 (s, 9H), 0.92–0.85 (m, 2H), 0.79–0.75 (m, 2H); <sup>13</sup>C NMR (CDCl<sub>3</sub>, 100 MHz):  $\delta$  156.4, 149.0, 135.6, 135.5, 132.9, 132.8, 129.9, 127.8, 126.2, 112.5, 103.8, 97.1, 89.1, 84.1, 68.0, 66.3, 65.1, 55.8, 27.3, 26.8, 25.1,

19.2, 8.7, 0.2; HRMS (ESI-Q-TOF)  $m/z$   $[M + H]^+$  for  $C_{35}H_{41}N_4O_3SSi$  calculated 625.2663, found 625.2667.

3.2.29. (2R,3R,4S,5R)-2-(4-Amino-5-(prop-1-yn-1-yl)-7H-pyrrolo[2,3-d]pyrimidin-7-yl)-5-(hydroxymethyl)tetrahydrothiophene-3,4-diol (**1h**)

Compound **15a** (150 mg, 0.25 mmol) was converted to **1h** (66.4 mg, 83%) yielding white solid, using the procedure described for **1a**; silica gel column chromatography ( $CH_2Cl_2/MeOH$ , 47:3); mp 190–192 °C;  $[\alpha]_D^{25}$   $-51.14$  ( $c$  0.05,  $CH_3OH$ ); UV ( $CH_3OH$ )  $\lambda_{max}$  282.77 nm;  $^1H$  NMR ( $DMSO-d_6$ , 500 MHz):  $\delta$  8.10 (s, 1H), 7.75 (s, 1H), 6.05 (d,  $J$  = 6.7 Hz, 1H), 5.40 (d,  $J$  = 6.2 Hz, 1H), 5.25 (d,  $J$  = 4.1 Hz, 1H), 5.16 (t,  $J$  = 5.3 Hz, 1H), 4.42–4.39 (m, 1H), 4.16–4.13 (m, 1H), 3.75–3.70 (m, 1H), 3.61–3.56 (m, 1H), 3.27–3.24 (m, 1H), 2.08 (s, 3H);  $^{13}C$  NMR ( $DMSO-d_6$ , 125 MHz):  $\delta$  157.4, 152.5, 149.7, 125.8, 102.1, 95.7, 88.4, 77.3, 73.2, 72.6, 63.1, 61.1, 52.9, 4.2; HRMS (ESI-Q-TOF)  $m/z$   $[M + H]^+$  for  $C_{14}H_{17}N_4O_3S$  calculated 321.1016, found 321.1013; purity  $\geq 95\%$ .

3.2.30. (2R,3R,4S,5R)-2-(4-Amino-5-(but-1-yn-1-yl)-7H-pyrrolo[2,3-d]pyrimidin-7-yl)-5-(hydroxymethyl)tetrahydrothiophene-3,4-diol (**1i**)

Following the procedure described for **1a**; compound **15b** (176 mg, 0.28 mmol) yielded **1i** (80.4 mg, 86%) as white solid; silica gel column chromatography ( $CH_2Cl_2/MeOH$ , 47:3); mp 161–162 °C;  $[\alpha]_D^{25}$   $-32.48$  ( $c$  0.05,  $CH_3OH$ ); UV ( $CH_3OH$ )  $\lambda_{max}$  283.86 nm;  $^1H$  NMR ( $DMSO-d_6$ , 500 MHz):  $\delta$  8.10 (s, 1H), 7.76 (s, 1H), 6.06 (d,  $J$  = 6.8 Hz, 1H), 5.40 ( $J$  = 6.3 Hz, 1H), 5.26 ( $J$  = 4.4 Hz, 1H), 5.16 (t,  $J$  = 5.4 Hz, 1H), 4.43–4.40 (m, 1H), 4.16–4.13 (m, 1H), 3.75–3.70 (m, 1H), 3.60–3.56 (m, 1H), 3.27–3.24 (m, 1H), 2.47 (q,  $J$  = 14.9, 7.4 Hz, 2H), 1.17 (t,  $J$  = 7.4 Hz, 3H);  $^{13}C$  NMR ( $CD_3OD$ , 100 MHz):  $\delta$  157.6, 151.6, 149.2, 126.0, 103.1, 97.0, 93.8, 78.8, 74.2, 72.0, 63.0, 62.5, 52.7, 12.9, 12.5; HRMS (ESI-Q-TOF)  $m/z$   $[M + H]^+$  for  $C_{15}H_{19}N_4O_3S$  calculated 335.1172, found 335.1157; purity  $\geq 95\%$ .

3.2.31. (2R,3R,4S,5R)-2-(4-Amino-5-(3,3-dimethylbut-1-yn-1-yl)-7H-pyrrolo[2,3-d]pyrimidin-7-yl)-5-(hydroxymethyl)tetrahydrothiophene-3,4-diol (**1j**)

Compound **15c** (200 mg, 0.31 mmol) was converted to **1j** (91.8 mg, 82%) as white solid, by following the procedure described for **1a**; silica gel column chromatography ( $CH_2Cl_2/MeOH$ , 47:3); mp 144–146 °C;  $[\alpha]_D^{25}$   $-61.72$  ( $c$  0.06,  $CH_3OH$ ); UV ( $CH_3OH$ )  $\lambda_{max}$  287.50 nm;  $^1H$  NMR ( $DMSO-d_6$ , 500 MHz):  $\delta$  8.11 (s, 1H), 7.76 (s, 1H), 6.06 (d,  $J$  = 7.0 Hz, 1H), 5.39 (d,  $J$  = 6.4 Hz, 1H), 5.27 (d,  $J$  = 4.4 Hz, 1H), 5.16 (t,  $J$  = 5.5 Hz, 1H), 4.45–4.41 (m, 1H), 4.16–4.13 (m, 1H), 3.76–3.71 (m, 1H), 3.61–3.55 (m, 1H), 3.27–3.24 (m, 1H), 1.31 (s, 9H);  $^{13}C$  NMR ( $DMSO-d_6$ , 100 MHz):  $\delta$  157.5, 152.6, 149.8, 125.7, 102.2, 100.3, 95.3, 77.3, 73.2, 72.5, 63.2, 60.9, 52.9, 30.6, 27.8; HRMS (ESI-Q-TOF)  $m/z$   $[M + H]^+$  for  $C_{17}H_{23}N_4O_3S$  calculated 363.1485, found 363.1492; purity  $\geq 95\%$ .

3.2.32. (2R,3R,4S,5R)-2-(4-Amino-5-(cyclopropylethynyl)-7H-pyrrolo[2,3-d]pyrimidin-7-yl)-5-(hydroxymethyl)tetrahydrothiophene-3,4-diol (**1k**)

Compound **15d** (156 mg, 0.24 mmol) was converted to **1k** (71.4 mg, 86%) as white solid, by following the procedure described for **1a**; silica gel column chromatography ( $CH_2Cl_2/MeOH$ , 47:3); mp 166–168 °C;  $[\alpha]_D^{25}$   $-50.34$  ( $c$  0.05,  $CH_3OH$ ); UV ( $CH_3OH$ )  $\lambda_{max}$  284.22 nm;  $^1H$  NMR ( $CD_3OD$ , 400 MHz):  $\delta$  8.09 (s, 1H), 7.67 (s, 1H), 6.11 (d,  $J$  = 5.6 Hz, 1H), 4.44 (dd,  $J$  = 5.6, 3.6 Hz, 1H), 4.24 (merged dd,  $J_1 = J_2 = 4.0$  Hz, 1H), 3.89–3.79 (m, 2H), 3.49–3.44 (m, 1H), 1.57–1.50 (m, 1H), 0.94–0.88 (m, 2H), 0.78–0.74 (m, 2H);  $^{13}C$  NMR ( $CD_3OD$ , 100 MHz):  $\delta$  159.2, 153.2, 150.7, 127.8, 104.7, 98.3, 97.1, 80.2, 75.6, 69.1, 64.5, 64.0, 54.2, 9.1, 0.9; HRMS (ESI-Q-TOF)  $m/z$   $[M + H]^+$  for  $C_{16}H_{19}N_4O_3S$  calculated 347.1172, found 347.1159; purity  $\geq 95\%$ .

### 3.3. Cell Proliferation Inhibition Assay (SRB Assay)

Human lung cancer cells (A549), colorectal cancer (HCT116) cells, breast cancer cells (MDA-MB-231), liver cancer cells (SK-HEP-1), and prostate cancer cells (PC-3) were pur-

chased from the American Type Culture Collection (Manassas, VA, USA). Human gastric cancer cells (SNU-638) were purchased from the Korean Cell Line Bank (Seoul, Korea). Cells were cultured in medium (Dulbecco's modified Eagle's medium for MDA-MB-231 and SK-HEP-1 cells; Roswell Park Memorial Institute 1640 for A549, HCT116, SNU-638, PC-3 cells) supplemented with penicillin-streptomycin and 10% fetal bovine serum at 37 °C in a humidified incubator with 5% carbon dioxide. Cells were seeded at a density of  $4\text{--}7 \times 10^4$  cells/mL in 96-well culture plates, and then treated with indicated compounds for 72 h. At the end of the experiment, cells were fixed with 10% trichloroacetic acid (TCA) solution and subjected to sulforhodamine B (SRB) assay to determine cell proliferation [42]. The percentage of cell proliferation was calculated with the following formula:

$$\text{Cell proliferation (\%)} = 100 \times [(A \text{ treated} - A \text{ zero day}) / (A \text{ control} - A \text{ zero day})],$$

where A is the average absorbance. The IC<sub>50</sub> values were calculated through non-linear regression analysis using TableCurve 2D v5.01 (Systat Software Inc., San Jose, CA, USA). All experiments were performed in triplicate and data shown are representative of two or three independent experiments.

### Cell Culture

The human colon cancer (KM12) and renal cancer (ACHN) cell lines were obtained from the Korean Cell Line Bank (Seoul, Korea). Cells were grown in DMEM supplemented with 10% fetal bovine serum (FBS) and antibiotics-antimycotics (PSF: 100 units/mL penicillin G sodium, 100 µg/mL streptomycin and 250 ng/mL amphotericin B). All cells were incubated at 37 °C in a humidified atmosphere containing 5% CO<sub>2</sub> and subcultured twice a week.

### 3.4. Kinome Scan Assays

The kinome scan assays were carried out at Eurofins DiscoverX Corporation. For kinome scan profiling of compound **1g**, it was screened at 1 µM against 96 kinases ( $N = 2$  independent experiments) [26]. The results for binding interactions are reported as % inhibition, where higher values indicate strong affinity; see the Supporting Information, Table S1 for full kinome profile. For kinase inhibition profile of compounds **1a–k** [see the Supporting information, Table S2, whose IC<sub>50</sub> values were determined using an 11-point 3-fold serial dilution of each test compound using their KINOMEscan assay and  $K_i$  was determined by the Cheng-Prusoff equation.

### 3.5. Metabolic Stability

Phosphate buffer (0.1 M, pH 7.4) containing human liver microsomes (0.5 mg/mL) and test compound (a final concentration of 1 µM) were pre-incubated for 5 min at 37 °C. NADPH regeneration system solution was added to it and incubated for 30 min at 37 °C. Acetonitrile solution containing chlorpropamide was added at the end of the reaction. The sample was centrifuged for 5 min (14,000 × g rpm, 4 °C) and the supernatant was injected into the LC-MS/MS system for the analysis. The amount of substrate that remained after the reaction was analyzed using the Shimadzu Nexera XR system and TSQ vantage (Thermo). Kinetex C18 column (2.1 × 100 mm, 2.6 µm particle size; Phenomenex) was used for HPLC. The mobile phase used contained 0.1% formic acid in distilled water (A) and 0.1% formic acid containing acetonitrile (B). Xcalibur (version 1.6.1) was used for data analysis. Verapamil was used as a positive control [48,49].

### 3.6. CYP Inhibition Assay

Human liver microsomes (0.25 mg/mL), 0.1 M phosphate buffer (pH 7.4), a cocktail of five coenzyme substrates (Phenacetin 50 µM, Diclofenac 10 µM, S-mephenytoin 100 µM, Dextromethorphan 5 µM, Midazolam 2.5 µM), and test compound (10 µM concentration) was pre-incubated for 5 min at 37 °C. NADPH generation system solution was added and incubated for 15 min at 37 °C. In order to terminate the reaction, acetonitrile solu-

tion containing an internal standard (Terfenadine) was added and centrifuged for 5 min (14,000 × g rpm, 4 °C). The supernatant was injected into the LC-MS/MS system to analyze the metabolites of the substrates simultaneously. Metabolites of each substrate produced during the reaction were analyzed using the Shimadzu Nexera XR system and TSQ vantage (Thermo). Kinetex C18 column (2.1 × 100 mm, 2.6 μm particle size; Phenomenex, USA) was used for HPLC. The mobile phase used contained 0.1% formic acid in distilled water (A) and 0.1% formic acid containing acetonitrile (B). The generated metabolites were quantified using MRM (Multiple Reaction Monitoring) and Xcalibur (version 1.6.1) was used for data analysis [50,51].

### 3.7. Computational Docking Simulation

Ligand binding site for docking was defined as a 30 Å<sup>3</sup> grid box for DYRK1A and 20 × 24 × 20 Å<sup>3</sup> grid box for TRKA centered on the centroid of co-crystallized native ligands. The crystal structures of DYRK1A (PDB ID: 7A51) [46] and TRKA (PDB ID: 5JFV) [47] were downloaded from RCSB PDB and computational docking was performed using AutoDock Vina version 1.5.6 (The Scripps Research Institute, La Jolla, CA, USA) [52]. For the macromolecule-ligand pair, the binding model of the ligand with the lowest binding free energy (kcal/mol) was used for further analysis. Figure to show the molecular modeling results were visualized using PyMOL (Schrödinger, LLC, New York, NY, USA) [53]. LIGPLOT<sup>+</sup> (version 2.2.4) was used to view the interactions between amino acid residues of enzyme and compound [54].

## 4. Conclusions

Protein kinases represent a promising target for the development of anticancer agents due to their association with cancer growth and progression [10–12]. In the present study, we designed molecules using the nucleoside skeleton with the intention to simultaneously occupy the hinge and the hydrophobic region I (buried region), along with the ribose region of the ATP-binding site. We sought to identify whether the hydrophobic pocket I acts as a pharmacophore in kinase inhibition. Thus, we designed and synthesized 7-substituted 7-deaza-4'-thioadenosine derivatives **1** with a nucleoside skeleton by modifying the hydrophobic residue (R), based on ATP-kinase interactions. Among all the synthesized compounds, compound **1g** with acetylene at the 7-position of 7-deaza-4'-thioadenosine (R = acetylene) exhibited markedly potent anticancer activity in vitro against six different cancer cell lines and potent kinase inhibition of TRKA, DYRK1A/1B, and CK1δ at a concentration of 1 μM among the panel of 96 kinases. The results showed that the C-7 substituent of 7-deazaadenine was optimal for substituting extremely small and linear acetylene, indicating that a very small linear hydrophobic group is required to inhibit TRKA, DYRK1A/1B, and CK1δ. These results will contribute greatly to the further development of new anticancer agents with multi-kinase inhibition.

**Supplementary Materials:** The following are available online at <https://www.mdpi.com/article/10.3390/ph14121290/s1>, <sup>1</sup>H and <sup>13</sup>C NMR spectra, HRMS (ESI-Q-TOF) data for **1g**, Figure S1: ORTEP diagram of compound **1g** showing thermal ellipsoid at 50% probability, X-ray crystallographic data for **1g**, HPLC chromatograms, Table S1: Kinome scan data of compound **1g**, Table S2: Kinase inhibition profile of **1a–k** against TRKA, CK1δ, and DYRK1A/1B.

**Author Contributions:** Conceptualization, L.S.J.; methodology, K.K.M., K.S., S.K.T., Y.A.Y., H.W.L., J.Y.K. and M.K.; software, K.K.M. and G.K.; validation, L.S.J.; formal analysis, K.K.M., W.S.B., H.K. and S.A.; investigation, K.K.M., W.S.B., H.K., S.A., E.-J.K., M.N. and S.K.L.; data curation, K.K.M., W.S.B., H.K. and S.A.; writing—original draft preparation, K.K.M. and L.S.J.; writing—review and editing, L.S.J.; supervision, L.S.J.; project administration, L.S.J.; funding acquisition, L.S.J. All authors have read and agreed to the published version of the manuscript.

**Funding:** This work was supported by the National Research Foundation (NRF) grants (NRF-2021R1A2B5B02001544) of Korea.

**Institutional Review Board Statement:** Not applicable.

**Informed Consent Statement:** Not applicable.

**Data Availability Statement:** Data is contained within the article and supplementary files.

**Conflicts of Interest:** The authors declare no conflict of interest.

## References

- Nikolaou, M.; Pavlopoulou, A.; Georgakilas, A.G.; Kyrodimos, E. The challenge of drug resistance in cancer treatment: A current overview. *Clin. Exp. Metastasis* **2018**, *35*, 309–318. [CrossRef]
- Khamisipour, G.; Jadidi-Niaragh, F.; Jahromi, A.S.; Zandi, K.; Hojjat-Farsangi, M. Mechanisms of tumor cell resistance to the current targeted-therapy agents. *Tumor Biol.* **2016**, *37*, 10021–10039. [CrossRef]
- Potapova, O.; Laird, A.D.; Nannini, M.A.; Barone, A.; Li, G.; Moss, K.G.; Cherrington, J.M.; Mendel, D.B. Contribution of individual targets to the antitumor efficacy of the multitargeted receptor tyrosine kinase inhibitor SU11248. *Mol. Cancer Ther.* **2006**, *5*, 1280–1289. [CrossRef]
- Peters, J.-U. Polypharmacology-foe or friend? *J. Med. Chem.* **2013**, *56*, 8955–8971. [CrossRef]
- Anighoro, A.; Bajorath, J.; Rastelli, G. Polypharmacology: Challenges and opportunities in drug discovery. *J. Med. Chem.* **2014**, *57*, 7874–7887. [CrossRef]
- Bolognesi, M.L.; Cavalli, A. Multitarget drug discovery and polypharmacology. *Chem. Med. Chem.* **2016**, *11*, 1190–1192. [CrossRef] [PubMed]
- Proschak, E.; Stark, H.; Merk, D. Polypharmacology by design: A medicinal chemist's perspective on multitargeting compounds. *J. Med. Chem.* **2019**, *62*, 420–444. [CrossRef]
- Chaudhari, R.; Fong, L.W.; Tan, Z.; Huang, B.; Zhang, S. An up-to-date overview of computational polypharmacology in modern drug discovery. *Expert Opin. Drug Discov.* **2020**, *15*, 1025–1044. [CrossRef] [PubMed]
- Cicenas, J.; Zalyte, E.; Bairoch, A.; Gaudet, P. Kinases and cancer. *Cancers* **2018**, *10*, 63. [CrossRef]
- Futreal, P.A.; Coin, L.; Marshall, M.; Down, T.; Hubbard, T.; Wooster, R.; Rahman, N.; Stratton, M.R. A census of human cancer genes. *Nat. Rev. Cancer* **2004**, *4*, 177–183. [CrossRef] [PubMed]
- Du, Z.; Lovly, C.M. Mechanisms of receptor tyrosine kinase activation in cancer. *Mol. Cancer* **2018**, *17*, 58. [CrossRef] [PubMed]
- Ferguson, F.M.; Gray, N.S. Kinase inhibitors: The road ahead. *Nat. Rev. Drug Discov.* **2018**, *17*, 353–377. [CrossRef] [PubMed]
- Bracarda, S.; Caserta, C.; Sordini, L.; Rossi, M.; Hamzay, A.; Crino, L. Protein kinase inhibitors in the treatment of renal cell carcinoma: Sorafenib. *Ann. Oncol.* **2007**, *18*, vi22–vi25. [CrossRef]
- Demetri, G.D.; van Oosterom, A.T.; Garrett, C.R.; Blackstein, M.E.; Shah, M.H.; Verweij, J.; McArthur, G.; Judson, I.R.; Heinrich, M.C.; Morgan, J.A.; et al. Efficacy and safety of sunitinib in patients with advanced gastrointestinal stromal tumour after failure of imatinib: A randomised controlled trial. *Lancet* **2006**, *368*, 1329–1338. [CrossRef]
- Ardini, E.; Menichincheri, M.; Banfi, P.; Bosotti, R.; De Ponti, C.; Pulci, R.; Ballinari, D.; Ciomei, M.; Texido, G.; Degrassi, A.; et al. Entrectinib, a pan-TRK, ROS1, and ALK inhibitor with activity in multiple molecularly defined cancer indications. *Mol. Cancer Ther.* **2016**, *15*, 628–639. [CrossRef]
- Roskoski, R., Jr. Properties of FDA-approved small molecule protein kinase inhibitors: A 2021 update. *Pharmacol. Res.* **2021**, *165*, 105463. [CrossRef]
- Bhullar, K.S.; Lagarón, N.O.; McGowan, E.M.; Parmar, I.; Jha, A.; Hubbard, B.P.; Rupasinghe, H.P.V. Kinase-targeted cancer therapies: Progress, challenges and future directions. *Mol. Cancer* **2018**, *17*, 48. [CrossRef]
- Okamoto, K.; Ikemori-Kawada, M.; Jestel, A.; von Konig, K.; Funahashi, Y.; Matsushima, T.; Tsuruoka, A.; Inoue, A.; Matsui, J. Distinct binding mode of multikinase inhibitor lenvatinib revealed by biochemical characterization. *ACS Med. Chem. Lett.* **2015**, *6*, 89–94. [CrossRef] [PubMed]
- Attwood, M.M.; Fabbro, D.; Sokolov, A.V.; Knapp, S.; Schiöth, H.B. Trends in kinase drug discovery: Targets, indications and inhibitor design. *Nat. Rev. Drug Discov.* **2021**, *20*, 839–861. [CrossRef]
- Vulpetti, A.; Bosotti, R. Sequence and structural analysis of kinase ATP pocket residues. *IL Farmaco* **2004**, *59*, 759–765. [CrossRef]
- Zheng, J.; Knighton, D.R.; Ten Eyck, L.F.; Karlsson, R.; Xuong, N.; Taylor, S.S.; Sowadski, J.M. Crystal structure of the catalytic subunit of cAMP-dependent protein kinase complexed with MgATP and peptide inhibitor. *Biochemistry* **1993**, *32*, 2154–2161. [CrossRef]
- Davis, M.I.; Hunt, J.P.; Herrgard, S.; Ciceri, P.; Wodicka, L.M.; Pallares, G.; Hocker, M.; Treiber, D.K.; Zarrinkar, P.P. Comprehensive analysis of kinase inhibitor selectivity. *Nat. Biotechnol.* **2011**, *29*, 1046–1051. [CrossRef]
- Gandin, V.; Ferrarese, A.; Dalla Via, M.; Marzano, C.; Chilin, A.; Marzaro, G. Targeting kinases with anilinopyrimidines: Discovery of *N*-phenyl-*N'*-[4-(pyrimidin-4-ylamino)phenyl]urea derivatives as selective inhibitors of class III receptor tyrosine kinase subfamily. *Sci. Rep.* **2015**, *5*, 16750. [CrossRef]
- Morphy, R. Selectively nonselective kinase inhibition: Striking the right balance. *J. Med. Chem.* **2010**, *53*, 1413–1437. [CrossRef] [PubMed]
- Anastassiadis, T.; Deacon, S.W.; Devarajan, K.; Ma, H.; Peterson, J.R. Comprehensive assay of kinase catalytic activity reveals features of kinase inhibitor selectivity. *Nat. Biotechnol.* **2011**, *29*, 1039–1045. [CrossRef]



26. Fabian, M.A.; Biggs, W.H., III; Treiber, D.K.; Atteridge, C.E.; Azimioara, M.D.; Benedetti, M.G.; Carter, T.A.; Ciceri, P.; Edeen, P.T.; Floyd, M.; et al. A small molecule-kinase interaction map for clinical kinase inhibitor. *Nat. Biotechnol.* **2005**, *23*, 329–336. [CrossRef] [PubMed]
27. Wells, C.I.; Al-Ali, H.; Andrews, D.M.; Asquith, C.R.M.; Axtman, A.D.; Dikic, I.; Ebner, D.; Etmayer, P.; Fischer, C.; Frederiksen, M.; et al. The kinase chemogenomic set (KCGS): An open science resource for kinase vulnerability identification. *Int. J. Mol. Sci.* **2021**, *22*, 566. [CrossRef]
28. Klaeger, S.; Heinzlmeier, S.; Wilhelm, M.; Polzer, H.; Vick, B.; Koenig, P.-A.; Reinecke, M.; Ruprecht, B.; Petzoldt, S.; Meng, C.; et al. The target landscape of clinical kinase drugs. *Science* **2017**, *358*, 1148. [CrossRef] [PubMed]
29. Biabani, M.F.; Gunasekera, S.P.; Longley, R.E.; Wright, A.E.; Pomponi, S.A. Tubercidin, a cytotoxic agent from the marine sponge *Caulospongia biflabellata*. *Pharm. Biol.* **2002**, *40*, 302–303. [CrossRef]
30. Grage, T.B.; Rochlin, D.B.; Weiss, A.J.; Wilson, W.L. Clinical studies with tubercidin administered after absorption into human erythrocytes. *Cancer Res.* **1970**, *30*, 79–81. [PubMed]
31. Bourderioux, A.; Nauš, P.; Perlíková, P.; Pohl, R.; Pichová, I.; Votruba, I.; Džubák, P.; Konečný, P.; Hajdúch, M.; Stray, K.M.; et al. Synthesis and significant cytostatic activity of 7-hetaryl-7-deazaadenosines. *J. Med. Chem.* **2011**, *54*, 5498–5507. [CrossRef] [PubMed]
32. Tiwari, K.N.; Shortnacy-fowler, A.T.; Cappellacci, L.; Parker, W.B.; Waud, W.R.; Montgomery, J.A.; Secrist, J.A., III. Synthesis of 4'-thio-β-D-arabinofuranosylcytosine (4'-thio-ara-C) and comparison of its anticancer activity with that of ara-C. *Nucleosides Nucleotides Nucleic Acids* **2000**, *19*, 329–340. [CrossRef] [PubMed]
33. Shelton, J.; Lu, X.; Hollenbaugh, J.A.; Cho, J.H.; Amblard, F.; Schinazi, R.F. Metabolism, biochemical actions, and chemical synthesis of anticancer nucleosides, nucleotides, and base analogs. *Chem. Rev.* **2016**, *116*, 14379–14455. [CrossRef] [PubMed]
34. Reist, E.J.; Gueffroy, D.E.; Goodman, L. Synthesis of 4-thio-D- and -L-ribofuranose and the corresponding adenine nucleosides. *J. Am. Chem. Soc.* **1964**, *86*, 5658–5663. [CrossRef]
35. Gunaga, P.; Moon, H.R.; Choi, W.J.; Shin, D.H.; Park, J.G.; Jeong, L.S. Recent advances in 4'-thionucleosides as potential antiviral and antitumor agents. *Curr. Med. Chem.* **2004**, *11*, 2585–2637. [CrossRef]
36. Parker, W.B.; Shaddix, S.C.; Rose, L.M.; Waud, W.R.; Shewach, D.S.; Tiwari, K.N.; Secrist, J.A., III. Metabolism of 4'-thio-β-D-arabinofuranosylcytosine in CEM cells. *Biochem. Pharmacol.* **2000**, *60*, 1925–1932. [CrossRef]
37. Radhakrishnan, A.; Nanjappa, V.; Raja, R.; Sathe, G.; Puttamalles, V.N.; Jain, A.P.; Pinto, S.M.; Balaji, S.A.; Chavan, S.; Sahasrabuddhe, N.A.; et al. A dual specificity kinase, DYRK1A, as a potential therapeutic target for head and neck squamous cell carcinoma. *Sci. Rep.* **2016**, *6*, 36132. [CrossRef]
38. Friedman, E. Mirk/Dyrk1B in cancer. *J. Cell. Biochem.* **2007**, *102*, 274–279. [CrossRef]
39. Knippschild, U.; Wolff, S.; Giamas, G.; Brockschmidt, C.; Wittau, M.; Wurl, P.U.; Eismann, T.; Stoter, M. The role of the casein kinase 1 (CK1) family in different signaling pathways linked to cancer development. *Onkologie* **2005**, *28*, 508–514. [CrossRef]
40. Batra, H.; Moriarty, R.M.; Penmasta, R.; Sharma, V.; Stanciu, G.; Staszewski, J.P.; Tuladhar, S.M.; Walsh, D.A.; Datta, S.; Krishnaswamy, S. A concise, efficient and production-scale synthesis of a protected L-lyxonolactone derivative: An important aldololactone core. *Org. Process Res. Dev.* **2006**, *10*, 484–486. [CrossRef]
41. Haraguchi, K.; Shimada, H.; Kimura, K.; Akutsu, G.; Tanaka, H.; Abe, H.; Hamasaki, T.; Baba, M.; Gullen, E.A.; Dutschman, G.E.; et al. Synthesis of 4'-ethynyl-2'-deoxy-4'-thioribonucleosides and discovery of a highly potent and less toxic NRTI. *ACS Med. Chem. Lett.* **2011**, *2*, 692–697. [CrossRef]
42. Molloy, J.J.; Seath, C.P.; West, M.J.; McLaughlin, C.; Fazakerley, N.J.; Kennedy, A.R.; Nelson, D.J.; Watson, A.J.B. Interrogating Pd(II) anion metathesis using a bifunctional chemical probe: A transmetalation switch. *J. Am. Chem. Soc.* **2018**, *140*, 126–130. [CrossRef]
43. The CIF file for X-ray crystal structure of 1g has been deposited at the Cambridge Crystallographic Data Centre (CCDC, 12 Union Road, Cambridge, CB2 1EZ (UK); Tel: (+44)1223-336-408, Fax: (+44) 1223-336-033, e-mail: Deposit@ccdc.cam.ac.uk) with deposition number: CCDC 1575257.
44. Vichai, V.; Kirtikara, K. Sulforhodamine B colorimetric assay for cytotoxicity screening. *Nat. Protoc.* **2006**, *1*, 1112–1116. [CrossRef]
45. Song, J.; Yu, J.; Jeong, L.S.; Lee, S.K. A novel cytarabine analog evokes synthetic lethality by targeting MK2 in p53-deficient cancer cells. *Cancer Lett.* **2021**, *497*, 54–65. [CrossRef]
46. Walmsley, D.L.; Murray, J.B.; Dokurno, P.; Massey, A.J.; Benwell, K.; Fiumana, A.; Foloppe, N.; Ray, S.; Smith, J.; Surgenor, A.E.; et al. Fragment-derived selective inhibitors of dual-specificity kinases DYRK1A and DYRK1B. *J. Med. Chem.* **2021**, *64*, 8971–8991. [CrossRef]
47. Skerratt, A.E.; Andrews, M.; Bagal, S.K.; Bilsland, J.; Brown, D.; Bungay, P.J.; Cole, S.; Gibson, K.R.; Jones, R.; Morao, I.; et al. The discovery of a potent, selective, and peripherally restricted pan-Trk inhibitor (PF-06273340) for the treatment of pain. *J. Med. Chem.* **2016**, *59*, 10084–10099. [CrossRef] [PubMed]
48. Di, L.; Kerns, E.H.; Gao, N.; Li, S.Q.; Huang, Y.; Bourassa, J.L.; Hury, D.M. Experimental design on single-time-point high-throughput microsomal stability assay. *J. Pharm. Sci.* **2004**, *93*, 1537–1544. [CrossRef]
49. Kerns, E.H.; Di, L. (Eds.) *Chapter 29—Metabolic Stability Methods. Drug-Like Properties: Concepts, Structure Design and Methods*; Academic Press: San Diego, CA, USA, 2008; pp. 329–347.

50. Kim, M.-J.; Kim, H.; Cha, I.-J.; Park, J.-S.; Shon, J.-H.; Liu, K.-H.; Shin, J.-G. High-throughput screening of inhibitory potential of nine cytochrome P450 enzymes in vitro using liquid chromatography/tandem mass spectrometry. *Rapid Commun. Mass Spectrom.* **2005**, *19*, 2651–2658. [CrossRef] [PubMed]
51. Kerns, E.H.; Di, L. (Eds.) *Chapter 32—CYP Inhibition Methods. Drug-like Properties: Concepts, Structure Design and Methods*; Academic Press: San Diego, CA, USA, 2008; pp. 360–371.
52. Trott, O.; Olson, A.J. AutoDock Vina: Improving the speed and accuracy of docking with a new scoring function, efficient optimization and multithreading. *J. Comput. Chem.* **2010**, *31*, 455–461. [CrossRef]
53. DeLano, W.L. *The PyMOL Molecular Graphics System (Version 2.4.0)*; Schrödinger, LLC: New York, NY, USA, 2002.
54. Laskowski, R.A.; Swindells, M.B. LigPlot+: Multiple ligand-protein interaction diagrams for drug discovery. *J. Chem. Inf. Model.* **2011**, *51*, 2778–2786. [CrossRef] [PubMed]



Article

# Exploring the Anti-Cancer Mechanism of Novel 3,4'-Substituted Diaryl Guanidinium Derivatives

Viola Previtali <sup>1</sup>, Helene B. Mihigo <sup>1</sup>, Rebecca Amet <sup>2</sup>, Anthony M. McElligott <sup>3</sup>, Daniela M. Zisterer <sup>2</sup> and Isabel Rozas <sup>1,\*</sup>

<sup>1</sup> School of Chemistry, Trinity Biomedical Sciences Institute (TBSI), Trinity College Dublin (TCD), 152-160 Pearse Street, D02R590 Dublin 2, Ireland; Viola.Previtali@iit.it (V.P.); mihigoh@tcd.ie (H.B.M.)

<sup>2</sup> School of Biochemistry and Immunology, Trinity Biomedical Sciences Institute (TBSI), Trinity College Dublin (TCD), 152-160 Pearse Street, D02R590 Dublin 2, Ireland; ametr@tcd.ie (R.A.); dzisterer@tcd.ie (D.M.Z.)

<sup>3</sup> Trinity Translational Medicine Institute, Trinity College and St James's Hospital, D02R590 Dublin 8, Ireland; Tony.McElligott@tcd.ie

\* Correspondence: rozasi@tcd.ie

Received: 16 November 2020; Accepted: 16 December 2020; Published: 21 December 2020

**Abstract:** We previously identified a guanidinium-based lead compound that inhibited BRAF through a hypothetic type-III allosteric mechanism. Considering the pharmacophore identified in this lead compound (i.e., “lipophilic group”, “di-substituted guanidine”, “phenylguanidine polar end”), several modifications were investigated to improve its cytotoxicity in different cancer cell lines. Thus, several *lipophilic groups* were explored, the *di-substituted guanidine* was replaced by a secondary amine and the phenyl ring in the *polar end* was substituted by a pyridine. In a structure-based design approach, four representative derivatives were docked into an in-house model of an active triphosphate-containing BRAF protein, and the interactions established were analysed. Based on these computational studies, a variety of derivatives was synthesized, and their predicted drug-like properties calculated. Next, the effect on cell viability of these compounds was assessed in cell line models of promyelocytic leukaemia and breast, cervical and colorectal carcinomas. The potential of a selection of these compounds as apoptotic agents was assessed by screening in the promyelocytic leukaemia cell line HL-60. The toxicity against non-tumorigenic epithelial MCF10A cells was also investigated. These studies allowed for several structure-activity relationships to be derived. Investigations on the mechanism of action of representative compounds suggest a divergent effect on inhibition of the MAPK/ERK signalling pathway.

**Keywords:** 3,4'-bis-guanidino; 3-amino-4'-guanidino; diphenyl ether; phenyl pyridyl ether; intramolecular hydrogen bond; cancer cell viability; HL-60; BRAF; apoptosis

## 1. Introduction

Various interlinked signalling pathways are involved in cell proliferation, apoptosis or survival, and these processes are even more relevant in the case of tumour formation [? ]. Oncogenic mutations in one of these signalling pathways, the Ras/RAF/MEK/ERK (MAPK/ERK) pathway, are observed frequently in many cancers [? ? ]. Additionally, since mutations in RAF kinases are common events, these kinases (i.e., ARAF, BRAF and CRAF) have become very interesting therapeutic targets [? ? ].

Most of the protein kinase inhibitors developed so far are ATP competitive and, based on the conformation of the protein kinase they bind to, have been broadly classified as type I (bind to the  $\alpha$ C-helix-IN/DFG-IN conformation), type II (bind to the  $\alpha$ C-helix-IN/DFG-OUT conformation), or type I/II (bind to the  $\alpha$ C-helix-OUT/DFG-IN conformation) [? ]. In addition, there are allosteric inhibitors, known as type III protein kinase inhibitors, which do not compete with ATP. These inhibitors tend

to exhibit the highest degree of kinase selectivity because they exploit binding sites and regulatory mechanisms unique to particular kinases [? ].

Previously, we had identified a 3,4'-bis-guanidinium diphenyl derivative (**1**, Figure ??) that demonstrated strong cytotoxicity, mediated through induction of apoptosis, in colorectal cancer cells containing wild type(wt)-BRAF and mutated <sup>V600E</sup>BRAF [? ? ]. Compound **1** also inhibited ERK1/2 signalling, EGFR activation, as well as Src, STAT3 and Akt phosphorylation. We also showed that **1** did not inhibit ATP binding to BRAF, but a radiometric assay of BRAF activity indicated that this was inhibited in vitro. From these studies, we hypothesised that **1** could inhibit BRAF as a type III inhibitor. We propose that the positively charged guanidines present in compound **1** could interact with the negatively charged phosphates of the ATP present in the active state of all kinases [? ].

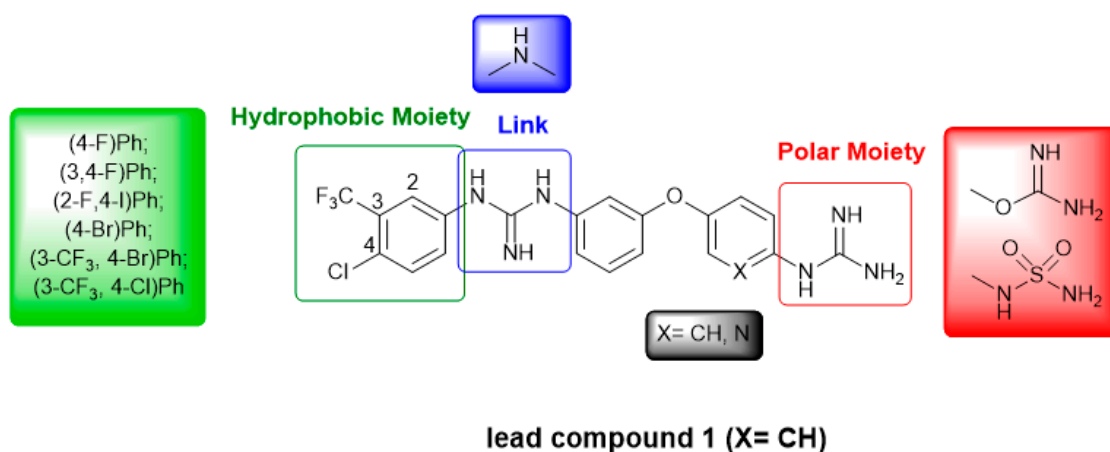


**Figure 1.** Structural modifications proposed for the optimization of the compound **1**.

Considering that only very recently a crystal structure of a BRAF protein kinase in complex with an ATP analogue (AMP-PCP) and MEK has been resolved (PDB 6U2G) [? ], we had previously constructed a model that reproduced an active form of this kinase including ATP to model potential type III inhibitors [? ]. This in-house model allowed us to explore the potential allosteric inhibition through ATP binding of compound **1** and it was considered a good target model for structure-based design when no crystallographic data was available.

Accordingly, in this article, we first present a computational study of a series of guanidine-based di-aromatic systems representative of all the compounds proposed with a simplified version of our in-house active BRAF model to explore their potential as type-III allosteric inhibitors. Additionally, we describe the preparation of the compounds proposed and the study of the anti-proliferative and pro-apoptotic activity on cancerous cell lines as well as their effect on the MAPK/ERK signalling pathway.

## 2. Results

Considering the structure of compound **1** ("link" -blue box-, "polar moiety" -red box- and "hydrophobic moiety" -green box-; see Figure ??), we explored a number of modifications in the different moieties, while maintaining the diaryl ether core due to its versatility and suitability for synthesis. First, several "hydrophobic" substituents have been considered (green box in Figure ??), since in our previously reported computational model [? ], this section of the molecule seems to interact with a hydrophobic pocket. Next, based on previous computational studies [? ], the effect of the length of the molecule on its activity has been studied by replacing the disubstituted guanidinium in the "link" by a secondary amine (blue box in Figure ??). Additionally, we explored the effect of substituting one of the phenyl rings by a pyridine to lock the orientation of the guanidinium by means of intramolecular hydrogen bonds (IMHBs) [? ]. Finally, in the "polar" region, different guanidine surrogates (i.e., isourea and sulfamide) have been tested (red box in Figure ??).

### 2.1. Molecular Modelling Studies

We had previously reported the docking of compound **1** into our in-house ATP-containing BRAF model [? ]; here, we are using a simplified model containing triphosphate (TP) instead of ATP since the interactions of interest only occur with the phosphates and adjacent hydrophobic pocket. Thus, in order to validate our TP-containing BRAF model, we first docked compound **1** (Figure ??) and considering that similar outcomes were observed, we used the TP-containing structure and similar conditions for the rest of the computational studies. Accordingly, a set of representative structures of all the compounds proposed were selected; compound **2** contains a pyridine instead of a phenyl ring as it was in compound **1**, in compound **3** the di-substituted guanidine of **1** has been changed to a secondary amine and compound **4** shows both modifications (Figure ??).

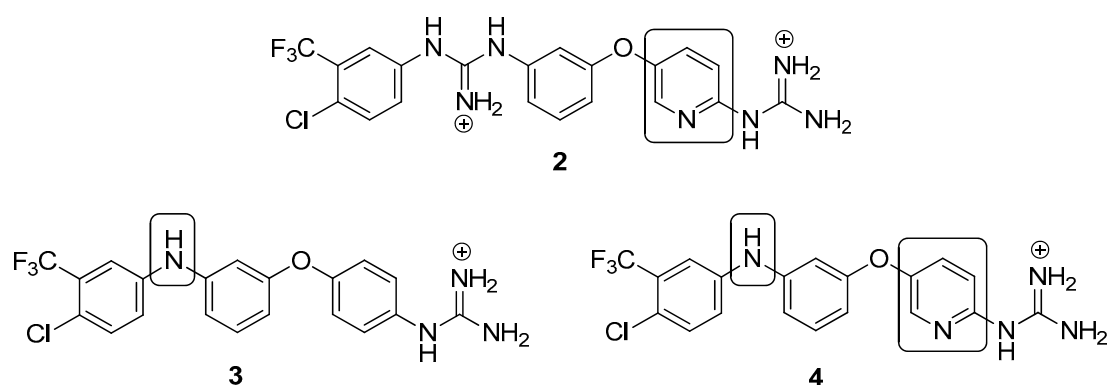


**Figure 2.** Structures of the proposed new derivatives of **1** (compounds **2**, **3** and **4**), which docking to the in-house triphosphate (TP)-containing BRAF simplified model was studied.

As in our previous modelling studies [? ], we found that compound **1** interacts with BRAF through an allosteric region found near the ATP binding site and with the TP system. The main interactions established involved bifurcated hydrogen bonds (HBs) between the mono-substituted guanidinium and two negatively charged O atoms of a phosphate (NH $\cdots$ O distances: 1.6, 2.9 and 2.7 Å, Figure S1) and a parallel HB interaction between the di-substituted guanidinium and the carboxylate of Glu648 (NH $\cdots$ O distances: of 2.0 and 2.6 Å, Figure S1). Both sets of HBs are reinforced by ionic interactions due to the charged nature of guanidinium, phosphate and carboxylate groups. Additionally, interactions are observed in the lipophilic pocket with the (4-Cl,3-CF<sub>3</sub>)Ph moiety; thus, the CF<sub>3</sub> group interacts with Met620 and the Cl with Trp619 (Figure S1).

Likewise, when derivative **2** is docked into the TP-BRAF simplified model, it forms ionically reinforced bifurcated HBs between the mono-substituted guanidinium and two negatively charged O atoms of TP (Figure ??). Likewise, a bifurcated HB interaction between the di-substituted guanidinium and Glu648 and van der Waals contacts at the lipophilic pocket with the (4-Cl,3-CF<sub>3</sub>)Ph moiety were also found for compound **2** (Figure ??). The newly introduced pyridine seems to form a HB with Asn137 as well as an IMHB that locks the mono-substituted guanidinium (Figure ??). This conformational restriction could result in increased affinity.

Replacement of the di-substituted guanidine by an -NH- leads to a significantly shorter molecule as in system **3** (Figure ??). Upon docking to the TP-containing simplified BRAF, we observed that the mono-substituted guanidinium still forms the expected bifurcated HBs. Compound **3** also fits within the hydrophobic pocket of the target establishing weaker contacts (longer interaction distances) with Met620 and Trp619. Additionally, the newly introduced -NH- group forms a HB with one of the O atoms of Glu648 (Figure S2).

Finally, the docking study of compound **4** (Figure ??) into the aforementioned target reproduce the results observed for the mono-substituted guanidinium pyridine system in analogue **2** by establishing bifurcated HBs with the TP, IMHB between guanidinium and pyridine as well as contacts between the

pyridine N and Asn137. Additionally, as the -NH- shortens the structure, similar interactions to those seen for compound 3 are observed, i.e., the -NH- group forms a HB with Glu648 and contacts within the hydrophobic pocket are found (Figure S3).

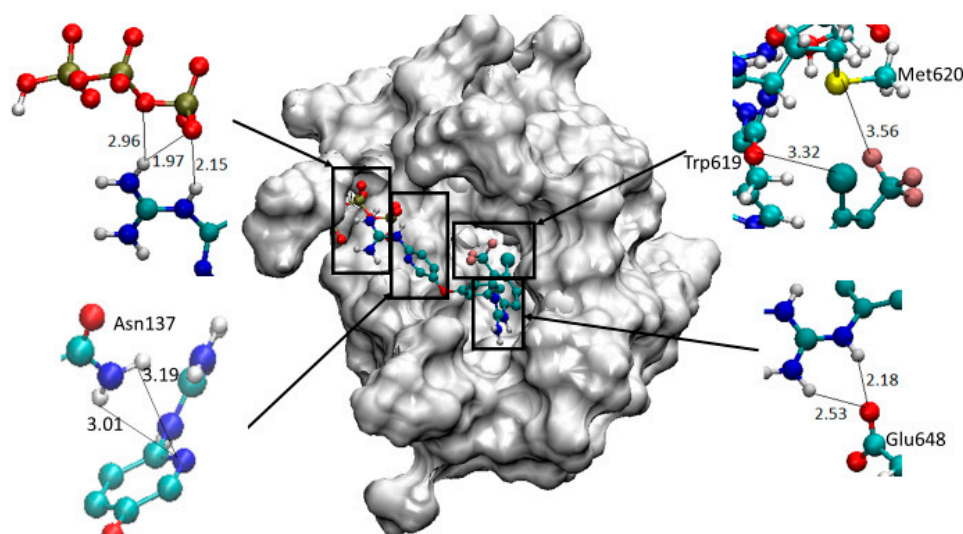


**Figure 3.** Docking of derivative 2 in the TP-containing BRAF simplified model indicating the bifurcated (up left, bottom left and right) and single (up right) hydrogen bond (HB) interactions observed. Distances are expressed in Å.

All this work was carried out prior to the recent publication of the crystal structure of BRAF containing an analogue of ATP (AMP-PCP) [? ], and in order to validate our in-house BRAF-ATP model [? ] we now superimposed both the reported crystal structure with our model finding an RMSD of 2.53 Å between them and with both ATP-like systems occupying the same pocket and with very similar orientations (Figures S4 and S5). This level of similarity gives us confidence on the docking studies performed with our BRAF-TP model.

The G-scores obtained for the best-poses obtained were very similar for the four compounds studied (around  $-7.7$  kcal/mol); hence, the interaction with the target was favoured in all the cases but did not help to discriminate among the four compounds. In summary, according to the docking studies all the compounds proposed seem to establish favourable interactions with BRAF, suggesting a possible type III allosteric binding.

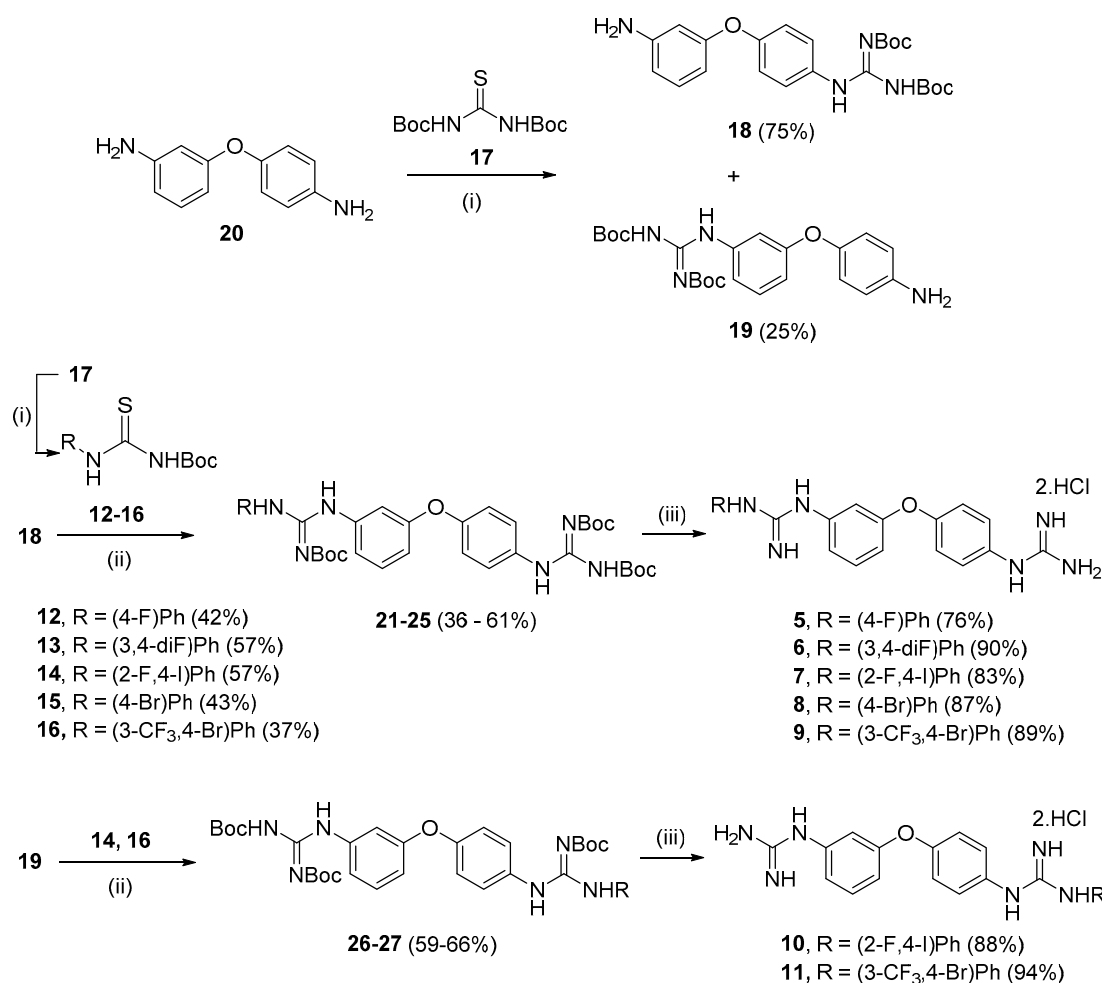
## 2.2. Synthesis

The synthesis of the analogues of compound 1, 3,4'-bis-guanidino diphenyl ethers 5–11, required the preparation of the corresponding *N*-aryl-*N'*-Boc-protected thioureas (12–16) following a procedure previously developed in the group starting from *N,N'*-bis-(*tert*-butoxycarbonyl)thiourea 17 (Scheme ??) [? ]. Given the diverse electron-withdrawing effect of differently substituted commercially available anilines, different yields of the corresponding thioureas 12–16 were obtained (37–57%, see details in ESI). The corresponding Boc-protected mono-guanidines 18 and 19 were prepared by reaction of commercially available 3,4'-dianiline ether 20 and *N,N'*-bis-(*tert*-butoxycarbonyl)thiourea 17 in the presence of  $\text{HgCl}_2$  and  $\text{NEt}_3$  yielding 18 and 19 as a mixture that was separated by column chromatography in good and moderate yields (Scheme ??) [? ].

Next, the *N*-aryl-*N'*-Boc-protected thioureas 12–16 were reacted with 18 or 19 under our standard conditions ( $\text{HgCl}_2$  and  $\text{NEt}_3$ ) to yield the corresponding Boc-protected 3-arylguanidino-4'-guanidino (21–25) and 3-guanidino-4'-arylguanidino (26–27) diphenyl ether derivatives (Scheme ??).

In order to prepare compound 3 and its analogues 28–30, the nitrophenyl precursor 31 was synthesised by a  $\text{S}_{\text{N}}\text{Ar}$  reaction between commercially available 3-aminophenol and 1-fluoro-4-nitrobenzene [? ]. Compounds 32–35 were synthesized using a Buchwald–Hartwig cross-coupling;

the success of this reaction depends on variables such as ligand, Pd source, base and solvent [? ]. The conditions chosen ( $\text{Pd}_2(\text{dba})_3$  3 mol%, BINAP 3 mol%, NaOtBu 1.4 eq. in dry toluene ( $2 \text{ mL mmol}^{-1}$ ) at  $90^\circ\text{C}$ ) afforded the proposed compounds **32–35** in high yields (62–87%, Scheme ??).



**Conditions:** (i)  $\text{HgCl}_2$ ,  $\text{NEt}_3$ ,  $\text{CH}_2\text{Cl}_2$   $0^\circ\text{C}$  to rt; (ii) NaH, TFAA, THF,  $0^\circ\text{C}$  to rt; (iii) 0.2M HCl/dioxane,  $55^\circ\text{C}$ , 8 h.

**Scheme 1.** Preparation of mono-substituted 3,4'-bis-guanidinium diphenyl ether derivatives.

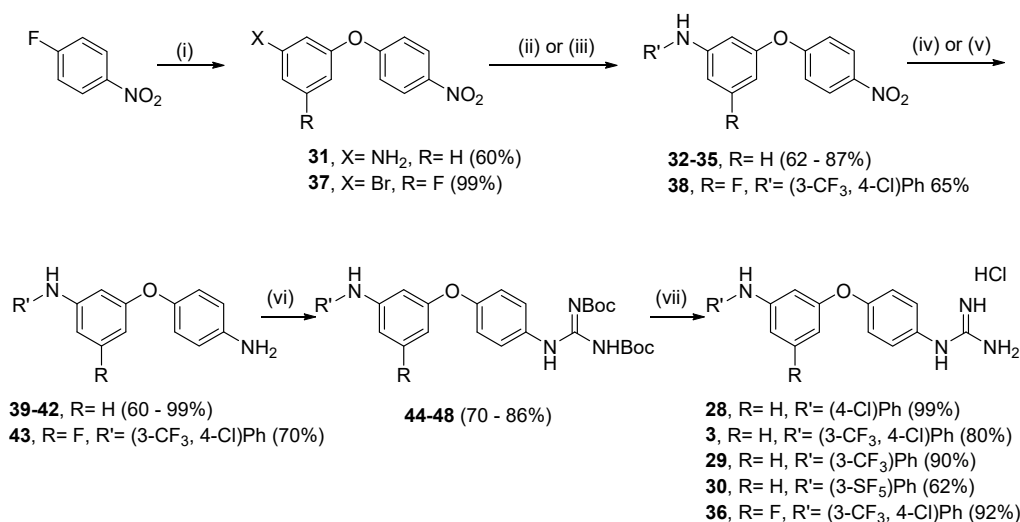
With the intention of probing the effect of branching in the diphenyl ether core, we prepared the fluoro derivative **36** for which we synthesised precursor **37** by using commercially available 3-bromo-5-fluorophenol that in the presence of  $\text{K}_2\text{CO}_3$  and DMF quantitatively reacted with 4-fluoronitrobenzene. Then, **37** was used for the Buchwald–Hartwig coupling with 4-chloro-3-(trifluoromethyl)aniline to afford compound **38** in good yield (Scheme ??).

Precursors **32–35** and **38** were then subjected to selective reduction of the nitro group to the amine that will serve as handle for the introduction of the guanidine moiety. Nitro reduction of compounds **34** and **35** was achieved using catalytic hydrogenation ( $\text{H}_2$ , Pd/C 10 mol%) yielding aniline derivatives **41** and **42**; however, in the case of chloro-derivatives **32**, **33**, and **38**, selective reduction was achieved with the use of tin(II) chloride dihydrate ( $\text{SnCl}_2 \cdot 2\text{H}_2\text{O}$ ) to produce anilines **39**, **40**, and **43** [? ]. Utilising our standard conditions, a guanidine moiety was introduced affording Boc-protected mono-guanidines **44–48** (Scheme ??).

In order to prepare the 3,4'-bis-guanidino phenyloxypyridines **2**, **4**, and **49–52**, the starting 5-(3-aminophenoxy)pyridin-2-amine (**53**) was synthesized. Thus,  $\text{S}_{\text{N}}\text{Ar}$  between 5-bromo-2-nitropyridine and 3-nitrophenol yielded the previously reported mixture of isomers (**54** and **55**) [? ], which were

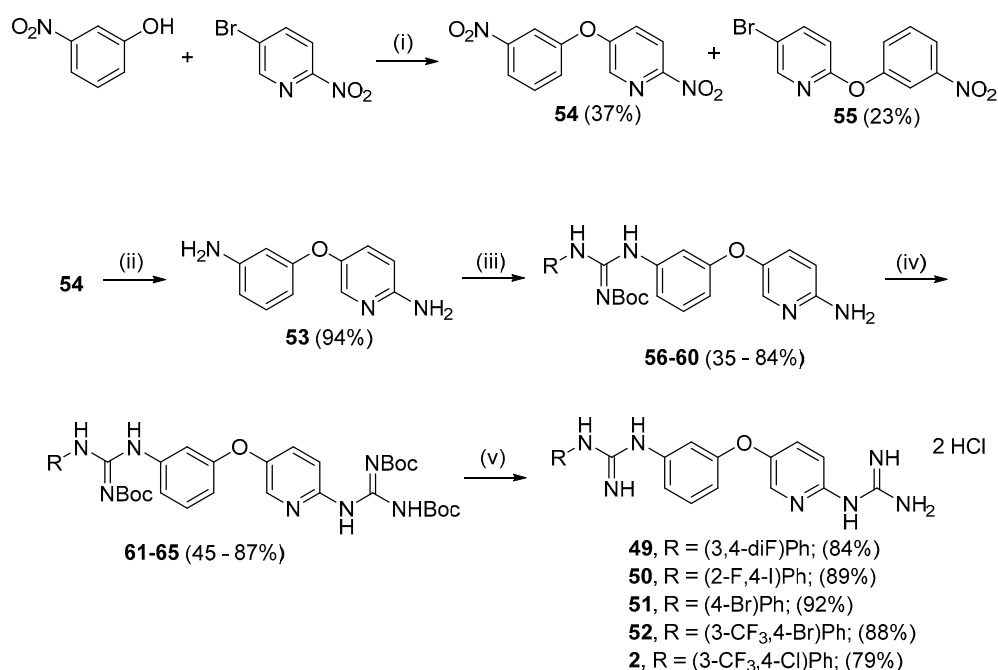


separated by chromatography. Further hydrogenation of **54** gave the desired product **53** in good yield (Scheme ??) [? ?].



**Conditions:** (i) 3-Aminophenol or, for **37**, 3-bromo-5-fluorophenol, K<sub>2</sub>CO<sub>3</sub>, DMF, 80 °C, 12 h; (ii) R-Br, Pd<sub>2</sub>(dba)<sub>3</sub>, BINAP, NaO<sup>t</sup>Bu, toluene, 90 °C, 24 h; (iii) for **38**, 4-chloro-3-(trifluoromethyl)aniline, Pd<sub>2</sub>(dba)<sub>3</sub>, BINAP, NaO<sup>t</sup>Bu, toluene, 90 °C 24 h; (iv) H<sub>2</sub>, Pd/C, EtOH, rt, 24 h; (v) SnCl<sub>2</sub>·2H<sub>2</sub>O, EtOAc, 70 °C, 3 h; (vi) *N,N'*-bis-(*tert*-butoxycarbonyl)-*S*-methylisothiourea, HgCl<sub>2</sub>, NEt<sub>3</sub>, CH<sub>2</sub>Cl<sub>2</sub>, 0 °C to rt; (vii) 0.2M HCl/dioxane, 55 °C, 8 h.

**Scheme 2.** Preparation of 3-amino,4'-guanidine diphenyl ether derivatives.

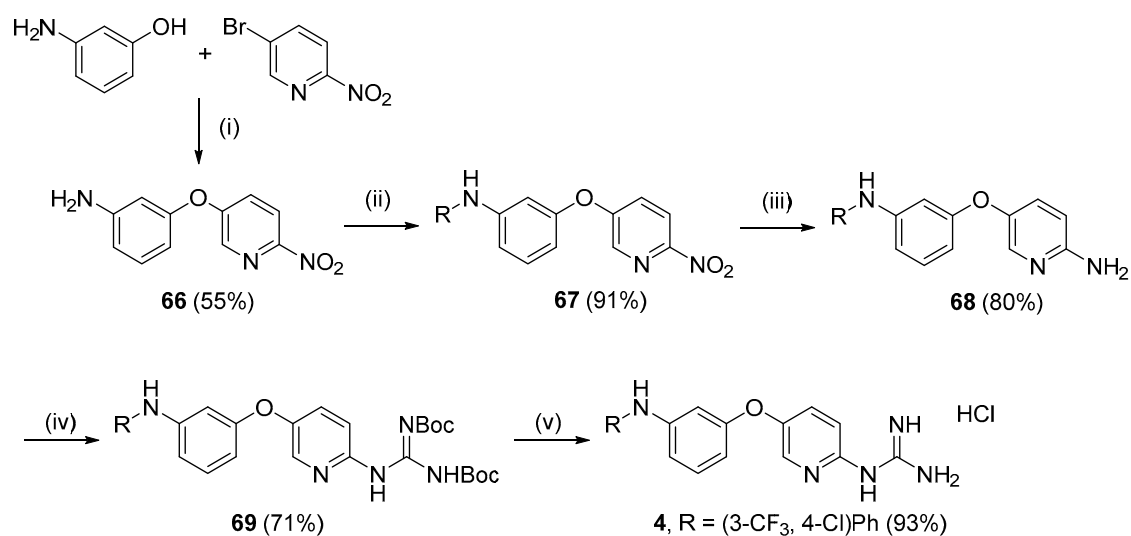


**Conditions:** (i) Cs<sub>2</sub>CO<sub>3</sub>, DMF, 80 °C, 12 h; (ii) H<sub>2</sub>, Pd/C, EtOH/THF/EtOAc, rt, 24 h; (iii) Boc-protected thioureas 12-16, HgCl<sub>2</sub>, NEt<sub>3</sub>, CH<sub>2</sub>Cl<sub>2</sub> 0 °C to rt, 12h; (iv) Boc-protected S-methylisothiourea, HgCl<sub>2</sub>, NEt<sub>3</sub>, CH<sub>2</sub>Cl<sub>2</sub> 0 °C to rt, 12h; (v) 0.2M HCl/dioxane, 55 °C, 8 h.

**Scheme 3.** Preparation of 3,4'-bis-guanidine perylpyridyl ether derivatives.

Compound **53** was then reacted with Boc-protected thioureas **12–16**, under our standard conditions to yield Boc-protected mono-guanidines **56–60** [?]. Subsequent guanidylation at position 2 of the pyridine ring was carried out with commercial *N,N'*-bis-(*tert*-butoxycarbonyl)-*S*-methylisothiurea to obtain Boc-protected compounds **61–65** (Scheme ??).

Preparation of the corresponding precursors for compound **4** required the synthesis of 3-((6-nitropyridin-3-yl)oxy)aniline **66** through a  $S_NAr$  between 5-bromo-2-nitropyridine and 3-aminophenol (Scheme ??).



Conditions: (i)  $\text{Cs}_2\text{CO}_3$ , DMF, 80 °C, 12 h; (ii) R-Br,  $\text{Pd}_2(\text{dba})_3$ , Xantphos,  $\text{Cs}_2\text{CO}_3$ , toluene, 90 °C 24 h; (iii)  $\text{SnCl}_2 \cdot 2\text{H}_2\text{O}$ , EtOAc, 70 °C, 3 h; (iv) Boc-protected *S*-isomethylthiourea,  $\text{HgCl}_2$ ,  $\text{NEt}_3$ ,  $\text{CH}_2\text{Cl}_2$ , 0 °C to rt; (v) 0.2M HCl/dioxane, 55 °C, 8 h.

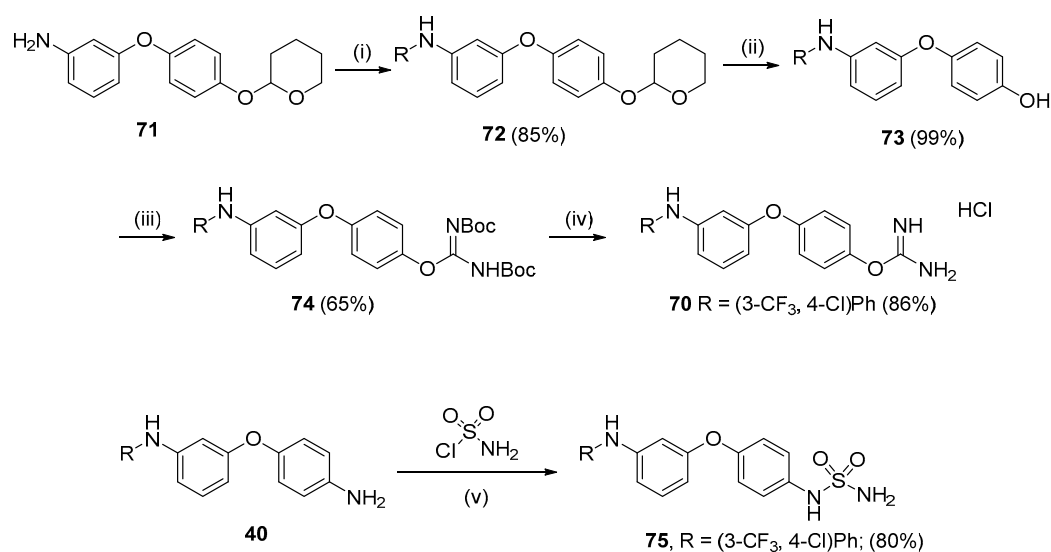
**Scheme 4.** Preparation of 3-amino-4'-guanidine phenylpyridyl ether derivatives.

Preparation of the arylanilino nitropyridine **67** was next attempted following the previous conditions described for the synthesis of **32–35** and **38** with poor results. However, Pd-catalysed reaction using of Xantphos and  $\text{Cs}_2\text{CO}_3$  yielded compound **67** in good yield. Next,  $\text{SnCl}_2 \cdot 2\text{H}_2\text{O}$  reduction conditions afforded compound **68** that was then subjected to guanidylation using *N,N'*-bis-(*tert*-butoxycarbonyl)-*S*-methylisothiurea to obtain Boc-protected compound **69** (Scheme ??).

With the aim of introducing diversity to the “polar” moiety of compound **3**, we also explored the substitution of the guanidinium system by an isouronium cation or a sulfamide (Scheme ??). Thus, preparation of the 3-anilino-4'-*O*-isourea phenylpyridyl ether derivative **70** involved the use of the previously synthesised compound **71** [?] as starting material for the synthesis of the intermediate **72** through the mentioned conditions for a Buchwald–Hartwig coupling ( $\text{Pd}_2(\text{dba})_3$ , Xantphos,  $\text{Cs}_2\text{CO}_3$ , toluene, 90 °C, 24 h).

Compound **72** was then deprotected with montmorillonite KSF to obtain the corresponding phenol **73**, which OH was then amidylated using standard conditions previously described by us [?] to yield the corresponding Boc-protected isouronium **74** (Scheme ??). Sulfamide **75** was synthesised by treating amine **40** with sulfamoyl chloride (previously prepared from chlorosulfonyl isocyanate and formic acid [? ?]) to afford compound **75** in good yield (Scheme ??).

All Boc-protected precursors were deprotected using HCl 4M/dioxane to yield compounds **2–11**, **28–30**, **36**, **49–52** (???????) and  $\text{SnCl}_4$  to obtain compound **70**. The purity of all the final hydrochloride salts was determined by HPLC, where a minimum purity of 95% was required before proceeding to biological testing (ESI).



Conditions: (i) R-Br, Pd2(dba)<sub>3</sub>, Xantphos, Cs<sub>2</sub>CO<sub>3</sub>, toluene, 90 °C, 24 h; (ii) KSF, MeOH, 50 °C; 4 h; (iii) Boc-protected S-methylisothiourea, HgCl<sub>2</sub>, NEt<sub>3</sub>, CH<sub>2</sub>Cl<sub>2</sub>, 0 °C to rt; (iv) SnCl<sub>4</sub>, H<sub>2</sub>O, EtOAc, rt, 1 h; (v) NEt<sub>3</sub>, CH<sub>2</sub>Cl<sub>2</sub>, rt, 2 h.

**Scheme 5.** Preparation of 3-amino-4'-isourea and 3-amino-4'-sulfamido diphenyl ether derivatives.

### 2.3. Predicted Physicochemical and In Vitro ADME Properties

Attention to physicochemical and pharmacokinetic properties of active molecules should be given at the early stages of their design in order to shorten their development to a drug. However, these properties are not always easy to be experimentally evaluated and, hence, computational approaches represent a good solution to get a general idea of the potential of compounds as drugs. Thus, to assess the drug-likeness of the compounds studied, we utilized SwissADME [?] and ChemAxon's Marvin [?] to computationally evaluate the mentioned properties and the calculated values are reported in Tables S1–S3 (ESI). All proposed compounds have a molecular weight (MW) <500 Da, except for 3,4'-bis-guanidine phenyloxybenzenes **7**, **9**, **10** and **11** or phenyloxy pyridines **50** and **52**, in which the MW exceeds by 7–10 units this threshold; such small exceptions are considered acceptable [?]. The consensus logP<sub>o/w</sub> [?] for all synthesised compounds is reported in Table S2 (ESI) indicating that, overall, all the compounds have a logP < 5. Topological Polar Surface Area (TPSA), which is an indicator of HB formation and a commonly used metric for a drug's ability to permeate cells, was calculated for all the synthesised molecules and all of them have values <140 Å<sup>2</sup>, which is the limit suggested in the literature for poor cell membrane permeation [? ? ?]. Specifically, shorter 3-amino-4'-guanidines have much lower TPSA (80–100 Å<sup>2</sup>) than 3,4'-bis-guanidinium analogues (120–135 Å<sup>2</sup>).

The BOILED egg graph presents a correlation between calculated logP and calculated TPSA and is an intuitive simultaneous prediction of two key ADME parameters, i.e., the passive gastrointestinal (GI) absorption and brain access (blood brain barrier, BBB) [? ?]. Compounds that fall into the white part of the graph are likely to undergo GI absorption and those that fall into the yellow part of the graph are likely to be brain permeant. Accordingly, all of our derivatives could undertake passive GI absorption (except pentafluorosulfanyl derivative **30** and sulfamide **75**), but none of them can cross the BBB (Figure S6). In addition, SwissADME enables the estimation for a chemical to be a substrate of the permeability glycoprotein (P-gp), which is the most important ATP-binding cassette transporter responsible for an active efflux through biological membranes, e.g., from the GI wall to the lumen or exiting the brain [? ?]. Thus, as reported in the legend of Figure S6, red dots indicate that all of our compounds, except compounds **49–51** (blue dots), are non-substrates of P-gp (Table S3).

The theoretical  $pK_{aH}$  values of all the synthesised compounds calculated with Marvin are reported in Table S1. The results indicate that exchanging the *para* mono-substituted guanidinium (compound **3**) by an isouronium moiety (compound **70**) results in a  $pK_{aH}$  decrease (less basic molecule). Interestingly, the pyridine derivatives (**49–52**, **2** and **4**) show lower  $pK_{aH}$  values than their diphenyl counterparts (**6–9**, **1** and **3**, respectively), probably due to the IMHB formed between the *para* guanidinium and the pyridine ring.

Solubility is not an easy parameter to model *in silico*, but SwissADME gives an estimation of the solubility class based on three predictors, two topological and one fragmental method [? ]. According to this program, all our molecules are poorly soluble in aqueous environments (Table S2). For the preclinical evaluation of our molecules, their solubility in EtOH/DMSO is still acceptable, but future work will have to be carried out to achieve full water solubility.

Other numerical descriptors are used to assess drug-likeness including the number of HB acceptors and donors (HBAs and HBDs) or the number of rotatable bonds (RotB) and the results obtained for this set of compounds are shown in Table S1 [? ]. According to these descriptors, in general, all studied compounds fulfil drug-like conditions.

## 2.4. Biochemical Studies

### 2.4.1. Cell Viability in Cancerous and Non-Cancerous Cell Lines

Cell viability and proliferation assays were used to evaluate the *in vitro* cytotoxicity of all synthesised compounds in a variety of different cancer cell lines using the alamarBlue® viability assay and the results are presented in ????. The sensitivity of cancer cells to drugs can often be compromised by PIK3CA, Ras and BRAF mutations. To determine whether such mutations are critical to the efficacy of our new compounds we tested them in a range of cancerous cell lines expressing different mutations. Firstly, we used the HL-60 (human promyelocytic leukaemia, NRas mutated) cell line for general cytotoxicity screening of all compounds. Next, the most active derivatives were studied in MCF-7 (breast adenocarcinoma, Ras/RAF wild type, and PIK3CA mutant), HeLa (cervical carcinoma, Ras/RAF and PIK3CA wild type), as well as HCT-116 and HKH-2 (colorectal carcinoma, KRas mutant and mutated KRas disrupted, respectively) cell lines [? ]. Lastly, toxicity against MCF-10A, which is a non-tumorigenic epithelial cell line, was also assessed for one of the most promising compounds (**4**). The graphs representing the viability results with the HL-60, MCF-7, HeLa, HCT-116, and HKH-2 cancer cell lines for compound **1** and derivatives **2**, **3**, and **4** are shown in Figures S7–S10 (ESI). Sorafenib (a known inhibitor of protein kinases including VEGFR, PDGFR and RAF [? ? ]) was used as a positive control in all viability assays.

**Table 1.** Effect on the viability of HL-60 cells ( $IC_{50}$ ,  $\mu M$ ) of compounds **1–11**, **28–30**, **36**, **49–52**, **70**, **75** and sorafenib with alamarBlue® assays.

Compounds.	HL-60 $IC_{50} \pm SEM$	Compounds.	HL-60 $IC_{50} \pm SEM$	Compounds.	HL-60 $IC_{50} \pm SEM$
<b>Sorafenib</b>	2.53 $\pm$ 0.68	<b>8</b>	15.26 $\pm$ 1.98	<b>49</b>	11.61 $\pm$ 0.27
<b>1<sup>7</sup></b>	9.72 $\pm$ 0.9	<b>9</b>	2.07 $\pm$ 0.33	<b>50</b>	8.33 $\pm$ 0.32
<b>2</b>	2.36 $\pm$ 0.14	<b>10</b>	8.85 $\pm$ 0.55	<b>51</b>	9.37 $\pm$ 0.54
<b>3</b>	3.08 $\pm$ 0.15	<b>11</b>	10.99 $\pm$ 0.64	<b>52</b>	1.53 $\pm$ 0.23
<b>4</b>	3.48 $\pm$ 0.28	<b>28</b>	7.50 $\pm$ 0.05	<b>70</b>	4.22 $\pm$ 0.04
<b>5</b>	>100	<b>29</b>	4.64 $\pm$ 0.83	<b>75</b>	9.14 $\pm$ 0.69
<b>6</b>	>100	<b>30</b>	3.23 $\pm$ 0.36		
<b>7</b>	8.63 $\pm$ 0.51	<b>36</b>	4.07 $\pm$ 0.10		

(a) Cells were seeded at a density of  $2 \times 10^5$  cells/mL (HL-60) in a 96-well plate and treated with different concentrations of the compounds dissolved in EtOH or DMSO (1% *v/v* and 0.1% *v/v*, respectively). Sorafenib was used as a reference and tested in the same manner. Once treated, cells were incubated for 72 h at 37 °C after which they were treated with alamarBlue® and left in darkness in an incubator for 5 h. The resulting fluorescence ( $\lambda_{excitation} = 544$  nm,  $\lambda_{emission} = 590$  nm) was read using a plate reader from which percentage viability was calculated.  $IC_{50}$  values were calculated using Prism GraphPad Prism software from at least three independent experiments performed in triplicate. Highlighted in grey are those  $IC_{50}$  values better than or similar to the control used, Sorafenib.

**Table 2.** Effect in viability of MCF-7, HeLa, HCT116, and HKH-2 cancer cells (IC<sub>50</sub>, μM) of compounds 1–4, 70 and sorafenib on the alamarBlue® assays.

Comps.	MCF-7	HeLa	HCT116	HKH-2
	IC <sub>50</sub> ± SEM	IC <sub>50</sub> ± SEM	IC <sub>50</sub> ± SEM	IC <sub>50</sub> ± SEM
Sorafenib	3.07 ± 0.10	4.59 ± 0.45	6.79 ± 0.18	4.43 ± 0.39
1	9.30 ± 1.87	9.48 ± 0.16	9.96 ± 0.60	19.18 ± 0.84
2	4.91 ± 1.04	4.87 ± 0.27	7.29 ± 0.53	8.09 ± 0.78
3	2.02 ± 0.27	4.33 ± 0.54	15.88 ± 2.73	10.34 ± 0.74
4	3.73 ± 0.35	1.33 ± 0.08	4.59 ± 0.40	2.88 ± 0.15
70	7.32 ± 0.35			

(a) Cells were seeded at a density of  $25 \times 10^3$  cells/mL (MCF-7 and HeLa) or  $1 \times 10^5$  cells/mL (HCT-116 and HKH-2) in a 96-well plate and treated with different concentrations of the compounds dissolved in EtOH or DMSO (1% *v/v* and 0.1% *v/v*, respectively). Sorafenib was used as a reference and tested in the same manner. Once treated, cells were incubated for 72 h at 37 °C after which they were treated with alamarBlue® and left in darkness in an incubator for 5 h. The resulting fluorescence ( $\lambda_{\text{excitation}} = 544$  nm,  $\lambda_{\text{emission}} = 590$  nm) was read using a plate reader from which percentage viability was calculated. IC<sub>50</sub> values were calculated using Prism GraphPad Prism software from at least three independent experiments performed in triplicate. Highlighted in grey are those IC<sub>50</sub> values better than or similar to the control used, Sorafenib, in each particular cell line.

The results obtained with the HL-60 cell line (Table ??) for the 3,4'-bis-guanidine derivatives 5–11 show, in general, more cytotoxicity than the previously tested compound 1 [? ]. However, compounds 5 and 6, which carry 3-F and 3,4-diF phenyl groups, respectively, give IC<sub>50</sub> values above 100 μM; this drop in activity is a clear indication of the importance of the size and nature of the substituents on the phenyl ring [? ]. The presence of 2-F and 4-I substituents in the hydrophobic moiety of derivative 7 resulted in an IC<sub>50</sub> value (8.63 μM) similar to 1. Substitution of the 4-Cl in compound 1 by a 4-Br (i.e., compound 9), gave a four-fold increase in activity, indicating that the halogen in this hydrophobic moiety could establish a halogen-bond with a Lewis base in the protein binding site. Additionally, compound 8 had decreased activity because of the absence of the 3-CF<sub>3</sub> substituent; this is an indication that such a big and polarized halogen atom can only result in a beneficial increment in activity when a bulky lipophilic substituent as CF<sub>3</sub> is present at position 3.

Cytotoxicity results of compounds 10 and 11 (lipophilic moiety in 4'-position of the phenyloxyphenyl core instead of the 3-position) with HL-60 cells show that compound 10 maintains a similar IC<sub>50</sub> value as 7; however, 11 has a reduction of activity compared to 9.

Compound 3, which is a shorter version of 1 (-NH- link instead of a di-substituted guanidinium) shows increased cytotoxicity in HL-60 cells (IC<sub>50</sub> = 3.08 μM). Similar to what was observed for the 3,4'-bis-guanidine derivatives, removal of the 3-CF<sub>3</sub> group in the lipophilic section caused decreased activity in the shorter analogue 28 (7.50 μM). Interestingly, removal of the 4-halogen in this lipophilic section did not affect the IC<sub>50</sub> value of compounds 29 and 30 compared to their analogue 3. This could be explained by the compensation of bulky and lipophilic effects when going from trifluoromethyl (-CF<sub>3</sub>) to bulkier pentafluorosulfanyl (-SF<sub>5</sub>) substitution.

The 3,4'-bis-guanidines phenyloxy pyridines 49–52, 2 and 4 show, overall, increased HL-60 cytotoxicity than the previously discussed derivatives. Compound 2, the pyridine analogue of 1, has an IC<sub>50</sub> value of 2.36 μM, a four-fold increased activity compared to 1. Likewise, compound 52 with a 3-CF<sub>3</sub>-4-Br phenyl system, shows a low IC<sub>50</sub> of 1.53 μM. Surprisingly, the introduction of a pyridinoguanidinium system as in compound 49 (11.61 μM) instead of a phenylguanidinium moiety as in 3 (>100 μM) results in increased HL-60 cytotoxicity. Even though this is not the most active compound of the series, it is a clear indication of the importance of the pyridinoguanidinium system in improving cytotoxicity in HL-60 cells.

Interestingly, compound 4, which includes both a shorter -NH- link and the pyridinoguanidinium moiety has a relatively low IC<sub>50</sub> value of 3.48 μM. Compound 70, with a -NH- link and an isouronium instead of the para guanidinium, shows similar cell viability as the guanidinium analogue 3. From these results we can deduce that the isouronium cation has a similar behaviour to the guanidinium cation, as we had previously observed in the 3,4'-bis-guanidinium series [? ]. Finally, compound 75, where the

*para* guanidinium is replaced by a sulfamide, shows a decreased cytotoxicity in HL-60 cells to 9.14  $\mu\text{M}$ , indicating the importance of the guanidinium or isouronium cations.

The  $\text{IC}_{50}$  values obtained for selected compounds in the MCF-7 cell line (Table ??, Figure S8) were similar to the results obtained for the HL-60 cell line with most values in the low  $\mu\text{M}$  range. Compounds **3** and **4** ( $\text{IC}_{50}$  = 2.02 and 3.73  $\mu\text{M}$ , respectively) are still the most cytotoxic agents compared to compound **1** ( $\text{IC}_{50}$  of 9.30  $\mu\text{M}$ ). The pyridine ring present in compounds **4** and **2** still appears responsible for the improved activity, even though less accentuated than in the HL-60 cell line. Instead, the isouronium version of compound **3**, compound **70**, has an increased  $\text{IC}_{50}$  in MCF-7 cells compared with HL-60 cells indicating a certain degree of cell selectivity.

We have also evaluated the effect of compounds **2**, **3**, **4**, and **1** on the viability of the HeLa cell line and the results are reported in Table ?? (Figure S9). In this cell line, compound **4** showed again the lowest  $\text{IC}_{50}$  value (1.33  $\mu\text{M}$ ). The rest of the compounds maintained similar cytotoxic activity in HeLa cells compared to HL-60 and MCF-7 cells.

It is known that sorafenib was originally developed as an inhibitor of the Ras effector RAF, and there are studies showing that sorafenib enhances the therapeutic efficacy of rapamycin in certain colorectal cancers [? ]. The  $\text{IC}_{50}$  results in Table ?? (Figure S10) show that compound **1** has more potency in the HCT116 *KRAS* mutated cancer cell line (9.96  $\mu\text{M}$ ) than in the HKH-2 *KRAS* wt isogenic form (19.18  $\mu\text{M}$ ). Remarkably, its cytotoxic effect is like that of sorafenib in HCT116 (6.79  $\mu\text{M}$ ), but not in HKH-2, where sorafenib has a much lower  $\text{IC}_{50}$ . Similar activity in both cell lines is reached with compound **2**, while **4** is revealed to be the most active of the series with an  $\text{IC}_{50}$  of 4.59  $\mu\text{M}$  in HCT116 and 2.88  $\mu\text{M}$  in HKH-2. Interestingly, compound **3**, which has a phenyl group instead of the 2-pyridinyl of compounds **2** and **4**, shows poor cytotoxic activity in both cell lines.

Searching for a relationship between physicochemical properties and cytotoxicity, we observed a trend between the calculated logP and the HL-60  $\text{IC}_{50}$  values obtained for all synthesised compounds (except the inactive **5** and **6**,  $\text{IC}_{50}$  > 100  $\mu\text{M}$ ) (Figure S11). This supports our hypothesis that the hydrophobic moiety of our molecules interacts with a specific allosteric hydrophobic pocket in protein kinases, justifying the use of bulkier and more lipophilic substituents (larger logP) in order to obtain improved anti-cancer activity (lower  $\text{IC}_{50}$  values).

Therefore, some structure–activity relationships (SARs) can be drawn from the cell viability assays (Figure ??): (i) the hydrophobic moiety is necessary for the activity; particularly, bulky and lipophilic substituents improve the cytotoxicity of these compounds (I- or Br- substitution at the 4-position better than Cl-), and a substituent at the 3-position is required to maintain efficacy ( $\text{CF}_3$  or  $\text{SF}_5$ ); (ii) replacement of the di-substituted guanidinium in compound **1** (position 3 of the phenyloxyaryl core) by a shorter -NH- link results in compounds with better cytotoxicity; (iii) a mono-substituted guanidinium group as in compound **1** (position 4' of the phenyloxyaryl core) gives the greatest cytotoxic activity; additionally, incorporating a 2-pyridinyl instead of a phenyl group, attached to this guanidinium facilitates forming an IMHB that seems to affect positively the cytotoxic activity.

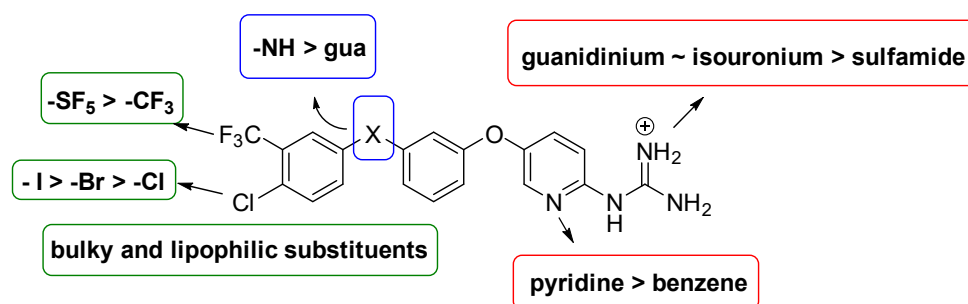


**Figure 4.** Structure Activity Relationship (SAR) deduced from the analysis of the HL-60 cytotoxicity results.

Considering the promising cytotoxicity results obtained with the cancer cell lines, we also evaluated the potential toxicity of the most efficient derivative (compound **4**) in the non-cancerous cell

line MCF10A (human mammary epithelial cell line). We observed that this compound **4** only shows toxicity towards MCF10A at a high concentration of 100  $\mu\text{M}$  while at lower concentrations of 10 and 1  $\mu\text{M}$  the compound does not appear to affect in any way cell viability (Figure S12).

#### 2.4.2. Apoptosis Assay in HL-60

We have previously reported that compound **1** induces  $68.9 \pm 0.1\%$  apoptosis in HL-60 cells at a 10  $\mu\text{M}$  concentration after 48 h [? ]. Accordingly, in order to evaluate the apoptotic effect of the most relevant derivatives (**2**, **3**, and **4**), HL-60 cells were treated with these compounds (at 5  $\mu\text{M}$ , 5  $\mu\text{M}$ , and 4  $\mu\text{M}$  concentration, respectively) for 48 h, stained with annexin V-FITC/PI and analysed using flow cytometry (Figure ??).

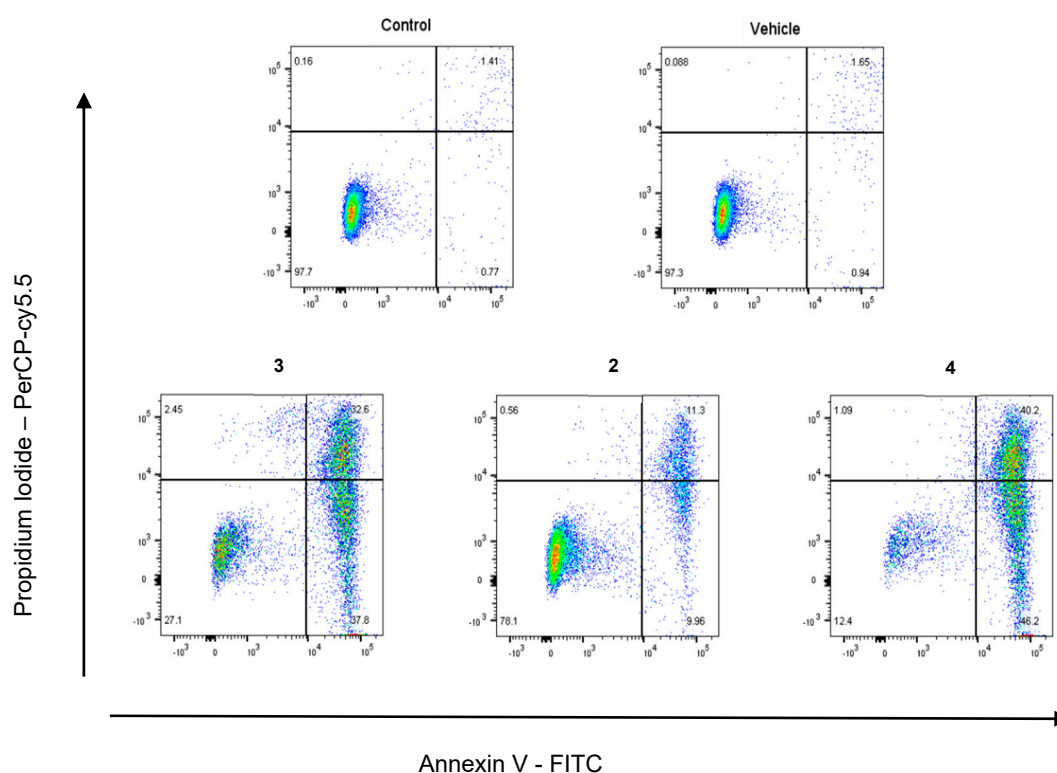


**Figure 5.** Annexin V-FITC vs. PI flow cytometry analysis of HL-60 cancer cells treated with compounds **3** (5  $\mu\text{M}$ ), **2** (5  $\mu\text{M}$ ) and **4** (4  $\mu\text{M}$ ) for 48 h. These figures are representative of three independent experiments. The viable cells, early apoptotic, necrotic and late apoptotic cells are represented by the lower left, lower right, upper left and upper right quadrants, respectively.

The results presented in Figure ?? and Figure S13 show that, under these conditions, a more potent induction of apoptosis was observed with **3** ( $82.5 \pm 11.3\%$ ) and **4** ( $92.7 \pm 5.5\%$ ) compared to compound **2** ( $30.7 \pm 11.6\%$ ). As the alamarBlue assay indirectly assesses cytotoxicity by quantifying cell viability and proliferation, these data suggest that compound **2** may have a predominantly cytostatic mechanism of action.

#### 2.4.3. Effect on the MAPK/ERK Pathway

Taking into account the positive binding results obtained in the docking studies to the BRAF-ATP model and the promising cytotoxicity shown in several cancer cells, we next explored the effect of compounds with  $\text{IC}_{50}$  near to that of sorafenib (**1**, **2**, **3**, **4**, **9**, and **52**) on the MAPK/ERK pathway. Thus, using Western immunoblot analysis of HL-60 extracts, we investigated the expression and phosphorylation levels of ERK (as an indication of ERK activation), which is the downstream effector of the Ras/BRAF signalling pathway (Figure ??).

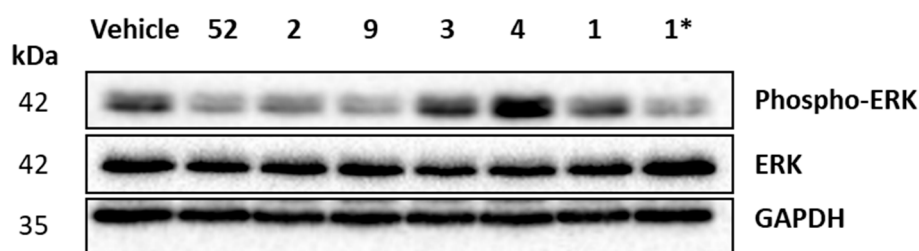


**Figure 6.** Western immunoblot of HL-60 cell extracts following incubation with compounds **2**, **3**, **4**, **9**, **52** and **1** (as a control). HL60 cells were seeded at  $2 \times 10^5$  cells/mL and were treated with either vehicle [0.5% EtOH (*v/v*)], compounds **52**, **2**, **9**, **3** and **4** (5  $\mu$ M) or compound **1** (5 and (\*) 10  $\mu$ M, as in reference [? ]) for 16 h. Cells were lysed and equal amounts of protein were loaded and separated on 15% SDS-PAGE gels, transferred to PVDF membrane and probed with antibodies against total and phosphorylated ERK. Anti-GAPDH was used as a loading control. Results are representative of 2 independent experiments.

We observed that compounds **3** and **4** do not appear to interfere with the Ras/BRAF signalling pathway; however, compounds **2**, **9**, and **52** have a similar effect as lead compound **1** (both at 5 and 10  $\mu$ M) in inhibiting ERK phosphorylation and therefore inhibiting the Ras/BRAF pathway. These results may suggest that the potent cytotoxicity observed with these derivatives may be due to different mechanisms of action. Therefore, compounds **2**, **9**, and **52**, which are all 3,4'-bis-guanidino phenyloxy(phenyl or pyridyl) analogues of **1** with similar lipophilic moieties (3-CF<sub>3</sub>,4-(Br/Cl)-Ph), may exert their cytotoxicity by interfering with the Ras/BRAF pathway. On the contrary, compounds **3** and **4** (shorter 3-amino-4'-guanidino phenyloxy(phenyl or pyridyl) derivatives) may act in a different signalling pathway or in the same pathway but through a different mechanism from compound **1** [? ]. Pulikakos and co-workers have reported that the biochemical effect of a RAF inhibitor on ERK signalling would be the combined outcome of different mechanisms [? ], clearly indicating the complexity of the biological target and opening the door to future studies to understand the mechanism of action of these compounds.

### 3. Discussion

Considering the promising results previously obtained for lead compound **1** we explored several modifications to improve its cytotoxicity in different cancer cell lines. Accordingly, we designed a variety of compounds where different changes have been introduced: several lipophilic groups were considered; the di-substituted guanidine was replaced by a secondary amine; the phenyl ring was exchanged with a pyridine; and the mono-substituted guanidine in the polar side was switched to an isourea or a sulfanylamide group.

Molecular docking was utilised to understand the interactions between the proposed biological target and model compounds **1–4**. Thus, considering the putative activity of **1** as a type-III kinase inhibitor, compounds **1–4** were docked into an in-house model of an active TP-containing BRAF kinase. All final poses exhibit similar interactions between the lipophilic moiety and the lipophilic pocket, as well as between the mono-substituted guanidinium and one of the phosphate groups of TP.

Based on this computational study, 3,4'-bis-guanidino diphenyl ether derivatives **5–11** were prepared by reacting the corresponding 3,4'-diamino diphenyl ether with conveniently substituted Boc-protected thioureas. Additionally, synthesis of the 3-amino-4'-guanidino diphenyl ethers **3**, **28–30** and **36** required the preparation of the corresponding starting diamines. Furthermore, preparation of 3,4'-bis-guanidino and 3-amino-4'-guanidino phenylpyridyl ether derivatives **2**, **49–52**, and **4**, required different synthetic approaches involving Buchwald–Hartwig coupling. Finally, the 3-amino-4'-isouronium **70** and 3-amino-4'-sulfonamido **75** derivatives were prepared following specific synthetic routes. All compounds were obtained as hydrochloride salts and their purity was determined to be >95% by HPLC before proceeding to biological testing.



A screening of the cytotoxicity of all compounds was performed in the HL-60 cell line and the more potent compounds were selected for further biological evaluation in MCF-7, HeLa, HCT116, and HKH-2 cell lines. These cell viability studies revealed that these compounds can inhibit cell proliferation in the low  $\mu\text{M}$  range, showing up to a nine-fold increase in cytotoxicity compared to lead compound **1**. All modifications explored generated SAR information which helped to understand the structural requirements for a more potent cytotoxicity. Cytotoxicity of compound **4** was also evaluated against non-tumorigenic MCF10A and the results show that, at active concentration in cancer cell lines, compound **4** has no toxic effects to non-tumorigenic cells.

Flow cytometry in HL-60 cell lines was also performed to assess the apoptotic effect of compounds **2**, **3**, and **4**. The results are in agreement with the corresponding structures; thus, mono-guanidinium compounds (**3** and **4**) induce a stronger apoptotic effect in HL-60 cells (82% and 92%, respectively) compared to the bis-guanidinium compounds (**1** and **2**, around 60%<sup>7</sup> and 30%, respectively).

With the aim of determining whether compounds **1–4**, **9**, and **52** exert their anticancer activity by interfering with the Ras/BRAF pathway (as previously suggested by us for lead compound **1**), Western immunoblot analysis was performed with HL-60 cell extracts measuring the activation of the downstream effector ERK. Thus, we observed that compounds **1**, **2**, **9**, and **52** (3,4'-bis-guanidine phenyloxy(phenyl or pyridyl) derivatives) abrogates ERK activation, suggesting potential inhibition of the Ras/BRAF pathway; however, compounds **3** and **4** (shorter derivatives) do not act in the same way.

## 4. Materials and Methods

### 4.1. Computational Details

#### 4.1.1. Ligand Optimization

All ligands were fully optimized at DFT level using the M06-2X functional with the 6-311+G\* basis set as implemented in the Gaussian16 package [?]. Frequency calculations were performed at the same computational level to confirm that the resulting optimized structures were energetic minima. The effect of water solvation was accounted for by using the SCRF-PCM approach implemented in the Gaussian16 package including dispersion, repulsion and cavitation energy terms of the solvent in the optimization.

#### 4.1.2. Docking Experiments

The program AutoDock Vina 4.2 was used to carry out docking studies [?]. The ligands were flexibly docked into the rigid in-house TP-containing BRAF model (see details in ESI). The corresponding docking scores (G-scores) were measured in kcal/mol and are only indicative of the quality of the interaction with the target; they do not provide a quantitative measure of binding. Poses obtained from the docking were visualised with VMD [?].

### 4.2. Chemistry

#### 4.2.1. 1-(4-Fluorophenyl)-2-(3-(4-guanidinophenoxy)phenyl)guanidine dihydrochloride (**5**)

Following Method A (see ESI), **21** (80 mg, 0.12 mmol) was dissolved in 4 M HCl in dioxane (0.54 mL, 2.16 mmol) and in additional dioxane (0.07 mL) until a final concentration of 0.2 M was reached. After 8 h stirring at 55 °C, the reaction was adjudged complete (TLC), solvents were evaporated and the residue was purified by silica gel (CH<sub>3</sub>Cl:MeOH) chromatography to afford the pure hydrochloride salt as a white-yellow solid (35 mg, 76%). Mp: decomp. > 180 °C.  $\delta_{\text{H}}$  (400 MHz, CD<sub>3</sub>OD): 7.00 (dd,  $J = 8.3, 2.4$ , 1H, H-4), 7.04 (t,  $J = 2.1$  Hz, 1H, H-2), 7.13–7.17 (m, 3H, H-8 and H-8' and H-6), 7.19–7.24 (m, 2H, H-13 and H-13'), 7.31 (d,  $J = 8.9$  Hz, 2H, H-9 and H-9'), 7.36–7.39 (m, 2H, H-12 and H-12'), 7.47 (t,  $J = 8.1$  Hz, 1H, H-5).  $\delta_{\text{C}}$  (100 MHz, CD<sub>3</sub>OD): 116.5 (CH Ar, C-2), 117.8 (d,  $J = 23.3$  Hz, 2 CH Ar, C-13 and C-13'), 118.6 (CH Ar, C-4), 121.1 (CH Ar, C-6), 121.5 (2 CH Ar, C-8 and C-8'), 129.95 (d,  $J = 8.8$  Hz, 2 CH Ar, C-12 and C-12'), 128.96 (2 CH Ar, C-9 and C-9'), 131.6 (qC,

132.3 (d,  $J = 3.1$  Hz, qC, C-11), 132.4 (CH Ar, C-5), 138.0 (qC), 156.6 (qC), 157.4 (qC), 158.4 (qC), 159.5 (qC), 163.2 (d,  $J = 246.1$  Hz, qC, C-14).  $\delta_F$  (376 MHz, CD<sub>3</sub>OD):  $-115.93$  (m).  $\nu_{\max}$ (ATR)/cm<sup>-1</sup>: 3110 (NH), 3052 (NH), 2922, 2330, 2134, 1655 (C=N), 1582 (C=N), 1505 (C-N), 1486, 1404, 1212 (C-O), 1066 (C-F), 834, 792, 552. HRMS ( $m/z$  ESI<sup>+</sup>): found: 379.1687 (M<sup>+</sup> + H), C<sub>20</sub>H<sub>20</sub>N<sub>6</sub>O requires: 379.1683. HPLC: 99.7% (*t*R: 22.9 min).

#### 4.2.2. 1-(3:4-Di-fluorophenyl)-2-(3-(4-guanidinophenoxy)phenyl)guanidine dihydrochloride (6)

Following Method A (see ESI), **22** (53 mg, 0.08 mmol) was dissolved in 4 M HCl in dioxane (0.36 mL, 1.37 mmol) and in additional dioxane (0.06 mL) until a final concentration of 0.2 M was reached. After 8 h stirring at 55 °C, the reaction was adjudged complete (TLC), solvents were evaporated and the residue was purified by silica gel chromatography (CHCl<sub>3</sub>:MeOH) to afford the pure hydrochloride salt as a white solid (34 mg, 90%). Mp: 158–160 °C.  $\delta_H$  (400 MHz, CD<sub>3</sub>OD): 7.00 (dd,  $J = 8.3, 2.4$  Hz, 1H, H-4), 7.05 (t,  $J = 2.2$  Hz, 1H, H-2), 7.13–7.20 (m, 4H, H-8 and H-8', H-6 and H-16), 7.32 (d,  $J = 8.9$  Hz, 2H, H-9 and H-9'), 7.34–7.41 (m, 2H, H-12 and H-15), 7.47 (t,  $J = 8.1$  Hz, 1H, H-5).  $\delta_C$  (100 MHz, CD<sub>3</sub>OD): 116.3 (d,  $J = 19.7$  Hz, C-12 or C-15), 116.5 (CH Ar, C-2), 118.6 (CH Ar, C-4), 119.5 (d,  $J = 18.8$  Hz, C-12 or C-15), 121.1 (CH Ar, C-6), 121.5 (2 CH Ar, C-8 and C-8'), 123.4 (dd,  $J = 6.7, 3.7$  Hz, C-16), 129.0 (2 CH Ar, C-9 and C-9'), 131.6 (qC), 132.4 (CH Ar, C-5), 133.0 (dd,  $J = 8.3, 3.6$  Hz, qC, C-11), 137.9 (qC), 150.8 (dd,  $J = 247.8, 12.6$  Hz, qC, C-13 or C-14), 151.8 (dd,  $J = 248.7, 13.7$  Hz, qC, C-13 or C-14), 156.5 (qC), 157.4 (qC), 158.3 (qC), 159.5 (qC).  $\delta_F$  (376 MHz, CD<sub>3</sub>OD):  $-137.23$  (m),  $-141.12$  (m).  $\nu_{\max}$ (ATR)/cm<sup>-1</sup>: 3228 (NH), 3040 (NH), 2923, 2853, 1655 (C=N), 1579 (C=N), 1505, 1485, 1401, 1259, 1211 (C-F), 1149, 972, 825, 771, 694, 649, 609, 587. HRMS ( $m/z$  ESI<sup>+</sup>): found: 397.1598 (M<sup>+</sup> + H), C<sub>20</sub>H<sub>19</sub>N<sub>6</sub>O<sub>2</sub> requires: 397.1588. HPLC: 96.8% (*t*R: 23.2 min).

#### 4.2.3. 1-(2-Fluoro-4-iodophenyl)-2-(3-(4-guanidinophenoxy)phenyl)guanidine dihydrochloride (7)

Following Method A (see ESI), **23** (357 mg, 0.44 mmol) was dissolved in 4 M HCl in dioxane (2 mL, 7.92 mmol) and in additional dioxane (0.2 mL) until a final concentration of 0.2 M was reached. After 8 h stirring at 55 °C, the reaction was adjudged complete (TLC), solvents were evaporated and the residue was purified by silica gel chromatography (CH<sub>3</sub>Cl:MeOH) to afford the pure hydrochloride salt as a white solid (210 mg, 83%). Mp: decomp. > 180 °C.  $\delta_H$  (400 MHz, CD<sub>3</sub>OD): 6.99–7.01 (m, 2H, H-2 and H-4), 7.11–7.14 (m, 1H, H-6), 7.15 (d,  $J = 8.9$  Hz, 2H, H-8 and H-8'), 7.20 (t,  $J = 8.2$  Hz, 1H, H-5), 7.33 (d,  $J = 8.9$  Hz, 2H, H-9 and H-9'), 7.44–7.49 (m, 1H, H-15), 7.64–7.66 (m, 1H, H-16), 7.69 (dd,  $J = 9.6, 1.8$  Hz, 1H, H-13).  $\delta_C$  (100 MHz, CD<sub>3</sub>OD): 93.4 (d,  $J = 7.5$  Hz, qC, C-14), 116.4 (CH Ar, C-2), 118.6 (CH Ar, C-4), 121.0 (CH Ar, C-6), 121.5 (2 CH Ar, C-8 and C-8'), 124.1 (d,  $J = 12.4$  Hz, qC, C-11), 127.3 (d,  $J = 22.2$  Hz, CH Ar, C-13), 128.9 (2 CH Ar, C-9 and C-9'), 130.9 (CH Ar, C-5), 131.5 (qC), 132.4 (CH Ar, C-15), 136.0 (d,  $J = 3.9$  Hz, CH Ar, C-16), 137.9 (qC), 156.4 (qC), 158.0 (d,  $J = 254.4$  Hz, qC, C-12), 157.3 (qC), 158.3 (qC), 159.5 (qC).  $\delta_F$  (376, CD<sub>3</sub>OD):  $-121.10$  (t,  $J = 8.9$  Hz).  $\nu_{\max}$ (ATR)/cm<sup>-1</sup>: 3318 (NH), 3098 (NH), 2958, 1661 (C=N), 1620, 1579, 1485, 1214 (C-F), 1149, 625, 609, 576 (C-I), 566. HRMS ( $m/z$  ESI<sup>+</sup>): found 505.0646 (M<sup>+</sup> + H), C<sub>20</sub>H<sub>19</sub>N<sub>6</sub>O<sub>2</sub>I requires: 505.0649. HPLC: 99.2% (*t*R: 25.3 min).

#### 4.2.4. 1-(4-Bromophenyl)-2-(3-(4-guanidinophenoxy)phenyl)guanidine dihydrochloride (8)

Following Method A (see ESI), **24** (212 mg, 0.29 mmol) was dissolved in 4 M HCl in dioxane (1.30 mL, 5.22 mmol) and in additional dioxane (0.12 mL) until a final concentration of 0.2 M was reached. After 8 h stirring at 55 °C, the reaction was adjudged complete (TLC), solvents were evaporated and the residue was purified by flash chromatography to afford the pure hydrochloride salt as a light-yellow solid (128 mg, 87%). Mp: decomp. > 110 °C.  $\delta_H$  (400 MHz, CD<sub>3</sub>OD): 6.99 (dd,  $J = 8.2, 2.3$  Hz, 1H, H-4), 7.03 (t,  $J = 2.2$  Hz, 1H, H-2), 7.12–7.16 (m, 3H, H-6 and H-8 and H-8'), 7.27 (d,  $J = 8.7$  Hz, 2H, H-12 and H-12' or H-13 and H-13'), 7.31 (d,  $J = 8.8$  Hz, 2H, H-9 and H-9'), 7.46 (t,  $J = 8.1$  Hz, 1H, H-5), 7.61 (d,  $J = 8.7$  Hz, 2H, H-12 and H-12' or H-13 and H-13').  $\delta_C$  (100 MHz, CD<sub>3</sub>OD): 116.3 (CH Ar, C-2), 118.5 (CH Ar, C-4), 120.9 (CH Ar, C-6), 121.5 (2 CH Ar, C-8 and C-8'), 121.7 (qC, C-14), 127.9 (2 CH Ar,

C-12 and C-12' or C-13 and C-13'), 128.9 (2 CH Ar, C-9 and C-9'), 131.5 (qC), 132.4 (CH Ar, C-5), 134.1 (CH Ar, C-12 and C-12' or C-13 and C-13'), 135.8 (qC), 138.0 (qC), 156.2 (qC), 157.4 (qC), 158.3 (qC), 159.5 (qC).  $\nu_{\max}(\text{ATR})/\text{cm}^{-1}$ : 3124 (NH), 3044 (NH), 1655, 1571 (C=N), 1504 (C=N), 1484, 1405, 1213 (C-O), 1070 (C-Br), 1010, 617–567. HRMS ( $m/z$  APCI<sup>+</sup>): found: 439.0857 (M<sup>+</sup> + H), C<sub>20</sub>H<sub>20</sub>BrN<sub>6</sub>O requires: 439.0876. HPLC: 99.8% (t<sub>R</sub>: 24.8 min).

#### 4.2.5. 1-(4-Bromo-3-(trifluoromethyl)phenyl)-2-(3-(4-guanidinophenoxy)phenyl)guanidine dihydrochloride (9)

Following Method A (see ESI), **25** (566 mg, 0.70 mmol) was dissolved in 4 M HCl in dioxane (3.15 mL, 12.6 mmol) and in additional dioxane (0.35 mL) until a final concentration of 0.2 M was reached. After 8 h stirring at 55 °C, the reaction was adjudged complete (TLC), solvents were evaporated and the residue was purified by silica gel chromatography (CHCl<sub>3</sub>:MeOH) to afford the pure hydrochloride salt as a white solid (361 mg, 89%). Mp: decomp. >136 °C.  $\delta_{\text{H}}$  (400 MHz, CD<sub>3</sub>OD): 6.99 (dd,  $J$  = 8.0, 1.9 Hz, 1H, H-4), 7.06 (t,  $J$  = 2.1 Hz, 1H, H-2), 7.14–7.16 (m, 3H, H-8 and H-8' and H-6), 7.32 (d,  $J$  = 8.9 Hz, 2H, H-9 and H-9'), 7.46 (t,  $J$  = 8.1 Hz, 1H, H-5), 7.51 (dd,  $J$  = 8.6, 2.4 Hz, 1H, H-16), 7.74 (d,  $J$  = 2.4 Hz, 1H, H-12), 7.88 (d,  $J$  = 8.6 Hz, 1H, H-15).  $\delta_{\text{C}}$  (100 MHz, CD<sub>3</sub>OD): 116.2 (CH Ar, C-2), 118.3 (qC, C-14), 118.5 (CH Ar, C-4), 120.8 (CH Ar, C-6), 121.5 (2 CH Ar, C-8 and C-8'), 123.9 (d,  $J$  = 260.3 Hz, qCF<sub>3</sub>), 125.3 (m, CH Ar, C-12), 128.9 (2 CH Ar, C-9 and C-9'), 130.5 (CH Ar, C-16), 131.6 (qC), 132.3 (d,  $J$  = 31.7 Hz, qC, C-13), 132.4 (CH Ar, C-5), 136.9 (qC), 137.8 (CH Ar, C-15), 138.0 (qC), 156.1 (qC), 157.3 (qC), 158.3 (qC), 159.6 (qC).  $\delta_{\text{F}}$  (376 MHz, CD<sub>3</sub>OD): –64.73 (s).  $\nu_{\max}(\text{ATR})/\text{cm}^{-1}$ : 3119 (NH), 3053 (NH), 1663 (C=O), 1584 (C=N), 1478, 1412, 1320 (C-F), 1238, 1214, 1174, 1129 (CF<sub>3</sub>), 1099 (C-Br), 1023, 828, 581–558. HRMS ( $m/z$  ESI<sup>+</sup>): found 507.0766 (M<sup>+</sup> + H), C<sub>21</sub>H<sub>19</sub>N<sub>6</sub>OF<sub>3</sub>Br requires: 507.0756. HPLC: 99.9% (t<sub>R</sub>: 26.3 min).

#### 4.2.6. 1-(2-Fluoro-4-iodophenyl)-2-(4-(3-guanidinophenoxy)phenyl)guanidine dihydrochloride (10)

Following Method A (see ESI), **26** (310 mg, 0.39 mmol) was dissolved in 4 M HCl in dioxane (1.73 mL, 6.93 mmol) and in additional dioxane (0.17 mL) until a final concentration of 0.2 M was reached. After 8 h stirring at 55 °C, the reaction was adjudged complete (TLC), solvents were evaporated and the residue was purified by flash chromatography to afford the pure hydrochloride salt as a white solid (198 mg, 88%). Mp: decomp. >150 °C.  $\delta_{\text{H}}$  (400 MHz, CD<sub>3</sub>OD): 6.97 (t,  $J$  = 2.1 Hz, 1H, H-2), 7.00 (dd,  $J$  = 8.2, 2.3 Hz, 1H, H-4), 7.08 (dd,  $J$  = 7.6, 1.5 Hz, 1H, H-6), 7.16 (d,  $J$  = 8.8 Hz, 2H, H-8 and H-8'), 7.22 (t,  $J$  = 8.2 Hz, 1H, H-5 or H-15), 7.36 (d,  $J$  = 8.8 Hz, 2H, H-9 and H-9'), 7.47 (t,  $J$  = 8.1 Hz, 1H, H-5 or H-15), 7.66 (d,  $J$  = 9.1 Hz, 1H, H-16), 7.70 (dd,  $J$  = 9.6, 1.7 Hz, 1H, H-13).  $\delta_{\text{C}}$  (100 MHz, CD<sub>3</sub>OD): 93.5 (d,  $J$  = 7.5 Hz, qC, C-14), 116.6 (CH Ar, C-2), 118.6 (CH Ar, C-4), 121.3 (CH Ar, C-6), 121.6 (2 CH Ar, C-8 and C-8'), 124.0 (d,  $J$  = 12.5 Hz, qC, C-11), 127.3 (d,  $J$  = 22.2 Hz, C-13), 128.7 (2 CH Ar, C-9 and C-9'), 131.1 (CH Ar, C-5 or C-15), 131.6 (qC), 132.4 (CH Ar, C-5 or C-15), 136.0 (d,  $J$  = 3.9 Hz, C-16), 137.7 (qC), 156.8 (qC), 157.3 (qC), 157.9 (qC), 158.2 (d,  $J$  = 254.5 Hz, qC, C-12), 159.5 (qC).  $\delta_{\text{F}}$  (376 MHz, CD<sub>3</sub>OD): –121.04 (t,  $J$  = 8.8 Hz).  $\nu_{\max}(\text{ATR})/\text{cm}^{-1}$ : 3335 (NH), 3265 (NH), 3180 (NH), 3052, 2868, 2325, 1616 (C=N), 1560 (C=N), 1504, 1400, 1226 (C-F), 1162, 1109, 971, 875, 789, 684–573 (C-I). HRMS ( $m/z$  ESI<sup>+</sup>): found: 505.0645 (M<sup>+</sup> + H), C<sub>20</sub>H<sub>19</sub>N<sub>6</sub>OFl requires: 505.0649. HPLC: 99.9% (t<sub>R</sub>: 25.9 min).

#### 4.2.7. 1-(4-Bromo-3-(trifluoromethyl)phenyl)-2-(4-(3-guanidinophenoxy)phenyl)guanidine dihydrochloride (11)

Following Method A (see ESI), **27** (148 mg, 0.18 mmol) was dissolved in 4 M HCl in dioxane (0.81 mL, 3.24 mmol) and in additional dioxane (0.10 mL) until a final concentration of 0.2 M was reached. After 8 h stirring at 55 °C, the reaction was adjudged complete (TLC), solvents were evaporated and the residue was purified by flash chromatography to afford the pure hydrochloride salt as a white solid (100 mg, 94%). Mp: decomp. > 95 °C.  $\delta_{\text{H}}$  (400 MHz, CD<sub>3</sub>OD): 6.98–7.02 (m, 2H, H-2 and H-4), 7.09 (ddd, 1H,  $J$  = 8.0, 1.9, 0.9 Hz, H-6), 7.17 (d,  $J$  = 8.9 Hz, 2H, H-8 and H-8'), 7.41 (d,  $J$  = 9.0 Hz, 2H, H-9 and H-9'), 7.49 (t,  $J$  = 8.0 Hz, 1H, H-5), 7.55 (dd,  $J$  = 8.5, 2.6 Hz, 1H, H-16), 7.77 (d,  $J$  = 2.6 Hz, 1H,

H-12), 7.91 (d,  $J = 8.6$  Hz, 1H, H-15).  $\delta_C$  (100 MHz, CD<sub>3</sub>OD): 116.6 (CH Ar, C-2 or C-4), 118.5 (qC, C-14), 118.6 (CH Ar, C-2 or C-4), 121.3 (CH Ar, C-6), 121.6 (2 CH Ar, C-8 and C-8'), 123.9 (d,  $J = 272.8$  Hz, qCF<sub>3</sub>), 125.5 (q,  $J = 5.6$  Hz, CH Ar, C-12), 128.5 (2 CH Ar, C-9 and C-9'), 130.8 (CH Ar, C-16), 131.7 (qC), 132.3 (q,  $J = 31.6$  Hz, qC, C-13), 132.4 (CH Ar, C-5), 136.7 (qC), 137.7 (qC), 137.8 (CH Ar, C-15), 156.5 (qC), 157.3 (qC), 157.9 (qC), 159.6 (qC).  $\delta_F$  (376 MHz, CD<sub>3</sub>OD): -64.30 (s).  $\nu_{\max}$ (ATR)/cm<sup>-1</sup>: 3309 (NH), 3116 (NH), 3053 (NH), 2837, 2280, 1663 (C=N), 1577 (C=N), 1505, 1486, 1405, 1320, 1258 (C-O), 1214 (CF<sub>3</sub>), 1129, 1023 (C-Br), 829, 595–575. HRMS ( $m/z$  ESI<sup>+</sup>): found: 507.0750 (M<sup>+</sup> + H), C<sub>21</sub>H<sub>19</sub>N<sub>6</sub>OBrF<sub>3</sub> requires: 507.0756. HPLC: 99.9% ( $t_R$ : 26.6 min).

#### 4.2.8. 1-(4-(3-((4-Chlorophenyl)amino)phenoxy)phenyl)guanidine hydrochloride (28)

Following Method A (see ESI), **44** (97 mg, 0.18 mmol) was dissolved in 4 M HCl in dioxane (0.53 mL, 2.10 mmol) and in additional dioxane (0.9 mL) until a final concentration of 0.2 M was reached. After 8 h stirring at 55 °C, the reaction was adjudged complete (TLC), solvents were evaporated and the residue was purified by silica gel chromatography (CHCl<sub>3</sub>:MeOH) to afford the pure hydrochloride salt as a purple solid (69 mg, 99%). Mp: 50–52 °C.  $\delta_H$  (400 MHz, CD<sub>3</sub>OD): 6.51 (dd,  $J = 8.3, 1.9$  Hz, 1H, H-4), 6.73 (t,  $J = 2.2$  Hz, 1H, H-2), 6.85 (dd,  $J = 7.8, 1.8$  Hz, 1H, H-6), 7.05 (d,  $J = 8.9$  Hz, 2H, H-12 and H-12'), 7.08 (d,  $J = 8.9$  Hz, 2H, H-8 and H-8'), 7.18 (d,  $J = 8.9$  Hz, 2H, H-13 and H-13'), 7.22 (t,  $J = 8.2$  Hz, 1H, H-5), 7.27 (d,  $J = 8.9$  Hz, 2H, H-9 and H-9').  $\delta_C$  (100 MHz, CD<sub>3</sub>OD): 108.6 (CH Ar, C-2), 111.8 (CH Ar, C-4), 113.7 (CH Ar, C-6), 120.0 (2 CH Ar, C-12 and C-12'), 120.7 (2 CH Ar, C-8 and C-8'), 126.1 (qC, C-14), 128.8 (2 CH Ar, C-9 and C-9'), 130.1 (2 CH Ar, C-13 and C-13'), 130.6 (qC), 131.5 (CH Ar, C-5), 143.4 (qC), 146.7 (qC), 158.4 (qC), 158.5 (qC), 158.9 (qC).  $\nu_{\max}$ (ATR)/cm<sup>-1</sup>: 3297 (N-H), 3126 (N-H), 1688, 1586 (C=N), 1502, 1485 (C-N), 1325, 1216 (C-O), 1142 (C-Cl), 997, 972, 823, 770, 689, 604, 588, 570. HRMS ( $m/z$  ESI<sup>+</sup>): found 353.1177 (M<sup>+</sup> + H). C<sub>19</sub>H<sub>18</sub>N<sub>4</sub>OCl requires: 353.1169. HPLC: 98.0% ( $t_R$ : 32.3 min).

#### 4.2.9. 1-(4-(3-((4-Chloro-3-(trifluoromethyl)phenyl)amino)phenoxy)phenyl)guanidine hydrochloride (3)

Following Method A (see ESI), **45** (112 mg, 0.18 mmol) was dissolved in 4 M HCl in dioxane (0.54 mL, 2.16 mmol) and in additional dioxane (0.36 mL) until a final concentration of 0.2 M was reached. After 8 h stirring at 55 °C, the reaction was adjudged complete (TLC), solvents were evaporated and the residue was purified by flash chromatography to afford the pure hydrochloride salt as a light brown solid (59 mg, 80%). Mp: 58–60 °C.  $\delta_H$  (400 MHz, CD<sub>3</sub>OD): 6.62 (dd,  $J = 8.7, 2.3$  Hz, 1H, H-4), 6.78 (t,  $J = 2.2$  Hz, 1H, H-2), 6.90 (dd,  $J = 8.1, 2.1$  Hz, 1H, H-6), 7.11 (d,  $J = 8.9$  Hz, 2H, H-8 and H-8'), 7.24 (dd,  $J = 8.8, 2.8$  Hz, 1H, H-16), 7.27–7.31 (m, 3H, H-9, H-9' and H-5) 7.36–7.39 (m, 2H, H-12, H-15).  $\delta_C$  (100 MHz, CD<sub>3</sub>OD): 109.8 (CH Ar, C-2), 113.1 (CH Ar, C-4), 114.8 (CH Ar, C-6), 116.1 (q,  $J = 5.6$  Hz, CH Ar, C-12), 121.0 (2 CH Ar, C-8 and C-8'), 121.5 (CH Ar, C-16), 122.1 (qC, C-14), 124.4 (d,  $J = 272.5$  Hz, qCF<sub>3</sub>), 129.0 (2 CH Ar, C-9 and C-9'), 129.6 (q,  $J = 31.0$ , qC, C-13), 131.0 (qC), 131.8 (CH Ar, C-5), 133.4 (CH Ar, C-15), 144.4 (qC), 145.3 (qC), 158.2 (qC), 158.4 (qC), 159.2 (qC).  $\delta_F$  (376 MHz, CD<sub>3</sub>OD): -64.18 (s).  $\nu_{\max}$ (ATR)/cm<sup>-1</sup>: 3295 (NH), 3163, 2923, 2853, 2400, 1664 (C=O), 1595 (C=N), 1504, 1482, 1441, 1333, 1258, 1217 (CF<sub>3</sub>), 1127, 1112 (C-Cl), 1027, 999, 977, 825. HRMS ( $m/z$  ESI<sup>+</sup>): found 421.1044 (M<sup>+</sup> + H). C<sub>20</sub>H<sub>17</sub>ClF<sub>3</sub>N<sub>4</sub>O requires: 421.1043. HPLC: 97.8% ( $t_R$ : 32.9 min).

#### 4.2.10. 1-(4-(3-((3-(Trifluoromethyl)phenyl)amino)phenoxy)phenyl)guanidine hydrochloride (29)

Following Method A (see ESI), **46** (371 mg, 0.63 mmol) was dissolved in 4 M HCl in dioxane (1.90 mL, 7.56 mmol) and in additional dioxane (1.25 mL) until a final concentration of 0.2 M was reached. After 6 h stirring at 55 °C, the reaction was adjudged complete (TLC), solvents were evaporated and the residue was purified by flash chromatography to afford the pure hydrochloride salt as a white solid (242 mg, 90%). Mp: 93–95 °C.  $\delta_H$  (400 MHz, CD<sub>3</sub>OD): 6.59 (dd,  $J = 8.1, 2.3$  Hz, 1H, H-4), 6.78 (t,  $J = 2.2$  Hz, 1H, H-2), 6.90 (dd,  $J = 7.9, 1.9$  Hz, 1H, H-6), 7.07–7.13 (m, 3H, H-8 and 8' and H-12 or H-14), 7.26–7.30 (m, 5H, H-9 and 9', H-12 or H-14, H-16 and H-5 or H-15), 7.37 (t,  $J = 8.3$  Hz, 1H, H-5 or H-15).  $\delta_C$  (100 MHz, CD<sub>3</sub>OD): 109.4 (CH Ar, C-2), 112.6 (CH Ar, C-4), 113.9 (q,  $J = 4.0$  Hz, CH Ar,

C-12 or C-14), 114.6 (CH Ar, C-6), 117.3 (q,  $J = 4.0$  Hz, CH Ar, C-12 or C-14), 119.9 (d,  $J = 280.7$  Hz, qCF<sub>3</sub>), 120.9 (2 CH Ar, C-8 and C-8'), 121.2 (CH Ar, C-16), 128.9 (2 CH Ar, C-9 and C-9'), 130.8 (qC), 131.1 (CH Ar, C-5 or C-15), 131.7 (CH Ar, C-5 or C-15), 132.6 (d,  $J = 31.9$  Hz, qC, C-13), 145.7 (qC), 145.9 (qC), 158.3 (qC), 158.4 (qC), 159.1 (qC).  $\delta_F$  (376 MHz, CD<sub>3</sub>OD):  $-64.42$  (s).  $\nu_{\max}$ (ATR)/cm<sup>-1</sup>: 3301 (NH), 3135 (NH), 1665, 1587 (C=N), 1490, 1486, 1335 (C-N), 1216 (C-O), 1161, 1116 (CF<sub>3</sub>), 1067 (C-Cl), 976, 836, 785, 689. HRMS ( $m/z$  ESI<sup>+</sup>): found 387.1438 (M<sup>+</sup> + H. C<sub>20</sub>H<sub>18</sub>N<sub>4</sub>O<sub>F</sub><sub>3</sub> requires: 387.1433). HPLC: 97.5% ( $t_R$ : 31.7 min).

#### 4.2.11. 1-(4-(3-((3-(Pentafluorosulfanyl)phenyl)amino)phenoxy)phenyl)guanidine hydrochloride (30)

Following Method A (see ESI), **47** (272 mg, 0.42 mmol) was dissolved in 4 M HCl in dioxane (1.27 mL, 5.06 mmol) and in additional dioxane (0.83 mL) until a final concentration of 0.2 M was reached. After 6 h stirring at 55 °C, the reaction was adjudged complete (TLC), solvents were evaporated and the residue was purified by silica gel chromatography (CHCl<sub>3</sub>:MeOH) to afford the pure hydrochloride salt as an orange solid (127 mg, 62%). Mp: 104–106 °C.  $\delta_H$  (400 MHz, CD<sub>3</sub>OD): 6.61 (dd,  $J = 8.2$ , 2.3 Hz, 1H, H-4), 6.78 (t,  $J = 2.2$  Hz, 1H, H-2), 6.90 (dd,  $J = 8.1$ , 2.1 Hz, 1H, H-6), 7.11 (d,  $J = 8.9$  Hz, H-8 and H-8'), 7.22–7.31 (m, 5H, H-9 and H-9', H-5 or H-15, H-14 and H-16), 7.34–7.38 (m, 1H, H-5 or H-15), 7.44 (t,  $J = 2.2$  Hz, 1H, H-12).  $\delta_C$  (100 MHz, CD<sub>3</sub>OD): 109.6 (CH Ar, C-2), 112.9 (CH Ar, C-4), 114.6 (CH Ar, C-6), 114.9 (p,  $J = 4.6$  Hz, CH Ar, C-12), 118.0 (p,  $J = 4.7$  Hz, CH Ar, C-14), 120.8 (CH Ar, C-16), 120.9 (2 CH Ar, C-8 and C-8'), 128.8 (2 CH Ar, C-9 and C-9'), 130.6 (CH Ar, C-5 or C-15), 130.8 (qC), 131.8 (CH Ar, C-5 or C-15), 145.6 (qC), 145.7 (qC), 155.9 (p,  $J = 16.4$  Hz, qC, C-13), 158.2 (qC), 158.3 (qC), 159.2 (qC).  $\delta_F$  (376 MHz, CD<sub>3</sub>OD):  $-64.34$  (s).  $\nu_{\max}$ (ATR)/cm<sup>-1</sup>: 3273 (NH), 3150 (NH), 1669, 1593 (C=N), 1487 (C-N), 1218 (C-O), 834 (SF<sub>5</sub>), 567. HRMS ( $m/z$  ESI<sup>+</sup>): found 445.1124 (M<sup>+</sup> + H. C<sub>19</sub>H<sub>18</sub>N<sub>4</sub>OSF<sub>5</sub> requires: 445.1121). HPLC: 95.4% ( $t_R$ : 32.3 min).

#### 4.2.12. 1-(4-(3-((4-Chloro-3-(trifluoromethyl)phenyl)amino)-5-fluorophenoxy)phenyl)guanidine hydrochloride (36)

Following Method A (see ESI), **48** (166 mg, 0.26 mmol) was dissolved in 4 M HCl in dioxane (0.78 mL, 3.12 mmol) and in additional dioxane (0.51 mL) until a final concentration of 0.2 M was reached. After 8 h stirring at 55 °C, the reaction was adjudged complete (TLC), solvents were evaporated and the residue was purified by silica gel chromatography (CHCl<sub>3</sub>:MeOH) to afford the pure hydrochloride salt as a light brown solid (114 mg, 92%). Mp: 92–94 °C.  $\delta_H$  (600 MHz, CD<sub>3</sub>OD): 6.31 (dt,  $J = 9.9$ , 2.1 Hz, 1H, H-4), 6.55 (s, 1H, H-2), 6.58 (dt,  $J = 10.7$ , 2.0 Hz, 1H, H-6), 7.16 (d,  $J = 8.8$  Hz, 2H, H-8 and H-8'), 7.29 (dd,  $J = 8.8$ , 2.7 Hz, 1H, H-16), 7.32 (d,  $J = 8.8$  Hz, 2H, H-9 and H-9'), 7.40 (d,  $J = 2.6$  Hz, 1H, H-12), 7.43 (d,  $J = 8.7$  Hz, 1H, H-15).  $\delta_C$  (150 MHz, CD<sub>3</sub>OD): 99.4 (d,  $J = 25.7$  Hz, CH Ar, C-4), 100.3 (d,  $J = 25.5$  Hz, CH Ar, C-6), 103.8 (d,  $J = 2.6$  Hz, CH Ar, C-2), 117.4 (q,  $J = 5.5$  Hz, CH Ar, C-12), 121.8 (2 CH Ar, C-8 and C-8'), 122.7 (CH Ar, C-16), 123.4 (qC, C-14), 124.3 (d,  $J = 272.2$  Hz, qCF<sub>3</sub>), 128.9 (2 CH Ar, C-9 and C-9'), 129.8 (q,  $J = 31.0$ , qC, C-13), 131.7 (qC), 133.5 (CH Ar, C-15), 143.4 (qC), 146.7 (d,  $J = 13.2$  Hz, qC, C-1 or C-3), 157.1 (qC), 158.4 (qC), 160.7 (d,  $J = 13.7$  Hz, qC, C-1 or C-3), 165.8 (d,  $J = 243.4$  Hz, qC, C-5).  $\delta_F$  (376 MHz, CD<sub>3</sub>OD):  $-64.67$  (s),  $-112.53$  (s).  $\nu_{\max}$ (ATR)/cm<sup>-1</sup>: 3285 (NH), 3139 (NH), 1666, 1601 (C=N), 1504, 1476, 1323 (CF<sub>3</sub>), 1216 (C-O), 1112 (C-F), 1020 (C-Cl), 994, 823, 660. HRMS ( $m/z$  ESI<sup>+</sup>): found 439.0945 (M<sup>+</sup> + H. C<sub>20</sub>H<sub>16</sub>N<sub>4</sub>O<sub>F</sub><sub>4</sub>Cl requires: 439.0943). HPLC: 95.7% ( $t_R$ : 33.1 min).

#### 4.2.13. 1-(3,4-Di-fluorophenyl)-3-(3-((6-guanidinopyridin-3-yl)oxy)phenyl)guanidine dihydrochloride (49)

Following Method A (see ESI), **61** (176 mg, 0.25 mmol) was dissolved in 4 M HCl in dioxane (1.14 mL, 4.54 mmol) and in additional dioxane (0.11 mL) until a final concentration of 0.2 M was reached. After 8 h stirring at 55 °C, the reaction was adjudged complete (TLC), solvents were evaporated and the residue was purified by silica gel chromatography (CHCl<sub>3</sub>:MeOH) to afford the pure hydrochloride salt as a white solid (101 mg, 84%). Mp: decomp. above 110 °C.  $\delta_H$  (400 MHz, CD<sub>3</sub>OD): 6.62 (dd,  $J = 7.5$ ,

2.4 Hz, 1H, H-4), 6.77–6.81 (m, 1H, H-17), 6.93 (dd,  $J = 8.0, 1.8$  Hz, 1H, H-6), 6.99 (d,  $J = 8.9$  Hz, 1H, H-9), 7.00–7.13 (m, 3H, H-2, H-13 and H-16), 7.25 (t,  $J = 8.1$  Hz, 1H, H-5), 7.49 (dd,  $J = 8.9, 2.9$  Hz, 1H, H-8), 8.05 (d,  $J = 2.9$  Hz, 1H, H-11).  $\delta_C$  (100 MHz, CD<sub>3</sub>OD): 112.0 (d,  $J = 18.8$  Hz, CH Ar, C-13 or C-16), 112.4 (CH Ar, C-2), 113.0 (CH Ar, C-4), 116.4 (CH Ar, C-9), 118.0 (CH Ar, C-6), 118.1 (d,  $J = 17.9$  Hz, CH Ar, C-13 or C-16), 119.1 (dd,  $J = 5.6, 3.1$  Hz, CH Ar, C-17), 131.3 (CH Ar, C-5), 131.4 (CH Ar, C-8), 138.5 (CH Ar, C-11), 143.9 (dd,  $J = 7.4, 2.2$  Hz, qC, C-12), 146.6 (qC), 147.2 (dd,  $J = 240.4, 12.9$  Hz, qC, C-14 or C-15), 150.1 (qC), 151.1 (qC), 151.4 (dd,  $J = 245.1, 13.4$  Hz, qC, C-14 or C-15), 152.5 (qC), 157.4 (qC), 159.0 (qC).  $\delta_F$  (376 MHz, CD<sub>3</sub>OD): –139.72 (m), –149.19 (m).  $\nu_{\max}$ (ATR)/cm<sup>–1</sup>: 3313 (NH), 3154 (NH), 2922, 2861, 1682, 1625 (C=N), 1507, 1473 (C-F), 1375, 1228 (C-F), 1166, 1146 (C-O), 866, 830, 770, 570, 557. HRMS ( $m/z$  ESI<sup>+</sup>): found 398.1548 (M<sup>+</sup> + H. C<sub>19</sub>H<sub>18</sub>N<sub>7</sub>OF<sub>2</sub> requires: 398.1541). HPLC: 99.8% (tR: 23.6 min).

#### 4.2.14. 1-(2-Fluoro-4-iodophenyl)-3-(3-((6-guanidinopyridin-3-yl)oxy)phenyl)guanidine dihydrochloride (50)

Following Method A (see ESI), **62** (104 mg, 0.13 mmol) was dissolved in 4 M HCl in dioxane (0.58 mL, 2.32 mmol) and in additional dioxane (0.10 mL) until a final concentration of 0.2 M was reached. After 8 h stirring at 55 °C, the reaction was adjudged complete (TLC), solvents were evaporated and the residue was purified by silica gel chromatography (CHCl<sub>3</sub>:MeOH) to afford the pure hydrochloride salt as a white solid (67 mg, 89%). Mp: decomp. above 120 °C.  $\delta_H$  (400 MHz, CD<sub>3</sub>OD): 6.98 (ddd,  $J = 8.3, 2.4, 0.7$  Hz, 1H, H-4), 7.02 (t,  $J = 2.2$  Hz, 1H, H-2), 7.11–7.18 (m, 3H, H-5 or H-16, H-6 and H-9), 7.46 (t,  $J = 8.1$  Hz, 1H, H-5 or H-16), 7.61–7.64 (m, 2H, H-17 and H-8), 7.67 (dd,  $J = 9.7, 1.8$  Hz, 1H, H-14), 8.16 (d,  $J = 2.9$  Hz, 1H, H-11).  $\delta_C$  (100 MHz, CD<sub>3</sub>OD): 92.7 (qC, C-15), 115.5 (CH Ar, C-2), 115.6 (CH Ar, C-9), 117.6 (CH Ar, C-4), 120.9 (CH Ar, C-6), 127.2 (d,  $J = 22.2$  Hz, CH Ar, C-14), 127.3 (d,  $J = 14.1$  Hz, qC, C-12), 130.6 (CH Ar, C-5 or C-16), 132.1 (CH Ar, C-8), 132.5 (CH Ar, C-5 or C-16), 136.0 (CH Ar,  $J = 3.9$  Hz, C-17), 138.7 (qC), 139.1 (CH Ar, C-11), 149.2 (qC), 151.2 (qC), 156.2 (qC), 156.9 (qC), 157.9 (qAr,  $J = 253.9$  Hz, C-13), 159.4 (qC).  $\delta_F$  (376 MHz CD<sub>3</sub>OD): –121.55 (t,  $J = 8.3$  Hz).  $\nu_{\max}$ (ATR)/cm<sup>–1</sup>: 3277 (NH), 3122 (NH), 2923, 2849, 1680, 1660, 1623–1570 (C=N), 1474 (C-F), 1227 (C-O), 1160, 1026, 945, 600 (C-I). HRMS ( $m/z$  ESI<sup>+</sup>): found 506.0609 (M<sup>+</sup> + H. C<sub>19</sub>H<sub>18</sub>N<sub>7</sub>OFI requires: 506.0602). HPLC: 98.1% (tR: 25.7 min).

#### 4.2.15. 1-(4-Bromophenyl)-3-(3-((6-guanidinopyridin-3-yl)oxy)phenyl)guanidine dihydrochloride (51)

Following Method A (see ESI), **63** (184 mg, 0.24 mmol) was dissolved in 4 M HCl in dioxane (1.08 mL, 4.4 mmol) and in additional dioxane (0.12 mL) until a final concentration of 0.2 M was reached. After 8 h stirring at 55 °C, the reaction was adjudged complete (TLC), solvents were evaporated and the residue was purified by silica gel chromatography (CHCl<sub>3</sub>:MeOH) to afford the pure hydrochloride salt as a white solid (113 mg, 92%). Mp: decomp. above 124 °C.  $\delta_H$  (400 MHz, CD<sub>3</sub>OD): 6.99–7.01 (m, 1H, H-4), 7.04 (bs, 1H, H-2), 7.14–7.16 (m, 2H, H-6 and H-9), 7.28 (d,  $J = 8.5$  Hz, 2H, H-13 and H-13' or H-14 and H-14'), 7.48 (t,  $J = 8.1$  Hz, 1H, H-5), 7.60–7.63 (m, 3H, H-13 and H-13' or H-14 and H-14' and H-8), 8.16 (d,  $J = 2.6$  Hz, 1H, H-11).  $\delta_C$  (100 MHz, CD<sub>3</sub>OD): 115.6 (CH Ar, C-6 or C-9), 115.8 (CH Ar, C-2), 118.0 (CH Ar, C-4), 121.1 (CH Ar, C-6 or C-9), 121.7 (qC, C-15), 127.9 (CH Ar, C-13 and C-13' or C-14 and C-14'), 132.1 (CH Ar, C-8), 132.5 (CH Ar, C-5), 134.1 (CH Ar, C-13 and C-13' or C-14 and C-14'), 135.7 (qC), 138.2 (qC), 139.0 (CH Ar, C-11), 149.2 (qC), 151.2 (qC), 156.1 (qC), 156.8 (qC), 159.4 (qC).  $\nu_{\max}$ (ATR)/cm<sup>–1</sup>: 3256 (NH), 3114 (NH), 2971, 1680, 1660, 1619 (C=N), 1566 (C=N), 1474, 1376 (C-N), 1226 (C-O), 1069 (C-Br), 1010, 832, 637–584. HRMS ( $m/z$  ESI<sup>+</sup>): found 440.0837 (M<sup>+</sup> + H. C<sub>19</sub>H<sub>19</sub>N<sub>7</sub>OBr requires: 440.0834). HPLC: 97.5% (tR: 25.2 min).

#### 4.2.16. 1-(4-Bromo-3-(trifluoromethyl)phenyl)-3-(3-((6-guanidinopyridin-3-yl)oxy)phenyl) guanidine dihydrochloride (52)

Following Method A (see ESI), **64** (358 mg, 0.44 mmol) was dissolved in 4 M HCl in dioxane (2 mL, 7.97 mmol) and in additional dioxane (0.2 mL) until a final concentration of 0.2 M was reached.

After 8 h stirring at 55 °C, the reaction was adjudged complete (TLC), solvents were evaporated and the residue was purified by silica gel chromatography (CHCl<sub>3</sub>:MeOH) to afford the pure hydrochloride salt as a white solid (225 mg, 88%). Mp: decomp. above 170 °C.  $\delta_{\text{H}}$  (400 MHz, CD<sub>3</sub>OD): 6.66 (dd,  $J = 8.1$ , 2.4 Hz, 1H, H-4), 6.96 (dd,  $J = 8.0$ , 1.9 Hz, 1H, H-6), 7.04 (d,  $J = 8.9$  Hz, 1H, H-9), 7.08 (t,  $J = 2.1$  Hz, 1H, H-2), 7.20 (dd,  $J = 8.6$ , 2.5 Hz, 1H, H-17), 7.28 (t,  $J = 8.1$  Hz, 1H, H-5), 7.48 (d,  $J = 2.5$ , 1H, H-13), 7.56 (dd,  $J = 8.9$ , 2.9 Hz, 1H, H-8), 7.60 (d,  $J = 8.6$  Hz, 1H, H-16), 8.10 (d,  $J = 2.7$  Hz, 1H, H-11).  $\delta_{\text{C}}$  (100 MHz, CD<sub>3</sub>OD): 111.8 (d,  $J = 1.8$  Hz, qC, C-15), 112.4 (CH Ar, C-2), 113.3 (CH Ar, C-4), 115.5 (CH Ar, C-9), 117.8 (CH Ar, C-6), 122.4 (q,  $J = 5.5$  Hz, CH Ar, C-13), 124.4 (d,  $J = 272.6$  Hz, qCF<sub>3</sub>), 127.7 (CH Ar, C-17), 130.9 (d,  $J = 30.8$  Hz, qC, C-14), 131.4 (CH Ar, C-5), 131.6 (CH Ar, C-8), 136.6 (CH Ar, C-16), 138.6 (CH Ar, C-11), 146.1 (qC), 147.2 (qC), 148.9 (qC), 151.8 (qC), 152.4 (qC), 156.9 (qC), 159.0 (qC).  $\delta_{\text{F}}$  (376 MHz, CD<sub>3</sub>OD): -63.96 (s).  $\nu_{\text{max}}$ (ATR)/cm<sup>-1</sup>: 3281 (NH), 3142 (NH), 2922, 2849, 1680, 1625 (C=N), 1566 (C=N), 1473, 1319, 1227 (CF<sub>3</sub>), 1129 (C-Br), 1023, 832, 592-583. HRMS ( $m/z$  ESI<sup>+</sup>): found 508.0710 (M<sup>+</sup> + H. C<sub>20</sub>H<sub>18</sub>N<sub>7</sub>OF<sub>3</sub>Br requires: 508.0708). HPLC: 99.8% ( $t_{\text{R}}$ : 27.5 min).

#### 4.2.17. 1-(4-Chloro-3-(trifluoromethyl)phenyl)-3-(3-((6-guanidinopyridin-3-yl)oxy)phenyl) guanidine dihydrochloride (2)

Following Method A (see ESI), **65** (113 mg, 0.15 mmol) was dissolved in 4 M HCl in dioxane (0.67 mL, 2.70 mmol) and in additional dioxane (0.10 mL) until a final concentration of 0.2 M was reached. After 6 h stirring at 55 °C, the reaction was adjudged complete (TLC), solvents were evaporated and the residue was purified by flash chromatography to afford the pure hydrochloride salt as a white solid (63 mg, 79%). Mp: 169–171 °C.  $\delta_{\text{H}}$  (400 MHz, CD<sub>3</sub>OD): 6.93 (dd,  $J = 8.3$ , 2.3 Hz, 1H, H-4), 7.06 (t,  $J = 2.1$  Hz, 1H, H-2), 7.11–7.13 (m, 2H, H-6 and H-9), 7.44 (t,  $J = 8.2$  Hz, 1H, H-5), 7.53 (dd,  $J = 8.6$ , 2.5 Hz, 1H, H-17), 7.60–7.65 (m, 2H, H-16 and H-8), 7.69 (d,  $J = 2.4$  Hz, 1H, H-13), 8.15 (d,  $J = 2.9$  Hz, 1H, H-11).  $\delta_{\text{C}}$  (100 MHz, CD<sub>3</sub>OD): 115.1 (CH Ar, C-2), 115.6 (CH Ar, C-9), 117.1 (CH Ar, C-4), 120.5 (CH Ar, C-6), 123.9 (d,  $J = 272.5$  Hz, qCF<sub>3</sub>), 124.5 (q,  $J = 5.5$  Hz, CH Ar, C-13), 129.9 (qC, C-15), 130.1 (CH Ar, C-17), 130.2 (d,  $J = 34.7$  Hz, qC, C-14), 132.0 (CH Ar, C-8 or C-16), 132.3 (CH Ar, C-5), 134.0 (CH Ar, C-8 or C-16), 138.3 (qC), 139.0 (CH Ar, C-11), 139.7 (qC), 149.1 (qC), 151.3 (qC), 155.5 (qC), 156.9 (qC), 159.3 (qC).  $\delta_{\text{F}}$  (376 MHz, CD<sub>3</sub>OD): -64.24 (s).  $\nu_{\text{max}}$ (ATR)/cm<sup>-1</sup>: 3297 (NH), 3121 (NH), 2923, 2854, 1625 (C=N), 1581 (C=N), 1474 (CF<sub>3</sub>), 1320, 1227 (C-O), 1130 (C-Cl), 1032, 832, 589, 557. HRMS ( $m/z$  ESI<sup>+</sup>): found: 464.1222 (M<sup>+</sup> + H. C<sub>20</sub>H<sub>18</sub>N<sub>7</sub>OF<sub>3</sub>Cl requires: 464.1213). HPLC: 96.9% ( $t_{\text{R}}$ : 26.8 min).

#### 4.2.18. 1-(5-(3-((4-Chloro-3-(trifluoromethyl)phenyl)amino)phenoxy)pyridin-2-yl)guanidine hydrochloride (4)

Following Method A (see ESI), **69** (200 mg, 0.32 mmol) was dissolved in 4 M HCl in dioxane (0.96 mL, 3.86 mmol) and in additional dioxane (0.65 mL) until a final concentration of 0.2 M was reached. After 8 h stirring at 55 °C, the reaction was adjudged complete (TLC), solvents were evaporated and the residue was purified by silica gel chromatography (CHCl<sub>3</sub>:MeOH) to afford the pure hydrochloride salt as a white solid (136 mg, 93%). Mp: 89–91 °C.  $\delta_{\text{H}}$  (400 MHz, CD<sub>3</sub>OD): 6.60 (dd,  $J = 8.2$ , 2.3 Hz, 1H, H-4), 6.75 (t,  $J = 2.2$  Hz, 1H, H-2), 6.90 (dd,  $J = 8.1$ , 2.0 Hz, 1H, H-6), 7.08 (d,  $J = 8.9$  Hz, 1H, H-9), 7.24 (dd,  $J = 8.7$ , 2.7 Hz, 1H, H-17), 7.29 (t,  $J = 8.1$  Hz, 1H, H-5), 7.37–7.39 (m, 2H, H-13 and H-16), 7.59 (dd,  $J = 8.9$ , 2.9 Hz, 1H, H-8), 8.13 (d,  $J = 2.9$  Hz, 1H, H-11).  $\delta_{\text{C}}$  (100 MHz, CD<sub>3</sub>OD): 108.7 (CH Ar, C-2), 112.2 (CH Ar, C-4), 114.7 (CH Ar, C-6), 115.5 (CH Ar, C-9), 116.2 (q,  $J = 5.5$  Hz, CH Ar, C-13), 121.8 (CH Ar, C-17), 122.4 (qC, C-15), 124.3 (d,  $J = 272.4$  Hz, qCF<sub>3</sub>), 129.6 (d,  $J = 31.0$  Hz, qC, C-14), 131.8 (CH Ar, C-8), 132.0 (CH Ar, C-5), 133.4 (CH Ar, C-16), 138.7 (CH Ar, C-11), 144.2 (qC), 145.6 (qC), 148.8 (qC), 151.8 (qC), 156.9 (qC), 159.4 (qC).  $\delta_{\text{F}}$  (376 MHz, CD<sub>3</sub>OD): -64.15 (s).  $\nu_{\text{max}}$ (ATR)/cm<sup>-1</sup>: 3264 (NH), 2923, 2863, 1684, 1629, 1595, 1474 (C=N), 1400, 1332, 1229 (C-O), 1129 (CF<sub>3</sub>), 1115 (C-Cl), 977, 998. HRMS ( $m/z$  ESI<sup>+</sup>): found 422.0987 (M<sup>+</sup> + H. C<sub>19</sub>H<sub>16</sub>N<sub>5</sub>OCIF<sub>3</sub> requires: 422.0995). HPLC: 98.6% ( $t_{\text{R}}$ : 33.3 min).

#### 4.2.19. 4-(3-((4-Chloro-3-(trifluoromethyl)phenyl)amino)phenoxy)phenyl carbamimidate hydrochloride (70)

To a stirred solution of **74** (205 mg, 0.33 mmol, 1eq) in EtOAc was added SnCl<sub>4</sub> (0.15 mL, 1.32 mmol, 4 eq). After 2 h of stirring at room temperature, the solvent and the excess of SnCl<sub>4</sub> were evaporated in vacuo. The remaining liquid was purified by silica gel chromatography (CHCl<sub>3</sub>:Acetone) to afford the pure hydrochloride salt (130 mg, 86%) as a colourless gum.  $\delta_{\text{H}}$  (400 MHz, DMSO-*d*<sub>6</sub>): 6.61 (dd, *J* = 7.6, 2.3 Hz, 1H, H-4), 6.76 (t, *J* = 2.2 Hz, 1H, H-2), 6.92 (dd, *J* = 7.8, 1.7 Hz, 1H, H-6), 7.16 (d, *J* = 9.1 Hz, 2H, H-8 and H-8' or H-9 and H-9'), 7.30–7.34 (m, 2H, H-5 and H-16), 7.37 (d, *J* = 9.0 Hz, 2H, H-8 and H-8' or H-9 and H-9'), 7.40 (d, *J* = 2.7 Hz, 1H, H-12), 7.50 (d, *J* = 8.8 Hz, 1H, H-15), 8.61 (bs, 4H, NH), 8.88 (bs, NH).  $\delta_{\text{C}}$  (100 MHz, DMSO-*d*<sub>6</sub>): 107.8 (CH Ar, C-2), 111.2 (CH Ar, C-4), 113.1 (CH Ar, C-6), 114.7 (q, *J* = 5.5 Hz, CH Ar, C-12), 119.4 (qC, C-14), 120.4 (CH Ar, C-5 or C-16), 120.5 (2 CH Ar, C-8 and C-8' or C-9 and C-9'), 122.0 (d, *J* = 227.5 Hz, qCF<sub>3</sub>), 123.1 (2 CH Ar, C-8 and C-8' or C-9 and C-9'), 127.2 (d, *J* = 30.7 Hz, qC, C-13), 130.9 (CH Ar, C-5 or C-16), 132.7 (CH Ar, C-15), 142.8 (qC), 143.5 (qC), 145.2 (qC), 155.2 (qC), 157.6 (qC), 161.1 (qC).  $\delta_{\text{F}}$  (376 MHz, CD<sub>3</sub>OD): –61.59 (s).  $\nu_{\text{max}}$  (ATR)/cm<sup>–1</sup>: 3285 (NH), 2924, 2854, 1693, 1655, 1593 (C=N), 1481 (C-N), 1400, 1258, 1231, 1195, 1175 (C-O), 1128 (CF<sub>3</sub>), 1111 (C-Cl), 1027, 824, 681, 665. HRMS (*m/z* ESI<sup>+</sup>): found: 422.0883 (M<sup>+</sup> + H. C<sub>20</sub>H<sub>16</sub>N<sub>3</sub>O<sub>2</sub>ClF<sub>3</sub> requires: 422.0883). HPLC: 96.2% (*t*<sub>R</sub>: 32.2 min).

#### 4.2.20. 4'-Sulfonamide-3-[4-chloro-3 trifluoromethylphenylamino]diphenylether (75)

Compound **40** (100 mg, 0.26 mmol, 1 eq.), sulfamoyl chloride (30 mg, 0.26 mmol, 1 eq.) and NEt<sub>3</sub> (0.05 mL, 0.29 mmol, 1.1 eq.) were dissolved in CH<sub>2</sub>Cl<sub>2</sub> (2 mL) and stirred at overnight at room temperature. The mixture was then washed with water and the organic layer extracted with EtOAc, washed with brine, dried over MgSO<sub>4</sub>, concentrated under vacuum and purified by silica gel chromatography (hexanes:EtOAc) to get **75** as a light brown solid (95 mg, 80%). Mp: 124–126 °C.  $\delta_{\text{H}}$  (400 MHz, CD<sub>3</sub>OD): 6.54 (dd, *J* = 8.2, 2.3 Hz, 1H, H-4), 6.69 (t, *J* = 2.2 Hz, 1H, H-2), 6.84 (dd, *J* = 8.1, 2.1 Hz, 1H, H-6), 6.99 (d, *J* = 9.0 Hz, 2H, H-8 and H-8'), 7.21–7.26 (m, 4H, H-9 and H-9', H-16, H-5), 7.34–7.38 (m, 2H, H-12, H-15).  $\delta_{\text{C}}$  (100 MHz, CD<sub>3</sub>OD): 109.1 (CH Ar, C-2), 112.2 (CH Ar, C-4), 113.8 (CH Ar, C-6), 116.1 (q, *J* = 5.5 Hz, C-12, CH Ar), 121.1 (2 CH Ar, C-8 and C-8'), 121.2 (CH Ar, C-16), 121.9 (qC, C-14), 123.2 (2 CH Ar, C-9 and C-9'), 124.4 (d, *J* = 272.5 Hz, qCF<sub>3</sub>), 129.7 (d, *J* = 30.9 Hz, qC, C-13), 131.5 (CH Ar, C-5), 133.3 (CH Ar, C-15), 136.1 (qC), 144.6 (qC), 145.1 (qC), 154.4 (qC), 160.5 (qC).  $\delta_{\text{F}}$  (376 MHz, CD<sub>3</sub>OD): –64.19 (s).  $\nu_{\text{max}}$  (ATR)/cm<sup>–1</sup>: 3404 (NH), 3279 (NH), 1596 (S=O), 1489 (S=O), 1143 (C-O), 1153 (CF<sub>3</sub>), 1125 (C-N), 830 (C-Cl), 821. HRMS (*m/z* ESI<sup>–</sup>): found: 456.0397 (M<sup>–</sup> – H. C<sub>19</sub>H<sub>14</sub>N<sub>3</sub>O<sub>3</sub>SClF<sub>3</sub> requires: 456.0397). HPLC: 99.3% (*t*<sub>R</sub>: 35.4 min).

### 4.3. Biochemistry

#### 4.3.1. Cell Viability Studies (alamarBlue)

Cells were counted and seeded in 96-well plates at a density of 2 × 10<sup>5</sup> cells/mL for HL-60, 2.5 × 10<sup>4</sup> cells/mL for MCF-7, MCF10A and HeLa, 1 × 10<sup>5</sup> cells/mL for HCT116 and HKH-2, all of them in their respective media. The 96-well plates were then treated with a 1:100 dilution of stock concentrations of drugs or EtOH (1% *v/v*)/DMSO (0.1% *v/v*) as vehicle control in triplicate. Three blank wells containing 200 μL RPMI with no cells were also set-up as blanks. After a 72 h incubation, 20 μL of alamarBlue was added to each well. The plates were incubated in darkness at 37 °C for 4–5 h using a Molecular Devices microplate reader, the fluorescence (F) was then read at an excitation wavelength of 544 nm and an emission wavelength of 590 nm. Cell viability was then determined by subtracting the mean blank fluorescence (F<sub>b</sub>) from the treated sample fluorescence (F<sub>s</sub>) and expressing this as a percentage of the fluorescence of the blanked vehicle control (F<sub>c</sub>). This is demonstrated in the equation below. The results were then plotted as a nonlinear regression, sigmoidal dose-response curves on Prism, from which the IC<sub>50</sub> value for each drug was determined.



### 4.3.2. Flow Cytometry

Apoptosis was analysed using annexin V fluorescein isothiocyanate (FITC) and propidium iodide (PI). HL-60 cells were seeded at a density of  $2 \times 10^5$  cells/mL in 12 well plates. Cells were then treated with either vehicle (0.5% ethanol), **2** (5  $\mu$ M), **3** (5  $\mu$ M), or **4** (4  $\mu$ M) for 48 h. Following treatment, HL60 cells were collected and washed with annexin V binding buffer (5 mM HEPES, 70 mM NaCl, 1.25 mM CaCl<sub>2</sub> pH 7.4) and stained with annexin V-FITC (iQ Corporation, Groningen, The Netherlands) for 20 min. Following washing with annexin V binding buffer, cells were resuspended in PI (0.5  $\mu$ g/mL) in binding buffer and analysed on BD FACS Canto II flow cytometer (BD Sciences) using FloJo software (Ashland, OR, USA).

### 4.3.3. Western Blotting

HL60s were seeded in T25 flasks at  $50 \times 10^4$  cells/mL and cells were treated with either vehicle [0.5% EtOH (*v/v*)], **1–4**, **9** or **52** (5  $\mu$ M), as well as **1** (10  $\mu$ M as reported [? ]). After 16 h, cells were collected and washed with PBS. Cell pellets were re-suspended in cold cell lysis buffer (radio-immunoprecipitation assay buffer) supplemented with 1% phosphatase inhibitor cocktail 2 and 3 (Sigma) and 10% protease inhibitor (Roche). Cells were lysed for 30 min on ice. Protein concentration was then determined by BCA assay. Lysates were boiled with Laemmli sample buffer [Tris-HCL 50 mM (pH 6.7), glycerol 10% (*w/v*), sodium dodecyl sulphate 2% (*w/v*), bromophenol blue 0.02% (*w/v*)] containing DTT 50  $\mu$ M for 10 min at 90 °C. Moreover, 20  $\mu$ g of lysates were resolved by sodium dodecyl sulphate polyacrylamide gel electrophoresis (SDS-PAGE) and transferred onto PVDF transfer membrane (EMD Millipore). Membranes were blocked with 5% non-fat milk and probed with primary antibodies for ERK and phospho-ERK (Cell Signalling). Anti-GAPDH was used as a loading control (Calbiochem).

## 5. Conclusions

Taking all of these results into account, the following SARs were drawn in terms of HL-60 cytotoxicity; for example, for a good cytotoxicity bulky substituents (4-Br/Cl and 3-CF<sub>3</sub>) in the phenyl ring of the hydrophobic moiety are needed; replacement of the di-substituted guanidinium as in compound **1** by a shorter -NH- link is also beneficial; a mono-substituted guanidinium group at the position 4' of the phenyloxyaryl core gives good cytotoxic activity; additionally, substituting one of the phenyl rings by a 2-pyridinyl to facilitate IMHB seems also to increase the cytotoxic activity in the 3,4'-bis-guanidinium series. On the negative side, in the bis-guanidinium diphenyl ether series, when only one substituent is kept in the phenyl ring of the hydrophobic moiety (4-Br or 4-F as in **8** or **5**) or both are very small (3,4-diF as in **6**), cytotoxicity decreases or is completely abolished. This is not the case either in the amino-guanidinium diphenyl ether or in the bis-guanidinium phenyloxypyridine series where mono-substituted or di-fluoro phenyl rings in the hydrophobic moiety still exhibit good HL-60 cytotoxicity (i.e., compounds **28–30** or **49** and **51**).

Future work will be required to investigate the molecular target(s) of our guanidinium derivatives, but nonetheless, while compound **2**, **9**, and **52** seem to be improved derivatives of previous *lead* molecule **1**, compounds **3** and **4** can be considered excellent *hit* molecules in the search for new anticancer therapies.

**Supplementary Materials:** The following are available online at <http://www.mdpi.com/1424-8247/13/12/485/s1>, synthetic details (general information, general procedures, characterisation of intermediates); computational details (Figure S1, Figure S2, Figure S3, Figure S4 and Figure S5); theoretical physicochemical and pharmacokinetic parameters (Table S1, Table S2, and Table S3, Figure S6); biochemical protocols (Figure S7, Figure S8, Figure S9, Figure S10, Figure S11, Figure S12, Figure S13); NMR spectra of final salts; and HPLC chromatograms of final salts.

**Author Contributions:** Conceptualization, V.P., A.M.M., D.M.Z., and I.R.; Formal analysis, V.P., H.B.M., R.A., and I.R.; Funding acquisition, A.M.M., D.M.Z., and I.R.; Investigation, V.P., H.B.M., and R.A.; Methodology, V.P.; Supervision, A.M.M., D.M.Z., and I.R.; Writing—original draft, V.P., and I.R.; Writing—review and editing, V.P., H.B.M., R.A., A.M.M., D.M.Z., and I.R. All authors have read and agreed to the published version of the manuscript.

**Funding:** This research was funded by the School of Chemistry at Trinity College Dublin (V.P.), the Irish Research Council (GOIPG/2017/834, H.B.M.), and the John Scott PhD fellowship from the School of Biochemistry & Immunology and the School of Medicine at Trinity College Dublin (R.A.).

**Acknowledgments:** Thanks are given to the Irish Centre for High-End Computing (ICHEC) for the provision of computational facilities.

**Conflicts of Interest:** The authors declare no conflict of interest.

## References

1. Hanahan, D.; Weinberg, R.A. The hallmarks of cancer. *Cell* **2000**, *100*, 57–70. [CrossRef]
2. Roberts, P.J.; Der, C.J. Targeting the Raf-MEK-ERK mitogen-activated protein kinase cascade for the treatment of cancer. *Oncogene* **2007**, *26*, 3291–3310. [CrossRef] [PubMed]
3. Davies, H.; Bignell, G.R.; Cox, C.; Stephens, P.; Edkins, S.; Clegg, S.; Teague, J.; Woffendin, H.; Garnett, M.J.; Bottomley, W.; et al. Mutations of the BRAF gene in human cancer. *Nature* **2002**, *417*, 949–954. [CrossRef] [PubMed]
4. Michaloglou, C.; Vredeveld, L.C.; Mooi, W.J.; Peeper, D.S. BRAF (E600) in benign and malignant human tumours. *Oncogene* **2008**, *27*, 877–895. [CrossRef] [PubMed]
5. Wimmer, R.; Baccarini, M. Partner exchange: Protein-protein interactions in the Raf pathway. *Trends Biochem. Sci.* **2010**, *35*, 660–668. [CrossRef]
6. Agianian, B.; Gavathiotis, E. Current insights of BRAF inhibitors in cancer. *J. Med. Chem.* **2018**, *61*, 5775–5793. [CrossRef]
7. Zhang, J.; Yang, P.L.; Gray, N.S. Targeting cancer with small molecule kinase inhibitors. *Nat. Rev. Cancer* **2009**, *9*, 28–39. [CrossRef]
8. Diez-Cecilia, E.; Kelly, B.; Perez, C.; Zisterer, D.M.; Nevin, D.K.; Lloyd, D.G.; Rozas, I. Guanidinium-based derivatives: Searching for new kinase inhibitors. *Eur. J. Med. Chem.* **2014**, *81*, 427–441. [CrossRef]
9. Diez-Cecilia, E.; Carson, R.; Kelly, B.; van Schaeybroeck, S.; Murray, J.T.; Rozas, I. Probing a 3,4'-bis-guanidinium diaryl derivative as an allosteric inhibitor of the Ras pathway. *Bioorg. Med. Chem. Lett.* **2015**, *25*, 4287–4292. [CrossRef]
10. Trujillo, C.; Previtali, V.; Rozas, I. A theoretical model of the interaction between phosphates in the ATP molecule and guanidinium systems. *Theor. Chem. Acc.* **2016**, *135*, 260. [CrossRef]
11. Liao, N.P.D.; Wendorff, T.J.; Quinn, J.G.; Steffek, M.; Phung, W.; Liu, P.; Tang, J.; Irudayanathan, F.J.; Izadi, S.; Shaw, A.S.; et al. Negative regulation of RAF kinase activity by ATP is overcome by 14-3-3-induced dimerization. *Nat. Struct. Mol. Biol.* **2020**, *27*, 134–141. [CrossRef]
12. Previtali, V.; Trujillo, C.; Boisson, J.-C.; Khartabil, H.; Hénon, E.; Rozas, I. Development of the first model of a phosphorylated, ATP/Mg<sup>2+</sup>-containing B-Raf monomer by molecular dynamics simulations: A tool for structure-based design. *Phys. Chem. Chem. Phys.* **2017**, *19*, 31177–31185. [CrossRef]
13. Kelly, B.; O'Donovan, D.H.; O'Brien, J.; Blanco, F.; Rozas, I. Pyridin-2-yl Guanidine derivatives: Conformational control induced by intramolecular hydrogen bonding interactions. *J. Org. Chem.* **2011**, *76*, 9216–9227. [CrossRef] [PubMed]
14. Dardonville, C.; Goya, P.; Rozas, I.; Alsasua, A.; Martín, M.I.; Borrego, M.J. New aromatic iminoimidazolidine derivatives as alpha1-adrenoceptor antagonists: A novel synthetic approach and pharmacological activity. *Bioorg. Med. Chem.* **2000**, *8*, 1567–1577. [CrossRef]
15. Okaniwa, M.; Hirose, M.; Imada, T.; Ohashi, T.; Hayashi, Y.; Miyazaki, T.; Arita, T.; Yabuki, M.; Kakoi, K.; Kato, J.; et al. Design and synthesis of novel DFG-out RAF/vascular endothelial growth factor receptor 2 (VEGFR2) inhibitors. 1. Exploration of [5,6]-fused bicyclic scaffolds. *J. Med. Chem.* **2012**, *55*, 3452–3478. [CrossRef] [PubMed]
16. Surrya, D.S.; Buchwald, S.L. Dialkylbiaryl phosphines in Pd-catalyzed amination: A user's guide. *Chem. Sci.* **2011**, *2*, 27–50. [CrossRef] [PubMed]
17. Bellamy, F.D.; Ou, K. Selective reduction of aromatic nitro compounds with stannous chloride in non acidic and non aqueous medium. *Tetrahedron Lett.* **1984**, *25*, 839–842. [CrossRef]
18. Ishimoto, K.; Fukuda, N.; Nagata, T.; Sawai, Y.; Ikemoto, T. Development of a scalable synthesis of a vascular endothelial growth factor receptor-2 kinase inhibitor: Efficient construction of a 6-Etherified [1,2,4]Triazololo[1,5-a]pyridine-2-amine core. *Org. Process Res. Dev.* **2014**, *18*, 122. [CrossRef]

19. Oguro, Y.; Cary, D.R.; Miyamoto, N.; Tawada, M.; Iwata, H.; Miki, H.; Hori, A.; Imamura, S. Design, synthesis, and evaluation of novel VEGFR2 kinase inhibitors: Discovery of [1,2,4]triazolo[1,5-a]pyridine derivatives with slow dissociation kinetics. *Biorg. Med. Chem.* **2013**, *21*, 4714–4729. [CrossRef]
20. Previtali, V.; Trujillo, C.; Amet, R.; Zisterer, D.M.; Rozas, I. Effect of isouronium/ guanidinium substitution on the efficacy of a series of novel anti-cancer agents. *Med. Chem. Comm.* **2018**, *9*, 735–743. [CrossRef]
21. Appel, R.; Berger, G. Hydrazinsulfonsäure-amide, I. Über das Hydrazidisulfamid. *Eur. J. Inorg. Chem.* **1958**, *91*, 1339–1341. [CrossRef]
22. Shahani, V.M.; Ball, D.P.; Ramos, A.V.; Li, Z.H.; Spagnuolo, P.A.; Haftchenary, S.; Schimmer, A.D.; Trudel, S.; Gunning, P.T. A 2,6,9-hetero-trisubstituted purine inhibitor exhibits potent biological effects against multiple myeloma cells. *Bioorg. Med. Chem.* **2013**, *21*, 5618–5628. [CrossRef] [PubMed]
23. Daina, A.; Michielin, O.; Zoete, V. SwissADME: A free web tool to evaluate pharmacokinetics, drug-likeness and medicinal chemistry friendliness of small molecules. *Sci. Rep.* **2017**, *7*, 42717. [CrossRef] [PubMed]
24. Marvin was used for calculating basicity (pKaH) of chemical structures, Marvin 17.21.0, ChemAxon. Available online: <https://www.chemaxon.com> (accessed on 28 June 2019).
25. Wu, P.; Nielsen, T.E.; Clausen, M.H. Small-molecule kinase inhibitors: An analysis of FDA-approved drugs. *Drug Discov. Today* **2016**, *21*, 5–10. [CrossRef] [PubMed]
26. Ertl, P.; Rohde, B.; Selzer, P. Fast calculation of molecular polar surface area as a sum of fragment-based contributions and its application to the prediction of drug transport properties. *J. Med. Chem.* **2000**, *43*, 3714–3717. [CrossRef] [PubMed]
27. Davis, A.; Ward, S.E. *The Handbook of Medicinal Chemistry: Principles and Practice*; Royal Society of Chemistry: London, UK, 2014.
28. Daina, A.; Zoete, V. A Boiled-Egg to predict gastrointestinal absorption and brain penetration of small molecules. *Chem. Med. Chem.* **2016**, *11*, 1117–1121. [CrossRef] [PubMed]
29. Montanari, F.; Ecker, G.F. Prediction of drug-ABC-transporter interaction—Recent advances and future challenges. *Adv. Drug Deliv. Rev.* **2015**, *86*, 17–26. [CrossRef]
30. Wilhelm, S.M.; Adnane, L.; Newell, P.; Villanueva, A.; Llovet, J.M.; Lynch, M. Preclinical overview of sorafenib, a multikinase inhibitor that targets both Raf and VEGF and PDGF receptor tyrosine kinase signaling. *Mol. Cancer Ther.* **2008**, *7*, 3129–3140. [CrossRef]
31. Keating, G.M.; Santoro, A. Sorafenib: A review of its use in advanced hepatocellular carcinoma. *Drugs* **2009**, *69*, 223–240. [CrossRef]
32. Barrett, S.D.; Bridges, A.J.; Dudley, D.T.; Saltiel, A.R.; Fergus, J.H.; Flamme, C.M.; Delaney, A.M.; Kaufman, M.; LePage, S.; Leopold, W.R. The discovery of the benzhydroxamate MEK inhibitors CI-1040 and PD 0325901. *Bioorg. Med. Chem. Lett.* **2008**, *18*, 6501–6504. [CrossRef]
33. Gulhati, P.; Zaytseva, Y.Y.; Valentino, J.D.; Stevens, P.D.; Kim, J.T.; Sasazuki, T.; Shirasawa, S.; Lee, E.Y.; Weiss, H.L.; Dong, J.; et al. Sorafenib enhances the therapeutic efficacy of rapamycin in colorectal cancers harboring oncogenic KRAS and PIK3CA. *Carcinogenesis* **2012**, *33*, 1782–1790. [CrossRef] [PubMed]
34. Karoulia, Z.; Wu, Y.; Ahmed, T.; Xin, Q.; Bollard, J.; Krepler, C.; Wu, X.; Zhang, C.; Bollag, G.; Herlyn, M.; et al. An integrated model of RAF inhibitor action predicts inhibitor activity against oncogenic BRAF signaling. *Cancer Cell.* **2016**, *30*, 485–498. [CrossRef] [PubMed]
35. Frisch, M.J.; Trucks, G.W.; Schlegel, H.B.; Scuseria, G.E.; Robb, M.A.; Cheeseman, J.R.; Scalmani, G.; Barone, V.; Petersson, G.A.; Nakatsuji, H.; et al. *Gaussian 16, Revision C.01*; Gaussian, Inc.: Wallingford, CT, USA, 2016.
36. Trott, O.; Olson, A.J. AutoDock Vina: Improving the speed and accuracy of docking with a new scoring function, efficient optimization and multithreading. *J. Comput. Chem.* **2010**, *31*, 455–461. [CrossRef] [PubMed]
37. Humphrey, W.; Dalke, A.; Schulten, K. VMD—visual molecular dynamics. *J. Mol. Graph.* **1996**, *14*, 33–38. [CrossRef]

**Publisher’s Note:** MDPI stays neutral with regard to jurisdictional claims in published maps and institutional affiliations.



© 2020 by the authors. Licensee MDPI, Basel, Switzerland. This article is an open access article distributed under the terms and conditions of the Creative Commons Attribution (CC BY) license (<http://creativecommons.org/licenses/by/4.0/>).



## Article

# Discovery of Potent Dual EGFR/HER2 Inhibitors Based on Thiophene Scaffold Targeting H1299 Lung Cancer Cell Line

Ranza Elrayess<sup>1,†</sup>, Yasmine M. Abdel Aziz<sup>1,\*</sup>, Mohamed Saleh Elgawish<sup>2,†</sup>, Marwa Elewa<sup>1</sup>, Asmaa S. A. Yassen<sup>1,\*</sup>, Sameh S. Elhady<sup>3</sup>, Hosam A. Elshihawy<sup>1</sup> and Mohamed M. Said<sup>1</sup>

- <sup>1</sup> Pharmaceutical Organic Chemistry Department, Faculty of Pharmacy, Suez Canal University, Ismailia 41522, Egypt; ranza.el-rayes@pharm.suez.edu.eg (R.E.); Marwa\_elewa@pharm.suez.edu.eg (M.E.); hosamelshihawy74@hotmail.com (H.A.E.); msaid123eg@yahoo.com (M.M.S.)
- <sup>2</sup> Medicinal Chemistry Department, Faculty of Pharmacy, Suez Canal University, Ismailia 41522, Egypt; mohamed\_elgawish@pharm.suez.edu.eg
- <sup>3</sup> Department of Natural Products, Faculty of Pharmacy, King Abdulaziz University, Jeddah 21589, Saudi Arabia; ssahmed@kau.edu.sa
- \* Correspondence: yassmin\_morsy@pharm.suez.edu.eg (Y.M.A.A.); asmaa\_yaseen@pharm.suez.edu.eg (A.S.A.Y.); Tel.: +20-1277718225 (Y.M.A.A.); +20-1096206738 (A.S.A.Y.); Fax: +20-064-3230741 (Y.M.A.A. & A.S.A.Y.)
- † The authors contributed equally.

**Abstract:** Dual targeting of epidermal growth factor receptor (EGFR) and human EGFR-related receptor 2 (HER2) is a proven approach for the treatment of lung cancer. With the aim of discovering effective dual EGFR/HER2 inhibitors targeting non-small cell lung cancer cell line H1299, three series of thieno[2,3-d][1,2,3]triazine and acetamide derivatives were designed, synthesized, and biologically evaluated. The synthesized compounds displayed IC<sub>50</sub> values ranging from 12 to 54 nM against H1299, which were superior to that of gefitinib (**2**) at 40 μM. Of the synthesized compounds, 2-(1*H*-pyrazolo[3,4-*b*]pyridin-3-ylamino)-*N*-(3-cyano-4,5,6,7-tetrahydrobenzo[*b*]thiophen-2-yl)acetamide (**21a**) achieved the highest in vitro cytotoxic activity against H1299, with an IC<sub>50</sub> value of 12.5 nM in situ, and 0.47 and 0.14 nM against EGFR and HER2, respectively, values comparable to the IC<sub>50</sub> of the approved drug imatinib (**1**). Our synthesized compounds were promising, demonstrating high selectivity and affinity for EGFR/HER2, especially the hinge region forming a hydrophobic pocket, which was mediated by hydrogen bonding as well as hydrophobic and electrostatic interactions, as indicated by molecular modeling. Moreover, the designed compounds showed good affinity for T790M EGFR, one of the main mutants resulting in acquired drug resistance. Furthermore, both pharmacokinetic and physicochemical properties of the designed compounds were within the appropriate range for human usage as predicted by the in Silico ADME study. The designed compound (**21a**) might serve as an encouraging lead compound for the discovery of promising anti-lung cancer agents targeting EGFR/HER2.

**Keywords:** thieno[2,3-d][1,2,3]triazine; acetamide; H1299; HER2; EGFR

**Citation:** Elrayess, R.; Abdel Aziz, Y.M.; Elgawish, M.S.; Elewa, M.; Yassen, A.S.A.; Elhady, S.S.; Elshihawy, H.A.; Said, M.M. Discovery of Potent Dual EGFR/HER2 Inhibitors Based on Thiophene Scaffold Targeting H1299 Lung Cancer Cell Line. *Pharmaceuticals* **2021**, *14*, 9. <https://dx.doi.org/10.3390/ph14010009>

Received: 24 November 2020

Accepted: 21 December 2020

Published: 24 December 2020

**Publisher's Note:** MDPI stays neutral with regard to jurisdictional claims in published maps and institutional affiliations.



**Copyright:** © 2020 by the authors. Licensee MDPI, Basel, Switzerland. This article is an open access article distributed under the terms and conditions of the Creative Commons Attribution (CC BY) license (<https://creativecommons.org/licenses/by/4.0/>).

## 1. Introduction

Lung cancer continues to be one of the major causes of cancer-related mortality, and non-small cell lung cancer (NSCLC) cases account for approximately 90% of all lung cancer [1]. Treatment options for patients with advanced lung cancer, including chemotherapy, radiation, or surgery, are still insufficient, and around half of limited-stage lung cancer patients relapse [2,3]. Receptor tyrosine kinases (RTKs) play a significant role in cellular signaling pathways and regulate the majority of cellular processes, such as cell metabolism, differentiation, proliferation, and apoptosis. Among the well-known RTKs, members of the ERBB receptor tyrosine kinase family, including epidermal growth factor receptor (EGFR; HER1/erbB-1), human EGFR-related receptor 2 (HER2; erbB-2/neu), HER3 (erbB-3), and

HER4 (erbB-4), represent a promising strategy for targeted therapy in patients with NSCLC due to observed patterns of oncogenic mutations of EGFR and HER2 [4]. Therefore, targeting the ERbB receptor could be a promising strategy in NSCLC eradication. HER2 overexpression currently serves as a biomarker of poor prognosis in many forms of human cancer and is considered to be responsible for around 11–32% of NSCLC tumors, with increased gene copy numbers recognized in 2–23% of cases. As HER2 overexpression is found to potentiate EGFR signaling, dual inhibition of these two pathways is of great clinical interest [5].

First-generation EGFR tyrosine kinase inhibitors (TKIs) such as gefitinib (2), imatinib (1), lapatinib (4), and erlotinib (3) have been approved by the US Food and Drug Administration (FDA) for treatment of EGFR-activating mutation-positive NSCLC patients (Figure 1). Acquired drug resistance, however, often occurs after approximately 12 months of treatment with gefitinib (2) or imatinib (1) [6,7]. Lapatinib (4), the first dual oral inhibitor of EGFR and HER2, was approved by the FDA in 2007 for patients with advanced or metastatic breast cancer (Figure 1). These drugs bind competitively and reversibly to the adenosine triphosphate (ATP) binding site of EGFR/HER2, achieving target selectivity by identifying unique characteristics of specific ATP-binding features [5–7]. Unfortunately, the ability of these EGFR inhibitors to successfully treat NSCLC is short-lived in subsequent therapies due to acquired T790M missense secondary mutations in EGFR, contributing to drug resistance in around 50% of patients. The mutation of EGFR T790M restores ATP affinity to levels close to those of wild type EGFR, preventing the first generation of TKIs from binding ATP at higher levels. To overcome this resistance, second-generation TKIs, represented by afatinib (5) (Vizimpro™, Pfizer Inc., New York, NY, USA) and neratinib (6) (Nerlynx™, Puma Biotechnology Inc.), were developed. They have been reported to be superior to first-generation EGFR TKIs in cases of EGFR mutation [6,7].

The majority of the second generation has been developed by structure-guided incorporation of an electrophilic moiety into inhibitors possessing binding affinity to the target of interest. This electrophilic moiety is designed to be attacked by the highly nucleophilic sulfhydryl of cysteine residues, forming a covalent bond [8]. Initially, covalent inhibitors will bind noncovalently and, then, if the reactive moiety trajectory is suitable, covalent bond formation will take place, permanently deactivating TK activity. High selectivity is one big benefit of covalent kinase inhibitors. Additionally, the covalency could allow for extension of the pharmacodynamic period without for the need for elevated drug concentrations [9,10]. Despite the therapeutic success of first- and second-generation EGFR TKIs, EGFR-TK mutation-related resistance remains a significant clinical problem. Great effort has been made to develop alternative strategies, resulting in third-generation TKIs. Third-generation irreversible EGFR inhibitors containing a Michael acceptor functional group have been developed in order to resolve the problem of second-generation irreversible inhibitors with limited wild type (WT) EGFR activity. These inhibitors have acquired increased ATP binding through irreversible alkylation of a cysteine residue. However, these irreversible inhibitors have so far demonstrated only partial clinical efficacy, except in a few cases [11]. Recently, however, interest in irreversible TK inhibitors has had a resurgence from a risk–benefit perspective. The reactivity of electrophilic moieties must be tuned to prevent rapid *in vivo* quenching and the formation of protein adducts, ultimately leading to hepatotoxicity and mutagenicity [9,10]. High toxicity and weak binding to mutant kinase are the causes of limited clinical efficacy of third-generation TKIs such as avitinib (7). (Figure 1) C797S mutations have been reported in cell-free plasma DNA samples from patients who acquired resistance [12]. These data indicate that the development of drugs that do not depend on covalent reaction with Cys797 is important for potency or selectivity.

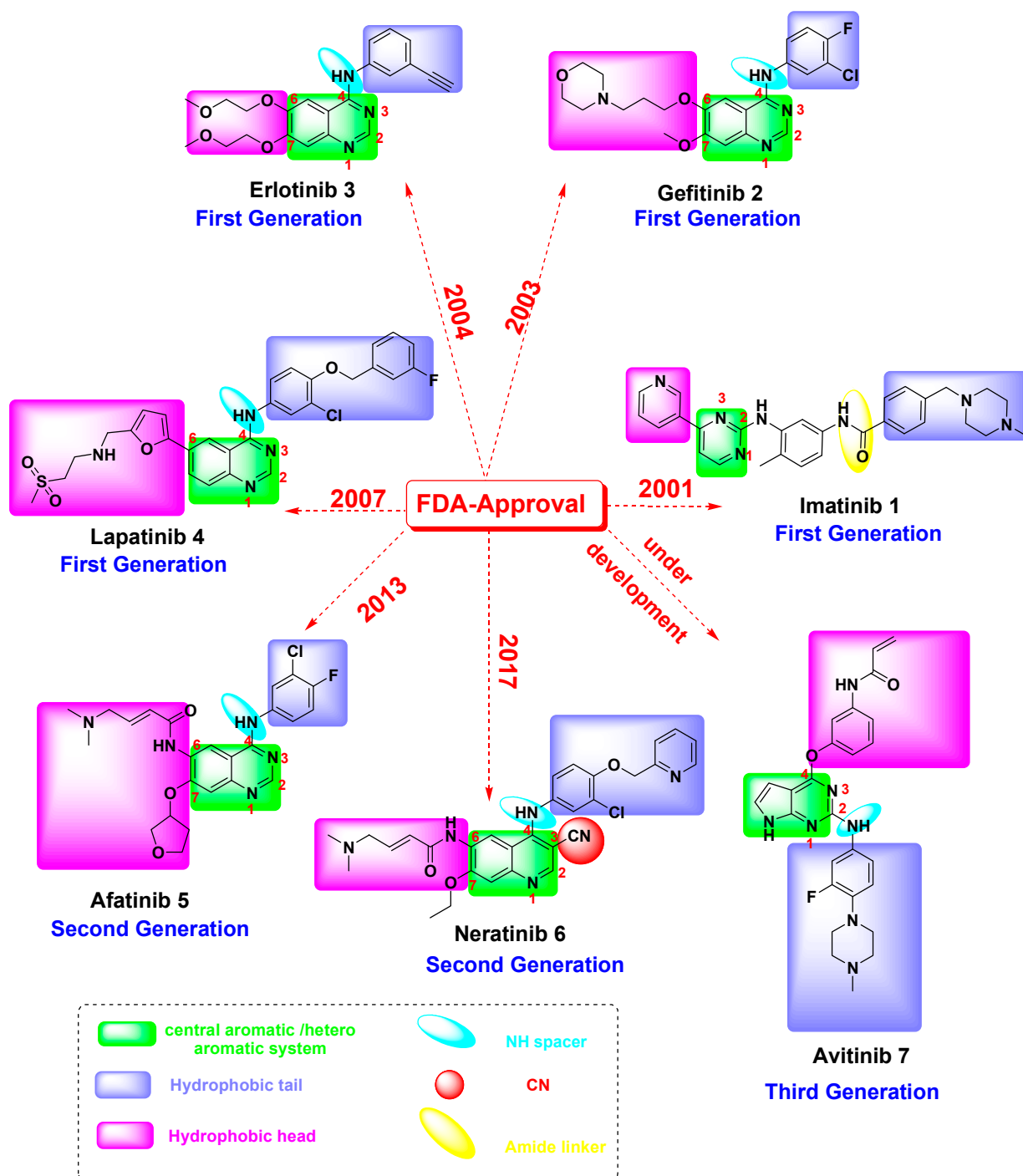


**Figure 1.** Representation of chemical structures of first-, second-, and third-generation tyrosine kinase inhibitors (TKIs).

Recently, it has been proposed that HER2/EGFR heterodimers or HER2/HER2 homodimers trigger a cascade of signal transduction pathways that are responsible for tumor invasion, progression, and metastasis. Therefore, dual EGFR/HER2 inhibition could be more effective than individual EGFR or HER2 inhibition [13]. In view of this, and in continuing the ongoing strategy aimed at developing new scaffolds for the discovery of potent TKIs, in the current study, a new series of thienotriazine and *N*-(3-cyanothiophen-2-yl)acetamide derivatives was designed and chemically synthesized (Figure 2).

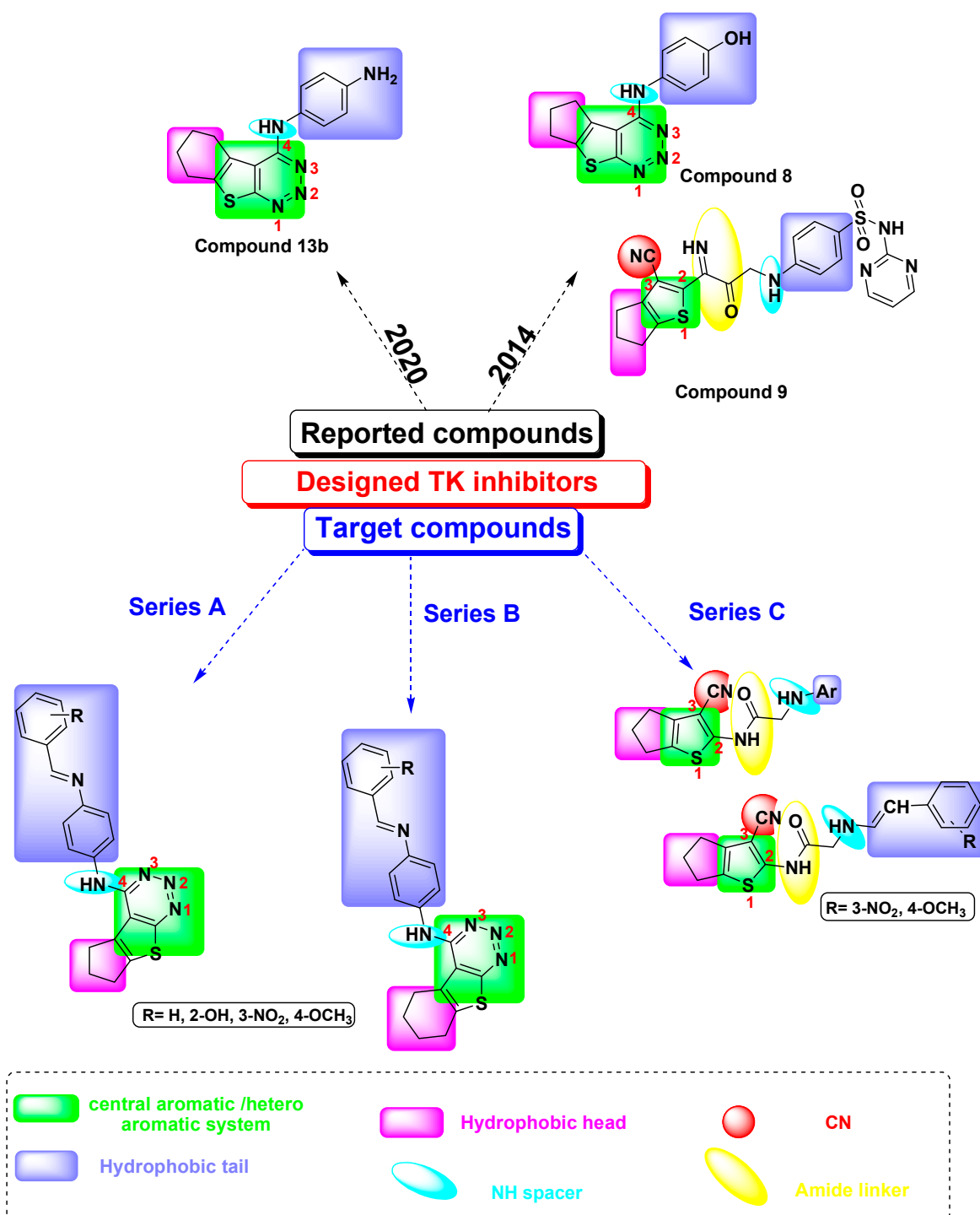


**Figure 2.** Reported and designed derivatives as dual epidermal growth factor receptor (EGFR)/human EGFR-related receptor 2 (HER2) inhibitors targeting H1299.

### Rationale and Design

It was found that most of the quinazoline-based anticancer agents that selectively inhibit EGFR/HER2 overexpression develop resistance over a long course of treatment [14,15]. Thus, there is an urgent need to create novel core structures that could replace this quinazoline core, retaining the advantage of the two nitrogen atoms necessary for binding with key amino acids in kinase active sites. In 2014, a study published by our group

reported the synthesis of a promising thieno[2,3-d][1,2,3]triazine-based structure as an EGFR inhibitor (**8**) with an  $IC_{50}$  of about 38 nM [15]. Moreover, our group designed and synthesized another thiophene-based derivative (**9**) with an  $IC_{50}$  of about 30.8 nM against EGFR (Figure 2) [15]. In 2020, our research group succeeded in designing a novel *m*-phenylenediamine thieno [1–3] triazine derivative (**13b**) as a promising EGFR inhibitor with an  $IC_{50}$  of about 0.33 nM. Compound (**13b**) was targeted to inhibit the growth of the challenging H1299 lung cancer cell line with an  $IC_{50}$  of about 25 nM [16]. This success prompted us to develop a novel series of EGFR/HER2 inhibitors targeting H1299.

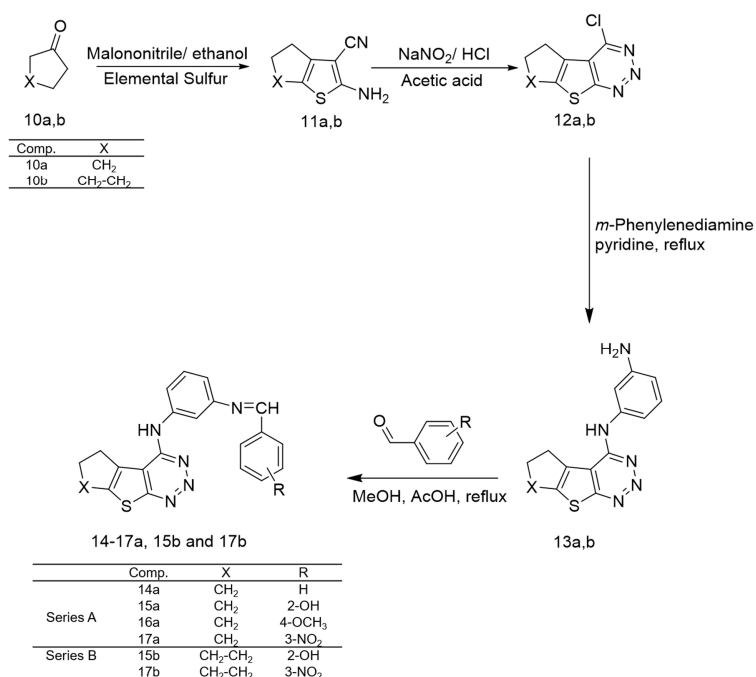
Moreover, it was observed that the structure of the majority of clinically approved TKIs is characterized by a hydrophobic head and hydrophobic tail linked to a central heteroaromatic system and NH spacer, as shown in Figure 1. A literature survey based on the leading dual EGFR/HER2 targeting compounds lapatinib (**4**) and neratinib (**6**) shows that the upper right warhead, or the hydrophobic tail, is essential for potency of kinase inhibition, while the lower left warhead, the hydrophobic head, is crucial for the dual EGFR/HER2 inhibitory activity. Therefore, to design dual TKIs, we kept the 4-aminoaniline with modified substitution at the meta position as the upper right warhead. On the other hand, the lower right warhead serves as an electrophilic moiety for covalent bond formation in the majority of second- and third-generation agents, and owing to the limited clinical benefit and toxicity, the left warhead was modified in the current study to cyclopentyl and/or cyclohexyl (series A and B) in an attempt to abolish the cytotoxicity. In addition, the hinge region of TKIs, which is occupied by the adenine ring of ATP, was modified to be occupied by thienotriazine in series A and B, and tetrahydrobenzothiophene in series C. Modification of the core scaffold was intended to diminish the cellular resistance common with quinazoline and improve the potency based on our previous publication. Another new modification in this study is a change in the position of the upper warhead from position 4 of quinoline and quinazoline in the majority of approved TKIs to position 2 of tetrahydrobenzothiophene, keeping the hydrophobic tail to mimic the dual EGFR/HER2 inhibitors. The cyano group, which is characteristic of neratinib (**6**), was kept at position 3 to mimic N3 of quinazoline-based TKIs. In this way, various regions of ATP-binding sites could be targeted by such substitution patterns on the mutant EGFR protein kinase domain to design molecules that are differentially selective. The design strategies are displayed in Figures 1 and 2.

## 2. Results and Discussion

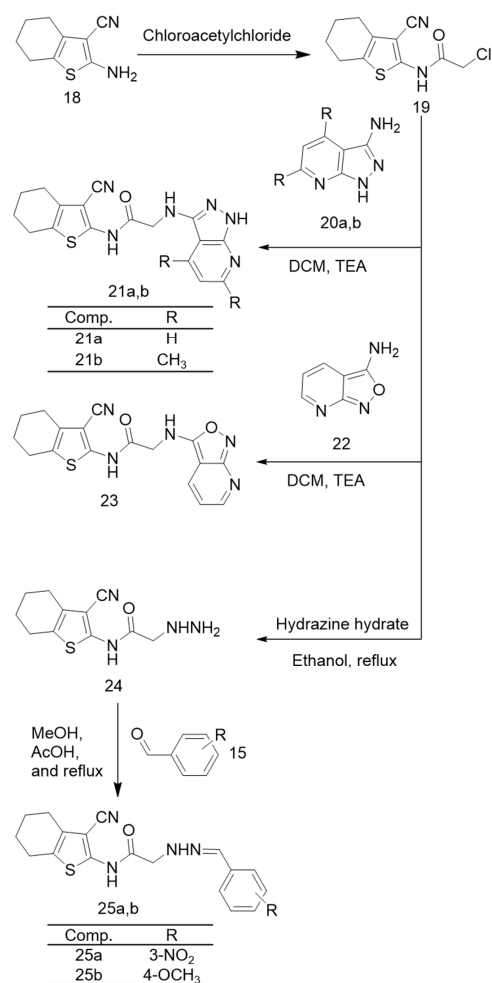
### 2.1. Chemistry

The synthetic methods for series compounds A/B and C were illustrated in Schemes 1 and 2. Compounds (**11–13**) were synthesized as reported in our earlier research [16]. Series A and B compounds were obtained by condensation of compounds (**13a,b**) with different aromatic aldehydes (Scheme 1) [17]. Scheme 2, involving the synthesis of series C, started with the reaction of 2-amino-5,6-dihydro-4H-cyclohexa[b]thiophene-3-carbonitrile (**18**) with chloroacetyl chloride to yield compound (**19**). Then, coupling of compound (**19**) with heteroaryl amines (**20a,b** and **22**) [18] and hydrazine hydrate gave compounds (**21a,b**), (**23**), and (**24**) respectively [19]. The hydrazide derivative (**24**) was condensed with different aromatic aldehydes, yielding compounds (**25a,b**) [17].





**Scheme 1.** Synthesis of dihydrocyclopentathienotriazine and tetrahydrobenzothienotriazine derivatives (series A, B).



**Scheme 2.** Synthesis of tetrahydrobenzothieno-acetamide derivatives (series C).

The structures of the synthesized compounds were confirmed by microanalyses and spectral data (IR,  $^1\text{H}$  NMR, and EI-MS). Mass spectra showed the expected molecular ion peaks. IR spectra of the synthesized compounds (**21a,b**) collectively showed secondary amine signals at around  $3300\text{--}3500\text{ cm}^{-1}$ , which indicates coupling between 2-chloro-*N*-(3-cyano-4,5,6,7-tetrahydrobenzo[*b*] thiophen-2-yl)acetamide (**19**) and heteroaryl amines (**20a,b** and **22**) with the disappearance of signal corresponding to  $\text{NH}_2$ .  $^1\text{H}$  NMR spectra of compounds (**14–17a**) showed multiple peaks of aromatic protons in the range of 7.80 to 8.70  $\delta$  (ppm) and a single peak for CH proton in the range of 7.4 to 8.4  $\delta$  (ppm). The spectrum of compound (**15a**) showed a single peak corresponding to OH proton at 10.15  $\delta$  (ppm), and the spectrum of compound (**16a**) showed a single sharp peak at 4.06  $\delta$  (ppm) corresponding to the  $\text{OCH}_3$  group of anisaldehyde. A single peak for CH proton appeared at 7.85  $\delta$  (ppm) and 7.64  $\delta$  (ppm) for compounds (**15b**) and (**17b**), respectively. The  $^1\text{H}$  NMR spectrum of compound (**15b**) showed a single peak corresponding to OH proton at 8.25  $\delta$  (ppm). The  $^1\text{H}$  NMR spectrum of compound (**21a**) showed the appearance of single peak at 11.88  $\delta$  (ppm) and multiple peaks at 6.95  $\delta$  (ppm) corresponding to NH proton and three aromatic protons of heteroarylamine, respectively. The NH proton of the coupling reaction appeared as a single peak at 3.65  $\delta$  (ppm). Another single peak belonging to proton of NH of thiophene appeared at 5.49  $\delta$  (ppm). Finally, a single sharp peak accounting for  $\text{CH}_2$  appeared at 3.08  $\delta$  (ppm). The  $^1\text{H}$  NMR spectrum of compound (**21b**) showed the appearance of single peaks at 11.69 and 6.58  $\delta$  (ppm), corresponding to NH proton and single aromatic proton of the heteroaryl amine, respectively. A single peak for NH proton of thiophene appeared at 5.01  $\delta$  (ppm) and a sharp peak of  $\text{CH}_2$  appeared at 3.65  $\delta$  (ppm). The spectrum also showed two single sharp peaks for the two methyl groups of the heteroarylamine at 2.42 and 2.54  $\delta$  (ppm).

## 2.2. Biological Evaluation

### 2.2.1. In Vitro Cytotoxic Activity against H1299 Cell Line

The in vitro cytotoxic activities of the synthesized compounds (**13–25a,b**) were measured using sulfo-rhodamine B (SRB) assay [20] against the NSCLC cell line H1299 and gefitinib (**2**) as a reference drug. This cancer cell line has high expression of EGFR and HER2 enzymes [3]. As seen in Table 1, the results revealed that the synthesized compounds showed versatile antitumor activity against the tested cell line. The synthesized compounds (**13–25a,b**) showed  $\text{IC}_{50}$  values in the range of 12 to 54 nM, superior to that of gefitinib (**2**) at 40  $\mu\text{M}$ . Compound (**21a**) was the most potent, with  $\text{IC}_{50} = 12.5\text{ nM}$ , followed by compound (**21b**), with  $\text{IC}_{50} = 13.68\text{ nM}$ . The viability curve of compound (**21a**), with the most potent anticancer activity, is displayed in Figure 3.

**Table 1.** In vitro cytotoxic activity of compounds (**13–25a,b**) against non-small cell lung cancer (NSCLC) cell line H1299.

Compound No.	$\text{IC}_{50}$ against H1299
<b>13a</b>	28.79 nM
<b>14a</b>	25.68 nM
<b>15a</b>	32.81 nM
<b>16a</b>	34.91 nM
<b>17a</b>	54.80 nM
<b>13b</b>	25 nM
<b>15b</b>	34.00 nM
<b>17b</b>	38.13 nM
<b>21a</b>	12.50 nM
<b>21b</b>	13.68 nM
<b>23</b>	18.41 nM
<b>25a</b>	18.53 nM
<b>25b</b>	18.47 nM
Gefitinib ( <b>2</b> )	40 $\mu\text{M}$

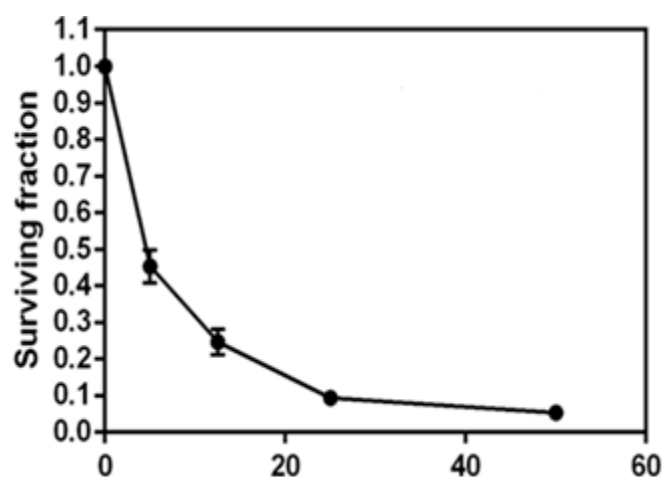


**Figure 3.** Viability curve of compound (21a), with cytotoxic activity against H1299 NSCLC cell line.

### 2.2.2. EGFR and HER2 Kinase Inhibitory Assay

The most active compound (21a) was chosen for further evaluation of in vitro EGFR and HER2 kinase inhibitory activity. The results showed that the  $IC_{50}$  values of compound (21a) were 0.47 and 0.14 nM against EGFR and HER2, respectively. This is superior to the value of gefitinib (2) against EGFR (1.9 nM). It is comparable to  $IC_{50}$  values for imatinib (1) 0.11 nM against EGFR and 0.06 nM against HER2 (Table 2).

**Table 2.** In vitro inhibitory activity of compound 21a against EGFR and HER2 enzymes.

Compound No.	$IC_{50}$ against EGFR (nM)	$IC_{50}$ against HER2 (nM)
(21a)	0.47	0.14
Gefitinib (2)	1.9	–
Imatinib (1)	0.11	0.06
Neratinib (6)	92 [21]	59 [21]

### 2.3. Molecular Modeling

#### 2.3.1. Molecular Docking

Computer-aided simulation of drug design saves effort, time, and energy compared to conventional methods of drug production. Molecular-based drug design was proposed in order to predict the possible interactions of the target compounds with EGFR/HER2. Using Glide in the Schrodinger program for docking, the modulation activity of erlotinib (3) and afatinib (5) derivatives against the EGFR/HER2 receptor was determined, as shown in Figure 4. The designed compounds were docked into the ATP-binding pocket as a thienotriazine and tetrahydrobenzothiophene scaffold, mimicking the ATP adenine ring occupying the hinge region motif of TKs. The positions of thienotriazine (14a), tetrahydrobenzothiophene (21a), erlotinib (3), and afatinib (5) were similar, which implies that they might share the same biological activity. The docking results show, in detail, that the designed TKI formed hydrogen bonds, hydrophobic contacts, and hydrophobic–hydrophilic interactions with the target TKs. N1 of the triazine motif in series A and B could act as a hydrogen bond acceptor and form hydrogen bonds with MET769 (distance 2.4 Å, angle 143.6) in the hinge region, mimicking the N1 of quinazoline in the approved drug erlotinib (3) (distance 2.2 Å, angle 135.7). In series C, a tetrahydrobenzothiophene scaffold occupied the hinge region in the same position of quinazoline, forming a hydrogen bond with crystal water, mimicking the N3 of erlotinib’s quinazoline. The phenyleneimine and pyrazolopyridine moieties deeply penetrated the hydrophobic pocket, forming hydrophobic–hydrophobic, Van der Waals, and  $\pi$ – $\pi$  interactions with key amino acids such as ALA719, ILE720, MET742, LEU753, and LEU764, mimicking the phenylacetylene of erlotinib (3). Modifying these moieties, such as by adding hydroxy, nitro, or methoxy groups, could enhance affinity

through the formation of hydrogen bonds with GLU738 and LYS721. The incorporation of CN at position 3 of tetrahydrobenzothiophene could confer series C with a certain superiority by forming hydrophobic interactions with LEU694 and VAL702. Extra precision glide docking of compounds (**14a**) and (**21a**) with the active domain of EGFR showed reasonable docking scores of  $-6.78$  and  $-7.69$  and glide E-model values of  $-64.6$  and  $-71.2$  kcal mol $^{-1}$ , respectively.

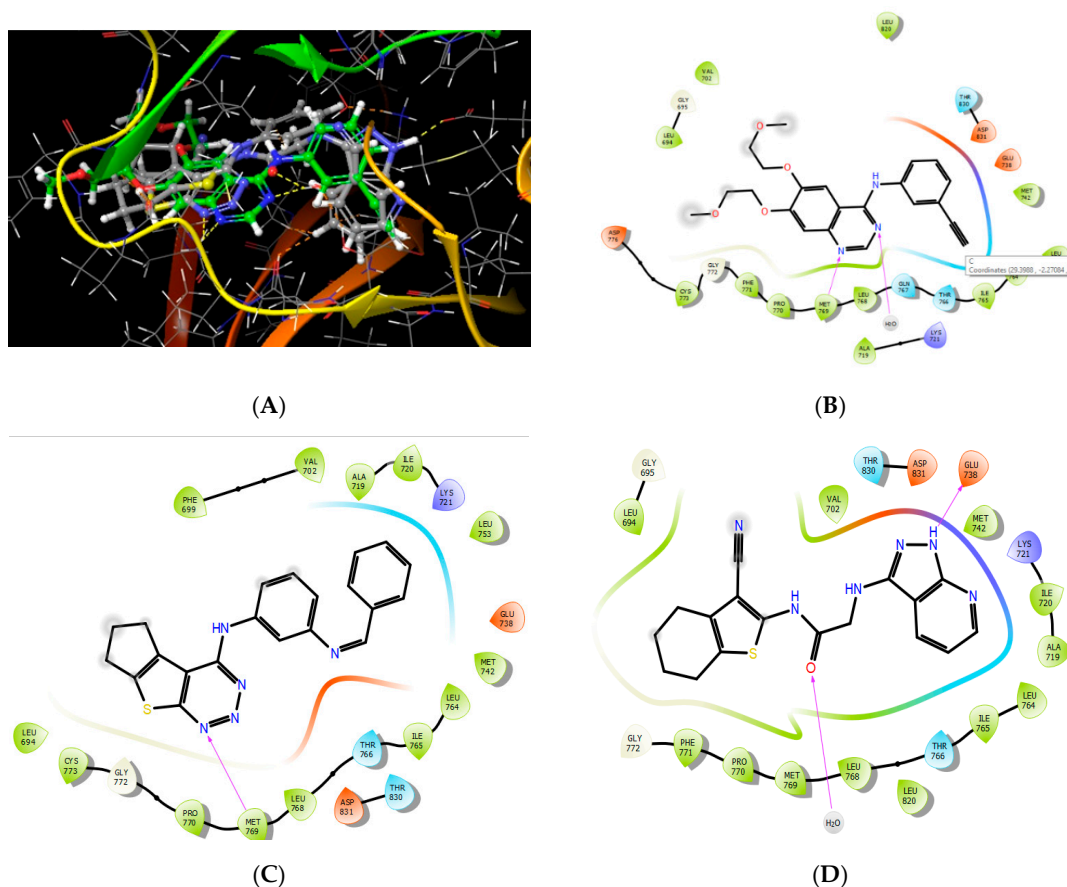


**Figure 4.** (A) Three-dimensional binding modes and overlay of erlotinib (**3**), compound (**14a**), and compound (**21a**) in the catalytic domain of EGFR (PDB 1M17). (B) 2D representation of erlotinib (**3**) in the EGFR catalytic domain. (C) 2D representation of compound (**14a**) in the EGFR catalytic domain. (D) 2D representation of compound (**21a**) in the EGFR catalytic domain.

On the other hand, the docking study of the designed compounds in human HER2 showed high affinity of these compounds toward this receptor. Thienotriazine and tetrahydrobenzothiophene occupied the hinge region, forming hydrogen bonds with the MET803 and water molecules there, as shown in Figure 5. Additionally, the hydrophobic heads in the upper right position of series A and B and at position 2 of series C deeply penetrated the hydrophobic pocket in HER2, forming hydrogen bond, hydrophobic, Van der Waals, and  $\pi$ - $\pi$  interactions. The inclusion of large substitutions was intended to improve the affinity of the designed compounds toward HER2, generating dual-acting compounds mimicking lapatinib (**4**) and neratinib (**6**). The extra precision docking score and glide energy showed the highest affinity of the design compounds compared to lapatinib (**4**) and neratinib (**6**). For (**15a**) and (**21a**), the docking scores were  $-10.5$  and  $-8.8$ , and the glide energy values were  $-81.4$  and  $-77.03$  kcal mol $^{-1}$ , respectively. These values are higher than those of lapatinib (**4**) ( $-7.8$  and  $-79.8$  kcal mol $^{-1}$ ) and neratinib (**6**) ( $-4.3$  and  $-52.6$  kcal mol $^{-1}$ ). These results are in agreement with those of in situ and in vitro screening studies.

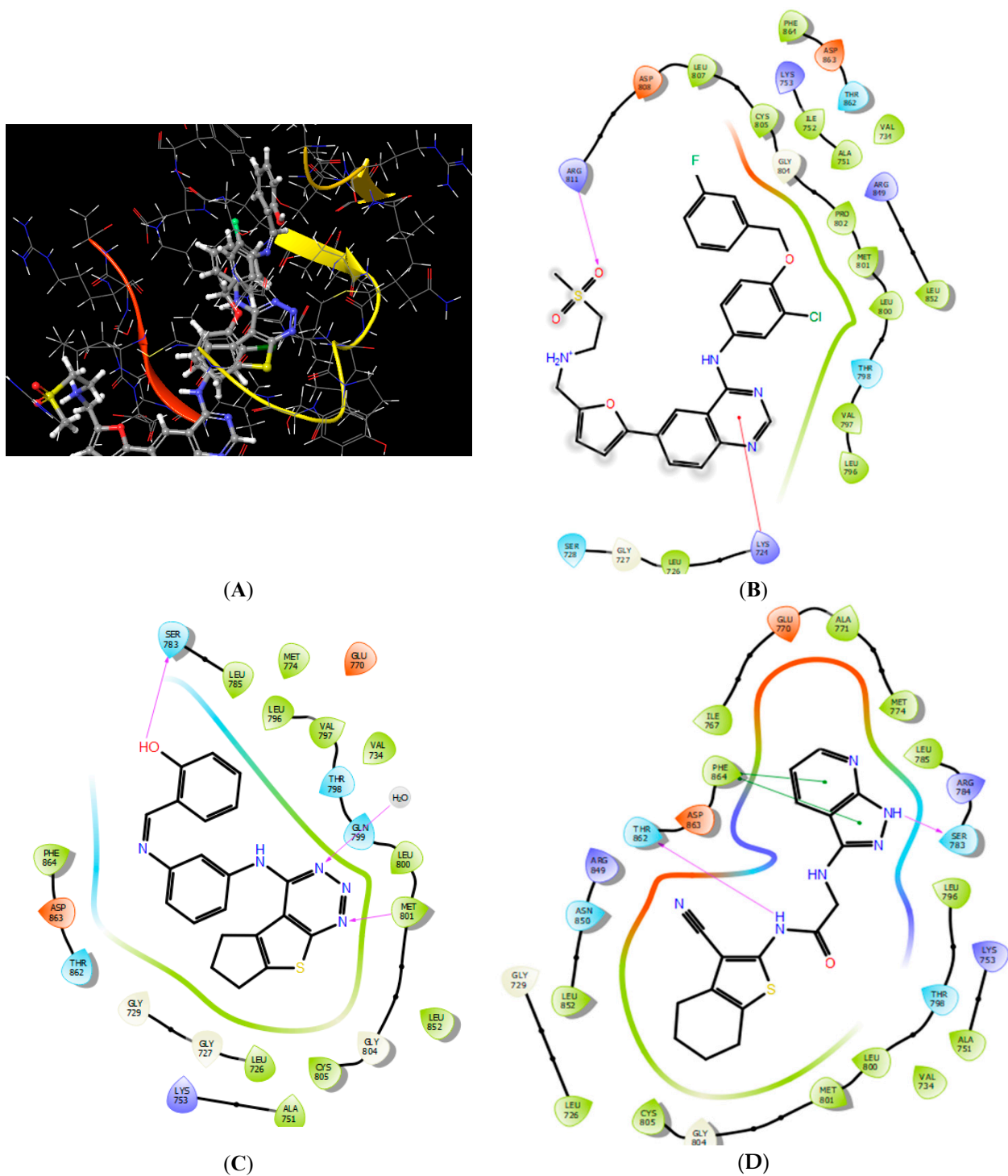


**Figure 5.** (A) Three-dimensional binding modes and overlay of lapatinib (4), compound (15a), and compound (21a) in the catalytic domain of HER2 (PDB 3PP0). (B) 2D representation of lapatinib (4) in the catalytic domain of HER2. (C) 2D representation of compound (15a) in the catalytic domain of HER2. (D) 2D representation of compound (21a) in the catalytic domain of HER2.

Acquired drug resistance normally develops after about 12 months of treatment with gefitinib (2) or erlotinib (3), which is attributed to secondary T790M mutation. To confirm the benefits of the designed compounds in terms of their affinity toward mutated TKs, the molecular docking study was extended to include mutated T790M protein (PDB 4G5P), as shown in Figure 6. The designed compounds occupied the same position as afatinib

(5). The amide link at position 2 of the thiophene ring and the cyano group at position 3 of the highest potent compound (**21a**) formed a hydrogen bond (2.01 Å, angle 108.9) with MET793 in the hinge region, mimicking the hydrogen bond of N1 of the quinazoline ring in afatinib (**5**) (2.19 Å, angle 116.8). Pyrazolopyridine participated in hydrophobic interactions, enforcing the binding affinity. The electrophilic moiety and hydrophobic tail at the left side of quinazoline formed extra hydrogen bonds, hydrophobic interactions, and covalent bonds with CYS797. Extra precision glide docking of compounds (**14a**) and (**21a**) with the active domain of T790M EGFR showed reasonable docking scores of  $-7.7$  and  $-7.5$  and glide E-model values of  $-72.12$  and  $-66.88$  kcal mol $^{-1}$ , respectively. These values were not as high as to those of afatinib (**5**) ( $-10.5$  and  $-103.4$  kcal mol $^{-1}$ ); however, they might better than those of lapatinib (**4**) ( $-6.2$  and  $-87.2$  kcal mol $^{-1}$ ).

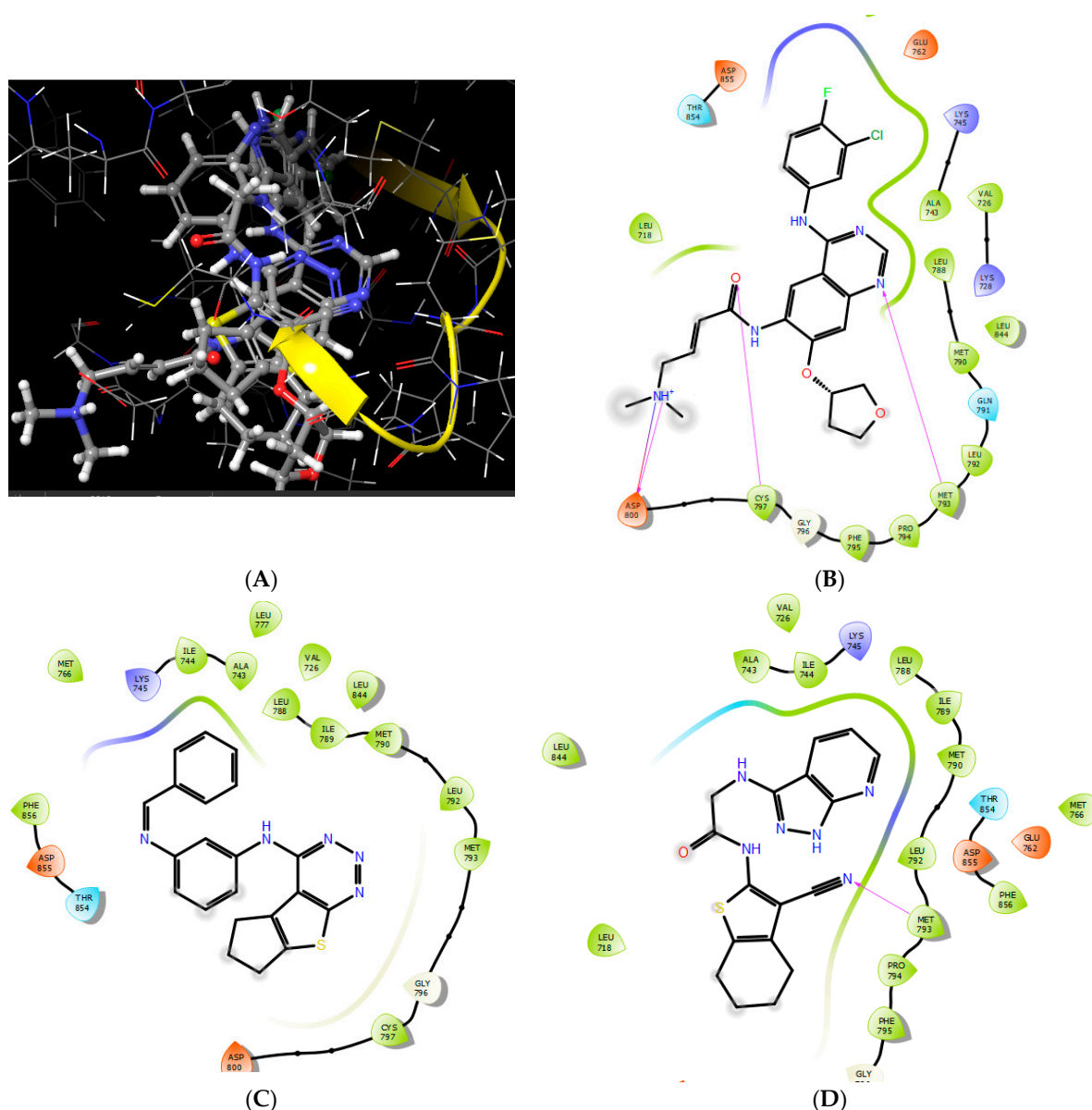


**Figure 6.** (A) Three-dimensional binding modes and overlay of afatinib (**5**) and compounds (**14a**) and (**21a**) in the catalytic domain of T790M EGFR (PDB 4G5P). (B) 2D representation of afatinib (**5**) in the catalytic domain of T790M EGFR. (C) 2D representation of compound (**14a**) in the catalytic domain of T790M EGFR. (D) 2D representation of compound (**21a**) in the catalytic domain of T790M EGFR.

### 2.3.2. Physicochemical Properties and In Silico ADME Prediction

The pharmacokinetic properties of drug-like molecules are primarily determined by the physicochemical properties of the designed molecules, such as solubility in aqueous solution, lipophilicity, hydrogen bonding capability, polar surface area, chemical stability, etc. Significantly, the physicochemical properties of a compound are the key to turning a biologically active compound into a therapeutically effective drug [16]. Therefore, our promising novel compound (**21a**) and moderately active compound (**15a**) were subjected to prediction of physicochemical properties using ADME predictions made by the QikProp v4.3 function of Schrodinger 10-1 prior to in vivo studies, with the licensed drug lapatinib (**4**) used as a reference compound. According to the QikProp suite, polar surface area (PSA), partition coefficient (log PO/W), and number of rotatable bonds were predicted in order to test the possible drug-like properties of compounds. As seen in Table 3, compounds (**15a**) and (**21a**) exhibited appropriate physicochemical properties compared to lapatinib (**4**). Caco-2 cell permeability (QPPCaco) was used as a marker for intestinal absorption or permeation. Compound (**15a**) showed a high partition coefficient and, consequently, the highest cell permeability. The most active compound (**21a**) and compound (**15a**) might be considered as promising lead molecules for designing potent EGFR inhibitors with excellent membrane permeability and oral bioavailability.

**Table 3.** In Silico ADME prediction parameters of designed and reference molecules.

ADME Prediction Parameters	Compound (15a)	Compound (21a)	Lapatinib (4)
mol MW <sup>a</sup>	371.4	352.1	581.06
Donor-HB <sup>b</sup>	1	2.25	1
Accept-HB <sup>c</sup>	5	5.7	8.25
QPlogPo/w <sup>d</sup>	4.3	2.4	6.3
PSA <sup>e</sup>	62.2	116.8	95.35
QPlogS <sup>f</sup>	-5.6	-6.2	-8.2
QPPCaco <sup>g</sup>	1143.7	96.8	187.5
QPlogBB <sup>h</sup>	-0.6	-1.9	0.8
QPPMDCK <sup>i</sup>	1080	59.5	376.5
QPlogKhsa <sup>j</sup>	0.55	0.26	1.19
#rotor <sup>k</sup>	5	5	10
% Human Oral Absorption <sup>l</sup>	100	76.9	78.8

Acceptable ranges: <sup>a</sup>: mol MW (molecular weight) < 500 amu; <sup>b</sup>: Donor-HB (hydrogen bond donor) < 5; <sup>c</sup>: Accept-HB (hydrogen bond acceptor) < 10; <sup>d</sup>: QPlogPo/w (octanol/water partition coefficient) < 5; <sup>e</sup>: PSA (Van der Waals surface area of polar nitrogen and oxygen atoms) = 7–200; <sup>f</sup>: QPlogS (Conformation-independent predicted aqueous solubility) < 0.5; <sup>g</sup>: QPPCaco (Caco-2 cell permeability) ≤ 5; <sup>h</sup>: QPlogBB (Predicted brain/blood partition coefficient) < 25 poor, h > 500 great; <sup>i</sup>: QPPMDCK (Predicted apparent MDCK cell permeability in nm/s. MDCK cells are considered to be a good mimic for the blood–brain barrier) < 25 poor, i > 500 great; <sup>j</sup>: QPlogKhsa (Prediction of binding to human serum albumin) = -1.5 to 1.5; <sup>k</sup>: rotatable bond = 0–15, <sup>l</sup>: % Human Oral Absorption (Predicted qualitative human oral absorption) > 80% is high, l < 25% is poor [16].

### 2.3.3. Molecular Orbital Energy Study and Molecular Electrostatic Potential (MESP)

A molecular electrostatic potential (MESP) map is a useful tool for understanding the sites for nucleophilic reactions, electrophilic attacks, and intermolecular interactions. Additionally, it widely used for the detection of iso-surface values, showing the locations of positive and negative electrostatic potential of designed compounds [16]. The MESP values of compounds (**21a**) and lapatinib (**4**) are shown in Figure 7. Red indicates the most electronegative region, blue the most electropositive region, and green the region of zero potential. The nitrogen atoms of quinazoline and aniline and the oxygen group of the furan ring of lapatinib (**4**) have a greater negative charge surrounded by some carbon atoms with greater positive charge. Thus, electrophilic attack and nucleophilic interaction with the receptor are more favorable for these parts of lapatinib (**4**). The remaining parts of

the structure are shown in green, which means they can bind through hydrophobic and Van der Waals interactions. In the same manner, the electronegative and electropositive regions of the designed compounds are located around 3-cyanotetrahydrothiophen and pyrazolopyridine, making these regions better able to interact with charged parts of the EGFR/HER2 receptors. The electronegative region around pyrazolopyridine distinguished it somewhat from lapatinib (4), which lacks this. The docking study showed that the designed compounds have higher affinity toward EGFR/HER2 compared to lapatinib (4). Therefore, we attributed the high affinity and biological activity observed in the in vitro study to the inclusion of a heterocyclic rather than aromatic system in this region that is common in TKIs.

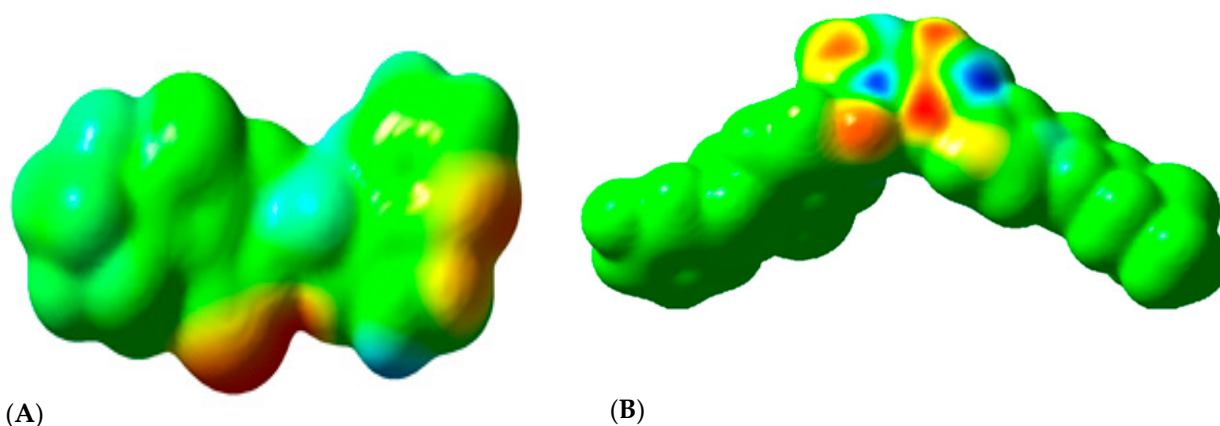


**Figure 7.** Molecular electrostatic potential mapping for (A) the most potent compound (21a) and (B) lapatinib (4) from density functional theory (DFT) calculations. Green indicates zero potential regions, blue indicates electropositive regions, and red indicates electronegative regions.

Moreover, the Mulliken atomic charges (Figure 8) are in agreement with the MESP results. The negative charge is mainly located on nitrogen atoms of the quinazoline of lapatinib (4) and on the cyano group and nitrogen of the amide link and nitrogen atoms of pyrazolopyridine in the most potent compound (21a). The highest negative charge in both lapatinib (4) and the representative compound give this atom the highest reactivity in the interaction with EGFR and HER2 receptors.

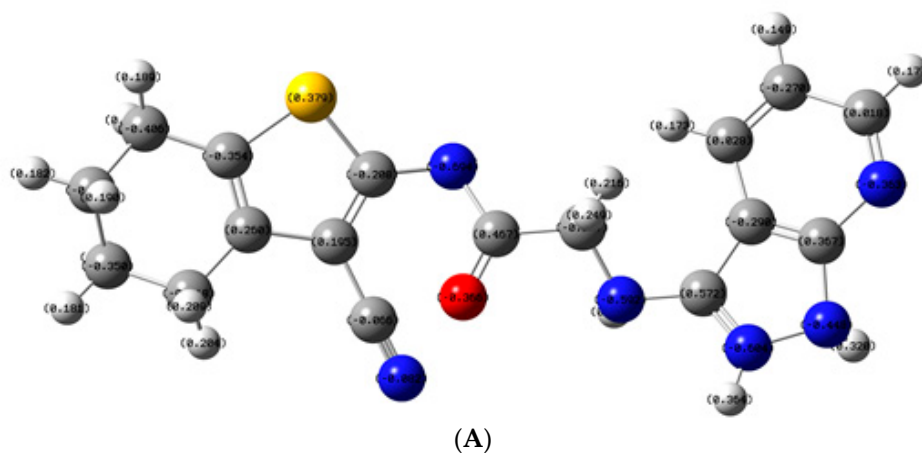


**Figure 8.** Cont.



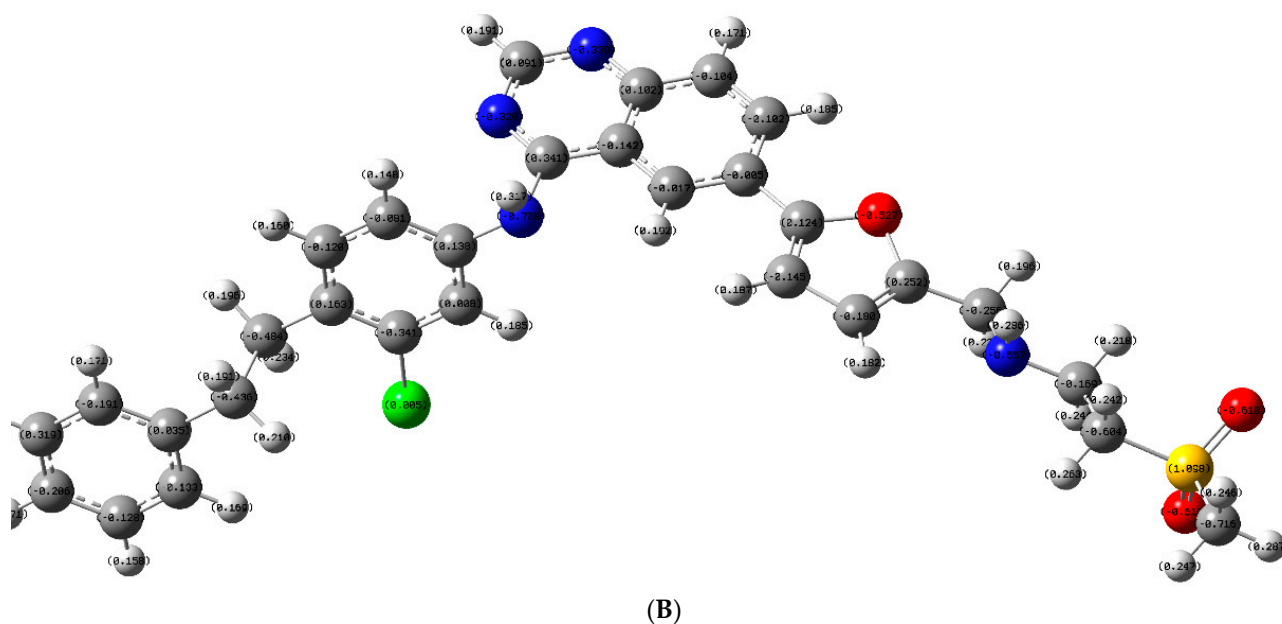


**Figure 8.** Mulliken atomic charges for (A) the most potent compound (21a) and (B) lapatinib (4).

The highest occupied molecular orbital (HOMO) and lowest unoccupied molecular orbital (LUMO) maps of the representative compound (21a) and lapatinib (4) are shown in Figure 9. On the one hand, it was observed that the electrons were delocalized on quinazoline, aniline, furan, and amino moieties in the HOMO map, whereas on the LUMO map, the electrons are mainly delocalized on quinazoline and aniline groups. On the other hand, the HOMO and LUMO maps of the target compounds are delocalized around the 3-cyanothiophene and amide linkage. The frontier molecular orbitals are mainly delocalized on the moieties or groups that mainly participate in drug–receptor interaction. Therefore, we can conclude that the biological activity might be facilitated via the quinazoline moiety of lapatinib (4) and the 3-cyanothiophene moiety of the designed compound through hydrophobic, hydrophilic, Van der Waals, and  $\pi$ – $\pi$  interactions or via hydrogen bond formation with key amino acids in the catalytic domain. The LUMO map and part of the HOMO map of the designed compounds and lapatinib (4) are concentrated on 3-cyanothiophene and quinazoline, making these moieties superior in drug–receptor interaction. Besides this, the amide linkage also participated in this interaction. The results of density functional theory (DFT) study are in accordance with those of the docking and in vitro cytotoxicity studies. Gaussian 09 software (Gauss View 5.0, Gaussian, Inc., Wallingford, CT, USA) was utilized for all computational calculation.

TK proteins are ATP-dependent, and the ATP-binding domain is conserved in TKs and serves as the receptor for anticancer agents. The discovery of novel inhibitors is focused mainly on searching for compounds containing the proper chemical moieties that can fulfill the requirements for interaction with the adenine-binding site (hinge region); 4-anilinoquinoline and/or quinazoline are features common in several approved TKIs. However, it was found that for most of the quinazoline-based anticancer agents that selectively inhibit EGFR/HER2 overexpression, resistance is developed over long courses of treatment. The discovery of a novel core structure with various substitutions at different positions is thus of great importance.

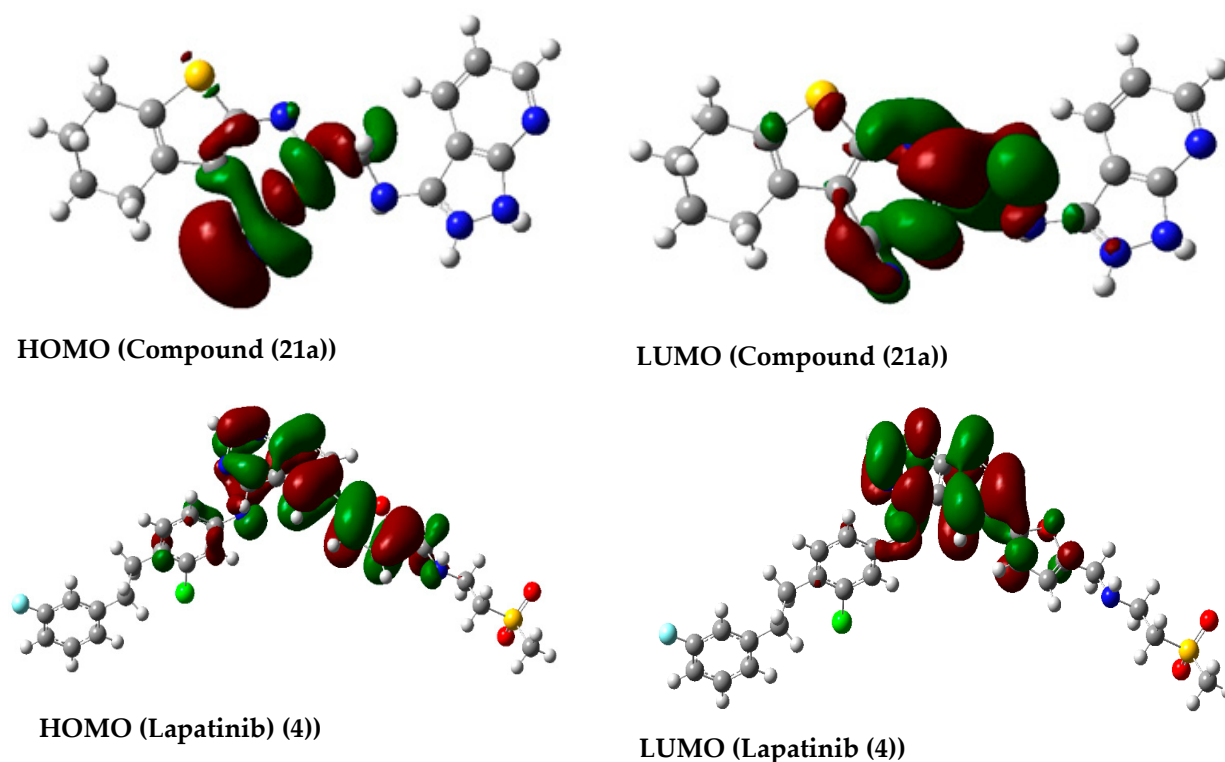


**Figure 9.** Highest occupied molecular orbital (HOMO) and lowest unoccupied molecular orbital (LUMO) maps for compound (21a) and lapatinib (4) from DFT calculations. Green indicates positive molecular orbital and red indicates negative molecular orbital.

In this study, and based on our previous publication, thienotriazine and 3-cyanotetrahydrobenzothiothiophene were selected as the core scaffold to design novel dual-acting EGFR/HER2 drug-like molecules. The designed compounds displayed promising in situ cytotoxicity against H1299 NSCLC and in vitro activity against EGFR and HER2, comparable to the approved TKIs imatinib (1) and gefitinib (2). The molecular modeling along with the computational studies revealed the significance of the two core moieties—thienotriazine and 3-cyanotetrahydrobenzothiothiophene, which functioned as the adenine of ATP in the hinge region, forming hydrogen bonding interactions. Modifying the upper right hydrophobic head through the addition of some heterocyclic systems (pyrazolopyridine and isoxazolopyridine) resulted in superior activity of the designed compound compared with the approved dual-acting drug lapatinib (4). Heterocyclic systems succeeded in forming extra hydrogen bonding in addition to the hydrophobic interaction in the hydrophobic region. The red electronic map of MESP and the highly negative charge localized in these systems, shown by Mulliken charge distribution, potentiated the merit of these moieties. Furthermore, alteration in the position of the substitution from position 4 on quinazoline in the common approved TKI drugs to position 2 in our series C enforced the potency and conferred to the designed compounds a certain benefit in strongly interacting with TKs at different sites. Molecular modeling also revealed that these modifications increased the interaction of the designed compounds with the protein kinase harboring the T790M mutation, which is responsible for acquired drug resistance. Figure 10 can summarize the cytotoxic activity of the designed molecules based on the observed structure–activity relationships (SAR).

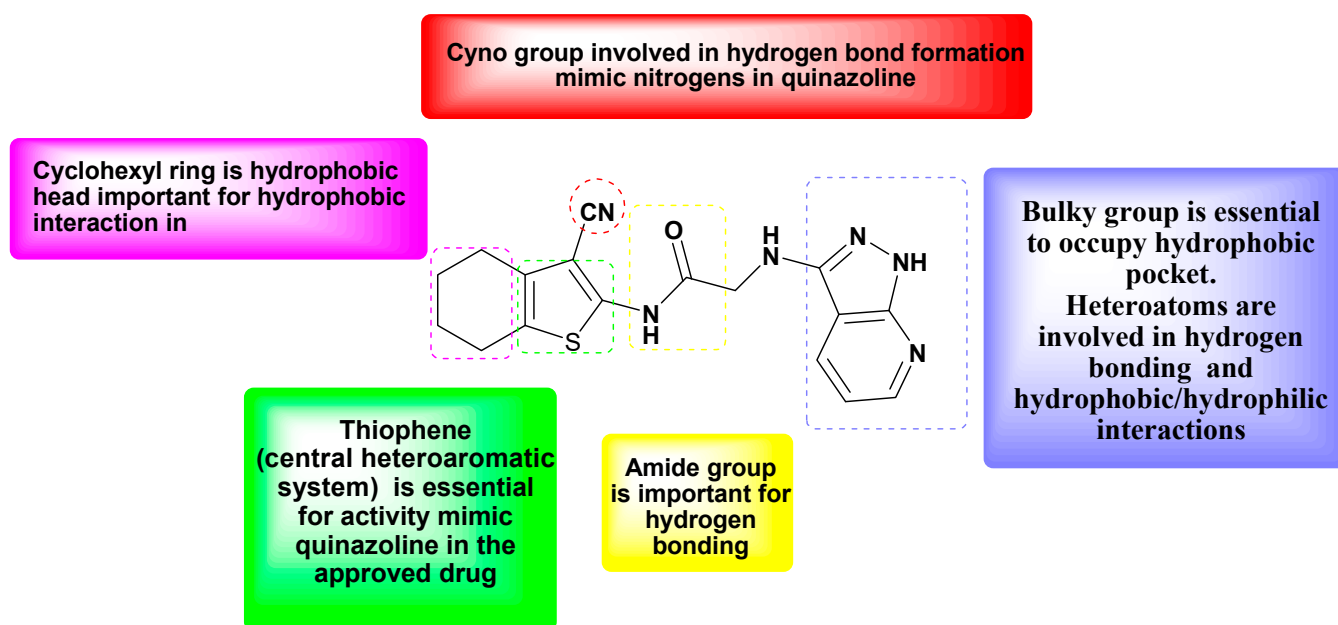


**Figure 10.** The observed structure–activity relationships of the designed molecules as promising dual EGFR/HER2 inhibitors.

### 3. Materials and Methods

#### 3.1. Instrument

The Varian Mercury Vx 300 NMR spectrometer or JEOL LA (300 MHz for  $^1\text{H}$  NMR) were used to measure  $^1\text{H}$  NMR spectra. Electron impact mass spectra (EI-MS) were recorded on a Shimadzu GCMS-QP 5050A gas chromatograph mass spectrometer (70 eV). Melting points were calculated in open capillaries using a Gallenkamp melting point apparatus and are uncorrected. Infrared (IR) spectra were recorded on a Shimadzu FT-IR 8101 PC IR spectrophotometer (KBr pellets).

#### 3.2. Chemicals and Reagents

Commercial chemicals and solvents of reagent grade were used directly in synthesis without further purification.

#### 3.3. Experimental

##### Chemistry

##### General procedure for synthesis of compounds (14a–17a)

A mixture of 3-(5,6-dihydro-7H-cyclopenta[4:5]thieno[2,3-d][1,2,3]triazin-4-ylamino)benzene-1,3-diamine (**13a**) [16] (0.01 mol) and suitable aromatic aldehyde (0.01 mol) in methanol (20 mL) in the presence of a catalytic amount of glacial acetic acid was refluxed for 5 h, with the progression of reaction monitored using TLC. The solvent was removed under reduced pressure, and the product recrystallized from chloroform [17].

##### 3-(5,6-Dihydro-7H-cyclopenta[4:5]thieno[2,3-d][1,2,3]triazin-4-ylamino)-N-benzylidenebenzene-1,3-diamine (14a)

Mass spectrum:  $m/z$  (%): 371 ( $\text{M}^+$ , 1.50%), 361 (1.33%), 353 (1.21%), 343 (7.82%), 316 (11.55%), 108 (100%). IR ( $\text{cm}^{-1}$ ): 752 (C–S), 1261 (C–N), 1624 (C=N), 3429 (N–H).  $^1\text{H}$  NMR (DMSO, 300 MHz):  $\delta$  (ppm) 1.29 (m, 2H), 3.08 (t, 2H), 3.27 (t, 2H), 7.08 (m, 8H), 7.71 (s, 1H), 7.80 (s, 1H), 11.81 (s, 1H). Elemental analysis calculated for  $\text{C}_{21}\text{H}_{17}\text{N}_5\text{S}$ : C, 67.90; H, 4.61; N, 18.85. Found: C, 68.09; H, 4.66; N, 19.08.

##### 3-(5,6-Dihydro-7H-cyclopenta[4:5]thieno[2,3-d][1,2,3]triazin-4-ylamino)-N-(2-hydroxybenzylidene)benzene-1,3-diamine (15a)

Mass spectrum:  $m/z$  (%): 387 ( $\text{M}^+$ , 0.76%), 375 (2.45%), 347 (6.59%), 345 (9.14%), 212 (85.96%), 119 (100%). IR ( $\text{cm}^{-1}$ ): 756 (C–S), 1149 (C–O), 1276 (C–N), 1616 (C=N), 3221

(N–H), 3352 (OH). <sup>1</sup>H NMR (DMSO, 300 MHz):  $\delta$  (ppm) 1.14 (m, 2H), 2.12 (t, 2H), 2.73 (t, 2H), 4.54 (s, 1H), 7.84 (m, 7H), 7.90 (s, 1H), 8.52 (s, 1H), 10.15 (s, 1H). Elemental analysis calculated for C<sub>21</sub>H<sub>17</sub>N<sub>5</sub>OS: C, 65.10; H, 4.42; N, 18.08. Found: C, 65.34; H, 4.47; N, 18.39.

**3-(5,6-Dihydro-7H-cyclopenta[4:5]thieno[2,3-d][1,2,3]triazin-4-ylamino)-N-(3-nitrobenzylidene)benzene-1,3-diamine (16a)**

Mass spectrum:  $m/z$  (%): 401 (M<sup>+</sup>, 3.10%), 389 (79.4%), 362 (1.80%), 322 (1.20%), 293 (2.40%), 261 (1.50%), 249 (100%). IR (cm<sup>-1</sup>): 690 (C–S), 1246 (C–O–C), 1261 (C–N), 1678 (C=N), 3444 (N–H). <sup>1</sup>H NMR (DMSO, 300 MHz):  $\delta$  (ppm): 1.15 (m, 2H), 3.65 (t, 2H), 3.70 (t, 2H), 4.06 (s, 3H), 7.30 (m, 7H), 7.85 (s, 1H), 8.70 (s, 1H), 10.20 (s, 1H). Elemental analysis calculated for C<sub>22</sub>H<sub>19</sub>N<sub>5</sub>OS: C, 65.81; H, 4.77; N, 17.44. Found: C, 66.04; H, 4.84; N, 17.68.

**3-(5,6-Dihydro-7H-cyclopenta[4:5]thieno[2,3-d][1,2,3]triazin-4-ylamino)-N-(4-methoxybenzylidene)benzene-1,3-diamine (17a)**

Mass spectrum:  $m/z$  (%): 416 (M<sup>+</sup>, 0.88%), 407 (2.47%), 403 (2.56%), 376 (4.56%), 222 (12.24%), 108 (100%). IR (cm<sup>-1</sup>): 732 (C–S), 1350 (NO<sub>2</sub>), 1527 (NO<sub>2</sub>), 1612 (C=N), 3363 (N–H). <sup>1</sup>H NMR (DMSO, 300 MHz):  $\delta$  (ppm): 1.80 (m, 2H), 2.62 (t, 2H), 2.64 (t, 2H), 4.80 (s, 1H), 7.28 (m, 6H), 7.31 (s, 1H), 7.34 (s, 1H), 8.50 (s, 1H). Elemental analysis calculated for C<sub>21</sub>H<sub>16</sub>N<sub>6</sub>O<sub>2</sub>S: C, 60.56; H, 3.87; N, 20.18. Found: C, 60.73; H, 3.91; N, 20.43.

**General procedure for synthesis of compounds (15b) and (17b)**

A mixture of 3-(5,6,7,8-Tetrahydro-7H-cyclohexa[4:5]thieno[2,3-d][1,2,3]triazin-4-ylamino)benzene-1,3-diamine (**13b**) [16] (0.01 mol) and suitable aromatic aldehyde (0.01 mol) in methanol (20 mL) in the presence of a catalytic amount of glacial acetic acid was refluxed for 5 h, with the progression of reaction monitored using TLC. The solvent was removed under reduced pressure, and the product recrystallized from chloroform [17].

**3-(5,6,7,8-Tetrahydro-7H-cyclohexa[4:5]thieno[2,3-d][1,2,3]triazin-4-ylamino)-N-(2-hydroxybenzylidene)benzene-1,3-diamine (15b)**

Mass spectrum:  $m/z$  (%): 401 (M<sup>+</sup>, 7.20%), 390 (3.80%), 375 (2.10%), 361 (6.49%), 346 (100%), 303 (5.30%). IR (cm<sup>-1</sup>): 756 (C–S), 1678 (C=N), 3228 (N–H), 3363 (OH). <sup>1</sup>H NMR (DMSO, 300 MHz):  $\delta$  (ppm): 1.13 (m, 4H), 3.05 (t, 2H), 3.10 (t, 2H), 3.60 (s, 1H), 7.13 (m, 7H), 7.81 (s, 1H), 7.85 (s, 1H), 8.25 (s, 1H). Elemental analysis calculated for C<sub>22</sub>H<sub>19</sub>N<sub>5</sub>OS: C, 65.81; H, 4.77; N, 17.44. Found: C, 65.58; H, 4.39; N, 17.76.

**3-(5,6,7,8-Tetrahydro-7H-cyclohexa[4:5]thieno[2,3-d][1,2,3]triazin-4-ylamino)-N-(3-nitrobenzylidene)benzene-1,3-diamine (17b)**

Mass spectrum:  $m/z$  (%): 430 (M<sup>+</sup>, 5.10%), 384 (8.60%), 354 (10.40%), 296 (6.30%), 103 (100%). IR (cm<sup>-1</sup>): 732 (C–S), 1350 (NO<sub>2</sub>), 1527 (NO<sub>2</sub>), 3360 (N–H). <sup>1</sup>H NMR (DMSO, 300 MHz):  $\delta$  (ppm): 1.14 (m, 4H), 3.04 (t, 2H), 3.11 (t, 2H), 3.20 (s, 1H), 7.31 (m, 6H), 7.37 (s, 1H), 7.45 (s, 1H), 7.64 (s, 1H).

**2-Chloro-N-(3-cyano-4,5,6,7-tetrahydrobenzo[b]thiophen-2-yl)acetamide (19)**

To a stirred solution of 2-amino-4,5,6,7-tetrahydrobenzo[b]thiophene-3-carbonitrile (**11**) [22] (0.10 mol) in acetone (20 mL), chloroacetyl chloride (0.05 mol) at 0–5 °C was added dropwise and maintained in an ice bath. The reaction mixture was stirred at room temperature for an additional 4 h. Then, 40 mL of 10% HCl was added to the mixture. The formed precipitate was filtered and washed with HCl (10%) and water. Melting point: 175–177 °C [23].

**General procedure for synthesis of compounds (21a,b)**

The amine derivatives (**20a,b**) (0.009 mol) [24] were dissolved in dry dichloromethane (DCM) (25.0 mL) and triethylamine (TEA) (1.5 mL) under nitrogen atmosphere. Compound (19) (0.0045 mol) was slowly added to the stirred solution, and the solution was then refluxed for 6–9 h. The mixture was then cooled and poured onto crushed ice. The formed precipitate was filtered, washed with water, dried and recrystallized from absolute ethanol [4].

**2-(1H-Pyrazolo[3,4-b]pyridin-3-ylamino)-N-(3-cyano-4,5,6,7-tetrahydrobenzo[b]thiophen-2-yl)acetamide (21a)**

Mass spectrum:  $m/z$  (%): 354 (M<sup>+</sup>, 4.29%), 353 (4.83%), 352 (6.96%), 320 (57.61%), 291 (38.64%), 178 (100%). IR (cm<sup>-1</sup>): 789 (C–S), 1689 (C=O), 2224 (C≡N), 3214 (N–H), 3338

(N–H), 3443 (N–H). <sup>1</sup>H NMR (DMSO, 300 MHz):  $\delta$  (ppm): 1.20 (m, 4H), 3.06 (m, 4H), 3.08 (s, 2H), 3.65 (s, 1H), 5.49 (s, 1H), 6.95 (m, 3H), 11.88 (s, 1H). Elemental analysis calculated for C<sub>17</sub>H<sub>16</sub>N<sub>6</sub>O<sub>2</sub>S: C, 57.94; H, 4.58; N, 23.85. Found: C, 58.21; H, 4.42; N, 24.18.

**N-(3-Cyano-4,5,6,7-tetrahydrobenzo[b]thiophen-2-yl)-2-(4,6-dimethyl-1H-pyrazolo[3,4-b]pyridin-3-ylamino)acetamide (21b)**

Mass spectrum:  $m/z$  (%) 382 (M<sup>+</sup>, 1.22%), 381 (1.08%), 380 (3.65%), 348 (1.44%), 320 (13.61%), 143 (100%). IR (cm<sup>-1</sup>): 778 (C–S), 1689 (C=O), 2224 (C≡N), 3285 (N–H), 3388 (N–H), 3444 (N–H). <sup>1</sup>H NMR (DMSO, 300 MHz):  $\delta$  (ppm): 1.18 (m, 4H), 1.75 (s, 1H), 2.42 (s, 3H), 2.54 (s, 3H), 3.02 (m, 4H), 3.65 (s, 2H), 5.01 (s, 1H), 6.58 (s, 1H), 11.69 (s, 1H). Elemental analysis calculated for C<sub>19</sub>H<sub>20</sub>N<sub>6</sub>O<sub>2</sub>S: C, 59.98; H, 5.30; N, 22.09. Found: C, 60.29; H, 5.43; N, 22.41.

**N-(3-Cyano-4,5,6,7-tetrahydrobenzo[b]thiophen-2-yl)-2-(isoxazolo[3,4-b]pyridin-3-ylamino)acetamide (23)**

Compound (22) [24] was dissolved in dry DCM (25.0 mL) and TEA (1.5 mL) under nitrogen atmosphere. Compound (19) (0.0045 mol) was added slowly to the stirred solution, then heated under reflux for 6–9 h. The mixture was then cooled and poured onto crushed ice. The formed precipitate was filtered and washed with water, dried and recrystallized from absolute ethanol [4].

Mass spectrum:  $m/z$  (%): 355 (M<sup>+</sup>, 0.39%), 354 (1.95%), 353 (0.60%), 343 (4.50%), 313 (6.29%), 144 (100%). IR (cm<sup>-1</sup>): 692 (C–S), 1689 (C=O), 2224 (C≡N), 3220 (N–H), 3446 (N–H). <sup>1</sup>H NMR (DMSO, 300 MHz):  $\delta$  (ppm): 1.79 (m, 4H), 3.17 (m, 4H), 3.82 (s, 2H), 4.09 (s, 1H), 7.09 (m, 3H), 9.78 (s, 1H). Elemental analysis calculated for C<sub>17</sub>H<sub>15</sub>N<sub>5</sub>O<sub>2</sub>S: C, 57.78; H, 4.28; N, 19.82. Found: C, 58.01; H, 4.37; N, 20.09.

**N-(3-Cyano-4,5,6,7-tetrahydrobenzo[b]thiophen-2-yl)-2-hydrazinyl acetamide (24)**

A mixture of hydrazine hydrate 80% (0.05 mol, 0.25 mL) and 2-chloro-N-(3-cyano-4,5,6,7-tetrahydrobenzo[b]thiophen-2-yl)acetamide (19) (0.0015 mol) in absolute ethanol (20 mL) was refluxed for 4 h, with the progression of reaction monitored using TLC. The reaction mixture was cooled and poured into water. The formed precipitate was filtered and recrystallized from ethanol to give the desired hydrazide. Melting point: 140–142 °C [19].

**General procedure for synthesis of compounds (25a,b)**

A mixture of compound (24) (0.01 mol) and the suitable aromatic aldehyde (0.01 mol) dissolved in methanol (20 mL) in the presence of a catalytic amount of glacial acetic acid was refluxed for 5 h, with the progression of reaction monitored using TLC. The solvent was removed under reduced pressure, and the product recrystallized from chloroform [17].

**N-(3-Cyano-4,5,6,7-tetrahydrobenzo[b]thiophen-2-yl)-2-(2-(3-nitrobenzylidene)hydrazinyl)acetamide (25a)**

Mass spectrum:  $m/z$  (%) 385 (M<sup>+</sup>, 0.66%), 384 (1.26%), 383 (2.27%), 369 (16.60%), 339 (5.59%), 311 (100%). IR (cm<sup>-1</sup>): 736 (C–S), 1265 (NO<sub>2</sub>), 1526 (NO<sub>2</sub>), 1689 (C=O), 2221 (C≡N), 3088 (N–H), 3443 (N–H). <sup>1</sup>H NMR (DMSO, 300 MHz):  $\delta$  (ppm): 1.78 (m, 4H), 2.15 (s, 1H), 2.45 (m, 4H), 3.62 (s, 2H), 7.80 (m, 3H), 8.71 (s, 1H), 8.88 (s, 1H), 11.63 (s, 1H). Elemental analysis calculated for C<sub>18</sub>H<sub>17</sub>N<sub>5</sub>O<sub>3</sub>S: C, 56.38; H, 4.47; N, 18.27. Found: C, 56.70; H, 4.58; N, 18.49.

**N-(3-Cyano-4,5,6,7-tetrahydrobenzo[b]thiophen-2-yl)-2-(2-(4-methoxybenzylidene)hydrazinyl)acetamide (25b)**

Mass spectrum:  $m/z$  (%) 370 (M<sup>+</sup>, 2.36%), 369 (6.14%), 368 (21.44%), 354 (100%), 338 (5.20%), 296 (39.14%). IR (cm<sup>-1</sup>): 695 (C–S), 1256 (OCH<sub>3</sub>), 1689 (C=O), 2225 (C≡N), 3220 (N–H), 3446 (N–H). <sup>1</sup>H NMR (DMSO, 300 MHz):  $\delta$  (ppm): 1.74 (m, 4H), 2.16 (s, 1H), 2.56 (m, 4H), 3.63 (s, 2H), 3.82 (s, 3H), 7.04 (m, 4H), 8.62 (s, 1H), 11.64 (s, 1H). Elemental analysis calculated for C<sub>19</sub>H<sub>20</sub>N<sub>4</sub>O<sub>2</sub>S: C, 61.94; H, 5.47; N, 15.21. Found: C, 62.23; H, 5.60; N, 15.49.

### 3.4. Biological Assays

#### 3.4.1. Cytotoxic Activity against H1299

The potential cytotoxic activity of the target compounds on H1299 lung cancer cell line was tested using sulfo-rhodamine B (SRB) assay according to Skehan method [20]. Single

cells were plated in 96-multiwell plates for 24 h before treatment with the compounds. A single concentration of the tested compounds was added to the cell monolayer. Monolayer cell was incubated with the compounds for 48 h at 37 °C and in atmosphere of 5% CO<sub>2</sub>. After 48 h, cell was fixed, washed and stained with Sulforhodamine-B stain. Acetic acid was then used to wash excess stain and attached stain was recovered with Tris ethylenediaminetetraacetic acid (EDTA) buffer. Color intensity was measured in an enzyme-linked immunosorbent assay (ELISA). Percentage of the surviving and inhibition were tabulated.

### 3.4.2. Measurement of Potential EGFR/HER2 Inhibitory Activity (IC<sub>50</sub>)

Measurement of potential EGFR/HER2 inhibitory activities was performed using Kinase-Glo Plus luminescence kinase assay kit (Promega Corporation, Madison, WI, USA) [25]. Mix kinases, ATP, substrates, and compounds in the reaction buffer of 25 mM HEPES (pH 7.4), 10 mM MgCl<sub>2</sub>, 0.01% Triton X-100, 100 µg/mL BSA, 2.5 mM DTT in a 384-well plate. Total reaction volume was 10 µL. The assay plate was incubated at 30 °C for 1 h, and the reaction was stopped by the addition of equal volume of kinase glo plus reagent. The fluorescence was measured. The signal was correlated with the remaining amount of ATP in the reaction and was inversely correlated with the kinase activity.

## 3.5. Molecular Modeling Study

### 3.5.1. Protein Preparation for Docking Study

The X-ray crystal structure of the catalytic domain of the EGFR enzyme complex with erlotinib (3) (PDB 1M17 resolution 2.6 Å), the human HER2 kinase domain with ligand 03Q (PDB 3PP0 resolution 2.25 Å), and EGFR kinase T790M in complex with BIBW2992 (afatinib (5)) (PDB 4G5P resolution 3.17Å) were obtained from Protein Data Bank and further prepared by the protein preparation wizards available in the Glide program of Schrodinger 10.1. The preparation portion adds hydrogen after ensuring chemical accuracy and neutralizes side chains that are neither close to the binding cavity nor involved in the formation of salt bridges. For this reason, the OPLS-2005 force field was used, and then the active site of the protein was established. Water molecules were extracted in the next step, and H atoms were added to the crystal structure, most likely hydroxyl and thiol hydrogen atom positions, protonation states, and tautomers of the His residue and chi “flip” assignment were selected by the protein assignment script provided by Schrodinger for Asn, Gln, and His residues. Using the OPLS2005 force field, minimization was carried out to alleviate steric clashes until the average root mean square deviation (RMSD) of the non-hydrogen atoms reached a maximum value of 0.3 Å [16,26,27].

### 3.5.2. Ligand Preparation

All compounds were constructed using the Maestro 10.1 fragment library and prepared using LigPrep 2.1, which can generate several structures with different ionization states, tautomers, stereochemistry, and ring conformations from each input structure. For optimization, the OPLS-2005 force field was used, which generates the ligand’s low-energy conformer. Partial atomic charges were allocated, and potential ionization states were issued at a pH of 7.0. For each ligand, energy minimization was carried out until it met the RMSD cutoff of 0.010 Å. The resulting structures were then adopted to carry out modeling studies [27,28].

### 3.5.3. Molecular Docking

The designed compounds were docked to the EGFR (PDB 1M17), HER2 (PDB 3PP0), and EGFR kinase T790M in complex with BIBW2992 (afatinib (5)) (PDB 4G5P resolution 3.17Å) binding sites using Glide, grid-based ligand docking with energetics software from Schrodinger 10.1, to test the docking parameters. We scaled the Van der Waals radii of receptor atoms by 0.8 with a partial atomic charge of 0.15 to soften the potential for nonpolar parts of the receptor. At the center of the active site, a grid box with coordinates X = 10, Y = 10, and Z = 10 was created. The ligands were docked with the active site using “extra-

precision" glide docking (Glide XP), which flexibly docks ligands. Glide internally creates conformations and passes them through a series of filters. The XP docking technique has been clarified elsewhere. Using a Glide score feature, the final best docked structure was selected. In most comparable docking conformations, the lowest energy docking complex was found. Finally, for further analysis, the lowest energy docked complex was chosen [16].

#### 3.5.4. In Silico ADME Prediction

Drug-like properties of the synthesized compounds were evaluated in accordance with Lipinski's rule of five ADME. This was used to evaluate whether these compounds have properties that would allow them to be orally active drugs for humans. The drug-like action of our compounds was predicted using module QikProp (v4.2; Schrodinger 2015-1) [16,26].

## 4. Conclusions

New chemical compounds belonging to tetrahydrobenzothieno[2,3-d][1,2,3]triazine, dihydrocyclopentathieno[2,3-d][1,2,3]triazine, and 3-cyanotetrahydrobenzothiophene bearing various heterocyclic systems at positions 4 and 2 were designed, synthesized, structurally elucidated, and biologically evaluated as anti-lung cancer agents. The synthesized compounds exhibited potent in situ cytotoxic activity toward human lung carcinoma cell line H1299 compared to gefitinib (2), with IC<sub>50</sub> values ranging from 12.5 to 54.8 nM. The designed compounds showed antiproliferative activity through competitive inhibition of EGFR and/or HER2 receptors. The designed compound (21a) has shown comparable potency to imatinib (1) but more potent than neratinib (6) in in vitro kinase inhibition against EGFR and HER2. Results of molecular modeling further supported the potent inhibitory activity of the proposed compounds, which helps in understanding the various interactions between ligands and receptor sites. The tetrahydrobenzothieno[2,3-d][1,2,3]triazine scaffold and 3-cyanotetrahydrobenzothiophene occupied the ATP-binding site, showing the same drug–receptor interactions as two approved drugs: lapatinib (4) and neratinib (6). Additional binding sites, especially in hydrophobic pockets, were provided by our structural modification. The introduction of new functional groups with positions different to those commonly found in approved drugs could allow the designed compounds to interact with alternative binding sites, which could solve the problem of acquired drug resistance. Our new scaffolds might also serve as promising lead compounds for the discovery of new drugs to overcome acquired resistance in NSCLC patients.

**Author Contributions:** Conceptualization, R.E., Y.M.A.A., M.E., A.S.A.Y., H.A.E., and M.M.S.; methodology, R.E., Y.M.A.A., M.E., A.S.A.Y., and H.A.E.; software, M.S.E.; writing—original draft preparation, R.E., Y.M.A.A., M.E., A.S.A.Y., and H.A.E.; writing—review and editing, R.E., Y.M.A.A., M.E., A.S.A.Y., and H.A.E.; resources, S.S.E.; funding acquisition, S.S.E.; R.E and M.S.E. contributed equally. All authors have read and agreed to the published version of the manuscript.

**Funding:** This research was funded by the Deanship of Scientific Research (DSR) at King Abdulaziz University, Jeddah, Saudi Arabia, under grant no. FP-127-42.

**Acknowledgments:** The Deanship of Scientific Research (DSR) at King Abdulaziz University, Jeddah, Saudi Arabia, funded this project under grant no. FP-127-42. The authors, therefore, acknowledge and thank DSR for technical and financial support.

**Conflicts of Interest:** The authors declare no conflict of interest.

## References

1. Zhao, J.; Xia, Y. Targeting Her2 Alterations in Non-Small-Cell Lung Cancer: A Comprehensive Review. *JCO Precis. Oncol.* **2020**, *4*, 411–425. [CrossRef]
2. Li, X.; Wu, J.; Cao, H.; Ma, R.; Wu, J.; Zhong, Y.; Feng, J. Blockade of DNA Methylation Enhances the Therapeutic Effect of Gefitinib in Non-Small Cell Lung Cancer Cells. *Oncol. Rep.* **2013**, *29*, 1975–1982. [CrossRef]

3. Kang, H.N.; Kim, S.; Yun, M.R.; Kim, H.R.; Lim, S.M.; Kim, M.; Hong, K.; Kim, S.; Kim, H.; Pyo, K.; et al. Er2, a Novel Human Anti-Egfr Monoclonal Antibody Inhibit Tumor Activity in Non-Small Cell Lung Cancer Models. *Lung Cancer* **2016**, *95*, 57–64. [CrossRef] [PubMed]
4. Yassen, A.S.A.; Elshihawy, H.E.A.E.A.; Said, M.M.A.; Abouzid, K.A.M. Molecular Modelling and Synthesis of Quinazoline-Based Compounds as Potential Antiproliferative Agents. *Chem. Pharm. Bull.* **2014**, *62*, 454–466. [CrossRef] [PubMed]
5. Charles, S.; Futreal, A.; Eisen, T. Her2-Targeted Therapies in Non-Small Cell Lung Cancer. *Clin. Cancer Res.* **2006**, *12*, 4377s–4383s.
6. Jianming, Z.; Yang, P.L.; Gray, N.S. Targeting Cancer with Small Molecule Kinase Inhibitors. *Nat. Rev. Cancer* **2009**, *9*, 28–39.
7. Elmetwally, S.A.; Saied, K.F.; Eissa, I.H.; Elkaeed, E.B. Design, Synthesis and Anticancer Evaluation of Thieno [2, 3-D] Pyrimidine Derivatives as Dual Egfr/Her2 Inhibitors and Apoptosis Inducers. *Bioorgan. Chem.* **2019**, *88*, 102944. [CrossRef]
8. Emeline, L.; Barluenga, S.; Moras, D.; Wurtz, J.; Winssinger, N. Cysteine Mapping in Conformationally Distinct Kinase Nucleotide Binding Sites: Application to the Design of Selective Covalent Inhibitors. *J. Med. Chem.* **2011**, *54*, 1347–1355.
9. Smith, A.J.; Zhang, X.; Leach, A.G.; Houk, K.N. Beyond Picomolar Affinities: Quantitative Aspects of Noncovalent and Covalent Binding of Drugs to Proteins. *J. Med. Chem.* **2009**, *52*, 225–233. [CrossRef]
10. Lanning, B.R.; Whitby, L.R.; Dix, M.M.; Douhan, J.; Gilbert, A.M.; Hett, E.C.; Johnson, T.O.; Joslyn, C.; Kath, J.C.; Niessen, S. A Road Map to Evaluate the Proteome-Wide Selectivity of Covalent Kinase Inhibitors. *Nat. Chem. Biol.* **2014**, *10*, 760–767. [CrossRef]
11. Shuhang, W.; Cang, S.; Liu, D. Third-Generation Inhibitors Targeting Egfr T790 m Mutation in Advanced Non-Small Cell Lung Cancer. *J. Hematol. Oncol.* **2016**, *9*, 34.
12. Yu, H.A.; Tian, S.K.; Drilon, A.E.; Borsu, L.; Riely, G.J.; Arcila, M.E.; Ladanyi, M. Acquired Resistance of Egfr-Mutant Lung Cancer to a T790m-Specific Egfr Inhibitor: Emergence of a Third Mutation (C797s) in the Egfr Tyrosine Kinase Domain. *JAMA Oncol.* **2015**, *1*, 982–984. [CrossRef] [PubMed]
13. Zhuo, L.; Wang, L.; Feng, M.; Yi, Y.; Zhang, W.; Liu, W.; Li, L.; Liu, Z.; Li, Y.; Ma, X. New Acrylamide-Substituted Quinazoline Derivatives with Enhanced Potency for the Treatment of Egfr T790m-Mutant Non-Small-Cell Lung Cancers. *Bioorgan. Chem.* **2018**, *77*, 593–599.
14. Siyuan, Y.; Tang, C.; Wang, B.; Zhang, Y.; Zhou, L.; Xue, L.; Zhang, C. Design, Synthesis and Biological Evaluation of Novel Egfr/Her2 Dual Inhibitors Bearing a Oxazolo [4, 5-G] Quinazolin-2 (1h)-One Scaffold. *Eur. J. Med. Chem.* **2016**, *120*, 26–36.
15. Mohamed, S.; Elshihawy, H. Synthesis, Anticancer Activity and Structure-Activity Relationship of Some Anticancer Agents Based on Cyclopenta (B) Thiophene Scaffold. *Pak. J. Pharm. Sci.* **2014**, *27*.
16. Ranza, E.; Aziz, Y.M.A.; Elgawish, M.S.; Elewa, M.; Elshihawy, H.A.; Said, M.M. Pharmacophore Modeling, 3d-Qsar, Synthesis, and Anti-Lung Cancer Evaluation of Novel Thieno [2, 3-D] [1, 2, 3] Triazines Targeting Egfr. *Arch. Pharm.* **2020**, *353*, 1900108.
17. Adesh, D.; Srivastava, S.K.; Srivastava, S.D. Conventional and Microwave Assisted Synthesis of 2-Oxo-4-Substituted Aryl-Azetidine Derivatives of Benzotriazole: A New Class of Biological Compounds. *Bioorgan. Med. Chem. Lett.* **2011**, *21*, 569–573.
18. Al-Obaid, A.M.; Abdel-Hamide, S.G.; El-Kashef, H.A.; Alaa, A.M.; El-Azab, A.S.; Al-Khamees, H.A.; El-Subbagh, H.I. Substituted Quinazolines, Part 3. Synthesis, in Vitro Antitumor Activity and Molecular Modeling Study of Certain 2-Thieno-4 (3h)-Quinazolinone Analogs. *Eur. J. Med. Chem.* **2009**, *44*, 2379–2391. [CrossRef]
19. Canan, K.; Ayhan-Kılıçgil, G.; Özbey, S.; Kaynak, F.B.; Kaya, M.; Çoban, T.; Can-Eke, B. Synthesis and Antioxidant Properties of Novel N-Methyl-1, 3, 4-Thiadiazol-2-Amine and 4-Methyl-2h-1, 2, 4-Triazole-3 (4h)-Thione Derivatives of Benzimidazole Class. *Bioorgan. Med. Chem.* **2008**, *16*, 4294–4303.
20. Philip, S.; Storeng, R.; Scudiero, D.; Monks, A.; McMahon, J.; Vistica, D.; Warren, J.T.; Bokesch, H.; Kenney, S.; Boyd, M.R. New Colorimetric Cytotoxicity Assay for Anticancer-Drug Screening. *JNCI J. Nat. Cancer Inst.* **1990**, *28*, 1107–1112.
21. 1 Product Results for Neratinib. Available online: [https://www.selleckchem.com/search.html?searchParam=Neratinib&sp=Neratinib](https://www.selleckchem.com/search.html?searchDTO.searchParam=Neratinib&sp=Neratinib) (accessed on 20 November 2020).
22. Gewalt, K. Heterocyclen Aus Ch-Aciden Nitrilen, Vii. 2-Amino-Thiophene Aus A-Oxo-Mercaptanen Und Methylenaktiven Nitrilen. *Chem. Berichte* **1965**, *98*, 3571–3577. [CrossRef]
23. Lou, Z.; Li, Z.; Chunfen, X.; Yong, Y.; Fanbo, Z.; Kaixun, H. Anticancer Activities of Some Arylcarbamoylalkyltriphenylphosphonium Chlorides. *Med. Chem. Res.* **2007**, *16*, 380–391.
24. Kundariya, D.S.; Bheshdadia, B.M.; Joshi, N.K.; Patel, P.K. Synthesis, Characterization and Pharmacological Evaluation of Some Novel Schiff Bases Containing 1h-Pyrazolo [3, 4-B] Pyridine Moiety. *Int. J. ChemTech. Res.* **2011**, *44*, 4385–4392.
25. Available online: <http://www.bpsbioscience.com/biochemical-based-assays> (accessed on 21 November 2020).
26. Elrayess, R.; Elgawish, M.S.; Elewa, M.; Nafie, M.S.; Elhady, S.S.; Yassen, A.S.A. Synthesis, 3d-Qsar, and Molecular Modeling Studies of Triazole Bearing Compounds as a Promising Scaffold for Cyclooxygenase-2 Inhibition. *Pharmaceuticals* **2020**, *13*, 370. [CrossRef] [PubMed]
27. Ghareb, N.; El-Sayed, N.M.; Abdelhameed, R.; Yamad, K.; Elgawish, M.S. Toward a treatment of diabetes: Rational design, synthesis and biological evaluation of benzene-sulfonamide derivatives as a new class of PTP-1B inhibitors. *Bioorgan. Chem.* **2019**, *86*, 322–338. [CrossRef] [PubMed]
28. Elgawish, M.S.; Kishikawa, N.; Helal, M.A.; Ohyama, K.; Kuroda, N. Molecular modeling and spectroscopic study of quinone-protein adducts: Insight into toxicity, selectivity, and reversibility. *Toxicol. Res.* **2015**, *4*, 843–847. [CrossRef]







## Article

# Design, Synthesis, In Vitro Anticancer Evaluation and Molecular Modelling Studies of 3,4,5-Trimethoxyphenyl-Based Derivatives as Dual EGFR/HDAC Hybrid Inhibitors

Tarek S. Ibrahim <sup>1,2,\*</sup>, Azizah M. Malebari <sup>1</sup> and Mamdouh F. A. Mohamed <sup>3,\*</sup>

<sup>1</sup> Department of Pharmaceutical Chemistry, Faculty of Pharmacy, King Abdulaziz University, Jeddah 21589, Saudi Arabia

<sup>2</sup> Department of Pharmaceutical Organic Chemistry, Faculty of Pharmacy, Zagazig University, Zagazig 44519, Egypt; amelibary@kau.edu.sa

<sup>3</sup> Department of Pharmaceutical Chemistry, Faculty of Pharmacy, Sohag University, Sohag 82524, Egypt

\* Correspondence: tmabraham@kau.edu.sa (T.S.I.); mamdouh.fawzi@pharm.sohag.edu.eg (M.F.A.M.)

**Citation:** Ibrahim, T.S.; Malebari, A.M.; Mohamed, M.F.A. Design, Synthesis, In Vitro Anticancer Evaluation and Molecular Modelling Studies of 3,4,5-Trimethoxyphenyl-Based Derivatives as Dual EGFR/HDAC Hybrid Inhibitors. *Pharmaceuticals* **2021**, *14*, 1177. <https://doi.org/10.3390/ph14111177>

Academic Editor: Maria Emília de Sousa

Received: 28 October 2021

Accepted: 15 November 2021

Published: 17 November 2021

**Publisher's Note:** MDPI stays neutral with regard to jurisdictional claims in published maps and institutional affiliations.

**Abstract:** Recently, combining histone deacetylase (HDAC) inhibitors with chemotherapeutic drugs or agents, in particular epidermal growth factor receptor (EGFR) inhibitors, is considered to be one of the most encouraging strategy to enhance the efficacy of the antineoplastic agents and decrease or avoid drug resistance. Therefore, in this work, based on introducing 3,4,5-trimethoxy phenyl group as a part of the CAP moiety, in addition to incorporating 4–6 aliphatic carbons linker and using COOH or hydroxamic acid as ZBG, 12 novel EGFR/HDAC hybrid inhibitors **2a–c**, **3a–c**, **4a–c** and **5a–c** were designed, constructed, and evaluated for their anticancer activities against 4 cancer cell lines (HepG2, MCF-7, HCT116 and A549). Among all, hybrids with hydroxamic acid **4a–c** and **5a**, exhibited the highest inhibition against all cancer cell lines with IC<sub>50</sub> ranging from 0.536 to 4.892 μM compared to Vorinostat (SAHA) with IC<sub>50</sub> ranging from 2.43 to 3.63 μM and Gefitinib with IC<sub>50</sub> ranging from 1.439 to 3.366 μM. Mechanistically, the most potent hybrids **4a–c** and **5a** were further tested for their EGFR and HDACs inhibitory activities. The findings disclosed that hybrid **4b** displayed IC<sub>50</sub> = 0.063 μM on the target EGFR enzyme which is slightly less potent than the standard Staurosporine (IC<sub>50</sub> = 0.044 μM). Furthermore, hybrid **4b** showed less HDAC inhibitory activity IC<sub>50</sub> against HDAC1 (0.148), 2 (0.168), 4 (5.852), 6 (0.06) and 8 (2.257) than SAHA. In addition, the investigation of apoptotic action of the most potent hybrid **4b** showed a significant increase in Bax level up to 3.75-folds, with down-regulation in Bcl2 to 0.42-fold, compared to the control. Furthermore, hybrid **4b** displayed an increase in the levels of Caspases 3 and 8 by 5.1 and 3.15 folds, respectively. Additionally, the cell cycle analysis of hybrid **4b** revealed that it showed programmed cell death and cell cycle arrest at G1/S phase. Moreover, all these outcomes together with the molecular docking study recommended the rationalized target hybrids **4a–c** and **5a**, particularly **4b**, may be considered to be promising lead candidates for discovery of novel anticancer agents via dual inhibition of both EGFR/HDAC enzymes.

**Keywords:** cancer; hybrid compounds; EGFR; HDAC inhibitors; chalcone; dual inhibitors



**Copyright:** © 2021 by the authors. Licensee MDPI, Basel, Switzerland. This article is an open access article distributed under the terms and conditions of the Creative Commons Attribution (CC BY) license (<https://creativecommons.org/licenses/by/4.0/>).

## 1. Introduction

Cancer, with about 15 million deaths per year in 2030 according to the estimations, is still emerging a panic as a real disaster for health systems globally [1,2]. Cancer was initially considered to be a genetic disease; however, it is now well-known that cancer is genetic and/or epigenetic disease [3] with complicated signaling networks and required perturbation of multiple targets at the same time as its cells can use different compensatory pathways for survival [4]. Accordingly, most of the existing authorized drugs that were designed through the “single-target single drug” strategy become less effective in the treatment of the mixed, complicated and multigenic cancer illness [4]. This may be

related to their systemic toxicity, drug-resistance, dose-related side effects as well as lack of selectivity [5,6]. Thus, there is an urgent medical necessity for innovation and discovery of innovative tactics and strategies to develop and design new potent anti-cancer candidates with high efficacy, less side effects, more desirable safety profile and low cost to manage the cancer global health crisis [7]. One of the favorable approaches in this issue is the multitarget or smart hybrids with two or more pharmacophores targeting cancer [4]. Indeed, histone deacetylases (HDACs) correspond to one of the most attractive targets for cancer therapy [8,9]. The oppositely acting histone acetyltransferases (HATs) and histone deacetylases (HDACs) are of the best two recognized enzymes groups involved in post-translational histone modifications [10]. Histone deacetylases perform a crucial role in the regulation of gene expression. It also regulates epigenetic and non-epigenetic mechanisms such as differentiation, cell cycle arrest and apoptosis and different forms of cancer cell death [4]. Consequently, overexpression of HDACs is related to tumor cell invasion and metastasis [4]. Thus, HDACs inhibition has been emerged as a promising strategy for cancer treatment [11]. Up to date, there are six HDAC inhibitors (Figure 1) have been FDA-approved; Vorinostat (SAHA) **1** [12], Romidepsin (FK228) **2a** and its active metabolite RedFK **2b** [13], Belinostat (PXD101) **3** [14], Pracinostat **4** [15], Panobinostat (LBH-589) **5** [16] are approved by the FDA while (Chidamide) **6** is approved by the Chinese FDA for the therapy of hematological malignancies (CS055) [17,18]. The X-ray arrangement disclosed that HDAC inhibitors consist of the following pharmacophores, namely; a cap group (CAP), the zinc-binding group (ZBG); and a spacer (hydrophobic linker) and a polar connection unit (CU, evidently unessential for HDAC8 selective inhibitors) (Figure 1) [19].

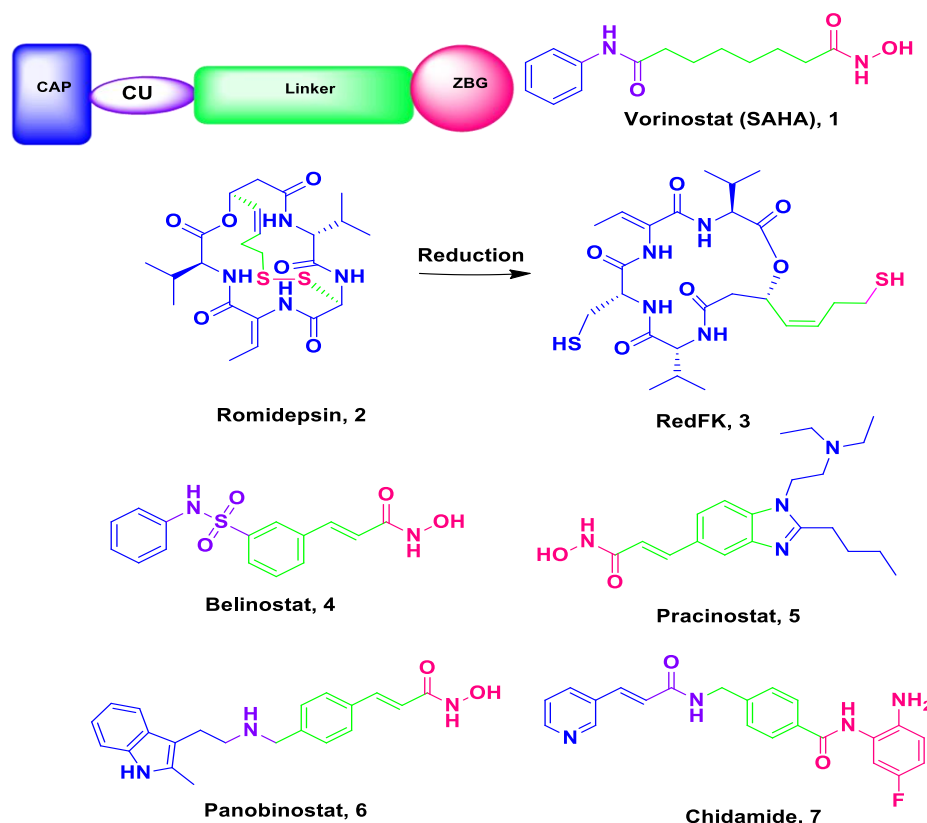


**Figure 1.** Pharmacophoric elements and structures of the official HDAC inhibitors.

HDAC inhibitors have shown encouraging findings against hematological malignancies, but varying on the cancer type and genetic factors, the response to HDAC inhibitors may be based on a certain biological response [20]. Moreover, HDAC inhibitors are not able to induce tumor remissions alone [21] and their clinical use is limited due to their severe side effects and its low oral bioavailability [22].

On the other hand, with numerous FDA approved tyrosine kinases inhibitors and several other in clinical trials, tyrosine kinases represent promising goals for the improvement of new chemotherapeutic agents [23–25]. Nevertheless, kinase inhibitors' as well as HDAC inhibitors effectiveness is often diminished and their use is restricted because of acquired drug resistance and consequently poor response rates [26,27]. To overcome this problem, medicinal chemistry investigators adopted the hybridization idea, principally with HDAC inhibitors due to either the ease of their structure modification or the likely synergism between HDAC and tyrosine kinase inhibitors which has been widely documented [28–35].

Recent studies revealed that dual blockade of EGFR/HDAC forcefully inhibited the proliferation of different cancer cell lines. For instant, Cai X. and co-workers [36] constructed a series of dual EGFR/HDAC hybrid inhibitors using erlotinib **8** (Figure 2) [37]. Among them, hybrid CUDC-101 **9** exhibited the most powerful in vitro inhibition against EGFR, HER2 and HDACs. Moreover, CUDC-101 **9** exhibited a strong anticancer activity greater than that of erlotinib, lapatinib, vorinostat (SAHA), and combinations of vorinostat/lapatinib or vorinostat/erlotinib [38]. CUDC-101 is currently in phase I clinical trials in patients with solid tumors [38]. In addition, many other EGFR/HDAC hybrid inhibitors are under investigation preclinically and exhibited promising results against different types of cancer [4].

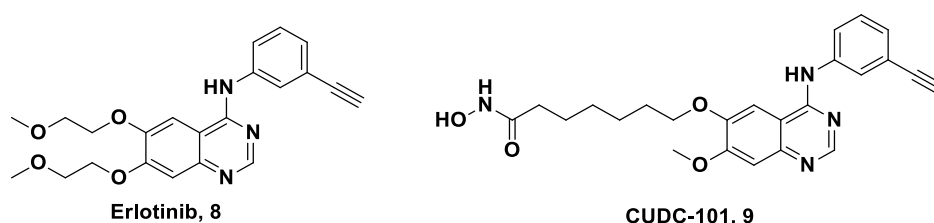


**Figure 2.** HDAC inhibitors with Erlotinib-based conjugates using SAHA as lead compound.

It is now obvious from previously mentioned data that dual inhibition of EGFR/HDAC is a favorable strategy for cancer control because of its advantages in producing synergistic effects and overcoming potential resistance. In continuation to our previous work on HDAC inhibitors [19,39–42] and EGFR inhibitors 1M17 [43,44], the present study was designed for synthesis of novel dual EGFR/HDAC hybrid inhibitors in one solid structure for the aim of synergism and/or reducing the expected undesirable effects. The synthesis of the novel dual EGFR/HDAC hybrid compounds is based on incorporation of trimethoxy phenyl group (as a part of the cap group of the HDAC inhibitors pharmacophore), in addition to incorporating 4–6 aliphatic carbons linker and using COOH or hydroxamic acid as ZBG. Moreover, the work involves the synthesis of chalcone derivatives and cyclization of chalcones into 3-cyano-2-oxo-pyridine derivatives (Figure 3).

All target compounds were evaluated for their in vitro anticancer activities against four cancer cell lines (MCF-7, HepG2, HCT116, and A549 cancer cell lines). Furthermore, the most potent hybrids were chosen for studying mechanistic pathways such as HDACs, EGFR assay, cell cycle analysis, and apoptosis markers.

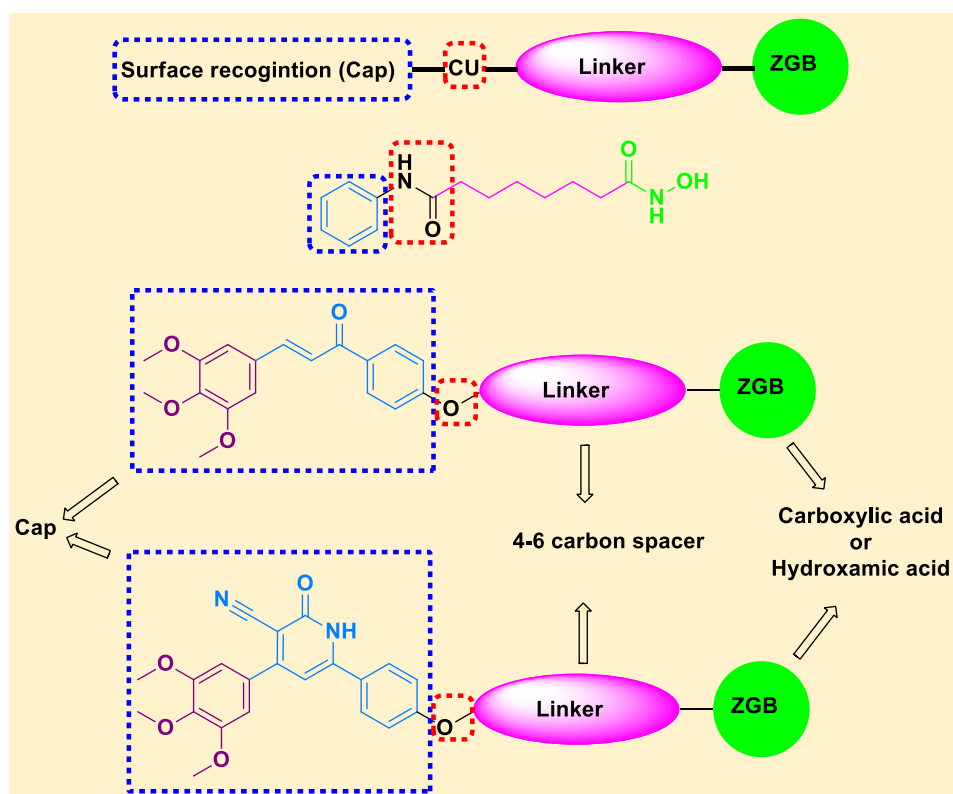


**Figure 3.** Designed structure of SAHA and the target EGFR/HDAC hybrid inhibitors.

## 2. Results and Discussion

### 2.1. Chemistry

The chemical synthesis of target hybrids **2a–c**, **3a–c**, **4a–c** and **5a–c** are described in Scheme 1. The (E)-1-(4-hydroxyphenyl)-3-(3,4,5-trimethoxyphenyl)prop-2-en-1-one **1** was prepared by Claisen condensation of 4-hydroxyacetophenone and 3,4,5-trimethoxybenzaldehyde in the presence of KOH and using ethanol as a solvent to afford the desired compound **1** according to the reported procedure [45]. Chalcone **1** was alkylated with the appropriate bromo esters in dry DMF containing excess of anhydrous  $K_2CO_3$  and stirring over night at 70–80 °C to afford the corresponding esters, which were subjected to alkaline hydrolysis to yield the target compounds **2a–c**.

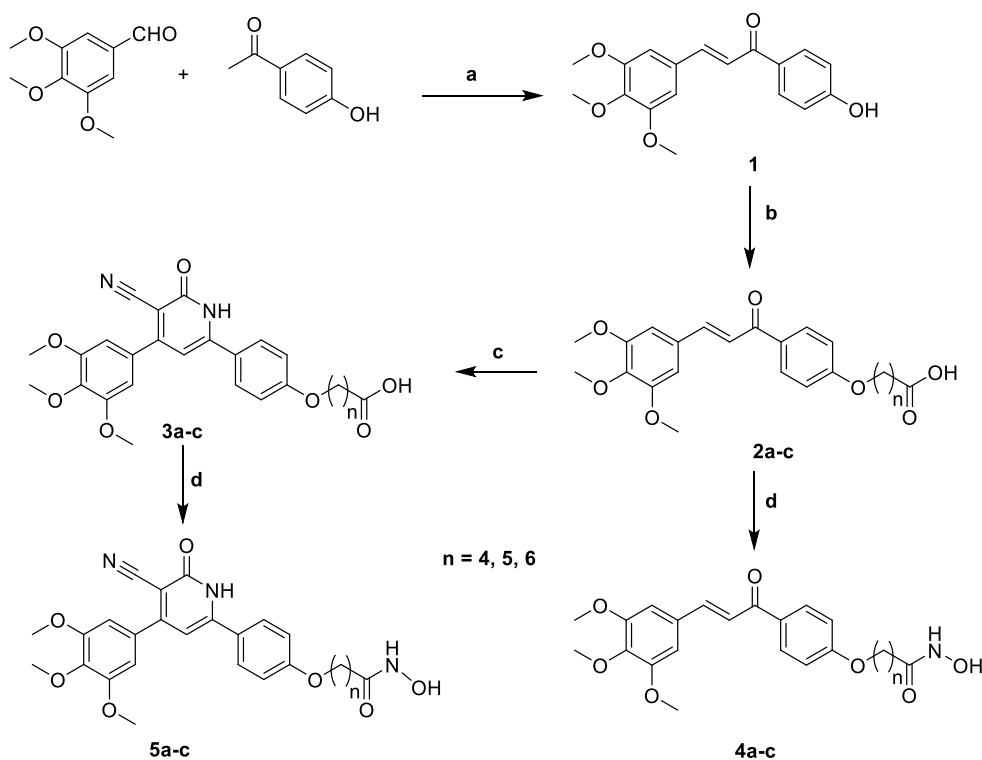
Treating the synthesized chalcone-acids **2a–c** with ethyl cyanoacetate and excess amount of ammonium acetate in refluxing ethanol gave the desired target compounds **3a–c**. Treating **2a–c** or **3a–c** with *N,N'*-carbonyldiimidazole (CDI) in dichloromethane as a solvent for 4 h followed by the addition of hydroxylamine hydrochloride an stirring at room temperature afforded the target hydroxamic acid derivatives **4a–c** and **5a–c**, respectively.

### 2.2. Biological Evaluation

#### 2.2.1. In Vitro Anticancer Activity

##### Cell Viability Assay

Cell viability test was brought out using human mammary gland epithelial cell line (MCF-10A). All new hybrids **2a–c**, **3a–c**, **4a–c** and **5a–c** were treated with MCF-10A cells for 4 days and MTT assay was used to determine the viability of cells. All newly compounds were demonstrated non-toxic with the majority of revealing more than 80% cell viability at 50  $\mu$ M concentration [43].



**Scheme 1.** Synthesis of the target hybrid **2a–c**, **3a–c**, **4a–c** and **5a–c**. **Reagents and conditions:** (a) KOH, Ethanol; (b) i, appropriate bromo esters,  $K_2CO_3$ , DMF, 70–80 °C, 12 h.; ii, MeOH, methanolic. KOH, rt, 7–8 h.; (c) Ethyl cyanoacetate, ammonium acetate, ethanol, reflux, 24 h.; (d) CDI, THF, 4 h,  $NH_2OH \cdot HCl$ , rt, 12 h.

#### Antiproliferative Activity

All final target hybrids **2a–c**, **3a–c**, **4a–c** and **5a–c** were tested for their antiproliferative action against four cancer cell lines, breast cancer (MCF-7), hepatocellular cancer (HepG2), colon cancer (HCT-119) and epithelial cancer (A-549), by means of MTT assay and SAHA and Gefitinib were used as the control compound.

The obtained results as shown in Table 1, displayed that the three hybrids **4a–c**, with hydroxamic acid as ZBG, were found to be the most potent against the four tested cancer cell lines with  $IC_{50}$  ranging from 0.536 to 3.619  $\mu M$ . Among them, hybrid **4b**, with 5 carbons linker, is the most potent and it displayed very strong anticancer activity with  $IC_{50} \leq 2 \mu M$  against the tested cell lines ( $IC_{50}$  values ranging from 0.536 to 1.206  $\mu M$ ). Hybrid **4c**, with six carbons spacer, comes next to **4b** and it exhibited very strong anticancer activity against MCF-7 (1.183), HCT116 (1.587) and A549 (1.934), while it showed strong anticancer activity against HepG2 (2.536). Finally, hybrid **4a**, with four carbons linker, displayed very strong anticancer activity against MCF-7 (1.971) and A549 (2.067) and it exhibited strong anticancer activity against HCT116 (3.213) and HepG2 (3.619), respectively. Despite the previously reported toxicity of some chalcones [46] due to the presence of  $\alpha,\beta$ -unsaturated carbonyl system, together with the cell viability test (less than 80%), it could be suggested that the higher activity of hybrids **4a–c** is attributed to its effect on cancer cells rather than normal cell. It is worth mentioning that the substituents on chalcone aromatic rings affect the electron density on the ring and consequently electronegativity of  $\alpha,\beta$ -unsaturated ketone system which has significant effect on binding affinity and biological activity. For instant, the presence of donating methoxy groups in hybrids **4a–c** decreases the electrophilic characters of the olefinic carbons and accordingly their binding with thiol group and this may explain their low toxicity on normal cells [1,46]. Cyclization of chalcone hybrids **4a–c** into 3-cyano-2-oxopyridine derivatives **5a–c**, lead to decrease in the activity in the case of four carbons linker as in hybrid **5a** with  $IC_{50}$  values 4.892, 3.456,

4.669 and 2.297 against MCF-7, HepG2, HCT116 and A549, respectively. However, the significant decrease in activity was obvious in the case of using six carbons linker as in hybrid **5c** and using five carbons spacer as in hybrid **5b**. Replacement of hydroxamic acid functionality with COOH as ZGB either in chalcone hybrids **2a–c**, or 3-cyano-2-oxopyridine derivatives **3a–c**, dramatically decreases anti-proliferative inhibitory activity. However, we could conclude that 3-cyano-2-oxopyridine derivatives **3a–c** showed higher activity than chalcone hybrids **2a–c**. Moreover, in the case of chalcone hybrids **2a–c**, hybrid **2c** with six carbons linker >**2b**, with 5 carbons linker > **2a**, with 4 carbons linker. On the other hand, 3-cyano-2-oxopyridine derivatives **3a–c**, hybrid **3b**, with five carbons linker, displayed the highest activity, followed by hybrid **3c**, with six carbons linker, and finally the least active hybrid **3a**, with four carbons linker. From these results, it is noticeable that both the linker and the ZGB of the target EGFR/HDAC inhibitor hybrids perform an important role in the anti-proliferative activity and extensiveness.

**Table 1.** Antiproliferative activity of the hybrids **2a–c**, **3a–c**, **4a–c** and **5a–c**.

Compound №	Antiproliferative Activity IC <sub>50</sub> ± SEM (µM)			
	MCF-7	HepG2	HCT116	A549
<b>2a</b>	59.94 ± 3.23	88.41 ± 4.76	40.11 ± 2.16	44.37 ± 2.39
<b>2b</b>	39.4 ± 2.12	30.35 ± 1.64	23.73 ± 1.28	33.74 ± 1.82
<b>2c</b>	14.77 ± 0.8	17.12 ± 0.92	16.49 ± 0.89	22.67 ± 1.22
<b>3a</b>	46.4 ± 2.54	65.82 ± 3.55	23.51 ± 1.27	31.03 ± 1.67
<b>3b</b>	12.15 ± 0.65	16.23 ± 0.87	15.71 ± 0.85	15.29 ± 0.82
<b>3c</b>	23.7 ± 1.28	21.09 ± 1.14	13.89 ± 0.75	21.31 ± 1.15
<b>4a</b>	1.971 ± 0.11	3.619 ± 0.2	3.213 ± 0.17	2.067 ± 0.11
<b>4b</b>	0.621 ± 0.03	0.536 ± 0.03	1.206 ± 0.07	0.797 ± 0.04
<b>4c</b>	1.183 ± 0.06	2.536 ± 0.14	1.587 ± 0.09	1.934 ± 0.14
<b>5a</b>	4.892 ± 0.26	3.456 ± 0.19	4.669 ± 0.25	2.297 ± 0.12
<b>5b</b>	19.55 ± 1.05	28.34 ± 0.99	16.89 ± 3.71	18.78 ± 1.01
<b>5c</b>	12.05 ± 0.65	27.64 ± 1.49	9.466 ± 0.51	8.577 ± 0.46
<b>SAHA</b>	2.43 ± 0.27	3.63 ± 0.24	2.53 ± 0.14	2.83 ± 0.13
<b>Gefitinib</b>	1.855 ± 0.13	2.848 ± 0.15	3.366 ± 0.18	1.439 ± 0.08

## 2.2.2. In Vitro Enzymatic Inhibitory Activity Assay

### Epidermal Growth Factor Receptor Activity (EGFR-TK) Inhibition

EGFR-TK testing was carried out to evaluate the EGFR inhibitory strength of new most potent hybrids **4a–c** and **5a** as illustrated in Table 2. The findings from this assay complement the outcomes of cancer cell-based assay. All examined hybrids **4a–c** and **5a** exhibited inhibitions of EGFR with IC<sub>50</sub> ranging from 0.063 to 0.214 µM. According to the obtained data, chalcone hybrid **4b** was found to be the most potent and its EGFR inhibitory activity (IC<sub>50</sub> = 0.063 µM) was close to the positive standard Gefitinib (IC<sub>50</sub> = 0.044 µM). This assay shows that these hybrids, particularly **4b**, are potent EGFR inhibitors and can possibly be used as anticancer agents.

**Table 2.** Effects of hybrids **4a–c**, **5a**, **Gefitinib**, **staurosporine** and **SAHA** on EGFR and HDAC1, 2, 4, 6 and 8 (IC<sub>50</sub> μM).

Compd. №	EGFR	HDAC1	HDAC2	HDAC4	HDAC6	HDAC8
<b>4a</b>	0.111 ± 0.002	0.121	0.119	6.685	0.086	6.354
<b>4b</b>	0.063 ± 0.002	0.148	0.168	5.852	0.06	2.257
<b>4c</b>	0.091 ± 0.001	0.07	0.277	8.716	0.113	5.015
<b>5a</b>	0.214 ± 0.004	0.051	0.256	17.53	0.222	19.56
<b>Gefitinib</b>	0.044 ± 0.001	nd	nd	nd	nd	nd
<b>Staurosporine</b>	0.4	nd	nd	nd	nd	nd
<b>SAHA</b>	nd	0.037	0.112	4.062	0.019	1.133

nd = not determined.

### In Vitro HDAC Inhibition Assay

To explore the mechanism of action of the most potent newly synthesized derivatives; hybrids **4a–c** and **5a** were tested for their in vitro HDAC inhibitory activity against HDAC1, HDAC2, HDAC4, HDAC6 and HDAC8 using SAHA as positive control. The HDAC inhibitory activity of the target compounds was measured using HDAC1 Human Colorimetric SimpleStep ELISA™ Kit (ABCAM, Cambridge, MA), HDAC2 Colorimetric ELISA KIT (MYBiosource, San Diego, CA, USA), HDAC4, 6 and 8 colorimetric Assay Kit (EpiGentek, Farmingdale, NY, USA), according to the manufacturer's instructions [42,47,48].

Analysis of the obtained results, presented in Table 2, revealed that the four selected hybrids possess variable high potency in HDAC inhibitory activity. For instant, hybrid **5a** was the most potent against HDAC1 followed by **4c** and **4a**, while **4b** displayed the lowest activity. Regarding HDAC2, hybrid **4a** exhibited the highest activity followed by **4b** and **5a**, while **4c** showed the lowest activity. Concerning HDAC4 and HDAC6, hybrid **4b** (with five carbons linker) were the most potent followed by **4a** (with four carbons linker) and **4c** (with six carbons linker), while **5a** (with four carbons linker) presented the lowest activity. Finally, the results of HDAC8 inhibitory activity showed that hybrid **4b** was the most potent one, followed by **4c** and **4a**, while **5a** exhibited the lowest inhibitory activity. From these results, it could be concluded that hybrids **4b**, in general, was the most potent and showed the highest selectivity towards HDAC6 followed by **4a**. on the hand, hybrid **5a** displayed the highest selectivity towards HDAC1 followed by hybrid **4c**.

Collectively, from the EGFR and HDAC inhibitory assay results, we could conclude that hybrid **4a–c** and **5a**, in particular, hybrid **4b**, could be considered to be promising anticancer candidates with potential dual EGFR/HDAC inhibitory activities. This could be explained based on the lower activity of hybrid **4b** against HDAC isozyme than the positive reference drug SAHA and EGFR inhibitory activity than the reference drug Gefitinib, and its higher anticancer activity against the tested cancer cell lines than both SAHA and Gefitinib, this can be attributed to its dual inhibitory activity against both HDAC1, 2, 4, 6, 8 and EGFR.

### 2.2.3. Western Blot Assay

Western blot assay [49] of **4b** was carried out on HepG2 cancer cell line (using its IC<sub>50</sub> of 0.536 μM) to detect its effect on EGFR and HDAC6. The obtained results as shown in Figure 4 agreed with the enzymatic assays as hybrid **4b** displayed decrease in both of EGFR and HDAC6 expression in concentration dependent manner using SAHA and Gefitinib as reference drugs, respectively.



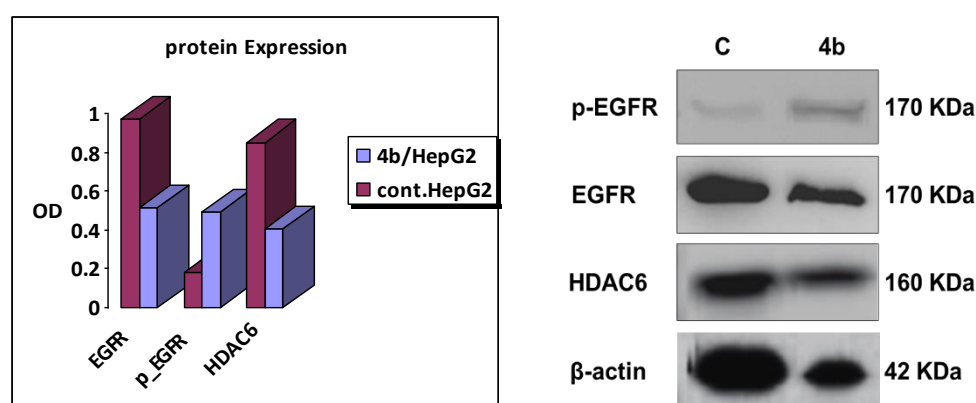


**Figure 4.** Western blot analysis of **4b** on EGFR and HDAC6 in HepG2 cancer cell line.

#### 2.2.4. Apoptotic Markers Activation Assay

The process of the programmed cell death, also known as apoptosis, is characterized by distinct various morphological and energy-dependent biochemical events [50,51]. There are proapoptotic proteins for instance Bad, Bax, Bid, Bcl-Xs and Bim, as well as antiapoptotic members such as Bcl-2, Bcl-XL and Bcl-W [52]. Anti-apoptotic proteins function as apoptosis inhibitors by preventing the discharge of Cytochrome-C while proapoptotic members act as activators for its release. Once the percentage of proapoptotic proteins beats antiapoptotic ones, the exterior mitochondrial membrane turns permeable leading to a cascade of actions. The release Cytochrome-c stimulates caspase-8 and caspase-9 which then triggers caspase-3 which in turn activates apoptosis by attacking various valuable proteins necessary by the cell [53,54].

#### Caspase-3, Caspase-8, Bax and Bcl-2 Levels Assay

Chalcone hybrid **4b** was evaluated as caspase-3 activator against HepG2 cancer cell line as shown in Table 3. The obtained results showed that hybrid **4b** has a remarkable caspase-3 protein level over expression of (483.2 pg/mL) in comparison to the reference drug, staurosporine (445.9 pg/mL). The over-expression level of caspase 3 caused by chalcone hybrid **4b** in HepG2 cancer cell line is about 5.1 folds higher than control, and higher than that of staurosporine (4.71 folds). Therefore, from these results we could suggest that apoptosis may be attributed to caspase-3 over-expression which induced by hybrid **4b**.

**Table 3.** Caspase-3, Caspase-8, Bax and Bcl-2 levels for hybrid **4b** and staurosporine on HepG2 cancer cell line.

Compound №	Caspase-3		Caspase-8		Bax		Bcl-2	
	Conc (pg/mL)	Fold Change	Conc (ng/mL)	Fold Change	Conc (Pg/mL)	Fold Change	Conc (ng/mL)	Fold Change
<b>4b</b>	483.2 ± 14.72	5.1	1.078 ± 0.046	3.15	398.9 ± 14.3	3.75	3.659 ± 0.09	0.42
<b>Staurosporine</b>	445.9 ± 15.39	4.71	1.343 ± 0.026	3.93	362.2 ± 9.61	3.4	3.146 ± 0.31	0.36
<b>Control</b>	94.61 ± 6.5	1	0.342 ± 0.038	1	106.5 ± 5.85	1	8.623 ± 0.19	1

Furthermore, the effect of hybrid **4b** on caspase-8, Bax and Bcl-2 levels against HepG2 cancer cell line using staurosporine as a reference drug, is illustrated in Table 3. The results displayed that hybrid **4b** revealed a remarkable increase in both caspase-8 and Bax levels compared to staurosporine. Hybrid **4b** possessed comparable caspase-8 level over-expression (1.078 ng/mL) compared to that of the reference staurosporine (1.343 ng/mL) (Table 3). Moreover, chalcone hybrid **4b** exhibited a comparable induction of Bax (398.9 ± 14.3 pg/mL) compared to staurosporine (362.2 pg/mL) with 3.75-fold higher than control untreated HepG2 cancer cells. Finally, chalcone hybrid **4b** caused

slightly higher down-regulation of Bcl-2 protein level (3.659 ng/mL) in HepG2 cell line compared to staurosporine (3.146 ng/mL).

### 2.2.5. Flow Cytometric Cell Cycle Analysis

Cell cycle analysis was carried out for the most active hybrid **4b** as a standard drug against HepG2 cancer cell line. Hybrid **4b** markedly increased the proportion of accumulation of cells at the Pre-G1 phase from 2.16 to 47.21%. Moreover, the percentages of HepG2 cell in G0-G1 increased from 42.97 to 53.04% and in S phase from 36.58 to 39.11% that combined with the decrease in the percentage of accumulation of cells at G2/M phase from 20.45 to 7.85% upon treatment with hybrid **4b** (Table 4) indicating that hybrid **4b** arrest cell cycle at G1/S phase. Moreover, it is obvious that the percentage of cell apoptosis increased from 0.12% for control untreated HepG2 cell to 24.67% in treated cells (Table 5, Figure 5). The outcomes revealed that the proportion of the late apoptosis is more than that of early apoptosis which is good proof for irreversible apoptosis caused by hybrid **4b** (Table 5, Figure 5). Corresponding to the above findings, it is apparent that the hybrid **4b** displayed pre G1 apoptosis and cell cycle arrest at G1/S phase. The results demonstrated that the hybrid **4b** are not cytotoxic and induced cell apoptosis in HepG2 cancer cells.

**Table 4.** Cell cycle analysis and apoptosis detection of hybrid **4b**.

Compound	%G0–G1	%S	%G2/M	%Pre-G1	Comment
<b>4b/HepG2</b>	53.04	39.11	7.85	47.21	cell growth arrest at G1/S
<b>cont. HepG2</b>	42.97	36.58	20.45	2.16	

**Table 5.** Results of Apoptotic assay of compound **4b**.

Compound	Total	Apoptosis		Necrosis
		Early	Late	
<b>4b/HepG2</b>	47.21	9.33	24.67	13.21
<b>cont. HepG2</b>	2.16	0.34	0.12	1.7

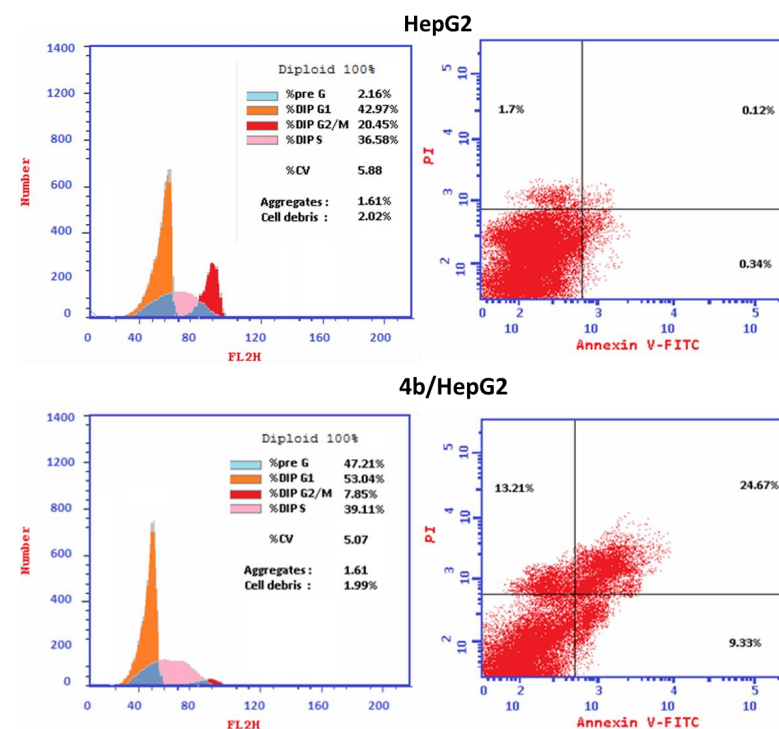


**Figure 5.** Cell cycle analysis and Apoptosis induction analysis using Annexin V/PI of hybrid **4b** in HepG2 cancer cell.

### 2.3. Docking Study

To achieve better understanding of binding mode of target compounds at the molecular level, hybrid **4b** was chosen to be docked into the active site of the 3D crystal structure of EGFR (PDB ID: 1M17) [43], HDAC 1 (PDB entry: 5ICN), HDAC 2 (PDB code: 4LXZ), HDAC 4 (PDB entry: 4CBT), HDAC 6 (PDB entry: 5EF8) and HDAC 8 (PDB entry: 3SFH) [42]. CDOCKER embedded in the Discovery Studio software (Accelrys<sup>®</sup> software corporation, San Diego, CA, USA) was used for performing the docking study. First, validation step was done via redocking of the ligands in all used crystal structures and RMSD values were less than 2 which indicates the validity and confidence in the produced docking results.

#### 2.3.1. EGFR Docking Study

Analysis of the docking results of Gefitinib (Figure 6A,B) revealed that it engaged with one hydrogen bond with Cys773. Additionally, attractive charge, Pi-Cation and Pi-Anion with Lys721 and Asp831 was observed. Additionally, it formed one Halogen interaction between Cl atom and Leu764. Moreover, it was incorporated in many hydrophobic interactions as Pi-Sigma with Leu820, Pi-Sulfur with Met742, van der Waal, Alkyl, Pi-Alkyl and Carbon Hydrogen bond with Leu694, Val702, Lys721 and Gly772. Interestingly, the docking results of hybrid **4b** (Figure 6C,D) showed that it binds nicely with the pocket through formation of 4 hydrogen bonds with Thr766, Met769, Phe771 and Cys773. In addition, Carbon Hydrogen bond with Glu738 and Pro770 and Pi-Alkyl with Leu694, Val702, Ala719 and Leu820 was detected.

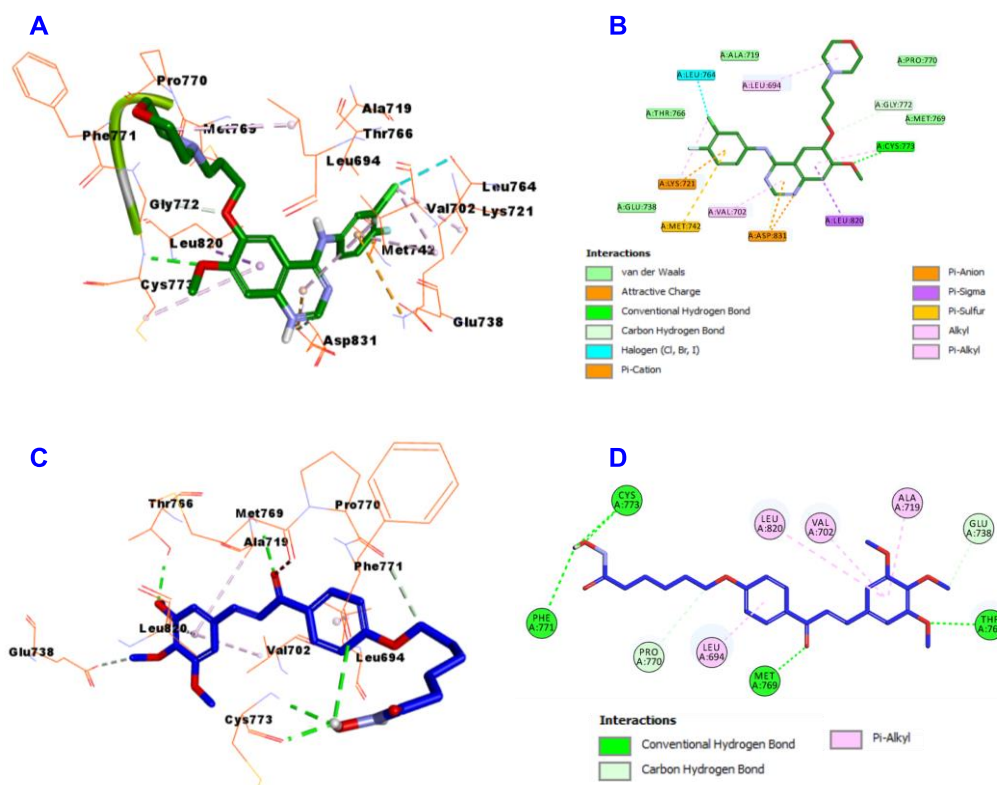


**Figure 6.** Docking and binding mode of **Gefitinib** (green) and **4b** (blue) into ATP-active site of EGFR kinase (PDB code: 1M17); (A) 3D structure of **Gefitinib**, (B) 2D structure of **Gefitinib**, (C) 3D structure of **4b**, (D) 2D structure of **4b**.

#### 2.3.2. HDAC1 Docking Study

Concerning the docking study results of **SAHA** (Figure 7A,B) and hybrid **4b** (Figure 7C,D) into the active site of the structure of HDAC1, the data displayed that **SAHA** engaged in the formation of 4 hydrogen bonds with Hist18, Gly27, Lys31 and Lys331. Ad-

ditionally, it forms many hydrophobic interactions such as Pi-cation with Lys331, Carbon Hydrogen bond with Pro29 and Pi-pi T-shaped interaction with Tyr336. Meanwhile, hybrid **4b** engaged in the formation of 4 hydrogen bonds with Lys31, Lys305, Lys331 and Gln339. In addition, it also involved in many hydrophobic interactions such as Pi-cation with Ar270, van der Waal and Carbon Hydrogen bond with Lys331, Glu335 and Tyr336.

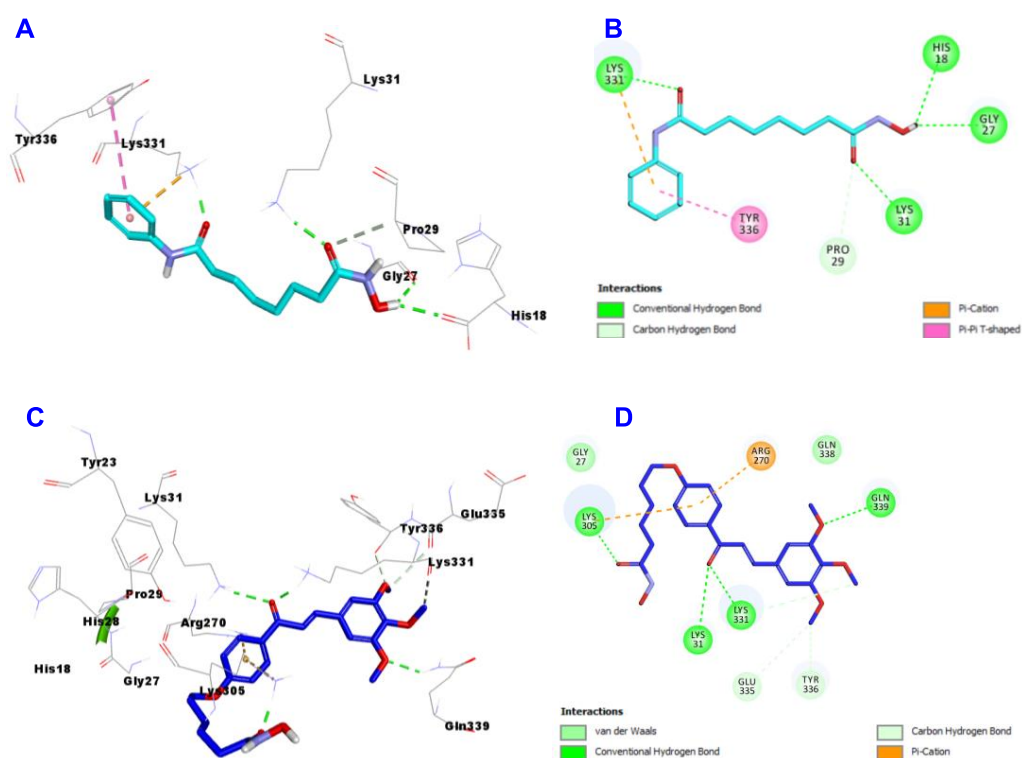


**Figure 7.** Docking and binding mode of SAHA (cyan) and **4b** (blue) into the active site of HDAC 1 (PDB entry: 5ICN); (A) 3D structure of SAHA, (B) 2D structure of SAHA, (C) 3D structure of **4b**, (D) 2D structure of **4b**.

### 2.3.3. HDAC2 Docking Study

HDAC2 docking results exhibited that SAHA (Figure 8A,B) formed 5 hydrogen bonds with Asp104, His145, His146, Asp181 and Tyr208, two metal acceptors with Zn:401 and one Pi-Alkyl with Pro34.

Hybrid **4b** (Figure 8C,D) was incorporated in formation of 3 hydrogen bonds with His145 (two) and Tyr208 and two metal acceptor interactions with Zn:401. Hybrid **4b** also showed many hydrophobic interactions as Amide-Pi stacked with Gly32, Pi-Alkyl with Pro34 and Leu276, van der Waal and Carbon Hydrogen bond with Glu103 and Asp104.

### 2.3.4. HDAC4 Docking Study

Regarding the docking results of SAHA (Figure 9A,B) and hybrid **4b** (Figure 9C,D) into the active site of HDAC4, the data showed that SAHA formed 3 hydrogen bonds with His802, Asp840 and His842, one metallic acceptor with Zn:2036 and one Pi-Alkyl with Pro676. On the hand, hybrid **4b** engaged in two hydrogen bonds with Asp840 and His842 and one metallic acceptor with Zn:2036. Hybrid **4b** showed more hydrophobic interactions than SAHA such as Pi-Pi Stacked and Pi-Pi T-shaped with Phe812, Phe871 and Gly975.

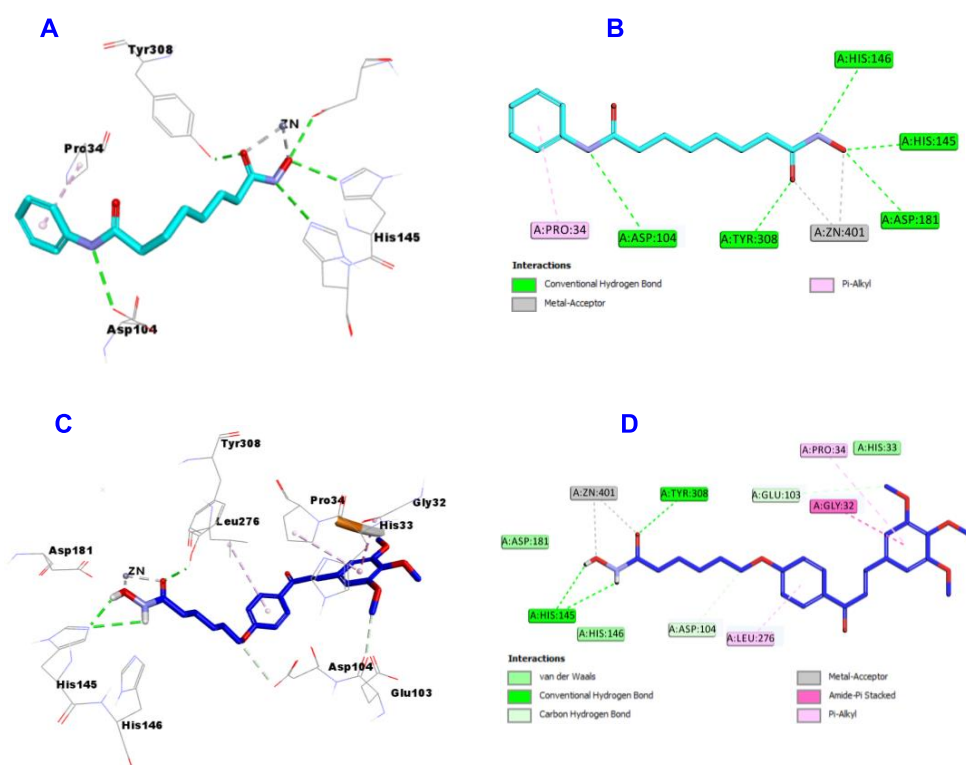


**Figure 8.** Docking and binding mode of SAHA (cyan) and 4b (blue) into the active site of HDAC2 (PDB: 4LXZ); (A) 3D structure of SAHA, (B) 2D structure of SAHA, (C) 3D structure of 4b, (D) 2D structure of 4b.

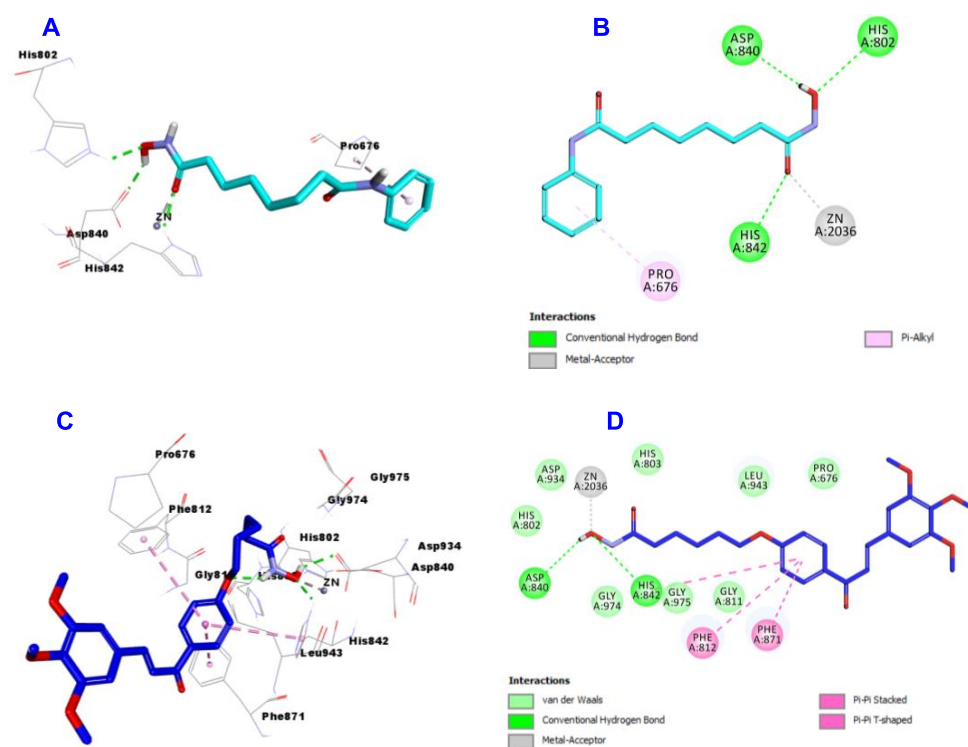


**Figure 9.** Docking and binding mode of SAHA (cyan) and 4b (blue) into the active site of HDAC4 (PDB entry: 4CBT); (A) 3D structure of SAHA, (B) 2D structure of SAHA, (C) 3D structure of 4b, (D) 2D structure of 4b.

### 2.3.5. HDAC6 Docking Study

Inspection of the docking results of SAHA (Figure 10A,B) and hybrid **4b** (Figure 10C,D) into the active site of HDAC6, the data showed that SAHA binds through the formation of 3 hydrogen bonds with Gly582 (two) and His614, one metal acceptor with Zn:2001, one Pi-Sigma with Phe583, Pi-Pi T-shaped with His463 and Pi-Alkyl with Pro464. Meanwhile, hybrid **4b** engaged in 3 hydrogen bonds with Gly582, His573 and His614, one metal acceptor with Zn:2001, Pi-Pi T-shaped with His463, van der Waal and Carbon Hydrogen bond with Asp460 and Ileu532.

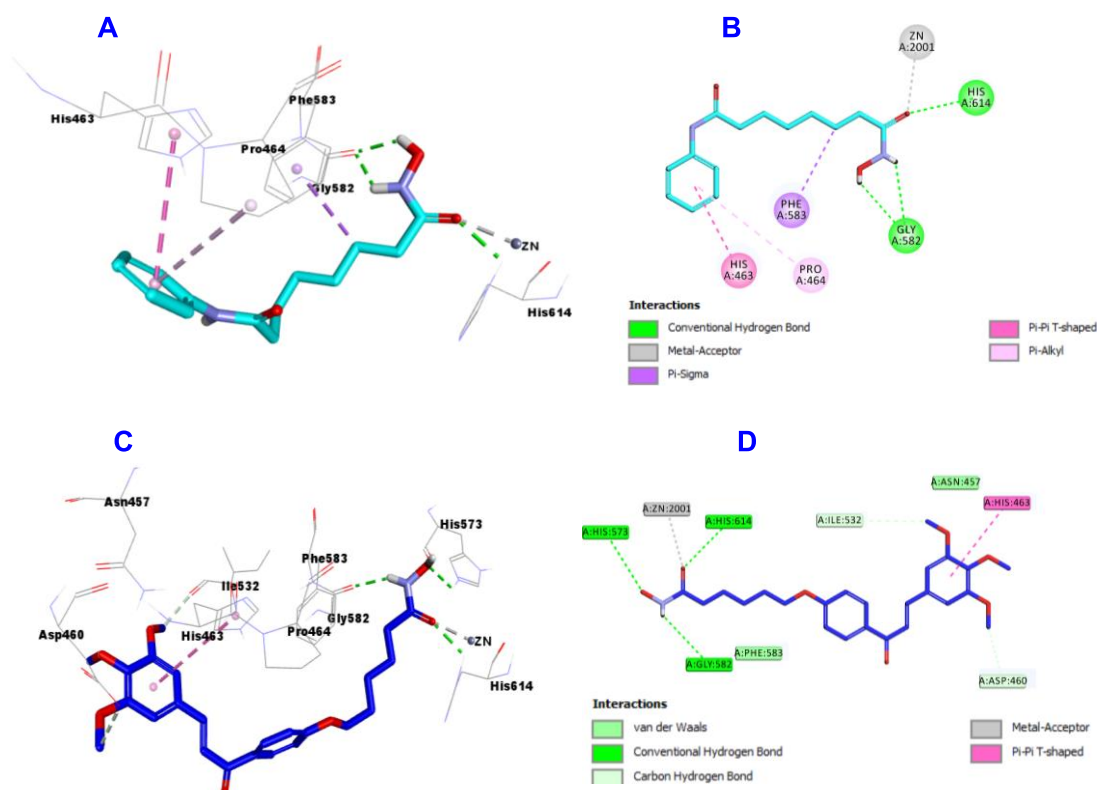


**Figure 10.** Docking and binding mode of SAHA (cyan) and **4b** (blue) into the active site of HDAC 6 (PDB entry: 5EF8); (A) 3D structure of SAHA, (B) 2D structure of SAHA, (C) 3D structure of **4b**, (D) 2D structure of **4b**.

### 2.3.6. HDAC8 Docking Study

Finally, the HDAC8 docking results revealed that SAHA incorporated in 3 hydrogen bonds with Lys33 (two) and Gly151, one metal acceptor with Zn:403 and one Pi-Sulfur with Cys153 (Figure 11A,B).

Regarding hybrid **4b**, it was involved in the formation of 4 hydrogen bonds with one hydrogen bond more than SAHA with His142, His143, Asp178 and His180. Additionally, hybrid **4b** formed the same metal acceptor with Zn:403. Additionally, hybrid **4b** form more hydrophobic interactions than SAHA such as Pi-Pi Stacked and Pi-Pi T-shaped with Phe152, His180 and Tyr306. Moreover, it formed van der Waal and Carbon Hydrogen bond with Gly206 and Tyr306 and one Pi-Cation with Zn:403 (Figure 11C,D).

All the above results together with the docking study suggest that hybrids **4a–c** and **5a**, in particular **4b**, may be considered to be promising lead candidates for the design and innovation of novel anticancer agents with dual EGFR/HDAC inhibitory activities, which merits further study and modifications that is underwork in our lab.

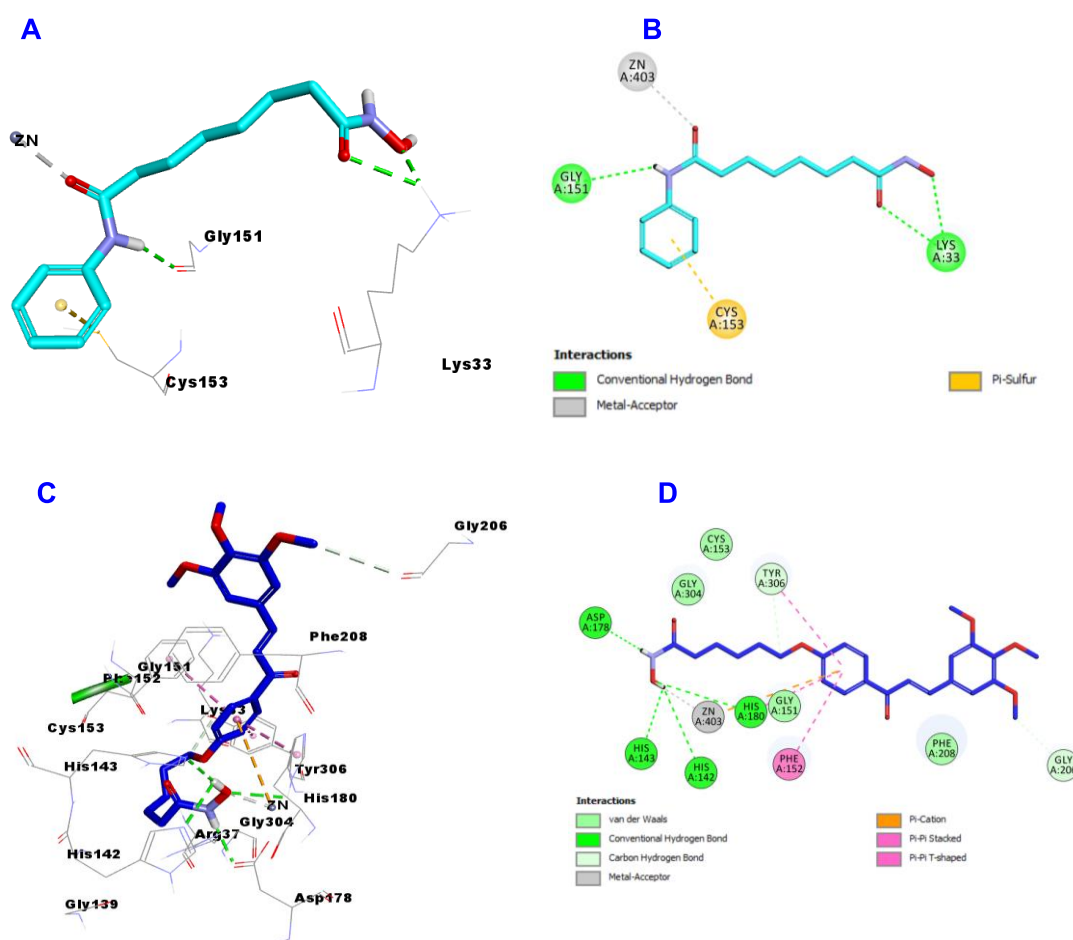


**Figure 11.** Docking and binding mode of SAHA (cyan) and **4b** (blue) into the active site of HDAC 8 (PDB entry: 3SFH); (A) 3D structure of SAHA, (B) 2D structure of SAHA, (C) 3D structure of **4b**, (D) 2D structure of **4b**.

### 3. Experimental

#### 3.1. Chemistry

For experimental details, See Section 1.1 in Supplementary Materials.

Compound **1** was prepared according to the previously reported procedure [45].

##### 3.1.1. General Procedure for Synthesis of Hybrids (**2a–c**)

A mixture of compound **1** (5 mmol), anhydrous potassium carbonate (10 mmol) and the appropriate ester (5 mmol) namely; ethyl 5-bromopentanoate (1.045 g), ethyl 6-bromohexanoate (1.115 g) and ethyl 7-bromoheptanoate (1.185 g) was stirred in DMF (20 mL) at 70–80 °C for 12 h. Then the reaction mixture was diluted with crushed ice and the resulting precipitate was filtered, washed with water and dried. Then, to the produced ester residue in methanol 2.5 equivalent of KOH were added and the reaction mixture was stirred at 40–50 °C heated for 7–8 h. After cooling to room temperature and acidification with dilute HCl, the separated solid was filtered and washed with water. The crude product is dried and recrystallized from ethyl acetate to afford **2a–c**.

##### (E)-5-(4-(3-(3,4,5-Trimethoxyphenyl)Acryloyl)Phenoxy)Pentanoic Acid (**2a**)

Yellow solid; 68% yield; mp = 102–105 °C,  $^1\text{H}$  NMR (400 MHz, DMSO- $d_6$ )  $\delta$  = 12.31 (s, 1H, OH); 8.36 (d, 2H,  $J$  = 8 Hz); 8.08 (d, 1H,  $J$  = 12 Hz); 7.89 (d, 1H,  $J$  = 12 Hz); 7.40 (s, 2H); 7.24 (d, 2H,  $J$  = 8 Hz); 4.25 (br s, 2H); 4.07 (br s, 6H); 3.93 (s, 3H); 2.50 (br s, 2H); 1.95 (br s, 1H), 1.94–1.45 (m, 4H).  $^{13}\text{C}$  NMR (101 MHz, DMSO- $d_6$ )  $\delta$  = 187.8, 174.9, 163.0, 153.6, 144.0, 140.1, 131.3, 130.9, 130.9, 121.6, 114.7, 114.6, 106.8, 68.0, 60.5, 56.5, 56.2, 33.7, 28.5, 21.6. Anal. Calcd. for  $\text{C}_{23}\text{H}_{26}\text{O}_7$ : C, 66.65; H, 6.32. Found: C, 66.62; H, 6.22.

**(E)-6-(4-(3-(3,4,5-Trimethoxyphenyl)Acryloyl)Phenoxy)Hexanoic Acid (2b)**

Yellow solid; 72% yield; mp = 138–140 °C,  $^1\text{H}$  NMR (400 MHz, DMSO- $d_6$ )  $\delta$  = 12.07 (s, 1H, OH); 8.19 (d, 2H, J = 8 Hz); 7.93 (d, 1H, J = 12 Hz); 7.69 (d, 1H, J = 12 Hz); 7.24 (s, 2H); 7.05 (d, 2H, J = 8 Hz); 4.04 (t, 2H, J = 8 Hz); 3.88 (br s, 6H); 3.73 (s, 3H); 2.25 (t, 2H, J = 8 Hz); 1.73 (d, 2H, J = 8 Hz), 1.58 (t, 2H, J = 8 Hz); 1.44 (d, 2H, J = 8 Hz).  $^{13}\text{C}$  NMR (101 MHz, DMSO- $d_6$ )  $\delta$  = 187.8, 174.9, 163.1, 153.6, 144.0, 140.1, 131.4, 130.9, 121.6, 114.8, 114.6, 106.8, 68.21, 60.55, 60.12, 56.51, 34.1, 33.9, 28.8, 25.6, 25.4, 24.7, 14.5. Anal. Calcd. for  $\text{C}_{24}\text{H}_{28}\text{O}_7$ : C, 67.28; H, 6.59. Found: C, 66.99; H, 6.62.

**(E)-7-(4-(3-(3,4,5-Trimethoxyphenyl)Acryloyl)Phenoxy)Heptanoic Acid (2c)**

Yellow solid; 75% yield; mp = 112–115 °C,  $^1\text{H}$  NMR (400 MHz, DMSO- $d_6$ )  $\delta$  = 12.03 (s, 1H, OH); 8.18 (d, 2H, J = 8 Hz); 7.91 (d, 1H, J = 16 Hz); 7.70 (d, 1H, J = 16 Hz); 7.23 (s, 2H); 7.06 (d, 2H, J = 8 Hz); 4.04 (t, 2H, J = 8 Hz); 3.88 (s, 6H); 3.74 (s, 3H); 2.22 (t, 2H, J = 8 Hz), 1.72 (t, 2H, J = 8 Hz), 1.55 (t, 2H, J = 8 Hz), 1.43–1.25 (m, 4H).  $^{13}\text{C}$  NMR (101 MHz, DMSO- $d_6$ )  $\delta$  = 187.7, 175.0, 163.1, 162.9, 153.6, 144.0, 140.1, 140.0, 131.4, 130.9, 130.2, 121.6, 114.8, 114.6, 106.8, 68.3, 60.5, 56.6, 56.5, 34.1, 28.9, 28.8, 26.7, 25.7, 24.9. Anal. Calcd. for  $\text{C}_{25}\text{H}_{30}\text{O}_7$ : C, 67.86; H, 6.83. Found: C, 67.65; H, 6.77.

**3.1.2. General Procedure for Synthesis of Hybrids (3a–c)**

To a mixture of the above prepared chalcone **2a–c** (10 mmol), ethyl cyanoacetate (1.1 g, 10 mmol), and ammonium acetate (6.2 g, 80 mmol) in absolute ethanol (30 mL) was heated under reflux for 24 h. The reaction was monitored by TLC. The reaction mixture was left behind to cool at room temperature and the formed solid product was filtered, washed with water, dried, and recrystallized from ethanol.

**5-(4-(5-Cyano-6-Oxo-4-(3,4,5-Trimethoxyphenyl)-1,6-Dihydropyridin-2-yl)Phenoxy)Pentanoic Acid (3a)**

Pale yellow solid; 70% yield; mp = 224–228 °C,  $^1\text{H}$  NMR (400 MHz, DMSO- $d_6$ )  $\delta$  = 7.88 (d, 2H, J = 8 Hz); 7.06–7.04 (m, 4H); 6.83 (s, 1H, pyridine-H); 4.05 (br s, 2H); 3.88 (br s, 6H); 3.76 (s, 3H); 2.39–1.99 (m, 4H); 1.97–1.70 (m, 2H); 1.69–1.43 (m, 2H).  $^{13}\text{C}$  NMR (101 MHz, DMSO- $d_6$ )  $\delta$  = 175.0, 162.8, 161.5, 159.9, 153.3, 151.5, 139.6, 131.8, 130.9, 129.9, 124.7, 117.5, 115.2, 114.8, 114.6, 106.5, 105.5, 97.3, 68.0, 60.6, 56.6, 33.8, 28.5, 21.6. Anal. Calcd. for  $\text{C}_{26}\text{H}_{26}\text{N}_2\text{O}_7$ : C, 65.26; H, 5.48; N, 5.85. Found: C, 65.55; H, 5.34; N, 6.01.

**6-(4-(5-Cyano-6-Oxo-4-(3,4,5-Trimethoxyphenyl)-1,6-Dihydropyridin-2-yl)Phenoxy)Hexanoic Acid (3b)**

Yellowish white solid; 77% yield (97mg); mp = 192–194 °C,  $^1\text{H}$  NMR (400 MHz, DMSO- $d_6$ )  $\delta$  = 12.31 (br. s, 2H, OH, NH); 7.87 (d, 2H, J = 8 Hz); 7.06–7.04 (m, 4H); 6.82 (s, 1H, pyridine-H); 4.04 (t, 2H, J = 8 Hz); 3.87 (s, 6H); 3.76 (s, 3H); 2.24 (t, 2H, J = 8 Hz); 1.77–1.70 (m, 2H); 1.61–1.53 (m, 2H); 1.46–1.41 (m, 2H).  $^{13}\text{C}$  NMR (101 MHz, DMSO- $d_6$ )  $\delta$  = 174.9, 162.6, 161.6, 160.0, 153.3, 151.3, 139.6, 131.8, 129.9, 124.6, 117.4, 115.2, 106.5, 105.5, 97.5, 68.2, 60.6, 56.6, 34.1, 28.8, 25.5, 24.7. Anal. Calcd. for  $\text{C}_{27}\text{H}_{28}\text{N}_2\text{O}_7$ : C, 65.84; H, 5.73; N, 5.69. Found: C, 65.89; H, 5.65; N, 5.94.

**7-(4-(5-Cyano-6-Oxo-4-(3,4,5-Trimethoxyphenyl)-1,6-Dihydropyridin-2-yl)Phenoxy)Heptanoic Acid (3c)**

Yellow solid; 79% yield (97mg); mp = 168–170 °C,  $^1\text{H}$  NMR (400 MHz, DMSO- $d_6$ )  $\delta$  = 12.20 (br. s, 2H, OH, NH); 7.89 (d, 2H, J = 8 Hz); 7.06 (s, 2H); 6.99 (d, 2H, J = 8 Hz); 6.82 (s, 1H, pyridine-H); 4.02 (t, 2H, J = 8 Hz); 3.89 (s, 6H); 3.78 (s, 3H); 2.22 (br s, 2H); 1.80–1.62 (m, 2H); 1.61–1.46 (m, 2H); 1.45–1.25 (m, 4H).  $^{13}\text{C}$  NMR (101 MHz, DMSO- $d_6$ )  $\delta$  = 175.0, 163.0, 162.6, 161.6, 160.0, 153.3, 153.2, 151.3, 139.6, 131.8, 130.9, 130.1, 129.8, 124.4, 117.4, 115.1, 114.6, 106.4, 105.4, 97.4, 68.2, 60.6, 56.5, 34.0, 28.9, 28.7, 25.6, 24.9. Anal. Calcd. for  $\text{C}_{28}\text{H}_{30}\text{N}_2\text{O}_7$ : C, 66.39; H, 5.97; N, 5.53. Found: C, 66.56; H, 6.02; N, 5.89.



### 3.1.3. General Procedure for Synthesis of Hybrids (4a–c)

The chalcone-acids **2a–c** (1 mmol) was dissolved in dichloromethane (10 mL) then *N,N'*-carbonyldiimidazole (CDI) (4 mmol, 0.648 g) was added at 25–30 °C and stirred for 4 h. Hydroxylamine hydrochloride (4 mmol, 0.278 g) was added, and the stirring was continued for another 12 h. The solvent was distilled off, ethylacetate (10 mL) was added, washed with water (2 × 10 mL), and the organic layer was collected, dried over anhydrous sodium sulphate, filtered, and evaporated under vacuum to afford **4a–c**.

#### (*E*)-*N*-Hydroxy-5-(4-(3-(3,4,5-Trimethoxyphenyl)Acryloyl)Phenoxy) Pentanamide (**4a**)

Yellow solid; 60% yield; mp = 220–224 °C, <sup>1</sup>H NMR (400 MHz, DMSO-d<sub>6</sub>) δ = 10.54 (s, 1H, NH); 8.72 (s, 1H, OH); 8.22 (s, 2H); 7.93 (d, 1H, J = 16 Hz); 7.68 (d, 1H, J = 16 Hz); 7.32 (s, 2H); 7.08 (s, 2H); 4.05 (br s, 2H); 3.86 (s, 6H); 3.75 (s, 3H); 2.34–2.01 (m, 2H); 1.95–1.35 (m, 4H). <sup>13</sup>C NMR (101 MHz, DMSO-d<sub>6</sub>) δ = 203.6, 187.7, 169.0, 163.0, 153.6, 144.1, 140.1, 131.4, 130.9, 130.4, 127.7, 121.6, 117.5, 114.9, 106.9, 105.0, 67.8, 60.6, 56.6, 56.4, 32.2, 28.6, 22.4. Anal. Calcd. for C<sub>23</sub>H<sub>27</sub>NO<sub>7</sub>: C, 64.32; H, 6.34; N, 3.26. Found: C, 64.02; H, 6.25; N, 3.46.

#### (*E*)-*N*-Hydroxy-6-(4-(3-(3,4,5-Trimethoxyphenyl)Acryloyl)Phenoxy) Hexanamide (**4b**)

Yellow solid; 69% yield; mp = 98–102 °C, <sup>1</sup>H NMR (400 MHz, DMSO-d<sub>6</sub>) δ = 10.43 (s, 1H, NH); 8.75 (s, 1H, OH); 8.19 (s, 2H); 7.90 (d, 1H, J = 16 Hz); 7.69 (d, 1H, J = 16 Hz); 7.22 (s, 2H); 7.08 (s, 2H); 4.06 (br s, 2H); 3.88 (s, 6H); 3.73 (s, 3H); 2.29–1.99 (m, 2H); 1.85–1.25 (m, 5H). <sup>13</sup>C NMR (101 MHz, DMSO-d<sub>6</sub>) δ = 188.0, 173.5, 170.0, 163.1, 153.5, 153.1, 144.1, 140.0, 131.4, 130.8, 130.0, 127.7, 121.6, 114.8, 114.6, 106.7, 68.2, 60.6, 56.5, 34.0, 32.6, 28.7, 25.5, 24.9. Anal. Calcd. for C<sub>24</sub>H<sub>29</sub>NO<sub>7</sub>: C, 65.00; H, 6.59; N, 3.16. Found: C, 64.92; H, 6.48; N, 3.35.

#### (*E*)-*N*-Hydroxy-7-(4-(3-(3,4,5-Trimethoxyphenyl)Acryloyl)Phenoxy)Heptanamide (**4c**)

Pale yellow solid; 64% yield; mp = 122–128 °C, <sup>1</sup>H NMR (400 MHz, DMSO-d<sub>6</sub>) δ = 10.49 (s, 1H, NH); 9.14 (s, 1H, OH); 8.16 (d, 2H, J = 8 Hz); 7.89 (d, 1H, J = 16 Hz); 7.66 (d, 2H, J = 16 Hz); 7.21 (s, 1H); 7.04 (d, 2H, J = 8 Hz); 4.03 (br s, 2H); 3.85 (s, 6H); 3.78 (s, 3H); 2.12–1.88 (m, 2H); 1.74–1.58 (m, 2H); 1.55–1.45 (m, 2H); 1.44–1.19 (m, 4H). <sup>13</sup>C NMR (101 MHz, DMSO-d<sub>6</sub>) δ = 187.8, 169.8, 163.1, 159.5, 153.6, 152.8, 144.1, 140.1, 134.5, 131.4, 130.4, 130.8, 127.9, 121.7, 119.6, 114.8, 114.6, 106.9, 69.3, 60.6, 56.6, 32.7, 28.9, 25.6, 25.5. Anal. Calcd. for C<sub>25</sub>H<sub>31</sub>NO<sub>7</sub>: C, 65.63; H, 6.83; N, 3.06. Found: C, 65.66; H, 6.96; N, 3.15.

### 3.1.4. General Procedure for Synthesis of Hybrids (5a–c)

The 3-cyano-2-oxopyridine carboxylic acid derivatives **3a–c** (1 mmol) was dissolved in dry dichloromethane (10 mL) then *N,N'*-carbonyldiimidazole (4 mmol, 0.648 g) was added at 25–30 °C and stirred for 4 h. Hydroxylamine hydrochloride (4 mmol, 0.278 g) was added, and the stirring was continued for another 12 h. The solvent was distilled off, ethyl acetate (10 mL) was added, washed with water (2 × 10 mL), and the organic layer was collected, dried over anhydrous sodium sulphate, filtered, and evaporated under vacuum to obtain the desired products **5a–c**.

#### 5-(4-(5-Cyano-6-Oxo-4-(3,4,5-Trimethoxyphenyl)-1,6-Dihydropyridin-2-yl)Phenoxy)-*N*-Hydroxypentanamide (**5a**)

Yellow solid; 61% yield; mp = 232–238 °C, <sup>1</sup>H NMR (400 MHz, DMSO-d<sub>6</sub>) δ = 12.59 (s, 1H, NH); 10.44 (s, 1H, NH); 8.75 (s, 1H, OH); 7.89 (d, 2H, J = 8 Hz); 7.07 (d, 4H, J = 8 Hz); 6.83 (s, 1H, pyridine-H); 4.04 (br s, 2H); 3.88 (s, 6H); 3.76 (s, 3H); 2.64–2.44 (m, 1H); 2.15–1.95 (m, 2H); 1.85–1.55 (m, 4H). <sup>13</sup>C NMR (101 MHz, DMSO-d<sub>6</sub>) δ = 169.5, 162.6, 161.6, 160.0, 153.3, 139.6, 131.8, 129.9, 124.6, 117.4, 115.2, 105.5, 105.6, 68.0, 60.6, 56.6, 32.3, 28.5, 22.2. Anal. Calcd. for C<sub>26</sub>H<sub>27</sub>N<sub>3</sub>O<sub>7</sub>: C, 63.28; H, 5.51; N, 8.51. Found: C, 63.33; H, 5.23; N, 8.74.

6-(4-(5-Cyano-6-Oxo-4-(3,4,5-Trimethoxyphenyl)-1,6-Dihydropyridin-2-yl)Phenoxy)-*N*-Hydroxyhexanamide (**5b**)

Yellow solid; 65% yield; mp = 198–204 °C, <sup>1</sup>H NMR (400 MHz, DMSO-*d*<sub>6</sub>) δ = 12.30 (s, 1H, NH); 10.36 (s, 1H, NH); 8.86 (s, 1H, OH); 7.88 (d, 2H, J = 8 Hz); 7.07–7.04 (m, 4H); 6.83 (s, 1H, pyridine-H); 4.04 (br s, 2H); 3.86 (s, 6H); 3.75 (s, 3H); 1.98 (s, 2H); 1.96–1.41 (m, 6H); 1.61–1.53 (m, 2H); 1.46–1.41 (m, 2H). <sup>13</sup>C NMR (101 MHz, DMSO-*d*<sub>6</sub>) δ = 170.0, 162.6, 161.6, 160.0, 157.6, 153.3, 152.9, 139.6, 131.8, 129.9, 122.5, 117.4, 115.8, 115.3, 106.5, 105.2, 104.9, 68.2, 60.6, 56.6, 32.7, 28.7, 25.6, 25.3. Anal. Calcd. for C<sub>27</sub>H<sub>29</sub>N<sub>3</sub>O<sub>7</sub>: C, 63.90; H, 5.76; N, 8.28. Found: C, 63.99; H, 5.87; N, 8.51.

7-(4-(5-Cyano-6-Oxo-4-(3,4,5-Trimethoxyphenyl)-1,6-dihydropyridin-2-yl)phenoxy)-*N*-Hydroxyheptanamide (**5c**)

Yellow solid; 72% yield; mp = 170–176 °C, <sup>1</sup>H NMR (400 MHz, DMSO-*d*<sub>6</sub>) δ = 12.60 (br s, 1H, NH); 10.34 (s, 1H, NH); 8.67 (s, 1H, OH); 7.89 (d, 1H, J = 16 Hz); 7.49–7.05 (m, 4H); 6.83 (s, 1H, pyridine-H); 4.32 (br s, 2H); 3.86 (s, 6H); 3.79 (s, 3H); 2.05 (s, 2H); 1.96–1.31 (m, 8H). <sup>13</sup>C NMR (101 MHz, DMSO-*d*<sub>6</sub>) δ = 170.0, 162.5, 161.7, 155.4, 153.3, 142.5, 139.6, 131.8, 130.9, 129.9, 126.9, 116.5, 115.2, 109.3, 106.5, 101.2, 68.3, 62.8, 60.8, 60.6, 58.3, 56.6, 56.5, 35.5, 32.7, 28.9, 25.6, 25.5. Anal. Calcd. for C<sub>28</sub>H<sub>31</sub>N<sub>3</sub>O<sub>7</sub>: C, 64.48; H, 5.99; N, 8.06. Found: C, 64.55; H, 6.02; N, 8.32.

### 3.2. Biological Evaluation

#### 3.2.1. Cytotoxic Activity Using MTT Assay and Evaluation of IC<sub>50</sub>.

##### MTT Assay

MTT assay was performed to investigate the effect of the synthesized compounds on mammary epithelial cells (MCF-10A) [55]. **See Section 4.2.1.1 in Supplementary Materials.**

##### Assay for Antiproliferative Effect

To explore the antiproliferative potential of compounds propidium iodide fluorescence assay was performed [55] using different cell lines. **See Section 4.2.1.2 in Supplementary Materials.**

#### 3.2.2. EGFR Inhibitory Assay

A cell-free assay was used to explore the mechanism of inhibition of EGFR kinase of the most active compounds according to the reported method [43]. **See Section 4.2.2 in Supplementary Materials.**

#### 3.2.3. In Vitro HDAC Isoforms Inhibitory Activity

All of the enzymatic reactions for HDAC1, HDAC2, HDAC4, HDAC6 and HDAC8 were conducted at 37 °C for 30 min software [42,47,48]. **See Section 4.2.6 in Supplementary Materials.**

#### 3.2.4. Western Blot Assay

Western blot assay was carried out according to the previously reported protocol [49].

#### 3.2.5. Caspase-3 and 8 Activation Assay

Cell line cells of MCF-7 and HepG2 were obtained from ATCC. RPMI 1640 containing 10% FBS was used to allow cells to grow at 37 °C, stimulated with the compounds to be tested for caspase-3 or caspase-8 [43]. **See Section 4.2.3 in Supplementary Materials.**

#### 3.2.6. Evaluation of Bax and Bcl-2 Expressions

m RNA isolation was carried out using RNeasy extraction kit, up to 1 × 10<sup>7</sup> cells. They were disrupted in Buffer RLT and homogenized [43]. **See Section 4.2.4 in Supplementary Materials.**

### 3.2.7. Cell Apoptosis Assay

Apoptosis was determined by flow cytometry based on the Annexin-V-fluoresce in isothiocyanate (FITC) and propidium iodide (PI) staining kit (BD Pharmingen, San Diego, CA, USA) [43]. See Section 4.2.5 in Supplementary Materials.

### 3.3. Docking Study

The 3.5 Å 3D structures of EGFR (PDB ID: 1M17) [43], HDAC 1 (PDB entry: 5ICN), HDAC 2 (PDB code: 4LXZ), HDAC 4 (PDB entry: 4CBT), HDAC 6 (PDB entry: 5EF8) and HDAC 8 (PDB entry: 3SFH) [43] were downloaded from protein data bank [56]. All molecular modeling calculations and docking studies were carried out using Discovery Studio software 2016 client v16.1.0.15350 (San Diego, CA, USA) with CDOCKER program. See Section 4.4 in Supplementary Materials.

## 4. Conclusions

In this work, 12 new final target hybrids **2a–c**, **3a–c**, **4a–c** and **5a–c** were designed, synthesized, characterized, and evaluated for their in vitro anti-proliferative activity against four cancer cell lines. Hybrids **4a–c** and **5a** displayed potent growth inhibition of cancer cells compared to SAHA and Gefitinib as reference drugs. Furthermore, Hybrids **4a–c** and **5a** were evaluated for their EGFR and HDAC inhibitory effect. Hybrid **4b** showed  $IC_{50} = 0.063 \pm 0.002 \mu\text{M}$  on the target EGFR enzyme which is slightly less potent than staurosporine reference drug ( $IC_{50} = 0.044 \pm 0.001 \mu\text{M}$ ). Furthermore, hybrid **4b** showed promising HDAC inhibitory activity against HDAC1 (0.148), 2 (0.168), 4 (5.852), 6 (0.06) and 8 (2.257) that was less potent than SAHA with  $IC_{50}$  values of 0.037, 0.112, 4.062, 0.019 and 1.133 against HDAC1, 2, 4, 6 and 8, respectively. The investigation of apoptotic effect of the most potent hybrid **4b** showed a noticeable increase in Bax level up to 3.75 folds, and down-regulation in Bcl2 to 0.42-fold, in comparison to the control. Moreover, hybrid **4b** showed increase in the level of Caspases 3 and 8 by 5.1 and 3.15 folds, respectively. The results of cell cycle analysis of hybrid **4b** revealed that it showed programmed cell death and cell cycle arrest at G1/S phase. Taken together with molecular docking study; suggested the rationalized target of hybrids **4a–c** and **5a**, particularly **4b**, may be promising lead candidates for discovery of novel anticancer agents via dual inhibition of both EGFR/HDAC enzymes.

**Supplementary Materials:** The following are available online at <https://www.mdpi.com/article/10.3390/ph14111177/s1>. Figure S1.  $^1\text{H}$ NMR spectrum for compound 2a; Figure S2.  $^{13}\text{C}$ NMR spectrum for compound 2a; Figure S3.  $^1\text{H}$ NMR spectrum for compound 2b; Figure S4.  $^{13}\text{C}$ NMR spectrum for compound 2b; Figure S5.  $^1\text{H}$ NMR spectrum for compound 2c; Figure S6.  $^{13}\text{C}$ NMR spectrum for compound 2c; Figure S7.  $^1\text{H}$ NMR spectrum for compound 3a; Figure S8.  $^{13}\text{C}$ NMR spectrum for compound 3a; Figure S9.  $^1\text{H}$ NMR spectrum for compound 3b; Figure S10.  $^{13}\text{C}$ NMR spectrum for compound 3b; Figure S11.  $^1\text{H}$ NMR spectrum for compound 3c; Figure S12.  $^{13}\text{C}$ NMR spectrum for compound 3c; Figure S13.  $^1\text{H}$ NMR spectrum for compound 4a; Figure S14.  $^{13}\text{C}$ NMR spectrum for compound 4a; Figure S15.  $^1\text{H}$ NMR spectrum for compound 4b; Figure S16.  $^{13}\text{C}$ NMR spectrum for compound 4b; Figure S17.  $^1\text{H}$ NMR spectrum for compound 4c; Figure S18.  $^{13}\text{C}$ NMR spectrum for compound 4c; Figure S19.  $^1\text{H}$ NMR spectrum for compound 5a; Figure S20.  $^{13}\text{C}$ NMR spectrum for compound 5a; Figure S21.  $^1\text{H}$ NMR spectrum for compound 5b; Figure S22.  $^{13}\text{C}$ NMR spectrum for compound 5b; Figure S23.  $^1\text{H}$ NMR spectrum for compound 5c; Figure S24.  $^{13}\text{C}$ NMR spectrum for compound 5c.

**Author Contributions:** Conceptualization, T.S.I., A.M.M. and M.F.A.M.; methodology, A.M.M. and M.F.A.M.; software, M.F.A.M.; validation, T.S.I., A.M.M. and M.F.A.M.; formal analysis, T.S.I., A.M.M. and M.F.A.M.; investigation, T.S.I., A.M.M. and M.F.A.M.; resources, T.S.I.; data curation, T.S.I.; writing—original draft preparation, M.F.A.M.; writing—review and editing, A.M.M.; visualization, M.F.A.M.; supervision, T.S.I.; project administration, T.S.I.; funding acquisition, T.S.I., A.M.M. All authors have read and agreed to the published version of the manuscript.

**Funding:** The authors extend their appreciation to the Deputyship for Research & Innovation, Ministry of Education in Saudi Arabia for funding this research work through the project number IFPHI-092-166-2020 and King Abdulaziz University, DSR, Jeddah, Saudi Arabia.

**Institutional Review Board Statement:** Not applicable.

**Informed Consent Statement:** Not applicable.

**Data Availability Statement:** Data is contained within the article and supplementary files.

**Conflicts of Interest:** The authors declare no conflict of interest.

## References

- Mohamed, M.F.; Abuo-Rahma, G.E.-D.A. Molecular targets and anticancer activity of quinoline–chalcone hybrids: Literature review. *RSC Adv.* **2020**, *10*, 31139–31155. [CrossRef]
- Neganova, M.E.; Klochkov, S.G.; Aleksandrova, Y.R.; Aliev, G. Histone modifications in epigenetic regulation of cancer: Perspectives and achieved progress. *Semin. Cancer Biol.* **2020**, *16*, 1044–1057. [CrossRef]
- Stazi, G.; Fioravanti, R.; Mai, A.; Mattevi, A.; Valente, S. Histone deacetylases as an epigenetic pillar for the development of hybrid inhibitors in cancer. *Curr. Opin. Chem. Biol.* **2019**, *50*, 89–100. [CrossRef]
- Bass, A.K.A.; El-Zoghbi, M.S.; Nageeb, E.-S.M.; Mohamed, M.F.A.; Badr, M.; Abuo-Rahma, G.E.-D.A. Comprehensive review for anticancer hybridized multitargeting HDAC inhibitors. *Eur. J. Med. Chem.* **2021**, *209*, 112904. [CrossRef] [PubMed]
- Pérez-Villanueva, J.; Matadamas-Martínez, F.; Yépez-Mulia, L.; Pérez-Koldenkova, V.; Leyte-Lugo, M.; Rodríguez-Villar, K.; Cortés-Benítez, F.; Macías-Jiménez, A.P.; González-Sánchez, I.; Romero-Velásquez, A.J.P. Synthesis and Cytotoxic Activity of Combretastatin A-4 and 2, 3-Diphenyl-2H-indazole Hybrids. *Pharmaceuticals* **2021**, *14*, 815. [CrossRef]
- Dobbelstein, M.; Moll, U. Targeting tumour-supportive cellular machineries in anticancer drug development. *Nat. Rev. Drug Discov.* **2014**, *13*, 179–196. [CrossRef] [PubMed]
- Barone, I.; Giordano, C.; Bonofiglio, D.; Andò, S.; Catalano, S. Phosphodiesterase type 5 and cancers: Progress and challenges. *Oncotarget* **2017**, *8*, 99179–99202. [CrossRef]
- Werner, R.J.; Kelly, A.D.; Issa, J.J. Epigenetics and Precision Oncology. *Cancer J.* **2017**, *23*, 262–269. [CrossRef]
- Qin, J.; Wen, B.; Liang, Y.; Yu, W.; Li, H. Histone Modifications and their Role in Colorectal Cancer (Review). *Pathol. Oncol. Res.* **2020**, *26*, 2023–2033. [CrossRef]
- Cheng, Y.; He, C.; Wang, M.; Ma, X.; Mo, F.; Yang, S.; Han, J.; Wei, X. Targeting epigenetic regulators for cancer therapy: Mechanisms and advances in clinical trials. *Signal Transduct. Target. Ther.* **2019**, *4*, 62. [CrossRef] [PubMed]
- Zhang, L.; Han, Y.; Jiang, Q.; Wang, C.; Chen, X.; Li, X.; Xu, F.; Jiang, Y.; Wang, Q.; Xu, W. Trend of histone deacetylase inhibitors in cancer therapy: Isoform selectivity or multitargeted strategy. *Med. Res. Rev.* **2015**, *35*, 63–84. [CrossRef]
- Kelly, W.K.; O'Connor, O.A.; Krug, L.M.; Chiao, J.H.; Heaney, M.; Curley, T.; MacGregore-Cortelli, B.; Tong, W.; Secrist, J.P.; Schwartz, L.; et al. Phase I study of an oral histone deacetylase inhibitor, suberoylanilide hydroxamic acid, in patients with advanced cancer. *J. Clin. Oncol. Off. J. Am. Soc. Clin. Oncol.* **2005**, *23*, 3923–3931. [CrossRef] [PubMed]
- Ueda, H.; Nakajima, H.; Hori, Y.; Fujita, T.; Nishimura, M.; Goto, T.; Okuhara, M. FR901228, a novel antitumor bicyclic depsipeptide produced by *Chromobacterium violaceum* No. 968. I. Taxonomy, fermentation, isolation, physico-chemical and biological properties, and antitumor activity. *J. Antibiot.* **1994**, *47*, 301–310. [CrossRef]
- Coiffier, B.; Pro, B.; Prince, H.M.; Foss, F.; Sokol, L.; Greenwood, M.; Caballero, D.; Borchmann, P.; Morschhauser, F.; Wilhelm, M.; et al. Results from a pivotal, open-label, phase II study of romidepsin in relapsed or refractory peripheral T-cell lymphoma after prior systemic therapy. *J. Clin. Oncol. Off. J. Am. Soc. Clin. Oncol.* **2012**, *30*, 631–636. [CrossRef] [PubMed]
- Novotny-Diermayr, V.; Hart, S.; Goh, K.C.; Cheong, A.; Ong, L.C.; Hentze, H.; Pasha, M.K.; Jayaraman, R.; Ethirajulu, K.; Wood, J.M. The oral HDAC inhibitor pracinostat (SB939) is efficacious and synergistic with the JAK2 inhibitor pacritinib (SB1518) in preclinical models of AML. *Blood Cancer J.* **2012**, *2*, e69. [CrossRef]
- Mottamal, M.; Zheng, S.; Huang, T.L.; Wang, G. Histone deacetylase inhibitors in clinical studies as templates for new anticancer agents. *Molecules* **2015**, *20*, 3898–3941. [CrossRef]
- Qiao, Z.; Ren, S.; Li, W.; Wang, X.; He, M.; Guo, Y.; Sun, L.; He, Y.; Ge, Y.; Yu, Q. Chidamide, a novel histone deacetylase inhibitor, synergistically enhances gemcitabine cytotoxicity in pancreatic cancer cells. *Biochem. Biophys. Res. Commun.* **2013**, *434*, 95–101. [CrossRef]
- McClure, J.J.; Li, X.; Chou, C.J. Advances and Challenges of HDAC Inhibitors in Cancer Therapeutics. *Adv. Cancer Res.* **2018**, *138*, 183–211. [CrossRef]
- Abbass, S.A.; Hassan, H.A.; Mohamed, M.F.; Moustafa, G.A.; Abuo-Rahma, G.E.-D.A. Recent Prospectives of Anticancer Histone Deacetylase Inhibitors. *J. Adv. Biomed. Pharm. Sci.* **2019**, *2*, 135–151. [CrossRef]
- Guerra, F.S.; Rodrigues, D.A.; Fraga, C.A.M.; Fernandes, P.D. Novel Single Inhibitor of HDAC6/8 and Dual Inhibitor of PI3K/HDAC6 as Potential Alternative Treatments for Prostate Cancer. *Pharmaceuticals* **2021**, *14*, 387. [CrossRef] [PubMed]
- Luan, Y.; Li, J.; Bernatchez, J.A.; Li, R. Kinase and Histone Deacetylase Hybrid Inhibitors for Cancer Therapy. *J. Med. Chem.* **2019**, *62*, 3171–3183. [CrossRef]

22. Fu, R.G.; Sun, Y.; Sheng, W.B.; Liao, D.F. Designing multi-targeted agents: An emerging anticancer drug discovery paradigm. *Eur. J. Med. Chem.* **2017**, *136*, 195–211. [CrossRef] [PubMed]
23. Yarden, Y.; Pines, G. The ERBB network: At last, cancer therapy meets systems biology. *Nat. Rev. Cancer* **2012**, *12*, 553–563. [CrossRef]
24. Shibuya, M. Vascular endothelial growth factor and its receptor system: Physiological functions in angiogenesis and pathological roles in various diseases. *J. Biochem.* **2013**, *153*, 13–19. [CrossRef]
25. Teng, Y.; Lu, K.; Zhang, Q.; Zhao, L.; Huang, Y.; Ingarra, A.M.; Galons, H.; Li, T.; Cui, S.; Yu, P. Recent advances in the development of cyclin-dependent kinase 7 inhibitors. *Eur. J. Med. Chem.* **2019**, *183*, 111641. [CrossRef]
26. Pao, W.; Miller, V.A.; Politi, K.A.; Riely, G.J.; Somwar, R.; Zakowski, M.F.; Kris, M.G.; Varmus, H. Acquired resistance of lung adenocarcinomas to gefitinib or erlotinib is associated with a second mutation in the EGFR kinase domain. *PLoS Med.* **2005**, *2*, e73. [CrossRef] [PubMed]
27. Avizienyte, E.; Ward, R.A.; Garner, A.P. Comparison of the EGFR resistance mutation profiles generated by EGFR-targeted tyrosine kinase inhibitors and the impact of drug combinations. *Biochem. J.* **2008**, *415*, 197–206. [CrossRef]
28. Zhou, N.; Xu, W.; Zhang, Y. Histone deacetylase inhibitors merged with protein tyrosine kinase inhibitors. *Drug Discov. Ther.* **2015**, *9*, 147–155. [CrossRef] [PubMed]
29. Kim, M.J.; Kim, D.E.; Jeong, I.G.; Choi, J.; Jang, S.; Lee, J.-H.; Ro, S.; Hwang, J.J.; Kim, C.-S. HDAC inhibitors synergize antiproliferative effect of sorafenib in renal cell carcinoma cells. *Anticancer. Res.* **2012**, *32*, 3161–3168.
30. Nakagawa, T.; Takeuchi, S.; Yamada, T.; Ebi, H.; Sano, T.; Nanjo, S.; Ishikawa, D.; Sato, M.; Hasegawa, Y.; Sekido, Y. EGFR-TKI resistance due to BIM polymorphism can be circumvented in combination with HDAC inhibition. *Cancer Res.* **2013**, *73*, 2428–2434. [CrossRef]
31. Chen, M.; Chen, C.; Wang, J.; Tsai, A.; Liou, J.; Pan, S.; Teng, C. The HDAC inhibitor, MPT0E028, enhances erlotinib-induced cell death in EGFR-TKI-resistant NSCLC cells. *Cell Death Dis.* **2013**, *4*, e810. [CrossRef]
32. Chen, C.-H.; Chen, M.-C.; Wang, J.-C.; Tsai, A.-C.; Chen, C.-S.; Liou, J.-P.; Pan, S.-L.; Teng, C.-M. Synergistic interaction between the HDAC inhibitor, MPT0E028, and sorafenib in liver cancer cells in vitro and in vivo. *Clin. Cancer Res.* **2014**, *20*, 1274–1287. [CrossRef]
33. Greve, G.; Schiffmann, I.; Pfeifer, D.; Pantic, M.; Schüller, J.; Lübbert, M. The pan-HDAC inhibitor panobinostat acts as a sensitizer for erlotinib activity in EGFR-mutated and-wildtype non-small cell lung cancer cells. *BMC Cancer* **2015**, *15*, 947. [CrossRef]
34. Tanimoto, A.; Takeuchi, S.; Arai, S.; Fukuda, K.; Yamada, T.; Roca, X.; Ong, S.T.; Yano, S. Histone Deacetylase 3 Inhibition Overcomes BIM Deletion Polymorphism-Mediated Osimertinib Resistance in EGFR-Mutant Lung Cancer. *Clin. Cancer Res.* **2017**, *23*, 3139–3149. [CrossRef]
35. Mahboobi, S.; Pilsl, B.; Sellmer, A. Generation and assessment of fusions between HDACi and TKi. In *HDAC/HAT Function Assessment and Inhibitor Development*; Methods in Molecular Biology; Humana Press: New York, NY, USA, 2017; Volume 1510, pp. 405–412. [CrossRef]
36. Cai, X.; Zhai, H.X.; Wang, J.; Forrester, J.; Qu, H.; Yin, L.; Lai, C.J.; Bao, R.; Qian, C. Discovery of 7-(4-(3-ethynylphenylamino)-7-methoxyquinazolin-6-yloxy)-N-hydroxyheptanamide (CUDc-101) as a potent multi-acting HDAC, EGFR, and HER2 inhibitor for the treatment of cancer. *J. Med. Chem.* **2010**, *53*, 2000–2009. [CrossRef]
37. Press, M.F.; Lenz, H.-J. Egfr, her2 and vegf pathways. *Drugs* **2007**, *67*, 2045–2075. [CrossRef]
38. Wang, J.; Pursell, N.W.; Samson, M.E.S.; Atoyian, R.; Ma, A.W.; Selmi, A.; Xu, W.; Cai, X.; Voi, M.; Savagner, P.; et al. Potential advantages of CUDC-101, a multitargeted HDAC, EGFR, and HER2 inhibitor, in treating drug resistance and preventing cancer cell migration and invasion. *Mol. Cancer Ther.* **2013**, *12*, 925–936. [CrossRef]
39. Mohamed, M.F.A.; Shaykoon, M.S.A.; Abdelrahman, M.H.; Elsadek, B.E.M.; Aboraia, A.S.; Abuo-Rahma, G. Design, synthesis, docking studies and biological evaluation of novel chalcone derivatives as potential histone deacetylase inhibitors. *Bioorg. Chem.* **2017**, *72*, 32–41. [CrossRef] [PubMed]
40. Mohamed, M.F.A.; Youssif, B.G.M.; Shaykoon, M.S.A.; Abdelrahman, M.H.; Elsadek, B.E.M.; Aboraia, A.S.; Abuo-Rahma, G.E.A. Utilization of tetrahydrobenzo [4,5] thieno [2,3-d] pyrimidinone as a cap moiety in design of novel histone deacetylase inhibitors. *Bioorg. Chem.* **2019**, *91*, 103127. [CrossRef]
41. Al-Sanea, M.M.; Gotina, L.; Mohamed, M.F.; Parambi, D.G.T.; Gomaa, H.A.; Mathew, B.; Youssif, B.G.; Alharbi, K.S.; Elsayed, Z.M.; Abdelgawad, M.A. Design, Synthesis and Biological Evaluation of New HDAC1 and HDAC2 Inhibitors Endowed with Ligustrazine as a Novel Cap Moiety. *Drug Des. Dev. Ther.* **2020**, *14*, 497. [CrossRef]
42. Ibrahim, T.S.; Sheha, T.A.; Abo-Dya, N.E.; AlAwadh, M.A.; Alhakamy, N.A.; Abdel-Samii, Z.K.; Panda, S.S.; Abuo-Rahma, G.E.-D.A.; Mohamed, M.F.A. Design, synthesis and anticancer activity of novel valproic acid conjugates with improved histone deacetylase (HDAC) inhibitory activity. *Bioorg. Chem.* **2020**, *99*, 103797. [CrossRef]
43. Abou-Zied, H.A.; Youssif, B.G.M.; Mohamed, M.F.A.; Hayallah, A.M.; Abdel-Aziz, M. EGFR inhibitors and apoptotic inducers: Design, synthesis, anticancer activity and docking studies of novel xanthine derivatives carrying chalcone moiety as hybrid molecules. *Bioorg. Chem.* **2019**, *89*, 102997. [CrossRef]
44. Abdelbaset, M.S.; Abdel-Aziz, M.; Ramadan, M.; Abdelrahman, M.H.; Abbas Bukhari, S.N.; Ali, T.F.S.; Abuo-Rahma, G.E.A. Discovery of novel thienoquinoline-2-carboxamide chalcone derivatives as antiproliferative EGFR tyrosine kinase inhibitors. *Bioorg. Med. Chem.* **2019**, *27*, 1076–1086. [CrossRef] [PubMed]

45. Gayam, V.; Ravi, S. Cinnamoylated chloroquine analogues: A new structural class of antimalarial agents. *Eur. J. Med. Chem.* **2017**, *135*, 382–391. [CrossRef]
46. Jasim, H.A.; Nahar, L.; Jasim, M.A.; Moore, S.A.; Ritchie, K.J.; Sarker, S.D. Chalcones: Synthetic Chemistry Follows Where Nature Leads. *Biomolecules* **2021**, *11*, 1203. [CrossRef]
47. Sangwan, R.; Rajan, R.; Mandal, P.K. HDAC as onco target: Reviewing the synthetic approaches with SAR study of their inhibitors. *Eur. J. Med. Chem.* **2018**, *158*, 620–706. [CrossRef]
48. Chen, C.; Hou, X.; Wang, G.; Pan, W.; Yang, X.; Zhang, Y.; Fang, H. Design, synthesis and biological evaluation of quinoline derivatives as HDAC class I inhibitors. *Eur. J. Med. Chem.* **2017**, *133*, 11–23. [CrossRef]
49. Mahmood, T.; Yang, P.-C. Western blot: Technique, theory, and trouble shooting. *N. Am. J. Med Sci.* **2012**, *4*, 429–434. [CrossRef]
50. Nagata, S. Apoptosis mediated by Fas and its related diseases. *Nippon Ika Daigaku Zasshi* **1997**, *64*, 459–462. [CrossRef] [PubMed]
51. Elmore, S. Apoptosis: A review of programmed cell death. *Toxicol. Pathol.* **2007**, *35*, 495–516. [CrossRef]
52. Cory, S.; Adams, J.M. The Bcl2 family: Regulators of the cellular life-or-death switch. *Nat. Rev. Cancer* **2002**, *2*, 647–656. [CrossRef] [PubMed]
53. Giaccia, A.J.; Kastan, M.B. The complexity of p53 modulation: Emerging patterns from divergent signals. *Genes Dev.* **1998**, *12*, 2973–2983. [CrossRef] [PubMed]
54. Pan, J.; Xu, G.; Yeung, S.-C.J. Cytochrome c Release Is Upstream to Activation of Caspase-9, Caspase-8, and Caspase-3 in the Enhanced Apoptosis of Anaplastic Thyroid Cancer Cells Induced by Manumycin and Paclitaxel. *J. Clin. Endocrinol. Metab.* **2001**, *86*, 4731–4740. [CrossRef] [PubMed]
55. Bukhari, S.N.A.; Jantan, I.; Unsal Tan, O.; Sher, M.; Naeem-Ul-Hassan, M.; Qin, H.-L. Biological activity and molecular docking studies of curcumin-related  $\alpha$ ,  $\beta$ -unsaturated carbonyl-based synthetic compounds as anticancer agents and mushroom tyrosinase inhibitors. *J. Agric. Food Chem.* **2014**, *62*, 5538–5547. [CrossRef] [PubMed]
56. Ravelli, R.B.; Gigant, B.; Curmi, P.A.; Jourdain, I.; Lachkar, S.; Sobel, A.; Knossow, M. Insight into tubulin regulation from a complex with colchicine and a stathmin-like domain. *Nature* **2004**, *428*, 198. [CrossRef] [PubMed]





## Article

# Repurposing FDA Drug Compounds against Breast Cancer by Targeting EGFR/HER2

Irving Balbuena-Rebolledo <sup>1,2</sup>, Itzia Irene Padilla-Martínez <sup>2</sup> , Martha Cecilia Rosales-Hernández <sup>3</sup> and Martiniano Bello <sup>1,\*</sup>

- <sup>1</sup> Laboratorio de Diseño y Desarrollo de Nuevos Fármacos e Innovación Biotecnológica, Escuela Superior de Medicina, Instituto Politécnico Nacional, Plan de San Luis y Diaz Mirón, s/n, Col. Casco de Santo Tomas, Ciudad de México 11340, Mexico; irving.balbu@gmail.com
  - <sup>2</sup> Laboratorio de Química Supramolecular y Nanociencias, Unidad Profesional Interdisciplinaria de Biotecnología, Instituto Politécnico Nacional, Av. Acueducto s/n, Barrio La Laguna Ticomán, Ciudad de México 07340, Mexico; ipadillamar@ipn.mx
  - <sup>3</sup> Laboratorio de Biofísica y Biocatálisis, Sección de Estudios de Posgrado e Investigación, Escuela Superior de Medicina, Instituto Politécnico Nacional, Plan de San Luis y Diaz Mirón, s/n, Col. Casco de Santo Tomas, Ciudad de México 11340, Mexico; marcrh2002@yahoo.com.mx
- \* Correspondence: bellomartini@gmail.com or mbellor@ipn.mx

**Abstract:** Repurposing studies have identified several FDA-approved compounds as potential inhibitors of the intracellular domain of epidermal growth factor receptor 1 (EGFR) and human epidermal receptor 2 (HER2). EGFR and HER2 represent important targets for the design of new drugs against different types of cancer, and recently, differences in affinity depending on active or inactive states of EGFR or HER2 have been identified. In this study, we first identified FDA-approved compounds with similar structures in the DrugBank to lapatinib and gefitinib, two known inhibitors of EGFR and HER2. The selected compounds were submitted to docking and molecular dynamics MD simulations with the molecular mechanics generalized Born surface area approach to discover the conformational and thermodynamic basis for the recognition of these compounds on EGFR and HER2. These theoretical studies showed that compounds reached the ligand-binding site of EGFR and HER2, and some of the repurposed compounds did not interact with residues involved in drug resistance. An *in vitro* assay performed on two different breast cancer cell lines, MCF-7, and MDA-MB-23, showed growth inhibitory activity for these repurposed compounds on tumorigenic cells at micromolar concentrations. These repurposed compounds open up the possibility of generating new anticancer treatments by targeting HER2 and EGFR.

**Keywords:** HER2; EGFR; doxazosin; docking; MD simulations

**Citation:** Balbuena-Rebolledo, I.; Padilla-Martínez, I.I.; Rosales-Hernández, M.C.; Bello, M. Repurposing FDA Drug Compounds against Breast Cancer by Targeting EGFR/HER2. *Pharmaceuticals* **2021**, *14*, 791. <https://doi.org/10.3390/ph14080791>

Academic Editors: Mary J. Meegan and Niamh M O'Boyle

Received: 18 July 2021

Accepted: 5 August 2021

Published: 12 August 2021

**Publisher's Note:** MDPI stays neutral with regard to jurisdictional claims in published maps and institutional affiliations.



**Copyright:** © 2021 by the authors. Licensee MDPI, Basel, Switzerland. This article is an open access article distributed under the terms and conditions of the Creative Commons Attribution (CC BY) license (<https://creativecommons.org/licenses/by/4.0/>).

## 1. Introduction

Human epidermal receptor type 2 (HER2) is part of a superfamily of human epidermal growth factor (EGF) receptors that include four receptors: ErbB1 (HER1 or EGFR), ErbB2 (HER2), ErbB3 (HER3), and ErbB4 [1]. Of these receptors, EGFR and HER2 are the most significant targets for anticancer therapy. These receptors are composed of a transmembrane region, extracellular domain, and receptor tyrosine kinase (RTK) domain, and the latter has been one of the major targets for anticancer drug design [2]. Activation of these receptors begins with the binding of endogenous growth factors at the extracellular region, which encourages homo and heterodimerization of RTK of both receptors [3,4]. This produces a structural change in the activation loop of the RTK domain and a change in the N-lobe  $\alpha$ -C helix to create active conformation [5–8]. The transition from the inactive to the active state is a two-step process for EGFR [5–7], whereas inactive, intermediate, and active states have been reported for HER2 [9–11]. Active and inactive EGFR conformations are used in drug design, identifying high specificity ligands by targeting the inactive



conformation, whereas the active state is only promising when mutations promote the activated state [12]. Mutations, radiotherapy, and chemotherapy resistance give rise to the constitutive activation of both receptors, which is linked with the progression of different kinds of cancer, such as breast and lung cancers [13–17]. Food and Drug Administration (FDA)-drug kinase inhibitors are divided into two groups: those targeting the active and inactive EGFR states [18–22]. Of these, lapatinib and gefitinib are shown to be dual inhibitors of the inactive state of EGFR and HER2 [2,10,23–27]. Lapatinib and gefitinib are competitive inhibitors of ATP and are approved to treat colorectal, lung, pancreatic, and breast cancers [28,29]. However, the employment of these compounds is associated with drug resistance [30]. Therefore, it is necessary to find new EGFR and HER2 inhibitors. Recently, new EGFR inhibitors with similar structures to lapatinib were investigated [31–35]. Given that, we screened DrugBank in the quest for new FDA-approved compounds with structures similar to lapatinib and gefitinib. The twenty-four identified compounds were submitted to docking and molecular dynamics (MD) simulations with the molecular mechanics generalized Born surface area approach (MMGBSA) considering the inactive state of EGFR and HER2. In addition, calculations of the binding free energy values and per-residue free energy were determined to check the affinities of each ligand for both receptors. The repurposed compounds with the highest affinity for EGFR and HER2 showed growth inhibitory activity in two different breast cancer cell lines, MCF-7 and MDA-MB-231, at micromolar concentrations.

## 2. Results and Discussion

### 2.1. Docking Studies

Blind docking studies showed that alfuzosin, amodiaquine, antrafenine, bopindolol, carvedilol, doxazosin, irinotecan, pindolol, prazosin, quinacrine, reserpine, saprisartan, sildenafil, terazosin, topotecan, trimetrexate, and udenafil reached the binding site of HER2 with a binding score between  $-7.6$  and  $-9.4$  kcal, whereas deserpidine, rifaximin, vardenafil, vinblastine, vincristine, vindesine, and vinorelbine did not (Table S1). The HER2-binding group of compounds, in addition to deserpidine and vardenafil, exhibited affinity to EGFR that ranged between  $-6.9$  and  $-9.1$  kcal mol<sup>-1</sup> (Table S1). However, a lack of affinity of rifaximin, vinblastine, vincristine, vindesine, and vinorelbine for both EGFR and HER2 was observed. All HER2-ligand complexes were stabilized by between 17 and 27 residues at the HER2 binding site, from which the following residues, L726, F731, V734, A751, I752, K753, M774, S783, L785, L796, V797, T798, Q799, L800, M801, Y803, G804, C805, L852, T862, D863, and F864, were mostly present (Table S2). EGFR-ligand complexes were also stabilized by between 17 and 27 residues at the EGFR binding site; of these residues, L718, V726, A743, K745, T790, Q791, L792, M793, G796, C797, D800, R841, L844, T854, D855, F856, and L858 were present in most of the complexes (Table S3). Both HER2- and EGFR-ligand complexes were further submitted to MD simulation to evaluate the prevalence of the interactions predicted by docking studies.

### 2.2. Convergence and Equilibrium

Complexes between HER2 and alfuzosin, antrafenine, bopindolol, carvedilol, doxazosin, irinotecan, pindolol, prazosin, quinacrine, saprisartan, sildenafil, terazosin, topotecan, and trimetrexate showed stable protein-ligand complexes during simulation, whereas amodiaquine, reserpine, and udenafil dissociated from the HER2 receptor during simulation; therefore, these three compounds were discarded from the analysis. For EGFR, stable protein-ligand complexes with alfuzosin, amodiaquine, antrafenine, bopindolol, carvedilol, doxazosin, pindolol, prazosin, quinacrine, saprisartan, terazosin, topotecan, trimetrexate, udenafil, and vardenafil were observed, whereas deserpidine, irinotecan, reserpine, and sildenafil diffused from the EGFR binding site through simulation, therefore these four compounds were discarded from the study. The RMSD analysis showed that the HER2-ligand and EGFR-ligand complexes reached constancy between 20 and 50 ns with RMSD values oscillating between 1.65 and 3.47 Å. The radius of gyration (RG) analysis

revealed that these complexes also exhibited permanence from 20 to 50 ns with values fluctuating between 18.90 and 20.24 Å (Table S4). Therefore, additional analyses were performed removing the first 50 ns.

### 2.3. Structural Analysis of HER2-Ligand Complexes

Clustering analysis over the equilibrated simulation time was performed to obtain the most populated conformation that allowed for exploration of the structural differences between compounds on EGFR and HER2. Analysis of the complexes between HER2 and alfuzosin, antrafenine, bopindolol, carvedilol, doxazosin, irinotecan, pindolol, prazosin, quinacrine, saprisartan, sildenafil, terazosin, topotecan, and trimetrexate showed that these complexes were stabilized by between 17 and 27 residues (Table 1). From these residues, L726, F731, V734, A751, I752, K753, M774, S783, R784, L785, L796, V797, T798, Q799, L800, M801, Y803, G804, C805, L852, T862, D863, and F864 were present in most of the complexes. Some of these residues participate in forming hydrogen bonds with compounds. Alfuzosin was stabilized by four hydrogen bonds with backbone atoms of M801 and F864 and through side chain atoms of S783 and D863 (Figure 1A). Bopindolol formed two hydrogen bonds with backbone atoms of L726 and C805 and one hydrogen bond with side chain atoms of D863 (Figure 1C). Carvedilol formed one hydrogen bond with side chain atoms of D863 (Figure 1D). Doxazosin forms two hydrogen bonds with backbone atoms of M801 and Y803 and two hydrogen bonds through side chain atoms of S783 and T798 (Figure 1E). Irinotecan formed two hydrogen bonds with backbone atoms L726 and Y803 and a Pi-Cation interaction with Phe864 (Figure 2A). Pindolol forms two hydrogen bonds with C805 and D808 through backbone and side chain atoms, respectively (Figure 2B).

**Table 1.** Interactions between inhibitors selected in DrugBank and HER2 during simulations.

Drug	Residues
Alfuzosin	L726, F731, V734, A751, I752, K753, M774, S783, R784, L785, L796, V797, T798, Q799, L800, M801, Y803, G804, C805, L852, T862, D863, F864.
Antrafenine	L726, F731, V734, A751, I752, K753, M774, S783, L785, L796, V797, T798, L800, M801, Y803, G804, C805, D808, H809, L852, V853, T862, D863, F864.
Bopindolol	L726, G727, F731, V734, A751, K753, S783, T798, Q799, L800, M801, P802, Y803, G804, C805, L852, T862, D863.
Carvedilol	L726, F731, V734, A751, K753, M774, S783, L785, L796, T798, Q799, L800, M801, Y803, G804, C805, L852, T862, D863, F864.
Doxazosin	V725, L726, S728, G727, K736, V734, K753, G804, C805, L807, D808, R849, N850, L852, T862, D863, L866
Irinotecan	L726, F731, V734, A751, K753, V754, L755, R756, I767, M774, S783, L785, L796, V797, T798, Q799, L800, M801, P802, Y803, G804, C805, L852, T862, D863, F864, G865.
Pindolol	L726, V734, A751, I752, K753, M774, S783, L785, L796, V797, T798, Q799, L800, M801, Y803, G804, L852, T862, D863, F864.
Prazosin	L726, F731, V734, A751, I752, K753, R756, M774, S783, R784, L785, L796, V797, T798, M801, Y803, G804, C805, L852, T862, D863, F864.
Quinacrine	L726, F731, V734, A751, I752, K753, M774, S783, L785, L796, V797, T798, Q799, L800, M801, Y803, G804, C805, R849, N850, L852, T862, D863, F864.
Saprisartan	L726, F731, V734, A751, I752, K753, V754, L755, R756, M774, S783, L785, L796, V797, T798, Q799, L800, M801, P802, Y803, G804, C805, L852, T862, D863, F864.
Sildenafil	L726, F731, V734, A751, K753, S783, L785, L796, V797, T798, Q799, L800, M801, Y803, G804, C805, L852, T862, D863, F864.
Terazosin	L726, F731, V734, A751, I752, K753, M774, S783, R784, L785, L796, V797, T798, Q799, L800, M801, Y803, G804, C805, L852, T862, D863, F864.
Topotecan	L726, F731, V734, A751, K753, S783, T798, Q799, L800, M801, Y803, G804, C805, D808, L852, T862, D863.
Trimetrexate	F731, V734, A751, I752, K753, M774, S783, R784, L785, L796, V797, T798, M801, Y803, G804, C805, L852, T862, D863, F864.

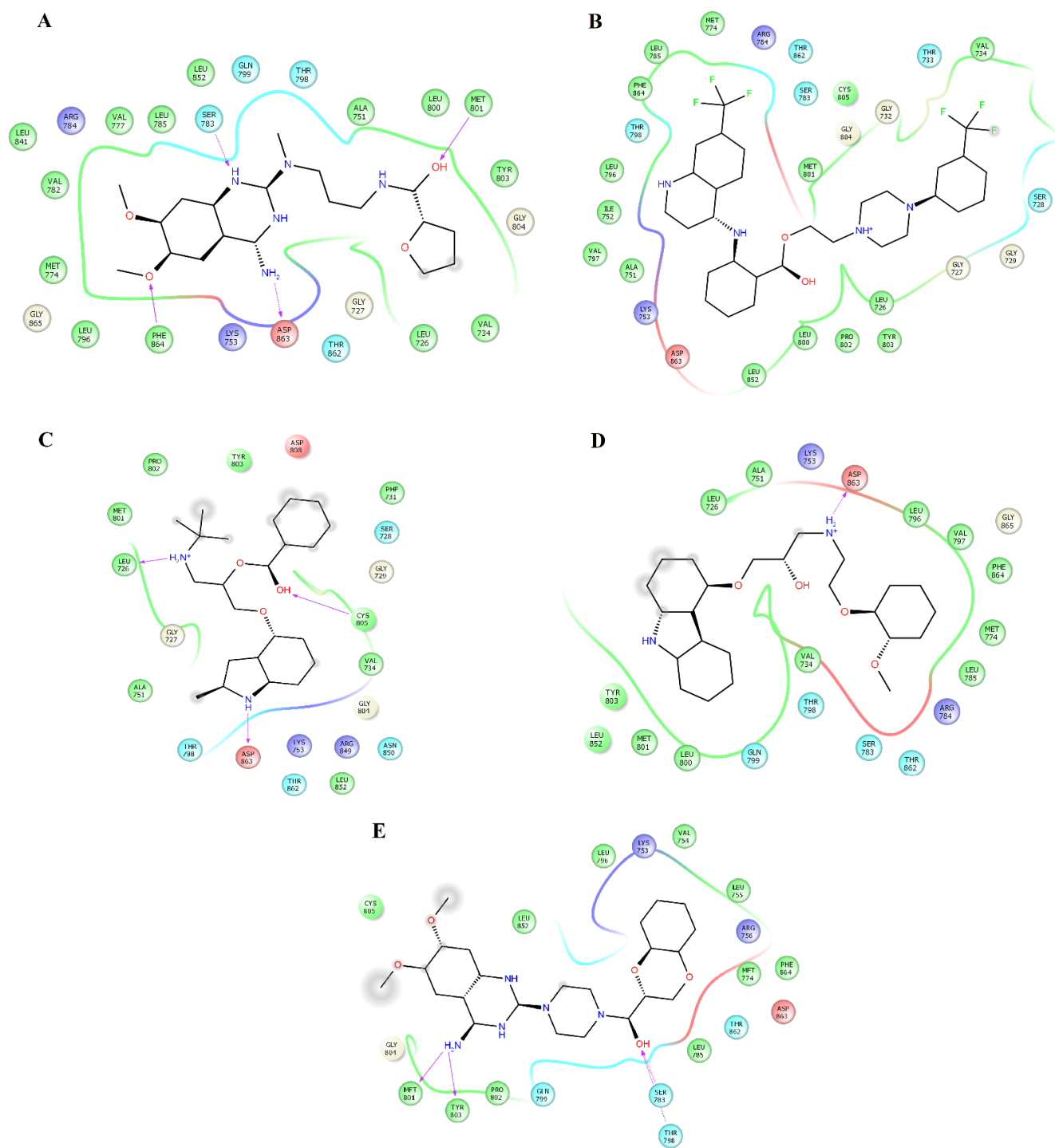


**Figure 1.** Map of contacts for the complexes between HER2 and alfuzosin, antrafenine, bipindolol, carvedilol, and doxazosin. Binding conformations for HER2<sub>alfuzosin</sub> (A); HER2<sub>antrafenine</sub> (B); HER2<sub>bopindolol</sub> (C); HER2<sub>carvedilol</sub> (D) and HER2<sub>doxazosin</sub> (E). The figure was constructed with Maestro Schrödinger version 10.5.

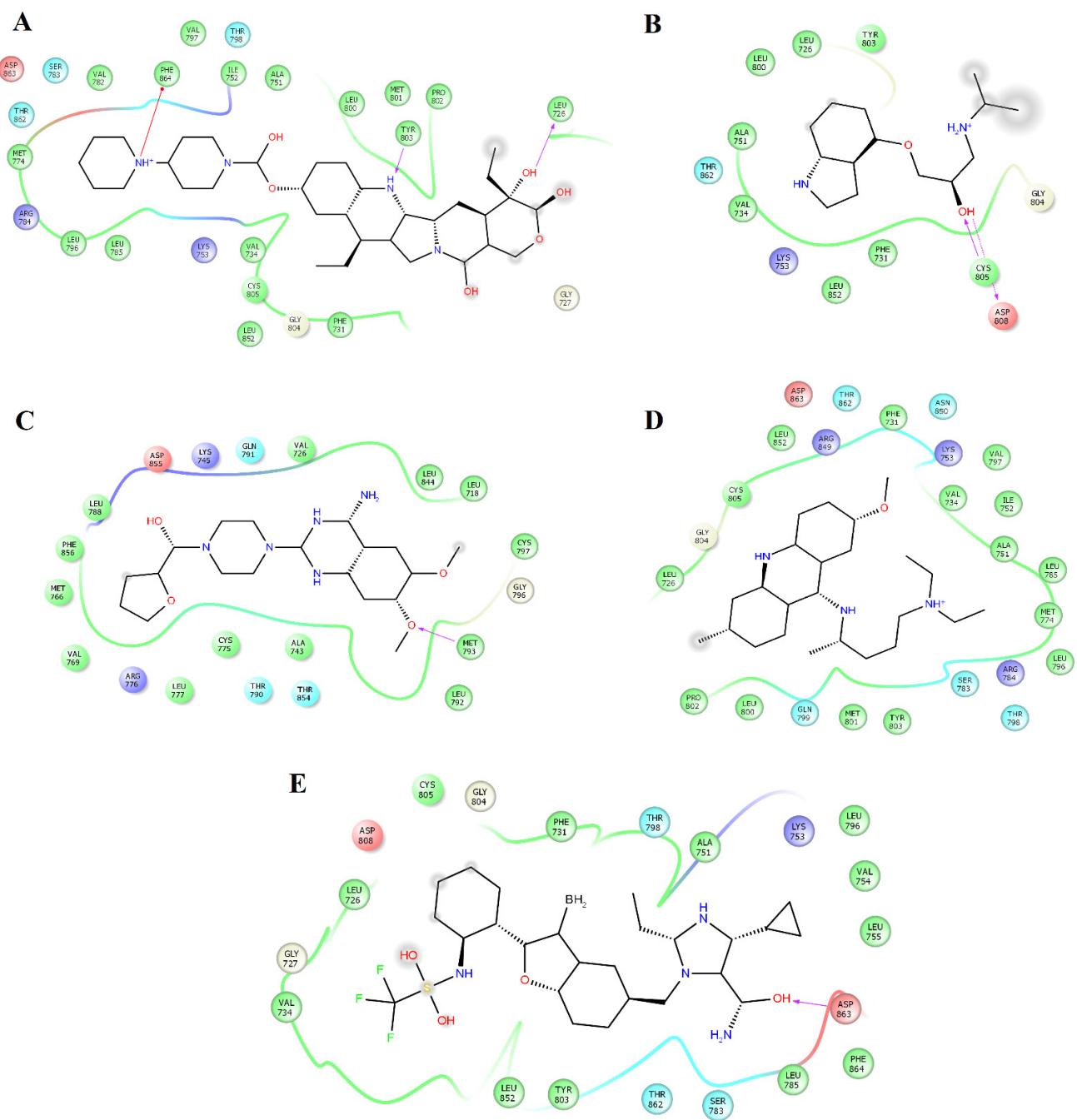


**Figure 2.** Map of interactions for the complexes between HER2 and irinotecan, pindolol, prazosin, quinacrine, and saprisartan. Binding conformations for HER2<sub>irinotecan</sub> (A); HER2<sub>pindolol</sub> (B); HER2<sub>prazosin</sub> (C); HER2<sub>quinacrine</sub> (D) and HER2<sub>saprisartan</sub> (E).

Prazosin forms one hydrogen bond with the backbone atoms of M793 (Figure 2C). Saprisartan forms one hydrogen bond with backbone atoms of D863. Y803 and T798 form hydrogen bonds with sildenafil through backbone and side chain atoms, respectively (Figure 2E). The side chain atoms of S783, T798, and D863 form hydrogen bonds with terazosin, and F864 forms through backbone atoms (Figure 3B). Topotecan formed one hydrogen bond with side chain atoms of D808 (Figure 3C). Trimetrexate established three hydrogen bonds with backbone atoms of M801, Y803, and F864 and one hydrogen bond with side chain atoms of T862 (Figure 3D). Analysis of frequent residues revealed the presence of characteristic interactions with M801, which is found for other inhibitors of HER2 [36,37]. In addition, F864 and Y803 formed hydrogen bonds in five HER2-ligand complexes.

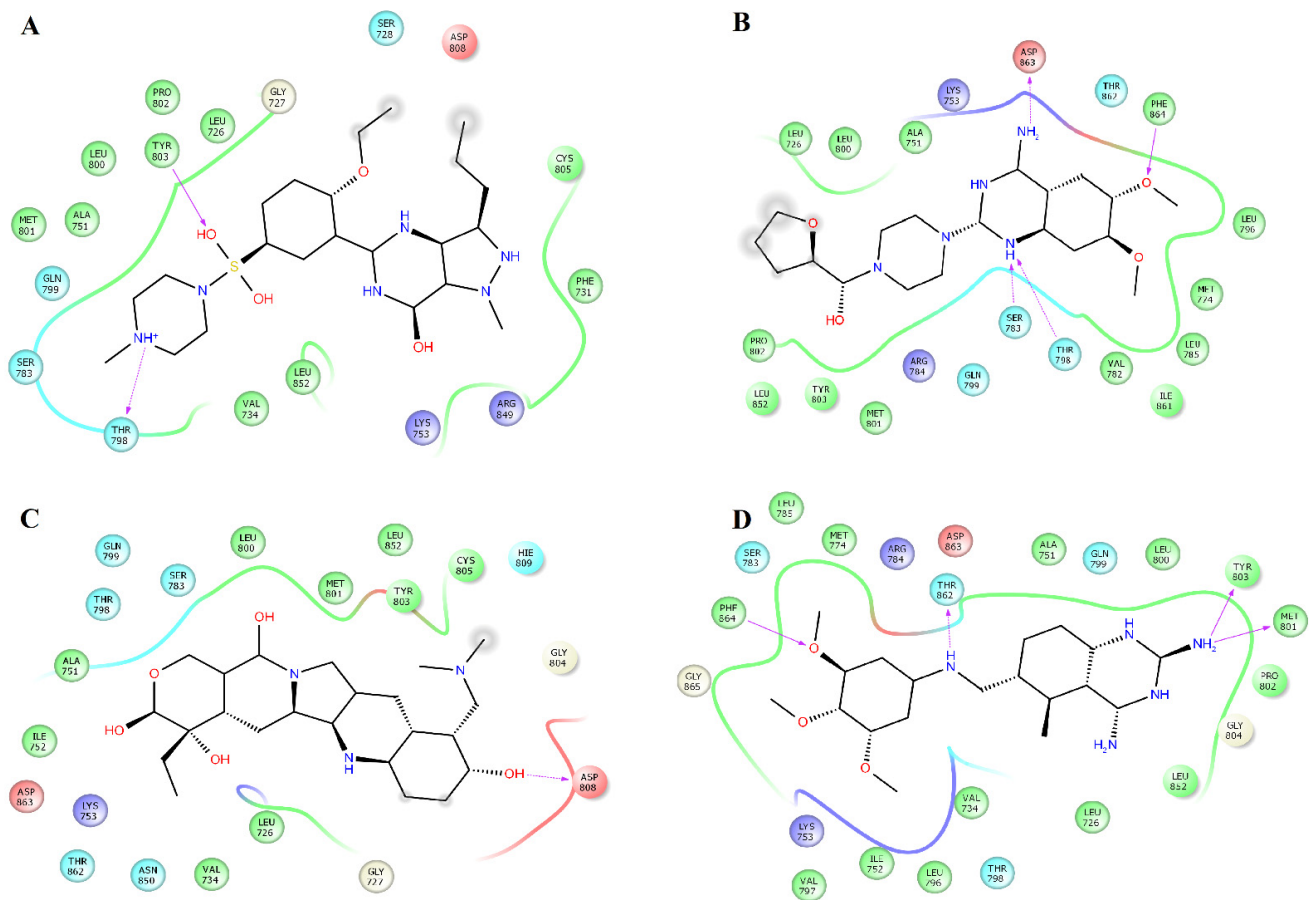


**Figure 3.** Map of interactions for the complexes between HER2 and sildenafil, terazosin, topotecan, and trimetrexate. Binding conformations for HER2<sub>sildenafil</sub> (A); HER2<sub>terazosin</sub> (B); HER2<sub>topotecan</sub> (C) and HER2<sub>trimetrexate</sub> (D).

#### 2.4. Structural Analysis of EGFR-Ligand Complexes

Analysis of the complexes between EGFR and alfuzosin, amodiaquine, antrafenine, bopindolol, carvedilol, doxazosin, pindolol, prazosin, quinacrine, saprisartan, terazosin, topotecan, trimetrexate, udenafil, and vardenafil showed that these complexes were stabilized by between 13 and 24 residues (Table 2). From these protein-ligand complexes, L718, G719, S720, V726, A743, K745, T790, L792, M793, G796, C797, R841, and L844 appear in most complexes. The formation of hydrogen bonds was observed in some complexes. Alfuzosin forms hydrogen bonds with backbone atoms of D855 and side chains of T790 and D855 (Figure 4A). Amodiaquine makes hydrogen bonds with backbone atoms of L792 and C797 and with side chain atoms of D800 (Figure 4B). Bopindolol forms hydrogen bonds with side chain atoms of N842 and D855 (Figure 4D). Carvedilol forms one hydrogen bond with side chain atoms of D837 and one Pi-Cation interaction with F723 (Figure 4E). Doxazosin established two hydrogen bonds with backbone atoms of M793 and P794 and through side chain atoms of D804 (Figure 5A).

**Table 2.** Interactions between inhibitors selected in DrugBank and EGFR during simulations.

Drug	Residues
Alfuzosin	L718, V726, A743, I744, K745, M766, C775, L777, L788, I789, T790, L792, M793, G796, C797, D800, R841, L844, N842, T854, D855, F856, L858.
Amodiaquine	L718, G719, V726, A743, Q791, L792, M793, P794, F795, G796, C797, D800, L844.
Antrafenine	L718, G719, S720, G721, G724, F723, T725, V726, K745, E746, L747, R803, L858, K913.
Bopindolol	L718, G719, V726, A743, I744, K745, L777, L788, I789, T790, L792, G796, C797, R841, N842, L844, T854, D855.
Carvedilol	L718, G719, S720, F723, T725, V726, K745, D746, L747, L788, D837, R841, N842, D855, L858, L862.
Doxazosin	L718, V726, A743, K745, Q791, L792, M793, P794, F795, G796, Y801, E804, H805, L844.
Pindolol	L718, S720, G721, V726, A743, K745, T790, Q791, L792, M793, G796, C797, R841, N842, L844, T854, D855.
Prazosin	L718, V726, A743, K745, M766, V769, C775, R776, L777, L788, T790, Q791, L792, M793, G796, C797, L844, T854, D855, F856.
Quinacrine	L718, G719, V726, A743, K745, T790, Q791, L792, M793, G796, C797, D800, R803, R841, L844, T854, D855.
Saprisartan	L718, G719, S720, G721, F723, G724, T725, V726, A743, K745, L747, T790, Q791, L792, M793, G796, C797, R841, L844, T854, L858, L862, K875, P877.
Terazosin	L718, G719, V726, A743, K745, C775, R776, M766, L777, L788, T790, M793, G796, C797, D800, L844, T854, D855, F856.
Topotecan	L718, G719, S720, G721, V726, A743, L792, M793, P794, G796, C797, D800, R841, N842, L844, D855.
Trimetrexate	L718, G721, A722, F723, V726, A743, K745, T790, Q791, L792, M793, G796, C797, R841, N842, L844, T854, D855, L858.
Udenafil	V717, L718, A743, Q791, L792, M793, P794, F795, G796, C797, L799, D800, R803, R841, L844.
Vardenafil	L718, G719, S720, G721, F723, G724, T725, V726, K745, E746, L747, L788, L792, G796, C797, D800, R841, N842, D855, L858.

Pindolol makes four hydrogen bonds with side chain atoms of K745, N842, T854, and D855 (Figure 5B). Prazosin forms one hydrogen bond with backbone atoms of M793 (Figure 5C). Quinacrine forms one hydrogen bond with the backbone atoms of M793 and a salt bridge with D800 (Figure 5D). Saprisartan forms two hydrogen bonds with side chain atoms of K745 and R841 (Figure 5E). Terazosin forms one hydrogen bond with the backbone atoms of C797 (Figure 6A). Topotecan forms one hydrogen bond with backbone atoms of M793 (Figure 6B). Trimetrexate establishes two hydrogen bonds with side chain atoms of K745 and D855 (Figure 6C). Udenafil forms two hydrogen bonds through the backbone and side chain atoms of M793 and D800, respectively (Figure 6D). Vardenafil establishes one hydrogen bond through side chain atoms of R841 (Figure 6E). Stabilization of ligands at the ligand-binding site of EGFR establishes interactions with T790, whose mutations are associated with EGFR drug resistance [38,39]. We also identified characteristic interactions with M793, which was previously observed for other inhibitors of EGFR [36,37].

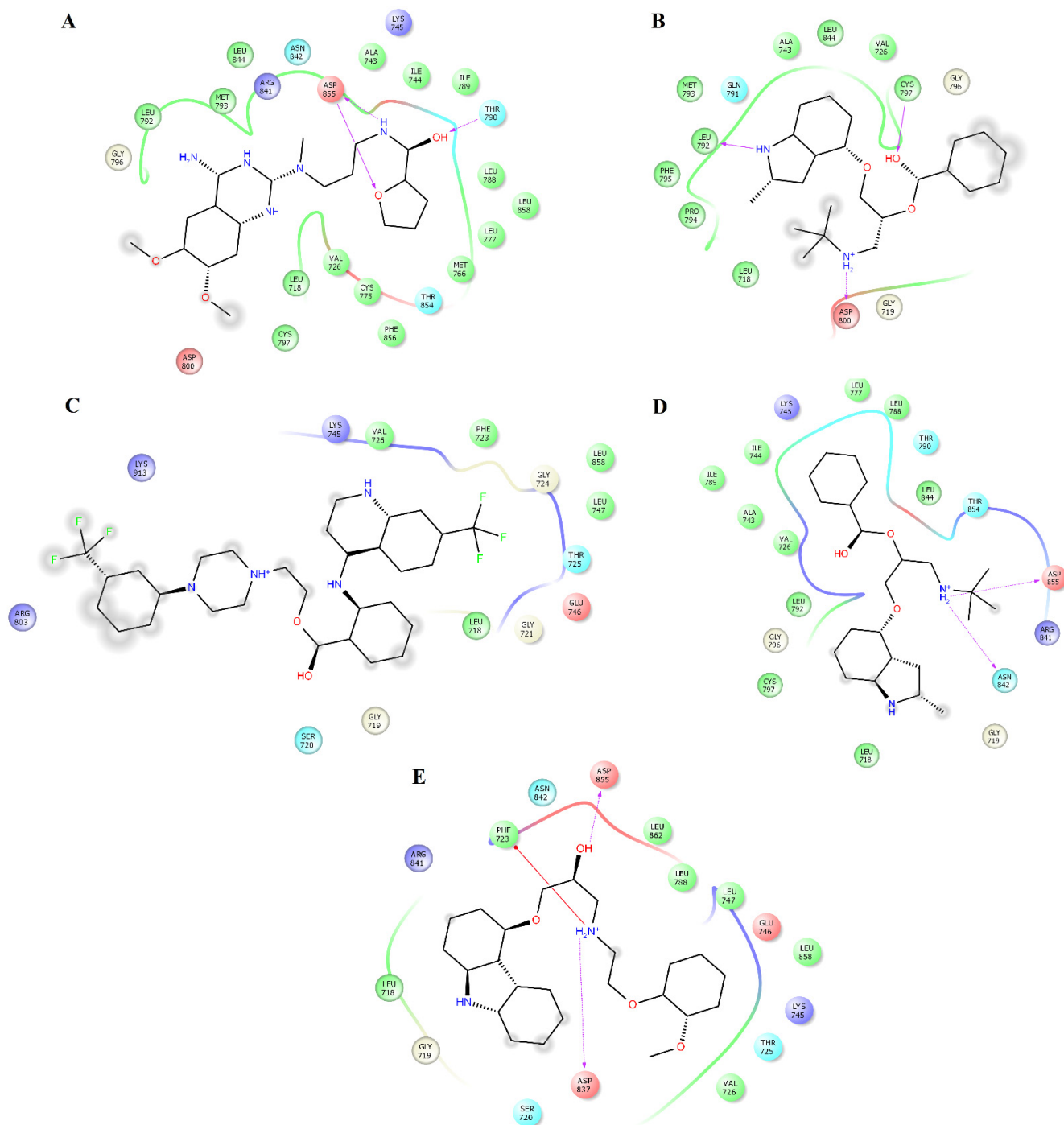


**Figure 4.** Interactions of the complexes between EGFR and alfuzosin, amodiaquine, antrafenine, bipindolol, and carvedilol. Binding complex for EGFR<sub>alfuzosin</sub> (A); EGFR<sub>amodiaquine</sub> (B); EGFR<sub>antrafenine</sub> (C); EGFR<sub>bipindolol</sub> (D) and EGFR<sub>carvedilol</sub> (E).

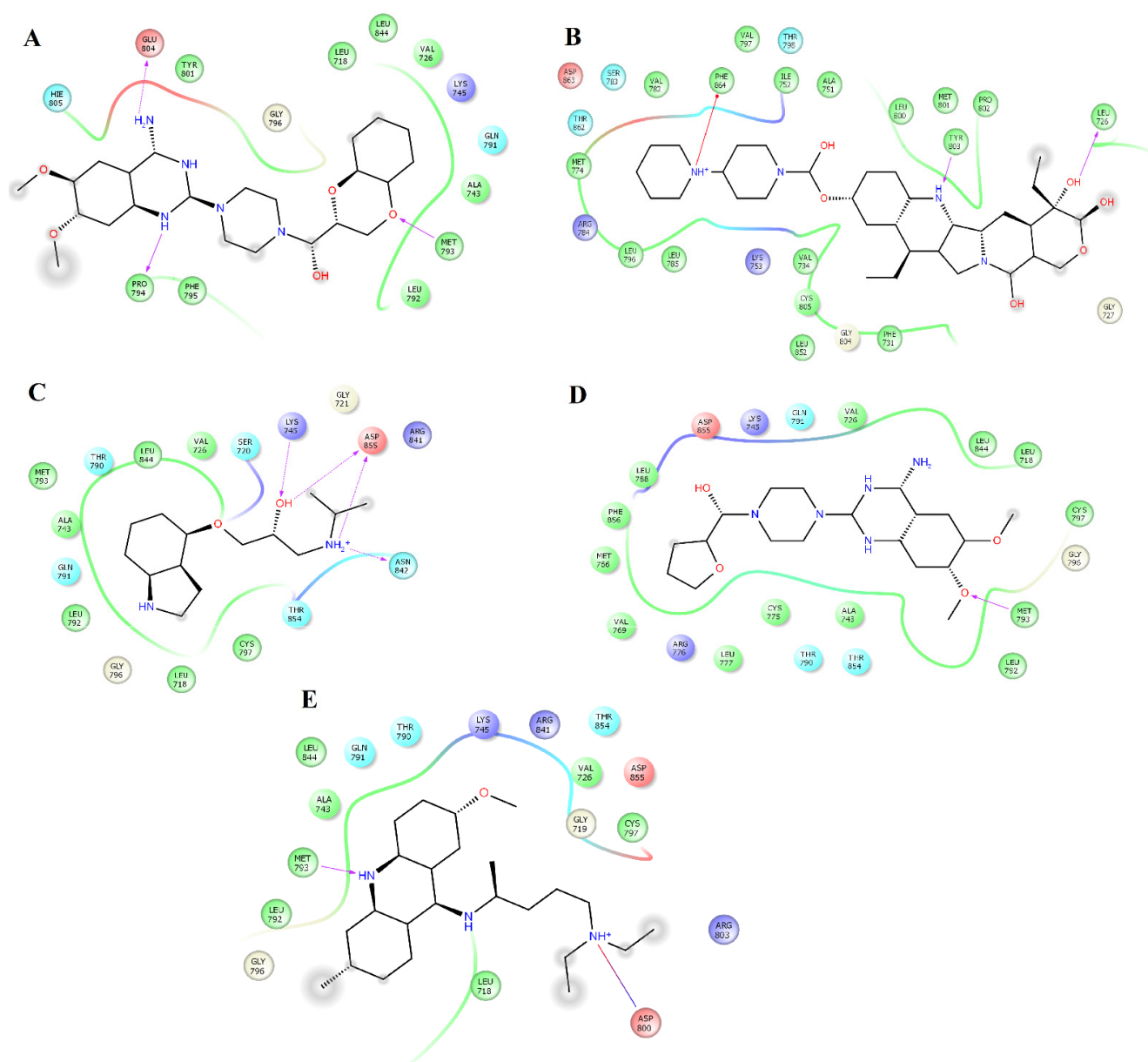


**Figure 5.** Interactions of the complexes between EGFR and doxazosin, pindolol, prazosin, quinacrine, and saprisartan. Binding complex for EGFR<sub>doxazosin</sub> (A); EGFR<sub>pindolol</sub> (B); EGFR<sub>prazosin</sub> (C); EGFR<sub>quinacrine</sub> (D) and EGFR<sub>saprisartan</sub> (E).



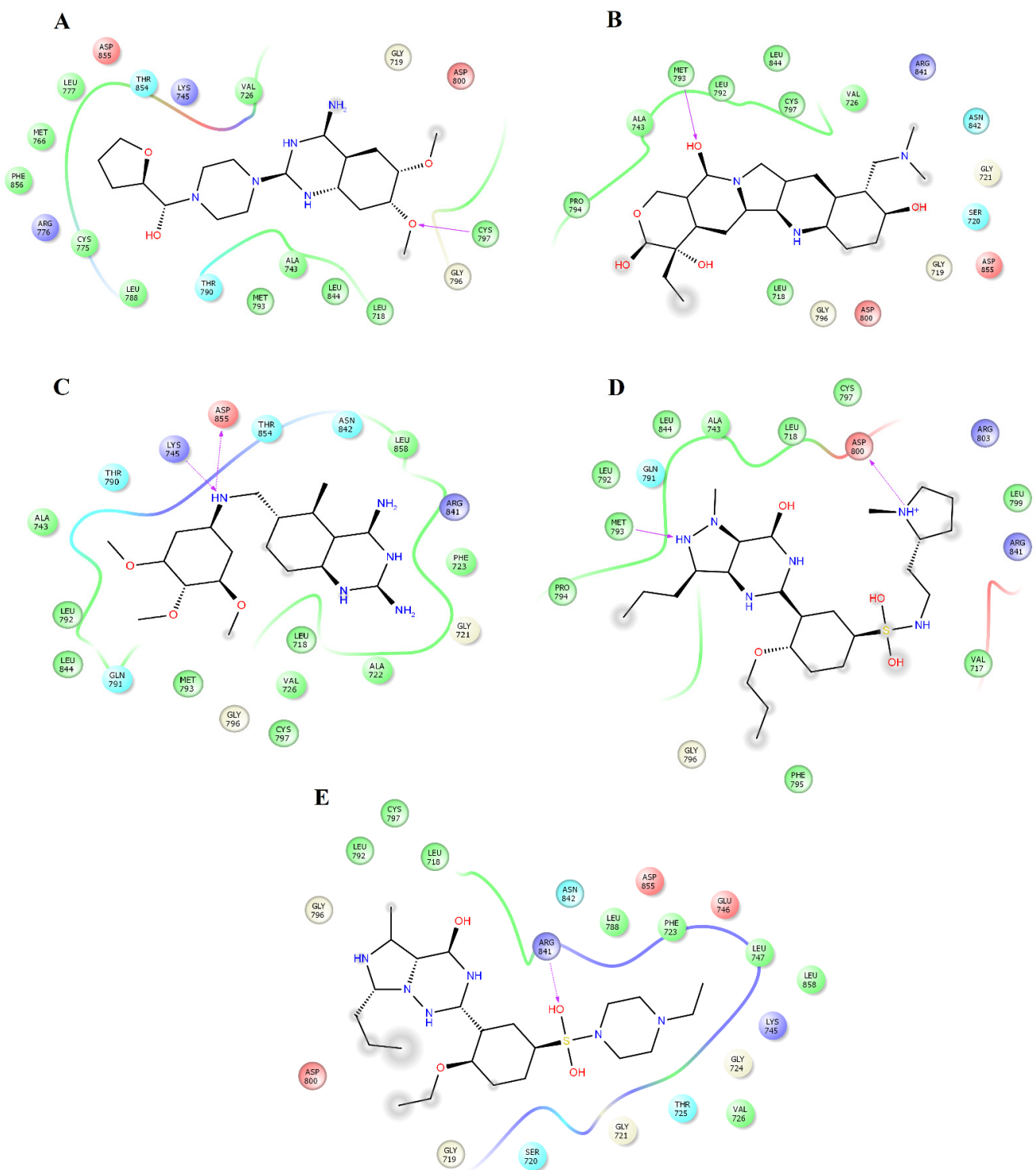


**Figure 6.** Interactions of the complexes between EGFR and terazosin, topotecan, trimetrexate, udenafil, and vardenafil. Binding complex for EGFR<sub>terazosin</sub> (A); EGFR<sub>topotecan</sub> (B); EGFR<sub>trimetrexate</sub> (C); EGFR<sub>udenafil</sub> (D) and EGFR<sub>vardenafil</sub> (E).

### 2.5. Affinity of Compounds

The difference in binding affinity for all complexes was determined using the MMG-BSA approach. All systems showed thermodynamically favorable binding free energy ( $\Delta G_{bind}$ ) values, where nonpolar interactions established by van der Waals energy ( $\Delta E_{vdw}$ ) and nonpolar desolvation ( $\Delta G_{npol,sol}$ ) dominated the binding of the protein-ligand complexes. Comparative analysis between both systems indicated that all the compounds exhibited a more favorable affinity to HER2 than EGFR (Table 3). HER2-ligand com-

plexes showed that irinotecan ( $-56.4 \pm 5$  kcal/mol), quinacrine ( $-54.9 \pm 3$  kcal/mol), alfuzosin ( $-51.9 \pm 6$  kcal/mol), and antrafenine ( $-51.1 \pm 3$  kcal/mol) showed the highest binding free energy for HER2. The affinity of irinotecan and quinacrine was higher than that reported between HER2 and lapatinib ( $-51 \pm 4$  kcal/mol) [10] and gefitinib ( $-26 \pm 6.0$ ) [21]. The affinity observed for alfuzosin and antrafenine was similar to that of lapatinib [10] but higher than that of gefitinib [21]. Vardenafil ( $-48.2 \pm 7$  kcal/mol), alfuzosin ( $-45.4 \pm 4$  kcal/mol), terazosin ( $-44.7 \pm 6$  kcal/mol), and prazosin ( $-40.2 \pm 4$  kcal/mol) exhibited the highest affinity for EGFR. These four compounds showed a slightly lower affinity for EGFR than lapatinib ( $-58 \pm 5$  kcal/mol) [13] but a higher affinity than that reported between EGFR and gefitinib ( $-39 \pm 2$  kcal/mol) [21]. These results suggest that quinacrine, alfuzosin, and antrafenine could act as dual inhibitors of HER2 and EGFR with higher selectivity to HER2, whereas irinotecan only exhibited selectivity to HER2. Alfuzosin, terazosin, and prazosin could act as dual inhibitors of EGFR and HER2, whereas vardenafil only exhibited selectivity for EGFR.

**Table 3.** Binding affinity for the protein-ligand systems (in units of kcal/mol).

System	$\Delta E_{vdw}$	$\Delta E_{ele}$	$\Delta G_{ele,sol}$	$\Delta G_{npol,sol}$	$\Delta G_{mmgsa}$
HER2 <sub>alfuzosin</sub>	$-57.0 \pm 4$	$-33.2 \pm 6$	$45.4 \pm 4$	$-7.1 \pm 0.3$	$-51.9 \pm 6$
HER2 <sub>antrafenine</sub>	$-66.3 \pm 3$	$24.4 \pm 8$	$-0.9 \pm 0.1$	$-8.3 \pm 0.2$	$-51.1 \pm 3$
HER2 <sub>bopindolol</sub>	$-40.0 \pm 4$	$18.7 \pm 10$	$-7.8 \pm 1$	$-5.5 \pm 0.5$	$-34.6 \pm 5$
HER2 <sub>carvedilol</sub>	$-51.1 \pm 6$	$16.0 \pm 4$	$4.6 \pm 1$	$-6.8 \pm 0.6$	$-37.3 \pm 5$
HER2 <sub>doxazosin</sub>	$-49.0 \pm 4$	$24.0 \pm 9$	$-7.4 \pm 1$	$-6.0 \pm 0.3$	$-38.4 \pm 4$
HER2 <sub>irinotecan</sub>	$-68.0 \pm 4$	$40.2 \pm 12$	$-21.0 \pm 8$	$-7.6 \pm 0.3$	$-56.4 \pm 5$
HER2 <sub>pindolol</sub>	$-26.0 \pm 3$	$4.0 \pm 0.5$	$3.4 \pm 0.6$	$-3.8 \pm 0.4$	$-22.4 \pm 4$
HER2 <sub>prazosin</sub>	$-56.0 \pm 3$	$-24.5 \pm 7$	$42.7 \pm 5$	$-6.9 \pm 0.2$	$-44.7 \pm 4$
HER2 <sub>quinacrine</sub>	$-57.5 \pm 3$	$34.0 \pm 8$	$-24.0 \pm 7$	$-7.4 \pm 0.2$	$-54.9 \pm 3$
HER2 <sub>saprisartan</sub>	$-57.0 \pm 4$	$-17.8 \pm 5$	$46.3 \pm 4$	$-7.2 \pm 0.4$	$-35.7 \pm 4$
HER2 <sub>sildenafil</sub>	$-49.1 \pm 3$	$34.7 \pm 9$	$-22.7 \pm 9$	$-6.2 \pm 0.3$	$-43.3 \pm 3$
HER2 <sub>terazosin</sub>	$-46.0 \pm 4$	$-38.3 \pm 11$	$50.0 \pm 7$	$-5.7 \pm 0.4$	$-40.0 \pm 7$
HER2 <sub>topotecan</sub>	$-45.1 \pm 3$	$-26.3 \pm 4$	$43.0 \pm 12$	$-5.3 \pm 0.4$	$-33.7 \pm 5$
HER2 <sub>trimetrexate</sub>	$-51.6 \pm 3$	$-23.6 \pm 4$	$33.9 \pm 3$	$-6.5 \pm 0.3$	$-47.8 \pm 4$
EGFR <sub>alfuzosin</sub>	$-55.5 \pm 4$	$-30.3 \pm 6$	$47.4 \pm 5$	$-7.0 \pm 0.3$	$-45.4 \pm 4$
EGFR <sub>amodiaquine</sub>	$-30.8 \pm 4$	$43.3 \pm 20$	$-35.2 \pm 15$	$-4.1 \pm 0.6$	$-26.8 \pm 8$
EGFR <sub>antrafenine</sub>	$-32.6 \pm 4$	$65.4 \pm 10$	$-48.5 \pm 10$	$-4.0 \pm 0.6$	$-19.7 \pm 3$
EGFR <sub>bopindolol</sub>	$-40.6 \pm 4$	$17.7 \pm 9$	$-8.4 \pm 1$	$-5.8 \pm 0.4$	$-37.1 \pm 3$
EGFR <sub>carvedilol</sub>	$-35.8 \pm 5$	$-21.4 \pm 11$	$25.8 \pm 7$	$-5.4 \pm 0.5$	$-36.8 \pm 7$
EGFR <sub>doxazosin</sub>	$-38.8 \pm 4$	$3.2 \pm 0.9$	$9.7 \pm 3$	$-4.6 \pm 0.4$	$-30.5 \pm 4$
EGFR <sub>pindolol</sub>	$-25.4 \pm 5$	$4.7 \pm 0.5$	$-4.1 \pm 1$	$-4.4 \pm 0.7$	$-29.2 \pm 5$
EGFR <sub>prazosin</sub>	$-52.8 \pm 3$	$-19.0 \pm 6$	$38.2 \pm 4$	$-6.6 \pm 0.2$	$-40.2 \pm 4$
EGFR <sub>quinacrine</sub>	$-40.6 \pm 4$	$12.9 \pm 3$	$-4.7 \pm 0.5$	$-5.4 \pm 0.5$	$-37.8 \pm 4$
EGFR <sub>saprisartan</sub>	$-46.4 \pm 3$	$-15.3 \pm 2$	$46.2 \pm 10$	$-6.4 \pm 0.5$	$-21.9 \pm 5$
EGFR <sub>terazosin</sub>	$-55.8 \pm 4$	$-22.7 \pm 7$	$40.4 \pm 6$	$-6.6 \pm 0.3$	$-44.7 \pm 6$
EGFR <sub>topotecan</sub>	$-35.2 \pm 7$	$-6.3 \pm 1$	$22.7 \pm 9$	$-3.9 \pm 0.8$	$-22.7 \pm 7$
EGFR <sub>trimetrexate</sub>	$-42.6 \pm 3$	$-29.8 \pm 7$	$48.5 \pm 6$	$-5.6 \pm 0.4$	$-29.5 \pm 4$
EGFR <sub>udenafil</sub>	$-40.3 \pm 3$	$10.0 \pm 2$	$5.6 \pm 0.5$	$-5.0 \pm 0.3$	$-29.7 \pm 3$
EGFR <sub>vardenafil</sub>	$-53.6 \pm 5$	$-35.0 \pm 12$	$46.8 \pm 11$	$-6.4 \pm 0.7$	$-48.2 \pm 7$

## 2.6. Per-Residue Decomposition Free Energy

This analysis allowed the identification of the residues that provided the most  $\Delta G_{bind}$  values for compounds that exhibited more energetically favorable  $\Delta G_{bind}$  values. Table 4 shows that L726, F731, V734, A751, K753, M774, S783, L785, L796, V797, T798, M801, C805, L852, T862, D863, and F864 were the main contributors to the stabilization of the HER2<sub>alfuzosin</sub> complex, from which S783, M801, D863 and F864 established hydrogen bonds with polar atoms of alfuzosin (Figure 1A). In the HER2<sub>antrafenine</sub> complex, Val726, G727, T733, V734, A751, K753, L785, L796, V797, T798, M801, C805, L852, T862, and D863 contributed the most to the maintenance of the complex (Figure 1B). In the HER2<sub>irinotecan</sub>

complex, Val726, G727, F731, V734, A751, K753, S783, L785, L796, V797, T798, P802, Y803, C805, L852, T862, and F864 supported the highest preservation of the complex, from which Y803 and Val726 formed hydrogen bonds, and F864 formed Pi-cation interactions with irinotecan (Figure 2A). In the HER2<sub>quinacrine</sub> complex, Val726, F731, V734, A751, K753, S783, L785, T798, L800, P802, Y803, G804, C805, L852, and T862 contributed the most to the conservation of this complex (Figure 2D).

**Table 4.** Per-residue free energy for complexes formed between alfuzosin, antrafenine, irinotecan, and quinacrine with HER2 (values kcal/mol).

Residue	HER2 <sub>alfuzosin</sub>	HER2 <sub>antrafenine</sub>	HER2 <sub>irinotecan</sub>	HER2 <sub>quinacrine</sub>
L726	−1.0	−1.1	−2.6	−1.8
G727		−1.0	−0.9	
F731	−1.1		−1.9	−1.6
T733		−0.7		
V734	−1.6	−3.0	−2.6	−2.1
A751	−0.9	−1.0	−1.6	−1.1
K753	−1.3	−1.2	−1.7	−1.5
M774	−1.1			
S783	−0.6		−0.5	−0.7
L785	−1.8	−0.9	−1.0	−0.9
L796	−1.4	−1.9	−0.5	
V797	−0.5	−0.9	−1.0	
T798	−1.8	−1.8	−1.8	−5.7
L800				−0.7
M801	−0.9	−1.8		
P802			−1.7	−1.0
Y803			−1.7	−2.0
G804				−0.6
C805	−0.6	−0.6	−0.5	−0.6
L852	−1.8	−1.4	−1.3	−1.9
T862	−1.1	−1.2	−1.1	−2.0
D863	−1.9	−0.7		
F864	−1.6		−0.5	

Table 5 shows that L718, V726, A743, K745, L788, I789, T790, M793, G796, C797, L844, T854, F856, and L858 contributed the most to the  $\Delta G_{bind}$  value of the EGFR<sub>alfuzosin</sub> complex, and of these residues, T790 forms hydrogen bonds with alfuzosin (Figure 4A). In the EGFR<sub>prazosin</sub> complex, L718, V726, A743, K745, L777, L788, T790, L792, M793, G796, C797, L844, T854, and F856 are the main contributors to the affinity of this complex, of which M793 established one hydrogen bond with prazosin (Figure 5C). In the EGFR<sub>terazosin</sub> complex, L718, V726, A743, I744, K745, M766, L777, L788, I789, T790, L792, M793, G796, C797, L844, T854, and F856 are major sources of the stability of this complex, of which C797 formed one hydrogen bond with a polar atom of prazosin (Figure 6A). L718, G719, G721, F723, T725, V726, A743, K745, L792, M793, G796, C797, R841, L844, and L858 represent the main origin of the permanence of the EGFR<sub>vardeanafil</sub> complex, of which R841 established one hydrogen bond with vardenafil (Figure 6E).

**Table 5.** Per-residue free energy for complexes formed between alfuzosin, prazosin, terazosin, and vardenafil with EGFR (values kcal/mol).

Residue	EGFR <sub>alfuzosin</sub>	EGFR <sub>prazosin</sub>	EGFR <sub>terazosin</sub>	EGFR <sub>vardenafil</sub>
L718	−2.2	−1.2	−2.2	−2.4
G719				−0.9
G721				−1.2
F723				−0.6
T725				−0.7
V726	−1.9	−2.0	−2.1	−3.0
A743	−1.0	−0.9	−1.0	−0.7
I744			−0.7	
K745	−1.4	−1.2	−2.0	−3.2
M766			−0.6	
L777		−1.9	−1.1	
L788	−1.0	−1.1	−1.6	
I789	−1.3		−0.5	
T790	−0.5	−1.2	−1.1	
L792		−0.9	−0.8	−0.9
M793	−1.0	−1.1	−0.7	−0.5
G796	−1.0	−0.5	−1.0	−0.7
C797	−1.0	−0.4	−0.9	−1.3
R841				−2.0
L844	−2.0	−2.2	−2.2	−0.8
T854	−1.3	−1.7	−1.7	
F856	−1.0	−0.6	−0.5	
L858	−0.6			−0.6

### 2.7. Antiproliferative Assays

HER2 and EGFR are rare important watchdogs for normal cellular activities, and their dysregulation has been linked to protein overexpression that promotes the progression of several kinds of cancer [40,41]. MDA-MB-231 and MCF-7 cell lines are estrogen receptor-negative and positive, respectively [42], and both expressed EGFR and HER2, although MDA-MB-231 cells expressed HER2 and EGFR at higher concentrations than MCF-7 cells [43]. The evaluation of growth inhibition by alfuzosin, quinacrine, terazosin, prazosin, and irinotecan was conducted using the MTT assay in selected MDA-MB-231 (Figure 7) and MCF-7 (Figure 8) cell lines and compared with that of gefitinib and lapatinib. Although vardenafil and antrafenine exhibited good theoretical affinities for EGFR or HER2, they were not included in this study because they were not commercially available at the time this research was performed.

As shown in Table 6, all evaluated compounds exhibited IC<sub>50</sub> values in the μM range. The compounds with the best antiproliferative activity in the MCF-7 cell line were irinotecan and quinacrine, which exhibited greater antiproliferative activity than gefitinib or lapatinib. In the MDA-MB-231 cell line, quinacrine exhibited better antiproliferative activity than lapatinib or gefitinib. Prazosin and irinotecan exhibited better antiproliferative activity than terazosin and alfuzosin but lower antiproliferative activity than lapatinib and gefitinib. Although the affinity tendency predicted by the MMGBSA approach was not in line with the antiproliferative activity, the results support the affinity observed through theoretical methods of alfuzosin, terazosin, prazosin, and irinotecan over HER2 and EGFR.

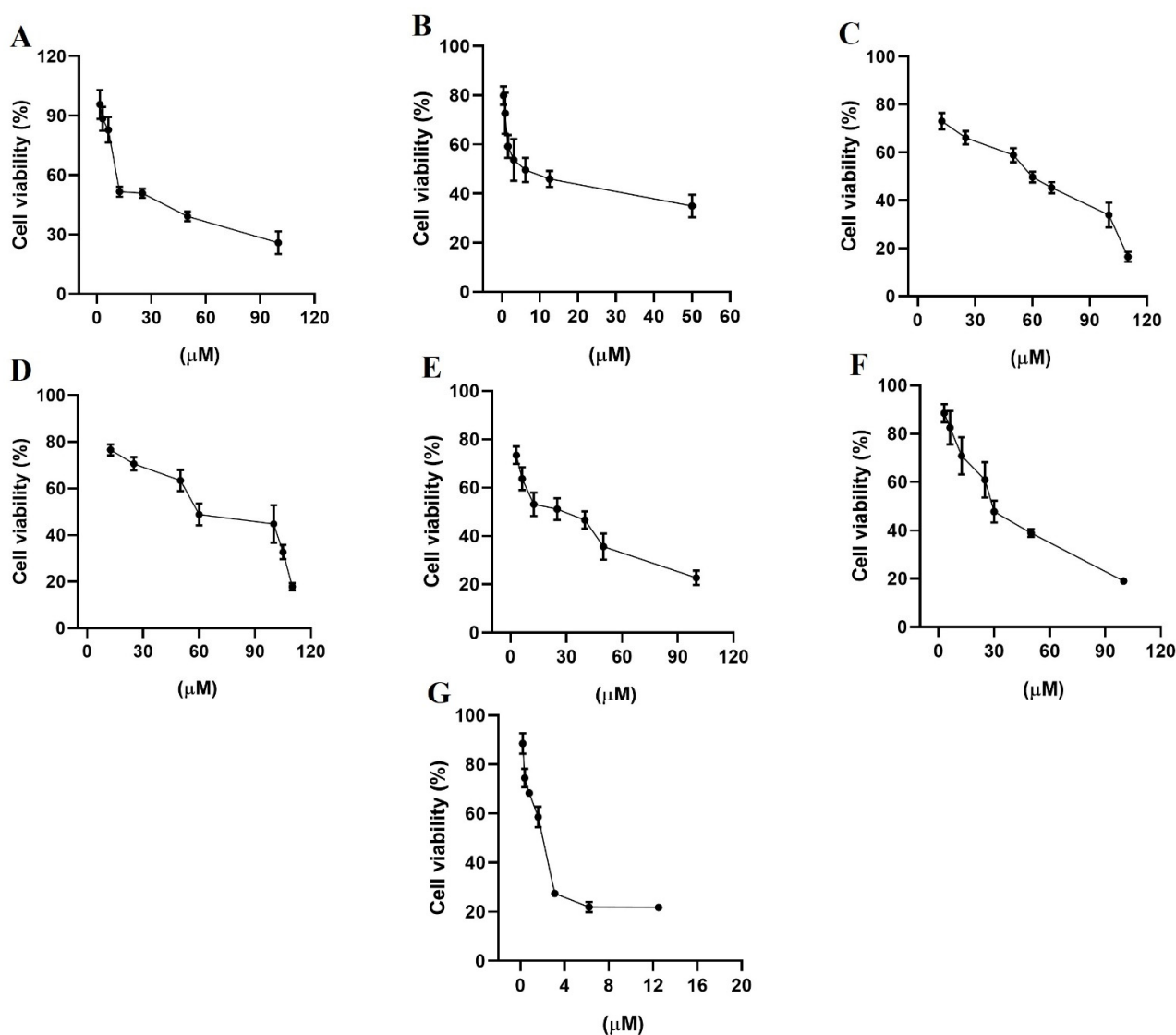


**Figure 7.** Percentage of cell viability from the biological study in the breast cancer cell line MDA-MB-231, (A) gefitinib; (B) lapatinib; (C) terazosin; (D) alfuzosin; (E) prazosin; (F) irinotecan; and (G) quinacrine. All assays were performed in triplicate.

**Table 6.** Cytotoxic activity ( $IC_{50}$  values in  $\mu M$  \*) in two breast cancer cell lines at 48 h of incubation.

Compounds	MCF-7	MDA-MB-231
Gefitinib	$10 \pm 1$	$13 \pm 1$
Lapatinib	$7 \pm 1$	$10 \pm 1$
Terazosin hydrochloride	$70 \pm 1$	$68 \pm 2$
Alfuzosin hydrochloride	$85 \pm 2$	$69 \pm 1$
Prazosin hydrochloride	$41 \pm 2$	$25 \pm 1$
Irinotecan hydrochloride	$0.37 \pm 0.8$	$27 \pm 1$
Quinacrine dihydrochloride	$1.4 \pm 1$	$1.3 \pm 1$

\* The calculation of Inhibitory concentration 50 ( $IC_{50}$ ) of the compounds was determined by the cell viability percentage curve vs the logarithmic of concentration.

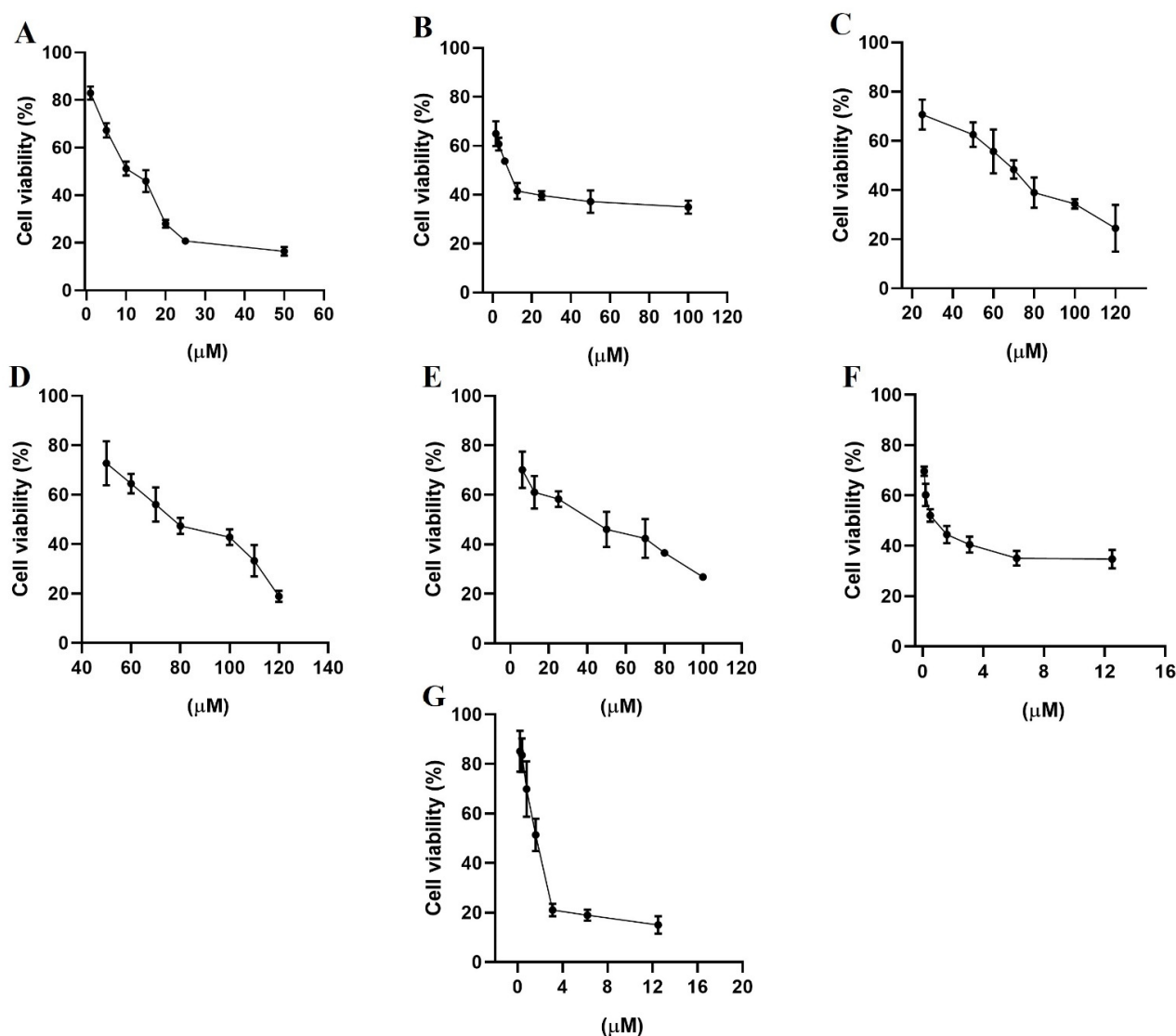


**Figure 8.** Percentage of cell viability from the biological study in the breast cancer cell line MCF-7, (A) gefitinib; (B) lapatinib; (C) terazosin; (D) alfuzosin; (E) prazosin; (F) irinotecan; and (G) quinacrine. All assays were performed in triplicate.

### 3. Methods

#### 3.1. Preparation of Systems

Twenty-four FDA small drugs structurally similar to lapatinib and gefitinib, alfuzosin, amodiaquine, antrafenine, bopindolol, carvedilol, deserpidine, doxazosin, irinotecan, pindolol, prazosin, quinacrine, rifaximin, sildenafil, reserpine, saprisartan, terazosin, topotecan, trimetrexate, udenafil, vardenafil, vinblastine, vincristine, vindesine, and vinorelbine (Scheme S1 and Table S5), were taken from the DrugBank [44] by retrieving the lapatinib and gefitinib charts via the option: show similar structures for approved drugs. These compounds were optimized at the AM1 level with Gaussian 09 W software [45]. The inactive state of EGFR was retrieved from the protein data bank (PDB code 1XKK). The inactive state of HER2 was selected from a previous study [10].

#### 3.2. Docking Studies

The twenty-four FDA small compounds were docked with EGFR and HER2 with AutoDock Tools 1.5.6 and AutoDock 4.2 programs [46]. Hydrogen atoms were included in ligands and receptors, and partial charges were assigned to receptors (Kollman) and ligands (Gasteiger). A grid size of  $70 \times 70 \times 70 \text{ \AA}$  and  $0.370 \text{ \AA}$  spacing was built on the receptor. A Lamarckian genetic algorithm was selected to evaluate a global conformational examination

with a maximum of  $1 \times 10^7$  energy calculations and 200 separate populations. For each compound, 20 runs were calculated, and the best binding structures were chosen using the criteria of the lowest energetic ligand conformations at the binding site of the receptor.

### 3.3. Molecular Dynamics Simulations

Docking complexes were examined via MD simulation studies employing the AMBER16 package [47] and the ff14SB force field [48]. Systems were simulated in a dodecahedral box of 12 Å and solvated with the TIP3P water model [49]. Systems were neutralized with NaCl (0.15 M) to establish physiological strength. Ligand forcefields were constructed considering AM1-BCC atomic charges with the general Amber force field [50]. Solvated and neutralized systems were minimized using steepest descent through 4000 steps and equilibrated through 1 nanosecond (ns). Minimized and equilibrated systems were run by MD simulations for 100 ns with an NPT ensemble at 310 K, with each MD simulation run in triplicate. The time step for simulations was set to 2.0 fs. The SHAKE algorithm [51] was selected to restrict bonds at their equilibrium values. The PME method [52] was employed to describe the electrostatic term, and a 10 Å cutoff was chosen for the van der Waals forces. Constant temperature and pressure of 310 K and 1 atm, respectively, were kept using a weak-coupling algorithm [53], with coupling constants  $\tau_T$  and  $\tau_P$  of 1.0 and 0.2 ps, respectively. The results of the MD simulations were evaluated with the cpptraj tool in Amber16 to determine the root mean squared deviation (RMSD), the radius of gyration ( $R_G$ ), and clustering analysis. Figures were constructed using PyMOL [54] and Maestro Schrödinger version 10.5 [55].

### 3.4. Affinity Prediction and Per-Residue Decomposition

Binding free energy ( $\Delta G_{bind}$ ) values and per residue energetic contribution were calculated using the MMGBSA approach [56–59]. Calculations were performed considering 500 protein-ligand complexes at intervals of 100 ps (last 50 ns of simulation) using implicit solvent models [60], a salt concentration of 0.10 M.  $\Delta G_{bind}$ , and per-residue contributions for each protein-ligand complex were determined as previously described [11] and correspond to the median result of triplicate trials.

### 3.5. Biological Assays on Cell Lines

Gefitinib, lapatinib, terazosin, alfuzosin, prazosin, irinotecan, and quinacrine were purchased from Sigma Chemical (St. Louis, MO, USA). The breast cancer cell lines used in this study, MCF-7 and MDA-MB-231, were obtained from the American Type Tissue Culture Collection (ATCC), Rockville, MD, USA. MCF-7 and MDA-MB-231 cells were grown in Dulbecco's modified Eagle's medium (DMEM) high glucose with phenol red, and the culture medium was supplemented with 10% fetal bovine serum (FBS) (BioWest, Riverside, MO, USA) and 1% penicillin/streptomycin as an antibiotic. The cells were incubated in culture flasks (75 cm<sup>3</sup>) at 37 °C in a humidified atmosphere of 5% CO<sub>2</sub> and 95% air, all of which were carried out under sterile conditions using a laminar flow hood.

### 3.6. Antiproliferative Assays on Cell Cultures

Breast cancer cell lines were detached with trypsin-EDTA (1%) for 5 min at 37 °C. After trypsin-EDTA inactivation with DMEM, the cells were centrifuged and resuspended in 4 mL of medium. Afterwards, cells were counted with CytoSmart cell counting (CytoSMART Technologies, Eindhoven, The Netherlands). Each cell line was seeded at  $5 \times 10^3$  cells in 96-well tissue culture plates and allowed to attach overnight (24 h) in a CO<sub>2</sub> incubator before the assays. Cells were treated with the compounds at different concentrations, all compounds were dissolved in DMSO (0.1% final concentration), and the control contained medium with DMSO (0.1%). The assays were performed in triplicate for each concentration and incubated at 37 °C under a humid atmosphere with 5% CO<sub>2</sub> for 48 h.

### 3.7. Cell Viability Assays

Further cell viability was determined using MTT [3-(4,5-dimethyl-2-thiazolyl)-2,5-diphenyl-2H-tetrazolium bromide (Sigma)]. After 48 h of incubation, the medium was removed and replaced by 100  $\mu$ L of MTT (0.500 mg/mL), dissolved in PBS, and incubated for 3 h at 37 °C and 5% CO<sub>2</sub>. After that, the MTT/PBS was discarded, and 100  $\mu$ L of DMSO was applied to each well to dissolve the dark-blue formazan crystals in intact cells. The resulting solution was measured by spectrophotometry with a microplate reader (Thermo Scientific, Multiskan™ Sky) at a wavelength of 550 nm, and the quantity of formazan produced was directly proportional to the number of living cells. The results are expressed as the percentage of viable cells in relation to the control, whose viability was designated as 100%. Each data point was determined with  $n = 8$  in three independent experiments, and the results are reported as the mean absorption  $\pm$  SD using the GraphPad Prism 8 software.

## 4. Conclusions

We performed repurposing studies by screening DrugBank in the search for new FDA-approved drugs with chemical structures similar to lapatinib and gefitinib. Docking and MD simulations coupled to the MMGBSA approach using the selected DrugBank compounds, and considering the inactive state of EGFR and HER2, allowed us to identify that quinacrine, alfuzosin, and antrafenine could act as dual inhibitors of HER2 and EGFR but with higher selectivity to HER2, whereas irinotecan exhibited high selectivity to HER2. Alfuzosin, terazosin, and prazosin could act as dual inhibitors of EGFR and HER2, whereas vardenafil exhibited selectivity exclusively to EGFR. Per-residue decomposition analysis identified the main residues stabilizing the protein-ligand complexes with HER2 and EGFR systems, showing that V726, V734, A751, K753, L785, C805, L852, and T862 were present in the stabilization of HER2<sub>alfuzosin</sub>, HER2<sub>antrafenine</sub>, HER2<sub>irinotecan</sub>, and HER2<sub>quinacrine</sub>. In the stabilization of these complexes, the characteristic interaction with M801 in HER2<sub>alfuzosin</sub> and HER2<sub>antrafenine</sub> complexes was observed, which has been observed for other HER2 inhibitors were also observed. In the case of EGFR, L718, V726, A743, K745, M793, G796, C797, and L844 were present in the stabilization of EGFR<sub>alfuzosin</sub>, EGFR<sub>prazosin</sub>, EGFR<sub>terazosin</sub>, and EGFR<sub>vardenafil</sub>. All complexes formed interactions with M793, a characteristic interaction that has been observed for other inhibitors of EGFR. Finally, MTT assays showed that repurposed compounds exhibited antiproliferative activity on breast cancer cell lines, with irinotecan and quinacrine exhibiting greater antiproliferative activity than lapatinib and gefitinib in the MCF-7 cell line, and quinacrine exhibiting greater antiproliferative activity than lapatinib and gefitinib in the MCF-7 and MDA-MB-231 cell lines. Finally, we could show that our structure-based screening approach identifies novel repositioning candidates for the cancer target EGFR/HER2. Not only did we identify candidates structurally related to gefitinib and lapatinib, but also showed that they show the desired inhibitory activity on the target receptors. Particularly, the FDA-approved drugs irinotecan and quinacrine, which appeared as the top hit from our screen and were later validated, demonstrates the potential of our approach for drug repositioning.

**Supplementary Materials:** The following are available online at <https://www.mdpi.com/article/10.3390/ph14080791/s1>, Scheme S1: FDA-drugs with structural similarity with lapatinib and gefitinib, Table S1: Docking studies of candidates to inactive EGFR/HER2 inhibitors selected in the DrugBank, Table S2: Interacting residues between inhibitors selected in the DrugBank with HER2, Table S3: Interacting residues between inhibitors selected in the DrugBank with EGFR, Table S4: Average RMSD and RG values (Å) during the last 50 ns of MD simulations, and Table S5: FDA-drugs with structural similarity with lapatinib and gefitinib.

**Author Contributions:** It would be as follow: Conceptualization, M.B., I.B.-R.; methodology, M.B., I.B.-R., I.I.P.-M., M.C.R.-H.; software, M.B., I.B.-R.; validation, M.B., I.B.-R.; formal analysis, M.B., I.B.-R., I.I.P.-M., M.C.R.-H.; investigation, M.B., I.B.-R.; resources, M.B.; data curation, M.B., I.B.-R.; writing—original draft preparation, M.B., I.B.-R.; writing—review and editing, M.B.; visualization,



M.B., I.B.-R.; supervision, M.B.; project administration, M.B.; funding acquisition, M.B. All authors have read and agreed to the published version of the manuscript.

**Funding:** This is an unpublished original article. The work was supported by grants from CONACYT (CB-A1-S-21278) and SIP/IPN (20210516).

**Institutional Review Board Statement:** Not applicable.

**Informed Consent Statement:** Not applicable.

**Data Availability Statement:** Not applicable.

**Conflicts of Interest:** The authors declare no conflict of interest.

## References

- de Bono, J.S.; Rowinsky, E.K. The ErbB receptor family: A therapeutic target for cancer. *Trends Mol. Med.* **2002**, *8*, S19–S26. [CrossRef]
- Lurje, G.; Lenz, H.-J. EGFR signaling and drug discovery. *Oncology* **2009**, *77*, 400–410. [CrossRef]
- Tzahar, E.; Waterman, H.; Chen, X.; Levkowitz, G.; Karunakaran, D.; Lavi, S.; Ratzkin, B.J.; Yarden, Y. A hierarchical network of interreceptor interactions determines signal transduction by Neu differentiation factor/neuregulin and epidermal growth factor. *Mol. Cell. Biol.* **1996**, *16*, 5276–5287. [CrossRef] [PubMed]
- Qian, X.; LeVe, C.M.; Freeman, J.K.; Dougall, W.C.; Greene, M.I. Heterodimerization of epidermal growth factor receptor and wild-type or kinase-deficient Neu: A mechanism of interreceptor kinase activation and transphosphorylation. *Proc. Natl. Acad. Sci. USA* **1994**, *91*, 1500–1504. [CrossRef]
- Riese, D.J., II; Gallo, R.M.; Settleman, J. Mutational activation of ErbB family receptor tyrosine kinases: Insights into mechanisms of signal transduction and tumorigenesis. *BioEssays* **2007**, *29*, 558–565. [CrossRef]
- Zhang, X.; Gureasko, J.; Shen, K.; Cole, P.A.; Kuriyan, J. An allosteric mechanism for activation of the kinase domain of epidermal growth factor receptor. *Cell* **2006**, *125*, 1137–1149. [CrossRef]
- Hubbard, S.R.; Miller, W.T. Receptor tyrosine kinases: Mechanisms of activation and signaling. *Curr. Opin. Cell Biol.* **2007**, *19*, 117–123. [CrossRef]
- Balius, T.E.; Rizzo, R.C. Quantitative prediction of fold resistance for inhibitors of EGFR. *Biochemistry* **2009**, *48*, 435–448. [CrossRef]
- Aertgeerts, K.; Skene, R.; Yano, J.; Sang, B.-C.; Zou, H.; Snell, G.; Jennings, A.; Iwamoto, K.; Habuka, N.; Hirokawa, A.; et al. Structural analysis of the mechanism of inhibition and allosteric activation of the kinase domain of HER2 protein. *J. Biol. Chem.* **2011**, *286*, 18756–18765. [CrossRef]
- Bello, M.; Guadarrama-García, C.; Rodríguez-Fonseca, R.A. Dissecting the Molecular Recognition of Dual Lapatinib Derivatives for EGFR/HER2. *J. Comput. Aided. Mol. Des.* **2020**, *34*, 293–303. [CrossRef]
- Bello, M.; Saldaña-Rivero, L.; Correa-Basurto, J.; García, B.; Sánchez-Espinosa, V.A. Structural and energetic basis for the molecular recognition of dual synthetic vs. natural inhibitors of EGFR/HER2. *Int. J. Biol. Macromol.* **2018**, *111*, 569–586. [CrossRef] [PubMed]
- Johnson, L.N. Protein kinase inhibitors: Contributions from structure to clinical compounds. *Q. Rev. Biophys.* **2009**, *42*, 1–40. [CrossRef] [PubMed]
- Sharma, S.V.; Bell, D.W.; Settleman, J.; Haber, D.A. Epidermal growth factor receptor mutations in lung cancer. *Nat. Rev. Cancer* **2007**, *7*, 169–181. [CrossRef] [PubMed]
- Sainsbury, J.R.C.; Farndon, J.R.; Needham, G.K.; Malcolm, A.J.; Harris, A.L. Epidermal growth factor receptor status as predictor of early recurrence of and death from breast-cancer. *Lancet* **1987**, *1*, 1398–1402.
- Ciardello, F.; Tortora, G. A novel approach in the treatment of cancer: Targeting the epidermal growth factor receptor. *Clin. Cancer Res.* **2001**, *7*, 2958–2970. [PubMed]
- Rexer, B.N.; Ghosh, R.; Narasanna, A. Human breast cancer cells harboring a gatekeeper T798M mutation in HER2 overexpress EGFR ligands and are sensitive to dual inhibition of EGFR and HER2. *Clin. Cancer Res.* **2013**, *19*, 5390–5401. [CrossRef]
- Gonzaga, I.M.; Soares-Lima, S.C.; de Santos, P.T. Alterations in epidermal growth factor receptors 1 and 2 in esophageal squamous cell carcinomas. *BMC Cancer* **2012**, *12*, 56. [CrossRef]
- Wood, E.R.; Truesdale, A.T.; McDonald, O.B.; Yuan, D.; Hassell, A.; Dickerson, S.H.; Ellis, B.; Pennisi, C.; Horne, E.; Lackey, K.; et al. Equally potent inhibition of c-Src and Abl by compounds that recognize inactive kinase conformations. *Cancer Res.* **2009**, *69*, 2384–2392.
- Bello, M. Binding mechanism of kinase inhibitors to EGFR and T790M, L858R and L858R/T790M mutants through structural and energetic analysis. *Int. J. Biol. Macromol.* **2018**, *118*, 1948–1962. [CrossRef]
- Saldaña-Rivera, L.; Bello, M.; Méndez-Luna, D. Structural insight into the binding mechanism of ATP to EGFR and L858R, and T790M and L858R/T790 mutants. *J. Biomol. Struct. Dyn.* **2019**, *37*, 4671–4684. [CrossRef]
- Bello, M.; Mejía, M.V. Structural Insight of the Anticancer Properties of Doxazosin on Overexpressing EGFR/HER2 Cell Lines. In *Breast Cancer*; IntechOpen: London, UK, 2021. [CrossRef]

22. Wood, E.R.; Truesdale, A.T.; McDonald, O.B.; Yuan, D.; Hassell, A.; Dickerson, S.H.; Ellis, B.; Pennisi, C.; Horne, E.; Lackey, K.; et al. A unique structure for epidermal growth factor receptor bound to GW572016 (Lapatinib): Relationships among protein conformation, inhibitor off-rate, and receptor activity in tumor cells. *Cancer Res.* **2004**, *64*, 6652–6659. [CrossRef]
23. Rusnak, D.W.; Lackey, K.; Affleck, K. The effects of the novel, reversible epidermal growth factor receptor/ErbB-2 tyrosine kinase inhibitor, GW2016, on the growth of human normal and tumor-derived cell lines in vitro and in vivo. *Mol. Cancer Ther.* **2001**, *1*, 85–89. [PubMed]
24. Konecny, G.E.; Pegram, M.D.; Venkatesan, N.; Finn, R.; Yang, G. Activity of the dual kinase inhibitor lapatinib (GW572016) against HER-2- overexpressing and trastuzumab-treated breast cancer cells. *Cancer Res.* **2006**, *66*, 1630–1639. [CrossRef] [PubMed]
25. Johnston, S.R.D.; Leary, A. Lapatinib: A novel EGFR/HER2 tyrosine kinase inhibitor for cancer. *Drugs Today* **2006**, *42*, 441–453. [CrossRef]
26. Zhou, Y.; Li, S.; Hu, Y.P.; Wang, J.; Hauser, J. Blockade of EGFR and ErbB2 by the novel dual EGFR and ErbB2 tyrosine kinase inhibitor GW572016 sensitizes human colon carcinoma GEO cells to apoptosis. *Cancer Res.* **2006**, *66*, 404–411. [CrossRef]
27. Medina, P.J.; Goodin, S. Lapatinib: A dual inhibitor of human epidermal growth factor receptor tyrosine kinases. *Clin. Ther.* **2008**, *30*, 1426–1447. [CrossRef] [PubMed]
28. Zhang, H.; Berezov, A.; Wang, Q.; Zhang, G.; Drebin, J.; Murali, R.; Greene, M.I. ErbB receptors: From oncogenes to targeted cancer therapies. *J. Clin. Investig.* **2007**, *117*, 2051–2058. [CrossRef]
29. Camp, E.R.; Summy, J.; Bauer, T.W.; Liu, W.; Gallick, G.E.; Ellis, L.M. Molecular mechanisms of resistance to therapies targeting the epidermal growth factor receptor. *Clin. Cancer Res.* **2005**, *11*, 397–405. [PubMed]
30. Liao, Q.H.; Gao, Q.Z.; Wei, J.; Chou, K.C. Docking and molecular dynamics study on the inhibitory activity of novel inhibitors on epidermal growth factor receptor (EGFR). *Med. Chem.* **2011**, *7*, 24–31. [CrossRef]
31. Waterson, A.G.; Petrov, K.G.; Hornberger, K.R.; Hubbard, R.D.; Sammond, D.M.; Smith, S.C.; Dickson, H.D.; Caferro, T.R.; Hinkle, K.W.; Stevens, K.L.; et al. Synthesis and evaluation of aniline headgroups for alkynyl thienopyrimidine dual EGFR/ErbB-2kinase inhibitors. *Bioorg. Med. Chem. Lett.* **2009**, *19*, 1332–1336. [CrossRef]
32. Rheault, T.R.; Caferro, T.R.; Dickerson, S.H.; Donaldson, K.H.; Gaul, M.D.; Goetz, A.S.; Mullin, R.J.; McDonald, O.B.; Petrov, K.G.; Rusnak, D.W.; et al. Thienopyrimidine-based dual EGFR/ErbB-2 inhibitors. *Bioorg. Med. Chem. Lett.* **2009**, *19*, 817–820. [CrossRef] [PubMed]
33. Lin, R.; Johnson, S.G.; Connolly, P.J.; Wetter, S.K.; Binnun, E.; Hughes, T.V.; Murray, W.V.; Pandey, N.B.; Moreno-Mazza, S.J.; Adams, M.; et al. Synthesis and evaluation of 2,7-diamino-thiazolo [4,5-d] pyrimidine analogues as anti-tumor epidermal growth factor receptor (EGFR) tyrosine kinase inhibitors. *Bioorg. Med. Chem. Lett.* **2009**, *19*, 2333–2337. [CrossRef] [PubMed]
34. Xu, G.; Abad, M.C.; Connolly, P.J.; Neeper, M.P.; Struble, G.T.; Springer, B.A.; Emanuel, S.L.; Pandey, N.; Gruninger, R.H.; Adams, M.; et al. 4-Amino-6-arylamino-pyrimidine-5-carbaldehyde hydrazones as potent ErbB-2/EGFR dual kinase inhibitors. *Bioorg. Med. Chem. Lett.* **2008**, *18*, 4615–4619. [CrossRef]
35. Ducray, R.; Ballard, P.; Barlaam, B.C.; Hickinson, M.D.; Kettle, J.G.; Ogilvie, D.J.; Trigwell, C.B. Novel 3-alkoxy-1H-pyrazolo [3,4-d]pyrimidines as EGFR and erbB2 receptor tyrosine kinase inhibitors. *Bioorg. Med. Chem. Lett.* **2008**, *18*, 959–962. [CrossRef] [PubMed]
36. Xing, L.; Klug-Mcleod, J.; Rai, B.; Lunney, E.A. Kinase hinge binding scaffolds and their hydrogen bond patterns. *Bioorg. Med. Chem.* **2015**, *23*, 6520–6527. [CrossRef] [PubMed]
37. Ahmed, M.; Sadek, M.; Abouzid, K.A.; Wang, F. In silico design: Extended molecular dynamic simulations of a new series of dually acting inhibitors against EGFR and HER2. *J. Mol. Graph. Model.* **2013**, *44*, 220–231. [CrossRef]
38. Yun, C.H.; Mengwasser, K.E.; Toms, A.V.; Woo, M.S.; Greulich, H.; Wong, K.K.; Meyerson, M.; Eck, M.J. The T790M mutation in EGFR kinase causes drug resistance by increasing the affinity for ATP. *Proc. Natl. Acad. Sci. USA* **2008**, *105*, 2070–2075. [CrossRef]
39. Ruan, Z.; Katiyar, S.; Kannan, N. Computational and experimental characterization of patient derived mutations reveal an unusual mode of regulatory spine assembly and drug sensitivity in EGFR kinase. *Biochemistry* **2017**, *56*, 22–32. [CrossRef]
40. Olayioye, M.A.; Neve, R.M.; Lane, H.A.; Hynes, N.E. The ErbB signaling network: Receptor heterodimerization in development and cancer. *EMBO J.* **2000**, *19*, 3159–3167. [CrossRef]
41. Graus-Porta, D.; Beerli, R.R.; Daly, J.M.; Hynes, N.E. ErbB-2, the preferred heterodimerization partner of all ErbB receptors, is a mediator of lateral signaling. *EMBO J.* **1997**, *16*, 1647–1655. [CrossRef]
42. Ford, C.H.; Al-Bader, M.; Al-Ayadhi, B.; Francis, I. Reassessment of estrogen receptor expression in human breast cancer cell lines. *Anticancer Res.* **2011**, *2*, 521–527.
43. Stanley, A.; Ashrafi, G.H.; Seddon, A.M.; Modjtahedi, H. Synergistic effects of various Her inhibitors in combination with IGF-1R, C-MET and Src targeting agents in breast cancer cell lines. *Sci. Rep.* **2017**, *7*, 1–15. [CrossRef] [PubMed]
44. Wishart, D.S.; Feunang, Y.D.; Guo, A.C.; Lo, E.J.; Marcu, A.; Grant, J.R.; Sajed, T.; Johnson, D.; Li, C.; Sayeeda, C.; et al. DrugBank 5.0, a major update to the DrugBank database for 2018. *Nucleic Acids Res.* **2018**, *46*, D1074–D1082. [CrossRef]
45. Frisch, M.J.T.; Schlegel, H.B.G.W.; Scuseria, G.E.; Robb, M.A.; Cheeseman, J.R.; Scalmani, G.; Barone, V.; Petersson, G.A.; Nakatsuji, H. *Gaussian 09, Revision A.02*; Gaussian, Inc.: Wallingford, CT, USA, 2016.
46. Morris, G.M.; Huey, R.; Lindstrom, W.; Sanner, M.F.; Belew, R.K.; Goodsell, D.S.; Olson, A.J. AutoDock4 and AutoDockTools4, automated docking with selective receptor flexibility. *J. Comput Chem* **2009**, *30*, 2785–2791. [CrossRef]
47. Case, D.A.; Cheatham, T.E.; Darden, T.; Gohlke, H.; Luo, R.; Merz, K.M., Jr.; Woods, R.J. The Amber biomolecular simulation programs. *J. Comput. Chem.* **2005**, *26*, 1668–1688. [CrossRef]

48. Duan, Y.; Wu, C.; Chowdhury, S.; Lee, M.C.; Xiong, G.; Zhang, W.; Yang, R.; Cieplak, P.; Luo, R.; Lee, T.; et al. A point-charge force field for molecular mechanics simulations of proteins based on condensed phase quantum mechanical calculations. *J. Comput. Chem.* **2003**, *24*, 1999–2012. [CrossRef]
49. Jorgensen, W.L.; Chandrasekhar, J.; Madura, J.D.; Impey, R.W.; Klein, M.L. Comparison of simple potential functions for simulating liquid water. *J. Chem. Phys.* **1983**, *79*, 926–935. [CrossRef]
50. Wang, J.; Wolf, R.M.; Caldwell, J.W.; Kollman, P.A.; Case, D.A. Development and testing of a general amber force field. *J. Comput. Chem.* **2004**, *25*, 1157–1174. [CrossRef] [PubMed]
51. van Gunsteren, W.F.; Berendsen, H.J.C. Algorithms for macromolecular dynamics and constraint dynamics. *Mol. Phys.* **1977**, *34*, 1311–1327. [CrossRef]
52. Darden, T.; York, D.; Pedersen, L. Particle mesh Ewald—an N. log(N) method for calculating sums in large systems. *J. Chem. Phys.* **1993**, *98*, 10089–10092. [CrossRef]
53. Berendsen, H.J.C.; Postma, J.P.M.; van Gunsteren, W.F.; DiNola, A.; Haak, J.R. Molecular dynamics with coupling to an external bath. *J. Chem. Phys.* **1984**, *81*, 3684–3690. [CrossRef]
54. DeLano, W.L. *The PyMOL Molecular Graphics System*; DeLano Scientific: San Francisco, CA, USA; Palo Alto: Santa Clara, CA, USA, 2002.
55. *Maestro, Version 10.1*; Schrödinger, LLC: New York, NY, USA, 2015; Volume 1.
56. Miller, B.R.; McGee, T.D.; Swails, J.M.; Homeyer, N.; Gohlke, H.; Roitberg, A.E. MMPBSA.py: An efficient program for end-state free energy calculations. *J. Chem. Theory Comput.* **2012**, *8*, 3314–3321. [CrossRef] [PubMed]
57. Gohlke, H.; Kiel, C.; Case, D.A.J. Insights into protein-protein binding by binding free energy calculation and free energy decomposition for the Ras-Raf and Ras-RalGDS complexes. *Mol. Biol.* **2003**, *330*, 891–913. [CrossRef]
58. Kollman, P.A.; Massova, I.; Reyes, C.; Kuhn, B.; Huo, S.; Chong, L. Calculating structures and free energies of complex molecules: Combining molecular mechanics and continuum models. *Acc. Chem. Res.* **2000**, *33*, 889–897. [CrossRef] [PubMed]
59. Wang, J.M.; Hou, T.J.; Xu, X.J. Recent advances in free energy calculations with a combination of molecular mechanics and continuum model. *Drug Des.* **2006**, *2*, 287–306. [CrossRef]
60. Onufriev, A.; Bashford, V.; Case, D.A. Exploring protein native states and large-scale conformational changes with a modified generalized born model. *Proteins* **2004**, *55*, 383–394. [CrossRef]



## Article

# Mechanistic Modelling Identifies and Addresses the Risks of Empiric Concentration-Guided Sorafenib Dosing

Warit Ruanglertboon <sup>\*</sup>, Michael J. Sorich , Ashley M. Hopkins and Andrew Rowland

College of Medicine and Public Health, Flinders University, Bedford Park, SA 5042, Australia; michael.sorich@flinders.edu.au (M.J.S.); ashley.hopkins@flinders.edu.au (A.M.H.); andrew.rowland@flinders.edu.au (A.R.)

\* Correspondence: warit.ruanglertboon@flinders.edu.au

**Abstract:** The primary objective of this study is to evaluate the capacity of concentration-guided sorafenib dosing protocols to increase the proportion of patients that achieve a sorafenib maximal concentration ( $C_{max}$ ) within the range 4.78 to 5.78  $\mu\text{g}/\text{mL}$ . A full physiologically based pharmacokinetic model was built and validated using Simcyp<sup>®</sup> (version 19.1). The model was used to simulate sorafenib exposure in 1000 Sim-Cancer subjects over 14 days. The capacity of concentration-guided sorafenib dose adjustment, with/without model-informed dose selection (MIDS), to achieve a sorafenib  $C_{max}$  within the range 4.78 to 5.78  $\mu\text{g}/\text{mL}$  was evaluated in 500 Sim-Cancer subjects. A multivariable linear regression model incorporating hepatic cytochrome P450 (CYP) 3A4 abundance, albumin concentration, body mass index, body surface area, sex and weight provided robust prediction of steady-state sorafenib  $C_{max}$  ( $R^2 = 0.883$ ;  $p < 0.001$ ). These covariates identified subjects at risk of failing to achieve a sorafenib  $C_{max} \geq 4.78 \mu\text{g}/\text{mL}$  with 95.0% specificity and 95.2% sensitivity. Concentration-guided sorafenib dosing with MIDS achieved a sorafenib  $C_{max}$  within the range 4.78 to 5.78  $\mu\text{g}/\text{mL}$  for 38 of 52 patients who failed to achieve a  $C_{max} \geq 4.78 \mu\text{g}/\text{mL}$  with standard dosing. In a simulation setting, concentration-guided dosing with MIDS was the quickest and most effective approach to achieve a sorafenib  $C_{max}$  within a designated range.

**Keywords:** concentration-guided dosing; model informed dosing; physiologically based pharmacokinetics; sorafenib

**Citation:** Ruanglertboon, W.; Sorich, M.J.; Hopkins, A.M.; Rowland, A. Mechanistic Modelling Identifies and Addresses the Risks of Empiric Concentration-Guided Sorafenib Dosing. *Pharmaceuticals* **2021**, *14*, 389. <https://doi.org/10.3390/ph14050389>

Academic Editors: Mary J. Meegan and Niamh M O'Boyle

Received: 11 March 2021

Accepted: 19 April 2021

Published: 21 April 2021

**Publisher's Note:** MDPI stays neutral with regard to jurisdictional claims in published maps and institutional affiliations.



**Copyright:** © 2021 by the authors. Licensee MDPI, Basel, Switzerland. This article is an open access article distributed under the terms and conditions of the Creative Commons Attribution (CC BY) license (<https://creativecommons.org/licenses/by/4.0/>).

## 1. Introduction

Sorafenib is an orally administered small molecule kinase inhibitor (KI) used in the treatment of advanced hepatocellular (HCC) and renal cell (RCC) carcinomas. Sorafenib is a potent inhibitor of multiple kinase receptors including the vascular endothelial growth factor receptor (VEGFR), endothelial growth factor (subtype 1, 2 and 3), platelet-derived growth factor-beta (PDGFR $\beta$ ) and fibroblast growth factor receptor 1 (FGFR1). Variability in sorafenib exposure between individuals and within an individual over time has been identified as a potential source of heterogeneity in treatment efficacy and tolerability [1,2]. The area under the plasma concentration curve (AUC) and maximal concentration ( $C_{max}$ ) for sorafenib following has been reported to vary more than 50% with standard 400 mg dosing [3–5]. Variability in gastrointestinal absorption due to limited and pH dependent solubility has been proposed as a major source of variability in exposure [6], however concomitant proton pump inhibitor (PPI) use, which is reported to reduce KI absorption [7], has been demonstrated to have no impact on survival outcomes in HCC [8] and RCC [9,10] patients treated with sorafenib.

A sorafenib  $C_{max} \geq 4.78 \mu\text{g}/\text{mL}$  has been associated with superior overall survival in RCC and HCC patients, albeit with a higher incidence of hypertension, while a sorafenib  $C_{max} \geq 5.78 \mu\text{g}/\text{mL}$  has been associated with an increased incidence of grade II toxicity, the most common of which is hand foot skin reactions [11,12]. While the evidence for these thresholds is derived from a single observational study in 52 individuals, these values

have been cited as target concentrations in multiple reviews addressing individualised sorafenib dosing [13,14]. The dose escalation protocol that has been proposed for sorafenib to increase from 400 mg to 600 mg twice daily [15]. This approach is based on a sub-analysis of a phase II trial demonstrating a clinical benefit in patients who increased from 400 mg to 600 mg sorafenib twice daily following disease progression at the 400 mg dose [16]. Notably the association of this dose escalation with sorafenib plasma concentration has not been evaluated.

The potential benefits of individualised KI dosing have gained interest in recent years [17–19] and a number of strategies are available to both inform initial dose selection and facilitate dose adaptation [20]. Therapeutic drug monitoring (TDM) is an established method to facilitate concentration-guided dose adaptation but requires significant clinical and analytical resources to quantify the drug of interest and establish a robust evidence base. To date, few cancer medicines have met the level of evidence required to implement TDM in a clinical setting [21–23].

Model-informed initial dose selection (MIDS), often underpinned by a population pharmacokinetic (pop-PK) or physiologically based pharmacokinetic (PBPK) model, has emerged as a strategy to assist initial dose selection either to complement or replace TDM [24–27]. PBPK modelling and simulation is an established tool in drug discovery and development, where it is used to predict factors affecting PK and support the design of clinical trials [28,29]. PBPK is a ‘bottom-up’ approach whereby the concentration–time profile of a drug is simulated based on physiochemical and *in vitro* data [30,31]. Novel clinical applications for PBPK have been proposed involving the prediction of clinical drug–drug interactions, identification of physiological covariates impacting drug exposure and informing initial dose selection [25,31–33].

The primary objective of this study is to evaluate the capacity of concentration-guided sorafenib dose adjustment, with and without MIDS, to increase the proportion of patients that achieve a sorafenib  $C_{\max}$  within a concentration range of 4.78 to 5.78  $\mu\text{g}/\text{mL}$ . A full body PBPK model for sorafenib was first developed and validated, then used to identify physiological and molecular covariates associated with between subject variability in sorafenib exposure.

## 2. Results

### 2.1. Verification of the Sorafenib PBPK Compound Model

The accuracy of the sorafenib compound model was assessed in nineteen age and sex matched cohorts from single or multiple ascending dose (100 to 800 mg) trials. Mean simulated and observed AUC and  $C_{\max}$  values and the corresponding simulated/observed ratios are presented in Table S1 along with a summary of the verification trial characteristics (i.e., age range, sex, sample size and dose). The mean ( $\pm$ standard deviation; SD) simulated/observed AUC and  $C_{\max}$  ratios for the single-dose cohorts ( $n = 37$ ) were 1.92 ( $\pm 1.11$ ) and 1.50 ( $\pm 1.7$ ), respectively. The mean ( $\pm$ SD) simulated/observed AUC and  $C_{\max}$  ratios for the multiple-dose (typically 14 days) cohorts ( $n = 14$ ) were 1.50 ( $\pm 0.72$ ) and 1.17 ( $\pm 0.63$ ), respectively. Variability in model performance, indicated by large SD for parameter ratios, was driven by heterogeneity in observed parameters between trials. A representative sorafenib concentration–time profile depicting overlaid with the mean concentration–time profile and 90% confidence interval (CI) for the observed data is shown in Figure 1. The accuracy of the sorafenib compound model was considered acceptable on the basis that mean simulated parameters were within two-fold of the respective mean observed parameter and contained within the 90% CI for the observed parameter. Simulated Day 14 and Day 28 sorafenib  $C_{\max}$  values were divided by 1.17 to account for simulation to observed MFE in multiple dose studies when evaluating the simulated parameters against the observed target  $C_{\max}$  range. Results of sensitivity analyses performed to evaluate the impact of input parameters with measurement uncertainty ( $C_{\text{int}}$  for CYP3A4 and UGT1A9 pathways, fraction unbound, B/P ratio and LogP) on sorafenib kinetic parameters are shown in Figure S1.

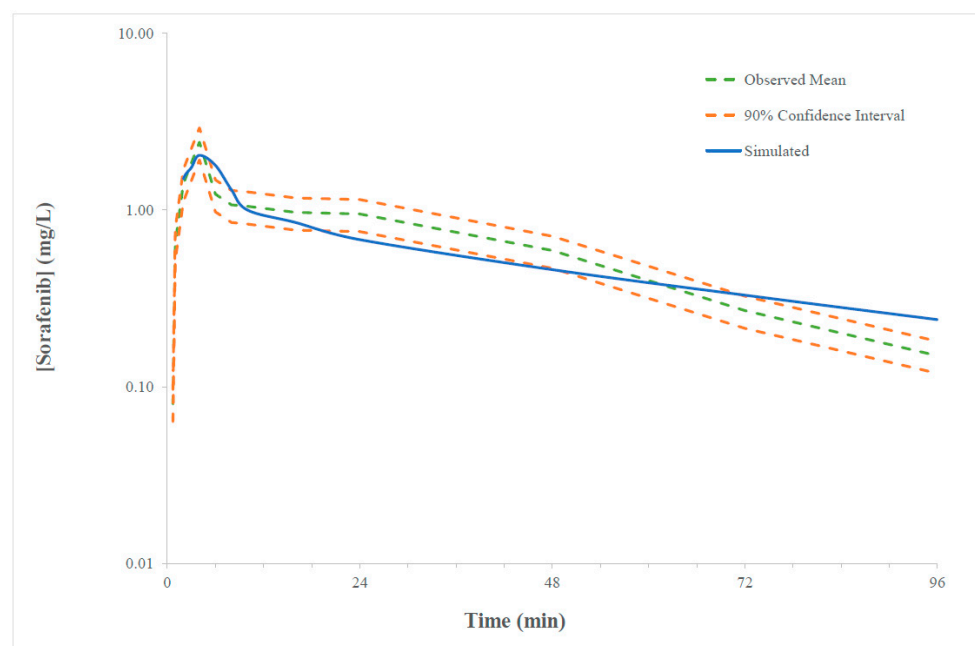


**Figure 1.** Representative overlay of simulated and observed (range) plasma concentration time curve of sorafenib (0–96 h) following 400 mg twice a day dosing. Solid blue line represented the mean model predicted exposure, dashed green line represented the mean observed exposure and dashed orange represented minimal and maximal 90% confidence intervals for the observed data.

### 2.2. Sorafenib Exposure in Cancer Patient

The summary of the mean, SD and range of steady-state sorafenib AUC and  $C_{\max}$  parameters defining exposure in 1000 virtual cancer patients is presented in Table S2. Consistent with the reported clinical trial data [4,5,34], the simulation revealed variability of greater than an order of magnitude in sorafenib exposure; the steady state AUC ranged from 22.7 to 270 mg/L·h (mean 99.2 mg/L·h), while  $C_{\max}$  ranged from 2.3 to 23.2  $\mu\text{g}/\text{mL}$  (mean 8.9  $\mu\text{g}/\text{mL}$ ).

### 2.3. Physiological and Molecular Characteristics Driving Variability in Sorafenib Exposure

Univariate logistic regression analysis evaluated correlations between physiological and molecular characteristics and sorafenib steady state  $C_{\max}$  threshold at  $> 4.78 \text{ mg}/\text{L}$  (Table S3) in a cohort of 1000 Sim-Cancer subjects. Statistical analysis of multivariable linear regression with stepwise inclusion of parameters revealed the primary covariates driving variability in sorafenib AUC were hepatic CYP3A4 abundance, albumin concentration, body mass index (BMI), body surface area (BSA), sex and weight (Figure 2).

A summary of the performance characteristics for the multivariable linear regression model is shown in Table 1. The covariate most strongly associated with variability in sorafenib AUC was hepatic CYP3A4 abundance, inclusion of albumin concentration and BMI resulted in substantial improvement in multivariable model fit. Stepwise inclusion of additional the covariates BSA, sex and weight resulted in minor improvements in model performance ( $R^2$  change  $\leq 0.010$ ). No other covariate met the stepwise inclusion criteria (probability of F to enter  $\leq 0.05$ ). These parameters formed the basis of the MIDS. The AUC of the ROC for the MIDS predicted steady state AUC was 0.991 (Figure 3). Sixty-three subjects (6.3%) from the Sim-Cancer cohort failed to achieve a Day 14  $C_{\max} > 4.78 \text{ }\mu\text{g}/\text{mL}$ . MIDS predicted individuals that failed to achieve a therapeutic sorafenib  $C_{\max}$  with 95.2% sensitivity (60/63 sub-therapeutic individuals) and 95.0% specificity (809/937 therapeutic individuals) (Table 2, Figure 3). Shown in Figure S2, differences in albumin concentration between participants were associated with changes in  $f_u$ .

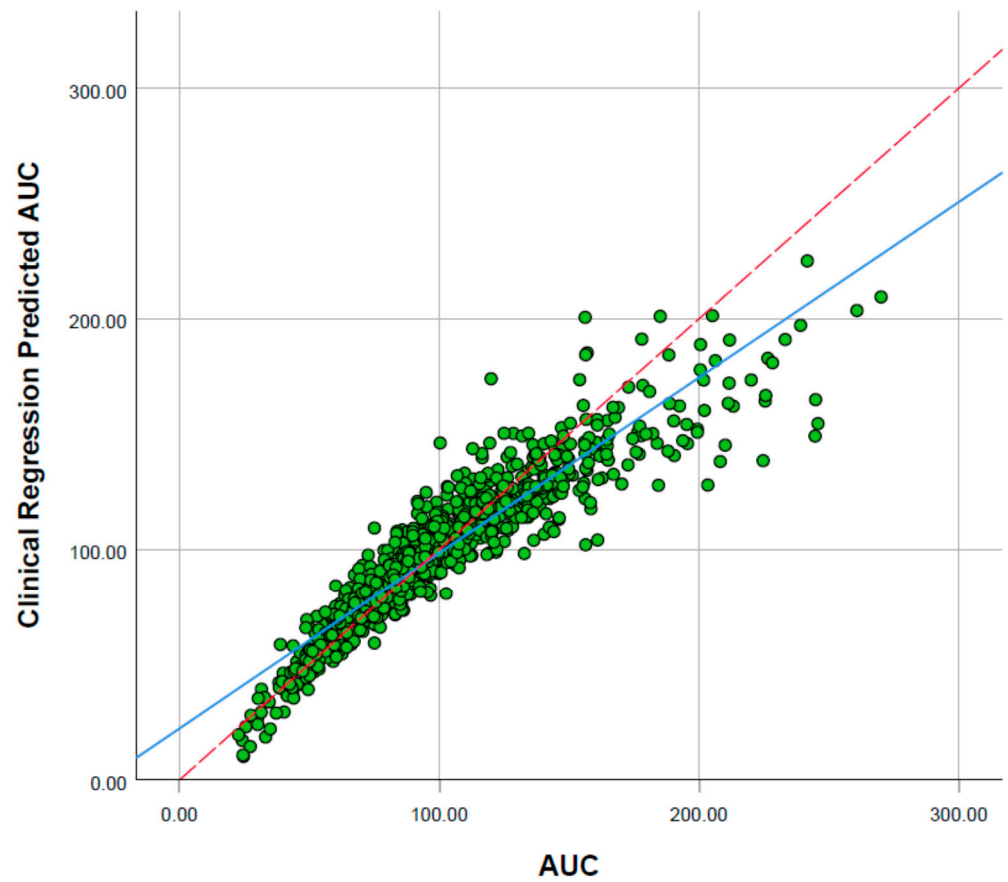


Figure 2. Correlation of model predicted steady-state sorafenib concentration predicted sorafenib AUC.

Table 1. Multivariable linear regression model performance characteristics.

Model	R <sup>2</sup>	Std. Error of the Estimate	R <sup>2</sup> Change	AUC ROC	AUC ROC Change
a	0.631	0.24141	0.631	0.953	0.953
b	0.781	0.18614	0.150	0.981	0.028
c	0.868	0.14458	0.087	0.990	0.009
d	0.873	0.14156	0.006	0.991	0.001
e	0.883	0.13619	0.010	0.991	-
f	0.883	0.13595	0.001	0.991	-

Model predictors (a) hepatic CYP3A4 abundance; (b) hepatic CYP3A4 abundance, albumin concentration; (c) hepatic CYP3A4 abundance, albumin concentration, BMI; (d) hepatic CYP3A4 abundance, albumin concentration, BMI, body surface area; (e) hepatic CYP3A4 abundance, albumin concentration, BMI, body surface area, sex; (f) hepatic CYP3A4 abundance, albumin concentration, BMI, body surface area, sex, weight; (g) hepatic CYP3A4 abundance, albumin concentration, BMI, body surface area, sex and weight.

Table 2. Classification matrixes describing the capability of linear regression models to identify individuals with a sub-therapeutic sorafenib steady state C<sub>max</sub>.

		Predicted Therapeutic C <sub>max</sub>		Percentage Correct
		Sub-Therapeutic	Therapeutic	
Observed Therapeutic C <sub>max</sub>	Sub-therapeutic	60 (true negative)	3 (false negative)	95.2
	Therapeutic	47 (false positive)	890 (true positive)	95.0

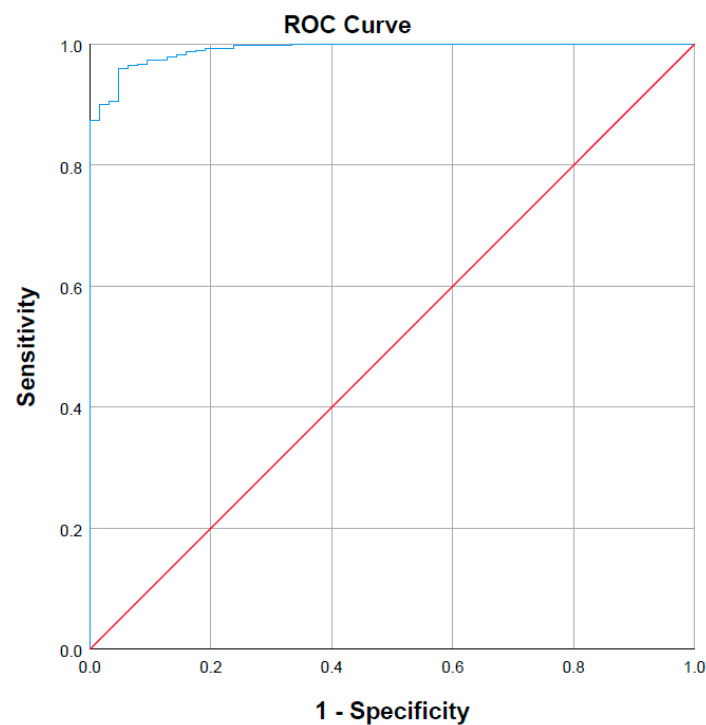


**Figure 3.** Receiver operating characteristic (ROC) curve demonstrating the prediction performance of a predicted steady state sorafenib AUC.

#### 2.4. Impact of Dose Individualisation

The proportion of participants with a simulated sorafenib  $C_{max}$  below, within and above the target 4.78 to 5.78  $\mu\text{g}/\text{mL}$  range at Day 14 and Day 28 based on following flat 400 mg dosing, concentration-guided dosing and concentration-guided dosing with MIDS is reported in Table 3. Concentration-guided sorafenib dosing without MIDS identified that 12.4% of subject (62/500) failed to achieve a Day 14  $C_{max} \geq 4.78 \mu\text{g}/\text{mL}$  with 400 mg twice daily dosing. Increasing the sorafenib dose to 600 mg twice daily in individuals who failed to achieve a Day 14 sorafenib  $C_{max} > 4.78 \mu\text{g}/\text{mL}$ , while retaining the 400 mg twice daily dose for those who did achieve a Day 14 sorafenib  $C_{max} \geq 4.78 \mu\text{g}/\text{mL}$  resulted in 99% of subjects (495/500) achieving a Day 28  $C_{max} \geq 4.78 \mu\text{g}/\text{mL}$ . Concentration-guided sorafenib dosing without MIDS resulted in an additional 43 subjects achieving a Day 28  $C_{max} > 5.78 \mu\text{g}/\text{mL}$  compared to flat 400 mg dosing.

**Table 3.** Number of participant below, within and above target concentration range with different sorafenib dosing protocols.

Dosing Protocol	Day 14			Day 28		
	<4.78 $\mu\text{g}/\text{mL}$	4.78 to 5.78 $\mu\text{g}/\text{mL}$	>5.78 $\mu\text{g}/\text{mL}$	<4.78 $\mu\text{g}/\text{mL}$	4.78 to 5.78 $\mu\text{g}/\text{mL}$	>5.78 $\mu\text{g}/\text{mL}$
Flat dosing	62	116	322	62	116	322
Concentration-guided dosing	62	116	322	5	130	365
Concentration-guided dosing with MIDS	34	135	331	5	164	336

On the basis of MIDS, 52 subjects were allocated to receive an initial sorafenib dose of 500 mg and 448 subjects were allocated to receive an initial sorafenib dose of 400 mg. Concentration-guided sorafenib dosing with MIDS resulted in 6.8% (34/500) subjects failing to achieve a Day 14  $C_{max} \geq 4.78 \mu\text{g}/\text{mL}$ . Increasing the sorafenib dose to 600 mg twice daily in individuals who failed to achieve a Day 14 sorafenib  $C_{max} \geq 4.78 \mu\text{g}/\text{mL}$ , while retaining the MIDS informed twice daily dose for those who did achieve a Day 14



sorafenib  $C_{\max} \geq 4.78 \mu\text{g/mL}$  resulted in 99% (495/500) of subjects achieving a Day 28  $C_{\max} \geq 4.78 \mu\text{g/mL}$ . Concentration-guided dosing with MIDS resulted in an additional 9 subjects achieving a Day 28  $C_{\max} > 5.78 \mu\text{g/mL}$  compared to flat 400 mg dosing. Post-hoc analysis demonstrated that three of these subjects would have a  $C_{\max} < 4.78 \mu\text{g/mL}$  with 400 mg dosing, while the remaining six subjects could have retained a Day 28  $C_{\max} \geq 4.78 \mu\text{g/mL}$  while avoiding a Day 28  $C_{\max} > 5.78 \mu\text{g/mL}$  with a dose reduction from 500 mg to 400 mg following assessment of  $C_{\max}$  on Day 14, however dose reduction was not incorporated into the simulation protocol.

### 3. Discussion

The present study demonstrated that concentration-guided dosing with MIDS facilitates therapeutic sorafenib exposure in 99% of subjects within 28 days while minimising the number of additional subjects at risk of supra-therapeutic dosing compared to concentration-guided dosing alone. Multivariable linear regression modelling demonstrated that variability in simulated sorafenib AUC and  $C_{\max}$  is associated with hepatic CYP3A4 abundance, albumin concentration, BMI, sex, age and weight. Logistic regression modelling of these covariates predicted individuals likely to fail to achieve sorafenib  $C_{\max} \geq 4.78 \text{ mg/L}$  with high sensitivity and specificity (95.2% and 95%, respectively). Incorporation of these parameters into an MIDS algorithm that allocated subjects to a 400 mg or 500 mg initial sorafenib dose resulted in a 50% reduction in the number of subjects that failed to achieve a Day 14  $C_{\max} \geq 4.78 \text{ mg/L}$ . When used in conjunction with concentration-guided dosing at Day 14, this protocol resulted in 99% of subjects attaining a Day 28  $C_{\max} \geq 4.78 \text{ mg/L}$ .

The current study also highlights the potential danger of empiric concentration-guided dosing in terms of placing patients at an increased risk of toxicity. In the absence of MIDS, 69% of subjects (43/62) that underwent a dose escalation from 400 to 600 mg on Day 14 experienced a  $C_{\max}$  on Day 28 that is associated with increased risk of grade II toxicity. Compared to concentration-guided dosing alone, the concentration-guided dosing with MIDS protocol reduced the number of additional subjects at increased risk of grade II toxicity on Day 28 ( $C_{\max} \geq 5.78 \text{ mg/L}$ ) from 43 to 9.

PBPK modelling and simulation is an established tool to support drug discovery and development, and is a core element of the regulatory approval process in many jurisdictions [35]. Recent studies have further demonstrated the potential role of PBPK in predicting covariates affecting variability in drug exposure resulting from either patient characteristics or the drugs' physicochemical properties [24,25], giving rise to the intriguing potential for this platform to support model informed precision dosing [26,32]. Since the introduction of imatinib in 2001 there has been a growing evidence base supporting a role for concentration-guided KI dosing, despite this implementation of KI dose individualisation has remained challenging. Many early studies focussed on a potential role for TDM-guided KI dosing, however, sufficient evidence has yet to be generated to support widespread implementation for any KI. This has led to the exploration of novel approaches to facilitate precision KI dosing, which have included model informed precision dosing based on integrated simulation/prediction platforms such as PK-Sim<sup>®</sup>, GastroPlus<sup>™</sup>, Phoenix<sup>™</sup>, and Simcyp<sup>®</sup> [26,36–38].

The target concentration range and dose escalation protocol used in the current study were based on the best current evidence [11,16]. The main limitation to this study remains the lack of independent verification of the 4.78 to 5.78  $\mu\text{g/mL}$  target  $C_{\max}$  range. Further, when considering the clinical implementation, it is also important to note that the rate at which sorafenib is absorbed from the GIT varies >five-fold [6]. Variability in the rate of intestinal absorption results in marked variability in the time taken to reach  $C_{\max}$  for sorafenib (1 to 6 h). As such, in the absence of full PK (AUC) sampling, which is not practical in a clinical setting, concentration-guided sorafenib dosing based on a  $C_{\max}$  target is unlikely to be robust.

Liver CYP3A4 abundance was identified as the dominant characteristic driving variability in sorafenib AUC and  $C_{\max}$ . By accounting for this characteristic alone, it was possible to identify subjects with a sub-therapeutic sorafenib  $C_{\max}$  with a specificity of 74.6% and a sensitivity of 96.3%. When hepatic CYP3A4 abundance was considered along with readily attained data regarding albumin concentration, BMI, BSA, sex and weight in combination with albumin concentration, these two parameters accounted for >88% of multivariable model performance in terms of  $R^2$ , specificity and sensitivity (Table 1). These data suggest that consideration of liver CYP3A4 abundance may provide sufficient power to prospectively identify patients who are likely to require a higher sorafenib dose in order to achieve a therapeutic plasma concentration. Importantly, recent work in this [39] and other [40,41] laboratories has demonstrated that quantification of extracellular vesicle (EV)-derived CYP3A protein, mRNA and ex vivo activity robustly describes variability in CYP3A activity in humans.

This study identified the major physiological and molecular characteristics associated with between subject variability in sorafenib exposure to be hepatic CYP3A4 abundance, albumin concentration, BMI, BSA, sex and weight. Initial dose selection informed by a model accounting for these covariates resulted in a quicker and more effective concentration-guided sorafenib dosing.

#### 4. Materials and Methods

##### 4.1. Development and Verification of the Sorafenib PBPK Model Structural Model

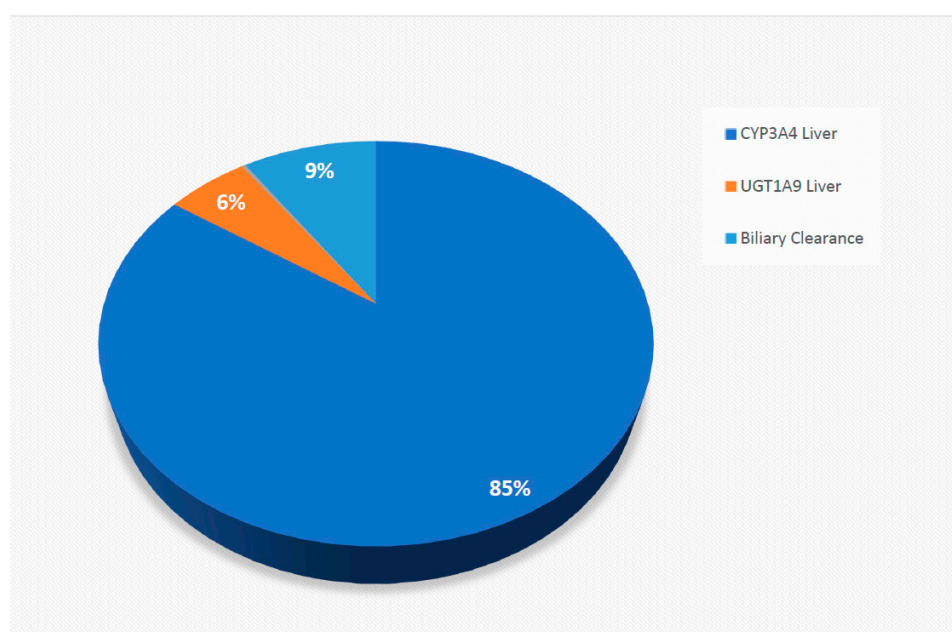
Sorafenib absorption was simulated using the advanced dissolution, absorption, and metabolism (ADAM) sub-model which incorporates membrane permeability, intestinal metabolism and transporter-mediated uptake and efflux. The ADAM sub-model was used in conjunction with a full-body PBPK model, containing compartments and drug distribution characteristics for all organs. All simulations were performed using Simcyp® (version 19.1, Certara, UK). The differential equations underpinning the model have been described previously [42].

##### 4.2. Development of the Sorafenib Compound Model

The physicochemical, blood binding, absorption, distribution, elimination parameters utilised to construct the sorafenib compound model are summarised in Table 4. Physicochemical properties were based on published literature and documents [43,44]. Metabolism and elimination parameters were incorporated based on reported intersystem extrapolation factor (ISEF) adjusted in vitro CYP and UDP-glucuronosyltransferase (UGT) data (Figure 4).

**Table 4.** Model inputs used to build the sorafenib compound model.

Parameter	Value	Source
<b>Physicochemical properties</b>		
Molecular weight	464.82 g/mol	
Log P <sub>o.w</sub>	4.54	[43]
Hydrogen bond donor	3	
Species	Base	[43]
<b>Protein binding</b>		
B/P	0.55	[43]
f <sub>up</sub>	0.0048	[43]
<b>Absorption (ADAM model)</b>		
f <sub>a</sub>	0.99	Predicted
k <sub>a</sub> (L/h)	1.75	Predicted
<b>Permeability</b>		
P <sub>eff, man</sub> (10 <sup>-4</sup> cm/s)	4.01	Predicted
Caco-2 (10 <sup>-6</sup> cm/s)	24.1	
<b>Formulation</b>		
Solid formulation	Immediate release	[43]
<b>In vivo pharmacokinetic properties (full PBPK model)</b>		
Prediction model	1	
K <sub>p</sub> scalar	0.7	Predicted
<b>CYP metabolism: ISEF adjusted recombinant enzyme kinetics (CL<sub>int</sub>; μL/min/pmol)</b>		
CYP3A4	2.6	[18]
<b>UGT metabolism: ISEF adjusted recombinant enzyme kinetics (CL<sub>int</sub>; μL/min/mg)</b>		
UGT1A9	20.1	[18]

**Figure 4.** The pie chart demonstrated the relative contribution of CYP and UGT to simulated sorafenib elimination based on the predicted model.

#### 4.3. Population Model

As no clinical trials evaluating sorafenib exposure have been performed in healthy volunteers, verification of the sorafenib compound model was performed using Sim-Cancer population cohort. Simulations performed to assess the physiological and molecular characteristics driving between-subject variability in sorafenib exposure at steady state also

utilised the Sim-Cancer population cohort. The physiological and pathological characteristics of the Sim-cancer population have been determined based on a meta-analysis of cancer patients enrolled in clinical trials [45].

#### 4.4. Simulated Trial Designs

During the model development stage, simulations included 10 trials with 10 subjects per trial (100 subjects total). During the verification stage, simulations were performed in 10 trials matched for sample size, dose, age range and sex distribution in the protocol described for the observed trial. Unless specified otherwise, parameters defining sorafenib exposure were assessed over 24 h following a single dose at 9:00 a.m. on day 1.

#### 4.5. Validation of the Sorafenib Compound Model

The sorafenib compound model was validated by comparing simulated AUC and  $C_{\max}$  values to reported observed values from matched clinical trials undertaken in cancer patients. A mean simulated parameter estimated within two-fold of the mean observed parameter and contained within the 90% confidence interval for the observed parameter was applied as the criteria to accept the model accuracy. The model goodness-of-fit was further verified by visual inspection of the overlay of mean simulated and observed sorafenib concentration-time profiles from individual clinical trials. Simulated  $C_{\max}$  values were normalised to account for the mean fold error (MFE) between simulated and observed values determined from multiple dose validation studies when evaluating simulations against the observed target concentration range (4.78 to 5.78  $\mu\text{g}/\text{mL}$ ).

#### 4.6. Physiological and Molecular Characteristics Driving Variability in Sorafenib Exposure

The validated sorafenib compound model was used to evaluate associations between physiological and molecular covariates and steady-state sorafenib AUC and  $C_{\max}$  [24]. A trial comprising 1000 subjects from the Sim-Cancer population was simulated over 15 days with 400 mg of sorafenib administered orally in a fasted-state every 12 h for 14 days starting at 9:00 a.m. on Day 1. The steady state sorafenib AUC was determined over 12 h following the final dose of sorafenib at 9:00 p.m. on Day 14. The steady state sorafenib  $C_{\max}$  was determined as the maximum concentration following the final dose at 9:00 p.m. on Day 14.

Associations between physiological and molecular characteristics and sorafenib log transformed AUC and  $C_{\max}$  were evaluated by univariate and multivariate linear regression. Continuous variables were checked for normality and non-linearity of association, sex was coded as a binary variable. A multivariable linear regression model to predict the log transformed sorafenib  $C_{\max}$  was developed by stepwise forward inclusion of individually significant characteristics identified in the univariable regression analysis based on a probability of F to enter  $\leq 0.05$ . The multivariable model (MIDS) predicted  $C_{\max}$  was determined by back transformation of the model predicted log transformed  $C_{\max}$ . The capacity of MIDS to identify subjects with a sub-therapeutic simulated sorafenib  $C_{\max}$  determined by scaling the reported threshold for simulation accuracy was evaluated using classification matrix analysis and is summarised as model sensitivity and specificity. The predictive performance of MIDS was assessed by receiver operating characteristic curve (ROC) analysis. Statistical analysis was conducted using R version 4.0.2 and IBM SPSS Statistics for Windows version 23 (Release 2015, IBM, Armonk, NY, USA).

#### 4.7. Impact of Dose Individualisation

A simulation was conducted to evaluate the capacity of concentration-guided sorafenib dose adjustment to achieve a steady state sorafenib  $C_{\max}$  within the range 4.78 to 5.78  $\mu\text{g}/\text{mL}$ . Sorafenib exposure was simulated in a cohort of 500 subjects from the Sim-Cancer population (20 to 50 years old, 50% female) over 14 days with 400 mg sorafenib administered orally in a fasted-state every 12 h starting at 9:00 a.m. on Day 1. Sorafenib  $C_{\max}$  was determined following the final dose at 9:00 p.m. on Day 14. Sorafenib exposure

in subjects who failed to achieve a Day 14 normalised simulated  $C_{\max} \geq 4.78 \mu\text{g/mL}$  was simulated over an additional 14 days with sorafenib administered at a dose of 600 mg every 12 h starting at 9:00 a.m. on Day 15. The post dose adjustment sorafenib  $C_{\max}$  was determined following the final dose at 9:00 p.m. on Day 28.

A simulation was conducted in the same cohort to evaluate the benefit of MIDS at baseline in conjunction with concentration-guided sorafenib dose adjustment. Demographic characteristics for the Sim-Cancer cohort were used to predict the normalised simulated Day 14 sorafenib  $C_{\max}$  based on the multivariable model described previously. Based on MIDS subjects with a predicted sorafenib  $C_{\max} \geq 4.78 \mu\text{g/mL}$  received 400 mg sorafenib twice daily, while subjects with predicted sorafenib  $C_{\max} < 4.78 \mu\text{g/mL}$  received 500 mg sorafenib twice daily. Sorafenib exposure was simulated over 28 days as described for concentration-guided sorafenib dose adjustment without MIDS, with  $C_{\max}$  evaluated at Day 14 and Day 28 and a dose increase to 600 mg between Day 15 and Day 28 for individuals who failed to achieve a Day 14  $C_{\max} \geq 4.78 \mu\text{g/mL}$ .

**Supplementary Materials:** The following are available online at <https://www.mdpi.com/article/10.3390/ph14050389/s1>. Table S1: Verification of the impact of drug interactions on sorafenib exposure. Table S2: Summary of physiological and molecular characteristic considered in regression analyses. Table S3: Logistic regression analysis of therapeutic  $C_{\max}$  threshold of  $>5.5926 \text{ mg/L}$ .

**Author Contributions:** Conceptualisation, W.R., M.J.S., A.M.H. and A.R.; methodology, W.R., M.J.S., A.M.H. and A.R.; software, A.R.; validation, A.R. and W.R.; formal analysis, W.R. and A.R.; investigation, W.R. and A.R.; resource, A.R.; data curation, W.R. and A.R.; writing—original draft preparation, W.R.; writing—review and editing, W.R., A.R., A.M.H. and M.J.S.; visualisation, W.R. and A.R.; supervision, M.J.S., A.M.H. and A.R.; project administration, M.J.S., A.M.H. and A.R.; funding acquisition, A.R. All authors have read and agreed to the published version of the manuscript.

**Funding:** WR is supported by a Royal Thai Government Scholarship. A.R. and M.J.S. are supported by Cancer Council Beat Cancer Fellowships. A.M.H. is supported by a National Breast Cancer Foundation Fellowship.

**Institutional Review Board Statement:** Not applicable.

**Informed Consent Statement:** Not applicable.

**Data Availability Statement:** The data that support the findings of this study are available from the corresponding author upon reasonable request.

**Conflicts of Interest:** A.R. and M.J.S. report investigator-initiated project grants from Pfizer, outside the scope of the submitted work. W.R. and A.M.H. have no conflicts of interest to disclose.

## References

1. Vogel, A.; Cervantes, A.; Chau, I.; Daniele, B.; Llovet, J.M.; Meyer, T.; Nault, J.C.; Neumann, U.; Ricke, J.; Sangro, B.; et al. Hepatocellular carcinoma: ESMO Clinical Practice Guidelines for diagnosis, treatment and follow-up. *Ann Oncol.* **2018**, *29* (Suppl. 4), 238–255. [CrossRef]
2. Wang, H.-T.; Xia, M. A meta-analysis of efficacy and safety of sorafenib versus other targeted agents for metastatic renal cell carcinoma. *Medicine* **2019**, *98*, e13779. [CrossRef]
3. Strumberg, D.; Clark, J.W.; Awada, A.; Moore, M.J.; Richly, H.; Hendlisz, A.; Hirte, H.W.; Eder, J.P.; Lenz, H.-J.; Schwartz, B. Safety, Pharmacokinetics, and Preliminary Antitumor Activity of Sorafenib: A Review of Four Phase I Trials in Patients with Advanced Refractory Solid Tumors. *Oncologist* **2007**, *12*, 426–437. [CrossRef] [PubMed]
4. Awada, A.; Hendlisz, A.; Gil, T.; Bartholomeus, S.; Mano, M.; de Valeriola, D.; Strumberg, D.; Brendel, E.; Haase, C.G.; Schwartz, B.; et al. Phase I safety and pharmacokinetics of BAY 43-9006 administered for 21 days on/7 days off in patients with advanced, refractory solid tumours. *Br. J. Cancer* **2005**, *92*, 1855–1861. [CrossRef]
5. Moore, M.; Hirte, H.W.; Siu, L.; Oza, A.; Hotte, S.J.; Petrenciuc, O.; Cihon, F.; Lathia, C.; Schwartz, B. Phase I study to determine the safety and pharmacokinetics of the novel Raf kinase and VEGFR inhibitor BAY 43-9006, administered for 28 days on/7 days off in patients with advanced, refractory solid tumors. *Ann. Oncol.* **2005**, *16*, 1688–1694. [CrossRef]
6. Jain, L.; Woo, S.; Gardner, E.R.; Dahut, W.L.; Kohn, E.C.; Kummur, S.; Mould, D.R.; Giaccone, G.; Yarchoan, R.; Venitz, J.; et al. Population pharmacokinetic analysis of sorafenib in patients with solid tumours. *Br. J. Clin. Pharmacol.* **2011**, *72*, 294–305. [CrossRef]

7. Sharma, M.; Holmes, H.M.; Mehta, H.B.; Chen, H.; Aparasu, R.R.; Shih, Y.-C.T.; Giordano, S.H.; Johnson, M.L. The concomitant use of tyrosine kinase inhibitors and proton pump inhibitors: Prevalence, predictors, and impact on survival and discontinuation of therapy in older adults with cancer. *Cancer* **2019**, *125*, 1155–1162. [CrossRef] [PubMed]
8. Ruanglertboon, W.; Sorich, M.J.; Logan, J.M.; Rowland, A.; Hopkins, A.M. The effect of proton pump inhibitors on survival outcomes in advanced hepatocellular carcinoma treated with sorafenib. *J. Cancer Res. Clin. Oncol.* **2020**, *146*, 2693–2697. [CrossRef] [PubMed]
9. Lalani, A.A.; McKay, R.R.; Lin, X.; Simantov, R.; Kaymakcalan, M.D.; Choueiri, T.K. Proton Pump Inhibitors and Survival Outcomes in Patients With Metastatic Renal Cell Carcinoma. *Clin. Genitourin. Cancer* **2017**, *15*, 724–732. [CrossRef] [PubMed]
10. Au, T.H.; Bailey, E.B.; Patel, S.B.; Tantravahi, S.K.; Agarwal, N.; Stenejem, D.D. Effect of concomitant proton pump inhibitor (PPI) on effectiveness of tyrosine kinase inhibitor (TKI) in patients with metastatic renal cell carcinoma (mRCC). *J. Clin. Oncol.* **2016**, *34* (Suppl. 2), 608. [CrossRef]
11. Fukudo, M.; Ito, T.; Mizuno, T.; Shinsako, K.; Hatano, E.; Uemoto, S.; Kamba, T.; Yamasaki, T.; Ogawa, O.; Seno, H.; et al. Exposure-toxicity relationship of sorafenib in Japanese patients with renal cell carcinoma and hepatocellular carcinoma. *Clin. Pharmacokinet.* **2014**, *53*, 185–196. [CrossRef] [PubMed]
12. Ruanglertboon, W.; Sorich, M.J.; Rowland, A.; Hopkins, A.M. Effect of early adverse events resulting in sorafenib dose adjustments on survival outcomes of advanced hepatocellular carcinoma patients. *Int. J. Clin. Oncol.* **2020**, *25*, 1672–1677. [CrossRef] [PubMed]
13. de Wit, D.; Guchelaar, H.J.; den Hartigh, J.; Gelderblom, H.; van Erp, N.P. Individualized dosing of tyrosine kinase inhibitors: Are we there yet? *Drug Discov. Today* **2015**, *20*, 18–36. [CrossRef] [PubMed]
14. Mueller-Schoell, A.; Groenland, S.L.; Scherf-Clavel, O.; van Dyk, M.; Huisinga, W.; Michelet, R.; Jaehde, U.; Steeghs, N.; Huitema, A.D.R.; Kloft, C. Therapeutic drug monitoring of oral targeted antineoplastic drugs. *Eur. J. Clin. Pharmacol.* **2020**, *29*, iv238–iv255. [CrossRef]
15. Semrad, T.J.; Gandara, D.R.; Lara, P.N., Jr. Enhancing the clinical activity of sorafenib through dose escalation: Rationale and current experience. *Ther. Adv. Med. Oncol.* **2011**, *3*, 95–100. [CrossRef]
16. Escudier, B.; Szczylik, C.; Hutson, T.E.; Demkow, T.; Staehler, M.; Rolland, F.; Negrier, S.; Laferriere, N.; Scheuring, U.J.; Cella, D.; et al. Randomized phase II trial of first-line treatment with sorafenib versus interferon Alfa-2a in patients with metastatic renal cell carcinoma. *J. Clin. Oncol.* **2009**, *27*, 1280–1289. [CrossRef] [PubMed]
17. Verheijen, R.B.; Yu, H.; Schellens, J.H.M.; Beijnen, J.H.; Steeghs, N.; Huitema, A.D.R. Practical Recommendations for Therapeutic Drug Monitoring of Kinase Inhibitors in Oncology. *Clin. Pharmacol. Ther.* **2017**, *102*, 765–776. [CrossRef]
18. Rowland, A.; van Dyk, M.; Mangoni, A.A.; Miners, J.O.; McKinnon, R.A.; Wiese, M.D.; Rowland, A.; Kichenadasse, G.; Gurney, H.; Sorich, M.J. Kinase inhibitor pharmacokinetics: Comprehensive summary and roadmap for addressing inter-individual variability in exposure. *Expert Opin. Drug Metab. Toxicol.* **2017**, *13*, 31–49. [CrossRef] [PubMed]
19. Darwich, A.; Ogungbenro, K.; Hatley, O.; Rostami-Hodjegan, A. Role of pharmacokinetic modeling and simulation in precision dosing of anticancer drugs. *Transl. Cancer Res.* **2017**. [CrossRef]
20. Hopkins, A.M.; Menz, B.D.; Wiese, M.D.; Kichenadasse, G.; Gurney, H.; McKinnon, R.A.; Rowland, A.; Sorich, M.J. Nuances to precision dosing strategies of targeted cancer medicines. *Pharmacol. Res. Perspect.* **2020**, *8*, e00625. [CrossRef]
21. Kang, J.S.; Lee, M.H. Overview of therapeutic drug monitoring. *Korean J. Intern. Med.* **2009**, *24*, 1–10. [CrossRef] [PubMed]
22. Thomson, A. TDM—A Multidisciplinary Approach. *Ther. Drug Monit.* **1997**, *19*, 490. [CrossRef]
23. Sánchez-Hernández, J.G.; Rebollo, N.; Martin-Suarez, A.; Calvo, M.V.; Muñoz, F. A 3-year prospective study of a multidisciplinary early proactive therapeutic drug monitoring programme of infliximab treatments in inflammatory bowel disease. *Br. J. Clin. Pharmacol.* **2020**, *86*, 1165–1175. [CrossRef] [PubMed]
24. Sorich, M.J.; Mutlib, F.; van Dyk, M.; Hopkins, A.M.; Polasek, T.M.; Marshall, J.C.; Rodrigues, A.D.; Rowland, A. Use of Physiologically Based Pharmacokinetic Modeling to Identify Physiological and Molecular Characteristics Driving Variability in Axitinib Exposure: A Fresh Approach to Precision Dosing in Oncology. *J. Clin. Pharmacol.* **2019**, *59*, 872–879. [CrossRef] [PubMed]
25. Rowland, A.; van Dyk, M.; Hopkins, A.M.; Mounzer, R.; Polasek, T.M.; Rostami-Hodjegan, A.; Sorich, M.J. Physiologically Based Pharmacokinetic Modeling to Identify Physiological and Molecular Characteristics Driving Variability in Drug Exposure. *Clin. Pharmacol. Ther.* **2018**, *104*, 1219–1228. [CrossRef] [PubMed]
26. Polasek, T.M.; Rostami-Hodjegan, A. Virtual Twins: Understanding the Data Required for Model-Informed Precision Dosing. *Clin. Pharmacol. Ther.* **2020**, *107*, 742–745. [CrossRef]
27. Kluwe, F.; Michelet, R.; Mueller-Schoell, A.; Maier, C.; Klopp-Schulze, L.; van Dyk, M.; Mikus, G.; Huisinga, W.; Kloft, C. Perspectives on Model-Informed Precision Dosing in the Digital Health Era: Challenges, Opportunities, and Recommendations. *Clin. Pharmacol. Ther.* **2020**, *109*, 29–36. [CrossRef]
28. Polasek, T.M.; Polak, S.; Doogue, M.P.; Rostami-Hodjegan, A.; Miners, J.O. Assessment of inter-individual variability in predicted phenytoin clearance. *Eur. J. Clin. Pharmacol.* **2009**, *65*, 1203–1210. [CrossRef]
29. Chetty, M.; Cain, T.; Wedagedera, J.; Rostami-Hodjegan, A.; Jamei, M. Application of Physiologically Based Pharmacokinetic (PBPK) Modeling Within a Bayesian Framework to Identify Poor Metabolizers of Efavirenz (PM), Using a Test Dose of Efavirenz. *Front. Pharmacol.* **2018**, *9*, 247. [CrossRef]
30. Tsamandouras, N.; Rostami-Hodjegan, A.; Aarons, L. Combining the ‘bottom up’ and ‘top down’ approaches in pharmacokinetic modelling: Fitting PBPK models to observed clinical data. *Br. J. Clin. Pharmacol.* **2015**, *79*, 48–55. [CrossRef]

31. Tylutki, Z.; Polak, S.; Wiśniowska, B. Top-down, Bottom-up and Middle-out Strategies for Drug Cardiac Safety Assessment via Modeling and Simulations. *Curr. Pharmacol. Rep.* **2016**, *2*, 171–177. [CrossRef]
32. Polasek, T.M.; Tucker, G.T.; Sorich, M.J.; Wiese, M.D.; Mohan, T.; Rostami-Hodjegan, A.; Korprasertthaworn, P.; Perera, V.; Rowland, A. Prediction of olanzapine exposure in individual patients using physiologically based pharmacokinetic modelling and simulation. *Br. J. Clin. Pharmacol.* **2018**, *84*, 462–476. [CrossRef]
33. Van Dyk, M.; Rowland, A. PBPK modeling as an approach to evaluate the effect of covariates and drug-drug interactions on variability in EGFR kinase inhibitor exposure. *Transl. Cancer Res.* **2017**, *6*, S1600–S1615. [CrossRef]
34. Minami, H.; Kawada, K.; Ebi, H.; Kitagawa, K.; Kim, Y.-I.; Araki, K.; Mukai, H.; Tahara, M.; Nakajima, H.; Nakajima, K. Phase I and pharmacokinetic study of sorafenib, an oral multikinase inhibitor, in Japanese patients with advanced refractory solid tumors. *Cancer Sci.* **2008**, *99*, 1492–1498. [CrossRef] [PubMed]
35. Shebley, M.; Sandhu, P.; Riedmaier, A.E.; Jamei, M.; Narayanan, R.; Patel, A.; Peters, S.A.; Reddy, V.P.; Zheng, M.; de Zwart, L.; et al. Physiologically Based Pharmacokinetic Model Qualification and Reporting Procedures for Regulatory Submissions: A Consortium Perspective. *Clin. Pharmacol. Ther.* **2018**, *104*, 88–110. [CrossRef]
36. Basu, S.; Lien, Y.T.; Vozmediano, V.; Schlender, J.-F.; Eissing, T.; Schmidt, S.; Niederalt, C. Physiologically Based Pharmacokinetic Modeling of Monoclonal Antibodies in Pediatric Populations Using PK-Sim. *Front. Pharmacol.* **2020**, *11*, 868. [CrossRef] [PubMed]
37. Hennig, S.; Holthouse, F.; Staatz, C.E. Comparing dosage adjustment methods for once-daily tobramycin in paediatric and adolescent patients with cystic fibrosis. *Clin. Pharmacokinet.* **2015**, *54*, 409–421. [CrossRef] [PubMed]
38. Song, L.; He, C.-Y.; Yin, N.-G.; Liu, F.; Jia, Y.-T.; Liu, Y. A population pharmacokinetic model for individualised dosage regimens of vancomycin in Chinese neonates and young infants. *Oncotarget* **2017**, *8*, 105211–105221. [CrossRef]
39. Rowland, A.; Ruanglertboon, W.; van Dyk, M.; Wijayakumara, D.; Wood, L.; Meech, R.; Mackenzie, P.; Rodrigues, A.; Marshall, J.; Sorich, M. Plasma Extracellular Nanovesicle (Exosome) derived biomarkers for ADME pathways: A novel approach to characterise variability in drug exposure. *Br. J. Clin. Pharmacol.* **2019**, *85*, 216–226. [CrossRef]
40. Kumar, S.; Sinha, N.; Gerth, K.A.; Rahman, M.A.; Yallapu, M.M.; Midde, N.M. Specific packaging and circulation of cytochromes P450, especially 2E1 isozyme, in human plasma exosomes and their implications in cellular communications. *Biochem. Biophys. Res. Commun.* **2017**, *491*, 675–680. [CrossRef]
41. Achour, B.; Al-Majdoub, Z.M.; Grybos-Gajniak, A.; Lea, K.; Kilford, P.; Zhang, M.; Knight, D.; Barber, J.; Schageman, J.; Rostami-Hodjegan, A. Liquid Biopsy Enables Quantification of the Abundance and Interindividual Variability of Hepatic Enzymes and Transporters. *Clin. Pharmacol. Ther.* **2021**, *109*, 222. [CrossRef] [PubMed]
42. Rowland Yeo, K.; Jamei, M.; Yang, J.; Tucker, G.T.; Rostami-Hodjegan, A. Physiologically based mechanistic modelling to predict complex drug-drug interactions involving simultaneous competitive and time-dependent enzyme inhibition by parent compound and its metabolite in both liver and gut—the effect of diltiazem on the time-course of exposure to triazolam. *Eur. J. Pharm. Sci.* **2010**, *39*, 298–309. [PubMed]
43. European Medicines Agency. Nexavar: European Public Assessment Reports (EPAR)-Scientific Discussion. 3 March 2007. Available online: [http://www.ema.europa.eu/docs/en\\_GB/document\\_library/EPAR-Scientific\\_Discussion/human/000690/WC500027707.pdf](http://www.ema.europa.eu/docs/en_GB/document_library/EPAR-Scientific_Discussion/human/000690/WC500027707.pdf) (accessed on 20 February 2021).
44. Liu, B.; Crewe, H.K.; Ozdemir, M.; Yeo, K.R.; Tucker, G.; Rostami-Hodjegan, A. The absorption kinetics of ketoconazole plays a major role in explaining the reported variability in the level of interaction with midazolam: Interplay between formulation and inhibition of gut wall and liver metabolism. *Biopharm. Drug Dispos.* **2017**, *38*, 260–270. [CrossRef] [PubMed]
45. Schwenger, E.; Reddy, V.P.; Moorthy, G.; Sharma, P.; Tomkinson, H.; Masson, E.; Vishwanathan, K. Harnessing Meta-analysis to Refine an Oncology Patient Population for Physiology-Based Pharmacokinetic Modeling of Drugs. *Clin. Pharmacol. Ther.* **2018**, *103*, 271–280. [CrossRef]



## Article

# Design, Synthesis, Anticancer Activity, and Solid Lipid Nanoparticle Formulation of Indole- and Benzimidazole-Based Compounds as Pro-Apoptotic Agents Targeting Bcl-2 Protein

Manar I. Nagy<sup>1</sup>, Khaled M. Darwish<sup>1</sup> , Safaa M. Kishk<sup>1</sup> , Mohamed A. Tantawy<sup>2</sup> , Ali M. Nasr<sup>3,4</sup> , Mona Qushawy<sup>4,5</sup> , Shady A. Swidan<sup>6,7</sup> , Samia M. Mostafa<sup>1</sup> and Ismail Salama<sup>1,\*</sup>

<sup>1</sup> Department of Medicinal Chemistry, Faculty of Pharmacy, Suez Canal University, Ismailia 41522, Egypt; manar.nagy@pharm.suez.edu.eg (M.I.N.); khaled\_darwish@pharm.suez.edu.eg (K.M.D.); safaa\_keshk@pharm.suez.edu.eg (S.M.K.); samiamostafa2010@hotmail.com (S.M.M.)

<sup>2</sup> National Research Center, Hormones Department, Medical Research Division, Dokki, Giza 12622, Egypt; mohamed\_tantawy@daad-alumni.de

<sup>3</sup> Department of Pharmaceutics, Faculty of Pharmacy, Port Said University, Port Said 42526, Egypt; a.nasr@pharm.psu.edu.eg

<sup>4</sup> Department of Pharmaceutics, Faculty of Pharmacy, Sinai University, Alarish, North Sinai 45511, Egypt; mqushawy@ut.edu.sa

<sup>5</sup> Department of Pharmaceutics, Faculty of Pharmacy, University of Tabuk, Tabuk 71491, Saudi Arabia

<sup>6</sup> Department of Pharmaceutics, Faculty of Pharmacy, The British University in Egypt, El-Sherouk City, Cairo 11837, Egypt; shady.swidan@bue.edu.eg

<sup>7</sup> The Center for Drug Research and Development (CDRD), Faculty of Pharmacy, The British University in Egypt, El-Sherouk City, Cairo 11837, Egypt

\* Correspondence: ismail\_mohamed@pharm.suez.edu.eg; Tel.: +20-102-225-7643

**Citation:** Nagy, M.I.; Darwish, K.M.; Kishk, S.M.; Tantawy, M.A.; Nasr, A.M.; Qushawy, M.; Swidan, S.A.; Mostafa, S.M.; Salama, I. Design, Synthesis, Anticancer Activity, and Solid Lipid Nanoparticle Formulation of Indole- and Benzimidazole-Based Compounds as Pro-Apoptotic Agents Targeting Bcl-2 Protein. *Pharmaceuticals* **2021**, *14*, 113. <http://doi.org/10.3390/ph14020113>

Academic Editors: Mary Meegan and Maria Emilia de Sousa

Received: 27 December 2020

Accepted: 26 January 2021

Published: 1 February 2021

**Publisher's Note:** MDPI stays neutral with regard to jurisdictional claims in published maps and institutional affiliations.



**Copyright:** © 2021 by the authors. Licensee MDPI, Basel, Switzerland. This article is an open access article distributed under the terms and conditions of the Creative Commons Attribution (CC BY) license (<https://creativecommons.org/licenses/by/4.0/>).

**Abstract:** Cancer is a multifactorial disease necessitating identification of novel targets for its treatment. Inhibition of Bcl-2 for triggered pro-apoptotic signaling is considered a promising strategy for cancer treatment. Within the current work, we aimed to design and synthesize a new series of benzimidazole- and indole-based derivatives as inhibitors of Bcl-2 protein. The market pan-Bcl-2 inhibitor, obatoclax, was the lead framework compound for adopted structural modifications. The obatoclax's pyrrolylmethine linker was replaced with straight alkylamine or carboxyhydrazine methylene linkers providing the new compounds. This strategy permitted improved structural flexibility of synthesized compounds adopting favored maneuvers for better fitting at the Bcl-2 major hydrophobic pocket. Anti-cancer activity of the synthesized compounds was further investigated through MTT-cytotoxic assay, cell cycle analysis, RT-PCR, ELISA and DNA fragmentation. Cytotoxic results showed compounds **8a**, **8b** and **8c** with promising cytotoxicity against MDA-MB-231/breast cancer cells ( $IC_{50} = 12.69 \pm 0.84$  to  $12.83 \pm 3.50 \mu M$ ), while **8a** and **8c** depicted noticeable activities against A549/lung adenocarcinoma cells ( $IC_{50} = 23.05 \pm 1.45$  and  $11.63 \pm 2.57 \mu M$ , respectively). The signaling Bcl-2 inhibition pathway was confirmed by molecular docking where significant docking energies and interactions with key Bcl-2 pocket residues were depicted. Moreover, the top active compound, **8b**, showed significant upregulated expression levels of pro-apoptotic/anti-apoptotic of genes; *Bax*, *Bcl-2*, *caspase-3*, *-8*, and *-9* through RT-PCR assay. Improving the compound's pharmaceutical profile was undertaken by introducing **8b** within drug-solid/lipid nanoparticle formulation prepared by hot melting homogenization technique and evaluated for encapsulation efficiency, particle size, and zeta potential. Significant improvement was seen at the compound's cytotoxic activity. In conclusion, **8b** is introduced as a promising anti-cancer lead candidate that worth future fine-tuned lead optimization and development studies while exploring its potentiality through in-vivo preclinical investigation.

**Keywords:** Bcl-2 inhibitors; Indole-based analogues; benzimidazole; MTT cytotoxic assay; cell cycle analysis; DNA fragmentation; ELISA; docking; solid/lipid nanoparticles



## 1. Introduction

The failure of most cancer cells to undergo apoptosis confers them a survival advantage over normal cells. Apoptosis is a genetically programmed cell death to get rid of an undesirable cell, which is necessary for cell turnover [1]. Apoptosis is controlled by two major modes: the extrinsic and the intrinsic pathways. Both pathways lead to activation of caspases that result in morphological changes such as chromatin condensation, nuclear fragmentation, formation of apoptotic bodies and finally cell death [2].

The extrinsic pathway comprises external signals, that bind to the cell's surface death receptors resulting in the formation of the death-induced signaling complex [3]. Bcl-2 (B cell lymphoma gene 2) family proteins control the intrinsic pathway. These proteins prevent the release of cytochrome C from mitochondria [4]. The Bcl-2 family of proteins can be classified as proapoptotic and antiapoptotic proteins. The conserved Bcl-2 homology domain-3 (BH3) of pro-apoptotic Bcl-2 members is responsible for the mitochondrial apoptosis [5]. Anti-apoptotic Bcl-2 proteins have a hydrophobic groove, containing both of the conserved Bcl-2 homology domains BH1 and BH2 which sequesters the BH3 of pro-apoptotic Bcl-2 members [6].

There are three approaches for targeting Bcl-2 in cancer therapy. The first one depends on the use of antisense oligonucleotide, which can bind to the complementary mRNA of Bcl-2, resulting in blocking expression at the protein level. The second strategy develops peptides against Bcl-2 protein [7,8]. Lastly, the third approach utilizes small molecules that can bind to the hydrophobic groove of anti-apoptotic Bcl-2 [9]. These molecules target one or more of P1–P4 sub-pockets in the BH3 groove of anti-apoptotic proteins. This binding results in releasing pro-apoptotic BH3-only proteins that can activate Bax and Bak and lead to apoptosis [10]. Several small molecules have been identified and synthesized, such as venetoclax, disarib, and obatoclax (Figure 1).

Venetoclax is a highly potent BH3 mimetic molecule. It showed a subnanomolar affinity to Bcl-2 ( $K_i < 0.010$  nM) with no measurable affinities for other apoptotic proteins. It showed cytotoxicity against non-Hodgkin's lymphoma, chronic lymphocytic leukemia (CLL) and acute leukemias [11]. Disarib is another selective Bcl-2 inhibitor [12]. Disarib was proven to inhibit the growth of Bcl-2 high cancer cell lines and CLL patient primary cell lines with minimum effect on Bcl-2 low cancer cell lines. In addition, disarib exhibited fewer side effects in treated animals with respect to platelet count, body weight, and liver and kidney functions [13]. Obatoclax is an oligopyrrole which antagonizes Bcl-2 and Bcl-xL [14]. Obatoclax binds to the BH3 domain of Bcl-2 and interrupts the interaction with proapoptotic proteins. The combination of obatoclax and lapatinib, giffitinib, bortezomib, and entinostat showed synergistic repression of cell growth in human breast cancer cells [15]. Furthermore, obatoclax synergizes chemotherapeutic agents as cisplatin, in cancer cell lines [16].

For Bcl-2 inhibitors development, we have described several series of compounds with chemical scaffolds that mimic obatoclax by either replacement of the pyrrole ring of obatoclax with benzimidazole or extending the structure after the indole ring. Additionally, comprehensive biological and molecular docking investigation, within the crystallised Bcl-2 crystal structure, provided further insights regarding the molecular pro-apoptotic mechanisms of the presented small synthesized molecules. Finally, formulating the most promising lead within an optimized solid lipid nanoparticle formulation provided beneficial results concerning improved cytotoxic activity, drug release and pharmaceutical properties, particularly drug's aqueous solubility and bioavailability.

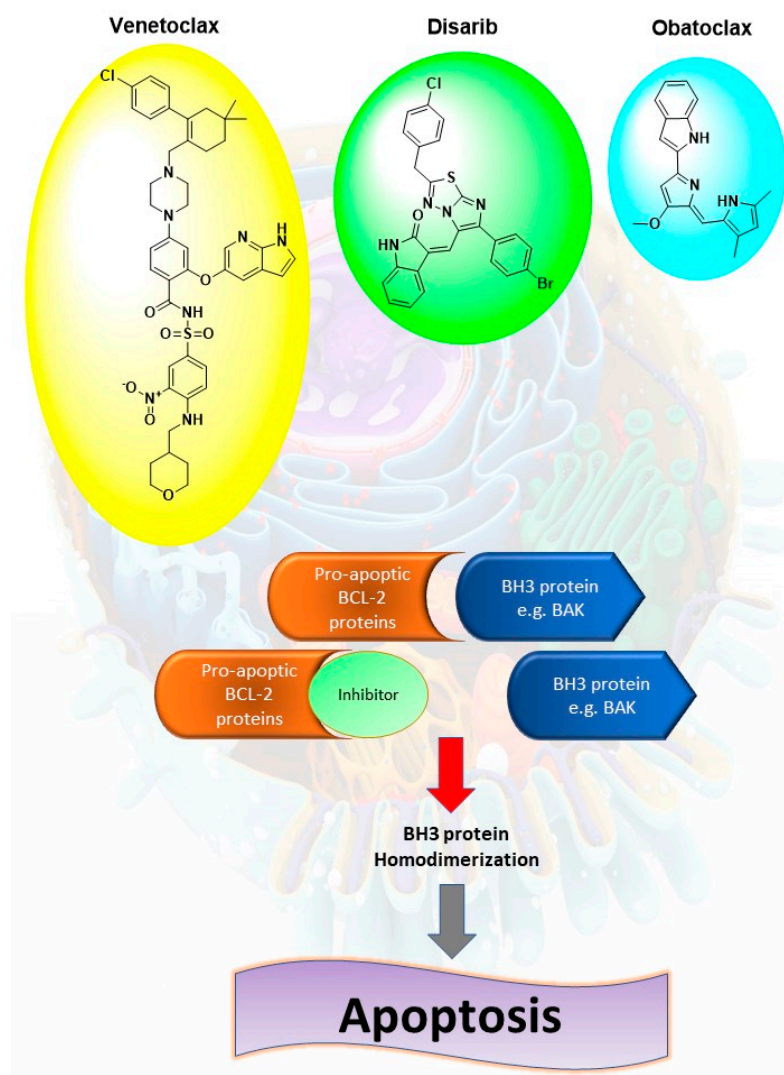


**Figure 1.** Mechanism of action of pro-apoptotic Bcl-2 proteins small molecules inhibitors such as venetoclax, disarib and obatoclax, where they can disrupt the interactions of Bcl-2 and BH3 proteins such as BAK, leading to homodimerization of the BH3 proteins and activation of apoptotic cascade.

## 2. Results and Discussion

### 2.1. Compounds Design

The reported drug-like pan Bcl-2 inhibitor, obatoclax (GX15\_070), was adopted as the lead framework for structural modifications and manipulations. Obatoclax is BH3-mimetic small molecule (317.4 Da) acting on several anti-apoptotic proteins such as Mcl-1, Bcl-2, Bcl-W, and Bcl-XL [17]. Preclinical studies illustrated the drug capability in reversing BH3-mediated binding of Bcl-2 family proteins to apoptotic proteins, Bak and Bax, allowing unopposed Bak/Bax dimerization and subsequent initiation of intrinsic apoptotic signaling [18,19]. Several additional mechanisms of action have been accounted for obatoclax anticancer activity, including induction of autophagic cell death and necroptosis [19–22]. Moreover, obatoclax can inhibit cell proliferation through seizing cell cycle development at G1/S-phases [19,23]. Many reported studies confirmed the clinical advent of obatoclax for inducing apoptosis within cells derived from solid tumors and hematological cancers such as small cell lung cancer, acute myeloid leukemia, and Hodgkin's lymphoma as well as potentiating cytotoxicity of targeted therapy drugs and conventional chemotherapeutics.

Currently, there is no reported atomic resolution data concerning the obatoclax being bounded to pre-survival Bcl-2 protein. Nevertheless, Zacarias-Lara et al. have reported seven recognized Bcl-2 inhibitors, including obatoclax, to be investigated for their re-

spective affinities and binding interactions through molecular docking calculations [24]. Interestingly, the authors suggested anchoring of obatoclax just adjacent the hydrophobic cleft (H1-3) which may compromise the drug's ability to dissociate BH3-only pro-apoptotic proteins for subsequent programmed cell death. Driven by the above findings, the presented study aimed for developing new pro-apoptotic agents, based on obatoclax principal pharmacophore, with an extra goal of improved Bcl-2 hydrophobic cleft accommodation. Obatoclax belongs to the class of organic compounds, designated as dipyrrens, incorporating two pyrrole rings within their chemical architectures where the two 5-membered rings are being fused via a trivalent methine (-CH=) bridge. Here within the presented manuscript, three structural modification strategies have been adopted to design the newly synthesized compounds, Series-I-to-III (Figure 2). The first modification strategy was to improve the obatoclax flexibility through replacing the drug's central pyrrolylmethine linker with straight alkylamine or carboxyhydrazine methylene linkers furnishing the members of the Series-I or -II, respectively. The aim of such tactic was to permit enhanced maneuver for these newly synthesized compounds to better accommodate the Bcl-2 major hydrophobic pockets (S1-to-5). Additionally, the terminal obatoclax pyrrole ring was replaced with substituted phenyl groups to permit an enriched  $\pi$ - $\pi$  stacking and other non-polar interactions with the hydrophobic residues at the Bcl-2 pocket.

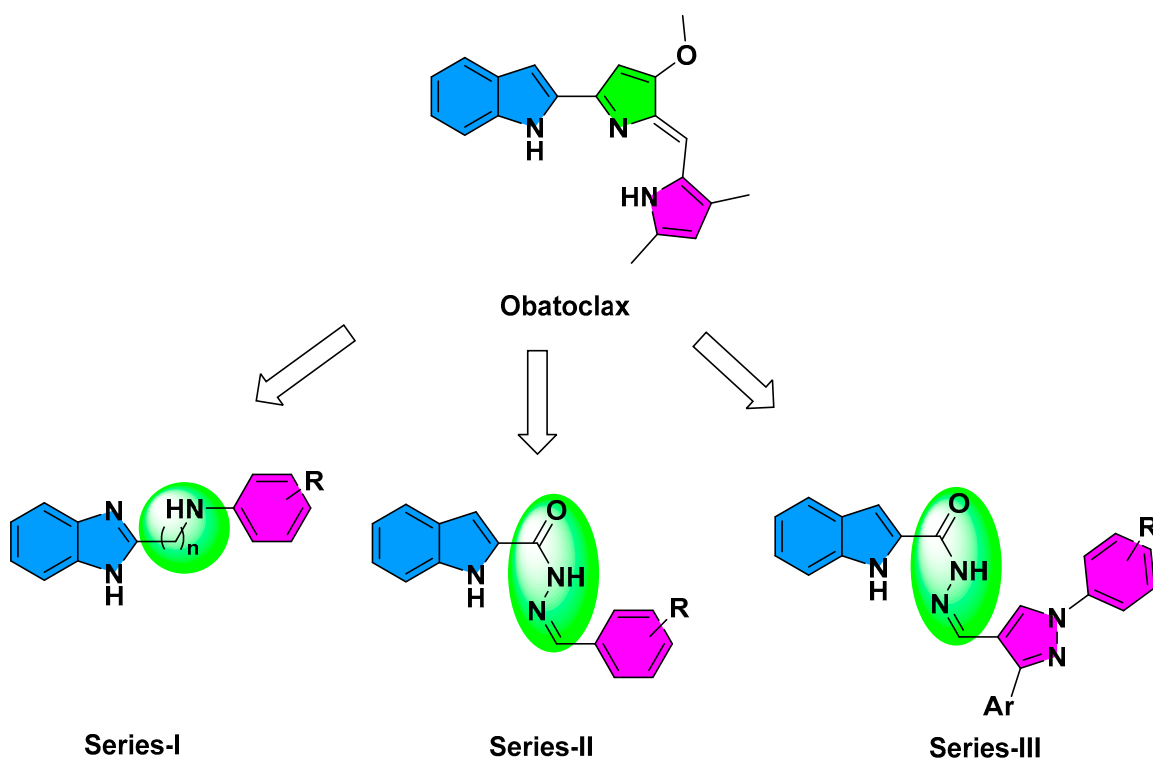


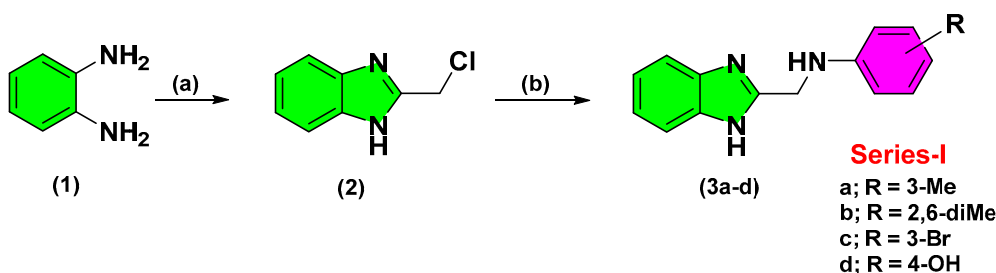
**Figure 2.** Rationalized design of the proposed new pro-apoptotic agents (Series-I-to-III), relying on the pan Bcl-2 inhibitor, obatoclax.

Within a comparable bases, members of Series-I possess the benzimidazole scaffold as the classical isostere of the indole moiety present within the obatoclax chemical architecture. Such introduced second structural modification relied on the ability of the benzimidazole ring to permit extra H-bonding with the surface polar residues of the Bcl-2 pocket and thus further ligand fixation. Notably, both members of Series-I and -II were of comparable overall size as that of the obatoclax, the thing that can limit the extension of the synthesized compounds to the farthest hydrophobic pockets. Therefore, a third and last structural modification strategy has been adopted where the terminal substituted phenyl moieties at Series-II were replaced with the highly extended substituted bisaryl pyrazole scaffold

resulting in the members of Series-III. The latter members possess the double advent of great flexibility and extended size. Finally, the adoption of the central pyrazole scaffold was rationalized for its straightforward synthesis as well as easily derivatized during the pyrazole ring closure. Based on the adopted three structural modification strategies, fourteen compounds were synthesized as well as evaluated for respective predicted anti-cancer activities through in-vitro and in-vivo biological analyses as well as molecular docking investigations.

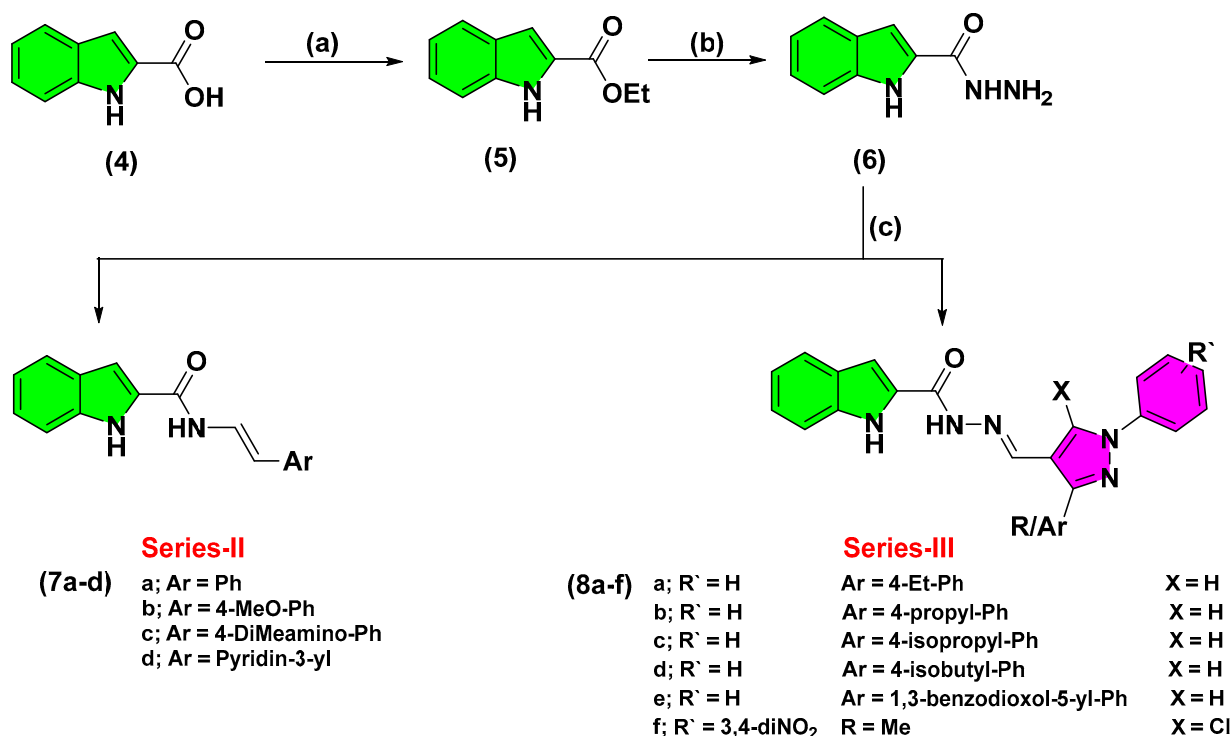
## 2.2. Chemistry

The synthesized compounds of the three designed series were obtained from straightforward schematic pathways. Structural diversity for synthesizing the target compounds was performed at the final steps of the synthetic pathways. Adopting such strategy was beneficial for minimizing the number of needed reactions that would provide each individual analogue. Within Scheme 1, Series-I benzimidazole derivatives were synthesized from the commercially available, ortho-phenylene diamine (1) through Phillips-Ladenburg reaction [25]. Cyclization was proceeded through refluxing ortho-phenylene diamine with chloroacetic acid, under acidic conditions, to yield the corresponding intermediate 2-(chloromethyl)-1H-benzimidazole (2). Introduction of 2-chloromethyl arm, within the benzimidazole skeleton, served as a handy scaffold for introducing structural diversity at the final synthetic pathway. Subsequent  $S_N2$  nucleophilic substitution at 2-methyl benzimidazole with various aromatic amines furnished the target substituted 2-aminomethyl-benzimidazole derivatives (3a–d) depicting extra aromatic signals at their  $^1H$ -NMR spectra [26].

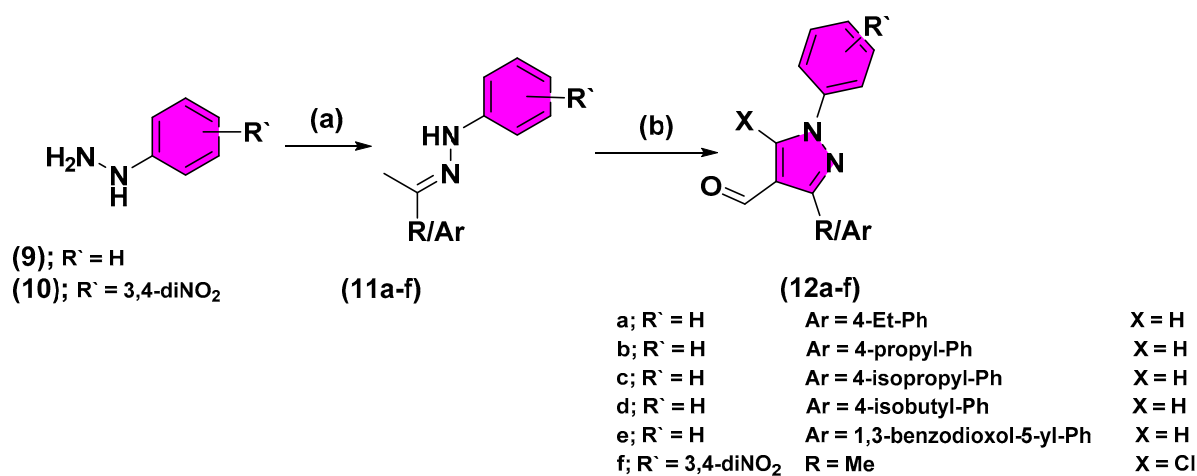


**Scheme 1.** Reagents and conditions for Series-I: (a)  $ClCH_2COOH$ , 4N HCL, reflux, overnight, 40%; (b)  $Ar-NH_2$ , 51–73%.

The indole-based derivatives (Series-II and -III) were synthesized starting from the commercially available indole-2-carboxylic acid (4) (Scheme 2). Throughout Fischer reaction, refluxing 4 with concentrated  $H_2SO_4$  and ethanol yielded the corresponding ethyl,1H-indole-2-carboxylate (5) [27]. Subsequent, condensation of the obtained ester intermediate with hydrazine hydrate furnished the hydrazide key intermediate (6). Finally, Schiff's base condensation of 6 with different commercially available and synthesized aromatic aldehydes, under acidic conditions, provided the target hydrazone analogues (7a–d and 8a–f) [28]. Appearance of the characteristic methylene hydrogen at NMR spectra ( $\delta_H = 8.16$ – $8.98$  ppm;  $\delta_C = 146.8$ – $148.9$  ppm) confirmed successful Schiff's base formation. Preparation of several pyrazole-based aldehydes was proceeded through three-step chemical synthesis [29]. Synthesis of the pyrazole aldehydes, that served as the structural building blocks of the Series-III compounds, was proceeded through initial acidic condensation of different ketones with phenylhydrazine derivatives yielded the corresponding imine analogues (10a–f) (Scheme 3). Subsequently, Vilsmeier-Haack reaction, with the advent of phosphorous oxychloride, provided the target pyrazole-based aldehydes (12a–f) exhibiting characteristic NMR signals of CHO groups ( $\delta_H = 9.97$ – $10.00$  ppm;  $\delta_C = 185.1$ – $185.3$  ppm).



**Scheme 2.** Reagents and conditions for Series-II and -III: (a) EtOH, Conc. H<sub>2</sub>SO<sub>4</sub>, reflux, 1.5 h, 92%; (b) Hydrazine hydrate, absolute EtOH, reflux, 6 h, 44%; (c) Ar-CHO, EtOH, glacial acetic acid, reflux, 1.5–3 h, 30–45%.



**Scheme 3.** Reagents and conditions for the synthesis of pyrazole aldehydes: (a) EtOH, Ar/R-COCH<sub>3</sub>, 80 °C, 1 h, 80–97%; (b) POCl<sub>3</sub>, DMF, reflux, 4 h, 61–81%.

### 2.3. Biological Activity

#### 2.3.1. In-Vitro Cytotoxic Activity

The potential anti-cancer activity of all fourteen final synthesized compounds was investigated through MTT cytotoxic assay against two different human solid cancerous cell lines; A549/lung and MDA-MB-231/breast adenocarcinoma. The adopted cell-proliferation assay assessed % cell viability in relation to the reducing activity of cellular NADPH-dependent cellular oxidoreductases on tetrazolium dye, MTT [2,5-diphenyl-3-(4,5-dimethylthiazol-2-yl)tetrazolium bromide salt], for furnishing an easily quantified insoluble chromogenic formazan [30]. For each drug concentration, 0.1, 1, 10, and 100 μM, the % cell-viability was estimated relative to negative control following a complete 48 h of drug treatment. Both 5-fluorouracil (5-FU) and doxorubicin (DOX) were set as posi-

tive index comparators. Moreover, the safety profile of the synthesized compounds was further investigated by examining their in-vitro cytotoxicity on non-cancerous cell line; MDCK/kidney cells.

Findings within Figure 3A illustrate a dose-dependent impact of several synthesized compounds on MDA-MB-231/breast cell proliferation. Rising drug concentration was directly related with elevated cell growth inhibition up to the highest applied concentration (100  $\mu\text{M}$ ) ( $p < 0.05$ ). Interestingly, most of the tested compounds had a dose dependent cytotoxicity or a plateau effect, except for compound **3c** on MDA-MB-231/breast cancer where it enhanced cell proliferation at 100  $\mu\text{M}$  drug concentration. The steepest decline within the cell proliferation was seen with **7c,d** and **8a–d** reaching down to very low % cell viabilities (12% and 14%) at 100  $\mu\text{M}$  concentrations. The latter suggests great susceptibility of MDA-MB-231/breast cancer cells towards indole derivatives, particularly those having pyrazole-based scaffolds (Series-III). The rest of compounds exhibited comparable cytotoxicity patterns as those for positive reference controls, 5-FU and DOX, since minor %viability fluctuations were depicted across the applied drug concentrations. Regarding the drug's impact on A549/lung adenocarcinoma cell proliferation, both investigated and positive control compounds showed quite lower overall anticancer activity as compared to their actions up on the MDA-MB-231/breast cancer cells. Nevertheless, comparable differential activity profiles were depicted among the investigated compounds, where compounds **8a–c** exhibited the highest activity profiles with steepest decrease in % cell viability (70–79%;  $p < 0.001$ ) at 100  $\mu\text{M}$  concentrations (Figure 3B). This again suggests promising anticancer activity of the indole-based compounds on A549/lung cancer cells, particularly for the ones incorporating the pyrazole scaffolds. The rest of the compounds exhibited comparable pattern of cell growth inhibition across their concentration range which was also quite similar to that of positive control drugs. However, it was only for compound **3b** where its anticancer activity on A549/lung cancer cells depicted irregular effects with tendency to increase the cell proliferation. Evaluating drug's cytotoxicity on non-cancerous kidney cells, Figure 3C showed higher safety profiles for synthesized compounds compared to controls, 5-FU and DOX. Significantly higher vitality patterns were illustrated for all compounds, particularly over the concentration range 0.1–10  $\mu\text{M}$ , as compared to those of reference compounds ( $p < 0.001$ ).

For gaining more insights about the efficacy/safety profiles of the synthesized compounds,  $\text{IC}_{50}$  values for promising cytotoxic compounds were estimated over the three cell lines. Only compounds exhibiting significant cytotoxicity, with cut-off value  $< 85\%$  vitality at 100  $\mu\text{M}$  on both cancerous cell lines, were considered relevant for  $\text{IC}_{50}$  estimating and warrant further consideration. Interestingly, the selected compounds for MDA-MB-231/breast cancer cells (**3a**, **7b**, **7d**, and **8a–d**) illustrated relevant  $\text{IC}_{50}$  values reaching down to two-digit micromolar activity (Table 1). Members of Series-III showed the lowest  $\text{IC}_{50}$  (down to 12.69  $\mu\text{M}$ ) suggesting the preferential cytotoxicity of their substituted pyrazole arms. Both **8d** and **8f** showed higher  $\text{IC}_{50}$  (21.64 and 31.46  $\mu\text{M}$ , respectively) suggesting activity preferentiality for aromatic substitution, at C3 pyrazole ring, while tolerating small-sized aliphatic chains. Compound **7d** was comparable to the top-active members of Series-III with  $\text{IC}_{50}$  17.38  $\mu\text{M}$ , suggesting Series-II preferentiality for pyridine ring substitution over methoxy phenyl synthon. Regarding  $\text{IC}_{50}$  on MDA-MB-231/lung adenocarcinoma, only **8b** and **8c** were evaluated suggesting preferential activity for pyrazole substitution with branched aliphatic chains. Finally, the  $\text{IC}_{50}$  for selected Series-III compounds on non-cancerous/kidney cells were much higher than the other two Series, reaching up to  $\text{IC}_{50}$  92  $\mu\text{M}$  activity for **8b**. Based on all the above findings, significant cytotoxic activity has been assigned for members of Series-III which were also presented with high safety profile, particularly **8b**, on non-cancerous cell line. Therefore, compound **8b** was considered promising with double the benefits of high efficacy/safety profiles making it worthy of further investigations.

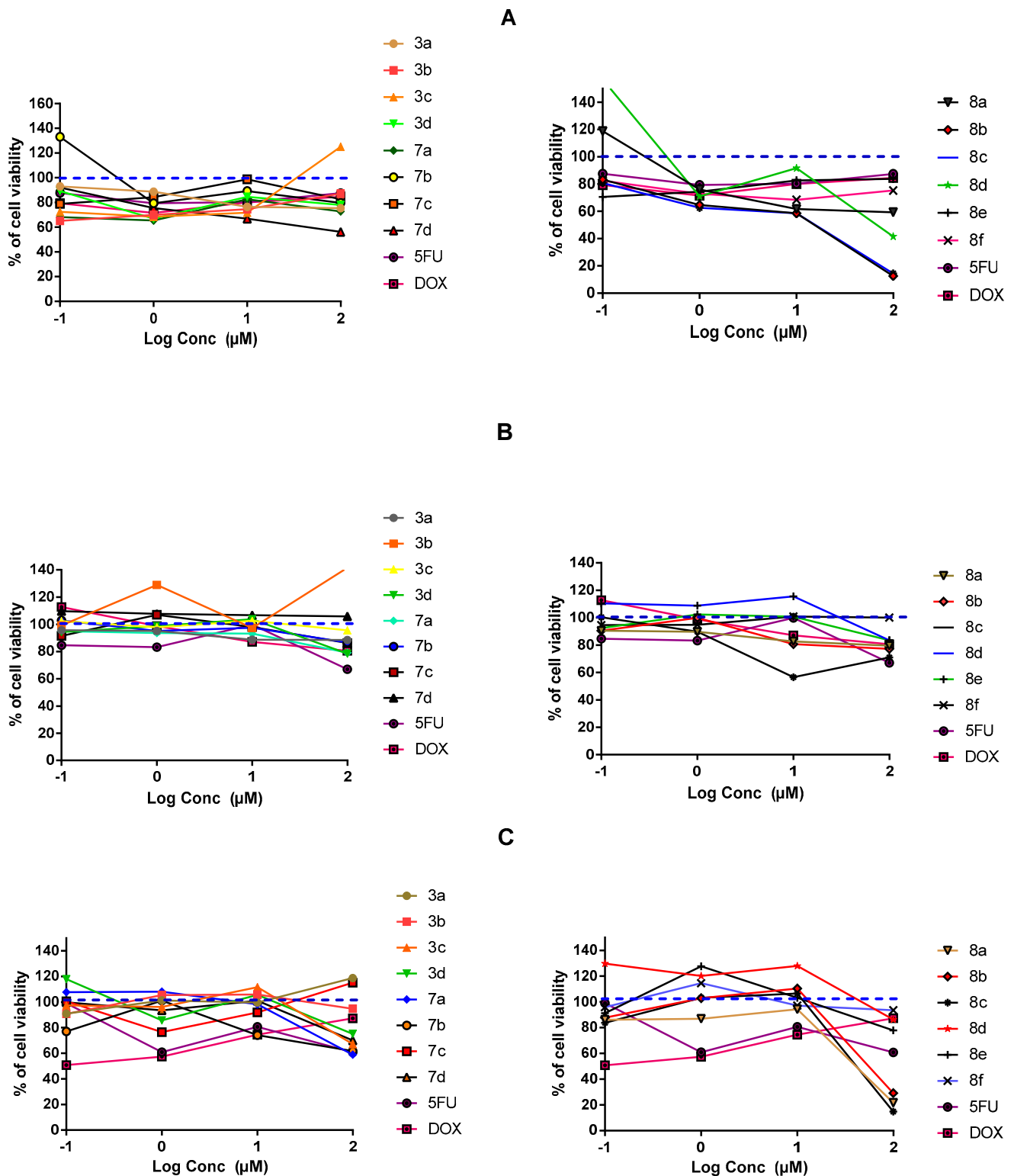


**Figure 3.** In-vitro cytotoxicity of the fourteen final synthesized compounds on cancerous and non-cancerous cell lines. (A) MDA-MB-231/breast cancer cells; (B) A549/lung adenocarcinoma cells; (C) MDCK/kidney non-cancerous cells. At  $1 \times 10^4$  cells/well cell density, cells were treated with several drug concentrations (0.1, 1, 10, and 100  $\mu\text{M}$ ) of investigated compounds or positive comparator; 5-FU and DOX, for 48 h exposure time. Cytotoxicity was identified via MTT-based colorimetric assay (490 nm) and % cell growth viability was estimated in triplicates as compared to vehicle negative controls representing the untreated cells. Blue dotted line indicates this control.

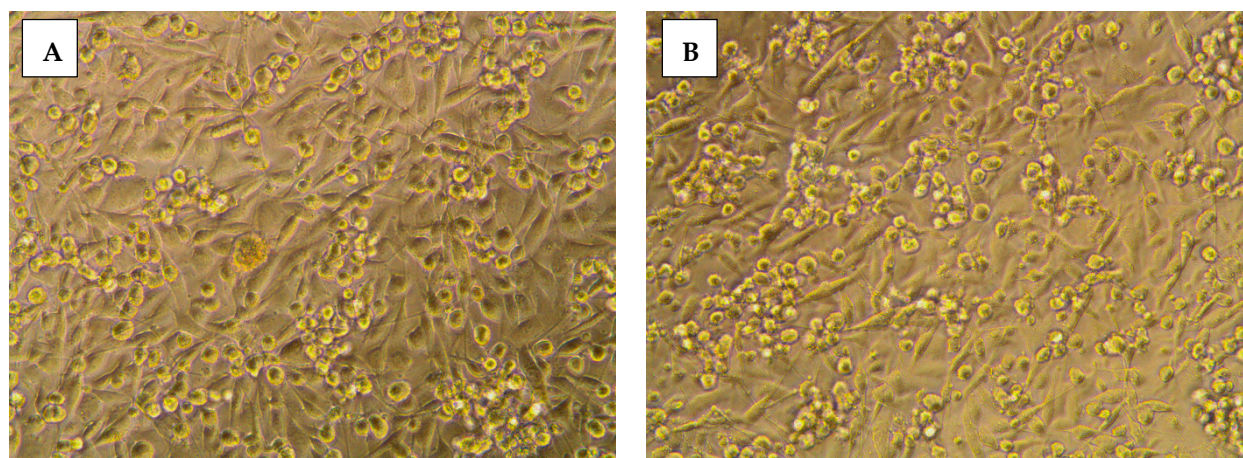
**Table 1.** In-vitro <sup>a</sup> data of MTT-cell proliferation assay for promising synthesized compounds on both cancerous and non-cancerous cell lines.

Compound <sup>b</sup> No.	MDA-MB-231 IC <sub>50</sub> (μM) <sup>c</sup>	A549 IC <sub>50</sub> (μM) <sup>c</sup>	MDCK IC <sub>50</sub> (μM) <sup>c</sup>
<b>3a</b>	29.68 ± 4.03	ND	ND
<b>7b</b>	43.77 ± 1.09	ND	28.92 ± 1.49
<b>7d</b>	17.38 ± 3.23	ND	ND
<b>8a</b>	12.69 ± 0.84	ND	73.86 ± 2.30
<b>8b</b>	12.71 ± 2.48	23.05 ± 1.45	92.75 ± 0.43
<b>8c</b>	12.83 ± 3.50	11.63 ± 2.57	87.29 ± 3.00
<b>8d</b>	31.46 ± 4.66	ND	ND
<b>8f</b>	21.64 ± 0.28	ND	ND

<sup>a</sup> In-vitro data are reported as mean of three independent experiments ± SEM; <sup>b</sup> Tested compounds were those depicted % cell viability < 85%, on both cancerous cell lines, at their respective 100 μM concentrations; <sup>c</sup> IC<sub>50</sub> values represent effective concentration of given small molecule being capable of inducing 50% inhibitory response of its own intrinsic maximum response following 48 h of drug exposure; ND = Not-detected.

### 2.3.2. Morphological Assessment

The impact of **8b** on cancerous cellular morphology was evaluated over different concentrations following 48 h exposure time. In MDA-MB-231/breast cancer cells, normal membrane integrity and control group nucleus morphology was depicted for cells within vehicle negative control group (Figure 4A). Contrarily, cells treated with **8b** exhibited significant cell morphology alteration, intercellular space dilatation, and cellular shrinkage (Figure 4B). Alterations proceeded within a dose-dependent manner as escalated drug concentrations showed cells being gradually shrunk, unable to adhere well, floated, and clustered together (Figure 4C,D). At 100 μM concentration, the cell number became highly declined and great loss of cellular polyhedral shape was observed as cells acquired the tentacled spindle-shaped morphology (Figure 4E). These morphological changes were more drastic with **8b** as compared to 5-FU for similar concentrations (100 μM) (Figure 4F). Comparable cell morphology changes were observed with A549/lung adenocarcinoma (Figure 5A–E). Nevertheless, an epithelial-mesenchymal transition was observed within 5-FU group, rather than **8b**, at same drug concentration (100 μM) (Figure 5F). The later finding presents a significant advantage for **8b** as it did not trigger this evolutionarily-conserved developmental program conferring metastatic properties upon cancerous cells through enhanced mobility, invasion, and apoptotic stimuli resistance [31].

**Figure 4.** Cont.



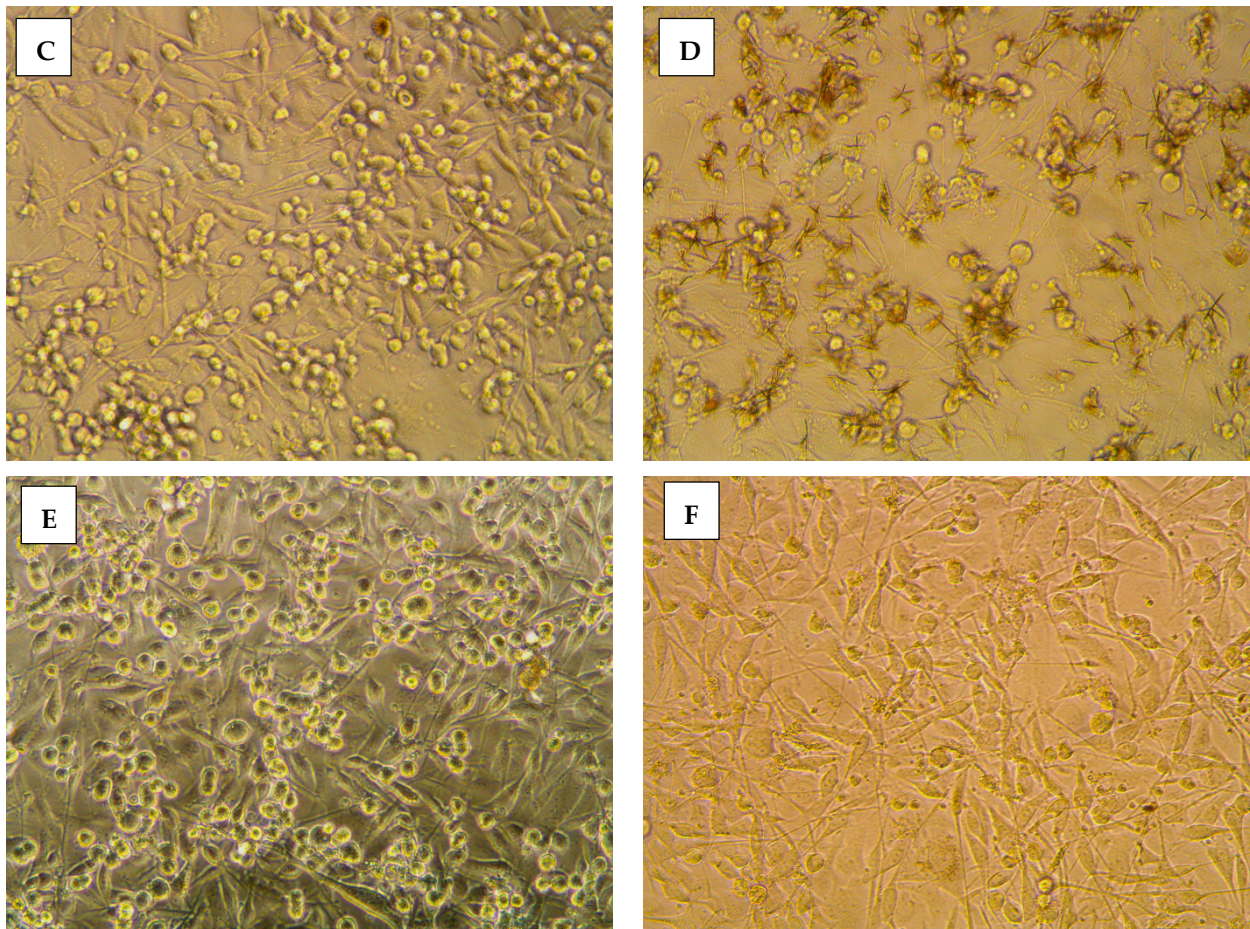


**Figure 4.** Morphological alterations of MDA-MB-231/breast cancer cells following 48 h incubation and photographed with phase-contrast microscope. (A) vehicle control; (B) 0.1  $\mu\text{M}$  8b; (C) 1  $\mu\text{M}$  8b; (D) 10  $\mu\text{M}$  8b; (E) 100  $\mu\text{M}$  8b; (F) 100  $\mu\text{M}$  5-FU; Magnification power  $\times 20$ .

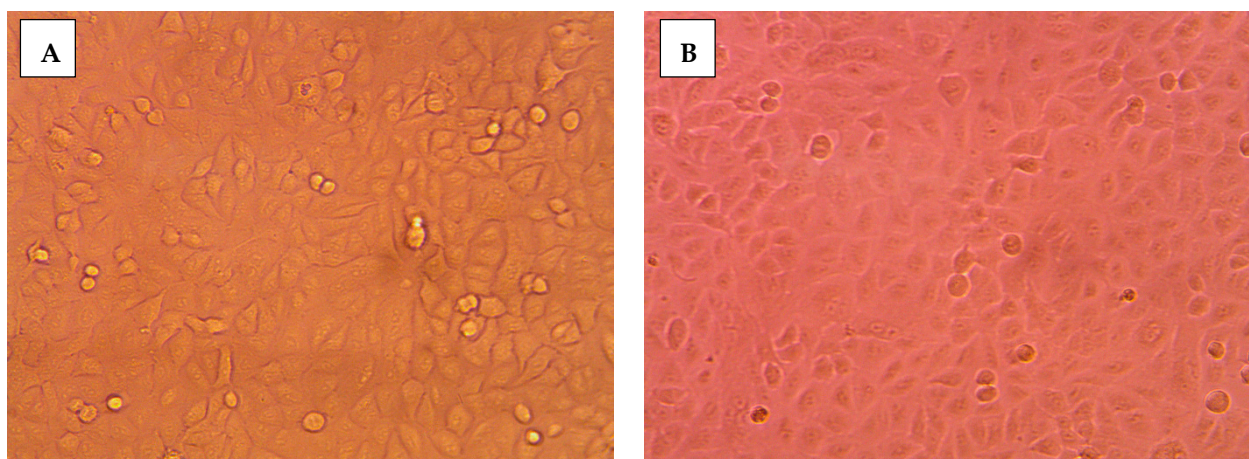


**Figure 5.** Cont.

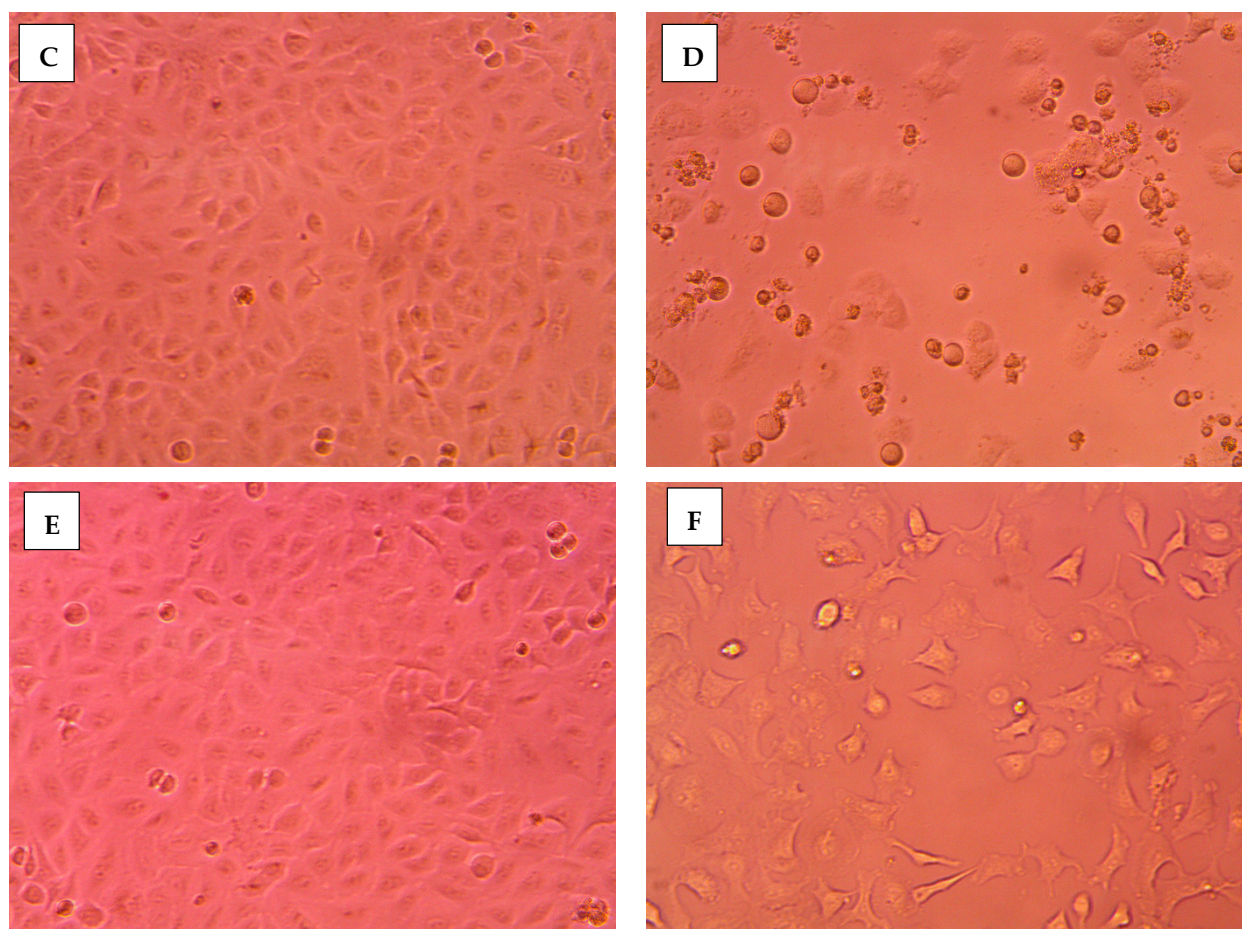


**Figure 5.** Morphological alterations of A549/lung carcinoma following 48 h incubation and photographed with phase-contrast microscope. (A) vehicle control; (B) 0.1  $\mu\text{M}$  8b; (C) 1  $\mu\text{M}$  8b; (D) 10  $\mu\text{M}$  8b; (E) 100  $\mu\text{M}$  8b; (F) 100  $\mu\text{M}$  5-FU; Magnification power  $\times 20$ .

### 2.3.3. Apoptosis Rate and Cell Cycle Analysis

Further investigation of **8b** mechanistic growth inhibitory action on MDA-MB-231/breast cancer, both cell cycle, and apoptosis rate analysis were conducted at the compound's approximated  $\text{IC}_{50}$  value (13  $\mu\text{M}$ ). Using flow cytometry, apoptosis rate analysis was proceeded through staining the cell surface-translocating phosphatidylserine with Annexin-V fluorescent conjugate, the calcium-dependent phospholipid binding protein [32]. However, cell cycle analysis was achieved using propidium iodide fluorescent dye to stoichiometrically stain cell DNA contents allowing quantitation and identification of all cell phase rates; G0-G1, S, G2/M, and pre-G1 [33,34]. The impact of **8b** on cell cycle distribution depicted predominant cell population at G2/M stage (25.32%) was significantly higher than that of untreated cell line (6.15%;  $p < 0.001$ ) (Figure 6A). The elevated cell population at G2/M stage was complemented by significant reduction at pre-G1 stage of treated cells as compared to negative controls (1.72% vs. 18.93%; Figure 6B). For identifying the mode of cell death promoted by **8b** within MDA-MB-231/breast cancer cells, apoptosis rate analysis was performed following 48 h exposure time. Compound **8b** (13  $\mu\text{M}$ ) induced both early and late stages of apoptosis in breast cancer cell line with significantly elevated % apoptotic cell levels as compared to controls ( $p < 0.01$  and  $p < 0.001$ , respectively) (Figure 7). Moreover, the average proportion of Annexin-V stained positive cells (total apoptotic cells) elevated from 1.72% within untreated cells to 18.93% in treated ones ( $p < 0.001$ ). Interestingly, compound **8b** showed no influence on the necrosis of MDA-MB-231/breast

cancer cells. The above provided findings are supported by the previous cell cycle analysis confirming the potentiality of **8b** as promising anticancer agent.

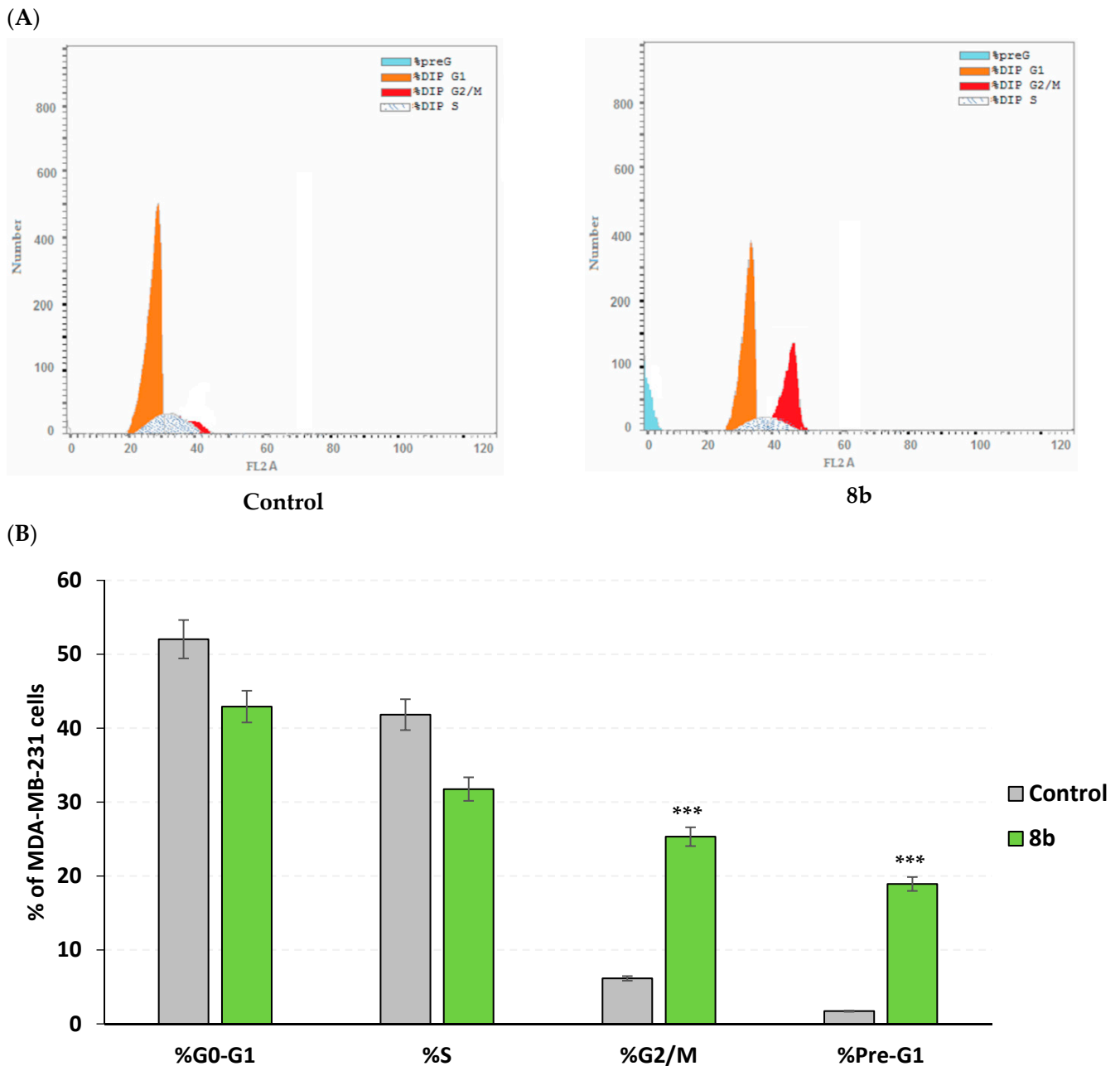


**Figure 6.** Impact of compound **8b** upon cell cycle distribution within MDA-MB-231/breast cancer cell line. Following 48 h-period incubation of cells with either **8b** (13  $\mu$ M; approximated  $IC_{50}$ ) or vehicle negative control [0.1% DMSO (*v/v*)], cells were fixed, stained with propidium iodide (PI), and assessed via flow cytometry; (A) DNA histograms for cell cycle distribution of untreated cells (left panel) and **8b** group (right panel) at in 2N (G0G1), >2N (S), 4N (G2/M), and <2N (pre-G1), where cell number was correlated against gated counts/DNA area (FL2-A) using CellQuest<sup>®</sup> software; (B) Bar-chart representation of cell accumulation percentage within each stage of cell development. All data are represented as mean of three independent experiments  $\pm$  SEM. Statistical analysis was performed using Student-*t*-test (\*\*\*,  $p < 0.001$ ).

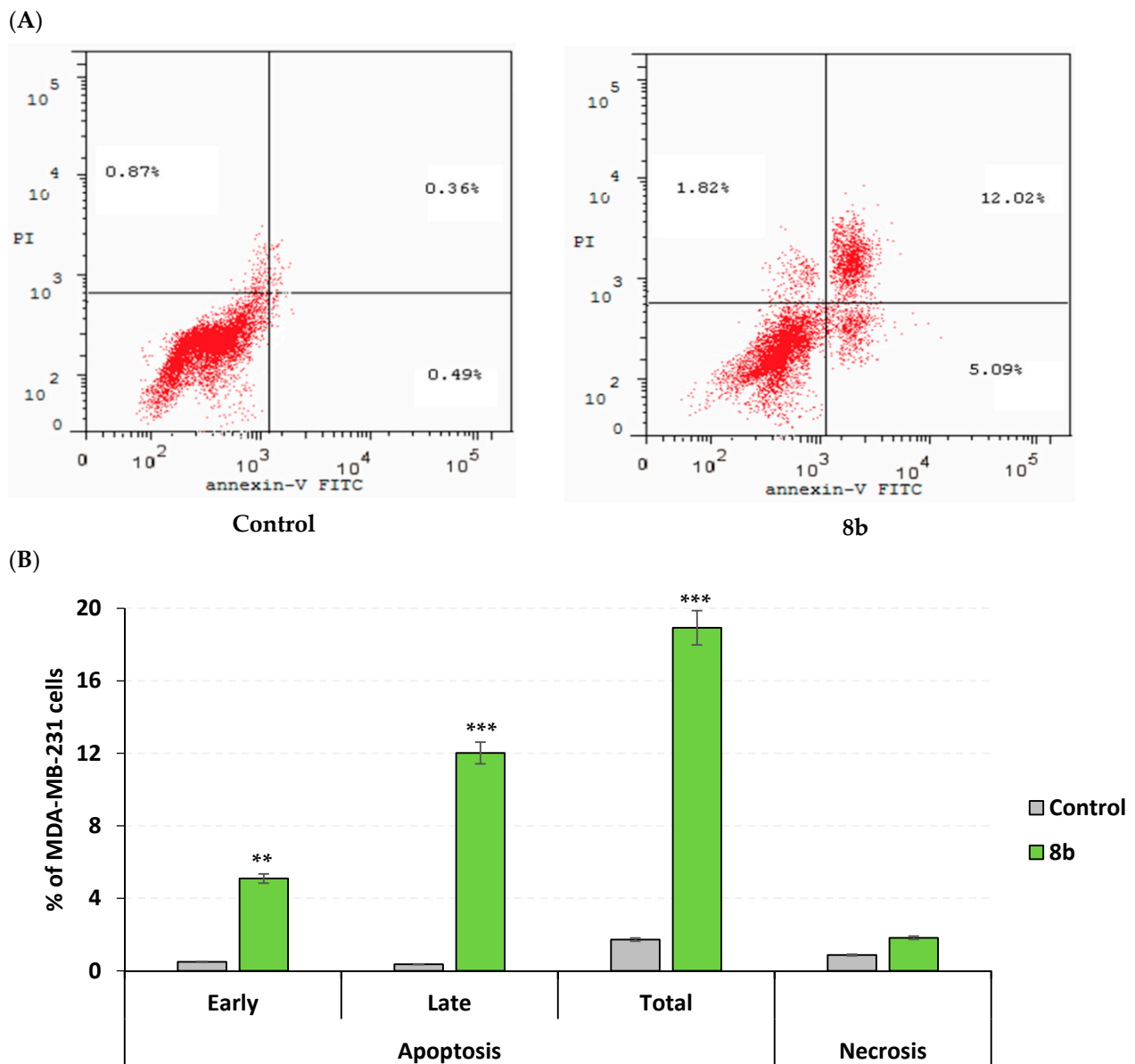


**Figure 7.** Impact of compound **8b** on apoptosis rate within MDA-MB-231/breast cancer cell line (Annexin-V/FACS). (A) Apoptotic impact of **8b** following cell double staining via Annexin-V-FITC then PI, and then 48 h incubation time with either **8b** (13  $\mu$ M; approximated  $IC_{50}$ ) or vehicle negative control [0.1% DMSO (*v/v*)]; (B) Bar-chart representation of quantitative analysis of apoptosis, across different stages, as well as necrosis. The four quadrants are recognised as: LL, LR, UR, and UL for viable, early apoptotic, late apoptotic, and necrotic cell populations, respectively. All data are represented as mean of three independent experiments  $\pm$  SEM. Statistical analysis was conducted via Student-*t*-test (\*\*,  $p < 0.01$ ; \*\*\*,  $p < 0.001$ ).

#### 2.3.4. DNA Fragmentation Determination

In order to delineate the mechanistic aspects of MDA-MB-231/breast cancer cell death mediated by **8b**, the DNA fragmentation assay was conducted as being highly characteristic for apoptosis. Significant DNA fragmentation was depicted with **8b** at  $IC_{50}$  doses (13  $\mu$ M) at various time-intervals; 48 h and 72 h following cell treatments. A typical ladder pattern of internucleosomal fragmentation was observed from cell homogenates within both incubation periods (Figure 8). Such findings further confirm the significant activity of **8b** as a potent inducer of apoptosis.

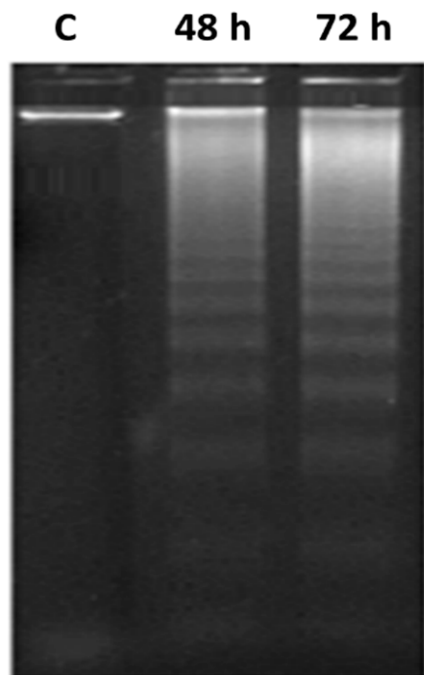


**Figure 8.** DNA fragmentation of MDA-MB-231/breast cancer cell line treated with **8b**. Fragmentations of genomic DNA in breast cancer cells were treated with **8b** (13  $\mu\text{M}$ ) for 48 or 72 h exposure time. Low-molecular-weight DNA from homogenized cells was resolved and visualized on ethidium bromide-stained 1.5% agarose gel while being photographed by UV-illumination electrophoresis; C = DMSO vehicle control.

### 2.3.5. Apoptotic Gene Expression and Protein Level Analysis

Compound **8b** demonstrated strong cytotoxic impact upon breast cancer cell lines, as it accomplished significantly low  $\text{IC}_{50}$  value (12.71  $\mu\text{M}$ ) with confirmed apoptosis induction. Dissection of the compound's proapoptotic activity was proceeded through gene expression analysis for key genes, controlling apoptosis pathway, as well as protein level determination. Following **8b** treatment for 48 h, alterations within MDA-MB-231/breast cancer cell expression of *Bcl-2*, *Bax*, *caspase-3*, *-8*, and *-9* genes, as well as cytochrome c and class-III  $\beta$ -tubulin proteins levels were determined using real-time polymerase chain reaction (RT-PCR) or ELISA technique, respectively. Typically, *Bcl-2*, *Bax*, caspases, and cytochrome c proteins contributes within the regulation of apoptotic signaling. Acting as apoptotic activator (*Bax*) or inhibitor (*Bcl-2*), the *Bcl-2* family proteins play their significant role in apoptosis [35]. The caspases family are cysteine proteases being classified as either executioners; caspase-3, -6, or -7 or initiators; caspase-8 and -9 [36]. Regrading caspase-8, its activation is proceeded through extrinsic death-receptor dependent apoptotic pathway, while, caspase-9 activation is within the event of intrinsic mitochondrial cytochrome c leakage [37]. Additionally, participation of activated caspase-3 is to be essential for caspase-8 activation [38]. Class-III  $\beta$ -tubulin are pure prognostic biomarker within cancer patients being associated with aggressive phenotypic/drug-resistant cancers and part of complicated pro-survival molecular pathway, being triggered via poor nutrient supply and hypoxia [39].

Findings within Figure 9A illustrated strong stimulated expression of pro-apoptotic *BAX* gene (3.61 folds), and apoptotic genes; *Caspase-3* (4.28 folds), *Caspase-8* (1.53 folds), and *Caspase-9* (7.65 folds) as compared to negative controls ( $p < 0.05$  and  $p < 0.001$ ). Nevertheless, significant downregulation of anti-apoptotic gene *Bcl-2* (0.165 folds) was depicted and have been translated into elevated *Bax/Bcl* expression ratio (1  $\rightarrow$  21.88;  $p < 0.001$ ). The *Bax/Bcl-2* gene expression ratio can serve as early predictor for cancer in patients as well as sensitive monitor of cancer progression [40]. On the other hand, compound **8b** illustrated increased

levels of the apoptotic stimulator cytochrome c (0.675 ng/mL vs. 0.295 ng/mL;  $p < 0.01$ ) and down-regulated levels of class-III  $\beta$ -tubulin (0.23 vs. 0.73 ng/mL; 68.36% inhibition;  $p < 0.001$ ) as compared to controls (Figure 9B). Gathering up all the provided evidence, up-regulation of *Caspase-3*, *-8*, *-9* and *Bax*, while down-regulation of *Bcl-2* genes and class-III  $\beta$ -tubulins are suggested believed to be related to compound **8b**-induced apoptosis within breast cancer cell line.

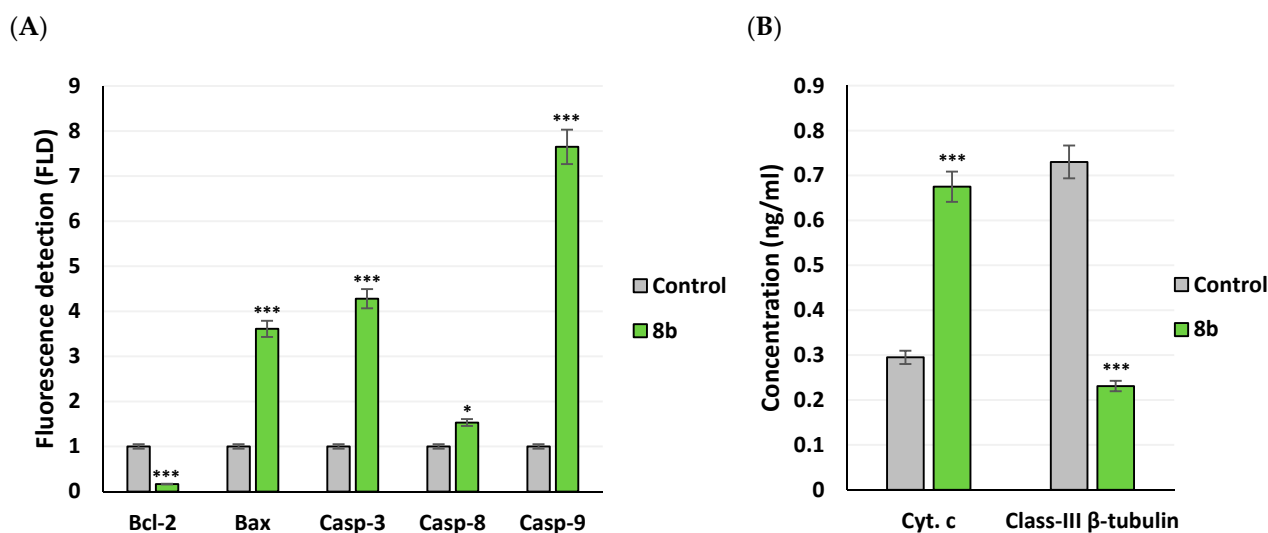


**Figure 9.** Apoptotic gene expressions and protein level analysis of MDA-MB-231/breast cancer cells exposed to **8b**. (A) Expression of pro-apoptotic/anti-apoptotic of genes; *Bax*, *Bcl-2*, *caspase-3*, *-8*, and *-9* using RT-PCR method; (B) Evaluation of cytochrome c and class-III  $\beta$ -tubulin protein levels in MDA-MB-231/breast cancer cells using ELISA technique. Within both assays, cultivated MDA-MB-231/breast cancer cells were treated with **8b** at its  $IC_{50}$  concentration (13  $\mu$ M) for 48 h exposure period. All data are represented as average of three independent experiments  $\pm$  SEM. Statistical analysis was performed using Student-*t*-test (\*,  $p < 0.05$ ; \*\*\*,  $p < 0.001$ ).

#### 2.4. Computational Study

To gain more insights about differential cytotoxic activity of synthesized compounds, molecular docking simulations were conducted for all agents. The binary complex of X-ray crystallized Bcl-2 (PDB ID: 6qgk; resolution 1.80 Å) [41], bounded to tetrahydroisoquinoline-phenyl pyrazole derivative, was adopted for the docking studies. Adopting such complex for the presented in-silico investigation was owing to structural similarities of crystallized ligand with the synthesized compounds as well as its extended orientation within the target protein. Typically, the Bcl-2 pocket is a narrow, long grooved site comprised of two larger nearby sub-pockets (P2 and P4), in addition to, three small hydrophobic pockets (P1, P3 and P5) [9]. The P1 through P4 sub-pockets are the key Bcl-2 binding sites for the class of single BH3-only pro-apoptotic proteins. Owing to the hydrophobic nature of the binding site residues, it has been challenging for inhibitors to competitively overcome the natural substrate-Bcl-2 interactions. However, significant polar residues (Tyr108, Asp111, Glu136, Met115, and Arg146) represent relevant anchoring sites for stabilizing the bounded ligands. The crystallized ligand showed extended accommodation within the target pocket, reaching from P1-to-P4 subsites (Figure 10). Significant non-polar contacts are depicted with the hydrophobic residues of four sub-pockets, while the ligand's polar functionalities exhibit close proximity towards Tyr108, Asp111, and Arg146. Interactions with these polar residues are suggested to be significant for the ligand/target stability [41].

Proceeding throughout the docking studies, validation of the adopted docking protocol was achieved through redocking the crystallized ligand (PDB ID: J1Q) showing a root-mean standard deviation (RMSD) below 2 Å. Depicting RMSD values below 2 Å indicates that both the adopted algorithms and parameters were sufficient for determining the best docking pose [42]. Regarding the docking results of the top cytotoxic drugs,

limited binding of the Series-I compound (**3b**) towards Bcl-2 pockets was illustrated. The benzimidazole-based ligand adopted V-shaped conformation with limited binding to P2 and P3 hydrophobic pockets. The benzimidazole scaffold predicted relevant anchoring within P3 through H-bonding with Asp111, while the substituted phenyl group finely overlaid at P2 pocket (Figure 11A). This orientation was further stabilized through  $\pi$ - $\pi$  stacking of the benzimidazole ring with Tyr108 (Supplementary Materials; Table S1). More extended orientations were depicted for the Series-II indole derivatives (**7a** and **7b**). Binding was extended at P2 through P4 sub-pockets showing their indole rings being docked at P2. Higher docking score was assigned for **7d** ( $S = -4.8585$  Kcal/mol vs.  $-4.76959$  Kcal/mol for **7b**), where double polar interactions between its pyridine ring and Arg146 side chain justified significant anchoring within pocket P4 (Figure 11B). Moreover, the pyridine ring was further stabilized through double  $\pi$ -hydrogen interaction with Leu137 of P4 subsite suggesting its great affinity to Bcl-2 protein. Owing to its amide linker flexibility, **7d** indole ring showed better overlay with the crystallized ligand than does the **3a** benzimidazole scaffold.

For the pyrazole-based Series-III ligands, comparable binding modes, to the crystallized ligand, were suggested (RMSD = 1.211 to 1.7374 Å) owing to a similar topology of central pyrazole with substituted aromatic arms. Extended orientations and conformations over P1-P4, with much closer proximity towards P5 subsite, have been predicted for Series-III ligands. Compound **8b** showed one of the highest docking scores ( $S = -6.1846$  Kcal/mol), which was explained by its exhibiting significant hydrogen bonding between its amide linker and Arg146 side chain at P4 subsite (Figure 10C). The same polar interaction was predicted for the other Series-III members confirming their superior Bcl-2 affinity ( $S = -5.7070$  to  $-6.2460$  Kcal/mol) and the importance of Arg146 in ligand binding. Notably, compound **8f** was suggested with the lowest member docking score ( $S = -4.9429$  Kcal/mol) for lacking contacts with P1 due to its short methyl arm instead of the substituted aromatic side chain in all Series-III members. Additionally, the 5-chloro substituent on the pyrazole ring exhibited great solvent exposure suggesting high solvation penalty (Figure 10D).

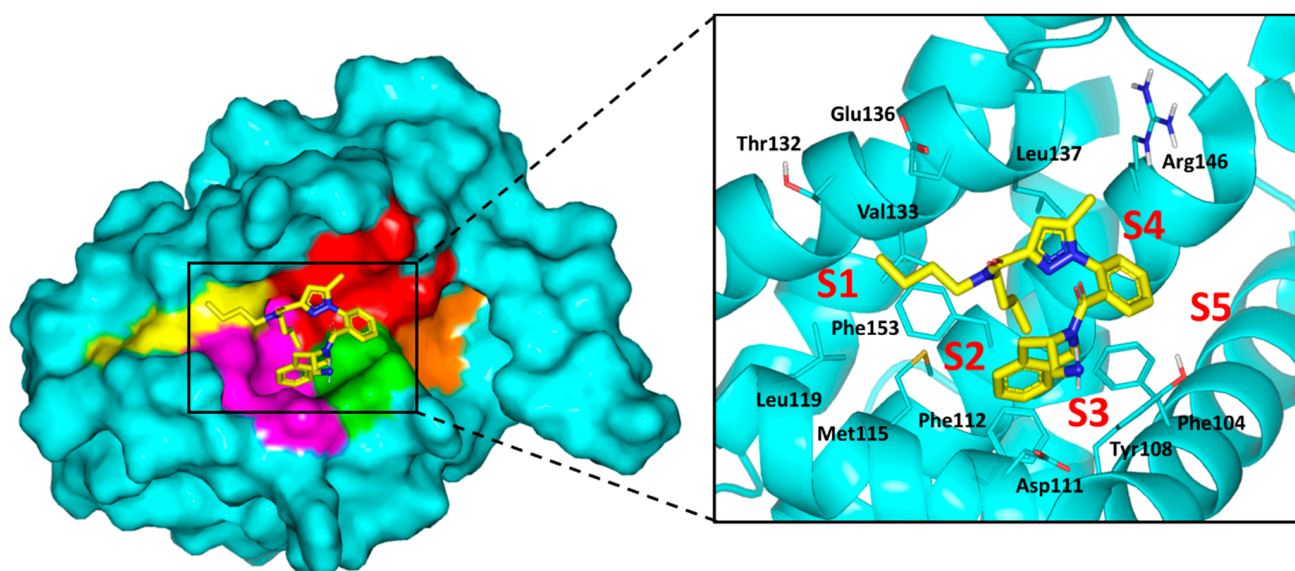


**Figure 10.** Structure of X-ray crystallized Bcl-2 (PDB ID: 6qgk) bounded to tetrahydroisoquinoline-phenyl pyrazole derivative along the binding site. Five hydrophobic pockets (P1–5), constituting the binding site, are shown in 3D-surface presentation and differently colored; P1 yellow, P2 magenta, P3 green, P4 red, P5 orange. Zoomed image is stereoview of crystallized ligand (yellow sticks) at binding site. Sub-pockets are labeled with red letters and only significant residues (cyan lines) located within 4 Å radius of bound ligand are displayed and labeled with sequence number.

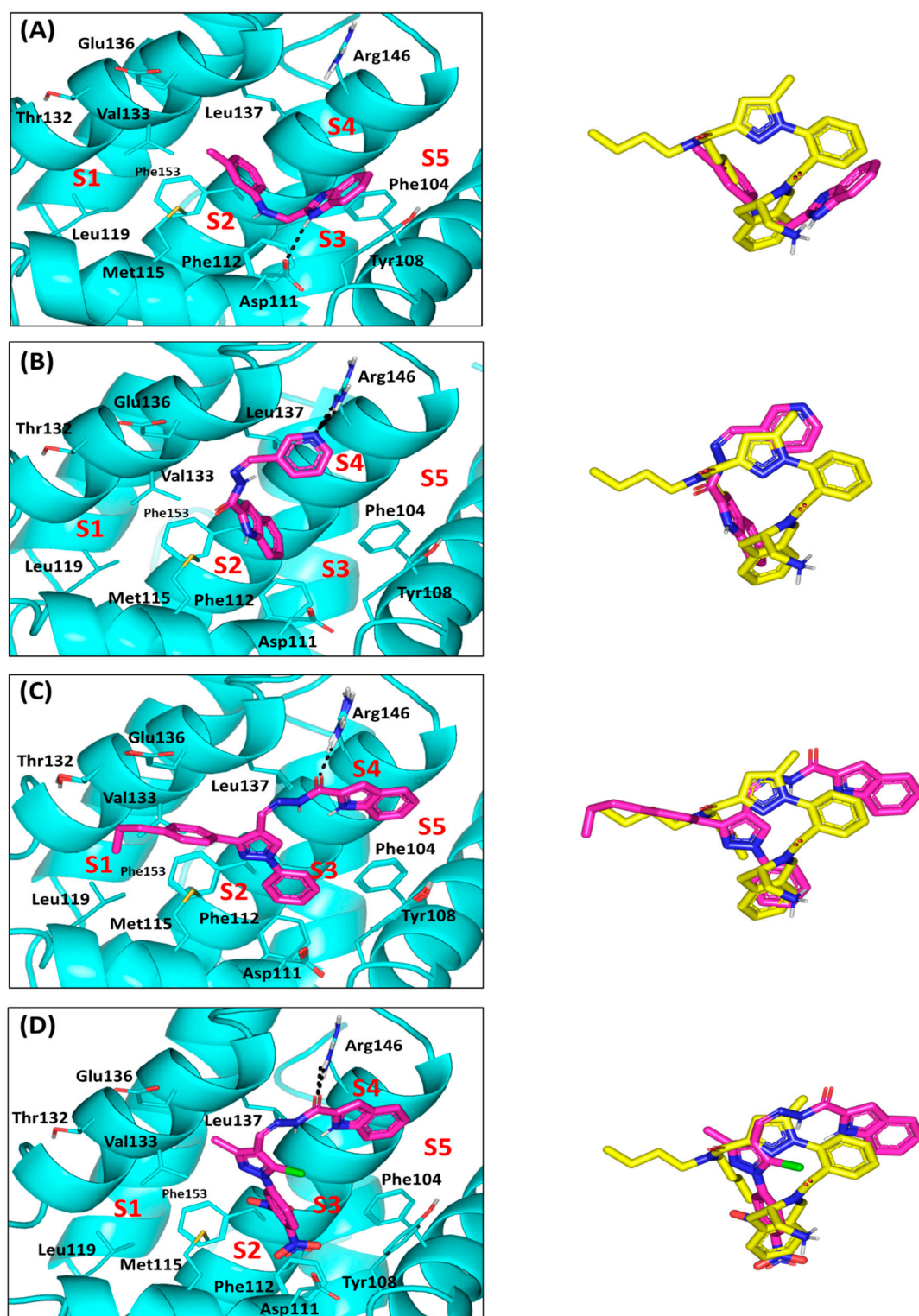


**Figure 11.** Docking results of synthesized compounds within Bcl-2 protein target (PDB ID: 6qgk). Left panels illustrate the proposed docking poses for the investigated compounds (magenta sticks) at the hydrophobic surface binding site of Bcl-2 target (cyan cartoon); (A) 3a; (B) 7d; (C) 8b; (D) 8f. On the right is the overlay of docked synthesized compounds (magenta sticks) and crystallized ligand (yellow sticks), depicting their comparative orientations within the binding site. Only significant residues (cyan lines) located within 4 Å radius of docked synthesized compounds are displayed and labeled with sequence number and colored. Hydrogen bonds are displayed as black-dashed lines.



## 2.5. Solid Lipid Nanoparticle Formulation Studies

In an attempt to the clinical suitability of **8b**, the *in-silico* pharmacokinetic properties and drug-likeness of compound was investigated using free web-based tool SwissADME (<http://www.swissadme.ch/>). Notably, the predicted poor water-solubility of **8b** ( $\text{LogS}_{\text{SILICOS-IT}} = -7.62$ ;  $1.06 \times 10^{-5}$  mg/mL;  $2.38 \times 10^{-8}$  mol/L) was identified as a significant parameter that might hinder the compound's full potential cytotoxic activity. Thus, Solid lipid nanoparticles (SLNs) formulation was adopted as a simple cost-effective approach for optimizing the compound's kinetic parameters. The main target of SLNs is to enhance the drug absorption, enhance the pharmacological response, and decrease the side effects. SLNs are colloidal dispersions made of solid lipid (possessing high melting point) and a hydrophilic surfactant [43]. SLNs are considered a new generation of submicron-sized lipid emulsions where solid lipids are utilized instead of liquid lipids (oil) [44]. Due to their unique characteristics, such as small size, large surface area, and increased drug loading capacity, SLNs are attracting great attention of formulators world-wide to improve performance and bioavailability of pharmaceuticals [45]. It was reported that SLNs have the ability to release entrapped drug in controlled manner and enhance stability of the entrapped drug [46]. Therefore, formulating **8b** as SLNs was expected to enhance its bioavailability at the tumor site and hence improve its cytotoxic activity.

### 2.5.1. Design, Preparation and Optimization of Drug-SLN

Eight drug-SLNs formulations were prepared via hot-melting homogenization technique. The formulations were designed by  $2^3$ -factorial design using Stat-Ease<sup>®</sup> V.11 software (Design-Expert<sup>™</sup>; Minneapolis, MN, USA) (Table 2). The selected factors (independent variables) were type of lipid (A;  $X_1$ ) and Surfactant (B;  $X_2$ ), as well as the concentration of surfactant (C;  $X_3$ ). According to the adopted  $2^3$ -factorial design, eight formulations were prepared and evaluated for encapsulation efficiency ( $Y_1$ : EE%), particle size ( $Y_2$ : PS) and zeta potential ( $Y_3$ : ZP). Compositions of eight drug-SLNs formulations are presented in Table 3. Drug analysis at different concentration was done using HPLC at  $\lambda_{\text{max}}$  254 nm, showing linear relationship between the drug concentration and peak area, obeying Beer-Lambert's law ( $R^2 = 0.999$ ) (Supplementary Materials; Figure S1).

**Table 2.** The formulation factors and responses of  $2^3$  factorial design for drug-solid lipid nanoparticles (SLNs).

Factors and Responses		Level Used	
Factor	Name	Low (−1)	High (+1)
A: $X_1$	Type of lipid	Compritol 888 ATO (COMP)	Glyceryl Monostearate (GMS)
B: $X_2$	Type of surfactant	Cremophor RH40	Poloxamer 188
C: $X_3$	Surfactant conc. (% w/v)	1%	1.5%
Response	Name	Goal	
$Y_1$	EE (%)	<b>Maximize</b>	
$Y_2$	PS (nm)	<b>Minimize</b>	
$Y_3$	ZP (mV)	<b>Maximize</b>	

**Table 3.** The eight designed drug-SLNs according to  $2^3$ -factorial design.

SNP Formulation No.	$X_1$	$X_2$	$X_3$
	A: Lipid Type	B: Surfactant Lipid	C: Surfactant Conc. (% w/v)
1	COMP	Cremophor RH40	1.5
2	COMP	Cremophor RH40	1
3	COMP	Poloxamer 188	1
4	GMS	Cremophor RH40	1
5	COMP	Poloxamer 188	1.5
6	GMS	Cremophor RH40	1.5
7	GMS	Poloxamer 188	1
8	GMS	Poloxamer 188	1.5

### 2.5.2. The Effect of Formulation Factors in the Responses

The prepared formulations of drug-SLNs were evaluated for the preselected responses; Encapsulation Efficiency (Y1: EE%), the particle size (Y2: PS) and zeta potential (Y3: ZP). As represented in Table 4, it was found that there was a difference in the results of the responses which gave an indication that the formulation factors have a great effect of the responses.

**Table 4.** The measured responses of prepared drug-SLNs according to 2<sup>3</sup> factorial design.

SNP Formulation No.	(Y1) EE%	(Y2) PS (nm)	(Y3) ZP (mV)	Polydispersity Index (PDI)
F1	37.1 ± 2.45	140.9 ± 3.2	−12.3 ± 0.77	0.352 ± 0.03
F2	53.4 ± 1.65	135.1 ± 1.0	−13.6 ± 0.32	0.282 ± 0.01
F3	95.3 ± 1.34	329.4 ± 6.1	−21.7 ± 0.15	0.563 ± 0.03
F4	82.8 ± 2.55	189.8 ± 3.3	−36.1 ± 1.90	0.432 ± 0.04
F5	86.8 ± 3.32	181.5 ± 2.1	−16.4 ± 1.10	0.442 ± 0.02
F6	67.7 ± 1.52	100.4 ± 0.4	−39.4 ± 0.095	0.433 ± 0.01
F7	94.6 ± 2.67	537.3 ± 10.4	−37.5 ± 0.58	0.582 ± 0.04
F8	92.8 ± 2.38	226.1 ± 10.5	−29.3 ± 1.17	0.639 ± 0.12

With the prepared formulations of drug-SLNs, significant impact on the preselected responses was depicted in response to the formulation factors. The EE% of all prepared drug-SLNs ranged from 37.1 ± 2.45% for F1 to 95.3 ± 1.34% for F3. As represented by model Equation (1), the EE% was increased by increasing the level of X1 and X2 from −1 to +1. These results infer that the formulations prepared by GMS and Poloxamer 188 had a higher EE% than those prepared using COMP or Cremophor RH40. Moreover, EE% showed an inverse relationship with X3: surfactant concentration where higher EE% was seen with 1.5% *w/v* surfactant.

$$Y_1 \text{ (EE\%)} = 76.31 + 8.16 X_1 + 16.06 X_2 - 5.21 X_3 \quad (1)$$

For better illustration, a 3D-response surface plot showing the impact of formulation factors on EE% was constructed (Figure 12). Interestingly, GMS-prepared SLNs exhibited higher EE% than those constituted by COMP. These findings might be for the large encapsulation space in case of GMS resulting from less-ordered SLNs structure by the virtue of their long carbon chains (C21) [10,30]. Additionally, higher EE% was assigned for Poloxamer 188-prepared SLNs as compared to Cremophor RH40 which may be correlated to the higher hydrophilic-lipophilic balance (HLB) value proposed by Poloxamer 188 [47]. Latter findings are in good agreement with Qushawy et al., where the prepared carbamazepine-SLNs depicted increased EE% through using GMS and Poloxamer 188 as solid lipid and surfactant, respectively [48]. The increase of surfactant concentration from 1% to 1.5% resulted in decreased EE% which may be for increased drug solubility within the aqueous phase [49]. The same results were depicted by Joseph et al. where olanzapine-SLNs EE% showed an inverse relationship with surfactant concentration [50].

Regarding the PS of all prepared drug-SLNs, values ranged from 135.1 ± 1.0 nm for F2 to 537.3 ± 10.4 nm for F7. The model Equation (2) of PS, revealed that PS had a direct relationship with X1 and X2 while, an inverse relationship with X3. As shown by Figure 13, the 3D response surface plot studied the impact of formulation factors (X1, X2 and X3) on PS of the prepared SLNs. It was found that PS was increased in case of CMS than in case of COMP which might be correlated to the fact of using solid lipid with high melting point, resulted in slow crystallization and large particle size [51]. The results in good agreement with Priyanka and Hasan found that the particle size of prepared montelukast SLNs was influenced by lipid type and the decreasing order of particle size for the three lipids was Compritol < GMS < stearic acid [52].

$$Y_2 \text{ (PS)} = 250.06 + 33.34 X_1 + 88.51 X_2 - 67.84 X_3 \quad (2)$$

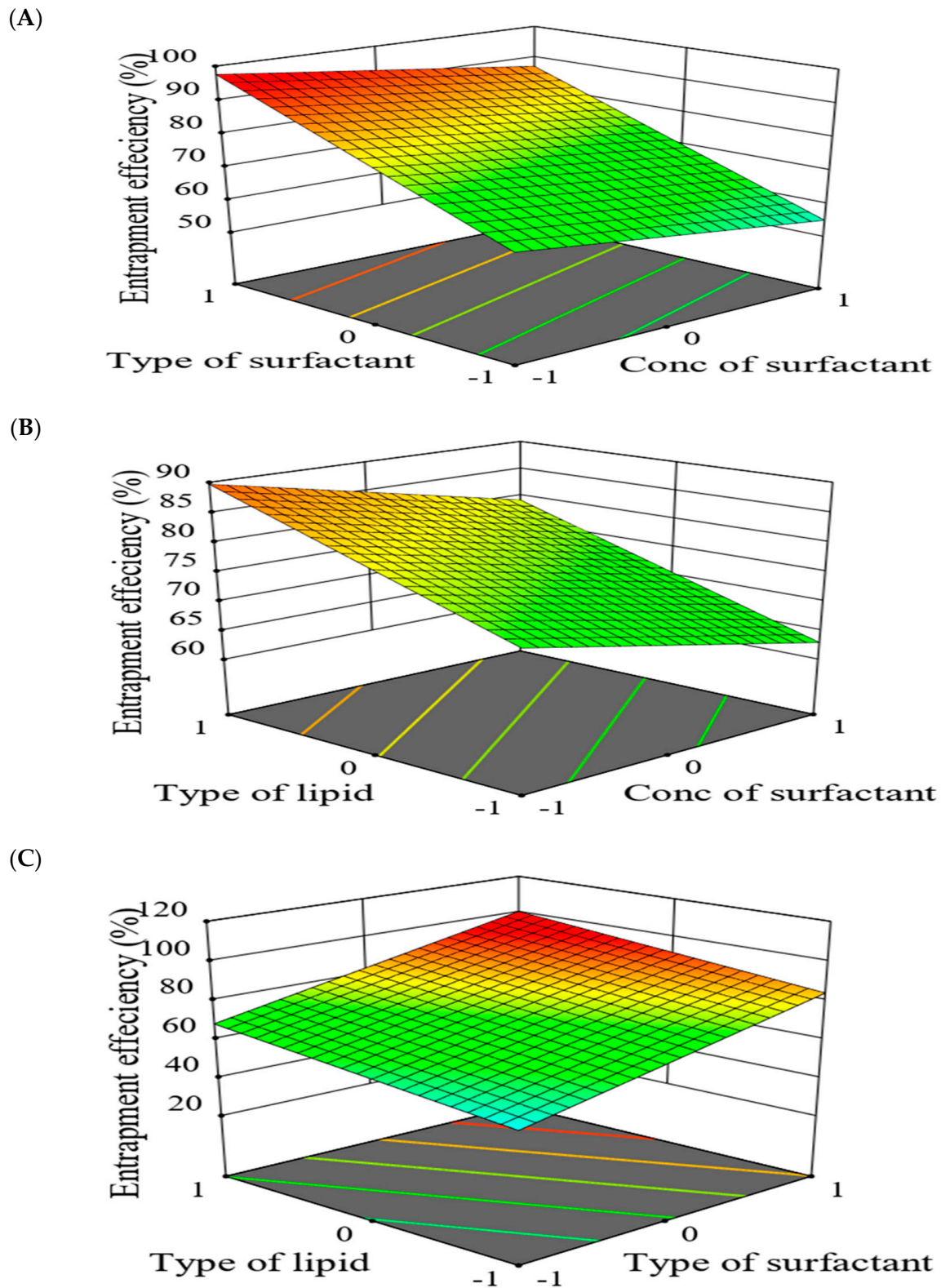


**Figure 12.** 3D-response surface plots showing combined effect of formulation factors on encapsulation efficiency (EE%;  $Y_1$ ). The adopted  $2^3$  model analysis evaluated two variable parameters while keeping (A) type of lipid ( $X_1$ ); (B) type of surfactant ( $X_2$ ); (C) concentration of surfactant ( $X_3$ ) constant.

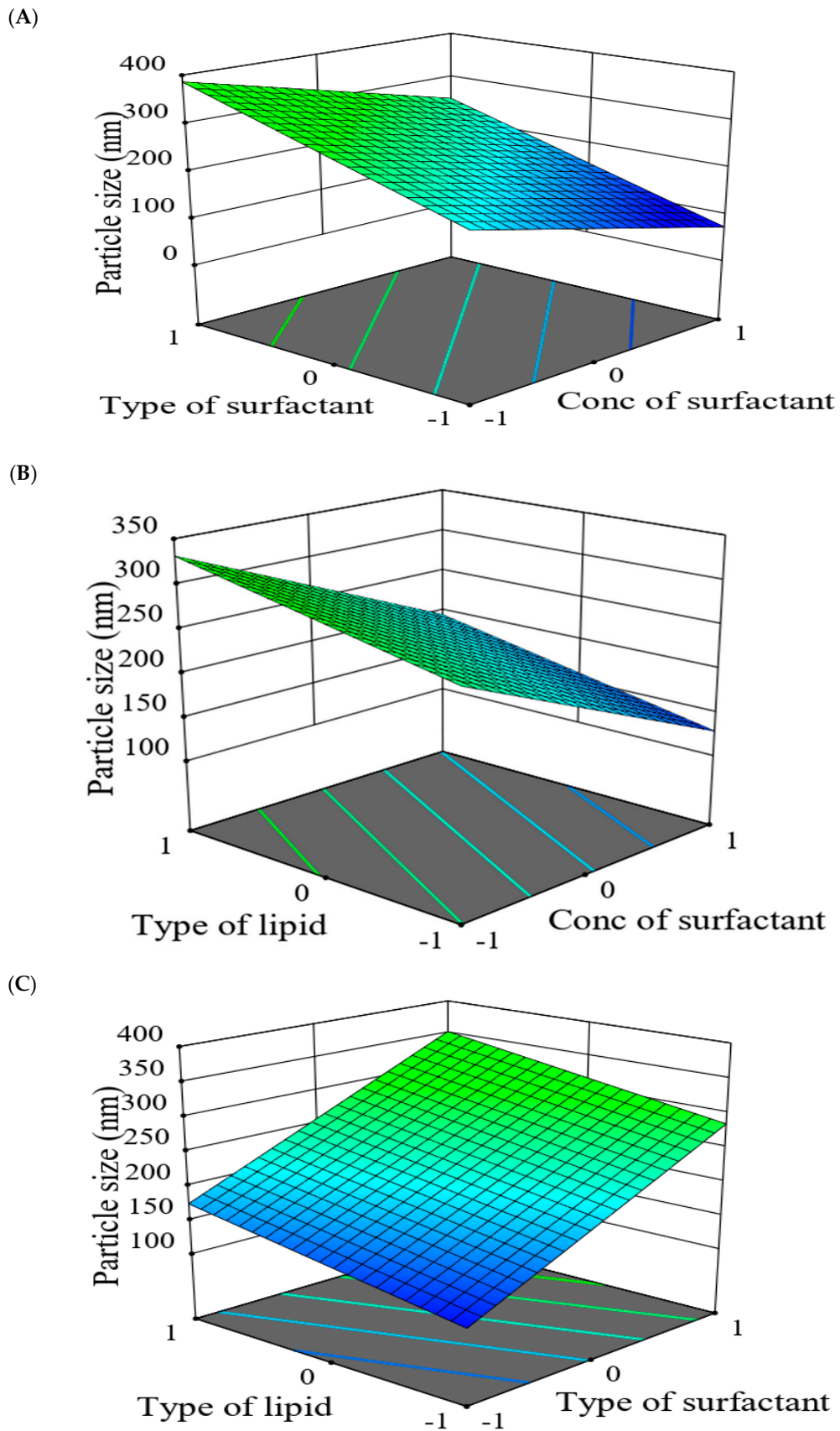


**Figure 13.** 3D-response surface plots showing combined effect of formulation factors on particle size (PP;  $Y_2$ ). The adopted  $2^3$  model analysis evaluated two variable parameters while keeping (A) type of lipid ( $X_1$ ); (B) type of surfactant ( $X_2$ ); (C) concentration of surfactant ( $X_3$ ) constant.

The PS of the prepared SLNs was also affected by surfactant type, where using Poloxamer 188 resulted in SLNs larger sizes than those prepared by Cremophor RH40. This may be reasoned to the conception of using surfactant with higher HLB can result in preparation of SLNs with larger size [53]. Additionally, as the surfactant concentration elevated from 1% to 1.5%, the particle size of SLNs decreased. This might be assigned to reduction within interfacial tension between the emulsion phases by increasing the concentration of surfactant which led to smaller PS of SLNs after congealing [50,52].

Moving towards the final parameter, The ZP of all prepared drug-SLNs was ranged from  $-12.3 \pm 0.77$  mV for F1 to  $-39.4 \pm 0.095$  mV for F6. zeta potential (ZP) is defined as potential difference existing within the stationary layer between the dispersion medium and the dispersed phase (solid particles) [54]. The value of ZP provides indication for the preparation stability, where higher values correlate to higher formulation stability [55]. Within the presented model Equation (3), the ZP of prepared drug-SLNs increased by increasing the level of lipid and surfactant types yet decreased by increasing the level of surfactant concentration.

$$Y_3 \text{ (ZP)} = 25.79 + 9.79 X_1 + 0.4375 X_2 - 1.44 X_3 \quad (3)$$

Corresponding 3D-response surface plot showed the effect factors on ZP responses (Figure 14). The type of lipid had a significant impact on negative value of ZP. The value was increased by using GMS than in case of COMP which might be related to longer carbon-chain of GMS resulted in the larger size of SLNs and larger surface area. It was found that negative zeta potential of the prepared SLNs was slightly decreased by using Cremophor RH40 while increased in case of Poloxamer 188 which may be attributed to differences within respective HLB values [56]. Moreover, ZP was decreased with increased surfactant concentration which may be due to the masking of surface charge by increasing the surfactant concentration [50,57]. It worth mentioning that the PDI values of all prepared drug-SLNs ranged from  $0.282 \pm 0.01$  to  $0.639 \pm 0.12$  for F2 and F8, respectively. Findings from PDI values indicated a narrow size distribution [54].

### 2.5.3. Optimization of Formulation Variables to Select the Best Formula

Purpose of optimization was to maximize EE%, minimize PS, as well as maximize values of the ZP. The Design-Expert V.11 software was used for obtaining an optimum level of each single formulation factor to achieve the desired goals for every response and obtain the optimized formulation of drug-SLNs. According to  $2^3$ -factorial design, formulation F8 was the optimized formulation in which prepared using GMS as a solid lipid and poloxamer 188 as a surfactant in concentration 1.5%. The predicted values of responses for the optimized formulation were 95.325% for EE% (Y1), 284.075 nm for PS (Y2), and  $-34.575$  mV for ZP (Y3). Interestingly, these predicted values were close to the actual values of responses with desirability value 0.781 which indicate the validity of  $2^3$ -factorial design. The transmission electron microscopic (TEM) image of F8 illustrated the spherical shape of the prepared SLNs within the nano size (Figure 15A). Size analysis for TEM image, using Nano-Measurer<sup>®</sup> V.1.2 software (Shanghai, China), exhibited narrow size distribution (Figure 15B). These findings were in good agreement with Qushawy et al. preparing carbamazepine-SLNs using GMS and stearic acid where the prepared SLNs were spherical in shape with nano size [44].

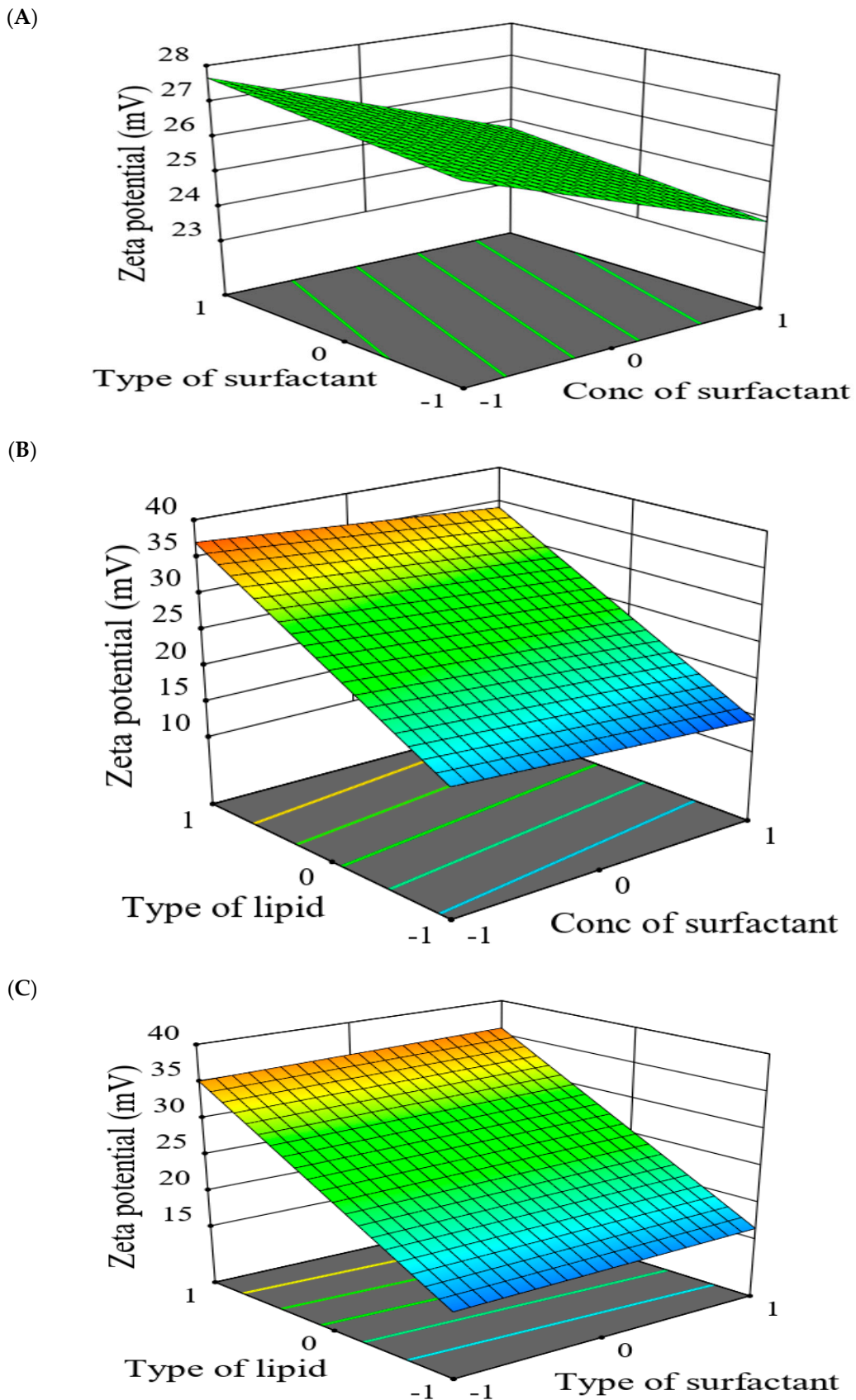


**Figure 14.** 3D-response surface plots showing combined effect of formulation factors on zeta potential (ZP;  $Y_3$ ). The adopted model analysis evaluated two variable parameters while keeping (A) type of lipid ( $X_1$ ); (B) type of surfactant ( $X_2$ ); (C) concentration of surfactant ( $X_3$ ) constant.

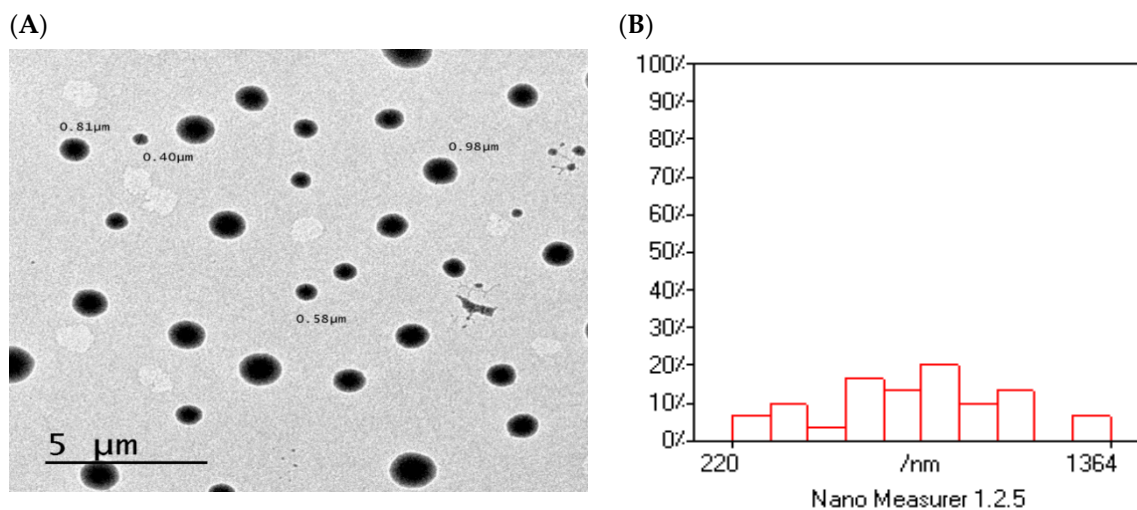


**Figure 15.** The surface morphology of the optimized formulation (F8). (A) TEM image; (B) size distribution analysis of TEM image.

#### 2.5.4. In-Vitro Release Study of Optimized Formulation (F8) in Comparison with **8b**

The in-vitro drug release profile of drug-SLNs was conducted for evaluating the stability and release behavior of drug-SLNs. The drug release from F8 was prolonged over 48 h, where the total released amount of drug from F8 was  $91.47 \pm 2.78\%$ , while being  $21.48 \pm 1.17\%$  for **8b** ( $p < 0.001$ ) (Figure 16). Thus, drug-SLNs may be expected to assist as stable nanoparticles for prolonged time and help in increasing the accumulation of drug in tumor site [58]. These results may be attributed to presence of the drug in more solubilized form and the prolonged effect might be the result of the drug diffusion from the lipid matrix [59].

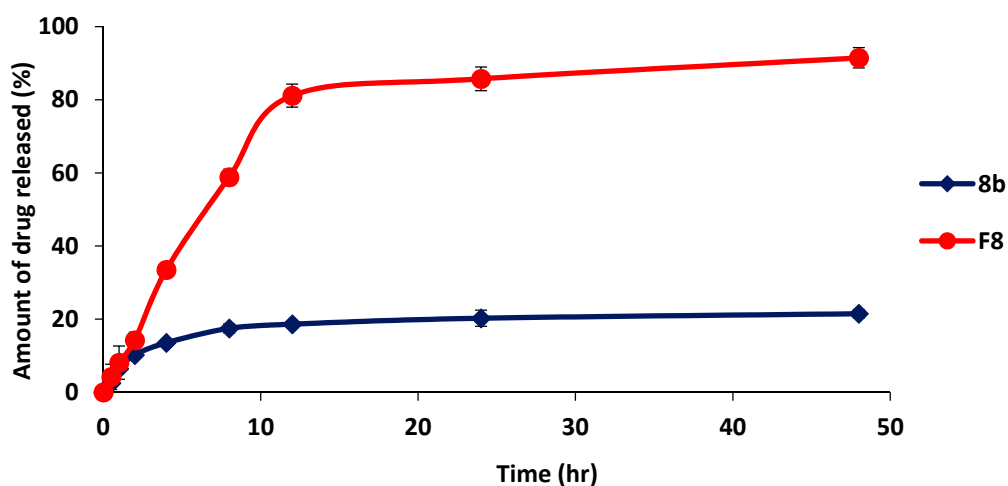


**Figure 16.** In-vitro drug release analysis of drug-optimized SLNs formula (F8) in comparison with **8b** as free drug form. All data are represented as mean of three independent experiments  $\pm$  SEM.

#### 2.5.5. Cytotoxicity Study of Optimized Formulation

The cytotoxic efficacy of compound **8b** was assayed in its pure form and in optimized SLN formulation (F8). From the Sulforhodamine B (SRB) assay, the compound's  $IC_{50}$  within MDA-MB-231/breast cancer cell line was significantly decreased from  $12.43 \pm 0.50 \mu\text{M}$  to  $9.27 \pm 0.34 \mu\text{M}$  for **8b** and formulated form, respectively ( $p < 0.05$ ) (Figure 17). Based

on the fact that **8b** is lipophilic (Consensus  $\text{Log}P_{o/w} = 5.16$ ) with poor aqueous solubility, it was predicted to possess low bioavailability [60]. Incorporation of the drug into lipid-based nanoparticles might offer significant improvement in its anticancer efficacy as the lipid nature of the SLN increases its solubility and allows the presence of the drug in its amorphous form. The latter might cause an increase within the drug **8b** penetration into the tumor cells [61]. Wang and colleagues found similar results when evaluated the cytotoxic effect of Resveratrol on MDA-MB-231/breast cancer cell line [62]. The authors mentioned that the enhanced cytotoxic effect of Resveratrol SLNs as compared to pure resveratrol may be due to the carrier hydrophobic nature facilitating the intra-cellular uptake.

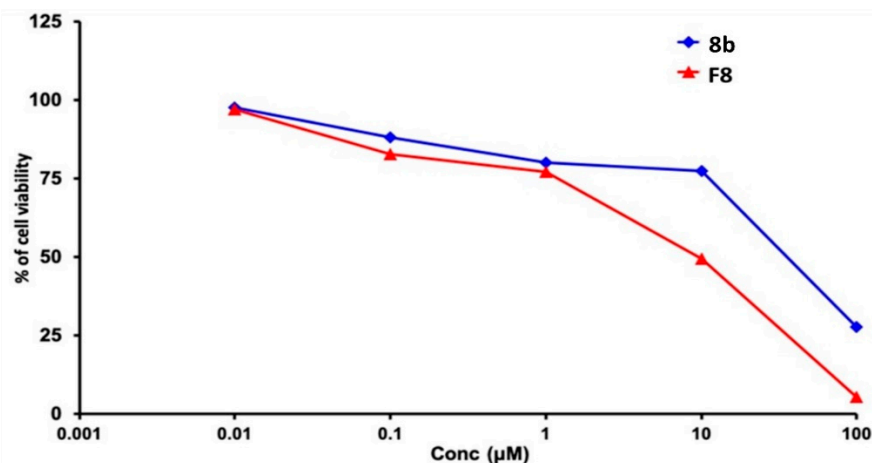


**Figure 17.** The Sulforhodamine B (SRB) cytotoxicity assay of the tested **8b** as compared to drug-optimized SLNs formula (F8) on MDA-MB-231/breast cancer cells. At  $5 \times 10^3$  cells/well cell density, cells were treated with various **8b** concentrations (0.01, 0.1, 1, 10, and 100  $\mu\text{M}$ ) for 72 h exposure time frame. Cytotoxic effect was detected via protein-bound SRB colorimetric assay (540 nm) and % cell growth viability was estimated in triplicates as compared to vehicle negative controls representing the untreated cells.

### 3. Materials and Methods

#### 3.1. General Experimental

All chemicals, reagents and solvents were purchased from Sigma-Aldrich, Fisher Scientific, Alfa-Aesar, Fluka and Acros Chemicals. Whenever required, solvents were dried prior to use as described by the handbook Purification of Laboratory Chemicals and stored over  $4\text{\AA}$  molecular sieves under nitrogen. Flash column chromatography was performed with silica gel (230–400 mesh) (Merck) and TLC was performed on pre-coated silica gel plates (Merck Kiesel gel 60F254, BDH). Melting points were determined on an electrothermal instrument (Gallenkamp) and are uncorrected. Compounds were visualized by irradiation with UV light at 254 nm and 365 nm. The NMR spectra of all new compounds were recorded on a Bruker AVANCE DPX500 spectrometer operating at 500 and 125 MHz for  $^1\text{H}$  and  $^{13}\text{C}$  NMR, respectively, and auto calibrated to the deuterated solvent reference peak (Supplementary Materials; Figure S2). Chemical shifts are given in  $\delta$  relative to tetramethylsilane (TMS); the coupling constants ( $J$ ) are given in Hertz. TMS was used as an internal standard ( $\delta = 0$  ppm) for  $^1\text{H}$  NMR and  $\text{CDCl}_3$  served as an internal standard ( $\delta = 77.0$  ppm) for  $^{13}\text{C}$  NMR. Multiplicity is denoted as s (singlet), d (doublet), t (triplet), q (quartet), m (multiplet) or combinations thereof. The compounds imines **11a–f** and aldehydes **12a–f** were prepared according to Kishk et al. [29]. The DI Analysis Shimadzu QP2010-Plus<sup>®</sup> GC/MS (Shimadzu<sup>TM</sup>, Tokyo, Japan) was adopted for recording the low-resolution mass spectra (MS) of the synthesized compounds at electron impact ( $\text{EI}^+$ ) mode. Regarding purity analysis, the elemental analyses were recorded on Vario<sup>®</sup> EL-CHNS Elemental Analyzer (GmbH<sup>TM</sup>, Hanau, Germany). The results of elemental



analyses (C, H, N) were found to be in good agreement ( $\pm 0.45\%$ ) with the calculated values. All compounds were  $>95\%$  pure.

### 3.2. Chemical Synthesis

#### 3.2.1. Synthesis of 2-(chloromethyl)-1H-Benzimidazole (2)

A mixture of ortho-phenylene diamine (1.0 g, 9.25 mmol) and chloroacetic acid (1.32 g, 13.97 mmol) in 4 N HCl (60 mL) was refluxed for 24 h. The purified product was obtained by re-crystallization from water after neutralization with 6 N  $\text{NH}_4\text{OH}$ , yield 0.4 g (40%). The product was used in the following step without further purification [63]. M.p. 149–151 °C (Lit. 147.8–148.2 °C).  $^1\text{H}$  NMR (DMSO- $d_6$ ):  $\delta$  4.91 (s, 2H,  $\text{CH}_2$ ), 7.25–7.29 (m, 2H, CH, Ar), and 7.57–7.59 (m, 2H, CH, Ar).

#### 3.2.2. Synthesis of 2-Aminomethyl-Benzimidazole Derivatives (3a–d)

A mixture of compound (2) (1 mmol) and the appropriate aromatic amine (1 mmol) in the presence of potassium iodide (1 mmol) were refluxed in absolute ethanol for 6 h, then potassium iodide (1 mmol) dissolved in 5 mL water was added and refluxed overnight. After cooling to room temperature, the solution was poured into ice, filtered and crude product was purified by flash column chromatography using gradient EtOAc: *n*-hexane [26].

##### *N*-((1H-benzo[*d*]imidazol-2-yl)methyl)-3-methylaniline (3a).

Prepared from 3-methylaniline, yield 0.07 g (71%), as an off-white powder. M.p. 139–141 °C. TLC (EtOAc: *n*-Hexane 2:3),  $R_f$ : 0.23.  $^1\text{H}$  NMR (DMSO- $d_6$ ):  $\delta$  2.39 (m, 3H,  $\text{CH}_3$ ), 4.46 (d,  $J = 5.38$  Hz, 2H,  $\text{CH}_2$ ), 6.17 (t,  $J = 7.2$  Hz, 1H, NH), 6.50 (s, 1H, NH), 6.96 (s, 1H, CH, Ar), 7.28 (d,  $J = 7.2$  Hz, 2H, CH, Ar), 7.49 (m, 1H, CH, Ar), 7.56 (t,  $J = 7.4$  Hz, 2H, CH, Ar), 7.76 (d,  $J = 7.4$  Hz, 2H, CH, Ar).  $^{13}\text{C}$  NMR (DMSO- $d_6$ ):  $\delta$  21.79 ( $\text{CH}_3$ ), 42.29 ( $\text{CH}_2$ ), 110 (2  $\times$  CH, Ar), 113.6 (2  $\times$  CH, Ar), 117.8 (CH, Ar), 129.2 (2  $\times$  CH, Ar), 129.75 (CH, Ar), 138.34 (3C, Ar), 143.4 (C, Ar). MS (EI $^+$ )  $m/z$ : 237.38 [ $\text{M}^+$ ]. Anal. Calcd for  $\text{C}_{15}\text{H}_{15}\text{N}_3$  (237.31): C, 75.92; H, 6.38; N, 17.72. Found: C, 75.81; H, 6.22; N, 17.60

##### *N*-((1H-benzo[*d*]imidazol-2-yl)methyl)-2,6-dimethylaniline (3b).

Prepared from 3,5-dimethylaniline, yield 0.06 g (61%), as an off-white powder. M.p. 159–161 °C. TLC (EtOAc: *n*-Hexane 1:2),  $R_f$ : 0.5.  $^1\text{H}$  NMR (DMSO- $d_6$ ):  $\delta$  2.30 (m, 6H, 2  $\times$   $\text{CH}_3$ ), 4.36 (s, 2H,  $\text{CH}_2$ ), 4.54 (s, 1H, NH), 6.81–6.89 (m, 1H, Ar), 6.94 (d,  $J = 7.34$  Hz, 2H, Ar), 7.16–7.19 (m, 2H, Ar), 7.54 (d,  $J = 7.5$  Hz, 2H, Ar).  $^{13}\text{C}$  NMR (DMSO- $d_6$ ):  $\delta$  18.9 (2  $\times$   $\text{CH}_3$ ), 46.2 ( $\text{CH}_2$ ), 111.8 (2  $\times$  CH, Ar), 118.8 (CH, Ar), 122 (2  $\times$  CH, Ar), 129.3 (2  $\times$  CH, Ar), 129.6 (2C, Ar), 138.8 (2C, Ar), 146.1 (C, Ar), 154.4 (C, Ar). MS (EI $^+$ )  $m/z$ : 251.17 [ $\text{M}^+$ ]. Anal. Calcd for  $\text{C}_{16}\text{H}_{17}\text{N}_3$  (251.33): C, 76.46; H, 6.82; N, 16.72. Found: C, 76.37; H, 6.89; N, 16.73.

##### *N*-((1H-benzo[*d*]imidazol-2-yl)methyl)-3-bromoaniline (3c) [64].

Prepared from 3-bromoaniline, yield 0.07 g (73%), as a light brown powder. M.p. 139–141 °C. TLC (EtOAc: *n*-hexane 1:2),  $R_f$ : 0.27.  $^1\text{H}$  NMR (DMSO- $d_6$ ):  $\delta$  4.16 (s, 2H,  $\text{CH}_2$ ), 7.21–7.24 (m, 2H, Ar), 7.57 (d,  $J = 7.4$  Hz, 2H, Ar), 7.59 (s, 1H, NH), 7.75 (d,  $J = 7.5$  Hz, 1H, Ar), 7.91–8.12 (m, 3H, Ar).  $^{13}\text{C}$  NMR (DMSO- $d_6$ ):  $\delta$  41.9 ( $\text{CH}_2$ ), 111.7 (2  $\times$  CH, Ar), 115.1 (2  $\times$  CH, Ar), 119.1 (CH, Ar), 121.8 (CH, Ar), 122.7 (2  $\times$  CH, Ar), 131.1 (1C, Ar), 150.5 (2C, Ar), 153.5 (1C, Ar), 169. (1C, Ar). MS (EI $^+$ )  $m/z$ : 302.72 [ $\text{M}^+$ ]. Anal. Calcd for  $\text{C}_{14}\text{H}_{12}\text{BrN}_3$  (302.18): C, 55.65; H, 4.01; N, 13.92. Found: C, 55.62; H, 3.93; N, 13.51.

##### 4-(((1H-benzo[*d*]imidazol-2-yl)methyl)amino)phenol (3d).

Prepared from 4-hydroxyaniline, yield 0.05 g (51%), as a brown powder. M.p. 139–141 °C. TLC (EtOAc: *n*-hexane 1:2),  $R_f$ : 0.4.  $^1\text{H}$  NMR (DMSO- $d_6$ ):  $\delta$  4.14 (s, 2H,  $\text{CH}_2$ ), 7.22 (d,  $J = 7.5$  Hz, 2H, Ar), 7.32 (d,  $J = 7.4$  Hz, 2H, Ar), 7.47–7.49 (m, 1H, CH, Ar), 7.57 (d,  $J = 7.5$  Hz, 2H, Ar), 7.59 (s, 1H, NH), 7.75 (d,  $J = 7.5$  Hz, 1H, Ar), 9.45 (s, 1H, OH), 12.18 (s, 1H, NH-indole).  $^{13}\text{C}$  NMR (DMSO- $d_6$ ):  $\delta$  43.6 ( $\text{CH}_2$ ), 115.2 (2  $\times$  CH, Ar), 116.3 (2  $\times$  CH, Ar), 116.7 (2  $\times$  CH, Ar), 124.1 (2  $\times$  CH, Ar), 139.1 (2C, Ar), 141.5 (1C, Ar), 142.1 (1C, Ar), 146.9 (1C, Ar). MS (EI $^+$ )  $m/z$ : 239.11 [ $\text{M}^+$ ]. Anal. Calcd for  $\text{C}_{14}\text{H}_{13}\text{N}_3\text{O}$  (239.28): C, 70.28; H, 5.48; N, 17.56. Found: C, 70.29; H, 5.49; N, 17.45.

### 3.2.3. Synthesis of Ethyl, 1H-Indole-2-Carboxylate (5)

To a stirred solution of 1H-indole-2-carboxylic acid (4) (1.5 g, 9.31 mmol) in dry ethanol (25 mL), sulfuric acid (0.5 mL) was added as catalyst. The reaction mixture was refluxed for 1.5 h. After the reaction was complete, water (25 mL) was added, and the mixture was extracted with ethyl acetate (3 × 50 mL). The combined organic phases were washed with brine, water, and dried over anhydrous Na<sub>2</sub>SO<sub>4</sub>. The solvent was evaporated under vacuum to give ethyl-1H-indole-2-carboxylate (6) as a white powder [65]. M.p. 126–127 °C (Lit. M.p. 123–124 °C). <sup>1</sup>H NMR (CDCl<sub>3</sub>) δ 1.43 (t, *J* = 7.4 Hz, 3H, CH<sub>3</sub>), 4.51 (q, *J* = 7.2 Hz, 2H, CH<sub>2</sub>), 6.96–6.99 (m, 1H, Ar), 7.12 (d, *J* = 7.0 Hz, 2H, Ar), 7.35 (d, *J* = 7.2 Hz, 2H, Ar), 9.31 (s, 1H, NH).

### 3.2.4. Synthesis of 1H-Indole-2-Carbohydrazide (6)

To a stirred solution of ethyl 1H-indole-2-carboxylate (5) (0.46 g, 7.93 mmol) was added hydrazine monohydrate (4 mL, 79.90 mmol) in the presence of 15 mL of absolute ethanol. The reaction mixture was refluxed for 6 h. After the reaction was complete, the solution was evaporated under vacuum, the remaining residue after evaporation (0.50 g) was washed with dichloromethane (0.5 mL × 3). The product was obtained as colorless crystals and was used directly in the following reaction without any further purifications [66]. M.p. 245–246 °C (Lit. M.p. 247–248 °C), <sup>1</sup>H-NMR (DMSO-d<sub>6</sub>): δ 4.49 (s, 2H, NH<sub>2</sub>), 7.13 (d, *J* = 4.6 Hz, 1H, Ar), 7.19 (s, 1H, Ar), 7.25 (d, *J* = 7.4 Hz, 1H, Ar), 7.49 (d, *J* = 7.4 Hz, 1H, Ar), 7.65 (d, *J* = 7.5 Hz, 1H, Ar), 9.79 (s, 1H, NH), 11.68 (s, 1H, NH, indole).

### 3.2.5. Synthesis of Different Carbohydrazide Derivatives (7, 8)

Equimolar amount of appropriate aromatic aldehyde was added to a solution of the hydrazide compound (6) (10 mmol) in absolute ethanol (5 mL), in presence of catalytic amount of glacial acetic acid (0.4 mL). Reaction mixture was allowed to reflux with continuous stirring for about 1.5 h and poured into ice/water mixture. The precipitate was filtered, washed with cold water and purified by flash column chromatography using gradient elution of EtOAc: *n*-hexane to give the corresponding carbohydrazide [67–69].

*N'*-benzylidene-1H-indole-2-carbohydrazide (7a) [67].

Prepared from benzaldehyde, yield 0.045 g (45%), as an off-white powder. M.p. 111–113 °C. TLC (EtOAc: *n*-Hexane 1:2), R<sub>f</sub>: 0.40. <sup>1</sup>H NMR (DMSO-d<sub>6</sub>): δ 7.08 (d, *J* = 7.34 Hz, 2H, CH, Ar), 7.28 (s, 1H, CH, indole), 7.54–7.59 (m, 5H, CH, Ar), 7.78 (d, *J* = 6.11 Hz, 2H, CH, Ar), 8.47 (s, 1H, CH=N), 11.76 (s, 1H, NH, indole), 11.92 (s, 1H, NH, amide). <sup>13</sup>C NMR (DMSO-d<sub>6</sub>): δ 111.1 (CH, Ar), 114.9 (CH, Ar), 119.8 (CH, Ar), 120.7 (CH, Ar), 121.7 (CH, Ar), 128.8 (2 × CH, Ar), 129.3 (2 × CH, Ar), 131.3 (C, Ar), 133.7 (C, Ar), 138.5 (C, Ar), 139.8 (C, Ar), 146.8 (2 × CH, Ar), 157.6 (C=O). MS (EI<sup>+</sup>) *m/z*: 263.55 [M<sup>+</sup>]. Anal. Calcd for C<sub>16</sub>H<sub>13</sub>N<sub>3</sub>O (263.30): C, 72.99; H, 4.98; N, 15.96. Found: C, 72.92; H, 5.03; N, 16.14

*N'*-(4-methoxybenzylidene)-1H-indole-2-carbohydrazide (7b) [69].

Prepared from 4-methoxybenzaldehyde, yield 0.03 g (30%), as an off-white powder. M.p. 104–106 °C (Lit. M.p. 98.9 °C). TLC (EtOAc: *n*-Hexane 1:2), R<sub>f</sub>: 0.35. <sup>1</sup>H NMR (DMSO-d<sub>6</sub>): δ 4.33 (s, 3H, CH<sub>3</sub>), 7.18 (d, *J* = 7.33 Hz, 2H, CH, Ar), 7.29 (s, 1H, CH, indole), 7.56–7.63 (m, 5H, CH, Ar), 7.82 (d, *J* = 6.15 Hz, 2H, CH, Ar), 8.49 (s, 1H, CH=N), 11.79 (s, 1H, NH, indole), 11.97 (s, 1H, NH, amide). <sup>13</sup>C NMR (DMSO-d<sub>6</sub>): δ 55.3 (CH<sub>3</sub>), 111.3 (CH, Ar), 115.2 (CH, Ar), 120.1 (CH, Ar), 120.8 (CH, Ar), 121.6 (CH, Ar), 129.1 (2 × CH, Ar), 129.5 (2 × CH, Ar), 131.7 (C, Ar), 133.5 (C, Ar), 138.4 (C, Ar), 140.1 (C, Ar), 146.5 (2 × CH, Ar), 157.4 (C=O). MS (EI<sup>+</sup>) *m/z*: 293.87 [M<sup>+</sup>]. Anal. Calcd for C<sub>17</sub>H<sub>15</sub>N<sub>3</sub>O<sub>2</sub> (293.30): C, 69.61; H, 5.15; N, 14.30. Found: C, 69.9; H, 5.11; N, 14.35

*N'*-(4-(dimethylamino)benzylidene)-1H-indole-2-carbohydrazide (7c) [69].

Prepared from 4-(dimethylamino)benzaldehyde, yield 0.04 g (35%), as a yellow powder. M.p. 90–92 °C (Lit. M.p. 82 °C). TLC (EtOAc: *n*-Hexane 1:2), R<sub>f</sub>: 0.35. <sup>1</sup>H NMR (DMSO-d<sub>6</sub>): δ 3.05 (m, 6H, 2 × CH<sub>3</sub>), 6.77 (t, *J* = 7.33 Hz, 1H, CH, Ar), 7.07 (s, 1H, CH, indole), 7.19 (d, *J* = 7.34 Hz, 2H, CH, Ar), 7.24 (d, *J* = 7.34 Hz, 2H, CH, Ar), 7.55 (d, *J* = 7.35 Hz, 2H, CH, Ar), 7.63–7.65 (m, 1H, CH, Ar), 8.31 (s, 1H, CH=N), 11.64 (s, 1H, NH, indole), 11.82

(s, 1H, NH, amide).  $^{13}\text{C}$  NMR (DMSO- $d_6$ ):  $\delta$  41.3 ( $2 \times \text{CH}_3$ ), 103.1 (CH, Ar), 111.8 ( $2 \times \text{CH}$ , Ar), 112.3 (CH, Ar), 119.9 (CH, Ar), 121.6 (CH, Ar), 121.8 (CH, Ar), 123.6 (C, Ar), 127.1 (CH, Ar), 128.4 (CH, Ar), 130.4 (C, Ar), 136.8 (2C, Ar), 148.1 (CH, Ar), 151.4 (C, Ar), 157.2 (C=O). MS (EI $^+$ )  $m/z$ : 306.82 [ $\text{M}^+$ ]. Anal. Calcd for  $\text{C}_{18}\text{H}_{18}\text{N}_4\text{O}$  (306.37): C, 70.57; H, 5.92; N, 18.29. Found: C, 70.51; H, 5.94; N, 17.91.

*N'*-(pyridin-3-ylmethylene)-1*H*-indole-2-carbohydrazide (**7d**) [68].

Prepared from nicotinaldehyde, yield 0.03 g (29%), as an off-white powder. M.p. 252–254 °C (Lit. M.p. 250–251 °C). TLC (EtOAc: *n*-Hexane 1:2),  $R_f$ : 0.29.  $^1\text{H}$  NMR (DMSO- $d_6$ ):  $\delta$  6.23 (t,  $J = 7.56$  Hz, 2H, CH, Ar), 7.44–7.64 (m, 4H, CH, Ar), 7.33 (d,  $J = 7.56$  Hz, 1H, CH, Ar), 7.66 (s, 1H, CH, Ar), 7.78 (d,  $J = 7.44$  Hz, 2H), 8.34 (s, 1H, CH=N), 11.66 (s, 1H, NH, indole), 11.83 (s, 1H, NH, amide).  $^{13}\text{C}$  NMR (DMSO- $d_6$ ):  $\delta$  103.8 (CH, Ar), 112.4 (CH, Ar), 120.1 (CH, Ar), 121.9 (CH, Ar), 124.1 (CH, Ar), 126.9 (CH, Ar), 129.8 (C, Ar), 130.2 (C, Ar), 133.4 (CH, Ar), 136.9 (C, Ar), 144.3 (C, Ar), 148.7 (CH, Ar), 150.7 ( $2 \times \text{CH}$ , Ar), 157.7 (C=O). MS (EI $^+$ )  $m/z$ : 264.75 [ $\text{M}^+$ ]. Anal. Calcd for  $\text{C}_{15}\text{H}_{12}\text{N}_4\text{O}$  (264.29): C, 68.17; H, 4.58; N, 21.2. Found: C, 68.21; H, 4.55; N, 20.90.

*N'*-((3-(4-ethylphenyl)-1-phenyl-1*H*-pyrazol-4-yl)methylene)-1*H*-indole-2-carbohydrazide (**8a**).

Prepared from 3-(4-ethylphenyl)-1-phenyl-1*H*-pyrazole-4-carbaldehyde (**12a**), yield 0.04 g (41%), as an off-white powder. M.p. 254–256 °C. TLC (EtOAc: *n*-Hexane 1:1),  $R_f$ : 0.42.  $^1\text{H}$  NMR (DMSO- $d_6$ ):  $\delta$  1.24 (t,  $J = 7.56$  Hz, 3H,  $\text{CH}_3$ ), 2.69 (q,  $J = 7.56$  Hz, 2H,  $\text{CH}_2$ ), 6.23 (t,  $J = 7.22$  Hz, 1H, Ar), 6.35 (t, 1H, Ar), 6.43 (s, 1H, Ar), 6.51–6.59 (m, 3H, CH, Ar), 6.71 (d,  $J = 8.25$  Hz, 2H, CH, Ar), 6.89 (d,  $J = 7.56$  Hz, 2H, CH, Ar), 6.95 (d,  $J = 8.25$  Hz, 2H, CH, Ar), 7.20 (d,  $J = 7.56$  Hz, 2H, CH, Ar), 7.71 (s, 1H, CH, Ar), 8.33 (s, 1H, CH=N), 11.76 (s, 1H, NH, indole), 11.85 (s, 1H, NH, amide).  $^{13}\text{C}$  NMR (DMSO- $d_6$ ):  $\delta$  15.6 ( $\text{CH}_3$ ), 28.2 ( $\text{CH}_2$ ), 103.2 (CH, Ar), 112.3 (C, Ar), 116.8 (CH, Ar), 118.8 ( $2 \times \text{CH}$ , Ar), 119.9 (CH, Ar), 121.7 (CH, Ar), 123.7 (CH, Ar), 126.8 ( $2 \times \text{CH}$ , Ar), 126.9 (CH, Ar), 128.2 (CH), 128.5 (CH, Ar), 129.4 ( $3 \times \text{CH}$ , Ar), 129.6 (C, Ar), 130.2 (C, Ar), 136.7 (2C, Ar), 139.1 (CH, Ar), 140.4 (C, Ar), 144.3 (C, Ar), 152.1 (C, Ar), 157.3 (C=O). MS (EI $^+$ )  $m/z$ : 233.14 [ $\text{M}^+$ ]. Anal. Calcd for  $\text{C}_{27}\text{H}_{23}\text{N}_5\text{O}$  (433.52): C, 74.81; H, 5.84; N, 15.35. Found: C, 74.85; H, 5.49; N, 15.24.

*N'*-((1-phenyl-3-(4-propylphenyl)-1*H*-pyrazol-4-yl)methylene)-1*H*-indole-2-carbohydrazide (**8b**).

Prepared from 1-phenyl-3-(4-propylphenyl)-1*H*-pyrazole-4-carbaldehyde (**12b**), yield 0.04 g (39%), as an off-white powder. M.p. 219–221 °C. TLC (EtOAc: *n*-Hexane 1:2),  $R_f$ : 0.51.  $^1\text{H}$  NMR (DMSO- $d_6$ ):  $\delta$  0.93 (t,  $J = 7.4$  Hz, 3H,  $\text{CH}_3$ ), 1.65 (sext,  $J = 7.3$  Hz, 2H,  $\text{CH}_2$ ), 2.63 (t,  $J = 7.4$  Hz, 2H,  $\text{CH}_2$ ), 6.22 (t,  $J = 7.56$  Hz, 1H, CH, Ar), 6.33 (t,  $J = 7.56$  Hz, 1H, CH, Ar), 6.44 (s, 1H, CH, Ar), 6.55–6.61 (m, 3H, CH, Ar), 6.69 (d,  $J = 8.25$  Hz, 2H, CH, Ar), 6.75 (t,  $J = 7.90$  Hz, 2H, CH, Ar), 6.81 (d,  $J = 8.25$  Hz, 2H, CH, Ar), 7.19 (d,  $J = 7.56$  Hz, 2H, CH, Ar), 7.73 (s, 1H, CH, Ar), 8.33 (s, 1H, CH=N), 11.76 (s, 1H, NH, indole), 11.85 (s, 1H, NH, amide).  $^{13}\text{C}$  NMR (DMSO- $d_6$ ):  $\delta$  13.7 ( $\text{CH}_3$ ), 24.1 ( $\text{CH}_2$ ), 37.9 ( $\text{CH}_2$ ), 103.4 (CH, Ar), 112.5 (C, Ar), 116.8 (CH, Ar), 118.8 ( $2 \times \text{CH}$ , Ar), 119.9 (CH, Ar), 121.7 (CH, Ar), 123.8 (CH, Ar), 126.8 (CH, Ar), 126.9 (CH, Ar), 127.1 (CH, Ar), 128.3 (CH), 128.7 (CH, Ar), 129.4 ( $2 \times \text{CH}$ , Ar), 129.5 ( $2 \times \text{CH}$ , Ar), 130.2 (C, Ar), 137.8 (2C, Ar), 139.5 (C, Ar), 140.3 (C, Ar), 143.5 (C, Ar), 152.5 (C, Ar), 156.5 (C=O). MS (EI $^+$ )  $m/z$ : 447.79 [ $\text{M}^+$ ]. Anal. Calcd for  $\text{C}_{28}\text{H}_{25}\text{N}_5\text{O}$  (447.54): C, 75.15; H, 5.63; N, 15.65. Found: C, 75.11; H, 5.89; N, 15.64.

*N'*-((3-(4-isopropylphenyl)-1-phenyl-1*H*-pyrazol-4-yl)methylene)-1*H*-indole-2-carbohydrazide (**8c**).

Prepared from 3-(4-isopropylphenyl)-1-phenyl-1*H*-pyrazole-4-carbaldehyde (**12c**), yield 0.03 g (39%), as an off-white powder. M.p. 219–221 °C. TLC (EtOAc: *n*-Hexane 1:2),  $R_f$ : 0.52.  $^1\text{H}$  NMR (DMSO- $d_6$ ):  $\delta$  1.26 (d,  $J = 6.9$  Hz, 6H,  $2 \times \text{CH}_3$ ), 2.97 (sept,  $J = 6.8$  Hz, 1H, CH), 7.07 (t,  $J = 7.56$  Hz, 1H, CH, Ar), 7.16 (t,  $J = 7.56$  Hz, 1H, CH, Ar), 7.29 (s, 1H, CH, Ar), 7.32–7.39 (m, 3H, CH, Ar), 7.43–7.52 (m, 3H, CH, Ar), 7.61 (d,  $J = 7.61$  Hz, 2H, CH, Ar), 7.73 (d,  $J = 7.58$  Hz, 2H, CH, Ar), 7.94 (d,  $J = 7.57$  Hz, 2H, CH, Ar), 8.52 (s, 1H, CH, Ar), 8.64 (s, 1H, CH=N), 11.79 (s, 1H, NH, indole), 11.93 (s, 1H, NH, amide).  $^{13}\text{C}$  NMR (DMSO- $d_6$ ):  $\delta$  23.8 ( $2 \times \text{CH}_3$ ), 33.3 (CH), 103.7 (CH, Ar), 113.1 (C, Ar), 116.9 (CH, Ar), 118.8 ( $2 \times \text{CH}$ ,

Ar), 119.9 (CH, Ar), 121.1 (CH, Ar), 123.7 (CH, Ar), 126.7 (2 × CH, Ar), 126.9 (2 × CH, Ar), 127.0 (2 × CH, Ar), 128.5 (2 × CH, Ar), 129.6 (C, Ar), 130.1 (C, Ar), 136.8 (2C, Ar), 139.1 (CH, Ar), 140.4 (C, Ar), 149.9 (C, Ar), 153.3 (C, Ar), 157.8 (C=O). MS (EI<sup>+</sup>) *m/z*: 447.45 [M<sup>+</sup>]. Anal. Calcd for C<sub>28</sub>H<sub>25</sub>N<sub>5</sub>O (447.54): C, 75.15; H, 5.63; N, 15.65. Found: C, 75.11; H, 5.89; N, 15.85.

*N'*-((3-(4-isobutylphenyl)-1-phenyl-1*H*-pyrazol-4-yl)methylene)-1*H*-indole-2-carbohydrazide (**8d**).

Prepared from 3-(4-isobutylphenyl)-1-phenyl-1*H*-pyrazole-4-carbaldehyde (**12d**), yield 0.04 g (42%), as an off-white powder. M.p. 229–231 °C. TLC (EtOAc: Hexane 1:2), R<sub>f</sub>: 0.45. <sup>1</sup>H NMR (DMSO-*d*<sub>6</sub>): δ 0.88 (d, *J* = 6.7 Hz, 6H, 2 × CH<sub>3</sub>) 1.88 (m, 1 H, CH), 2.51 (d, *J* = 6.8 Hz, 2H, CH<sub>2</sub>), 7.07 (t, *J* = 6.6 Hz, 1H, CH, Ar), 7.21 (t, *J* = 7.5 Hz, 1H, CH, Ar), 7.29 (s, 1H, CH, Ar), 7.35 (t, *J* = 6.9 Hz, 2H, CH, Ar), 7.49–7.56 (m, 2H, CH, Ar), 7.63 (d, *J* = 7.4 Hz, 2H, CH, Ar), 7.68–7.72 (m, 3H, CH, Ar), 8.03 (d, *J* = 7.5 Hz, 2H, CH, Ar), 8.53 (s, 1H, CH, Ar), 8.69 (s, 1H, CH=N), 11.78 (s, 1H, NH, indole), 11.92 (s, 1H, NH, amide). <sup>13</sup>C NMR (DMSO-*d*<sub>6</sub>): δ 22.1 (2 × CH<sub>3</sub>), 29.6 (CH), 44.3 (CH<sub>2</sub>), 103.2 (CH, Ar), 112.4 (C, Ar), 116.8 (CH, Ar), 118.8 (CH, Ar), 119.9 (CH, Ar), 121.7 (CH, Ar), 123.7 (2 × CH, Ar), 126.8 (CH, Ar), 126.9 (CH, Ar), 127 (CH, Ar), 128.2 (CH, Ar), 129.4 (C, Ar), 129.5 (2 × CH, Ar), 129.6 (2 × CH, Ar), 130.1 (C, Ar), 136.8 (C, Ar), 139.1 (C, Ar), 141.3 (C, Ar), 141.8 (CH, Ar), 151.8 (2C, Ar), 157.2 (C=O). MS (EI<sup>+</sup>) *m/z*: 461 [M<sup>+</sup>]. Anal. Calcd for C<sub>29</sub>H<sub>27</sub>N<sub>5</sub>O (461.57): C, 75.46; H, 5.90; N, 15.17. Found: C, 75.30; H, 6.11; N, 15.20.

*N'*-((3-(benzo[*d*][1,3]dioxol-5-yl)-1-phenyl-1*H*-pyrazol-4-yl)methylene)-1*H*-indole-2-carbohydrazide (**8e**).

Prepared from 3-(benzo[*d*][1,3]dioxol-5-yl)-1-phenyl-1*H*-pyrazole-4-carbaldehyde (**12e**), yield 0.03 g (33%), as an off-white powder. M.p. 239–241 °C. TLC (EtOAc: *n*-Hexane 1:2), R<sub>f</sub>: 0.35. <sup>1</sup>H NMR (DMSO-*d*<sub>6</sub>): δ 5.29 (s, 2H, CH<sub>2</sub>), 6.31–6.37 (m, 2H, CH, Ar), 6.49 (s, 1H, CH, Ar), 6.57–6.62 (m, 3H, CH, Ar), 6.62 (d, *J* = 8.25 Hz, 1H, CH, Ar), 6.73 (d, *J* = 7.90 Hz, 4H, CH, Ar), 6.89 (d, *J* = 8.25 Hz, 1H, CH, Ar), 7.20 (s, 1H, CH, Ar), 7.71 (s, 1H, CH, Ar), 8.33 (s, 1H, CH=N), 11.76 (s, 1H, NH, indole), 11.85 (s, 1H, NH, amide). <sup>13</sup>C NMR (DMSO-*d*<sub>6</sub>): δ 101.3 (CH<sub>2</sub>), 103.3 (CH, Ar), 108.6 (CH, Ar), 108.7 (CH, Ar), 112.3 (C, Ar), 116.7 (2 × CH, Ar), 118.8 (C, Ar), 119.9 (CH, Ar), 121.7 (CH, Ar), 122.5 (CH, Ar), 123.7 (CH, Ar), 124.1 (CH, Ar), 126.9 (2C, Ar), 127.2 (CH, Ar), 127.5 (CH, Ar), 130.2 (CH, Ar), 130.5 (CH, Ar), 136.8 (C, Ar), 139.0 (C, Ar), 140.3 (CH, Ar), 147.6 (C, Ar), 147.7 (C, Ar), 151.6 (C, Ar), 157.2 (C=O). MS (EI<sup>+</sup>) *m/z*: 449 [M<sup>+</sup>]. Anal. Calcd for C<sub>29</sub>H<sub>27</sub>N<sub>5</sub>O (461.57): C, 69.48; H, 4.26; N, 15.58. It was Found: H, 4.16; C, 69.03; N, 15.22.

*N'*-((5-chloro-1-(3,4-dinitrophenyl)-3-methyl-1*H*-pyrazol-4-yl)methylene)-1*H*-indole-2-carbohydrazide (**8f**).

Prepared from 5-chloro-1-(3,4-dinitrophenyl)-3-methyl-1*H*-pyrazole-4-carbaldehyde, yield 0.04 g (37%), as an off-white powder. M.p. 204–206 °C. TLC (EtOAc: *n*-Hexane 1:2), R<sub>f</sub>: 0.37. <sup>1</sup>H NMR (DMSO-*d*<sub>6</sub>): δ 1.65 (s, 3H, CH<sub>3</sub>), 6.24–6.26 (m, 2H, CH, Ar), 6.49 (s, 1H, CH, Ar), 6.59 (d, *J* = 7.4 Hz, 2H, CH, Ar), 6.78 (d, *J* = 8.26 Hz, 2H, CH, Ar), 8.02 (s, 1H, CH, Ar), 8.63 (s, 1H, CH=N), 11.76 (s, 1H, NH, indole), 11.85 (s, 1H, NH, amide). <sup>13</sup>C NMR (DMSO-*d*<sub>6</sub>): δ 18.4 (CH<sub>3</sub>), 101.8 (CH, Ar), 103.1 (CH, Ar), 112.2 (CH, Ar), 112.3 (C, Ar), 119.6 (C, Ar), 119.8 (C, Ar), 121.3 (CH, Ar), 121.6 (CH, Ar), 123.0 (CH, Ar), 123.6 (CH, Ar), 127.0 (CH, Ar), 127.1 (CH, Ar), 130.1 (C, Ar), 130.4 (C, Ar), 136.2 (C, Ar), 136.6 (C, Ar), 147.7 (C, Ar), 157.3 (C, Ar), 161.3 (C=O). MS (EI<sup>+</sup>) *m/z*: 467.79 [M<sup>+</sup>]. Anal. Calcd for C<sub>20</sub>H<sub>14</sub>ClN<sub>7</sub>O<sub>5</sub> (467.83): C, 51.35; H, 3.02; N, 20.96. Found: C, 51.34; H, 3.04; N, 20.91

### 3.3. MTT-Cell Proliferation Assay and Morphological Evaluation

Evaluating the cytotoxicity of tested compounds on two cancer cell lines (A549/lung and MDA-MB-231/breast adenocarcinoma) and non-cancerous (MDCK/kidney cells) was performed while adopting the formerly described method with small alterations [70]. Cancer cell lines were propagated within Dulbecco's Modified Eagle Medium-High Glucose (Cat.#: P0103; DMEM\_High Glucose with Na.Pyruvate and stable Glutamine, Biowest<sup>TM</sup>, Nuaillé, France), while MDA-MB-231 cells were propagated within RPMI-1640 L-Glutamine medium

(Cat.#:12-604F; Lonza-Verviers SPRL<sup>TM</sup>, Verviers, Belgium). The culturing media were supplemented via 1% antibiotic-antimycotic 100X (Cat.#: L0010; Biowest<sup>TM</sup>, Nuaille, France) and 10% fetal bovine serum (FBS) (Cat.#: EU-000-H; Seralab<sup>TM</sup>, West Sussex, UK). Cells were seeded as triplicates within 96-well plate, at  $1 \times 10^4$  cells per well density, after being counted and viability checked using the trypan blue staining solution (Cat.# ab233465; Abcam<sup>TM</sup>, Cambridge, MA, USA). Seeded cells were permitted to adhere for 24 h under 5% CO<sub>2</sub> and at 37 °C incubating conditions. The assigned compounds were dissolved in 500 µL DMSO affording the stock solution (100 mM) being ready for more diluting within the whole medium to obtain the compound's final concentrations; 0.1, 1, 10, 100 µM for cell treatments. Notably, the final DMSO-culture medium concentration was not allowed to exceed 0.2% (*v/v*) [71]. Following 24 h compound-cell treatment, the medium was substituted by fresh one and cells were permitted to develop for 48 h. At four hours prior the end of incubation, 10 µL MTT Sigma-Aldrich<sup>TM</sup> (5 mg/mL in PBS 1X without magnesium and calcium; Cat.# 17-516F, Lonza-Verviers<sup>TM</sup>, Basel, Switzerland) were added to all wells. Following the complete 48 h incubation, 100 µL DMSO was all added to all wells where they were subsequently centrifuged at 4000 rpm for 5 min allowing the formazan crystals of formazan to precipitate. Color was established and intensities were recorded at 490 nm using Synergy-Neo2<sup>®</sup> Hybrid MultiMode Plate Reader (BioTek<sup>TM</sup>, Winooski, VT, USA), while subtracting the multi-well plates background absorbance at 690 nm. Percentage cell viability was estimated using the subsequent formula: % cell-viability = (average absorbance of treated wells/average absorbance of controls) × 100.

### 3.4. SRB Cytotoxicity Assay

MDA-MB-231: Breast Cancer cell line was obtained from Nawah<sup>TM</sup> Scientific Inc., (Cairo, Egypt). Cells were maintained within DMEM provided by 100 units/mL of penicillin, 100 mg/mL streptomycin, and 10% of heat-inactivated FBS within 5% (*v/v*) CO<sub>2</sub> humidified atmosphere (37 °C). The validity of cell line was evaluated adopting the previously reported approach [72]. Briefly, an accurate volume (100 µL) of cell line suspension ( $5 \times 10^3$  cells) was placed in 96-well plates and incubated for 24 h within complete media [73]. Cell line suspensions were then treated with another 100 µL media spiked with various drug concentrations (0.01, 0.1, 1, 10, 100 µM/mL) and kept for 72 h. Then the media were replaced with 150 µL of 10% trichloroacetic acid (TCA) for fixing cells through subsequent 1 h incubation at 4 °C [74]. Following incubation, TCA was removed, and cells were washed via distilled water 5 times. Aliquots of 70 µL SRB solution (0.4% *w/v*; Cat.# S1402; Sigma-Aldrich<sup>TM</sup>, Taufkirchen, Germany) were added and cell were then incubated in dark for 10 min at 25 °C. Plates were subjected to triplicate washing via 1% acetic acid and then permitted to be air-dried overnight [62]. Protein-bound SRB stain was extracted by addition of tris base (150 µL, 10 mM) and the absorbance was measured at 540 nm using FLUOstar-Omega<sup>®</sup> microplate reader (BMG-Labtech<sup>TM</sup> GmbH, Ortenberg, Germany) [75].

### 3.5. Morphological Evaluation

The impact of this tested final compounds on the morphology of treated MDA-MB-231/breast cancer cell line was investigated, through planting cells within 6-well plates and subsequently incubated with 0.1, 1, 10, 100 µM of **8b** for 24 h. Variations within the cells' morphology were identified via Olympus<sup>®</sup>-CKX53 Inverted Metallurgical light microscope (Olympus<sup>TM</sup>, Center Valley, PA, USA), snapped by Olympus<sup>®</sup> Digital Camera, and analyzed by OLYMPUS<sup>®</sup> Stream image analysis software [76].

### 3.6. Flow Cytometer Analysis

Apoptotic assay and cell cycle analysis were proceeded according to previous literatures [77]. In brief, cells were planted in  $1.0 \times 10^6$  cells/flask density for 24 h. Subsequently, **8b** was added at its IC<sub>50</sub> value and incubated for 48 h. Following incubation, MDA-MB-231 cells were trypsinized, harvested, and fixed according to information cited within Annexin<sup>®</sup> V-FITC Detection Kit (Cat.#: K101-25, BioVision<sup>TM</sup>, Milpitas, CA, USA), for quantifying

cell's DNA contents being treated with **8b** relative to control sample using propidium iodide stain (Cat.#: ab139418; Abcam™, Cambridge, MA, USA). Finally, flow cytometry analysis was done using BD-FACSCalibur® cell analyzer platform (Becton Dickinson-Biosciences-SG™, Singapore, Thailand) to estimate which cell cycle phase, the treated cells would be arrested in, as well as computing the percentage of apoptotic cells.

### 3.7. DNA Fragmentation Assay

DNA isolation was performed through planting MDA-MB-231/breast cells at  $0.16 \times 10^6$  density, prior to incubation at 37 °C/humidified 5% CO<sub>2</sub> overnight [78]. Following 48 h exposure time, cells were harvested, washed and lysed via DNA-extraction buffer at 37 °C overnight. The lysate was incubated after that with 100 µg/mL Micro-pestle® DNase/RNase-free (Cat.#: 9097.1; Carl-Roth™, Karlsruhe, Germany) at 37 °C for 2 h, which was followed by three extraction processes using phenol:CHCl<sub>3</sub> (1:1 v/v) (Bioflux™, Selangor, Malaysia). A consequent re-extraction was done using CHCl<sub>3</sub> and then the organic solvent was centrifuged for 5 min at 12,000 rpm within 4 °C conditions. Extracted DNA was precipitated via ice-cold 3 M sodium acetate and absolute ethanol for 1 h at -20 °C, which was then proceeded through centrifugation (15 min—at 12,000 rpm—4 °C). After washed with 70% ethyl alcohol, DNA pellets were air-dried, dissolved within 40 µL Tris-HCl/EDTA (pH 8.0), and then electrophoresed on 1.5% agarose gel for their final staining using ethidium bromide within Tris/acetate/EDTA buffer. DNA fragments were photographed using GelDoc-Go® System (Bio-Rad™, Hercules, CA, USA).

### 3.8. Real-Time PCR Analysis

Quantitative Real-time PCR was operated on Rotor-Gene Q® PCR system as a reader (Cat.#: 204774; Qiagen™, Milan, Italy) via GenElute® RNA extraction/SIGMA PCR kit (Cat.#: REI10; Qiagen™, Milan, Italy)<sup>86</sup>. Cells were treated with IC<sub>50</sub> of **8b** for 48 h and total RNA was extracted from the non-treated and treated cells. RNA purity was assessed via Nanodrop® 2000/2000c UV-Vis spectrophotometer (Thermo-Scientific™, Bilbao, Spain). Synthesis of cDNA was proceeded using QuantiNova® Reverse Transcription Kit (Cat.#: RTN30; Qiagen™, Milan, Italy) and the subsequent PCR tests were conducted via single tubes. Specific forward/reverse primer pairs were selected for investigated (*Casp-3*, *-8*, *-9*, *BAX*, and *Bcl2*). Obtained results were expressed within Cycle threshold (Ct) values, while relative quantitation of each measured gene was assessed based on  $\Delta\Delta Ct$  calculations as represented in Table 5 [79].

**Table 5.** Specific forward/reverse primer sequence of *Casp-3*, *-8*, *-9*, *BAX* and *Bcl2*.

Gene	Forward	Reverse
<i>BAX</i>	5'-AGTGGCAGCTGACATGTTTT-3'	5'-GGAGGAAGTCCAATGTCCAG-3'
<i>Casp-3</i>	5'-GGCCCTGAAATACGAAGTC-3'	5'-GGCAGTAGTCCACTCTGAAG-3'
<i>Casp-8</i>	5'-GCCTCCCTCAAGTTCCT-3'	5'-CCTGGAGTCTCTGGAATAACA-3'
<i>Casp-9</i>	5'-CGAACTAACAGGCAAGCAG-3'	5'-ACCTCACCAAATCCTCCAGAAC-3'
<i>Bcl-2</i>	5'-CCTGTGGATGACTGAGTACC-3'	5'-GAGACAGCCAGGAGAAATCA-3'

### 3.9. ELISA Assay

Quantikine® Colorimetric Sandwich-ELISA Kit (Cat.#: DCTC0; R&D Systems, Minneapolis, MN, USA) was used for quantitating the targeted human cytochrome c protein through immunoassay protocol [80]. Based on manufacturer's instructions, MDA-MB-231/breast cancer cells were incubated with **8b** at its approximated IC<sub>50</sub>, for 48 h. Following incubation, both non-treated and treated cells were subjected to lysis via cell extraction buffer. Lysates were then diluted by standard diluent buffer over the assay range, and then estimated for human cytochrome-c protein.

### 3.10. Molecular Docking Studies

Molecular docking experiments were performed on the 14 investigated using Molecular Operating Environment (MOE) software as reported in previous work with few modifications [81–83]. In brief, ligands were constructed via the MOE “builder” tool, and then proceeded through the minimization step, adopting MMFF94x forcefield and 2000 steps of conjugate-gradient approach till a gradient of 0.001 Kcal/Å was reached 0.1 RMS Kcal/mol/Å<sup>2</sup>. The atomic structure of the target protein was prepared by the MOE through 3D-protonation, at physiological pH (7), temperature of 300 K, and 0.1 mol/L salt within implicit solvent at Generalized-Born/Volume-Integral implicit solvent model. Moreover, the protein was auto-corrected for partial charges, types of atoms, and bond connectivity [11]. The adopted protocol was proceeded through the rigid receptor docking approach since the RMSD of the superimposed apo (PDB ID: 1g5m) and complexed states of Bcl-2 (PDB ID: 6qgk) showed RMSD of 0.934 Å. Thus, ligand binding would suggest non-significant impact on the protein conformational change either on local or global aspects. Throughout the adopted docking protocol, the ligand conformations were developed through the method of bond rotation, lodged within in the defined active site guided by triangular-matching approach, and then conformations were ranked via the London\_dG scores. The top ten docked poses were retained for subsequent refinement and then an energy minimization stage, within the target pocket, before they were rescored using GBVI/WSA forcefield [84]. High docking energy, RMSD values (2.0 Å threshold), and ligand interaction with relevant pocket residues, all were considered for selecting the best docking pose for each investigated ligand. Analysis and visual inspection of ligand-protein interactions was achieved using PyMol v2.0.6 Graphics System (Schrödinger<sup>TM</sup>, NY, USA) [85]. The hydrophobic interactions were determined via MOE ligand interactions tool as well as manual measurements using PyMol bond distance measurement tools.

### 3.11. Preparation of Drug-Loaded SLNs

Eight formulations of drug-SLNs were successfully prepared by the hot melting homogenization technique [48,61]. An accurate amount (450 mg) of selected lipid; either COMP (Cat.#: 3123; Gattefosse<sup>TM</sup>, Lyon, France) or GMS (Cat.#: 23A70; Sasol<sup>TM</sup>, Hamburg, Germany), was melted in a small glass vial at temperature 80 °C which exceed the melting point of both lipid. Consequently, 10 mg of drug was added and dissolved completely forming oily phase. Considering the aqueous phase, it was prepared via addition of accurate amount of surfactant (COMP or Poloxamer 188; Cat.#: 9003-11-6; Sigma-Aldrich<sup>TM</sup>, St. Louis, MO, USA) to distilled water and allowed to heat at the same temperature of oily phase. Subsequently, aqueous phase was added slowly to oily phase with stirring while keeping the temperature to yield coarse emulsion using a hot plate with stirrer (Brandstead/Thermolyne<sup>TM</sup>, Ramsey, MN, USA). The resultant preparation was homogenized at 15,000 rpm for 15 min to form fine o/w emulsion using Heidolph<sup>®</sup> silent crusher homogenizer (Heidolph<sup>TM</sup>, Schwabach, Germany) [86]. The final preparation was allowed to cool at *r.t.* to solidify the SLNs the stored at refrigerator for further study.

### 3.12. HPLC Analysis

Drug stock solution of 1 mg/mL in mobile phase: Buffer (0.1% Trifluoroacetic acid/water) and acetonitrile was prepared, and seven dilutions were prepared in concentrations of 5, 10, 25, 50, 100, 200, and 300 µg/mL. All solutions were filtered using 0.22 µm syringe filter and then 10 µl was subjected to HPLC analysis using Waters-2690 Alliance<sup>®</sup> HPLC system (Waters<sup>TM</sup>, Milford, MA, USA) [87]. Peak area of drug was noted at 254 nm. Each experiment was performed within a triplicate manner and mean peak area was plotted against the drug concentration.

### 3.13. Determination of the Drug-SLNs Parameters (Y1–3)

For estimating the encapsulation efficiency (EE%; Y1), samples of the eight formulations of drug-SLNs were subjected to vortexing for 1 min followed by centrifugation

at 15,000 rpm for 30 min using Biofuge<sup>®</sup> centrifuge (Primo-Heraeus<sup>™</sup>, Germany) [61]. For each sample, the clear supernatant collected and filtered using 0.22 µm syringe filter then 10 µl of each sample was injected and subjected to HPLC analysis at 254 nm [62]. Equation (4) was used to calculate the EE% of drug [62,88]. Dynamic light scattering (DLS) technique was applied to determine PS (Y2), ZP (Y3), and PDI of all prepared drug-SLNs using Zetasizer<sup>®</sup> (Malvern<sup>™</sup> Instruments Ltd., Malvern, UK) [86]. The measurements were done at 25 °C after appropriate dilution of each sample [49].

$$EE\% = (\text{Total amount of drug} - \text{Unentrapped amount of drug}) / (\text{Total amount of drug}) \times 100 \quad (4)$$

### 3.14. Surface Morphology of Optimized Formulation

Morphology of optimized formulation was determined by JTEM<sup>®</sup> transmission electron microscope (TEM; model 1010, JEOL<sup>®</sup>, Tokyo, Japan). A small sample of optimized formulation was spread upon collodion-coated copper grid then left to be dried for nearly 2 min allowing the SLNs-collodion adherence [74,89]. The samples were subjected to stain by addition of one drop of uranyl acetate solution. Following drying, samples were examined with TEM.

### 3.15. In-Vitro Release Study of the Optimized Formulation

The in-vitro drug-release behavior of SLNs was determined through the dialysis method [58]. The release of drug from SLNs was done using phosphate buffer saline (pH 7.4) as dissolution medium. An accurate amount of SLNs (equivalent to 5 mg drug) was taken and placed within the dialysis bag (MWCO: 12 kDa). The dialysis bag was closed from both ends and placed within 75 mL Phosphate Buffer Saline (pH 7.4) as dissolution medium. The analysis was conducted while maintaining the dissolution medium at 37 ± 1 °C and being stirred via magnetic stirrer at 100 rpm. Dissolution medium samples (2 mL) were withdrawn at pre-determined time intervals (0.5, 1, 2, 4, 8, 12, 24 and 48 h). Equal volumes of fresh dissolution medium were added to replace the withdrawn volumes for keeping sink condition [90]. The experiment was done in triplicate and the amount of drug release was measured following the same procedure as in the entrapment efficiency section.

## 4. Conclusions

The presented manuscript reported indole- and benzimidazole-based compounds with promising pro-apoptotic activity targeting the Bcl-2 biological targets. The furnished synthesized compounds owned structural diversity and chemical scaffolds that mimic the market released Bcl-2 family pan-antagonist, obatoclox. Either through replacing the pyrrole ring of obatoclox with benzimidazole or extending the structure after the indole ring, fourteen compounds were afforded belonging to three chemical series. Biological evaluation through MTT-proliferation on two solid tumor cell lines, A549/lung and MDA-MB-231/breast adenocarcinoma, provided solid evidence concerning the compounds' cytotoxic activity. Compound **8b** was considered promising for further evaluation as it possessed impressive balanced cytotoxic/safety profile on non-cancerous MDCK/kidney cell line. Further, cell cycle analysis, DNA fragmentation, apoptotic gene expression, and protein level analysis have confirmed the compound's promising anti-cancer activity and provided valuable insights regarding its molecular mechanisms. Moreover, a validated molecular docking investigation, on Bcl-2 crystallized protein, has thoroughly investigated the differential compounds' bindings at the active site, while showing good correlation between the IC<sub>50</sub> values and furnished docking scores. Finally, the introduction of compound **8b** within a well-optimized solid lipid nanoparticle formulation has improved the compound's pharmaceutical profile leading to a significant improvement at the compound's cytotoxic activity. All the above findings have introduced **8b** as a promising anti-cancer lead candidate that is worthy of future fine-tuned lead optimization and development studies and exploration of its potentiality through in-vivo preclinical investigation.



**Supplementary Materials:** The following are available online at <https://www.mdpi.com/1424-8247/14/2/113/s1>, Figure S1: Standard calibration curve of **8b** using HPLC-UV analysis, Figure S2: NMR charts of all new compounds, Table S1: The Data of Ligand-Docking Studies on Bcl-2 anti-apoptotic protein target.

**Author Contributions:** Conceptualization, I.S., A.M.N., and S.A.S.; methodology, M.I.N., S.M.K., A.M.N., S.A.S., M.Q., and M.A.T.; data curation, I.S., M.I.N., K.M.D., S.M.K., A.M.N., and M.A.T.; software, K.M.D., M.A.T., A.M.N., S.A.S., and M.Q.; resources, M.I.N., S.M.K., S.A.S., M.Q., and M.A.T.; supervision, I.S., S.M.M., and K.M.D.; original draft preparation, M.I.N., K.M.D., M.A.T., A.M.N., S.A.S., and M.Q.; writing, review, and editing, all authors. All authors have read and agreed to the published version of the manuscript.

**Funding:** This research received no external funding.

**Institutional Review Board Statement:** Not applicable.

**Informed Consent Statement:** Not applicable.

**Data Availability Statement:** The data presented in this study are available within the article or on request from the corresponding author.

**Conflicts of Interest:** The authors declare no conflict of interest.

## References

- Portt, L.; Norman, G.; Clapp, C.; Greenwood, M.; Greenwood, M.T. Anti-apoptosis and cell survival: A review. *Biochim. Biophys. Acta* **2011**, *1813*, 238–259. [CrossRef]
- Okada, H.; Mak, T.W. Pathways of apoptotic and non-apoptotic death in tumour cells. *Nat. Rev. Cancer* **2004**, *4*, 592–603. [CrossRef]
- Hengartner, M.O. The biochemistry of apoptosis. *Nature* **2000**, *407*, 770–776. [CrossRef]
- Cory, S.; Adams, J.M. The Bcl2 family: Regulators of the cellular life-or-death switch. *Nat. Rev. Cancer* **2002**, *2*, 647–656. [CrossRef]
- Youle, R.J.; Strasser, A. The BCL-2 protein family: Opposing activities that mediate cell death. *Nat. Rev. Mol. Cell Biol.* **2008**, *9*, 47–59. [CrossRef]
- Garner, T.P.; Lopez, A.; Reyna, D.E.; Spitz, A.Z.; Gavathiotis, E. Progress in targeting the BCL-2 family of proteins. *Curr. Opin. Chem. Biol.* **2017**, *39*, 133–142. [CrossRef]
- Thomas, S.; Quinn, B.A.; Das, S.K.; Dash, R.; Emdad, L.; Dasgupta, S.; Wang, X.Y.; Dent, P.; Reed, J.C.; Pellecchia, M.; et al. Targeting the Bcl-2 family for cancer therapy. *Expert Opin. Ther. Targets* **2013**, *17*, 61–75. [CrossRef]
- Yip, K.W.; Reed, J.C. Bcl-2 family proteins and cancer. *Oncogene* **2008**, *27*, 6398–6406. [CrossRef]
- Birkinshaw, R.W.; Gong, J.-N.; Luo, C.S.; Lio, D.; White, C.A.; Anderson, M.A.; Blombery, P.; Lessene, G.; Majewski, I.J.; Thijssen, R.; et al. Structures of BCL-2 in complex with venetoclax reveal the molecular basis of resistance mutations. *Nat. Commun.* **2019**, *10*, 2385. [CrossRef]
- Besbes, S.; Mirshahi, M.; Pocard, M.; Billard, C. New dimension in therapeutic targeting of BCL-2 family proteins. *Oncotarget* **2015**, *6*, 12862–12871. [CrossRef]
- Souers, A.J.; Levenson, J.D.; Boghaert, E.R.; Ackler, S.L.; Catron, N.D.; Chen, J.; Dayton, B.D.; Ding, H.; Enschede, S.H.; Fairbrother, W.J.; et al. ABT-199, a potent and selective BCL-2 inhibitor, achieves antitumor activity while sparing platelets. *Nat. Med.* **2013**, *19*, 202–208. [CrossRef] [PubMed]
- Iyer, D.; Vartak, S.V.; Mishra, A.; Goldsmith, G.; Kumar, S.; Srivastava, M.; Hegde, M.; Gopalakrishnan, V.; Glenn, M.; Velusamy, M.; et al. Identification of a novel BCL2-specific inhibitor that binds predominantly to the BH1 domain. *Febs J.* **2016**, *283*, 3408–3437. [CrossRef] [PubMed]
- Vartak, S.V.; Hegde, M.; Iyer, D.; Gaikwad, S.; Gopalakrishnan, V.; Srivastava, M.; Karki, S.S.; Choudhary, B.; Ray, P.; Santhoshkumar, T.R.; et al. A novel inhibitor of BCL2, Disarib abrogates tumor growth while sparing platelets, by activating intrinsic pathway of apoptosis. *Biochem. Pharmacol.* **2016**, *122*, 10–22. [CrossRef]
- Kang, M.H.; Reynolds, C.P. Bcl-2 inhibitors: Targeting mitochondrial apoptotic pathways in cancer therapy. *Clin. Cancer Res. Off. J. Am. Assoc. Cancer Res.* **2009**, *15*, 1126–1132. [CrossRef]
- Paik, P.K.; Rudin, C.M.; Pietanza, M.C.; Brown, A.; Rizvi, N.A.; Takebe, N.; Travis, W.; James, L.; Ginsberg, M.S.; Juergens, R.; et al. A phase II study of obatoclax mesylate, a Bcl-2 antagonist, plus topotecan in relapsed small cell lung cancer. *Lung Cancer* **2011**, *74*, 481–485. [CrossRef]
- Li, J.; Viallet, J.; Haura, E.B. A small molecule pan-Bcl-2 family inhibitor, GX15-070, induces apoptosis and enhances cisplatin-induced apoptosis in non-small cell lung cancer cells. *Cancer Chemother. Pharmacol.* **2008**, *61*, 525–534. [CrossRef]
- Zhai, D.; Jin, C.; Satterthwait, A.C.; Reed, J.C. Comparison of chemical inhibitors of antiapoptotic Bcl-2-family proteins. *Cell Death Differ.* **2006**, *13*, 1419–1421. [CrossRef]
- Tse, C.; Shoemaker, A.R.; Adickes, J.; Anderson, M.G.; Chen, J.; Jin, S.; Johnson, E.F.; Marsh, K.C.; Mitten, M.J.; Nimmer, P.; et al. ABT-263: A potent and orally bioavailable Bcl-2 family inhibitor. *Cancer Res.* **2008**, *68*, 3421–3428. [CrossRef]

19. Koehler, B.C.; Jassowicz, A.; Scherr, A.L.; Lorenz, S.; Radhakrishnan, P.; Kautz, N.; Elssner, C.; Weiss, J.; Jaeger, D.; Schneider, M.; et al. Pan-Bcl-2 inhibitor Obatoclax is a potent late stage autophagy inhibitor in colorectal cancer cells independent of canonical autophagy signaling. *BMC Cancer* **2015**, *15*, 919. [CrossRef]
20. Schwartz-Roberts, J.L.; Shajahan, A.N.; Cook, K.L.; Wärrri, A.; Abu-Asab, M.; Clarke, R. GX15-070 (obatoclax) induces apoptosis and inhibits cathepsin D- and L-mediated autophagosomal lysis in antiestrogen-resistant breast cancer cells. *Mol. Cancer Ther.* **2013**, *12*, 448–459. [CrossRef]
21. Stamelos, V.A.; Fisher, N.; Bamrah, H.; Voisey, C.; Price, J.C.; Farrell, W.E.; Redman, C.W.; Richardson, A. The BH3 mimetic obatoclax accumulates in lysosomes and causes their alkalization. *PLoS ONE* **2016**, *11*, e0150696. [CrossRef] [PubMed]
22. Basit, F.; Cristofanon, S.; Fulda, S. Obatoclax (GX15-070) triggers necroptosis by promoting the assembly of the necrosome on autophagosomal membranes. *Cell Death Differ.* **2013**, *20*, 1161–1173. [CrossRef] [PubMed]
23. Zhong, D.; Gu, C.; Shi, L.; Xun, T.; Li, X.; Liu, S.; Yu, L. Obatoclax induces G1/G0-phase arrest via p38/p21(waf1/Cip1) signaling pathway in human esophageal cancer cells. *J. Cell Biochem.* **2014**, *115*, 1624–1635. [CrossRef]
24. Zacarias-Lara, O.J.; Correa-Basurto, J.; Bello, M. Exploring the conformational and binding properties of unphosphorylated/phosphorylated monomeric and trimeric Bcl-2 through docking and molecular dynamics simulations. *Biopolymers* **2016**, *105*, 393–413. [CrossRef]
25. Cornils, B. *Philips Reaction*. In *Catalysis from A to Z*; Herrmann, W., Cornils, B., Zanthoff, H., Xu, J.-H., Eds.; Wiley & Sons: New York, NY, USA, 2020. [CrossRef]
26. Achar, K.C.; Hosamani, K.M.; Seetharamareddy, H.R. In-vivo analgesic and anti-inflammatory activities of newly synthesized benzimidazole derivatives. *Eur. J. Med. Chem.* **2010**, *45*, 2048–2054. [CrossRef]
27. Colella, M.; Degennaro, L.; Luisi, R. Continuous flow synthesis of heterocycles: A recent update on the flow synthesis of indoles. *Molecules* **2020**, *25*, 3242. [CrossRef]
28. Kumar, S.; Kumar, P.; Sati, N. Synthesis and biological evaluation of Schiff bases and azetidiones of 1-naphthol. *J. Pharm. Bioallied Sci.* **2012**, *4*, 246–249. [CrossRef]
29. Kishk, S.M.; McLean, K.J.; Sood, S.; Smith, D.; Evans, J.W.D.; Helal, M.A.; Gomaa, M.S.; Salama, I.; Mostafa, S.M.; de Carvalho, L.P.S.; et al. Design and synthesis of imidazole and triazole pyrazoles as mycobacterium tuberculosis CYP121A1 inhibitors. *ChemistryOpen* **2019**, *8*, 995–1011. [CrossRef]
30. Berridge, M.V.; Herst, P.M.; Tan, A.S. Tetrazolium dyes as tools in cell biology: New insights into their cellular reduction. *Biotechnol. Ann. Rev.* **2005**, *11*, 127–152.
31. Kalluri, R.; Weinberg, R.A. The basics of epithelial-mesenchymal transition. *J. Clin. Investig.* **2009**, *119*, 1420–1428. [CrossRef]
32. Van den Eijnde, S.M.; Luijsterburg, A.J.; Boshart, L.; De Zeeuw, C.I.; van Dierendonck, J.H.; Reutelingsperger, C.P.; Vermeij-Keers, C. In situ detection of apoptosis during embryogenesis with annexin V: From whole mount to ultrastructure. *Cytometry* **1997**, *29*, 313–320. [CrossRef]
33. Darzynkiewicz, Z. Critical aspects in analysis of cellular DNA content. *Curr. Protoc. Cytom.* **2011**, *56*, 1–8. [CrossRef]
34. Darzynkiewicz, Z.; Juan, G. DNA content measurement for DNA ploidy and cell cycle analysis. *Curr. Protoc. Cytom.* **2001**, *1*, 1–24. [CrossRef] [PubMed]
35. Goldsmith, K.C.; Gross, M.; Peirce, S.; Luyindula, D.; Liu, X.; Vu, A.; Sliozberg, M.; Guo, R.; Zhao, H.; Reynolds, C.P.; et al. Mitochondrial Bcl-2 family dynamics define therapy response and resistance in neuroblastoma. *Cancer Res.* **2012**, *72*, 2565–2577. [CrossRef]
36. Kumar, S. Regulation of caspase activation in apoptosis: Implications in pathogenesis and treatment of disease. *Clin. Exp. Pharmacol. Physiol.* **1999**, *26*, 295–303. [CrossRef]
37. Ouyang, L.; Shi, Z.; Zhao, S.; Wang, F.T.; Zhou, T.T.; Liu, B.; Bao, J.K. Programmed cell death pathways in cancer: A review of apoptosis, autophagy and programmed necrosis. *Cell Prolif.* **2012**, *45*, 487–498. [CrossRef]
38. Ferreira, K.S.; Kreutz, C.; Macnelly, S.; Neubert, K.; Haber, A.; Bogyo, M.; Timmer, J.; Borner, C. Caspase-3 feeds back on caspase-8, Bid and XIAP in type I Fas signaling in primary mouse hepatocytes. *Apoptosis* **2012**, *17*, 503–515. [CrossRef]
39. Mariani, M.; Karki, R.; Spennato, M.; Pandya, D.; He, S.; Andreoli, M.; Fiedler, P.; Ferlini, C. Class III  $\beta$ -tubulin in normal and cancer tissues. *Gene* **2015**, *563*, 109–114. [CrossRef]
40. Sharifi, S.; Barar, J.; Hejazi, M.S.; Samadi, N. Roles of the Bcl-2/Bax ratio, caspase-8 and 9 in resistance of breast cancer cells to paclitaxel. *Asian Pac. J. Cancer Prev.* **2014**, *15*, 8617–8622. [CrossRef]
41. Murray, J.B.; Davidson, J.; Chen, I.; Davis, B.; Dokurno, P.; Graham, C.J.; Harris, R.; Jordan, A.; Matassova, N.; Pedder, C.; et al. Establishing drug discovery and identification of hit series for the anti-apoptotic proteins, Bcl-2 and Mcl-1. *ACS Omega* **2019**, *4*, 8892–8906. [CrossRef]
42. Kontoyianni, M.; McClellan, L.M.; Sokol, G.S. Evaluation of docking performance: Comparative data on docking algorithms. *J. Med. Chem.* **2004**, *47*, 558–565. [CrossRef]
43. Severino, P.; Andreani, T.; Macedo, A.S.; Fangueiro, J.F.; Santana, M.H.A.; Silva, A.M.; Souto, E.B. Current state-of-art and new trends on lipid nanoparticles (SLN and NLC) for oral drug delivery. *J. Drug Deliv.* **2012**, *2012*, 750891. [CrossRef] [PubMed]
44. Pardeshi, C.; Rajput, P.; Belgamwar, V.; Tekade, A.; Patil, G.; Chaudhary, K.; Sonje, A. Solid lipid based nanocarriers: An overview. *Acta Pharm.* **2012**, *62*, 433–472. [CrossRef] [PubMed]
45. Mukherjee, S.; Ray, S.; Thakur, R.S. Solid lipid nanoparticles: A modern formulation approach in drug delivery system. *Indian J. Pharm. Sci.* **2009**, *71*, 349–358. [CrossRef] [PubMed]

46. Müller, R.H.; Mäder, K.; Gohla, S. Solid lipid nanoparticles (SLN) for controlled drug delivery—A review of the state of the art. *Eur. J. Pharm. Biopharm.* **2000**, *50*, 161–177. [CrossRef]
47. Ekambaram, P.; Abdul, H.S.A. Formulation and evaluation of solid lipid nanoparticles of ramipril. *J. Young Pharm. JYP* **2011**, *3*, 216–220. [CrossRef]
48. Qushawy, M.; Prabahar, K.; Abd-Alhaseeb, M.; Swidan, S.; Nasr, A. Preparation and evaluation of carbamazepine solid lipid nanoparticle for alleviating seizure activity in pentylenetetrazole-kindled mice. *Molecules* **2019**, *24*, 3971. [CrossRef]
49. Fernandes, R.S.; Silva, J.O.; Seabra, H.A.; Oliveira, M.S.; Carregal, V.M.; Vilela, J.M.C.; Andrade, M.S.; Townsend, D.M.; Colletti, P.M.; Leite, E.A.; et al.  $\alpha$ -Tocopherol succinate loaded nano-structured lipid carriers improves antitumor activity of doxorubicin in breast cancer models in vivo. *Biomed. Pharmacother.* **2018**, *103*, 1348–1354. [CrossRef]
50. Joseph, E.; Reddi, S.; Rinwa, V.; Balwani, G.; Saha, R. Design and in vivo evaluation of solid lipid nanoparticulate systems of Olanzapine for acute phase schizophrenia treatment: Investigations on antipsychotic potential and adverse effects. *Eur. J. Pharm. Sci.* **2017**, *104*, 315–325. [CrossRef]
51. Sznitowska, M.; Wolska, E.; Baranska, H.; Cal, K.; Pietkiewicz, J. The effect of a lipid composition and a surfactant on the characteristics of the solid lipid microspheres and nanospheres (SLM and SLN). *Eur. J. Pharm. Biopharm.* **2017**, *110*, 24–30. [CrossRef]
52. Priyanka, K.; Sathali, A.A. Preparation and evaluation of montelukast sodium loaded solid lipid nanoparticles. *J. Young Pharm.* **2012**, *4*, 129–137. [CrossRef] [PubMed]
53. El-Housiny, S.; Shams Eldeen, M.A.; El-Attar, Y.A.; Salem, H.A.; Attia, D.; Bendas, E.R.; El-Nabarawi, M.A. Fluconazole-loaded solid lipid nanoparticles topical gel for treatment of pityriasis versicolor: Formulation and clinical study. *Drug Deliv.* **2018**, *25*, 78–90. [CrossRef] [PubMed]
54. Zielińska, A.; Ferreira, N.R.; Durazzo, A.; Lucarini, M.; Cicero, N.; Mamouni, S.E.; Silva, A.M.; Nowak, I.; Santini, A.; Souto, E.B. Development and optimization of alpha-pinene-loaded solid lipid nanoparticles (SLN) using experimental factorial design and dispersion analysis. *Molecules* **2019**, *24*, 2683. [CrossRef] [PubMed]
55. Gardouh, A.R.; Attia, M.A.; Enan, E.T.; Elbahaie, A.M.; Fouad, R.A.; El-Shafey, M.; Youssef, A.M.; Alomar, S.Y.; Ali, Z.A.-E.; Zaitone, S.A.; et al. Synthesis and antitumor activity of doxycycline polymeric nanoparticles: Effect on tumor apoptosis in solid ehrlich carcinoma. *Molecules* **2020**, *25*, 3230. [CrossRef] [PubMed]
56. Hong, I.K.; Kim, S.I.; Lee, S.B. Effects of HLB value on oil-in-water emulsions: Droplet size, rheological behavior, zeta-potential, and creaming index. *J. Ind. Eng. Chem.* **2018**, *67*, 123–131. [CrossRef]
57. Schwarz, C.; Mehnert, W. Solid lipid nanoparticles (SLN) for controlled drug delivery. II. Drug incorporation and physicochemical characterization. *J. Microencapsul.* **1999**, *16*, 205–213. [CrossRef]
58. Fasehee, H.; Dinarvand, R.; Ghavamzadeh, A.; Esfandyari-Manesh, M.; Moradian, H.; Faghihi, S.; Ghaffari, S.H. Delivery of disulfiram into breast cancer cells using folate-receptor-targeted PLGA-PEG nanoparticles: In vitro and in vivo investigations. *J. Nanobiotechnol.* **2016**, *14*, 32. [CrossRef]
59. Jain, A.; Agarwal, A.; Majumder, S.; Lariya, N.; Khaya, A.; Agrawal, H.; Majumdar, S.; Agrawal, G.P. Mannosylated solid lipid nanoparticles as vectors for site-specific delivery of an anti-cancer drug. *J. Control. Release* **2010**, *148*, 359–367. [CrossRef]
60. Kalepu, S.; Nekkanti, V. Insoluble drug delivery strategies: Review of recent advances and business prospects. *Acta Pharm. Sin. B* **2015**, *5*, 442–453. [CrossRef]
61. Swidan, S.; Ghonaim, H.; Samy, A.; Ghorab, M. Efficacy and in vitro cytotoxicity of nanostructured lipid carriers for paclitaxel delivery. *J. Appl. Pharm. Sci.* **2016**, *6*, 18–26. [CrossRef]
62. Wang, W.; Zhang, L.; Chen, T.; Guo, W.; Bao, X.; Wang, D.; Ren, B.; Wang, H.; Li, Y.; Wang, Y.; et al. Anticancer effects of resveratrol-loaded solid lipid nanoparticles on human breast cancer cells. *Molecules* **2017**, *22*, 1814. [CrossRef] [PubMed]
63. Gutierrez-Hernández, A.; Galván-Ciprés, Y.; Domínguez-Mendoza, E.A.; Aguirre-Vidal, Y.; Estrada-Soto, S.; Almanza-Pérez, J.C.; Navarrete-Vázquez, G. Design, Synthesis, Antihyperglycemic studies, and docking simulations of benzimidazole-thiazolidinedione hybrids. *J. Chem.* **2019**, *2019*, 1650145. [CrossRef]
64. Wang, W.; Pang, J.; Ha, E.H.; Zhou, M.; Li, Z.; Tian, S.; Li, H.; Hu, Q. Development of novel NLRP3-XOD dual inhibitors for the treatment of gout. *Bioorg Med Chem Lett.* **2020**, *30*, 126944. [CrossRef] [PubMed]
65. Basceken, S.; Kaya, S.; Balci, M. Intramolecular gold-catalyzed and NaH-supported cyclization reactions of N-propargyl indole derivatives with pyrazole and pyrrole rings: Synthesis of pyrazolodiazepinoindole, pyrazolopyrazinoindole, and pyrrolopyrazinoindole. *J. Org. Chem.* **2015**, *80*, 12552–12561. [CrossRef]
66. Demurtas, M.; Baldisserotto, A.; Lampronti, I.; Moi, D.; Balboni, G.; Pacifico, S.; Vertuani, S.; Manfredini, S.; Onnis, V. Indole derivatives as multifunctional drugs: Synthesis and evaluation of antioxidant, photoprotective and antiproliferative activity of indole hydrazones. *Bioorganic Chem.* **2019**, *85*, 568–576. [CrossRef]
67. Mirfazli, S.S.; Kobarfard, F.; Firoozpour, L.; Asadipour, A.; Esfahanizadeh, M.; Tabib, K.; Shafiee, A.; Foroumadi, A. N-substituted indole carbohydrazone derivatives: Synthesis and evaluation of their antiplatelet aggregation activity. *DARU* **2014**, *22*, 65. [CrossRef]
68. Boraie, A.T.; El Ashry, S.H.; Barakat, A.; Ghabbour, H.A. Synthesis of new functionalized indoles based on ethyl indol-2-carboxylate. *Molecules* **2016**, *21*, 333. [CrossRef]
69. Al-Ebaisat, H.S.; Ababne, T.S.; Al Shboul, T.M.; Jazazi, T.M. Synthesis, characterization and antifungal activity of some substituted 4-thiazolidinone derivatives. *J. Pure Appl. Chem. Res.* **2016**, *5*, 125–130. [CrossRef]

70. Maurya, D.K.; Nandakumar, N.; Devasagayam, T.P.A. Anticancer property of gallic acid in A549, a human lung adenocarcinoma cell line, and possible mechanisms. *J. Clin. Biochem. Nutr.* **2011**, *48*, 85–90. [CrossRef]
71. Ranganathan, S.; Halagowder, D.; Sivasithambaram, N.D. Quercetin suppresses twist to induce apoptosis in MCF-7 breast cancer cells. *PLoS ONE* **2015**, *10*, e0141370. [CrossRef]
72. Koulaouzidou, E.A.; Papazisis, K.T.; Economides, N.A.; Beltes, P.; Kortsaris, A.H. Antiproliferative effect of mineral trioxide aggregate, zinc oxide-eugenol cement, and glass-ionomer cement against three fibroblastic cell lines. *J. Endod.* **2005**, *31*, 44–46. [CrossRef] [PubMed]
73. Dey, N.S.; Mukherjee, B.; Maji, R.; Satapathy, B.S. Development of linker-conjugated nanosize lipid vesicles: A strategy for cell selective treatment in breast cancer. *Curr. Cancer Drug Targets* **2016**, *16*, 357–372. [PubMed]
74. Wang, W.; Chen, T.; Xu, H.; Ren, B.; Cheng, X.; Qi, R.; Liu, H.; Wang, Y.; Yan, L.; Chen, S.; et al. Curcumin-loaded solid lipid nanoparticles enhanced anticancer efficiency in breast cancer. *Molecules* **2018**, *23*, 1578. [CrossRef] [PubMed]
75. Jung, B.; Shim, M.K.; Park, M.J.; Jang, E.H.; Yoon, H.Y.; Kim, K.; Kim, J.H. Hydrophobically modified polysaccharide-based on polysialic acid nanoparticles as carriers for anticancer drugs. *Int. J. Pharm.* **2017**, *520*, 111–118. [CrossRef]
76. Hegazy, M.G.A.; Imam, A.M.; Abdelghany, B.E. Evaluation of cytotoxic and anticancer effect of *Orobancha crenata* methanolic extract on cancer cell lines. *Tumor Biol.* **2020**, *42*, 1010428320918685. [CrossRef]
77. Tantawy, M.A.; Sroor, F.M.; Mohamed, M.F.; El-Naggar, M.E.; Saleh, F.M.; Hassaneen, H.M.; Abdelhamid, I.A. Molecular docking study, cytotoxicity, cell cycle arrest and apoptotic induction of novel chalcones incorporating thiadiazolyl isoquinoline in cervical cancer. *Anticancer Agents Med. Chem.* **2020**, *20*, 70–83. [CrossRef]
78. Zhao, Y.; Xiang, S.; Dai, X.; Yang, K. A simplified diphenylamine colorimetric method for growth quantification. *Appl. Microbiol. Biotechnol.* **2013**, *97*, 5069–5077. [CrossRef]
79. Preusse, M.; Tantawy, M.A.; Klawonn, F.; Schughart, K.; Pessler, F. Infection- and procedure-dependent effects on pulmonary gene expression in the early phase of influenza A virus infection in mice. *BMC Microbiol.* **2013**, *13*, 293. [CrossRef]
80. Petersen, H.; Mostafa, A.; Tantawy, M.A.; Iqbal, A.A.; Hoffmann, D.; Tallam, A.; Selvakumar, B.; Pessler, F.; Beer, M.; Rautenschlein, S.; et al. NS segment of a 1918 influenza a virus-descendent enhances replication of H1N1pdm09 and virus-induced cellular immune response in mammalian and avian systems. *Front. Microbiol.* **2018**, *9*, 526. [CrossRef]
81. El Raey, M.A.; El-Hagrassi, A.M.; Osman, A.F.; Darwish, K.M.; Emam, M. *Acalypha wilkesiana* flowers: Phenolic profiling, cytotoxic activity of their biosynthesized silver nanoparticles and molecular docking study for its constituents as Topoisomerase-I inhibitors. *Biocatal. Agric. Biotechnol.* **2019**, *20*, 101243. [CrossRef]
82. Malebari, A.; Ibrahim, T.; Salem, I.; Salama, I.; Khayyat, A.; Mostafa, S.; El-Sabbagh, O.; Darwish, K. The anticancer activity for the bumetanide-based analogs via targeting the tumor-associated membrane bound human carbonic anhydrase-IX enzyme. *Pharmaceuticals* **2020**, *13*, 252. [CrossRef] [PubMed]
83. Wadie, M.A.; Kishk, S.M.; Darwish, K.M.; Mostafa, S.M.; Elgawish, M.S. Simultaneous determination of losartan and rosuvastatin in rat plasma using liquid chromatography–tandem mass spectrometric technique for application into pharmacokinetic and drug–drug interaction studies. *Chromatographia* **2020**, *83*, 1477–1494. [CrossRef]
84. Vilar, S.; Cozza, G.; Moro, S. Medicinal chemistry and the molecular operating environment (MOE): Application of QSAR and molecular docking to drug discovery. *Curr. Top. Med. Chem.* **2008**, *8*, 1555–1572. [CrossRef] [PubMed]
85. *The PyMOL Molecular Graphics System, 2.0.6*; Schrödinger, LLC: New York, NY, USA, 2016.
86. Souto, E.B.; Doktorovova, S.; Zielinska, A.; Silva, A.M. Key production parameters for the development of solid lipid nanoparticles by high shear homogenization. *Pharm. Dev. Technol.* **2019**, *24*, 1181–1185. [CrossRef] [PubMed]
87. Da Rocha Lindner, G.; Khalil, N.M.; Mainardes, R.M. Resveratrol-loaded polymeric nanoparticles: Validation of an HPLC-PDA method to determine the drug entrapment and evaluation of its antioxidant activity. *Sci. World J.* **2013**, *2013*, 506083. [CrossRef]
88. Nasr, A.M.; Qushawy, M.K.; Elkhoudary, M.M.; Gawish, A.Y.; Elhady, S.S.; Swidan, S.A. Quality by design for the development and analysis of enhanced in-situ forming vesicles for the improvement of the bioavailability of fexofenadine HCl in vitro and in vivo. *Pharmaceutics* **2020**, *12*, 409. [CrossRef]
89. Aldawsari, H.M.; Singh, S. Rapid microwave-assisted cisplatin-loaded solid lipid nanoparticles: Synthesis, characterization and anticancer study. *Nanomaterials* **2020**, *10*, 510. [CrossRef]
90. Mona, Q.; Ali, N. Solid lipid nanoparticles (SLNs) as nano drug delivery carriers: Preparation, characterization and application. *Int. J. Appl. Pharm.* **2019**, *12*, 1–9.





Article

# Tryptophanol-Derived Oxazolopyrrolidone Lactams as Potential Anticancer Agents against Gastric Adenocarcinoma

Margarida Espadinha<sup>1</sup>, Valentina Barcherini<sup>1</sup>, Lídia M. Gonçalves<sup>1</sup> , Elies Molins<sup>2</sup> ,  
Alexandra M. M. Antunes<sup>3</sup> and Maria M. M. Santos<sup>1,\*</sup>

<sup>1</sup> Research Institute for Medicines (iMed.Ulisboa), Faculty of Pharmacy, Universidade de Lisboa, Av. Prof. Gama Pinto, 1649-003 Lisboa, Portugal; mespadinha@ff.ulisboa.pt (M.E.); vbarcherini@ff.ulisboa.pt (V.B.); lgoncalves@ff.ulisboa.pt (L.M.G.)

<sup>2</sup> Institut de Ciència de Materials de Barcelona (ICMAB-CSIC), Campus UAB, 08193 Bellaterra, Spain; elies.molins@icmab.es

<sup>3</sup> Centro de Química Estrutural, Instituto Superior Técnico, ULisboa, 1049-001 Lisboa, Portugal; alexandra.antunes@tecnico.ulisboa.pt

\* Correspondence: mariasantos@ff.ulisboa.pt; Tel.: +351-21-794-6451

**Abstract:** Gastric cancer is one of the deadliest cancers in modern societies, so there is a high level of interest in discovering new drugs for this malignancy. Previously, we demonstrated the ability of tryptophanol-derived polycyclic compounds to activate the tumor suppressor protein p53, a relevant therapeutic target in cancer. In this work, we developed a novel series of enantiomerically pure tryptophanol-derived small molecules to target human gastric adenocarcinoma (AGS) cells. From an initial screening of fourteen compounds in AGS cell line, a hit compound was selected for optimization, leading to two derivatives selective for AGS gastric cells over other types of cancer cells (MDA-MB-231, A-549, DU-145, and MG-63). More importantly, the compounds were non-toxic in normal cells (HEK 293T). Additionally, we show that the growth inhibition of AGS cells induced by these compounds is mediated by apoptosis. Stability studies in human plasma and human liver microsomes indicate that the compounds are stable, and that the major metabolic transformations of these molecules are mono- and di-hydroxylation of the indole ring.

**Keywords:** anticancer agents; cytotoxicity; enantioselective synthesis; gastric adenocarcinoma; tryptophanol

**Citation:** Espadinha, M.; Barcherini, V.; Gonçalves, L.M.; Molins, E.; Antunes, A.M.M.; Santos, M.M.M. Tryptophanol-Derived Oxazolopyrrolidone Lactams as Potential Anticancer Agents against Gastric Adenocarcinoma. *Pharmaceuticals* **2021**, *14*, 208. <https://doi.org/10.3390/ph14030208>

Academic Editor: Mary J. Meegan

Received: 26 January 2021

Accepted: 26 February 2021

Published: 2 March 2021

**Publisher's Note:** MDPI stays neutral with regard to jurisdictional claims in published maps and institutional affiliations.



**Copyright:** © 2021 by the authors. Licensee MDPI, Basel, Switzerland. This article is an open access article distributed under the terms and conditions of the Creative Commons Attribution (CC BY) license (<https://creativecommons.org/licenses/by/4.0/>).

## 1. Introduction

Cancer is considered a worldwide health problem, and its occurrence can be associated to a combination of environmental factors and genetic alterations [1]. According to the World Health Organization (WHO), it is estimated that in 2018, cancer contributed to 9.5 million deaths worldwide [2]. Gastric cancer (GC) ranks third in the list of deadliest cancers [1], and its occurrence and mortality are highly influenced by region and culture [3]. The survival rate of GC has not improved much over the last years. Patients with GC in early-stage, usually, do not have symptoms, which hinders the early detection of this cancer. For this reason, most patients present advanced GC and, in these cases, radical surgery is the first-line approach and the only curative treatment [4]. In the cases that surgery is not recommended, alternative treatments can be used, such as chemotherapy, radiotherapy, and immunotherapy. However, these therapeutic options only achieve modest results, and the poor response of this cancer to chemotherapy is, typically, associated to chemoresistance mechanisms [5,6]. Moreover, the severe side effects associated to drug-related toxicity are frequent [7,8]. Consequently, the discovery of new alternative therapeutics for the treatment of GC, with low cost and minimal side effects, is still urgently needed. In the last decades, the discovery of cellular mechanisms associated to malignancies has been intensive, and many anticancer agents were developed to disrupt specific biological pathways. With this, the discovery of new scaffolds increased, as well as the interest in

new therapeutic applications to scaffolds already known. For example, the indole scaffold is associated to many pharmacological activities in medicinal chemistry, including antimicrobial, antioxidant, antiviral, and anticancer [9,10]. It is considered a privileged scaffold, commonly found in many natural products (e.g., alkaloids and microbial hormones) and synthetic molecules with medicinal value (e.g., compounds **1** and **2**, Figure 1) [11].

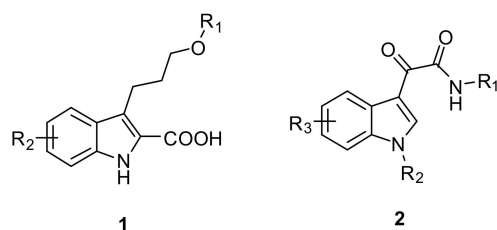
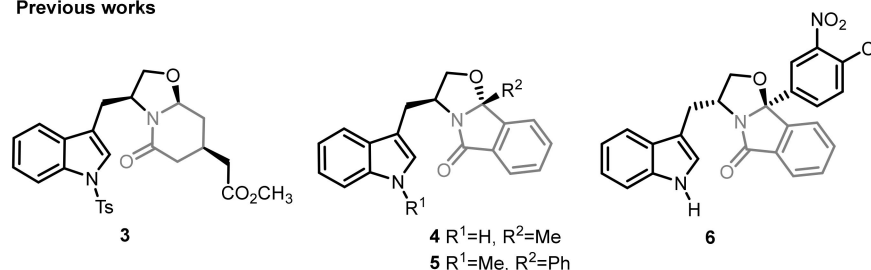


**Figure 1.** Chemical structures of indole-derived compounds with *in vitro* anticancer activity: Mcl-1 inhibitors (**1**) and tubulin inhibitors (**2**).

Other examples are tryptophanol-based small molecules (e.g., compounds **3–6**, Figure 2), reactivators of the p53 pathway, that showed *in vitro* antiproliferative activity in colon and breast cancer cells [12–17]. Specifically, tryptophanol-derived isoindolinones **4–5** presented promising *in vivo* antitumor results in xenograft mouse models, without cytotoxicity and genotoxicity [13,14,16]. Based on these results, and on reported results with pyrrolidone-based small molecules with anticancer activity [18,19], we envisioned that the merge of these two scaffolds could lead to compounds with interesting anticancer properties [15]. Herein, we report the synthesis of 29 enantiopure tryptophanol-derived oxazolopyrrolidone lactams (compounds **7** and **8**, Figure 2), their antiproliferative activity in human gastric adenocarcinoma (AGS) cell line, and *in vitro* stability and metabolic studies with this scaffold.

#### Previous works



#### This work

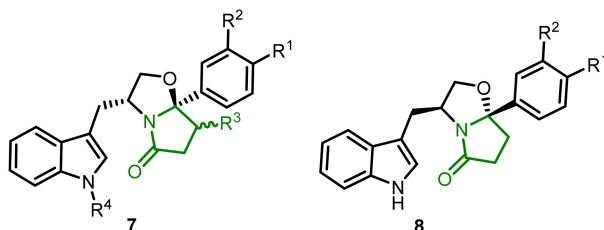


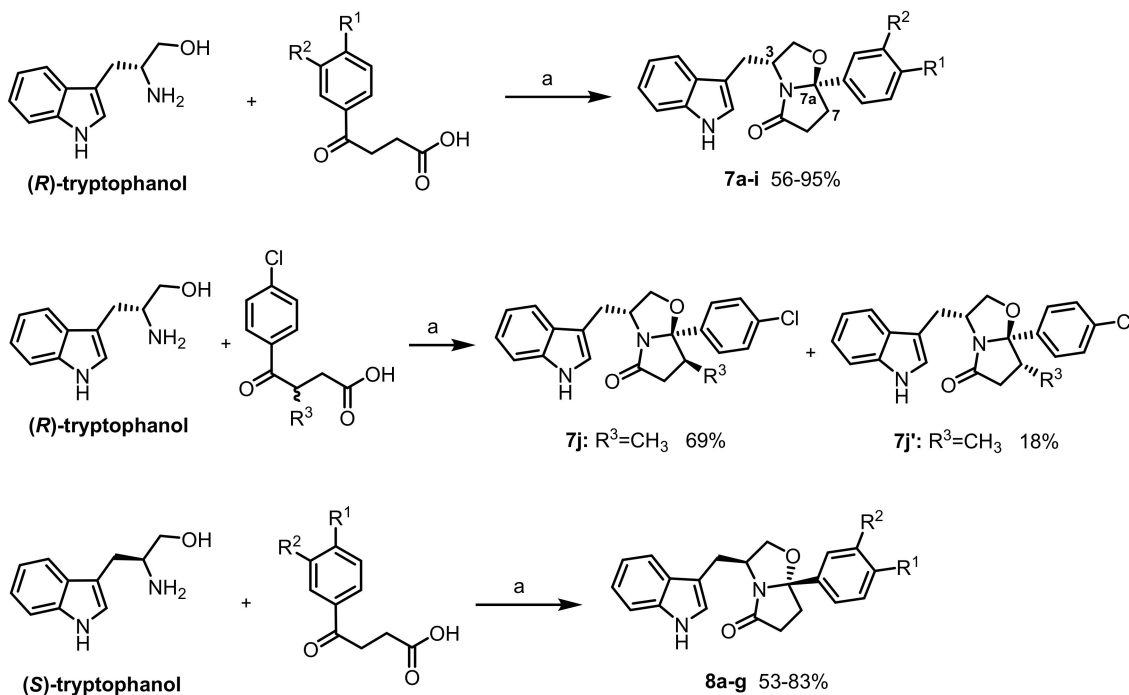
**Figure 2.** Previously reported tryptophanol-based scaffolds **3–6** and tryptophanol-derived oxazolopyrrolidones **7–8** studied in this work.

## 2. Results and Discussion

### 2.1. Chemistry

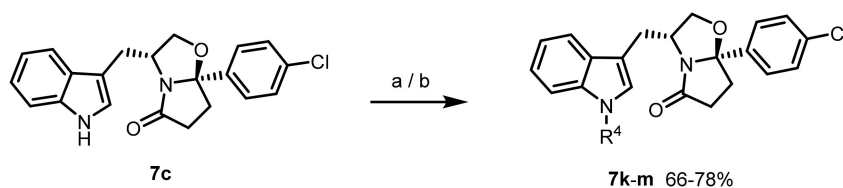
Enantiopure bicyclic lactams **7a–j**, **7j'**, and **8a–g** were easily accessed by a chiral-induced cyclocondensation reaction, starting from enantiopure tryptophanol and commercially available keto acids, in low to excellent yields (18–95%, Scheme 1) [20]. In almost all reactions, the formation of only one diastereomer was observed by thin-layer

chromatography (TLC) and proton nuclear magnetic resonance ( $^1\text{H}$  NMR). In the cyclocondensation reaction of (*R*)-tryptophanol with 4-(4-chlorophenyl)-3-methyl-4-oxobutanoic acid, in which an additional chirality center is formed, diastereomer **7j** (69% yield) was obtained, as well as the minor diastereoisomer **7j'** (18% yield).



**Scheme 1.** Synthesis of (*R*)- and (*S*)-tryptophanol-derived oxazolopyrrolidone lactams **7a–j**, **7j'**, and **8a–g**, respectively. Reaction conditions: (a) toluene, reflux, 10–25 h.

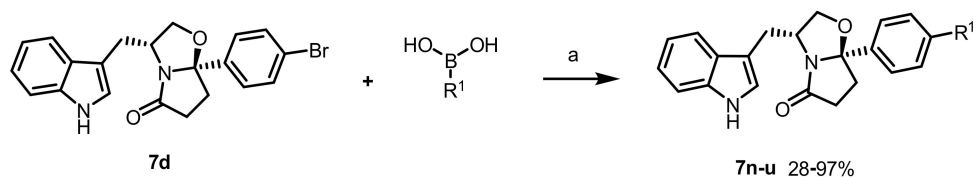
Tryptophanol-derived oxazolopyrrolidone lactams **7k–m**, with substituents on the indole nitrogen, were obtained in moderate to good yields (66–78%, Scheme 2). Specifically, compounds **7k–l** were synthesized by treatment of **7c** with sodium hydride in dimethylformamide, in the presence of iodoethane (compound **7k**) or acetic anhydride (compound **7l**). Compound **7m** was prepared by reaction of **7c** with di-*tert*-butyl dicarbonate, in the presence of 4-dimethylaminopyridine and triethylamine, in tetrahydrofuran.



**Scheme 2.** Synthesis of (*R*)-tryptophanol-derived oxazolopyrrolidone lactams **7k–m**. Reaction conditions: (a) compounds **7k–l**: ethyl iodide/acetic anhydride, NaH, DMF, 0 °C–r.t., 3–6 h; (b) compound **7m**: di-*tert*-butyl dicarbonate, DMAP, Et<sub>3</sub>N, THF, r.t., 3 h.

Compounds **7n–u** were obtained through Suzuki-Miyaura cross-coupling reaction between compound **7d** and different aryl boronic acids, using Pd(PPh<sub>3</sub>)<sub>2</sub>Cl<sub>2</sub> as catalyst (Scheme 3). Except for compound **7u**, which was obtained in low yield (28%) due to the low solubility of the boronic acid, all the other derivatives were obtained in high yields (71–97%).





**Scheme 3.** Synthesis of (*R*)-tryptophanol-derived oxazopyrrolidone lactams **7n–u**. Reaction conditions: (a) Pd(PPh<sub>3</sub>)<sub>2</sub>Cl<sub>2</sub>, aq. sol. Na<sub>2</sub>CO<sub>3</sub> (1 M), 1,4-dioxane, 100 °C, 2–5 h.

The absolute configuration of the new formed stereogenic center C-7a was established by X-ray analysis of compound **8b** (Figure 3). The <sup>13</sup>C NMR spectroscopy data of compound **8b** was used as reference to confirm the stereochemistry of the other derivatives. For compounds **7a–i** and **8a–g**, the signals of C-3, C-7a, and C-7 appear between 55.5–56.5, 101.7–102.6, and 35.0–35.4 ppm, respectively.

The spectral data obtained for compounds **7j** and **7j'** indicate that the major diastereomer **7j** has (*3R*, *7aR*, *7S*) configuration, while the minor diastereoisomer **7j'** has (*3R*, *7aR*, *7R*) configuration [21]. In particular, the methyl group appears in the <sup>1</sup>H NMR spectra as a doublet at 1.12 ppm for **7j** and at 0.60 ppm for **7j'**, and in the <sup>13</sup>C NMR spectra at 13.96 ppm for **7j** and at 16.40 ppm for **7j'**. Moreover, the methyl group induces a shift in the C-7 that appears at 39.7 ppm for compound **7j** and at 41.3 ppm for compound **7j'**. The chemical shift of C-3 appears in a higher field for diastereoisomer **7j'** (54.8 ppm). The absolute configuration of diastereomers **7j** and **7j'** was further confirmed by X-ray crystallography (Figure 3).

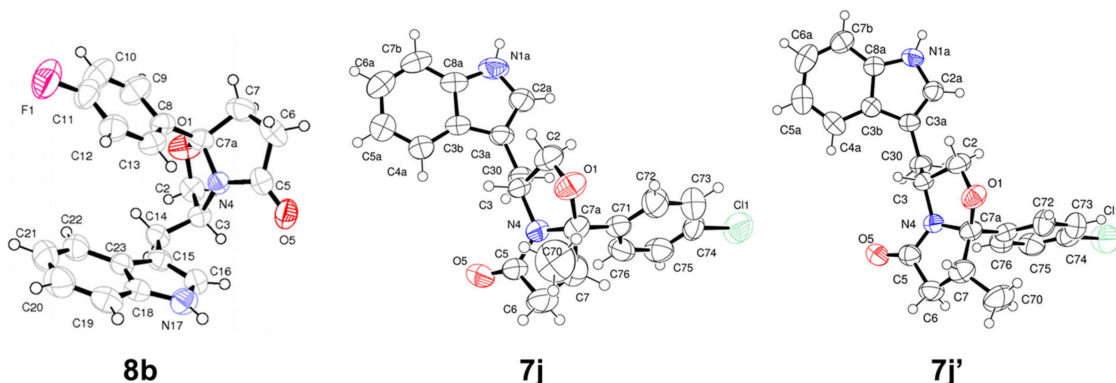


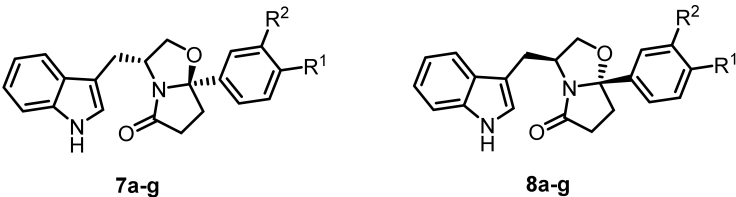
**Figure 3.** X-ray crystallographic structures of compounds **8b**, **7j**, and **7j'** (crystallographic information file (CIF) data can be found in the Supplementary Materials Tables S1–S15).

## 2.2. Effect of Tryptophanol-Derived Oxazopyrrolidone Lactams on Cell Viability and on Apoptosis

To perform a structure–activity relationship (SAR) study, a first series of tryptophanol-derived oxazopyrrolidone lactams containing different substituents on the phenyl ring (R<sup>1</sup>) at position C-7a was synthesized (compounds **7a–g** and **8a–g**, Table 1). In the design of this new compounds series, a diversity of substituents with electron donating properties (–CH<sub>3</sub> and –OCH<sub>3</sub> groups) and electron withdrawing properties (–F, –Cl, –Br, and –SO<sub>2</sub>CH<sub>3</sub> groups) were chosen. Both series of enantiomers, (*S*)- and (*R*)-tryptophanol derivatives, were synthesized to evaluate the impact of compound's stereochemistry on the antiproliferative response of AGS cells. The activity of the target compounds was assessed using the MTT reduction assay. In general, (*R*)-tryptophanol-derived oxazopyrrolidone lactams were more active than the corresponding enantiomers, except for derivative **8b** with a *para*-fluoro substituent (**7a–g** vs. **8a–g**). From the first screening at 100 μM, analogues **7a** (R<sup>1</sup> = H), **7b** (R<sup>1</sup> = F), and **8e** (R<sup>1</sup> = CH<sub>3</sub>) showed moderate antiproliferative activity, while compounds **7g** and **8g** (R<sup>1</sup> = SO<sub>2</sub>CH<sub>3</sub>) did not induce appreciable cytotoxicity. Remarkably,

compounds **7c–e** and **8c** revealed an antiproliferative response higher than 85%. The presence of chlorine or bromine substituents at R<sup>1</sup> had a positive impact on the antiproliferative activity, for both enantiomers (compounds **7c–d** and **8c–d**). The derivative **7c** (R<sup>1</sup> = Cl) exhibited the highest activity and was selected for chemical derivatizations to improve the antiproliferative activity of this scaffold in AGS cells.

**Table 1.** Screening of (*R*) and (*S*)-tryptophanol-derived oxazolopyrrolidone lactams **7a–g** and **8a–g** in AGS cell line.



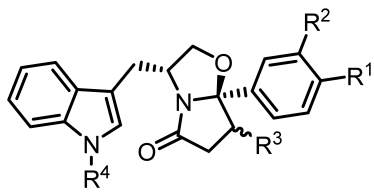
Compound	R <sup>1</sup>	R <sup>2</sup>	% CV at 100 μM <sup>1</sup>
<b>7a</b>	H	H	50 ± 5
<b>7b</b>	F	H	50 ± 8
<b>7c</b>	Cl	H	6 ± 1
<b>7d</b>	Br	H	14 ± 3
<b>7e</b>	CH <sub>3</sub>	H	14 ± 2
<b>7f</b>	OCH <sub>3</sub>	H	18 ± 2
<b>7g</b>	SO <sub>2</sub> CH <sub>3</sub>	H	94 ± 12
<b>8a</b>	H	H	58 ± 4
<b>8b</b>	F	H	22 ± 4
<b>8c</b>	Cl	H	11 ± 1
<b>8d</b>	Br	H	25 ± 4
<b>8e</b>	CH <sub>3</sub>	H	60 ± 3
<b>8f</b>	OCH <sub>3</sub>	H	30 ± 4
<b>8g</b>	SO <sub>2</sub> CH <sub>3</sub>	H	91 ± 11

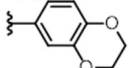
<sup>1</sup> Each % of CV (cell viability) value is the mean ± SD of triplicate of at least two different experiments. % CV determined by the MTT method after 48 h of compounds' incubation.

Four sites were identified for suitable structural modifications in compound **7c**: *meta*-position of the C-7a phenyl ring (compounds **7h** and **7i**, Scheme 1), position C-7 of the pyrrolidone ring (compounds **7j** and **7j'**, Scheme 1), alkylation of the *N*-indole (compounds **7k–m**, Scheme 2) and C–C couplings in the C-7a phenyl ring (compounds **7n–u**, Scheme 3).

The fifteen (*R*)-tryptophanol-derived oxazolopyrrolidone lactams **7h–u** and **7j'** obtained, as well as **7c**, were screened at 50 μM in AGS cell line (Table 2).

(*R*)-tryptophanol-derived oxazolopyrrolidones **7h** and **7r** showed similar antiproliferative activity to **7c**, while **7j**, **7o**, and **7s** were more active than the hit compound **7c**. The presence of a pyridine (compound **7t**) or a dioxane ring (compound **7u**) led to a decrease of the antiproliferative effect in AGS cells. Additionally, *meta*-fluoro and *para*-methoxy substituents on the phenyl ring (compound **7i**) resulted in a non-significant cell death. Compounds **7n** (R<sup>1</sup> = *p*-Cl-Ph), **7p** (R<sup>1</sup> = *p*-OH-Ph), and **7q** (R<sup>1</sup> = *p*-CH<sub>2</sub>OH-Ph), with bulky substituents, displayed moderate antiproliferative activity at 50 μM. The results also suggest that the presence of a *meta*-chloro substituent or electron withdrawing groups are important for the activity (**7r** and **7s** vs. **7n** and **7o**, **7r**, and **7s** vs. **7p** and **7q**). Interestingly, the two diastereomers **7j** and **7j'** had different effects in AGS cells. Diastereomer **7j**, with (3*R*, 7*R*, 7*a**S*) configuration, had a high antiproliferative effect, while diastereomer **7j'** (3*R*, 7*R*, 7*a**R*) had almost no effect, suggesting that the C-7a stereochemistry is also decisive for the antiproliferative activity of tryptophanol-derived oxazolopyrrolidone lactams in AGS cells.

**Table 2.** Screening of (*R*)-tryptophan-derived oxazopyrrolidone lactams **7c**, **7h–u**, and **7j'** in AGS cell line.


Compound	R <sup>1</sup>	R <sup>2</sup>	R <sup>3</sup>	R <sup>4</sup>	% CV at 50 μM <sup>1</sup>
<b>7c</b>	Cl	H	H	H	11 ± 1
<b>7h</b>	CH <sub>3</sub>	Cl	H	H	11 ± 2
<b>7i</b>	OCH <sub>3</sub>	F	H	H	84 ± 7
<b>7j</b>	Cl	H	( <i>S</i> )-CH <sub>3</sub>	H	8 ± 0
<b>7j'</b>	Cl	H	( <i>R</i> )-CH <sub>3</sub>	H	81 ± 3
<b>7k</b>	Cl	H	H	CH <sub>2</sub> CH <sub>3</sub>	40 ± 5
<b>7l</b>	Cl	H	H	COCH <sub>3</sub>	63 ± 13
<b>7m</b>	Cl	H	H	CO <sub>2</sub> C(CH <sub>3</sub> ) <sub>3</sub>	61 ± 9
<b>7n</b>	<i>p</i> -Cl-Ph	H	H	H	65 ± 13
<b>7o</b>	<i>p</i> -CF <sub>3</sub> -Ph	H	H	H	7 ± 1
<b>7p</b>	<i>p</i> -OH-Ph	H	H	H	56 ± 1
<b>7q</b>	<i>p</i> -CH <sub>2</sub> OH-Ph	H	H	H	55 ± 1
<b>7r</b>	<i>m</i> -Cl-Ph	H	H	H	17 ± 1
<b>7s</b>	3,4-Cl-Ph	H	H	H	8 ± 1
<b>7t</b>	pyridine	H	H	H	75 ± 14
<b>7u</b>		H	H	H	67 ± 6

<sup>1</sup> Each % of CV (cell viability) value is the mean ± SD of triplicate of at least two different experiments. % CV determined by the MTT method after 48 h of compounds' incubation.

The substitution of the *N*-indole hydrogen (compound **7c**) by ethyl (compound **7k**), acetyl (compound **7l**) or *tert*-butyloxycarbonyl (compound **7m**) groups led to a decrease of activity, probably due to steric effects or because the establishment of a hydrogen bond might be important for the antiproliferative effect.

The IC<sub>50</sub> values of the most promising derivatives (**7j**, **7o**, and **7s**), as well as of the hit compound **7c**, were determined in AGS cell line (Table 3). Trifluoromethyl derivative **7o** (R<sup>1</sup> = *p*-CF<sub>3</sub>-Ph) and di-halogenated derivative **7s** (R<sup>1</sup> = 3,4-Cl-Ph) were the most active derivatives with 2.3 times more potency than the hit **7c**, respectively. We then tested compounds **7o** and **7s** in four cancer cell lines of other tumor types (Table 3): MDA-MB-231 (breast adenocarcinoma), A-549 (lung carcinoma), DU-145 (prostate cancer), and MG-63 (osteosarcoma). Both compounds were much less potent in lung carcinoma cells (IC<sub>50</sub> higher than 60 μM) but presented moderate activity in prostate cancer cell line DU-145 (Table 3). In osteosarcoma and breast cells, compound **7o** was around two times more active than compound **7s**. Compounds **7o** and **7s** were then evaluated in HEK 293T normal cell line [22] and, except for A-549 cells, showed selectivity towards all cancer cell lines over the non-cancer derived cell line (Table 3).

The ability of compounds **7o** and **7s** to induce apoptosis was also explored by measuring caspase 3/7 activity in AGS cells. The assays showed that, after 48 h of compounds' incubation at 12.5 μM, there was a significant increase of caspase 3/7 activity, indicating that the antiproliferative activity is associated with apoptosis induction (Figure 4).

**Table 3.** IC<sub>50</sub> values<sup>1</sup> in cancer cell lines of selected compounds.

Compound	AGS IC <sub>50</sub> (μM)	MDA-MB-231 IC <sub>50</sub> (μM)	A-549 IC <sub>50</sub> (μM)	DU-145 IC <sub>50</sub> (μM)	MG-63 IC <sub>50</sub> (μM)	HEK 293T IC <sub>50</sub> (μM)
7c	(3.4 ± 0.2) × 10	-	-	-	-	-
7j	(2.8 ± 0.4) × 10	-	-	-	-	-
7o	(1.5 ± 0.6) × 10	(2.8 ± 0.2) × 10	(6.3 ± 1.8) × 10	(2.4 ± 0.5) × 10	26.8 ± 0.4	(5.2 ± 0.2) × 10
7s	(1.3 ± 0.4) × 10	(6.8 ± 0.6) × 10	(8.8 ± 1.7) × 10	(2.1 ± 1.2) × 10	(5.6 ± 0.7) × 10	(11.7 ± 0.6) × 10

<sup>1</sup> IC<sub>50</sub> values determined by the MTT method after 48 h of compounds' incubation. Each IC<sub>50</sub> value is the mean ± SD of, at least, three independent experiments with six replicates each.

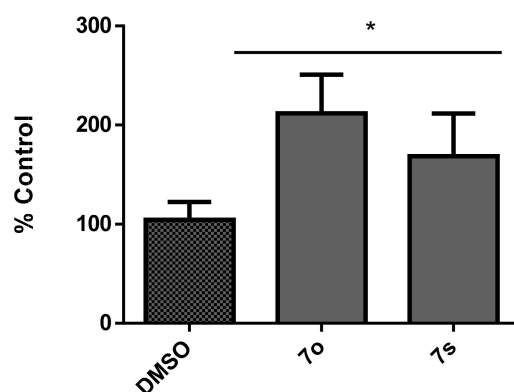


**Figure 4.** Percentage of the normalized caspase 3/7 activity in AGS cells after 48 h of exposure to the selected compounds at 12.5 μM. \* Significantly different from control for  $p < 0.05$ .

### 2.3. Stability Studies in PBS, Human Plasma, and Human Liver Microsomes and Identification of Metabolites

Preliminary stability studies can provide useful information about possible liabilities of new drug candidates. Understanding possible clearance mechanisms and how to modulate the metabolism to reduce metabolic liability of a new bioactive chemical entity is a fundamental step in drug development that allows access to a hit compound with desirable ADME attributes [23]. The in vitro phosphate saline buffer (PBS), plasma, and metabolic stabilities for compound **7s** were evaluated. This compound showed chemical stability in PBS conditions and under plasmatic enzyme activity after 24 h of incubation, at 37 °C (Figure 5A). The in vitro metabolic stability of compound **7s** was determined upon incubation in human liver microsomes, in the presence of the Phase I cofactor NADPH (Figure 5B). This compound demonstrated to be moderately stable [24,25], with a half-life ( $t_{1/2}$ ) of 45 min (see Supplementary Materials Figure S1) and an intrinsic hepatic clearance ( $CL_{int}$ ) of 22.8 min<sup>-1</sup>·mL<sup>-1</sup>·Kg<sup>-1</sup>. Three main Phase I metabolites, stemming from mono- and di-hydroxylation of the indole moiety, were identified by LC-HRMS/MS (liquid chromatography high resolution tandem mass spectrometry) analysis. The protonated molecule of the parent compound, **7s**, is observed in the HRMS-ESI(+) full scan spectrum at  $m/z$  477.1148 ± 3.6 ppm, with the characteristic dichlorine isotope cluster, and the base peak of the MS/MS spectrum is observed at  $m/z$  304.0289 ± 0.3 ppm, which corresponds to the loss of the dichloro-biphenyl-dihydropyrrolone moiety from the protonated molecule (see Supplementary Materials Figure S2). A mass increment of 15.9944  $u$  is observed for the protonated molecules of the two close eluting (major) metabolites at  $m/z$  493.1100 ± 4.0 and  $m/z$  493.1098 ± 3.7 ppm, which are, therefore, compatible with two isomer mono-hydroxylated metabolites of compound **7s**, indicated with abbreviation **mono-OH-7s** (Figure 5C, see Supplementary Materials Figure S3). The structural similarity of these two Phase I metabolites was further confirmed by the similar fragmentation patterns observed in the tandem mass spectra (see Supplementary Materials Figure S3B,C), whose base peaks correspond to the loss the dichloro-biphenyl-dihydropyrrolone moiety, similarly to what is observed for **7s**. Whereas the exact location of the hydroxyl group could not

be determined, the hydroxylation of the indole moiety is suggested by the observation of the diagnostic fragment ion at  $m/z$  146.0606  $\pm$  4.1 ppm in the MS/MS spectra of the two mono-hydroxylated metabolites (Figure 5C, see Supplementary Materials Figure S3B,C). With retention time of 15.9 min, a minor di-hydroxylated metabolite was also identified based on the observation of the monoisotopic signal at  $m/z$  509.1050  $\pm$  4.1 ppm, in the full scan HRMS-ESI(+) spectra (see Supplementary Materials Figure S4B). Identification of the diagnostic fragment ion at  $m/z$  150.0551  $\pm$  1.3 ppm in the MS/MS spectrum confirms the di-hydroxylation on the indole ring (Figure 5C, see Supplementary Materials Figure S4B). The observation of the fragment ion at  $m/z$  162.0551  $\pm$  1.2 ppm (the di-hydroxylated version of the mentioned diagnostic fragment ion for **mono-OH-7s** metabolites), represents an additional evidence that the main site of Phase I biotransformation is the indole ring. This constitutes an expected metabolic transformation [26], which is not linked with drug bioactivation processes [27], and, therefore, is not anticipated to be a toxicity red flag alert. Nonetheless, taking into consideration the moderate metabolic stability of the parent compound, it might be relevant to assess the activity of hydroxylated metabolites, following further improvement of this scaffold.

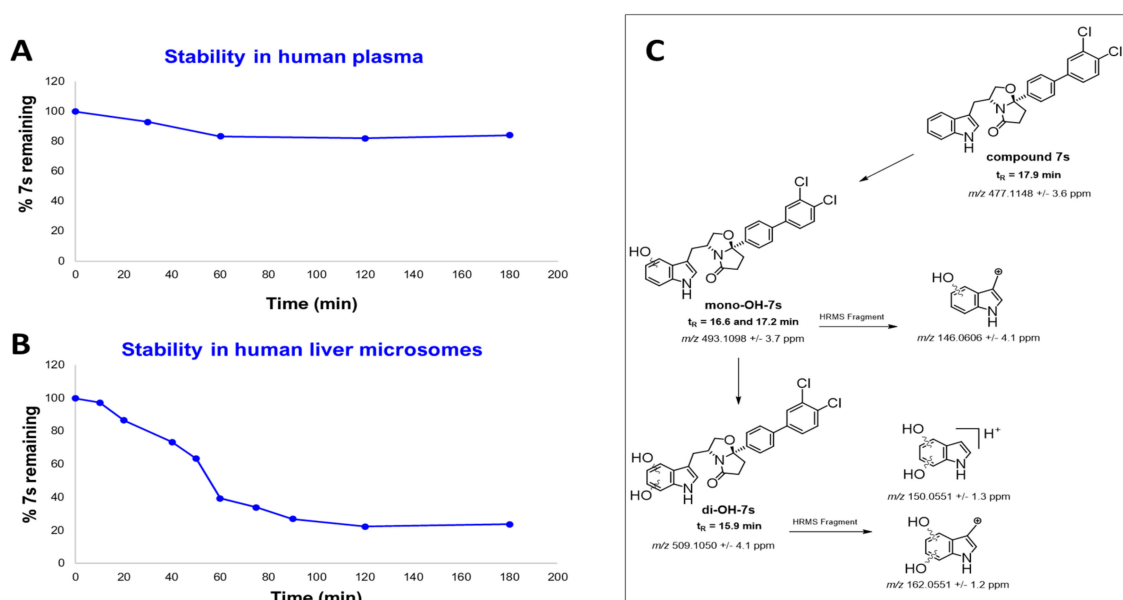


**Figure 5.** (A) Stability of compound 7s in human plasma; (B) stability of compound 7s in human liver microsomes; (C) HRMS evidence for the identification of the **mono-OH-7s** (major) and **di-OH-7s** (minor) metabolites.

### 3. Materials and Methods

#### 3.1. Chemistry

General information: THF was dried using sodium wire and benzophenone as indicator. (*R*)-Tryptophanol was obtained by reduction of (*R*)-tryptophan using lithium aluminum hydride [28]. Other reagents were obtained from commercial suppliers (Sigma-Aldrich, Alfa Aesar, and Fluorochem). General information concerning the equipment used for the elucidation of the products' chemical structures and product characterization (NMR, melting point, optical rotations, MS, and elemental analysis) are presented in our earlier publication [21]. Multiplicities in  $^1\text{H}$  NMR spectra are given as: s (singlet), d (doublet), dd (double doublet), ddd (doublet of doublets of doublets), t (triplet), and m (multiplet). Compounds 7h, 7j, and 7j' showed purity  $\geq$  95% by LC-MS, performed in a LaChrom HPLC constituted of a Merck Hitachi pump L-7100, Merck Hitachi autosampler L-7250, and a Merck Hitachi UV detector L-7400. Analyses were performed with a LiChrospher<sup>®</sup>100 RP-8 (5  $\mu\text{m}$ ) LiChroCART<sup>®</sup> 250-4 column at room temperature, using a mobile phase

solution constituted of 65% acetonitrile and 35% Milli-Q water. Peaks were detected at  $\lambda = 254$  nm.

General procedure for the synthesis of compounds **7a–j**, **7j'**, and **8a–g**: To a suspension of enantiopure tryptophanol (0.53 mmol, 1.0 eq.) in toluene (5 mL) was added the appropriate oxocarboxylic acid (0.58 mmol, 1.1 eq.). The mixture was heated at reflux for 10–25 h in a Dean–Stark apparatus. The reaction mixture was concentrated in vacuo and the residue obtained was dissolved in EtOAc (10 mL). The organic phase was washed with saturated aqueous solution of NaHCO<sub>3</sub> (15 mL) and brine (15 mL), dried over Na<sub>2</sub>SO<sub>4</sub>, filtered, and concentrated in vacuo. The residue was purified by silica gel flash chromatography using a mixture of EtOAc/*n*-hexane as eluent.

(3*R*,7*aR*)-3-((1*H*-indol-3-yl)methyl)-7*a*-phenyltetrahydropyrrolo[2,1-*b*]oxazol-5(6*H*)-one (**7a**): Following the general procedure, to a solution of (*R*)-tryptophanol (0.102 g, 0.536 mmol) in toluene (5 mL) was added 3-benzoyl propionic acid (0.105 g, 0.590 mmol). Reaction time: 19 h. The compound was purified by flash chromatography (EtOAc/*n*-hexane 1:1) and recrystallized from EtOAc/*n*-hexane to give pale pink crystalline solid (0.166 g, 95%);  $\alpha_D^{25} = -54.7^\circ$  ( $c = 2.0$ , MeOH); <sup>1</sup>H NMR spectra was found to be identical to the one reported [15] and obtained for compound **8a**. Anal. Calcd. for C<sub>21</sub>H<sub>20</sub>N<sub>2</sub>O<sub>2</sub>·0.05H<sub>2</sub>O: C, 75.67%; H, 6.09%; N, 8.41%. Found C: 75.22%; H: 5.87%; N: 8.23%. The m.p. value was found to be identical to the one reported for compound **8a**.

(3*S*,7*aS*)-3-((1*H*-indol-3-yl)methyl)-7*a*-phenyltetrahydropyrrolo[2,1-*b*]oxazol-5(6*H*)-one (**8a**): Following the general procedure, to a solution of (*S*)-tryptophanol (0.101 g, 0.529 mmol) in toluene (5 mL) was added 3-benzoyl propionic acid (0.104 g, 0.582 mmol). Reaction time: 24 h. The compound was purified by flash chromatography (EtOAc/*n*-hexane 1:1) and recrystallized from EtOAc/*n*-hexane to give pale pink crystalline solid (0.127 g, 72%);  $\alpha_D^{25} = +40.4^\circ$  ( $c = 2.0$ , MeOH); m.p.: 153–156 °C; <sup>1</sup>H NMR (300 MHz, CDCl<sub>3</sub>)  $\delta$  7.99 (s, 1H, NH), 7.50 (d,  $J = 6.0$  Hz, 2H, ArH), 7.46–7.29 (m, 5H, ArH), 7.17 (t,  $J = 7.5$  Hz, 1H, ArH), 7.10–7.05 (m, 2H, ArH), 4.62–4.52 (m, 1H, H-3), 4.16 (t,  $J = 8.1$  Hz, 1H, H-2), 3.63–3.58 (m, 1H, H-2), 3.07 (dd,  $J = 14.3, 6.2$  Hz, 1H, indole-CH<sub>2</sub>), 2.96–2.75 (m, 1H, CH<sub>2</sub>), 2.68–2.35 (m, 3H, CH<sub>2</sub>, and indole-CH<sub>2</sub>), 2.34–2.14 (m, 1H, CH<sub>2</sub>) ppm; Anal. Calcd. for C<sub>21</sub>H<sub>20</sub>N<sub>2</sub>O<sub>2</sub>: C: 75.88%; H: 6.06%; N: 8.43%. Found C: 75.95%; H: 5.76%; N: 8.36%. <sup>1</sup>H NMR spectra was found to be identical to the one reported [15].

(3*R*,7*aR*)-3-((1*H*-indol-3-yl)methyl)-7*a*-(4-fluorophenyl)tetrahydropyrrolo[2,1-*b*]oxazol-5(6*H*)-one (**7b**): Following the general procedure, to a solution of (*R*)-tryptophanol (0.100 g, 0.526 mmol) in toluene (5 mL) was added 3-(4-fluorobenzoyl) propionic acid (0.114 g, 0.581 mmol). Reaction time: 19 h. The compound was purified by flash chromatography (EtOAc/*n*-hexane 1:1) and recrystallized from EtOAc/*n*-hexane to give pale yellow crystalline solid (0.113 g, 70%);  $\alpha_D^{25} = -48.8^\circ$  ( $c = 2.0$ , MeOH); <sup>1</sup>H NMR was found to be identical to the one obtained for compound **8b**. Anal. Calcd. for C<sub>21</sub>H<sub>19</sub>FN<sub>2</sub>O<sub>2</sub>: C: 71.98%; H: 5.47%; N: 8.00%. Found C: 72.09%; H: 5.49%; N: 7.94%. The m.p. value was found to be identical to the one reported for compound **8b**.

(3*S*,7*aS*)-3-((1*H*-indol-3-yl)methyl)-7*a*-(4-fluorophenyl)tetrahydropyrrolo[2,1-*b*]oxazol-5(6*H*)-one (**8b**): Following the general procedure, to a solution of (*S*)-tryptophanol (0.102 g, 0.535 mmol) in toluene (5 mL) was added 3-(4-fluorobenzoyl) propionic acid (0.115 g, 0.588 mmol). Reaction time: 21 h. The compound was purified by flash chromatography (EtOAc/*n*-hexane 1:1) and recrystallized from EtOAc/*n*-hexane to give orange crystalline solid (0.156 g, 83%);  $\alpha_D^{25} = +39.5^\circ$  ( $c = 2.0$ , MeOH); m.p.: 197–198 °C; <sup>1</sup>H NMR (300 MHz, CDCl<sub>3</sub>)  $\delta$  8.00 (s, 1H, NH), 7.51–7.41 (m, 3H, ArH), 7.33 (d,  $J = 8.1$  Hz, 1H, ArH), 7.21–7.15 (m, 1H, ArH), 7.11–7.03 (m, 4H, ArH), 4.62–4.53 (m, 1H, H-3), 4.17 (dd,  $J = 8.8$  Hz, 7.4 Hz, 1H, H-2), 3.59 (dd,  $J = 8.8$  Hz, 6.9 Hz, 1H, H-2), 3.05 (dd,  $J = 14.7$  Hz, 6.2 Hz, 1H, indole-CH<sub>2</sub>), 2.90–2.78 (m, 1H, CH<sub>2</sub>), 2.65–2.43 (m, 3H, CH<sub>2</sub>, and indole-CH<sub>2</sub>), 2.24 – 2.15 (m, 1H, CH<sub>2</sub>) ppm; <sup>13</sup>C NMR (75 MHz, CDCl<sub>3</sub>)  $\delta$  180.3 (C=O), 162.8 (d, Cq,  $J_{C-F} = 245.3$  Hz), 138.8 (d, Cq,  $J = 3.1$  Hz), 136.3 (Cq), 127.5 (Cq), 126.9 (d, ArCH,  $J = 8.1$  Hz), 122.3 (ArCH), 122.2 (ArCH), 119.6 (ArCH), 118.9 (ArCH), 115.5 (d, ArCH,  $J = 21.5$  Hz), 111.6 (Cq), 111.3 (ArCH), 102.2

(C-7a), 72.8 (C-2), 55.8 (C-3), 35.2 (CH<sub>2</sub>), 32.7 (CH<sub>2</sub>), 29.8 (indole-CH<sub>2</sub>). Anal. Calcd. for C<sub>21</sub>H<sub>19</sub>FN<sub>2</sub>O<sub>2</sub>: C: 71.98%; H: 5.47%; N: 8.00%. Found C: 72.48%; H: 5.37%; N: 8.03%.

(3*R*,7*aR*)-3-((1*H*-indol-3-yl)methyl)-7*a*-(4-chlorophenyl)tetrahydropyrrolo[2,1-*b*]oxazol-5(6*H*)-one (**7c**): Following the general procedure, to a solution of (*R*)-tryptophanol (0.103 g, 0.541 mmol) in toluene (5 mL) was added 3-(4-chlorobenzoyl) propionic acid (0.127 g, 0.596 mmol). Reaction time: 18 h. The compound was purified by flash chromatography (EtOAc/*n*-hexane 1:1) and recrystallized from EtOAc/*n*-hexane to give pale yellow crystalline solid (0.133 g, 67%);  $\alpha_D^{25} = -63.1^\circ$  ( $c = 2.0$ , MeOH); <sup>1</sup>H NMR was found to be identical to the one obtained for compound **8c**. Anal. Calcd. for C<sub>21</sub>H<sub>19</sub>ClN<sub>2</sub>O<sub>2</sub>: C: 68.76%; H: 5.18%; N: 7.62%. Found C: 68.76%; H: 5.22%; N: 7.64%. The m.p. value was found to be identical to the one reported for compound **8c**.

(3*S*,7*aS*)-3-((1*H*-indol-3-yl)methyl)-7*a*-(4-chlorophenyl)tetrahydropyrrolo[2,1-*b*]oxazol-5(6*H*)-one (**8c**): Following the general procedure, to a solution of (*S*)-tryptophanol (0.104 g, 0.545 mmol) in toluene (5 mL) was added 3-(4-chlorobenzoyl) propionic acid (0.128 g, 0.600 mmol). Reaction time: 23 h. The compound was purified by flash chromatography (EtOAc/*n*-hexane 1/1) and recrystallized from EtOAc/*n*-hexane to give pale pink crystalline solid (0.164 g, 82%);  $\alpha_D^{25} = +54.5^\circ$  ( $c = 2.0$ , MeOH); m.p.: 206–208 °C; <sup>1</sup>H NMR (300 MHz, CDCl<sub>3</sub>)  $\delta$  7.98 (s, 1H, NH), 7.47–7.32 (m, 6H, ArH), 7.21–7.16 (m, 1H, ArH), 7.12–7.06 (m, 2H, ArH), 4.62–4.52 (m, 1H, H-3), 4.17 (dd,  $J = 8.8$  Hz, 7.5 Hz, 1H, H-2), 3.59 (dd,  $J = 8.8$  Hz, 6.9 Hz, 1H, H-2), 3.05 (dd,  $J = 15.1$  Hz, 7.5 Hz, 1H, indole-CH<sub>2</sub>), 2.89–2.78 (m, 1H, CH<sub>2</sub>), 2.65–2.44 (m, 3H, CH<sub>2</sub>, and indole-CH<sub>2</sub>), 2.22–2.14 (m, 1H, CH<sub>2</sub>) ppm; <sup>13</sup>C NMR (75 MHz, CDCl<sub>3</sub>)  $\delta$  180.3 (C=O), 141.5 (Cq), 136.3 (Cq), 134.3 (Cq), 129.0 (ArCH), 127.4 (Cq), 126.7 (ArCH), 122.3 (ArCH), 122.2 (ArCH), 119.5 (ArCH), 118.8 (ArCH), 111.4 (Cq), 111.3 (ArCH), 102.1 (C-7a), 72.9 (C-2), 55.8 (C-3), 35.1 (CH<sub>2</sub>), 32.6 (CH<sub>2</sub>), 29.8 (indole-CH<sub>2</sub>). Anal. Calcd. for C<sub>21</sub>H<sub>19</sub>ClN<sub>2</sub>O<sub>2</sub>: C: 68.76%; H: 5.22%; N: 7.62%. Found C: 68.94%; H: 5.06%; N: 7.60%.

(3*R*,7*aR*)-3-((1*H*-indol-3-yl)methyl)-7*a*-(4-bromophenyl)tetrahydropyrrolo[2,1-*b*]oxazol-5(6*H*)-one (**7d**): Following the general procedure, to a solution of (*R*)-tryptophanol (0.102 g, 0.536 mmol) in toluene (5 mL) was added 3-(4-bromobenzoyl) propionic acid (0.153 g, 0.590 mmol). Reaction time: 18 h. The compound was purified by flash chromatography (EtOAc/*n*-hexane 1:1) and recrystallized from EtOAc/*n*-hexane to give pale pink crystalline solid (0.182 g, 83%);  $\alpha_D^{25} = -53.6^\circ$  ( $c = 2.0$ , MeOH); <sup>1</sup>H NMR was found to be identical to the one obtained for compound **8d**. Anal. Calcd. for C<sub>21</sub>H<sub>19</sub>BrN<sub>2</sub>O<sub>2</sub>·0.15H<sub>2</sub>O: C: 60.92%; H: 4.71%; N: 6.77%. Found C: 60.47%; H: 4.55%; N: 6.55%. The m.p. value was found to be identical to the one reported for compound **8d**.

(3*S*,7*aS*)-3-((1*H*-indol-3-yl)methyl)-7*a*-(4-bromophenyl)tetrahydropyrrolo[2,1-*b*]oxazol-5(6*H*)-one (**8d**): Following the general procedure, to a solution of (*S*)-tryptophanol (0.102 g, 0.536 mmol) in toluene (5 mL) was added 3-(4-bromobenzoyl) propionic acid (0.151 g, 0.589 mmol). Reaction time: 18 h. The compound was purified by flash chromatography (EtOAc/*n*-hexane 1:1) and recrystallized from EtOAc/*n*-hexane to give pale yellow crystalline solid (0.159 g, 72%);  $\alpha_D^{25} = +52.3^\circ$  ( $c = 2.0$ , MeOH); m.p.: 207–210 °C. <sup>1</sup>H NMR (300 MHz, CDCl<sub>3</sub>)  $\delta$  7.97 (s, 1H, NH), 7.52–7.45 (m, 3H, ArH), 7.37–7.32 (m, 3H, ArH), 7.21–7.05 (m, 3H, ArH), 4.62–4.52 (m, 1H, H-3), 4.17 (dd,  $J = 8.8$  Hz, 7.4 Hz, 1H, H-2), 3.59 (dd,  $J = 8.8$  Hz, 6.9 Hz, 1H, H-2), 3.05 (dd,  $J = 14.7$  Hz, 6.1 Hz, 1H, indole-CH<sub>2</sub>), 2.89–2.78 (m, 1H, CH<sub>2</sub>), 2.65–2.44 (m, 3H, CH<sub>2</sub>, and indole-CH<sub>2</sub>), 2.22–2.14 (m, 1H, CH<sub>2</sub>) ppm; <sup>13</sup>C NMR (75 MHz, CDCl<sub>3</sub>)  $\delta$  180.3 (C=O), 142.1 (Cq), 136.3 (Cq), 131.8 (ArCH), 127.5 (Cq), 127.1 (ArCH), 122.5 (Cq), 122.2 (ArCH), 122.1 (ArCH), 119.7 (ArCH), 118.9 (ArCH), 111.6 (Cq), 111.3 (ArCH), 102.1 (C-7a), 72.9 (C-2), 55.8 (C-3), 35.1 (CH<sub>2</sub>), 32.7 (CH<sub>2</sub>), 29.8 (indole-CH<sub>2</sub>). Anal. Calcd. for C<sub>21</sub>H<sub>19</sub>BrN<sub>2</sub>O<sub>2</sub>: C: 61.33%; H: 4.66%; N: 6.81%. Found C: 61.26%; H: 4.48%; N: 6.76%.

(3*R*,7*aR*)-3-((1*H*-indol-3-yl)methyl)-7*a*-(*p*-tolyl)tetrahydropyrrolo[2,1-*b*]oxazol-5(6*H*)-one (**7e**): Following the general procedure, to a solution of (*R*)-tryptophanol (0.103 g, 0.541 mmol) in toluene (5 mL) was added 3-(4-methylbenzoyl) propionic acid (0.114 g, 0.596 mmol). Reaction time: 19 h. The compound was purified by flash chromatography (EtOAc/*n*-hexane

1:1) and recrystallized from EtOAc/*n*-hexane to give pale pink crystalline solid (0.160 g, 86%);  $\alpha_D^{25} = -58.7^\circ$  ( $c = 2.0$ , MeOH);  $^1\text{H NMR}$  was found to be identical to the one obtained for compound **8e**. Anal. Calcd. for  $\text{C}_{22}\text{H}_{22}\text{N}_2\text{O}_2$ : C: 76.28%; H: 6.40%; N: 8.09%. Found C: 75.87%; H: 6.23%; N: 8.06%. The m.p. value was found to be identical to the one reported for compound **8e**.

(3*S*,7*aS*)-3-((1*H*-indol-3-yl)methyl)-7*a*-(*p*-tolyl)tetrahydropyrrolo[2,1-*b*]oxazol-5(6*H*)-one (**8e**): Following the general procedure, to a solution of (*S*)-tryptophan (0.100 g, 0.526 mmol) in toluene (5 mL) was added 3-(4-methylbenzoyl) propionic acid (0.112 g, 0.583 mmol). Reaction time: 18 h. The compound was purified by flash chromatography (EtOAc/*n*-hexane 1:1) and recrystallized from EtOAc/*n*-hexane to give pale pink crystalline solid (0.097 g, 53%);  $\alpha_D^{25} = +45.1^\circ$  ( $c = 2.0$ , MeOH); m.p.: 210–213 °C.  $^1\text{H NMR}$  (300 MHz,  $\text{CDCl}_3$ )  $\delta$  8.00 (s, 1H, NH), 7.47–7.32 (m, 4H, ArH), 7.21–7.06 (m, 5H, ArH), 4.60–4.50 (m, 1H, H-3), 4.15 (dd,  $J = 8.7$  Hz, 7.4 Hz, 1H, H-2), 3.61 (dd,  $J = 8.8$  Hz, 6.9 Hz, 1H, H-2), 3.09 (dd,  $J = 14.7$  Hz, 6.1 Hz, 1H, indole- $\text{CH}_2$ ), 2.90–2.79 (m, 1H,  $\text{CH}_2$ ), 2.64–2.43 (m, 3H,  $\text{CH}_2$ , and indole- $\text{CH}_2$ ), 2.39 (s, 3H,  $\text{CH}_3$ ), 2.26–2.17 (m, 1H,  $\text{CH}_2$ ) ppm;  $^{13}\text{C NMR}$  (75 MHz,  $\text{CDCl}_3$ )  $\delta$  180.3 (C=O), 139.9 (Cq), 138.2 (Cq), 136.3 (Cq), 129.3 (ArCH), 127.5 (Cq), 125.2 (ArCH), 122.3 (ArCH), 122.2 (ArCH), 119.6 (ArCH), 119.0 (ArCH), 111.9 (Cq), 111.2 (ArCH), 102.6 (C-7*a*), 72.9 (C-2), 55.7 (C-3), 35.4 ( $\text{CH}_2$ ), 32.9 ( $\text{CH}_2$ ), 29.9 (indole- $\text{CH}_2$ ), 21.4 ( $\text{CH}_3$ ). Anal. Calcd. for  $\text{C}_{22}\text{H}_{22}\text{N}_2\text{O}_2$ : C: 76.28%; H: 6.40%; N: 8.09%. Found C: 76.49%; H: 6.27%; N: 8.16%.

(3*R*,7*aR*)-3-((1*H*-indol-3-yl)methyl)-7*a*-(4-methoxyphenyl)tetrahydropyrrolo[2,1-*b*]oxazol-5(6*H*)-one (**7f**): Following the general procedure, to a solution of (*R*)-tryptophan (0.100 g, 0.526 mmol) in toluene (5 mL) was added 3-(4-methoxybenzoyl) propionic acid (0.121 g, 0.581 mmol). Reaction time: 24 h. The compound was purified by flash chromatography (EtOAc/*n*-hexane 1:1) and recrystallized from EtOAc/*n*-hexane to give pale yellow crystalline solid (0.106 g, 56%);  $\alpha_D^{25} = -43.0^\circ$  ( $c = 1.0$ , MeOH);  $^1\text{H NMR}$  was found to be identical to the one obtained for compound **8f**. Anal. Calcd. for  $\text{C}_{22}\text{H}_{22}\text{N}_2\text{O}_3 \cdot 0.15\text{H}_2\text{O}$ : C: 72.36%; H: 6.17%; N: 7.67%. Found C: 72.22%; H: 6.21%; N: 7.53%. The m.p. value was found to be identical to the one reported for compound **8f**.

(3*S*,7*aS*)-3-((1*H*-indol-3-yl)methyl)-7*a*-(4-methoxyphenyl)tetrahydropyrrolo[2,1-*b*]oxazol-5(6*H*)-one (**8f**): Following the general procedure, to a solution of (*S*)-tryptophan (0.101 g, 0.533 mmol) in toluene (5 mL) was added 3-(4-methoxybenzoyl) propionic acid (0.122 g, 0.586 mmol). Reaction time: 25 h. The compound was purified by flash chromatography (EtOAc/*n*-hexane 1:1) and recrystallized from EtOAc/*n*-hexane to give pale yellow crystalline solid (0.134 g, 69%);  $\alpha_D^{25} = +48.1^\circ$  ( $c = 1.0$ , MeOH); m.p.: 185–187 °C.  $^1\text{H NMR}$  (300 MHz,  $\text{CDCl}_3$ )  $\delta$  8.00 (s, 1H, NH), 7.47–7.32 (m, 4H, ArH), 7.20–7.05 (m, 3H, ArH), 6.92–6.89 (m, 2H, ArH), 4.61–4.50 (m, 1H, H-3), 4.15 (dd,  $J = 8.4$  Hz, 7.7 Hz, 1H, H-2), 3.84 (s, 3H, O- $\text{CH}_3$ ), 3.61 (dd,  $J = 8.7$  Hz, 7.0 Hz, 1H, H-2), 3.08 (dd,  $J = 14.7$  Hz, 6.2 Hz, 1H, indole- $\text{CH}_2$ ), 2.90–2.79 (m, 1H,  $\text{CH}_2$ ), 2.64–2.44 (m, 3H,  $\text{CH}_2$ , and indole- $\text{CH}_2$ ), 2.25–2.17 (m, 1H,  $\text{CH}_2$ ) ppm;  $^{13}\text{C NMR}$  (75 MHz,  $\text{CDCl}_3$ )  $\delta$  180.2 (C=O), 159.7 (Cq), 136.3 (Cq), 134.9 (Cq), 127.5 (Cq), 126.6 (ArCH), 122.2 (ArCH), 119.5 (ArCH), 119.0 (ArCH), 114.1 (ArCH), 111.8 (Cq), 111.2 (ArCH), 102.5 (C-7*a*), 72.8 (C-2), 55.7 (O $\text{CH}_3$ ), 55.5 (C-3), 35.3 ( $\text{CH}_2$ ), 32.8 ( $\text{CH}_2$ ), 29.8 (indole- $\text{CH}_2$ ). Anal. Calcd. for  $\text{C}_{22}\text{H}_{22}\text{N}_2\text{O}_3$ : C: 72.91%; H: 6.12%; N: 7.73%. Found C: 72.73%; H: 5.76%; N: 7.73%.

(3*R*,7*aR*)-3-((1*H*-indol-3-yl)methyl)-7*a*-(4-(methylsulfonyl)phenyl)tetrahydropyrrolo[2,1-*b*]oxazol-5(6*H*)-one (**7g**): Following the general procedure, to a solution of (*R*)-tryptophan (0.106 g, 0.557 mmol) in toluene (5 mL) was added 3-(4-methylsulfonylbenzoyl) propionic acid (0.157 g, 0.613 mmol). Reaction time: 22 h. The compound was purified by flash chromatography (EtOAc/*n*-hexane 7:3) and recrystallized from EtOAc/*n*-hexane to give a pale yellow crystalline solid (0.171 g, 75%);  $\alpha_D^{25} = -57.2^\circ$  ( $c = 2.0$ , MeOH);  $^1\text{H NMR}$  was found to be identical to the one obtained for compound **8g**. Anal. Calcd. for  $\text{C}_{22}\text{H}_{22}\text{N}_2\text{O}_4\text{S}$ : C: 64.37%; H: 5.40%; N: 6.82%. Found C: 64.31%; H: 5.32%; N: 6.81%. The m.p. value was found to be identical to the one reported for compound **8g**.

(3*S*,7*aS*)-3-((1*H*-indol-3-yl)methyl)-7*a*-(4-(methylsulfonyl)phenyl)tetrahydropyrrolo[2,1-*b*]oxazol-5(6*H*)-one (**8g**): Following the general procedure, to a solution of (*S*)-tryptophan



(0.100 g, 0.526 mmol) in toluene (5 mL) was added 3-(4-methylsulfonylbenzoyl) propionic acid (0.148 g, 0.578 mmol). Reaction time: 23 h. The compound was purified by flash chromatography (EtOAc/*n*-hexane 7:3) and recrystallized from EtOAc/*n*-hexane to give yellow crystalline solid (0.131 g, 61%);  $\alpha_D^{25} = +66.9$  ( $c = 2.0$ , MeOH); m.p.: 205–207 °C.  $^1\text{H}$  NMR (300 MHz,  $\text{CDCl}_3$ )  $\delta$  8.01 (s, 1H, NH), 7.90–7.88 (m, 2H, ArH), 7.62–7.59 (m, 2H, ArH), 7.43 (d,  $J = 7.9$  Hz, 1H, ArH), 7.33 (d,  $J = 8.1$  Hz, 1H, ArH), 7.21–7.16 (m, 1H, ArH), 7.11–7.06 (m, 1H, ArH), 7.00 (d,  $J = 2.3$  Hz, 1H, ArH), 4.66–4.56 (m, 1H, H-3), 4.22 (dd,  $J = 8.9, 7.4$  Hz, 1H, H-2), 3.61 (dd,  $J = 8.9, 7.0$  Hz, 1H, H-2), 3.10 (s, 3H,  $\text{SO}_2\text{CH}_3$ ), 3.00 (dd,  $J = 15.5, 5.9$  Hz, 1H, indole- $\text{CH}_2$ ), 2.92–2.75 (m, 1H,  $\text{CH}_2$ ), 2.70–2.45 (m, 3H,  $\text{CH}_2$ , and indole- $\text{CH}_2$ ), 2.21–2.13 (m, 1H,  $\text{CH}_2$ ) ppm;  $^{13}\text{C}$  NMR (75 MHz,  $\text{CDCl}_3$ )  $\delta$  180.1 (C=O), 149.2 (Cq), 140.5 (Cq), 136.3 (Cq), 128.0 (ArCH), 127.5 (Cq), 126.2 (ArCH), 122.4 (ArCH), 119.7 (ArCH), 118.7 (ArCH), 111.4 (Cq), 111.1 (ArCH), 101.8 (C-7a), 72.9 (C-2), 56.0 (C-3), 44.6 ( $\text{SO}_2\text{CH}_3$ ), 35.1 ( $\text{CH}_2$ ), 32.6 ( $\text{CH}_2$ ), 29.5 (indole- $\text{CH}_2$ ). Anal. Calcd. for  $\text{C}_{22}\text{H}_{22}\text{N}_2\text{O}_4\text{S}$ : C: 64.37%; H: 5.40%; N: 6.82%. Found C: 64.59%; H: 5.51%; N: 6.69%.

(3*R*,7*aR*)-3-((1*H*-indol-3-yl)methyl)-7*a*-(3-chloro-4-methylphenyl)tetrahydropyrrolo[2,1-*b*]oxazol-5(6*H*)-one (7*h*): Following the general procedure, to a solution of (*R*)-tryptophanol (0.041 g, 0.218 mmol) in toluene (2 mL) was added 4-(3-chloro-4-methylphenyl)-4-oxobutanoic acid (0.058 g, 0.254 mmol). Reaction time: 10 h. The compound was purified by flash chromatography (EtOAc/*n*-hexane 1:1) and recrystallized from  $\text{CH}_2\text{Cl}_2$ /*n*-hexane to give a white solid (0.077 g, 93%);  $\alpha_D^{25} = -29.6^\circ$  ( $c = 1.0$ ,  $\text{CH}_2\text{Cl}_2$ ); m.p.: 171–172 °C.  $^1\text{H}$  NMR (300 MHz,  $\text{CDCl}_3$ )  $\delta$  7.97 (s, 1H, NH), 7.50 (d,  $J = 1.4$  Hz, 1H, ArH), 7.48 (d,  $J = 8.1$  Hz, 1H, ArH), 7.33 (d,  $J = 8.0$  Hz, 1H, ArH), 7.28–7.23 (m, 2H, ArH), 7.21–7.15 (m, 1H, ArH), 7.13–7.09 (m, 1H, ArH), 7.06 (d,  $J = 2.4$  Hz, 1H, ArH), 4.62–4.50 (m, 1H, H-3), 4.16 (dd,  $J = 8.8, 7.4$  Hz, 1H, H-2), 3.61 (dd,  $J = 8.8, 6.9$  Hz, 1H, H-2), 3.10 (dd,  $J = 14.6, 6.0$  Hz, 1H, indole- $\text{CH}_2$ ), 2.85 (ddd,  $J = 16.3, 9.8, 8.1$  Hz, 1H,  $\text{CH}_2$ ), 2.62 (dd,  $J = 10.1, 3.3$  Hz, 1H,  $\text{CH}_2$ ), 2.50 (ddd,  $J = 18.4, 9.6, 6.1$  Hz, 2H,  $\text{CH}_2$ , and indole- $\text{CH}_2$ ), 2.41 (s, 3H,  $\text{CH}_3$ ), 2.25–2.15 (m, 1H,  $\text{CH}_2$ );  $^{13}\text{C}$  NMR (75 MHz,  $\text{CDCl}_3$ )  $\delta$  180.1 (C=O), 160.6 (Cq), 142.3 (Cq), 136.2 (Cq), 134.9 (Cq), 131.4 (ArCH), 127.4 (Cq), 125.9 (ArCH), 123.5 (ArCH), 122.3 (ArCH), 122.2 (ArCH), 119.6 (Cq), 118.9 (ArCH), 111.6 (ArCH), 111.2 (ArCH), 101.8 (C-7a), 72.9 (C-2), 55.7 (C-3), 35.1 ( $\text{CH}_2$ ), 32.7 ( $\text{CH}_2$ ), 29.8 (indole- $\text{CH}_2$ ), 20.0 ( $\text{CH}_3$ ). LRMS (ESI)  $m/z$  calcd for  $\text{C}_{22}\text{H}_{21}\text{ClN}_2\text{O}_2$ : 380, found 381  $[\text{M}+\text{H}]^+$ .

(3*R*,7*aR*)-3-((1*H*-indol-3-yl)methyl)-7*a*-(3-fluoro-4-methoxyphenyl)tetrahydropyrrolo[2,1-*b*]oxazol-5(6*H*)-one (7*i*): Following the general procedure, to a solution of (*R*)-tryptophanol (0.100 g, 0.526 mmol) in toluene (5 mL) was added 3-(3-fluoro-4-methoxybenzoyl) propionic acid (0.131 g, 0.578 mmol). Reaction time: 22 h. The compound was purified by flash chromatography (EtOAc/*n*-hexane 1:1) and recrystallized from EtOAc/*n*-hexane to give a pale yellow crystalline solid (0.139 g, 69%);  $\alpha_D^{25} = -51.3^\circ$  ( $c = 2.0$ , MeOH); m.p.: 131–132 °C;  $^1\text{H}$  NMR (300 MHz,  $\text{CDCl}_3$ )  $\delta$  8.01 (s, 1H, NH), 7.47 (d,  $J = 7.9$  Hz, 1H, ArH), 7.33 (d,  $J = 8.0$  Hz, 1H, ArH), 7.23–7.04 (m, 5H, ArH), 6.93 (t,  $J = 8.4$  Hz, 1H, ArH), 4.61–4.41 (m, 1H, H-3), 4.16 (dd,  $J = 8.7, 7.4$  Hz, 1H, H-2), 3.92 (s, 3H, O- $\text{CH}_3$ ), 3.61 (dd,  $J = 8.8, 6.9$  Hz, 1H, H-2), 3.08 (dd,  $J = 13.9, 6.0$  Hz, 1H, indole- $\text{CH}_2$ ), 2.90–2.83 (m, 1H,  $\text{CH}_2$ ), 2.64–2.43 (m, 3H,  $\text{CH}_2$ , and indole- $\text{CH}_2$ ), 2.24–2.15 (m, 1H,  $\text{CH}_2$ ) ppm;  $^{13}\text{C}$  NMR (75 MHz,  $\text{CDCl}_3$ )  $\delta$  180.2 (C=O), 152.2 (d, Cq,  $J_{\text{C-F}} = 245.2$  Hz), 147.5 (Cq), 147.3 (Cq), 136.3 (Cq), 135.7 (d, Cq,  $J = 5.2$  Hz), 127.4 (Cq), 122.0 (d, ArCH,  $J = 6.3$  Hz), 120.8 (d, ArCH,  $J = 3.5$  Hz), 119.5 (ArCH), 118.8 (ArCH), 113.2 (d, ArCH,  $J = 1.6$  Hz), 113.2 (ArCH), 111.5 (Cq), 111.3 (ArCH), 101.9 (C-7a), 72.9 (C-2), 56.5 (C-3), 55.8 ( $\text{OCH}_3$ ), 35.2 ( $\text{CH}_2$ ), 32.9 ( $\text{CH}_2$ ), 29.8 (indole- $\text{CH}_2$ ). Anal. Calcd. for  $\text{C}_{22}\text{H}_{21}\text{FN}_2\text{O}_3$ : C: 69.46%; H: 5.56%; N: 7.36%. Found C: 69.49%; H: 5.76%; N: 7.12%.

(3*R*,7*aR*,7*S*)-3-((1*H*-indol-3-yl)methyl)-7*a*-(4-chlorophenyl)-7-methyltetrahydropyrrolo oxazol-5(6*H*)-one (7*j*) and (3*R*,7*aR*,7*R*)-3-((1*H*-indol-3-yl)methyl)-7*a*-(4-chlorophenyl)-7-methyltetrahydropyrrolo[2,1-*b*]oxazol-5(6*H*)-one (7*j'*): Following the general procedure, to a solution of (*R*)-tryptophanol (0.039 g, 0.207 mmol) in toluene (2 mL) was added 4-(4-chlorophenyl)-3-methyl-4-oxobutanoic acid (0.057 g, 0.239 mmol). Reaction time:

17 h. Two compounds were purified by flash chromatography (EtOAc/*n*-hexane 2:3) and recrystallized from CH<sub>2</sub>Cl<sub>2</sub>/*n*-hexane.

(7j): The product was obtained as a white solid (0.055 g, 69%);  $\alpha_D^{25} = -30.5^\circ$  ( $c = 1.0$ , CH<sub>2</sub>Cl<sub>2</sub>); m.p.: 201–202 °C. <sup>1</sup>H NMR (300 MHz, CDCl<sub>3</sub>):  $\delta$  8.00 (s, 1H, NH), 7.41 (d,  $J = 8.6$  Hz, 3H, ArH), 7.34 (d,  $J = 8.8$  Hz, 3H, ArH), 7.18 (t,  $J = 7.4$  Hz, 1H, ArH), 7.11 (s, 1H, ArH), 7.07 (d,  $J = 7.4$  Hz, 1H, ArH), 4.67–4.56 (m, 1H, H-3), 4.13 (t,  $J = 8.0$  Hz, 1H, H-2), 3.58 (dd,  $J = 8.5, 6.6$  Hz, 1H, H-2), 3.04–2.85 (m, 2H, CH<sub>2</sub>, and indole-CH<sub>2</sub>), 2.44 (td,  $J = 15.1, 8.1$  Hz, 2H, CH<sub>2</sub>, and indole-CH<sub>2</sub>), 2.18 (dd,  $J = 17.3, 5.6$  Hz, 1H, CH<sub>2</sub>), 1.12 (d,  $J = 7.1$  Hz, 3H, CH<sub>3</sub>); <sup>13</sup>C NMR (75 MHz, CDCl<sub>3</sub>)  $\delta$  181.1 (C=O), 141.4 (Cq), 136.2 (Cq), 134.2 (Cq), 128.9 (ArCH), 127.5 (Cq), 127.0 (ArCH), 122.3 (ArCH), 122.1 (ArCH), 119.6 (ArCH), 118.8 (ArCH), 111.8 (Cq), 111.2 (ArCH), 103.0 (C-7a), 72.3 (C-2), 56.5 (C-3), 40.0 (CH<sub>2</sub>), 39.7 (CH<sub>2</sub>), 29.7 (indole-CH<sub>2</sub>), 14.0 (CH<sub>3</sub>). LRMS (ESI)  $m/z$  calcd for C<sub>22</sub>H<sub>21</sub>ClN<sub>2</sub>O<sub>2</sub>: 380, found 381 [M+H]<sup>+</sup>.

(7j'): The product was obtained as white solid (0.014 g, 18%);  $\alpha_D^{25} = -45.7^\circ$  ( $c = 1.0$ , CH<sub>2</sub>Cl<sub>2</sub>); m.p.: 205–206 °C. <sup>1</sup>H NMR (300 MHz, CDCl<sub>3</sub>):  $\delta$  7.95 (s, 1H, NH), 7.48 (d,  $J = 7.9$  Hz, 1H, ArH), 7.34 (t,  $J = 8.7$  Hz, 5H, ArH), 7.19 (t,  $J = 7.3$  Hz, 1H, ArH), 7.10 (t,  $J = 7.3$  Hz, 1H, ArH), 6.99 (s, 1H, ArH), 4.55 (td,  $J = 12.4, 6.8$  Hz, 1H, H-3), 4.24–4.17 (m, 1H, H-2), 3.64 (dd,  $J = 8.6, 7.1$  Hz, 1H, H-2), 3.10 (dd,  $J = 14.7, 5.3$  Hz, 1H, indole-CH<sub>2</sub>), 2.78–2.63 (m, 2H, CH<sub>2</sub>), 2.48 (dt,  $J = 15.8, 8.1$  Hz, 2H, CH<sub>2</sub>, and indole-CH<sub>2</sub>), 0.65 (d,  $J = 6.5$  Hz, 3H, CH<sub>3</sub>); <sup>13</sup>C NMR (75 MHz, CDCl<sub>3</sub>)  $\delta$  177.1 (C=O), 137.9 (Cq), 136.3 (Cq), 134.4 (Cq), 128.7 (ArCH), 127.9 (ArCH), 127.5 (Cq), 122.4 (ArCH), 122.2 (ArCH), 119.7 (ArCH), 119.0 (ArCH), 111.6 (Cq), 111.2 (ArCH), 104.1 (C-7a), 73.5 (C-2), 54.8 (C-3), 42.1 (CH<sub>2</sub>), 41.3 (CH<sub>2</sub>), 29.6 (indole-CH<sub>2</sub>), 16.4 (CH<sub>3</sub>). LRMS (ESI)  $m/z$  calcd for C<sub>22</sub>H<sub>21</sub>ClN<sub>2</sub>O<sub>2</sub>: 380, found 381 [M+H]<sup>+</sup>.

General procedure for the synthesis of 7k–l: The (*R*)-tryptophanol-derived oxazopyrrolidone lactam (0.129 mmol) was dissolved in dry DMF (5 mL), and the solution was cooled to 0 °C, under N<sub>2</sub> atmosphere. Sodium hydride (NaH) in 60% dispersion in mineral oil (0.250 mmol, 2.0 eq.) was added portion wise and the mixture stirred for 15 min. The appropriate protecting reagent (0.320 mmol, 2.5 eq.) was added and the reaction mixture stirred at room temperature for 3–6 h. After reaction completion, water (10 mL) was added followed by EtOAc (10 mL). The aqueous phase was washed with EtOAc (2x10 mL); the combined organic phases were washed with brine (10 mL), dried with MgSO<sub>4</sub>, and concentrated in vacuo. The residue was purified by silica gel flash chromatography using EtOAc/*n*-hexane as eluent.

(3*R*,7*aR*)-7*a*-(4-chlorophenyl)-3-((1-ethyl-1*H*-indol-3-yl)methyl)tetrahydropyrrolo[2,1-*b*]oxazol-5(6*H*)-one (7k): Following the general procedure, to a solution of 7c (0.120 g, 0.327 mmol) in DMF (13.5 mL) was added NaH (0.016 g, 0.654 mmol) and ethyl iodide (65.4  $\mu$ L, 0.818 mmol). Reaction time: 3 h. The compound was purified by flash chromatography (EtOAc/*n*-hexane 1:2) to afford the title compound as a pale yellow oil (0.101 g, 78%); <sup>1</sup>H NMR (300 MHz, CDCl<sub>3</sub>)  $\delta$  7.39 (d,  $J = 7.9$  Hz, 1H, ArH), 7.36–7.17 (m, 5H, ArH), 7.16–7.08 (m, 1H, ArH), 7.04–6.97 (m, 1H, ArH), 6.87 (s, 1H, ArH), 4.48 (m, 1H, H-3), 4.08 (dd,  $J = 8.8, 7.5$  Hz, 1H, H-2), 4.01 (q,  $J = 7.3$  Hz, 2H, CH<sub>2</sub>CH<sub>3</sub>), 3.52 (dd,  $J = 8.8, 7.0$  Hz, 1H, H-2), 3.01 (dd,  $J = 14.6, 5.3$  Hz, 1H, indole-CH<sub>2</sub>), 2.84–2.70 (m, 1H, CH<sub>2</sub>), 2.58–2.36 (m, 3H, CH<sub>2</sub>, and indole-CH<sub>2</sub>), 2.15–2.07 (m, 1H, CH<sub>2</sub>), 1.33 (t,  $J = 7.3$  Hz, 3H, CH<sub>2</sub>CH<sub>3</sub>); <sup>13</sup>C NMR (75 MHz, CDCl<sub>3</sub>)  $\delta$  180.2 (C=O), 141.6 (Cq), 136.1 (Cq), 134.3 (Cq), 129.0 (ArCH), 128.1 (Cq), 126.8 (ArCH), 125.3 (ArCH), 121.7 (ArCH), 119.2 (ArCH), 119.1 (ArCH), 110.0 (Cq), 109.4 (ArCH), 102.1 (C-7a), 72.9 (C-2), 55.9 (C-3), 40.9 (CH<sub>2</sub>CH<sub>3</sub>), 35.2 (CH<sub>2</sub>), 32.8 (CH<sub>2</sub>), 29.7 (indole-CH<sub>2</sub>), 15.6 (CH<sub>2</sub>CH<sub>3</sub>). Anal. Calcd. for C<sub>23</sub>H<sub>23</sub>ClN<sub>2</sub>O<sub>2</sub>: C: 69.96%; H: 5.87%; N: 7.09%. Found C: 70.12%; H: 6.40%; N: 6.95%.

(3*R*,7*aR*)-3-((1-acetyl-1*H*-indol-3-yl)methyl)-7*a*-(4-chlorophenyl)tetrahydropyrrolo[2,1-*b*]oxazol-5(6*H*)-one (7l): Following the general procedure, to a solution of 7c (0.094 g, 0.256 mmol) in DMF (9.5 mL) was added NaH (12.3 mg, 0.512 mmol) and acetic anhydride (60.6  $\mu$ L, 0.641 mmol). Reaction time: 6 h. The compound was purified by flash chromatography (EtOAc/*n*-hexane 1:1) to afford the title compound as a white powder (0.072 g, 69%);

m.p.: 66–67 °C;  $^1\text{H}$  NMR (300 MHz,  $\text{CDCl}_3$ )  $\delta$  8.32 (d,  $J = 7.8$  Hz, 1H, ArH), 7.56 (s, 1H, ArH), 7.28–7.11 (m, 7H, ArH), 4.61–4.45 (m, 1H, H-3), 4.20 (dd,  $J = 8.7, 7.6$  Hz, 1H, H-2), 3.49 (dd,  $J = 8.7, 6.5$  Hz, 1H, H-2), 2.80–2.52 (m, 3H,  $\text{CH}_2$ , and indole- $\text{CH}_2$ ), 2.52 (s, 3H,  $\text{CH}_3$ ), 2.48–2.35 (m, 2H,  $\text{CH}_2$ , and indole- $\text{CH}_2$ ), 2.16–2.02 (m, 1H,  $\text{CH}_2$ );  $^{13}\text{C}$  NMR (75 MHz,  $\text{CDCl}_3$ )  $\delta$  180.9 (C=O), 168.9 (C=O), 141.2 (Cq), 135.9 (Cq), 134.5 (Cq), 130.6 (Cq), 129.1 (ArCH), 126.6 (ArCH), 125.5 (ArCH), 123.7 (ArCH), 123.3 (ArCH), 118.7 (ArCH), 118.3 (Cq), 116.8 (ArCH), 102.4 (C-7a), 72.6 (C-2), 54.9 (C-3), 34.7 ( $\text{CH}_2$ ), 32.4 ( $\text{CH}_2$ ), 29.6 (indole- $\text{CH}_2$ ), 24.2 ( $\text{CH}_3$ ). Anal. Calcd. for  $\text{C}_{23}\text{H}_{21}\text{ClN}_2\text{O}_3$ : C: 67.56%; H: 5.18%; N: 6.85%. Found C: 67.37%; H: 5.47%; N: 6.72%.

Procedure for the synthesis of *tert*-butyl 3-(((3*R*,7*aR*)-7*a*-(4-chlorophenyl)-5-oxohexahydropyrrolo[2,1-*b*]oxazol-3-yl)methyl)-1*H*-indole-1-carboxylate (**7m**): To a solution of **7c** (0.070 g, 0.191 mmol) in THF (7.0 mL) was added anhydrous  $\text{Et}_3\text{N}$  (58.6  $\mu\text{L}$ , 0.420 mmol), DMAP (0.006 g, 0.048 mmol), and  $\text{Boc}_2\text{O}$  (0.054 g, 0.248 mmol). The reaction mixture was stirred at room temperature for 3 h. After reaction completion, the mixture was concentrated in vacuo and the crude was dissolved in EtOAc (20 mL). The organic phase was washed with a sat. sol. of  $\text{NH}_4\text{Cl}$  ( $2 \times 15$  mL), a sat. sol. of  $\text{NaHCO}_3$  ( $2 \times 15$  mL) and brine (15 mL). The combined organic phases were dried with  $\text{MgSO}_4$ , concentrated in vacuo and the compound was purified by flash chromatography (EtOAc/*n*-hexane 2:3) to afford the title compound as a pale yellow powder (0.059 g, 66%); m.p.: 163–165 °C;  $^1\text{H}$  NMR (300 MHz,  $\text{CDCl}_3$ )  $\delta$  8.01 (d,  $J = 7.6$  Hz, 1H, ArH), 7.37–7.30 (m, 4H, ArH), 7.29–7.18 (m, 3H, ArH), 7.14 (td,  $J = 7.5, 1.1$  Hz, 1H, ArH), 4.57–4.40 (m, 1H, H-3), 4.14 (dd,  $J = 8.8, 7.5$  Hz, 1H, H-2), 3.51 (dd,  $J = 8.9, 7.0$  Hz, 1H, H-2), 2.90 (ddd,  $J = 14.7, 5.7, 1.2$  Hz, 1H, indole- $\text{CH}_2$ ), 2.85–2.70 (m, 1H,  $\text{CH}_2$ ), 2.59–2.30 (m, 3H,  $\text{CH}_2$ , and indole- $\text{CH}_2$ ), 2.16–2.05 (m, 1H,  $\text{CH}_2$ ), 1.58 (s, 9H,  $\text{C}(\text{CH}_3)_3$ );  $^{13}\text{C}$  NMR (75 MHz,  $\text{CDCl}_3$ )  $\delta$  180.3 (C=O), 149.8 (C=O), 141.4 (Cq), 134.4 (Cq), 130.4 (Cq), 129.1 (ArCH), 126.6 (ArCH), 124.7 (ArCH), 123.5 (ArCH), 122.7 (ArCH), 119.1 (ArCH), 116.1 (Cq), 115.4 (ArCH), 102.1 (C-7a), 83.8 ( $\text{C}(\text{CH}_3)_3$ ), 72.8 (C-2), 55.2 (C-3), 35.2 ( $\text{CH}_2$ ), 32.7 ( $\text{CH}_2$ ), 29.5 (indole- $\text{CH}_2$ ), 28.4 ( $\text{C}(\text{CH}_3)_3$ ); Anal. Calcd. for  $\text{C}_{26}\text{H}_{27}\text{ClN}_2\text{O}_4$ : C: 66.88%; H: 5.83%; N: 6.00%. Found C: 66.90%; H: 6.16%; N: 5.89%.

General procedure for the synthesis of **7n–u**: To a solution of the appropriate tryptophan-derived oxazolopiperidone lactams (0.230 mmol) in dioxane (2.3 mL) was added  $\text{Pd}(\text{PPh}_3)_2\text{Cl}_2$  (0.023 mmol, 0.1 eq) and 1 M aq. sol. of  $\text{Na}_2\text{CO}_3$  (690  $\mu\text{L}$ ), followed by the appropriate boronic acid (0.280 mmol, 1.2 eq.). The resulting mixture was degassed and stirred at 100 °C, under  $\text{N}_2$  atmosphere, for 2–5 h. After cooling to room temperature, the reaction mixture was diluted with  $\text{CH}_2\text{Cl}_2$ , filtered in celite, and concentrated in vacuo. The residue was purified by silica gel flash chromatography using EtOAc/*n*-hexane as eluent.

(3*R*,7*aR*)-3-((1*H*-indol-3-yl)methyl)-7*a*-(4'-chloro-[1,1'-biphenyl]-4-yl)tetrahydropyrrolo oxazol-5(6*H*)-one (**7n**): Following the general procedure, to a solution of **7d** (0.036 g, 0.088 mmol) in dioxane (1.0 mL) was added  $\text{Pd}(\text{PPh}_3)_2\text{Cl}_2$  (0.003 g, 8.8  $\mu\text{mol}$ ), 1 M aq. sol. of  $\text{Na}_2\text{CO}_3$  (266  $\mu\text{L}$ ), and 4-chlorophenylboronic acid (0.017 g, 0.107 mmol). Reaction time: 4 h. The compound was purified by flash chromatography (EtOAc/*n*-hexane 2:3) to afford the title compound as a white solid (0.036 g, 94%); m.p.: 201–204 °C;  $^1\text{H}$  NMR (300 MHz,  $\text{CDCl}_3$ )  $\delta$  8.08 (s, 1H, NH), 7.63–7.50 (m, 6H, ArH), 7.48–7.39 (m, 3H, ArH), 7.33 (d,  $J = 8.1$  Hz, 1H, ArH), 7.22–7.12 (m, 1H, ArH), 7.12–7.01 (m, 2H, ArH), 4.70–4.52 (m, 1H, H-3), 4.20 (dd,  $J = 8.7, 7.4$  Hz, 1H, H-2), 3.66 (dd,  $J = 8.8, 6.8$  Hz, 1H, H-2), 3.11 (dd,  $J = 15.1, 6.6$  Hz, 1H, indole- $\text{CH}_2$ ), 3.01–2.78 (m, 1H,  $\text{CH}_2$ ), 2.73–2.44 (m, 3H,  $\text{CH}_2$ , and indole- $\text{CH}_2$ ), 2.38–2.17 (m, 1H,  $\text{CH}_2$ );  $^{13}\text{C}$  NMR (75 MHz,  $\text{CDCl}_3$ )  $\delta$  180.3 (C=O), 142.3 (Cq), 140.1 (Cq), 139.1 (Cq), 136.3 (Cq), 133.9 (Cq), 129.2 (ArCH), 128.5 (ArCH), 127.5 (Cq), 127.4 (ArCH), 125.9 (ArCH), 122.3 (ArCH), 122.2 (ArCH), 119.6 (ArCH), 118.9 (ArCH), 111.8 (Cq), 111.3 (ArCH), 102.4 (C-7a), 73.0 (C-2), 55.8 (C-3), 35.2 ( $\text{CH}_2$ ), 32.8 ( $\text{CH}_2$ ), 29.9 (indole- $\text{CH}_2$ ); Anal. Calcd. for  $\text{C}_{27}\text{H}_{23}\text{ClN}_2\text{O}_2$ : C: 73.21%; H: 5.23%; N: 6.32%. Found C: 73.56%; H: 5.83%; N: 5.92%.

(3*R*,7*aR*)-3-((1*H*-indol-3-yl)methyl)-7*a*-(4'-(trifluoromethyl)-[1,1'-biphenyl]-4-yl)tetrahydropyrrolo [2,1-*b*]oxazol-5(6*H*)-one (**7o**): Following the general procedure, to a solution of **7d** (0.050 g, 0.122 mmol) in dioxane (1.4 mL) was added  $\text{Pd}(\text{PPh}_3)_2\text{Cl}_2$  (0.004 g, 12.2  $\mu\text{mol}$ ), 1 M aq. sol.

of Na<sub>2</sub>CO<sub>3</sub> (370 µL), and 4-(trifluoromethyl)phenylboronic acid (0.028 g, 0.148 mmol). Reaction time: 3 h. The compound was purified by flash chromatography (EtOAc/*n*-hexane 2:3) to afford the title compound as a white solid (0.050 g, 86%); m.p.: 201–203 °C; <sup>1</sup>H NMR (300 MHz, CDCl<sub>3</sub>) δ 7.99 (s, 1H, NH), 7.72 (s, 4H, ArH), 7.64–7.55 (m, 4H, ArH), 7.43 (d, *J* = 7.5 Hz, 1H, ArH), 7.33 (d, *J* = 8.1 Hz, 1H, ArH), 7.21–7.14 (m, 1H, ArH), 7.12–7.03 (m, 2H, ArH), 4.67–4.53 (m, 1H, H-3), 4.20 (dd, *J* = 8.8, 7.4 Hz, 1H, H-2), 3.65 (dd, *J* = 8.8, 6.8 Hz, 1H, H-2), 3.10 (dd, *J* = 15.0, 6.5 Hz, 1H, indole-CH<sub>2</sub>), 2.91–2.83 (m, 1H, CH<sub>2</sub>), 2.67–2.48 (m, 3H, CH<sub>2</sub>, and indole-CH<sub>2</sub>), 2.33–2.22 (m, 1H, CH<sub>2</sub>); <sup>13</sup>C NMR (75 MHz, CDCl<sub>3</sub>) δ 180.3 (C=O), 143.9 (Cq), 142.7 (Cq), 139.8 (Cq), 136.0 (Cq), 129.5 (q, Cq, *J* = 32.3 Hz), 127.8 (ArCH), 127.6 (ArCH), 127.1 (Cq), 125.8 (q, ArCH, *J* = 3.7 Hz), 125.7 (ArCH), 124.2 (q, Cq, *J*<sub>C-F</sub> = 270.2 Hz), 122.3 (ArCH), 122.2 (ArCH), 119.6 (ArCH), 118.1 (ArCH), 111.7 (Cq), 111.2 (ArCH), 102.4 (C-7a), 72.9 (C-2), 55.8 (C-3), 35.2 (CH<sub>2</sub>), 32.8 (CH<sub>2</sub>), 29.9 (indole-CH<sub>2</sub>); Anal. Calcd. for C<sub>28</sub>H<sub>23</sub>F<sub>3</sub>N<sub>2</sub>O<sub>2</sub>: C: 70.58%; H: 4.87%; N: 5.88%. Found C: 70.09%; H: 5.19%; N: 5.83%.

(3*R*,7*aR*)-3-((1*H*-indol-3-yl)methyl)-7*a*-(4'-hydroxy-[1,1'-biphenyl]-4-yl)tetrahydropyrrolo oxazol-5(6*H*)-one (**7p**): Following the general procedure, to a solution of **7d** (0.050 g, 0.122 mmol) in dioxane (1.4 mL) was added Pd(PPh<sub>3</sub>)<sub>2</sub>Cl<sub>2</sub> (0.004 g, 12.2 µmol), 1 M aq. sol. of Na<sub>2</sub>CO<sub>3</sub> (370 µL), and 4-hydroxyphenylboronic acid (0.021 g, 0.148 mmol). Reaction time: 2 h. The compound was purified by flash chromatography (EtOAc/*n*-hexane 3:2) to afford the title compound as a white solid (0.044 g, 85%); m.p.: 223–225 °C; <sup>1</sup>H NMR (300 MHz, CDCl<sub>3</sub>) δ 7.98 (s, 1H, NH), 7.62–7.43 (m, 7H, ArH), 7.34 (d, *J* = 7.8 Hz, 1H, ArH), 7.18 (t, *J* = 7.6 Hz, 1H, ArH), 7.10–7.05 (m, 2H, ArH), 6.95 (d, *J* = 8.5 Hz, 2H, ArH), 5.21 (s, 1H, OH), 4.68–4.51 (m, 1H, H-3), 4.20 (dd, *J* = 8.5, 7.8 Hz, 1H, H-2), 3.66 (dd, *J* = 8.6, 6.8 Hz, 1H, H-2), 3.13 (dd, *J* = 14.9, 6.3 Hz, 1H, indole-CH<sub>2</sub>), 2.98–2.76 (m, 1H, CH<sub>2</sub>), 2.75–2.46 (m, 3H, CH<sub>2</sub>, and indole-CH<sub>2</sub>), 2.33–2.24 (m, 1H, CH<sub>2</sub>); <sup>13</sup>C NMR (75 MHz, (CD<sub>3</sub>)<sub>2</sub>SO) δ 179.5 (C=O), 157.2 (Cq), 140.8 (Cq), 139.9 (Cq), 136.0 (Cq), 130.1 (Cq), 127.7 (ArCH), 126.9 (Cq), 126.0 (ArCH), 125.5 (ArCH), 122.9 (ArCH), 121.0 (ArCH), 118.3 (ArCH), 117.9 (ArCH), 115.8 (ArCH), 111.4 (ArCH), 109.9 (Cq), 101.7 (C-7a), 72.3 (C-2), 55.3 (C-3), 40.4 (CH<sub>2</sub>), 32.8 (CH<sub>2</sub>), 29.8 (indole-CH<sub>2</sub>); Anal. Calcd. for C<sub>27</sub>H<sub>24</sub>N<sub>2</sub>O<sub>3</sub>·0.15H<sub>2</sub>O: C: 75.91%; H: 5.75%; N: 6.56%. Found C: 75.74%; H: 5.85%; N: 6.57%.

(3*R*,7*aR*)-3-((1*H*-indol-3-yl)methyl)-7*a*-(4'-(hydroxymethyl)-[1,1'-biphenyl]-4-yl)tetrahydropyrrolo oxazol-5(6*H*)-one (**7q**): Following the general procedure, to a solution of **7d** (0.070 g, 0.170 mmol) in dioxane (2.0 mL) was added Pd(PPh<sub>3</sub>)<sub>2</sub>Cl<sub>2</sub> (0.005 g, 17.0 µmol), 1 M aq. sol. of Na<sub>2</sub>CO<sub>3</sub> (520 µL), and 4-(hydroxymethyl)phenylboronic acid (0.032 g, 0.208 mmol). Reaction time: 3 h. The compound was purified by flash chromatography (EtOAc/*n*-hexane 3:2) to afford the title compound as a pale yellow solid (0.053 g, 71%); m.p.: 213–215 °C; <sup>1</sup>H NMR (300 MHz, CDCl<sub>3</sub>) δ 8.00 (s, 1H, NH), 7.65–7.44 (m, 9H, ArH), 7.33 (d, *J* = 8.0 Hz, 1H, ArH), 7.17 (t, *J* = 7.3 Hz, 1H, ArH), 7.11–7.02 (m, 2H, ArH), 4.77 (s, 2H, CH<sub>2</sub>), 4.67–4.53 (m, 1H, H-3), 4.19 (t, *J* = 8.0 Hz, 1H, H-2), 3.66 (t, *J* = 8.0 Hz, 1H, H-2), 3.11 (dd, *J* = 14.7, 6.0 Hz, 1H, indole-CH<sub>2</sub>), 2.95–2.78 (m, 1H, CH<sub>2</sub>), 2.69–2.47 (m, 3H, CH<sub>2</sub>, and indole-CH<sub>2</sub>), 2.38–2.20 (m, 1H, CH<sub>2</sub>); <sup>13</sup>C NMR (75 MHz, CDCl<sub>3</sub>) δ 180.3 (C=O), 142.0 (Cq), 140.9 (Cq), 140.4 (Cq), 140.1 (Cq), 136.3 (Cq), 127.5 (ArCH), 127.4 (Cq), 127.3 (ArCH), 127.2 (ArCH), 125.8 (ArCH), 122.3 (ArCH), 122.2 (ArCH), 119.6 (ArCH), 119.0 (ArCH), 111.9 (Cq), 111.3 (ArCH), 102.5 (C-7a), 73.0 (C-2), 65.3 (CH<sub>2</sub>OH), 55.8 (C-3), 35.3 (CH<sub>2</sub>), 32.8 (CH<sub>2</sub>), 29.9 (indole-CH<sub>2</sub>); Anal. Calcd. (C<sub>28</sub>H<sub>26</sub>N<sub>2</sub>O<sub>3</sub>·0.40H<sub>2</sub>O): C: 75.44%; H: 6.07%; N: 6.29%. Found C: 75.18%; H: 6.21%; N: 6.14%.

(3*R*,7*aR*)-3-((1*H*-indol-3-yl)methyl)-7*a*-(3'-chloro-[1,1'-biphenyl]-4-yl)tetrahydropyrrolo oxazol-5(6*H*)-one (**7r**): Following the general procedure, to a solution of **7d** (0.070 g, 0.170 mmol) in dioxane (2.0 mL) was added Pd(PPh<sub>3</sub>)<sub>2</sub>Cl<sub>2</sub> (0.005 g, 17.0 µmol), 1 M aq. sol. of Na<sub>2</sub>CO<sub>3</sub> (520 µL), and 3-chlorophenylboronic acid (0.033 g, 0.208 mmol). Reaction time: 4 h. The compound was purified by flash chromatography (EtOAc/*n*-hexane 1:1) to afford the title compound as a pale yellow solid (0.059 g, 78%); m.p.: 204–206 °C; <sup>1</sup>H NMR (300 MHz, CDCl<sub>3</sub>) δ 7.98 (s, 1H, NH), 7.47 (t, *J* = 1.6 Hz, 1H, ArH), 7.43 (s, 4H, ArH), 7.36 (dt, *J* = 7.4 Hz, 1.6 Hz, 1H, ArH), 7.30 (d, *J* = 7.7 Hz, 1H, ArH), 7.25–7.17 (m, 3H, ArH), 7.06–7.00 (m, 1H, ArH), 6.95–6.91 (m, 2H, ArH), 4.51–4.42 (m, 1H, H-3), 4.05 (dd,

$J = 8.9, 6.9$  Hz, 1H, H-2), 3.51 (dd,  $J = 8.8, 6.8$  Hz, 1H, H-2), 2.95 (dd,  $J = 14.4, 6.6$  Hz, 1H, indole-CH<sub>2</sub>), 2.80–2.66 (m, 1H, CH<sub>2</sub>), 2.53–2.34 (m, 3H, CH<sub>2</sub>, and indole-CH<sub>2</sub>), 2.22–2.08 (m, 1H, CH<sub>2</sub>); <sup>13</sup>C NMR (75 MHz, CDCl<sub>3</sub>)  $\delta$  180.3 (C=O), 142.51 (Cq), 142.46 (Cq), 139.9 (Cq), 136.3 (Cq), 134.9 (Cq), 130.3 (ArCH), 127.8 (ArCH), 127.6 (ArCH), 127.6 (Cq), 127.5 (ArCH), 125.9 (ArCH), 125.4 (ArCH), 122.3 (ArCH), 119.6 (ArCH), 118.9 (ArCH), 111.7 (Cq), 111.3 (ArCH), 102.4 (C-7a), 72.9 (C-2), 55.7 (C-3), 35.2 (CH<sub>2</sub>), 32.8 (CH<sub>2</sub>), 29.8 (indole-CH<sub>2</sub>); Anal. Calcd. for C<sub>27</sub>H<sub>23</sub>ClN<sub>2</sub>O<sub>2</sub>: C: 73.21%; H: 5.23%; N: 6.32%. Found C: 72.91%; H: 5.70%; N: 6.24%.

(3*R*,7*aR*)-3-((1*H*-indol-3-yl)methyl)-7*a*-(3',4'-dichloro-[1,1'-biphenyl]-4-yl)tetrahydropyrrolo oxazol-5(6*H*)-one (**7s**): Following the general procedure, to a solution of **7d** (0.070 g, 0.170 mmol) in dioxane (2.0 mL) was added Pd(PPh<sub>3</sub>)<sub>2</sub>Cl<sub>2</sub> (0.005 g, 17.0  $\mu$ mol), 1 M aq. sol. of Na<sub>2</sub>CO<sub>3</sub> (520  $\mu$ L), and 3,4-dichlorophenylboronic acid (0.040 g, 0.208 mmol). Reaction time: 4 h. The compound was purified by flash chromatography (EtOAc/*n*-hexane 1:1) to afford the title compound as a pale yellow solid (0.069 g, 85%); m.p.: 176–178 °C; <sup>1</sup>H NMR (300 MHz, CDCl<sub>3</sub>)  $\delta$  7.98 (s, 1H, NH), 7.71 (d,  $J = 2.1$  Hz, 1H, ArH), 7.49 (s, 5H, ArH), 7.38 (dd,  $J = 8.4$  Hz, 2.2 Hz, 2H, ArH), 7.27 (d,  $J = 8.1$  Hz, 1H, ArH), 7.11 (d,  $J = 8.1$  Hz, 1H, ArH), 7.06–6.97 (m, 2H, ArH), 4.65–4.45 (m, 1H, H-3), 4.14 (dd,  $J = 8.7, 7.4$  Hz, 1H, H-2), 3.58 (dd,  $J = 8.8, 6.8$  Hz, 1H, H-2), 3.02 (dd,  $J = 15.0, 6.6$  Hz, 1H, indole-CH<sub>2</sub>), 2.87–2.76 (m, 1H, CH<sub>2</sub>), 2.65–2.38 (m, 3H, CH<sub>2</sub>, and indole-CH<sub>2</sub>), 2.26–2.15 (m, 1H, CH<sub>2</sub>); <sup>13</sup>C NMR (75 MHz, (CD<sub>3</sub>)<sub>2</sub>SO)  $\delta$  180.3 (C=O), 142.9 (Cq), 140.7 (Cq), 138.9 (Cq), 136.2 (Cq), 132.9 (Cq), 131.7 (Cq), 131.0 (ArCH), 128.9 (ArCH), 127.5 (Cq), 127.4 (ArCH), 126.3 (ArCH), 126.0 (ArCH), 122.3 (ArCH), 122.2 (ArCH), 119.6 (ArCH), 118.8 (ArCH), 111.7 (Cq), 111.3 (ArCH), 102.3 (C-7a), 72.8 (C-2), 55.8 (C-3), 35.2 (CH<sub>2</sub>), 32.9 (CH<sub>2</sub>), 29.9 (indole-CH<sub>2</sub>); Anal. Calcd. for C<sub>27</sub>H<sub>22</sub>Cl<sub>2</sub>N<sub>2</sub>O<sub>2</sub>: C: 67.93%; H: 4.65%; N: 5.87%. Found C: 67.96%; H: 4.90%; N: 5.73%. HRMS-ESI *m/z* calcd for C<sub>27</sub>H<sub>22</sub>Cl<sub>2</sub>N<sub>2</sub>O<sub>2</sub>: 476.1058, found 477.1143  $\pm$  3.6 ppm [M+H]<sup>+</sup>.

(3*R*,7*aR*)-3-((1*H*-indol-3-yl)methyl)-7*a*-(4-(pyridin-4-yl)phenyl)tetrahydropyrrolo[2,1-*b*]oxazol-5(6*H*)-one (**7t**): Following the general procedure, to a solution of **7d** (0.070 g, 0.170 mmol) in dioxane (2.0 mL) was added Pd(PPh<sub>3</sub>)<sub>2</sub>Cl<sub>2</sub> (0.005 g, 17.0  $\mu$ mol), 1 M aq. sol. of Na<sub>2</sub>CO<sub>3</sub> (520  $\mu$ L), and 4-pyridinylboronic acid (0.026 g, 0.208 mmol). Reaction time: 2 h. The compound was purified by flash chromatography (EtOAc/*n*-hexane 3:1) to afford the title compound as a pale yellow solid (0.068 g, 97%); m.p.: 214–215 °C; <sup>1</sup>H NMR (300 MHz, CDCl<sub>3</sub>)  $\delta$  8.69 (d,  $J = 5.6$  Hz, 2H, ArH), 8.23 (s, 1H, NH), 7.63 (q,  $J = 8.4$  Hz, 4H, ArH), 7.54 (d,  $J = 5.9$  Hz, 2H, ArH), 7.43 (d,  $J = 7.8$  Hz, 1H, ArH), 7.32 (d,  $J = 8.0$  Hz, 1H, ArH), 7.17 (t,  $J = 7.4$  Hz, 1H, ArH), 7.12–7.01 (m, 2H, ArH), 4.71–4.55 (m, 1H, H-3), 4.21 (t,  $J = 8.1$  Hz, 1H, H-2), 3.65 (dd,  $J = 8.6, 7.0$  Hz, 1H, H-2), 3.09 (dd,  $J = 14.7, 6.1$  Hz, 1H, indole-CH<sub>2</sub>), 2.88 (ddd,  $J = 24.1, 12.1, 6.3$  Hz, 1H, CH<sub>2</sub>), 2.72–2.45 (m, 3H, CH<sub>2</sub>, and indole-CH<sub>2</sub>), 2.37–2.20 (m, 1H, CH<sub>2</sub>); <sup>13</sup>C NMR (75 MHz, CDCl<sub>3</sub>)  $\delta$  180.3 (C=O), 150.5 (ArCH), 147.9 (Cq), 144.0 (Cq), 138.2 (Cq), 136.3 (Cq), 127.5 (ArCH), 126.1 (ArCH), 122.4 (ArCH), 122.3 (ArCH), 121.8 (ArCH), 119.6 (ArCH), 118.9 (ArCH), 111.6 (Cq), 111.3 (ArCH), 102.3 (C-7a), 73.0 (C-2), 55.81 (C-3), 35.19 (CH<sub>2</sub>), 32.75 (CH<sub>2</sub>), 29.85 (indole-CH<sub>2</sub>). Anal. Calcd. for C<sub>26</sub>H<sub>23</sub>N<sub>3</sub>O<sub>2</sub>·0.20H<sub>2</sub>O: C: 75.59%; H: 5.72%; N: 10.17%. Found C: 75.90%; H: 5.81%; N: 9.73%.

(3*R*,7*aR*)-3-((1*H*-indol-3-yl)methyl)-7*a*-(4-(2,3-dihydrobenzo[*b*][1,4]dioxin-6-yl)phenyl)tetrahydropyrrolo[2,1-*b*]oxazol-5(6*H*)-one (**7u**): Following the general procedure, to a solution of **7d** (0.070 g, 0.170 mmol) in dioxane (2.0 mL) was added Pd(PPh<sub>3</sub>)<sub>2</sub>Cl<sub>2</sub> (0.005 g, 17.0  $\mu$ mol), 1 M aq. sol. of Na<sub>2</sub>CO<sub>3</sub> (520  $\mu$ L), and 1,4-benzodioxane-6-boronic acid (0.037 g, 0.208 mmol). Reaction time: 5 h. The compound was purified by flash chromatography (EtOAc/*n*-hexane 1:1) to afford the title compound as a pale yellow solid (0.022 g, 28%); m.p.: 286–288 °C; <sup>1</sup>H NMR (300 MHz, CDCl<sub>3</sub>)  $\delta$  7.97 (s, 1H, NH), 7.56–7.44 (m, 5H, ArH), 7.33 (d,  $J = 8.0$  Hz, 1H, ArH), 7.19–7.08 (m, 5H, ArH), 6.95 (d,  $J = 8.3$  Hz, 1H, ArH), 4.64–4.54 (m, 1H, H-3), 4.31 (s, 4H, CH<sub>2</sub>), 4.18 (dd,  $J = 8.7, 7.5$  Hz, 1H, H-2), 3.65 (dd,  $J = 8.8, 6.9$  Hz, 1H, H-2), 3.11 (dd,  $J = 14.7, 6.1$  Hz, 1H, indole-CH<sub>2</sub>), 2.93–2.82 (m, 1H, CH<sub>2</sub>), 2.67–2.45 (m, 3H, CH<sub>2</sub>, and indole-CH<sub>2</sub>), 2.37–2.19 (m, 1H, CH<sub>2</sub>); <sup>13</sup>C NMR (75 MHz, CDCl<sub>3</sub>)  $\delta$  180.4 (C=O), 143.9 (Cq), 143.6 (Cq), 141.4 (Cq), 140.7 (Cq), 136.3 (Cq), 134.2 (Cq), 127.3 (Cq), 126.9 (ArCH), 125.4 (ArCH), 122.3 (ArCH), 122.0 (ArCH), 120.4 (ArCH), 119.4 (ArCH), 118.8

(ArCH), 117.6 (ArCH), 115.8 (ArCH), 111.8 (Cq), 111.2 (ArCH), 102.4 (C-7a), 72.9 (C-2), 64.7 (CH<sub>2</sub>), 55.7 (C-3), 35.2 (CH<sub>2</sub>), 32.9 (CH<sub>2</sub>), 29.9 (indole-CH<sub>2</sub>). Anal. Calcd. for C<sub>29</sub>H<sub>26</sub>N<sub>2</sub>O<sub>4</sub>: C: 74.66%; H: 5.68%; N: 6.00%. Found C: 74.65%; H: 5.70%; N: 5.67%.

### 3.2. Biological Assays

#### 3.2.1. Cytotoxicity Assays

The cytotoxicity was assessed in different cell lines with the endpoint MTT, using previously reported procedure [29–31]. The following cells were obtained from the American Type Culture Collection: human embryonic kidney epithelial cell line (HEK 293T, ATCC HBT-22<sup>TM</sup>), breast cancer cell line (MDA-MB-231, ATCC HTB-26<sup>TM</sup>), osteosarcoma cell line (MG-63, ATCC CRL-1427<sup>TM</sup>), gastric adenocarcinoma cell line (AGS, ATCC CRL-1739<sup>TM</sup>), prostate cancer cell line (DU-145, ATCC HTB-81<sup>TM</sup>), and lung carcinoma cell line (A-549, ATCC CCL-185<sup>TM</sup>). All cell lines were seeded at  $2 \times 10^4$  cells/well with exception of A-549 cell line, which was seeded at  $5 \times 10^3$  cells/well.

#### 3.2.2. Caspase 3/7 Activity Assay

The activity of caspase 3/7 was determined by fluorimetric assay based on the hydrolysis of the peptide substrate acetyl-Asp-Glu-Val-Asp-7-amido-4-methylcoumarin (Ac-DEVD-AMC) by caspase 3/7 using a previously reported procedure [32].

### 3.3. In Vitro Stability Assays

#### 3.3.1. Buffer and Human Plasma Stabilities for Compound 7s

Human plasma was obtained from healthy volunteers and provided by Instituto Português do Sangue, Lisbon, Portugal. Buffer and human plasma stabilities were determined by standard methodology [33]. Specifically, human plasma was centrifuged (5 min,  $2000 \times g$ , room temperature) and, then, diluted 50% in PBS buffer (pH 7.4). The reactions were initiated by the addition of a solution of compound 7s (4 mM in DMSO, 25  $\mu$ L) to 975  $\mu$ L of plasma solution, at 37 °C, obtaining a final concentration of 100  $\mu$ M. Solutions were stirred at 37 °C and 100  $\mu$ L aliquots were collected at different time points: 0, 30, 60, 120, and 180 min (one additional aliquot was collected at 24 h). A cold reserpine solution (internal standard, 5  $\mu$ M in acetonitrile, 300  $\mu$ L) was then added to quench the reactions. Following centrifugation (10 min,  $10,000 \times g$ , room temperature), the clear supernatants were stored at  $-20$  °C until further analysis by HPLC-DAD. Assays were run in duplicate and procaine was used as a positive control for plasma stability. Additional control assays were conducted using PBS (pH 7.4) instead of a plasma solution. HPLC-DAD analysis was performed as previously described [34].

#### 3.3.2. Metabolic Stability for Compound 7s

The evaluation of the metabolic stability of compound 7s was conducted in human liver microsomes (GIBCO<sup>TM</sup>, 20 donors) by a previously reported procedure [35]. Specifically, for a total incubation volume of 1 mL, in 100 mM phosphate buffer at pH 7.4, 7s (10  $\mu$ M), human liver microsomes (0.8 mg protein/mL), NADPH (1 mM), and NADPH regeneration system (10  $\mu$ L, Vivid<sup>®</sup> Regeneration System, 100 $\times$ ) were used. Nevirapine was used as a positive control. Additional control incubations were performed in the absence of 7s or NADPH, and using heat-denatured (90 °C, 15 min) microsomes. The resulting mixtures were incubated at 37 °C, and all assays were run in duplicate. Aliquots (50  $\mu$ L) were collected at different time points (0, 5, 10, 20, 30, 40, 50, 60, 75, 90, 120, and 180 min and 24 h) and 50  $\mu$ L of cold reserpine solution (2.5  $\mu$ M in acetonitrile) was then added to quench the reactions. Following centrifugation (10 min,  $10,000 \times g$ , 4 °C), the supernatants were stored at  $-20$  °C until LC-MS and LC-HRMS/MS analysis.

#### 3.3.3. Half-Life $t_{1/2}$ Determination

Samples from the metabolic stability assay were analyzed by LC-MS using the experimental conditions previously described [36]. The in vitro depletion half-life of 7s,  $t_{1/2}$ , was

calculated using Equation (1), assuming that the compound follows a first-order kinetic trend (see Supplementary Materials Figure S2). The “slope” was determined from linear fitting of the natural logarithm of the concentration of drug remaining plotted against time.

$$t_{1/2} = \frac{\ln 2}{\text{slope}} \quad (1)$$

The intrinsic clearance was calculated using Equation (2) [24,25]

$$CL_{int} = \frac{0.693}{t_{1/2}} \times \frac{mL \text{ incubation}}{mg \text{ microsomes}} \times \frac{45 \text{ mg microsomes}}{g \text{ liver}} \times \frac{26 \text{ g liver}}{Kg \text{ b.w.}} \quad (2)$$

#### 3.3.4. Metabolite Identification

The 60 min aliquot was analyzed by LC-HRMS/MS, as previously described [36]. All spectra corresponding to metabolites were then manually checked. The mass deviation from the accurate mass of the identified metabolites remained below 5 ppm for the precursor and product ions. After their detection, structural characterization of the potential metabolites was based on tandem mass data (see Supplementary Materials Figures S2–S4).

#### 4. Conclusions

A series of enantiopure tryptophanol-derived bicyclic lactams was prepared, and its antiproliferative activity was evaluated in AGS cells. From the first screening emerged compound **7c**, a (*R*)-tryptophanol derivative with a *para*-chloro phenyl substituent, which was selected for further optimization. Introduction of an additional di-halogenated aromatic ring in **7c** structure led to two derivatives 2.3- to 2.7-fold more active in AGS cells. These compounds also showed moderate activity in prostate cancer cells, representing useful hit compounds for further optimization in this type of cancer. More importantly, additional assays with the two compounds showed they are not toxic in normal HEK 293T cells, and that the antiproliferative activity in AGS cells occurs through apoptosis. Stability studies with the most potent derivative, compound **7s**, showed that the compound is stable in PBS and human plasma. Moreover, incubation assays in human liver microsomes, followed by LC-HRMS/MS analysis, showed that this compound is moderately metabolically stable and that the major metabolites stem from mono-hydroxylation of the indole ring, which is not anticipated to be a toxicity red flag alert.

**Supplementary Materials:** The following are available online at <https://www.mdpi.com/1424-8247/14/3/208/s1>: crystallographic information for compounds **7j**, **7j'**, and **8b**; LC-HRMS/MS data for compound **7s** and its metabolites; NMR spectra of compounds **7h**, **7j**, **7j'**, **7o**, and **7s**.

**Author Contributions:** Synthesis: M.E. and V.B.; stability assays: V.B. and A.M.M.A., cell assays: L.M.G.; X-ray crystallographic analysis: E.M.; supervision: M.M.M.S.; writing—original draft preparation: M.E. and M.M.M.S.; writing—review and editing: M.E., V.B., A.M.M.A., and M.M.M.S.; project administration and conceptualization: M.M.M.S. All authors have read and agreed to the published version of the manuscript.

**Funding:** This research was funded by FCT (Fundação para a Ciência e a Tecnologia) through iMed.Ulisboa (UIDB/04138/2020), CQE (UID/QUI/00100/2020), project PTDC/QUI-QOR/29664/2017, principal investigator grants CEECIND/02001/2017 (A. M. M. Antunes), and CEECIND/03143/2017 (L. M. Gonçalves), and PhD fellowships SFRH/BD/117931/2016 (M. Espadinha) and PD/BD/143126/2019 (V. Barcherini), and funded by Severo Ochoa FunFuture CEX2019-917-S.

**Institutional Review Board Statement:** Ethical review and approval were waived for this study. This plasma was obtained from “Instituto Português do Sangue” that is the Portuguese institute of blood. The plasma was obtained from blood that was already out of date for use in medical procedures. This blood was to be destroyed if it were not used by us. The IPS makes agreements with the institutions so that it can be used for research purposes.

**Informed Consent Statement:** Not applicable.

**Data Availability Statement:** CCDC 2050433-2050435 contains the supplementary crystallographic data for this paper. These data are provided free of charge by The Cambridge Crystallographic Data Centre.

**Conflicts of Interest:** The authors declare no conflict of interest. The funders had no role in the design of the study; in the collection, analyses, or interpretation of data; in the writing of the manuscript; or in the decision to publish the results.

## References

1. Bray, F.; Ferlay, J.; Soerjomataram, I.; Siegel, R.L.; Torre, L.A.; Jemal, A. Global cancer statistics 2018: GLOBOCAN estimates of incidence and mortality worldwide for 36 cancers in 185 countries. *CA Cancer J. Clin.* **2018**, *68*, 394–424. [CrossRef]
2. Available online: <https://www.who.int/news-room/fact-sheets/detail/cancer> (accessed on 25 January 2021).
3. Rawla, P.; Barsouk, A. Epidemiology of gastric cancer: Global trends, risk factors and prevention. *Prz. Gastroenterol.* **2019**, *14*, 26–38. [CrossRef] [PubMed]
4. Digkila, A.; Wagner, A.D. Advanced gastric cancer: Current treatment landscape and future perspectives. *World J. Gastroenterol.* **2016**, *22*, 2403–2414. [CrossRef]
5. Tomasello, G.; Ghidini, M.; Liguigli, W.; Ratti, M.; Toppo, L.; Passalacqua, R. Targeted therapies in gastric cancer treatment: Where we are and where we are going. *Investig. New Drugs* **2016**, *34*, 378–393. [CrossRef] [PubMed]
6. Lazăr, D.C.; Tăban, S.; Cornianu, M.; Faur, A.; Goldiș, A. New advances in targeted gastric cancer treatment. *World J. Gastroenterol.* **2016**, *22*, 6776–6799. [CrossRef]
7. Sitarz, R.; Skierucha, M.; Mielko, J.; Offerhaus, G.J.A.; Maciejewski, R.; Polkowski, W.P. Gastric cancer: Epidemiology, prevention, classification, and treatment. *Cancer Manag. Res.* **2018**, *10*, 239–248. [CrossRef] [PubMed]
8. Marin, J.J.; Al-Abdulla, R.; Lozano, E.; Briz, O.; Bujanda, L.; Banales, J.M.; Macias, R.I. Mechanisms of Resistance to Chemotherapy in Gastric Cancer. *Anticancer Agents Med. Chem.* **2016**, *16*, 318–334. [CrossRef] [PubMed]
9. Sravanthi, T.V.; Manju, S.L. Indoles—A promising scaffold for drug development. *Eur. J. Pharm. Sci.* **2016**, *91*, 1–10. [CrossRef]
10. Sharma, V.; Kumar, P.; Pathak, D. Biological Importance of the Indole Nucleus in Recent Years: A Comprehensive Review. *J. Heterocycl. Chem.* **2010**, *47*, 491–502. [CrossRef]
11. Wan, Y.; Li, Y.; Yan, C.; Yan, M.; Tang, Z. Indole: A privileged scaffold for the design of anti-cancer agents. *Eur. J. Med. Chem.* **2019**, *183*, 111691. [CrossRef]
12. Soares, J.; Raimundo, L.; Pereira, N.A.; dos Santos, D.J.; Pérez, M.; Queiroz, G.; Leão, M.; Santos, M.M.M.; Saraiva, L. A tryptophan-derived oxazolopiperidone lactam is cytotoxic against tumors via inhibition of p53 interaction with murine double minute proteins. *Pharmacol. Res.* **2015**, *95–96*, 42–52. [CrossRef]
13. Soares, J.; Raimundo, L.; Pereira, N.A.; Monteiro, Â.; Gomes, S.; Bessa, C.; Pereira, C.; Queiroz, G.; Bisio, A.; Fernandes, J.; et al. Reactivation of wild-type and mutant p53 by tryptophan-derived oxazoloisindolinone SLMP53-1, a novel anticancer small-molecule. *Oncotarget* **2016**, *7*, 4326–4343. [CrossRef]
14. Soares, J.; Espadinha, M.; Raimundo, L.; Ramos, H.; Gomes, A.S.; Gomes, S.; Loureiro, J.B.; Inga, A.; Reis, F.; Gomes, C.; et al. DIMP53-1: A novel small-molecule dual inhibitor of p53-MDM2/X interactions with multifunctional p53-dependent anticancer properties. *Mol. Oncol.* **2017**, *11*, 612–627. [CrossRef] [PubMed]
15. Raimundo, L.; Espadinha, M.; Soares, J.; Loureiro, J.B.; Alves, M.G.; Santos, M.M.M.; Saraiva, L. Improving anticancer activity towards colon cancer cells with a new p53-activating agent. *Br. J. Pharmacol.* **2018**, *175*, 3947–3962. [CrossRef]
16. Gomes, S.; Bosco, B.; Loureiro, J.B.; Ramos, H.; Raimundo, L.; Soares, J.; Nazareth, N.; Barcherini, V.; Domingues, L.; Oliveira, C.; et al. SLMP53-2 Restores Wild-Type-Like Function to Mutant p53 through Hsp70: Promising Activity in Hepatocellular Carcinoma. *Cancers* **2019**, *11*, 1151. [CrossRef]
17. Barcherini, V.; Almeida, J.; Lopes, E.A.; Wang, M.; Magalhães, E.; Silva, D.; Mori, M.; Wang, S.; Saraiva, L.; Santos, M.M.M. Potency and Selectivity Optimization of Tryptophan-Derived Oxazoloisindolinones: Novel p53 Activators in Human Colorectal Cancer. *ChemMedChem* **2020**, *16*, 250–258. [CrossRef]
18. Jiang, L.J.; Lv, S.M.; Cheng, C.; Dong, L.; Li, Y.; Yin, S.F. Synthesis and Antitumor Activity of a Novel Series of Helicid-Pyrrolidone Derivatives. *Chem. Nat. Compd.* **2015**, *51*, 121–126. [CrossRef]
19. Li, J.; Wu, Y.; Guo, Z.; Zhuang, C.; Yao, J.; Dong, G.; Yu, Z.; Min, X.; Wang, S.; Liu, Y.; et al. Discovery of 1-arylpyrrolidone derivatives as potent p53-MDM2 inhibitors based on molecule fusing strategy. *Bioorg. Med. Chem. Lett.* **2014**, *24*, 2648–2650. [CrossRef]
20. Pereira, N.A.; Monteiro, Â.; Machado, M.; Gut, J.; Molins, E.; Perry, M.J.; Dourado, J.; Moreira, R.; Rosenthal, P.J.; Prudêncio, M.; et al. Enantiopure Indolizinoindolones with in vitro Activity against Blood- and Liver-Stage Malaria Parasites. *ChemMedChem* **2015**, *10*, 2080–2089. [CrossRef] [PubMed]
21. Espadinha, M.; Viejo, L.; Lopes, R.M.R.M.; Herrera-Arozamena, C.; Molins, E.; Dos Santos, D.J.V.A.; Gonçalves, L.; Rodríguez-Franco, M.I.; Ríos, C.L.; Santos, M.M.M. Identification of tetracyclic lactams as NMDA receptor antagonists with potential application in neurological disorders. *Eur. J. Med. Chem.* **2020**, *194*, 112242. [CrossRef]
22. Shukla, S.J.; Huang, R.; Austin, C.P.; Xia, M. The future of toxicity testing: A focus on in vitro methods using a quantitative high-throughput screening platform. *Drug Discov. Today* **2010**, *15*, 997–1007. [CrossRef] [PubMed]



23. Cerny, M.A.; Kalgutkar, A.S.; Obach, R.S.; Sharma, R.; Spracklin, D.K.; Walker, G.S. Effective Application of Metabolite Profiling in Drug Design and Discovery. *J. Med. Chem.* **2020**, *63*, 6387–6406. [CrossRef] [PubMed]
24. McNaney, C.A.; Drexler, D.M.; Hnatyshyn, S.Y.; Zvyaga, T.A.; Knipe, J.O.; Belcastro, J.V.; Sanders, M. An automated liquid chromatography-mass spectrometry process to determine metabolic stability half-life and intrinsic clearance of drug candidates by substrate depletion. *Assay Drug Dev. Technol.* **2008**, *6*, 121–129. [CrossRef] [PubMed]
25. Słoczyńska, K.; Gunia-Krzyżak, A.; Koczurkiewicz, P.; Wójcik-Pszczola, K.; Żelaszczyk, D.; Popiół, J.; Pękala, E. Metabolic stability and its role in the discovery of new chemical entities. *Acta Pharm.* **2019**, *69*, 345–361. [CrossRef]
26. Gillam, E.M.; Notley, L.M.; Cai, H.; De Voss, J.J.; Guengerich, F.P. Oxidation of indole by cytochrome P450 enzymes. *Biochemistry* **2000**, *39*, 13817–13824. [CrossRef]
27. Wang, K.; Burton, R.; Anderson, S. Bioactivation of Indoles by Human Liver Microsomes with Glutathione as Trapping Agent: Formation of Novel Cyclic Cysteine and Cysteine-Glycine Adducts. *FASEB J.* **2015**, *29*, LB525. [CrossRef]
28. Bailey, P.D.; Collier, I.D.; Hollinshead, S.P.; Moore, M.H.; Morgan, K.M.; Smith, D.I.; Vernon, J.M. New asymmetric route to bridged indole alkaloids: Formal enantiospecific syntheses of (–)-suaveoline, (–)-raumacline and (–)-Nb methylraumacline. *J. Chem. Soc. Perkin Trans.* **1997**, *1*, 1209–1214. [CrossRef]
29. Mosmann, T. Rapid colorimetric assay for cellular growth and survival: Application to proliferation and cytotoxicity assays. *J. Immunol. Methods* **1983**, *65*, 55–63. [CrossRef]
30. Cadete, A.; Figueiredo, L.; Lopes, R.; Calado, C.C.; Almeida, A.J.; Gonçalves, L.M. Development and characterization of a new plasmid delivery system based on chitosan-sodium deoxycholate nanoparticles. *Eur. J. Pharm. Sci.* **2012**, *45*, 451–458. [CrossRef] [PubMed]
31. Monteiro, Â.; Gonçalves, L.M.; Santos, M.M.M. Synthesis of novel spiropyrazoline oxindoles and evaluation of cytotoxicity in cancer cell lines. *Eur. J. Med. Chem.* **2014**, *79*, 266–272. [CrossRef] [PubMed]
32. Marto, J.; Ascenso, A.; Gonçalves, L.M.; Gouveia, L.F.; Manteigas, P.; Pinto, P.; Oliveira, E.; Almeida, A.J.; Ribeiro, H.M. Melatonin-based pickering emulsion for skin's photoprotection. *Drug Deliv.* **2016**, *23*, 1594–1607. [CrossRef] [PubMed]
33. Hartman, D.A. Determination of the stability of drugs in plasma. *Curr. Protoc. Pharmacol.* **2003**, *19*, 7.6.1–7.6.8. [CrossRef]
34. Martins, I.L.; Nunes, J.; Charneira, C.; Morello, J.; Pereira, S.A.; Telo, J.P.; Marques, M.M.; Antunes, A.M.M. The first-line antiepileptic drug carbamazepine: Reaction with biologically relevant free radicals. *Free Radic. Biol. Med.* **2018**, *129*, 559–568. [CrossRef] [PubMed]
35. Lopes, B.T.; Caldeira, M.J.; Gaspar, H.; Antunes, A.M.M. Metabolic profile of four selected cathinones in microsome incubations: Identification of Phase I and II metabolites by Liquid Chromatography High Resolution Mass Spectrometry. *Front. Chem.* **2021**, *8*, 609251. [CrossRef] [PubMed]
36. Godinho, A.L.A.; Martins, I.L.; Nunes, J.; Charneira, C.; Grilo, J.; Silva, D.M.; Pereira, S.A.; Soto, K.; Oliveira, M.C.; Marques, M.M.; et al. High resolution mass spectrometry-based methodologies for identification of Etravirine bioactivation to reactive metabolites: In vitro and in vivo approaches. *Eur. J. Pharm. Sci.* **2018**, *119*, 70–82. [CrossRef] [PubMed]



## Article

# Synthesis and Anticancer Evaluation of New 1,3,4-Oxadiazole Derivatives

Camelia Elena Stecoza<sup>1</sup>, George Mihai Nitulescu<sup>1,\*</sup> , Constantin Draghici<sup>2</sup>, Miron Teodor Caproiu<sup>2</sup>, Octavian Tudorel Olaru<sup>1</sup>, Marinela Bostan<sup>3</sup> and Mirela Mihaila<sup>3</sup>

<sup>1</sup> Department of Pharmaceutical Chemistry, Faculty of Pharmacy, “Carol Davila” University of Medicine and Pharmacy, 6 Traian Vuia Street, 020956 Bucharest, Romania; camelia.stecoza@umfcd.ro (C.E.S.); octavian.olaru@umfcd.ro (O.T.O.)

<sup>2</sup> “Costin D. Nenişescu” Centre of Organic Chemistry Romanian Academy, 202 B Splaiul Independenţei, 060023 Bucharest, Romania; cst\_drag@yahoo.com (C.D.); mct@ccocdn.ro (M.T.C.)

<sup>3</sup> Center of Immunology, “Stefan S. Nicolau” Institute of Virology, 030304 Bucharest, Romania; marinela.bostan@virology.ro (M.B.); mirela.mihaila@virology.ro (M.M.)

\* Correspondence: george.nitulescu@umfcd.ro

**Abstract:** In order to develop novel chemotherapeutic agents with potent anticancer activities, a series of new 2,5-diaryl/heteroaryl-1,3,4-oxadiazoles were designed and synthesized. The structures of the new compounds were established using elemental analyses, IR and NMR spectral data. The compounds were evaluated for their anticancer potential on two standardized human cell lines, HT-29 (colon adenocarcinoma) and MDA-MB-231 (breast adenocarcinoma). Cytotoxicity was measured by MTS assay, while cell cycle arrest and apoptosis assays were conducted using a flow cytometer, the results showing that the cell line MDA-MB-231 is more sensitive to the compounds' action. The results of the predictive studies using the PASS application and the structural similarity analysis indicated STAT3 and miR-21 as the most probable pharmacological targets for the new compounds. The promising effect of compound **3e**, 2-[2-(phenylsulfanylmethyl)phenyl]-5-(4-pyridyl)-1,3,4-oxadiazole, especially on the MDA-MB-231 cell line motivates future studies to improve the anticancer profile and to reduce the toxicological risks. It is worth noting that **3e** produced a low toxic effect in the *D. magna* 24 h assay and the predictive studies on rat acute toxicity suggest a low degree of toxic risks.

**Keywords:** cytotoxic agents; apoptosis induction; HT-29 cells; MDA-MB-231 cells; mechanism prediction; STAT inhibitors; miR-21; hydrazide derivatives; nitrogen scaffolds

**Citation:** Stecoza, C.E.; Nitulescu, G.M.; Draghici, C.; Caproiu, M.T.; Olaru, O.T.; Bostan, M.; Mihaila, M. Synthesis and Anticancer Evaluation of New 1,3,4-Oxadiazole Derivatives. *Pharmaceuticals* **2021**, *14*, 438. <https://doi.org/10.3390/ph14050438>

Academic Editors: Mary Meegan and Niamh M O'Boyle

Received: 8 April 2021

Accepted: 3 May 2021

Published: 6 May 2021

**Publisher's Note:** MDPI stays neutral with regard to jurisdictional claims in published maps and institutional affiliations.



**Copyright:** © 2021 by the authors. Licensee MDPI, Basel, Switzerland. This article is an open access article distributed under the terms and conditions of the Creative Commons Attribution (CC BY) license (<https://creativecommons.org/licenses/by/4.0/>).

## 1. Introduction

Cancer, a severe human health issue, is among the leading causes of death on a global scale, and so far chemotherapy remains a main treatment option adopted worldwide either alone or in conjunction with surgery and/or radiotherapy [1]. Despite the significant advancement in chemotherapy over recent decades, which led to major changes in the treatment of various cancers, the main obstacles to the success of the therapy have remained the development of tumor-cell resistance to various chemotherapeutic agents. Drug resistance, either existing before treatment (intrinsic) or generated after therapy (acquired), is responsible for most the relapses of cancer, one of the major causes of death of the disease [2,3].

In the attempt of finding effective anticancer agents, the strategy of using simple druggable scaffolds proved to be successful in finding many relevant lead compounds [4]. A large number of nitrogen-containing heterocyclic compounds were identified as valuable anticancer solutions [5]. Among these, oxadiazoles are receiving particular interest. Depending on the position of the nitrogen and oxygen atoms, the heterocycle may occur in the form of one of the following four different isomers: 1,2,3-, 1,2,4-, 1,2,5-, and 1,3,4-oxadiazole (Figure 1) [6].



**Figure 1.** Chemical structures of oxadiazole isomers.

The greatest interest is involved with 1,3,4-oxadiazoles, as in the last years a large number of compounds with cytotoxicity for several tumor lines have been reported. The most active derivatives are more potent than the reference drugs, which proves the high anticancer potential of the 1,3,4-oxadiazole ring [7–11]. The 1,3,4-oxadiazole is an important scaffold in medicinal chemistry, with high versatility, giving rise to elevated structural diversity. In some cases, it acts as a bioisostere for carbonyl-containing compounds such as esters, amides, and carbamates or as a flat aromatic linker to provide the appropriate molecular geometry. The stability of the oxadiazole ring in aqueous medium, and its capability to easily interact with bio-targets establishing  $\pi$ – $\pi$  interactions or forming strong hydrogen bonds, justify the interest in the development of bioactive molecules containing this scaffold [6].

The versatility and the usefulness of the 1,3,4-oxadiazole scaffold is demonstrated by its use as a core structure in the inhibitors of methionine aminopeptidase (MetAP2) [12], telomerase [13,14], focal adhesion kinase (FAK) [15], thymidylate synthase (TS) [16], glycogen synthase kinase-3 (GSK-3) [17], and thymidine phosphorylase (TP) [18,19]. The antitumor potency of 1,3,4-oxadiazoles derivatives is also related to their ability to inhibit growth factors such as epidermal growth factor receptor (EGFR) [20,21] or vascular endothelial growth factor (VEGF) [22], to inhibit tubulin polymerization [23], histone deacetylases (HDAC) [24,25], or to interact with DNA structures [26]. The structures of the representative anticancer compounds sharing the 1,3,4-oxadiazole scaffold are presented in Figure 2.

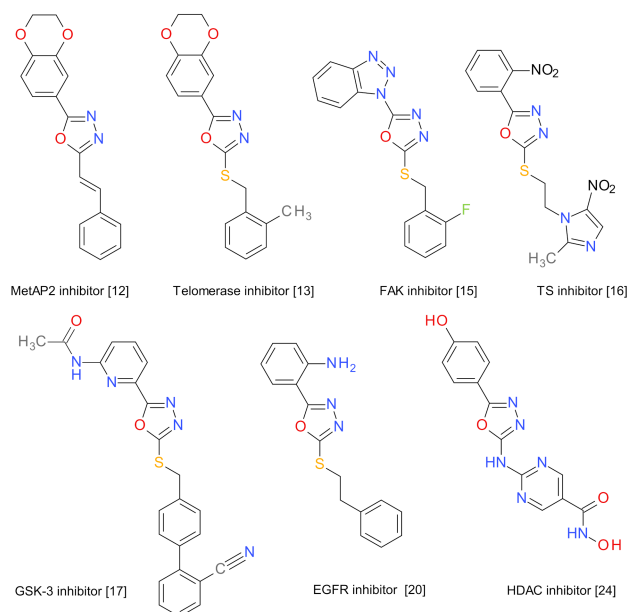


**Figure 2.** Structure of some representative bioactive compounds containing 1,3,4-oxadiazole moiety as anticancer agents.

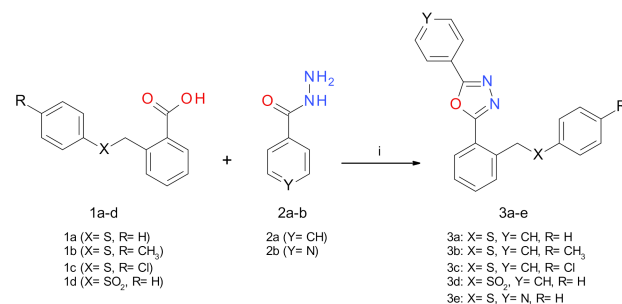
In view of the above findings, in order to develop novel chemotherapeutic agents with potent anticancer activities we hereby report the synthesis, characterization and biological evaluation of some new 2,5-diaryl/heteroaryl-1,3,4-oxadiazoles.

## 2. Results

### 2.1. Synthesis Procedures

The compounds were designed so that the molecular weight is under 500 g/mol, and the number of hydrogen donors and acceptors comply with the Lipinski rule.

The new 1,3,4-oxadiazole derivatives were prepared by heating under reflux and magnetic stirring of aromatic carboxylic acids **1a–d** with the hydrazide derivatives **2a–b** in the presence of phosphorus oxychloride in 59–70% yields (Scheme 1).

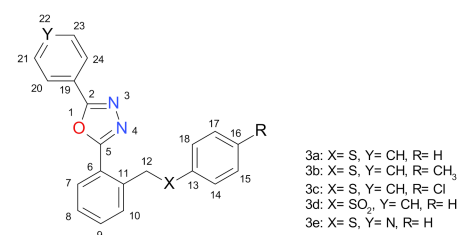


**Scheme 1.** Synthesis of the target compounds **3a–e**. Reagents and conditions: (i) POCl<sub>3</sub>, reflux, 9 h.

The aromatic carboxylic acids **1a–c** were prepared starting from thiophenol or the corresponding *p*-substituted thiophenols and phthalide, according to a previously reported procedure [27,28]. A synthetic procedure for the preparation of 2-[(benzenesulfonyl)methyl]benzoic acid (**1d**) was reported by Patra group [29], and it consists in the reaction of methyl 2-(bromomethyl)benzoate with sodium benzenesulfinate in dry dimethylformamide at room temperature, followed by the hydrolysis of the resulting ester with an aqueous solution of sodium hydroxide. The benefit of our synthesis method is the use of an alternative greener approach and the yield advantage.

The new 1,3,4-oxadiazole derivatives **3a–e** were prepared by the treatment of aromatic carboxylic acids **1a–d** with the hydrazide derivatives **2a–b** in the presence of phosphorus oxychloride. The method was adapted based on previously described procedures [30,31].

Scheme 2 presents the atoms' numbering used for assigning the NMR signals of the new oxadiazole derivatives.



**Scheme 2.** Structure of the new oxadiazole compounds and the numbering of their atoms.

In the <sup>1</sup>H-NMR spectra of the new compounds, the aromatic hydrogens gave signals in the range of 8.84–6.98 ppm. The methylene group CH<sub>2</sub> (H-12) presented a singlet in the range of 4.64–4.71 ppm for the compounds **3a–c** and **3e**. In the case of **3d**, the S-oxidation induces a deshielding effect that results in an approximately 1 ppm higher chemical shift for the protons of the methylenic group. The methyl group presented a singlet at 2.22 ppm.

In the <sup>13</sup>C-NMR spectra, the two signals in the range of 164.50–161.87 ppm are produced by the two carbons in the oxadiazole ring. The carbon atoms of the benzene and the pyridine rings produce signals in the range of 149.80–120.41 ppm. The methylene group (C-12) is characterized by a signal at 36.54–38.70 ppm in the compounds **3a–c** and **3e**, and 59.38 ppm in compound **3d**.

The IR spectra of the **3a–e** compounds differ significantly from the corresponding spectra of the hydrazide derivatives **2a–b** and those of the acids **1a–d**.

## 2.2. Anticancer Evaluation

The amplification of the cell division process is responsible for the formation of tumors. Most tumor cells have disorders in the development of the cell cycle, which are associated with an exacerbated proliferative process and this is responsible for the evolution of the tumor process. In addition, the apoptotic process is inhibited in tumor cells [32,33]. In general, cytostatic treatment aims either to induce the apoptotic process of the tumor cells or to cause cell cycle blockage.

To determine the role of the studied compounds on tumor processes, studies were performed on two different types of cancer (colon and breast) using the standardized cell lines HT-29 and MDA-MB-231. The cells treated with the compounds **3a–e** and the intermediates **2a–b** were subjected to flow cytometry techniques in order to examine the apoptotic process and the cell cycle analysis. The apoptotic cells were determined by flow cytometry using Annexin V-FITC and PI (propidium iodide) double labeling. The live cell population, and the cells undergoing early apoptosis (Annexin+/PI−) and late apoptosis (Annexin+/PI+) were quantified [34,35]. The distribution of the cell cycle phases in the tumor cells treated for 24 h with the studied compounds was analyzed for their DNA content by flow cytometry [36,37].

Cisplatin (CisPt) is frequently used for the treatment of colon adenocarcinoma, while doxorubicin (DOX) is routinely used in the treatment of breast cancers, and was therefore chosen as a reference (CisPt for HT-29 cells, DOX for MDA-MB-231 cells).

### 2.2.1. Effects on Cell Viability

The cell viability after treatment with the compounds and reference drugs was determined using the MTS (3-(4,5-dimethylthiazol-2-yl)-5-(3-carboxymethoxyphenyl)-2-(4-sulfophenyl)-2H-tetrazolium). The HT-29 and MDA-MB-231 tumor cells were preliminarily treated with the new compounds in concentrations from 6.25  $\mu\text{M}$  up to 200  $\mu\text{M}$  for 24 or 48 h in order to determine the optimal concentration. Two concentrations, 10  $\mu\text{M}$  and 50  $\mu\text{M}$ , were chosen to evaluate the compounds effect on the cells' viability.

The two cell lines responded differently to treatment with the tested compounds. In the HT-29 cell line, the tested compounds reduce viability in a similar way regardless of the concentration used (Figure 3). In contrast, in the MDA-MB231 line, the cell viability is affected more when the compounds are used in a higher concentration (50  $\mu\text{M}$ ) and the chemical structure has a greater impact, the compound **3e** having the strongest effect (Figure 4). It is noteworthy that all the compounds analyzed have a stronger cytotoxic effect than the effect induced by CisPt or DOX.

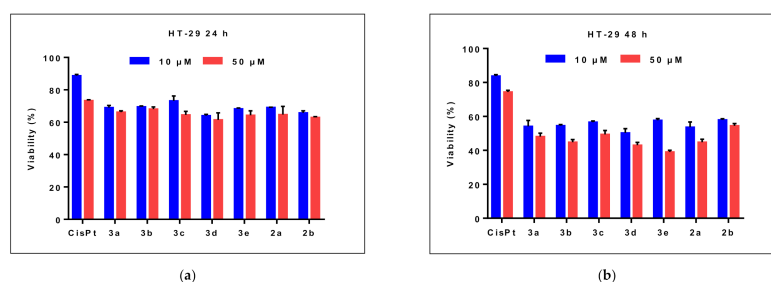


**Figure 3.** The tested compounds effects on HT-29 tumor cells' viability. The cells were treated with the compounds compared with cisplatin (CisPt) using two concentrations 10  $\mu\text{M}$  or 50  $\mu\text{M}$  for 24 h (a) or 48 h (b). Untreated cells were considered to have 100% viability.

The new oxadiazole derivatives **3a–e** reduced the HT-29 cells' viability with values in the range of 64.0% (**3d**) up to 73.2% (**3c**) when exposed for 24 h at 10  $\mu\text{M}$ , and with values between 61.5% (**3d**) and 68.1% (**3b**) when the concentration was 50  $\mu\text{M}$ . The effect of the compounds was higher when the exposure was doubled to 48 h. The cells' viability was between 50.3% (**3d**) and 57.7% (**3e**) for 10  $\mu\text{M}$ , and between 39.0% (**3e**) and 49.4% (**3c**) for the 50  $\mu\text{M}$  concentration.

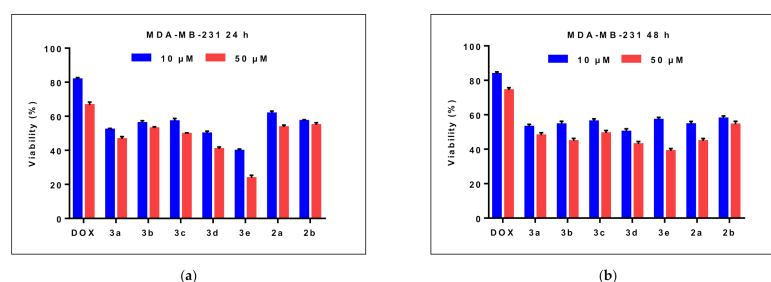


**Figure 4.** The tested compounds effects on MDA-MB-231 tumor cells' viability. The cells were treated with the compounds compared with doxorubicin (DOX) using two concentrations 10  $\mu$ M or 50  $\mu$ M for 24 h (a) or 48 h (b). Untreated cells were considered to have 100% viability.

The compounds **3a–e** reduced the MDA-MB-231 cells' viability with values in the range of 39.9% (**3e**) up to 57.2% (**3c**) when exposed for 24 h at 10  $\mu$ M. The viability values were between 23.8% (**3e**) and 53.1% (**3b**) when the concentration was 50  $\mu$ M. The cells' viability was between 50.8% (**3d**) and 56.9% (**3e**) after exposure for 48 h at 10  $\mu$ M, and between 38.7% (**3e**) and 48.9% (**3c**) for the 50  $\mu$ M concentration.

### 2.2.2. Effects on Cell Apoptosis

The HT-29 and MDA-MB-231 cells were treated for 24 h with the compounds **3a–e** and the intermediates **2a–b**, and subjected to a double Annexin/PI staining technique that allowed the detection of the apoptotic process by flow cytometry. CisPt and DOX were used as positive controls (Table 1).

**Table 1.** Apoptosis of HT-29 cells and MDA-MB-231 cells induced by 24 h treatment with the tested compounds **3a–e** and **2a–b**.

	HT-29 Cells			MDA-MB-231 Cells		
	Early Apoptosis (%)	Late Apoptosis (%)	Total Apoptosis (%)	Early Apoptosis (%)	Late Apoptosis (%)	Total Apoptosis (%)
Control	4.8	1.1	5.9	4.2	0.5	4.7
CisPt <sup>1</sup>	16.5	4.2	20.7	-	-	-
DOX <sup>1</sup>	-	-	-	11.4	2.3	13.7
<b>3a</b>	23.5	2.2	25.7	41.7	8.0	49.7
<b>3b</b>	21.7	4.8	26.5	40.5	4.7	45.2
<b>3c</b>	6.4	3	9.4	40.8	5.0	45.8
<b>3d</b>	16.5	2.7	19.2	44.3	6.6	50.9
<b>3e</b>	43.9	7.3	51.2	51.8	10.9	62.7
<b>2a</b>	53.0	12.7	65.7	45.9	12.9	58.8
<b>2b</b>	44.8	6.8	51.6	55.5	17.3	72.8

<sup>1</sup> positive controls cisplatin (CisPt) for HT-29 cells and doxorubicin (DOX) for MDA-MB-231 cells.

The treatment of the HT-29 cells for 24 h with 10  $\mu$ M of the compounds **3a–e** increased the total apoptosis in the range of 9.4% up to 51.2% compared to the untreated cells (control, 5.9%). Considering the compound **3a**, the introduction of a 4-chloro substituent is detrimental for the apoptotic effect (compound **3c**), while the transformation of the sulfur atom into a sulfone (compound **3d**) slightly reduced the effect. The exchange of the benzene ring with a pyridine (compound **3e**) almost doubled the proportion of apoptotic cells.

The new oxadiazole compounds had greater effects on the MDA-MB-231 cells compared to those observed on the HT-29 cells, with the total apoptosis percent's in the range of 45.2% up to 62.7%. All the compounds had close to three-fold stronger effects than those of the positive control. The observed structure activity relationships are similar, but the impact of the structural transformation is smaller. The compound **3e** determined the greatest effect in the oxadiazoles series, but it was smaller when compared with its precursor hydrazide **2b** (Figure 5).

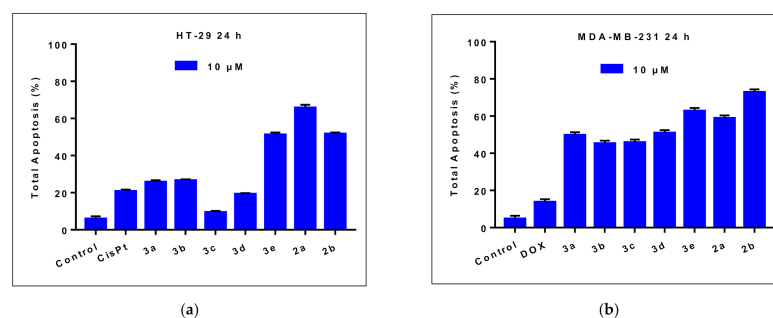


**Figure 5.** The tested compounds effects on cells' apoptosis. The cells were treated with the test compounds at 10  $\mu$ M for 24 h. The effects on HT-29 cells can be observed compared to cisplatin (CisPt) (a) and the effects on MDA-MB-231 cells are reported to doxorubicin (DOX) (b).

### 2.2.3. Cell Cycle Analysis

A flow cytometry method was used to analyze the effect induced by the studied compounds on the cell cycle of the HT-29 tumor cells compared to the effect induced by CisPt, and on the cell cycle of the MDA-MB-231 tumor cells using DOX as a positive control (Figure 6).

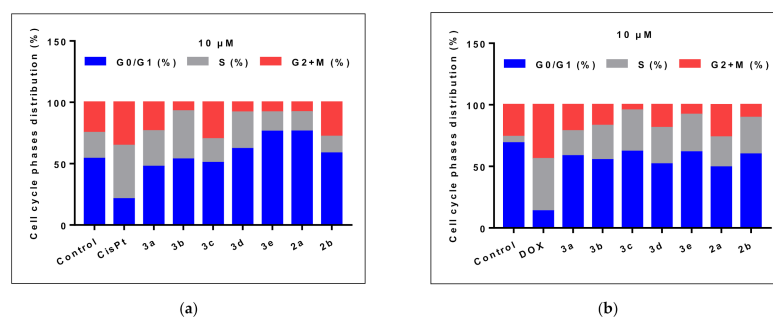


**Figure 6.** The tested compounds' effects on cell cycle phases. The cells were treated with the test compounds at 10  $\mu$ M for 24 h. The effects on HT-29 cells can be observed compared to cisplatin (CisPt) (a) and the effects on MDA-MB-231 cells are reported to doxorubicin (DOX) (b).

The treatment of the HT-29 cells for 24 h with CisPt 10  $\mu$ M induced a decrease in the G0/G1 phase from 54% to 21%, accompanied by an increase in the S phase of the cell cycle to 43.5% compared to the untreated cells (21.2%). The oxadiazoles **3a–d** did not significantly alter the proportion of G0/G1 phase cells compared to untreated cells, while increasing the number of S phase cells. The compound **3e** caused a different effect, augmenting the G0/G1 phase accompanied by a decrease in the S phase.

The flow cytometry analysis on the cell cycle of the MDA-MB-231 tumor cells showed a high percentage of G0/G1 phase (68.9%). The treatment with DOX 10  $\mu$ M induced a synchronization of the S and G2+M phases, registering an increase in the S phase (42.4%) versus the untreated cells (5.1%), accompanied by an increase in the G2+M phases (43.9%) versus 26% in the untreated cells. The analyzed compounds determined the arrest of the cells in the G0/G1 phase, accompanied by a decrease in the S and G2+M phases. The compound **3e** had the greatest impact of the oxadiazoles series, increasing the number of cells in G0/G1 and significantly reducing those in the S phase.

### 2.3. Daphnia Magna Toxicity Assay

The *Daphnia magna* (*D. magna*) bioassay results are summarized in Table 2. After 24 h of exposure, the compounds **3b–e** induced at all the tested concentrations a lethality rate (L%) lower than 50%, whereas **3a** induced an L% of 55% at the highest concentration. Due to the obtained results, the median lethal concentration (LC50) was calculated only for the compounds **3a**, **2a** and **2b**. Although the LC50 for **2b** was slightly lower than **2a**, the 95%CI of both compounds suggest a similar biological response.

**Table 2.** Daphnia magna bioassay: 24 h and 48 h values, 95% confidence intervals for newly synthesized compounds and their starting materials.

Compound	24 h		48 h	
	LC50 ( $\mu\text{M}$ )	95%CI of LC50 ( $\mu\text{M}$ )	LC50 ( $\mu\text{M}$ )	95%CI of LC50 ( $\mu\text{M}$ )
3a	115.8	43.6 to 307.4	ND*	ND*
3b	ND*	ND*	ND*	ND*
3c	ND*	ND*	11.5	ND*
3d	ND*	ND*	2.34	ND*
3e	ND*	ND*	3.5	2.0–7.3
2a	332.5	201.1–549.8	35.9	23.0–56.1
2b	296.0	205.3–426.7	21.8	11.5–41.1

ND\*—not determined due the results obtained.

After 48 h of exposure, all the newly tested compounds exhibited a significantly higher toxicity on *D. magna*. The LC50 value was not calculated for **3a** and **3b** because they induced an L% between 55 and 85% at all the concentrations. In the case of the compounds **3c–e**, the calculated LC50 values are between 2.34 and 11.5  $\mu\text{M}$ .

#### 2.4. Prediction of the Molecular Mechanism of Action and Toxicity

##### 2.4.1. PASS Prediction

The prediction of an activity spectra for substances (PASS) is an algorithm that predicts a large panel of biological activities of a given molecule using its structure as input data, and yields a probability to be active (Pa) and a probability to be inactive (Pi) for each target [38]. Each compound's target profile was manually analyzed, the relevant oncotargets were selected, and the corresponding Pa values are presented in Table 3.

**Table 3.** The probability of compounds **3a–e** to be active (Pa) as predicted by PASS analysis.

Target	3a	3b	3c	3d	3e
Transcription factor inhibitor	0.58	0.62	0.55	0.32	0.58
Transcription factor STAT inhibitor	0.61	0.64	0.61	0.42	0.65
Transcription factor STAT3 inhibitor	0.55	0.58	0.56	0.26	0.54
JAK2 expression inhibitor	0.40	0.33	0.40	0.33	0.22
Focal adhesion kinase inhibitor	0.23	0.22	0.22	0.24	0.27
Focal adhesion kinase 2 inhibitor	0.35	0.34	0.34	0.36	0.38
MAP3K5 inhibitor	0.28	0.26	-	-	0.29
Vascular endothelial growth factor 1 antagonist	0.27	0.22	0.22	0.30	0.30

The Pa values are an indication of the possibility that a compound interacts with a certain biological target, but not for the potency of the compound. The Pa values indicate the inhibition of STAT transcription factors, especially STAT3, as the most probable mechanism for the anti-proliferative effects of the compounds **3a–e**. The results for the compounds **3d** and **3a** indicate that the (phenylsulfonyl)methyl substitution reduces the probability to inhibit STAT3 compared to the phenylthiomethyl substitution.

##### 2.4.2. Structural Similarity Analysis

The similarity search on ChEMBL database returned 27 analog compounds, all sharing a 1,3,4-oxadiazole central scaffold. The highest degree of structural similarity (65.00%) was observed for the compound CHEMBL485773. The results highlight the originality of the new synthesized compounds. Depending on their structure, the ChEMBL compounds are registered to interact with various human targets. The most frequent targets are represented by microRNA 21 (77.78%), Ras-related protein Rab-9A (62.96%), Niemann–Pick C1 protein (59.26%), survival motor neuron protein (48.15%), and 15-hydroxyprostaglandin dehydrogenase (40.74%). In Figure 7 the corresponding pIC50 or pEC50 values are represented for the most relevant oncological target registered for the similar compounds.



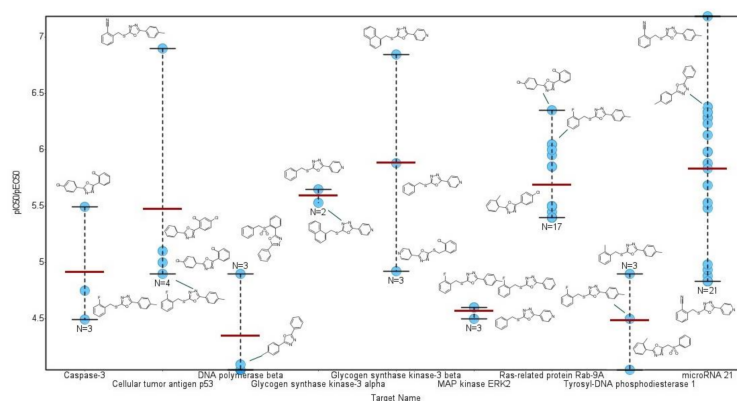


**Figure 7.** Structures and negative log of potency measurement for compounds structurally similar with the target structures **3a–e**. The compounds were extracted from the ChEMBL database and share a similarity over 50% with the new synthesized compounds. The red lines represent the average value for each target.

The target profile of the chemically similar compounds indicates the interaction with microRNA 21 (miR-21), Ras-related protein Rab-9A, glycogen synthase kinase-3 beta, and cellular tumor antigen p53, as the most probable interaction targets for the new synthesized compounds **3a–e**.

#### 2.4.3. Predicted Acute Rat Toxicity

For all the compounds, the predicted results fall in the applicability domain of the application. The predicted median lethal dose (LD50) of the new compounds after oral and intravenous (IV) administration on rats are presented in Table 4, and they indicate a relatively low degree of toxicity. All the new oxadiazole derivatives are predicted to be less toxic than their corresponding hydrazides synthesis precursors.

**Table 4.** The predicted toxicity of the compounds **3a–e** and **2a–b** expressed as median lethal doses (LD50) on rats using the GUSAR application.

Rat Acute Toxicity	3a	3b	3c	3d	3e	2a	2b
Oral LD50 (mg/kg)	1970	1977	1317	1417	1924	967	900
Oral LD50 Class	4	4	4	4	4	4	4
IV LD50 (mg/kg)	321.1	289.6	253.3	383.0	298.8	135.7	256.1
IV LD50 Class	5	4	4	5	4	4	4

### 3. Discussion

A series of new 2,5-diaryl/heteroaryl-1,3,4-oxadiazoles were synthesized and evaluated for their anticancer potential on two standardized cell lines, HT-29 and MDA-MB-231. At 10  $\mu$ M, all the compounds reduced the cell viability after 24 h of exposure, inducing apoptosis and perturbation of the cell cycle. The cell line MDA-MB-231 proved to be more sensitive to the compounds' action than HT-29.

The predictive studies using the PASS application indicated the inhibition of the STAT3 transcription factor as the most probable anticancer mechanism. Recent evidence shows that the 1,3,4-oxadiazole scaffold is frequently used in the structure of STAT3 inhibitors active against various cancer cells [39–41]. STAT3 is closely related to the occurrence of cancers and is an attractive therapeutic target for oncology and drug development. It acts in the regulation of many cellular events involving cell proliferation, differentiation, apoptosis and angiogenesis [42]. N-[2-(1,3,4-oxadiazolyl)]-4-quinolinecarboxamide, also known as STX-0119, is structurally similar to the **3a–e** compounds and functions as a STAT3 dimerization inhibitor [43]. HJC0123 was developed based on the structure of STX-0119, but it does not contain the oxadiazole scaffold. When administered in the MDA-MB-231

cells, the compound blocked the phosphorylation of STAT3, reduced the cells' viability, promoted apoptosis, and increased the proportion of S-phase cells while reducing the number of cells in G0/G1 [44]. The effects of HJC0123 in the MDA-MB-231 cells are similar with those observed for compound **3e**. In contrast to MDA-MB-231 tumor cell lines, STAT3 plays no major role in the colon carcinoma cell line HT-29 [45] and it could explain the lower effects of the new compounds on this cell line.

The structural similarity analysis indicated miR-21 as a highly probable target for the new compounds. MiR-21 is considered an oncomir because it is one of the most frequently up-regulated miRNA in a wide type of cancers. MiR-21 is overexpressed in the MDA-MB-231 cell line close to four-fold compared with the non-tumorigenic MCF-10A cell line. The knockdown of miR-21 suppressed the cell growth and proliferation of the MDA-MB-231 cells [46]. The levels of miR-21 are also significantly higher in the HT-29 cells and promote cell proliferation and migration [47].

The results of the predictive studies using the PASS application and the structural similarity analysis indicated STAT3 and miR-21 as the most probable pharmacological targets for the new compounds **3a–e**, but also that these compounds may have multitarget activities. This is suggested also by the significant toxic effects registered in the *D. magna* 48 h assay.

The chemical diversity of the **3a–e** structures, and the limited number of tested compounds, limits the development of structure activity relationships. The compound **3e** presented the best anticancer profile of the series, probably due to the presence of the pyridine ring next to the oxadiazole structure. The promising effect of the compound **3e**, especially on the MDA-MB-231 cell line, a triple-negative breast cancer line, motivates future studies to improve the anticancer profile and to reduce the toxicological risks. It is worth noting that **3e** produced a low toxic effect in the *D. magna* 24 h assay and the predictive studies on rat acute toxicity suggest a low degree of toxic risks.

## 4. Materials and Methods

### 4.1. Analytical Procedures

The melting points (m.p.) were measured in open capillary tubes on an Electrothermal 9100 apparatus and are uncorrected. The  $^1\text{H-NMR}$  and  $^{13}\text{C-NMR}$  spectra were recorded on a Gemini 300 BB instrument (Varian, Palo Alto, CA, USA) at room temperature, operating at 300 MHz for  $^1\text{H}$  and 75.075 MHz for  $^{13}\text{C}$ . The chemical shifts were recorded as  $\delta$  values in ppm units downfield to tetrametylsilane (TMS) used as internal standard, and  $\text{CDCl}_3$  and  $\text{DMSO-d}_6$  as solvents. The coupling constants values ( $J$ ) are reported in hertz (Hz) and the splitting patterns are abbreviated as follows: s, singlet; d, doublet; t, triplet; q, quartet; and b, broad. The carbons not attached to any protons are presented as Cq, while those attached to a hydrogen atom are designated as CH.

The IR spectra were recorded on a FT/IR-4200 spectrometer (JASCO, Tokyo, Japan) with an ATR PRO450-S accessory at a resolution of  $4\text{ cm}^{-1}$ . The elemental analyses were performed on a Perkin–Elmer 2400 Series II CHNS/O Elemental Analyzer (Shelton, CT, USA).

### 4.2. Synthesis Procedures

All the chemicals and reagents were purchased from commercial suppliers and used without purification, unless otherwise noted.

#### 4.2.1. Synthesis of 2-[(benzenesulfonyl)methyl]benzoic acid (**1d**)

To a solution of 2-(phenylthiomethyl)benzoic acid (**1a**) (0.02 mol) in glacial acetic acid (100 mL), 20 mL 30% aqueous hydrogen peroxide was added dropwise. The mixture was heated for 2 h and then left overnight at room temperature. The reaction mixture was diluted with water and extracted with chloroform. The separated organic phase was dried over sodium sulfate and then concentrated under reduced pressure. The crude product was recrystallized from ethanol.

White solid. Yield 93%, m.p. 154–155 °C. IR (cm<sup>-1</sup>). <sup>1</sup>H-NMR (300 MHz, CDCl<sub>3</sub>, δ ppm, *J* Hz): 8.86 (bs, 1H); 8.05 (dd, 1H, 1.4, 7.5); 7.64 (dd, 2H, 1.4, 7.5); 7.59 (tt, 1H, 1.4, 7.2); 7.55 (td, 1H, 1.4, 7.5); 7.49 (m, 1H); 7.46 (m, 2H); 7.35 (dd, 1H, 1.4, 7.5); 5.10 (s, 2H). <sup>13</sup>C-NMR (75.075 MHz, CDCl<sub>3</sub>, δ ppm): 171.88 (C-7); 137.90 (C-9); 129.97 (C-2); 129.45 (C-1); 129.04 (C-3); 128.98 (C-11, C-13); 128.62 (C-10, C-14); 133.88 (C-4 or C-5); 133.74 (C-12); 133.02 (C-5 or C-4); 131.86 (C-6); 59.46 (C-8). Elemental analysis calculated for C<sub>14</sub>H<sub>12</sub>O<sub>4</sub>S (276.31 g/mol): C 60.86%, H 4.38%, S 11.60% and found: C 60.94%, H 4.28%, S 11.69%.

#### 4.2.2. General Procedure for the Synthesis of the 1,3,4-oxadiazoles Derivatives (3a-e)

An equimolar mixture of benzoyl hydrazine (**2a**, 0.01 mol) or isonicotinic hydrazide (**2b**, 0.01 mol) and the appropriate aromatic acid (**1a–d**) (0.01 mol) in phosphorus oxychloride (45 mL) was refluxed for 9 h. The reaction mixture was slowly poured onto crushed ice and kept overnight. The solid thus separated out was filtered and washed with water, dried under vacuum and recrystallized from an appropriate solvent.

#### 4.2.3. 2-Phenyl-5-[2-(phenylsulfanylmethyl)phenyl]-1,3,4-oxadiazole (3a)

White solid. Yield 69%, m.p. 111–112 °C. <sup>1</sup>H-NMR (300 MHz, CDCl<sub>3</sub>, δ ppm, *J* Hz): 8.03 (dd, 7.7, 1.6, 2H, H-20, H-24); 7.95 (ddd, 1H, H-7); 7.42–7.49 m (3H, H-21, H-22, H-23); 7.27–7.35 m (3H; H-8, H-9, H-10); 7.22 td (2H, H-14, H-18); 7.07–7.15 m (3H, H-15, H-16, H-17); 4.64 (s, 2H, H-12). <sup>13</sup>C-NMR (75.075 MHz, CDCl<sub>3</sub>, δ ppm): 164.39 (C-2 or C-5); 164.26 (C-2 or C-5); 138.07 (Cq); 135.60 (Cq); 131.90 (CH); 131.61 (2CH); 131.44 (CH); 131.39 (CH); 129.51 (CH); 129.23 (2CH); 128.90 (2CH); 127.75 (CH); 127.13 (2CH); 127.02 (CH); 123.97 (CH); 122.84 (CH); 38.30 (C-12). Elemental analysis calculated for C<sub>21</sub>H<sub>16</sub>N<sub>2</sub>OS (344.44 g/mol): C 73.23%, H 4.68%, N 8.13%, S 9.31% and found: C 73.31%, H 4.60%, N 8.20%, S 9.24%.

#### 4.2.4. 2-Phenyl-5-[2-(p-tolylsulfanylmethyl)phenyl]-1,3,4-oxadiazole (3b)

White solid. Yield 68%, m.p. 116–117 °C. <sup>1</sup>H-NMR (300 MHz, CDCl<sub>3</sub>, δ ppm, *J* Hz): 8.11 (dd, 7.4, 1.5, 2H, H-20, H-24); 8.01 (dd, 7.0, 2.2, 1H, H-7); 7.48–7.58 (m, 3H, H-8, H-9, H-10); 7.40 (t, 6.5, 2H, H-21, H-23); 7.31 (t, 6.5, 1H, H-22); 7.17 (d, 8.1, 2H, H-15, H-17); 6.98 (d, 8.1, 2H, H-14, H-18); 4.66 (s, 2H, H-12); 2.22 (s, 3H, CH<sub>3</sub>). <sup>13</sup>C-NMR (75.075 MHz, CDCl<sub>3</sub>, δ ppm): 164.21 (C-2 or C-5); 164.16 (C-2 or C-5); 138.32 (Cq); 137.20 (Cq); 137.19 (Cq); 132.38 (CH); 132.28 (CH); 131.73 (CH); 131.34 (CH); 131.21 (CH); 129.51 (2CH); 129.32 (CH); 129.07 (2CH); 127.49 (CH); 126.96 (2CH); 123.83 (Cq); 122.64 (Cq); 38.70 (C-12); 21.01 (CH<sub>3</sub>). Elemental analysis calculated for C<sub>22</sub>H<sub>18</sub>N<sub>2</sub>OS (358.47 g/mol): C 73.72%, H 5.06%, N 7.81%, S 8.94% and found: C 73.81%, H 4.98%, N 7.72%, S 9.01%.

#### 4.2.5. 2-[2-(4-Chlorophenyl)sulfanylmethyl]phenyl]-5-phenyl-1,3,4-oxadiazole (3c)

White solid. Yield 60%, m.p. 126–128 °C. <sup>1</sup>H-NMR (CDCl<sub>3</sub>, δ ppm, *J* Hz): 8.06 (dd, 1.6, 7.5, 2H, H-20, H-24); 7.97 ddd (1H, H-7); 7.47–7.50 m (3H, H-21, H-22, H-23); 7.38–7.35 m (2H; H-9, H-10); 7.26 (dd, 1H, H-8); 7.16 (d, 8.8, 2H, H-14, H-18); 7.10 (d, 8.8, 2H, H-15, H-17); 4.65 (s, 2H, H-12); <sup>13</sup>C-NMR (CDCl<sub>3</sub>, δ ppm): 164.42 (C-2(5)); 164.16 (C-5(2)); 137.85 (C-13); 134.03 (Cq); 133.73 (Cq); 133.21 (2CH); 131.98 (CH); 131.43 (2CH); 129.53 (CH); 129.26 (2CH); 129.04 (2CH); 127.91 (CH); 127.16 (2CH); 123.92 (Cq); 122.87 (Cq); 38.56 (C-12). Elemental analysis calculated for C<sub>21</sub>H<sub>15</sub>ClN<sub>2</sub>OS (378.88 g/mol): C 66.57%, H 3.99%, N 7.39%, S 8.46% and found: C 66.68%, H 3.82%, N 7.48%, S 8.32%.

#### 4.2.6. 2-[2-(Benzenesulfonylmethyl)phenyl]-5-phenyl-1,3,4-oxadiazole (3d)

White solid. Yield 59%, m.p. 195–196 °C. <sup>1</sup>H-NMR (300 MHz, CDCl<sub>3</sub>, δ ppm, *J* Hz): 7.97 (dd, 8.0, 2.4, 2H, H-14, H-18); 7.77 (dd, 7.1, 1.8, 1H, H-7); 7.00–7.60 (m, 11H, H-arom); 5.26 (s, 2H, H-12). <sup>13</sup>C-NMR (75.075 MHz, CDCl<sub>3</sub>, δ ppm): 164.05 (C-2 or C-5); 163.46 (C-2 or C-5); 138.07 (Cq); 134.03 (CH); 133.48 (CH); 132.09 (CH); 131.60 (CH); 129.46 (CH); 129.27 (2CH); 129.09 (CH); 128.87 (CH); 128.72 (2CH); 128.69 (CH); 127.99 (Cq); 127.02 (2CH); 124.37 (Cq); 123.53 (Cq); 59.38 (C-12). Elemental analysis calculated for C<sub>21</sub>H<sub>16</sub>N<sub>2</sub>O<sub>3</sub>S

(376.44 g/mol): C 67.01%, H 4.28%, N 7.44%, S 8.52% and found: C 67.09%, H 4.19%, N 7.38%, S 8.60%.

#### 4.2.7. 2-[2-(Phenylsulfanylmethyl)phenyl]-5-(4-pyridyl)-1,3,4-oxadiazole (3e)

White solid. Yield 70%, m.p. 130–132 °C. <sup>1</sup>H-NMR (300 MHz, DMSO-d<sub>6</sub> + CDCl<sub>3</sub> 3:1, δ ppm, J Hz): 8.84 (d, 5.8, 2H, H-21, H-23); 8.07 (td, 4.0, 2.0, 1H, H-7); 8.03 (d, 5.8, 2H, H-20, H-24); 7.39–7.49 (m, 3H, H-8, H-9, H-10); 7.13–7.26 (m, 5H, H-14, H-15, H-16, H-17, H-18); 4.71 (s, 2H, H-12). <sup>13</sup>C-NMR (75.075 MHz, DMSO-d<sub>6</sub> + CDCl<sub>3</sub> 3:1, δ ppm): 164.50 (C-2 or C-5); 161.87 (C-2 or C-5); 149.90 (C-21, C-23); 137.56 (Cq); 135.07 (Cq); 131.63 (CH); 131.14 (CH); 131.03 (CH); 129.97 (2CH); 129.50 (CH); 128.64 (2CH); 127.73 (CH); 126.37 (CH); 121.70 (CH); 120.41 (2CH); 36.54 (C-12). Elemental analysis calculated for C<sub>20</sub>H<sub>15</sub>N<sub>3</sub>OS (345.43 g/mol): C 69.54%, H 4.38%, N 12.16%, S 9.28% and found: C 69.48%, H 4.46%, N 12.26%, S 9.19%.

### 4.3. Anticancer Evaluation

#### 4.3.1. Reagents

Cisplatin (CisPt), doxorubicin (DOX), and dimethyl sulfoxide (DMSO) were purchased from Sigma-Aldrich (St. Louis, MO, USA). The stock solutions were prepared by dissolving the compounds in a minimum amount of DMSO and kept at –20 °C. The working solutions were prepared before each experiment from the stocks and the culture medium. Annexin V-FITC/PI Apoptosis Detection Kit for flow cytometry was purchased from BioVision Inc., Milpitas, CA, USA. Cycletest Plus DNA Reagent Kit was provided by BD Biosciences (Becton Dickinson, USA).

#### 4.3.2. Cell Culture and Treatments

Human cancer cell lines HT-29 (colon adenocarcinoma) and MDA-MB-231 (breast adenocarcinoma) were purchased from American Type Culture Collection (ATCC). Adherent cells were routinely maintained in culture in Dulbecco's modified Eagle medium/nutrient mixture F-12 (DMEM:F12) medium added by 2 mM of L-glutamine, 10% fetal bovine serum, 100 units/mL penicillin, 100 µg/mL streptomycin (Sigma-Aldrich, St. Louis, Mo, USA) and incubated at 37 °C in 5% CO<sub>2</sub> humidified atmosphere. After 24 h, adherent cells were treated with different concentrations of the compounds for different periods of time. Cell treatments of compounds, CisPt and DOX were carried out using concentrations of 200, 100, 50, 25, 12.5 and 6.25 µM of the drug. Then cells were detached with a nonenzymatic solution of phosphate-buffered saline (PBS)/1 mM EDTA, washed twice in PBS.

#### 4.3.3. Cytotoxicity Assay

All assays were performed in triplicate in 96-well microtiter plates with flat bottom (Falcon), using CellTiter 96 Aqueous One Solution Cell Proliferation Assay (Promega), an MTS (3-(4,5-dimethylthiazol-2-yl)-5-(3-carboxymethoxyphenyl)-2-(4-sulfophenyl)-2H-tetrazolium)-based colorimetric assay. Briefly, 1 × 10<sup>4</sup> cells/wells were cultured in 100 µL for 24 h, culture supernatants were discarded, and then cells were treated for 24 h and 48 h with increasing concentrations of drugs. After the end of the incubation time, 20 µL reagent containing a) MTS, and b) phenazine ethosulfate (PES) were added in each well. PES has a high chemical stability that allows it to bind to MTS and form a stable solution. After adding the coloring solution, plates were incubated for 4 h at 37 °C, with mild agitation every 15 min. The method relies on the ability of metabolically active cells to reduce MTS, a yellow tetrazolium salt to the colored formazan that is soluble in the culture medium. The reduction in the tetrazolium compound to formazan was spectrophotometrically measured at λ = 492 nm, using a Dynex plate reader (DYNEX Technologies-MRS). The percentage of viability compared to untreated cells (considered 100% viable) was calculated based on the absorbance (Abs) values as follows:

$$\text{Cell viability (\%)} = \frac{(\text{Abs treated cells} - \text{Abs culture medium})}{(\text{Abs untreated cells} - \text{Abs culture medium})} \times 100, \quad (1)$$

Cell viability data were expressed as the mean values  $\pm$  standard deviations (SD) of the experiments. Data were obtained in triplicates ( $n = 3$ ), averaged and expressed as mean  $\pm$  SD.

#### 4.3.4. Apoptosis Analysis

The apoptosis assay was carried out using the Annexin V-FITC Kit and the manufacturer's protocol from BD Biosciences. The  $5 \times 10^5$  cells/mL treated and untreated were suspended in cold binding buffer and stained simultaneously with 5  $\mu$ L FITC-Annexin V (green fluorescence) and 5  $\mu$ L PI in a dark at room temperature for 15 min. The percentages of apoptotic cells were determined by double staining with Annexin V-FITC/PI. In each tube was added 400  $\mu$ L of Annexin V binding buffer and the 5000 cells/sample were collected using FACSCantoII flow cytometer (Becton Dickinson—BD) and the analysis was performed using DIVA 6.2 software in order to identify early apoptosis (Annexin+/PI−), late apoptosis (Annexin+/PI+) and necrosis (Annexin−/PI+) [48].

#### 4.3.5. Cell Cycle Analysis

The assay was carried out using Cycletest Plus DNA Reagent Kit and the manufacturer's protocol from BD Biosciences. Previously fixed cells ( $5 \times 10^5$ ) were washed twice in PBS and cell pellets were resuspended in PBS. The probes were kept in the dark and at 4 °C until data acquisition by flow cytometry using a FACSCantoII flow cytometer (Becton Dickinson—BD). The analysis was performed using ModFIT software in order to estimate the DNA index (DI) and progression through cell cycle phases [49].

#### 4.4. *Daphnia Magna* Toxicity Assay

*D. magna* Straus was maintained parthenogenetically at 'Carol Davila' University (Department of Pharmaceutical Botany and Cell Biology). The culture was maintained at 25 °C, a photoperiod of 16 h/8 h light/dark cycle. Prior to the determination, young daphnids were selected according to their size and maintained for 24 h in artificial medium. The bioassay was performed on 10 daphnids/replicates in tissue culture plates with 12 wells (Greiner Bio-One) according to the protocol described in our previous studies [50,51]. For each compound, six concentrations were tested, ranging from 5 to 128  $\mu$ M. The hydrazides **2a** (20–411  $\mu$ M) and **2b** (20–394  $\mu$ M) were used as positive controls, and a 1% DMSO solution as a negative control. The concentrations were selected based on the solubility and a pre-screening assay. The final volume/well was 4 mL, and the lethality was recorded at 24 and 48 h of exposure. All determinations were performed in duplicate. The 95% confidence intervals (95%CI) for LC50 values were also calculated using the least square fit method. All calculations were performed using GraphPad Prism v 5.1 software.

#### 4.5. Prediction of the Molecular Mechanism of Action and Toxicity

##### 4.5.1. PASS Prediction

A virtual screening was performed using the computer program PASS (prediction of activity spectra for substances), a software product designed to evaluate the general biological potential drug-like molecules. The compounds were inputted in PASS as mol files and the results were analyzed if the Pa values were above the corresponding Pi values. The resulted biological targets were manually selected based on their anticancer treatment potential.

##### 4.5.2. Structural Similarity Analysis

A similarity search was performed on the ChEMBL database for each compound **3a–e** using a 50% threshold. The resulting structures were extracted together with their assayed activities on human targets [52]. The entries were filtered using DataWarrior v5.2.1 software [53] to remove compounds with inexact potency values and to merge duplicate structures into single entries with calculated average pIC50 or pEC50 values expressed as mol/L (M).

#### 4.5.3. Prediction of the Compounds' Toxicity

The freely available program GUSAR was used to predict the LD50 values of the new compounds after oral and intravenous administration on rats [54].

#### 5. Patents

Patent application a202000446: Camelia Elena Stecoza, George Mihai Nitulescu, Mirela Antonela Mihaila, Marinela Bostan, Constantin Draghici, Miron Teodor Caproiu, 2-Aryl(heteroaryl)-5-[2-(phenylthiomethyl)phenyl]-1,3,4-oxadiazole derivatives, a pharmaceutical composition containing them and their use as antitumor agent, published in RO-BOPI, 11/2020 from 27 November 2020.

**Author Contributions:** Conceptualization, C.E.S.; methodology and investigation, C.E.S., G.M.N., C.D., M.T.C., O.T.O., M.B., M.M.; writing—original draft preparation, C.E.S., G.M.N., C.D., M.T.C., O.T.O., M.B., M.M.; writing—review and editing, C.E.S., G.M.N., M.M. All authors have read and agreed to the published version of the manuscript.

**Funding:** This research received no external funding. The APC was funded by the authors.

**Institutional Review Board Statement:** Not applicable.

**Informed Consent Statement:** Not applicable.

**Data Availability Statement:** The datasets used and/or analysed during the current study are available from the corresponding author on reasonable request.

**Conflicts of Interest:** The authors declare no conflict of interest.

#### References

- Sung, H.; Ferlay, J.; Siegel, R.L.; Laversanne, M.; Soerjomataram, I.; Jemal, A.; Bray, F. Global cancer statistics 2020: GLOBOCAN estimates of incidence and mortality worldwide for 36 cancers in 185 countries. *CA. Cancer J. Clin.* **2021**, *68*, 394–424.
- Wang, X.; Zhang, H.; Chen, X. Drug resistance and combating drug resistance in cancer. *Cancer Drug Resist.* **2019**, *2*, 141–160. [CrossRef]
- Schirrmacher, V. From chemotherapy to biological therapy: A review of novel concepts to reduce the side effects of systemic cancer treatment (Review). *Int. J. Oncol.* **2019**, *54*, 407–419.
- Ion, G.N.D.; Olaru, O.T.; Nitulescu, G.; Olaru, I.I.; Tsatsakis, A.; Burykina, T.I.; Spandidos, D.A.; Nitulescu, G.M. Improving the odds of success in antitumoral drug development using scoring approaches towards heterocyclic scaffolds. *Oncol. Rep.* **2020**, *44*, 589–598. [CrossRef]
- Lang, D.K.; Kaur, R.; Arora, R.; Saini, B.; Arora, S. Nitrogen-Containing Heterocycles as Anticancer Agents: An Overview. *Anti-Cancer Agents Med. Chem.* **2020**, *20*, 2150–2168. [CrossRef]
- Boström, J.; Hogner, A.; Llinàs, A.; Wellner, E.; Plowright, A.T. Oxadiazoles in medicinal chemistry. *J. Med. Chem.* **2012**, *55*, 1817–1830. [CrossRef]
- Benassi, A.; Doria, F.; Pirota, V. Groundbreaking anticancer activity of highly diversified oxadiazole scaffolds. *Int. J. Mol. Sci.* **2020**, *21*, 8692. [CrossRef]
- Glomb, T.; Szymankiewicz, K.; Świątek, P. Anti-cancer activity of derivatives of 1,3,4-oxadiazole. *Molecules* **2018**, *23*, 3361. [CrossRef]
- Akhtar, J.; Khan, A.A.; Ali, Z.; Haider, R.; Shahar Yar, M. Structure-activity relationship (SAR) study and design strategies of nitrogen-containing heterocyclic moieties for their anticancer activities. *Eur. J. Med. Chem.* **2017**, *125*, 143–189. [CrossRef] [PubMed]
- Sankhe, N.M.; Durgashivaprasad, E.; Gopalan Kutty, N.; Venkata Rao, J.; Narayanan, K.; Kumar, N.; Jain, P.; Udupa, N.; Vasanth Raj, P. Novel 2,5-disubstituted-1,3,4-oxadiazole derivatives induce apoptosis in HepG2 cells through p53 mediated intrinsic pathway. *Arab. J. Chem.* **2019**, *12*, 2548–2555. [CrossRef]
- Hamdy, R.; Elseginy, S.A.; Ziedan, N.I.; El-Sadek, M.; Lashin, E.; Jones, A.T.; Westwell, A.D. Design, synthesis and evaluation of new bioactive oxadiazole derivatives as anticancer agents targeting bcl-2. *Int. J. Mol. Sci.* **2020**, *21*, 8980. [CrossRef]
- Sun, J.; Li, M.H.; Qian, S.S.; Guo, F.J.; Dang, X.F.; Wang, X.M.; Xue, Y.R.; Zhu, H.L. Synthesis and antitumor activity of 1,3,4-oxadiazole possessing 1,4-benzodioxan moiety as a novel class of potent methionine aminopeptidase type II inhibitors. *Bioorg. Med. Chem. Lett.* **2013**, *23*, 2876–2879. [CrossRef]
- Zhang, X.M.; Qiu, M.; Sun, J.; Zhang, Y.B.; Yang, Y.S.; Wang, X.L.; Tang, J.F.; Zhu, H.L. Synthesis, biological evaluation, and molecular docking studies of 1,3,4-oxadiazole derivatives possessing 1,4-benzodioxan moiety as potential anticancer agents. *Bioorg. Med. Chem.* **2011**, *19*, 6518–6524. [CrossRef]

14. Bajaj, S.; Roy, P.P.; Singh, J. 1,3,4-Oxadiazoles as Telomerase Inhibitor: Potential Anticancer Agents. *Anti-Cancer Agents Med. Chem.* **2017**, *17*, 1869–1883. [CrossRef] [PubMed]
15. Zhang, S.; Luo, Y.; He, L.Q.; Liu, Z.J.; Jiang, A.Q.; Yang, Y.H.; Zhu, H.L. Synthesis, biological evaluation, and molecular docking studies of novel 1,3,4-oxadiazole derivatives possessing benzotriazole moiety as FAK inhibitors with anticancer activity. *Bioorg. Med. Chem.* **2013**, *21*, 3723–3729. [CrossRef]
16. Du, Q.R.; Li, D.D.; Pi, Y.Z.; Li, J.R.; Sun, J.; Fang, F.; Zhong, W.Q.; Gong, B.-H.; Zhu, H.L. Novel 1,3,4-oxadiazole thioether derivatives targeting thymidylate synthase as dual anticancer/antimicrobial agents. *Bioorg. Med. Chem.* **2013**, *21*, 2286–2297. [CrossRef] [PubMed]
17. Bajaj, S.; Asati, V.; Singh, J.; Roy, P.P. 1,3,4-Oxadiazoles: An emerging scaffold to target growth factors, enzymes and kinases as anticancer agents. *Eur. J. Med. Chem.* **2015**, *97*, 124–141. [CrossRef]
18. Khan, K.M.; Rani, M.; Ambreen, N.; Ali, M.; Hussain, S.; Perveen, S.; Choudhary, M.I. 2,5-Disubstituted-1,3,4-oxadiazoles: Thymidine phosphorylase inhibitors. *Med. Chem. Res.* **2013**, *22*, 6022–6028. [CrossRef]
19. Alam, M.M.; Almalki, A.S.; Neamatallah, T.; Ali, N.M.; Malebari, A.M.; Nazreen, S. Synthesis of New 1, 3, 4-Oxadiazole-Incorporated 1, 2, 3-Triazole Moieties as Potential Anticancer Agents Targeting Thymidylate Synthase and Their Docking Studies. *Pharmaceuticals* **2020**, *13*, 390. [CrossRef] [PubMed]
20. Liu, K.; Lu, X.; Zhang, H.J.; Sun, J.; Zhu, H.L. Synthesis, molecular modeling and biological evaluation of 2-(benzylthio)-5-aryloxadiazole derivatives as anti-tumor agents. *Eur. J. Med. Chem.* **2012**, *47*, 473–478. [CrossRef]
21. Akhtar, M.J.; Siddiqui, A.A.; Khan, A.A.; Ali, Z.; Dewangan, R.P.; Pasha, S.; Yar, M.S. Design, synthesis, docking and QSAR study of substituted benzimidazole linked oxadiazole as cytotoxic agents, EGFR and erbB2 receptor inhibitors. *Eur. J. Med. Chem.* **2017**, *126*, 853–869. [CrossRef] [PubMed]
22. Ruel, R.; Thibeault, C.; L'Heureux, A.; Martel, A.; Cai, Z.W.; Wei, D.; Qian, L.; Barrish, J.C.; Mathur, A.; D'Arienzo, C.; et al. Discovery and preclinical studies of 5-isopropyl-6-(5-methyl-1,3,4-oxadiazol-2-yl)-N-(2-methyl-1H-pyrrolo[2,3-b]pyridin-5-yl)pyrrolo[2,1-f][1,2,4]triazin-4-amine (BMS-645737), an in vivo active potent VEGFR-2 inhibitor. *Bioorg. Med. Chem. Lett.* **2008**, *18*, 2985–2989. [CrossRef] [PubMed]
23. Kamal, A.; Srikanth, P.S.; Vishnuvardhan, M.V.P.S.; Kumar, G.B.; Suresh Babu, K.; Hussaini, S.M.A.; Kapure, J.S.; Alarifi, A. Combretastatin linked 1,3,4-oxadiazole conjugates as a Potent Tubulin Polymerization inhibitors. *Bioorg. Chem.* **2016**, *65*, 126–136. [CrossRef] [PubMed]
24. Rajak, H.; Agarawal, A.; Parmar, P.; Thakur, B.S.; Veerasamy, R.; Sharma, P.C.; Kharya, M.D. 2,5-Disubstituted-1,3,4-oxadiazoles/thiadiazole as surface recognition moiety: Design and synthesis of novel hydroxamic acid based histone deacetylase inhibitors. *Bioorg. Med. Chem. Lett.* **2011**, *21*, 5735–5738. [CrossRef]
25. Valente, S.; Trisciuglio, D.; De Luca, T.; Nebbioso, A.; Labella, D.; Lenoci, A.; Bigogno, C.; Dondio, G.; Miceli, M.; Brosch, G.; et al. 1,3,4-Oxadiazole-containing histone deacetylase inhibitors: Anticancer activities in cancer cells. *J. Med. Chem.* **2014**, *57*, 6259–6265. [CrossRef] [PubMed]
26. Terenzi, A.; Fanelli, M.; Ambrosi, G.; Amatori, S.; Fusi, V.; Giorgi, L.; Turco Liveri, V.; Barone, G. DNA binding and antiproliferative activity toward human carcinoma cells of copper(ii) and zinc(ii) complexes of a 2,5-diphenyl[1,3,4]oxadiazole derivative. *Dalt. Trans.* **2012**, *41*, 4389–4395. [CrossRef]
27. Stecoza, C.; Majekova, M.; Majek, P.; Caproiu, M.; Marutescu, L. Novel Dibenzothiepins with Antibiofilm Activity Demonstrated by Microbiological Assays and Molecular Modeling. *Curr. Org. Chem.* **2013**, *17*, 113–124. [CrossRef]
28. Stecoza, C.E.; Ilie, C.; Caproiu, M.T.; Draghici, C. New 2-metyl-O-acyloximino-dibenzo [b,e] thiepins Synthesis and structural characterization. *Rev. Chim.* **2011**, *62*, 610–613.
29. Patra, A.; Ghorai, S.K.; De, S.R.; Mal, D. Regiospecific Synthesis of Benzo[b]fluorenones via Ring Contraction by Benzil-Benzilic Acid Rearrangement of Benz[a]anthracene-5,6-diones. *Synthesis* **2006**, *2006*, 2556–2562. [CrossRef]
30. Kumar, H.; Javed, S.A.; Khan, S.A.; Amir, M. 1,3,4-Oxadiazole/thiadiazole and 1,2,4-triazole derivatives of biphenyl-4-yloxy acetic acid: Synthesis and preliminary evaluation of biological properties. *Eur. J. Med. Chem.* **2008**, *43*, 2688–2698. [CrossRef]
31. Gamal El-Din, M.M.; El-Gamal, M.I.; Abdel-Maksoud, M.S.; Yoo, K.H.; Oh, C.H. Synthesis and in vitro antiproliferative activity of new 1,3,4-oxadiazole derivatives possessing sulfonamide moiety. *Eur. J. Med. Chem.* **2015**, *90*, 45–52. [CrossRef]
32. Hustedt, N.; Durocher, D. The control of DNA repair by the cell cycle. *Nat. Cell Biol.* **2017**, *19*, 1–9. [CrossRef]
33. Lezaja, A.; Altmeyer, M. Inherited DNA lesions determine G1 duration in the next cell cycle. *Cell Cycle* **2018**, *17*, 24–32. [CrossRef] [PubMed]
34. Bostan, M.; Petrică-Matei, G.G.; Ion, G.; Radu, N.; Mihăilă, M.; Hainăroșie, R.; Brașoveanu, L.I.; Roman, V.; Constantin, C.; Neagu, M.T. Cisplatin effect on head and neck squamous cell carcinoma cells is modulated by ERK1/2 protein kinases. *Exp. Ther. Med.* **2019**, *18*, 5041–5051. [CrossRef]
35. Mihaila, M.; Bostan, M.; Hotnog, D.; Ferdes, M.; Brasoveanu, L.I. Real-time analysis of quercetin, resveratrol and/or doxorubicin effects in mcf-7 cells. *Rom. Biotechnol. Lett.* **2013**, *18*, 8106–8114.
36. Maciucă, A.-M.; Munteanu, A.-C.; Mihaila, M.; Badea, M.; Olar, R.; Nitulescu, G.M.; Munteanu, C.V.A.; Bostan, M.; Uivarosi, V. Rare-Earth Metal Complexes of the Antibacterial Drug Oxolinic Acid: Synthesis, Characterization, DNA/Protein Binding and Cytotoxicity Studies. *Molecules* **2020**, *25*, 5418. [CrossRef]
37. Bostan, M.; Petrică-Matei, G.G.; Radu, N.; Hainăroșie, R.; Stefanescu, C.D.; Diaconu, C.C.; Roman, V. The Effect of Resveratrol or Curcumin on Head and Neck Cancer Cells Sensitivity to the Cytotoxic Effects of Cisplatin. *Nutrients* **2020**, *12*, 2596. [CrossRef]

38. Filimonov, D.A.; Lagunin, A.A.; Glorizova, T.A.; Rudik, A.V.; Druzhilovskii, D.S.; Pogodin, P.V.; Poroikov, V.V. Prediction of the biological activity spectra of organic compounds using the pass online web resource. *Chem. Heterocycl. Compd.* **2014**, *50*, 444–457. [CrossRef]
39. Choi, S.; Jung, H.J.; Kim, M.W.; Kang, J.H.; Shin, D.; Jang, Y.S.; Yoon, Y.S.; Oh, S.H. A novel STAT3 inhibitor, STX-0119, attenuates liver fibrosis by inactivating hepatic stellate cells in mice. *Biochem. Biophys. Res. Commun.* **2019**, *513*, 49–55. [CrossRef]
40. Malojirao, V.H.; Girimanhanaika, S.S.; Shanmugam, M.K.; Sherapura, A.; Dukanya; Metri, P.K.; Vigneshwaran, V.; Chinnathambi, A.; Alharbi, S.A.; Rangappa, S.; et al. Novel 1,3,4-oxadiazole targets STAT3 signaling to induce antitumor effect in lung cancer. *Biomedicines* **2020**, *8*, 368. [CrossRef] [PubMed]
41. Khanam, R.; Hejazi, I.I.; Shahabuddin, S.; Bhat, A.R.; Athar, F. Pharmacokinetic evaluation, molecular docking and in vitro biological evaluation of 1, 3, 4-oxadiazole derivatives as potent antioxidants and STAT3 inhibitors. *J. Pharm. Anal.* **2019**, *9*, 133–141. [CrossRef]
42. Verhoeven, Y.; Tilborghs, S.; Jacobs, J.; De Waele, J.; Quatannens, D.; Deben, C.; Prenen, H.; Pauwels, P.; Trinh, X.B.; Wouters, A.; et al. The potential and controversy of targeting STAT family members in cancer. *Semin. Cancer Biol.* **2020**, *60*, 41–56. [CrossRef] [PubMed]
43. Matsuno, K.; Masuda, Y.; Uehara, Y.; Sato, H.; Muroya, A.; Takahashi, O.; Yokotagawa, T.; Furuya, T.; Okawara, T.; Otsuka, M.; et al. Identification of a New Series of STAT3 Inhibitors by Virtual Screening. *ACS Med. Chem. Lett.* **2010**, *1*, 371–375. [CrossRef] [PubMed]
44. Chen, H.; Yang, Z.; Ding, C.; Chu, L.; Zhang, Y.; Terry, K.; Liu, H.; Shen, Q.; Zhou, J. Fragment-based drug design and identification of HJC0123, a novel orally bioavailable STAT3 inhibitor for cancer therapy. *Eur. J. Med. Chem.* **2013**, *62*, 498–507. [CrossRef]
45. Corvinus, F.M.; Orth, C.; Moriggl, R.; Tsareva, S.A.; Wagner, S.; Pfizner, E.B.; Baus, D.; Kaufmann, R.; Huber, L.A.; Zatloukal, K.; et al. Persistent STAT3 activation in colon cancer is associated with enhanced cell proliferation and tumor growth. *Neoplasia* **2005**, *7*, 545–555. [CrossRef] [PubMed]
46. Yan, L.X.; Wu, Q.N.; Zhang, Y.; Li, Y.Y.; Liao, D.Z.; Hou, J.H.; Fu, J.; Zeng, M.S.; Yun, J.P.; Wu, Q.L.; et al. Knockdown of miR-21 in human breast cancer cell lines inhibits proliferation, in vitro migration and in vivo tumor growth. *Breast Cancer Res.* **2011**, *13*, 1–14. [CrossRef] [PubMed]
47. Li, C.; Zhao, L.; Chen, Y.; He, T.; Chen, X.; Mao, J.; Li, C.; Lyu, J.; Meng, Q.H. MicroRNA-21 promotes proliferation, migration, and invasion of colorectal cancer, and tumor growth associated with down-regulation of sec23a expression. *BMC Cancer* **2016**, *16*, 605. [CrossRef]
48. Botezatu, A.; Iancu, I.V.; Plesa, A.; Manda, D.; Popa, O.; Bostan, M.; Mihaila, M.; Albulescu, A.; Fudulu, A.; Vladoiu, S.V.; et al. Methylation of tumour suppressor genes associated with thyroid cancer. *Cancer Biomark.* **2019**, *25*, 53–65. [CrossRef]
49. Hotnog, D.; Mihaila, M.; Botezatu, A.; Matei, G.G.; Hotnog, C.; Anton, G.; Bostan, M.; Brasoveanu, L.I. Genistein potentiates the apoptotic effect of 5-fluorouracyl in colon cancer cell lines. *Rom. Biotechnol. Lett.* **2013**, *18*, 7151–7160.
50. Nitulescu, G.; Mihai, D.P.; Nicorescu, I.M.; Olaru, O.T.; Ungurianu, A.; Zafiriescu, A.; Nitulescu, G.M.; Margina, D. Discovery of natural naphthoquinones as sortase A inhibitors and potential anti-infective solutions against *Staphylococcus aureus*. *Drug Dev. Res.* **2019**, *80*, 1136–1145. [CrossRef] [PubMed]
51. Seremet, O.C.; Olaru, O.T.; Gutu, C.M.; Nitulescu, G.M.; Ilie, M.; Negres, S.; Zbarcea, C.E.; Purdel, C.N.; Spandidos, D.A.; Tsatsakis, A.M.; et al. Toxicity of plant extracts containing pyrrolizidine alkaloids using alternative invertebrate models. *Mol. Med. Rep.* **2018**, *17*, 7757–7763. [CrossRef] [PubMed]
52. Mendez, D.; Gaulton, A.; Bento, A.P.; Chambers, J.; De Veij, M.; Félix, E.; Magariños, M.P.; Mosquera, J.F.; Mutowo, P.; Nowotka, M.; et al. ChEMBL: Towards direct deposition of bioassay data. *Nucleic Acids Res.* **2019**, *47*, D930–D940. [CrossRef]
53. Sander, T.; Freyss, J.; von Korff, M.; Rufener, C. DataWarrior: An Open-Source Program for Chemistry Aware Data Visualization and Analysis. *J. Chem. Inf. Model.* **2015**, *55*, 460–473. [CrossRef]
54. Zakharov, A.V.; Peach, M.L.; Sitzmann, M.; Nicklaus, M.C. A new approach to radial basis function approximation and its application to QSAR. *J. Chem. Inf. Model.* **2014**, *54*, 713–719. [CrossRef] [PubMed]







## Article

# Inhibition of XPO-1 Mediated Nuclear Export through the Michael-Acceptor Character of Chalcones

Marta Gargantilla <sup>1</sup>, José López-Fernández <sup>1</sup>, Maria-Jose Camarasa <sup>1</sup>, Leentje Persoons <sup>2</sup>, Dirk Daelemans <sup>2</sup>, Eva-Maria Priego <sup>1,\*</sup> and María-Jesús Pérez-Pérez <sup>1,\*</sup>

<sup>1</sup> Instituto de Química Médica (IQM, CSIC) c/Juan de la Cierva 3, 28006 Madrid, Spain; mgargantilla@iqm.csic.es (M.G.); jose.lopez@iiq.csic.es (J.L.-F.); mj.camarasa@iqm.csic.es (M.-J.C.)

<sup>2</sup> KU Leuven Department of Microbiology, Immunology and Transplantation, Laboratory of Virology and Chemotherapy, Rega Institute for Medical Research, KU Leuven, Herestraat 49, 3000 Leuven, Belgium; leentje.persoons@kuleuven.be (L.P.); dirk.daelemans@kuleuven.be (D.D.)

\* Correspondence: empriego@iqm.csic.es (E.-M.P.); mjperrez@iqm.csic.es (M.-J.P.-P.); Tel.: +34-91-5680040 (E.-M.P.); +34-91-2587516 (M.-J.P.-P.);

**Abstract:** The nuclear export receptor exportin-1 (XPO1, CRM1) mediates the nuclear export of proteins that contain a leucine-rich nuclear export signal (NES) towards the cytoplasm. XPO1 is considered a relevant target in different human diseases, particularly in hematological malignancies, tumor resistance, inflammation, neurodegeneration and viral infections. Thus, its pharmacological inhibition is of significant therapeutic interest. The best inhibitors described so far (leptomycin B and SINE compounds) interact with XPO1 through a covalent interaction with Cys528 located in the NES-binding cleft of XPO1. Based on the well-established feature of chalcone derivatives to react with thiol groups via hetero-Michael addition reactions, we have synthesized two series of chalcones. Their capacity to react with thiol groups was tested by incubation with GSH to afford the hetero-Michael adducts that evolved backwards to the initial chalcone through a retro-Michael reaction, supporting that the covalent interaction with thiols could be reversible. The chalcone derivatives were evaluated in antiproliferative assays against a panel of cancer cell lines and as XPO1 inhibitors, and a good correlation was observed with the results obtained in both assays. Moreover, no inhibition of the cargo export was observed when the two prototype chalcones **9** and **10** were tested against a XPO1-mutated Jurkat cell line (XPO1C528S), highlighting the importance of the Cys at the NES-binding cleft for inhibition. Finally, their interaction at the molecular level at the NES-binding cleft was studied by applying the computational tool CovDock.

**Keywords:** chalcones; exportin-1; covalent binding; CovDock; anticancer activity

**Citation:** Gargantilla, M.; López-Fernández, J.; Camarasa, M.-J.; Persoons, L.; Daelemans, D.; Priego, E.-M.; Pérez-Pérez, M.-J. Inhibition of XPO-1 Mediated Nuclear Export through the Michael-Acceptor Character of Chalcones. *Pharmaceuticals* **2021**, *14*, 1131. <https://doi.org/10.3390/ph14111131>

Academic Editors: Mary J. Meegan and Niamh M. O'Boyle

Received: 13 October 2021

Accepted: 4 November 2021

Published: 6 November 2021

**Publisher's Note:** MDPI stays neutral with regard to jurisdictional claims in published maps and institutional affiliations.



**Copyright:** © 2021 by the authors. Licensee MDPI, Basel, Switzerland. This article is an open access article distributed under the terms and conditions of the Creative Commons Attribution (CC BY) license (<https://creativecommons.org/licenses/by/4.0/>).

## 1. Introduction

Exportin-1 (XPO1, also known as chromosome region maintenance 1, CRM1) is the best-characterized nuclear transporter that mediates the traffic of high molecular weight molecules (i.e., proteins or RNA) from the nucleus to the cytoplasm [1,2]. Aberrant XPO1 function is implicated in different diseases, including different types of cancers, inflammation, neurodegeneration and viral infections [3–8]. In the nucleus, exportin-1 recognizes specific leucine-rich peptide stretches, known as nuclear export signals (NES) in cargo proteins, and forms a ternary complex with RanGTP. When this exportin-RanGTP-cargo complex reaches the cytoplasm, GTP is hydrolyzed to GDP, disrupting the ternary complex and releasing the cargo [2].

XPO1 has been found to be overexpressed in a variety of solid tumors and hematological cancers, and in many cases, elevated XPO1 levels have been correlated to poor prognosis [7,9]. Pharmacological inhibition of XPO1 has been considered an appealing anticancer strategy [2,4,5,10]. Indeed, XPO1 cargo proteins include many tumor suppressors and cell growth regulators, such as p53, Topo2, FOXOs, etc., [7,8], and XPO1 inhibition

has been shown to restore nuclear localization and function of these tumor suppressors, leading to apoptosis of the cancer cells [11].

The most potent XPO1 inhibitors described, either from natural or synthetic origin, are  $\alpha,\beta$ -unsaturated carbonyl compounds that bind into the NES-binding cleft of XPO1 through covalent interactions with Cys528 [2,4,10,12,13]. These inhibitors prevent the interaction of cargo proteins with XPO1 and, hence, block cargo export to the cytoplasm [14]. Only recently, a non-covalent XPO1 inhibitor has been described [15], while a first report on allosteric inhibitors with moderate affinity has been published [16].

The first XPO1 inhibitor clinically tested was the natural product leptomycin B (**1**, Figure 1). However, clinical trials were discontinued due to severe cytotoxicity [17], probably associated with irreversible inhibition. Among synthetic compounds, the *N*-azolylacrylate compounds [12,13], also known as selective inhibitors of nuclear export (SINE) exemplified by KPT-330 (selinexor) (**2**), KPT-185 (**3**) or the second generation compound KPT-8602 (eltanexor) (**4**) (Figure 1), have been described as very slowly reversible inhibitors [12,18–20]. Indeed, the recent FDA approval of selinexor (KPT-330, XPOVIO, **2**) for the treatment of patients with heavily pretreated relapsed or refractory multiple myeloma and diffuse B cell lymphoma supports the significance of XPO1 as a target in hematological malignancies [21]. Other interesting XPO1 inhibitors are the 1-(pyridin-2-ylamino)-1*H*-pyrrole-2,5-dione derivatives S109 (**5**) and CBS9106 (**6**) [22,23], with the latter being evaluated in Phase 1 clinical trials [24].

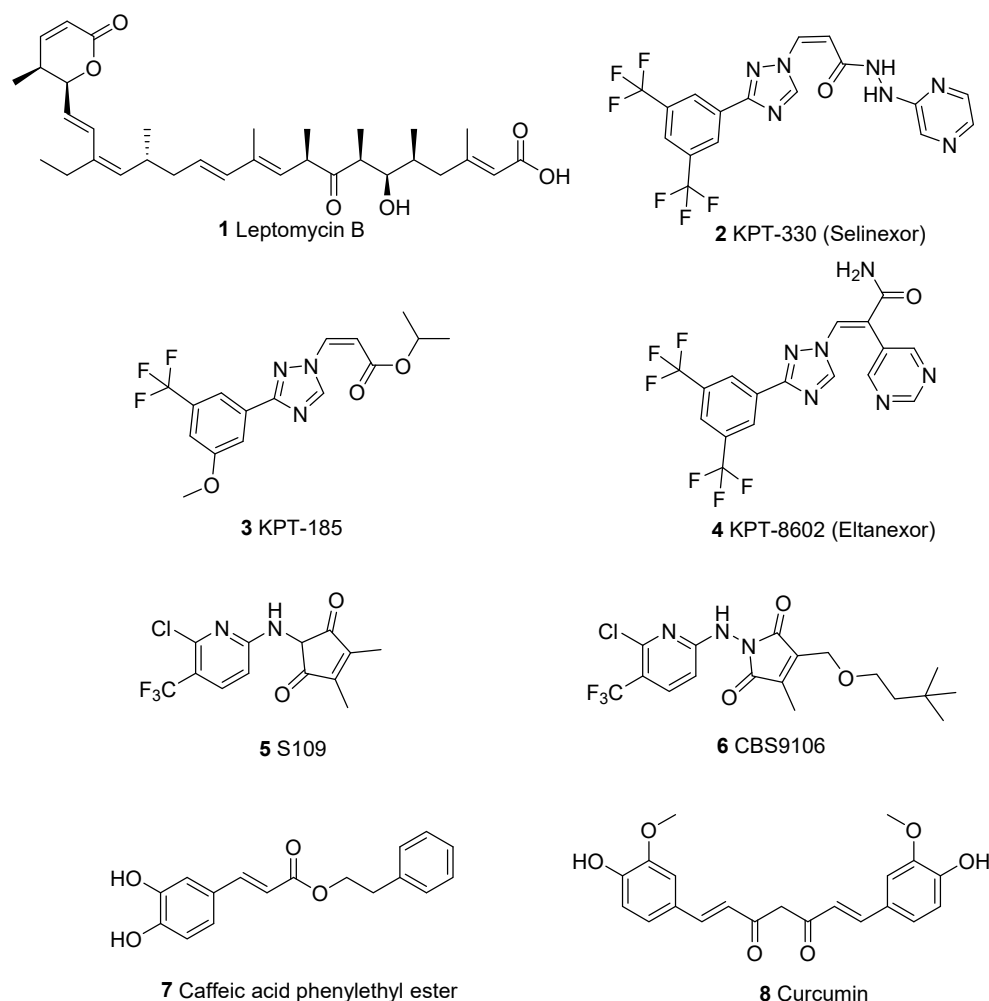


**Figure 1.** Chemical structures of several XPO1 inhibitors.

The overall structure of XPO1 complexed with Ran and RanBP1 is shown in Figure 2A, where the NES-binding cleft is colored in grey. Structurally, this cleft contains five hy-

drophobic pockets (named  $\Phi 0$ – $\Phi 4$ , Figure 2B) that lodge the hydrophobic key residues of the cargo protein. Cys528 (which corresponds to Cys539 in *Saccharomyces cerevisiae* in the X-ray structure) is located between the  $\Phi 3$  and  $\Phi 4$  pockets. While leptomycin B occupies almost all  $\Phi$  pockets [17], the KPT compounds exemplified by KPT-8602 (Figure 2C) only occupy a small part of the NES-binding cleft [25], demonstrating that XPO1 inhibition can be accomplished by only occupying part of the hydrophobic cleft. By analysing the binding mode of KPT-8602, it can be concluded that an aromatic hydrophobic core is located below the Cys-reactive residue, while more polar substituents (a pyrimidinyl ring in KPT-8602) can be lodged over the Cys in the proximities of the  $\Phi 4$  pocket.

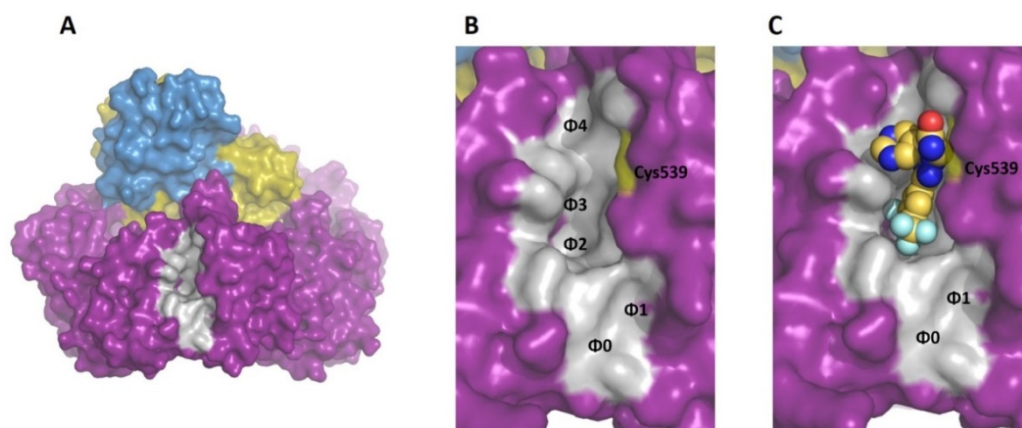


**Figure 2.** (A) Overall structure of the XPO1 protein (in deep purple), Ran (olive) and RanBP1 (sky blue). The NES-binding cleft is shown in grey. (B) Surface representation of the NES-binding cleft (grey) and the  $\Phi 0$ – $\Phi 4$  pockets. ScCys539 is shown in yellow and labelled. (C) Detailed view of KPT-8602 (yellow spheres, pdb id: 5jlj) inside of the NES-binding cleft.

Based on these precedents, we envisioned the chalcone scaffold as a suitable  $\alpha,\beta$ -unsaturated carbonyl construct for XPO1 inhibition by interaction with Cys528 based on their ability to behave as Michael acceptors. Indeed, quite similar  $\alpha,\beta$ -unsaturated carbonyl compounds such as caffeic acid phenylethyl ester (7, Figure 1) or curcumin (8) have been described as XPO1 inhibitors. Moreover, since chalcones can undergo a retro-Michael reaction, the expected inhibition should be reversible. Reversible covalent inhibitors may have some advantages versus their irreversible counterparts, such as the possibility to tune the residence time and/or to avoid the irreversible inhibition of off-targets [26], while as a disadvantage they may show lower potency. Compounds 9 and 10 (Figure 3) were proposed as prototypes, so that ring A should be lodged below the Cys where the covalent interaction takes place, while the pyrimidine (ring B) should be located closer to the  $\Phi 4$  pocket. The XPO1 inhibition obtained with these compounds triggered us to explore closely related structural analogues (Figure 3). Thus, their synthesis, antiproliferative activity against a panel of cancer cell lines, XPO1 inhibition and docking studies at the NES-binding cleft of XPO1 are here described.

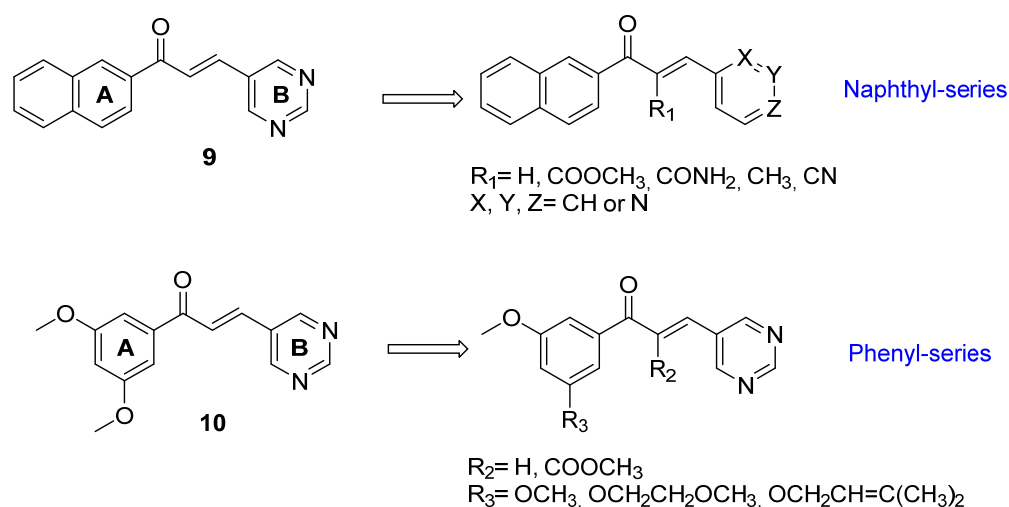
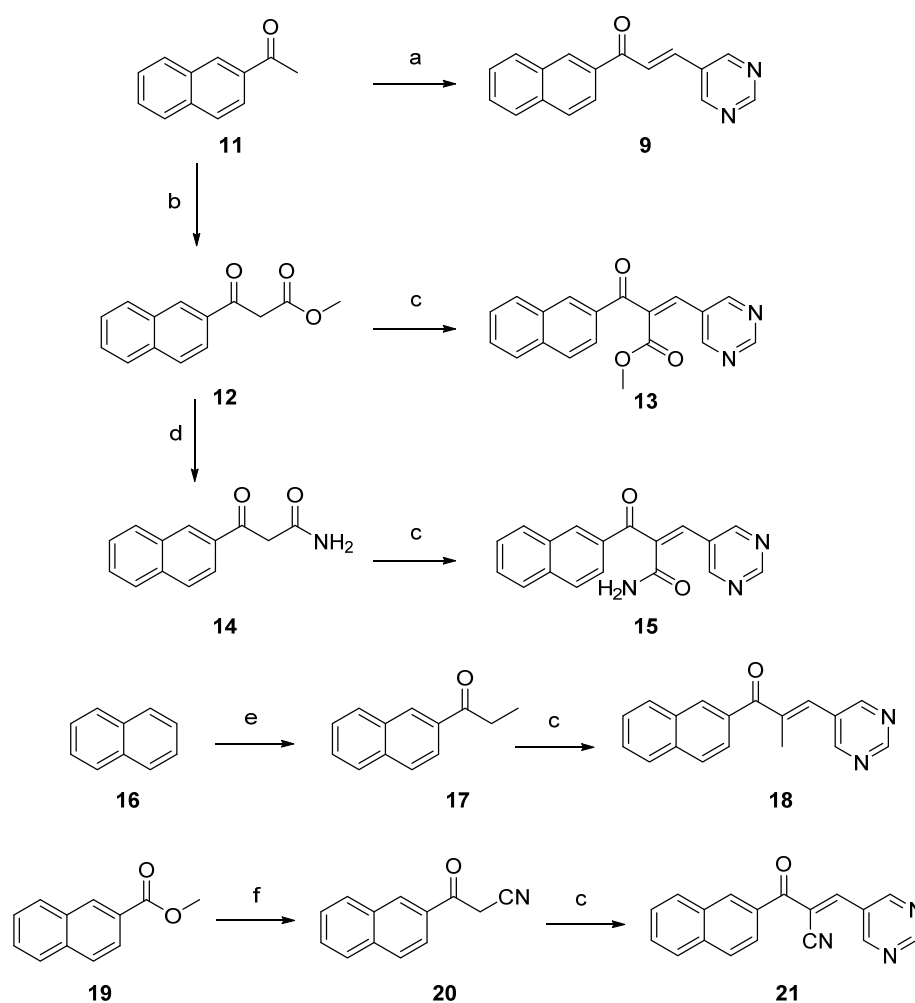


**Figure 3.** Chalcones synthesized and tested in this study as XPO1 inhibitors.

## 2. Results and Discussion

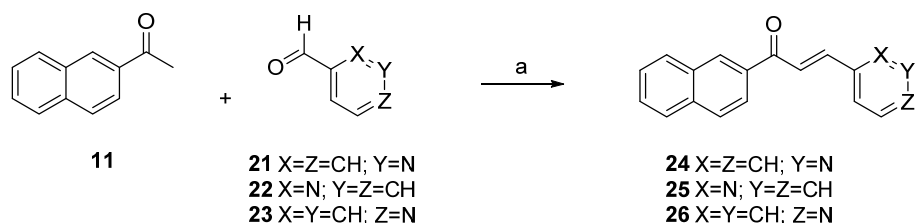
### 2.1. Synthesis

It has been described by performing kinetic measurements in  $\alpha$ -X-2',3,4,4'-tetramethylchalcones that the nature of the substituent at position  $\alpha$  of the chalcone affects their reactivity as electrophiles versus thiol groups [27]. In such series, the  $\alpha$ -COOEt substituent led to a similar reactivity as that of the  $\alpha$ -H chalcone; the  $\alpha$ -CH<sub>3</sub> chalcone was poorly electrophilic, while the  $\alpha$ -CN chalcone was the most electrophilic. Thus, in the naphthyl series (Figure 3), the synthesis of the chalcones where  $R_1 = \text{H, COOCH}_3, \text{CH}_3$  or CN was accomplished. The reaction of 1-(naphthalen-2-yl)ethan-1-one (**11**) with pyrimidine-5-carbaldehyde in the presence of Ba(OH)<sub>2</sub> afforded  $\alpha$ -H chalcone **9** in a 55% yield (Scheme 1). The ketone **11** reacted with dimethyl carbonate, as described, to provide the methyl 3-oxopropanoate **12** [28], whose reaction with pyrimidine-5-carbaldehyde resulted in the  $\alpha$ -COOCH<sub>3</sub> chalcone **13**. Reaction of the ester **12** with NH<sub>3</sub>/dioxane at 110 °C [29] led to the amide **14** that was further transformed into the chalcone **15**. On the other hand, reaction of naphthalene **16** with propionyl chloride under Friedel–Crafts acylation conditions, as described [30], provided the 2-acyl derivative **17**, together with a small proportion of its 1-isomer [31]. This mixture of isomers reacted with pyrimidine-5-carbaldehyde to yield the  $\alpha$ -CH<sub>3</sub> chalcone **18** (30%). Finally, the synthesis of the  $\alpha$ -CN derivative was addressed by the reaction of 2-methylnaphthoate (**19**) with acetonitrile to provide 3-oxopropanenitrile **20** [32], which was further transformed into the  $\alpha$ -CN chalcone **21**. Compound **21** proved to be very unstable and readily decomposed in phosphate-buffered solution (PBS), hampering its biological evaluation.



**Scheme 1.** Reagents and conditions: (a) pyrimidine-5-carbaldehyde, Ba(OH)<sub>2</sub>, methanol/water, rt, 2 h, 55% yield; (b) as described in [28]: dimethyl carbonate, NaH, 1,4-dioxane, 70 °C, 3.5 h; (c) pyrimidine-5-carbaldehyde, piperidine, AcOH, 70–100 °C, 2–48 h, 30–40% yield; (d) NH<sub>3</sub>, 1,4-dioxane, 110 °C, 16 h, 34% yield; (e) as described in [30]: propionyl chloride, AlCl<sub>3</sub>, 1,2-DCE, rt, 16 h; (f) as described in [32]: acetonitrile, NaH, toluene, 110 °C, 16 h.

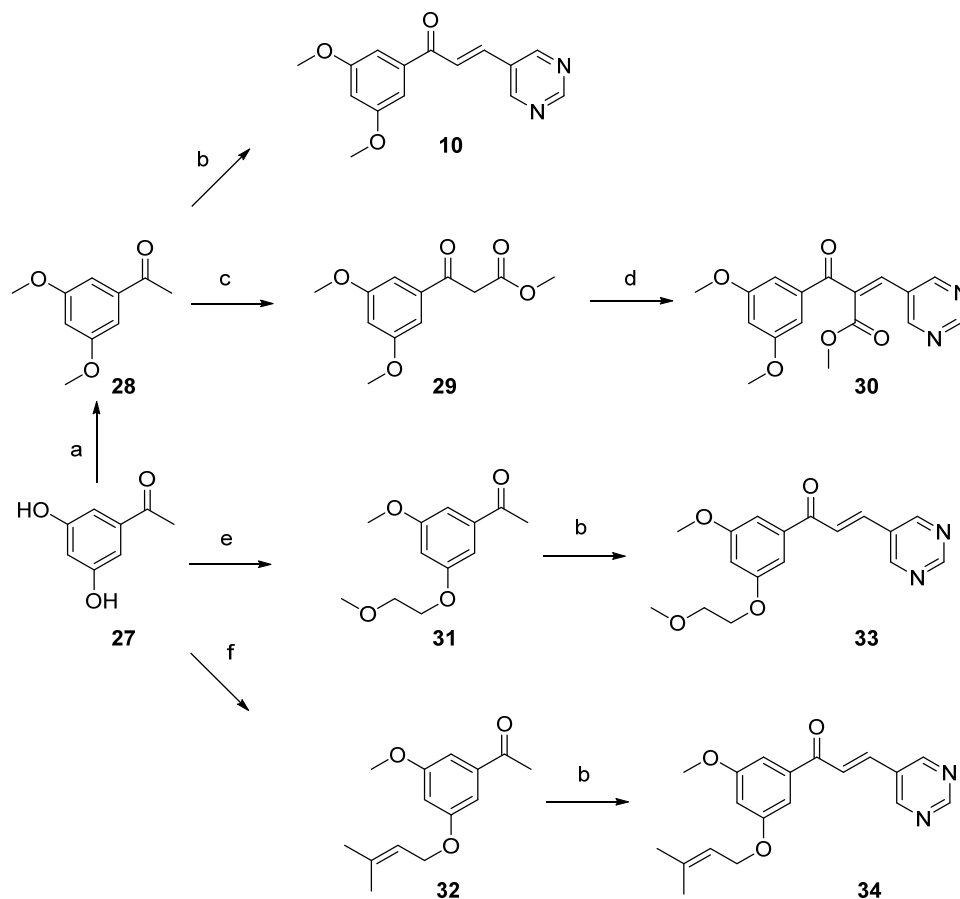
A second set of modifications involved the incorporation as ring B of different pyridines instead of the 5-pyrimidinyl of the prototype 9. To this end, the ketone 11 was reacted with different aldehydes (21–23) in the presence of Ba(OH)<sub>2</sub>, using a mixture of methanol and water at rt, to yield the chalcones 24–26 (Scheme 2).



**Scheme 2.** Reagents and conditions: (a) Ba(OH)<sub>2</sub>, methanol/water, rt, 2–7 h, 32–73% yield.

In parallel, we synthesized the 3,5-dimethoxyphenyl chalcone 10 (Scheme 3) by reaction of the 1-(3,5-dihydroxyphenyl)ethan-1-one 27 with methyl iodide to provide the ketone 28 [33], whose reaction with pyrimidine-5-carbaldehyde afforded the chalcone 10 (64% yield). Additionally, in this case, the α-COOCH<sub>3</sub> chalcone was synthesized through the transformation of the ketone 28 into the methylpropionate 29 [34], and further reaction

of this methyl ester with pyrimidine-5-carbaldehyde afforded the  $\alpha$ -COOCH<sub>3</sub> chalcone **30**. On the other hand, as will be later shown in the molecular modeling studies, one of the methoxy groups of the chalcone **10** seems to be pointing towards the lower part of the NES-binding cleft that lodges the aliphatic chain of leptomyacin B. Thus, one of the methoxy groups in the chalcone **10** was replaced by either a 2-methoxyethoxy or a 3,3-dimethylallyloxy group. To this end, the 3,5-dihydroxyacetophenone **27** was transformed in 2 steps into the corresponding ketones **31** and **32**, whose reaction with pyrimidine-5-carbaldehyde afforded the chalcones **33** and **34** in a 32% and 41% yield, respectively.



**Scheme 3.** Reagents and conditions: (a) as described in [33]: MeI, Cs<sub>2</sub>CO<sub>3</sub>, DMF, 80 °C, 1 h; (b) pyrimidine-5-carbaldehyde, Ba(OH)<sub>2</sub>, methanol/water, rt, 16 h, 32–64% yield; (c) as described in [34]: dimethyl carbonate, NaH, 1,4-dioxane, 70 °C, 3 h; (d) pyrimidine-5-carbaldehyde, piperidine, AcOH, 70 °C, 16 h, 39% yield; (e) (i) as described in [35]: MeI, Cs<sub>2</sub>CO<sub>3</sub>, DMF, rt, 16 h, (ii) 2-bromoethylmethyl ether, Cs<sub>2</sub>CO<sub>3</sub>, DMF, 80 °C, 1 h, 77% yield; (f) (i) as described in [35]: MeI, Cs<sub>2</sub>CO<sub>3</sub>, DMF, rt, 16 h; (ii) 3,3-dimethylallyl bromide, Cs<sub>2</sub>CO<sub>3</sub>, DMF, 80 °C, 1 h, 75% yield.

For the  $\alpha$ -H chalcones (**9**, **10**, **24–26**, **33**, **34**), the configuration of the double bond was easily assigned as *E*, as expected, based on the  $J_{H_2-H_3}$  value (15–16 Hz) in their <sup>1</sup>H-NMR spectra [36]. The configuration of the  $\alpha$ -substituted chalcones (**13**, **15**, **18**, **21**, **30**) was also assigned as *E*, based on previous reports [37,38].

## 2.2. Incubation with GSH

In order to determine if these chalcones could react with thiol groups through a hetero-Michael addition reaction, a few selected compounds (**9**, **10**, **13** and **18**) were incubated with glutathione (GSH). After different incubation times, the reactions were quenched by adding 5,5'-dithiobis(2-nitrobenzoic acid) (DTNB, Ellman's reagent) [39,40] (1:1 ratio with respect to the initial concentration of GSH). The course of the reaction was followed

by HPLC, adapting reported procedures [41,42]. The prototype  $\alpha$ -H chalcones **9** and **10** quickly reacted with GSH to provide the Michael addition products, as shown by HPLC-MS. These adducts underwent a retro-Michael addition reaction, generating the parent chalcone, demonstrating the reversibility of the reaction (see Figures S1 and S2). The  $\alpha$ -COOCH<sub>3</sub> chalcone **13** also provided the Michael adducts with GSH after a short reaction time, while longer incubations revealed that the adducts reverted to the parent chalcone (Figure S3). However, under the same incubation conditions with GSH, the  $\alpha$ -CH<sub>3</sub> chalcone **18** remained almost unaltered even after 4 h of incubation, and only a very small proportion of the addition products was detected (Figure S4). As already mentioned, the  $\alpha$ -CN chalcone **21** could not even be tested due to instability in PBS, suggesting a very high electrophilic character. Thus, although this assay is only qualitative, the tendency observed among these chalcones nicely fits the reactivity described for  $\alpha$ -X-2'-3,4,4'-tetramethylchalcones [27].

### 2.3. Biological Results

#### 2.3.1. Antiproliferative Activity

The synthesized compounds were tested for their antiproliferative activity against a panel of cancer cell lines using KPT-330 as a reference compound (Table 1).

**Table 1.** Antiproliferative activity of the synthesized chalcones against different tumor cell lines.

Comp	IC <sub>50</sub> (μM) <sup>a</sup>						
	Hap-1 <sup>b</sup>	HCT-116 <sup>b</sup>	NCI-H460 <sup>b</sup>	DND-41 <sup>b</sup>	HL-60 <sup>b</sup>	K-562 <sup>b</sup>	Z-138 <sup>b</sup>
<b>9</b>	2.3 ± 0.2	2.4 ± 0.2	2.1 ± 0.1	2.1 ± 0.5	2.0 ± 0.5	1.8 ± 0.08	1.8 ± 0.05
<b>10</b>	2.1 ± 0.2	4.7 ± 1.7	3.5 ± 1.5	1.5 ± 0.2	2.2 ± 0.3	7.2 ± 1.9	0.5 ± 0.05
<b>13</b>	≥54.9	≥15.5	≥47.1	≥30.6	>100	>100	>100
<b>15</b>	2.1 ± 0.7	5.3 ± 3.1	2.6 ± 0.7	8.9 ± 0.9	5.5 ± 3.6	2.1 ± 0.1	5.1 ± 2.7
<b>18</b>	>100	>100	>100	39.1 ± 5.3	≥40.9	48.5 ± 2.4	>100
<b>24</b>	1.6 ± 0.1	3.1 ± 0.9	4.3 ± 2.2	1.8 ± 0.5	3.5 ± 2.1	2.2 ± 0.03	1.6 ± 0.1
<b>25</b>	3.4 ± 0.5	3.9 ± 1.5	51.6 ± 11.7	2.6 ± 0.4	1.8 ± 0.05	4.8 ± 2.8	2.3 ± 0.5
<b>26</b>	2.3 ± 0.3	1.9 ± 0.4	7.7 ± 1.1	1.9 ± 0.4	0.9 ± 0.2	4.0 ± 0.2	1.1 ± 0.4
<b>30</b>	≥32.0	≥22.2	17.3 ± 4.6	43.2 ± 6.4	23.4 ± 1.9	42.9 ± 0.1	47.6 ± 1.1
<b>33</b>	4.3 ± 2.5	34.2 ± 6.5	16.9 ± 4.5	3.7 ± 1.6	10.0 ± 0.9	37.5 ± 0.9	1.5 ± 0.2
<b>34</b>	10.0 ± 2.0	52.9 ± 3.6	34.5 ± 5.2	10.1 ± 0.0	40.2 ± 10.1	4.1 ± 1.9	4.6 ± 2.7
<b>KPT-330</b>	0.07 ± 0.03	0.10 ± 0.1	0.12 ± 0.08	0.05 ± 0.0	0.11 ± 0.1	0.09 ± 0.0	0.40 ± 0.4

<sup>a</sup> IC<sub>50</sub>: concentration of compound at which 50% of cell proliferation is inhibited. Mean value of two independent experiments ±SEM.

<sup>b</sup> Hap-1: chronic myeloid leukemia; HCT-116: colorectal carcinoma; NCI-H460: lung carcinoma; DND-41: acute lymphoblastic leukemia; HL-60: acute myeloid leukemia; K-562: chronic myeloid leukemia; Z-138: non-Hodgkin lymphoma.

The two prototype compounds **9** and **10** inhibited proliferation against all cell lines tested at single digit μM IC<sub>50</sub> values, being between 5- to 30-fold less potent than the reference compound KPT-330. The  $\alpha$ -substituted chalcones in the naphthyl series with an ester (compound **13**) or methyl (compound **18**) group were almost inactive in the proliferation assays, while the  $\alpha$ -CONH<sub>2</sub> chalcone **15** was slightly less active than the parent chalcone **9**. When the 5-pyrimidinyl ring in **9** was replaced by different pyridines (pyridin-3-yl in **24**, pyridin-2-yl in **25** or pyridin-4-yl in **26**), the IC<sub>50</sub> values were maintained in the low μM range. Concerning the phenyl series, the  $\alpha$ -COOCH<sub>3</sub> chalcone **30** was considerably less active than the  $\alpha$ -H chalcone **10**. Moreover, replacement of one of the methoxy groups in compound **10** by longer ethers was compatible with antiproliferative activity, although up to a 20-fold increase in IC<sub>50</sub> values was obtained for certain cell lines.

#### 2.3.2. XPO1 Inhibition Studies

In order to determine if the observed antiproliferative activity was caused by XPO1 inhibition, the compounds were assayed in a reporter cell line based on the subcellular localization of a XPO1-dependent GFP reporter cargo protein [13]. Inhibition of XPO1-mediated nuclear export of the reporter is evident by its nuclear accumulation, which can



be visualized and quantified compared to the untreated control, where the GFP protein localizes in the cytoplasm. Using this reporter cell line, the capacity of the synthesized chalcones to inhibit XPO1-mediated nuclear export was determined (Table 2).

**Table 2.** XPO1 inhibition.

Comp	IC <sub>50</sub> (μM) <sup>a</sup>
<b>9</b>	2.46 ± 0.16
<b>10</b>	0.55 ± 0.19
<b>13</b>	>100
<b>5</b>	9.18 ± 3.28
<b>18</b>	>100
<b>24</b>	1.27 ± 0.29
<b>25</b>	7.28 ± 1.34
<b>26</b>	10.74 ± 3.24
<b>30</b>	87.34 ± 4.91
<b>33</b>	12.35 ± 1.28
<b>34</b>	1.59 ± 0.36
<b>KPT-330</b>	0.05

<sup>a</sup> IC<sub>50</sub> (50% inhibitory concentration) is given as the mean ± SEM of two independent experiments.

The prototype chalcones **9** and **10** both in the naphthyl and phenyl series showed significant XPO1 inhibition, with IC<sub>50</sub> values of 2.5 and 0.55 μM, respectively. Interestingly, among the naphthyl series, the chalcones substituted with an ester or a methyl group at the α-position of the double bond (compounds **13** and **18**, respectively) that were inactive in the antiproliferative activity assays, were also inactive against XPO1. On the other hand, the α-CONH<sub>2</sub> chalcone **15** or compounds with a pyridinyl ring (**24–26**) instead of the pyrimidinyl of the prototype **9**, which had shown significant antiproliferative activity, inhibited XPO1 with IC<sub>50</sub> values around or below 10 μM. Among the phenyl series, the α-COOCH<sub>3</sub> derivative **30** was almost inactive against XPO1, while the extended ethers **33** and **34** were active, particularly the 3,3-dimethylallyl derivative **34**, with an IC<sub>50</sub> value of 1.59 μM.

Once XPO1 inhibition was confirmed, an additional experiment was performed for compounds **9** and **10** employing a Jurkat leukemia cell line where the cysteine residue at position 528 of XPO1 had been replaced by a serine residue (Jurkat XPO1<sup>C528S</sup>) [19,43]. The effect of the mutation on the activity of the inhibitors was assessed by the visualization of the subcellular localization of the XPO1 cargo RanBP1. As shown in Figure 4A (control experiment), in both wild-type and mutant Jurkat cells, RanBP1 is localized in the cytoplasm as a consequence of the correct nuclear export mediated by XPO1. When both cell lines were treated with KPT-330 at 1 μM (used as a positive control, Figure 4B), in the wild-type cell line, RanBP1 was accumulated in the nucleus, since KPT-330 blocked its binding to XPO1, whereas in the mutant cell line, KPT-330 was unable to interact with XPO1; therefore, RanBP1 remained in the cytoplasm. Similarly, when both cell lines were treated with our prototype compounds **9** and **10** at 4 μM (Figure 4C, D, respectively), RanBP1 accumulated in the nucleus in the case of the wild-type cells, whereas its nuclear export was not inhibited in the mutant cell line.

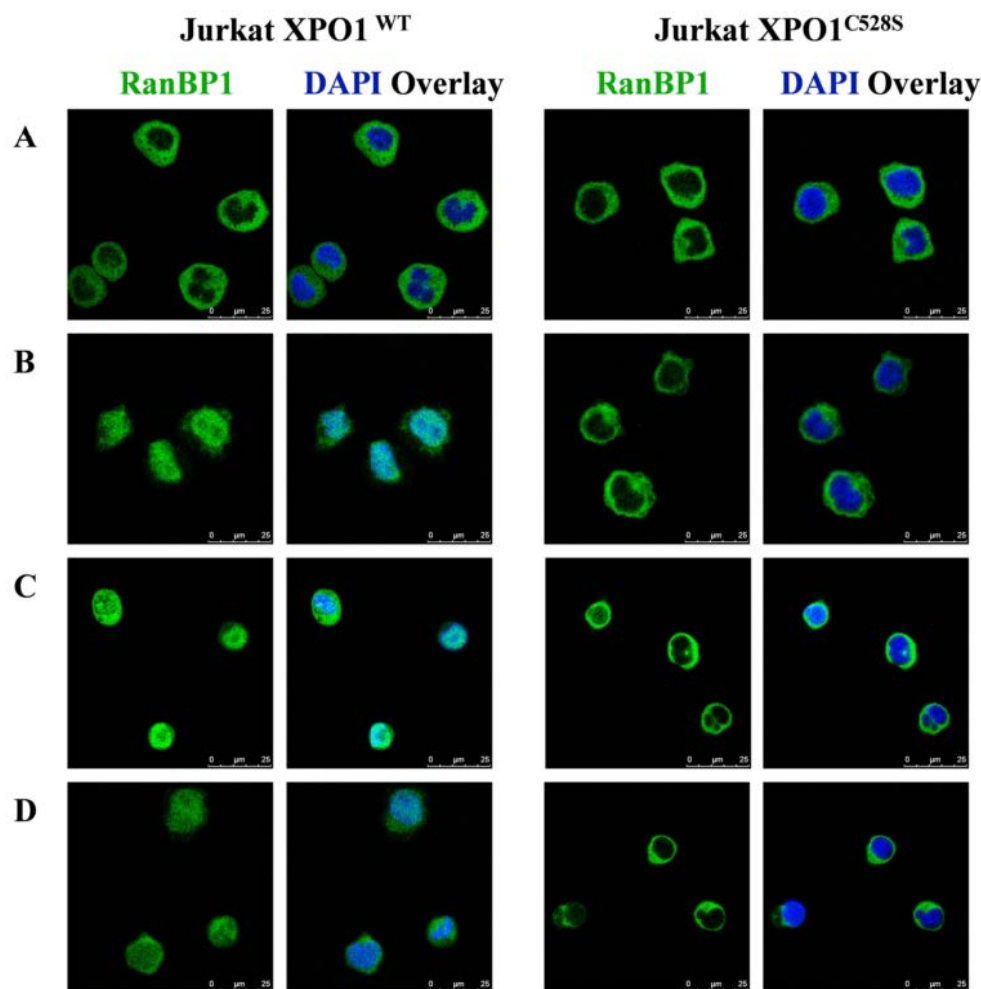


**Figure 4.** XPO1-mediated nuclear export of RanBP1 cargo protein. (A) Endogenous RanBP1 cargo protein (green) localized in the cytoplasm of untreated wild-type and mutant XPO1<sup>C528S</sup> Jurkat cells; (B) 3 h after treatment with 1  $\mu$ M KPT-330 (Selinexor), RanBP1 accumulates in the nucleus of wild-type cells (left) but remains localized in the cytoplasm of mutant XPO1<sup>C528S</sup> cells (right); (C,D) 3 h after treatment with 4  $\mu$ M of prototype compounds **9** or **10**, respectively, nuclear accumulation of RanBP1 is found in wild-type Jurkat cells. In contrast, no nuclear retention of the cargo was induced in the mutant XPO1<sup>C528S</sup> cells. Scale bar 25  $\mu$ m, and nuclei were counterstained with DAPI (blue).

The IC<sub>50</sub> values of compounds **9** and **10** regarding their XPO1 inhibitory activity in WT and C528S Jurkat cell lines are shown in Table 3. Both compounds **9** and **10** inhibited nuclear export of RanBP1 cargo protein with IC<sub>50</sub> values of 2.2 and 0.3  $\mu$ M, respectively, in the WT Jurkat cell line. These results were in agreement with the IC<sub>50</sub> values obtained for XPO1 inhibition in the HeLa reporter cell line (Table 2), where the chalcone **10** was the most potent of the two. What is most relevant is that both compounds lost their inhibitory activity against the Jurkat XPO1<sup>C528S</sup> cell line, similar to the positive control KPT-330. Thus, these experiments evidenced the importance of Cys528 for the XPO1 inhibitory activity of these chalcones.

**Table 3.** IC<sub>50</sub> values of **9** and **10** in means of XPO1 inhibition in wild-type and XPO1<sup>C528S</sup> mutant Jurkat cell lines.

Comp	IC <sub>50</sub> (μM) <sup>a</sup>	
	Jurkat XPO1 <sup>WT</sup>	Jurkat XPO1 <sup>C528S</sup>
KPT-330	0.07 ± 0.01	>5
<b>9</b>	2.2 ± 0.03	>5
<b>10</b>	0.3 ± 0.3	>5

<sup>a</sup> IC<sub>50</sub> (50% inhibitory concentration) is given as the mean ±SD of two independent experiments.

Thus, compounds **9** and **10**, able to react with GSH in incubation studies, were among the most potent XPO1 inhibitors and also showed good antiproliferative activity. On the other hand, the α-CH<sub>3</sub> chalcone **18**, which poorly reacted with GSH in the incubation assays, was unable to inhibit XPO1 and also did not show antiproliferative activity. The most puzzling data comes from the esters **13** and **30**, which were almost inactive against XPO1 and in antiproliferation assays. However, in the incubation studies with GSH, compound **13** seems to be as reactive as the α-H chalcone **9**. Certainly, many factors can be involved in the lack of activity of this chalcone. A potential explanation may arise by taking into account that the XPO1 inhibition assays are performed in a cell culture, so that the presence of esterases might convert the ester into the corresponding carboxylic acid. If this is the case, the resulting α-COOH chalcone would be very poorly electrophilic based on the reactivity described for α-X-2′3,4,4′-tetramethylchalcones [27], and thus, its capacity to behave as a Michael acceptor against XPO1 would be seriously compromised.

#### 2.4. Docking Studies

Docking molecular studies have been carried out for compounds **9** and **10** with CovDock [44,45], a computational tool developed by Schrödinger to perform covalent docking, using the coordinates of the *S. cerevisiae* XPO1 protein in its complex with KPT-8602 [20]. Using this tool, a covalent bond is created between the SH of Cys539 (Cys528 in human XPO1) in the NES-binding cleft and the β-position of the double bond of the chalcone.

The best-docked solution of compound **9** (Figure 5A) shows that the compound nicely fits within the upper part of the NES-binding cleft, so that the 2-naphthyl (ring A) has favorable interactions with the hydrophobic residues Ile555, Leu536, Phe583 and Val559, while the pyrimidin-5-yl ring (ring B) is buried in an inner region delimited by Ala552. As for compound **10** (Figure 5B), the best-docked solution indicates that the 3,5-dimethoxyphenyl ring lays in a hydrophobic cavity surrounded by the residues Ile555, Leu536 and Phe583, whereas ring B is directed to the upper part of the cleft. In addition, this binding mode is compatible with a hydrogen bond interaction between the carbonyl group of the ligand and the side chain of Lys579. This stabilizing interaction might help explain the higher inhibitory activity of compound **10** compared to **9** against XPO1. Additionally, this binding mode also suggests that one of the methoxy groups in ring A can be replaced by other longer ethers to gain additional interactions in the lower part of the cleft. Indeed, such ethers (compounds **33** and **34**) also showed XPO1 inhibition, but did not improve the inhibitory value of compound **10**.

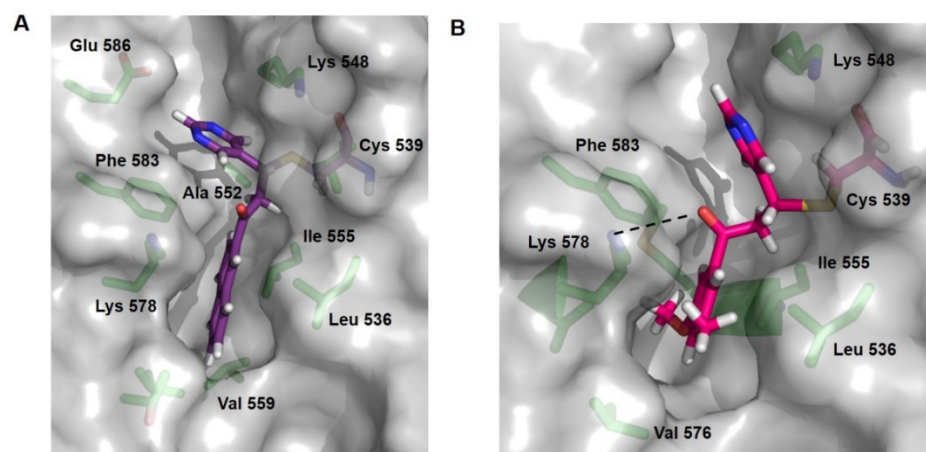


**Figure 5.** (A) Best CovDock solution of compound **9** (shown as purple sticks) at the NES-binding cleft of XPO1 (shown as light grey surface). (B) Best CovDock solution of compound **10** (shown as magenta sticks) at the NES-binding cleft of XPO1 (shown as light grey surface). Selected interacting residues from the NES-binding cleft are shown in green sticks and labeled, and hydrogen bond is shown as dashed lines.

### 3. Materials and Methods

#### 3.1. Chemistry Procedures

Melting points were measured on a M170 apparatus (Mettler Toledo, Columbus, Ohio, USA) apparatus and are uncorrected. The elemental analysis was performed with a CHN-O-RAPID instrument (Heraeus, Hanau, Germany). The elemental compositions of the compounds agreed within  $\pm 0.4\%$  of the calculated values.

$^1\text{H}$  and  $^{13}\text{C}$  NMR spectra were recorded on a Varian INNOVA (now Agilent, Santa Clara, CA, USA) 300 operating at 299 MHz ( $^1\text{H}$ ) and 75 MHz ( $^{13}\text{C}$ ), respectively, a Varian INNOVA-400 operating at 399 MHz ( $^1\text{H}$ ) and 99 MHz ( $^{13}\text{C}$ ), respectively, and a VARIAN SYSTEM-500 operating at 499 MHz ( $^1\text{H}$ ) and 125 MHz ( $^{13}\text{C}$ ), respectively. Monodimensional  $^1\text{H}$  and  $^{13}\text{C}$  spectra were obtained using standard conditions.

Compounds were also analyzed by HPLC/MS with a e2695 LC (Waters, Milford, Massachusetts, USA), coupled to a Waters 2996 photodiode array detector and a Waters Micromass ZQ. The column used is a Waters SunFire C18  $2.1 \times 50$  mm,  $3.5 \mu\text{m}$ , and the mobile phases were A: acetonitrile and B:  $\text{H}_2\text{O}$ , together with a constant 5% of C ( $\text{H}_2\text{O}$  with 2% formic acid) to assure 0.1% of formic acid along the run.

Analytical TLC was performed on silica gel 60 F<sub>254</sub> (Merck, Dramstand, Germany)-precoated plates (0.2 mm). Spots were detected under UV light (254 nm) and/or charring with ninhydrin or phosphomolibdic acid.

Separations on silica gel were performed by preparative centrifugal circular thin-layer chromatography (CCTLC) on a Chromatotron<sup>R</sup> (Kieselgel 60 PF<sub>254</sub> gipshaltig (Merck)), with a layer thickness of 1 and 2 mm and a flow rate of 4 or 8 mL/min, respectively.

General procedure for the reaction of aromatic ethanones with aldehydes under basic conditions (General procedure A) [46].

To a solution of  $\text{Ba}(\text{OH})_2 \cdot 8\text{H}_2\text{O}$  (1.0–1.2 mmol) in water (0.2 mL), the corresponding aldehyde (1.0–2.0 mmol) in methanol (1 mL) was added. To the resultant mixture, the appropriate aromatic ketone (1.0–1.2 mmol) in methanol (8 mL) was added dropwise over 10 min and the reaction was stirred at room temperature for 2–16 h. The workup and purification procedures are described individually.

General procedure for the reaction of aromatic ketones with pyrimidine-5-carboxaldehyde under acid conditions (General procedure B) [47].

To a mixture containing the corresponding aromatic ketone (1.0 mmol) and pyrimidine-5-carboxaldehyde (1.2–2.8 mmol) in glacial acetic acid (1 mL), piperidine (0.5 mmol) was

added dropwise, and then the reaction was stirred at 70–100 °C for 5–48 h. Volatiles were removed, and the residue was purified by CCTLC in the Chromatotron.

General procedure for the alkylation of phenol groups (General procedure C).

To a solution of the corresponding phenol (1.0 mmol) in anhydrous DMF (6 mL), Cs<sub>2</sub>CO<sub>3</sub> (1.2–1.5 mmol) was added. After stirring at rt for 10 min, the appropriate alkyl halide (1.2 mmol) in anhydrous DMF (2 mL) was added dropwise. The resulting mixture was heated at 80 °C for 0.5–5 h and then quenched with water (5 mL). Volatiles were removed and the residue was diluted with ethyl acetate (20 mL) and washed with a saturated solution of NH<sub>4</sub>Cl (10 mL). The organic layer was dried over Na<sub>2</sub>SO<sub>4</sub>, filtered and evaporated to dryness. The residue was purified by CCTLC in the Chromatotron.

#### (E)-1-(Naphthalen-2-yl)-3-(pyrimidin-5-yl)prop-2-en-1-one (9)

Following the general procedure A, to a solution of Ba(OH)<sub>2</sub>·8H<sub>2</sub>O (111 mg, 0.35 mmol) and pyrimidine-5-carboxaldehyde (76 mg, 0.70 mmol) in a mixture of water (70 µL) and methanol (0.4 mL), 1-(naphthalen-2-yl)ethanone (**11**) (60 mg, 0.35 mmol) in methanol (2.8 mL) was added and the reaction was stirred for 2 h. The reaction was filtered, and the solid obtained was washed with cooled methanol and then purified by CCTLC (petroleum ether/ethyl acetate, 1:1) to yield 50 mg (55%) of **9** as a white solid. Mp: 175–177 °C. MS (ES, positive mode): m/z 261 (M+H)<sup>+</sup>. <sup>1</sup>H NMR (300 MHz, DMSO-d<sub>6</sub>) δ: 7.61–7.77 (m, 2H, Ar), 7.81 (d, J = 15.8 Hz, 1H, CH=CH-Ar), 7.99–8.13 (m, 2H, Ar), 8.11–8.21 (m, 2H, Ar), 8.40 (d, J = 15.9 Hz, 1H, CH=CH-Ar), 8.99 (s, 1H, Ar), 9.23 (s, 1H, Ar), 9.37 (s, 2H, Ar). <sup>13</sup>C NMR (75 MHz, DMSO-d<sub>6</sub>) δ: 124.4, 125.8, 127.5, 128.1, 129.0, 129.2, 129.3, 130.0, 131.3, 132.6, 134.7, 135.6, 137.3, 157.0, 159.3 (Ar, CH=CH), 188.9 (CO). Anal. calc. for (C<sub>17</sub>H<sub>12</sub>N<sub>2</sub>O): C, 78.44; H, 4.65; N, 10.76. Found: C, 78.19; H, 4.81; N, 10.53.

#### (E)-2-Methoxycarbonyl-1-(naphthalene-2-yl)-3-(pyrimidin-5-yl)prop-2-en-1-one (13)

Following general procedure B, a solution of methyl 3-(naphthalen-2-yl)-3-oxopropanoate (**12**) [28] (58 mg, 0.25 mmol), pyrimidine-5-carboxaldehyde (80 mg, 0.70 mmol) and piperidine (13 µL, 0.13 mmol) in glacial acetic acid (1 mL) was stirred at 100 °C overnight and evaporated. The residue was purified by CCTLC in the Chromatotron (DCM/ethyl acetate, 12:1) to yield 32 mg (40%) of **13** as a white solid. Mp: 161–163 °C. MS (ES, positive mode): m/z 319 (M+H)<sup>+</sup>. <sup>1</sup>H NMR (400 MHz, DMSO-d<sub>6</sub>) δ: 3.76 (s, 3H, OCH<sub>3</sub>), 7.61 (ddd, J = 8.1, 6.8, 1.2 Hz, 1H, Ar), 7.70 (ddd, J = 8.2, 6.9, 1.3 Hz, 1H, Ar), 7.96–8.04 (m, 2H, Ar), 8.07 (d, J = 8.6 Hz, 1H, Ar), 8.08–8.15 (m, 2H, Ar, C=CH-Ar), 8.58 (d, J = 1.6 Hz, 1H, Ar), 8.77 (s, 2H, Ar), 9.04 (s, 1H, Ar). <sup>13</sup>C NMR (101 MHz, DMSO-d<sub>6</sub>) δ: 53.4 (CH<sub>3</sub>), 123.7, 127.7, 127.8, 128.3, 129.7, 130.1, 130.4, 132.6, 132.7, 132.8, 134.9, 136.2, 136.6, 157.3, 159.1 (Ar, C=CH), 164.6, 194.5 (CO). Anal. calc. for (C<sub>19</sub>H<sub>14</sub>N<sub>2</sub>O<sub>3</sub>): C, 71.69; H, 4.43; N, 8.80. Found: C, 71.49; H, 4.53; N, 9.04.

#### 3-(Naphthalen-2-yl)-3-oxopropanamide (14)

The ester **12** (118 mg, 0.52 mmol) was dissolved in NH<sub>3</sub>/dioxane 0.5 N (2.5 mL) and heated at 110 °C for 7 h. Then, volatiles were removed, and the residue was redissolved in NH<sub>3</sub>/dioxane 0.5 N (2.5 mL) and heated at 110 °C overnight. Volatiles were removed, and the residue was purified by CCTLC in the Chromatotron (hexane/ethyl acetate, 1:2) to yield 37 mg (34%) of **14** as an amorphous solid containing a tautomeric mixture of the 3-oxopropanamide and 3-hydroxyacrylamide species (ratio 7:3). MS (ES, positive mode): m/z 214 (M+H)<sup>+</sup>. <sup>1</sup>H NMR (400 MHz, DMSO-d<sub>6</sub>) δ: 4.00 (s, CH<sub>2</sub>), 5.89 (s, C(OH)=CH), 7.13 (br s, NH<sub>2</sub>), 7.38 (br s, NH<sub>2</sub>), 7.55–7.72 (m, Ar), 7.75 (dd, J = 8.7, 1.8 Hz, Ar), 7.94–8.07 (m, Ar), 8.09–8.14 (m, Ar), 8.33 (d, J = 1.9 Hz, Ar), 8.65–8.71 (m, Ar), 15.31 (s, C(OH)=CH).

#### (E)-2-Carbamoyl-1-(naphthalene-2-yl)-3-(pyrimidin-5-yl)prop-2-en-1-one (15)

Following the general procedure B, a solution of **14** (33 mg, 0.16 mmol), pyrimidine-5-carboxaldehyde (20 mg, 0.19 mmol) and piperidine (10 µL, 0.10 mmol) in glacial acetic acid (1 mL) was stirred at 70 °C for 5 h and evaporated. The residue was purified by CCTLC in the Chromatotron (DCM/methanol, 75:1) to yield 17 mg (36%) of **15** as an amorphous

solid. MS (ES, positive mode):  $m/z$  304 (M+H)<sup>+</sup>. <sup>1</sup>H NMR (500 MHz, DMSO-*d*<sub>6</sub>)  $\delta$ : 7.61 (ddd,  $J = 8.2, 6.8, 1.2$  Hz, 1H, Ar), 7.65 (br s, 1H, NH<sub>2</sub>), 7.69 (ddd,  $J = 8.2, 6.8, 1.3$  Hz, 1H, Ar), 7.74 (s, 1H, C=CH-Ar), 7.93–7.96 (m, 2H, NH<sub>2</sub>, Ar), 7.99 (d,  $J = 8.2$  Hz, 1H, Ar), 8.03 (d,  $J = 8.6$  Hz, 1H, Ar), 8.08 (d,  $J = 8.2$  Hz, 1H, Ar), 8.49 (s, 1H, Ar), 8.67 (s, 2H, Ar), 8.98 (s, 1H, Ar). <sup>13</sup>C NMR (126 MHz, DMSO-*d*<sub>6</sub>): 124.0, 127.7, 128.2, 128.6, 129.4, 129.8, 130.2, 130.5, 132.2, 132.5, 133.5, 135.9, 140.0, 156.7, 158.5 (Ar, C=CH), 166.4, 195.8 (CO). Anal. calc. for (C<sub>18</sub>H<sub>13</sub>N<sub>3</sub>O<sub>2</sub>·0.5H<sub>2</sub>O): C, 69.22; H, 4.52; N, 13.45. Found: C, 68.95; H, 4.44; N, 13.26.

#### (E)-2-Methyl-1-(naphthalen-2-yl)-3-(pyrimidin-5-yl)prop-2-en-1-one (18)

Naphthalene was reacted with propionyl chloride as described to provide 1-(naphthalen-2-yl)propan-1-one (17) [30] as the major product, together with a small proportion of its 1-isomer. MS (ES, positive mode):  $m/z$  185 (M+H)<sup>+</sup>. This mixture (91 mg, 0.49 mmol), pyrimidine-5-carboxaldehyde (144 mg, 1.33 mmol) and piperidine (24  $\mu$ L, 0.25 mmol) in glacial acetic acid (1 mL) was stirred at 100 °C for 48 h and evaporated, following the general procedure B. The residue was purified by CCTLC in the Chromatotron (DCM/ethyl acetate, 14:1) to yield 42 mg (30%) of 18 as an amorphous solid. MS (ES, positive mode):  $m/z$  275 (M+H)<sup>+</sup>. <sup>1</sup>H NMR (400 MHz, DMSO-*d*<sub>6</sub>)  $\delta$ : 2.26 (d,  $J = 1.5$  Hz, 3H, CH<sub>3</sub>), 7.17 (s, 1H, C=CH-Ar), 7.63 (ddd,  $J = 8.1, 6.8, 1.4$  Hz, 1H, Ar), 7.68 (ddd,  $J = 8.2, 6.9, 1.5$  Hz, 1H, Ar), 7.87 (dd,  $J = 8.5, 1.7$  Hz, 1H, Ar), 8.03 (d,  $J = 8.0$  Hz, 1H, Ar), 8.07 (d,  $J = 8.6$  Hz, 1H, Ar), 8.13 (d,  $J = 8.1$  Hz, 1H, Ar), 8.44 (s, 1H, Ar), 8.99 (s, 2H, Ar), 9.17 (s, 1H, Ar). <sup>13</sup>C NMR (126 MHz, DMSO-*d*<sub>6</sub>)  $\delta$ : 15.2 (CH<sub>3</sub>), 125.8, 127.4, 128.1, 128.8, 128.9, 129.9, 130.2, 131.5, 132.4, 133.7, 134.7, 135.1, 140.3, 157.5, 157.8 (Ar, C=CH), 198.2 (CO). Anal. calc. for (C<sub>18</sub>H<sub>14</sub>N<sub>2</sub>O): C, 78.81; H, 5.14; N, 10.21. Found: C, 78.39; H, 5.12; N, 9.89.

#### 3-(Naphthalen-2-yl)-3-oxopropanenitrile (20) [32]

An Ace pressure tube was charged with a solution of methyl 2-naphthoate (19) (250 mg, 1.34 mmol) and acetonitrile (210  $\mu$ L, 4.03 mmol) in anhydrous toluene (2.7 mL). Then, NaH (60% dispersion in mineral oil, 162 mg, 4.03 mmol) was added, and the resulting mixture was heated to 110 °C overnight. The reaction was allowed to warm to rt and quenched with water (5 mL). Then, it was diluted with DCM (15 mL) and washed with HCl 1N (10 mL) and brine. The organic layer was dried over Na<sub>2</sub>SO<sub>4</sub>, filtered and evaporated to dryness. The residue was purified by flash chromatography (DCM/methanol, 100:1) to yield 125 mg (48%) of 20 as an amorphous solid. MS (ES, positive mode):  $m/z$  196 (M+H)<sup>+</sup>. <sup>1</sup>H NMR (400 MHz, DMSO-*d*<sub>6</sub>)  $\delta$ : 4.89 (s, 2H, CH<sub>2</sub>), 7.66 (ddd,  $J = 8.1, 6.8, 1.4$  Hz, 1H, Ar), 7.72 (ddd,  $J = 8.2, 6.8, 1.4$  Hz, 1H, Ar), 7.96 (dd,  $J = 8.6, 1.8$  Hz, 1H, Ar), 8.03 (d,  $J = 8.0$  Hz, 1H, Ar), 8.06 (d,  $J = 8.7$  Hz, 1H, Ar), 8.12 (d,  $J = 7.9$  Hz, 1H, Ar), 8.65 (m, 1H, Ar). <sup>1</sup>H NMR data are similar to those previously described [32].

#### (E)-2-Cyano-1-(naphthalene-2-yl)-3-(pyrimidin-5-yl)prop-2-en-1-one (21)

Following the general procedure B, a solution of 20 (30 mg, 0.15 mmol), pyrimidine-5-carbaldehyde (23 mg, 0.21 mmol) and piperidine (8  $\mu$ L, 0.08 mmol) in glacial acetic acid (1 mL) was heated to 70 °C for 2 h and evaporated. After cooling down with an ice bath and adding cold ethanol (3 mL), a solid precipitated, which was filtered under vacuum and washed with cold ethanol to yield 16 mg (36%) of 21 as an amorphous yellow solid. MS (ES, positive mode):  $m/z$  286 (M+H)<sup>+</sup>. <sup>1</sup>H NMR (400 MHz, DMSO-*d*<sub>6</sub>)  $\delta$ : 7.65–7.77 (m, 2H, Ar), 7.94 (dd,  $J = 8.5, 1.8$  Hz, 1H, Ar), 8.07 (d,  $J = 8.1$  Hz, 1H, Ar), 8.11–8.18 (m, 2H, Ar), 8.34 (s, 1H, C=CH-Ar), 8.66 (d,  $J = 1.8$  Hz, 1H, Ar), 9.36 (s, 1H, Ar), 9.38 (s, 2H, Ar).

#### (E)-1-(Naphthalen-2-yl)-3-(pyridin-3-yl)prop-2-en-1-one (24)

Following the general procedure A, to a solution of Ba(OH)<sub>2</sub>·8H<sub>2</sub>O (111 mg, 0.35 mmol) and 3-pyridinecarboxaldehyde (21) (66  $\mu$ L, 0.70 mmol) in water (70  $\mu$ L) and methanol (0.4 mL), 1-(naphthalen-2-yl)ethanone (11) (60 mg, 0.35 mmol) in methanol (2.8 mL) was added, and the reaction was stirred for 3 h. Volatiles were removed, and the residue was purified by CCTLC (hexane/ethyl acetate, 1:1) to yield 67 mg (73%) of 24 as a pale yellow solid. Mp: 123–125 °C. MS (ES, positive mode):  $m/z$  260 (M+H)<sup>+</sup>. <sup>1</sup>H NMR (300 MHz,

DMSO- $d_6$ )  $\delta$ : 7.53 (dd,  $J = 8.0, 4.8$  Hz, 1H, Ar), 7.60–7.77 (m, 2H, Ar), 7.85 (d,  $J = 15.7$  Hz, 1H,  $\underline{\text{CH}}=\underline{\text{CH}}\text{-Ar}$ ), 7.97–8.13 (m, 2H, Ar), 8.10–8.22 (m, 2H, Ar), 8.28 (d,  $J = 15.7$  Hz, 1H,  $\underline{\text{CH}}=\underline{\text{CH}}\text{-Ar}$ ), 8.41 (dt,  $J = 8.1, 1.9$  Hz, 1H, Ar), 8.64 (dd,  $J = 4.8, 1.6$  Hz, 1H, Ar), 8.98 (s, 1H, Ar), 9.09 (d,  $J = 2.2$  Hz, 1H, Ar).  $^{13}\text{C}$  NMR (75 MHz, DMSO- $d_6$ )  $\delta$ : 124.3, 124.4, 127.4, 128.1, 128.9, 129.2, 130.0, 131.0, 131.1, 132.7, 135.0, 135.5, 135.6, 140.8, 150.7, 151.4 (Ar,  $\underline{\text{CH}}=\underline{\text{CH}}$ ), 189.0 (C=O). Anal. calc. for ( $\text{C}_{18}\text{H}_{13}\text{NO}$ ): C, 83.37; H, 5.05; N, 5.40. Found: C, 83.36; H, 5.23; N, 5.46. This compound has been recently described using slightly different reaction conditions [48].

(E)-1-(Naphthalen-2-yl)-3-(pyridin-2-yl)prop-2-en-1-one (**25**)

Following the general procedure A, to a solution of  $\text{Ba}(\text{OH})_2 \cdot 8\text{H}_2\text{O}$  (111 mg, 0.35 mmol) and 2-pyridinecarboxaldehyde (**22**) (67  $\mu\text{L}$ , 0.70 mmol) in water (70  $\mu\text{L}$ ) and methanol (0.4 mL), 1-(naphthalen-2-yl)ethanone (**11**) (60 mg, 0.35 mmol) in methanol (2.8 mL) was added, and the reaction was stirred for 7 h. Volatiles were removed, and the residue was purified by CCTLC (hexane/ethyl acetate, 6:1) to yield 37 mg (40%) of **25** as a pale yellow solid. Mp: 89–90  $^\circ\text{C}$ . MS (ES, positive mode):  $m/z$  260 ( $\text{M}+\text{H}$ ) $^+$ .  $^1\text{H}$  NMR (400 MHz, DMSO- $d_6$ )  $\delta$ : 7.47 (ddd,  $J = 6.9, 4.7, 2.4$  Hz, 1H, Ar), 7.62–7.73 (m, 2H, Ar), 7.80 (d,  $J = 15.4$  Hz, 1H,  $\underline{\text{CH}}=\underline{\text{CH}}\text{-Ar}$ ), 7.90–7.97 (m, 2H, Ar), 8.03 (d,  $J = 8.0$  Hz, 1H, Ar), 8.04–8.15 (m, 2H, Ar), 8.23 (d,  $J = 7.9$  Hz, 1H, Ar), 8.34 (d,  $J = 15.4$  Hz, 1H,  $\underline{\text{CH}}=\underline{\text{CH}}\text{-Ar}$ ), 8.72 (d,  $J = 4.5$  Hz, 1H, Ar), 8.88 (d,  $J = 1.8$  Hz, 1H, Ar).  $^{13}\text{C}$  NMR (101 MHz, DMSO- $d_6$ )  $\delta$ : 124.4, 125.3, 125.6, 127.5, 128.2, 129.1, 129.3, 130.3, 131.0, 132.8, 135.1, 135.6, 137.7, 143.5, 150.5, 153.3 (Ar,  $\underline{\text{CH}}=\underline{\text{CH}}$ ), 189.7 (CO). Anal. calc. for ( $\text{C}_{18}\text{H}_{13}\text{NO}$ ): C, 83.37; H, 5.05; N, 5.40. Found: C, 83.22; H, 5.08; N, 5.26. This compound has been recently described using slightly different reaction conditions [48].

(E)-1-(Naphthalen-2-yl)-3-(pyridin-4-yl)prop-2-en-1-one (**26**)

Following the general procedure A, to a solution of  $\text{Ba}(\text{OH})_2 \cdot 8\text{H}_2\text{O}$  (111 mg, 0.35 mmol) and 4-pyridinecarboxaldehyde (**23**) (52  $\mu\text{L}$ , 0.53 mmol) in water (70  $\mu\text{L}$ ) and methanol (0.5 mL), 1-(naphthalen-2-yl)ethanone (**11**) (60 mg, 0.35 mmol) in methanol (2.8 mL) was added and the reaction was stirred for 2 h. Water was added, and the resulting solid was isolated and then purified by CCTLC (hexane/ethyl acetate/triethylamine, 3:1:0.04) to yield 30 mg (32%) of **26** as a pale yellow solid. Mp: 135–137  $^\circ\text{C}$ . MS (ES, positive mode):  $m/z$  260 ( $\text{M}+\text{H}$ ) $^+$ .  $^1\text{H}$  NMR (400 MHz, DMSO- $d_6$ )  $\delta$ : 7.64–7.73 (m, 2H, Ar), 7.76 (d,  $J = 15.7$  Hz, 1H,  $\underline{\text{CH}}=\underline{\text{CH}}\text{-Ar}$ ), 7.87–7.92 (m, 2H, Ar), 8.01–8.10 (m, 2H, Ar), 8.12–8.20 (m, 2H, Ar), 8.35 (d,  $J = 15.7$  Hz, 1H,  $\underline{\text{CH}}=\underline{\text{CH}}\text{-Ar}$ ), 8.68–8.73 (m, 2H, Ar), 8.98 (s, 1H, Ar).  $^{13}\text{C}$  NMR (126 MHz, DMSO- $d_6$ )  $\delta$ : 123.0, 124.5, 126.8, 127.5, 128.2, 129.1, 129.4, 130.1, 131.4, 132.7, 134.8, 135.7, 141.4, 142.3, 150.8 (Ar,  $\underline{\text{CH}}=\underline{\text{CH}}$ ), 189.3 (CO). Anal. calc. for ( $\text{C}_{18}\text{H}_{13}\text{NO}$ ): C, 83.37; H, 5.05; N, 5.40. Found: C, 83.30; H, 5.00; N, 5.18. This compound has been recently described using slightly different reaction conditions [48].

(E)-1-(3',5'-Dimethoxyphenyl)-3-(pyrimidin-5'-yl)prop-2-en-1-one (**10**)

Following the general procedure A, to a solution of  $\text{Ba}(\text{OH})_2 \cdot 8\text{H}_2\text{O}$  (132 mg, 0.42 mmol) and pyrimidine-5-carbaldehyde (91 mg, 0.84 mmol) in water (84  $\mu\text{L}$ ) and methanol (0.5 mL), 1-(3,5-dimethoxyphenyl)ethan-1-one (**28**) [33] (76 mg, 0.42 mmol) in methanol (3.4 mL) was added, and the reaction was stirred overnight. The reaction was filtered and the solid obtained was washed with cooled methanol and then purified by CCTLC in the Chromatotron (hexane/ethyl acetate, 1:3) to yield 72 mg (64%) of **10** as a white solid. Mp: 184–185  $^\circ\text{C}$ . MS (ES, positive mode):  $m/z$  271 ( $\text{M}+\text{H}$ ) $^+$ .  $^1\text{H}$  NMR (400 MHz, DMSO- $d_6$ )  $\delta$ : 3.85 (s, 6H,  $\text{OCH}_3$ ), 6.83 (t,  $J = 2.3$  Hz, 1H, Ar), 7.31 (d,  $J = 2.3$  Hz, 2H, Ar), 7.74 (d,  $J = 15.8$  Hz, 1H,  $\underline{\text{CH}}=\underline{\text{CH}}\text{-Ar}$ ), 8.17 (d,  $J = 15.8$  Hz, 1H,  $\underline{\text{CH}}=\underline{\text{CH}}\text{-Ar}$ ), 9.21 (s, 1H, Ar), 9.34 (s, 2H, Ar).  $^{13}\text{C}$  NMR (101 MHz, DMSO- $d_6$ )  $\delta$ : 56.1 ( $\text{OCH}_3$ ), 105.9, 106.9, 125.8, 129.2, 137.8, 139.5, 157.2, 159.4, 161.2 (Ar,  $\underline{\text{CH}}=\underline{\text{CH}}$ ), 188.7 (CO). Anal. calc. for ( $\text{C}_{15}\text{H}_{14}\text{N}_2\text{O}_3$ ): C, 66.66; H, 5.22; N, 10.36. Found: C, 66.79; H, 5.24; N, 10.33.

(E)-2-Methoxycarbonyl-1-(3',5'-dimethoxybenzoyl)-3-(pyrimidin-5'-yl)prop-2-en-1-one (**30**)

Following the general procedure B, a solution of methyl 3-(3',5'-dimethoxyphenyl)-3-oxopropanoate (**29**) [34] (50 mg, 0.21 mmol), pyrimidine-5-carbaldehyde (31 mg, 0.29 mmol) and piperidine (10  $\mu$ L, 0.10 mmol) in acetic acid (1 mL) was stirred at 70 °C overnight and evaporated. The residue was purified by CCTLC in the Chromatotron (hexane/ethyl acetate, 1:1) to yield 27 mg (39%) of **30** as a pale yellow solid. Mp: 81–82 °C. MS (ES, positive mode):  $m/z$  329 (M+H)<sup>+</sup>. <sup>1</sup>H NMR (400 MHz, DMSO-*d*<sub>6</sub>)  $\delta$ : 3.76 (s, 3H, COOCH<sub>3</sub>), 3.77 (s, 6H, OCH<sub>3</sub>), 6.83 (t,  $J$  = 2.3 Hz, 1H, Ar), 7.00 (d,  $J$  = 2.3 Hz, 2H, Ar), 8.00 (s, 1H, C=CH-Ar), 8.73 (s, 2H, Ar), 9.10 (s, 1H, Ar). <sup>13</sup>C NMR (75 MHz, DMSO-*d*<sub>6</sub>)  $\delta$ : 53.1 (COOCH<sub>3</sub>), 55.9 (OCH<sub>3</sub>), 106.9, 127.6, 134.4, 136.4, 137.1, 157.2, 159.1, 161.3 (Ar, CH=CH), 164.4 (COOCH<sub>3</sub>), 193.83 (CO). Anal. calc. for (C<sub>17</sub>H<sub>16</sub>N<sub>2</sub>O<sub>5</sub>): C, 62.19; H, 4.91; N, 8.53. Found: C, 62.56; H, 4.99; N, 8.20.

#### 1-(3-Methoxy-5-(2-methoxyethoxy)phenyl)ethan-1-one (**31**)

3,5-Dihydroxyacetophenone (**27**) was reacted with methyl iodide as described [49] to provide 1-(3-hydroxy-5-methoxyphenyl)ethan-1-one (MS (ES, positive mode):  $m/z$  167 (M+H)<sup>+</sup>) together with 1-(3,5-dimethoxyphenyl)ethan-1-one (**28**). The 3-hydroxy derivative (52 mg, 0.31 mmol) was reacted with Cs<sub>2</sub>CO<sub>3</sub> (151 mg, 0.46 mmol) and 2-bromoethyl methyl ether (34  $\mu$ L, 0.37 mmol) in anhydrous DMF (0.9 mL) at 80 °C for 5 h, following the general procedure C. After workup, the residue was purified by CCTLC in the Chromatotron (DCM/ethyl acetate, 40:1) to yield 54 mg (77%) of **31** as a colourless oil. MS (ES, positive mode):  $m/z$  225 (M+H)<sup>+</sup>. <sup>1</sup>H NMR (400 MHz, DMSO-*d*<sub>6</sub>)  $\delta$ : 2.55 (s, 3H, COCH<sub>3</sub>), 3.31 (s, 3H, OCH<sub>3</sub>), 3.63–3.68 (m, 2H, OCH<sub>2</sub>), 3.80 (s, 3H, OCH<sub>3</sub>), 4.11–4.17 (m, 2H, OCH<sub>2</sub>), 6.78 (t,  $J$  = 2.3 Hz, 1H, Ar), 7.06 (m, 1H, Ar), 7.08 (m, 1H, Ar).

#### 1-(3-Methoxy-5-((3-methylbut-2-en-1-yl)oxy)phenyl)ethan-1-one (**32**)

As described for the synthesis of **31**, 1-(3-hydroxy-5-methoxyphenyl)ethan-1-one (67 mg, 0.40 mmol) was reacted with Cs<sub>2</sub>CO<sub>3</sub> (196 mg, 0.60 mmol) and 3,3-dimethylallylbromide (58  $\mu$ L, 0.48 mmol) in anhydrous DMF (1.2 mL) at 80 °C for 1 h, following the general procedure C. After workup, the residue was purified by CCTLC in the Chromatotron (DCM/ethyl acetate, 80:1) to yield 71 mg (75%) of **32** as a colourless oil. MS (ES, positive mode):  $m/z$  235 (M+H)<sup>+</sup>. <sup>1</sup>H NMR (400 MHz, DMSO-*d*<sub>6</sub>)  $\delta$ : 1.72 (s, 3H, CH<sub>3</sub>), 1.74 (s, 3H, CH<sub>3</sub>), 3.79 (s, 3H, OCH<sub>3</sub>), 4.58 (d,  $J$  = 6.8 Hz, 2H, OCH<sub>2</sub>CH), 5.42 (m, 1H, OCH<sub>2</sub>CH), 6.76 (t,  $J$  = 2.3 Hz, 1H, Ar), 7.04 (dd,  $J$  = 2.3, 1.4 Hz, 1H, Ar), 7.07 (dd,  $J$  = 2.3, 1.3 Hz, 1H, Ar).

#### (E)-1-(3'-Methoxy-5'-(2-methoxyethoxy)phenyl)-3-(pyrimidin-5''-yl)prop-2-en-1-one (**33**)

Following the general procedure A, to a solution of Ba(OH)<sub>2</sub>·8H<sub>2</sub>O (94 mg, 0.30 mmol) and pyrimidine-5-carbaldehyde (40 mg, 0.37 mmol) in water (60  $\mu$ L) and methanol (0.3 mL), the ketone **31** (69 mg, 0.30 mmol) in methanol (2.4 mL) was added, and the reaction was stirred for 1.5 h. Volatiles were removed, and the residue was purified by CCTLC in the Chromatotron (DCM/MeOH, 80:1) to yield 29 mg (32%) of **33** as an amorphous white solid. MS (ES, positive mode):  $m/z$  325 (M+H)<sup>+</sup>. <sup>1</sup>H NMR (400 MHz, DMSO-*d*<sub>6</sub>)  $\delta$ : 3.32 (s, 3H, OCH<sub>3</sub>), 3.67–3.71 (m, 2H, OCH<sub>2</sub>), 3.84 (s, 3H, OCH<sub>3</sub>), 4.17–4.22 (m, 2H, OCH<sub>2</sub>), 6.84 (d,  $J$  = 2.3 Hz, 1H, Ar), 7.29 (dd,  $J$  = 2.3, 1.3 Hz, 1H, Ar), 7.34 (dd,  $J$  = 2.3, 1.4 Hz, 1H, Ar), 7.74 (d,  $J$  = 15.8 Hz, 1H, CH=CH-Ar), 8.17 (d,  $J$  = 15.8 Hz, 1H, CH=CH-Ar), 9.20 (s, 1H, Ar), 9.34 (s, 2H, Ar). <sup>13</sup>C NMR (101 MHz, DMSO-*d*<sub>6</sub>)  $\delta$ : 56.1, 58.6, 67.8, 70.8 (CH<sub>2</sub>, CH<sub>3</sub>), 106.3, 106.8, 107.7, 125.8, 129.2, 137.8, 139.5, 157.2, 159.4, 160.5, 161.2 (Ar, CH=CH), 188.7 (CO). Anal. calc. for (C<sub>17</sub>H<sub>18</sub>N<sub>2</sub>O<sub>4</sub>): C, 64.96; H, 5.77; N, 8.91. Found: C, 64.59; H, 5.68; N, 8.78.

#### (E)-1-(3'-Methoxy-5'-((3-methylbut-2-en-1-yl)oxy)phenyl)-3-(pyrimidin-5''-yl)prop-2-en-1-one (**34**)

Following the general procedure A, to a solution of Ba(OH)<sub>2</sub>·8H<sub>2</sub>O (82 mg, 0.26 mmol) and pyrimidine-5-carbaldehyde (34 mg, 0.31 mmol) in water (52  $\mu$ L) and methanol (0.26 mL), the ketone **32** (61 mg, 0.26 mmol) in methanol (2.1 mL) was added and the reaction was stirred for 2 h. Water was added, and the resulting solid was isolated and then purified by CCTLC in the Chromatotron (hexane/ethyl acetate, 1:1) to yield 39 mg (41%) of **34** as an



amorphous white solid. MS (ES, positive mode):  $m/z$  325 (M+H)<sup>+</sup>. <sup>1</sup>H NMR (300 MHz, DMSO-*d*<sub>6</sub>)  $\delta$ : 1.74 (s, 3H, CH<sub>3</sub>), 1.75 (s, 3H, CH<sub>3</sub>), 3.84 (s, 3H, OCH<sub>3</sub>), 4.62 (d,  $J$  = 6.8 Hz, 2H, OCH<sub>2</sub>CH), 5.42 (m, 1H, OCH<sub>2</sub>CH), 6.82 (t,  $J$  = 2.2 Hz, 1H, Ar), 7.28 (t,  $J$  = 2.2 Hz, 1H, Ar), 7.32 (t,  $J$  = 2.3 Hz, 1H, Ar) 7.73 (d,  $J$  = 15.8 Hz, 1H, CH=CH-Ar), 8.16 (d,  $J$  = 15.8 Hz, 1H, CH=CH-Ar), 9.20 (s, 1H, Ar), 9.34 (s, 2H, Ar). <sup>13</sup>C NMR (101 MHz, DMSO-*d*<sub>6</sub>)  $\delta$ : 18.5, 25.9, 56.1, 65.2 (CH<sub>2</sub>, CH<sub>3</sub>), 106.5, 106.6, 107.9, 120.0, 125.80, 129.2, 137.7, 138.1, 139.4, 157.2, 159.3, 160.4, 161.2 (Ar, CH=CH, C(CH<sub>3</sub>)<sub>2</sub>=CH), 188.7 (CO). Anal. calc. for (C<sub>19</sub>H<sub>20</sub>N<sub>2</sub>O<sub>3</sub>): C, 70.35; H, 6.21; N, 8.64. Found: C, 70.21; H, 6.29; N, 8.35.

### 3.2. GSH Reactivity Assay

A 500  $\mu$ M sample of the tested compound was incubated with 5 mM reduced L-glutathione for 24 h at 37 °C with a final volume of 200  $\mu$ L. As a solvent system, 20 mM PBS buffer pH 7.4 with 2 mM EDTA:DMSO (1:1) was used [50]. To perform the assay, stock solutions of 20 mM of the chalcones (**9**, **10**, **13** and **18**) and 15 mM of reduced L-glutathione were freshly prepared for every experiment and then diluted properly to give the final electrophile:nucleophile ratio (1:10). A 5 mM solution of 5,5'-dithiobis(2-nitrobenzoic acid) (DTNB) was prepared in the same solvent system to quench the reaction. After different time points (10 min, 1 h, 4 h and 24 h), an aliquot of 20  $\mu$ L of the incubation mixture was quenched by adding 20  $\mu$ L of the DTNB stock solution, mixed thoroughly, and then analyzed by HPLC. HPLC analysis was performed in Agilent 1120 compact LC, column ACE 5 C18-300 (15 cm  $\times$  4.6 mm); UV detection was performed at  $\lambda$  = 254 nm. Solvents used were acetonitrile for bottle A and H<sub>2</sub>O (containing 0.05% TFA) for bottle B, and the flow rate was 1 mL/min. The gradients used were: (A) incubations with chalcone **9**: from 10% to 80% of solvent A in 10 min; (B) incubations with chalcones **10** and **18**: from 10% to 100% of solvent A in 10 min. The new peaks were analysed by LC-MS. As controls, a 500  $\mu$ M solution of the  $\alpha,\beta$ -unsaturated compound was also analysed, and a 5 mM reduced L-glutathione solution was quenched by adding DNTB at the same time points. In general, after 6 h of incubation, no GSH was detected.

### 3.3. Biological Assays

#### 3.3.1. Cell Culture and Reference Compounds

Cancer cell lines HCT-116, NCI-H460, HL-60, K-562 and Z-138 were acquired from the American Type Culture Collection (ATCC, Manassas, VA, USA). The DND-41 cell line was purchased from the Deutsche Sammlung von Mikroorganismen und Zellkulturen (DSMZ Leibniz-Institut, Brunswick, Germany), and the HAP-1 cell line was ordered from Horizon Discovery (Horizon Discovery Group, Water Beach, UK). All cell lines were cultured as recommended by the suppliers. Culture media were purchased from Gibco Life Technologies and supplemented with 10% fetal bovine serum (HyClone, GE Healthcare Life Sciences, Chicago, Illinois, USA).

Stably transfected HeLa NLS<sub>SV40</sub>-AcGFP-NES<sub>PKI</sub> were cultured as described in Ver-cruysse et al. [19] CRISPR/Cas9 genome editing of the Jurkat cell line was performed as in Neggers et al. [43] to generate a XPO1<sup>C528S</sup> mutant cell line.

Reference inhibitor KPT-330 was purchased from Selleckchem, and stock solutions were prepared in DMSO.

#### 3.3.2. Cell Proliferation Assays

Adherent cell lines HCT-116, NCI-H460 and Hap-1 cells were seeded at a density between 500 and 1500 cells per well in 384-well tissue culture plates (Greiner). After overnight incubation, cells were treated with different concentrations of the test compounds. Suspension cell lines HL-60, K-562, Z-138 and DND-41 were seeded at densities ranging from 2500 to 5500 cells per well in 384-well culture plates containing the test compounds at the same concentration points. The plates were incubated and monitored at 37 °C for 72 h in an IncuCyte (Essen BioScience Inc., Sartorius; Göttingen, Germany for real-time imaging of cell proliferation. Brightfield images were taken every 3 h, with one field imaged per well

under  $10\times$  magnification. Cell growth was then quantified based on the percent cellular confluence, as analysed by the IncuCyte image analysis software, and used to calculate  $IC_{50}$  values by logarithmic interpolation. Compounds were tested in two independent experiments and represented as mean  $\pm$  SEM.

### 3.3.3. XPO1 Phenotypic Reporter Assay

To study the XPO1-mediated nuclear export, stably transfected HeLa NLS<sub>SV40</sub>-AcGFP-NES<sub>PKI</sub> reporter cells were seeded at 8000 cells per well in 96-well all clear tissue culture plates (TPP). After overnight incubation, cells were treated with different doses of compound or solvent (DMSO) for 2 h and then fixed and counterstained with DAPI. Fluorescence was read on an ArrayScan XTI High Content Reader (Thermo Fisher Scientific, Waltham, MA, USA). Nuclear and cytoplasmic compartments were segmented and their average pixel intensities in the green channel were quantitated employing the HCS Studio software. Genedata Screener software was used for dose-response curve fitting, and calculation of  $EC_{50}$  values was based on the percentage of cells having a predominant nuclear localisation (ratio of nuclear to cytoplasmic signal equal or above 1.4) of the reporter construct. Compounds were tested in two independent experiments and represented as mean  $\pm$  SEM.

### 3.3.4. Immunofluorescence Staining of RanBP1

RanBP1 immunofluorescence staining was performed on both wild type and mutant XPO1<sup>C528S</sup> Jurkat cells treated with compound or solvent (DMSO) for 3 h. Cells were harvested at  $400\times g$ , washed in PBS and then transferred into an 8-well  $\mu$ -Slide (Ibidi) pretreated with 0.1% (*w/v*) poly-L-lysine (Sigma). Cells were allowed to adhere to the slides and then subsequently fixed (4% PFA in PBS), washed and permeabilized (0.2% Triton X-100 in PBS). Further immunofluorescence staining was then performed according to standard procedures. Employed antibodies were rabbit anti-RanBP1 (ab97659, Abcam, Cambridge, UK) at a 1:500 dilution and secondary Alexa Fluor 488 goat anti-rabbit antibody (A11008, Invitrogen, ThermoFisher Scientific). Cell nuclei were counterstained with DAPI, and the samples were imaged by confocal microscopy on a Leica TCS SP5 confocal microscope (Leica Microsystems, Weitzlar, Germany), employing a HCX PL APO 63 $\times$  (NA 1.2) water immersion objective. Subsequently, fluorescence was read on an ArrayScan XTI High Content Reader (Thermo Fisher Scientific, Waltham, MA, USA). Nuclear and cytoplasmic compartments were segmented, and their average pixel intensities in the green channel were quantitated similarly as for the XPO1 phenotypic reporter assay.

## 3.4. Computational Methods

The crystal structure of XPO1 complex with KPT-8602 was retrieved from the Protein Data Bank [51] (pdb id: 5JLJ [20]).

The Schrödinger Suite v2018-3 has been used for all the computational studies [52]. The 3D structure of all compounds used in the modelling studies were generated using the graphical interface Maestro, and these were then optimized using the tool MacroModel. For the docking studies, all ligands were prepared with LigPrep in Maestro, and the receptor protein was prepared with the Protein Preparation Wizard.

Covalent docking was performed with CovDock [44]. The KPT-8602-XPO1 X-Ray structure was used for all covalent docking studies. Cys539 was selected as the reactive residue and Michael addition was selected as the reaction type. A grid box of 10 Å was defined. CovDock was used with the default parameters published in reference [44], except for the number of final poses per ligand, which was set up to 10. MMGBSA analysis was also chosen. Results were visually inspected and analysed using the computer graphics program PyMOL [53].

#### 4. Conclusions

Most of the described XPO1 inhibitors are  $\alpha,\beta$ -unsaturated carbonyl compounds able to react with Cys528 at the NES-binding cleft of XPO1. Based on these examples, we synthesized two series of chalcones with a six-membered N-heterocycle as ring B and tested their XPO1 inhibitory activity. Most of the synthesized compounds inhibited XPO1 function in a reporter cell line, and this inhibition nicely correlated with their antiproliferative activity in cell culture assays, with compounds **9**, **10**, **24** and **34** as the most potent. Moreover, in a mutant Jurkat cell line where the Cys528 of XPO1 had been mutated to a Ser (Jurkat XPO1<sup>C528S</sup>), the capacity of the prototype compounds **9** and **10** to inhibit XPO1 mediated nuclear export of the cargo protein was abolished, indicating the importance of Cys at position 528 for the inhibitory activity of our compounds, as also demonstrated for KPT-330 [43]. Finally, the interaction of the chalcones **9** and **10** with the NES-binding cleft has been analyzed through covalent docking with CovDock. Thus, these chalcones may represent an alternative scaffold in the search for XPO1 inhibitors.

**Supplementary Materials:** The following are available online at <https://www.mdpi.com/article/10.3390/ph14111131/s1>, Figures S1–S4: Chromatograms of the incubations of chalcones **9**, **10**, **13** and **18** with GSH. <sup>1</sup>H and <sup>13</sup>C NMR spectra of the tested compounds.

**Author Contributions:** Conceptualization, M.-J.C., D.D., E.-M.P. and M.-J.P.-P.; formal analysis, E.-M.P.; investigation, M.G., J.L.-F. and L.P.; project administration, M.-J.P.-P.; supervision, D.D. and M.-J.P.-P.; validation, M.G. and L.P.; visualization, E.-M.P.; writing—original draft, M.G., D.D., E.-M.P. and M.-J.P.-P.; writing—review & editing, M.-J.C. and M.-J.P.-P. All authors have read and agreed to the published version of the manuscript.

**Funding:** This research was funded by AECSIC, grant number PIE-201980E100 and by Agencia Estatal de Investigación (PID2019-105117RR-C22/ AEI / 10.13039/501100011033 and PID2019-104070RB-C21).

**Institutional Review Board Statement:** Not applicable.

**Informed Consent Statement:** Not applicable.

**Data Availability Statement:** Data is contained within the article or supplementary material.

**Conflicts of Interest:** The authors declare no conflict of interest.

#### References

- Kim, Y.H.; Han, M.-E.; Oh, S.-O. The molecular mechanism for nuclear transport and its application. *Anat. Cell Biol.* **2017**, *50*, 77–85. [CrossRef] [PubMed]
- Kosyna, F.K.; Depping, R. Controlling the Gatekeeper: Therapeutic Targeting of Nuclear Transport. *Cells* **2018**, *7*, 221. [CrossRef] [PubMed]
- Pickens, J.A.; Tripp, R.A. Verdinexor Targeting of CRM1 is a Promising Therapeutic Approach against RSV and Influenza Viruses. *Viruses* **2018**, *10*, 48. [CrossRef]
- Çağatay, T.; Chook, Y.M. Karyopherins in cancer. *Curr. Opin. Cell Biol.* **2018**, *52*, 30–42. [CrossRef]
- Mathew, C.; Ghildyal, R. CRM1 Inhibitors for Antiviral Therapy. *Front. Microbiol.* **2017**, *8*, 1171. [CrossRef] [PubMed]
- Camus, V.; Miloudi, H.; Taly, A.; Sola, B.; Jardin, F. XPO1 in B cell hematological malignancies: From recurrent somatic mutations to targeted therapy. *J. Hematol. Oncol.* **2017**, *10*, 1–13. [CrossRef]
- Sun, Q.; Chen, X.; Zhou, Q.; Burstein, E.; Yang, S.; Jia, D. Inhibiting cancer cell hallmark features through nuclear export inhibition. *Signal Transduct. Target. Ther.* **2016**, *1*, 1–10. [CrossRef]
- Dickmanns, A.; Monecke, T.; Ficner, R. Structural Basis of Targeting the Exportin CRM1 in Cancer. *Cells* **2015**, *4*, 538–568. [CrossRef]
- Muqbil, I.; Azmi, A.S.; Mohammad, R.M. Nuclear Export Inhibition for Pancreatic Cancer Therapy. *Cancers* **2018**, *10*, 138. [CrossRef]
- A Jans, D.; Martin, A.J.; Wagstaff, K.M. Inhibitors of nuclear transport. *Curr. Opin. Cell Biol.* **2019**, *58*, 50–60. [CrossRef] [PubMed]
- Yoshimura, M.; Ishizawa, J.; Ruvolo, V.; Dilip, A.; Quintás-Cardama, A.; McDonnell, T.J.; Neelapu, S.S.; Kwak, L.; Shacham, S.; Kauffman, M.; et al. Induction of p53-mediated transcription and apoptosis by exportin-1 (XPO 1) inhibition in mantle cell lymphoma. *Cancer Sci.* **2014**, *105*, 795–801. [CrossRef] [PubMed]
- Daelemans, D.; Afonina, E.; Nilsson, J.; Werner, G.; Kjems, J.; De Clercq, E.; Pavlakakis, G.N.; Vandamme, A.-M. A synthetic HIV-1 Rev inhibitor interfering with the CRM1-mediated nuclear export. *Proc. Natl. Acad. Sci. USA* **2002**, *99*, 14440–14445. [CrossRef]

13. Van Neck, T.; Pannecouque, C.; Vanstreels, E.; Stevens, M.; Dehaen, W.; Daelemans, D. Inhibition of the CRM1-mediated nucleocytoplasmic transport by N-azolyacrylates: Structure–activity relationship and mechanism of action. *Bioorg. Med. Chem.* **2008**, *16*, 9487–9497. [CrossRef]
14. Lapalombella, R.; Sun, Q.; Williams, K.; Tangeman, L.; Jha, S.; Zhong, Y.; Goettl, V.; Mahoney, E.; Berglund, C.; Gupta, S.; et al. Selective inhibitors of nuclear export show that CRM1/XPO1 is a target in chronic lymphocytic leukemia. *Blood* **2012**, *120*, 4621–4634. [CrossRef]
15. Lei, Y.; An, Q.; Shen, X.-F.; Sui, M.; Li, C.; Jia, D.; Luo, Y.; Sun, Q. Structure-Guided Design of the First Noncovalent Small-Molecule Inhibitor of CRM1. *J. Med. Chem.* **2021**, *64*, 6596–6607. [CrossRef] [PubMed]
16. Shaikhqasem, A.; Dickmanns, A.; Neumann, P.; Ficner, R. Characterization of Inhibition Reveals Distinctive Properties for Human and *Saccharomyces cerevisiae* CRM1. *J. Med. Chem.* **2020**, *63*, 7545–7558. [CrossRef]
17. Sun, Q.; Carrasco, Y.P.; Hu, Y.; Guo, X.; Mirzaei, H.; MacMillan, J.; Chook, Y.M. Nuclear export inhibition through covalent conjugation and hydrolysis of Leptomycin B by CRM1. *Proc. Natl. Acad. Sci. USA* **2013**, *110*, 1303–1308. [CrossRef]
18. Van Der Watt, P.J.; Chi, R.-P.A.; Stelma, T.; Stowell, C.; Strydom, E.; Carden, S.; Angus, L.; Hadley, K.; Lang, D.; Wei, W.; et al. Targeting the Nuclear Import Receptor Kpn $\beta$ 1 as an Anticancer Therapeutic. *Mol. Cancer Ther.* **2016**, *15*, 560–573. [CrossRef]
19. Vercruyse, T.; De Bie, J.; Neggers, J.; Jacquemyn, M.; Vanstreels, E.; Schmid-Burgk, J.; Hornung, V.; Baloglu, E.; Landesman, Y.; Senapedis, W.; et al. The Second-Generation Exportin-1 Inhibitor KPT-8602 Demonstrates Potent Activity against Acute Lymphoblastic Leukemia. *Clin. Cancer Res.* **2017**, *23*, 2528–2541. [CrossRef] [PubMed]
20. Hing, Z.A.; Fung, H.Y.J.; Ranganathan, P.; Mitchell, S.; El-Gamal, D.; Woyach, J.A.; Williams, K.; Goettl, V.M.; Smith, J.; Yu, X.; et al. Next-generation XPO1 inhibitor shows improved efficacy and in vivo tolerability in hematological malignancies. *Leukemia* **2016**, *30*, 2364–2372. [CrossRef]
21. FDA Grants Accelerated Approval to Selinexor for Multiple Myeloma | FDA. Available online: <https://www.fda.gov/drugs/resources-information-approved-drugs/fda-grants-accelerated-approval-selinexor-multiple-myeloma> (accessed on 24 September 2021).
22. Sakakibara, K.; Saito, N.; Sato, T.; Suzuki, A.; Hasegawa, Y.; Friedman, J.; Kufe, D.W.; Vonhoff, D.D.; Iwami, T.; Kawabe, T. CBS9106 is a novel reversible oral CRM1 inhibitor with CRM1 degrading activity. *Blood* **2011**, *118*, 3922–3931. [CrossRef] [PubMed]
23. Liu, X.; Chong, Y.; Liu, H.; Han, Y.; Niu, M. Novel reversible selective inhibitor of CRM1 for targeted therapy in ovarian cancer. *J. Ovarian Res.* **2015**, *8*, 1–9. [CrossRef] [PubMed]
24. A Phase 1 Trial of a Novel XPO1 Inhibitor in Patients With Advanced Solid Tumors. Available online: <https://clinicaltrials.gov/ct2/show/NCT02667873> (accessed on 4 October 2021).
25. Etchin, J.; Sun, Q.; Kentsis, A.; Farmer, A.; Zhang, Z.C.; Sanda, T.; Mansour, M.; Barceló, C.; McCauley, D.; Kauffman, M.; et al. Antileukemic activity of nuclear export inhibitors that spare normal hematopoietic cells. *Leukemia* **2012**, *27*, 66–74. [CrossRef]
26. Bradshaw, J.M.; McFarland, J.M.; Paavilainen, V.O.; Bisconte, A.; Tam, D.; Phan, V.T.; Romanov, S.; Finkle, D.; Shu, J.; Patel, V.; et al. Prolonged and tunable residence time using reversible covalent kinase inhibitors. *Nat. Chem. Biol.* **2015**, *11*, 525–531. [CrossRef]
27. Al-Rifai, N.; Rücker, H.; Amslinger, S. Opening or Closing the Lock? When Reactivity Is the Key to Biological Activity. *Chem. A Eur. J.* **2013**, *19*, 15384–15395. [CrossRef] [PubMed]
28. Murphy, G.K.; Tao, J.; Tuck, T.N. Geminal Dichlorination of Phenyliodonium Ylides of  $\beta$ -Dicarbonyl Compounds through Double Ligand Transfer from (Dichloroiodo)benzene. *Synthesis* **2016**, *48*, 772–782. [CrossRef]
29. Zheng, X.; Kerr, M.A. Synthesis and Cross-Coupling Reactions of 7-Azaindoles via a New Donor–Acceptor Cyclopropane. *Org. Lett.* **2006**, *8*, 3777–3779. [CrossRef]
30. Ghosh, A.K.; Takayama, J.; Aubin, Y.; Ratia, K.; Chaudhuri, R.; Baez, Y.; Sleeman, K.; Coughlin, M.; Nichols, D.B.; Mulhearn, D.C.; et al. Structure-Based Design, Synthesis, and Biological Evaluation of a Series of Novel and Reversible Inhibitors for the Severe Acute Respiratory Syndrome–Coronavirus Papain-Like Protease. *J. Med. Chem.* **2009**, *52*, 5228–5240. [CrossRef]
31. Malmedy, F.; Wirth, T. Stereoselective Ketone Rearrangements with Hypervalent Iodine Reagents. *Chem. A Eur. J.* **2016**, *22*, 16072–16077. [CrossRef]
32. Romagnoli, R.; Baraldi, P.G.; Carrion, M.D.; Cara, C.L.; Salvador, M.K.; Preti, D.; Tabrizi, M.A.; Moorman, A.R.; Vincenzi, F.; Borea, P.A.; et al. Synthesis and biological effects of novel 2-amino-3-(4-chlorobenzoyl)-4-substituted thiophenes as allosteric enhancers of the A1 adenosine receptor. *Eur. J. Med. Chem.* **2013**, *67*, 409–427. [CrossRef] [PubMed]
33. Jimenez, L.R.; Tolentino, D.R.; Gallon, B.J.; Schrodi, Y. Development of a Method for the Preparation of Ruthenium Indenylidene-Ether Olefin Metathesis Catalysts. *Molecules* **2012**, *17*, 5675–5689. [CrossRef]
34. Parsons, D.E.; Frontier, A.J. Noncanonical Cation– $\pi$  Cyclizations of Alkylidene  $\beta$ -Ketoesters: Synthesis of Spiro-fused and Bridged Bicyclic Ring Systems. *Org. Lett.* **2019**, *21*, 2008–2012. [CrossRef] [PubMed]
35. Heinelt, U.; Wehner, V.; Herrmann, M.; Schoenafinger, K.; Steinhagen, H. Triazolium salts as PAR1 inhibitors, production thereof, and use as medicaments. *PCT Int. Appl. WO200909 7971A1*, 2009.
36. Ducki, S.; Forrest, R.; Hadfield, J.A.; Kendall, A.; Lawrence, N.J.; McGown, A.T.; Rennison, D. Potent antimetabolic and cell growth inhibitory properties of substituted chalcones. *Bioorg. Med. Chem. Lett.* **1998**, *8*, 1051–1056. [CrossRef]
37. Lawrence, N.J.; Patterson, R.P.; Ooi, L.-L.; Cook, D.; Ducki, S. Effects of  $\alpha$ -substitutions on structure and biological activity of anticancer chalcones. *Bioorg. Med. Chem. Lett.* **2006**, *16*, 5844–5848. [CrossRef] [PubMed]

38. Biddle, M.M.; Lin, M.; Scheidt, K.A. Catalytic Enantioselective Synthesis of Flavanones and Chromanones. *J. Am. Chem. Soc.* **2007**, *129*, 3830–3831. [CrossRef] [PubMed]
39. Böhme, A.; Thaens, D.; Paschke, A.; Schüürmann, G. Kinetic Glutathione Chemoassay To Quantify Thiol Reactivity of Organic Electrophiles—Application to  $\alpha,\beta$ -Unsaturated Ketones, Acrylates, and Propiolates. *Chem. Res. Toxicol.* **2009**, *22*, 742–750. [CrossRef]
40. Chan, K.; Poon, R.; O'Brien, P.J. Application of structure–activity relationships to investigate the molecular mechanisms of hepatocyte toxicity and electrophilic reactivity of  $\alpha,\beta$ -unsaturated aldehydes. *J. Appl. Toxicol.* **2008**, *28*, 1027–1039. [CrossRef]
41. Cee, V.J.; Volak, L.P.; Chen, Y.; Bartberger, M.D.; Tegley, C.; Arvedson, T.; McCarter, J.; Tasker, A.S.; Fotsch, C. Systematic Study of the Glutathione (GSH) Reactivity of N-Arylacrylamides: 1. Effects of Aryl Substitution. *J. Med. Chem.* **2015**, *58*, 9171–9178. [CrossRef] [PubMed]
42. Slawik, C.; Rickmeyer, C.; Brehm, M.; Böhme, A.; Schüürmann, G. Glutathione Adduct Patterns of Michael-Acceptor Carbonyls. *Environ. Sci. Technol.* **2017**, *51*, 4018–4026. [CrossRef]
43. Neggers, J.; Vercruyssen, T.; Jacquemyn, M.; Vanstreels, E.; Baloglu, E.; Shacham, S.; Crochiere, M.; Landesman, Y.; Daelemans, D. Identifying Drug-Target Selectivity of Small-Molecule CRM1/XPO1 Inhibitors by CRISPR/Cas9 Genome Editing. *Chem. Biol.* **2015**, *22*, 107–116. [CrossRef]
44. Warshaviak, D.T.; Golan, G.; Borrelli, K.W.; Zhu, K.; Kalid, O. Structure-Based Virtual Screening Approach for Discovery of Covalently Bound Ligands. *J. Chem. Inf. Model.* **2014**, *54*, 1941–1950. [CrossRef]
45. Zhu, K.; Borrelli, K.W.; Greenwood, J.R.; Day, T.; Abel, R.; Farid, R.S.; Harder, E. Docking Covalent Inhibitors: A Parameter Free Approach To Pose Prediction and Scoring. *J. Chem. Inf. Model.* **2014**, *54*, 1932–1940. [CrossRef] [PubMed]
46. Devraj, R.; Kumaravel, G.; Lecci, C.; Loke, P.; Meniconi, M.; Monck, N.; North, C.; Ridgill, M.; Tye, H. Preparation of heteroaryl inhibitors of peptidylarginine deiminase 4. PCT Int. Appl. WO2018049296A1, 2018.
47. Wang, K.-K.; Wang, P.; Ouyang, Q.; Du, W.; Chen, Y.-C. Substrate-controlled switchable asymmetric annulations to access polyheterocyclic skeletons. *Chem. Commun.* **2016**, *52*, 11104–11107. [CrossRef] [PubMed]
48. Wang, W.; Zhang, Y.-W.; Hu, S.-J.; Niu, W.-P.; Zhang, G.-N.; Zhu, M.; Wang, M.-H.; Zhang, F.; Li, X.-M.; Wang, J.-X. Design, synthesis, and antibacterial evaluation of PFK-158 derivatives as potent agents against drug-resistant bacteria. *Bioorg. Med. Chem. Lett.* **2021**, *41*, 127980. [CrossRef]
49. Parnell, K.M.; McCall, J.; Romero, D. Preparation of functionalized pyrazoles and other nitrogen-containing heterocycles as inhibitors of MCT4 for the treatment of MCT4-mediated diseases. U.S. Pat. Appl. Publ. US20180162822A1, 2018.
50. Amslinger, S.; Al-Rifai, N.; Winter, K.; Wörmann, K.; Scholz, R.; Baumeister, P.; Wild, M. Reactivity assessment of chalcones by a kinetic thiol assay. *Org. Biomol. Chem.* **2013**, *11*, 549–554. [CrossRef] [PubMed]
51. Berman, H.M.M.; Westbrook, J.; Feng, Z.; Gilliland, G.; Bhat, T.N.; Weissig, H.; Shindyalov, I.N.; Bourne, P.E. The Protein Data Bank. *Nucleic Acids Res.* **2000**, *28*, 235–242. [CrossRef]
52. *Schrödinger Release 2018-3*; Schrödinger, LLC: New York, NY, USA, 2018; Available online: <https://www.schrodinger.com/citations> (accessed on 13 October 2021).
53. *The PyMOL Molecular Graphics System*; Version 2.0; Schrödinger, LLC: New York, NY, USA, 2017.



Article

# Synthesis of New 1, 3, 4-Oxadiazole-Incorporated 1, 2, 3-Triazole Moieties as Potential Anticancer Agents Targeting Thymidylate Synthase and Their Docking Studies

Mohammad Mahboob Alam <sup>1</sup>, Abdulraheem SA Almalki <sup>2</sup> , Thikryat Neamatallah <sup>3,†</sup> ,  
Nada M. Ali <sup>1</sup>, Azizah M. Malebari <sup>4</sup> and Syed Nazreen <sup>1,\*</sup>

<sup>1</sup> Department of Chemistry, Faculty of Science, Albaha University, Albaha-1988, Saudi Arabia; mmalamchem@gmail.com (M.M.A.); umyousee@gmail.com (N.M.A.)

<sup>2</sup> Department of Chemistry, Faculty of Science, Taif University, Taif-21974, Saudi Arabia; drasaalmalki1@gmail.com

<sup>3</sup> Department of Pharmacology and Toxicology, Faculty of Pharmacy, King Abdulaziz University, Jeddah 21589, Saudi Arabia; Taneamatallah@kau.edu.sa

<sup>4</sup> Department of Pharmaceutical Chemistry, Faculty of Pharmacy, King Abdulaziz University, Jeddah 21589, Saudi Arabia; amelibary@kau.edu.sa

\* Correspondence: syed.nazreen22885@gmail.com

† These authors contributed equally to this work.

Received: 22 October 2020; Accepted: 12 November 2020; Published: 14 November 2020

**Abstract:** Thymidylate synthase (TS) has emerged as a hot spot in cancer treatment, as it is directly involved in DNA synthesis. In the present article, nine hybrids containing 1,2,3-triazole and 1,3,4-oxadiazole moieties (**6–14**) were synthesized and evaluated for anticancer and in vitro thymidylate synthase activities. According to in silico pharmacokinetic studies, the synthesized hybrids exhibited good drug likeness properties and bioavailability. The cytotoxicity results indicated that compounds **12** and **13** exhibited remarkable inhibition on the tested Michigan Cancer Foundation (MCF-7) and Human colorectal Carcinoma (HCT-116) cell lines. Compound **12** showed four-fold inhibition to a standard drug, 5-fluorouracil, and comparable inhibition to tamoxifen, whereas compound **13** exerted five-fold activity of tamoxifen and 24-fold activity of 5-fluorouracil for MCF-7 cells. Compounds **12** and **13** inhibited thymidylate synthase enzyme, with an half maximal inhibitory concentration, IC<sub>50</sub> of 2.52 μM and 4.38 μM, while a standard drug, pemetrexed, showed IC<sub>50</sub> = 6.75 μM. The molecular docking data of compounds **12** and **13** were found to be in support of biological activities data. In conclusion, hybrids (**12** and **13**) may inhibit thymidylate synthase enzyme, which could play a significant role as a chemotherapeutic agent.

**Keywords:** thymidylate synthase; cytotoxicity; 1,2,3-triazole; 1,3,4-oxadiazole; 5-fluorouracil; pemetrexed; docking

## 1. Introduction

Cancer is uncontrolled cell growth and cell proliferation, and remains a global burden despite the advancements in cancer diagnosis and treatment [1]. The available anticancer drugs on the market develop resistance against the chemotherapeutic agents and toxicity to normal cells [2,3]. Chemotherapy is the only effective treatment, causing the inhibition of cancer cell growth and induction of apoptosis, as the DNA levels in tumor cells are significantly higher than in normal cells [4,5]. Interestingly, thymidylate synthase (TS) has now emerged as an important target for chemotherapy for cancer treatment, as it is directly involved in DNA synthesis [6].

Thymidylate synthase enzyme catalyzes the reductive methylation of deoxyuridine monophosphate (dUMP) to deoxythymidine monophosphate (dTMP) and 5,10-methylenetetrahydrofolate (CH<sub>2</sub>THF) [7, 8]. This dTMP upon phosphorylation changes into thymine triphosphate (dTTP), which acts as a direct precursor for the synthesis of DNA [9,10]. The blocking of dTMP causes a decrease in deoxythymidine triphosphate (dTTP), thereby interrupting DNA biosynthesis causing DNA damage [11]. In addition, TS inhibition causes an increase in dUMP, leading to surge in the deoxyuridine triphosphate (dUTP) level [12]. One of the anticancer drugs, 5-fluorouracil (5-FU), acts as a strong thymidylate inhibitor for various cancers [13]. Also, a 5-FU metabolite, fluorodeoxyuridine monophosphate (FdUMP), binds with a TS active site to form a stable ternary complex, thus blocking the binding of the dUMP with TS and leading to the inhibition of dTMP synthesis [14].

Heterocycle has been a main pharmacophore in drug discovery and development. In the last few years, there is an emergence in the development of different 1,2,3-triazole-linked heterocycles, due to their excellent pharmacological properties, including anticancer [15], antiviral [16], antidiabetic [17], antimicrobial [18], anti-inflammatory [19], and antitubercular [20]. Compounds containing 1,2,3-triazoles have been reported to exert anticancer effect by inhibiting TS enzymes [21–23]. On the other hand, 1,3,4-oxadiazole plays a crucial part in medicinal chemistry. Zibotentan, an anticancer drug containing 1,3,4-oxadiazole as a pharmacophore, is used for various cancers [24]. Furthermore, 1,3,4-oxadiazole-linked heterocycles have also been reported to act as potential TS inhibitors [25,26]. Therefore, combining these two heterocycles in one molecule may lead to development of effective TS inhibitor (Figure 1).

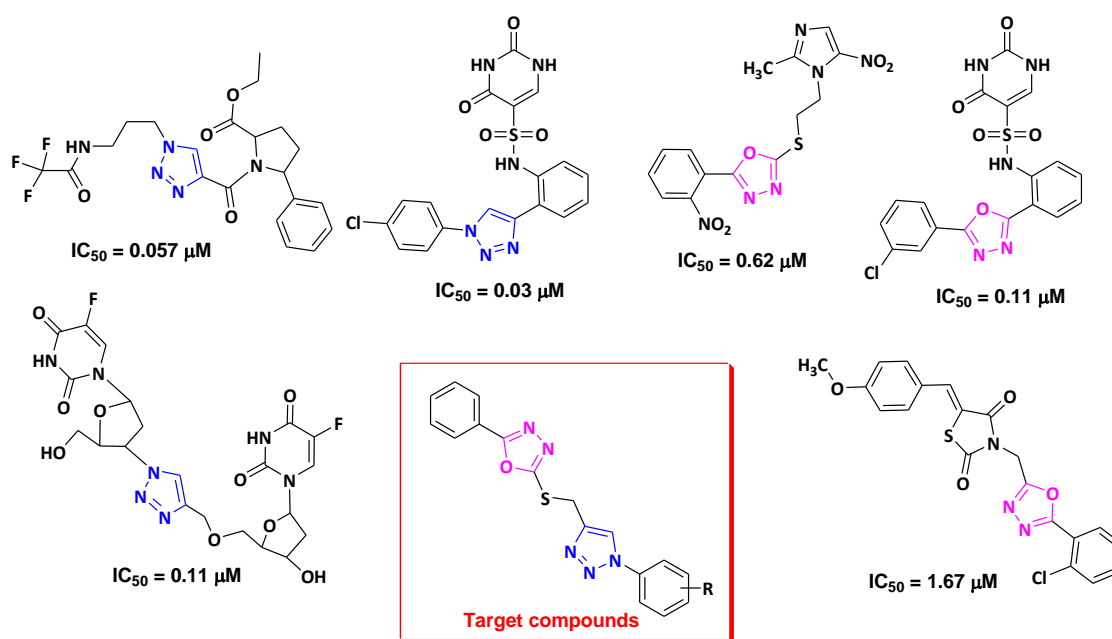


**Figure 1.** Reported thymidylate synthase inhibitors containing 1,3,4-oxadiazole and 1,2,3-triazoles.

In our previous work, we have reported thiazolidinedione-linked 1,3,4-oxadiazole as a promising TS inhibitor [27]. In continuation of our work to develop an effective TS inhibitor, we tried to conjugate 1,3,4-oxadiazole and 1,2,3-triazole pharmacophore in a single hybrid, which can inhibit the TS enzyme effectively. In this work, we describe the synthesis, pharmacokinetic study, anticancer, and TS inhibitory activities. The active compounds were docked against the thymidylate synthase enzymes to see the molecular interactions of active compounds with binding proteins.

## 2. Results and Discussion

### 2.1. Chemistry

Esterification of benzoic acid **1** in the presence of MeOH and concentrated H<sub>2</sub>SO<sub>4</sub> yielded methyl benzoate **2**, which further reacted with hydrazine monohydrate in absolute ethanol to give acid hydrazide **3**. To this acid hydrazide **3** were added ethanol, carbon disulphide, and KOH, and the mixture was stirred for 24 h and then refluxed for 14 h. After completion of the reaction, monitored by Thin Layer Chromatography (TLC), the reaction mixture was concentrated, and 100 mL cold water was added. The acidification of aqueous solution with concentrated HCl (pH 3–4) produced a white precipitate, which was filtered and recrystallized in ethanol to afford compound **4**. The propargylation of compound **4** in the presence of potassium carbonate and propargyl bromide yielded the key intermediate **5**. Finally, the key intermediate **5**, using a click chemistry approach with different aromatic azides in the presence of copper sulphate pentahydrate and sodium ascorbate, yielded final compounds **6–14** (Figure 2).

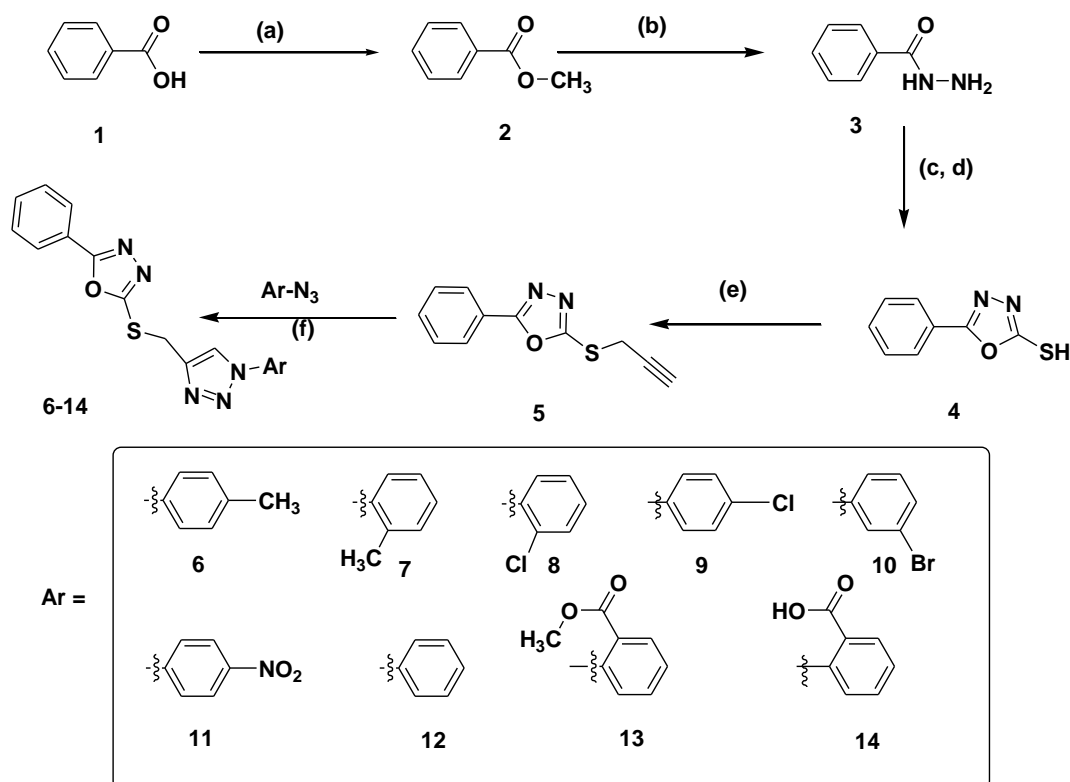


**Figure 2.** Synthesis of 1,3,4-oxadiazole linked 1,2,3-triazole hybrids. Reagents and conditions: (a) Methanol, Conc. H<sub>2</sub>SO<sub>4</sub>, reflux, 6h; (b) Absolute ethanol, H<sub>2</sub>N-NH<sub>2</sub>.H<sub>2</sub>O, reflux 4h; (c) Absolute ethanol, CS<sub>2</sub>, KOH, stir, 24 h; (d) reflux, 14 h, Conc. HCl; (e) Acetone, K<sub>2</sub>CO<sub>3</sub>, Propargyl bromide, stir, 50–60 °C, 6h; (f) tert.butanol:water (1:1), CuSO<sub>4</sub>.5H<sub>2</sub>O, sodium ascorbate, stir, 6–12 h.

All the synthesized conjugates have been confirmed using different analytical techniques, such as IR, NMR, and mass spectrometry. Formation of the compounds **2** and **3** were done by the presence of the molecular ion peak at 137 in Electron Spray Ionisation (ESI) mass spectra and from their boiling point and melting point, respectively [28]. Formation of compound **4** was done by the presence of stretching frequency of an oxadiazole ring at 1500–1600 cm<sup>-1</sup>, -SH bond stretching at 2400 cm<sup>-1</sup> in the IR spectrum, presence of an S-H singlet at δ 10.77 ppm in the <sup>1</sup>H NMR spectrum, and the molecular ion signal at δ 179 [M + H]<sup>+</sup> in mass spectrum. The propargylation of compound **4** to compound **5** was confirmed by the absence of chemical shift of an -SH proton at δ 10.77 ppm, as well as the presence



of a triplet at  $\delta$  2.34 ppm and a singlet at  $\delta$  4.5 ppm for terminal alkyne proton and S-CH<sub>2</sub>- protons, respectively. Finally, the formation of the compound **5** was supported by the presence of a molecular ion signal at 217 [M + H]<sup>+</sup> in the ESI mass spectrum. Structural confirmation of final hybrids **6–14** was observed by disappearance of terminal alkyne proton peak at  $\delta$  2.34 ppm, as well as the appearance of a 1,2,3-triazole ring proton in the range of  $\delta$  8.19–8.89 ppm with additional aromatic protons. Finally, the presence of molecular ion peaks in the mass spectrum confirmed the formation of all the final compounds (The spectra are provided in Supplementary Materials).

## 2.2. Pharmacokinetics Studies/ADME Predictions

Nowadays, *in silico* pharmacokinetic predictions are extensively used in drug discovery to reduce the cost and time. To be orally available, the molecule is not only required to have excellent biological activity, but it must follow the desired pharmacokinetic properties. The *in silico* studies that have been carried out on synthesized molecules **6–14** have been to check whether these molecules satisfy the desirable pharmacokinetics or not, which plays a crucial role in drug discovery. The physicochemical properties directly affect the pharmacokinetic behavior. The synthesized molecules should obey the Lipinski [29] and Veber [30] rules for an orally available drug. The molecule must follow the following parameters: molecular weight (MW) should be less than 500, the number of hydrogen bond acceptors (HBAs) should be fewer than 10, the number of hydrogen bond donors (HBD) should be fewer than 5, the partition coefficient (logP) should be less than 5, and the number of rotatable bonds should be  $\leq 10$  for drug likeness and good bioavailability (Table 1).

**Table 1.** Pharmacokinetic/Absorption, Distribution, Metabolism and Elimination (ADME) predictions of the target compounds **6–14**.

No.	Lipinski Parameters					nROTB <sup>e</sup>	TPSA <sup>f</sup>	%ABS <sup>g</sup>	BBB <sup>h</sup>	GI ABS <sup>i</sup>
	MW <sup>a</sup>	HBAs <sup>b</sup>	HBDs <sup>c</sup>	LogP <sup>d</sup>	Violations					
6	349.41	5	0	3.54	0	5	94.93	76.24	No	High
7	349.41	5	0	3.5	0	5	94.93	76.24	No	High
8	369.83	5	0	3.33	0	5	94.93	76.24	No	High
9	369.83	5	0	3.5	0	5	94.93	76.24	No	High
10	414.28	5	0	3.62	0	5	94.93	76.24	No	High
11	380.38	7	0	2.97	0	6	140.75	60.44	No	Low
12	335.38	5	0	3.21	0	5	94.93	76.24	No	High
13	393.42	7	0	3.39	0	7	121.23	67.17	No	High
14	379.39	7	1	2.48	0	6	132.23	63.38	No	High

<sup>a</sup> Molecular weight; <sup>b</sup> hydrogen bond acceptors; <sup>c</sup> hydrogen bond donors; <sup>d</sup> partition coefficient; <sup>e</sup> number of rotatable bonds; <sup>f</sup> topological polar surface area; <sup>g</sup> absorption (%); <sup>h</sup> blood–brain barrier; <sup>i</sup> gastro-intestinal absorption.

From the above data, it was noticed that the synthesized molecules **6–14** follow the desired pharmacokinetic properties. All the final compounds, except compound **11**, showed high gastrointestinal absorption. The % absorption of the molecules was found to be in the range 60.44–76.24. Compounds **6**, **7**, **8**, **9**, **10**, and **12** showed the highest absorption of 76.24%, while compound **11** showed the lowest absorption at 60.44%. All the compounds followed Lipinski and Veber rules, i.e., molecular weight ranging from 335–414, hydrogen bond acceptors ranging from 5–7, hydrogen bond donors ranging from 0–1, lipophilicity appearing in the range 2.48–3.62, and the number of rotatable bonds between 5 and 7. The synthesized compounds exhibited higher logP values, in the range 2.48–3.62, suggesting higher cell membrane permeability. The final hybrids exhibited topological polar surface areas (TPSAs) between 94.93–140.75 Å<sup>2</sup>, which suggests good intestinal absorption. The pharmacokinetic results indicate that these compounds satisfy the criteria for good drug likeness parameters and good bioavailability.

### 2.3. Biological Studies

#### 2.3.1. Cytotoxicity Assay

The final compounds **6–14** were screened for their antiproliferative effect using an MTT (3-(4,5-dimethylthiazol-2-yl)-2,5-diphenyl tetrazolium bromide) assay. These compounds were tested against breast MCF-7 and colorectal HCT-116 cell lines. These compounds exhibited moderate to significant activity compared to standard drugs tamoxifen and 5-fluorouracil (5-FU). The results are presented in Table 2.

**Table 2.** The IC<sub>50</sub> (μM) of the synthesized compounds (**6–14**) against tested human cancer cell lines (MCF-7 and HCT-116).<sup>a</sup>

Compound	MCF-7 <sup>b</sup>	HCT-116 <sup>c</sup>
6	79.80	89.20
7	30.70	34.30
8	73.30	107.50
9	34.40	36.70
10	25.90	32.70
11	98.20	102.30
12	5.80	14.80
13	1.26	17.30
14	40.60	46.80
Tam <sup>d</sup>	5.12	26.41
5-FU <sup>e</sup>	24.74	32.68

<sup>a</sup> IC<sub>50</sub> values are the concentrations that cause 50% inhibition of cancer cell growth. Data represent the mean values ± standard deviation of three independent experiments, performed in triplicate; <sup>b</sup> breast cancer (MCF-7); <sup>c</sup> colorectal cancer (HCT-116); <sup>d</sup> Tam: tamoxifen; <sup>e</sup> 5-FU: 5-fluorouracil, which was used as a reference drug (positive control).

Among the tested compounds, compounds **12** and **13** showed significant inhibitory effects on the viability of MCF-7 and HCT-116 cells (Figure 3). Compound **12** (IC<sub>50</sub> = 5.8 μM) showed comparable inhibition to the standard drug tamoxifen (IC<sub>50</sub> = 5.12 μM) and four-fold inhibition compared to the standard drug 5-fluorouracil (IC<sub>50</sub> = 24.74 μM). Compound **13**, however, was found to exhibit promising inhibition against MCF-7, with IC<sub>50</sub> = 1.26 μM, while the two standard drugs, tamoxifen and 5-fluorouracil, showed IC<sub>50</sub> = 5.12 μM and 24.74 μM, respectively. It is clear from the results that compound **13** was more potent in exerting the anticancer effect, with five times the activity of tamoxifen and 24 times the activity of 5-fluorouracil for MCF-7 (Figure 4).

The same two compounds (**12** and **13**) also displayed significant inhibition against HCT-116 cells. Compound **12** (IC<sub>50</sub> = 14.8 μM) revealed 1.7-fold activity compared to tamoxifen (IC<sub>50</sub> = 26.41 μM) and 2.2-fold activity compared to 5-fluorouracil (IC<sub>50</sub> = 32.68 μM) against HCT-116, while compound **13** (IC<sub>50</sub> = 17.3 μM) displayed 1.9-fold activity compared to 5-FU and 1.5-fold the activity of tamoxifen. Other compounds, **6**, **7**, **8**, **9**, **10**, **11**, and **14**, exhibited moderate cytotoxicity with the MCF-7, with IC<sub>50</sub> values in the range 25.9–98.28 μM. On the other hand, compounds **6**, **7**, **9**, **10**, and **14** displayed inhibition with IC<sub>50</sub> values in the range of 32.7–89.2 μM, whereas compounds **8** and **11** were found to be inactive (IC<sub>50</sub> > 100) against the HCT-116 cells.

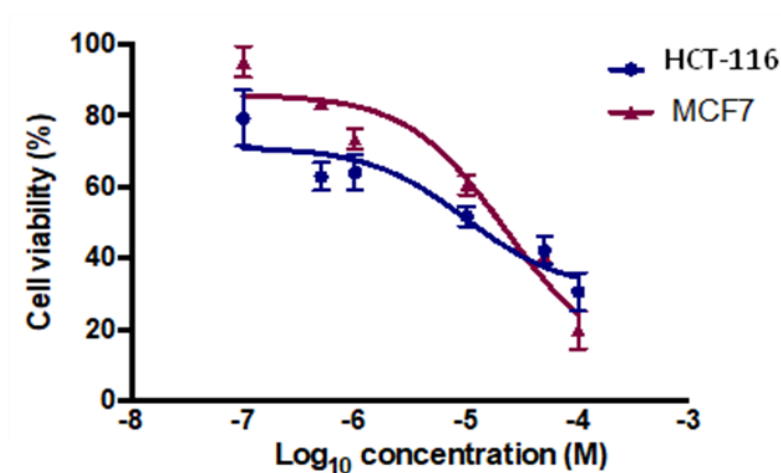


**Figure 3.** Antiproliferative effects of compound **12** in HCT-116 and MCF-7 cells. Cell viability was expressed as a percentage of vehicle control (ethanol 1% (*v/v*)) and was measured by MTT (3-(4,5-dimethylthiazol-2-yl)-2,5-diphenyl tetrazolium bromide) assay. The values represent the mean  $\pm$  standard error of the mean (SEM) for three independent experiments performed in triplicate.

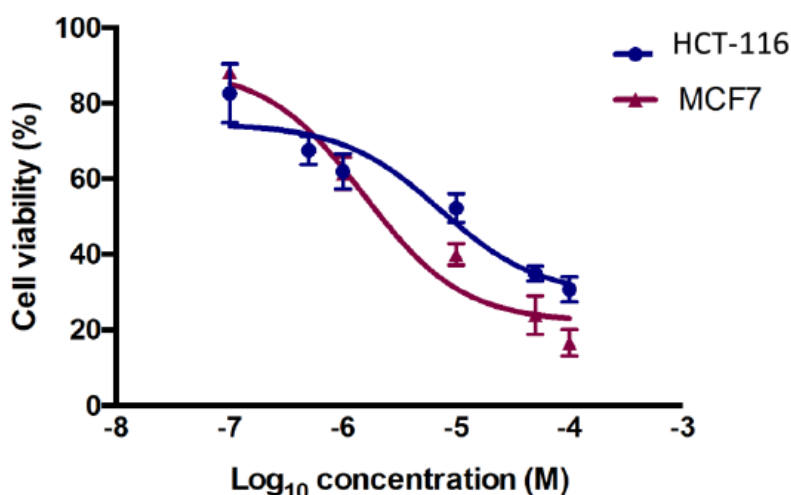


**Figure 4.** Antiproliferative effects of compound **13** in HCT-116 and MCF-7 cells. Cell viability was expressed as a percentage of vehicle control (ethanol 1% (*v/v*)) and was measured by MTT assay. The values represent the mean  $\pm$  SEM for three independent experiments performed in triplicate.

The most potent compounds, **12** and **13**, were also tested on non-tumorigenic cell line HEK 293 (normal human embryonic kidney) cells, in order to investigate the toxicity and selectivity of these two potent compounds (Figures 5 and 6). It was found that these two compounds (**12** and **13**) showed  $IC_{50}$  values above 50  $\mu$ M on HEK 293 cells, which was higher than those observed against the two cancer cell lines—MCF-7:  $IC_{50}$  = 5.8  $\mu$ M (**12**), 1.26  $\mu$ M (**13**); HCT-116:  $IC_{50}$  = 14.8  $\mu$ M (**12**), 17.3  $\mu$ M (**13**)—indicating that these molecules were less toxic to human normal cells and selective to cancerous cells. From these results, it is clear that compound **12** with no substituents and compound **13** with a  $-COOMe$  group at the ortho position exerted promising antiproliferative effects on both the tested cells, whereas the presence of halogens and electron withdrawing groups (nitro) on the aromatic ring did not play a significant role in exerting the anticancer effect.

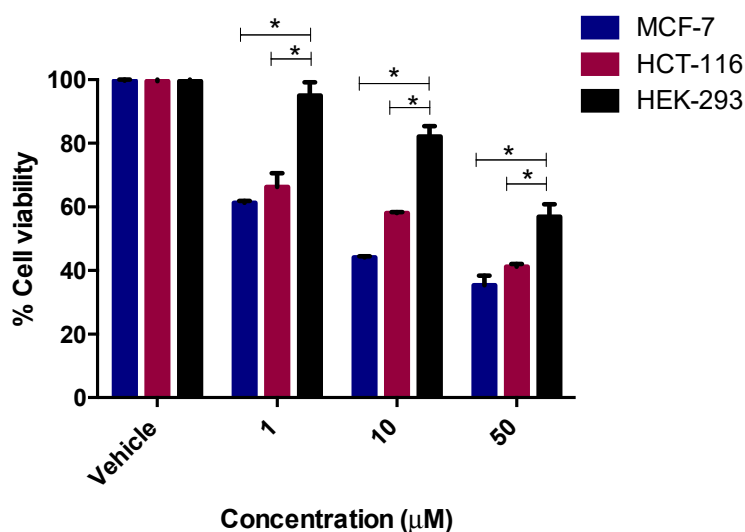


**Figure 5.** Antiproliferative effects of compound **12** on the viability of cancerous MCF-7 and HCT-116 cells, as well as non-tumorigenic HEK-293 cells. The values represent the mean  $\pm$  SEM for three independent experiments performed in triplicate. \*  $p < 0.05$  between the indicated groups, via two-way ANOVA (Bonferroni post-test).

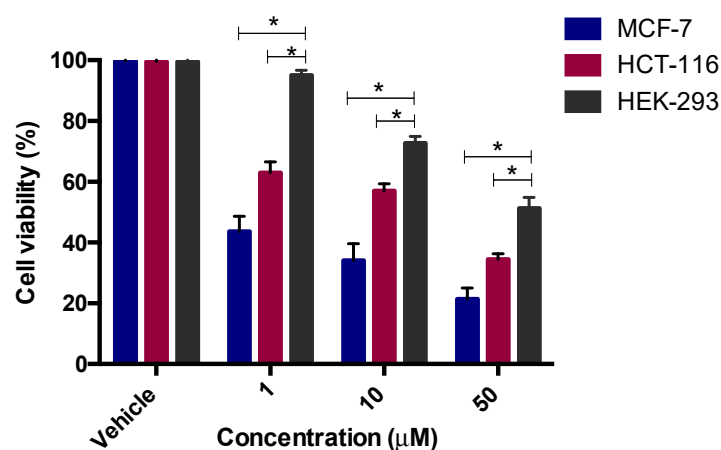


**Figure 6.** Antiproliferative effects of compound **13** on the viability of cancerous MCF-7 and HCT-116 cells, as well as non-tumorigenic HEK-293 cells. The values represent the mean  $\pm$  SEM for three independent experiments performed in triplicate. \*  $p < 0.05$  between indicate groups, via two-way ANOVA (Bonferroni post-test).

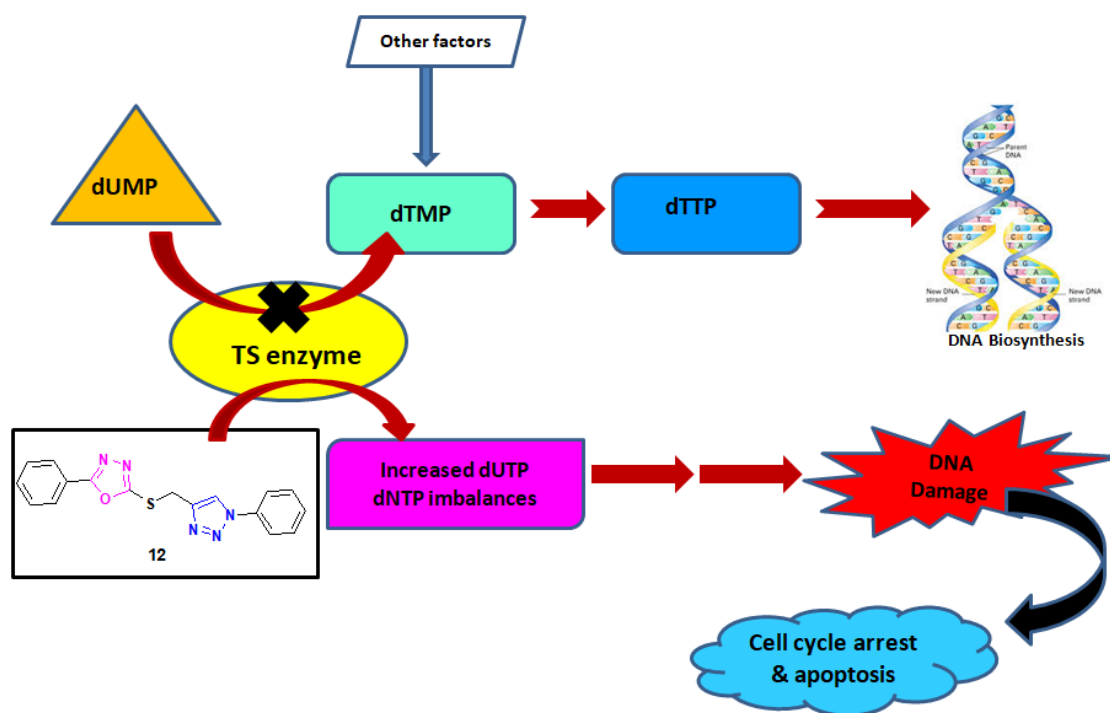
### 2.3.2. In Vitro Thymidylate Synthase Activity

Thymidylate synthase (TS) has become an important target for cancer treatment, as it is involved in DNA synthesis. The inhibition of this enzyme plays a vital role in chemotherapy treatment. The active compounds (**12** and **13**) from the MTT assay were screened for in vitro thymidylate synthase, to confirm its mechanism of action. These compounds inhibited the TS enzyme significantly compared to the standard drug pemetrexed. Compound **12** inhibited TS with  $IC_{50} = 2.52 \mu M$ , and **13** inhibited it with  $IC_{50} = 4.38$  (Table 3). It was observed that compounds **12** and **13** showed 2.6- and 1.5-fold activity compared to pemetrexed ( $IC_{50} = 6.75 \mu M$ ). From these results, it can be inferred that compounds **12** and **13** inhibit TS by binding with the active binding site of the enzyme, which results in the blocking of dUMP with TS, leading to inactivation of dTMP. This inactivation of dTMP results in a reduction of deoxythymidine triphosphate (dTTP), leading to the disruption of DNA synthesis and cessation of cell growth and proliferation (Figure 7). These results support our antiproliferative results.

**Table 3.** In vitro thymidylate synthase (TS) activity of the active compounds **12** and **13**, as well as PTX.

Compounds	IC <sub>50</sub> (μM)
12	2.52
13	4.38
PTX	6.75

IC<sub>50</sub> values are the mean ± SD of three separate experiments. PTX: pemetrexed.

**Figure 7.** Mechanism of action of compound **12** on thymidylate synthase enzyme.

#### 2.4. Molecular Docking

It is a computational technique used frequently to know the possible interactions of a molecule with a receptor. The active compounds from in vitro studies were docked against TS proteins (PDB = 6QXG) to support our in vitro thymidylate synthase results, as well as to know the possible binding modes with the protein. The 5-fluorouracil has been reported as a TS inhibitor that interacts with the active binding site of the protein through different residues [31,32]. Therefore, we have docked our active compounds **12** and **13** against this protein, in order to support our in vitro findings. The results are presented in Figure 8 and Table 4.

**Table 4.** Docking scores of active compounds **12** and **13** against human thymidylate synthase protein 6QXG.

Compound	Docking Score	Amino Acid Residue
12	−3.81	ASN 226
13	−4.25	ASN 226, PHE 225, HIE 196
5-FU	−3.5	ASP 218, ASN 226

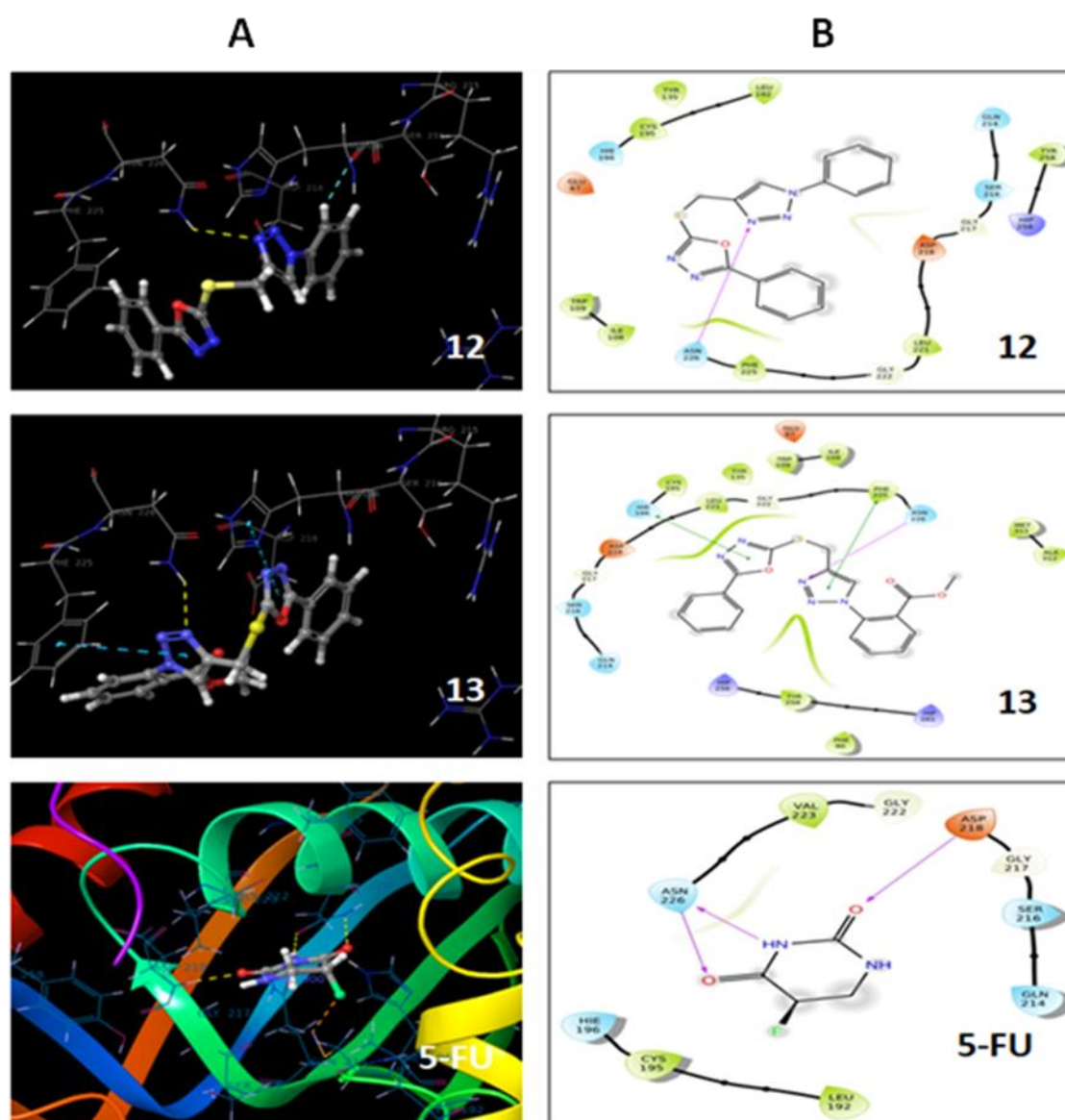


**Figure 8.** Molecular docking of the active compounds **12** and **13**, as well as 5-FU, against thymidylate synthase (TS) protein 6QXG. (A) Binding mode of **12**, **13**, and 5-FU at the TS binding site, with a three-dimensional (3D) plot. (B) Binding mode of **12**, **13**, and 5-FU at the TS binding site on a two-dimensional (2D) plot. 5-FU: 5-fluorouracil.

From the docking results, it was observed that compound **12** (−3.81) and **13** (−4.25) showed higher dock scores than the standard drug 5-fluorouracil (−3.5). The nitrogen of the 1,2,3-triazole ring in compounds **12** and **13** showed hydrogen bonding interactions with ASN 226 residues, while two pi–pi interactions were also observed in compound **13**. One pi interaction was between a 1,2,3-oxadiazole ring and HIE 196, and another was the interaction of a 1,2,3-triazole ring with a PHE 225 residue. The standard drug 5-FU showed H-bonding interactions of ASP 218 with a C=O group at the 2 position, and ASN 226 with N–H and a C=O group at the 3 and 4 positions. The binding pattern of compounds **12** and **13**, as well as 5-FU, was found to be similar to the thymidylate synthase protein. These findings suggest that these two compounds (**12** and **13**) exert anticancer effects by inhibiting the thymidylate synthase enzyme, which supports the *in vitro* TS results of hybrids **12** and **13**, with IC<sub>50</sub> values of 2.52 and 4.38 μM, respectively.

### 3. Experimental

#### 3.1. Chemistry

The chemicals and other reagents were procured from Sigma Aldrich (Germany) and Loba Chem (India), and were used without further purification. FTIR spectra were recorded on a Thermo Scientific iS 50 by ATR method. Nuclear magnetic resonance (NMR) analysis was performed on Bruker 300 and 850 MHz instruments in CDCl<sub>3</sub> or DMSO-d<sub>6</sub> solvents; tetramethylsilane (TMS) was used as an internal reference. Chemical shift and coupling constant are provided in parts per million (ppm) and Hertz, respectively. All the samples were analyzed by mass spectrometry on a Thermo Scientific-LCQ Fleet (LCF10605) using the electron spray ionization method, and are provided in *m/z*. The melting points of the compounds were determined on the electro-thermal melting point apparatus (Stuart SMP40). A LEECO Elementar Analyzer was used for elemental analysis of the synthesized compounds, which was reported in % standard; these were  $\pm 0.4\%$  of the calculated values. Monitoring of the reaction and purity of the compounds were checked on a silica gel G plate (Merck, Germany).

#### 3.2. General Procedure for the Synthesis of 1,3,4-Oxadiazole Linked 1,2,3-Triazole Hybrids (6–14)

Compound **5** (0.01 mmole) was charged in a 100 mL round-bottom flask, followed by addition of *tert*-BuOH–H<sub>2</sub>O (1:1, 30–50 mL). The reaction mixture was heated to get a clear solution and cooled to room temperature. To this reaction mixture, copper sulphate pentahydrate (0.0013 mmol) and sodium ascorbate (0.0013 mmol) was added and stirred for 30 mins, followed by drop-wise addition of aromatic azides (0.15 mmole). The reaction mixture was stirred for 5–12 hrs at room temperature, and the progress of the reaction was monitored by TLC, using *n*-hexane/ethylacetate (6:4) as eluents. After completion of the reaction, water (50 mL) was added to the reaction mixture and the products were extracted with dichloromethane (100 mL  $\times$  2). The dichloromethane layer was combined, dried over anhydrous sodium sulphate, concentrated, and recrystallized using dichloromethane and cyclohexane to get target compounds **6–14** in 65–85% yield.

##### 3.2.1. 4-((5-phenyl-1,3,4-oxadiazol-2-ylthio)methyl)-1-*p*-tolyl-1H-1,2,3-triazole (6)

Grey crystals, yield = 80%, melting point (MP) = 146–147 °C. IR (ATR)  $\nu_{\max}$ : 3086 (C–H), 1559 (C=C), 1518 1468, 1340, 1257, 1232 (C=N, C–N), 1192, 1079 (C–O), 700, 688 (C–S) cm<sup>-1</sup>. <sup>1</sup>H NMR (300 MHz, CDCl<sub>3</sub>):  $\delta$  2.40 (s, 3H), 4.69 (s, 2H), 7.28 (d, *J* = 8.1 Hz, 2H), 7.46–7.59 (m, 5H), 7.98 (d, *J* = 7.2 Hz, 2H), 8.19 (s, 1H). <sup>13</sup>C NMR (75 MHz, CDCl<sub>3</sub>):  $\delta$  21.01, 27.25, 120.41, 122.48, 123.49, 126.87, 129.86, 130.68, 132.49, 134.68, 138.86, 143.91, 163.40, 165.84. ESI MS: 350 (M<sup>+</sup> + H). C<sub>18</sub>H<sub>15</sub>N<sub>5</sub>OS (calculated): C = 61.87; H = 4.33; N = 20.04; O = 4.58; S = 9.18; observed: C = 61.42; H = 4.35; N = 20.01; O = 4.60; S = 9.16.

##### 3.2.2. 4-((5-phenyl-1,3,4-oxadiazol-2-ylthio)methyl)-1-*o*-tolyl-1H-1,2,3-triazole (7)

White powder, yield = 75%, MP = 112–113 °C. IR (ATR)  $\nu_{\max}$ : 3123 (C–H aromatic), (C–H), 2920 (C–H), 1606, 1557 (C=C), 1505, 1491, 1466, 1382, 1341 (C=N, C–N), 1185, 1076 (C–O), 701, 683 (C–S) cm<sup>-1</sup>. <sup>1</sup>H NMR (300 MHz, CDCl<sub>3</sub>):  $\delta$  2.52 (s, 3H), 4.75 (s, 2H), 7.11–7.14 (m, 2H), 7.57–7.66 (m, 3H), 7.77–8.0 (3, 4H), 8.72 (s, 1H). <sup>13</sup>C NMR (75 MHz, CDCl<sub>3</sub>):  $\delta$  17.75, 27.33, 123.51, 125.94, 126.41, 126.89, 127.43, 129.86, 130.31, 131.80, 132.50, 133.47, 136.57, 142.86, 163.36, 165.87. ESI MS: 350 (M<sup>+</sup> + H). C<sub>18</sub>H<sub>15</sub>N<sub>5</sub>OS (calculated): C = 61.87; H = 4.33; N = 20.04; O = 4.58; S = 9.18; observed: C = 61.82; H = 4.36; N = 20.01; O = 4.60; S = 9.17.

##### 3.2.3. 4-((5-phenyl-1,3,4-oxadiazol-2-ylthio)methyl)-1-(2-chlorophenyl)-1H-1,2,3-triazole (8)

White crystals, yield = 65%, MP = 111–112 °C. (ATR)  $\nu_{\max}$ : 3142, 3089 (C–H aromatic), 1557 (C=C), 1490, 1470, 1342 (C=N, C–N), 1192, 1073, 1064 (C–O), 769, 717 (C–Cl), 704, 686 (C–S) cm<sup>-1</sup>. <sup>1</sup>H NMR (300 MHz, CDCl<sub>3</sub>):  $\delta$  4.71 (s, 1H), 7.39–7.61 (m, 7H), 7.97–8.00 (m, 2H), 8.23 (s, 1H). <sup>13</sup>C NMR (75 MHz,

CDCl<sub>3</sub>):  $\delta$  27.19, 123.49, 126.51, 126.89, 128.77, 128.85, 128.92, 129.86, 130.99, 132.13, 132.50, 134.80, 142.98, 163.31, 165.87. ESI MS: 370 (M<sup>+</sup> + H), 372 (M<sup>+</sup> + 2 + H). C<sub>17</sub>H<sub>12</sub>N<sub>5</sub>OS (calculated): C = 55.21; H = 3.27; N = 18.94; O = 4.33; S = 8.67; observed: C = 55.16; H = 3.30; N = 18.89; O = 4.35; S = 8.64.

#### 3.2.4. 4-((5-phenyl-1,3,4-oxadiazol-2-ylthio)methyl)-1-(4-chlorophenyl)-1H-1,2,3-triazole (9)

Brown powder, yield = 75%, MP = 200–202 °C. (ATR)  $\nu_{\max}$ : 3082 (C–H, aromatic), 2920 (C–H), 1558 (C=C), 1490, 1473, 1448, 1427, 1339 (C=N, C–N), 1195, 1093, 1077, 1051 (C–O), 846, 827 (C–Cl), 702, 686 (C–S) cm<sup>-1</sup>. <sup>1</sup>H NMR (300 MHz, CDCl<sub>3</sub>):  $\delta$  4.68 (s, 2H), 7.26–7.28 (m, 5H), 7.49 (t, *J* = 7.8 Hz, 2H), 7.67 (d, *J* = 8.7 Hz, 2H), 7.87 (d, *J* = 6.6 Hz, 2H), 8.24 (s, 1H). <sup>13</sup>C NMR (75 MHz, CDCl<sub>3</sub>):  $\delta$  27.18, 119.06, 120.30, 122.77, 123.47, 126.83, 128.97, 129.81, 132.00, 132.45, 134.64, 137.92, 144.23, 163.33, 165.82. ESI MS: 370 (M<sup>+</sup>+H), 372 (M<sup>+</sup>+2+H). C<sub>17</sub>H<sub>12</sub>N<sub>5</sub>OS (calculated): C = 55.21; H = 3.27; N = 18.94; O = 4.33; S = 8.67; observed: C = 55.16; H = 3.30; N = 18.93; O = 4.37; S = 8.63.

#### 3.2.5. 4-((5-phenyl-1,3,4-oxadiazol-2-ylthio)methyl)-1-(3-bromophenyl)-1H-1,2,3-triazole (10)

White flakes, yield = 70%, MP = 146–148 °C. IR (ATR)  $\nu_{\max}$ : 3137, 3083 (C–H, aromatic), 1607, 1588 (C=C), 1558, 1486, 1471, 1461, 1341, 1289, 1255 (C=N, C–N), 1191, 1077, 1046 (C–O), 702 (C–S), 691 (C–Br) cm<sup>-1</sup>. <sup>1</sup>H NMR (300 MHz, CDCl<sub>3</sub>):  $\delta$  4.67 (s, 2H), 7.35–7.68 (m, 6H), 7.92–8.00 (m, 3H), 8.24 (s, 1H). <sup>13</sup>C NMR (75 MHz, CDCl<sub>3</sub>):  $\delta$  27.19, 119.53, 122.79, 122.89, 123.09, 123.50, 126.87, 129.86, 131.95, 132.28, 132.49, 138.02, 144.22, 163.32, 165.85. ESI MS: 414 (M<sup>+</sup> + H), 416 (M<sup>+</sup> + 2 + H). C<sub>17</sub>H<sub>12</sub>N<sub>5</sub>OS: (calculated): C = 49.29; H = 2.92; N = 16.90; O = 3.86; S = 7.74; observed: C = 49.31; H = 2.94; N = 16.87; O = 3.83; S = 7.76.

#### 3.2.6. 4-((5-phenyl-1,3,4-oxadiazol-2-ylthio)methyl)-1-(4-nitrophenyl)-1H-1,2,3-triazole (11)

Light orange solid, yield = 65%, MP = 202–204 °C. IR (ATR)  $\nu_{\max}$ : 3127, 3079 (C–H, aromatic), 1596 (C=C), 1558 (N–O) 1523, 1505, 1473, 1388 (C=N, C–N), 1260, 1232, 1191, 1109 (C–O), 703, 686 (C–S) cm<sup>-1</sup>. <sup>1</sup>H NMR (850 MHz, DMSO-*d*<sub>6</sub>)  $\delta$ : 4.79 (s, 2H), 7.27–8.01 (m, 9H), 8.26 (s, 1H). <sup>13</sup>C NMR (213 MHz, DMSO)  $\delta$ : 27.25, 120.17, 12.87, 123.38, 126.60, 127.47, 127.66, 128.54, 128.70, 131.98, 132.22, 137.11, 147.54, 163.52, 165.58. ESI MS: 381 (M + H). C<sub>17</sub>H<sub>12</sub>N<sub>6</sub>O<sub>3</sub>S (calculated): C = 53.68; H = 3.18; N = 22.09; O = 12.62; S = 8.43; observed: C = 53.69; H = 3.20; N = 22.07; O = 12.62; S = 8.42.

#### 3.2.7. 4-((5-phenyl-1,3,4-oxadiazol-2-ylthio)methyl)-1-phenyl-1H-1,2,3-triazole (12)

White flakes, yield = 75%, MP = 130–131 °C. IR (ATR)  $\nu_{\max}$ : 3144 (C–H), 1594 (C=C), 1506, 1466, 1344, 1290, 1256 (C=N, C–N), 1191, 1173, 1077, 1064 (C–O), 702, 683 (C–S) cm<sup>-1</sup>. <sup>1</sup>H NMR (300 MHz, CDCl<sub>3</sub>):  $\delta$  4.69 (s, 2H), 7.36–8.24 (m, 10H), 8.35 (s, 1H). <sup>13</sup>C NMR (75 MHz, CDCl<sub>3</sub>):  $\delta$  27.26, 120.55, 122.58, 123.51, 126.86, 129.21, 129.85, 130.34, 132.48, 136.92, 143.99, 163.37, 165.85; ESI MS: 336 (M<sup>+</sup> + H). C<sub>17</sub>H<sub>13</sub>N<sub>5</sub>OS (calculated): C = 60.88; H = 3.91; N = 20.88; O = 4.77; S = 9.56; observed: C = 60.81; H = 3.95; N = 20.85; O = 4.80; S = 9.55.

#### 3.2.8. Methyl 2-(4-((5-phenyl-1,3,4-oxadiazol-2-ylthio)methyl)-1H-1,2,3-triazol-1-yl)benzoate (13)

Brown flakes, yield = 70%, MP = 119–120 °C. IR (ATR)  $\nu_{\max}$ : 3127, 3083 (C–H, aromatic), 2953 (C–H), 1727 (C=O), 1602, 1558 (C=C), 1506, 1472, 1450, 1340, 1272 (C=N, C–N), 1192, 1134, 1053 (C–O), 702, 688 (C–S) cm<sup>-1</sup>. <sup>1</sup>H NMR (300 MHz, CDCl<sub>3</sub>):  $\delta$  3.85 (s, 3H), 4.68 (s, 2H), 6.99 (d, *J* = 9.0 Hz, 2H), 7.21–7.75 (m, 5H), 7.93–8.44 (m, 2H), 8.45 (s, 1H). <sup>13</sup>C NMR (75 MHz, DMSO)  $\delta$ : 27.30, 56.00, 115.32, 122.21, 122.51, 122.83, 123.51, 126.86, 129.84, 130.34, 132.46, 143.66, 163.40, 165.84, 169.77. ESI MS: 394 (M<sup>+</sup> + H). C<sub>19</sub>H<sub>15</sub>N<sub>5</sub>O<sub>3</sub>S (calculated): C = 58.01; H = 3.84; N = 17.80; O = 12.20; S = 8.15; observed: C = 58.02; H = 3.82; N = 17.81; O = 12.21; S = 8.14.



### 3.2.9. 2-(4-((5-phenyl-1,3,4-oxadiazol-2-ylthio)methyl)-1H-1,2,3-triazol-1-yl)benzoic acid (14)

White solid, yield = 72%, MP = 119–120 °C. IR (ATR)  $\nu_{\max}$ : 3127 (brs–OH) 3083, 2953 (C–H), 1727 (C = O), 1602, 1558 (C=C), 1506, 1472, 1450, 1340, 1272 (C=N, C–N), 1260, 1192, 1134, 1053 (C–O), 702, 688 (C–S)  $\text{cm}^{-1}$ .  $^1\text{H}$  NMR (400 MHz, DMSO):  $\delta$  4.69 (s, 2H), 7.13–7.24 (m, 2H), 7.41–7.99 (m, 7H), 8.89 (s, 1H), 10.66 (s, 1H).  $^{13}\text{C}$  NMR (213 MHz, DMSO):  $\delta$  27.26, 120.01, 125.48, 126.76, 132.57, 134.09, 135.61, 138.57, 143.77, 163.92, 165.21, 167.27; ESI MS: 380 ( $\text{M}^+ + \text{H}$ ).  $\text{C}_{18}\text{H}_{13}\text{N}_5\text{O}_3\text{S}$  (calculated): C = 56.98; H = 3.45; N = 18.46; O = 12.65; S = 8.45; observed: C = 56.99; H = 3.47; N = 18.43; O = 12.64; S = 8.45.

## 3.3. Anticancer Activity

### 3.3.1. Cell Lines and Culture Medium

The human breast cancer cell line (MCF-7) used in the present study was obtained from Dr. Neamatallah's lab. The cells were cultured in Dulbecco's Modified Eagle Medium (DMEM) supplemented with 10% (*v/v*) fetal bovine serum (FBS), 10,000 units/mL penicillin/streptomycin, and 1% (*v/v*) L-glutamine at 37 °C in humidified 5%  $\text{CO}_2$  incubator.

### 3.3.2. Cytotoxicity Assay

The cytotoxicity activity was done by MTT assay [33]. Breast MCF-7 and colorectal HCT-116 cancer cells were added at  $1 \times 10^5$  cells/mL into a 96-well plate with three replicates, and incubated overnight for attachment at 37 °C in a 5%  $\text{CO}_2$  humidified atmosphere. Drug concentrations at six serial dilutions (100.0, 50.0, 10.0, 1.0, 0.5, and 0.1  $\mu\text{M}$ ) were added in triplicate and incubated at 37 °C and 5%  $\text{CO}_2$  for 72 h. Drugs were dissolved in 0.1% DMSO as a vehicle. Untreated cells were used as control. Tamoxifen and 5-fluorouracil (5-FU) was used as positive controls. Thereafter, each well for each time point was removed and replaced with 100  $\mu\text{M}$  of full medium containing 10% 3-(4,5-dimethylthiazolyl-2)-2,5-diphenyltetrazoliumbromide (MTT) (10 mg/mL). Then the media was removed and 100  $\mu\text{l}$  of DMSO was added, and cells were incubated for a further 5 mins at 37 °C and 5%  $\text{CO}_2$ . Plates were quantified using the SpectraMax M3 plate reader at 570 nm. The percentage inhibition was calculated as  $100 - ((\text{mean OD of treated cell} \times 100) / \text{Mean OD of vehicle treated cells (DMSO)})$ . All the experiments were repeated in at least three independent experiments (Table 2, Figures 3–6).

### 3.4. In Vitro Thymidylate Synthase Enzyme Assay

A thymidylate synthase enzymatic assay was carried out according to the reported method [34,35]. It involves a mixture containing 2-mercaptoethanol (0.1 M), (6R,S)-tetrahydrofolate (0.0003 M), formaldehyde (0.012 M),  $\text{MgCl}_2$  (0.02 M), dUMP (0.001 M), TrisHCl (0.04 M), and NaEDTA (0.00075 M). This assay was done spectrophotometrically at 30 °C and pH 7.4. The reaction was initiated by the addition of an amount of enzyme, giving a change in absorbance at 340 nm of 0.016/min in the absence of inhibitor. The percent inhibition was determined at a minimum of four inhibitor concentrations within 20% of the 50% point. The standard deviations for determination of the 50% points were within  $\pm 10\%$  of the values given. The results are presented in Table 3 and Figure 7.

### 3.5. Molecular Docking

Molecular docking studies involve mainly protein selection and preparation, grid generation, ligand preparation, docking, and further analysis of docking studies. A protein with accession number 6QXG was selected and downloaded from Protein Data Bank. This protein is reported to act as a thymidylate synthase inhibitor. The protein was imported, optimized, and minimized by removing unwanted molecules and other defects reported by the software. The minimized protein was used for grid generation, which involves the selected ligand as the reference, as it signifies the binding sites of the drug with respect to the target. Molecules drawn in 3D form were refined by the LigPrep module.

The molecules were subjected to an OPLS-2005 force field to generate a single, low-energy 3D structure for each input structure. Docking studies were carried out using Glide software. It was carried out using extra precision and write XP descriptor information. This generates favorable ligand poses, which are further screened through filters to examine the spatial fit of the ligand in the active site. Ligand poses, which pass through an initial screening, are subjected to evaluation and minimization of grid approximation. Scoring was then carried out on energy-minimized poses to generate a Glide score [36] (Table 4, Figure 8).

#### 4. Conclusions

In the present article, a series of nine hybrids of 1,2,3-triazole and 1,3,4-oxadiazole moieties (6–14) have been described. The final compounds have been characterized using different analytical techniques. These hybrids have been tested for *in vitro* anticancer and thymidylate synthase activities. According to *in silico* pharmacokinetic studies, the synthesized hybrids exhibited good drug likeness properties and bioavailability. The cytotoxicity results indicated that compounds **12** and **13** exhibited remarkable inhibition on the tested MCF-7 and HCT-116 cell lines. Compound **12** showed four-fold inhibition compared to the standard drug 5-fluorouracil, and comparable inhibition to tamoxifen, whereas compound **13** exerted five-fold and 24 times the activity of tamoxifen and 5-fluorouracil, respectively, for MCF-7 cells. The same compounds (**12** and **13**) also revealed significant inhibition against HCT-116 cells. Compound **12** revealed 1.7-fold activity of tamoxifen and 2.2-fold activity of 5-fluorouracil, while compound **13** displayed 1.9-fold the activity of 5-FU and 1.5-fold that of tamoxifen against HCT-116. The *in vitro* thymidylate synthase activity results supported our cytotoxicity results. Compounds **12** and **13** inhibited thymidylate synthase enzyme with  $IC_{50}$  values of 2.52  $\mu$ M and 4.38  $\mu$ M, respectively, while the standard drug pemetrexed showed an  $IC_{50}$  of 6.75  $\mu$ M. The molecular docking data of compounds **12** and **13** supported the *in vitro* biological activity data. In conclusion, hybrids (**12** and **13**) may inhibit the thymidylate synthase enzyme, which could play a significant role as a chemotherapeutic agent.

**Supplementary Materials:** The following are available online at <http://www.mdpi.com/1424-8247/13/11/390/s1>, Figures S1–S9:  $^1H$  NMR spectra of all final compounds; Figures S10–S18:  $^{13}C$  NMR spectra of all final compounds; Figures S19–S27: Mass spectra of all final compounds.

**Author Contributions:** M.M.A. and S.N. designed the experiment and supervised. T.N. and N.M.A. carried out the pharmacology work, M.M.A. and A.S.A.A. performed the synthetic work, A.M.M. and S.N. analyzed the data, characterized the compounds, and wrote the manuscript. All authors have read and agreed to the published version of the manuscript.

**Funding:** Taif University Researchers Supporting Project (Number TURSP-2020/44) for financial assistance for the project work.

**Acknowledgments:** A.S.A.A. acknowledges the Taif University Researchers Supporting Project (Number TURSP-2020/44) for financial assistance. M.M.A. and S.N. thanks the Chemistry department, Albaha University, for providing the necessary facilities to carry out the project work. We also thank Safaa S. Bayashut, King Abdulaziz University (KAU) for helping perform the pharmacological activities. The non-tumorigenic HEK-293 cells (normal human embryonic kidney) were generously provided by Anwar Hashem, Vaccine and Immunotherapy Unit, King Fahd Medical Research Centre, KAU.

**Conflicts of Interest:** The authors declare no conflict of interest.

#### References

1. Mansoori, B.; Mohammadi, A.; Davudian, S.; Shirjang, S.; Baradaran, B. The different mechanism of Cancer drug resistance. A brief review. *Adv. Pharm. Bull.* **2017**, *7*, 339–348. [CrossRef] [PubMed]
2. Vasan, N.; Baselga, J.; Hyman, D.M. A view on drug resistance in cancer. *Nature* **2019**, *575*, 299–309. [CrossRef] [PubMed]
3. Housman, G.; Byler, S.; Heerboth, S.; Lapinska, K.; Longacre, M.; Snyder, N.; Sarkar, S. Drug resistance in cancer: An overview. *Cancers* **2014**, *6*, 769–1792. [CrossRef]

4. Hanahan, D.; Weinberg, R.A. Hallmarks of cancer: The next generation. *Cell* **2011**, *144*, 646–674. [CrossRef] [PubMed]
5. Li, X.Y.; Liang, J.W.; Mohamed, K.O.; Zhang, T.J.; Lu, G.Q.; Meng, F.H. Design, synthesis and biological evaluation of N-phenyl-(2,4- dihydroxypyrimidine-5-sulfonamido)benzoyl hydrazide derivatives as thymidylate synthase (TS) inhibitors and as potential antitumor drugs. *Eur. J. Med. Chem.* **2018**, *154*, 267–279. [CrossRef]
6. Carreras, C.W.; Santi, D.V. The catalytic mechanism and structure of thymidylate synthase. *Annu. Rev. Biochem.* **1995**, *64*, 721–762. [CrossRef]
7. Rode, W.; Les, A. Molecular mechanism of thymidylate synthase-catalyzed reaction and interaction of the enzyme with 2- and/or 4-substituted analogues of dUMP and 5-fluoro-dUMP. *Acta Biochim. Pol.* **1996**, *43*, 133–142. [CrossRef]
8. Hardy, L.W. Structural aspects of the inhibition and catalytic mechanism of thymidylate synthase. *Acta Biochim. Pol.* **1995**, *42*, 367–380. [CrossRef]
9. Kumar, V.P.; Cisneros, J.A.; Frey, K.M.; Castellanos-Gonzalez, A.; Wang, Y.; Gangjee, A.; White, A.C.; Jorgensen, W.L.; Anderson, K.S. Structural studies provide clues for analog design of specific inhibitors of *Cryptosporidium hominis* thymidylate synthase-dihydrofolate reductase. *Bioorg. Med. Chem. Lett.* **2014**, *24*, 4158–4161. [CrossRef]
10. Catalano, A.; Luciani, R.; Carocci, A.; Cortesi, D.; Pozzi, C.; Borsari, C.; Ferrari, S.; Mangani, S. X-ray crystal structures of *Enterococcus faecalis* thymidylate synthase with folate binding site inhibitors. *Eur. J. Med. Chem.* **2016**, *123*, 649–664. [CrossRef]
11. Houghton, J.A.; Tillman, D.M.; Harwood, F.G. Ratio of 2'-deoxyadenosine-5'-triphosphate/thymidine-5'-triphosphate influences the commitment of human colon carcinoma cells to thymineless death. *Clin. Cancer Res.* **1995**, *1*, 723–730. [PubMed]
12. Aherne, G.W.; Hardcastle, A.; Raynaud, F.; Jackman, A.L. Immunoreactive dUMP and TTP pools as an index of thymidylate synthase inhibition; effect of tomudex (ZD1694) and a non polyglutamated quinazoline antifolate (CB30900) in L1210 mouse leukaemia cells. *Biochem. Pharmacol.* **1996**, *51*, 1293–1301. [CrossRef]
13. Alvarez, P.; Marchal, J.A.; Boulaiz, H.; Carrillo, E.; Velez, C.; Rodríguez-Serrano, F.; Melguizo, C.; Prados, J.; Madeddu, R.; Aranega, A. 5-Fluorouracil derivatives: A patent review. *Expert Opin. Ther. Pat.* **2015**, *22*, 107–123. [CrossRef] [PubMed]
14. Santi, D.V.; McHenry, C.S.; Sommer, H. Mechanism of interaction of thymidylate synthetase with 5-fluorodeoxyuridylate. *Biochemistry* **1974**, *13*, 471–481. [CrossRef]
15. Pinheiro, S.; Pessoa, J.C.; Pinheiro, E.M.C.; Muri, E.M.F.; Greco, S.J. 2H-1,2,3-Triazole-chalcones as novel cytotoxic agents against prostate cancer. *Bioorg. Med. Chem. Lett.* **2020**, *30*, 127457–127463. [CrossRef]
16. Yan, L.; Yin, Z.; Niu, L.; Shao, J.; Chen, H.; Li, X. Synthesis of pentacyclic iminosugars with constrained butterfly-like conformation and their HIV-RT inhibitory activity. *Bioorg. Med. Chem. Lett.* **2018**, *28*, 425–428. [CrossRef]
17. Saeedi, M.; Mohammadi-Khanaposhtani, M.; Pourrabia, P.; Razzagi, N.; Ghadimi, R.; Imanparast, S.; Faramarzi, M.A.; Bandarian, F.; Esfahani, E.N.; Safavi, M.; et al. Design and synthesis of novel quinazolinone-1,2,3-triazole hybrids as new anti-diabetic agents: In vitro  $\alpha$ -glucosidase inhibition, kinetic, and docking study. *Bioorg Chem.* **2019**, *83*, 161–169. [CrossRef]
18. Bi, F.; Ji, S.; Venter, H.; Liu, J.; Semple, S.J.; Ma, S. Substitution of terminal amide with 1H-1,2,3-triazole: Identification of unexpected class of potent antibacterial agents. *Bioorg. Med. Chem. Lett.* **2018**, *28*, 884–891. [CrossRef]
19. Moussa, G.; Alaaeddine, R.; Alaaeddine, L.M.; Nasra, R.; Belal, A.S.F.; Ismail, A.; El-Yazbi, A.F.; Abdel-Ghany, Y.S.; Hazza, A. Novel click modifiable thioquinazolinones as anti-inflammatory agents: Design, synthesis, biological evaluation and docking study. *Eur. J. Med. Chem.* **2018**, *144*, 635–650. [CrossRef]
20. Yan, X.; Lv, Z.; Wen, J.; Zhao, S.; Xu, Z. Synthesis and in vitro evaluation of novel substituted isatin-propylene-1H-1,2,3-triazole-4- methylene-moxifloxacin hybrids for their anti-mycobacterial activities. *Eur. J. Med. Chem.* **2018**, *143*, 899–904. [CrossRef]
21. Lu, G.Q.; Li, X.Y.; Mohamed, O.K.; Wang, D.; Meng, F.H. Design, synthesis and biological evaluation of novel uracil derivatives bearing 1, 2, 3-triazole moiety as thymidylate synthase (TS) inhibitors and as potential antitumor drugs. *Eur. J. Med. Chem.* **2019**, *171*, 282–296. [CrossRef] [PubMed]

22. Baraniak, D.; Baranowski, D.; Ruszkowski, P.; Boryski, J. Nucleoside dimmers analogues with a 1,2,3-triazole linkage: Conjugation of floxuridine and thymidine provides novel tools for cancer treatment. *Nucleosides Nucleotides Nucleic Acids* **2019**, *38*, 807–835. [CrossRef] [PubMed]
23. Onen, F.E.; Boum, Y.; Jacquement, C.; Spanedda, M.V.; Jaber, N.; Scherman, D.; Myllykallio, H.; Herscovici, J. Design, synthesis and evaluation of potent thymidylate synthase X inhibitors. *Bioorg. Med. Chem. Lett.* **2008**, *18*, 3628–3631. [CrossRef] [PubMed]
24. Shen, W.; Xi, H.; Li, C.; Bian, S.; Cheng, H.; Cui, J.; Wang, N.; Wei, B.; Huang, X.; Chen, L. Endothelin-A receptor in gastric cancer and enhanced antitumor activity of trastuzumab in combination with the endothelin-A receptor antagonist ZD4054. *Ann. N.Y. Acad. Sci.* **2019**, *1448*, 30–41. [CrossRef]
25. Du, Q.R.; Li, D.D.; Pi, Y.Z.; Li, J.R.; Sun, J.; Fang, F.; Zhong, W.Q.; Gong, H.B.; Zhu, H.L. Novel 1,3,4-oxadiazole thioether derivatives targeting thymidylate synthase as dual anticancer/antimicrobial agents. *Bioorg. Med. Chem.* **2013**, *21*, 2286–2297. [CrossRef] [PubMed]
26. Li, X.; Wang, D.; Lu, G.; Lu, K.; Zhang, T.; Li, S.; Mohamed, K.O.; Xue, W.; Qian, X.; Meng, F. Development of a novel thymidylate synthase (TS) inhibitor capable of up-regulating P53 expression and inhibition angiogenesis in NSCLC. *J. Adv. Res.* **2020**, *26*, 95–110. [CrossRef]
27. Alzhrani, Z.M.M.; Alam, M.M.; Neamatallah, T.; Nazreen, S. Design, synthesis and in vitro antiproliferative activity of new thiazolidinedione-1,3,4-oxadiazole hybrids as thymidylate synthase inhibitors. *J. Enzyme Inhib. Med. Chem.* **2020**, *35*, 1116–1123. [CrossRef]
28. Jha, K.K.; Samad, A.; Kumar, Y.; Shaharyar, M.; Khosa, R.L.; Jain, J.; Kumar, V.; Singh, P. Design, synthesis and biological evaluation of 1,3,4-oxadiazole derivatives. *Eur. J. Med. Chem.* **2010**, *45*, 4963–4967. [CrossRef]
29. Lipinski, C.A.; Lombardo, F.; Dominy, B.W.; Freener, P.J. Experimental and computational approaches to estimate solubility and permeability in drug discovery and development settings. *Adv. Drug Deliv. Rev.* **2001**, *46*, 3–26. [CrossRef]
30. Veber, D.F.; Johnson, S.R.; Cheng, H.Y.; Smith, B.R.; Ward, K.W.; Kopple, K.D. Molecular properties that influence the oral bioavailability of drug candidates. *J. Med. Chem.* **2002**, *45*, 2615–2623. [CrossRef]
31. Lamia, H.T.A.; Taghreed, Z.S.; Abeer, M.N. Design, synthesis, anticancer evaluation and docking studies of new pyrimidine derivatives as potent thymidylate synthase inhibitors. *Bioorg. Chem.* **2019**, *9*, 103159–103173.
32. Ahmed, F.E.; Qasem, M.A.A.; Emad, S.I.H. Design, synthesis, molecular docking of new thiopyrimidine-5-carbonitrile derivatives and their cytotoxic activity against HepG2 cell line. *J. Appl. Pharm. Sci.* **2014**, *4*, 102–111.
33. Meerloo, J.V.; Kaspers, G.J.L.; Cloos, J. Cell sensitivity assays. *Methods Mol. Biol.* **2011**, *731*, 237–245. [PubMed]
34. Wahba, A.J.; Friedkin, M. The enzymatic synthesis of thymidylate: I. early steps in the purification of thymidylate synthetase of Escherichia coli. *J. Biol. Chem.* **1962**, *237*, 3794–3801.
35. Davisson, V.J.; Sirawaraporn, W.; Santi, D.V. Expression of human thymidylate synthase in Escherichia coli. *J. Biol. Chem.* **1989**, *264*, 9145–9148.
36. Nazreen, S.; Alam, M.S.; Hamid, H.; Yar, M.S.; Shafi, S.; Dhulap, A.; Alam, P.; Pasha, M.A.Q.; Bano, S.; Alam, M.M.; et al. Design, synthesis, in silico molecular docking and biological evaluation of novel oxadiazole based thiazolidine-2,4-diones bis-heterocycles as PPAR- $\gamma$  agonists. *Eur. J. Med. Chem.* **2014**, *87*, 175–185. [CrossRef]

**Publisher's Note:** MDPI stays neutral with regard to jurisdictional claims in published maps and institutional affiliations.



© 2020 by the authors. Licensee MDPI, Basel, Switzerland. This article is an open access article distributed under the terms and conditions of the Creative Commons Attribution (CC BY) license (<http://creativecommons.org/licenses/by/4.0/>).





## Article

# Design, Synthesis, and Molecular Docking Study of New Tyrosyl-DNA Phosphodiesterase 1 (TDP1) Inhibitors Combining Resin Acids and Adamantane Moieties

Kseniya Kovaleva <sup>1</sup>, Olga Yarovaya <sup>1,2,\*</sup>, Konstantin Ponomarev <sup>1</sup>, Sergey Cheresiz <sup>2</sup>, Amirhossein Azimirad <sup>2</sup>, Irina Chernyshova <sup>2</sup>, Alexandra Zakharenko <sup>3</sup>, Vasily Konev <sup>4</sup>, Tatiana Khlebnikova <sup>4</sup>, Evgenii Mozhaytsev <sup>1</sup>, Evgenii Suslov <sup>1</sup>, Dmitry Nilov <sup>5</sup>, Vytas Švedas <sup>5,6</sup>, Andrey Pokrovsky <sup>2</sup>, Olga Lavrik <sup>2,3</sup> and Nariman Salakhutdinov <sup>1</sup>

<sup>1</sup> N. N. Vorozhtsov Novosibirsk Institute of Organic Chemistry, Siberian Branch of the Russian Academy of Sciences, Lavrentiev Ave. 9, 630090 Novosibirsk, Russia; kseniya.kovaleva3103@yandex.ru (K.K.); ponomarev@nioch.nsc.ru (K.P.); mozh@nioch.nsc.ru (E.M.); suslov@nioch.nsc.ru (E.S.); anvar@nioch.nsc.ru (N.S.)

<sup>2</sup> V. Zelman Institute for the Medicine and Psychology, Novosibirsk State University, Pirogova St. 1, 630090 Novosibirsk, Russia; cheresiz@yandex.ru (S.C.); azimirad@mail.ru (A.A.); chernyshova0305@gmail.com (I.C.); agpok@inbox.ru (A.P.); lavrik@nioch.nsc.ru (O.L.)

<sup>3</sup> Novosibirsk Institute of Chemical Biology and Fundamental Medicine, Siberian Branch of the Russian Academy of Sciences, Lavrentiev Ave. 8, 630090 Novosibirsk, Russia; a.zakharenko73@gmail.com

<sup>4</sup> Borekov Institute of Catalysis, Siberian Branch of the Russian Academy of Sciences, Lavrentiev Ave. 5, 630090 Novosibirsk, Russia; konvasnik@gmail.com (V.K.); khleb@catalysis.nsk.su (T.K.)

<sup>5</sup> Belozersky Institute of Physicochemical Biology, Lomonosov Moscow State University, Lenin Hills 1, Bldg. 40, 119991 Moscow, Russia; nilovdm@gmail.com (D.N.); vyta@belozersky.msu.ru (V.Š.)

<sup>6</sup> Faculty of Bioengineering and Bioinformatics, Lomonosov Moscow State University, Lenin Hills 1, Bldg. 73, 119991 Moscow, Russia

\* Correspondence: ooo@nioch.nsc.ru

**Citation:** Kovaleva, K.; Yarovaya, O.; Ponomarev, K.; Cheresiz, S.; Azimirad, A.; Chernyshova, I.; Zakharenko, A.; Konev, V.; Khlebnikova, T.; Mozhaytsev, E.; et al. Design, Synthesis, and Molecular Docking Study of New Tyrosyl-DNA Phosphodiesterase 1 (TDP1) Inhibitors Combining Resin Acids and Adamantane Moieties. *Pharmaceuticals* **2021**, *14*, 422. <https://doi.org/10.3390/ph14050422>

Academic Editors: Mary Meegan and Niamh M O'Boyle

Received: 26 March 2021

Accepted: 23 April 2021

Published: 1 May 2021

**Publisher's Note:** MDPI stays neutral with regard to jurisdictional claims in published maps and institutional affiliations.



**Copyright:** © 2021 by the authors. Licensee MDPI, Basel, Switzerland. This article is an open access article distributed under the terms and conditions of the Creative Commons Attribution (CC BY) license (<https://creativecommons.org/licenses/by/4.0/>).

**Abstract:** In this paper, a series of novel abietyl and dehydroabietyl ureas, thioureas, amides, and thioamides bearing adamantane moieties were designed, synthesized, and evaluated for their inhibitory activities against tyrosyl-DNA-phosphodiesterase 1 (TDP1). The synthesized compounds were able to inhibit TDP1 at micromolar concentrations (0.19–2.3  $\mu$ M) and demonstrated low cytotoxicity in the T98G glioma cell line. The effect of the terpene fragment, the linker structure, and the adamantane residue on the biological properties of the new compounds was investigated. Based on molecular docking results, we suppose that adamantane derivatives of resin acids bind to the TDP1 covalent intermediate, forming a hydrogen bond with Ser463 and hydrophobic contacts with the Phe259 and Trp590 residues and the oligonucleotide fragment of the substrate.

**Keywords:** tyrosyl-DNA-phosphodiesterase 1; adamantane; resin acid; TDP1

## 1. Introduction

DNA in living organisms is constantly exposed to a variety of physical and chemical stresses, and damage occurs as a result. Bulk DNA damage is caused by UV light and environmental mutagens, and X-rays cause DNA double-strand breaks. Defects in the repair of DNA damage are implicated in a variety of diseases, many of which are typified by neurological dysfunction and/or increased genetic instability and cancer [1]. Traditional cancer chemotherapy is aimed at damaging the DNA of malignant cells, and the results depend on the effectiveness of their repair systems. Recently, compounds that act as DNA repair inhibitors have been considered as potential drugs [2,3]. The enzyme tyrosyl-DNA-phosphodiesterase 1 (TDP1) is one of the promising ones [4]. This enzyme is an important supplementary target for anticancer therapies based on topoisomerase

inhibitors 1 (TOP1), since it plays a key role in the removal of TOP1-DNA adducts stabilized by TOP1 inhibitors such as camptothecin [5] and its clinical derivatives [6]. TDP1 is also capable of hydrolysing apurinic sites, and thus leading to their repair. This may be the key activity needed for the repair of DNA damage caused by antitumour alkylating drugs such as temozolomide (TMZ), as well as ionising radiation [7]. Thus, the inhibition of TDP1 activity may significantly enhance the therapeutic effect of some anticancer agents. SCAN1 is a natural mutant of TDP1 where His493 is replaced with Arg493 in the binding pocket [8]. The mutation changes the geometry of the enzyme active site, and the enzyme remains covalently bound to DNA. This mutation leads to a severe neurodegenerative disease spinocerebellar ataxia syndrome with axonal neuropathy (SCAN1). It is currently suggested that the pathology is caused by the accumulation of the SCAN1-DNA covalent cleavage complexes [9]. It is assumed that nerve cells especially suffer from the accumulation of such adducts due to their nonproliferative nature leading to the progressive accumulation of unrepaired DNA lesions [10]. Therefore, suppression of SCAN1 activity could potentially improve the SCAN1 patients' condition and prevent the progression of the disease. The search for inhibitors of key DNA repair enzymes is a promising area of medical chemistry, as it represents one of the ways to design effective therapies for cancer, as well as cardiovascular and neurodegenerative diseases. Recently, a number of TDP1 inhibitor structural classes have been studied, including pyrimidine nucleosides [11], furamidine [12], compounds with benzopentathiepine moiety [13], indenoisoquinolines [14], and 5-arylidene-thioxothiazolidinones [15] (Figure 1).

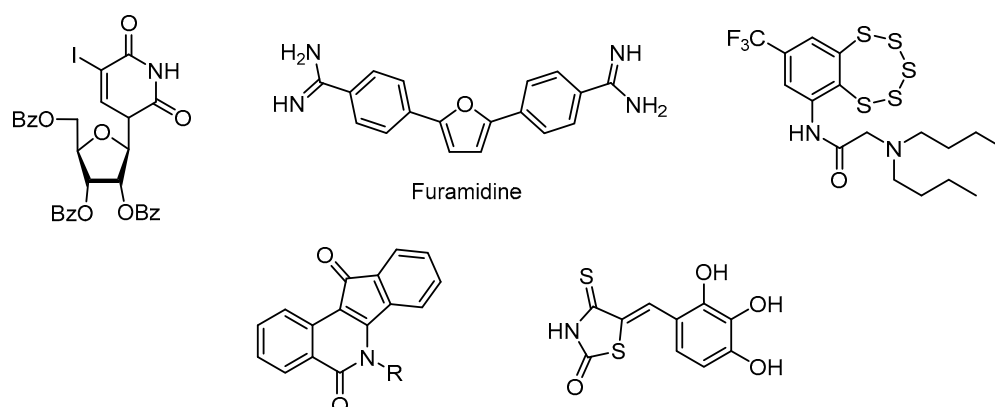


**Figure 1.** Structures of known TDP1 inhibitors.

Hybrid molecules created from different pharmacophores of natural and synthetic equivalents are successfully used in pharmaceutical practice [16]. New hybrid compounds have been synthesised starting from the pharmacophoric natural compounds with inhibitory properties against TDP1. These include phenolic usnic acid derivatives A [17], 7-hydroxycoumarins B [18], and 4-arylcoumarins C [19], derivatives of deoxycholic acid D [20] and adamantanecarboxylic acid monoterpene esters E [21] (Figure 2).

Our group previously obtained a set of ureas and thioureas based on the natural terpenoid dehydroabietylamine [22]. These compounds are able to inhibit TDP1 in the submicromolar range. They also lack toxicity against different cell lines in concentrations up to 100  $\mu$ M. For the first time, we have shown that dehydroabietylamine TDP1 inhibitors in combination with TMZ demonstrate a better cytotoxic effect on glioblastoma cells than TMZ alone, taken at the same concentration. Compound 1 (Figure 3), which has a fragment of resin acid and adamantane, was an efficient inhibitor of TDP1 activity *in vitro*, and enhanced the cytotoxic effect of TMZ on glioblastoma cells. We synthesised a series of dehydroabietylamine derivatives containing the heterocyclic fragment 2-thioxoimidazolidin-4-ones and studied their activity against TDP1 [23]. It is important to note that not all of the synthesized heterocyclic derivatives are suitable for studying inhibitory activity, as some of the substances proved to be extremely insoluble. In addition,

the combination of an adamantane fragment with terpenes of various structures has been shown to be successful in identifying new inhibitors of the TDP1 repair enzyme [23–27]. Since the combination of a terpene resin acid backbone with an adamantane fragment in compound **1** proved to be most successful and the compound had the most important biological properties, we set out in the present study to synthesise analogues of compound **1** to examine their structural activity. The design of the target derivatives is shown in Figure 3. It includes the variations of the linker type and length, diterpene, and adamantane moieties. Understanding which structural blocks are most important for the target biological activity and whether more active agents can be obtained by available synthetic methods is the main goal of the presented work.

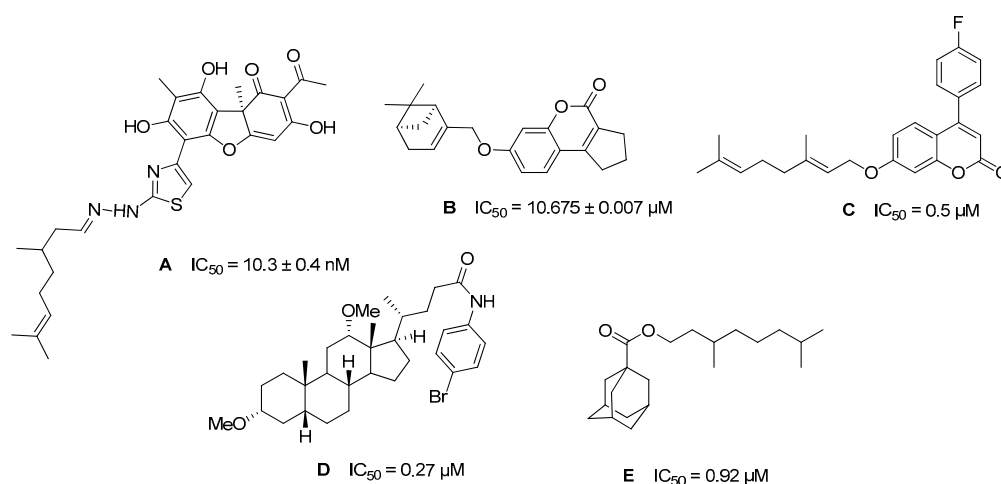


**Figure 2.** Structures of natural-based TDP1 inhibitors and their  $IC_{50}$  values.

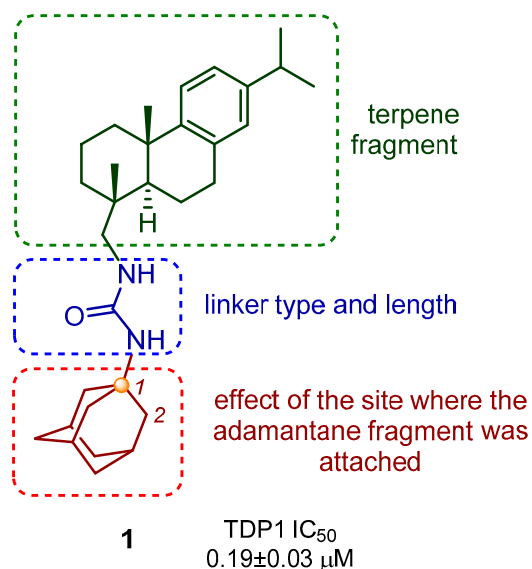


**Figure 3.** Design strategy for new abietylamine-based compounds.

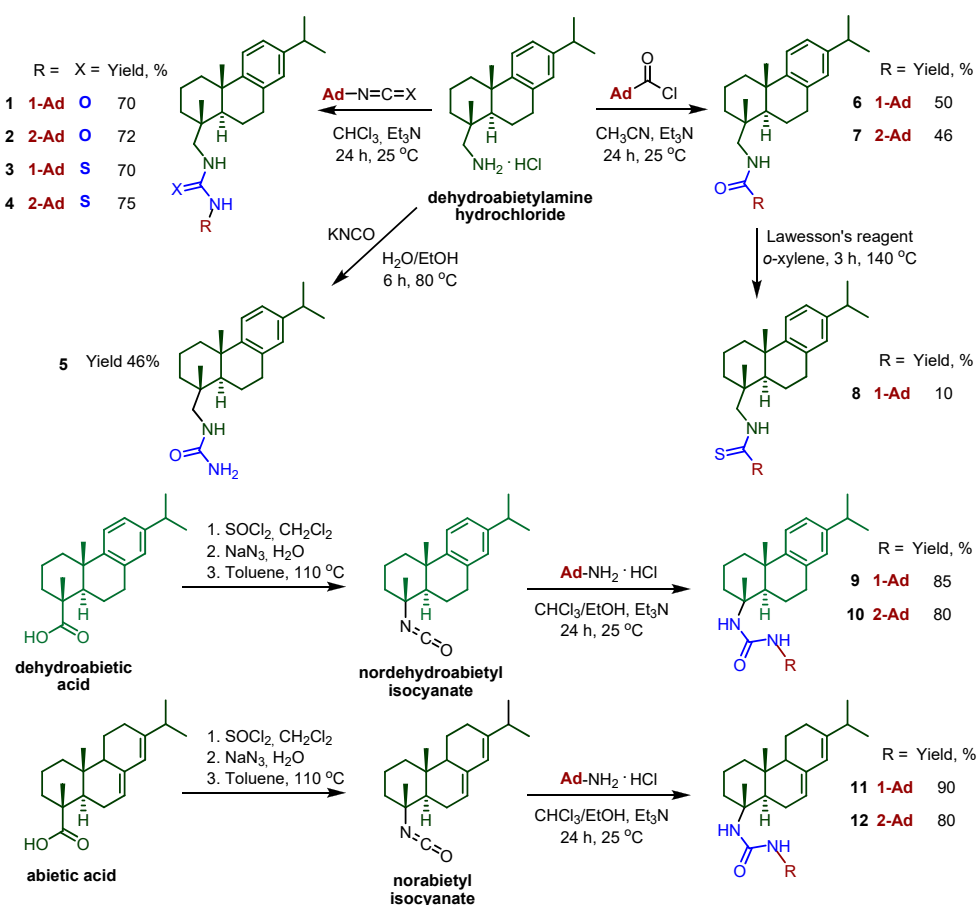
## 2. Results and Discussion

### 2.1. Chemistry

Dehydroabietylamine (DHAm) is a diterpenic primary amine obtained from dehydroabietic acid (DHA). Dehydroabietic and abietic acids are components of resins of coniferous plants; for example, the high acid content is found in the resin of *Picea obovata* [27]. Dehydroabietylamine can be directly obtained from the resin by the reduction of dehydroabietyl nitrile.



The synthetic route for obtaining compounds 1–12 is shown in Scheme 1. A set of ureas and thioureas 1–4 was obtained by the interaction of dehydroabietylamine hydrochloride with 1- and 2- adamantyl isocyanates and isothiocyanates. The starting isocyanates and isothiocyanates were synthesized using the methods described earlier. In particular, 1-adamantyl isocyanate was obtained by the Curtius rearrangement of 1-adamantyl acyl azide formed in situ by interaction of corresponding acyl chloride with sodium azide [28]. Isomeric 2-adamantyl isocyanate was synthesized by the reaction of 2-adamantylamine hydrochloride with triphosgene in the presence of sodium hydrocarbonate, with dichloromethane used as a solvent [29]. Refluxing of 1-adamantaneamine with phenyl isothiocyanate in dry toluene resulted in 1-adamantane isothiocyanate [30]. To obtain 2-adamantyl isothiocyanate, 2-adamantaneamine hydrochloride was treated by triethylamine followed by carbon disulfide and DMAP/Boc<sub>2</sub>O subsequently [31]. For the present study, we re-synthesised compound 1, which previously showed the best inhibitory characteristics and the ability to enhance the cytostatic properties of TMZ. Mono-substituted urea 5 was prepared by treating dehydroabietylamine hydrochloride with potassium cyanate. Amide and thioamide groups were considered as another variant of linker structurally similar to the ureas. The target amides 6 and 7 were obtained from dehydroabietylamine hydrochloride and 1- and 2-adamantanecarbonyl chlorides. The amide group of compound 6 was converted to thioamide using Lawesson's reagent. The reaction proceeded under harsh conditions. Refluxing in toluene led to the formation of thioamide 8. Compound 8 was isolated individually with a small yield. When the reaction was carried out in lower boiling solvents, the target product was not detected, even after a long period.



Scheme 1. General procedure for the synthesis of compounds 1–12.

To obtain the target compounds **9–12**, starting with the dehydroabietic and abietic acids, the following synthetic route was taken. Following the three-step procedure described previously [32], nordehydroabietyl and norabietyl isocyanates were prepared. According to this method, treatment of the resin acids with  $\text{SOCl}_2$  afforded the corresponding chlorides, which were then converted to azides by interaction with  $\text{NaN}_3$ . The azides underwent Curtius rearrangement by refluxing in toluene, resulting in decarboxylation and the formation of the corresponding isocyanates. Reaction of the obtained resin acid isocyanates with 1- and 2-adamantylamine hydrochlorides in the presence of a base provided good yields of the ureas **9–12** (80–90%).

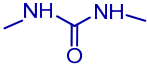
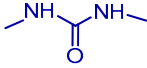
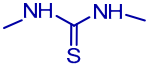
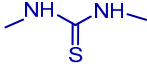
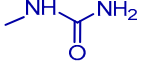
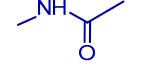
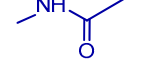
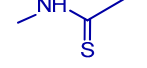
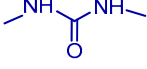
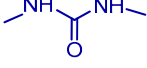
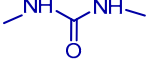
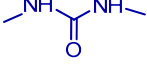
As a result of this work, compounds **2–12** (Scheme 1) were synthesised and characterized using physico-chemical methods. The ureas **1** and **2** (and thioureas **3** and **4**) differed from one another by the position of the adamantane fragment (1 and 2 respectively). Monosubstituted urea **5**, without the adamantane fragment in its structure, was prepared to clarify the contribution of this moiety to the studied compounds. Substances **6–8** have linkers of a different type. Ureas **9–10** differed from the leading compound **1** by lacking a  $\text{CH}_2$  group in the linker, while ureas **11–12**, in addition to the above, differed in the terpene part.

## 2.2. TDP1 Assay and Cytotoxicity Studies

The primary screening of the inhibitory activities against TDP1 was performed using an in vitro cell-free system involving the recombinant TDP1 and a fluorescent reporter probe as previously described [13]. The  $\text{IC}_{50}$  values were found for derivatives **2–12** (and are presented in Table 1), a commercially available TDP inhibitor Furamidine was used as a reference drug [12]. We show here that the obtained compounds have the capacity to inhibit TDP1 in vitro within a 0.19–2.3  $\mu\text{M}$  range. As can be seen from the data in the table, only compound **5**—monosubstituted urea (lacking the adamantane moiety)—showed no activity against TDP1.

All the compounds with the exception of **5** were able to inhibit TDP1 at micromolar concentrations (0.19–2.3  $\mu\text{M}$ ). We studied the structure–activity relationship for a number of the compounds synthesized. After considering the effect of the diterpene fragment on the inhibitory characteristics, we conclude that ureas with dehydroabietyl **1–2** and nordehydroabietyl **9–10** backbone work in lower concentrations than with norabietyl **11–12**. For ureas **1–2** and **9–10**, the  $\text{IC}_{50}$  values were in the 0.19–0.8  $\mu\text{M}$  range, and for ureas **11–12**, the  $\text{IC}_{50}$  values were higher—1.4–1.7  $\mu\text{M}$ . However, ureas **9–12**, lacking a  $\text{CH}_2$  group in the terpene part, demonstrated extremely low solubility in water and almost all organic solvents, which does not make them promising for further study. The choice of 1-adamantane or 2-adamantane substituent did not significantly affect the inhibitory characteristics, but their absence negatively affected them. Monosubstituted urea **5** (without any bulky fragment) showed no activity at concentrations up to 15  $\mu\text{M}$ . In a previous study [22], we showed that a decrease in the size of the substituent led to a decrease in activity, and the data obtain herein consistent with this. Among the compounds belonging to the urea, thiourea, amide, and thioamide classes, compound **8** with the thioamide linker inhibited TDP1 in the highest concentrations ( $\text{IC}_{50} = 2.3 \mu\text{M}$ ).

**Table 1.** Inhibitory activity of compounds 1–12 against TDP1 and predicted LogP (main determinant of brain tissue binding).

Compound	terpene fragment	linker type	adamantane fragment	IC <sub>50</sub> (TDP1), μM	LogP
1	DGAAm		1-Ad	0.19 ± 0.03	7.50
2	DGAAm		2-Ad	0.80 ± 0.20	7.31
3	DGAAm		1-Ad	1.50 ± 0.50	7.60
4	DGAAm		2-Ad	0.67 ± 0.19	7.38
5	DGAAm		-	>15	5.45
6	DGAAm		1-Ad	0.94 ± 0.18	7.48
7	DGAAm		2-Ad	1.80 ± 0.40	7.34
8	DGAAm		1-Ad	2.30 ± 0.80	8.28
9	nor-DGAA		1-Ad	0.57 ± 0.16	7.19
10	nor-DGAA		2-Ad	0.59 ± 0.15	7.27
11	nor-AA		1-Ad	1.70 ± 0.60	6.72
12	nor-AA		2-Ad	1.40 ± 0.30	6.30
Furamidine	-	-	-	1.20 ± 0.30	-

IC<sub>50</sub>: 50% inhibiting concentration.

QSAR prediction methods offer a useful tool to identify drug-like compounds [33,34], and therefore we have calculated LogP values for synthesized inhibitors as main determinant of brain tissue binding. Octanol/water LogP predicted with GALAS algorithm [35] and QSAR software ACD/Percepta ([www.acdlabs.com](http://www.acdlabs.com) accessed on 29 April 2021) indicate that the obtained adamantane derivatives have similar lipophilicity (Table 1). The corresponding rate of brain penetration LogPS and extent of brain penetration LogBB, calculated using LogP, molecular size, and H-bonding parameters as inputs, are suitable for penetration into the central nervous system (see Table S1).

Since dehydroabietylamine and its derivatives are known to possess high cytotoxicity against several cancer cells lines [36–38], the ureas, thioureas, amides, and thioamide (1–12) synthesised in the present study were tested against the T98G glioma cells. Since we used the T98G glioblastoma cell line for the first time for our experiments, we first attempted to perform the cytotoxicity study in a range of concentrations from 10 to 100 μM, as we did previously with the TDP1 inhibitory compounds when working with the other cell lines. However, the cytotoxicity at 50 and 100 μM of our compounds turned out to be rather high in the T98G cell line. We then measured the cytotoxicity of individual TDP1 inhibitors at 2.5, 5, 10, and 25 μM. The studied compounds were prepared as 50 mM stock solutions in DMSO

and added to T98G glioma cells at 2.5  $\mu\text{M}$  to 25  $\mu\text{M}$  concentrations, either individually or in combination with 1000 or 2000  $\mu\text{M}$  of TMZ. Preparation of stock solutions showed that the studied compounds varied in their solubility in DMSO. Compounds 9, 10, 11, and 12 failed to dissolve either at 50  $\mu\text{M}$  or at 10  $\mu\text{M}$  concentrations. They were therefore discarded from the later cytotoxicity studies.

When individual compounds were added to T98G glioma cells at 2.5, 5, 10, and 25  $\mu\text{M}$  concentrations, they demonstrated moderate toxicity. The cell viabilities at 2.5 and 5  $\mu\text{M}$  lay within the 90–100% range (Figure 4).

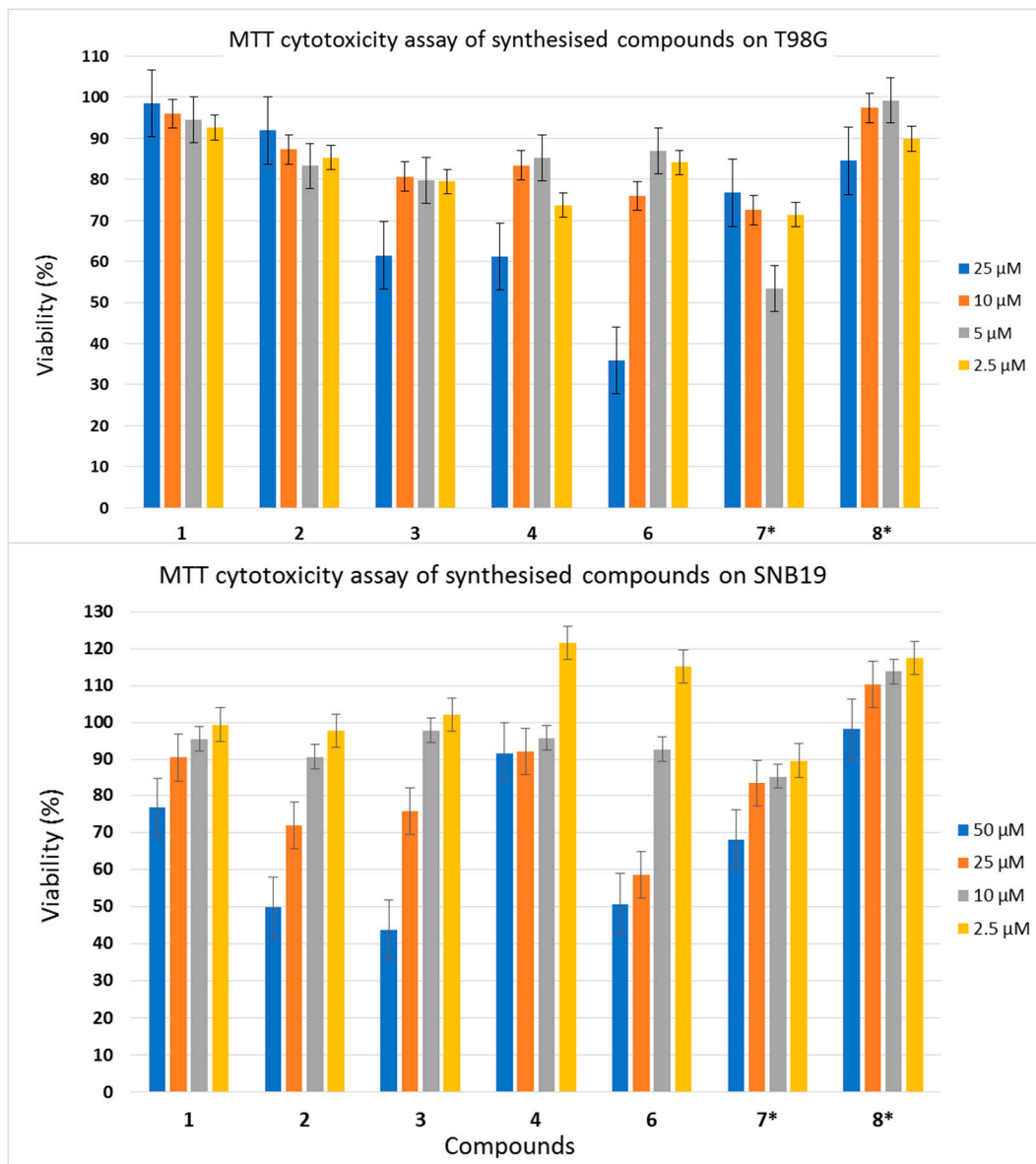


**Figure 4.** Individual cytotoxicity of studied compounds in the T98G and SNB19 glioma cell lines. \* Compounds 7 and 8 formed visible micelles when stock solutions were dissolved in a cell growth medium, as shown by light microscopy. The cytotoxicity of these compounds was studied; however, the concentrations of their solutions may be significantly different from those indicated in dilutions.

To investigate the cytotoxicity of combinations of the studied compounds with TMZ, we combined 5  $\mu\text{M}$  concentrations of each with 1000  $\mu\text{M}$  or 2000  $\mu\text{M}$  of TMZ and compared their toxicity with 1000  $\mu\text{M}$  and 2000  $\mu\text{M}$  of TMZ alone. At 1000  $\mu\text{M}$ , TMZ was almost non-toxic to our cell culture, with ~95% of cells surviving the treatment. Adding 5  $\mu\text{M}$  of

the compounds to 1000  $\mu\text{M}$  of TMZ did not increase the cytotoxicity to the glioma cells. Higher cytotoxicity was obtained with 2000  $\mu\text{M}$  of TMZ, which inhibited cell viability by  $\sim 40\%$ . Combining the compounds with 2000  $\mu\text{M}$  of TMZ resulted in considerably higher toxicity (i.e., an increase of 5–15%) compared with TMZ alone, which indicated the additive profile of the action of TDP1 inhibitors with TMZ. The effects of combinations of dehydroabietylamine derivatives 1–4 and 6–8 with TMZ on T98G viability are shown in Figure 5.

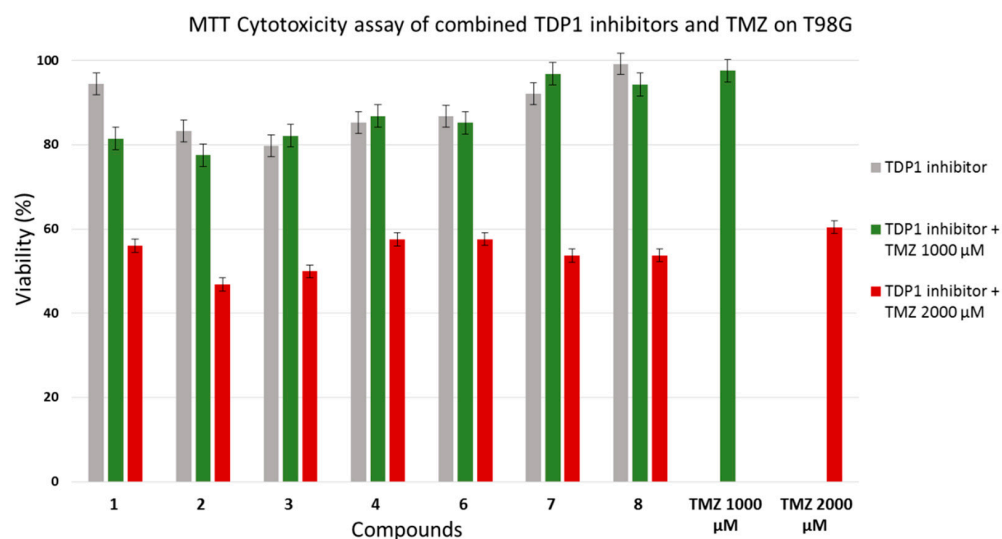


**Figure 5.** Cytotoxicities of combinations of studied compounds with temozolomide in T98G glioma cell line.

### 2.3. Molecular Docking Studies

The reaction catalyzed by TDP1 proceeds in two steps: the nucleophile His263 residue attacks the 3'-phosphotyrosyl bond of the substrate, and the His493 residue activates the water molecule to cleave the covalent intermediate [39–41]. This offers two potential therapeutic strategies: (1) the inhibition of the first step to prevent the formation of the 3'-phosphohistidine intermediate; and (2) the inhibition of the second step to prevent the intermediate hydrolysis [4,42]. Using molecular docking, we tested the discussed resin acid derivatives against both the molecular model of the apo form and that of the covalent intermediate. The inhibitors were found to bind preferentially to the intermediate structure, as demonstrated in Figure 6.

A resin acid fragment occupies part of the peptide binding site—peptide is released upon the intermediate formation—and forms hydrophobic contacts with the side chain of Trp590. An adamantane fragment interacts with both the Phe259 residue of the oligonucleotide binding site and with methylene (ribose) and the methyl (nucleobase) groups of the oligonucleotide. A carbamide linker forms a hydrogen bond with the Ser463 side chain, whilst its NH groups are orientated towards the solvent.

We conclude that adamantane derivatives of resin acids stabilize the TDP1 intermediate (covalent complex of TDP1 with DNA) in a manner that is analogous with the stabilisation of topoisomerase–DNA covalent complexes by camptothecins [43,44]. It is worth noting that compound 5, which lacked the adamantane fragment, failed to inhibit TDP1. Using our proposed model, this can be explained as follows: monosubstituted urea has an additional hydrogen bond donor, the  $-\text{NH}_2$  group, which is orientated towards a hydrophobic adamantane-binding region. This may result in the unfavourable interaction of compound 5 with the TDP1 intermediate.

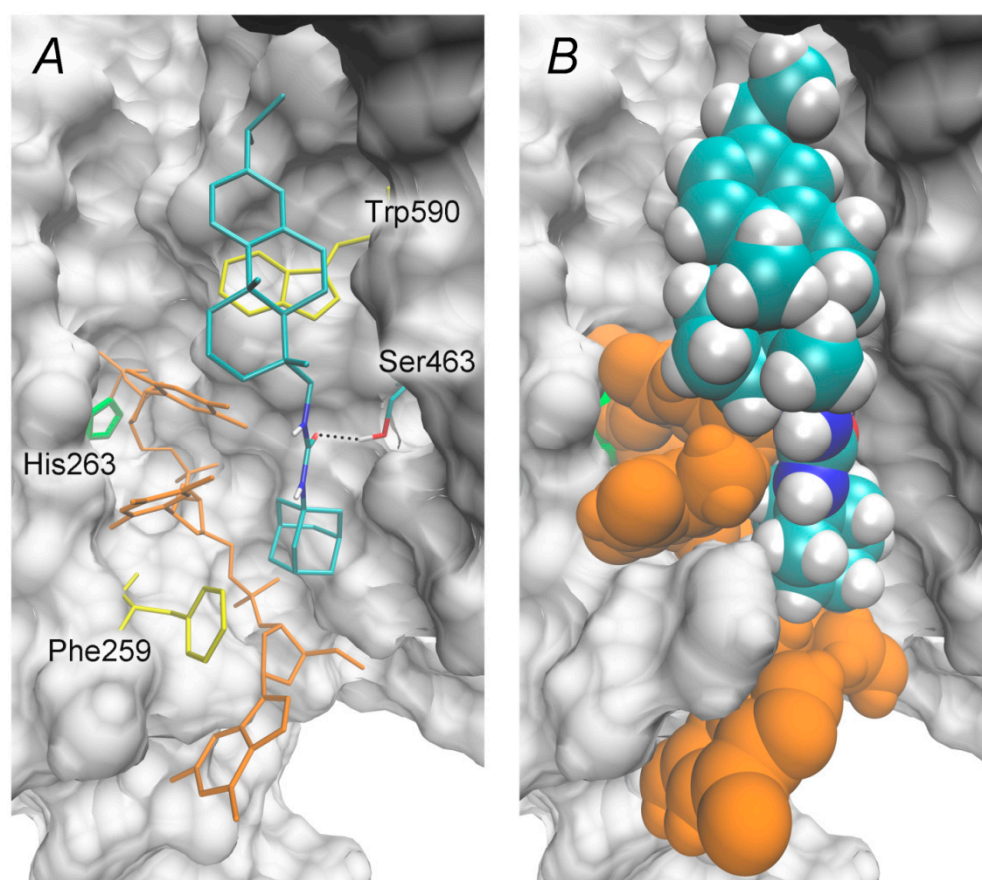


**Figure 6.** Position of the resin acid derivative **1** in the molecular model of human TDP1 intermediate,  $\Delta G^{\text{calc}} = -9.0$  kcal/mol. (A) Inhibitor's interactions with a covalently bound DNA fragment and TDP1 residues. The oligonucleotide is shown in orange, His263 in green, and hydrophobic Phe259 and Trp590 in yellow. The dotted line indicates a hydrogen bond. (B) Van der Waal's representation of the modeled TDP1–inhibitor complex.

### 3. Materials and Methods

#### 3.1. Chemistry

All reagents and solvents were purchased from commercial sources and were used as received without further purification. Reactions were monitored by thin-layer chromatography (TLC) in silica gel. The TLC plates were visualised by exposure to ultraviolet light (254 and 365 nm). Merck (Merck KGaA, Darmstadt, Germany) silica gel (63–200  $\mu\text{m}$ ) was used for column chromatography. The  $^1\text{H}$  and  $^{13}\text{C}$  NMR spectra in  $\text{CDCl}_3$ ,  $\text{CD}_3\text{OD}$ , and  $\text{DMSO-}d_6$  were recorded on a Bruker AV-400 spectrometer (400.13 and 100.61 MHz, respectively, Bruker, Billerica, MA, USA). The residual signals of the solvent were used as references ( $\delta\text{H}$  7.24,  $\delta\text{C}$  76.90 for  $\text{CDCl}_3$ ;  $\delta\text{H}$  2.50,  $\delta\text{C}$  39.50 for  $\text{DMSO-}d_6$ ). High-resolution mass spectra were recorded on a Thermo Scientific DFS instrument (Thermo Fisher Scientific Inc., Waltham, MA, USA) in full scan mode over the  $m/z$  range of 0–500 by ionisation with an electron impact of 70 eV, and direct introduction of samples. IR spectra were recorded on a Vector22 spectrometer (KBr, Bruker, Billerica, MA, USA). Thin-layer chromatography was performed on Silufol plates (UV-254, Merck KGaA, Darmstadt, Germany). The atomic numbering in the compounds is provided for the assignment of signals in the NMR spectra and is different from the atomic numbering in the systematic name. The analytical and spectroscopic studies were conducted at the Chemical Service Center for the collective use of the Siberian Branch of the Russian Academy of Sciences (SB RAS).

## 3.1.1. General Procedure for the Synthesis of Ureas and Thioureas 1–4

Dehydroabietylamine hydrochloride (0.5 g, 1.55 mmol) and triethylamine (0.28 mL, 2.0 mmol) were dissolved in  $\text{CHCl}_3$  (25 mL) and an equimolar amount of the appropriate adamantyl isocyanate or isothiocyanate was added. The reaction mixture was stirred on a magnetic stirrer for 24 h at room temperature. Conversion was monitored by TLC. The reaction mixture was washed with 10 mL of distilled water. The organic layer was dried over anhydrous  $\text{Na}_2\text{SO}_4$  and filtered. The resultant liquid was evaporated under vacuum. The residue was purified using column chromatography on silica gel with  $\text{CHCl}_3$  as an eluent and a MeOH gradient from 0 to 100%.

**N-abieta-8,11,13-trien-18-yl-N'-1-adamantylurea (1).** The spectral data for the compound **1** has been described previously [22].

**N-abieta-8,11,13-trien-18-yl-N'-2-adamantylurea (2).** Yield 72%, white powder. M.p. 150 °C. IR (KBr)  $\nu_{\text{max}}$  3361, 2908, 1629, 1562  $\text{cm}^{-1}$ .  $^1\text{H}$  NMR (400MHz,  $\text{CDCl}_3$ ,  $\delta$ , ppm, J/Hz): 6.86 (1H, s, H-14), 6.96 (1H, d,  $J_{11,12} = 8.2$ , H-12), 7.14 (1H, d,  $J_{11,12} = 8.2$ , H-11), 5.06 and 5.26 (1H both, s, NH), 0.87 (3H, s, Me-19), 1.20 (6H, d,  $J_{16,15} = 6.9$ , Me-16 and Me-17), 1.18 (3H, s, Me-20), 2.80 (1H, sept,  $J_{15,16} = 6.9$ , H-15), 2.82–2.95 (2H, m, 2H-7), 2.24 (1H, d,  $^2J = 12.3$ , H-1e), 3.72–3.83 (1H, m, H-23), 2.95–3.13 (2H, m, H-18), 1.65–1.91 (15H, m, H-22, H-26, H-27, H-28, 2H-25, 2H-24, 2H-30, 2H-29, H-3e, H-3a, H-6e), 1.27–1.65 (7H, m, 2H-31, H-5a, H-6a, H-2a, H-2e, H-1a).  $^{13}\text{C}$  NMR (100MHz,  $\text{CDCl}_3$ ,  $\delta$ , ppm): 158.10 (C-20), 147.21 (C-9), 145.31 (C-13), 134.77 (C-8), 126.68 (C-14), 124.05 (C-11), 123.59 (C-12), 18.43 (Me-19), 23.85 (Me-17 and Me-16), 25.16 (Me-20), 27.19 and 27.04 (C-22, C-26), 32.48 and 32.43 (C-27, C-28), 33.28 (C-15), 45.03 (C-5), 53.92 (C-23), 18.58 (C-2), 18.70 (C-6), 30.05 (C-7), 31.60 and 31.57 (C-25, C-30), 50.61 (C-18), 37.30 and 37.27 (C-23, C-28), 38.29 (C-4), 37.51 (C-3), 37.16 (C-10), 37.06 (C-1), 38.36 (C-30). Found,  $m/z$ : 462.3613  $[\text{M}]^+$ .  $\text{C}_{31}\text{H}_{46}\text{ON}_2$ . Calculated,  $m/z$ : 462.3605.

**N-abieta-8,11,13-trien-18-yl-N'-1-adamantylthiourea (3).** Yield 70%, white powder. M.p. 103 °C. IR (KBr)  $\nu_{\text{max}}$  3265, 2908, 1538  $\text{cm}^{-1}$ .  $^1\text{H}$  NMR (400MHz,  $\text{CDCl}_3$ ,  $\delta$ , ppm, J/Hz): 6.88 (1H, s, H-14), 6.95 (1H, d,  $J_{11,12} = 8.1$ , H-12), 7.13 (1H, d,  $J_{11,12} = 8.1$ , H-11), 0.98 (3H, s, Me-19), 1.18 (6H, d,  $J_{16,15} = 6.9$ , Me-16 and Me-17), 1.20 (3H, s, Me-20), 2.79 (1H, sept,  $J_{15,16} = 6.9$ , H-15), 2.82–2.98 (2H, m, 2H-7), 2.29 (1H, d,  $^2J = 13.0$ , H-1e), 2.00–2.21 (4H, m, H-26, H-27, H-28, H-6a), 1.83–1.99 (8H, m, 2H-23, 2H-24, 2H-25, H-6e, H-2a), 3.23–3.40 and 3.65–3.84 (2H, m, H-18), 1.36–1.44 (1H, d,  $^2J = 13.0$ , H-1a), 1.45–1.81 (9H, m, 2H-29, 2H-30, 2H-31, H-3, H-2e, H-5a).  $^{13}\text{C}$  NMR (100MHz,  $\text{CDCl}_3 + \text{CD}_3\text{OD}$ ,  $\delta$ , ppm): 181.35 (C-21), 146.72 (C-9), 145.42 (C-13), 134.17 (C-8), 126.48 (C-14), 123.75 (C-11), 123.51 (C-12), 18.26 (Me-19), 23.60 and 23.69 (Me-17 and Me-16), 24.66 (Me-20), 33.15 (C-15), 46.00 (C-5), 29.04 (C-26, C-27, C-28), 18.29 (C-2), 18.72 (C-6), 29.66 (C-7), 38.21 (C-4), 37.28 (C-1), 37.14 (C-10), 36.54 (C-3), 53.66 (C-18), 35.66 (C-29, C-30, C-31), 42.00 (C-23, C-24, C-25), 56.15 (C-22). Found,  $m/z$ : 478.3380  $[\text{M}]^+$ .  $\text{C}_{31}\text{H}_{46}\text{N}_2\text{S}$ . Calculated,  $m/z$ : 478.3376.

**N-abieta-8,11,13-trien-18-yl-N'-2-adamantylthiourea (4).** Yield 75%, white powder. M.p. 116 °C. IR (KBr)  $\nu_{\text{max}}$  3278, 2908, 1537  $\text{cm}^{-1}$ .  $^1\text{H}$  NMR (400MHz,  $\text{CDCl}_3$ ,  $\delta$ , ppm, J/Hz): 6.86 (1H, s, H-14), 6.95 (1H, d,  $J_{11,12} = 8.1$ , H-12), 7.12 (1H, d,  $J_{11,12} = 8.1$ , H-11), 6.94 and 5.21 (1H both, s, NH), 0.95 (3H, s, Me-18), 1.19 (6H, d,  $J_{16,15} = 6.9$ , Me-16 and Me-17), 1.19 (3H, s, Me-19), 2.79 (1H, sept,  $J_{15,16} = 6.9$ , H-15), 2.92–2.92 (2H, m, 2H-7), 4.05 (1H, br s, H-23), 3.09–3.62 (2H, m, 2H-18), 2.26 (1H,  $^2J = 12.6$ , H-1e), 1.94–2.10 (2H, m, H-22, H-26), 1.26–1.51 (4H, m, H-6, 2H-2, H-1a), 1.51–1.93 (16H, m, 2H-24, 2H-29, 2H-25, 2H-31, 2H-30, H-27, H-28, H-6, 2H-3, H-5).  $^{13}\text{C}$  NMR (100MHz,  $\text{CDCl}_3$ ,  $\delta$ , ppm): 181.06 (C-21), 146.72 (C-9), 145.47 (C-13), 134.37 (C-8), 126.67 (C-14), 123.89 (C-11), 123.65 (C-12), 18.44 (Me-19), 23.87 and 23.82 (Me-17 and Me-16), 25.02 (Me-20), 33.24 (C-15), 45.76 (C-5), 26.78 (C-27, C-28), 31.58 (C-22, C-26), 57.83 (C-23), 55.31 (C-18), 18.40 (C-2), 18.93 (C-6), 29.86 (C-7), 31.72 (C-25, C-31), 38.11 (C-4), 37.57 (C-1), 36.57 (C-30), 36.78 (C-24, C-29), 37.26 and 37.16 (C-10 and C-3). Found,  $m/z$ : 478.3368  $[\text{M}]^+$ .  $\text{C}_{31}\text{H}_{46}\text{N}_2\text{S}$ . Calculated,  $m/z$ : 478.3376.

### 3.1.2. Synthesis of Urea 5

Dehydroabietylamine hydrochloride (0.34 g, 1.06 mmol) was dissolved in EtOH (30 mL), and an aqueous solution of potassium cyanate (0.1 g of KNCO in 5 mL of water) was added. The mixture was refluxed for 6 h, then cooled to room temperature. The solvent was evaporated under vacuum. The solid residue was dissolved in CHCl<sub>3</sub> (20 mL) and washed with water (10 mL) and 5% aqueous NaOH solution (10 mL). The urea was purified using column chromatography on silica gel with CHCl<sub>3</sub> as an eluent and a MeOH gradient from 0 to 20%.

**N-abieta-8,11,13-trien-18-ylurea (5).** Yield 46%, white powder. M.p. 108 °C. IR (KBr)  $\nu_{\max}$  3430, 2927, 1652 cm<sup>-1</sup>. <sup>1</sup>H NMR (400MHz, CDCl<sub>3</sub>,  $\delta$ , ppm, J/Hz): 6.86 (1H, s, H-14), 6.96 (1H, d,  $J_{11,12}$  = 8.2, H-12), 7.14 (1H, d,  $J_{11,12}$  = 8.2, H-11), 0.89 (3H, s, Me-19), 1.19 (6H, d,  $J_{16,15}$  = 6.9, Me-16 and Me-17), 1.18 (3H, s, Me-20), 2.25 (1H, d,  $^2J$  = 12.3, H-1e), 2.79 (1H, sept,  $J_{15,16}$  = 6.9, H-15), 2.93–3.00 and 3.02–3.11 (1H both, m, H-18), 2.80–2.95 (2H, m, H-7), 1.77–1.94 (2H, m, H-6e, H-3a), 1.52–1.76 (3H, m, H-2e, H-3e, H-1a), 1.26–1.50 (3H, m, H-6e, H-2a H-5a), 4.53 (2H, s, NH<sub>2</sub>), 4.96 (1H, s, NH). <sup>13</sup>C NMR (100MHz, CDCl<sub>3</sub>,  $\delta$ , ppm): 159.18 (C-21), 147.17 (C-9), 145.47 (C-13), 134.72 (C-8), 126.72 (C-14), 124.02 (C-11), 123.65 (C-12), 23.85 (Me-17 and Me-16), 25.05 (Me-20), 33.29 (C-15), 44.87 (C-5), 29.95 (C-7), 38.28 (C-4), 37.27 (C-1, C-10), 35.89 (C-3), 50.73 (C-18), 18.76 (Me-19, C-2, C-6). Found,  $m/z$ : 328.2503 [M]<sup>+</sup>. C<sub>21</sub>H<sub>32</sub>ON<sub>2</sub>. Calculated,  $m/z$ : 328.2509.

**Norabietyl isocyanate.** Yield 56%, light-yellow oil. IR (KBr)  $\nu_{\max}$  2933, 2250, 1459 cm<sup>-1</sup>. <sup>1</sup>H NMR (400MHz, CDCl<sub>3</sub>,  $\delta$ , ppm, J/Hz): 5.77 (1H, s, H-14), 5.39–5.44 (1H, m, H-7), 1.00 and 0.99 (3H both,  $J_{16,15}$  = 6.9, Me-16 and Me-17), 0.75 (3H, s, Me-18), 1.34 (3H, s, Me-19), 2.21 (1H, sept,  $J_{15,16}$  = 6.9, H-15), 2.27 (1H, d,  $J$  = 18.2, H-5), 1.08 (1H, dt,  $J$  = 3.8,  $J$  = 13.3, H-11a), 0.81–0.88 (1H, m, H-1a), 1.15–1.29 (2H, m, H-2a, H-2e), 1.42–1.48 (1H, m, H-3), 1.54–1.70 (3H, m, H-1e, H-11e, H-9), 1.74–1.80 (1H, m, H-3e), 1.80–1.86 (1H, m, H-6a), 1.86–2.03 (3H, m, H-6e, H-12a, H-12e). <sup>13</sup>C NMR (100MHz, CDCl<sub>3</sub>,  $\delta$ , ppm): 145.18 (C-13), 135.22 (C-8), 122.13 (C-14), 119.97 (C-7), 21.17 and 20.62 (Me-17 and Me-16), 23.66 (Me-18), 13.32 (Me-19), 34.66 (C-15), 50.60 (C-9), 51.30 (C-5), 19.18 (C-2), 27.20 (C-12), 22.54 (C-11), 23.86 (C-6), 35.59 (C-10), 38.00 (C-1), 43.14 (C-3), 61.24 (C-4), 121.92 (C-20). Found,  $m/z$ : 299.2240 [M]<sup>+</sup>. C<sub>20</sub>H<sub>29</sub>ON. Calculated,  $m/z$ : 299.2244.

### 3.1.3. General Procedure for the Synthesis of Amides 6–7

Dehydroabietylamine hydrochloride (1.0 g, 3.1 mmol) was mixed with an equimolar amount of 1- or 2-adamantanecarbonyl chloride (0.62 g, 3.1 mmol) in 30 mL of CH<sub>3</sub>CN with the addition of Et<sub>3</sub>N (0.56 mL, 4.0 mmol). The reaction mixture was stirred on a magnetic stirrer for 24 h at room temperature. Upon completion, the solvent was evaporated under vacuum. The solid residue was dissolved in CHCl<sub>3</sub> (20 mL) and washed with water (15 mL). The organic layer was dried over anhydrous Na<sub>2</sub>SO<sub>4</sub> and filtered. The resultant liquid was evaporated under vacuum. The residue was purified using column chromatography on silica gel with hexane/ethyl acetate system, with a concentration gradient (EtOAc 0–25%) as an eluent.

**N-abieta-8,11,13-trien-18-yladamantan-1-carboxamide (6).** Yield 50%, white powder. M.p. 90 °C. IR (KBr)  $\nu_{\max}$  3363, 2906, 1639, 1525 cm<sup>-1</sup>. <sup>1</sup>H NMR (400MHz, CDCl<sub>3</sub>,  $\delta$ , ppm, J/Hz): 6.88 (1H, d,  $J_{12,14}$  = 1.7, H-14), 6.98 (1H, dd,  $J_{11,12}$  = 8.2,  $J_{12,14}$  = 1.7, H-12), 7.16 (1H, d,  $J_{11,12}$  = 8.2, H-11), 0.91 (3H, s, Me-19), 1.21 (6H, d,  $J_{16,15}$  = 6.9, Me-16 and Me-17), 1.20 (3H, s, Me-20), 2.81 (1H, sept,  $J_{15,16}$  = 6.9, H-15), 2.28 (1H, d,  $^2J$  = 12.3, H-1e), 3.17–3.22 and 3.08–3.13 (1H both, m, H-18), 2.85–2.91 and 2.73–2.79 (1H both, m, H-7), 1.99–2.02 (3H, m, H-26, H-27, H-28), 1.80–1.83 (6H, m, H-23, H-24, H-25), 1.84–1.89 (1H, m, H-6e), 1.42 (1H, d,  $^2J$  = 13.0, H-3e), 1.32–1.39 (2H, m, H-5a, H-1a), 1.62–1.75 (8H, m, H-29, H-30, H-31, H-3a, H-2e), 1.22–1.30 (2H, m, H-6e, H-2a). <sup>13</sup>C NMR (100MHz, CDCl<sub>3</sub>,  $\delta$ , ppm): 177.7 (C-21), 146.9 (C-9), 145.4 (C-13), 134.6 (C-8), 126.8 (C-14), 124.1 (C-11), 123.7 (C-12), 18.4 (Me-19), 23.84 and 23.80 (Me-17 and Me-16), 25.4 (Me-20), 33.3 (C-15), 46.2 (C-5), 28.0 (C-26, C-27, C-28), 18.5 (C-2), 18.9 (C-6), 30.4 (C-7), 36.4 (C-29, C-30, C-31), 39.3 (C-23, C-24, C-25), 38.3



(C-4), 37.5 (C-1), 37.3 (C-10), 36.2 (C-3), 49.5 (C-18), 40.8 (C-22). Found,  $m/z$ : 447.3490 [M]<sup>+</sup>. C<sub>31</sub>H<sub>45</sub>ON. Calculated,  $m/z$ : 447.3496.

**N-abieta-8,11,13-trien-18-yladamantan-2-carboxamide (7)**. Yield 46%, white powder. M.p. 94 °C. IR (KBr)  $\nu_{\max}$  3311, 2904, 1642, 1542 cm<sup>-1</sup>. <sup>1</sup>H NMR (400MHz, CDCl<sub>3</sub>,  $\delta$ , ppm, J/Hz): 6.87 (1H, s, H-14), 6.97 (1H, d,  $J_{11,12}$ =8.1, H-12), 7.15 (1H, d,  $J_{11,12}$ =8.1, H-11), 0.92 (3H, s, Me-19), 1.20 (6H, d,  $J_{16,15}$ =6.9, Me-16 and Me-17), 1.19 (3H, s, Me-20), 2.80 (1H, sept,  $J_{15,16}$ =6.9, H-15), 2.27 (1H, d,  $^2J$ =12.7, H-1e), 2.73-2.94 (2H, m, H-7), 5.59 (1H, s, NH), 3.13-3.26 (2H, m, H-18), 2.39-2.47 (1H, m, H-23), 2.16-2.23 (2H, m, H-22, H-26), 1.63-1.80 (7H, m, H-24, H-29, H-25, H-31, H-30, H-3, H-6), 1.52-1.63 (3H, m, H-5a, H-1e, H-3), 1.80-2.00 (6H, m, H-24, H-29, H-25, H-31, H-28, H-27), 1.29-1.46 (4H, m, H-6, 2H-2, H-1a). <sup>13</sup>C NMR (100MHz, CDCl<sub>3</sub>,  $\delta$ , ppm): 173.9 (C-21), 147.0 (C-9), 145.5 (C-13), 134.7 (C-8), 126.8 (C-14), 124.0 (C-11), 123.7 (C-12), 18.5 (Me-19), 23.8 and 23.9 (Me-17 and Me-16), 25.2 (Me-20), 33.3 (C-15), 45.6 (C-5), 50.0 (C-23), 29.96 and 30.04 (C-22, C-26), 27.24 and 27.36 (C-27, C-28), 18.5 (C-2), 18.9 (C-6), 30.2 (C-7), 49.5 (C-18), 33.16 and 33.21 (C-25, C-31), 38.20 and 38.26 (C-25, C-31, C-4), 36.3 (C-3), 37.22, 37.31, 37.33 (C-10, C-1, C-30). Found,  $m/z$ : 447.3503 [M]<sup>+</sup>. C<sub>31</sub>H<sub>45</sub>ON. Calculated,  $m/z$ : 447.3500.

### 3.1.4. Synthesis of Thioamide 8

Amide 6 (0.4 g, 0.9 mmol) and Lawesson's reagent (0.18 g, 0.45 mmol) were refluxed in *o*-xylene (20 mL) for 3 h. Conversion was monitored by TLC. The solvent was removed under vacuum. The residue was purified using column chromatography on silica gel with CHCl<sub>3</sub> as an eluent and a MeOH gradient from 0 to 20%.

**N-abieta-8,11,13-trien-18-yladamantan-1-carbothioamide (8)**. Yield 10%, light-yellow powder. M.p. 166 °C. IR (KBr)  $\nu_{\max}$  3386, 2904, 1525 cm<sup>-1</sup>. <sup>1</sup>H NMR (400MHz, CDCl<sub>3</sub>,  $\delta$ , ppm, J/Hz): 6.89 (1H, s, H-14), 6.99 (1H, d,  $J_{11,12}$ =8.2, H-12), 7.15 (1H, d,  $J_{11,12}$ =8.2, H-11), 7.42 (1H, s, NH), 0.99 (3H, s, Me-19), 1.21 (6H, d,  $J_{16,15}$ =6.9, Me-16 and Me-17), 1.22 (3H, s, Me-20), 2.81 (1H, sept,  $J_{15,16}$ =6.9, H-15), 2.72-2.93 (2H, m, 2H-7), 2.31 (1H, m, H-1e), 3.75-3.85 (1H, m, H-18), 3.48-3.56 (1H, m, H-18), 2.04-2.14 (3H, m, H-26, H-27, H-28), 1.50-1.56 (1H, m, H-3a), 1.91-2.03 (7H, m, 2H-23, 2H-24, 2H-25, H-6e), 1.28-1.47 (3H, m, H-5a, H-1a, H-3e), 1.60-1.91 (9H, m, 2H-28, 2H-29, 2H-30, H-6a, H-2a, H-2e). <sup>13</sup>C NMR (100MHz, CDCl<sub>3</sub>,  $\delta$ , ppm): 212.88 (C-21), 146.27 (C-9), 145.28 (C-13), 134.11 (C-8), 126.56 (C-14), 123.84 (C-11), 123.56 (C-12), 18.33 (Me-19), 23.54 and 23.49 (Me-17 and Me-16), 25.08 (Me-20), 32.97 (C-15), 46.75 (C-5), 28.14 (C-26, C-27, C-28), 18.18 (C-2), 18.79 (C-6), 30.04 (C-7), 35.93 (C-29, C-30, C-31), 41.53 (C-23, C-24, C-25), 37.85 (C-4), 37.27 (C-1), 37.18 (C-10), 36.56 (C-3), 56.12 (C-18), 46.08 (C-22). Found,  $m/z$ : 463.3264 [M]<sup>+</sup>. C<sub>31</sub>H<sub>45</sub>NS. Calculated,  $m/z$ : 463.3267.

### 3.1.5. General Procedure for the Synthesis of Norabietyl and Nordehydroabietyl Ureas

Norabietyl or nordehydroabietyl isocyanate (0.3 g, 1.0 mmol) was dissolved in CHCl<sub>3</sub> (15 mL). An equimolar amount (0.19 g, 1.0 mmol) of 1- or 2-adamantylamine hydrochloride with triethylamine (0.17 mL, 1.2 mmol) was dissolved in EtOH (15 mL) and added to isocyanate solution. The reaction mixture was stirred on a magnetic stirrer for 24 h at room temperature. The precipitated norabietyl ureas were filtered off and were not additionally purified. The nordehydroabietyl urea solutions were washed with water (15 mL) and dried over Na<sub>2</sub>SO<sub>4</sub>. The solvent was removed in vacuo. The solid residues were recrystallized from acetonitrile.

**N-1-adamantyl-N'-[(1R,4aS,10aR)-7-isopropyl-1,4a-dimethyl-1,2,3,4,4a,9,10,10a-octahydrophenanthren-1-yl]urea (9)**. Yield 85%, white powder. M.p. 235 °C. IR (KBr)  $\nu_{\max}$  3357, 2906, 1629, 1554 cm<sup>-1</sup>. <sup>1</sup>H NMR (400MHz, CDCl<sub>3</sub> + CD<sub>3</sub>OD,  $\delta$ , ppm, J/Hz): 6.76 (1H, s, H-14), 6.87 (1H, d,  $J_{11,12}$  = 8.2, H-12), 7.05 (1H, d,  $J_{11,12}$  = 8.2, H-11), 1.07 (3H, s, Me-18), 1.11 (6H, d,  $J_{16,15}$  = 6.9, Me-16 and Me-17), 1.10 (3H, s, Me-19), 2.71 (1H, sept,  $J_{15,16}$  = 6.9, H-15), 2.74-2.83 (2H, m, 2H-7), 2.10 (2H, m, H-1e, H-5a), 1.88-2.01 (4H, m, H-25, H-26, H-27, H-6e), 1.73-1.86 (8H, m, 2H-22, 2H-23, 2H-24, H-3e, H-3a), 1.47-1.66 (9H, m, 2H-28, 2H-29, 2H-30, H-6a, H-2a, H-2e), 1.30-1.40 (1H, m, H-1a). <sup>13</sup>C NMR (100MHz, CDCl<sub>3</sub> + CD<sub>3</sub>OD,  $\delta$ , ppm): 157.17 (C-20), 146.74 (C-9), 145.16 (C-13), 134.44 (C-8),

126.44 (C-14), 124.08 (C-11), 123.49 (C-12), 20.76 (Me-18), 23.62 and 23.66 (Me-17 and Me-16), 24.77 (Me-19), 33.15 (C-15), 46.93 (C-5), 29.25 (C-25, C-26, C-27), 18.59 (C-2), 19.46 (C-6), 30.11 (C-7), 36.18 (C-28, C-29, C-30), 42.13 (C-22, C-23, C-24), 55.77 (C-4), 37.89 (C-1), 37.50 and 37.46 (C-10 and C-3), 50.04 (C-21). Found,  $m/z$ : 448.3445 [M]<sup>+</sup>. C<sub>30</sub>H<sub>44</sub>ON<sub>2</sub>. Calculated,  $m/z$ : 448.3448.

**N-2-adamantyl-N'-[(1R,4aS,10aR)-7-isopropyl-1,4a-dimethyl-1,2,3,4,4a,9,10,10a-octahydrophenanthren-1-yl]urea (10)**. Yield 80%, white powder. M.p. 233 °C. IR (KBr)  $\nu_{\max}$  3357, 2912, 1623, 1556 cm<sup>-1</sup>. <sup>1</sup>H NMR (400MHz, CDCl<sub>3</sub>,  $\delta$ , ppm, J/Hz): 6.78 (1H, s, H-14), 6.89 (1H, d,  $J_{11,12}$  = 8.2, H-12), 7.07 (1H, d,  $J_{11,12}$  = 8.2, H-11), 1.20 (3H, s, Me-18), 1.11 (6H, d,  $J_{16,15}$  = 6.9, Me-16 and Me-17), 1.10 (3H, s, Me-19), 2.73 (1H, sept,  $J_{15,16}$  = 6.9, H-15), 2.74–2.87 (2H, m, 2H-7), 2.15 (1H, d,  $^2J$  = 12.3, H-1e), 3.64 (1H, s, H-22), 1.29–1.41 (1H, m, H-1a), 1.42–1.54 (2H, m, H-24, H-29), 1.94–2.08 (2H, m, H-23, H-28), 1.78–1.93 (2H, m, H-24, H-29), 1.55–1.65 (4H, m, H-26, H-27, 2H-30), 1.65–1.78 (11H, m, 2H-2, 2H-3, 2H-6, H-5, H-21, H-25, H-23, H-28). <sup>13</sup>C NMR (100MHz, DMSO-*d*<sub>6</sub>,  $\delta$ , ppm, J/Hz): 157.25 (C-20), 147.74 (C-9), 145.54 (C-13), 134.99 (C-8), 127.00 (C-14), 124.69 (C-11), 124.16 (C-12), 21.91 (Me-18), 24.14 and 24.48 (Me-17 and Me-16), 25.25 (Me-19), 46.53 (C-5), 30.43 (C-7), 18.89 (C-2), 20.06 (C-6), 55.76 (C-4), 53.25 (C-22), 27.46 and 27.52 (C-21, C-25), 31.80 and 31.92 (C-24, C-29), 32.86 and 32.94 (C-26, C-27), 33.43 (C-15), 37.57 (C-3), 37.73 (C-10), 38.32 and 38.36 (C-1, C-30), 37.97 and 37.92 (C-23, C-28). Found,  $m/z$ : 448.3449 [M]<sup>+</sup>. C<sub>30</sub>H<sub>44</sub>ON<sub>2</sub>. Calculated,  $m/z$ : 448.3448.

**N-1-adamantyl-N'-[(1R,4aR,10aR)-7-isopropyl-1,4a-dimethyl-1,2,3,4,4a,4b,5,6,10,10a-decahydrophenanthren-1-yl]urea (11)**. Yield 90%, white powder. M.p. 224 °C. IR (KBr)  $\nu_{\max}$  3346, 2906, 1633, 1560 cm<sup>-1</sup>. <sup>1</sup>H NMR (400MHz, CDCl<sub>3</sub> + CD<sub>3</sub>OD,  $\delta$ , ppm, J/Hz): 5.65 (1H, s, H-14), 5.30 (1H, s, H-7), 0.88 and 0.89 (3H both, d,  $J_{16,15}$  = 6.9, Me-16 and Me-17), 0.67 (3H, s, Me-18), 1.12 (3H, s, Me-19), 2.10 (1H, sept,  $J_{15,16}$  = 6.9, H-15), 0.95–1.10 (2H, m, H-1a, H-11a), 1.32–1.48 (2H, m, H-2a, H-2e), 1.63–1.73 (2H, m, H-3a, H-11e), 1.48–1.57 (6H, m, 2H-29, 2H-30, 2H-28), 1.72–1.87 (9H, m, 2H-22, 2H-23, 2H-24, H-1e, H-3e, H-9), 1.87–2.05 (8H, m, H-25, H-26, H-27, H-5, H-6a, H-6e, 2H-12). <sup>13</sup>C NMR (100MHz, CDCl<sub>3</sub> + CD<sub>3</sub>OD,  $\delta$ , ppm): 156.99 (C-20), 145.02 (C-13), 135.33 (C-8), 122.19 (C-14), 120.64 (C-7), 29.32 (C-25, C-26, C-27), 36.22 (C-28, C-29, C-30), 42.21 (C-22, C-23, C-24), 21.10 and 20.53 (Me-17 and Me-16), 21.38 (Me-18), 13.61 (Me-19), 34.65 (C-15), 50.65 (C-9), 47.00 (C-5), 19.15 (C-2), 27.20 (C-12), 35.44 (C-10), 38.14 (C-1), 37.92 (C-3), 22.49 (C-11), 23.50 (C-6), 55.45 (C-4), 50.17 (C-21). Found,  $m/z$ : 450.3600 [M]<sup>+</sup>. C<sub>30</sub>H<sub>46</sub>ON<sub>2</sub>. Calculated,  $m/z$ : 450.3605.

**N-2-adamantyl-N'-[(1R,4aR,10aR)-7-isopropyl-1,4a-dimethyl-1,2,3,4,4a,4b,5,6,10,10a-decahydrophenanthren-1-yl]urea (12)**. Yield 80%, white powder. M.p. 213 °C. IR (KBr)  $\nu_{\max}$  3395, 2908, 1629, 1556 cm<sup>-1</sup>. <sup>1</sup>H NMR (400MHz, CDCl<sub>3</sub> + CD<sub>3</sub>OD,  $\delta$ , ppm, J/Hz): 5.62 (1H, s, H-14), 5.27 (1H, s, H-7), 0.88 and 0.87 (3H both, d,  $J_{16,15}$  = 6.9, Me-16 and Me-17), 0.67 (3H, s, Me-18), 1.13 (3H, s, Me-19), 2.08 (1H, sept,  $J_{15,16}$  = 6.9, H-15), 0.93–1.10 (2H, m, H-1a, H-11a), 1.32–1.48 (4H, m, H-2a, H-2e, H-24, H-29), 1.54–1.61 (2H, m, 2H-30), 1.89–2.05 (5H, m, H-5, H-6a, H-6e, 2H-12), 1.73–1.89 (3H, m, H-1e, H-3e, H-9), 1.60–1.75 (10H, m, H-3a, H-11e, H-26, H-27, H-21, H-25, 2H-23, 2H-28, H-24, H-29), 3.59 (1H, s, H-22). <sup>13</sup>C NMR (100MHz, CDCl<sub>3</sub> + CD<sub>3</sub>OD,  $\delta$ , ppm): 157.29 (C-20), 144.82 (C-13), 135.25 (C-8), 122.11 (C-14), 120.52 (C-7), 13.53 (Me-19), 21.03 and 20.47 (Me-17 and Me-16), 21.28 (Me-18), 22.42 (C-11), 23.40 (C-6), 27.13 (C-12), 27.05 and 26.90 (C-21, C-25), 31.37 (C-24, C-29), 32.38 and 32.40 (C-26, C-27), 34.55 (C-15), 35.35 (C-10), 37.05 and 37.03 (C-23, C-28), 38.10 (C-1), 37.92 (C-3), 37.35 (C-30), 46.87 (C-5), 50.68 (C-9), 55.33 (C-4), 53.10 (C-22). Found,  $m/z$ : 450.3604 [M]<sup>+</sup>. C<sub>30</sub>H<sub>46</sub>ON<sub>2</sub>. Calculated,  $m/z$ : 450.3605.

### 3.2. TDP1 Assay

The recombinant TDP1 was purified to homogeneity by chromatography on Ni-chelating resin and phosphocellulose P11 as previously described [45], using plasmid pET 16B-TDP1, kindly provided by Dr. K.W. Caldecott (University of Sussex, United Kingdom). The TDP1 activity measurements were carried out as described [13]. Briefly, TDP1-biosensor

with fluorophore (FAM) at the 5'-end and a fluorescence quencher (BHQ1) at the 3'-end at a final concentration of 50 nM were incubated in a 200  $\mu$ L volume that contained TDP1 buffer (50 mM Tris-HCl pH 8.0, 50 mM NaCl, and 7 mM  $\beta$ -mercaptoethanol) supplemented with purified 1.5 nM TDP1 and various concentrations of inhibitor. Fluorescence measurements (Ex485/Em520 nm) were carried out during the linear phase of the reaction (from 0 to 8 min for TDP1) every 55 sec. The reactions were incubated at a constant temperature of 26  $^{\circ}$ C in a POLARstar OPTIMA fluorimeter (BMG LABTECH, GmbH). The influence of compounds was evaluated by comparing the fluorescence increase rate in the presence of compounds with that of DMSO control wells. The data were imported into the MARS Data Analysis 2.0 program (BMG LABTECH), and the IC<sub>50</sub> values (the concentration of a compound required to reduce the enzyme activity by 50%) were calculated. The TDP1-biosensor 5'-(5,6 FAM-aac gtc agg gtc ttc c-BHQ1)-3' was synthesised in the Laboratory of Biomedical Chemistry, Institute of Chemical Biology and Fundamental Medicine, Novosibirsk, Russia.

### 3.3. Cytotoxicity Experiments

Individual TDP1 inhibitors were prepared as 50 mM stock solutions in DMSO and were added to the cells at 2.5, 5, 10, or 25  $\mu$ M. Temozolomide was prepared as 200 mM stock solution in DMSO and was added at 1 mM or 2 mM concentrations, either alone or in combination with TDP1 inhibitors. T98G and SNB19 glioma cells were maintained in DMem/F12 medium supplemented with 10% foetal bovine serum, l-glutamine, and penicillin/streptomycin and were split at 10,000 cells/well into the 96-well plates for cytotoxicity experiments. The drugs or drug combinations were incubated with cells for 72 h, then the MTT reagent (3-(4,5-dimethylthiazol-2-yl)-2,5-diphenyltetrazolium bromide) was added for 4 h. The produced purple formazan dye reporting the activity of cellular oxidoreductases was dissolved overnight in 10% solution of acidified SDS and the absorbance was measured using a Tecan plate reader. Each concentration of individual substance or each drug combination was tested in triplicate. The data obtained were processed using MS Excel software and presented as histogram plots.

### 3.4. Molecular Docking

The models of the apo form and covalent intermediate of human TDP1 were based on the 1NOP crystal structure [46] and constructed as reported in our previous work [47,48]. Molecular docking of inhibitors was performed with Lead Finder 1.1.15 [49,50]. An energy grid box with edges of 35  $\text{Å}$  was centred on the N <sup>$\epsilon$ 2</sup> atom of the catalytic residue His263 and overlapped the active site and adjacent cavities. In our previous study, the TDP1 substrate-binding groove was identified and mapped based on the 1NOP structure (covalent complex with substrate analogue), and successfully tested in docking runs with diazaadamantane derivatives as reference TDP1 inhibitors [48]. Docking was done using a genetic algorithm in 'extra precision' mode. The protein structure was rigid, whereas rotating functional/rotatable groups of ligands was allowed. VMD 1.9.2 was used to visualise molecular structures [51].

## 4. Conclusions

As a result of this study, we synthesized a set of compounds containing the diterpene fragment. The effect of the terpene structural blocks, the length and structure of the ureide linker, and the site of attachment of the adamantane residue on the biological properties of the new abietylamine-based compounds were investigated, and in particular their ability both to inhibit the DNA repair enzyme TDP1 and to enhance the cytotoxic effect of TMZ. In this library of compounds, we studied the structure of compounds with demonstrated biological activity. The choice of 1-adamantane or 2-adamantane substituent did not significantly affect the inhibitory characteristics, but their absence negatively affected them. Ureas on nordehydroabietyl and norabietyl isocyanates lacking a CH<sub>2</sub> group in the terpene part, demonstrated extremely low solubility in water and almost all organic solvents, which does not make them promising for further study. The starting compound **1** was

the most effective in the inhibition of TDP1 and compound **2** was the most effective in the sensitization of glioma T98G cells to TMZ. We found some synergistic effects on cells T98G when using repair enzyme inhibitors, but they are not as high as we expected. At the same time, the substances we described could be of considerable interest when studied on other cancer cell lines or simultaneously with other cytostatics.

**Supplementary Materials:** The following are available online at <https://www.mdpi.com/article/10.3390/ph14050422/s1>.

**Author Contributions:** Conceptualization, K.K., O.Y.; methodology, K.K., O.Y., S.C., A.Z.; investigation, K.K., K.P., A.A., I.C., V.K., T.K., E.M., D.N.; writing—original draft preparation, K.K., O.Y., S.C., A.Z.; supervision, E.S., V.Š., A.P., O.L., N.S. All authors have read and agreed to the published version of the manuscript.

**Funding:** This work was supported by a grant from the Russian Science Foundation 19-73-00051.

**Institutional Review Board Statement:** Not applicable.

**Informed Consent Statement:** Not applicable.

**Data Availability Statement:** Not applicable.

**Acknowledgments:** The authors would like to acknowledge the Multi-Access Chemical Service Centre SB RAS for spectral and analytical measurements.

**Conflicts of Interest:** The authors declare no conflict of interest.

## References

- Caldecott, K.W. Single-strand break repair and genetic disease. *Nat. Rev. Genet.* **2008**, *9*, 619–631. [CrossRef]
- Baglini, E.; Salerno, S.; Barresi, E.; Robello, M.; Da Settimo, F.; Taliani, S.; Marini, A.M. Multiple Topoisomerase I (TopoI), Topoisomerase II (TopoII) and Tyrosyl-DNA Phosphodiesterase (TDP) inhibitors in the development of anticancer drugs. *Eur. J. Pharm. Sci.* **2021**, *156*, 105594. [CrossRef] [PubMed]
- Jain, P.G.; Patel, B.D. Medicinal chemistry approaches of poly ADP-Ribose polymerase 1 (PARP1) inhibitors as anticancer—A recent update. *Eur. J. Med. Chem.* **2019**, *165*, 198–215. [CrossRef] [PubMed]
- Laev, S.S.; Salakhutdinov, N.F.; Lavrik, O.I. Tyrosyl-DNA phosphodiesterase inhibitors: Progress and potential. *Bioorganic Med. Chem.* **2016**, *24*, 5017–5027. [CrossRef] [PubMed]
- Buzun, K.; Bielawska, A.; Bielawski, K.; Gornowicz, A. DNA topoisomerases as molecular targets for anticancer drugs. *J. Enzym. Inhib. Med. Chem.* **2020**, *35*, 1781–1799. [CrossRef]
- Liang, X.; Wu, Q.; Luan, S.; Yin, Z.; He, C.; Yin, L.; Zou, Y.; Yuan, Z.; Li, L.; Song, X.; et al. A comprehensive review of topoisomerase inhibitors as anticancer agents in the past decade. *Eur. J. Med. Chem.* **2019**, *171*, 129–168. [CrossRef]
- Boccard, S.G.; Marand, S.V.; Geraci, S.; Pycroft, L.; Berger, F.R.; Pelletier, L.A. Inhibition of DNA-repair genes Ercc1 and Mgmt enhances temozolomide efficacy in gliomas treatment: A pre-clinical study. *Oncotarget* **2015**, *6*, 29456–29468. [CrossRef]
- Takashima, H.; Boerkoel, C.F.; John, J.; Saifi, G.M.; Salih, M.A.M.; Armstrong, D.; Mao, Y.; Quioco, F.A.; Roa, B.B.; Nakagawa, M.; et al. Mutation of TDP1, encoding a topoisomerase I-dependent DNA damage repair enzyme, in spinocerebellar ataxia with axonal neuropathy. *Nat. Genet.* **2002**, *32*, 267–272. [CrossRef]
- Interthal, H.; Chen, H.J.; Kehl-Fie, T.E.; Zotzmann, J.; Leppard, J.B.; Champoux, J.J. SCAN1 mutant Tdp1 accumulates the enzyme-DNA intermediate and causes camptothecin hypersensitivity. *EMBO J.* **2005**, *24*, 2224–2233. [CrossRef]
- Rass, U.; Ahel, I.; West, S.C. Defective DNA Repair and Neurodegenerative Disease. *Cell* **2007**, *130*, 991–1004. [CrossRef]
- Zakharenko, A.L.; Drenichev, M.S.; Dyrkheeva, N.S.; Ivanov, G.A.; Oslovsky, V.E.; Ilina, E.S.; Chernyshova, I.A.; Lavrik, O.I.; Mikhailov, S.N. Inhibition of Tyrosyl-DNA Phosphodiesterase 1 by Lipophilic Pyrimidine Nucleosides. *Molecules* **2020**, *25*, 3694. [CrossRef]
- Antony, S.; Marchand, C.; Stephen, A.G.; Thibaut, L.; Agama, K.K.; Fisher, R.J.; Pommier, Y. Novel high-throughput electrochemiluminescent assay for identification of human tyrosyl-DNA phosphodiesterase (Tdp1) inhibitors and characterization of furamidine (NSC 305831) as an inhibitor of Tdp1. *Nucleic Acids Res.* **2007**, *35*, 4474–4484. [CrossRef]
- Zakharenko, A.; Khomenko, T.; Zhukova, S.; Koval, O.; Zakharova, O.; Anarbaev, R.; Lebedeva, N.; Korchagina, D.; Komarova, N.; Vasiliev, V.; et al. Synthesis and biological evaluation of novel tyrosyl-DNA phosphodiesterase 1 inhibitors with a benzopentathiepine moiety. *Bioorg. Med. Chem.* **2015**, *23*, 2044–2052. [CrossRef]
- Beck, D.E.; Reddy, P.V.N.; Lv, W.; Abdelmalak, M.; Tender, G.S.; Lopez, S.; Agama, K.; Marchand, C.; Pommier, Y.; Cushman, M. Investigation of the Structure–Activity Relationships of Aza-A-Ring Indenoisoquinoline Topoisomerase I Poisons. *J. Med. Chem.* **2015**, *59*, 3840–3853. [CrossRef]

15. Sirivolu, V.R.; Vernekar, S.K.V.; Marchand, C.; Naumova, A.; Chergui, A.; Renaud, A.; Stephen, A.G.; Chen, F.; Sham, Y.Y.; Pommier, Y.; et al. 5-Arylideneethiothiazolidinones as Inhibitors of Tyrosyl-DNA Phosphodiesterase I. *J. Med. Chem.* **2012**, *55*, 8671–8684. [CrossRef] [PubMed]
16. Salakhutdinov, N.F.; Volcho, K.P.; Yarovaya, O.I. Monoterpenes as a renewable source of biologically active compounds. *Pure Appl. Chem.* **2017**, *89*, 1105–1117. [CrossRef]
17. Luzina, O.; Filimonov, A.; Zakharenko, A.; Chepanova, A.; Zakharova, O.; Ilina, E.; Dyrkheeva, N.; Likhatskaya, G.; Salakhutdinov, N.; Lavrik, O. Usnic Acid Conjugates with Monoterpenoids as Potent Tyrosyl-DNA Phosphodiesterase 1 Inhibitors. *J. Nat. Prod.* **2020**, *83*, 2320–2329. [CrossRef] [PubMed]
18. Khomenko, T.; Zakharenko, A.; Odarchenko, T.; Arabshahi, H.J.; Sannikova, V.; Zakharova, O.; Korchagina, D.; Reynisson, J.; Volcho, K.; Salakhutdinov, N.; et al. New inhibitors of tyrosyl-DNA phosphodiesterase I (Tdp 1) combining 7-hydroxycoumarin and monoterpene moieties. *Bioorg. Med. Chem.* **2016**, *24*, 5573–5581. [CrossRef]
19. Khomenko, T.M.; Zakharenko, A.L.; Chepanova, A.A.; Ilina, E.S.; Zakharova, O.D.; Kaledin, V.I.; Nikolin, V.P.; Popova, N.A.; Korchagina, D.V.; Reynisson, J.; et al. Promising New Inhibitors of Tyrosyl-DNA Phosphodiesterase I (Tdp 1) Combining 4-Arylcoumarin and Monoterpene Moieties as Components of Complex Antitumor Therapy. *Int. J. Mol. Sci.* **2019**, *21*, 126. [CrossRef] [PubMed]
20. Salomatina, O.V.; Popadyuk, I.I.; Zakharenko, A.L.; Zakharova, O.D.; Chepanova, A.A.; Dyrkheeva, N.; Komarova, N.I.; Reynisson, J.; Anarbaev, R.O.; Salakhutdinov, N.F.; et al. Deoxycholic acid as a molecular scaffold for tyrosyl-DNA phosphodiesterase 1 inhibition: A synthesis, structure–activity relationship and molecular modeling study. *Steroids* **2021**, *165*, 108771. [CrossRef] [PubMed]
21. Mozhaitsev, E.S.; Zakharenko, A.L.; Suslov, E.V.; Korchagina, D.V.; Zakharova, O.D.; Vasil'eva, I.A.; Chepanova, A.A.; Black, E.; Patel, J.; Chand, R.; et al. Novel Inhibitors of DNA Repair Enzyme TDP1 Combining Monoterpene and Adamantane Fragments. *Anti-Cancer Agents Med. Chem.* **2019**, *19*, 463–472. [CrossRef]
22. Kovaleva, K.; Oleshko, O.; Mamontova, E.; Yarovaya, O.; Zakharova, O.; Zakharenko, A.; Kononova, A.; Dyrkheeva, N.; Cheresiz, S.; Pokrovsky, A.; et al. Dehydroabietylamine Ureas and Thioureas as Tyrosyl-DNA Phosphodiesterase 1 Inhibitors That Enhance the Antitumor Effect of Temozolomide on Glioblastoma Cells. *J. Nat. Prod.* **2019**, *82*, 2443–2450. [CrossRef] [PubMed]
23. Kovaleva, K.; Mamontova, E.; Yarovaya, O.; Zakharova, O.; Zakharenko, A.; Lavrik, O.; Salakhutdinov, N. Dehydroabietylamine-based thiazolidin-4-ones and 2-thioxoimidazolidin-4-ones as novel tyrosyl-DNA phosphodiesterase 1 inhibitors. *Mol. Divers.* **2020**, 1–9. [CrossRef]
24. Chepanova, A.A.; Mozhaitsev, E.S.; Munkuev, A.A.; Suslov, E.V.; Korchagina, D.V.; Zakharova, O.D.; Zakharenko, A.L.; Patel, J.; Ayine-Tora, D.M.; Reynisson, J.; et al. The Development of Tyrosyl-DNA Phosphodiesterase 1 Inhibitors. Combination of Monoterpene and Adamantine Moieties via Amide or Thioamide Bridges. *Appl. Sci.* **2019**, *9*, 2767. [CrossRef]
25. Zakharenko, A.L.; Ponomarev, K.U.; Suslov, E.V.; Korchagina, D.V.; Volcho, K.P.; Vasil'eva, I.A.; Salakhutdinov, N.F.; Lavrik, O.I. Inhibitory properties of nitrogen-containing adamantane derivatives with monoterpene fragments against tyrosyl-DNA phosphodiesterase 1. *Russ. J. Bioorg. Chem.* **2015**, *41*, 657–662. [CrossRef] [PubMed]
26. Ponomarev, K.Y.; Suslov, E.V.; Zakharenko, A.L.; Zakharova, O.D.; Rogachev, A.D.; Korchagina, D.V.; Zafar, A.; Reynisson, J.; Nefedov, A.A.; Volcho, K.P.; et al. Aminoadamantanes containing monoterpene-derived fragments as potent tyrosyl-DNA phosphodiesterase 1 inhibitors. *Bioorg. Chem.* **2018**, *76*, 392–399. [CrossRef]
27. Kugler, S.; Ossowicz, P.; Malarczyk-Matusiak, K.; Wierzbicka, E. Advances in Rosin-Based Chemicals: The Latest Recipes, Applications and Future Trends. *Molecules* **2019**, *24*, 1651. [CrossRef] [PubMed]
28. Butov, G.M.; Burmistrov, V.; Saad, K.R. Synthesis of Adamantyl-Containing Compounds: Structure Elements of Rotaxanes and Supramolecular Polymers. *Mod. Org. Chem. Res.* **2017**, *4*, 1910–1914. [CrossRef]
29. Claremon, D.A.; Zhuang, L.; Ye, Y.; Singh, S.B.; Tice, C.M. Carbamate and urea inhibitors of 11 $\beta$ -hydroxysteroid dehydrogenase. Patent Number WO2009131669A2, 29 October 2009.
30. Burmistrov, V.V.; Butov, G.M.; Pitushkin, D.A. Synthesis of adamantyl-containing isothiocyanates. *Russ. J. Org. Chem.* **2015**, *51*, 1795–1796. [CrossRef]
31. Pitushkin, D.A.; Burmistrov, V.V.; Butov, G.M. Synthesis of Homologs of 1-Isothiocyanatoadamantane. *Russ. J. Org. Chem.* **2018**, *54*, 1475–1479. [CrossRef]
32. Zeiss, H.H.; Martin, W.B. Synthesis and Stereochemistry of the 3-Keto- $\Delta^4$ -steroidal System from Diterpenic Acids 1a,b. *J. Am. Chem. Soc.* **1953**, *75*, 5935–5940. [CrossRef]
33. Righetti, G.; Casale, M.; Tonelli, M.; Liessi, N.; Fossa, P.; Pedemonte, N.; Millo, E.; Cichero, E. New Insights into the Binding Features of F508del CFTR Potentiators: A Molecular Docking, Pharmacophore Mapping and QSAR Analysis Approach. *Pharmaceuticals* **2020**, *13*, 445. [CrossRef] [PubMed]
34. Francesconi, V.; Cichero, E.; Schenone, S.; Naesens, L.; Tonelli, M. Synthesis and Biological Evaluation of Novel (thio)semicarbazone-Based Benzimidazoles as Antiviral Agents against Human Respiratory Viruses. *Molecules* **2020**, *25*, 1487. [CrossRef]
35. Pallicer, J.M.; Rosés, M.; Ràfols, C.; Bosch, E.; Pascual, R.; Port, A. Evaluation of log Po/w values of drugs from some molecular structure calculation softwares. *ADMET DMPK* **2014**, *2*, 107–114. [CrossRef]
36. Gowda, R.; Madhunapantula, S.V.; Kuzu, O.F.; Sharma, A.; Robertson, G.P. Targeting Multiple Key Signaling Pathways in Melanoma Using Leelamine. *Mol. Cancer Ther.* **2014**, *13*, 1679–1689. [CrossRef] [PubMed]

37. Kovaleva, K.S.; Kononova, A.A.; Korobeynikov, A.V.; Cheresiz, S.V.; Zarubaev, V.V.; Shtro, A.A.; Orshanskaya, Y.R.; Yarovaya, O.I.; Pokrovsky, A.G.; Salakhutdinov, N.F. Cytotoxic and Antiviral Properties of Novel Dehydroabietylamine Salts. *Med. Chem.* **2016**, *6*, 642–646. [CrossRef]
38. Chen, H.; Qiao, C.; Miao, T.T.; Li, A.L.; Wang, W.Y.; Gu, W. Synthesis and biological evaluation of novel N-(piperazin-1-yl)alkyl-1H-dibenzo[a,c]carbazole derivatives of dehydroabietic acid as potential MEK inhibitors. *J. Enzym. Inhib. Med. Chem.* **2019**, *34*, 1544–1561. [CrossRef]
39. Davies, U.R.; Interthal, H.; Champoux, J.J.; Hol, W.G.J. The crystal structure of human tyrosyl-DNA phosphodiesterase, Tdp1. *Structure* **2002**, *10*, 237–248. [CrossRef]
40. Gajewski, S.; Comeaux, E.Q.; Jafari, N.; Bharatham, N.; Bashford, D.; White, S.W.; Van Waardenburg, R.C. Analysis of the Active-Site Mechanism of Tyrosyl-DNA Phosphodiesterase I: A Member of the Phospholipase D Superfamily. *J. Mol. Biol.* **2012**, *415*, 741–758. [CrossRef]
41. DeYonker, N.J.; Webster, C.E. A Theoretical Study of Phosphoryl Transfers of Tyrosyl-DNA Phosphodiesterase I (Tdp1) and the Possibility of a “Dead-End” Phosphohistidine Intermediate. *Biochemistry* **2015**, *54*, 4236–4247. [CrossRef] [PubMed]
42. Comeaux, E.Q.; Van Waardenburg, R.C.A.M. Tyrosyl-DNA phosphodiesterase I resolves both naturally and chemically induced DNA adducts and its potential as a therapeutic target. *Drug Metab. Rev.* **2014**, *46*, 494–507. [CrossRef] [PubMed]
43. Pommier, Y.; Leo, E.; Zhang, H.; Marchand, C. DNA Topoisomerases and Their Poisoning by Anticancer and Antibacterial Drugs. *Chem. Biol.* **2010**, *17*, 421–433. [CrossRef]
44. Fujita, K.I.; Kubota, Y.; Ishida, H.; Sasaki, Y. Irinotecan, a key chemotherapeutic drug for metastatic colorectal cancer. *World J. Gastroenterol.* **2015**, *21*, 12234–12248. [CrossRef] [PubMed]
45. Lebedeva, N.A.; Rechkunova, N.I.; Lavrik, O.I. AP-site cleavage activity of tyrosyl-DNA phosphodiesterase 1. *FEBS Lett.* **2011**, *585*, 683–686. [CrossRef]
46. Davies, D.R.; Interthal, H.; Champoux, J.J.; Hol, W.G. Crystal Structure of a Transition State Mimic for Tdp1 Assembled from Vanadate, DNA, and a Topoisomerase I-Derived Peptide. *Chem. Biol.* **2003**, *10*, 139–147. [CrossRef]
47. Zakharenko, A.; Luzina, O.; Koval, O.; Nilov, D.; Gushchina, I.; Dyrkheeva, N.; Švedas, V.; Salakhutdinov, N.; Lavrik, O. Tyrosyl-DNA Phosphodiesterase 1 Inhibitors: Usnic Acid Enamines Enhance the Cytotoxic Effect of Camptothecin. *J. Nat. Prod.* **2016**, *79*, 2961–2967. [CrossRef] [PubMed]
48. Gushchina, I.V.; Nilov, D.K.; Zakharenko, A.L.; Lavrik, O.I.; Švedas, V.K. Structure Modeling of Human TyrosylDNA Phosphodiesterase 1 and Screening for Its Inhibitors. *Acta Nat.* **2017**, *9*, 59–66. [CrossRef]
49. Stroganov, O.V.; Novikov, F.N.; Stroylov, V.S.; Kulkov, V.; Chilov, G.G. Lead Finder: An Approach To Improve Accuracy of Protein-Ligand Docking, Binding Energy Estimation, and Virtual Screening. *J. Chem. Inf. Model.* **2008**, *48*, 2371–2385. [CrossRef] [PubMed]
50. Novikov, F.N.; Stroylov, V.S.; Zeifman, A.A.; Stroganov, O.V.; Kulkov, V.; Chilov, G.G. Lead Finder docking and virtual screening evaluation with Astex and DUD test sets. *J. Comput. Mol. Des.* **2012**, *26*, 725–735. [CrossRef] [PubMed]
51. Humphrey, W.; Dalke, A.; Schulten, K. VMD: Visual molecular dynamics. *J. Mol. Graph.* **1996**, *14*, 33–38. [CrossRef]





Review

# Mucin1 and Mucin16: Therapeutic Targets for Cancer Therapy

Dong-Hee Lee <sup>1</sup>, Seunghyun Choi <sup>2</sup>, Yoon Park <sup>2,\*</sup> and Hyung-seung Jin <sup>1,\*</sup>

<sup>1</sup> Department of Convergence Medicine, Asan Institute for Life Sciences, Asan Medical Center, University of Ulsan College of Medicine, Seoul 05505, Korea; dhlee3342@gmail.com

<sup>2</sup> Center for Theragnosis, Biomedical Research Institute, Korea Institute of Science and Technology (KIST), Seoul 02792, Korea; 221508@kist.re.kr

\* Correspondence: ypark@kist.re.kr (Y.P.); hsjin@amc.seoul.kr (H.-s.J.)

**Abstract:** The mucin (MUC) family is a group of highly glycosylated macromolecules that are abundantly expressed in mammalian epithelial cells. MUC proteins contribute to the formation of the mucus barrier and thus have protective functions against infection. Interestingly, some MUC proteins are aberrantly expressed in cancer cells and are involved in cancer development and progression, including cell growth, proliferation, the inhibition of apoptosis, chemoresistance, metabolic reprogramming, and immune evasion. With their unique biological and structural features, MUC proteins have been considered promising therapeutic targets and also biomarkers for human cancer. In this review, we discuss the biological roles of the transmembrane mucins MUC1 and MUC16 in the context of hallmarks of cancer and current efforts to develop MUC1- and MUC16-targeted therapies.

**Keywords:** mucin; MUC1; MUC16; immunotherapy; cancer vaccine; CAR (chimeric antigen receptor); ADC (antibody-drug conjugate)

**Citation:** Lee, D.-H.; Choi, S.; Park, Y.; Jin, H.-s. Mucin1 and Mucin16: Therapeutic Targets for Cancer Therapy. *Pharmaceuticals* **2021**, *14*, 1053. <https://doi.org/10.3390/ph14101053>

Academic Editors: Mary J. Meegan and Niamh M O'Boyle

Received: 29 September 2021

Accepted: 14 October 2021

Published: 17 October 2021

**Publisher's Note:** MDPI stays neutral with regard to jurisdictional claims in published maps and institutional affiliations.



**Copyright:** © 2021 by the authors. Licensee MDPI, Basel, Switzerland. This article is an open access article distributed under the terms and conditions of the Creative Commons Attribution (CC BY) license (<https://creativecommons.org/licenses/by/4.0/>).

## 1. Introduction

Mucins are large and highly glycosylated proteins that provide hydration and lubrication to the epithelial luminal surface of body duct, including the gastrointestinal, respiratory, and reproductive tracts. Mucins also act as a physical barrier against various pathogens in the epithelium [1,2]. Mucins are classified into two types: secreted or transmembrane (membrane-bound) mucins. Secreted mucins are comprised of gel-forming and non-gel-forming mucins, and include MUC2, MUC5AC, MUC5B, MUC6, MUC7, MUC8, MUC9 (OVGP1), and MUC19. Transmembrane mucins, comprising a single membrane-spanning domain and a cytoplasmic domain, have been identified as MUC1, MUC3A, MUC3B, MUC4, MUC12, MUC13, MUC14 (endomucin), MUC15, MUC16, MUC17, MUC20, MUC21 (epiglycanin), and MUC22 [3,4].

MUC1 was the first mucin to be identified [5]. After its initial identification in human pancreatic cancer [6,7], MUC1 expression has been detected in most epithelial cells [8]. In addition, it has been reported that MUC1 is overexpressed in a variety of cancer tissues including in pancreatic, breast, ovarian, lung, and colon carcinomas [9]. The aberrant expression of MUC1 can induce a loss of polarity of epithelial cells and altered downstream signals through its cytoplasmic domain [2,10]. Ectopically expressed MUC1 in rat fibroblasts induces their cellular transformation and tumor formation in the mouse [11]. In addition, a series of findings have indicated that MUC1 is an attractive target for anti-cancer treatment [12–15].

MUC16 (also known as carbohydrate antigen 125, CA125) is the largest transmembrane mucin and is normally expressed in the epithelium of the upper respiratory tract, ocular surface, mesothelium lining body cavities (pleural, peritoneal, and pelvic cavities), internal organs, and male and female reproductive organs [16–18]. Since MUC16 is known to be overexpressed on the surface of ovarian cancer cells and cleaved/shed into blood,



it is a well-established serum biomarker for ovarian cancer [19]. Even though signaling pathways via the MUC16 cytoplasmic domain are largely unknown, a strong correlation between the serum CA125/MUC16 level and ovarian cancer prognosis also suggests that MUC16 is a potential therapeutic target for the treatment of ovarian cancer [20].

A variety of therapeutic agents have been explored to target onco-mucins for cancer treatment. The extracellular domain of membrane-bound mucins on the surface of cancer cells can be a potential target for monoclonal antibody-based cancer therapeutics [21,22]. It is also feasible to modulate signaling pathways directly through the cytoplasmic domain of mucins or to boost the host immune reaction against tumor via vaccinations with mucin antigens [22]. The purpose of this review is to summarize both intrinsic and extrinsic roles of MUC1 and MUC16 in modulating tumorigenesis and the recent advances made in exploiting the therapeutic potential of these transmembrane mucins.

## 2. Transmembrane Mucin Structure

### 2.1. Core Structural Characteristics

Transmembrane mucins are type I membrane proteins with a single membrane span. Their N-terminal extracellular region comprises a tandem-repeat (TR) domain, SEA (sea urchin sperm protein enterokinase and agrin) domain, and/or an EGF (epidermal growth factor)-like domain [2]. The TR domain contains a variable number of repeated amino acid sequences and is rich in serine, threonine, and proline (S/T/P). These S/T/P residues are the sites for O-linked N-acetylgalactosamine (GalNAc) addition to initiate further N-linked glycosylation chain reactions [23]. The TR domain underlies the physical and chemical features of these molecules, such as lubrication or immune protection, due to its highly glycosylated structure. The SEA domain has a highly conserved cleavage site located close to the outside of the cell membrane. Proteolytic cleavage of transmembrane mucins divides them into an N-terminal subunit containing an extracellular TR and C-terminal subunit harboring the transmembrane and cytoplasmic domains. These two subunits can form a non-covalent and stable complex [10]. The EGF-like domain shares sequence homology with growth factors such as EGF or cytokines and interacts with growth factor receptors such as the ErbB receptor [24]. The cytoplasmic domain of transmembrane mucins is relatively short. Due to the presence of known protein-binding motifs and tyrosine residues for phosphorylation, this domain is considered to have a role in signal transduction. The specific structures of MUC1 and MUC16 are described below in more detail.

### 2.2. Structure of MUC1

MUC1, also known as EMA (tumor-associated epithelial membrane antigen) or CD227, is a large, glycosylated protein with expected molecular weights ranging from 120 to 500 kDa, depending on the glycosylation status. A variable number tandem repeat (VNTR) domain in MUC1 consists of 20–125 repeats of a 20 amino acid sequence (PAPGSTAPPAHGVTSAPDTR). MUC1 also contains a 110 amino acid long single SEA, short transmembrane region, and 74 amino acids of cytoplasmic region (Figure 1A). Its cytoplasmic domain has several short (4–9 amino acid long) protein-binding motifs that facilitate its interaction with GSK3 $\beta$  (glycogen synthase kinase 3 beta),  $\beta$ -catenin, GRB2 (growth factor receptor-bound protein 2), SRC, and ESR1 (estrogen receptor 1) [25–30]. It also possesses a p53 binding region, which is a relatively long 37 amino acid sequence [31]. MUC1 has several isoforms, some of which do not have TR regions, such as the J13 or Y variants [32–34].

### 2.3. Structure of MUC16

MUC16 is the largest transmembrane mucin and comprises ~14,000 amino acids with molecular weights ranging from 1.5 to 5 MDa. MUC16 contains three major domains: an N-terminal domain (MUC16-N), a tandem repeat domain (MUC16-TR), and a C-terminal domain (MUC16-C) (Figure 1B). Its N-terminal domain contains multiple serine-rich regions inside of a ~12,000 amino acid long threonine-rich region, which is

exclusively *O*-glycosylated. The TR domain contains 12~60 repeats of 156 amino acids with an interspersed SEA domain, which harbors both *O*-linked and *N*-linked glycosylation sites [35]. Unlike MUC1, MUC16 has been known to contain 16 SEA modules [36]. The C-terminal domain of MUC16 comprises an extracellular domain, short transmembrane region, and a 32 amino acid cytoplasmic domain. The cytoplasmic domain of MUC16 contains a polybasic amino acid motif (RRRKK) that associates with ezrin/radixin/moesin (ERM) actin-binding proteins [37]. The MUC16 cytoplasmic domain also contains several serine/threonine/tyrosine residues; the third tyrosine residue of the cytoplasmic domain is known to be phosphorylated by *c*-Src kinase [35,38].

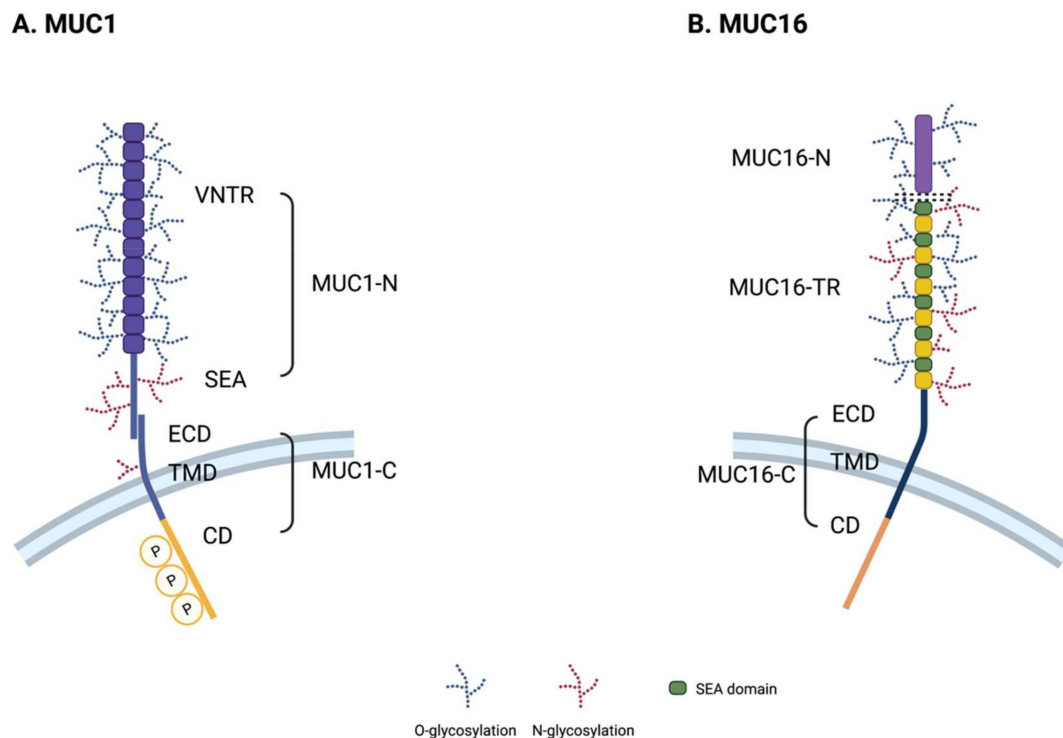


**Figure 1.** Schematic representation of the MUC1 and MUC16 structures. **(A)** MUC1 is a stable heterodimeric complex with an N-terminal subunit (MUC1-N) and C-terminal subunit (MUC1-C). The variable number tandem repeat (VNTR) region in MUC1-N is composed of a 20 amino acid repeat sequence that is extensively *O*-glycosylated at the serine and threonine residues. SEA domain is auto-cleaved and non-covalently linked to the extracellular domain (ECD) of the MUC1-C subunit. MUC1-C is anchored in the plasma membrane of cells via its transmembrane domain (TMD). The cytoplasmic domain (CD) of MUC1 contains potential binding motifs for various signaling proteins with phosphorylation sites. **(B)** MUC16 is a single transmembrane glycoprotein consisting of a large N-terminal domain (MUC16-N) and tandem repeat domain (MUC16-TR) that is interspersed with an SEA domain and C-terminal domain (MUC16-C).

### 3. The Role of Transmembrane Mucins in Tumorigenesis

Transmembrane mucins have long been considered promising anti-cancer targets because they are abnormally overexpressed in various carcinomas of the lung [39–41], breast [42–44], pancreas [45–47], digestive tract [48–51], and ovary [52,53]. Among the transmembrane mucin family, MUC1 and MUC16 are the most well-studied in terms of their clinical significance in tumorigenesis. To determine differences of *MUC1* and *MUC16* expression in tumor and normal tissues, the *MUC1* and *MUC16* mRNA levels in multiple types of tumor tissues were analyzed in the cancer genomics database TCGA (The Cancer Genome Atlas) (Figure 2). *MUC1* expression was higher in BRCA (breast invasive carcinoma), CESC (cervical squamous cell carcinoma and endocervical adenocarcinoma), GBM (glioblastoma), LGG (brain lower grade glioma), DLBC (lymphoid neoplasm diffuse large B-cell lymphoma), PAAD (pancreatic adenocarcinoma), OV (ovarian serous cystadenocar-

cinoma), THYM (thymoma), and UCEC (uterine corpus endometrial carcinoma) compared with adjacent normal tissues. On the contrary, lower expression was observed in ACC (adrenocortical carcinoma), KIRC (kidney renal clear cell carcinoma), KIRP (kidney renal papillary cell carcinoma), LAML (acute myeloid leukemia), LUSC (lung squamous cell carcinoma), SKCM (skin cutaneous melanoma), and TGCT (testicular germ cell tumors). *MUC16* expression was significantly higher in the LUAD (lung adenocarcinoma), OV, PAAD, UCEC, and UCS (uterine carcinosarcoma) compared with adjacent normal tissues.

Tumorigenesis is a complex process involving a variety of events inside and outside of transformed cells. Abnormal alterations of these biological events are well-characterized as “hallmarks of cancer” [54]. Although each hallmark of cancer is initiated by a specific gene, some genes are known as multifunctional master regulators of several hallmarks. Many reports have suggested that transmembrane mucins may play multiple roles in tumorigenesis and tumor progression. We here summarize the detailed tumorigenic roles of *MUC1* and *MUC16* in the context of cancer hallmarks.

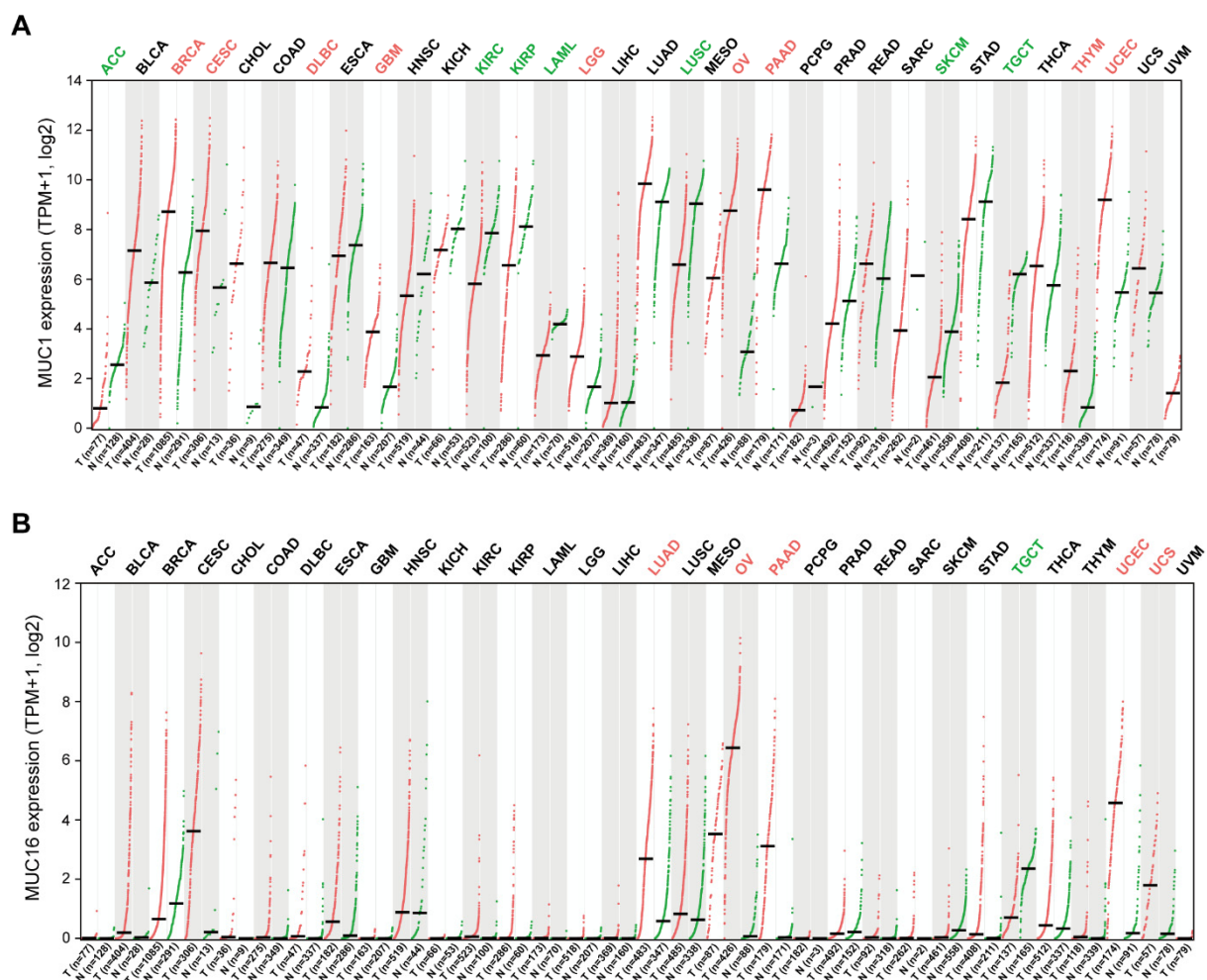


**Figure 2.** *MUC1* and *MUC16* mRNA expression in tumor and normal tissues. Pan-cancer expression analysis of *MUC1* and *MUC16* genes was conducted using the GEPIA2 web server [55]. Tumor tissues (T, red dots) represent TCGA tumors. Normal tissues (N, green dots) represent TCGA and GTEx normal tissues. Expression values are presented as log-normalized transcripts per million (TPM) with median values (horizontal black bar). The red and green colors of the cancer type abbreviations denote that *MUC1* or *MUC16* gene expression is significantly higher or lower in these tumor tissues compared with normal tissues. (A) *MUC1* is overexpressed in tumors of the breast (BRCA), cervix (CESC), brain (GBM, LGG), B-cell (DLBC), pancreas (PAAD), ovary (OV), thymus (THYM), and uterus (UCEC). (B) *MUC16* is overexpressed in tumors of the lung (LUAD), ovary (OV), pancreas (PAAD), and uterus (UCEC and UCS).

### 3.1. Uncontrolled Proliferation

One of the essential hallmarks of cancer cells is an unlimited proliferative potential sustained by abnormal growth signaling pathways. Constitutive activation of growth factor signaling is conferred by oncogenic mutations or by the overexpression of receptor tyrosine kinases (RTKs), followed by protein–protein interactions that transmit downstream signals [56]. The cytoplasmic domain of MUC1 has several protein-binding motifs and phosphorylation sites that are important for protein–protein interactions. RTKs are known to interact directly with MUC1 for oncogenic signaling. ErbB is a family of RTKs consisting of ErbB1 (also known as EGF receptor), ErbB2 (also known as HER2/Neu), ErbB3, and ErbB4. MUC1 interacts with all of the ErbB family receptors to transmit oncogenic signaling reciprocally. The cytoplasmic domain of MUC1 was found in breast cancer cell lines to be phosphorylated by ErbB1 at the YEKV motif, resulting in c-Src and  $\beta$ -catenin recruitment and downstream signaling [57]. Reciprocally, MUC1 also potentiates ErbB signaling. The increased expression of MUC1 activates MAPK signaling through a physical interaction with ErbB1 and inhibition of ErbB1 degradation in breast cancer cells [58,59]. MUC1 also binds to fibroblast growth factor receptor 3 (FGFR3), another key RTK in tumorigenesis. Upon FGF1 ligand stimulation, FGFR3 interacts with MUC1 and phosphorylates the YEKV motif of the MUC1 cytoplasmic domain. This phosphorylated MUC1 forms a complex with  $\beta$ -catenin and translocates into the nucleus [60]. MUC1 also increases cytosolic  $\beta$ -catenin levels by inhibiting GSK3 $\beta$ -mediated phosphorylation and degradation. A serine-rich motif (SRM) of MUC1 interacts directly with the Armadillo repeats of  $\beta$ -catenin [61].

Estrogen receptor alpha (ER $\alpha$ ) is a nuclear receptor that acts as an oncogene in a specific type of hormone-dependent (ER+) breast cancer. The nuclear localization and dimerization of ER $\alpha$  by estrogen stimuli activates the transcription of genes that contain an estrogen response element (ERE) within their regulatory regions. MUC1 interacts with the DNA-binding domain of ER $\alpha$  directly and thereby stabilizes ER $\alpha$  by blocking proteasomal degradation, resulting in enhanced ER $\alpha$  response gene transcription and the proliferation of breast cancer cells [29].

### 3.2. Evading Cell Death and Resistance to Stress

Another important hallmark of cancer is resistance to apoptotic cell death. Fast proliferating cancer cells face various stress conditions arising from internal (e.g., DNA replication, protein translation and degradation, and mitochondrial respiration) or external (e.g., tumor microenvironment and anti-cancer drugs) factors. Cellular stress pathways usually accompany apoptotic signals to eliminate damaged or transformed cells. Cancer cells evade stress-induced apoptosis through various mechanisms, and MUC1 has a protective role that contributes to this survival. First, MUC1 attenuates the genotoxic stress induced by DNA damage from DNA replication mechanisms or the actions of anti-cancer drugs. MUC1 regulates p53-dependent gene transcription through its direct association with the p53 regulatory domain and p53-responsive element. Upon treatment of cancer cells with DNA damage inducing agents (e.g., cisplatin and etoposide), MUC1 promotes transcription of growth arrest genes and suppresses p53-dependent apoptotic genes, thereby promoting the survival of these cells upon exposure to anti-cancer agents [31]. On the other hand, MUC1 directly exploits the drug efflux system through the transcription of multidrug resistance (MDR) genes, which has been reported to protect both lung and pancreatic cancer cells from chemotherapeutics [62,63].

MUC1 attenuates mitochondrial apoptotic factors such as cytochrome c or Bcl-xL (B-cell lymphoma-extra-large), protecting cancer cells from anti-cancer genotoxins such as cytarabine, gemcitabine, and cisplatin [64,65]. Upon genotoxic stress, c-Abl combined with 14-3-3 protein localizes in the nucleus where it activates the proapoptotic c-Jun N-terminal kinase (JNK) pathway [66]. MUC1 blocks this nuclear translocation of the c-Abl protein and thereby inhibits the apoptotic response to genotoxic anti-cancer drugs [67]. The constitutive activation of the NF- $\kappa$ B pathway is another anti-apoptotic mechanism activated

by genotoxic stress. Oncogenic MUC1 promotes the phosphorylation and degradation of I $\kappa$ B $\alpha$  via an association with IKK $\beta$  and IKK $\gamma$  [68].

MUC1 provides survival advantage to cancer cells by scavenging oxidative stress. MUC1 dephosphorylates and activates FOXO3a, which is tightly regulated by the PI3K/AKT pathway. FOXO3a activation induces its nuclear localization and the subsequent transcription activation of ROS scavenging genes. The stable downregulation of MUC1 has been shown to increase the intracellular ROS levels and sensitize breast cancer cells to ROS-induced necrosis [69].

Cancer cells are exposed to Fas (CD95/APO-1) and the Fas ligand (FasL) mediated apoptosis pathway when engaged by tumor-killing lymphocytes. The MUC1 cytoplasmic domain binds to Fas-associated death domain (FADD) and regulates FADD-induced caspase-8 activation. Hence, MUC1-high expressing cancer cells can evade the extrinsic apoptosis pathway [70].

MUC16 is also known to play an anti-apoptotic role in cancer cells. The ectopic expression of the c-terminal domain of MUC16 induces cisplatin resistance in ovarian cancer cells [71]. Lakshmanan et al. have also previously demonstrated a chemoresistant role of MUC16 in lung cancer cells that is mediated through the suppression of p53 [72]. Although its binding partners and precise molecular mechanisms underlying the resistance phenotypes are still unknown, the cytoplasmic domain of MUC16 is believed to have a signaling role that is comparable to MUC1.

### 3.3. Reprogramming Energy Metabolism

Since aerobic glycolysis was proposed as a unique glucose metabolic process in cancer, reprogramming pathways for acquiring nutrients and their subsequent metabolism are also an accepted cancer hallmark [54,73]. The altered expression of mucins in various cancer tissues is additionally suggested as a mediator of this reprogramming of energy metabolism. Chaika et al. demonstrated in an earlier study that MUC1 increases the glucose metabolism levels in pancreatic cancer. MUC1 overexpression also showed an association with increased glucose uptake, and with HIF-1 $\alpha$ , GLUT1, and LDHA protein expression, in an orthotopic mouse model of pancreatic cancer. MUC1, together with HIF-1 $\alpha$ , binds to the hypoxia response element (HRE) in the promoter region of the key glycolysis enzymes *ENO1* and *PGM2*. Furthermore, a prior metabolomics study has illustrated a global metabolic shift, including amino acid metabolism and the TCA cycle, as well as glycolysis, in MUC1-overexpressing pancreatic cells [74]. MUC16 also has a similar role in metabolic reprogramming in pancreatic cancer through the mTOR (mammalian target of rapamycin) and c-MYC pathways [75]. Another study has suggested a role of the cytoplasmic domain of MUC1 in these processes. Rat fibroblasts transformed via the ectopic expression of MUC1 show altered glucose uptake and lactate production. MUC1 stimulates pyruvate kinase M2 (PKM2), a key mediator of anaerobic glycolysis, through a direct association [76]. MUC1 also contributes to altering the pentose phosphate pathway (PPP) and the nucleotide metabolism of pancreatic cancer cells. Inducing sufficient DNA damage is necessary to kill cancer cells during radiation therapy. However, cancer cells can be protected from DNA damage stress by an upregulated PPP and stronger nucleotide metabolism to secure a larger nucleotide pool [77]. High MUC1 expression also reduces cancer cell sensitivity to radiation in vitro and in vivo. This resistance is reverted by inhibiting glycolysis and the PPP with 3-bromopyruvate (BrPA) and 6-amino nicotinamide (6AN), respectively [78].

Altered lipid metabolism is also associated with cancer progression. Since cancer cells use lipids as signaling molecules as well as building blocks or an energy source, altered lipid metabolism is observed in the pathogenesis of cancer [79]. Pitroda et al. proposed a 38-gene set, designated as MLMS (MUC1-induced lipid metabolism signature), that consists of differentially expressed genes associated with lipid metabolism in MUC1-transformed 3Y1 cells. The MLMS contains genes involved in cholesterol metabolism, lipid transport, and fatty acid synthesis. MLMS overexpression is associated with a poor prognosis in tamoxifen-treated breast cancer patients, suggesting that altered lipid metabolism may

induce tamoxifen resistance [80]. MLMS gene expression patterns are correlated with ER-dependent gene expression, as MUC1 binds to the ERE in association with ER $\alpha$  [29].

#### 3.4. EMT and Metastasis

Invasion and metastasis are closely related to a poor prognosis in cancer patients. The epithelial–mesenchymal transition (EMT) is the first stage in cancer cell movement, which is represented by a loss of cell polarity. Along with the concurrent phenotypic changes, the molecular mechanisms underlying EMT have been well-studied [81]. Recently, a series of studies has lent support to the role of the mucins in the EMT in breast and pancreatic cancers. Analyses of MUC1-overexpressing cells and knockout mouse models have demonstrated that the EMT process is strongly affected by MUC1 in pancreatic cancer. As an example of this, the EMT is blocked when all tyrosine residues in the MUC1 cytoplasmic domain are substituted for phenylalanine. This MUC1 mutant cannot bind to  $\beta$ -catenin and therefore fails to translocate to the nucleus to promote the transcription of EMT genes [82]. Grover et al. have reported similar findings—i.e., that the tyrosine residues of the MUC1 cytoplasmic domain are important for TGF- $\beta$ -induced EMT in pancreatic cancer [83]. The direct association of MUC1 to TWIST1 and ZEB1 (zinc-finger E-box-binding homeobox 1) has also been shown to regulate the EMT process in breast cancer when two major immune-related signal pathways are activated—i.e., STAT3 (signal transducer and activator of transcription 3) and NF- $\kappa$ B, respectively [84,85].

MUC16 is also a mediator of EMT in pancreatic cancer, and its knockdown results in a decreased migration of cancer cells *in vitro* and reduced metastasis *in vivo*. Indeed, the recently described interaction between MUC16 and FAK is suggested as a mechanism of pancreatic cancer metastasis [86]. Lakshmanan et al. have demonstrated that MUC16 is expressed in the metastatic lymph nodes of lung cancer patients. A MUC16 knockdown also markedly decreases lung cancer cell migration via JAK2/STAT3/GR (glucocorticoid receptor)-mediated TSPYL5 (testis-specific protein Y-encoded-like 5) downregulation [72].

#### 3.5. Avoiding Immune Surveillance

The host immune system continuously eliminates newly transformed cancerous cells by recognizing tumor-specific antigens or cellular stress-induced markers [87]. This process, referred to as “immune surveillance”, is a major hurdle to be overcome by cancer cells for their propagation [88]. Since mucins expressed in normal epithelial tracts have an important role in mucosal immunity against bacterial infection, cancer-associated mucins have been thought to modulate cancer immunity. Mucins engage several strategies to avoid host immunity, including (1) blocking the interaction between immune cells and cancer cells, (2) modulating immune cell signaling via co-stimulatory or co-inhibitory molecules, and (3) regulating proinflammatory cytokine production. Because of the large and glycosylated structure of their extracellular region, mucin proteins have an inhibitory role against cell–cell interactions [89,90].

Immune cell infiltration analysis of TCGA samples has indicated a strong negative correlation between mucin mRNA expression and cytotoxic lymphocyte infiltration of a tumor (Figures 2 and 3) [91]. The infiltration of CD8+ T cells was indicated to be significantly lower in MUC1-high tumors (BRCA, GBM, LGG, PAAD, THYM, and UCEC) and MUC16-high ovarian cancer, which was assessed by several prediction algorithms. Low NK cell infiltration was also predicted by MUC1-high BRCA, GBM, LGG, and UCEC, but this correlation was found to be relatively weaker than that for CD8+ T cell infiltration (Figure 3). Although the mechanism of reduced T or NK infiltration of mucin-high tumors is not yet fully elucidated, several studies have reported immune suppression mechanisms that support these aforementioned results.

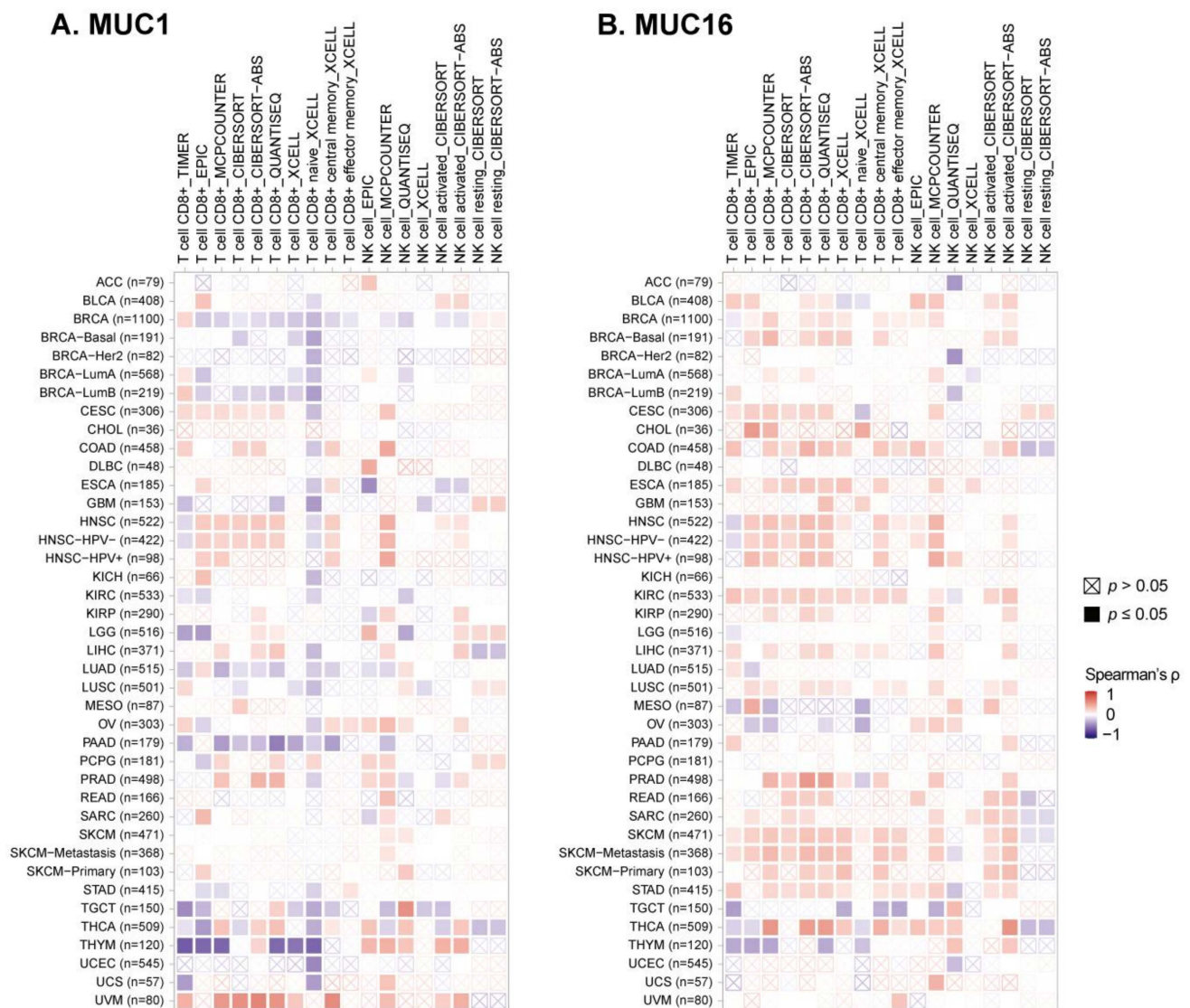


**Figure 3.** Correlation between mucin expression and tumor-infiltrating T and NK cells. Tumor infiltration analysis of CD8+ T cells and NK cells was conducted using the TIMER2.0 web portal [91]. The row names in the heatmap represent the TCGA tumor types and number of samples analyzed. Various deconvolution methods were applied to the prediction of tumor-infiltrating immune cells using TCGA bulk RNAseq data. The deconvolution methods are indicated by the column names, along with the type of lymphocyte, i.e., TIMER [92], EPIC [93], MCP-counter [94], CIBERSORT [95], quanTIseq [96] and xCell [97].

Overexpressed MUC1 and MUC4 on the surfaces of cancer cells provide steric hindrance for the conjugation between cancer cells and cytotoxic lymphocytes, resulting in a decreased cancer cell lysis [98,99]. Glycosylated MUC1 on cancer cells directly binds to selectin or siglec family proteins expressed on immune cells including macrophages and suppresses their functions [100–102]. Furthermore, MUC1 plays as an immune checkpoint molecule by binding to intercellular adhesion molecule 1 (ICAM-1) on T cells and inhibiting their functions [103,104]. Cancer-associated MUC1 inhibits dendritic cell (DC) maturation and promotes IL-10<sup>high</sup>IL-12<sup>low</sup> regulatory DC differentiation, which enables tumors to escape immune surveillance [105,106]. MUC1 is also expressed on DCs that contribute to the suppression of immune responses. In MUC1-deficient mice, DCs showed a more activated phenotype with higher expression of co-stimulatory molecules, including CD40, CD80, and CD86, leading to an augmented CD4+ T cell activation [107]. The ovarian cancer antigen MUC16 (CA125) is known to interact with the immune suppressive molecule galectin-1

and with mesothelin on leukocytes [108,109]. Ovarian cancer cell-derived MUC16 induces an attenuated cytotoxic activity of human NK cells with phenotypic alterations [110,111]. MUC1 also plays an intrinsic role in cancer cell immune evasion through its cytoplasmic domain. MUC1 upregulates programmed death-ligand 1 (PD-L1) expression in non-small cell lung cancer (NSCLC), and this is reversed by the MUC1 cytoplasmic domain inhibitor GO-203. The p53/ZEB1 pathway that regulates the transcription of PD-L1, as well as TLR9, IFN- $\gamma$ , MCP-1 (monocyte chemoattractant protein-1), and GM-CSF (granulocyte-macrophage colony-stimulating factor) in cancer cells, is activated by MUC1 [112]. The similar mechanism of PD-L1 upregulation by MUC1 was reported in triple-negative breast cancer (TNBC) [113]. Proinflammatory cytokines are important for boosting the immune response to cancer cells. Reciprocally, these cytokines also stimulate mucin overexpression in various cancer cells. Interleukin-6 (IL-6) and IFN- $\gamma$  activate STAT3 and STAT1 proteins, which bind to the MUC1 promoter region to enhance gene transcription in breast cancer cells [114]. TNF- $\alpha$  and IFN- $\gamma$  increase MUC16 expression in breast, endometrial, and ovarian cancers via NF- $\kappa$ B-mediated transcription regulation [115]. Conversely, MUC1 promotes the expression of proinflammatory cytokines such as IL-6 and TNF- $\alpha$  by binding to their promoter regions, resulting in a feedback loop that promotes chronic inflammation in the malignant microenvironment [116].

#### 4. Targeting Transmembrane Mucins for Cancer Treatment

Many studies have demonstrated that the mucin family of proteins are promising targets for cancer therapeutics. Due to their roles in cancer signal transduction pathways, the signaling pathways of transmembrane mucins may have particular potential in anti-tumor therapy research. The extracellular domain of membrane-bound mucins can also be a good target for antibody-mediated therapies such as neutralizing antibodies, chimeric antigen receptors (CARs), bi-specific T-cell engagers (BiTEs), and antibody–drug conjugates (ADCs). The cancer-specific expression of certain mucin proteins also suggests the possibility of developing a mucin antigen-based cancer vaccine [117]. We describe below the current attempts at developing mucin-targeted cancer therapeutics (Figure 4).

##### 4.1. Therapeutic Targeting of MUC1

MUC1 therapeutic candidates are under development for a variety of cancer types, including both solid and blood cancers (Table 1). The absence of an enzymatic pocket inside the MUC1 protein prevents its targeting by a small molecule inhibitor, but peptide inhibitors and RNA aptamers may be viable options for direct-binding inhibitors of MUC1. GO-203 is a cell-penetrating peptide inhibitor of MUC1 dimerization through its direct binding to the CQCRRK region of the MUC1 cytoplasmic domain [118]. The cytoplasmic domain of MUC1 binds a number of key oncogenic proteins, and a block of the dimerization of MUC1 could have anti-tumor effects through a variety of mechanisms, depending on the cell type. Since AKT-S6K1-eIF4A is one of the main pathways altered by MUC1, GO-203 has anti-tumor potency by blocking the AKT pathway in multiple tumor types, such as colon, esophageal, bladder, and breast [119–122]. GO-203 also shows potential in combination with standard chemotherapies in chemo-resistant cancer cells or hard-to-treat cancer types [121,122]. In TNBC, GO-203 combined with the PARP (poly (ADP-ribose) polymerase) inhibitor olaparib shows anti-cancer potency by blocking MUC1-C-induced epigenetic reprogramming and activating the DNA damage response [123]. In KRAS mutant lung adenocarcinoma, GO-203 suppresses MUC1-induced MYC transcription synergically when combined with the JQ-1 BET inhibitor [124]. GO-203 also shows synergism with lenalidomide and bortezomib against drug-resistant multiple myeloma by regulating TCF4/ $\beta$ -catenin and ER/oxidative stress mechanisms, respectively [125,126]. GO-203 further provides anti-cancer effects against FLT3-mutant leukemia and T cell lymphoma [127,128]. Moreover, in association with the tumor immune microenvironment, GO-203 is known to suppress PD-L1 and induce IFN- $\gamma$  in NSCLC [129].



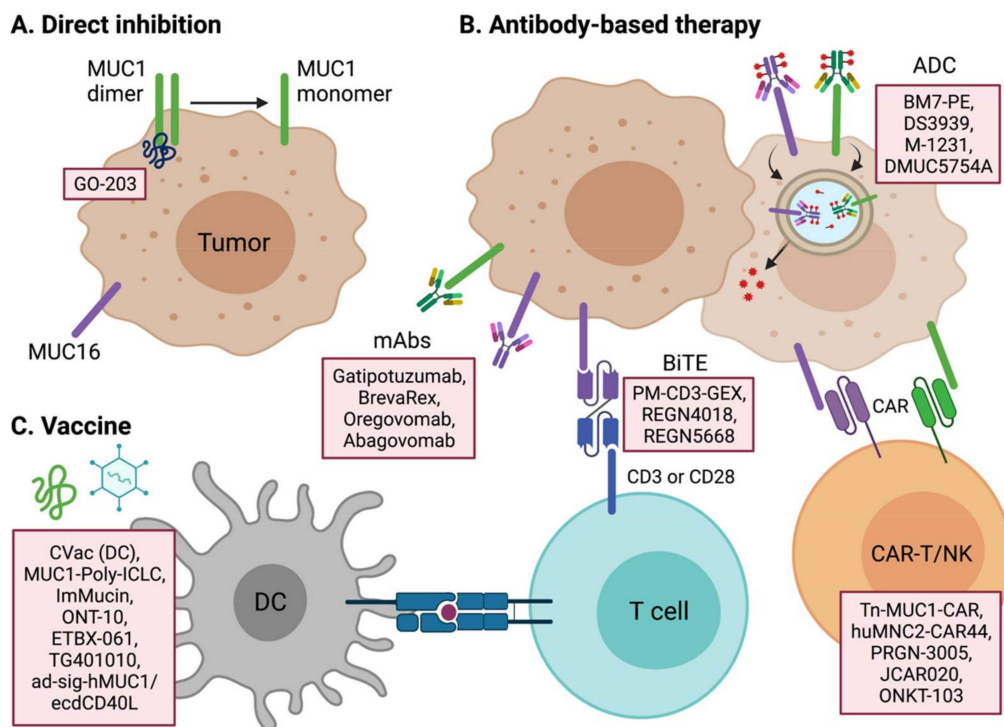


**Figure 4.** Anti-cancer therapeutic candidates that target MUC1 and MUC16. The aberrant expression of MUC1 and MUC16 in tumors provides potential strategies for targeting these molecules to kill cancer cells. (A) The direct MUC1 inhibitor GO-203 is a cell-permeable peptide that binds and blocks MUC1-C. (B) The extracellular domain of mucin in cancer cells is a potential target for monoclonal antibody-based therapies. ADCs dump toxins into cancer cells through the endocytosis of MUC1- and MUC16-binding antibodies. BiTE can recruit CD3+ or CD28+ cytotoxic T lymphocytes to MUC1- or MUC16-overexpressing cancer cells. CAR-T or NK cells directly kill cancer cells by recognizing MUC1 and MUC16 antigens. (C) Cancer vaccines elicit an active immune response by stimulating antigen-presenting cells (e.g., dendritic cells) against mucin protein antigens.

Selective RNA aptamer binding to the extracellular domain of MUC1 is another strategy for targeting MUC1-high cancer cells. Peregelyuk et al. have previously designed MUC1-aptamer-hybrid nanoparticles to deliver anti-tumor microRNAs into MUC1-overexpressing cancer cells. These miRNA-29b-loaded hybrid nanoparticles (MAFMIL-HNs) show anti-tumor effects in a lung cancer mouse model by downregulating DNMT3B (DNA methyltransferase 3 beta), a direct target of the miRNA payload [130]. Furthermore, using a dual payload strategy, geistein-miRNA-29b-biconjugate hybrid nanoparticles (GML-HNs) showed a greater potency than a single payload nanoparticle in a mouse lung cancer model by targeting AKT, PI3K, DNMT3B, and MCL-1 (myeloid cell leukemia-1) [131].

Table 1. Current therapeutic candidates that target MUC1 protein.

Drug Name	Company	Drug Type	Indication	Development Status	Identifiers or References	Recruitment Status	Start Date
Anti-mucin-1 antibodies	University of California Davis	scFv antibody	Cancer				
Mucin-1 inhibitor	Quest PharmaTech	IgE monoclonal antibody	Cancer	Preclinical			
MUC1 inhibitors	Minerva Biotechnologies Corp.	Humanized single chain antibody	Cancer	Discovery			
Yttrium civatuzumab tetraxetan	Garden State Cancer Center	Radio-labeled antibody	Cancer				
Pab-001	Peptron	ADC	Cancer	Preclinical			
DS-3939	Daiichi Sankyo	ADC	Cancer	Preclinical			
SPmAb	Vaxil BioTherapeutics	Monoclonal antibody	Cancer	Preclinical			
BrevaRex	Quest PharmaTech	Anti-idiotype mAb	Multiple Myeloma, Cancer	Phase 2			
BM7-PE	Oslo University Hospital	ADC	Metastatic colorectal cancer	Phase 2	NCT04550897	Recruiting	31 August 2020
Gatipotuzumab (PankoMab-GEX)	Glycotope GmbH	IgG1 antibody	Advanced ovarian cancer	Phase 2	NCT01899599	Completed	September 2013
PM-CD3-GEX	Glycotope GmbH	BiTE	NSCLC, Ovary tumor	Preclinical			
PM-IL15-GEX	Glycotope GmbH	Antibody fused to IL-15	Solid tumor	Preclinical			
PM-PDL-GEX	Glycotope GmbH	Trifunctional antibody (MUC1, PD-L1, and FcγR)	Ovary tumor	Preclinical			
HuMab-Tn	MabVax Therapeutics Holdings	Monoclonal antibody	Cancer	Discovery			
M-1231	EMD Serono; Sutro Biopharma	ADC	Metastatic cancer	Phase 1	NCT04695847	Recruiting	13 January 2021
Anti-CD3/anti-MUC1 BiTE CIK cell therapy	Benhealth Biopharmaceutical (Shenzhen)	BiTE; Cell therapy	Metastatic cancer	Phase 2	NCT03146637	Recruiting	1 May 2017
GO-203-2C	Genus Oncology LLC	Peptide	R/R AML	Phase 2	NCT02204085	Active, not recruiting	September 2014
GO-203-2C	Genus Oncology LLC	Peptide	Solid tumor	Phase 1	NCT01279603	Completed	19 January 2011
Mucin1-aptamer	Thomas Jefferson University	Aptamer	NSCLC	Preclinical			

Table 1. Cont.

Drug Name	Company	Drug Type	Indication	Development Status	Identifiers or References	Recruitment Status	Start Date
rHSP-MUC1 fusion protein	Chengdu Xinlibang Bio-pharmaceutical	Fusion protein	Breast tumor	Phase 1			
P-MUC1C-ALLO1	Poseida Therapeutics	CAR-T	Solid tumor	Preclinical			
P-MUC1C-101	Poseida Therapeutics	CAR-T	Solid tumor	Preclinical			
ICTCAR-052	Innovative Cellular Therapeutics	CAR-T	Breast tumor	Phase 1			
ICTCAR-046	Innovative Cellular Therapeutics	CAR-T	Pancreatic tumor	Phase 1			
ICTCAR-053	Innovative Cellular Therapeutics	CAR-T	Pancreatic tumor	Phase 1			
ICTCAR-043	Innovative Cellular Therapeutics	CAR-T	Breast tumor	Phase 1			
Tn MUC-1 CAR-T	Tmunity Therapeutics	CAR-T	Cancer	Phase 1	NCT04025216	Recruiting	10 October 2019
Anti-MUC1 CAR-T cell therapy (w or w/o) PD-1 knockout T cell	Guangzhou Anjie Biomedical Technology	CAR-T	Metastatic cancer	Phase 2/3	NCT03525782	Recruiting	1 February 2018
MUC-1 pCAR	Leucid Bio	CAR-T	Cancer	Preclinical			
huMNC2-CAR44 T cells	Minerva Biotechnologies Corp.	CAR-T	Cancer	Phase 1	NCT04020575	Recruiting	15 January 2020
Anti-MUC1 CAR-pNK	PersonGen Biomedicine (Suzhou)	CAR-NK	MUC1-positive R/R solid tumor	Phase 2	NCT02839954	Unknown	21 July 2016
Anti-MUC1 CAR-T cell therapy	PersonGen Biomedicine (Suzhou)	CAR-T	MUC1-positive advanced refractory solid tumor	Phase 2	NCT02587689	Unknown	27 October 2015
TAB-28z	OncoTab	CAR-T	Breast tumor	Preclinical			
Anti-MUC-1 CAR-T cell therapy	Baylor College of Medicine	CAR-T	Breast tumor	Preclinical			
ONKT-103	ONK Therapeutics	CAR-NK	Solid tumor	Preclinical			
Anti-MUC1 CAR-T cell therapy + anti-CTLA4 + anti-PD-1 antibodies	Shanghai Cell Therapy Research Institute	CAR-T	MUC1-positive advanced solid tumor	Phase 2	NCT03179007	Unknown	7 June 2017

Recent advances in antibody technology have led to a variety of antibody-based therapeutics, such as ADC, BiTE, and CAR therapies, as well as neutralizing therapeutic antibody approaches. BM7-PE and M-1231 are the leading candidates for MUC1 ADCs in present clinical trials. BM7-PE, developed at Oslo University Hospital, comprises anti-MUC1 antibody BM7, conjugated to pseudomonas exotoxin A (PE). In a preclinical study, BM7-PE has shown anti-metastatic effects and promoted long-term survival in a breast cancer nude rat model [132]. BM7-PE is now in a phase 1/2 clinical trial for metastatic colorectal cancer (NCT04550897). M-1231 is a bispecific antibody–drug conjugate targeting the epidermal growth factor receptor (EGFR) and MUC1, and it is now in a phase 1 clinical trial for various metastatic solid tumors. Pab-001 is the first-in-class therapeutic antibody to target OT-MUC1 (onco-tethered MUC1). The highly glycosylated region of transmembrane MUC1 is prone to cleavage by extracellular matrix proteases. The cleaved MUC1-N subunit is released into the blood, thereby sequestering the anti-MUC1 antibody that recognizes the shed MUC1-N domain. Pab-001 targets the extracellular portion of the cleaved MUC1-C subunit to overcome this drawback [133,134]. Pab-001-MMAE ADC has shown promising results against TNBC and other cancers in various preclinical settings. DS-3939 is a PankoMab-GEX (gatipotuzumab) ADC [135], targeting a tumor-specific mucin carbohydrate–protein epitope (TA-MUC1). Bispecific antibodies using PankoMab are under development. PM-CD3-GEX is a BiTE (bispecific T cell engager), which recruits anti-tumor CD3<sup>+</sup> T cells to MUC1-expressing cancer cells. PM-IL15-GEX is an immunocytokine that combines interleukin-15 with PankoMab-GEX to stimulate anti-tumorigenic NK or T cells. PM-PDL-GEX is a trifunctional antibody targeting MUC1, PD-L1, and FcγR. PD-L1 inhibition and FcγR activation act as an immunostimulant for anti-tumor leukocytes.

After remarkable successes against B cell lymphoma and multiple myeloma, chimeric antigen receptor (CAR) technology is seeking new target molecules for the expansion of its application to solid tumors. Since MUC1 is such a target candidate due to its aberrant expression in various solid tumors, several CAR therapies targeting MUC1 antigen are now under development. It must be noted however that the basal expression of MUC1 in normal tissues can induce significant adverse effects (Figure 2). This has led to new strategies in anti-MUC1 CAR therapies to ensure its safety and efficacy. We below describe recent advances in this regard.

Tn-MUC1 CAR developed by Tmunity Therapeutics is a leading MUC1 CAR-T cell therapy that is currently under phase 1 clinical trial (NCT04025216). Because Tn (GalNAcα1-O-Ser/Thr) is the most prevalent abnormal glycoform found in cancer tissues, the Tn glycoform of MUC1 (Tn-MUC1) is a promising target for CAR therapy. Tn-MUC1 CAR-T has shown anti-tumor potency against T cell lymphomas and pancreatic tumors in a target-specific manner [136]. The MUC-1 pCAR developed by Leucid Bio is a parallel CAR (pCAR) platform that introduces two chimeric antigen receptors side-by-side with different antigen-binding domains and with co-stimulatory domains or cytokine-stimulatory receptors, respectively (WO2020183158). This combination of dual receptors is expected to give T cells more specificity against MUC1-positive tumors and more efficacy than standard CAR-Ts, which have low potency against solid tumors. huMNC2-CAR44 T cells produced by Minerva Biotechnologies Corp are harboring scFv against a cleaved form of MUC1 present on solid cancer cells. huMNC2-CAR44 is in phase 1 clinical trials (NCT04020575) for breast, ovarian, pancreatic, and lung cancer, which are highly MUC1<sup>+</sup>-positive tumor types. NK cells are also considered as good hosts for CAR therapy. ONKT-103 is a MUC1 targeting CAR-NK cell therapy developed by ONK Therapeutics. ONKT-103 maximizes anti-tumor activity by introducing a DR5-TRAIL variant death receptor signaling pathway. TRAIL in NK cells stimulates the DR5 death receptor of cancer cells and leads to FADD-caspase-mediated apoptosis. ONKT-103 is currently at a preclinical stage and is being tested in the targeting of ovarian, breast, and lung cancers.

#### 4.2. Therapeutic Targeting of MUC16 and Other Mucins

Along with MUC1, other membrane-bound mucins have also been considered as potential targets for anti-cancer treatment. We summarize below the various attempts made at targeting MUC16 and other mucins (Table 2).

MUC16 is approved by the FDA for its diagnostic usage [137]. Targeting MUC16 for cancer therapeutics is expected to improve the poor prognosis of ovarian cancer. Oregovomab (OvaRex) is the first monoclonal antibody drug investigated in clinical trials. Oregovomab binds the glycosylated region of MUC16 with high affinity ( $1.16 \times 10^{10}$  /M) and induces indirect immune responses via an anti-idiotypic antibody induction cascade [138]. Oregovomab (Ab<sub>1</sub>) induces anti-oregovomab antibodies (anti-idiotypic antibodies; Ab<sub>2</sub>), which in turn induces anti-anti-idiotypic antibodies (Ab<sub>3</sub>). Ab<sub>3</sub> antibodies recognize the original MUC16 antigen, resulting in immune cell-mediated killing of MUC16-expressing tumor cells. Various clinical trials of this agent have been conducted in different settings for ovarian cancers [139]. Oregovomab has shown very promising results in a phase 2 trial in combination with carboplatin and paclitaxel (CP), as compared with CP only, for 97 patients with stage III/IV ovarian cancer. The progression-free survival (PFS) outcome was 41.8 months for CP plus oregovomab vs. 12.2 for CP only ( $p = 0.0027$ , HR = 0.46, 95% CI = 0.28–0.7) [140]. The co-administration of CP with oregovomab resulted in an increase in MUC16-specific IFN- $\gamma$ <sup>+</sup> CD8<sup>+</sup> T lymphocytes in the peripheral blood, demonstrating the activation of an immune response to oregovomab [141]. However, despite encouraging results from a combination study with standard chemotherapies, oregovomab monotherapy did not show a clinical benefit in phase 2 and phase 3 clinical trials [142,143]. Another phase 3 clinical trial (NCT04498117) of oregovomab is ongoing for newly diagnosed ovarian cancer patients in conjunction with carboplatin and paclitaxel chemotherapy.

Abagovomab is an anti-idiotypic antibody (Ab<sub>2</sub>), generated against the anti-MUC16 antibody OC125 (Ab<sub>1</sub>). Abagovomab induces a specific Ab<sub>3</sub> response, which in turn activates a cellular cytotoxic response against MUC16-expressing cancer cells. As an ovarian cancer vaccine for maintenance therapy, abagovomab has shown very promising results in terms of an immune response and overall survival (OS) improvements (median OS 23.5 vs. 4.9 months;  $p < 0.001$ ) in a phase 1b/2 trial [144]. However, a multicenter phase 3 MIMOSA study of abagovomab involving 888 patients (NCT00418574) failed to confirm these clinical benefits (HR for RFS = 1.099;  $p = 0.301$ , HR for OS = 1.150;  $p = 0.322$ ) [145]. Subsequent analysis of the MIMOSA study findings indicated that abagovomab does not augment MUC16-specific cytotoxic T lymphocytes (CTLs) [146]. A high level of MUC16-specific CTLs was found to be associated with a good prognosis, regardless of abagovomab treatment. Further analysis has suggested that the proportion of IFN- $\gamma$ <sup>+</sup> CD8<sup>+</sup> T cells is a factor determining the clinical benefits of abagovomab and could therefore be a predictive biomarker for this drug [147].

DMUC5754A (RG-7458, sofituzumab vedotin) is an ADC that comprises the humanized anti-MUC16 antibody conjugated to a potent anti-mitotic agent, monomethyl auristatin E (MMAE). A phase 1 study of DMUC5754A was performed for patients with platinum-resistant ovarian cancer (OC) and unresectable pancreatic cancer (PC). Despite the safe profile of DMUC5754A, the response rate was only 17% (5/29; 1 CR; 4 PRs) for the OC cases, with neither CR nor PR observed for any of the PC patients [148]. Regeneron is currently developing MUC16 BiTEs that co-target MUC16-positive cancer and T cells. REGN4018 (MUC16/CD3 BiTE) shows MUC16-dependent anti-tumor potency and good tolerability in both murine and monkey models [149]. REGN4018 is now under phase 2 clinical trials alone and in combination with the PD-1 antibody cemiplimab or with REGN5668 (MUC16/CD28 BiTE) for recurrent ovarian cancer patients (NCT03564340, NCT04590326). JCAR-020, developed by Juno/Celgene/Bristol-Myers Squibb, is a MUC16 CAR-T cell therapy that harbors an interleukin-12 receptor agonist. JCAR-020 is currently under a phase 1 clinical trial (NCT02498912).

Table 2. Current therapeutic candidates that target MUC16 and other membrane-bound mucin proteins.

Drug Name	Company	Drug Type	Indication	Development Status	Identifiers or References	Recruitment Status	Start Date
Mab-AR-9.6	Quest PharmaTech	Monoclonal antibody	Pancreas tumor	Preclinical			
Oregovomab (OvaRex)	Quest PharmaTech	Monoclonal antibody; Anti-idiotype induction therapy	Cancer	Phase 3	NCT04498117	Recruiting	25 August 2020
RG-7458 (DMUC-5754A)	Genentech	ADC	Ovarian cancer, Pancreatic cancer	Discontinued	NCT01335958	Completed	Day, April 2011
RG-7882 (DMUC-4064A)	Genentech	ADC	Ovarian cancer, Pancreatic cancer	Discontinued	NCT02146313	Completed	22 June 2014
EDO-772P	Mundipharma EDO GmbH	ADC	Ovarian cancer				
Abagovomab	Menarini; CellControl Biomedical	Anti-idiotype mAb	Ovarian cancer	Phase 2/3	NCT00418574	Terminated (Failed)	Day, December 2006
NAV-005	Navrogen	IgG1 Fc fusion protein	Cancer	Discovery			
REGN-4018	Regeneron Pharmaceuticals	BiTE (MUC16/CD3)	Ovarian cancer	Phase 2	NCT03564340	Recruiting	21 May 2018
REGN-5668	Regeneron Pharmaceuticals	BiTE (MUC16/CD28)	Ovarian cancer	Phase 2	NCT04590326	Recruiting	9 December 2020
PRGN-3005	Precigen	CAR-T	Ovarian cancer	Phase 1	NCT03907527	Recruiting	30 April 2019
TC-220	TCR2 Therapeutics	CAR-T	Ovarian cancer	Preclinical			
TC-410	TCR2 Therapeutics	CAR-T	Ovarian cancer	Discovery			
Anti-MUC16	Eureka Therapeutics	CAR-T	Solid tumor	Preclinical			
CAR-T/PD-1 scFv	Bristol-Myers Squibb	CAR-T	Cancer	Phase 1	NCT02498912	Active, not recruiting	Day, August 2015
JCAR-020							
Targeting other mucins							
MUC13 antibody	University of Tennessee	Monoclonal antibody	Cancer	Discovery			
AMG-199	Amgen	BiTE (MUC17/CD3)	Stomach cancer, Esophagus cancer	Phase 1	NCT04117958	Recruiting	20 January 2020

In addition to MUC1 and MUC16, other transmembrane mucins have been assessed as potential cancer targets. The aberrant expression and pathogenesis of MUC13 in pancreatic cancer leads to the development of anti-MUC13 antibodies that can be used for diagnostic and therapeutic purposes [150–152]. Amgen is developing a BiTE targeting CD3 and MUC17 for the treatment of gastric and esophageal cancer, and this is now in a phase 1 trial (WO2019133961A1, NCT04117958).

#### 4.3. Tumor Vaccines

Therapeutic cancer vaccines are designed to activate a host's immune system to eradicate cancer cells. The host immune system not only generates antibodies that recognize a specific cancer antigen but also induces a CTL-mediated tumor cell killing. Along with mucin-targeting passive immunotherapies such as the administration of a therapeutic antibody or engineered CTLs, vaccination with mucin antigens has also been vigorously attempted for treating various solid tumors.

CVac are autologous monocyte-derived DCs primed with a mannosylated MUC1 protein. Two phase 2 clinical studies have now been conducted with these cells: one for advanced OC patients with progressive disease after standard chemotherapy [153], and one for maintenance therapy after clinical remission in OC patients [154]. The CVac DC vaccine was found to have adequate safety with minimal adverse effects but failed to increase the PFS compared with standard chemotherapy alone. However, in a sub-group analysis that divided participants into first (CR1) and second clinical remission (CR2) groups, CVac produced a promising improvement in the PFS (HR = 0.32) and OS (HR = 0.17) in the CR2 group. This result however was from a small-sized randomized trial (n = 10 for each group), and a phase 3 clinical trial with a large cohort will be needed to verify this finding.

ImMucin is a 21-mer peptide vaccine comprising the signal peptide domain of the MUC1 protein that binds to various MHC class I and class II alleles [155]. A phase 1/2 study of ImMucin for multiple myeloma with co-administration of GM-CSF demonstrated a safe tolerability of this vaccination, the successful induction of a vaccine-mediated cellular and humoral immune response, and clinical disease control in 11/15 patients (duration: 17.5–41.3 months after study completion) [156].

Dr. Finn and colleagues have also designed a peptide sequence from MUC1 as a tumor vaccine. Direct administration of a 100-mer clinical grade peptide (5 repeats of 20-mer peptide) with adjuvants has shown the tolerability and immunogenicity of this vaccine in phase 1 and phase 2 clinical trials for pancreatic cancer and colon cancer patients [157,158]. This peptide has also been exploited as a MUC1 peptide pulsed autologous DC vaccine for patients with pancreatic and biliary tumors after resection of their primary tumors. In that particular clinical study, 4/12 patients survived without recurrence, with a median survival of 26 months (range, 13–69 months) [159].

ONT-10 is a liposome therapeutic vaccine consisting of two repeats of a 20-mer synthetic glycopeptide from MUC1 combined with pentaerythritol lipid A (PET Lipid A), a TLR4 agonist. A preclinical study of ONT-10 indicated an induction of a cellular and humoral immune response to MUC1 and anti-tumor effects in syngenic B16-MUC1 and MC38-MUC1 models [160]. A phase 1 study of 28 advanced solid cancer patients demonstrated that ONT-10 is safe and well-tolerated, but neither CR nor PR was observed [161]. Recently, a phase 1b study of ONT-10 in combination with varlilumab (anti-CD27 agonistic antibody) was performed in advanced ovarian and breast cancer patients (NCT02270372). Emepepimut-S (also known as Tecemotide or L-BLP25) is another developed peptide vaccine for MUC1. However, in a phase 3 study in NSCLC patients, no significant difference in OS was observed [162].

ETBX-061 is a therapeutic adenovirus vaccine targeting the MUC1 protein. Considering the heterogenous nature of solid tumors, ETBX-061 has been studied in combination with other vaccines or therapeutic agents in clinical trials. A triple (CEA/MUC1/Brachyury) vaccine combination regimen was studied in a phase 1 clinical trial for advanced cancer

patients that confirmed antigen-specific T cell generation and disease control (60% SD and 40% PD) [163]. Other clinical studies with different regimens have also been reported (Table 3). TG4010 is a modified vaccinia Ankara (MVA) expressing MUC1 and interleukin-2. In a phase 2b/3 trial for advanced NSCLC, TG4010 plus chemotherapy produced a significant improvement in the PFS relative to a placebo plus chemotherapy, but the survival benefit was marginal only (5.9 vs. 5.1 months) [164]. MicroVAC LLC is developing an ad-sig-hMUC1/eCdCD40L vaccine in which a fusion protein of MUC1 (TAA; tumor-associated antigen) is combined with the extracellular domain (ECD) of the CD40 ligand (CD40L) to boost DC activation and promote T and B cell expansion [165]. A small cohort phase 1 study of this vaccine has demonstrated that it is safe and has encouraging anti-tumor activity [166]. A phase 1 clinical study is now ongoing with a larger number of patients. Other mucin-targeting vaccines under development are summarized in Table 3.



Table 3. Tumor vaccines that target mucin family proteins.

Drug Name	Company	Drug Type	Indication	Development Status	Identifiers or References	Recruitment Status	Start Date
<i>Mucin-1 vaccines</i>							
Cvac	Sydys/Prima BioMed	Autologous DC vaccine	Ovarian cancer, Colorectal cancer, Triple-negative breast cancer	Phase 2	NCT01068509	Completed	July 2010
MUC1-Poly-ICLC	University of Pittsburgh	Peptide vaccine	Colon cancer, NSCLC	Phase 2	NCT00773097	Completed	October 2008
MUC1-DC-CTL	Beijing Doing Biomedical Technology	DC vaccine; T-cell stimulator	Stomach tumor	Preclinical			
ETBX-061	Etubics Corp	Adenovirus vaccine	Colon cancer	Phase 1/2	NCT03563157	Active, not recruiting	25 May 2018
ImMucin	Vaxil BioTherapeutics	Peptide vaccine	Advanced cancer	Phase 1	NCT03384316	Completed	31 January 2018
Enepepimut-S (Tecemotide/Stimuvax/L- BLP25)	Merck Serono	Liposome-encapsulated peptide vaccine	Hormone refractory prostate cancer	Phase 1	NCT03481816	Completed	24 July 2018
MTI	ViaMune/GeoVax	Peptide vaccine	Breast cancer, Multiple myeloma, Ovary tumor	Phase 2	NCT01232712	Completed	September 2010
GEO-CM01	GeoVax	Modified-vaccina Ankara virus-like particles (MVA-VLP)	Cancer	Phase 3 Discontinued	NCT00409188		
ONT-10	Cascadian Therapeutics	Glycopeptide vaccine	Cancer	Preclinical			
TG4010	Transgene SA	MVA	NSCLC	Phase 1b	NCT02270372	Completed	November 2014
TG4010	Transgene SA	MVA	NSCLC	Phase 2/3 (Suspended)	NCT01388148	Terminated	April 2012
Ad-sig-hMUC-1/ecdCD40L vaccine	MicroVAX LLC	Adenovirus vaccine	NSCLC Cancer	Phase 2	NCT02823990	Active, not recruiting	14 December 2016
GI-6108	NantCell/Ceigene/GlobeImmune	Tarmogen vaccine	Cancer	Phase 1	NCT02140996	Unknown	September 2014
<i>Mucin-16 vaccine</i>							
OvcaVax	Theralink Technologies	CA-125/IL-2/GM-CSF vaccine	Ovary tumor	Preclinical			

## 5. Conclusions and Perspectives

Transmembrane mucins have important functions in maintaining mucosal structure and physiological homeostasis. Mucins are heavily glycosylated proteins that overexpress in different types of cancers. Many efforts have been continued to find new therapeutic strategies for exploiting the overexpression and aberrant glycosylation of some transmembrane mucins. Many therapeutic agents targeting mucins are under different stages of clinical trial for several cancers. These agents include antibody-based therapeutics, small molecule inhibitors, vaccines, and cell therapy. A better understanding of mucin glycoproteins in terms of shedding mechanism, aberrant glycosylation, possible splice variants, oncogenic signaling cascades, and interacting binding partners would be required to develop more effective mucin-based therapeutic strategies.

**Author Contributions:** Conceptualization, D.-H.L., Y.P. and H.-s.J.; writing—original draft preparation and editing, D.-H.L., S.C., Y.P. and H.-s.J.; funding acquisition, Y.P. and H.-s.J. All authors have read and agreed to the published version of the manuscript.

**Funding:** This research was funded by the National Research Foundation of Korea (NRF-2020R1A4A1016695 and NRF-2020M3A9G7103935) and the KIST institutional program.

**Institutional Review Board Statement:** Not applicable.

**Informed Consent Statement:** Not applicable.

**Data Availability Statement:** All data is contained within the article.

**Acknowledgments:** Figures 1 and 4 were created with BioRender.com.

**Conflicts of Interest:** The authors declare no competing financial or other interests in relation to this article.

## References

- Dekker, J.; Rossen, J.W.; Buller, H.A.; Einerhand, A.W. The MUC family: An obituary. *Trends Biochem. Sci.* **2002**, *27*, 126–131. [CrossRef]
- Hollingsworth, M.A.; Swanson, B.J. Mucins in cancer: Protection and control of the cell surface. *Nat. Rev. Cancer* **2004**, *4*, 45–60. [CrossRef]
- Bhatia, R.; Gautam, S.K.; Cannon, A.; Thompson, C.; Hall, B.R.; Aithal, A.; Banerjee, K.; Jain, M.; Solheim, J.C.; Kumar, S.; et al. Cancer-associated mucins: Role in immune modulation and metastasis. *Cancer Metastasis Rev.* **2019**, *38*, 223–236. [CrossRef]
- Dhanisha, S.S.; Guruvayoorappan, C.; Drishya, S.; Abeesh, P. Mucins: Structural diversity, biosynthesis, its role in pathogenesis and as possible therapeutic targets. *Crit. Rev. Oncol. Hematol.* **2018**, *122*, 98–122. [CrossRef]
- Gendler, S.J.; Lancaster, C.A.; Taylor-Papadimitriou, J.; Duhig, T.; Peat, N.; Burchell, J.; Pemberton, L.; Lalani, E.N.; Wilson, D. Molecular cloning and expression of human tumor-associated polymorphic epithelial mucin. *J. Biol. Chem.* **1990**, *265*, 15286–15293. [CrossRef]
- Batra, S.K.; Hollingsworth, M.A. Expression of the human mucin gene, Muc 1, in normal tissues and metastatic pancreatic tumors. *Int. J. Pancreatol.* **1991**, *10*, 287–292. [CrossRef] [PubMed]
- Lan, M.S.; Batra, S.K.; Qi, W.N.; Metzgar, R.S.; Hollingsworth, M.A. Cloning and sequencing of a human pancreatic tumor mucin cDNA. *J. Biol. Chem.* **1990**, *265*, 15294–15299. [CrossRef]
- Patton, S.; Gendler, S.J.; Spicer, A.P. The epithelial mucin, MUC1, of milk, mammary gland and other tissues. *Biochim. Biophys. Acta* **1995**, *1241*, 407–423. [CrossRef]
- Gendler, S.J. MUC1, the renaissance molecule. *J. Mammary Gland Biol. Neoplasia* **2001**, *6*, 339–353. [CrossRef] [PubMed]
- Kufe, D.W. Mucins in cancer: Function, prognosis and therapy. *Nat. Rev. Cancer* **2009**, *9*, 874–885. [CrossRef] [PubMed]
- Li, Y.; Liu, D.; Chen, D.; Kharbanda, S.; Kufe, D. Human DF3/MUC1 carcinoma-associated protein functions as an oncogene. *Oncogene* **2003**, *22*, 6107–6110. [CrossRef] [PubMed]
- Li, Y.; Cozzi, P.J. MUC1 is a promising therapeutic target for prostate cancer therapy. *Curr. Cancer Drug. Targets* **2007**, *7*, 259–271. [CrossRef]
- Joshi, M.D.; Ahmad, R.; Yin, L.; Raina, D.; Rajabi, H.; Bublely, G.; Kharbanda, S.; Kufe, D. MUC1 oncoprotein is a druggable target in human prostate cancer cells. *Mol. Cancer Ther.* **2009**, *8*, 3056–3065. [CrossRef]
- Hu, X.F.; Yang, E.; Li, J.; Xing, P.X. MUC1 cytoplasmic tail: A potential therapeutic target for ovarian carcinoma. *Exp. Rev. Anticancer Ther.* **2006**, *6*, 1261–1271. [CrossRef] [PubMed]
- Kufe, D.W. MUC1-C oncoprotein as a target in breast cancer: Activation of signaling pathways and therapeutic approaches. *Oncogene* **2013**, *32*, 1073–1081. [CrossRef]

16. Zeimet, A.G.; Offner, F.A.; Muller-Holzner, E.; Widschwendter, M.; Abendstein, B.; Fuith, L.C.; Daxenbichler, G.; Marth, C. Peritoneum and tissues of the female reproductive tract as physiological sources of CA-125. *Tumour Biol.* **1998**, *19*, 275–282. [CrossRef] [PubMed]
17. Argueso, P.; Spurr-Michaud, S.; Russo, C.L.; Tisdale, A.; Gipson, I.K. MUC16 mucin is expressed by the human ocular surface epithelia and carries the H185 carbohydrate epitope. *Investig. Ophthalmol. Vis. Sci.* **2003**, *44*, 2487–2495. [CrossRef] [PubMed]
18. Matsuoka, Y.; Endo, K.; Kawamura, Y.; Yoshida, T.; Saga, T.; Watanabe, Y.; Koizumi, M.; Nakashima, T.; Konishi, J.; Yamaguchi, N.; et al. Normal bronchial mucus contains high levels of cancer-associated antigens, CA125, CA19-9, and carcinoembryonic antigen. *Cancer* **1990**, *65*, 506–510. [CrossRef]
19. Bast, R.C., Jr.; Xu, F.J.; Yu, Y.H.; Barnhill, S.; Zhang, Z.; Mills, G.B. CA 125: The past and the future. *Int. J. Biol. Markers* **1998**, *13*, 179–187. [CrossRef] [PubMed]
20. Capstick, V.; Maclean, G.D.; Suresh, M.R.; Bodnar, D.; Lloyd, S.; Shepert, L.; Longenecker, B.M.; Krantz, M. Clinical evaluation of a new two-site assay for CA125 antigen. *Int. J. Biol. Markers* **1991**, *6*, 129–135. [CrossRef] [PubMed]
21. Singh, R.; Samant, U.; Hyland, S.; Chaudhari, P.R.; Wels, W.S.; Bandyopadhyay, D. Target-specific cytotoxic activity of recombinant immunotoxin scFv(MUC1)-ETA on breast carcinoma cells and primary breast tumors. *Mol. Cancer Ther.* **2007**, *6*, 562–569. [CrossRef]
22. Singh, R.; Bandyopadhyay, D. MUC1: A target molecule for cancer therapy. *Cancer Biol. Ther.* **2007**, *6*, 481–486. [CrossRef] [PubMed]
23. Hanisch, F.G. O-glycosylation of the mucin type. *Biol. Chem.* **2001**, *382*, 143–149. [CrossRef] [PubMed]
24. Carraway, K.L., 3rd; Rossi, E.A.; Komatsu, M.; Price-Schiavi, S.A.; Huang, D.; Guy, P.M.; Carvajal, M.E.; Fregien, N.; Carraway, C.A.; Carraway, K.L. An intramembrane modulator of the ErbB2 receptor tyrosine kinase that potentiates neuregulin signaling. *J. Biol. Chem.* **1999**, *274*, 5263–5266. [CrossRef]
25. Al Masri, A.; Gendler, S.J. Muc1 affects c-Src signaling in PyV MT-induced mammary tumorigenesis. *Oncogene* **2005**, *24*, 5799–5808. [CrossRef]
26. Kinlough, C.L.; Poland, P.A.; Bruns, J.B.; Harkleroad, K.L.; Hughey, R.P. MUC1 membrane trafficking is modulated by multiple interactions. *J. Biol. Chem.* **2004**, *279*, 53071–53077. [CrossRef]
27. Li, Y.; Bharti, A.; Chen, D.; Gong, J.; Kufe, D. Interaction of glycogen synthase kinase 3beta with the DF3/MUC1 carcinoma-associated antigen and beta-catenin. *Mol. Cell Biol.* **1998**, *18*, 7216–7224. [CrossRef] [PubMed]
28. Pandey, P.; Kharbanda, S.; Kufe, D. Association of the DF3/MUC1 breast cancer antigen with Grb2 and the Sos/Ras exchange protein. *Cancer Res.* **1995**, *55*, 4000–4003.
29. Wei, X.; Xu, H.; Kufe, D. MUC1 oncoprotein stabilizes and activates estrogen receptor alpha. *Mol. Cell* **2006**, *21*, 295–305. [CrossRef]
30. Yamamoto, M.; Bharti, A.; Li, Y.; Kufe, D. Interaction of the DF3/MUC1 breast carcinoma-associated antigen and beta-catenin in cell adhesion. *J. Biol. Chem.* **1997**, *272*, 12492–12494. [CrossRef]
31. Wei, X.; Xu, H.; Kufe, D. Human MUC1 oncoprotein regulates p53-responsive gene transcription in the genotoxic stress response. *Cancer Cell* **2005**, *7*, 167–178. [CrossRef]
32. Oosterkamp, H.M.; Scheiner, L.; Stefanova, M.C.; Lloyd, K.O.; Finstad, C.L. Comparison of MUC-1 mucin expression in epithelial and non-epithelial cancer cell lines and demonstration of a new short variant form (MUC-1/Z). *Int. J. Cancer* **1997**, *72*, 87–94. [CrossRef]
33. Zrihan-Licht, S.; Vos, H.L.; Baruch, A.; Elroy-Stein, O.; Sagiv, D.; Keydar, I.; Hilkens, J.; Wreschner, D.H. Characterization and molecular cloning of a novel MUC1 protein, devoid of tandem repeats, expressed in human breast cancer tissue. *Eur. J. Biochem.* **1994**, *224*, 787–795. [CrossRef]
34. Zhang, L.; Vlad, A.; Milcarek, C.; Finn, O.J. Human mucin MUC1 RNA undergoes different types of alternative splicing resulting in multiple isoforms. *Cancer Immunol. Immunother.* **2013**, *62*, 423–435. [CrossRef] [PubMed]
35. Haridas, D.; Ponnusamy, M.P.; Chugh, S.; Lakshmanan, I.; Seshacharyulu, P.; Batra, S.K. MUC16: Molecular analysis and its functional implications in benign and malignant conditions. *FASEB J.* **2014**, *28*, 4183–4199. [CrossRef] [PubMed]
36. Duraisamy, S.; Ramasamy, S.; Kharbanda, S.; Kufe, D. Distinct evolution of the human carcinoma-associated transmembrane mucins, MUC1, MUC4 AND MUC16. *Gene* **2006**, *373*, 28–34. [CrossRef] [PubMed]
37. Blalock, T.D.; Spurr-Michaud, S.J.; Tisdale, A.S.; Heimer, S.R.; Gilmore, M.S.; Ramesh, V.; Gipson, I.K. Functions of MUC16 in corneal epithelial cells. *Investig. Ophthalmol. Vis. Sci.* **2007**, *48*, 4509–4518. [CrossRef]
38. Akita, K.; Tanaka, M.; Tanida, S.; Mori, Y.; Toda, M.; Nakada, H. CA125/MUC16 interacts with Src family kinases, and over-expression of its C-terminal fragment in human epithelial cancer cells reduces cell-cell adhesion. *Eur. J. Cell Biol.* **2013**, *92*, 257–263. [CrossRef]
39. Tsutsumida, H.; Goto, M.; Kitajima, S.; Kubota, I.; Hirotsu, Y.; Wakimoto, J.; Batra, S.K.; Imai, K.; Yonezawa, S. MUC4 expression correlates with poor prognosis in small-sized lung adenocarcinoma. *Lung Cancer* **2007**, *55*, 195–203. [CrossRef]
40. Hanaoka, J.; Kontani, K.; Sawai, S.; Ichinose, M.; Tezuka, N.; Inoue, S.; Fujino, S.; Ohkubo, I. Analysis of MUC4 mucin expression in lung carcinoma cells and its immunogenicity. *Cancer* **2001**, *92*, 2148–2157. [CrossRef]
41. Guddo, F.; Giatromanolaki, A.; Koukourakis, M.I.; Reina, C.; Vignola, A.M.; Chlouverakis, G.; Hilkens, J.; Gatter, K.C.; Harris, A.L.; Bonsignore, G. MUC1 (episialin) expression in non-small cell lung cancer is independent of EGFR and c-erbB-2 expression and correlates with poor survival in node positive patients. *J. Clin. Pathol.* **1998**, *51*, 667–671. [CrossRef] [PubMed]

42. Rakha, E.A.; Boyce, R.W.; Abd El-Rehim, D.; Kurien, T.; Green, A.R.; Paish, E.C.; Robertson, J.F.; Ellis, I.O. Expression of mucins (MUC1, MUC2, MUC3, MUC4, MUC5AC and MUC6) and their prognostic significance in human breast cancer. *Mod. Pathol.* **2005**, *18*, 1295–1304. [CrossRef] [PubMed]
43. Hayes, D.F.; Sekine, H.; Ohno, T.; Abe, M.; Keefe, K.; Kufe, D.W. Use of a murine monoclonal antibody for detection of circulating plasma DF3 antigen levels in breast cancer patients. *J. Clin. Investig.* **1985**, *75*, 1671–1678. [CrossRef] [PubMed]
44. Apostolopoulos, V.; McKenzie, I.F. Cellular mucins: Targets for immunotherapy. *Crit. Rev. Immunol.* **1994**, *14*, 293–309. [CrossRef]
45. Choudhury, A.; Moniaux, N.; Winpenny, J.P.; Hollingsworth, M.A.; Aubert, J.P.; Batra, S.K. Human MUC4 mucin cDNA and its variants in pancreatic carcinoma. *J. Biochem.* **2000**, *128*, 233–243. [CrossRef]
46. Balague, C.; Gambus, G.; Carrato, C.; Porchet, N.; Aubert, J.P.; Kim, Y.S.; Real, F.X. Altered expression of MUC2, MUC4, and MUC5 mucin genes in pancreas tissues and cancer cell lines. *Gastroenterology* **1994**, *106*, 1054–1061. [CrossRef]
47. Andrianifahanana, M.; Moniaux, N.; Schmied, B.M.; Ringel, J.; Friess, H.; Hollingsworth, M.A.; Buchler, M.W.; Aubert, J.P.; Batra, S.K. Mucin (MUC) gene expression in human pancreatic adenocarcinoma and chronic pancreatitis: A potential role of MUC4 as a tumor marker of diagnostic significance. *Clin. Cancer Res.* **2001**, *7*, 4033–4040.
48. Wang, R.Q.; Fang, D.C. Alterations of MUC1 and MUC3 expression in gastric carcinoma: Relevance to patient clinicopathological features. *J. Clin. Pathol.* **2003**, *56*, 378–384. [CrossRef]
49. Utsunomiya, T.; Yonezawa, S.; Sakamoto, H.; Kitamura, H.; Hokita, S.; Aiko, T.; Tanaka, S.; Irimura, T.; Kim, Y.S.; Sato, E. Expression of MUC1 and MUC2 mucins in gastric carcinomas: Its relationship with the prognosis of the patients. *Clin. Cancer Res.* **1998**, *4*, 2605–2614.
50. Walsh, M.D.; Young, J.P.; Leggett, B.A.; Williams, S.H.; Jass, J.R.; McGuckin, M.A. The MUC13 cell surface mucin is highly expressed by human colorectal carcinomas. *Hum. Pathol.* **2007**, *38*, 883–892. [CrossRef]
51. Duncan, T.J.; Watson, N.F.; Al-Attar, A.H.; Scholefield, J.H.; Durrant, L.G. The role of MUC1 and MUC3 in the biology and prognosis of colorectal cancer. *World J. Surg. Oncol.* **2007**, *5*, 31. [CrossRef]
52. Fritsche, H.A.; Bast, R.C. CA 125 in ovarian cancer: Advances and controversy. *Clin. Chem.* **1998**, *44*, 1379–1380. [CrossRef] [PubMed]
53. Chauhan, S.C.; Singh, A.P.; Ruiz, F.; Johansson, S.L.; Jain, M.; Smith, L.M.; Moniaux, N.; Batra, S.K. Aberrant expression of MUC4 in ovarian carcinoma: Diagnostic significance alone and in combination with MUC1 and MUC16 (CA125). *Mod. Pathol.* **2006**, *19*, 1386–1394. [CrossRef]
54. Hanahan, D.; Weinberg, R.A. Hallmarks of cancer: The next generation. *Cell* **2011**, *144*, 646–674. [CrossRef]
55. Tang, Z.; Kang, B.; Li, C.; Chen, T.; Zhang, Z. GEPIA2: An enhanced web server for large-scale expression profiling and interactive analysis. *Nucleic Acids Res.* **2019**, *47*, W556–W560. [CrossRef] [PubMed]
56. Regad, T. Targeting RTK Signaling Pathways in Cancer. *Cancers* **2015**, *7*, 1758–1784. [CrossRef]
57. Li, Y.; Ren, J.; Yu, W.; Li, Q.; Kuwahara, H.; Yin, L.; Carraway, K.L., 3rd; Kufe, D. The epidermal growth factor receptor regulates interaction of the human DF3/MUC1 carcinoma antigen with c-Src and beta-catenin. *J. Biol. Chem.* **2001**, *276*, 35239–35242. [CrossRef]
58. Pochampalli, M.R.; el Bejjani, R.M.; Schroeder, J.A. MUC1 is a novel regulator of ErbB1 receptor trafficking. *Oncogene* **2007**, *26*, 1693–1701. [CrossRef] [PubMed]
59. Schroeder, J.A.; Thompson, M.C.; Gardner, M.M.; Gendler, S.J. Transgenic MUC1 interacts with epidermal growth factor receptor and correlates with mitogen-activated protein kinase activation in the mouse mammary gland. *J. Biol. Chem.* **2001**, *276*, 13057–13064. [CrossRef] [PubMed]
60. Ren, J.; Raina, D.; Chen, W.; Li, G.; Huang, L.; Kufe, D. MUC1 oncoprotein functions in activation of fibroblast growth factor receptor signaling. *Mol. Cancer Res.* **2006**, *4*, 873–883. [CrossRef] [PubMed]
61. Huang, L.; Chen, D.; Liu, D.; Yin, L.; Kharbanda, S.; Kufe, D. MUC1 oncoprotein blocks glycogen synthase kinase 3beta-mediated phosphorylation and degradation of beta-catenin. *Cancer Res.* **2005**, *65*, 10413–10422. [CrossRef]
62. Jin, W.; Liao, X.; Lv, Y.; Pang, Z.; Wang, Y.; Li, Q.; Liao, Y.; Ye, Q.; Chen, G.; Zhao, K.; et al. MUC1 induces acquired chemoresistance by upregulating ABCB1 in EGFR-dependent manner. *Cell Death Dis.* **2017**, *8*, e2980. [CrossRef] [PubMed]
63. Nath, S.; Daneshvar, K.; Roy, L.D.; Grover, P.; Kidiyoor, A.; Mosley, L.; Sahraei, M.; Mukherjee, P. MUC1 induces drug resistance in pancreatic cancer cells via upregulation of multidrug resistance genes. *Oncogenesis* **2013**, *2*, e51. [CrossRef]
64. Ren, J.; Agata, N.; Chen, D.; Li, Y.; Yu, W.H.; Huang, L.; Raina, D.; Chen, W.; Kharbanda, S.; Kufe, D. Human MUC1 carcinoma-associated protein confers resistance to genotoxic anticancer agents. *Cancer Cell* **2004**, *5*, 163–175. [CrossRef]
65. Raina, D.; Kharbanda, S.; Kufe, D. The MUC1 oncoprotein activates the anti-apoptotic phosphoinositide 3-kinase/Akt and Bcl-xL pathways in rat 3Y1 fibroblasts. *J. Biol. Chem.* **2004**, *279*, 20607–20612. [CrossRef]
66. Kharbanda, S.; Ren, R.; Pandey, P.; Shafman, T.D.; Feller, S.M.; Weichselbaum, R.R.; Kufe, D.W. Activation of the c-Abl tyrosine kinase in the stress response to DNA-damaging agents. *Nature* **1995**, *376*, 785–788. [CrossRef]
67. Raina, D.; Ahmad, R.; Kumar, S.; Ren, J.; Yoshida, K.; Kharbanda, S.; Kufe, D. MUC1 oncoprotein blocks nuclear targeting of c-Abl in the apoptotic response to DNA damage. *EMBO J.* **2006**, *25*, 3774–3783. [CrossRef]
68. Ahmad, R.; Raina, D.; Trivedi, V.; Ren, J.; Rajabi, H.; Kharbanda, S.; Kufe, D. MUC1 oncoprotein activates the I $\kappa$ B kinase beta complex and constitutive NF- $\kappa$ B signalling. *Nat. Cell Biol.* **2007**, *9*, 1419–1427. [CrossRef]
69. Yin, L.; Huang, L.; Kufe, D. MUC1 oncoprotein activates the FOXO3a transcription factor in a survival response to oxidative stress. *J. Biol. Chem.* **2004**, *279*, 45721–45727. [CrossRef]

70. Agata, N.; Ahmad, R.; Kawano, T.; Raina, D.; Kharbanda, S.; Kufe, D. MUC1 oncoprotein blocks death receptor-mediated apoptosis by inhibiting recruitment of caspase-8. *Cancer Res.* **2008**, *68*, 6136–6144. [CrossRef] [PubMed]
71. Boivin, M.; Lane, D.; Piche, A.; Rancourt, C. CA125 (MUC16) tumor antigen selectively modulates the sensitivity of ovarian cancer cells to genotoxic drug-induced apoptosis. *Gynecol Oncol.* **2009**, *115*, 407–413. [CrossRef]
72. Lakshmanan, I.; Salfity, S.; Seshacharyulu, P.; Rachagani, S.; Thomas, A.; Das, S.; Majhi, P.D.; Nimmakayala, R.K.; Vengoji, R.; Lele, S.M.; et al. MUC16 Regulates TSPYL5 for Lung Cancer Cell Growth and Chemoresistance by Suppressing p53. *Clin. Cancer Res.* **2017**, *23*, 3906–3917. [CrossRef] [PubMed]
73. DeBerardinis, R.J.; Chandel, N.S. Fundamentals of cancer metabolism. *Sci. Adv.* **2016**, *2*, e1600200. [CrossRef] [PubMed]
74. Chaika, N.V.; Gebregiorgis, T.; Lewallen, M.E.; Purohit, V.; Radhakrishnan, P.; Liu, X.; Zhang, B.; Mehla, K.; Brown, R.B.; Caffrey, T.; et al. MUC1 mucin stabilizes and activates hypoxia-inducible factor 1 alpha to regulate metabolism in pancreatic cancer. *Proc. Natl. Acad. Sci. USA* **2012**, *109*, 13787–13792. [CrossRef] [PubMed]
75. Shukla, S.K.; Gunda, V.; Abrego, J.; Haridas, D.; Mishra, A.; Soucek, J.; Chaika, N.V.; Yu, F.; Sasson, A.R.; Lazenby, A.J.; et al. MUC16-mediated activation of mTOR and c-Myc reprograms pancreatic cancer metabolism. *Oncotarget* **2015**, *6*, 19118–19131. [CrossRef]
76. Kosugi, M.; Ahmad, R.; Alam, M.; Uchida, Y.; Kufe, D. MUC1-C oncoprotein regulates glycolysis and pyruvate kinase M2 activity in cancer cells. *PLoS ONE* **2011**, *6*, e28234. [CrossRef]
77. Turgeon, M.O.; Perry, N.J.S.; Pouligiannis, G. DNA Damage, Repair, and Cancer Metabolism. *Front. Oncol.* **2018**, *8*, 15. [CrossRef]
78. Gunda, V.; Soucek, J.; Abrego, J.; Shukla, S.K.; Goode, G.D.; Vernucci, E.; Dasgupta, A.; Chaika, N.V.; King, R.J.; Li, S.; et al. MUC1-Mediated Metabolic Alterations Regulate Response to Radiotherapy in Pancreatic Cancer. *Clin. Cancer Res.* **2017**, *23*, 5881–5891. [CrossRef]
79. Snaebjornsson, M.T.; Janaki-Raman, S.; Schulze, A. Greasing the Wheels of the Cancer Machine: The Role of Lipid Metabolism in Cancer. *Cell Metab.* **2020**, *31*, 62–76. [CrossRef]
80. Pitroda, S.P.; Khodarev, N.N.; Beckett, M.A.; Kufe, D.W.; Weichselbaum, R.R. MUC1-induced alterations in a lipid metabolic gene network predict response of human breast cancers to tamoxifen treatment. *Proc. Natl. Acad. Sci. USA* **2009**, *106*, 5837–5841. [CrossRef]
81. Ribatti, D.; Tamma, R.; Annese, T. Epithelial-Mesenchymal Transition in Cancer: A Historical Overview. *Transl. Oncol.* **2020**, *13*, 100773. [CrossRef] [PubMed]
82. Roy, L.D.; Sahraei, M.; Subramani, D.B.; Besmer, D.; Nath, S.; Tinder, T.L.; Bajaj, E.; Shanmugam, K.; Lee, Y.Y.; Hwang, S.I.; et al. MUC1 enhances invasiveness of pancreatic cancer cells by inducing epithelial to mesenchymal transition. *Oncogene* **2011**, *30*, 1449–1459. [CrossRef] [PubMed]
83. Grover, P.; Nath, S.; Nye, M.D.; Zhou, R.; Ahmad, M.; Mukherjee, P. SMAD4-independent activation of TGF-beta signaling by MUC1 in a human pancreatic cancer cell line. *Oncotarget* **2018**, *9*, 6897–6910. [CrossRef] [PubMed]
84. Rajabi, H.; Alam, M.; Takahashi, H.; Kharbanda, A.; Guha, M.; Ahmad, R.; Kufe, D. MUC1-C oncoprotein activates the ZEB1/miR-200c regulatory loop and epithelial-mesenchymal transition. *Oncogene* **2014**, *33*, 1680–1689. [CrossRef]
85. Hata, T.; Rajabi, H.; Yamamoto, M.; Jin, C.; Ahmad, R.; Zhang, Y.; Kui, L.; Li, W.; Yasumizu, Y.; Hong, D.; et al. Targeting MUC1-C Inhibits TWIST1 Signaling in Triple-Negative Breast Cancer. *Mol. Cancer Ther.* **2019**, *18*, 1744–1754. [CrossRef]
86. Muniyan, S.; Haridas, D.; Chugh, S.; Rachagani, S.; Lakshmanan, I.; Gupta, S.; Seshacharyulu, P.; Smith, L.M.; Ponnusamy, M.P.; Batra, S.K. MUC16 contributes to the metastasis of pancreatic ductal adenocarcinoma through focal adhesion mediated signaling mechanism. *Genes Cancer* **2016**, *7*, 110–124. [CrossRef] [PubMed]
87. Swann, J.B.; Smyth, M.J. Immune surveillance of tumors. *J. Clin. Investig.* **2007**, *117*, 1137–1146. [CrossRef]
88. Vinay, D.S.; Ryan, E.P.; Pawelec, G.; Talib, W.H.; Stagg, J.; Elkord, E.; Lichtor, T.; Decker, W.K.; Whelan, R.L.; Kumara, H.; et al. Immune evasion in cancer: Mechanistic basis and therapeutic strategies. *Semin. Cancer Biol.* **2015**, *35*, S185–S198. [CrossRef]
89. Wesseling, J.; van der Valk, S.W.; Hilken, J. A mechanism for inhibition of E-cadherin-mediated cell-cell adhesion by the membrane-associated mucin episialin/MUC1. *Mol. Biol. Cell* **1996**, *7*, 565–577. [CrossRef]
90. Zhang, K.; Baeckstrom, D.; Brevinge, H.; Hansson, G.C. Secreted MUC1 mucins lacking their cytoplasmic part and carrying sialyl-Lewis a and x epitopes from a tumor cell line and sera of colon carcinoma patients can inhibit HL-60 leukocyte adhesion to E-selectin-expressing endothelial cells. *J. Cell Biochem.* **1996**, *60*, 538–549. [CrossRef]
91. Li, T.; Fu, J.; Zeng, Z.; Cohen, D.; Li, J.; Chen, Q.; Li, B.; Liu, X.S. TIMER2.0 for analysis of tumor-infiltrating immune cells. *Nucleic Acids Res.* **2020**, *48*, W509–W514. [CrossRef] [PubMed]
92. Li, B.; Severson, E.; Pignon, J.C.; Zhao, H.; Li, T.; Novak, J.; Jiang, P.; Shen, H.; Aster, J.C.; Rodig, S.; et al. Comprehensive analyses of tumor immunity: Implications for cancer immunotherapy. *Genome Biol.* **2016**, *17*, 174. [CrossRef]
93. Racle, J.; de Jonge, K.; Baumgaertner, P.; Speiser, D.E.; Gfeller, D. Simultaneous enumeration of cancer and immune cell types from bulk tumor gene expression data. *eLife* **2017**, *6*, e26476. [CrossRef] [PubMed]
94. Becht, E.; Giraldo, N.A.; Lacroix, L.; Buttard, B.; Elarouci, N.; Petitprez, F.; Selves, J.; Laurent-Puig, P.; Sautes-Fridman, C.; Fridman, W.H.; et al. Estimating the population abundance of tissue-infiltrating immune and stromal cell populations using gene expression. *Genome Biol.* **2016**, *17*, 218. [CrossRef]
95. Newman, A.M.; Liu, C.L.; Green, M.R.; Gentles, A.J.; Feng, W.; Xu, Y.; Hoang, C.D.; Diehn, M.; Alizadeh, A.A. Robust enumeration of cell subsets from tissue expression profiles. *Nat. Methods* **2015**, *12*, 453–457. [CrossRef]

96. Finotello, F.; Mayer, C.; Plattner, C.; Laschober, G.; Rieder, D.; Hackl, H.; Krogsdam, A.; Loncova, Z.; Posch, W.; Wilflingseder, D.; et al. Molecular and pharmacological modulators of the tumor immune contexture revealed by deconvolution of RNA-seq data. *Genome Med.* **2019**, *11*, 34. [CrossRef] [PubMed]
97. Aran, D.; Hu, Z.; Butte, A.J. xCell: Digitally portraying the tissue cellular heterogeneity landscape. *Genome Biol.* **2017**, *18*, 220. [CrossRef]
98. Komatsu, M.; Yee, L.; Carraway, K.L. Overexpression of sialomucin complex, a rat homologue of MUC4, inhibits tumor killing by lymphokine-activated killer cells. *Cancer Res.* **1999**, *59*, 2229–2236.
99. Van de Wiel-van Kemenade, E.; Ligtenberg, M.J.; de Boer, A.J.; Buijs, F.; Vos, H.L.; Melief, C.J.; Hilken, J.; Figdor, C.G. Episialin (MUC1) inhibits cytotoxic lymphocyte-target cell interaction. *J. Immunol.* **1993**, *151*, 767–776.
100. Kim, Y.J.; Borsig, L.; Han, H.L.; Varki, N.M.; Varki, A. Distinct selectin ligands on colon carcinoma mucins can mediate pathological interactions among platelets, leukocytes, and endothelium. *Am. J. Pathol.* **1999**, *155*, 461–472. [CrossRef]
101. Nath, D.; Hartnell, A.; Happerfield, L.; Miles, D.W.; Burchell, J.; Taylor-Papadimitriou, J.; Crocker, P.R. Macrophage-tumour cell interactions: Identification of MUC1 on breast cancer cells as a potential counter-receptor for the macrophage-restricted receptor, sialoadhesin. *Immunology* **1999**, *98*, 213–219. [CrossRef] [PubMed]
102. Brinkman-Van der Linden, E.C.; Varki, A. New aspects of siglec binding specificities, including the significance of fucosylation and of the sialyl-Tn epitope. Sialic acid-binding immunoglobulin superfamily lectins. *J. Biol. Chem.* **2000**, *275*, 8625–8632. [CrossRef]
103. Regimbald, L.H.; Pilarski, L.M.; Longenecker, B.M.; Reddish, M.A.; Zimmermann, G.; Hugh, J.C. The breast mucin MUC1 as a novel adhesion ligand for endothelial intercellular adhesion molecule 1 in breast cancer. *Cancer Res.* **1996**, *56*, 4244–4249.
104. Agrawal, B.; Krantz, M.J.; Reddish, M.A.; Longenecker, B.M. Cancer-associated MUC1 mucin inhibits human T-cell proliferation, which is reversible by IL-2. *Nat. Med.* **1998**, *4*, 43–49. [CrossRef] [PubMed]
105. Rughetti, A.; Pellicciotta, I.; Biffoni, M.; Backstrom, M.; Link, T.; Bennet, E.P.; Clausen, H.; Noll, T.; Hansson, G.C.; Burchell, J.M.; et al. Recombinant tumor-associated MUC1 glycoprotein impairs the differentiation and function of dendritic cells. *J. Immunol.* **2005**, *174*, 7764–7772. [CrossRef]
106. Monti, P.; Leone, B.E.; Zerbi, A.; Balzano, G.; Cainarca, S.; Sordi, V.; Pontillo, M.; Mercalli, A.; Di Carlo, V.; Allavena, P.; et al. Tumor-derived MUC1 mucins interact with differentiating monocytes and induce IL-10<sup>high</sup>IL-12<sup>low</sup> regulatory dendritic cell. *J. Immunol.* **2004**, *172*, 7341–7349. [CrossRef]
107. Williams, M.A.; Bauer, S.; Lu, W.; Guo, J.; Walter, S.; Bushnell, T.P.; Lillehoj, E.P.; Georas, S.N. Deletion of the mucin-like molecule muc1 enhances dendritic cell activation in response to toll-like receptor ligands. *J. Innate Immunol.* **2010**, *2*, 123–143. [CrossRef]
108. Gubbels, J.A.; Belisle, J.; Onda, M.; Rancourt, C.; Migneault, M.; Ho, M.; Bera, T.K.; Connor, J.; Sathyanarayana, B.K.; Lee, B.; et al. Mesothelin-MUC16 binding is a high affinity, N-glycan dependent interaction that facilitates peritoneal metastasis of ovarian tumors. *Mol. Cancer* **2006**, *5*, 50. [CrossRef] [PubMed]
109. Seelenmeyer, C.; Wegehangel, S.; Lechner, J.; Nickel, W. The cancer antigen CA125 represents a novel counter receptor for galectin-1. *J. Cell Sci.* **2003**, *116*, 1305–1318. [CrossRef] [PubMed]
110. Belisle, J.A.; Gubbels, J.A.; Raphael, C.A.; Migneault, M.; Rancourt, C.; Connor, J.P.; Patankar, M.S. Peritoneal natural killer cells from epithelial ovarian cancer patients show an altered phenotype and bind to the tumour marker MUC16 (CA125). *Immunology* **2007**, *122*, 418–429. [CrossRef] [PubMed]
111. Patankar, M.S.; Jing, Y.; Morrison, J.C.; Belisle, J.A.; Lattanzio, F.A.; Deng, Y.; Wong, N.K.; Morris, H.R.; Dell, A.; Clark, G.F. Potent suppression of natural killer cell response mediated by the ovarian tumor marker CA125. *Gynecol. Oncol.* **2005**, *99*, 704–713. [CrossRef]
112. Bouillez, A.; Rajabi, H.; Jin, C.; Samur, M.; Tagde, A.; Alam, M.; Hiraki, M.; Maeda, T.; Hu, X.; Adegebe, D.; et al. MUC1-C integrates PD-L1 induction with repression of immune effectors in non-small-cell lung cancer. *Oncogene* **2017**, *36*, 4037–4046. [CrossRef]
113. Maeda, T.; Hiraki, M.; Jin, C.; Rajabi, H.; Tagde, A.; Alam, M.; Bouillez, A.; Hu, X.; Suzuki, Y.; Miyo, M.; et al. MUC1-C Induces PD-L1 and Immune Evasion in Triple-Negative Breast Cancer. *Cancer Res.* **2018**, *78*, 205–215. [CrossRef]
114. Gaemers, I.C.; Vos, H.L.; Volders, H.H.; van der Valk, S.W.; Hilken, J. A stat-responsive element in the promoter of the episialin/MUC1 gene is involved in its overexpression in carcinoma cells. *J. Biol. Chem.* **2001**, *276*, 6191–6199. [CrossRef]
115. Morgado, M.; Sutton, M.N.; Simmons, M.; Warren, C.R.; Lu, Z.; Constantinou, P.E.; Liu, J.; Francis, L.L.; Conlan, R.S.; Bast, R.C., Jr.; et al. Tumor necrosis factor-alpha and interferon-gamma stimulate MUC16 (CA125) expression in breast, endometrial and ovarian cancers through NFkappaB. *Oncotarget* **2016**, *7*, 14871–14884. [CrossRef]
116. Cascio, S.; Zhang, L.; Finn, O.J. MUC1 protein expression in tumor cells regulates transcription of proinflammatory cytokines by forming a complex with nuclear factor-kappaB p65 and binding to cytokine promoters: Importance of extracellular domain. *J. Biol. Chem.* **2011**, *286*, 42248–42256. [CrossRef]
117. Graham, R.A.; Burchell, J.M.; Taylor-Papadimitriou, J. The polymorphic epithelial mucin: Potential as an immunogen for a cancer vaccine. *Cancer Immunol. Immunother.* **1996**, *42*, 71–80. [CrossRef] [PubMed]
118. Raina, D.; Agarwal, P.; Lee, J.; Bharti, A.; McKnight, C.J.; Sharma, P.; Kharbanda, S.; Kufe, D. Characterization of the MUC1-C Cytoplasmic Domain as a Cancer Target. *PLoS ONE* **2015**, *10*, e0135156. [CrossRef]
119. Ahmad, R.; Alam, M.; Hasegawa, M.; Uchida, Y.; Al-Obaid, O.; Kharbanda, S.; Kufe, D. Targeting MUC1-C inhibits the AKT-S6K1-eIF4A pathway regulating TIGAR translation in colorectal cancer. *Mol. Cancer* **2017**, *16*, 33. [CrossRef] [PubMed]

120. GongSun, X.; Zhao, Y.; Jiang, B.; Xin, Z.; Shi, M.; Song, L.; Qin, Q.; Wang, Q.; Liu, X. Inhibition of MUC1-C regulates metabolism by AKT pathway in esophageal squamous cell carcinoma. *J. Cell Physiol.* **2019**, *234*, 12019–12028. [CrossRef] [PubMed]
121. Shigeta, K.; Hasegawa, M.; Kikuchi, E.; Yasumizu, Y.; Kosaka, T.; Mizuno, R.; Mikami, S.; Miyajima, A.; Kufe, D.; Oya, M. Role of the MUC1-C oncoprotein in the acquisition of cisplatin resistance by urothelial carcinoma. *Cancer Sci.* **2020**, *111*, 3639–3652. [CrossRef]
122. Raina, D.; Uchida, Y.; Kharbanda, A.; Rajabi, H.; Panchamoorthy, G.; Jin, C.; Kharbanda, S.; Scaltriti, M.; Baselga, J.; Kufe, D. Targeting the MUC1-C oncoprotein downregulates HER2 activation and abrogates trastuzumab resistance in breast cancer cells. *Oncogene* **2014**, *33*, 3422–3431. [CrossRef]
123. Yamamoto, M.; Jin, C.; Hata, T.; Yasumizu, Y.; Zhang, Y.; Hong, D.; Maeda, T.; Miyo, M.; Hiraki, M.; Suzuki, Y.; et al. MUC1-C Integrates Chromatin Remodeling and PARP1 Activity in the DNA Damage Response of Triple-Negative Breast Cancer Cells. *Cancer Res.* **2019**, *79*, 2031–2041. [CrossRef]
124. Bouillez, A.; Rajabi, H.; Pitroda, S.; Jin, C.; Alam, M.; Kharbanda, A.; Tagde, A.; Wong, K.K.; Kufe, D. Inhibition of MUC1-C Suppresses MYC Expression and Attenuates Malignant Growth in KRAS Mutant Lung Adenocarcinomas. *Cancer Res.* **2016**, *76*, 1538–1548. [CrossRef] [PubMed]
125. Yin, L.; Kufe, T.; Avigan, D.; Kufe, D. Targeting MUC1-C is synergistic with bortezomib in downregulating TIGAR and inducing ROS-mediated myeloma cell death. *Blood* **2014**, *123*, 2997–3006. [CrossRef] [PubMed]
126. Yin, L.; Tagde, A.; Gali, R.; Tai, Y.T.; Hideshima, T.; Anderson, K.; Avigan, D.; Kufe, D. MUC1-C is a target in lenalidomide resistant multiple myeloma. *Br. J. Haematol.* **2017**, *178*, 914–926. [CrossRef] [PubMed]
127. Jain, S.; Washington, A.; Leaf, R.K.; Bhargava, P.; Clark, R.A.; Kupper, T.S.; Stroopinsky, D.; Pyzer, A.; Cole, L.; Nahas, M.; et al. Decitabine Priming Enhances Mucin 1 Inhibition Mediated Disruption of Redox Homeostasis in Cutaneous T-Cell Lymphoma. *Mol. Cancer Ther.* **2017**, *16*, 2304–2314. [CrossRef]
128. Liu, S.; Yin, L.; Stroopinsky, D.; Rajabi, H.; Puissant, A.; Stegmaier, K.; Avigan, D.; Kharbanda, S.; Kufe, D.; Stone, R. MUC1-C oncoprotein promotes FLT3 receptor activation in acute myeloid leukemia cells. *Blood* **2014**, *123*, 734–742. [CrossRef]
129. Bouillez, A.; Adeegbe, D.; Jin, C.; Hu, X.; Tagde, A.; Alam, M.; Rajabi, H.; Wong, K.K.; Kufe, D. MUC1-C promotes the suppressive immune microenvironment in non-small cell lung cancer. *Oncoimmunology* **2017**, *6*, e1338998. [CrossRef]
130. Pereplyuk, M.; Sacko, K.; Thangavel, K.; Shoyele, S.A. Evaluation of MUC1-Aptamer Functionalized Hybrid Nanoparticles for Targeted Delivery of miRNA-29b to Nonsmall Cell Lung Cancer. *Mol. Pharm.* **2018**, *15*, 985–993. [CrossRef]
131. Sacko, K.; Thangavel, K.; Shoyele, S.A. Codelivery of Genistein and miRNA-29b to A549 Cells Using Aptamer-Hybrid Nanoparticle Bioconjugates. *Nanomaterials* **2019**, *9*, 1052. [CrossRef]
132. Engebraaten, O.; Sivam, G.; Juell, S.; Fodstad, O. Systemic immunotoxin treatment inhibits formation of human breast cancer metastasis and tumor growth in nude rats. *Int. J. Cancer* **2000**, *88*, 970–976. [CrossRef]
133. Wu, G.; Kim, D.; Kim, J.N.; Park, S.; Maharjan, S.; Koh, H.; Moon, K.; Lee, Y.; Kwon, H.J. A Mucin1 C-terminal Subunit-directed Monoclonal Antibody Targets Overexpressed Mucin1 in Breast Cancer. *Theranostics* **2018**, *8*, 78–91. [CrossRef]
134. Wu, G.; Maharjan, S.; Kim, D.; Kim, J.N.; Park, B.K.; Koh, H.; Moon, K.; Lee, Y.; Kwon, H.J. A Novel Monoclonal Antibody Targets Mucin1 and Attenuates Growth in Pancreatic Cancer Model. *Int. J. Mol. Sci.* **2018**, *19*, 4. [CrossRef] [PubMed]
135. Danielczyk, A.; Stahn, R.; Faulstich, D.; Loffler, A.; Marten, A.; Karsten, U.; Goletz, S. PankoMab: A potent new generation anti-tumour MUC1 antibody. *Cancer Immunol. Immunother.* **2006**, *55*, 1337–1347. [CrossRef]
136. Posey, A.D., Jr.; Schwab, R.D.; Boesteanu, A.C.; Steentoft, C.; Mandel, U.; Engels, B.; Stone, J.D.; Madsen, T.D.; Schreiber, K.; Haines, K.M.; et al. Engineered CAR T Cells Targeting the Cancer-Associated Tn-Glycoform of the Membrane Mucin MUC1 Control Adenocarcinoma. *Immunity* **2016**, *44*, 1444–1454. [CrossRef]
137. Bottoni, P.; Scatena, R. The Role of CA 125 as Tumor Marker: Biochemical and Clinical Aspects. *Adv. Exp. Med. Biol.* **2015**, *867*, 229–244. [CrossRef] [PubMed]
138. Schultes, B.C.; Baum, R.P.; Niesen, A.; Noujaim, A.A.; Madiyalakan, R. Anti-idiotype induction therapy: Anti-CA125 antibodies (Ab3) mediated tumor killing in patients treated with Ovarex mAb B43.13 (Ab1). *Cancer Immunol. Immunother.* **1998**, *46*, 201–212. [CrossRef] [PubMed]
139. Pietragalla, A.; Duranti, S.; Daniele, G.; Nero, C.; Ciccarone, F.; Lorusso, D.; Fagotti, A.; Scambia, G. Oregovomab: An investigational agent for the treatment of advanced ovarian cancer. *Expert Opin. Investig. Drugs* **2021**, *30*, 103–110. [CrossRef]
140. Brewer, M.; Angioli, R.; Scambia, G.; Lorusso, D.; Terranova, C.; Panici, P.B.; Raspagliesi, F.; Scollo, P.; Plotti, F.; Ferrandina, G.; et al. Front-line chemo-immunotherapy with carboplatin-paclitaxel using oregovomab indirect immunization in advanced ovarian cancer: A randomized phase II study. *Gynecol. Oncol.* **2020**, *156*, 523–529. [CrossRef] [PubMed]
141. Battaglia, A.; Buzzonetti, A.; Fossati, M.; Scambia, G.; Fattorossi, A.; Madiyalakan, M.R.; Mahnke, Y.D.; Nicodemus, C. Translational immune correlates of indirect antibody immunization in a randomized phase II study using scheduled combination therapy with carboplatin/paclitaxel plus oregovomab in ovarian cancer patients. *Cancer Immunol. Immunother.* **2020**, *69*, 383–397. [CrossRef]
142. Berek, J.S.; Taylor, P.T.; Gordon, A.; Cunningham, M.J.; Finkler, N.; Orr, J., Jr.; Rivkin, S.; Schultes, B.C.; Whiteside, T.L.; Nicodemus, C.F. Randomized, placebo-controlled study of oregovomab for consolidation of clinical remission in patients with advanced ovarian cancer. *J. Clin. Oncol.* **2004**, *22*, 3507–3516. [CrossRef] [PubMed]
143. Berek, J.; Taylor, P.; McGuire, W.; Smith, L.M.; Schultes, B.; Nicodemus, C.F. Oregovomab maintenance monoimmunotherapy does not improve outcomes in advanced ovarian cancer. *J. Clin. Oncol.* **2009**, *27*, 418–425. [CrossRef]

144. Reinartz, S.; Kohler, S.; Schlebusch, H.; Krista, K.; Giffels, P.; Renke, K.; Huober, J.; Mobus, V.; Kreienberg, R.; DuBois, A.; et al. Vaccination of patients with advanced ovarian carcinoma with the anti-idiotype ACA125: Immunological response and survival (phase Ib/II). *Clin. Cancer Res.* **2004**, *10*, 1580–1587. [CrossRef]
145. Sabbatini, P.; Harter, P.; Scambia, G.; Sehouli, J.; Meier, W.; Wimberger, P.; Baumann, K.H.; Kurzeder, C.; Schmalfeldt, B.; Cibula, D.; et al. Abagovomab as maintenance therapy in patients with epithelial ovarian cancer: A phase III trial of the AGO OVAR, COGI, GINECO, and GEICO—the MIMOSA study. *J. Clin. Oncol.* **2013**, *31*, 1554–1561. [CrossRef] [PubMed]
146. Buzzonetti, A.; Fossati, M.; Catzola, V.; Scambia, G.; Fattorossi, A.; Battaglia, A. Immunological response induced by abagovomab as a maintenance therapy in patients with epithelial ovarian cancer: Relationship with survival—a substudy of the MIMOSA trial. *Cancer Immunol. Immunother.* **2014**, *63*, 1037–1045. [CrossRef]
147. Battaglia, A.; Fossati, M.; Buzzonetti, A.; Scambia, G.; Fattorossi, A. A robust immune system conditions the response to abagovomab (anti-idiotypic monoclonal antibody mimicking the CA125 protein) vaccination in ovarian cancer patients. *Immunol. Lett.* **2017**, *191*, 35–39. [CrossRef]
148. Liu, J.F.; Moore, K.N.; Birrer, M.J.; Berlin, S.; Matulonis, U.A.; Infante, J.R.; Wolpin, B.; Poon, K.A.; Firestein, R.; Xu, J.; et al. Phase I study of safety and pharmacokinetics of the anti-MUC16 antibody-drug conjugate DMUC5754A in patients with platinum-resistant ovarian cancer or unresectable pancreatic cancer. *Ann. Oncol.* **2016**, *27*, 2124–2130. [CrossRef] [PubMed]
149. Crawford, A.; Haber, L.; Kelly, M.P.; Vazzana, K.; Canova, L.; Ram, P.; Pawashe, A.; Finney, J.; Jalal, S.; Chiu, D.; et al. A Mucin 16 bispecific T cell-engaging antibody for the treatment of ovarian cancer. *Sci. Transl. Med.* **2019**, *11*, 7534. [CrossRef]
150. Khan, S.; Zafar, N.; Khan, S.S.; Setua, S.; Behrman, S.W.; Stiles, Z.E.; Yallapu, M.M.; Sahay, P.; Ghimire, H.; Ise, T.; et al. Clinical significance of MUC13 in pancreatic ductal adenocarcinoma. *HPB* **2018**, *20*, 563–572. [CrossRef]
151. Nishii, Y.; Yamaguchi, M.; Kimura, Y.; Hasegawa, T.; Aburatani, H.; Uchida, H.; Hirata, K.; Sakuma, Y. A newly developed anti-Mucin 13 monoclonal antibody targets pancreatic ductal adenocarcinoma cells. *Int. J. Oncol.* **2015**, *46*, 1781–1787. [CrossRef]
152. Chauhan, S.C.; Ebeling, M.C.; Maher, D.M.; Koch, M.D.; Watanabe, A.; Aburatani, H.; Lio, Y.; Jaggi, M. MUC13 mucin augments pancreatic tumorigenesis. *Mol. Cancer Ther.* **2012**, *11*, 24–33. [CrossRef] [PubMed]
153. Mitchell, P.L.; Quinn, M.A.; Grant, P.T.; Allen, D.G.; Jobling, T.W.; White, S.C.; Zhao, A.; Karanikas, V.; Vaughan, H.; Pietersz, G.; et al. A phase 2, single-arm study of an autologous dendritic cell treatment against mucin 1 in patients with advanced epithelial ovarian cancer. *J. Immunother. Cancer* **2014**, *2*, 16. [CrossRef] [PubMed]
154. Gray, H.J.; Benigno, B.; Berek, J.; Chang, J.; Mason, J.; Mileskin, L.; Mitchell, P.; Moradi, M.; Recio, F.O.; Michener, C.M.; et al. Progression-free and overall survival in ovarian cancer patients treated with CVac, a mucin 1 dendritic cell therapy in a randomized phase 2 trial. *J. Immunother. Cancer* **2016**, *4*, 34. [CrossRef]
155. Kovjazin, R.; Volovitz, I.; Kundel, Y.; Rosenbaum, E.; Medalia, G.; Horn, G.; Smorodinsky, N.I.; Brenner, B.; Carmon, L. ImMucin: A novel therapeutic vaccine with promiscuous MHC binding for the treatment of MUC1-expressing tumors. *Vaccine* **2011**, *29*, 4676–4686. [CrossRef]
156. Carmon, L.; Avivi, I.; Kovjazin, R.; Zuckerman, T.; Dray, L.; Gatt, M.E.; Or, R.; Shapira, M.Y. Phase I/II study exploring ImMucin, a pan-major histocompatibility complex, anti-MUC1 signal peptide vaccine, in multiple myeloma patients. *Br. J. Haematol.* **2015**, *169*, 44–56. [CrossRef]
157. Kimura, T.; McKolanis, J.R.; Dzubinski, L.A.; Islam, K.; Potter, D.M.; Salazar, A.M.; Schoen, R.E.; Finn, O.J. MUC1 vaccine for individuals with advanced adenoma of the colon: A cancer immunoprevention feasibility study. *Cancer Prev. Res.* **2013**, *6*, 18–26. [CrossRef]
158. Ramanathan, R.K.; Lee, K.M.; McKolanis, J.; Hitbold, E.; Schraut, W.; Moser, A.J.; Warnick, E.; Whiteside, T.; Osborne, J.; Kim, H.; et al. Phase I study of a MUC1 vaccine composed of different doses of MUC1 peptide with SB-AS2 adjuvant in resected and locally advanced pancreatic cancer. *Cancer Immunol. Immunother.* **2005**, *54*, 254–264. [CrossRef]
159. Lepisto, A.J.; Moser, A.J.; Zeh, H.; Lee, K.; Bartlett, D.; McKolanis, J.R.; Geller, B.A.; Schmotzer, A.; Potter, D.P.; Whiteside, T.; et al. A phase I/II study of a MUC1 peptide pulsed autologous dendritic cell vaccine as adjuvant therapy in patients with resected pancreatic and biliary tumors. *Cancer Ther.* **2008**, *6*, 955–964. [PubMed]
160. Pestano, L.A.; Christian, B.; Koppenol, S.; Millard, J.; Christianson, G.; Klucher, K.; Rosler, R.; Peterson, S.R. Abstract 762: ONT-10, a liposomal vaccine targeting hypoglycosylated MUC1, induces a potent cellular and humoral response and suppresses the growth of MUC1 expressing tumors. *Cancer Res.* **2011**, *71*, 762. [CrossRef]
161. Nemunaitis, J.; Bedell, C.; Klucher, K.; Vo, A.; Whiting, S. Phase 1 dose escalation of ONT-10, a therapeutic MUC1 vaccine, in patients with advanced cancer. *J. Immunother. Cancer* **2013**, *1*, P240. [CrossRef]
162. Butts, C.; Socinski, M.A.; Mitchell, P.L.; Thatcher, N.; Havel, L.; Krzakowski, M.; Nawrocki, S.; Ciuleanu, T.E.; Bosquee, L.; Trigo, J.M.; et al. Tecemotide (L-BLP25) versus placebo after chemoradiotherapy for stage III non-small-cell lung cancer (START): A randomised, double-blind, phase 3 trial. *Lancet Oncol.* **2014**, *15*, 59–68. [CrossRef]
163. Gatti-Mays, M.E.; Redman, J.M.; Donahue, R.N.; Palena, C.; Madan, R.A.; Karzai, F.; Bilusic, M.; Sater, H.A.; Marte, J.L.; Cordes, L.M.; et al. A Phase I Trial Using a Multitargeted Recombinant Adenovirus 5 (CEA/MUC1/Brachyury)-Based Immunotherapy Vaccine Regimen in Patients with Advanced Cancer. *Oncologist* **2020**, *25*, 479.e899. [CrossRef] [PubMed]
164. Quoix, E.; Lena, H.; Losonczy, G.; Forget, F.; Chouaid, C.; Papai, Z.; Gervais, R.; Ottensmeier, C.; Szczesna, A.; Kazarnowicz, A.; et al. TG4010 immunotherapy and first-line chemotherapy for advanced non-small-cell lung cancer (TIME): Results from the phase 2b part of a randomised, double-blind, placebo-controlled, phase 2b/3 trial. *Lancet Oncol.* **2016**, *17*, 212–223. [CrossRef]



165. Deisseroth, A.; Tang, Y.; Zhang, L.; Akbulut, H.; Habib, N. TAA/ecdCD40L adenoviral prime-protein boost vaccine for cancer and infectious diseases. *Cancer Gene Ther.* **2013**, *20*, 65–69. [CrossRef] [PubMed]
166. Tan, T.J.Y.; Chia, J.W.K.; Chong, H.-S.; Li, X.; Tan, S.H.; Hopkins, R.; Wang, W.-W.; Toh, H.C. First-in-man study of Ad-sig-hMUC1/ecdCD40L vaccine for immunotherapy of MUC1 overexpressing epithelial cancers. *J. Clin. Oncol.* **2018**, *36*, 3098. [CrossRef]



## Article

# Synthesis and Biological Evaluation of 1-(Diarylmethyl)-1*H*-1,2,4-triazoles and 1-(Diarylmethyl)-1*H*-imidazoles as a Novel Class of Anti-Mitotic Agent for Activity in Breast Cancer

Gloria Ana <sup>1</sup>, Patrick M. Kelly <sup>1</sup>, Azizah M. Malebari <sup>2</sup>, Sara Noorani <sup>1</sup>, Seema M. Nathwani <sup>3</sup>, Brendan Twamley <sup>4</sup>, Darren Fayne <sup>3</sup>, Niamh M. O'Boyle <sup>1</sup> , Daniela M. Zisterer <sup>3</sup>, Elisangela Flavia Pimentel <sup>5</sup>, Denise Coutinho Endringer <sup>5</sup> and Mary J. Meegan <sup>1,\*</sup>

<sup>1</sup> School of Pharmacy and Pharmaceutical Sciences, Trinity College Dublin, Trinity Biomedical Sciences Institute, 152-160 Pearse Street, Dublin 2, DO2R590 Dublin, Ireland; anag@tcd.ie (G.A.); kellyp9@tcd.ie (P.M.K.); noorani87@gmail.com (S.N.); NIOBOYLE@tcd.ie (N.M.O.)

<sup>2</sup> Department of Pharmaceutical Chemistry, College of Pharmacy, King Abdulaziz University, Jeddah 21589, Saudi Arabia; amelibrary@kau.edu.sa

<sup>3</sup> School of Biochemistry and Immunology, Trinity College Dublin, Trinity Biomedical Sciences Institute, 152-160 Pearse Street, Dublin 2, DO2R590 Dublin, Ireland; seema.nathwani@outlook.com (S.M.N.); FAYNED@tcd.ie (D.F.); dzistrer@tcd.ie (D.M.Z.)

<sup>4</sup> School of Chemistry, Trinity College Dublin, Dublin 2, DO2R590 Dublin, Ireland; TWAMLEYB@tcd.ie

<sup>5</sup> Department of Pharmaceutical Sciences, University Vila Velha, Av. Comissário José Dantas de Melo, n°21, Boa Vista Vila Velha—Espírito Santo, Vila Velha 29102-920, Brazil; eflapim@hotmail.com (E.F.P.); endringer@gmail.com (D.C.E.)

\* Correspondence: mmeegan@tcd.ie; Tel.: +353-1-896-2798

**Citation:** Ana, G.; Kelly, P.M.; Malebari, A.M.; Noorani, S.; Nathwani, S.M.; Twamley, B.; Fayne, D.; O'Boyle, N.M.; Zisterer, D.M.; Pimentel, E.F.; et al. Synthesis and Biological Evaluation of 1-(Diarylmethyl)-1*H*-1,2,4-triazoles and 1-(Diarylmethyl)-1*H*-imidazoles as a Novel Class of Anti-Mitotic Agent for Activity in Breast Cancer. *Pharmaceuticals* **2021**, *14*, 169. <https://doi.org/10.3390/ph14020169>

Academic Editor:  
Marialuigia Fantacuzzi

Received: 5 January 2021  
Accepted: 18 February 2021  
Published: 22 February 2021

**Publisher's Note:** MDPI stays neutral with regard to jurisdictional claims in published maps and institutional affiliations.



**Copyright:** © 2021 by the authors. Licensee MDPI, Basel, Switzerland. This article is an open access article distributed under the terms and conditions of the Creative Commons Attribution (CC BY) license (<https://creativecommons.org/licenses/by/4.0/>).

**Abstract:** We report the synthesis and biochemical evaluation of compounds that are designed as hybrids of the microtubule targeting benzophenone phenstatin and the aromatase inhibitor letrozole. A preliminary screening in estrogen receptor (ER)-positive MCF-7 breast cancer cells identified 5-((2*H*-1,2,3-triazol-1-yl)(3,4,5-trimethoxyphenyl)methyl)-2-methoxyphenol **24** as a potent antiproliferative compound with an IC<sub>50</sub> value of 52 nM in MCF-7 breast cancer cells (ER+/PR+) and 74 nM in triple-negative MDA-MB-231 breast cancer cells. The compounds demonstrated significant G<sub>2</sub>/M phase cell cycle arrest and induction of apoptosis in the MCF-7 cell line, inhibited tubulin polymerisation, and were selective for cancer cells when evaluated in non-tumorigenic MCF-10A breast cells. The immunofluorescence staining of MCF-7 cells confirmed that the compounds targeted tubulin and induced multinucleation, which is a recognised sign of mitotic catastrophe. Computational docking studies of compounds **19e**, **21I**, and **24** in the colchicine binding site of tubulin indicated potential binding conformations for the compounds. Compounds **19e** and **21I** were also shown to selectively inhibit aromatase. These compounds are promising candidates for development as antiproliferative, aromatase inhibitory, and microtubule-disrupting agents for breast cancer.

**Keywords:** phenstatin; letrozole; tubulin polymerisation inhibitor; aromatase inhibitor; breast cancer; hybrid molecule; dual-targeting molecule; apoptosis; designed multiple ligand

## 1. Introduction

Designing single agents that act against multiple biological targets is of increasing interest and prominence in medicinal chemistry [1–4]. Dual-targeting drugs are designed with the potential to be more potent and efficient and overcome many of the disadvantages of single drugs such as low solubility, side effects [5], and multidrug resistance (MDR). While the molecular mechanisms of resistance to chemotherapeutics have been identified, MDR is known to be a key factor in the failure of breast cancer chemotherapy [6]. Traditionally, drugs have been designed to target a single biological target (protein), aiming for high

selectivity and thus avoiding unwanted effects due to off-target events. The interaction of a drug with multiple target proteins has been regarded as potentially associated with adverse side effects. However, for complex diseases such as cancer, it is now recognised that a single-target drug may not achieve the optimum therapeutic effect. Molecules that are effective at more than one target protein may overcome incomplete efficacy and demonstrate an increased safety profile compared to single-targeted ones [2]. Dual-targeting strategies may offer a more favourable outcome of cancer treatment.

A possible strategy to improve the outcome for postmenopausal breast cancer patients is to design compounds with dual aromatase and tubulin targeting activities, which may offer the potential benefits of improved efficacy and fewer side effects [7,8]. The objective of our research is to investigate a new series of 1-(diarylmethyl)-1*H*-1,2,4-triazoles and 1-(diarylmethyl)-1*H*-imidazoles as a novel class of antimetabolic compounds with an interesting biochemical profile particularly as tubulin-targeting agents and aromatase inhibitors for the treatment of breast cancer.

Breast cancer is the most commonly diagnosed cancer in women; it is estimated that approximately one in eight women will develop breast cancer during their lifetime, and it is the most frequent cause of death for women in the age group 35–55 [9]. There were over two million new cases in 2018 [10], and the number of cases is predicted to rise due to an ageing population [11,12]. Mortality has decreased due to improved screening and early detection together with the use of adjuvant therapy [13]. Approximately 70–80% of breast cancers are hormone-dependent; their growth is stimulated in response to the hormone estrogen, with the majority of these estrogen receptor positive (ER+) cancers also expressing the progesterone receptor (ER+/PR+ cancers). Upregulation of the gene encoding the PR is directly mediated by ER, and PR modulates ER $\alpha$  action in breast cancer [14].

Aromatase (CYP19A1), a member of the cytochrome P-450 enzyme superfamily, catalyses the aromatisation of C-19 androgens to C-18 estrogens in the final step in estrogen biosynthesis, and it is an attractive target for selective inhibition [15–17]. Estrogen deprivation is an effective therapeutic intervention for hormone-dependent breast cancer (HDBC) and has been clinically established by the inhibition of the aromatase enzyme. The aromatase inhibitors (AIs), e.g., letrozole **1** [18], anastrozole **2** [19], and exemestane [20] (Figure 1a), prevent the stimulating effects of estrogen in breast tissue [19], and they are approved in the treatment of a wide spectrum of breast cancers [21]. These AIs have demonstrated superior efficacy in postmenopausal women and have few associated risks apart from reduction in bone density [8,21–23], and emerging resistance [24,25].

The selective estrogen receptor modulator (SERM) tamoxifen **3a** (Figure 1a) is effective for the treatment of ER+ breast cancer [13]; however, resistance is a clinical problem [26] together with a small increase in incidences of blood clots and endometrial cancers for postmenopausal women [27,28]. The potential advantage of the tamoxifen metabolites endoxifen (**3b**) and norendoxifen (**3c**) in endocrine-refractory metastatic breast cancer is reported [29]. Breast cancers that are (ER+/PR+) are likely to respond to hormone therapy such as tamoxifen and anastrozole [23], while the prophylactic use of tamoxifen, raloxifene, or anastrozole is recommended for postmenopausal women at high risk of developing breast cancer [30,31]. Approximately 20% of breast cancers overexpress the human epidermal growth factor receptor 2 (HER2), which promotes the growth of cancer cells.

Effective treatments for HER2+ breast cancers include the monoclonal antibody trastuzumab [32], the antibody–drug conjugate ado-trastuzumab emtansine [33], and the dual tyrosine kinase inhibitor lapatinib which targets both the HER/neu and the epidermal growth factor receptor (EGFR) [34]. Breast cancers are classified as triple negative (TNBC) when their growth is not supported by estrogen and progesterone nor by the presence of HER2 receptors. The clinical options for treatment of TNBC are limited due to poor response to hormonal therapy, resulting in low 5-year survival rates [35]. There is extensive diversity among breast cancer patients, and each sub-type of breast cancer has unique characteristics. The identification of sub-type-specific network biomarkers can be useful in predicting the survivability of breast cancer patients [36].

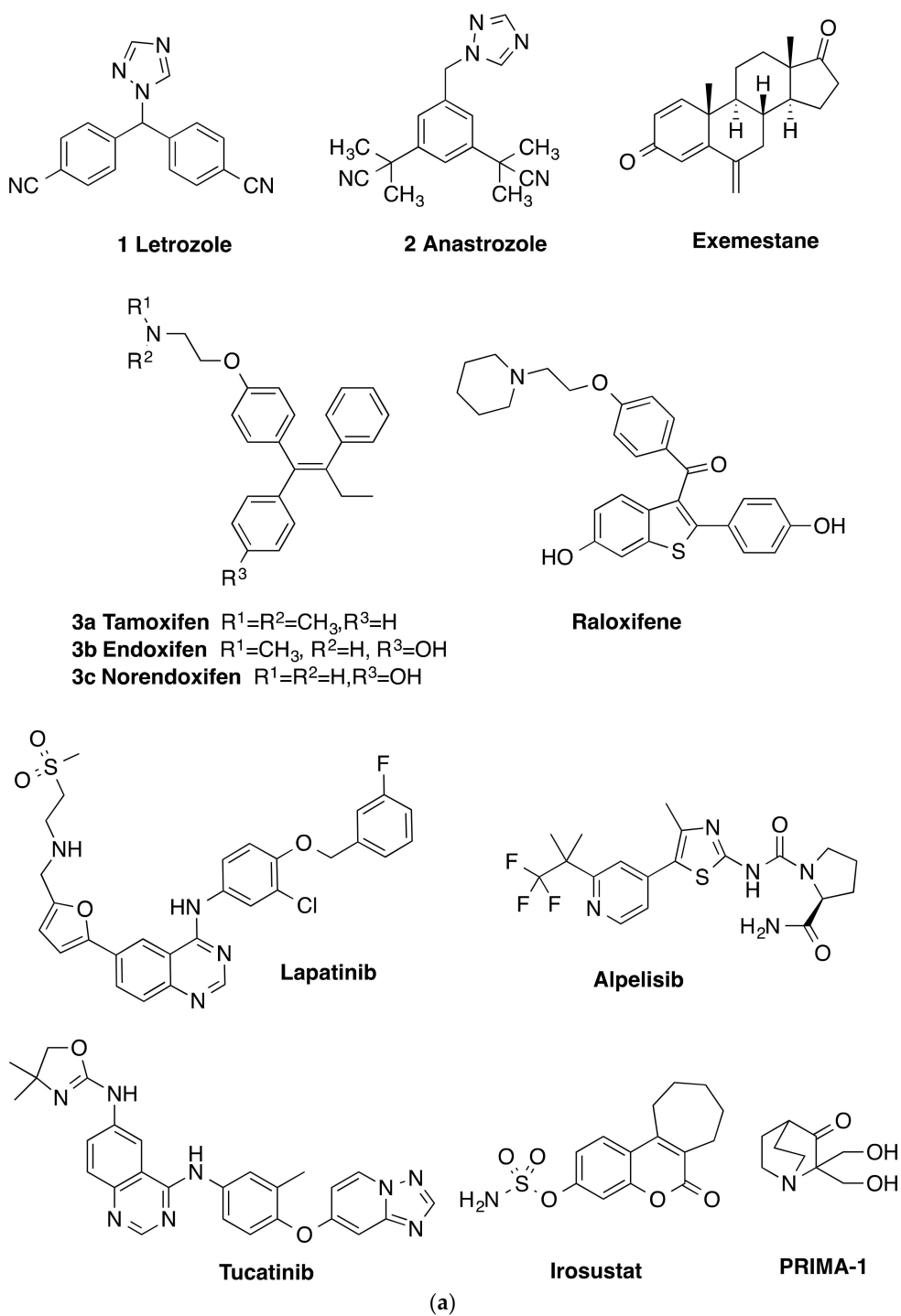
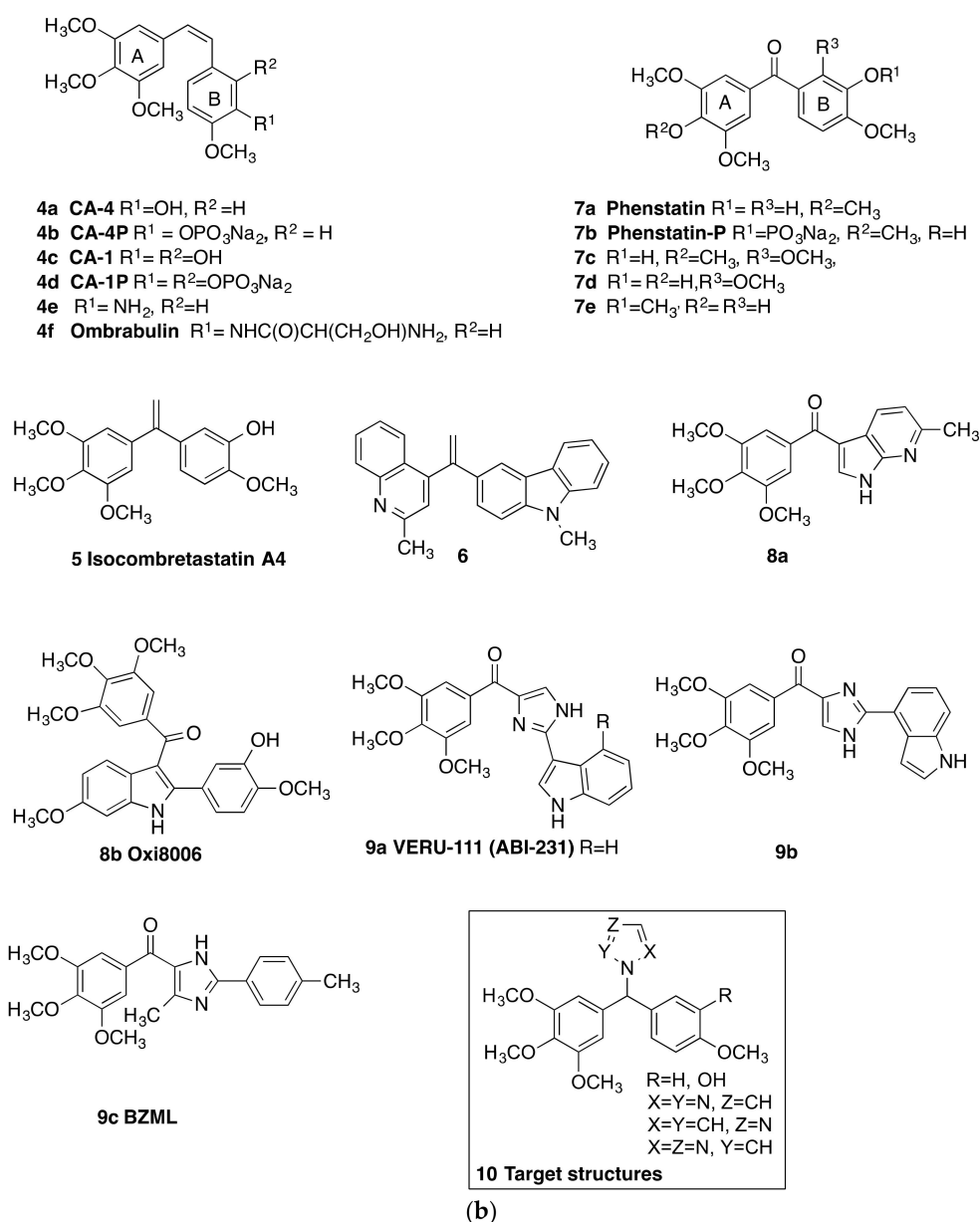


Figure 1. Cont.



**Figure 1.** (a) Aromatase inhibitors (letrozole, anastrozole, Exemestane), SERMs (Tamoxifen, Endoxifen, Norendoxifen, Raloxifene), kinase inhibitors Lapatinib, Alpelisib, Tucatinib, steroid sulfatase inhibitor Irosustat and mutant p53 inhibitor PRIMA-1, (b) Combretastatins **4a–f**, Isocombretastatins **5,6**, phenstatins **7a–e**, colchicine binding site inhibitors **8a,b, 9a–c** and target structures **10**.

FDA-approved drugs for breast cancer in 2019 include the antibody–drug conjugate Fam-trastuzumab deruxtecan [37] (HER2-directed antibody and topoisomerase inhibitor) for the treatment of unresectable or metastatic HER2-positive breast cancer [38], the phosphoinositide-3-kinase (PI3K $\alpha$ ) inhibitor alpelisib [39] for the treatment of HER2-negative, PIK3CA-mutated, advanced or metastatic breast cancer [40] and in 2020, tucatinib, an orally bioavailable, small molecule tyrosine kinase inhibitor for patients with HER2-positive metastatic breast cancer [41]. The microtubule-stabilising drugs paclitaxel, docetaxel, and the epothilone ixabepilone were approved for use in patients with metastatic breast cancer (MBC), alongside the microtubule destabilising vinca alkaloid eribulin [42,43]. The FDA recently granted accelerated approval to the antibody–drug conjugate sacituzumab govitecan (Trodelvy) for previously treated metastatic TNBC [44], while ladiratuzumab vedotin (a LIV-1-targeted antibody

linked to the microtubule-disrupting agent monomethyl auristatin E (MMAE)) is in clinical trials for locally advanced or metastatic triple-negative breast cancer [45]. The steroid sulfatase inhibitor (STS) e.g., STX64 (Irosustat) has entered clinical trials for ER+ locally advanced or metastatic breast cancer [46], while inhibitors of mutant p53, e.g., PRIMA-1 and PRIMA-1<sup>MET</sup>, overexpressed in TNBC have been demonstrated to be effective in vitro [47].

Combretastatins CA-4 **4a**, (phosphate prodrug **4b**), CA-1 **4c** (phosphate prodrug **4d**), **4e**, and serine prodrug ombrabulin **4f** (Figure 1b) have demonstrated impressive antiproliferative potency with microtubule destabilising and anti-vascular effects in many cancers, including breast cancer [48–50]. While many structurally related colchicine binding site inhibitors have been reported [51–53], problems associated with the poor water solubility and isomerisation causing an extensive loss of potency have hampered the progression of combretastatins in clinical trials [54,55]. We have previously reported the synthesis of a series of CA-4 analogues with structures based on the conformationally constrained 2-azetidinone ring, demonstrating potent activity in breast cancer cells [56]. Triazole [57,58] imidazole [59,60], and pyridine-containing analogs [61] of CA-4 are also reported with antiproliferative activity in human cancer cell lines. *Isocombretastatin A4* **5** [62] and 1,1-diheterocyclic ethylenes derived from quinaldine and carbazole e.g., **6** [63] and related conjugates [64] display potent antiproliferative effects in cancer cells and induce G<sub>2</sub>/M cell cycle arrest [65]. The related benzophenone phenstatin **7a** (Figure 1b) [66], together with its sodium phosphate prodrug (**7b**) and metabolites **7c–e** [67], show potent activity in cancer cells and microtubule destabilising activity. The imidazole and indole heterocycles are widely recognised as nuclei of great interest in the design of molecules with anti-tumour activity [68,69]. Related fused-ring heterocyclic structures such as imidazo[2,1-*b*][1,3,4]thiadiazoles with potent antiproliferative activity have also been reported [70]. A variety of compounds structurally related to phenstatin, which contain the heterocycles indole and imidazole, have been synthesised and subsequently evaluated for antimitotic effects and vascular-disrupting effects in cancer cells [71,72]. The azaindole **8a** and 2-aryl-3-aryloindole (OXi8006) **8b** are cytotoxic against selected human cancer cell lines and strongly inhibit tubulin assembly [73,74]. Examples of novel imidazole and indole containing compounds e.g., **9a** [75], **9b** [76], and **9c** (BZML) [77] have been developed as potent tubulin polymerisation-targeting antiproliferative agents. The imidazole derivative BZML **9c** is a novel colchicine binding site inhibitor, which also overcomes multidrug resistance by inhibiting P-gp function and inducing mitotic catastrophe [77]. Compounds such as **9a** (VERU-111), **9b**, and **9c** (BZML) containing both imidazole and indole nuclei exhibit potent activity against a panel of cancer cell lines, are not substrates of P-glycoprotein, and inhibit tumour growth in paclitaxel-resistant cell lines. **9c** inhibits tumour growth and metastasis in vivo [75–77].

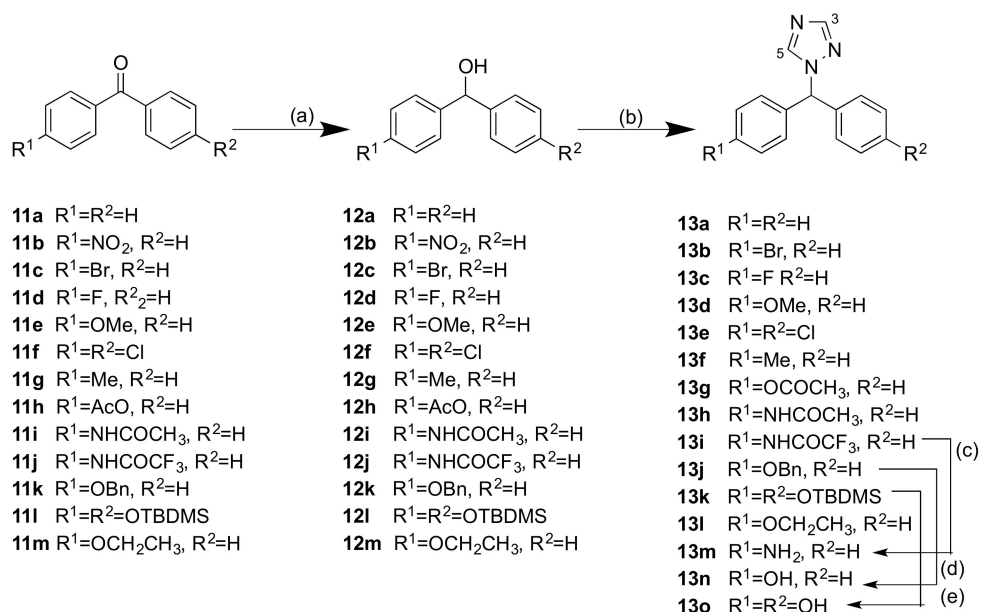
A number of approaches to the design of dual targeting breast cancer agents have been reported e.g., ER/tubulin [78], tubulin/HSP90 [79], tubulin/HSP27 [80], ER/AI e.g., norendoxifen [81,82], and endoxifen [83], sulfatase/AI [84], tubulin/sulfatase [85,86] and tubulin/angiogenesis (vascular endothelial growth factor receptor-2 (VEGFR2) [87]. We now report the synthesis and biological evaluation of a series of 1-(diarylmethyl)-1*H*-1,2,4-triazoles, 1-(diarylmethyl)-2*H*-1,2,3-triazoles, and 1-(diarylmethyl)-1*H*-imidazoles, which are designed as hybrid scaffolds derived from the benzophenone structure of the tubulin targeting phenstatin **7a**, together with the 1,2,4-triazole of the aromatase inhibitor letrozole **2** [88]. These compounds are designed to provide a selective anti-tumour effect by targeting tubulin polymerisation and also would be effective by inhibiting estrogen production. Although aromatase inhibitors such as letrozole are widely used in the treatment of breast cancer, dual tubulin–aromatase inhibitors have not been reported to date. 1-(Diarylmethyl)-1*H*-1,2,4-triazole and 1-(diarylmethyl)-1*H*-1,2,4-imidazole derivatives have been previously investigated as dual aromatase-steroid sulfatase inhibitors [89]. The target structures **10** are shown in Figure 1b. In addition, a number of related compounds containing the cyclic amines pyrrolidine, piperidine, and piperazine are investigated. We wished to develop

this strategic approach with the aim of targeting dual tubulin–aromatase inhibition and have investigated a series of dual-targeting inhibitors.

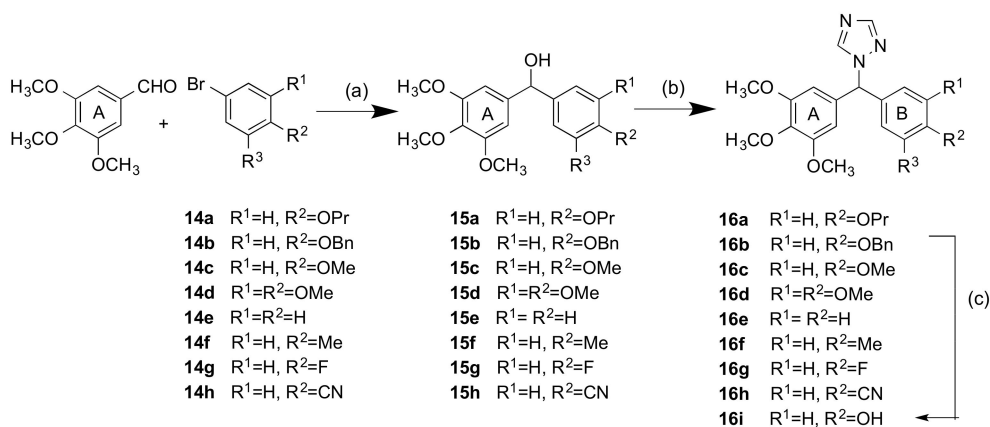
## 2. Results and Discussion

### 2.1. Chemistry

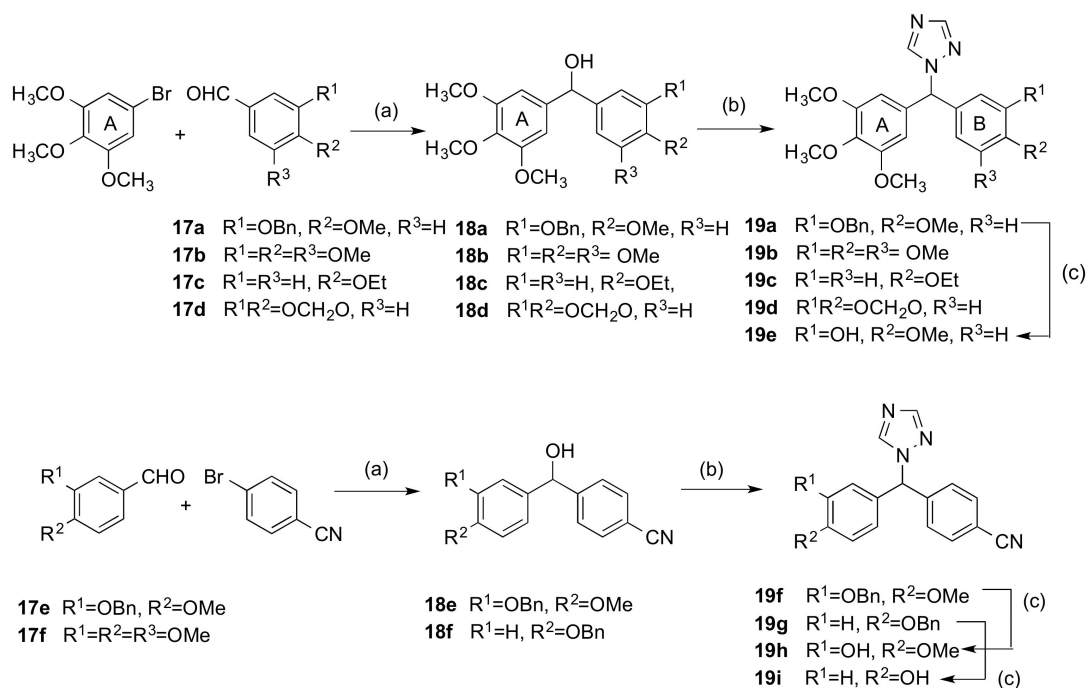
A series of benzophenone-like compounds related in structure to phenstatin **7a** were first prepared (**11a–11m**). The carbonyl group of the benzophenone was subsequently reduced to afford a benzhydryl alcohol; the heterocycles 1,2,4-triazole, 1,2,3-triazole, imidazole, piperidine, pyrrolidine, and piperazine were introduced in order to afford the N-benzhydryl-heterocyclic products (Schemes 1–8). These compounds were investigated as potential dual-active hybrids: the benzophenone scaffold was designed to interact with tubulin, while the heterocyclic ring was incorporated to target the aromatase enzyme.



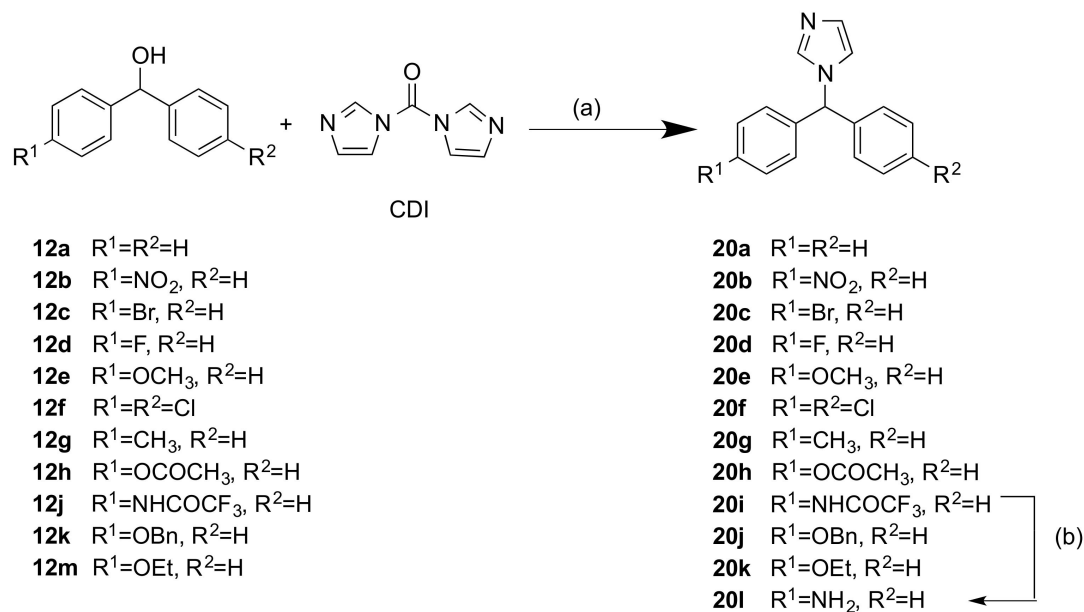
**Scheme 1.** Synthesis of compounds **13a–13o** (Series 1). Reagents and conditions: (a) NaBH<sub>4</sub>, MeOH, 0 °C, (38–100%); (b) 1,2,4-triazole, *p*-TSA, toluene, 4 h, 120 °C, microwave open vessel, (3–98%); (c) K<sub>2</sub>CO<sub>3</sub>, MeOH, H<sub>2</sub>O, 20 °C, 72 h, (16%); (d) H<sub>2</sub>, Pd(OH)<sub>2</sub>, ethyl acetate, 20 °C, (67%); (e) TBAF, THF, 0 °C, (90%) [TBDMS, *tert*-butyldimethylsilyl; Bn, CH<sub>2</sub>C<sub>6</sub>H<sub>5</sub>].



**Scheme 2.** Synthesis of letrozole-phenstatin hybrid compounds **16a–16i** (Series 2a). Reagents and conditions: (a) *n*-BuLi, THF, –78 °C, 1.5 h, (21–89%); (b) 1,2,4-triazole, *p*-TSA, toluene, 4 h, 120 °C, microwave open vessel, (34–93%); (c) Pd(OH)<sub>2</sub>, H<sub>2</sub>, ethyl acetate, 20 °C, (49%). [Bn, CH<sub>2</sub>C<sub>6</sub>H<sub>5</sub>].

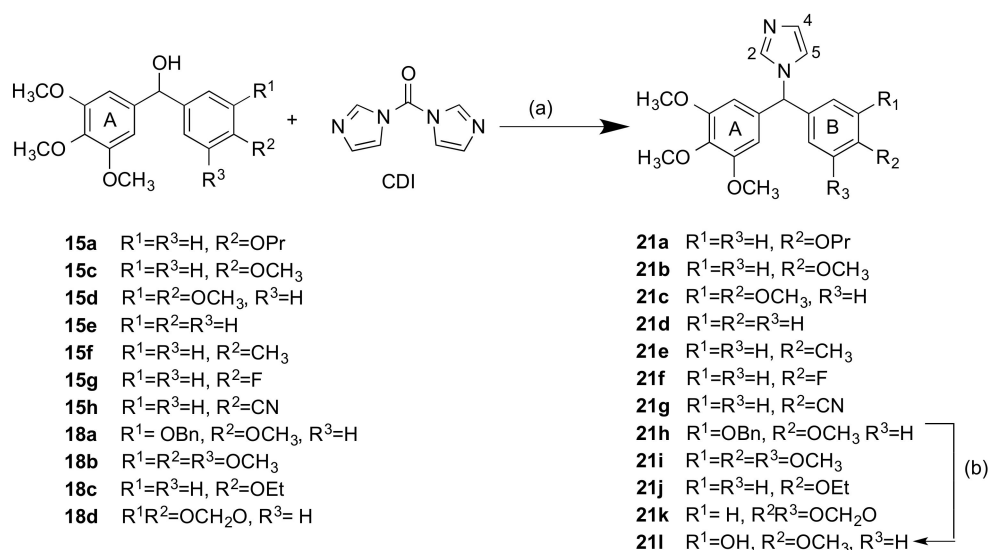


**Scheme 3.** Synthesis of letrozole-phenstatin hybrid compounds **19a–19e** (Series 2a) and **19f–19i** (Series 2b). Reagents and conditions: (a): *n*-BuLi, dry THF,  $-78\text{ }^\circ\text{C}$ , 1.5 h, (16–88%); (b) 1,2,4-triazole, *p*-TSA, microwave open vessel, 4h, (64–95%); (c) Pd(OH)<sub>2</sub>, H<sub>2</sub>, (66–82%). [Bn: CH<sub>2</sub>C<sub>6</sub>H<sub>5</sub>].

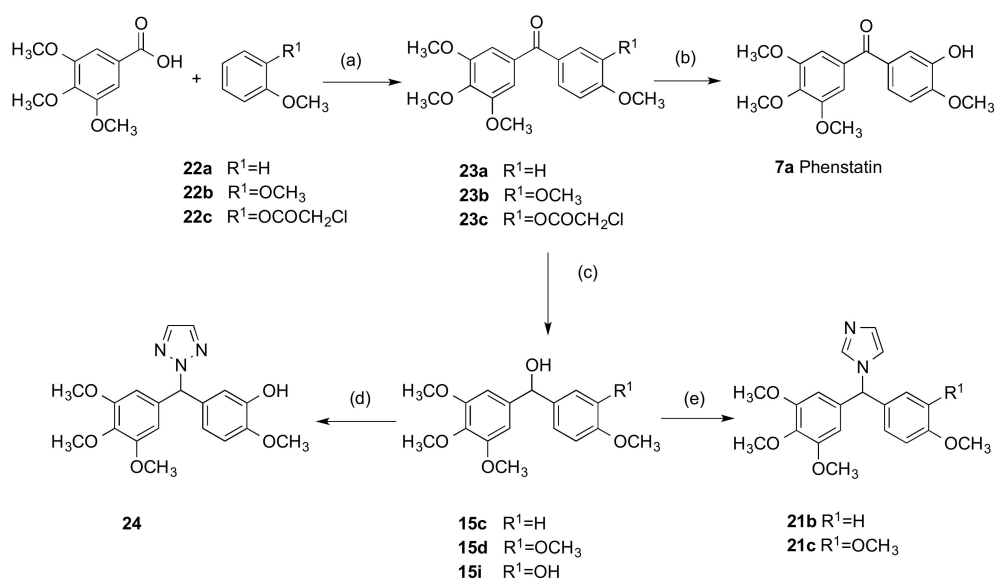


**Scheme 4.** Synthesis of hybrid imidazole-phenstatin compounds **20a–20l** (Series 3). Reagents and conditions: (a) CDI, CH<sub>3</sub>CN, reflux, 3 h, (10–64%); (b) K<sub>2</sub>CO<sub>3</sub>, MeOH, H<sub>2</sub>O, 20 °C, 72, (50%). [Bn: CH<sub>2</sub>C<sub>6</sub>H<sub>5</sub>].





**Scheme 5.** Synthesis of hybrid imidazole-phenstatin compounds **21a–21l**, (Series 4). Reagents and conditions: (a) CDI, CH<sub>3</sub>CN, reflux, 3 h, (30–100%). (b) H<sub>2</sub>, Pd(OH)<sub>2</sub>, ethyl acetate, 20 °C, (93%). [Bn: CH<sub>2</sub>C<sub>6</sub>H<sub>5</sub>].



**Scheme 6.** Synthesis of phenstatin **7a** and phenstatin hybrids **21b**, **21c**, **24**, (Series 4). Reagents and conditions: (a) Eaton's reagent (P<sub>2</sub>O<sub>5</sub>, CH<sub>3</sub>SO<sub>3</sub>H), 60 °C, 3 h, [**23a** (60%), **23b** (57%), **23c** (17%)]; (b) sodium acetate, methanol, reflux, 2 h, (89%); (c) NaBH<sub>4</sub>, MeOH, 0 °C, [**15c** (50%), **15d** (89%), **15i** (96%)]; (d) 1,2,3-triazole, *p*-TSA, toluene, 4 h, 120 °C, microwave open vessel, (77%); (e) CDI, CH<sub>3</sub>CN, reflux, 3 h, [**21b** (39%), **21c** (67%)].

The target compounds are arranged as follows:

Series 1: 1-(Diarylmethyl)-1*H*-1,2,4-triazoles **13a–13o**

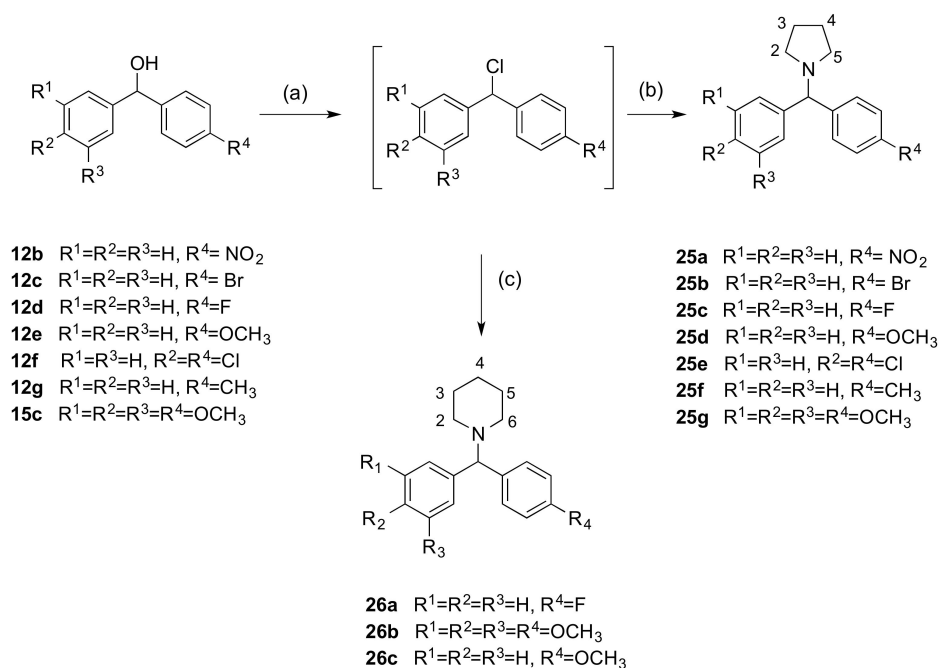
Series 2a: 1-(Aryl-(3,4,5-trimethoxyphenyl)methyl)-1*H*-1,2,4-triazoles **16a–i**, **19a–e**,  
1-(aryl-(3,4,5-trimethoxyphenyl)methyl)-1*H*-1,2,3-triazole **24**

Series 2b: 4-(Aryl-(1*H*-1,2,4-triazol-1-yl)methyl)benzotriazoles **19f–i**

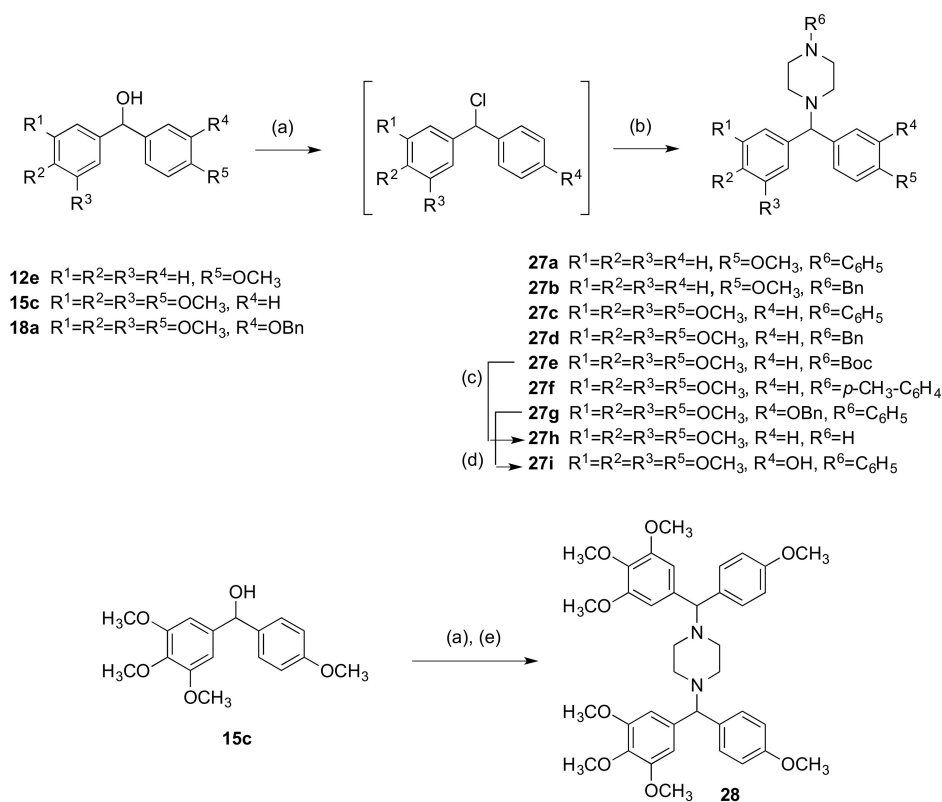
Series 3: 1-(Diarylmethyl)-1*H*-imidazoles **20a–l**

Series 4: 1-(Aryl-(3,4,5-trimethoxyphenyl)methyl)-1*H*-imidazoles **21a–l**,

Series 5: 1-(Diarylmethyl)pyrrolidines **25a–g**, 1-(diarylmethyl)piperidines **26a–c** and  
1-(diarylmethyl)piperazines **27a–i**, **28**



**Scheme 7.** Synthesis of pyrrolidine **25a–g** and piperidine derivatives **26a–c**, (Series 5). Reagents and conditions: (a)  $SOCl_2, CH_2Cl_2$ , 12 h, 20 °C; (b) pyrrolidine, acetonitrile, 12 h, reflux (23–93%); (c) piperidine, acetonitrile, 12 h, reflux (84–91%).



**Scheme 8.** Synthesis of piperazine-phenstatin compounds **27a–g**, **28**, (Series 5). Reagents and conditions: (a)  $SOCl_2, CH_2Cl_2$ , 12 h, 20 °C; (b) N-phenylpiperazine, N-benzylpiperazine, N-Boc-piperazine or *p*-methoxyphenylpiperazine, acetonitrile, reflux, 12 h (6–80%) (c) TFA,  $CH_2Cl_2$ , 30 min, 20 °C (42%); (d)  $H_2, Pd(OH)_2$  (45%); (e) piperazine, ACN, acetonitrile, reflux, 12 h (12%). [Boc: *tert*-Butoxycarbonyl; Bn:  $CH_2C_6H_5$ ].

### 2.1.1. 1-(Diarylmethyl)-1*H*-1,2,4-triazoles (Series 1 and 2)

The general reaction scheme for the preparation of the 1-(diarylmethyl)-1*H*-1,2,4-triazoles **13a–o** (Series 1) heterocyclic derivatives of benzophenones is shown in Scheme 1. These initial compounds carry a single substituent at the *para* position on one or both of the aryl rings (Cl, F, Br, OH, OCH<sub>3</sub>, CH<sub>3</sub> etc.). The benzophenones (**11a–m**) were reduced with sodium borohydride to afford the secondary alcohols **12a–m**, in good yields, Scheme 1. Coupling of 1,2,4-triazole with the secondary alcohols **12a–12m** to afford the benzhydryl-1*H*-1,2,4-triazoles **13a–l** was achieved using *p*-TSA as a catalyst in an open-vessel microwave reactor. Amine **13m** was obtained on treatment of amide **13i** with potassium carbonate, while the phenol **13n** was obtained by hydrogenolysis of the benzyl ether **13j** with palladium hydroxide. Deprotection of the silyl ether **13k** with TBAF afforded the diphenol **13o**. In the <sup>1</sup>H-NMR spectrum of compound **13o**, the singlets (8.41 and 7.97 ppm) were identified as the triazole H5 and H3 respectively, while the singlet at 6.75 ppm corresponds to the methine proton. In the <sup>13</sup>C-NMR spectrum of **13o**, the signal at 65.12 ppm was assigned to the tertiary carbon, while the signals at 151.52 and 143.93 ppm are assigned to C3 and C5 of the triazole (see Supplementary Information).

Since the potent tubulin-inhibiting activity of the 3,4,5-trimethoxyaryl function is very well documented in colchicine-binding site inhibitors [90], the 1,2,4-triazole heterocycle was next reacted with several phenstatin-type 3,4,5-trimethoxyaryl substituted benzhydryl alcohols in order to maximise the potential tubulin activity in the scaffold structures with aromatase-inhibiting action (Series 2). It was decided to retain in most compounds the 3,4,5-trimethoxyaryl group substitution (ring A) and introduce alternative substituents on the second ring (ring B). A modified synthetic procedure allowing access to the desired benzhydryl alcohol intermediates **15a–h** and **18a–f** is shown in Schemes 2 and 3 (step *a*) [91]. Scheme 2 shows the alcohols (**15a–h**) obtained by treatment of the appropriate aryl bromides **14a–h** with *n*-butyllithium followed by reaction with 3,4,5-trimethoxybenzaldehyde (A ring) to afford the alcohols **15a–h** in yields of 21–89%. For the preparation of compounds (**18a–d**) (Scheme 3), the A ring was derived from 3,4,5-trimethoxybromobenzene followed by reaction with the appropriate aldehyde **17a–d**. The nitrile-containing compounds **18e,f** were similarly obtained from the aldehydes **17e,f** and 4-bromobenzonitrile (Scheme 3). The benzhydryl compounds were obtained in good yield after purification via flash column chromatography and the presence of the hydroxyl group was confirmed from IR ( $\nu$  3200–3600 cm<sup>-1</sup>).

Then, the secondary alcohols **15a–h** and **18a–f** were reacted with 1,2,4-triazole to afford the hybrid phenstatin/letrozole compounds **16a–h** and **19a–d,f,g** as racemates, except for **19b**, (Schemes 2 and 3, step *b*). The phenolic compounds **16i**, **19e**, **19h**, and **19i** were obtained by hydrogenolysis over palladium hydroxide of the benzyl ethers **16b**, **19a**, **19f**, and **19g** respectively. From the <sup>1</sup>H-NMR spectrum of compound **16c**, the singlet at 6.62 ppm was assigned the tertiary aliphatic proton. The singlets at 7.91 and 8.01 ppm were assigned to the triazole H-3 and H-5. In the <sup>13</sup>C-NMR spectrum, the tertiary CH signal was identified at 67.4 ppm, while the triazole ring C3 and C5 signals were identified at 143.5 and 152.3 ppm, respectively.

X-ray crystal structures of the triazole compounds **16e**, **16f**, and **19c** (recrystallised from dichloromethane/*n*-hexane) are displayed in Figure 2, while the crystal data and structure refinement are displayed in Table 1. The length of the C-N bond between the methine carbon and the triazole N-1 for compounds **16e**, **16f**, and **19c** was measured at 1.470, 1.471, and 1.479 Å, respectively. The N1-N2 bond length was 1.366 Å (**16e**), 1.363 Å (**16f**), and 1.365 Å (**19c**). The N1-C5 bond length of the triazole ring was observed as 1.334 Å (**16e**), 1.342 Å (**16f**), and 1.343 Å (**19c**). The angle between the methine carbon and the two aromatic rings (Ar-C1-Ar) was measured as 112.51°, 115.08°, and 113.53° respectively for compounds **16e**, **16f**, and **19c**. The corresponding value for the letrozole structure is 114.0°, while the C-N bond between the methine carbon and the triazole N-1 was 1.46 Å [92].

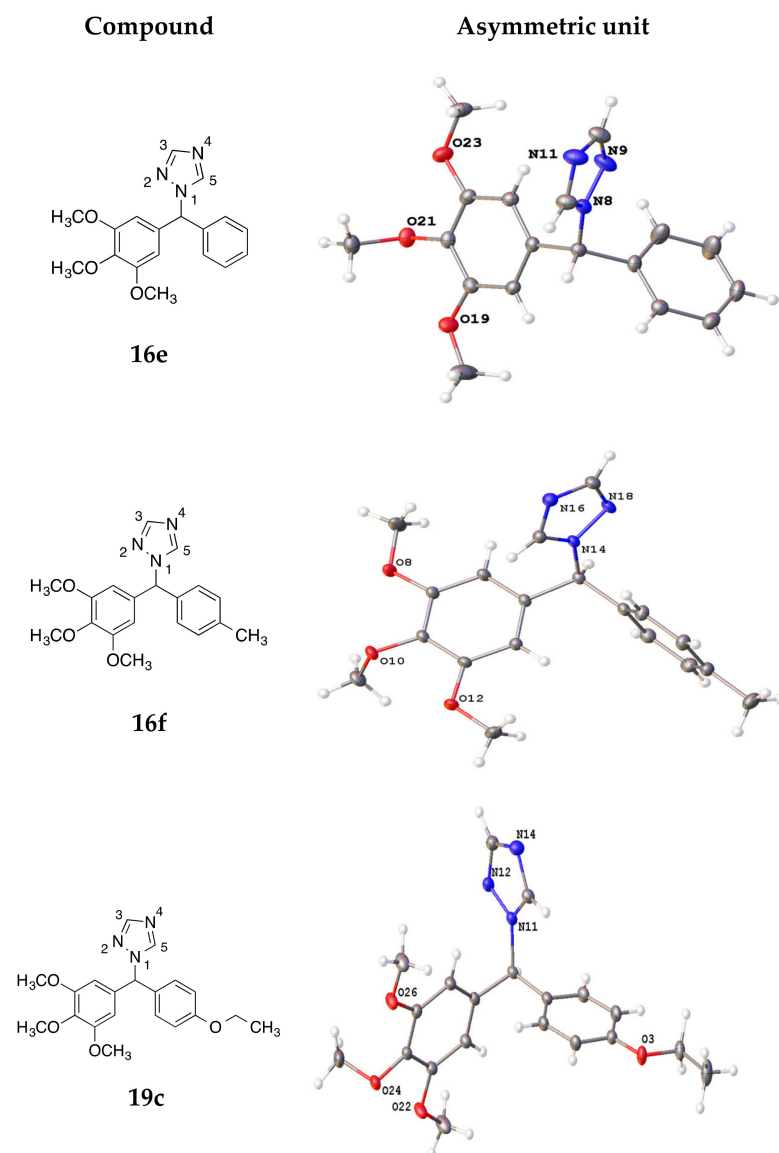


**Figure 2.** X-ray crystallography structures of **16e**, **16f**, and **19c** with heteroatoms labelled and displacement shown at 50% probability.

### 2.1.2. 1-(Diarylmethyl)-1*H*-imidazoles (Series 3 and 4)

A series of related imidazole-containing compounds were also prepared **20a–l** (Series 3) and **21a–k** (Series 4). The secondary alcohols **12a–h**, **j**, **k**, and **m** were coupled to imidazole using CDI (carbonyldiimidazole) [93] to afford products **20a–k**, Series 3, (Scheme 4, step *a*). The associated carbamate derivatives were not isolated in our reactions [94]. The hydrolysis of **20i** afforded the amine **20i** in 50% yield (Scheme 4, step *b*). Structures were optimised with variations in electron-releasing and electron-withdrawing substituents on the aryl rings. A further series of compounds containing the ring A type 3,4,5-trimethoxyaryl substituents was prepared by reacting alcohols **15a,c–h**, and **18a–d** with CDI to afford imidazole products **21a–k**, Series 4, (Scheme 5, step *a*). The benzyl ether **21h** was treated with Pd(OH)<sub>2</sub> to afford the phenol **21i** as a racemate in 93% yield (Scheme 5, step *b*). In the <sup>1</sup>H NMR spectrum of compound **21i**, the imidazole H4 was observed as a singlet at 6.88 ppm, while the H2 and H5 were observed at 7.44, and 7.12 ppm, respectively. The singlet at 6.38 ppm was assigned to the tertiary aliphatic CH. From the <sup>13</sup>C-NMR spectrum, the aliphatic tertiary CH was identified at 65.2, while the signals at 138.0, 129.4, and 119.4 ppm were assigned to the imidazole C2, C4, and C5, respectively.

**Table 1.** Crystal data and structure refinement details for compounds **16e**, **16f**, **19c**, **21i**, and **26a**.

Compound	16e	16f	19c	21i	26a
CCDC no.	2015431	2015432	2015433	2015434	2015435
Empirical formula	C <sub>18</sub> H <sub>19</sub> N <sub>3</sub> O <sub>3</sub>	C <sub>19</sub> H <sub>21</sub> N <sub>3</sub> O <sub>3</sub>	C <sub>20</sub> H <sub>23</sub> N <sub>3</sub> O <sub>4</sub>	C <sub>22</sub> H <sub>26</sub> N <sub>2</sub> O <sub>6</sub>	C <sub>18</sub> H <sub>20</sub> FN
M (g/mol)	325.36	339.39	369.41	414.45	269.35
T (K)	100(2)	100(2)	100(2)	100(2)	100(2)
Crystal System	monoclinic	monoclinic	monoclinic	monoclinic	monoclinic
SG	P2 <sub>1</sub> /n	P2 <sub>1</sub> /c	P2 <sub>1</sub> /c	P2 <sub>1</sub> /c	P2 <sub>1</sub> /c
a (Å)	8.1796(5)	9.2487(4)	12.8748(6)	14.1937(6)	5.9228(2)
b (Å)	14.1725(10)	9.6620(4)	9.8550(5)	13.1553(5)	14.0705(5)
c (Å)	14.4742(10)	20.0006(9)	14.8091(7)	12.4613(5)	17.7920(6)
α (°)	90	90	90	90	90
β (°)	98.7882(11)	97.8110(10)	93.1792(8)	113.2250(10)	98.275(2)
γ (°)	90	90	90	90	90
V (Å <sup>3</sup> )	1658.23(19)	1770.69(13)	1876.10(16)	2138.25(15)	1467.29(9)
Z	4	4	4	4	4
D <sub>calc</sub> (g/cm <sup>3</sup> )	1.303	1.273	1.308	1.287	1.219
μ (mm <sup>-1</sup> )	0.09	0.088	0.092	0.094	0.628
F(000)	688	720	784	880	576
Radiation	MoKα (λ = 0.71073)	MoKα (λ = 0.71073)	MoKα (λ = 0.71073)	MoKα (λ = 0.71073)	CuKα (λ = 1.54178)
Reflections collected	61043	115661	95764	85391	20214
Independent reflections	4298 [R <sub>int</sub> = 0.0532, R <sub>sigma</sub> = 0.0237]	5438 [R <sub>int</sub> = 0.0264, R <sub>sigma</sub> = 0.0097]	5504 [R <sub>int</sub> = 0.0364, R <sub>sigma</sub> = 0.0143]	6261 [R <sub>int</sub> = 0.0385, R <sub>sigma</sub> = 0.0188]	2684 [R <sub>int</sub> = 0.0634, R <sub>sigma</sub> = 0.0356]
Data/restraints/ parameters	4298/0/217	5438/0/230	5504/0/248	6261/0/277	2684/1/191
Goodness-of-fit on F <sup>2</sup> (S)	1.018	1.043	1.046	1.005	1.063
Final R indexes [I ≥ 2σ (I)] *	R <sub>1</sub> = 0.0407, wR <sub>2</sub> = 0.0904	R <sub>1</sub> = 0.0374, wR <sub>2</sub> = 0.1018	R <sub>1</sub> = 0.0381, wR <sub>2</sub> = 0.0938	R <sub>1</sub> = 0.0405, wR <sub>2</sub> = 0.0967	R <sub>1</sub> = 0.0479, wR <sub>2</sub> = 0.1325
Final R indexes [all data]	R <sub>1</sub> = 0.0613, wR <sub>2</sub> = 0.1005	R <sub>1</sub> = 0.0445, wR <sub>2</sub> = 0.1083	R <sub>1</sub> = 0.0506, wR <sub>2</sub> = 0.1025	R <sub>1</sub> = 0.0580, wR <sub>2</sub> = 0.1079	R <sub>1</sub> = 0.0547, wR <sub>2</sub> = 0.1369
Largest diff. peak/hole/e Å <sup>-3</sup>	0.31/−0.21	0.42/−0.39	0.42/−0.21	0.38/−0.24	0.19/−0.21

$$* R_1 = \sum | |F_o| - |F_c| | / \sum |F_o|, wR_2 = [\sum w(F_o^2 - F_c^2)^2 / \sum w(F_o^2)^2]^{1/2}.$$

Single crystal X-ray analysis was obtained for compound **21i** (recrystallised from dichloromethane/*n*-hexane), and the crystal structure is shown in Figure 3. The crystal data and structure refinement for compound **21i** are displayed in Table 1. The angle between the methine carbon and the aryl rings (114.16°) and also the bond length between the methine carbon and the N-1 imidazole nitrogen (1.471 Å) were similar to the corresponding values obtained for the triazole compounds **16e**, **16f**, and **19c** (Table 1). The bond angles between the aryl rings and the imidazole ring were determined as 111.36° and 111.80°, also similar to the corresponding values of 109.99° and 112.6° reported for letrozole [92].

An alternative approach for the preparation of phenstatin and related azole compounds using a Friedel–Crafts acylation with Eaton’s reagent was also investigated (Scheme 6) [67]. 3,4,5-Trimethoxybenzoic acid was reacted with anisole (**22a**), 1,2-dimethoxybenzene (**22b**), or compound **22c** (prepared by the protection of 2-methoxyphenol with chloroacetyl chloride) using Eaton’s reagent (readily prepared from phosphorus pentoxide and methane-sulfonic acid) to afford respectively benzophenones **23a**, **23b**, and **23c** (Scheme 6, Step a). Then, these benzophenones were reduced to the benzhydryl alcohols **15c**, **15d**, and **15i**, respectively with sodium borohydride (Scheme 6, step a), with the concomitant removal of the chloroacetyl protecting group of **23c**. Although requiring an additional step, this method was followed after the reaction of the aryl bromide with the aldehyde to afford the alcohol as shown in Schemes 2 and 3 was not successful or did not afford a sufficient

quantity of product for the next step e.g., for compound **15d**, the overall yield increased to 51% compared with 30%. Then, compounds **15c** and **15d** were treated with CDI azole to afford the imidazole-containing products **21b** and **21c** (Scheme 6, step e).

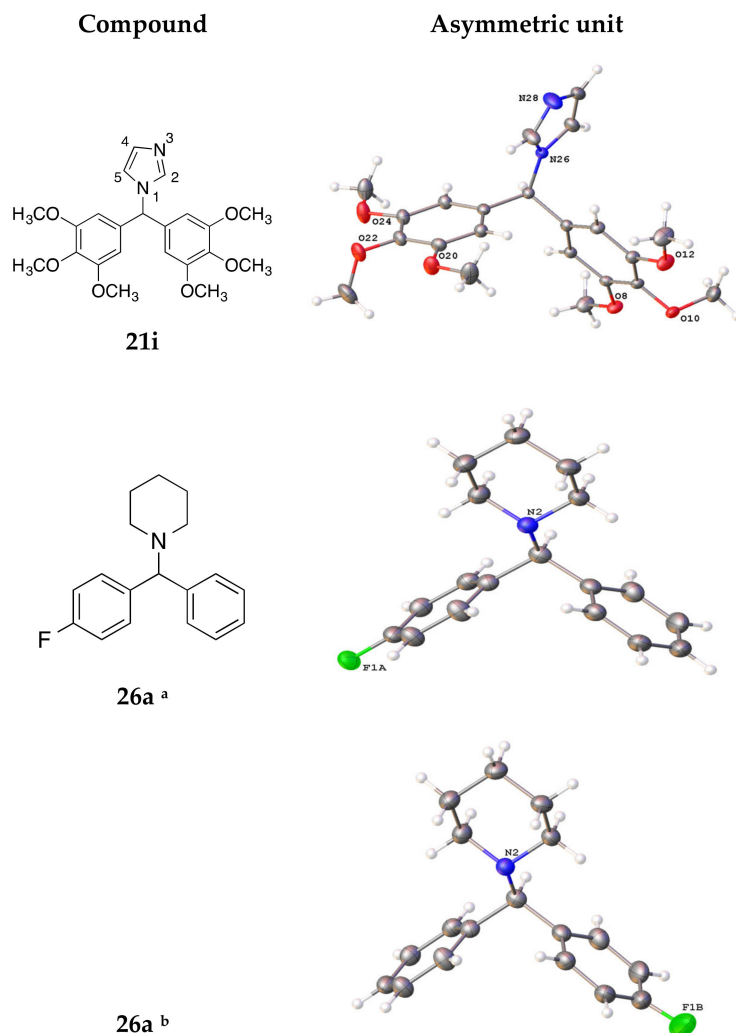


**Figure 3.** X-ray crystallography of compounds **21i** and **26a** with heteroatoms labelled and displacement shown at 50% probability. <sup>a</sup> Disordered molecular structure of **26a** showing the major occupied moiety F1a. <sup>b</sup> Disordered molecular structure of **26a** showing the minor occupied moiety F1B.

The phenol **15i** was also reacted with 1,2,3-triazole to afford the product **24** in 77% yield, Series 4, (Scheme 6, step d). Compound **24** is the only phenstatin derivative substituted with 1,2,3-triazole synthesised in this project and was investigated for comparison with the 1,3,4-triazole compound series. In the <sup>1</sup>H NMR spectrum of **24**, the signal at 6.99 ppm was assigned to the tertiary CH. Interestingly, the two protons of the 1,2,3-triazole ring were observed as a singlet with an integration of 2H at 7.83 ppm, while the signal at 134.9 ppm in the <sup>13</sup>C-NMR spectrum of **24** was assigned to the C4 and C5 of the triazole ring, indicating that alkylation occurred at N2 of the 1,2,3-triazole [95]. The alkylation of 1,2,3-triazoles may result in the formation of regioisomers depending on the reaction conditions e.g., solvent, temperature, and catalyst used [96]. The signal for the tertiary CH was observed at 71.0 ppm. The benzophenone **23c** was also used in the preparation of phenstatin **7a** [67]; the deprotection of **23c** by reaction with sodium acetate afforded **7a** in 89% yield (Scheme 6, step b), which was used as a positive control in the cell viability tests.

### 2.1.3. 1-(Diarylmethyl)Pyrrolidines, 1-(Diarylmethyl)Piperidines, and 1-(Diarylmethyl)Piperazines (Series 5)

The preparation of a series of benzhydryl derivatives substituted on the tertiary carbon with the heterocycles pyrrolidine, piperidine, and piperazine was next investigated (Series 5, Schemes 7 and 8). These products allow a comparison of biochemical activity with the related imidazole and triazole compounds from Series 1–4. The advantages of incorporating such heterocyclic rings into drugs are well known; i.e., they can increase the lipophilicity, polarity, and aqueous solubility of the drug [97]. In particular, piperazine is ranked 3<sup>rd</sup> among the 25 most common heterocycles contained in FDA-approved drugs [98]. In the present work, the corresponding secondary benzhydryl chloride was prepared from the secondary alcohols **12b–12g**, **15c**, and **18a** using thionyl chloride (Schemes 7 and 8, step *a*) [93]. The intermediate alkyl chlorides were reacted with piperidine to afford products **26a–c** (Scheme 7, step *c*), while reaction with pyrrolidine yielded derivatives **25a–g** (Scheme 7, step *b*).

An alternative synthesis of 1-(diarylmethyl)piperidines is reported using a copper(I)-catalysed coupling reaction of aryl boronic acids with N,O-acetals and N,N-aminals [99]. All compounds are racemates apart from compound **25e** and were obtained in moderate yields (23–93%). In the <sup>1</sup>H-NMR spectrum of compound **25b**, the multiplets at 1.71–1.80 and 2.35–2.43 ppm were assigned to the pyrrolidine methylene protons at H-3,4 and H-2,5 respectively, while the tertiary CH was observed as a singlet at 4.11 ppm. In the <sup>13</sup>C-NMR spectrum, the pyrrolidine C-3 and C-2 signals were at 23.5 and 53.6 ppm, respectively. The signal at 75.7 ppm was assigned to the tertiary carbon. Single crystal X-ray analysis for compound **26a** is shown below in Figure 3 (obtained by crystallisation in dichloromethane/*n*-hexane). The crystal data and structure refinement for compound **26a** are displayed in Table 1. In **26a**, the disordered fluorine was modelled in two positions with occupancies of 84% and 16%. The C1-N bond length was observed as 1.473 Å and the central C<sub>14</sub>-C<sub>1</sub>-C<sub>8</sub> and C<sub>14</sub>-C<sub>1</sub>-N<sub>2</sub> angles were observed as 109.28° and 112.09°, respectively. The piperidine ring bond lengths were 1.471 Å (N2-C3), 1.474 Å (N2-C7), and 1.514 Å (C3-C4), which differ from the N1-C bond length of the triazole ring 1.334 Å due to unsaturation.

As a further extension of this research, a related series of piperazine-containing compounds was prepared by coupling selected secondary alcohols with the appropriate piperazine derivative (Series 5, Scheme 8). The preparation of diarylmethylamines has been reported by Le Gall et al. by reaction of the aldehyde and piperidine derivative to a solution of the organozinc reagent in acetonitrile in a Mannich-type reaction [100,101]. The secondary alcohols **12e**, **15c**, and **18a** were treated with thionyl chloride (Scheme 8, step *a*), and the resulting alkyl chloride was used immediately for the next reaction step (step *b*) by addition of the appropriate piperazine (N-phenylpiperazine, N-benzylpiperazine, *p*-methoxyphenylpiperazine, or N-Boc-piperazine) to afford the products **27a–g** in yields up to 80%. For the preparation of compound **27e**, Boc-protected piperazine was used to avoid the possible formation of the dimer. In the <sup>1</sup>H-NMR spectrum of compound **27d**, the broad signal at 2.47 ppm is assigned to piperazine methylene protons; the singlet at 3.50 ppm is assigned to the benzyl methylene, while the singlet at 4.09 ppm corresponds to the tertiary C-1 proton. The <sup>13</sup>C-NMR spectrum of compound **27d** further confirms the proposed structure. The signals at 51.8 and 53.3 ppm were characteristic of the piperazine ring protons, the signals at 63.0 ppm and 75.6 ppm are assigned to the benzyl methylene and tertiary CH, respectively. The deprotection of compound **27e** with TFA afforded compound **27h** as a yellow oil (42%), (Scheme 8, step *c*). A palladium-catalysed hydrogenolysis of **27g** afforded the phenolic compound **27i** in 45% yield (step *d*), which is the phenylpiperazine derivative of phenstatin. Its formation was confirmed by IR spectroscopy (3475 cm<sup>-1</sup>).

When the secondary alcohol **15c** was treated with thionyl chloride followed by an excess of piperazine (5 equivalents), the product obtained was a piperazine dimer **28** (Scheme 8). In the <sup>1</sup>H-NMR spectrum of the dimer **28**, the broad signal (2.40 ppm) is characteristic of the piperazine methylene protons, while the signal at 4.08 ppm integrating for 2H was assigned to the two tertiary CH protons. In the <sup>13</sup>C-NMR spectrum, the signal

at 52.0 ppm was assigned to the piperazine ring carbons; the signal at 75.7 ppm was assigned to the CH, while the duplication of the aromatic signals confirmed the formation of the product.

## 2.2. Stability Studies

HPLC stability studies were performed on representative compounds **211** and **24** to establish their stability at different pH systems, which mimic in vivo conditions. Compound **211** was chosen among these imidazole compounds for HPLC stability studies at three different pH systems; acidic pH 4, pH 7.4, and basic pH 9 (acid pH found in the stomach, basic found in the intestine, and pH 7.4 in the plasma). The degradation of compound **211** was minimal with 80% of **231** remaining at both pH 7.4 and pH 9 and 90% at pH 4 after 24 h. The 1,2,3-triazole compound **24** was observed to be most stable at pH 4 with 65% remaining after 24 h compared to 60% at pH 9 and 50% at pH 7.4.

## 3. Biochemical Results and Discussion

### 3.1. In Vitro Antiproliferative Activity in MCF-7 Breast Cancer Cells

The antiproliferative activity of the panel of hybrid compounds 1-(diarylmethyl)-1*H*-1,2,4-triazoles (Series 1 and 2) and 1-(diarylmethyl)-1*H*-imidazoles (Series 3 and 4) was initially evaluated in the MCF-7 human breast cancer cell using the standard alamarBlue assay. In addition, a number of related compounds containing the aliphatic amines pyrrolidine, piperidine, and piperazine were investigated (Series 5). The MCF-7 human breast cancer cell line is estrogen receptor (ER)-positive, progesterone receptor (PR)-positive, and HER2 negative. Compounds were initially screened at two concentrations (1 and 0.1  $\mu\text{M}$ ) for antiproliferative activity in MCF-7 cells to determine the structure–activity relationship for these hybrid compounds and to identify the most potent compounds for further investigation. Compounds that were synthetic intermediates for the final compound were not screened, as they were not considered as potential actives in the study. The results obtained from this preliminary screen are displayed in Figures 4–6. Then, those compounds showing potential activity (cell viability <50%) were selected for further evaluation at different concentrations and in other cell lines. CA-4 (**4a**) (24% viable cells at 1  $\mu\text{M}$ ) and phenstatin (**7a**) (30% viable cells at 1  $\mu\text{M}$ ) induced a potent antiproliferative effect and were used as positive controls. Ethanol (1% *v/v*) was used as the vehicle control (with 99% cell viability). The preliminary results obtained for these novel compounds (Series 1–5) are discussed by structural type.

#### 3.1.1. Series 1: 1-(Diarylmethyl)-1*H*-1,2,4-triazoles **13b–g**, **1–o**

The first class of compounds tested 1-(diarylmethyl)-1*H*-1,2,4-triazoles (**13b–g**, **13l–o**, Figure 4A) were weakly active, with 68–90% viability for the two concentrations tested (1  $\mu\text{M}$  and 0.1  $\mu\text{M}$ ). These compounds carry a single substituent at the *para* position on one or both aryl rings (Cl, F, Br, OH, OCH<sub>3</sub>, CH<sub>3</sub>, etc.) indicating that the triazole ring alone is not sufficient for the induction of antiproliferative activity in MCF-7 cells. The most active compounds were the diphenolic derivative **13o** with 68% viability (1  $\mu\text{M}$ ) and the amino compound **13m** (72% viability 1  $\mu\text{M}$ ). It appears that specific substituents are required on both the A and B rings of the benzophenone for activity, as also observed for phenstatin and analogues [67].

#### 3.1.2. Series 2: 1-(Aryl-(3,4,5-Trimethoxyphenyl)Methyl)-1*H*-1,2,4-Triazoles **16a,c–i**, **19b–e**, **19h**, **19i** and 1-(Phenyl(3,4,5-Trimethoxyphenyl)Methyl)-1*H*-1,2,3-Triazole **24**

Since the potent tubulin inhibiting activity of the 3,4,5-trimethoxyaryl function is very well documented [90], the preliminary screening in MCF-7 cells of the panel of 1,2,4-triazole containing compounds (**16a**, **c–i**, **19b–e**) synthesised having the 3,4,5-trimethoxyphenyl motif (A ring) together with various substituents on the B ring was next investigated (Figure 4B, two concentrations of 1  $\mu\text{M}$  and 0.1  $\mu\text{M}$ ). The most potent compound was identified as **19e** having the characteristic 3-hydroxy-4-methoxyaryl B ring as in phenstatin



and CA-4 (29% viability at 1  $\mu$ M), while the ethanol control (1% *v/v*) resulted in 99% viability. Two compounds with moderate activity were identified as **16c** (4-methoxy group in the B ring) with 75% cell viability at 1  $\mu$ M and **16g** (4-fluoro in B ring) with 77% viable cells at 1  $\mu$ M. The remaining 3,4,5-trimethoxyphenylmethyl-1*H*-1,2,4-triazole compounds investigated having various substituents on the B ring e.g., 4-F, 4-CN, 4-OH, 4-CH<sub>3</sub> were not as potent as the lead compound with viability >80% at 1  $\mu$ M, while compounds **19h** and **19i** were found to be inactive with half maximal inhibitory concentration (IC<sub>50</sub>) values greater than 100  $\mu$ M. This result demonstrated that even small changes to the phenstatin scaffold were unfavourable for antiproliferative activity. From the initial screening results, it was concluded that the 1,2,4-triazole heterocycle alone was not sufficient to improve activity in the benzhydryl compounds compared to phenstatin.

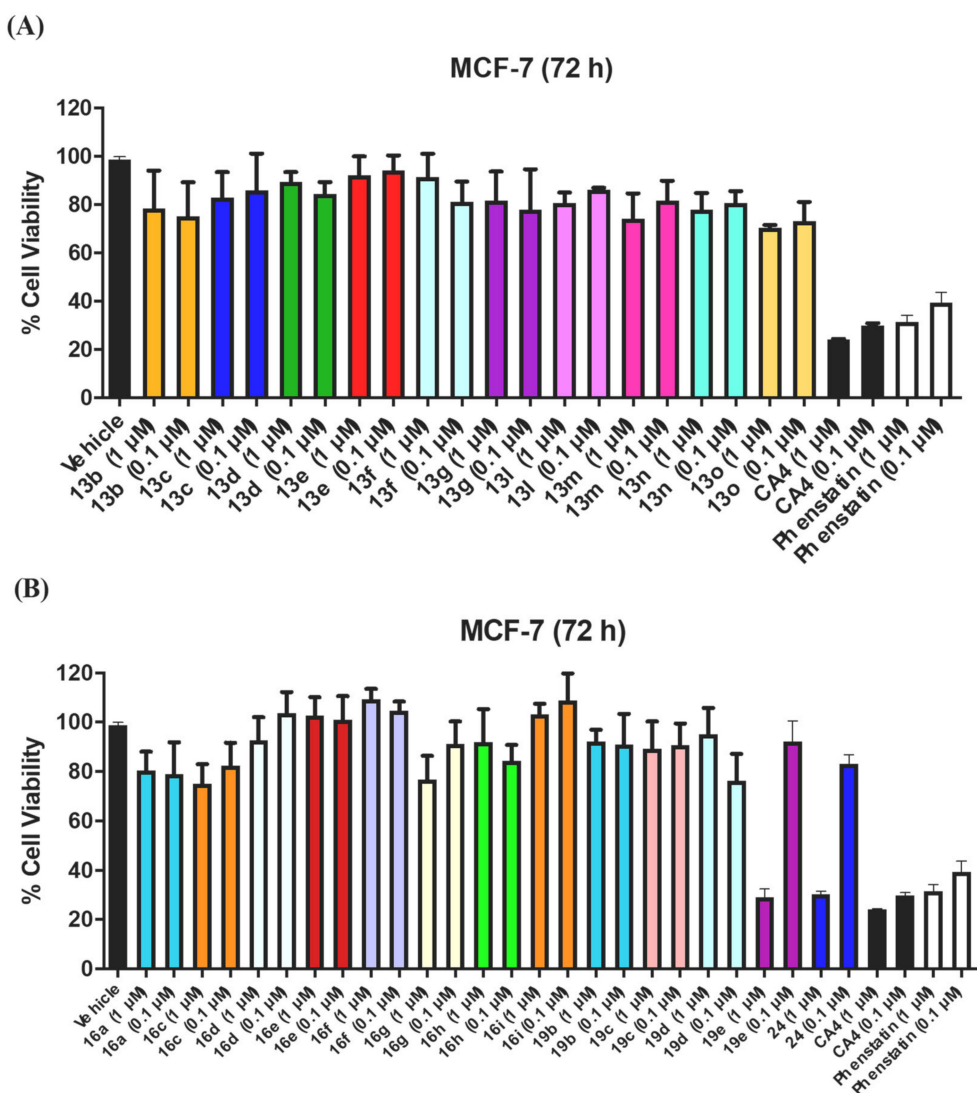


**Figure 4.** Preliminary cell viability data for (A) Series 1: 1-(diarylmethyl)-1*H*-1,2,4-triazoles **13b–g**, **1–o** (B) Series 2: 1-(diarylmethyl)-1*H*-1,2,4-triazoles **16a**, **c–i**, **19b–e**, 1-(diarylmethyl)-2*H*-1,2,3-triazole **24** in MCF-7 breast cancer cells. Cell proliferation of MCF-7 cells was determined with an alamarBlue assay (seeding density  $2.5 \times 10^4$  cells/mL per well for 96-well plates). Compound concentrations of either 1 or 0.1  $\mu$ M for 72 h were used to treat the cells (in triplicate) with control wells containing vehicle ethanol (1% *v/v*). The mean value + SEM for three independent experiments is shown. The positive controls used are CA-4 and phenstatin.

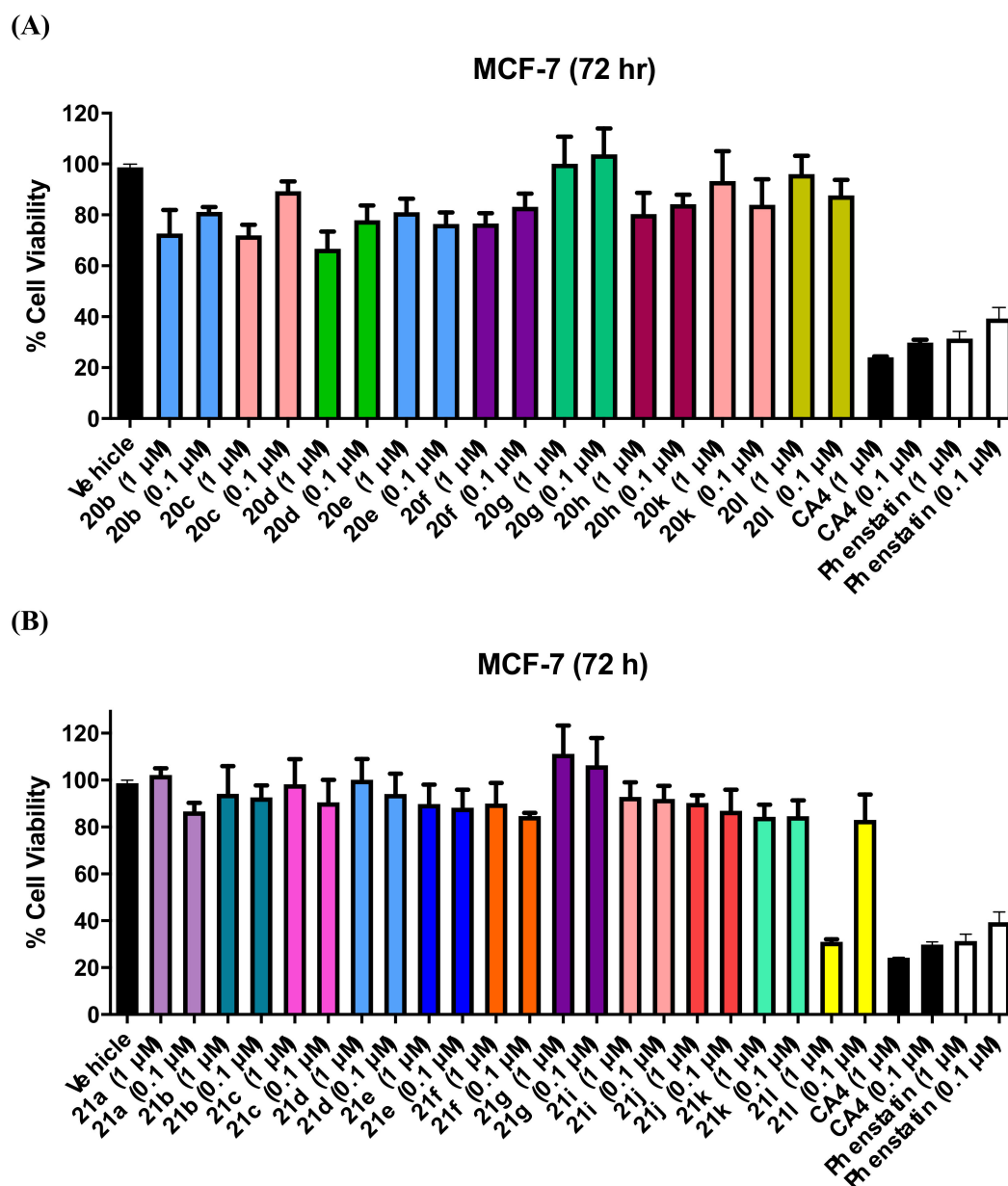


**Figure 5.** Preliminary cell viability data for (A) Series 3: 1-(diarylmethyl)-1*H*-imidazoles **20b–h, k, l** and (B) Series 4: 1-(diarylmethyl)-1*H*-imidazoles **21a–g, i–l** in MCF-7 breast cancer cells. Cell proliferation of MCF-7 cells was determined with an alamarBlue assay (seeding density  $2.5 \times 10^4$  cells/mL per well for 96-well plates). Compound concentrations of either 1 or 0.1  $\mu\text{M}$  for 72 h were used to treat the cells (in triplicate) with control wells containing vehicle ethanol (1% *v/v*). The mean value  $\pm$  SEM for three independent experiments is shown. The positive controls used are CA-4 and phenstatin.

The  $\text{IC}_{50}$  value for the most potent triazole–phenstatin hybrid compound **19e** was determined in MCF-7 as  $0.42 \pm 0.07 \mu\text{M}$  at 72 h (Table 2). **19e** is a hybrid of phenstatin with the 3,4,5-trimethoxyaryl motif (ring A) and the 3-hydroxy-4-methoxyaryl B ring, but it is also related to the aromatase inhibitor letrozole due to the 1,2,4-triazole heterocycle. The hybrid structure suggests a potential for dual tubulin/aromatase activity, and therefore, this compound was selected for aromatase inhibition assay.

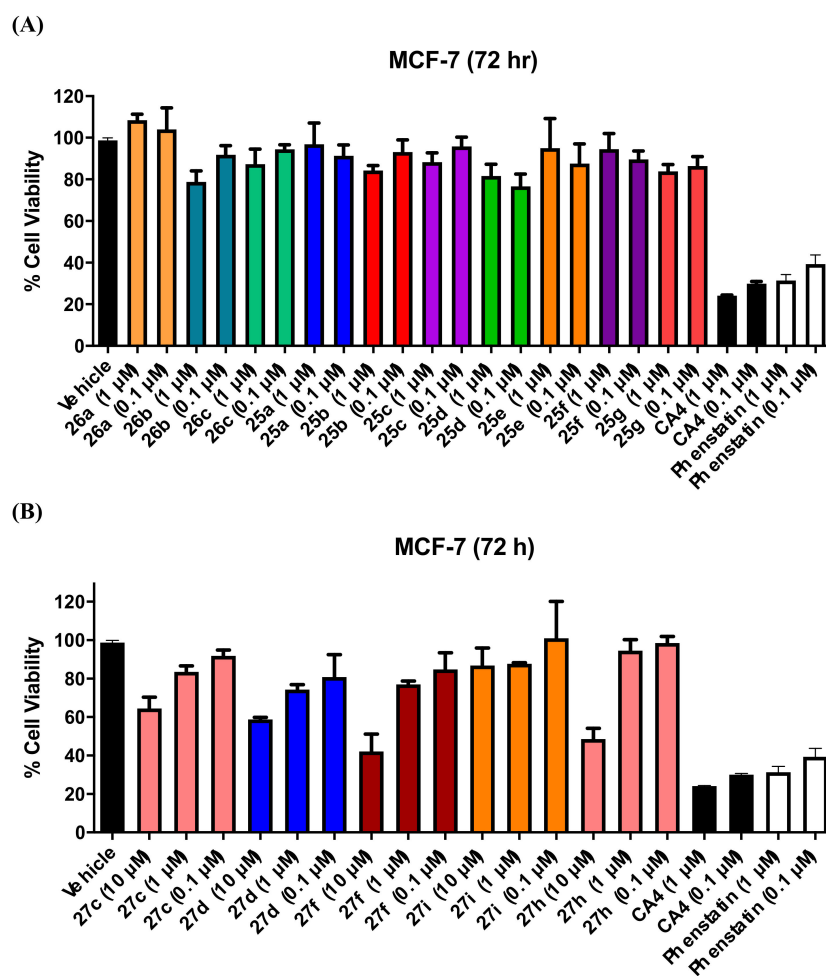


**Figure 6.** Preliminary cell viability data for (A) Series 5: 1-(diarylmethyl)pyrrolidines and 1-(diarylmethyl)piperidines **25a–g**, **26a–c** and (B) Series 5: 1-(diarylmethyl)piperazines **27c,d,f,i**, and **h** in MCF-7 breast cancer cells. Cell proliferation of MCF-7 cells was determined with an alamarBlue assay (seeding density  $2.5 \times 10^4$  cells/mL per well for 96-well plates). Compound concentrations of either 10, 1, or 0.1  $\mu\text{M}$  for 72 h were used to treat the cells (in triplicate) with control wells containing vehicle ethanol (1% *v/v*). The mean value  $\pm$  SEM for three independent experiments is shown. The positive controls used are CA-4 and phenstatin.

**Table 2.** Antiproliferative effects of selected azole compounds **19e**, **211**, and **24** in MCF-7, MDA-MB-231 human breast cancer cells, and HL-60 leukaemia cell line.

Compound	Antiproliferative Activity <sup>a</sup> MCF-7 Cells IC <sub>50</sub> ( $\mu\text{M}$ )	Antiproliferative Activity <sup>a</sup> MDA-MB-231 Cells IC <sub>50</sub> ( $\mu\text{M}$ )	Antiproliferative Activity <sup>a</sup> HL-60 Cells IC <sub>50</sub> ( $\mu\text{M}$ )
<b>19e</b>	$0.042 \pm 0.070$	$0.978 \pm 0.130$	$0.261^b$
<b>211</b>	$0.132 \pm 0.007$	$0.237 \pm 0.040$	$0.156 \pm 0.052$
<b>24</b>	$0.052 \pm 0.040$	$0.074 \pm 0.030$	$0.173 \pm 0.055$
<b>CA-4</b>	$0.0039 \pm 0.00032^c$	$0.0430^c$	$0.0019 \pm 0.0005^c$

<sup>a</sup> IC<sub>50</sub> values are half maximal inhibitory concentrations required to block the growth stimulation of MCF-7, MDA-MB-231, and HL-60 cells. Values represent the mean (SEM (error values  $10^{-6}$ )) for three experiments performed in triplicate. <sup>b</sup> Antiproliferative activity for compound **19e** against HL-60 from NCI. <sup>c</sup> The IC<sub>50</sub> value obtained for CA-4 in this assay are in agreement with the reported values for CA-4 in MCF-7 and MDA-MB-231 human breast cancer and leukaemia cell lines (see Refs. [62,102,103]).

Compound **24** is the only example synthesised containing the 1,2,3-triazole heterocycle and is also a direct analogue of phenstatin because of the presence of the 3,4,5-trimethoxyaryl motif (ring A) and the 3-hydroxy-4-methoxyaryl B ring. This structure showed excellent activity in MCF-7 cells with 27% cell viability at 1  $\mu\text{M}$  and the  $\text{IC}_{50}$  value for the compound was determined as 52 nM (Table 2), which compares with CA-4 ( $\text{IC}_{50} = 3.9$  nM) [102,103]. **24** was selected for further studies on different cell lines and for cell cycle analysis. Phenstatin (**7a**) was synthesised in our laboratory for use as a positive control ( $\text{IC}_{50} = 1.61 \pm 2.7$  nM) [104].

### 3.1.3. Series 3: 1-(Diarylmethyl)-1*H*-Imidazoles **20b–h,k,l**

The results obtained from the preliminary screening of the benzhydryl imidazole derivatives, **20b–k** and **l** are shown in Figure 5A. These compounds carry a single substituent at the *para* position on one or both aryl rings (Cl, F, Br, OH,  $\text{OCH}_3$ ,  $\text{CH}_3$ , etc). This library of compounds did not show any significant activity, with cell viability of 67–90% at concentrations of 1 and 0.1  $\mu\text{M}$ , as observed for the Series 1 1,2,4-triazole derivatives **13b–g** and **l–o**, indicating that the imidazole ring alone is not sufficient for antiproliferative activity. The most active compounds in this panel were identified as the 4-nitro derivative **20b** and the 4-fluoro substituted compound **20d** (73% and 67% cell viability respectively at 1  $\mu\text{M}$ ).

### 3.1.4. Series 4: 1-(Aryl-(3,4,5-Trimethoxyphenyl)Methyl)-1*H*-Imidazoles **21a–g, i–l**

The results obtained from the preliminary screening of the panel of phenstatin hybrid compounds carrying imidazole as the heterocyclic ring (**21a–g, i–l**) in MCF-7 cells are shown in Figure 5B. From the library of 3,4,5-trimethoxydiphenylmethyl-1*H*-imidazole derivatives (**21a–g, i–l**), compound **21l** was significantly the most active (31% viable cells at 1  $\mu\text{M}$ ), confirming the observation that the phenstatin scaffold is required for optimum activity. The remaining compounds in the series demonstrated weak activity, with viability >80% at 1  $\mu\text{M}$ . The  $\text{IC}_{50}$  value of the most potent imidazole containing compound **21l** was determined as  $0.132 \pm 0.007$   $\mu\text{M}$  in MCF-7 cells (Table 2), and this compound was selected for further evaluations in other cancer cell lines and cell cycle analysis in MCF-7 cells.

### 3.1.5. Series 5: 1-(Diarylmethyl)Pyrrolidines **25a–g** and 1-(Diarylmethyl)Piperidines **26a–c**, and 1-(Diarylmethyl)Piperazines **27a–g, 28**

The results of preliminary evaluation of the panel of pyrrolidine and piperidine derivatives **25a–g** and **26a–c** in MCF-7 cells are shown Figure 6A. These compounds were not sufficiently active when compared to the positive controls CA-4 and phenstatin (**7a**). The most potent examples were identified as the piperidine derivative **26b**, showing the lowest percentage of viable cells (78%) at 1  $\mu\text{M}$  and containing the 3,4,5-trimethoxyphenyl (ring A) and 4-methoxyphenyl (Ring B), together with the corresponding pyrrolidine containing compounds **25g** and **25d** (82% and 80% viability at 1  $\mu\text{M}$ ). The (3,4,5-trimethoxyphenyl)(methyl)piperazine derivatives (**27c,d,f,h,i**) were screened at three concentrations (10, 1, 0.1  $\mu\text{M}$ ) (Figure 6B). Compound **27f** was identified as the most active, with a percentage of viable cells of 42% at 10  $\mu\text{M}$ , 76% at 1  $\mu\text{M}$  and 84% at 0.1  $\mu\text{M}$ . Benzylpiperazine **27i**, which is more closely related in structure to phenstatin, displayed promising antiproliferative activity at 10  $\mu\text{M}$  (48% cell viability).

From the results obtained above, it is interesting to see that inclusion of the triazole heterocycle on the phenstatin scaffold (as in compounds **21l** and **24**) results in greater antiproliferative effects in the MCF-7 cell line than the corresponding imidazole compound (**19e**). By comparison, replacement of the azole with pyrrolidine, piperidine, or piperazine resulted in decreased antiproliferative activity. The antiproliferative activity of the most potent azole compounds **19e**, **21l**, and **24** may be correlated to the logP values (see Supplementary Information). The imidazole compound **19e** has a lower logP (2.41) when compared to the 1,2,4-triazole compound **21l** (logP of 2.91) and the 1,2,3-triazole compound **24** (logP 3.50); the antiproliferative activity of the compounds **19e**, **21l**, and **24** in MCF-7 cells are determined as  $\text{IC}_{50} = 0.42$ , 0.13, and 0.052  $\mu\text{M}$ , respectively. In addition, the total

polar surface (TPSA) area for these compounds is in the range  $74.22\text{--}87.86 \text{ \AA}^2 < 140 \text{ \AA}^2$ . However, compounds with higher logP values e.g., the piperazine compounds **27f** (5.50) and **27d** (4.67) display poor activity.

### 3.2. Antiproliferative Activity of Selected Analogues in MDA-MB-231 and HL60 Cell Lines

A number of the more potent compounds synthesised were evaluated in the triple-negative MDA-MB-231 cell line with 72 h incubation time (see Table 2). For the triazole compound **19e**, an  $IC_{50}$  value of  $0.98 \mu\text{M}$  was obtained in MDA-MB-231 cells, although this is not as potent as observed in the MCF-7 cells ( $IC_{50} = 0.42 \mu\text{M}$ , Table 2). The lower  $IC_{50}$  value for the imidazole compound **211** ( $0.237 \mu\text{M}$ ) indicates that the imidazole heterocycle in **211** contributes to the antiproliferative activity more effectively than the 1,2,4-triazole ring in compound **19e**. The novel 1,2,3-triazole compound **24** was the best of all analogues tested in MCF-7 cells ( $IC_{50} = 0.052 \mu\text{M}$ ). The result obtained for **24** in the MDA-MB-231 cell line was also very promising ( $IC_{50} = 0.074 \mu\text{M}$ ), Table 2, and compares very favourably with the reported activity of phenstatin in MDA-MB-231 cells ( $IC_{50} = 1.5 \mu\text{M}$  [105]), indicating that the 1,2,3-triazole has very potent antiproliferative effects compared to imidazole or 1,2,4-triazole present in the related compounds **211** and **19e**. Since the antiproliferative effects of 1,2,3-triazole–phenstatin hybrid compounds has not previously been investigated, this heterocycle is especially interesting for further development.

In a further study, the antiproliferative effects of the novel imidazole compound **211**, 1,3,4-triazole compound **19e**, and the 1,2,3-triazole compound **24** (structurally related to letrozole and phenstatin) in HL-60 leukaemia cells was also investigated. HL-60 leukaemia cells were used as an in vitro model for acute myeloid leukaemia. Both MCF-7 and HL-60 cell lines are CA-4 sensitive and are highly susceptible to the effects of tubulin-targeting compounds [102]. The  $IC_{50}$  value of  $0.156 \mu\text{M}$  obtained for imidazole compound **211** identifies it as a lead compound for future development. The 1,2,3-triazole compound **24** was also potent in the leukaemia HL-60 cell line with an  $IC_{50}$  value of  $0.173 \mu\text{M}$ , while **19e** was less potent,  $IC_{50} = 261 \mu\text{M}$ . ( $IC_{50}$  value for phenstatin =  $0.031 \mu\text{M}$  [106]). This experiment demonstrated the selective effect of interchanging the imidazole, 1,3,4-triazole, and 1,2,3-triazole heterocycles on cell viability in HL-60 cells.

### 3.3. NCI Cell Line Screening for **19e**, **211**, **25g**, **26b**, and **27d**

Five novel substituted phenstatin compounds from the present work (**19e**, (Series 2) **211**, (Series 4), **25g**, **26b** and **27d** (Series 5)) were selected for evaluation in the NCI 60 cell line screen [107] following initial analysis of the Lipinski (drug-like) properties from the Tier-1 profiling screen, together with predictions of the relevant absorption, distribution, metabolism, excretion, and toxicity (ADMET) properties e.g., metabolic stability, permeability, blood–brain barrier partition, plasma protein binding, and human intestinal absorption properties (see Tables S1 and S2 Supplementary Information). The compounds are predicted to be moderately lipophilic–hydrophilic, revealing their drug-like pharmacokinetic profiles and are potentially suitable candidates for further investigation.

The results obtained for the triazole compound **19e** in the NCI 60 cancer cell line screening ( $GI_{50}$  values, five doses) [107] are shown in Table 3. ( $GI_{50}$  is defined as the concentration for 50% of maximal inhibition of cell proliferation). In general, **19e** showed good activity on most of the cell lines with  $GI_{50}$  values in the sub-micromolar range. The activity was particularly potent in all of the leukaemia, CNS, and prostate cancer cell lines. The activity in MCF-7 cells ( $GI_{50} = 0.347 \mu\text{M}$ ) was in close agreement with the value obtained from our in-house viability assay of  $0.424 \mu\text{M}$ . The compound displayed significant activity in the TNBC cell lines HS-578T ( $GI_{50} = 0.548 \mu\text{M}$ ) and MDA-MB-468 ( $GI_{50} = 0.371 \mu\text{M}$ ) and in the BT-549 invasive ductal carcinoma cell line ( $GI_{50} = 0.618 \mu\text{M}$ ). Potent anti-cancer activity was also observed against the ovarian cancer cells, e.g., OVOCAR-3 cell line ( $0.323 \mu\text{M}$ ) and colon cancer, e.g., chemoresistant HT-29 cells ( $GI_{50} = 0.330 \mu\text{M}$ ). The best activity for **19e** among all of the 60 cell lines tested was the melanoma cell line MDA-MB-435 in which the  $GI_{50}$  value was  $0.181 \mu\text{M}$ . The MID  $GI_{50}$  was calculated as  $0.243 \mu\text{M}$  over

all 60 cell lines. The MID value obtained for TGI (total growth inhibition) was 53.7  $\mu\text{M}$ , and for  $\text{LC}_{50}$ , it was 97.7  $\mu\text{M}$ , indicating that the lethal concentration of the drug is very high and well above the  $\text{GI}_{50}$  value, indicating that **19e** has low toxicity. The results of the NCI COMPARE analysis for compound **19e** are shown in Table 4. Based on the  $\text{GI}_{50}$  mean graph and on the TGI mean graph, the compound with the highest rank was vinblastine sulphate with  $r$  values of 0.586 and 0.737, respectively. Correlation values ( $r$ ) are Pearson correlation coefficients.

**Table 3.** Antiproliferative evaluation of compounds **211** and **19e** in the NCI 60 cell line in vitro screen <sup>a</sup>.

Cell Line	Compound 211 <sup>c</sup>	Compound 19e <sup>d</sup>	Cell Line	Compound 211 <sup>c</sup>	Compound 19e <sup>d</sup>
	$\text{GI}_{50}$ ( $\mu\text{M}$ ) <sup>b</sup>	$\text{GI}_{50}$ ( $\mu\text{M}$ ) <sup>b</sup>		$\text{GI}_{50}$ ( $\mu\text{M}$ ) <sup>b</sup>	$\text{GI}_{50}$ ( $\mu\text{M}$ ) <sup>b</sup>
<i>Leukemia</i>			<i>Melanoma</i>		
CCRF-CEM	0.289	0.402	LOX IMV1	0.523	0.523
HL-60 (TB)	0.229	0.261	MALME-3M	Nd <sup>e</sup>	Nd <sup>e</sup>
K-562	0.225	0.427	M14	0.180	0.374
MOLT-4	0.565	0.510	MDA-MB-435	0.119	0.181
RPMI-8226	0.385	0.452	SK-MEL-2	0.324	0.361
SR	0.182	0.376	UACC-62	0.668	0.550
<i>Non-Small Cell Lung Cancer</i>			SK-MEL-28	Nd <sup>e</sup>	Nd <sup>e</sup>
A549/ATCC	0.836	0.969	SK-MEL-5	0.367	0.440
HOP-62	0.516	0.514	UACC-257	1.44	>100
HOP-92	28.6	9.69	<i>Ovarian Cancer</i>		
EKVX	0.702	2.24	IGROV1	0.862	0.959
NCI-H226	0.640	1.43	OVCAR-3	0.264	0.323
NCI-H23	0.882	0.977	OVCAR-4	3.44	3.02
NCI-H332M	0.789	0.696	OVCAR-5	0.648	1.99
NCI-H460	0.377	0.414	OVCAR-8	0.450	1.14
NCI-H552	0.247	0.395	NCI/ADR-RES	1.92	1.18
<i>Colon Cancer</i>			SK-OV-3	0.465	0.402
COLO 205	0.361	0.332	<i>Renal Cancer</i>		
HCT-2998	1.72	1.35	786-0	0.369	0.475
HCT-116	0.249	0.448	A498	0.304	0.324
HCT-15	0.264	0.438	ACHN	0.693	0.653
HT29	0.312	0.330	CAKI-1	0.681	0.567
KM12	0.389	0.418	RXF 393	Nd <sup>e</sup>	0.321
SW-620	0.387	0.431	SN12C	0.910	0.853
<i>CNS Cancer</i>			TK-10	Nd <sup>e</sup>	>100
SF-268	0.731	0.469	UO-31	0.883	0.903
SF295	0.307	0.325	<i>Breast Cancer</i>		
SF539	0.217	0.300	MCF-7	0.339	0.347
SNB-19	0.532	0.578	MDA-MB-231/ATCC	0.664	1.50
SNB-75	0.192	Nd <sup>e</sup>	HS 578T	0.414	0.548
AC	0.391	0.446	BT-549	0.306	0.618
<i>Prostate cancer</i>			T-47D	Nd <sup>e</sup>	Nd <sup>e</sup>
PC-3	0.384	0.431	MDA-MB-468	0.316	0.371
DU-145	0.407	0.530			
<b>MG-MID (<math>\mu\text{M}</math>) <sup>f</sup></b>	0.234	0.243			

<sup>a</sup> Data obtained from NCI in vitro human tumour cell screen 5 dose assay. <sup>b</sup>  $\text{GI}_{50}$  is the molar concentration of the compound causing 50% inhibition of growth of the tumour cells; <sup>c</sup> NSC 78806; <sup>d</sup> NSC 788805; <sup>e</sup> Nd: Not determined; <sup>f</sup> MG-MID: the mean of  $\text{GI}_{50}$  values over all cell lines for the tested compound.

The National Cancer Institute (NCI) screening of imidazole compound **211** also demonstrated very good results showing that the compound not only is active against breast cancer cells but also against other types of cancer (see Table 2). Compound **211** proved active against all of the leukaemia cell lines; in particular, very promising activity was measured in SR cells ( $\text{GI}_{50} = 0.182 \mu\text{M}$ ) and HL60 ( $\text{GI}_{50} = 0.229 \mu\text{M}$ ), confirming our in-house evaluation. The activity against CNS cancer varied in a range between  $\text{GI}_{50} = 0.192$

and 0.731  $\mu\text{M}$ . Particularly good was also the activity against the breast cancer panel with  $\text{GI}_{50}$  values in the range of 0.306–0.664  $\mu\text{M}$ , including the TNBC cell line MDA-MB-468 ( $\text{GI}_{50} = 0.316 \mu\text{M}$ ). Of all the cell lines evaluated in the panel, compound **211** was most potent against melanoma MDA-MB-435 cells with  $\text{GI}_{50} = 0.119 \mu\text{M}$ . The MID  $\text{GI}_{50}$  value for the 60 cell line panel was 0.234  $\mu\text{M}$ . MID TGI and  $\text{LC}_{50}$  values of 40.7 and 100  $\mu\text{M}$  respectively are an indication of the low toxicity of the compound, as the median lethal dose is very high compared to the  $\text{GI}_{50}$  values. From the COMPARE analysis results shown in Table 3, it was observed that based on the mean  $\text{GI}_{50}$  value, the activity of our **211** is most closely related to paclitaxel ( $r = 0.587$ ). Based on TGI values, the compound with the highest ranking was maytansine ( $r = 0.775$ ); both are tubulin-targeting agents. Correlation values ( $r$ ) are Pearson correlation coefficients and  $\text{LC}_{50}$  values all  $>0.1 \text{ mM}$ .

**Table 4.** Standard COMPARE analysis of compounds **19e** and **211**<sup>a</sup>.

Rank	19e	$r$	211	$r$
	<b>Based on <math>\text{GI}_{50}</math> mean graph</b>		<b>Based on <math>\text{GI}_{50}</math> mean graph</b>	
1	Vinblastine sulphate, hiConc:-7.6	0.586	Paclitaxel (Taxol) hiConc:-6.0	0.587
2	S-Trityl-L-cysteine	0.575	S-Trityl-L-cysteine	0.58
3	Maytansine	0.547	Paclitaxel (Taxol) hiConc:-4.0	0.544
4	Rhizoxin	0.544	Maytansine	0.53
5	Vinblastine sulphate, hiConc:-5.6	0.509	Paclitaxel (Taxol) hiConc:-4.6	0.518
	<b>Based on TGI mean graph</b>		<b>Based on TGI mean graph</b>	
1	Vinblastine sulfate	0.737	Maytansine hiConc: -9.0	0.775
2	Rhizoxin	0.726	Vinblastine sulfate	0.765
3	Paclitaxel (Taxol)	0.704	Rhizoxin	0.748
4	Maytansine hiConc:-9.0	0.696	Paclitaxel (Taxol)	0.703
5	Maytansine hiConc:-4.0	0.689	Maytansine hiConc:-9.0	0.700

<sup>a</sup> The target set was the standard agent database and the target set endpoints were selected to be equal to the seed endpoints. Standard COMPARE analysis was performed. Correlation values ( $r$ ) are Pearson correlation coefficients. Vinblastine sulfate and maytansine appear at different concentrations, as it has been tested by the NCI at multiple concentration ranges (see reference 107).

Compounds **25g**, **26b**, and **27d** were also selected for evaluation in the NCI 60 cell line one-dose screen (see Table S4, Supplementary Information). The mean growth percentages for **25g**, **26b**, and **27d** were 73.1%, 34.2%, and 65.5% over the 60 cell line panel at 10  $\mu\text{M}$ . Interestingly, the piperidine compound **26b** displayed significant potency in the breast cancer panel, with mean growth of 30.3% over this cell panel, with notable potency in the triple negative breast cancer cell lines HS587T (16.6% growth) and MDA-MB-468 (9.3% growth). In the leukaemia panel, the mean growth obtained is 23.5% over this 60 cell panel and significantly 4.36% growth for the acute myeloid leukaemia HL-60 cell line. Compound **26b** also displayed notable potency in the CA-4 resistant colon cancer cell line HT-29 with 7.93% growth recorded.

#### 3.4. Evaluation of Toxicity in MCF-10A Cells

The potent phenstatin derivatives **19e**, **211**, and **24** were selected for toxicity evaluation in the non-tumorigenic MCF-10A epithelial breast cancer cell line. The human mammary

epithelial cell line MCF10A is widely used as an in vitro model for normal breast cell function and transformation [108]. The viability of the MCF-10A cells was determined after treatment with compounds **19e** and **211** at four different concentrations of 10, 1, 0.5, and 0.4  $\mu\text{M}$  for 24 h (Figure 7A,B). It was observed that at the highest concentration (10  $\mu\text{M}$ ), compounds **19e** and **211** show a cell death of approximately 50%. At 1  $\mu\text{M}$  concentration, compound **19e** does not show any loss in cell viability (99% viability), while compound **211** resulted in 73% cell viability, still above the  $\text{IC}_{50}$  values of 0.42  $\mu\text{M}$  (**19e**) and 0.13  $\mu\text{M}$  (**211**) in MCF-7 cells. When the experiment was repeated with an increased incubation time of 48 h, it was observed that the percentage of viable cells at 10  $\mu\text{M}$  concentration decreased for compounds **19e** and **211** to approximately 30% (Figure 7A,B). The percentage of viable cells at 1  $\mu\text{M}$  decreased to 64% for compound **211**, while it did not change significantly for **19e** (>94%). For both compounds, viability at 0.5  $\mu\text{M}$  and 0.4  $\mu\text{M}$  is close to 100%, which means that the compounds are not toxic toward healthy cells at lower concentrations corresponding to their  $\text{IC}_{50}$  values. The third screening for **19e** and **211** was performed at 72 h, which is the incubation time used through all the screenings in MCF-7 (Figure 7A,B). It is interesting to note that as the concentration of the drug decreases from 1 to 0.5 and 0.4  $\mu\text{M}$ , the percentage of viable cells increases significantly, with viable cells percentage >80% at 0.4  $\mu\text{M}$  for all compounds tested. This demonstrates that even at concentrations that are toxic to the MCF-7 cancer cells, the MCF-10A are not killed by the drug. Therefore, the compounds selected demonstrate good antiproliferative activity and additionally show good selectivity and low cytotoxicity to normal cells. Compound **24** was evaluated in MCF-10A cells at three different concentrations: 10, 1, and 0.1  $\mu\text{M}$  over 72 h (Figure 7C). The percentage of viable cells at the three different concentrations was 61%, 71%, and 96%, respectively, with higher percentage of cells alive at the lower concentration. Compound **24** demonstrates good selectivity for cancer cells and low cytotoxicity even if the percentage of viable cells at 1  $\mu\text{M}$  was slightly lower than the value observed previously for compounds **19e** and **211** (>80%) at 72 h. These results are also supported by the low toxicity of the compounds determined from the NCI evaluation. Tubulin-targeting drugs such as taxanes and vinca alkaloids are among the most effective anti-cancer therapeutics in the treatment of castration-resistant prostate cancer and triple-negative breast cancer. However, their use is limited by toxicities including neutropenia and neurotoxicity; additionally, tumour cells can develop resistance to these drugs [109]. Our results demonstrate that azoles **19e**, **211**, and **24** were less toxic to normal human breast cells than to breast cancer cells, providing a potential window of selectivity.

### 3.5. Effects of Compounds **211** and **24** on Cell Cycle Arrest and Apoptosis

To investigate further the mechanism of action of the novel azole compounds synthesised, the effect of selected potent compounds **211** and **24** was investigated in MCF-7 cells by flow cytometry and propidium iodide (PI) staining, allowing the percentage of cells in each phase of the cell cycle to be quantified (Figure 8). For the imidazole compound **211**, three time points were analysed (24, 48, and 72 h), and the values obtained for apoptosis and the  $\text{G}_2/\text{M}$  phase of the cell cycle were quantified (concentration 1  $\mu\text{M}$ ), as shown in Figure 8A. It was observed that the percentage of cells undergoing apoptosis (sub- $\text{G}_1$ ) increases significantly at all three time points to 15%, 31%, and 37% respectively compared to the background level of apoptosis with the vehicle ethanol (2%, 4%, and 2%) at the corresponding time points. It is also interesting to notice how the percentage of cells in the  $\text{G}_2/\text{M}$  phase for the treated sample (47%, 43%, and 40%) is statistically higher than the cells in the same phase for the control sample treated with the vehicle (26%, 25%, 25%) at the corresponding time points.  $\text{G}_2/\text{M}$  cell cycle arrest is strongly associated with an inhibition of tubulin polymerisation. CA-4 and related tubulin targeting compounds cause  $\text{G}_2/\text{M}$  arrest. Hence, the higher percentage of cells observed in cells treated with **211** may suggest that the mechanism of action is indeed the inhibition of tubulin polymerisation.



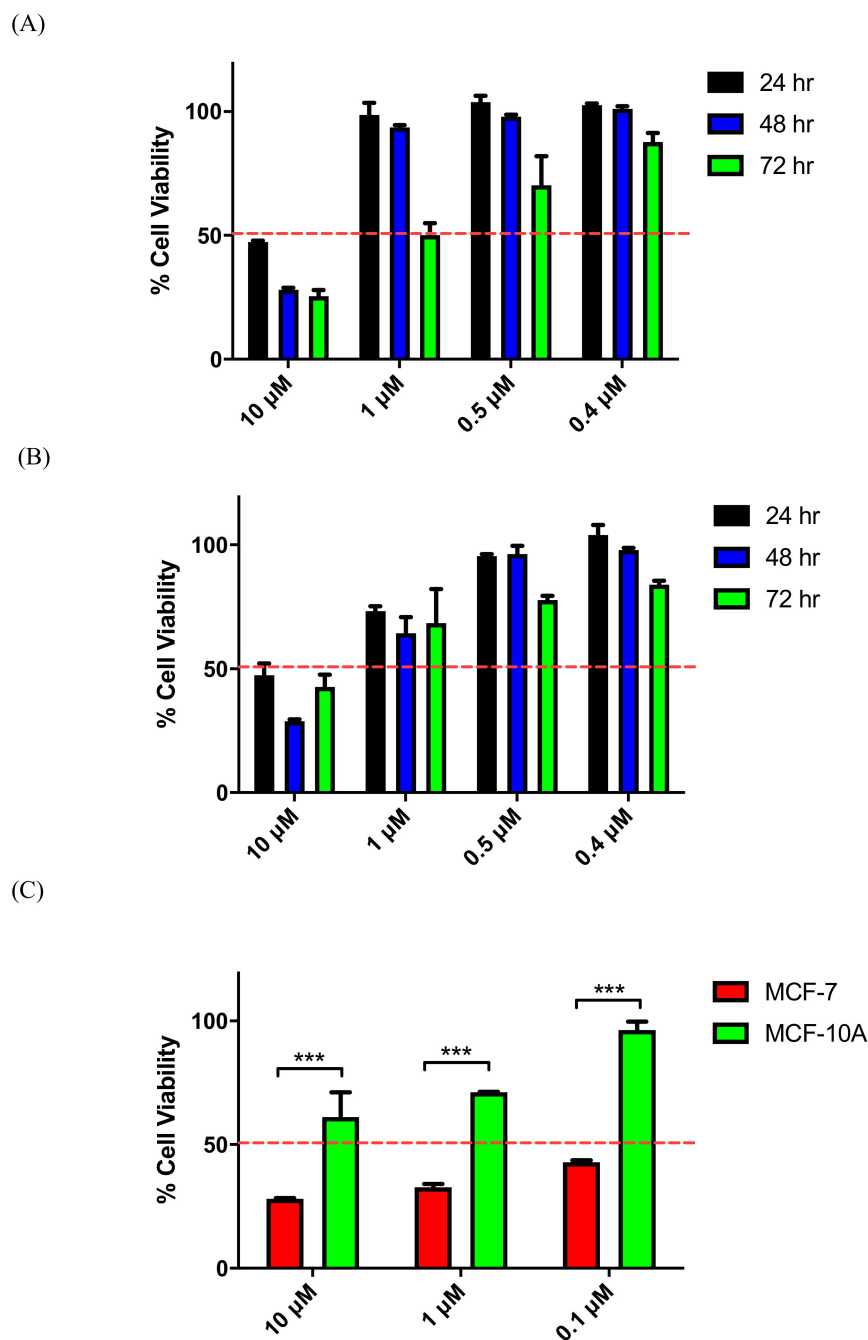


**Figure 7.** Screening of phenstatin derivatives **19e** (A) and **211** (B) in MCF-10A cells at 24, 48, 72 h and (C) 24 in MCF-10A and MCF-7 cells at 72 h. (A,B) Effect of compounds **19e** and **211** on the viability of non-tumorigenic MCF-10A human mammary epithelial cells. Cells were treated with the indicated concentrations for 21, 48, or 72 h. Cell viability was expressed as a percentage of vehicle control (ethanol 1% (*v/v*)) and was determined by alamarBlue assay (average + SEM of three independent experiments). (C) Effect of compound **24** on the viability of non-tumorigenic MCF-10A human mammary epithelial cells and MCF-7 breast cancer cells. Cells were treated with the indicated concentrations for 72 h. Cell viability was expressed as a percentage of vehicle control (ethanol 1% (*v/v*)) and was determined by alamarBlue assay (average  $\pm$  SEM of three independent experiments). Statistical analysis was performed using two-way ANOVA (\*\*\*,  $p < 0.001$ ).

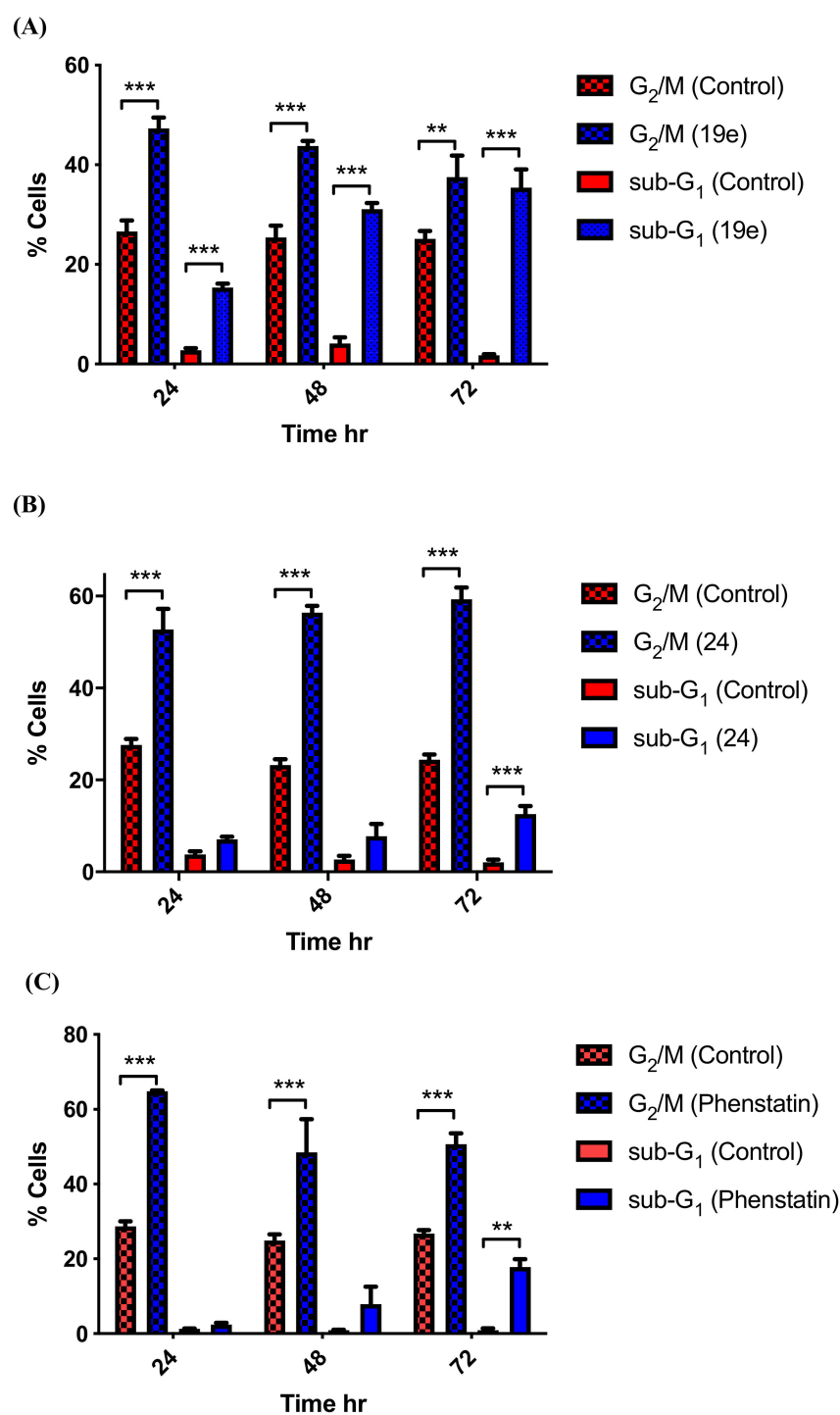


**Figure 8.** Compound (A) 19e, (B) 24, and (C) phenstatin (7a) in MCF-7 induced G<sub>2</sub>/M arrest followed by apoptosis in a time-dependent manner in MCF-7 cells. Cells were treated with either vehicle control (v) (0.1% ethanol (v/v)) or compound 19e, 24, or phenstatin (7a) (1 μM) for 24, 48, and 72 h). Then, cells were fixed, stained with PI, and analysed by flow cytometry. Cell cycle analysis was performed on histograms of gated counts per DNA area (FL2-A). The number of cells with <2 N (sub-G<sub>1</sub>), 2 N (G<sub>0</sub>G<sub>1</sub>), and 4 N (G<sub>2</sub>/M) DNA content was determined with CellQuest software. Values represent as the mean ± SEM for three separate experiments. Statistical analysis was performed using two-way ANOVA (\*\*,  $p < 0.01$ , \*\*\*,  $p < 0.001$ ).

The 1,2,3-triazole compound 24, which was the most potent compound evaluated in the viability assay, demonstrated the same effects on the relative percentages of cells in

apoptosis and the G<sub>2</sub>/M phase, as shown in Figure 8B. Apoptosis increased with time, with a statistically significant difference compared to vehicle control at 72 h. A high percentage of cells were arrested in the G<sub>2</sub>/M phase (52%, 56%, and 59%) at time points 24, 48, and 72 h respectively, following treatment with compound **24** with a much lower percentage of cells in the G<sub>2</sub>/M phase for the sample treated with the vehicle (28%, 23%, and 24%) at the same time points.

Phenstatin **7a** was used as a positive control through all the biological experiments. Cell cycle analysis of MCF-7 cells treated with phenstatin at time points 24, 48, and 72 h and a concentration of 1 µM showed a very low percentage of cells undergoing apoptosis at 24 and 48 h, as shown in Figure 8C. Apoptosis increased to 18% between 48 and 72 h, while the percentage of cells in the G<sub>2</sub>/M phase was correspondingly high (65%, 49%, and 51% at 24, 48, and 72 h, respectively). This pattern was also observed in the compounds **211** and **24** tested, but the percentage of cells in apoptosis was always higher than for phenstatin, possibly suggesting differences in the effects of these compounds on tubulin arising from the presence of the azole in the modified structures.

The role of apoptosis in the inhibition of MCF-7 and MDA-MB-231 cell growth was further examined. MCF-7 and MDA-MB-231 cells were treated with compound **211** for 48 h and stained with Annexin V-fluorescein isothiocyanate (FITC)/propidium iodide (PI) and then analysed by flow cytometry. Dual staining with Annexin-V and PI facilitates discrimination between live cells (annexin-V<sup>-</sup>/PI<sup>-</sup>), early apoptotic cells (annexin-V<sup>+</sup>/PI<sup>-</sup>), late apoptotic cells (annexin-V<sup>+</sup>/PI<sup>+</sup>), and necrotic cells (annexin-V<sup>-</sup>/PI<sup>+</sup>). Compound **211** induced both early and late apoptosis in MCF-7 cells in a concentration-dependent manner when compared to the untreated control cells (Figure 9A). When MCF-7 cells were treated with **211** (0.1, 0.5, and 1 µM), the average proportion of Annexin V-stained positive cells (total apoptotic cells) increased from 0.9% in control cells to 14.1%, 17.5%, and 19.3%, respectively. These results suggested that compound **211** induces the apoptosis of MCF-7 cells in a dose-dependent manner. In MDA-MB-231 cells, the percentage of cells observed in apoptosis following treatment with **211** was significantly lower with 3.6%, 5.9%, and 6.9% at 0.1, 0.5, and 1.0 µM respectively, as shown in Figure 9B. In contrast, for phenstatin, the Annexin V-stained positive cells (total apoptotic) cells were determined as 36.1% and 46% in MCF-7 cells at 0.1 µM and 0.5 µM, respectively, as shown in Figure 9A. The total apoptotic MDA-MB-231 cells were determined as 16.6% and 17.9% following treatment with phenstatin (0.1 and 0.5 µM), respectively, as shown in Figure 9B.

### 3.6. Tubulin Polymerisation

Compound **211** was selected for further analysis using a tubulin polymerisation assay. Its promising antiproliferative activity (IC<sub>50</sub> = 0.237 µM in MCF-7 cells) combined with structural features related to phenstatin **7a** and CA-4 indicate that the mechanism of action of this compound could be the inhibition of tubulin polymerisation. The assay is based on the capacity of microtubules to scatter light proportionally to their concentration. The imidazole compound **211** (red) showed good inhibition of tubulin polymerisation after 60 min (V<sub>max</sub> value 2.84 ± 0.10 mOD/min at 10 µM), corresponding to a 1.34-fold reduction of the polymer mass compared to the vehicle, as shown in Figure 10A. Paclitaxel (in green) was used as a positive control as it stabilises polymerised tubulin, as shown in Figure 10A. Phenstatin **7a** is a potent inhibitor of tubulin polymerisation comparable to CA-4 [66], as shown in Figure 10B. Incubation with either imidazole **211** or phenstatin resulted in a significant inhibition of tubulin polymerisation and assembly.

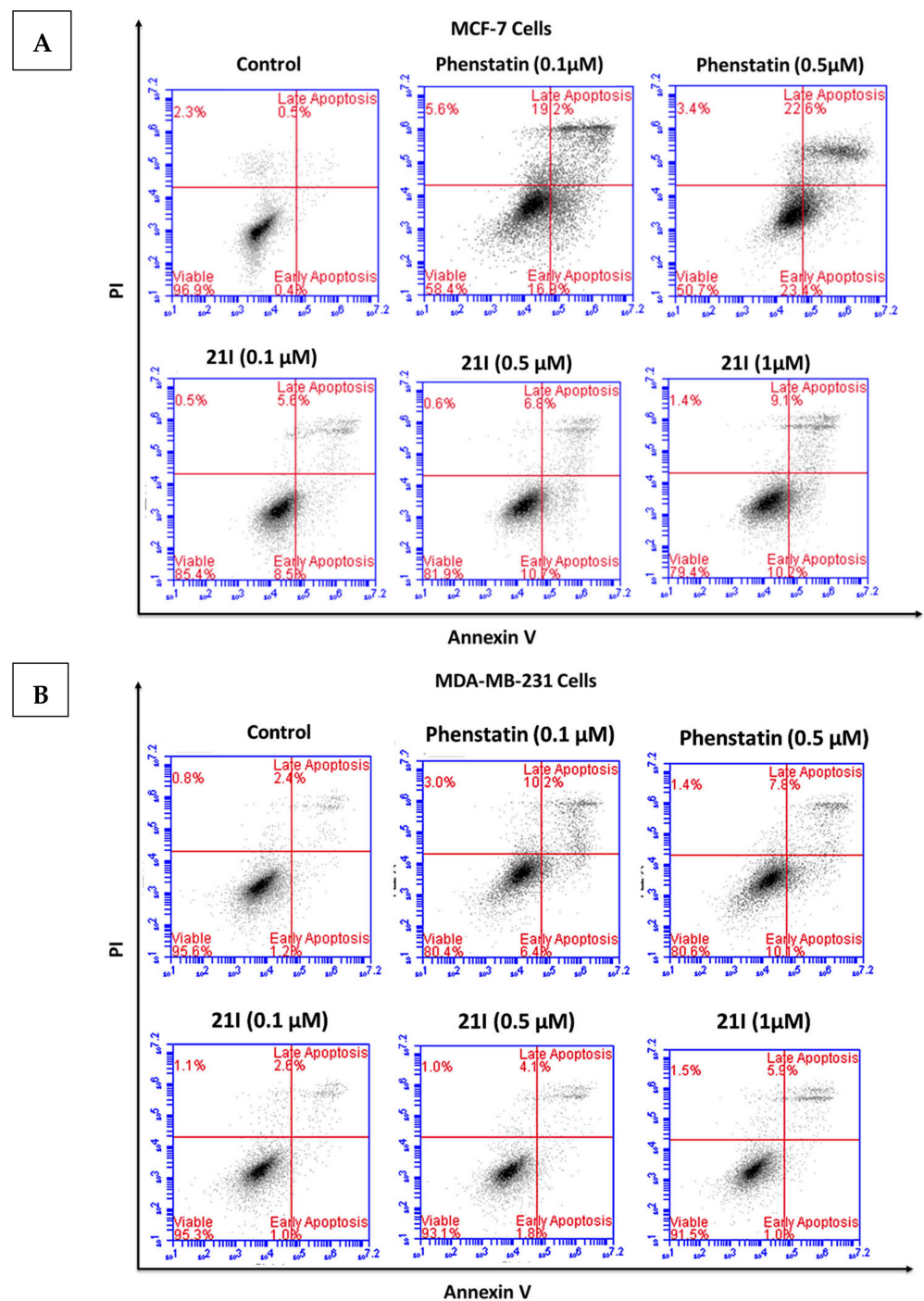


**Figure 9.** Compound **21I** induced cell apoptosis in (A) MCF-7 breast cancer cells and (B) MDA-MB-231 breast cancer cells. MCF-7 breast cancer cells and MDA-MB-231 breast cancer cells were treated with **21I** or phenstatin (**7a**) (1 µM) or control vehicle (0.1% ethanol (*v/v*)), and the percentage of apoptotic cells was determined by staining with Annexin V-FITC and PI. In each panel, the lower left quadrant shows cells that are negative for both PI and Annexin V-FITC, the upper left shows only PI cells that are necrotic. The lower right quadrant shows Annexin-positive cells that are in the early apoptotic stage and the upper right shows both Annexin/PI positive, which are in late apoptosis/necrosis. Control cells and cells treated with phenstatin **7a** and **21I** at 48 h are shown, respectively. Values represent the mean of three independent experiments.

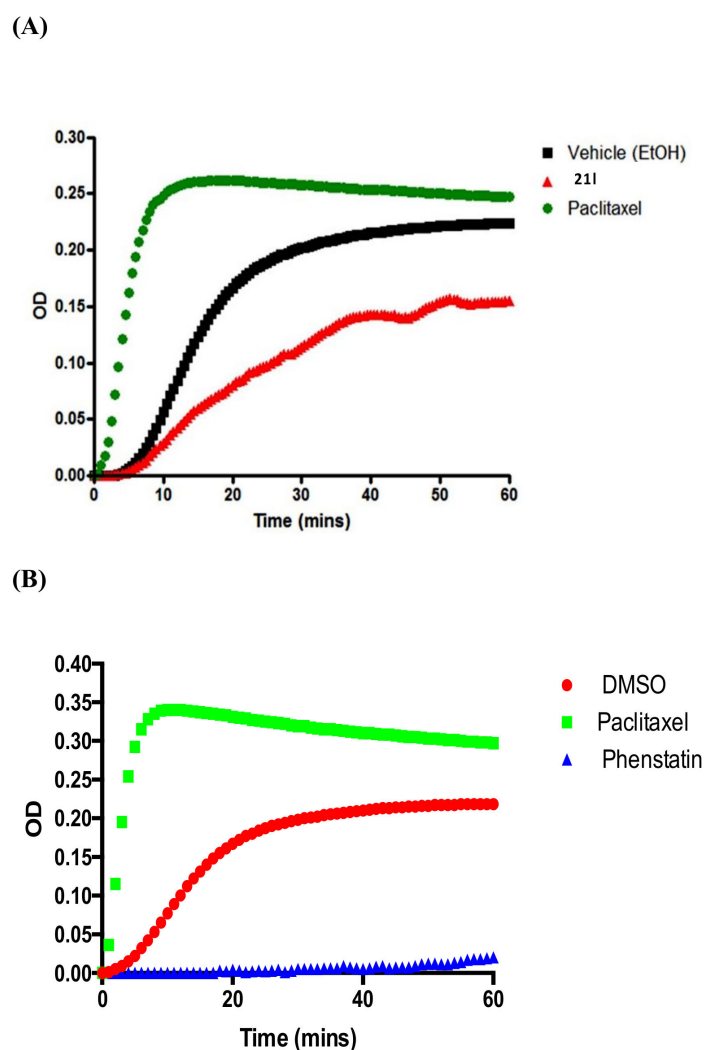


**Figure 10.** Effect of compound **211** on tubulin polymerisation in vitro. **(A)** Tubulin polymerisation assay for compound **211** at 10  $\mu\text{M}$ . **(B)** Paclitaxel (10  $\mu\text{M}$ ) and phenstatin (**7a**) (10  $\mu\text{M}$ ) were used as references while ethanol (1% *v/v*) and DMSO (1% *v/v*) were used as vehicle controls. Purified bovine tubulin and guanosine-5'-triphosphate (GTP) were mixed in a 96-well plate. The polymerisation reaction was initiated by warming the solution from 4 to 37  $^{\circ}\text{C}$ . The effect on tubulin assembly was monitored in a Spectramax 340PC spectrophotometer at 340 nm at 30 s intervals for 60 min at 37  $^{\circ}\text{C}$ . DMSO. Fold inhibition of tubulin polymerisation was calculated using the  $V_{\text{max}}$  value for each reaction. The results represent the mean for three separate experiments.

Following the experiment above, the in vitro effects of compounds **19e** and **211** were examined on the microtubule structure of MCF-7 breast cancer cells with confocal microscopy using anti-tubulin antibodies. Paclitaxel and phenstatin, a known polymeriser and depolymeriser of tubulin respectively, were used as controls. In Figure 11A, a well-organised microtubule network (stained green) is clearly seen for the vehicle control, together with the MCF-7 cell nuclei (stained blue). Hyperpolymerisation of tubulin was demonstrated in the paclitaxel-treated sample (Figure 11B), whereas the phenstatin-treated sample Figure 11C shows an extensive depolymerisation of tubulin. Cells treated with the azoles **19e** (Figure 11D) and **211** (Figure 11E) displayed disorganised microtubule networks with similar effects to phenstatin, together with multinucleation (formation of multiple micronuclei), which is a recognised sign of mitotic catastrophe [110] previously observed by us and others upon treatment with tubulin-targeting agents such as CA-4 and related compounds in non-small cell lung cancer cells and breast cancer MCF-7 cells [111,112].

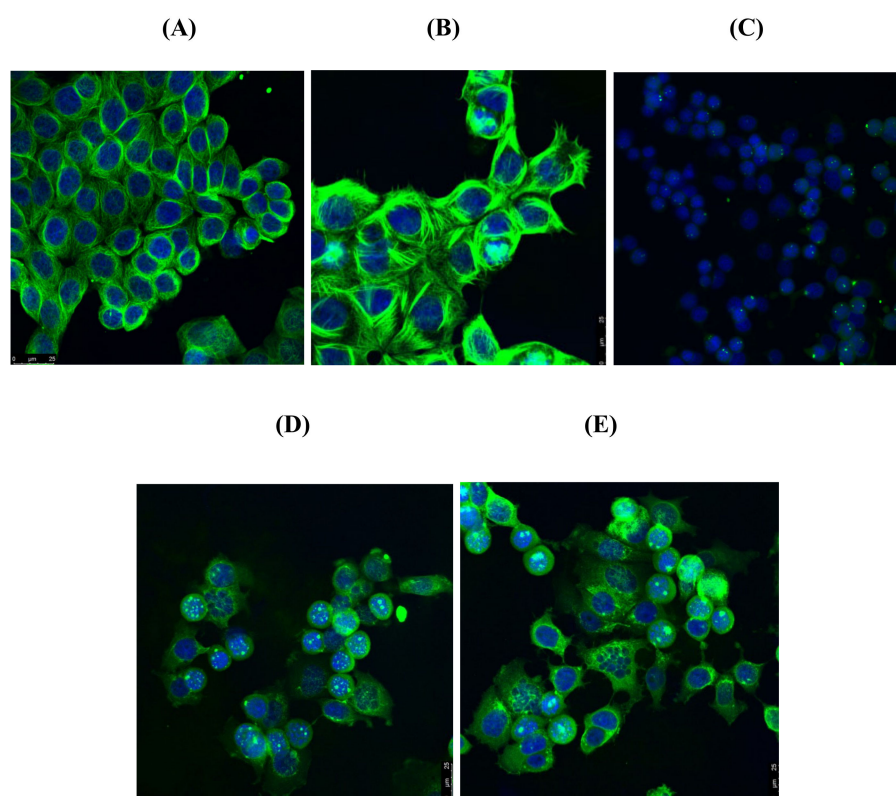


**Figure 11.** Compounds **19e** and **211** depolymerise the microtubule network of MCF-7 breast cancer cells. Cells were treated with (A) vehicle control (0.1% ethanol (*v/v*)), (B) paclitaxel (1  $\mu$ M), (C) phenstatin (**7a**) (1  $\mu$ M), (D) compound **19e** (10  $\mu$ M), or (E) compound **211** (10  $\mu$ M) for 16 h. Cells were fixed in ice-cold methanol and stained with mouse monoclonal anti- $\alpha$ -tubulin–fluorescein isothiocyanate (FITC) antibody (clone DM1A) (green), Alexa Fluor 488 dye, and counterstained with DAPI 4'-6'-diamidino-2-phenylindole (blue). Images obtained with Leica SP8 confocal microscopy, Leica application suite X software. Representative confocal micrographs of three separate experiments are shown. Scale bar indicates 25  $\mu$ m.

### 3.7. Effects of Compounds **211** and **24** on Expression Levels of Apoptosis-Associated Proteins

Some of the novel compounds synthesised during the project were selected for further investigation of their mechanism of action as pro-apoptotic agents based on their effect on the expression of proteins that can regulate apoptosis or proteins involved in the regulation of DNA repair. The effects of compounds **211** and **24** on apoptosis were evaluated by Western blotting. Apoptosis regulating proteins Bcl-2 and Mcl-1 were investigated along with PARP. PARP (poly ADP-ribose polymerase) is involved in the repair of DNA single-strand breaks in response to environmental stress [113]; and PARP cleavage is considered a hallmark of apoptosis. Bcl-2 is an anti-apoptotic protein that prevents apoptosis by sequestering caspases (apoptosis promoters) or by preventing the release of pro-apoptotic cytochrome c and AIF (apoptosis inducing factor) from the mitochondria into the cytoplasm [114]. The Mcl-1 protein belongs to the Bcl-2 family; it is also an anti-apoptotic protein localised in the mitochondrial outer membrane that acts at a very early stage in the cascade, leading to the release of the cytochrome c [115]. Pro- and anti-apoptotic members of the Bcl-2 family can heterodimerise and titrate each other's functions. If the expression levels of Mcl-1 and Bcl-2 are reduced (by drug treatment), apoptosis may be triggered.

From the results obtained, no change in the expression levels of two anti-apoptotic proteins was observed, indicating that Bcl-2 and Mcl-1 may not play a critical role in the pro-apoptotic mechanism of action of the compounds (Figure 12). A significant reduction in the expression of full-length PARP (116 kDa) between the vehicle and the treated MCF-7 cells was observed (Figure 12), suggesting that **211** and **24** cause PARP cleavage. PARP

enzymes play a crucial role in the DNA repair, and PARP cleavage is affected by caspase 3 activity. PARP enzymes are found in the cell nucleus and are activated by damage of the DNA single strand; therefore, the inhibition of DNA repair in cancer cells represents an attractive strategy in cancer therapy [116]. In conclusion, the proposed mechanism of action of these compounds as pro-apoptotic drugs is supported by the observed increase in the percentage of cell in subG1 in the cell cycle profile, the flow cytometric analysis of Annexin V/PI-stained cells, and also by PARP cleavage.

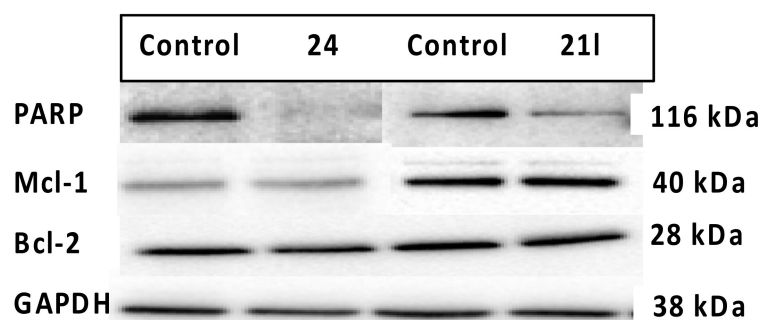


**Figure 12.** Effects of **21I** and **24** on expression of PARP (poly ADP-ribose polymerase) and anti-apoptotic proteins Bcl-2 and Mcl-1. MCF-7 cells were treated with either vehicle control (ethanol, 0.1% *v/v*) or with compounds **21I** and **24** (1  $\mu$ M) for 24 h. After the required time, cells were harvested and separated by SDS-PAGE to detect the level of the apoptosis-related proteins. The membrane was probed with anti-PARP or anti-cleaved PARP antibodies. Results are representative of three separate experiments. To confirm equal protein loading, each membrane was stripped and re-probed with glyceraldehyde 3-phosphate dehydrogenase (GAPDH) antibody.

### 3.8. Aromatase Inhibition

An objective of this research was the design of dual-acting tubulin/aromatase inhibitors. The evaluation of the aromatase inhibitory activity of the most potent compounds prepared was next investigated. Three compounds of the phenstatin hybrid panel **21I**, **24** and **19e** were selected for evaluation against two cytochrome members of the P450 family: CYP19 and CYP1A1. CYP19 is the aromatase cytochrome directly responsible for the synthesis of estradiol by the aromatisation of its steroid precursors testosterone and androstenedione, while CYP1A1 is involved in the metabolism of estrogen. The specificity of aromatase inhibition was evaluated by an assay carried out with xenobiotic-metabolising cytochrome P450 enzymes CYP1A1. The methodology applied in this study requires the detection of the hydrolysed dibenzylfluorescein (DBF) by the aromatase enzyme [117]. Aromatase and CYP1A1 inhibition were quantified by measuring the fluorescent intensity of fluorescein, the hydrolysis product of dibenzylfluorescein (DBF), by aromatase as previously described [118,119]. Naringenin was used as a positive control, yielding  $IC_{50}$  values of 4.9  $\mu$ M. The test was initially conducted at one concentration (20  $\mu$ g/mL). Further experiments to determine the  $IC_{50}$  value were performed if the compound caused greater than 90% inhibition at 20  $\mu$ g/mL. The results are presented in Table 5. Of these, 1,2,3-triazole **24** was inactive, as it did not show any inhibition of the enzyme at 20  $\mu$ g/mL, 0.05  $\mu$ M (0.01% for CYP19 and 12.81% for CYP1A1), whereas imidazole **21I** (0.05  $\mu$ M) and 1,2,4-triazole **19e** (0.05  $\mu$ M) were active in the first screen against CYP19 (Table 5). The inhibition for imidazole **21I**, although potent, was not concentration-dependent, and the  $IC_{50}$  could not be determined. 1,2,4-Triazole **19e** inhibited aromatase in a concentration-dependent manner, and its  $IC_{50}$  was determined as 29  $\mu$ M. Of all the tested compounds (**21I**, **24**, and **19e**), none showed significant inhibition of CYP1A1, yielding  $IC_{50}$  values above 53  $\mu$ M, which is regarded as inactive [119,120]. From the results obtained, we can suggest that the 1,2,4-triazole heterocycle is required for aromatase inhibition in the phenstatin related compound **19e**. Therefore, the 1,2,4-triazole compound **19e** could be identified as

a potential dual-acting drug for the treatment of breast cancer targeting both aromatase inhibition and tubulin polymerisation.

**Table 5.** Inhibitory effect of compounds **19e**, **21l**, and **24** on aromatase and CYP1A1 activity.

Compound	% Inhibition at 20 µg/mL <sup>a</sup>		IC <sub>50</sub> (µM) <sup>a,b</sup>	
	CYP19	CYP1A1	CYP19	CYP1A1
19e	85.34	18.08	29.62	>53.85
21l	74.73	18.44	>53.99	>53.99
24	0.01	12.81	>53.85	>53.85

<sup>a</sup> The values are mean values of at least three experiments; <sup>b</sup> Concentration required to decrease the aromatase and CYP1A1 inhibition activity by 50%.

### 3.9. Molecular Docking of Phenstatin Hybrids **19e**, **21l**, and **24**

Compounds **19e**, **21l**, and **24** were next examined in tubulin molecular docking experiments to rationalise the observed biochemical activities. These three molecules contain a 3-hydroxy-4-methoxy substituted aromatic ring and a 3,4,5-trimethoxyphenyl ring and differ in the nitrogen heterocycle that is substituted on the benzyldryl linkage. The compounds phenstatin **7a** and N-deacetyl-N-(2-mercaptoacetyl)colchicine (DAMA-colchicine) were used as reference compounds in the docking experiments. Since the compounds **19e**, **21l**, and **24** were synthesised as racemates, both R and S enantiomers of each compound were docked in the crystallised tubulin structure 1SA0 [121] and ranked based on the substituent and enantiomer giving the best binding results as illustrated in Figure 13. The co-crystallised tubulin DAMA-colchicine structure 1SA0 [121] was used for this study, as it has been demonstrated that both CA-4 **4a** and phenstatin **7a** interact at the colchicine-binding site of tubulin. Figure 13A–C shows the binding of the S enantiomers, the ranking for the binding of the three different compounds in order: **S-21l**, **S-24**, and **S-19e**. All three compounds demonstrate a strong interaction with the same amino acid residue Lys352. Compound **S-21l** forms a hydrogen bond acceptor interaction between an imidazole nitrogen and Ser178. The imidazole also forms a  $\pi$ -CH interaction with Leu248. Compounds **S-24** and **S-19e** show very similar behaviour; they do not bind Ser178 but still have the same interaction with Leu248. In the R-enantiomer series, the heterocycle is directed differently, and very different binding poses and less favourable binding interactions between the ligands and the tubulin binding site are predicted for these compounds (Figure 13D–F). In order to maintain the A and C-ring overlays, the heterocycle would clash with binding site amino acids, so for the three R-enantiomers, the heterocycle overlays with either the A or C-ring and the 3,4,5-trimethoxyphenyl mapping is no longer possible or not as ideal.

Compound **S-21l** was the highest ranked compound in the series; therefore, it would be of interest to obtain in vitro results for the enantiomerically pure compound. Phenstatin **7a** also maps well to the colchicine binding pose with the 3,4-5-trimethoxyaryl residues overlaying effectively and the B-ring 4-methoxy group positioned to form a hydrogen bond with Lys352 (Figure 12G). The results provide rationalisation of the observed biochemical experiments in which cell cycle and tubulin binding was confirmed, indicating that these compounds are apoptotic and tubulin depolymerising agents.



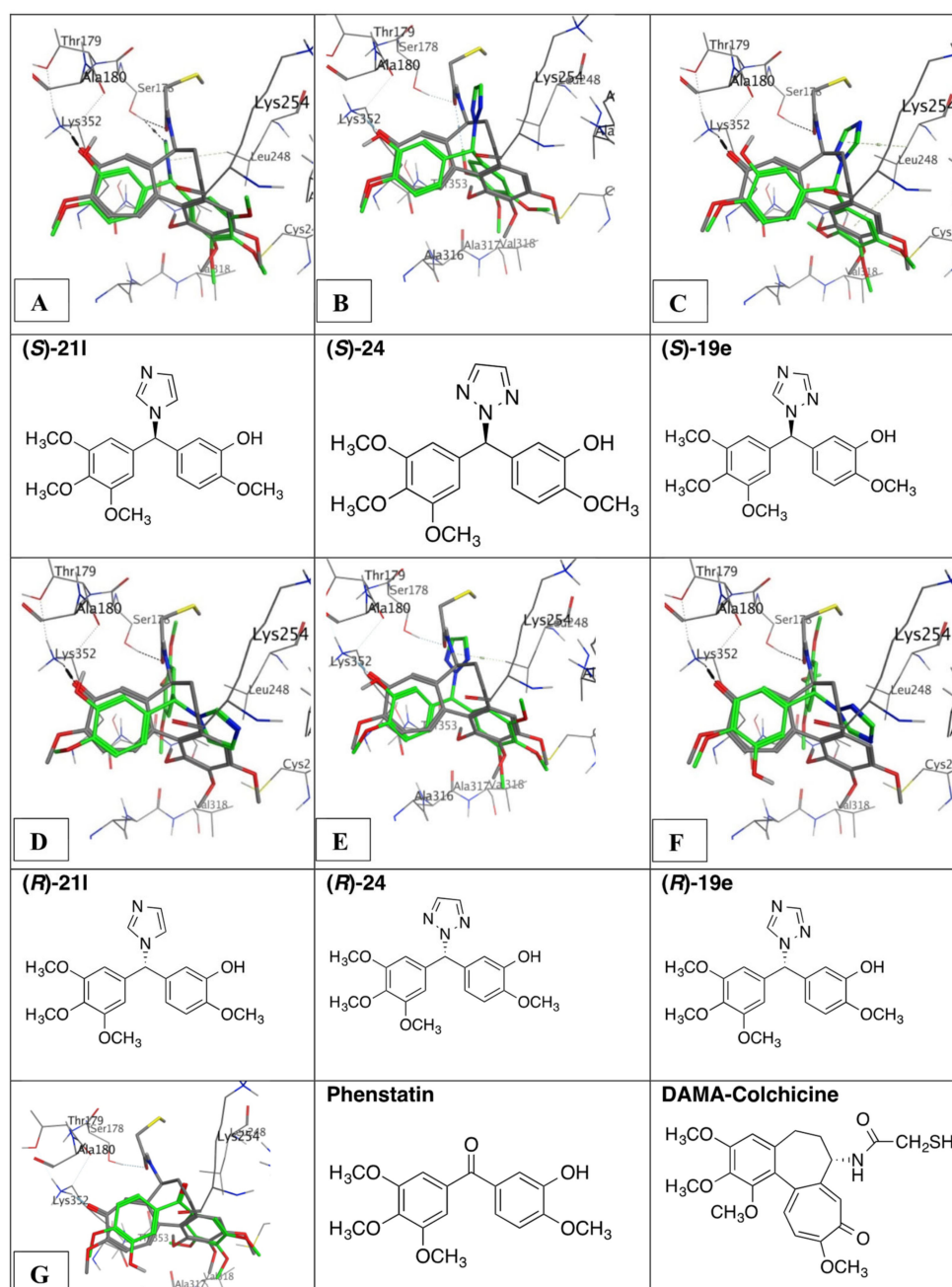


**Figure 13.** Docking of compounds **19e**, **211**, and **24** in the colchicine binding site of tubulin. Overlay of the X-ray structure of tubulin co-crystallised with DAMA-colchicine (PDB entry 1SA0) on the best-ranked docked poses of the three *S* enantiomers (**A**) **211**, (**B**) **24**, and (**C**) **19e**. Overlay of the X-ray structure of tubulin co-crystallised with DAMA-colchicine (PDB entry 1SA0) on the best ranked docked poses of the three *R* enantiomers (**D**) **211**, (**E**) **24**, (**F**) **19e**, and (**G**) Phenstatin (**7a**). Ligands are rendered as tube and amino acids as a line. Tubulin amino acids and DAMA-colchicine are coloured by atom type; the three heterocycles are coloured green. The atoms are coloured by element type, carbon = grey, hydrogen = white, oxygen = red, nitrogen = blue, sulphur = yellow. Key amino acid residues are labelled, and multiple residues are hidden to enable a clearer view.

## 4. Materials and Methods

### 4.1. Chemistry

All reagents were commercially available and were used without further purification unless otherwise indicated. Anhydrous solvents were purchased from Sigma. Uncorrected melting points were measured on a Gallenkamp apparatus. Infrared (IR) spectra were

recorded on a Perkin Elmer FT-IR Paragon 1000 spectrometer.  $^1\text{H}$  and  $^{13}\text{C}$  nuclear magnetic resonance spectra (NMR) were recorded at 27 °C on a Bruker DPX 400 spectrometer (400.13 MHz,  $^1\text{H}$ ; 100.61 MHz,  $^{13}\text{C}$ ) in  $\text{CDCl}_3$  (internal standard tetramethylsilane (TMS)). For  $\text{CDCl}_3$ ,  $^1\text{H}$  NMR spectra were assigned relative to the TMS peak at 0.00 ppm, and  $^{13}\text{C}$  NMR spectra were assigned relative to the middle  $\text{CDCl}_3$  peak at 77.0 ppm. Electrospray ionisation mass spectrometry (ESI-MS) was performed in the positive ion mode on a liquid chromatography time-of-flight mass spectrometer (Micromass LCT, Waters Ltd., Manchester, UK). The samples were introduced to the ion source by an LC system (Waters Alliance 2795, Waters Corporation, Milford, MA, USA) in acetonitrile/water (60:40% *v/v*) at 200  $\mu\text{L}/\text{min}$ . The capillary voltage of the mass spectrometer was at 3 kV. The sample cone (de-clustering) voltage was set at 40 V. For exact mass determination, the instrument was externally calibrated for the mass range  $m/z$  100 to 1000. A lock (reference) mass ( $m/z$  556.2771) was used. Mass measurement accuracies of  $< \pm 5$  ppm were obtained. Thin-layer chromatography (TLC) was performed using Merck Silica gel 60 TLC aluminium sheets with fluorescent indicator visualising with UV light at 254 nm. Flash chromatography was carried out using standard silica gel 60 (230–400 mesh) obtained from Merck. All products isolated were homogenous on TLC. The purity of the tested compounds was determined by HPLC. Analytical high-performance liquid chromatography (HPLC) was performed using a Waters 2487 Dual Wavelength Absorbance detector, a Waters 1525 binary HPLC pump, and a Waters 717 plus Autosampler. The column used was a Varian Pursuit XRs C18 reverse phase 150  $\times$  4.6 mm chromatography column. Samples were detected using a wavelength of 254 nm. All samples were analysed using acetonitrile (60%)/water (40%) over 10 min and a flow rate of 1 mL/min. Microwave experiments were carried using a Biotage Discover CEM microwave synthesiser on a standard power setting (maximum power supplied is 300 watts) unless otherwise stated. Details of the synthesis and characterisation of intermediate compounds and target azole products are available in the Supporting Information.

#### 4.1.1. (3-Hydroxy-4-Methoxyphenyl)(3,4,5-Trimethoxyphenyl)Methanone, Phenstatin (7a)

2-Methoxy-5-(3,4,5-trimethoxybenzoyl)phenyl 2-chloroacetate (23c) (1 eq, 1.28 mmol, 0.51 g) was reacted with sodium acetate (4.5 eq, 5.76 mmol, 0.47 g) in methanol (10 mL) at reflux for 2 h. After cooling, the mixture was concentrated under reduced pressure. Distilled water was added to the residue, and the resulting precipitate was filtered and recrystallised from ethanol. Yield: 89% (0.361 g) white solid Mp: 152–156 °C [66,67].  $^1\text{H}$  NMR (400 MHz,  $\text{CDCl}_3$ )  $\delta$  7.42 (d,  $J = 2.1$  Hz, 1H, Ar-H), 7.37 (dd,  $J = 8.3, 2.1$  Hz, 1H, Ar-H), 7.01 (s, 2H, Ar-H), 6.90 (d,  $J = 8.4$  Hz, 1H, Ar-H), 3.96 (s, 3H,  $\text{OCH}_3$ ), 3.91 (s, 3H,  $\text{OCH}_3$ ), 3.86 (s, 6H,  $\text{OCH}_3$ ).  $^{13}\text{C}$  NMR (101 MHz,  $\text{CDCl}_3$ )  $\delta$  194.63 (C=O), 152.75 (2  $\times$  C-O), 150.17 (C-O), 145.29 (C-OH), 141.61 (C-O), 133.13 (C), 131.03 (C), 123.61 (CH), 116.19 (CH), 109.66 (CH), 107.49 (2  $\times$  CH), 60.93 ( $\text{OCH}_3$ ), 56.28 (2  $\times$   $\text{OCH}_3$ ), 56.07 ( $\text{OCH}_3$ ). LRMS (EI): found 319.37 (M+H) $^+$ ;  $\text{C}_{17}\text{H}_{19}\text{O}_6$  requires 319.12. IR:  $\nu_{\text{max}}$  (ATR)  $\text{cm}^{-1}$ : 3249, 3003, 2840, 1632, 1578, 1505, 1443, 1414, 1331, 1236, 1222, 1118, 1002, 931, 892, 870, 758, 736, 670, 639, 576.

#### 4.1.2. General Method A: Preparation of Alcohols

To a solution of the benzophenone in methanol (25 mL),  $\text{NaBH}_4$  (1 eq) was added in small portions. The solution was stirred at 0 °C until the reaction was complete from TLC. Dilute HCl (10%) was added, and the solvent was removed with the rotary evaporator. Then, the product was dissolved in ethyl acetate (30 mL) and washed with water (20 mL) and brine (10 mL), dried over sodium sulphate, filtered, and concentrated. Purification via flash column chromatography (eluent: *n*-hexane/ethyl acetate 1:1) afforded the product.

#### *N*-(4-(Hydroxy(Phenyl)Methyl)Phenyl)Acetamide (12i)

As per general method A, a solution of compound 11i (1 eq, 0.5 mmol, 0.12 g) in methanol (25 mL) was treated with sodium borohydride (1 eq, 0.5 mmol, 0.02 g). The product was isolated without further purification, as an oil (0.1 g, 83%). IR:  $\nu_{\text{max}}$  (ATR)

cm<sup>-1</sup>: 3058, 1653, 1601, 1512, 1408, 1370, 1250, 1174, 1092, 1018. <sup>1</sup>H NMR (400 MHz, CDCl<sub>3</sub>) δ 7.43 (s, 2H, Ar-H), 7.32 (s, 2H, Ar-H), 7.31 (d, *J* = 1.4 Hz, 2H, Ar-H), 7.29 (d, *J* = 2.4 Hz, 2H, Ar-H), 7.27 (s, 1H, Ar-H), 5.20 (s, 1H, CH-OH), 2.14 (s, 3H, CH<sub>3</sub>). <sup>13</sup>C NMR (101 MHz, CDCl<sub>3</sub>) δ 168.28 (NH-C=O), 143.72 (C), 138.02 (C), 137.10 (C-NH), 128.36 (2 × CH), 127.59 (2 × CH), 127.44 (CH), 126.82 (2 × CH), 119.80 (2 × CH), 84.92 (CH-OH), 30.91 (CH<sub>3</sub>). LRMS (EI): C<sub>15</sub>H<sub>16</sub>NO<sub>2</sub>, 242.27 (M+H)<sup>+</sup>.

#### 4-(Hydroxy(Phenyl)Methyl)Phenyl 2,2,2-Trifluoroacetate (**12j**)

As per general method A, a solution of compound **11j** (1 eq, 2.12 mmol, 0.622 g) was treated with sodium borohydride (1 eq, 2.12 mmol, 0.08 g). Following purification via flash column chromatography (eluent: *n*-hexane/ethyl acetate 1:1), the product was isolated as a white solid, 89% (0.562 g) Mp. 145–147 °C. IR: ν<sub>max</sub> (ATR) cm<sup>-1</sup>: 3299, 1701, 1602, 1542, 1494, 1448, 1420, 1246, 1178, 1152, 1016. <sup>1</sup>H NMR (400 MHz, CDCl<sub>3</sub>) δ 7.73–7.66 (m, 1H, Ar-H), 7.52 (d, *J* = 8.6 Hz, 2H, Ar-H), 7.41 (d, *J* = 8.6 Hz, 2H, Ar-H), 7.35–7.32 (m, 4H, Ar-H), 5.84 (s, 1H, CH-OH). <sup>13</sup>C NMR (101 MHz, CDCl<sub>3</sub>) δ 163.43 (C=O), 143.40 (C-O), 141.94 (C), 132.90 (C), 128.62 (2 × CH), 127.84 (CH), 127.47 (2 × CH), 126.49 (2 × CH), 120.45 (2 × CH), 113.60 (CF<sub>3</sub>), 75.65 (CH-OH). HRMS (EI): found 294.0745 (M – 2H)<sup>+</sup>; C<sub>15</sub>H<sub>9</sub>F<sub>3</sub>O<sub>3</sub> requires 294.0504.

#### 4.1.3. General Method B: Preparation of 1-(Diarylmethyl)-1*H*-1,2,4-Triazoles

To a solution of the secondary alcohol (1 eq) in toluene (60 mL), in a round-bottom flask connected to a Dean-Stark trap was added 1,2,4-triazole (3 eq) and *p*-toluenesulfonic acid (200 mg, 0.61 eq). The source of heating used for the reaction was a Biotage open vessel microwave reactor (90–250 W). The reaction mixture was heated at reflux for 4 h, the toluene was evaporated, and the crude product was dissolved in ethyl acetate (30 mL) and washed with water (20 mL) and brine (10 mL). The solution was dried over sodium sulphate, filtered, and concentrated under reduced pressure. The crude product was purified via flash chromatography (*n*-hexane/ethyl acetate, 1:1) over silica gel to afford the desired product.

#### 1-((4-Fluorophenyl)(Phenyl)Methyl)-1*H*-1,2,4-Triazole (**13c**)

As per general method B, compound **12d** (1 eq, 2.47 mmol, 0.5 g) was reacted with 1,2,4-triazole and *p*-TSA in toluene. The crude product was purified via flash chromatography (eluent: *n*-hexane/ethyl acetate 5:3), white crystals, 26% (0.16 g), Mp. 96–99 °C, (HPLC 97%). IR: ν<sub>max</sub> (ATR) cm<sup>-1</sup>: 3120, 3051, 3010, 1605, 1509, 1496, 1276, 1228, 1207, 1160, 1137, 1015. <sup>1</sup>H NMR (400 MHz, CDCl<sub>3</sub>) δ 6.72 (s, 1 H, CH-N-R), 7.02–7.08 (m, 2 H, Ar-H), 7.08–7.13 (m, 4 H, Ar-H), 7.35–7.39 (m, 3 H, Ar-H), 7.91 (s, 1 H, CH-N), 8.01 (s, 1 H, CH-N). <sup>13</sup>C NMR (101 MHz, CDCl<sub>3</sub>) δ 67.13 (CH-N-R), 115.83 (CH), 116.05 (CH), 128.00 (2 × CH), 128.76 (CH), 129.04 (2 × CH), 129.90 (CH), 129.98 (CH), 133.85 (C), 137.74 (C), 143.47 (CH-N), 152.41 (CH-N), 163.87 (C-F). HRMS (EI): found 252.0941 (M – H)<sup>+</sup>; C<sub>15</sub>H<sub>11</sub>FN<sub>3</sub> requires 252.0937.

#### 2,2,2-Trifluoro-*N*-(4-(Phenyl(1*H*-1,2,4-Triazol-1-yl)Methyl)Phenyl)Acetamide (**13i**)

As per general method B, compound **12j** (1 eq, 1.67 mmol, 0.49 g) was reacted with 1,2,4-triazole and *p*-TSA in toluene. The crude product was purified via flash chromatography (eluent: *n*-hexane/ethyl acetate 1:1) to afford a pale yellow solid, 26%, 0.154 g, Mp. 143–145 °C. IR: ν<sub>max</sub> (ATR) cm<sup>-1</sup>: 3112, 3039, 1725, 1612, 1560, 1503, 1252, 1209, 1186, 1159, 1135. <sup>1</sup>H NMR (400 MHz, CDCl<sub>3</sub>) δ 6.74 (s, 1 H, CH-N-R), 7.16 (d, *J* = 8.54 Hz, 4 H, Ar-H), 7.36 (d, *J* = 1.83 Hz, 3 H, Ar-H), 7.58 (d, *J* = 8.54 Hz, 2 H, Ar-H), 7.92 (s, 1 H, CH-N), 8.02 (s, 1 H, CH-N). <sup>13</sup>C NMR (101 MHz, CDCl<sub>3</sub>) δ 154.64 (C=O), 152.33 (CH-N), 143.54 (CH-N), 137.34 (C), 135.97 (C-NH), 135.40 (C), 129.08 (2 × CH), 128.88 (CH), 128.11 (2 × CH), 120.80 (2 × CH), 114.14 (CF<sub>3</sub>), 67.23 (CH-N-R). HRMS (EI): found 347.1116 (M + H)<sup>+</sup>; C<sub>17</sub>H<sub>14</sub>F<sub>3</sub>N<sub>4</sub>O requires 347.1119.

1-((4-(Benzyloxy)Phenyl)(Phenyl)Methyl)-1*H*-1,2,4-Triazole (**13j**)

As per general method B, compound **12k** (1 eq, 2.41 mmol, 0.7 g) was reacted with 1,2,4-triazole and *p*-TSA in toluene. The crude product was purified via flash chromatography (eluent: *n*-hexane/ethyl acetate 1:2) to afford a white solid, 54%, 0.44 g, Mp. 132–134 °C. IR:  $\nu_{\max}$  (ATR)  $\text{cm}^{-1}$ : 3089, 3033, 3050, 2888, 2853, 1576, 1452, 1379, 1289, 1276, 1245, 1171, 1041.  $^1\text{H}$  NMR (400 MHz,  $\text{CDCl}_3$ )  $\delta$  5.04 (s, 2 H,  $\text{CH}_2$ ), 6.69 (s, 1 H, CH-N-R), 6.95 (d,  $J = 8.54$  Hz, 2 H, Ar-H), 7.05–7.09 (m, 4 H, Ar-H), 7.31–7.42 (m, 8 H, Ar-H), 7.89 (s, 1 H, CH-N), 8.00 (s, 1 H, CH-N).  $^{13}\text{C}$  NMR (101 MHz,  $\text{CDCl}_3$ )  $\delta$  158.93 (C-O), 152.24 (CH-N), 143.43 (CH-N), 138.32 (C), 136.57 (C), 130.10 (C), 129.63 (2  $\times$  CH), 128.86 (2  $\times$  CH), 128.60 (2  $\times$  CH), 128.40 (2  $\times$  CH), 128.07 (CH), 127.75 (2  $\times$  CH), 127.42 (CH), 115.19 (2  $\times$  CH), 70.07 (CH-N-R), 67.35 ( $\text{CH}_2$ ). LRMS (EI): found 341.90 ( $\text{M}^+$ );  $\text{C}_{22}\text{H}_{19}\text{N}_3\text{O}$  requires 341.15.

1-((4-Ethoxyphenyl)(Phenyl)Methyl)-1*H*-1,2,4-Triazole (**13l**)

As per general method B, compound **12m** (1 eq, 1.98 mmol, 0.45 g) was reacted with 1,2,4-triazole and *p*-TSA in toluene. The crude product was purified via flash chromatography (eluent: *n*-hexane/ethyl acetate 1:1) to afford white crystals, 98%, 0.54 g, Mp. 98–100 °C, (HPLC 97%). IR:  $\nu_{\max}$  (ATR)  $\text{cm}^{-1}$ : 3091, 2926, 1611, 1579, 1468, 1458, 1430, 1390, 1375, 1248, 1138, 1015.  $^1\text{H}$  NMR (400 MHz,  $\text{CDCl}_3$ )  $\delta$  1.41 (t,  $J = 7.02$  Hz, 3 H,  $\text{CH}_3$ ), 4.03 (q,  $J = 6.71$  Hz, 2 H,  $\text{CH}_2$ ), 6.71 (s, 1 H, CH-N-R), 6.86–6.90 (m, 2 H, Ar-H), 7.05–7.11 (m, 4 H, Ar-H), 7.32–7.40 (m, 3 H, Ar-H), 7.90 (s, 1 H, CH-N), 8.02 (s, 1 H, CH-N).  $^{13}\text{C}$  NMR (101 MHz,  $\text{CDCl}_3$ )  $\delta$  14.76 ( $\text{CH}_3$ ), 63.55 ( $\text{CH}_2$ ), 67.42 (CH-N-R), 114.82 (2  $\times$  CH), 127.74 (CH), 128.38 (2  $\times$  CH), 128.86 (2  $\times$  CH), 129.63 (2  $\times$  CH, C), 138.43 (C), 143.45 (CH-N), 152.22 (CH-N), 159.14 (C-O). HRMS (EI): found 280.1447 ( $\text{M} + \text{H}^+$ );  $\text{C}_{17}\text{H}_{18}\text{N}_3\text{O}$  requires 280.1450.

1-((4-(Benzyloxy)phenyl)(3,4,5-trimethoxyphenyl)methyl)-1*H*-1,2,4-triazole (**16b**)

As per general method B, compound **15b** (1 eq, 1.06 mmol, 0.405 g) was reacted with 1,2,4-triazole (3 eq, 3.19 mmol, 0.22 g) and *p*-TSA (0.61 eq, 200 mg) in toluene (60 mL). The crude product was purified via flash chromatography (eluent: *n*-hexane/ethyl acetate 1:1), pale yellow oil, 72%, 0.33 g. IR:  $\nu_{\max}$  (ATR)  $\text{cm}^{-1}$ : 1589, 1504, 1453, 1330, 1230, 1175, 1120, 1005.  $^1\text{H}$  NMR (400 MHz,  $\text{CDCl}_3$ )  $\delta$  3.73 (s, 6 H,  $\text{OCH}_3$ ), 3.82 (s, 3 H,  $\text{OCH}_3$ ), 5.06 (s, 2 H,  $\text{CH}_2$ ), 6.28 (s, 2 H, Ar-H), 6.62 (s, 1 H, CH-N-R), 6.96 (d,  $J = 8.54$  Hz, 2 H, Ar-H), 7.08 (d,  $J = 8.54$  Hz, 2 H, Ar-H), 7.31–7.42 (m, 5 H, Ar-H), 7.91 (s, 1 H, CH-N), 8.01 (s, 1 H, CHN).  $^{13}\text{C}$  NMR (101 MHz,  $\text{CDCl}_3$ )  $\delta$  158.98 (C), 153.54 (2  $\times$  C), 152.25 (CH), 143.47 (CH), 137.97 (C), 136.53 (C), 133.76 (C), 129.84 (C), 129.55 (2  $\times$  CH), 128.62 (2  $\times$  CH), 128.11 (CH), 127.44 (2  $\times$  CH), 115.24 (2  $\times$  CH), 104.98 (2  $\times$  CH), 70.09 ( $\text{CH}_2$ ), 67.43 (CH), 60.84 ( $\text{OCH}_3$ ), 56.12 (2  $\times$   $\text{OCH}_3$ ). HRMS (EI): found 454.1748 ( $\text{M} + \text{Na}^+$ );  $\text{C}_{25}\text{H}_{25}\text{N}_3\text{NaO}_4$  requires 454.1743.

1-(Phenyl(3,4,5-Trimethoxyphenyl)Methyl)-1*H*-1,2,4-Triazole (**16e**)

As per general method B, compound **15e** (1 eq, 3.2 mmol, 0.87 g) was reacted with 1,2,4-triazole (3 eq, 9.6 mmol, 0.66 g) and *p*-TSA (0.6 eq, 200 mg) in toluene (60 mL). The crude product was purified via flash chromatography (eluent: *n*-hexane/ethyl acetate 1:1), white crystals, 70%, 0.735 g, Mp. 139–140 °C, (HPLC 100%). IR:  $\nu_{\max}$  (ATR)  $\text{cm}^{-1}$ : 3119, 2944, 1592, 1502, 1454, 1434, 1420, 1332, 1270, 1219, 1120.  $^1\text{H}$  NMR (400 MHz,  $\text{CDCl}_3$ )  $\delta$  3.74 (s, 6 H,  $\text{OCH}_3$ ), 3.83 (s, 3 H,  $\text{OCH}_3$ ), 6.32 (s, 2 H, Ar-H), 6.67 (s, 1 H, CH-N-R), 7.13 (d,  $J = 7.32$  Hz, 2 H, Ar-H), 7.35–7.40 (m, 3 H, Ar-H), 7.93 (s, 1 H, CH-N), 8.02 (s, 1 H, CH-N).  $^{13}\text{C}$  NMR (101 MHz,  $\text{CDCl}_3$ )  $\delta$  56.10 (2  $\times$   $\text{OCH}_3$ ), 60.83 ( $\text{OCH}_3$ ), 67.89 (CH-N-R), 105.32 (2  $\times$  CH), 128.01 (2  $\times$  CH), 128.70 (CH), 128.94 (2  $\times$  CH), 133.32 (C), 137.69 (C-O), 138.10 (C), 143.55 (CH-N), 152.32 (CH-N), 153.56 (2  $\times$  C-O). HRMS (EI): found 348.1314 ( $\text{M} + \text{Na}^+$ );  $\text{C}_{18}\text{H}_{19}\text{N}_3\text{NaO}_3$  requires 348.1324.

1-((3-(Benzyloxy)-4-Methoxyphenyl)(3,4,5-Trimethoxyphenyl)Methyl)-1*H*-1,2,4-Triazole (**19a**)

As per general method B, compound **18a** (1 eq, 2.43 mmol, 1.0 g) was reacted with 1,2,4-triazole (3 eq, 7.3 mmol, 0.5 g) and *p*-TSA (200 mg) in toluene (60 mL). The toluene

was evaporated, and the crude product was dissolved in ethyl acetate (30 mL), washed with water (20 mL), brine (10 mL), dried over sodium sulphate and concentrated under reduced pressure, white solid, 64%, 0.71 g, Mp. 98–100 °C. IR:  $\nu_{\max}$  (ATR)  $\text{cm}^{-1}$ : 3440, 2938, 1591, 1517, 1464, 1416, 1253, 1127, 1006.  $^1\text{H}$  NMR ( $\text{CDCl}_3$ , 400 MHz)  $\delta$  8.02 (s, 1H, CH-N), 7.83 (s, 1H, CH-N), 7.29–7.35 (m, 5H, Ar-H), 6.89 (d,  $J$  = 8.53 Hz, 1H, Ar-H), 6.69–6.74 (m, 1H, Ar-H), 6.66 (d,  $J$  = 2.01 Hz, 1H, Ar-H), 6.59 (s, 1H, CH-N-R), 6.23 (s, 2H, Ar-H), 5.08 (s, 2H,  $\text{CH}_2$ ), 3.91 (s, 3H,  $\text{OCH}_3$ ), 3.86 (s, 3H,  $\text{OCH}_3$ ), 3.72 (s, 6H,  $\text{OCH}_3$ ).  $^{13}\text{C}$  NMR ( $\text{CDCl}_3$ , 100 MHz)  $\delta$  153.0 (COBn), 151.8 (CH-N), 149.5 (C), 147.6 (C), 143.0 (CH-N), 137.4 (C), 136.0 (C), 133.2 (C), 129.3 (C), 128.1 (2  $\times$  CH), 127.6 (2  $\times$  CH), 126.8 (CH), 120.9 (CH), 113.7 (CH), 111.2 (CH), 104.3 (2  $\times$  CH), 77.0 ( $\text{CH}_2$ ), 70.5 (CH-N-R), 67.0 ( $\text{OCH}_3$ ), 60.4 ( $\text{OCH}_3$ ), 55.6 ( $\text{OCH}_3$ ), 55.5 ( $\text{OCH}_3$ ). HRMS (EI): 484.1833 (M + Na) $^+$ ;  $\text{C}_{26}\text{H}_{27}\text{N}_3\text{NaO}_5$  requires 484.1848.

#### 4-((3-(Benzyloxy)-4-Methoxyphenyl)(1*H*-1,2,4-Triazol-1-yl)methyl)Benzonitrile (19f)

As per the general method B, **18e** (1 eq., 600 mg, 1.73 mmol), 1,2,4-triazole (3 eq., 360 mg, 5.21 mmol) and *p*-TSA (0.5 eq, 0.87 mmol, 150 mg) were reacted in a microwave reactor. The fixed microwave was set to 120 W for the duration of the reaction. The product was purified via flash chromatography on silica gel (DCM: EtOAc, gradient 25:1 to 10:1) to afford a yellow solid, 507 mg, 74%, Mp. 91–93 °C. IR:  $\nu_{\max}$  (KBr)  $\text{cm}^{-1}$ : 3032, 2934, 2228, 1607, 1513, 1441, 1264, 1139, 1015.  $^1\text{H}$  NMR ( $\text{CDCl}_3$ , 400 MHz)  $\delta$  8.04 (s, 1H, CH), 7.88 (s, 1H, CH), 7.61 (d,  $J$  = 8.53 Hz, 2H, Ar-H), 7.30–7.37 (m, 5H, Ar-H), 7.06 (d,  $J$  = 8.03 Hz, 2H, Ar-H), 6.91 (d,  $J$  = 8.03 Hz, 1H, Ar-H), 6.76 (dd,  $J$  = 1.51, 8.03 Hz, 1H, Ar-H), 6.64 (d,  $J$  = 13.55 Hz, 2H, Ar-H), 5.10 (s, 2H,  $\text{CH}_2$ ), 3.92 (s, 3H,  $\text{OCH}_3$ ).  $^{13}\text{C}$  NMR ( $\text{CDCl}_3$ , 100 MHz)  $\delta$  151.9 (NCHN), 150.0 ( $\text{C}_q$ ), 147.8 ( $\text{C}_q$ ), 143.1 (NCHN), 135.9 ( $\text{C}_q$ ), 132.1, 128.2, 127.7, 127.7, 127.6, 126.7, 121.5, 117.8 ( $\text{C}_q$ ), 114.2, 111.8, 111.3 ( $\text{C}_q$ ), 70.6 ( $\text{CH}_2$ ), 66.5 (CH), 55.6 ( $\text{OCH}_3$ ). HRMS (EI): 395.1516 (M – H) $^-$ ;  $\text{C}_{24}\text{H}_{19}\text{N}_4\text{O}_2$  requires 395.1508.

#### 4-((4-(Benzyloxy)Phenyl)(1*H*-1,2,4-Triazol-1-yl)methyl)Benzonitrile (19g)

As per general method B, **18f** (1 eq., 3 g, 9.51 mmol), 1,2,4-triazole (3 eq., 1.69 g, 24.5 mmol) and *p*-TSA (1.0 eq, 1.74 mmol, 300 mg) were reacted for 4 h. The fixed microwave was set to 95 W for the duration of the reaction. The material was purified via flash chromatography on silica gel (DCM: EtOAc, gradient 25:1 to 10:1) to afford a pale yellow solid, 2.33 g, 67%, Mp. 79–81 °C. IR:  $\nu_{\max}$  (KBr)  $\text{cm}^{-1}$ : 3443, 3118, 2920, 2227, 1608, 1561, 1511, 1418, 1394, 1217, 1169, 1154, 1039.  $^1\text{H}$  NMR ( $\text{CDCl}_3$ , 400 MHz)  $\delta$  8.07 (s, 1H, CH), 7.99 (s, 1H, CH), 7.68 (d,  $J$  = 8.53 Hz, 2H, Ar-H), 7.33–7.48 (m, 5H, Ar-H), 7.19 (d,  $J$  = 8.53 Hz, 2H, Ar-H), 7.11–7.16 (m, 2H, Ar-H), 6.98–7.05 (m, 2H, Ar-H), 6.75 (s, 1H, CH), 5.10 (s, 2H,  $\text{CH}_2$ ).  $^{13}\text{C}$  NMR ( $\text{CDCl}_3$ , 100 MHz)  $\delta$  159.0 (COBn), 152.2 (NCHN), 143.4 (NCHN), 135.9 ( $\text{C}_q$ ), 132.2, 129.7, 128.3, 128.0, 127.8 ( $\text{C}_q$ ), 127.0, 117.8 ( $\text{C}_q$ ), 115.1, 111.9 ( $\text{C}_q$ ), 69.7 ( $\text{CH}_2$ ), 66.4 (CH). HRMS (EI): 365.1408 (M – H) $^-$ ;  $\text{C}_{23}\text{H}_{17}\text{N}_4\text{O}$  requires 365.1402.

#### 5-((2*H*-1,2,3-Triazol-1-yl)(3,4,5-Trimethoxyphenyl)methyl)-2-Methoxyphenol (24)

As per general method B, compound **15i** (1 eq, 0.2 mmol, 0.5 g) was reacted with 1,2,3-triazole (3 eq, 1.5 mmol, 0.33 g) of and *p*-TSA (0.61 eq, 200 mg) in toluene (60 mL). The crude product was purified via flash column chromatography (eluent: *n*-hexane/ethyl acetate 1:1), yellow oil, 77%, 0.143 g, (HPLC 98%). IR:  $\nu_{\max}$  (ATR)  $\text{cm}^{-1}$ : 3392, 2939, 2838, 1590, 1507, 1458, 1419, 1330, 1275, 1236, 1120, 1001, 1025.  $^1\text{H}$  NMR (400 MHz,  $\text{DMSO}-d_6$ )  $\delta$  9.01 (s, 1H, OH), 7.83 (s, 2H, Ar-H), 6.99 (s, 1H, CH), 6.83 (d,  $J$  = 8.4 Hz, 1H, Ar-H), 6.65 (d,  $J$  = 2.2 Hz, 1H, Ar-H), 6.60 (s, 2H, Ar-H), 6.56 (dd,  $J$  = 8.4, 2.1 Hz, 1H, Ar-H), 3.70 (s, 3H,  $\text{OCH}_3$ ), 3.65 (s, 6H,  $\text{OCH}_3$ ), 3.62 (s, 3H,  $\text{OCH}_3$ ).  $^{13}\text{C}$  NMR (101 MHz,  $\text{DMSO}-d_6$ )  $\delta$  153.12 (2  $\times$  C-O), 147.78 (C-O), 146.67 (C-O), 137.49 (C), 135.21 (C), 134.90 (CH), 131.93 (CH, C), 119.34 (CH), 115.79 (CH), 112.28 (CH), 105.96 (2  $\times$  CH), 70.96 (CH-N-R), 60.42 ( $\text{OCH}_3$ ), 56.29 (2  $\times$   $\text{OCH}_3$ ), 56.01 ( $\text{OCH}_3$ ). LRMS (EI): found 394.26 (M + Na) $^+$ ;  $\text{C}_{19}\text{H}_{21}\text{N}_3\text{NaO}_5$  requires 394.14.

#### 4.1.4. 4-(Phenyl(1*H*-1,2,4-Triazol-1-yl)Methyl)Aniline (**13m**)

To a solution of compound **13i** (1 eq, 0.44 mmol, 0.154 g) in MeOH and water, K<sub>2</sub>CO<sub>3</sub> (4 eq, 1.78 mmol, 0.25 g) was added. The mixture was stirred for 72 h; then, it was acidified with HCl 10% (50 mL) and extracted with DCM (3 × 25 mL). The acid phase was made alkaline with aqueous NaOH (15%) and extracted with DCM (3 × 25 mL). The organic extracts were combined, dried over Na<sub>2</sub>SO<sub>4</sub>, filtered and concentrated under reduced pressure, orange solid, 16%, 0.043 g, Mp. 149–151 °C. IR:  $\nu_{\max}$  (ATR) cm<sup>-1</sup>: 3357, 3194, 3124, 1611, 1517, 1504, 1273, 1209, 1184, 1134, 1022. <sup>1</sup>H NMR (400 MHz, DMSO-*d*<sub>6</sub>)  $\delta$  5.15 (s, 2 H, NH), 6.49 (m, 2 H, Ar-H), 6.77 (s, 1 H, CH-N-R), 6.88 (d, *J* = 8.54 Hz, 2 H, Ar-H), 7.09 (d, *J* = 7.32 Hz, 2 H, Ar-H), 7.22–7.35 (m, 3 H, Ar-H), 7.98 (s, 1 H, CH-N), 8.40 (s, 1 H, CH-N). <sup>13</sup>C NMR (101 MHz, DMSO-*d*<sub>6</sub>)  $\delta$  65.76 (CH-N-R), 113.57 (2 × CH), 125.32 (2 × CH), 127.44 (2 × CH), 127.51 (C), 128.38 (CH), 129.15 (2 × CH), 140.02 (C), 143.92 (CH-N), 148.58 (C-NH<sub>2</sub>), 151.60 (CH-N). LRMS (EI): found 251.18 (M<sup>+</sup>); C<sub>15</sub>H<sub>16</sub>N<sub>4</sub> requires 251.13.

#### 4.1.5. 4-(Phenyl(1*H*-1,2,4-Triazol-1-yl)Methyl)Phenol (**13n**)

Compound **13j** (1 eq, 1.28 mmol, 0.44 g) was stirred in ethyl acetate (20 mL) and palladium hydroxide (0.05 g) under hydrogen atmosphere for 3 h. Then, the crude product was purified via flash chromatography (eluent: *n*-hexane/ethyl acetate 1:2), off-white solid, 67%, 0.217 g, Mp. 189–191 °C, (HPLC 93%). IR:  $\nu_{\max}$  (ATR) cm<sup>-1</sup>: 3104, 2599, 1612, 1590, 1512, 1493, 1449, 1372, 1283, 1238, 1217, 1025. <sup>1</sup>H NMR (400 MHz, CDCl<sub>3</sub>)  $\delta$  6.68 (s, 1 H, CH-N-R), 6.81 (d, *J* = 7.93 Hz, 2 H, Ar-H), 7.01 (s, 2 H, Ar-H), 7.07 (d, *J* = 6.10 Hz, 2 H, Ar-H), 7.34 (s, 3 H, Ar-H), 7.89 (s, 1 H, CH-N), 8.00 (s, 1 H, CH-N). <sup>13</sup>C NMR (101 MHz, CDCl<sub>3</sub>)  $\delta$  156.13 (C-OH), 151.53 (CH-N), 142.78 (CH-N), 138.00 (C), 129.82 (2 × CH), 129.53 (C), 128.92 (2 × CH), 128.52 (CH), 127.70 (2 × CH), 115.89 (2 × CH), 67.62 (CH-N-R). HRMS (EI): found 250.0981 (M - H)<sup>+</sup>; C<sub>15</sub>H<sub>12</sub>N<sub>3</sub>O requires 250.0981.

#### 4.1.6. General Method C: Preparation of Secondary Alcohols **15b**, **15c**, **15d**, **15g**, **15h**

A solution of the aryl bromide in dry THF was cooled to –78 °C under nitrogen. *n*-BuLi was added dropwise, and the mixture was allowed to stir for 1 h under nitrogen. After 1 h, a solution of the aryl aldehyde in dry THF was added, and the mixture was stirred for a further 1.5 h at –78 °C. The mixture was stirred at room temperature for 2 h; then, it was concentrated under reduced pressure to remove the THF. The residue was dissolved in DCM (30 mL) and washed with water (20 mL) and brine (10 mL), dried over sodium sulfate, filtered, and concentrated. Then, the crude product was purified via flash chromatography (eluent: *n*-hexane/ethyl acetate).

#### (4-(Benzyloxy)Phenyl)(3,4,5-Trimethoxyphenyl)Methanol (**15b**)

As per general method C, compound **14b** (1 eq, 5.2 mmol, 1.37 g) in dry THF (50 mL) was treated with *n*-BuLi (2.4 mL) followed by the addition 3,4,5-trimethoxybenzaldehyde (1 eq, 5.2 mmol, 1 g). The crude product was purified via flash chromatography (eluent: *n*-hexane/ethyl acetate 1:1), white solid, 21%, 0.405 g, Mp. 98–102 °C. IR:  $\nu_{\max}$  (ATR) cm<sup>-1</sup>: 3477, 2935, 2833, 1590, 1503, 1451, 1418, 1329, 1301, 1287, 1231, 1178, 1121, 1002. <sup>1</sup>H NMR (400 MHz, CDCl<sub>3</sub>)  $\delta$  3.81 (s, 9 H, CH<sub>3</sub>), 5.04 (s, 2 H, CH<sub>2</sub>), 5.72 (s, 1 H, CH-OH), 6.58 (s, 2 H, Ar-H), 6.93 (d, *J* = 8.54 Hz, 2 H, Ar-H), 7.24–7.31 (m, 3 H, Ar-H), 7.31–7.37 (m, 2 H, Ar-H), 7.40 (t, *J* = 7.02 Hz, 2 H, Ar-H). <sup>13</sup>C NMR (101 MHz, CDCl<sub>3</sub>)  $\delta$  56.08 (2 × OCH<sub>3</sub>), 60.81 (OCH<sub>3</sub>), 70.03 (CH<sub>2</sub>), 75.85 (CH-OH), 103.38 (2 × CH), 114.83 (2 × CH), 127.44 (2 × CH), 127.90 (CH), 127.98 (C), 128.42 (2 × CH), 136.16 (C-O), 136.88 (2 × C), 139.58 (2 × CH), 153.23 (2 × C-O), 158.34 (C-OBn). LRMS (EI): Found 403.21 (M + Na)<sup>+</sup>; C<sub>23</sub>H<sub>24</sub>NaO<sub>5</sub> requires 403.15.

#### (4-Methoxyphenyl)(3,4,5-Trimethoxyphenyl)Methanol (**15c**)

*Method (i)* As per general method C, 1-bromo-4-methoxybenzene **14c** (1 eq, 7.2 mmol, 1.34 g) in dry THF (50 mL) was treated with *n*-BuLi (3.3 mL) followed by the addition after 1 h of 3,4,5-trimethoxybenzaldehyde (1 eq, 7.2 mmol, 1.41 g). The crude product was

purified via flash chromatography (eluent: *n*-hexane/ethyl acetate gradient 7:3 to 1:1), pink solid, 22%, 0.5 g, Mp. 107–109 °C [103]. IR:  $\nu_{\max}$  (ATR)  $\text{cm}^{-1}$ : 3358, 2936, 2837, 1611, 1590, 1508, 1459, 1423, 1325, 1234, 1125, 1055, 1034, 1000.  $^1\text{H}$  NMR (400 MHz,  $\text{CDCl}_3$ )  $\delta$  3.79 (s, 3 H,  $\text{CH}_3$ ), 3.81 (s, 9 H,  $\text{CH}_3$ ), 5.73 (d,  $J = 2.44$  Hz, 1 H, CH-OH), 6.59 (s, 2 H, Ar-H), 6.86 (d,  $J = 8.54$  Hz, 2 H, Ar-H), 7.28 (d,  $J = 8.54$  Hz, 2 H, Ar-H).  $^{13}\text{C}$  NMR (101 MHz,  $\text{CDCl}_3$ )  $\delta$  55.26 ( $\text{OCH}_3$ ), 56.07 ( $2 \times \text{OCH}_3$ ), 60.80 ( $\text{OCH}_3$ ), 75.85 (CH-OH), 103.36 ( $2 \times \text{CH}$ ), 113.87 ( $2 \times \text{CH}$ ), 127.86 (C), 135.89 (C), 137.13 (C-O), 139.63 ( $2 \times \text{CH}$ ), 153.21 ( $2 \times \text{C-O}$ ), 159.11 (C-O). HRMS (EI): found 327.1221 ( $\text{M}+\text{Na}$ ) $^+$   $\text{C}_{17}\text{H}_{20}\text{NaO}_5$  requires 327.1209. *Method (ii)* As per general method A, compound **22c** (1 eq, 4.16 mmol, 1.26 g) was treated with sodium borohydride (3 eq, 12.48 mmol, 0.47 g). The product was obtained as a pink solid, 50%, 0.6 g, Mp. 107–109 °C, which was identical ( $^1\text{H}$ -NMR,  $^{13}\text{C}$ -NMR, HRMS, IR) to the sample obtained through general method C.

#### (3,4-Dimethoxyphenyl)(3,4,5-Trimethoxyphenyl)Methanol (**15d**)

*Method (i)* As per general method C, compound **14d** (1 eq, 7.2 mmol, 1.56 g) in dry THF (50 mL) was treated with *n*-BuLi (3.3 mL) followed by the addition of 3,4,5-trimethoxybenzaldehyde (1 eq, 7.2 mmol, 1.41 g). The crude product was purified via flash chromatography (eluent: *n*-hexane/ethyl acetate 5:3) as a dark oil, 30%, 0.725 g [67]. IR:  $\nu_{\max}$  (ATR)  $\text{cm}^{-1}$ : 3503, 2936, 2835, 1587, 1504, 1452, 1413, 1328, 1259, 1229, 1120, 1024, 1003.  $^1\text{H}$  NMR (400 MHz,  $\text{CDCl}_3$ )  $\delta$  3.82–3.83 (m, 9 H,  $\text{CH}_3$ ), 3.86 (s, 3 H,  $\text{CH}_3$ ), 3.86 (s, 3 H,  $\text{CH}_3$ ), 5.71 (d,  $J = 2.90$  Hz, 1 H, CH-OH), 6.60 (s, 2 H, Ar-H), 6.83 (d,  $J = 8.29$  Hz, 1 H, Ar-H), 6.88 (dd,  $J = 8.29, 1.66$  Hz, 1 H, Ar-H), 6.93 (d,  $J = 2.07$  Hz, 1 H, Ar-H).  $^{13}\text{C}$  NMR (101 MHz,  $\text{CDCl}_3$ )  $\delta$  55.82 ( $2 \times \text{OCH}_3$ ), 56.02 ( $2 \times \text{OCH}_3$ ), 60.74 ( $\text{OCH}_3$ ), 75.90 (CH-OH), 103.44 ( $2 \times \text{CH}$ ), 109.74 (CH), 110.86 (CH), 118.93 (CH), 136.25 (C), 137.10 (C), 139.50 (C-O), 148.45 (C-O), 148.94 (C-O), 153.11 ( $2 \times \text{C-O}$ ). HRMS (EI): found 357.1305 ( $\text{M} + \text{Na}$ ) $^+$ ;  $\text{C}_{18}\text{H}_{22}\text{NaO}_6$  requires 357.1314. *Method (ii)* As per general method A, compound **20a** (1 eq, 3.9 mmol, 1.3 g) was treated with sodium borohydride (3 eq, 11.73 mmol, 0.44 g). The product was afforded as a dark oil, 89%, 1.16 g which was identical ( $^1\text{H}$ -NMR,  $^{13}\text{C}$ -NMR, HRMS, IR) to the sample obtained by general method C.

#### 4.1.7. 4-((1*H*-1,2,4-Triazol-1-yl)(3,4,5-Trimethoxyphenyl)Methyl)Phenol (**16i**)

Compound **16b** (1 eq, 0.76 mmol, 0.330 g) was dissolved in ethyl acetate (20 mL) and stirred with palladium hydroxide (0.05 g) under a hydrogen atmosphere. The reaction mixture was filtered through Celite, and the solvent was concentrated. The crude product was purified via flash chromatography (eluent: *n*-hexane/ethyl acetate 1:2), yellow oil, 49%, 0.16 g, (HPLC 96%). IR:  $\nu_{\max}$  (ATR)  $\text{cm}^{-1}$ : 3113, 2999, 2939, 2837, 1592, 1505, 1459, 1420, 1332, 1274, 1236, 1123.  $^1\text{H}$  NMR (400 MHz,  $\text{CDCl}_3$ )  $\delta$  3.76 (s, 6 H,  $\text{OCH}_3$ ), 3.85 (s, 3 H,  $\text{OCH}_3$ ), 6.31 (s, 2 H, Ar-H), 6.63 (s, 1 H, CH-N-R), 6.85 (d,  $J = 8.54$  Hz, 2 H, Ar-H), 7.06 (d,  $J = 8.54$  Hz, 2 H, Ar-H), 7.94 (s, 1 H, CH-N), 8.04 (s, 1 H, CH-N).  $^{13}\text{C}$  NMR (101 MHz,  $\text{CDCl}_3$ )  $\delta$  56.13 ( $2 \times \text{OCH}_3$ ), 60.85 ( $\text{OCH}_3$ ), 67.58 (CH-N-R), 105.01 ( $2 \times \text{CH}$ ), 115.94 ( $2 \times \text{CH}$ ), 129.67 ( $2 \times \text{CH}$ ), 133.64 ( $2 \times \text{C}$ ), 137.41 (C-O), 143.43 (CH-N), 151.97 (CH-N), 153.55 ( $2 \times \text{C-O}$ ), 156.58 (C-OH). HRMS (EI): found 340.1302 ( $\text{M} - \text{H}$ ) $^+$ ;  $\text{C}_{18}\text{H}_{18}\text{N}_3\text{O}_4$  requires 340.1297.

#### 4.1.8. 5-((1*H*-1,2,4-Triazol-1-yl)(3,4,5-Trimethoxyphenyl)methyl)-2-Methoxyphenol (**19e**)

Compound **19a** (1 eq, 0.43 mmol, 0.2 g) was dissolved in ethyl acetate (20 mL) and stirred with palladium hydroxide (0.05 g) under hydrogen atmosphere. The reaction mixture was filtered through Celite, and the solvent was concentrated. The crude product was purified via flash chromatography (eluent: *n*-hexane/ethyl acetate 1:2), white solid, 76%, 0.12 g, Mp. 61–63 °C. IR:  $\nu_{\max}$  (ATR)  $\text{cm}^{-1}$ : 3389, 2936, 1591, 1508, 1461, 1276, 1127, 1010.  $^1\text{H}$  NMR ( $\text{CDCl}_3$ , 400 MHz)  $\delta$  8.04 (s, 1H, CH-N), 7.97 (s, 1H, CH-N), 6.86 (d,  $J = 8.53$  Hz, 1H, Ar-H), 6.76 (d,  $J = 2.01$  Hz, 1H, Ar-H), 6.67 (dd,  $J = 2.01, 8.03$  Hz, 1H, Ar-H), 6.61 (s, 1H, CH-N-R), 6.33 (s, 2H, Ar-H), 3.90 (s, 3H,  $\text{OCH}_3$ ), 3.85 (s, 3H,  $\text{OCH}_3$ ), 3.77 (s, 6H,  $\text{OCH}_3$ ).  $^{13}\text{C}$  NMR ( $\text{CDCl}_3$ , 100 MHz)  $\delta$  153.1 ( $2 \times \text{C-O}$ ), 151.6 (CH-N), 146.5 (C-OH), 145.6

(C-O), 143.0 (CH-N), 137.4 (C-O), 133.2 (C), 130.0 (C), 119.6 (CH), 114.2 (CH), 110.4 (CH), 104.5 (2 × CH), 67.1 (CH-N-R), 60.4 (OCH<sub>3</sub>), 55.7 (2 × OCH<sub>3</sub>), 55.5 (OCH<sub>3</sub>). HRMS (EI): 394.1363 (M + Na)<sup>+</sup>; C<sub>19</sub>H<sub>21</sub>N<sub>3</sub>NaO<sub>5</sub> requires 394.1379.

#### 4.1.9. 4-((3-Hydroxy-4-Methoxyphenyl)(1*H*-1,2,4-Triazol-1-yl)methyl)Benzonitrile (**19h**)

Compound **19f** (190 mg, 0.479 mmol) and Pd(OH)<sub>2</sub> (20%, 20 mg) were reacted in ethyl acetate (25 mL) for 60 min under a hydrogen atmosphere. The material was purified via flash chromatography over silica gel (DCM: EtOAc, gradient 10:1 to 5:1) to afford the product as a white solid, 120 mg, 82%, Mp. 168–170 °C. IR:  $\nu_{\max}$  (KBr) cm<sup>-1</sup>: 3123, 2937, 2842, 2230, 1609, 1592, 1505, 1442, 1278, 1132, and 1022. <sup>1</sup>H NMR (CDCl<sub>3</sub>, 400 MHz)  $\delta$  8.07 (s, 1H, CH), 8.05 (s, 1H, CH), 7.68 (d, *J* = 8.53 Hz, 2H, Ar-H), 7.19 (d, *J* = 8.03 Hz, 2H, Ar-H), 6.88 (d, *J* = 8.03 Hz, 1H, Ar-H), 6.77 (s, 1H, CH), 6.66–6.74 (m, 2H, Ar-H), 3.93 (s, 3H, OCH<sub>3</sub>), <sup>13</sup>C NMR (CDCl<sub>3</sub>, 100 MHz),  $\delta$  151.8 (NCHN), 146.9 (C<sub>q</sub>), 145.9 (C<sub>q</sub>), 143.2 (NCHN), 132.2, 128.6 (C<sub>q</sub>), 127.8, 120.2, 117.8 (C<sub>q</sub>), 114.5, 111.9 (C<sub>q</sub>), 110.5, 66.5 (CH), 55.6 (OCH<sub>3</sub>), HRMS (EI): 305.1039 (M – H)<sup>-</sup>, C<sub>17</sub>H<sub>13</sub>N<sub>4</sub>O<sub>2</sub> requires 305.1039.

#### 4.1.10. 4-((4-Hydroxyphenyl)(1*H*-1,2,4-Triazol-1-yl)methyl)Benzonitrile (**19i**)

Compound **19g** (400 mg, 1.09 mmol) and Pd(OH)<sub>2</sub> (20%, 20 mg) were reacted in ethyl acetate (25 mL) for 60 min under a hydrogen atmosphere. The material was purified via flash chromatography over silica gel (DCM: EtOAc, gradient 10:1 to 5:1) to afford the product as a brown solid, 200 mg, 66%, Mp. 78–81 °C [89]. IR:  $\nu_{\max}$  (KBr) cm<sup>-1</sup>: 3409 (br.), 2333 (CN), 1641, 1607, 1284, 1169. <sup>1</sup>H NMR (DMSO-d<sub>6</sub>, 400 MHz)  $\delta$  10.60 (br. s., 1H, OH), 8.01 (d, *J* = 8.03 Hz, 2H, Ar-H), 7.80 (d, *J* = 8.03 Hz, 2H, Ar-H), 7.67 (d, *J* = 8.53 Hz, 2H, Ar-H), 6.91 (d, *J* = 8.53 Hz, 2H, Ar-H) <sup>13</sup>C NMR (DMSO-d<sub>6</sub>, 100 MHz)  $\delta$  193.1 (C=O), 162.7 (COH), 142.2 (C<sub>q</sub>), 132.8, 132.5, 129.5, 126.9 (C<sub>q</sub>), 118.3 (C<sub>q</sub>), 115.5, 113.8 (C<sub>q</sub>) HRMS (EI): 222.0557 (M – H)<sup>-</sup>, C<sub>14</sub>H<sub>8</sub>NO<sub>2</sub> requires 222.0555.

#### 4.1.11. General Method D: Preparation of 1-(Diarylmethyl)-1*H*-Imidazoles

To a solution of the secondary alcohol (1 eq) in dry acetonitrile (60 mL), CDI was added (1.3 eq). The mixture was refluxed for 3 h under nitrogen, the acetonitrile was evaporated, and the crude product was dissolved in DCM (30 mL) and washed with water (20 mL) and brine (10 mL). The product was dried over sodium sulphate and concentrated under reduced pressure. The crude product was purified via flash chromatography over silica gel to afford the desired product (eluent: *n*-hexane/ethyl acetate 1:1).

#### 1-((4-Bromophenyl)(Phenyl)methyl)-1*H*-Imidazole (**20c**)

As per general method D, compound (**12c**) was reacted with CDI in ACN at reflux for 3 h. Then, the crude product was purified via flash chromatography (eluent: *n*-hexane/ethyl acetate 1:2), white solid, 10%, 0.06 g, Mp. 126–128 °C. IR:  $\nu_{\max}$  (ATR) cm<sup>-1</sup>: 3130, 1758, 1487, 1475, 1387, 1289, 1253, 1061. <sup>1</sup>H NMR (400 MHz, CDCl<sub>3</sub>)  $\delta$  6.98 (s, 1 H, CH-N-R), 7.09 (s, 1 H, CH-N), 7.26 (s, 1H, CH-N), 7.34–7.42 (m, 6 H, Ar-H), 7.47 (s, 1 H, Ar-H), 7.52 (d, *J* = 8.54 Hz, 2 H, Ar-H), 8.20 (s, 1 H, CH-N). <sup>13</sup>C NMR (101 MHz, CDCl<sub>3</sub>)  $\delta$  80.51 (CH-N-H), 117.12 (CH-N), 122.91 (C), 127.06 (2 × CH), 128.83 (CH), 128.93 (CH-N), 128.95 (2 × CH), 130.91 (2 × CH), 132.00 (2 × CH), 137.07 (C), 137.36 (C), and 137.74 (CH-N). HRMS (EI): found 313.0337 (M + H)<sup>+</sup>; C<sub>16</sub>H<sub>14</sub><sup>79</sup>BrN<sub>2</sub> requires 313.0340.

#### 1-((3-(Benzyloxy)-4-Methoxyphenyl)(3,4,5-Trimethoxyphenyl)methyl)-1*H*-Imidazole (**21h**)

As per general method D, compound **18a** (1 eq, 1.71 mmol, 0.70 g) was reacted with CDI in ACN (50 mL) at reflux for 1 h. The crude product was then purified via flash chromatography (eluent: *n*-hexane/ethyl acetate/methanol 10:2:1), colourless oil, 49%, 0.380 g. IR:  $\nu_{\max}$  (ATR) cm<sup>-1</sup>: 2937, 2836, 1590, 1506, 1455, 1419, 1330, 1229, 1122, 1076, 1004. <sup>1</sup>H NMR (400 MHz, CDCl<sub>3</sub>)  $\delta$  3.68 (s, 6 H, OCH<sub>3</sub>), 3.84 (s, 3 H, OCH<sub>3</sub>), 3.88 (s, 3 H, OCH<sub>3</sub>), 5.04 (s, 2 H, CH<sub>2</sub>), 6.16 (s, 2 H, Ar-H), 6.31 (s, 1 H, CH-N-R), 6.58 (d, *J* = 2.07 Hz, 1 H), 6.66 (dd, *J* = 8.29, 2.07 Hz, 1 H, Ar-H), 6.73 (s, 1 H, Ar-H), 6.84 (d, *J* = 8.71 Hz, 1 H, CH-N), 7.05



(s, 1 H, CH-N), 7.26–7.31 (m, 5 H, Ar-H), 7.33 (s, 1 H, CH-N).  $^{13}\text{C}$  NMR (101 MHz,  $\text{CDCl}_3$ ),  $\delta$  56.00 ( $\text{OCH}_3$ ), 56.07 ( $2 \times \text{OCH}_3$ ), 60.85 ( $\text{OCH}_3$ ), 64.60 ( $\text{CH}_2$ ), 70.98 (CH-N-R), 104.79 ( $2 \times \text{CH}$ ), 111.60 (CH), 114.16 (CH), 119.21 (CH), 121.16 (CH), 127.29 ( $3 \times \text{CH}$ ), 127.94 (CH), 128.52 ( $2 \times \text{CH}$ ), 129.29 (C), 131.14 (C), 136.56 ( $2 \times \text{C}$ ), 137.71 (CH), 147.98 (C-O), 149.75 (C-OBn), 153.41 ( $2 \times \text{C-O}$ ). HRMS (EI): found 461.2056 ( $\text{M}+\text{H}$ ) $^+$ ;  $\text{C}_{27}\text{H}_{29}\text{N}_2\text{O}_5$  requires 461.2076.

#### 1-(Bis(3,4,5-Trimethoxyphenyl)Methyl)-1H-Imidazole (21i)

As per general method D, compound **18b** (1 eq, 1.38 mmol, 0.51 g) was reacted with CDI in ACN (50 mL) at reflux for 3 h. Then, the crude product was purified via flash chromatography (eluent: *n*-hexane/ethyl acetate 1:1) to afford an orange solid, 52%, 0.3 g, Mp. 154–156 °C, (HPLC 100%). IR:  $\nu_{\text{max}}$  (ATR)  $\text{cm}^{-1}$ : 2934, 2830, 1589, 1504, 1455, 1329, 1226, 1121, 1106, 1003.  $^1\text{H}$  NMR (400 MHz,  $\text{CDCl}_3$ )  $\delta$  3.77 (s, 12 H,  $\text{OCH}_3$ ), 3.87 (s, 6 H,  $\text{OCH}_3$ ), 6.32 (s, 4 H, Ar-H), 6.38 (s, 1 H, CH-N-R), 6.88 (s, 1 H, CH-N), 7.12 (s, 1 H, CH-N), 7.44 (s, 1 H, CH-N).  $^{13}\text{C}$  NMR (101 MHz,  $\text{CDCl}_3$ )  $\delta$  56.22 ( $4 \times \text{OCH}_3$ ), 60.91 ( $2 \times \text{CH}_3$ ), 65.15 (CH-N-R), 105.24 ( $4 \times \text{CH}$ ), 119.35 (CH-N), 129.44 (CH-N), 134.47 ( $2 \times \text{C}$ ), 137.44 ( $2 \times \text{C-O}$ ), 138.02 (CH-N), 153.53 ( $4 \times \text{C-O}$ ). HRMS (EI): found 413.1718 ( $\text{M} - \text{H}$ ) $^+$ ;  $\text{C}_{22}\text{H}_{25}\text{N}_2\text{O}_6$  requires 413.1713.

#### 4.1.12. 4-((1H-Imidazol-1-yl)(Phenyl)Methyl)Aniline (20i)

To a solution of compound **20i** (1 eq, 0.20 mmol, 0.07 g) in MeOH and water  $\text{K}_2\text{CO}_3$  (4 eq, 0.81 mmol, 0.11 g) was added. The mixture was stirred for 72 h and then acidified with HCl 10% (50 mL) and extracted with DCM ( $3 \times 25$  mL). The acid phase was made basic with NaOH (15%) and extracted with DCM ( $3 \times 25$  mL). Organic phases combined, dried over  $\text{Na}_2\text{SO}_4$ , filtered, and concentrated. The crude product was purified via flash chromatography (eluent: *n*-hexane/ethyl acetate 1:1), orange oil, [122] 50%, 0.01 g. IR:  $\nu_{\text{max}}$  (ATR)  $\text{cm}^{-1}$ : 3130, 1696, 1613, 1560, 1515, 1491, 1283, 1259, 1215, 1151, 1103, 1068.  $^1\text{H}$  NMR (400 MHz,  $\text{CDCl}_3$ )  $\delta$  3.72 (br. s., 2 H,  $\text{NH}_2$ ), 6.39 (s, 1 H, CH-N-R), 6.62 (d,  $J = 8.54$  Hz, 2 H, Ar-H), 6.82 (s, 1 H, CH-N), 6.89 (d,  $J = 7.93$  Hz, 2 H, Ar-H), 7.02–7.07 (m, 3 H, Ar-H), 7.27–7.35 (m, 3 H, Ar-H), 7.38 (s, 1 H, CH-N).  $^{13}\text{C}$  NMR (101 MHz,  $\text{CDCl}_3$ ),  $\delta$  64.62 (CH-N-R), 115.01 ( $2 \times \text{CH}$ ), 118.07 (CH), 127.60 ( $3 \times \text{CH}$ ), 127.99 (C), 128.67 ( $3 \times \text{CH}$ ), 129.42 ( $2 \times \text{CH}$ ), 139.90 (C, CH), 146.52 (C- $\text{NH}_2$ ), HRMS (EI): found 250.1338 ( $\text{M}+\text{H}$ ) $^+$ ;  $\text{C}_{16}\text{H}_{16}\text{N}_3$  requires 250.1344.

#### 4.1.13. 5-((1H-Imidazol-1-yl)(3,4,5-Trimethoxyphenyl)Methyl)-2-Methoxyphenol (21i)

1-((3-(Benzyloxy)-4-methoxyphenyl)(3,4,5-trimethoxyphenyl)methyl)-1H-imidazole (**21h**) (1 eq, 0.83 mmol, 0.38 g) was stirred in ethyl acetate (20 mL) and palladium hydroxide (0.05 g) under hydrogen atmosphere for 1 h. The product was filtered through Celite, and the solvent was removed under reduced pressure, off-white solid, 93%, 0.28 g, Mp. 154–157 °C, (HPLC 97%). IR:  $\nu_{\text{max}}$  (ATR)  $\text{cm}^{-1}$ : 3136, 2932, 2836, 1589, 1532, 1452, 1437, 1331, 1294, 1223, 1121, and 1084.  $^1\text{H}$  NMR (400 MHz,  $\text{DMSO}-d_6$ )  $\delta$  9.05 (s, 1H, OH), 7.58 (s, 1H, Ar-H), 7.07 (s, 1H, Ar-H), 6.91 (s, 1H, Ar-H), 6.87 (d,  $J = 8.4$  Hz, 1H, Ar-H), 6.57 (s, 1H, CH-N-R), 6.54 (d,  $J = 2.2$  Hz, 1H, Ar-H), 6.47 (dd,  $J = 8.3, 2.1$  Hz, 1H, Ar-H), 6.43 (s, 2H, Ar-H), 3.71 (s, 3H,  $\text{OCH}_3$ ), 3.65 (s, 6H,  $\text{OCH}_3$ ), 3.62 (s, 3H,  $\text{OCH}_3$ ).  $^{13}\text{C}$  NMR (101 MHz,  $\text{DMSO}-d_6$ )  $\delta$  153.34 ( $2 \times \text{C-O}$ ), 147.72 (C-OH), 146.90 (C-O), 137.45 (CH-N), 136.30 (C-O), 132.66 ( $2 \times \text{C}$ ), 128.84 (CH-N), 119.69 (CH-N), 118.98 (CH), 115.48 (CH), 112.53 (CH), 105.71 ( $2 \times \text{CH}$ ), 63.56 (CH), 60.44 ( $\text{OCH}_3$ ), 56.32 ( $2 \times \text{OCH}_3$ ), 56.01 ( $\text{OCH}_3$ ). HRMS (EI): found 369.1453 ( $\text{M} - \text{H}$ ) $^+$ ;  $\text{C}_{20}\text{H}_{21}\text{N}_2\text{O}_5$  requires 369.1451.

#### 4.1.14. (4-Methoxyphenyl)(3,4,5-trimethoxyphenyl)methanone (23a)

Anisole (1 eq, 7.0 mmol, 0.75 g 0.75 mL) was reacted with 3,4,5-trimethoxybenzoic acid (1.5 eq, 10.5 mmol, 2.23 g) in Eaton's reagent (0.99 g  $\text{P}_2\text{O}_5$ /6.69 mL  $\text{CH}_3\text{SO}_3\text{H}$ ). The mixture was stirred at 60 °C for 3 h under  $\text{N}_2$ . The product was diluted in DCM (60 mL) and poured in a separatory funnel containing  $\text{NaHCO}_3$  50% (40 mL) and extracted. The crude product was purified via flash chromatography (eluent: *n*-hexane/ethyl acetate 5:4) to afford a pink

solid, 60%, 1.26 g, Mp. 76–81 °C [103]. IR:  $\nu_{\max}$  (ATR)  $\text{cm}^{-1}$ : 3401, 2951, 2837, 1641, 1600, 1510, 1494, 1445, 1332, 1305, 1233, 1250, 1111, 1018, 1025, 922, 840, 696, 761, 738, 696, 611.  $^1\text{H}$  NMR (400 MHz,  $\text{CDCl}_3$ )  $\delta$  3.88 (s, 6 H,  $\text{OCH}_3$ ), 3.90 (s, 3 H,  $\text{OCH}_3$ ), 3.94 (s, 3 H,  $\text{OCH}_3$ ), 6.98 (d,  $J = 8.53$  Hz, 2 H, Ar-H), 7.02 (s, 2 H, Ar-H), 7.83 (d,  $J = 9.03$  Hz, 2 H, Ar-H).  $^{13}\text{C}$  NMR (101 MHz,  $\text{CDCl}_3$ )  $\delta$  55.46 ( $\text{OCH}_3$ ), 56.25 ( $2 \times \text{OCH}_3$ ), 60.92 ( $\text{OCH}_3$ ), 107.40 ( $2 \times \text{CH}$ ), 113.50 ( $2 \times \text{CH}$ ), 130.23 (C), 132.34 ( $2 \times \text{CH}$ ), 133.30 (C), 141.54 (C-O), 152.78 ( $2 \times \text{C-O}$ ), 163.08 (C-O), 194.61 (C=O). HRMS (EI): Found 325.1056 ( $\text{M}+\text{Na}$ ) $^+$ ;  $\text{C}_{17}\text{H}_{18}\text{NaO}_5$  requires 325.1052. (Eaton's reagent was prepared from phosphorus pentoxide and methanesulfonic acid in a weight ratio  $\text{P}_2\text{O}_5:\text{CH}_3\text{SO}_3\text{H}$  of 1:10, mixed in a round-bottomed flask and heated at 40 °C under nitrogen atmosphere until homogenous).

#### 4.1.15. (3,4-Dimethoxyphenyl)(3,4,5-Trimethoxyphenyl)Methanone (23b)

1,2-Dimethoxybenzene (1 eq, 7.24 mmol, 1 g) was reacted with 3,4,5-trimethoxybenzoic acid (1.5 eq, 10.86 mmol, 2.30 g) in Eaton's reagent (1.02 g  $\text{P}_2\text{O}_5$ /7.24 mL  $\text{CH}_3\text{SO}_3\text{H}$ ). The mixture was stirred at 60 °C for 3 h under  $\text{N}_2$ . The product was diluted in DCM (60 mL) and poured in a separatory funnel containing  $\text{NaHCO}_3$  50% (40 mL) and extracted. The crude product was purified via flash chromatography (eluent: *n*-hexane/ethyl acetate 5:4) to afford an orange solid, 57%, 1.37 g, Mp. 128–131 °C [67]. IR:  $\nu_{\max}$  (ATR)  $\text{cm}^{-1}$ : 2942, 1640, 1599, 1576, 1411, 1330, 1256, 1232, 1118, 1026.  $^1\text{H}$  NMR (400 MHz,  $\text{CDCl}_3$ )  $\delta$  3.89 (s, 6 H,  $\text{OCH}_3$ ), 3.94 (s, 3 H,  $\text{OCH}_3$ ), 3.95 (s, 3 H,  $\text{OCH}_3$ ), 3.98 (s, 3 H,  $\text{OCH}_3$ ), 6.92 (d,  $J = 8.29$  Hz, 1 H, CH), 7.04 (s, 2 H, Ar-H), 7.40 (d,  $J = 2.07$  Hz, 1 H, Ar-H), 7.47 (d,  $J = 2.07$  Hz, 1 H, Ar-H).  $^{13}\text{C}$  NMR (101 MHz,  $\text{CDCl}_3$ )  $\delta$  56.07 ( $2 \times \text{OCH}_3$ ), 56.30 ( $2 \times \text{OCH}_3$ ), 60.96 ( $\text{OCH}_3$ ), 107.44 ( $2 \times \text{CH}$ ), 109.76 (CH), 112.25 (CH), 125.04 (CH), 130.30 ( $2 \times \text{C}$ ), 148.95 ( $2 \times \text{C-O}$ ), 152.80 ( $3 \times \text{C-O}$ ), 194.62 (C=O). HRMS (EI): Found 333.1330 ( $\text{M}+\text{H}$ ) $^+$ ;  $\text{C}_{18}\text{H}_{21}\text{O}_6$  requires 333.1338.

#### 4.1.16. General Method E for the Preparation of Diarylmethylpyrrolidines, Diarylmethylpiperidines and Diarylmethylpiperazines

The benzhydryl alcohol (1 eq) was reacted with thionyl chloride (5 eq) in dry DCM (30 mL) for 12 h. The reaction mixture was concentrated under reduced pressure, and the crude product was used in the next step without any further purification. The chlorinated benzhydryl alcohol was reacted with pyrrolidine or piperidine (5 eq) in dry ACN (30 mL) and refluxed for 12 h. The solvent was removed, and the residue was dissolved in DCM (50 mL) and washed with 1 M NaOH (30 mL). The organic phase was dried over sodium sulphate, filtered, and concentrated. Then, the crude product was purified via flash chromatography (eluent: *n*-hexane/ethyl acetate).

#### 1-((4-Bromophenyl)(Phenyl)methyl)Pyrrolidine (25b)

As per general method E, compound 12c (1 eq, 2.9 mmol, 0.82 g) was treated with thionyl chloride followed by reaction with pyrrolidine (5 eq, 14.5 mmol, 1.03 g, 1.20 mL) in acetonitrile (ACN) (50 mL) at reflux for 12 h. The crude product was purified via flash chromatography (eluent: *n*-hexane/ethyl acetate 9:1), white solid, 37%, 0.345 g, Mp. 70–72 °C, (HPLC 95%). IR:  $\nu_{\max}$  (ATR)  $\text{cm}^{-1}$ : 2964, 2784, 1648, 1585, 1484, 1450, 1280, 1194, 1070, 1009.  $^1\text{H}$  NMR (400 MHz,  $\text{CDCl}_3$ )  $\delta$  1.71–1.80 (m, 4 H,  $\text{CH}_2$ ), 2.35–2.43 (m, 4 H,  $\text{CH}_2$ ), 4.11 (s, 1 H, CH-N.R), 7.14–7.19 (m, 1 H, Ar-H), 7.23 (s, 1 H, Ar-H), 7.27 (s, 1 H, Ar-H), 7.31–7.42 (m, 6 H, Ar-H).  $^{13}\text{C}$  NMR (101 MHz,  $\text{CDCl}_3$ )  $\delta$  23.53 ( $2 \times \text{CH}_2$ ), 53.55 ( $2 \times \text{CH}_2$ ), 75.72 (CH-N.R), 120.44 (C-Br), 127.00 (CH), 127.36 ( $2 \times \text{CH}$ ), 128.45 ( $2 \times \text{CH}$ ), 129.15 ( $2 \times \text{CH}$ ), 131.46 ( $2 \times \text{CH}$ ), 143.44 (C), 143.75 (C). HRMS (EI): found 316.0711 ( $\text{M}+\text{H}$ ) $^+$ ;  $\text{C}_{17}\text{H}_{19}^{79}\text{BrN}$  requires 316.0701.

#### 1-((4-Methoxyphenyl)(3,4,5-Trimethoxyphenyl)methyl)Piperidine (26b)

As per general method E, compound 15c (1 eq, 1.83 mmol, 0.59 g) was treated with thionyl chloride (5 eq) in dry DCM (30 mL) for 12 h, then reacted with piperidine (5 eq, 9.15 mmol, 0.78 g, 0.90 mL) in dry ACN (50 mL) and refluxed for 12 h. The product did not require any further purification, brown oil, 54%, 0.37 g, (HPLC 95%). IR:  $\nu_{\max}$  (ATR)  $\text{cm}^{-1}$ : 2956, 2813, 1598, 1507, 1450, 1419, 1331, 1230, 1174, 1145, 1125, 1031.  $^1\text{H}$  NMR (400 MHz,

CDCl<sub>3</sub>) δ 1.42 (d, *J* = 4.98 Hz, 2 H, CH<sub>2</sub>), 1.52–1.57 (m, 4 H, CH<sub>2</sub>), 2.28 (d, *J* = 4.15 Hz, 4 H, CH<sub>2</sub>), 3.76 (s, 3 H, OCH<sub>3</sub>), 3.78 (s, 3 H, OCH<sub>3</sub>), 3.82 (s, 6 H, OCH<sub>3</sub>), 4.06 (s, 1 H, CH-N-R), 6.63 (s, 2 H, Ar-H), 6.80 (d, *J* = 8.71 Hz, 2 H, Ar-H), 7.27 (d, *J* = 8.71 Hz, 2 H, Ar-H). <sup>13</sup>C NMR (101 MHz, CDCl<sub>3</sub>) δ 158.38 (C-O), 153.00 (2 × C-O), 139.44 (C), 136.40 (C-O), 134.97 (C), 128.97 (2 × CH), 113.60 (2 × CH), 104.46 (2 × CH), 76.03 (CH-N-R), 60.74 (OCH<sub>3</sub>), 56.03 (2 × OCH<sub>3</sub>), 55.14 (OCH<sub>3</sub>), 53.04 (2 × CH<sub>2</sub>), 26.23 (2 × CH<sub>2</sub>), 24.68 (2 × CH<sub>2</sub>). LRMS (EI): found 372.17 (M+H)<sup>+</sup>; C<sub>22</sub>H<sub>30</sub>NO<sub>4</sub> requires 372.21.

#### 1-((4-Methoxyphenyl)(3,4,5-Trimethoxyphenyl)Methyl)-4-Phenylpiperazine (27c)

As per general method E, compound **15c** (1 eq, 0.805 mmol, 0.26 g) was reacted with 1-phenyl-piperazine (5 eq, 4.02 mmol, 0.81 g, 0.79 mL) in dry ACN (40 mL) and refluxed for 12 h under nitrogen atmosphere. The crude product was purified via flash chromatography (eluent: *n*-hexane/ethyl acetate 1:1) to afford a white solid, 74%, 0.26 g, Mp. 125 °C, (HPLC 98%). IR: ν<sub>max</sub> (ATR) cm<sup>-1</sup>: 2950, 2823, 1590, 1501, 1451, 1418, 1386, 1301, 1227, 1122, 1176, 1032, 1004. <sup>1</sup>H NMR (400 MHz, CDCl<sub>3</sub>) δ 2.53 (dt, *J* = 10.47, 4.92 Hz, 4 H, CH<sub>2</sub>), 3.18 (t, *J* = 4.77 Hz, 4 H, CH<sub>2</sub>), 3.77 (s, 3 H, OCH<sub>3</sub>), 3.78 (s, 3 H, OCH<sub>3</sub>), 3.83 (s, 6 H, OCH<sub>3</sub>), 4.11 (s, 1 H, CH-N-R), 6.67 (s, 2 H, Ar-H), 6.83 (d, *J* = 8.71 Hz, 2 H, Ar-H), 6.89 (d, *J* = 8.29 Hz, 2 H, Ar-H), 7.21–7.26 (m, 3 H, Ar-H), 7.33 (d, *J* = 8.71 Hz, 2 H, Ar-H). <sup>13</sup>C NMR (101 MHz, CDCl<sub>3</sub>) δ 158.65 (C-O), 153.20 (2 × C-O), 151.26 (C), 138.76 (C), 136.65 (C-O), 134.42 (C), 129.04 (2 × CH), 128.88 (2 × CH), 119.48 (CH), 115.74 (2 × CH), 113.87 (2 × CH), 104.37 (2 × CH), 75.56 (CH-N-R), 60.76 (OCH<sub>3</sub>), 56.07 (2 × OCH<sub>3</sub>), 55.18 (OCH<sub>3</sub>), 51.86 (CH<sub>2</sub>), 49.18 (CH<sub>2</sub>). LRMS (EI): found 449.19 (M+H)<sup>+</sup>; C<sub>27</sub>H<sub>33</sub>N<sub>2</sub>O<sub>4</sub> requires 449.24.

#### Tert-Butyl 4-((4-Methoxyphenyl)(3,4,5-Trimethoxyphenyl)Methyl)Piperazine-1-Carboxylate (27e)

As per general method E, compound **15c** (1 eq, 0.86 mmol, 0.28 g) was treated with excess thionyl chloride and then reacted with BOC-piperazine (5 eq, 4.3 mmol, 0.8 g) in dry ACN (40 mL) and refluxed for 12 h under nitrogen atmosphere. The product was obtained as a yellow oil, 80%, 0.32 g. IR: ν<sub>max</sub> (ATR) cm<sup>-1</sup>: 3475, 2938, 2835, 1682, 1591, 1503, 1451, 1418, 1240, 1120, 1175, 1120, 1002, 1078. <sup>1</sup>H NMR (400 MHz, CDCl<sub>3</sub>) δ 2.07 (s, 9 H, CH<sub>3</sub>), 2.78 (s, 4 H, CH<sub>2</sub>), 3.37 (s, 4 H, CH<sub>2</sub>), 3.74 (s, 3 H, OCH<sub>3</sub>), 3.75 (s, 3 H, OCH<sub>3</sub>), 3.80 (s, 6 H, OCH<sub>3</sub>), 4.04 (s, 1 H, CH-N-R), 6.61 (s, 2 H, Ar-H), 6.80 (d, *J* = 8.8 Hz, 2 H, Ar-H), 7.27 (d, *J* = 8.7 Hz, 2 H, Ar-H). <sup>13</sup>C NMR (101 MHz, CDCl<sub>3</sub>) δ 158.64 (C-O), 154.77 (C=O), 153.17 (2 × C-O), 138.50 (C), 136.67 (C-O), 134.12 (C), 128.85 (2 × CH), 113.85 (2 × CH), 104.37 (2 × CH), 79.60 (CH-N-R), 75.42 (C-(CH<sub>3</sub>)<sub>3</sub>), 60.73 (OCH<sub>3</sub>), 56.04 (2 × OCH<sub>3</sub>), 55.15 (OCH<sub>3</sub>), 51.62 (2 × CH<sub>2</sub>), 45.73 (2 × CH<sub>2</sub>), 28.38 (3 × CH<sub>3</sub>). LRMS (EI): found 473.26 (M+H)<sup>+</sup>; C<sub>26</sub>H<sub>37</sub>N<sub>2</sub>O<sub>6</sub> requires 473.26.

#### 1-((3-(Benzyloxy)-4-Methoxyphenyl)(3,4,5-Trimethoxyphenyl)Methyl)-4-Phenylpiperazine (27g)

As per general method E, compound **18a** (1 eq, 0.58 mmol, 0.25 g) was first reacted with thionyl chloride; then, it was treated with phenylpiperazine (5 eq, 2.91 mmol, 0.47 g, 0.44 mL) in dry ACN (50 mL) at reflux for 12 h. The crude product was purified via flash column chromatography (eluent: *n*-hexane/ethyl acetate 1:1) to afford the product as off-white powder, 67%, 0.21 g, Mp. 124–126 °C, (HPLC 99%). IR: ν<sub>max</sub> (ATR) cm<sup>-1</sup>: 2957, 2831, 1599, 1507, 1450, 1419, 1232, 1174, 1119, 1031, 925, 823, 726, 698. <sup>1</sup>H NMR (400 MHz, CDCl<sub>3</sub>) δ 2.41–2.54 (m, 4 H, CH<sub>2</sub>), 3.11–3.13 (m, 4 H, CH<sub>2</sub>), 3.80 (s, 9 H, OCH<sub>3</sub>), 3.86 (s, 3 H, OCH<sub>3</sub>), 4.05 (s, 1 H, CH-N-R), 5.16 (s, 2 H, CH<sub>2</sub>), 6.60 (s, 2 H, Ar-H), 6.81–6.85 (m, 1 H, Ar-H), 6.90 (d, *J* = 8.29 Hz, 2 H, Ar-H), 6.92–6.95 (m, 1 H, Ar-H), 6.99–7.01 (s, 1 H, Ar-H), 7.23–7.29 (m, 4 H, Ar-H), 7.32–7.34 (m, 2 H, Ar-H), 7.38–7.43 (m, 2 H, Ar-H). <sup>13</sup>C NMR (101 MHz, CDCl<sub>3</sub>) δ 49.15 (2 × CH<sub>2</sub>), 51.73 (2 × CH<sub>2</sub>), 55.95 (2 × OCH<sub>3</sub>), 56.08 (OCH<sub>3</sub>), 60.79 (OCH<sub>3</sub>), 71.06 (CH<sub>2</sub>), 75.51 (CH-N-R), 104.37 (2 × CH), 111.56 (C), 113.85 (CH), 115.72 (2 × CH), 119.48 (CH), 120.84 (CH), 127.25 (CH), 127.79 (2 × CH), 128.48 (2 × CH), 129.07

(2 × CH), 134.78 (C-O), 137.16 (2 × C), 138.48 (C), 147.93 (C-O), 148.84 (C), 151.26 (C-OBn), 153.17 (2 × C-O). LRMS (EI): found 555.16 (M+H)<sup>+</sup>; C<sub>34</sub>H<sub>39</sub>N<sub>2</sub>O<sub>5</sub> requires 555.29.

#### 1,4-bis((4-Methoxyphenyl)(3,4,5-Trimethoxyphenyl)Methyl)Piperazine (28)

As per general method E, compound **15c** (1 eq, 0.99 mmol, 0.32 g) was treated with excess thionyl chloride, followed by a reaction with piperazine (5 eq, 4.95 mmol, 0.42 g) in dry ACN (40 mL), and the reaction mixture was refluxed for 12 h under nitrogen atmosphere. The crude product was purified via flash chromatography (eluent: *n*-hexane/ethyl acetate 1:1). The product was obtained as a brown solid, 12%, 0.08 g, Mp. 220 °C. IR:  $\nu_{\max}$  (ATR) cm<sup>-1</sup>: 3059, 3025, 2957, 2819, 1599, 1450, 1419, 1331, 1300, 1287, 1232, 1174, 1108, 1031. <sup>1</sup>H NMR (400 MHz, CDCl<sub>3</sub>)  $\delta$  2.40 (br. s, 8 H, CH<sub>2</sub>), 3.73 (s, 6 H, OCH<sub>3</sub>), 3.75 (s, 6 H, OCH<sub>3</sub>), 3.80 (s, 12 H, OCH<sub>3</sub>), 4.08 (s, 2 H, CH-N-R), 6.62 (s, 4 H, Ar-H), 6.78 (d, *J* = 7.88 Hz, 4 H, Ar-H), 7.28 (d, *J* = 7.46 Hz, 4 H, Ar-H). <sup>13</sup>C NMR (101 MHz, CDCl<sub>3</sub>)  $\delta$  158.57 (2 × C-O), 153.10 (4x C-O), 138.59 (2 × C), 136.62 (2 × C-O), 134.27 (2 × C), 128.91 (4x CH), 113.74 (4x CH), 104.49 (4x CH), 75.70 (2 × CH), 60.73 (2 × OCH<sub>3</sub>), 56.06 (4x OCH<sub>3</sub>), 55.16 (2 × OCH<sub>3</sub>), 52.00 (4x CH<sub>2</sub>). LRMS (EI): found 658.77 (M)<sup>+</sup>; C<sub>38</sub>H<sub>46</sub>N<sub>2</sub>O<sub>8</sub> requires 658.33.

#### 4.1.17. 1-((4-Methoxyphenyl)(3,4,5-Trimethoxyphenyl)Methyl)Piperazine (27h)

A solution of **27e** (0.21 mmol, 0.1 g) in DCM (15 mL) was treated with trifluoroacetic acid (TFA) (1 mL) for 30 min at 20 °C. The reaction mixture was quenched with NaHCO<sub>3</sub>, washed with water and brine, dried over sodium sulphate, filtered, and concentrated to afford the product as a yellow oil, 42%, 0.03 g. IR:  $\nu_{\max}$  (ATR) cm<sup>-1</sup>: 3477, 2937, 2835, 1689, 1591, 1504, 1451, 1418, 1326, 1234, 1119, 1078, 1034. <sup>1</sup>H NMR (400 MHz, CDCl<sub>3</sub>)  $\delta$  3.41 (br. s., 4 H, CH<sub>2</sub>), 3.46 (br. s., 4 H, CH<sub>2</sub>), 3.77 (s, 3 H, OCH<sub>3</sub>), 3.79 (s, 3 H, OCH<sub>3</sub>), 3.83 (s, 6 H, OCH<sub>3</sub>), 4.07 (s, 1 H, CH-N-R), 6.64 (s, 2 H, Ar-H), 6.83 (d, *J* = 8.71 Hz, 2 H, Ar-H), 7.30 (d, *J* = 8.29 Hz, 2 H, Ar-H). <sup>13</sup>C NMR (101 MHz, CDCl<sub>3</sub>)  $\delta$  45.22 (2 × CH<sub>2</sub>), 51.65 (2 × CH<sub>2</sub>), 55.19 (OCH<sub>3</sub>), 56.07 (2 × OCH<sub>3</sub>), 60.76 (OCH<sub>3</sub>), 75.44 (CH-N-R), 103.71 (2 × CH), 104.40 (2 × CH), 113.82 (2 × CH), 128.89 (C), 129.25 (C), 134.16 (C-O), 138.53 (C), 153.20 (2 × C-O), 158.68 (C-O). LRMS (EI): found 372.09 (M)<sup>+</sup> C<sub>21</sub>H<sub>28</sub>N<sub>2</sub>O<sub>4</sub> requires 372.20.

#### 4.1.18. 2-Methoxy-5-((4-Phenylpiperazin-1-yl)(3,4,5-Trimethoxyphenyl)Methyl)Phenol (27i)

Compound **(27g)** (1 eq, 0.21 mmol, 0.1 g) was stirred in ethyl acetate (25 mL) and palladium hydroxide (0.05 g) under a hydrogen atmosphere. The reaction mixture was filtered through Celite and the solvent evaporated to afford the product as a light brown oil, 45%, 0.04 g, (HPLC 97%). IR:  $\nu_{\max}$  (ATR) cm<sup>-1</sup>: 3475, 2937, 2834, 1591, 1503, 1451, 1418, 1327, 1231, 1119, 1077. <sup>1</sup>H NMR (400 MHz, CDCl<sub>3</sub>)  $\delta$  2.47–2.62 (m, 4 H, CH<sub>2</sub>), 3.18–3.20 (m, 4 H, CH<sub>2</sub>), 3.80 (s, 3 H, OCH<sub>3</sub>), 3.83–3.88 (d, 9H, OCH<sub>3</sub>), 4.06 (s, 1 H, CH-N-R), 5.58 (s, 1 H, OH), 6.69 (s, 2 H, Ar-H), 6.78 (d, *J* = 8.29 Hz, 1 H, Ar-H), 6.84 (t, 1 H, Ar-H), 6.91 (d, *J* = 7.88 Hz, 3 H, Ar-H), 7.05 (s, 1 H, Ar-H), 7.25–7.27 (m, 2 H, Ar-H). <sup>13</sup>C NMR (101 MHz, CDCl<sub>3</sub>)  $\delta$  49.21 (2 × CH<sub>2</sub>), 51.88 (2 × CH<sub>2</sub>), 55.89 (OCH<sub>3</sub>), 56.09 (2 × OCH<sub>3</sub>), 60.77 (OCH<sub>3</sub>), 75.74 (CH), 104.34 (2 × CH), 110.44 (CH), 113.82 (2 × CH), 115.75 (CH), 119.40 (2 × CH), 128.20 (2 × CH), 135.78 (C-O), 138.70 (C), 145.63 (C), 151.30 (2 × C-O), 153.22 (C), 156.37 (2 × C-O). LRMS (EI): found 464.95 (M+H)<sup>+</sup> C<sub>27</sub>H<sub>33</sub>N<sub>2</sub>O<sub>5</sub> requires 464.23.

## 4.2. Stability Study of Compounds 211 and 24

Stability studies for compounds **211** and **24** were performed by analytical HPLC using a Symmetry<sup>®</sup> column (C18, 5 mm, 4.6 × 150 mm), a Waters 2487 Dual Wavelength Absorbance detector, a Waters 1525 binary HPLC pump, and a Waters 717 plus Autosampler (Waters Corporation, Milford, MA, USA). Samples were detected at  $\lambda$  254 nm using acetonitrile (70%)/water (30%) as the mobile phase over 15 min and a flow rate of 1 mL/min. Stock solutions of the compounds are prepared using 10 mg of compounds **211** and **24** in 10 mL of mobile phase (1 mg/mL). Phosphate buffers at the desired pH values (4, 7.4, and 9) were prepared following the British Pharmacopoeia monograph 2020. Then, 30  $\mu$ L of stock solution was diluted with 1 mL of appropriate buffer, shaken, and injected immediately.

Samples were withdrawn and analysed at time intervals of  $t = 0$  min, 5 min, 30 min, 60 min, and hourly for 24 h.

#### 4.3. X-ray Crystallography

Data for samples **16e**, **16f**, **19c**, **21e**, and **26a** were collected on a Bruker APEX DUO using Mo  $K\alpha$  and Cu  $K\alpha$  radiation ( $\lambda = 0.71073$  and  $1.54178$  Å). Each sample was mounted on a MiTeGen cryoloop and data were collected at 100(2) K using an Oxford Cobra cryosystem. Bruker APEX [123] software was used to collect and reduce data, determine the space group, solve, and refine the structures. Absorption corrections were applied using SADABS 2014 [124]. Structures were solved with the XT structure solution program [125] using Intrinsic Phasing and refined with the XL refinement package [126] using Least Squares minimisation. All non-hydrogen atoms were refined anisotropically. Hydrogen atoms were assigned to calculated positions using a riding model with appropriately fixed isotropic thermal parameters. Molecular graphics were generated using OLEX2 [127]. All structures are racemates. In **26a**, the disordered fluorine was modelled in two positions with occupancies of 84% and 16%. Geometric restraints (SADI) were used to model the C-F bond lengths. Crystallographic data for the structures in this paper have been deposited with the Cambridge Crystallographic Data Centre as supplementary publication nos. 201543, 2015432, 2015433, 2015434, and 2015435. Copies of the data can be obtained, free of charge, on application to CCDC, 12 Union Road, Cambridge CB2 1EZ, UK, (fax: +44-(0)1223-336033 or e-mail:deposit@ccdc.cam.ac.uk).

#### 4.4. Biochemical Evaluation of Activity

All biochemical assays were performed in triplicate and on at least three independent occasions for the determination of mean values reported.

##### 4.4.1. Cell Culture

The human breast carcinoma cell line MCF-7 was purchased from the European Collection of Animal Cell Cultures (ECACC) and cultured in Eagles minimum essential medium with 10% foetal bovine serum, 2 mM L-glutamine, and 100  $\mu\text{g}/\text{mL}$  penicillin/streptomycin. The medium was supplemented with 1% non-essential amino acids. The human breast carcinoma cell line MDA-MB-231 was purchased from the ECACC. MDA-MB-231 cells were maintained in Dulbecco's modified Eagle's medium (DMEM) supplemented with 10% (*v/v*) foetal bovine serum, 2 mM L-glutamine, and 100  $\mu\text{g}/\text{mL}$  penicillin/streptomycin (complete medium). HL-60 cells were derived from a patient with acute myeloid leukaemia and were obtained from the ECACC (Salisbury, UK). Cells were cultured in RPMI-1640 Glutamax medium supplemented with 10% FCS media and 100  $\mu\text{g}/\text{mL}$  penicillin/streptomycin. MCF-10A cells were obtained as a kind gift from Dr Susan McDonnell, School of Chemical and Bioprocess Engineering, University College Dublin and were cultured in Dulbecco's Modified Eagle Medium: Nutrient Mixture F-12 (DMEM/F12; Gibco) supplemented with 5% horse serum (Invitrogen), 20  $\text{ng mL}^{-1}$  epidermal growth factor (Merck Millipore), 0.5  $\mu\text{g mL}^{-1}$  hydrocortisone (Sigma, Aldrich, Arklow, Co. Wicklow, Ireland), 100  $\text{ng mL}^{-1}$  cholera toxin (Sigma, Aldrich, Arklow, Co. Wicklow, Ireland), 10  $\mu\text{g mL}^{-1}$  insulin (Sigma, Aldrich, Arklow, Co. Wicklow, Ireland), and penicillin/streptomycin 5000  $\text{U mL}^{-1}$  (1%)(Gibco, Biosciences, 3 Charlemont Terrace, Crofton Road, Dun Laoghaire, Co Dublin, A96 K7H7, Ireland). Cells were maintained at 37 °C in 5%  $\text{CO}_2$  in a humidified incubator. All cells were sub-cultured 3 times/week by trypsinisation using TrypLE Express (1 $\times$ ).

##### 4.4.2. Cell Viability Assay

Cells were seeded at a density of  $2.5 \times 10^4$  cells/well (MCF-7, MDA-MB-231, MCF-10A cells) and  $1 \times 10^4$  cells/well (HL-60) in 96-well plates (200  $\mu\text{L}$  per well). After 24 h, cells were then treated with either medium alone, vehicle control (1% ethanol (*v/v*)) or with serial dilutions of CA-4 (**4a**), phenstatin (**7a**) or selected compounds (0.001–100  $\mu\text{M}$ ) in triplicate. Cell proliferation for MCF-7, MDA-MB-231, and MCF-10A cells was analysed

using the alamarBlue assay (Invitrogen Corp.) according to the manufacturer's instructions. After 67–69 h, alamarBlue (10% (*v/v*)) was added to each well, and plates were incubated for 3–5 h at 37 °C in the dark. Fluorescence was read using a 96-well fluorimeter with excitation at 530 nm and emission at 590 nm. Results were expressed as percentage viability relative to vehicle control (100%). Dose–response curves were plotted, and IC<sub>50</sub> values (concentration of drug resulting in 50% reduction in cell survival) were obtained using the commercial software package Prism (GraphPad Software, Inc., La Jolla, CA, USA).

#### 4.4.3. Cell Cycle Analysis

Cells were seeded at a density of  $1 \times 10^5$  cells/well in 6-well plates (3 mL) and treated with indicated compound **19e**, **24**, and phenstatin (**7a**), (1 μM) for 24, 48, or 72 h. The cells were collected by trypsinisation and centrifuged at  $800 \times g$  for 15 min. Cells were washed twice with ice-cold phosphate-buffered saline (PBS) and fixed in ice-cold 70% ethanol overnight at –20 °C. Fixed cells were centrifuged at  $800 \times g$  for 15 min and stained with 50 μg/mL of PI, containing 50 μg/mL of DNase-free RNase A, at 37 °C for 30 min. The DNA content of cells (10,000 cells/experimental group) was analysed by flow cytometer at 488 nm using a FACSCalibur flow cytometer (BD Biosciences, San Jose, CA, USA), and all data were recorded and analysed using the CellQuest Software (Becton-Dickinson)

#### 4.4.4. Annexin V/PI Apoptotic Assay

Apoptotic cell death was detected by flow cytometry using Annexin V and propidium iodide (PI). MCF-7 and MDA-MB-231 cells were seeded in 6-well plates at a density of  $1 \times 10^5$  cells/mL (3 mL) and treated with either vehicle (0.1% (*v/v*) EtOH), Phenstatin (**7a**), or **211** at different concentrations for the selected time. Then, cells were harvested and prepared for flow cytometric analysis. Cells were washed in 1X binding buffer (20× binding buffer: 0.1M 4-(2-hydroxyethyl)-1-piperazineethanesulfonic acid (HEPES), pH 7.4; 1.4 M NaCl; 25 mM CaCl<sub>2</sub> diluted in dH<sub>2</sub>O) and incubated in the dark for 30 min on ice in Annexin V-containing binding buffer (1:100). Then, cells were washed once in binding buffer and then re-suspended in PI-containing binding buffer (1:1000). Samples were analysed immediately using the BD Accuri flow cytometer (BD Biosciences, 2350 Qume Dr, San Jose, CA, USA) and prism software for analysis of the data (GraphPad Software, Inc., 2365 Northside Dr., Suite 560, San Diego, CA, USA). Four populations are produced during the assay: Annexin V and PI negative (Q4, healthy cells), Annexin V positive and PI negative (Q3, early apoptosis), Annexin V and PI positive (Q2, late apoptosis), and Annexin V negative and PI positive (Q1, necrosis).

#### 4.4.5. Immunofluorescence Microscopy

Confocal microscopy was used to study the effects of drug treatment on MCF-7 cytoskeleton. For immunofluorescence, MCF-7 cells were seeded at  $1 \times 10^5$  cells/mL on eight chamber glass slides (BD Biosciences). Cells were treated with vehicle (1% ethanol (*v/v*)), CA-4 (0.01 μM), paclitaxel (1 μM), phenstatin (1 μM), compound **19e** (10 μM), or compound **211** (10 μM) for 16 h. Following treatment, cells were gently washed in PBS, fixed for 20 min with 4% paraformaldehyde in PBS, and permeabilised in 0.5% Triton X-100. Following washes in PBS containing 0.1% Tween (PBST), cells were blocked in 5% bovine serum albumin diluted in PBST. Then, cells were incubated with mouse monoclonal anti-α-tubulin–FITC antibody (clone DM1A) (Sigma) (1:100) for 2 h at room temperature (rt). Following washes in Phosphate Buffered Saline with Tween®20 (PBST), cells were incubated with Alexa Fluor 488 dye (1:500) for 1 h at rt. Following washes in PBST, the cells were mounted in Ultra Cruz Mounting Media (Santa Cruz Biotechnology, Santa Cruz, CA) containing 4,6-diamino-2-phenolindol dihydrochloride (DAPI). Images were captured by Leica SP8 confocal microscopy with Leica application suite X software. All images in each experiment were collected on the same day using identical parameters. Experiments were performed on three independent occasions.

#### 4.4.6. Evaluation of Expression Levels of Anti-Apoptotic Proteins Mcl-1, Bcl-2 and PARP Cleavage

MCF-7 cells were seeded at a density of  $1 \times 10^5$  cells/flask (10 mL) in T25 flasks. After 48 h, whole cell lysates were prepared from untreated cells or cells treated with vehicle control (EtOH, 0.1% *v/v*) or selected compound **211** or **24** (1  $\mu$ M). MCF-7 cells were harvested in Radioimmunoprecipitation assay buffer (RIPA) buffer supplemented with protease inhibitors (Roche Diagnostics), phosphatase inhibitor cocktail 2 (Sigma-Aldrich), and phosphatase inhibitor cocktail 3 (Sigma-Aldrich). Equal quantities of protein (as determined by a bicinchoninic acid assay (BCA assay)) were resolved by SDS-PAGE (12%) followed by transfer to polyvinylidene fluoride PVDF membranes. Membranes were blocked in 5% bovine serum albumin/Tris-buffered saline with 0.1% Tween®20 Detergent (TBST) for 1 h. Membranes were incubated in the relevant primary antibodies at 4 °C overnight, washed with TBST, and incubated in horseradish peroxidase-conjugated secondary antibody for 1 h at rt and washed again. Western blot analysis was performed as described above using antibodies directed against Mcl-1 (1:1000) (Millipore), Bcl-2 [1:500] (Millipore), and PARP followed by incubation with a horseradish peroxidase-conjugated anti-mouse antibody (1:2000) (Promega, Madison, WI, USA). All blots were probed with anti-glyceraldehyde 3-phosphate dehydrogenase (GAPDH) antibody (1:5000) (Millipore) to confirm equal loading. Proteins were detected using enhanced chemiluminescent Western blot detection (Clarity Western ECL substrate) (Bio Rad) on the ChemiDoc MP System (Bio Rad). Experiments were performed on three independent occasions.

#### 4.4.7. Tubulin Polymerisation Assay

The assembly of purified bovine tubulin was monitored using a kit, BK006, purchased from Cytoskeleton Inc. (Denver, CO, USA). The assay was carried out in accordance with the manufacturer's instructions using the standard assay conditions [128]. Briefly, purified (>99%) bovine brain tubulin (3 mg/mL) in a buffer consisting of 80 mM piperazine-N,N'-bis(2-ethanesulfonic acid) (PIPES) (pH 6.9), 0.5 mM ethylene glycol tetraacetic acid (EGTA), 2 mM MgCl<sub>2</sub>, 1 mM guanosine-5'-triphosphate (GTP) and 10% glycerol was incubated at 37 °C in the presence of either vehicle (2% (*v/v*) ddH<sub>2</sub>O) paclitaxel, phenstatin (**7a**), or **211** (all at 10  $\mu$ M). Light is scattered proportionally to the concentration of polymerised microtubules in the assay. Therefore, tubulin assembly was monitored turbidimetrically at 340 nm in a Spectramax 340 PC spectrophotometer (Molecular Devices, Sunnyvale, CA, USA). The absorbance was measured at 30 s intervals for 60 min.

#### 4.4.8. Cytochrome P450 Assays (CYP19 (Aromatase) and CYP1A1)

The substrate DBF (dibenzylfluorescein) was obtained from Gentest Corporation (Woburn, MA). All human recombinant cytochrome P450 enzymes were purchased from BD Biosciences, San Jose, CA. Aromatase and CYP1A1 inhibition were quantified by measuring the fluorescent intensity of fluorescein, the hydrolysis product of dibenzylfluorescein (DBF), by aromatase, as previously described [118,119]. In brief, the test substance (10  $\mu$ L) was pre-incubated with a NADPH regenerating system (90  $\mu$ L of 2.6 mM NADP<sup>+</sup>, 7.6 mM glucose 6-phosphate, 0.8 U/mL glucose 6-phosphate dehydrogenase, 13.9 mM MgCl<sub>2</sub>, and 1 mg/mL albumin in 50 mM potassium phosphate, pH 7.4), for 10 min, at 37 °C, before 100  $\mu$ L of the enzyme and substrate (E/S) mixture were added (4.0 pmol/well of CYP19/0.4  $\mu$ M DBF; 5.0 pmol/well of CYP2C8/2.0  $\mu$ M DBF; 5.0 pmol/well of CYP3A4/2.0  $\mu$ M DBF and 0.5 pmol/well of CYP1A1/2.0  $\mu$ M DBF). The reaction mixtures were incubated for 30 min (excepting CYP1A1, 25 min) at 37 °C to allow the generation of product, quenched with 75  $\mu$ L of 2 N NaOH, shaken for 5 min, and incubated for 2 h at 37 °C to enhance the noise/background ratio. Finally, fluorescence was measured at 485 nm (excitation) and 530 nm (emission). Three independent experiments were performed, each one in triplicate, and the average values were used to construct dose-response curves. At least four concentrations of the test substance were used, and the IC<sub>50</sub> value was calculated (*Tablecurve*<sup>TM</sup>2D, AISN Software, EUA, 1996). Naringenin was used as positive

controls, yielding an  $IC_{50}$  value of 4.9  $\mu M$ . Compounds **19e**, **211**, and **24** were dissolved in dimethyl sulfoxide (DMSO) and diluted to final concentrations. An equivalent volume of DMSO was added to control wells, and this had no measurable effect on cultured cells or enzymes. Compounds are considered for further experiments when showing inhibition great than 90%.

#### 4.5. Molecular Modelling and Docking Study

The X-ray structure of bovine tubulin co-crystallised with N-deacetyl-N-(2-mercaptoacetyl)-colchicine (DAMA-colchicine) 1SA0 [121] was downloaded from the PDB website. A UniProt Align analysis confirmed a 100% sequence identity between human and bovine  $\beta$  tubulin. The crystal structure was prepared using QuickPrep (minimised to a gradient of 0.001 kcal/mol/Å), Protonate 3D, Residue pKa and Partial Charges protocols in MOE 2015 with the MMFF94x force field [129]. Both enantiomers of selected compounds **19e**, **24**, and **211** were drawn in ChemBioDraw 13.0, saved as mol files, and opened in MOE. For both enantiomers of each compound, MMFF94x partial charges were calculated, and each was minimised to a gradient of 0.001 kcal/mol/Å. Default parameters were used for docking, except that 300 poses were sampled for each enantiomer, and the top 50 docked poses were retained for subsequent analysis.

## 5. Conclusions

In this work, a novel series of heterocyclic phenstatin-based compounds have been designed and synthesised as tubulin-targeting agents. The structural modifications introduced on the phenstatin moiety included the nitrogen heterocycles 1,2,4-triazole, 1,2,3-triazole, and imidazole to afford a hybrid structure of the vascular targeting agent phenstatin and the aromatase inhibitor letrozole, which contains a 1,2,4-triazole heterocycle. The introduction of aliphatic amines such as pyrrolidine, piperazine, and various piperidine derivatives was also achieved. The resulting compounds were investigated for potential dual activity as tubulin and aromatase inhibitors. All novel compounds were initially evaluated in the MCF-7 breast cancer cell line and of particular interest were compounds **19e**, **211**, and **24**, which displayed antiproliferative activity in the nanomolar range e.g., **19e** ( $IC_{50}$  = 424 nM, **211** ( $IC_{50}$  = 132 nM), and **24** ( $IC_{50}$  = 52 nM). They were selected for further studies to provide a better understanding of their mechanism of action in breast cancer cells.

The most potent compounds **211** and **24** were evaluated in MCF-10A cells (normal breast epithelial cells) for cytotoxicity. Minimal cell death was observed when treated at a concentration similar to the  $IC_{50}$  value of the compounds in MCF-7 cells, indicating that the compounds were selective towards cancer cells. Compounds showed impressive antiproliferative activity at nanomolar levels against a range of susceptible human cancer cell lines when tested in the 60 cancer cell line panel of the NCI. Cell cycle analysis of compounds **211** and **24** resulted in an increase in  $G_2/M$  arrest and apoptotic cell death in MCF-7 cells. Flow cytometric analysis of Annexin V/PI-stained cells indicated that compound **211** induces the apoptosis of MCF-7 cells in a dose-dependent manner. Compounds **211** and **24** were also shown to promote PARP cleavage and an inhibition of tubulin polymerisation. The tubulin effects were confirmed when MCF-7 cells treated with the azoles **19e** and **211** displayed disorganised microtubule networks with similar effects to phenstatin, together with multinucleation.

The molecular docking of selected compounds indicated possible binding to the colchicine-binding site of tubulin and a preference for the *S* enantiomer. The results showed an efficient introduction of the azoles 1,2,4-triazole, 1,2,3-triazole, and imidazole on the phenstatin scaffold structure to retain antiproliferative effects. The selective inhibition of aromatase is an important tool to select compounds that act as chemopreventative agents for hormone-dependent cancer [130]. The aromatase inhibition of the most potent antiproliferative compounds **19e**, **211**, and **24** was evaluated, and compound **19e** was identified as the most potent with over 85% inhibition of CYP19 at 20  $\mu M$  and an  $IC_{50}$  of 29  $\mu M$ . We can



conclude that the 1,2,4-triazole heterocycle is essential for aromatase inhibition in these compounds, and its activity was optimised when included in a phenstatin-related scaffold such as **19e**. On the basis of the structural modifications of phenstatin described in this work, e.g., introduction of the azoles 1,2,4-triazole, 1,2,3-triazole, and imidazole on the phenstatin scaffold, we have developed lead compounds that exhibit promising anti-cancer properties with potential for further development. The investigation of the stereoselective effects of the compounds together with the optimisation of the dual aromatase–antiproliferative action of compound **19e** is in progress.

**Supplementary Materials:** The following are available online at <https://www.mdpi.com/1424-8247/14/2/169/s1>. Tier-1 profiling and Lipinski properties of selected compounds; details of experimental procedures and spectroscopic data; full NCI60 cell line data for compounds **19e**, **21l**, **25g**, **26b** and **27d**.

**Author Contributions:** Conceptualisation, G.A., M.J.M.; Formal analysis, G.A., P.M.K., A.M.M., B.T., S.N., S.M.N., D.F., D.C.E., N.M.O. and M.J.M.; Funding acquisition, A.M.M. and M.J.M.; Investigation, G.A., P.M.K., A.M.M., S.N., S.M.N., E.F.P.; Methodology, G.A., D.F., B.T., P.M.K.; Supervision, M.J.M. and D.M.Z.; Writing—original draft, M.J.M., G.A. and D.C.E.; Writing—review and editing, M.J.M., G.A., D.M.Z., D.F., N.M.O. and D.C.E. All authors have read and agreed to the published version of the manuscript.

**Funding:** A Trinity College Dublin postgraduate research award (G.A. and P.M.K.), and Agenzia Regionale per il Lavoro, Sardinia, Programme Master and Back (G.A.) are gratefully acknowledged. A postgraduate research scholarship from King Abdulaziz University (KAU) is gratefully acknowledged (AMM). This work was also supported by the Irish Research Council Postdoctoral Fellowship (GOIPD/2013/188; NMO'B).

**Institutional Review Board Statement:** Not applicable.

**Informed Consent Statement:** Not applicable.

**Data Availability Statement:** Data sharing not applicable.

**Acknowledgments:** The Trinity Biomedical Sciences Institute (TBSI) is supported by a capital infrastructure investment from Cycle 5 of the Irish Higher Education Authority's Programme for Research in Third Level Institutions (PRTL). This study was also co-funded under the European Regional Development. We thank Susan McDonnell, School of Chemical and Bioprocess Engineering, University College Dublin for the kind gift of MCF-10A cells, Gavin McManus for assistance with confocal microscopy, and Barry Moran for flow cytometry. Synthetic contributions from Rebecca Hirschberger and Ayat Sherif are also appreciated. We thank John O'Brien and Manuel Ruether for NMR spectra. DF thanks the software vendors for their continuing support of academic research efforts, in particular the contributions of the Chemical Computing Group, Biovia, and OpenEye Scientific. The support and provisions of Dell Ireland, the Trinity Centre for High Performance Computing (TCHPC), and the Irish Centre for High-End Computing (ICHEC) are also gratefully acknowledged.

**Conflicts of Interest:** The authors declare no conflict of interest.

## Abbreviations

The following abbreviations are used in this manuscript:

AI	Aromatase inhibitor
ADC	Antibody–drug conjugate
ATR	Attenuated total reflection
CDI	1,1'-Carbonyldiimidazole
DEPT	Distortionless Enhancement by Polarization Transfer
DMEM	Dulbecco's Modified Eagle Medium
DMSO	Dimethyl sulfoxide
ECACC	European Collection of Animal Cell Cultures
EGFR	Epidermal growth factor receptor
ER	Estrogen receptor

FACS	Fluorescence activated cell sorting
FBS	Foetal bovine serum
GI50	50% Growth inhibitory concentration
HER2	Human epidermal growth factor receptor 2
HER/neu	Receptor tyrosine-protein kinase erbB-2, CD340
HDBC	Hormone-dependent breast cancer
HR	Hormone receptor
LC50	Median lethal concentration
MBC	Metastatic breast cancer
MDR	Multidrug resistance
MEM	Minimum essential media
NCI	National Cancer Institute
NMR	Nuclear magnetic resonance
PARP	Poly (ADP-ribose) polymerase
PBS	Phosphate buffered saline
PI	Propidium iodide
PIK3CA	Phosphatidylinositol-4,5-Bisphosphate 3-Kinase Catalytic Subunit Alpha
PR	Progesterone receptor
RIPA	Radioimmunoprecipitation assay
SERM	Selective estrogen receptor modulator
STS	Steroid sulfatase
TGI	Total growth inhibitory concentration
TLC	Thin layer chromatography
TNBC	Triple negative breast cancer

## References

- O'Boyle, N.M.; Meegan, M.J. Designed multiple ligands for cancer therapy. *Curr. Med. Chem.* **2011**, *18*, 4722–4737. [PubMed]
- Ramsay, R.R.; Popovic-Nikolic, M.R.; Nikolic, K.; Uliassi, E.; Bolognesi, M.L. A perspective on multi-target drug discovery and design for complex diseases. *Clin. Transl. Med.* **2018**, *7*, 3. [CrossRef]
- Gediya, L.K.; Njar, V.C.O. Promise and challenges in drug discovery and development of hybrid anticancer drugs. *Expert Opin. Drug Discov.* **2009**, *4*, 1099–1111. [CrossRef] [PubMed]
- Morphy, R.; Kay, C.; Rankovic, Z. From magic bullets to designed multiple ligands. *Drug Discov. Today* **2004**, *9*, 641–651. [CrossRef]
- Fortin, S.; Berube, G. Advances in the development of hybrid anticancer drugs. *Expert Opin. Drug Discov.* **2013**, *8*, 1029–1047. [CrossRef]
- Ji, X.; Lu, Y.; Tian, H.; Meng, X.; Wei, M.; Cho, W.C. Chemoresistance mechanisms of breast cancer and their countermeasures. *Biomed. Pharm.* **2019**, *114*, 108800. [CrossRef] [PubMed]
- Jelovac, D.; Macedo, L.; Goloubeva, O.G.; Handratta, V.; Brodie, A.M. Additive antitumor effect of aromatase inhibitor letrozole and antiestrogen fulvestrant in a postmenopausal breast cancer model. *Cancer Res.* **2005**, *65*, 5439–5444. [CrossRef]
- Howell, A.; Czuzick, J.; Baum, M.; Buzdar, A.; Dowsett, M.; Forbes, J.F.; Hochtin-Boes, G.; Houghton, J.; Locker, G.Y.; Tobias, J.S.; et al. Results of the ATAC (arimidex, tamoxifen, alone or in combination) trial after completion of 5 years' adjuvant treatment for breast cancer. *Lancet* **2005**, *365*, 60–62.
- American Cancer Society. *Breast Cancer Facts & Figures 2019–2020*; American Cancer Society Inc.: Atlanta, GA, USA, 2019.
- World Cancer Research Fund, Breast Cancer Statistics. Available online: <https://www.Wcrf.Org/dietandcancer/cancer-trends/breast-cancer-statistics> (accessed on 4 November 2020).
- Cancer Trends 37—Breast Cancer, 1994–2016. Available online: <https://www.Ncri.Ie/publications/cancer-trends-and-projections/cancer-trends-37-breast-cancer-1994-2016> (accessed on 4 November 2020).
- Cancer Incidence Projections for Ireland, 2020–2045. Available online: <https://www.Ncri.Ie/publications/cancer-trends-and-projections/cancer-incidence-projections-ireland-2020-2045> (accessed on 4 November 2020).
- Early Breast Cancer Trialists' Collaborative Group. Tamoxifen for early breast cancer: An overview of the randomised trials. *Lancet* **1998**, *351*, 1451–1467. [CrossRef]
- Mohammed, H.; Russell, I.A.; Stark, R.; Rueda, O.M.; Hickey, T.E.; Tarulli, G.A.; Serandour, A.A.; Birrell, S.N.; Bruna, A.; Saadi, A.; et al. Progesterone receptor modulates  $\alpha$  action in breast cancer. *Nature* **2015**, *523*, 313–317. [CrossRef] [PubMed]
- Blakemore, J.; Naftolin, F. Aromatase: Contributions to physiology and disease in women and men. *Physiology* **2016**, *31*, 258–269. [CrossRef]
- Spinello, A.; Ritacco, I.; Magistrato, A. Recent advances in computational design of potent aromatase inhibitors: Open-eye on endocrine-resistant breast cancers. *Expert Opin. Drug Discov.* **2019**, *14*, 1065–1076. [CrossRef]
- Khodarahmi, G.; Asadi, P.; Farrokhpour, H.; Hassanzadeh, F.; Dinari, M. Design of novel potential aromatase inhibitors via hybrid pharmacophore approach: Docking improvement using the qm/mm method. *RSC Adv.* **2015**, *5*, 58055–58064. [CrossRef]

18. Bhatnagar, A.S. The discovery and mechanism of action of letrozole. *Breast Cancer Res. Treat.* **2007**, *105* (Suppl. 1), 7–17. [CrossRef] [PubMed]
19. Fabian, C.J. The what, why and how of aromatase inhibitors: Hormonal agents for treatment and prevention of breast cancer. *Int. J. Clin. Pract.* **2007**, *61*, 2051–2063. [CrossRef]
20. Deeks, E.D.; Scott, L.J. Exemestane: A review of its use in postmenopausal women with breast cancer. *Drugs* **2009**, *69*, 889–918. [CrossRef] [PubMed]
21. Kumler, I.; Knoop, A.S.; Jessing, C.A.; Ejlersten, B.; Nielsen, D.L. Review of hormone-based treatments in postmenopausal patients with advanced breast cancer focusing on aromatase inhibitors and fulvestrant. *ESMO Open* **2016**, *1*, e000062. [CrossRef]
22. Pistelli, M.; Mora, A.D.; Ballatore, Z.; Berardi, R. Aromatase inhibitors in premenopausal women with breast cancer: The state of the art and future prospects. *Curr. Oncol.* **2018**, *25*, e168–e175. [CrossRef]
23. Needleman, S.J.; Tobias, J.S. Review of the ATAC study: Tamoxifen versus anastrozole in early-stage breast cancer. *Expert Rev. Anticancer Ther.* **2008**, *8*, 1871–1881. [CrossRef] [PubMed]
24. Miller, W.R.; Larionov, A.A. Understanding the mechanisms of aromatase inhibitor resistance. *Breast Cancer Res.* **2012**, *14*, 201. [CrossRef] [PubMed]
25. Hanka, A.B.; Sudhan, D.R.; Arteaga, C.L. Overcoming endocrine resistance in breast cancer. *Cancer Cell* **2020**, *37*, 496–513. [CrossRef]
26. Chang, M. Tamoxifen resistance in breast cancer. *Biomol. Ther.* **2012**, *20*, 256–267. [CrossRef] [PubMed]
27. Ali, S.; Coombes, R.C. Endocrine-responsive breast cancer and strategies for combating resistance. *Nat. Rev. Cancer* **2002**, *2*, 101–112. [CrossRef]
28. Fleming, C.A.; Heneghan, H.M.; O'Brien, D.; McCartan, D.P.; McDermott, E.W.; Prichard, R.S. Meta-analysis of the cumulative risk of endometrial malignancy and systematic review of endometrial surveillance in extended tamoxifen therapy. *Br. J. Surg.* **2018**, *105*, 1098–1106. [CrossRef] [PubMed]
29. Goetz, M.P.; Suman, V.J.; Reid, J.M.; Northfelt, D.W.; Mahr, M.A.; Ralya, A.T.; Kuffel, M.; Buhrow, S.A.; Safgren, S.L.; McGovern, R.M.; et al. First-in-human phase I study of the tamoxifen metabolite z-endoxifen in women with endocrine-refractory metastatic breast cancer. *J. Clin. Oncol.* **2017**, *35*, 3391–3400. [CrossRef] [PubMed]
30. Sestak, I. Preventative therapies for healthy women at high risk of breast cancer. *Cancer Manag. Res.* **2014**, *6*, 423–430. [CrossRef]
31. Cuzick, J.; Sestak, I.; Cawthorn, S.; Hamed, H.; Holli, K.; Howell, A.; Forbes, J.F.; Investigators, I.-I. Tamoxifen for prevention of breast cancer: Extended long-term follow-up of the ibis-i breast cancer prevention trial. *Lancet Oncol.* **2015**, *16*, 67–75. [CrossRef]
32. Costa, R.L.B.; Czerniecki, B.J. Clinical development of immunotherapies for her2(+) breast cancer: A review of HER2-directed monoclonal antibodies and beyond. *NPJ Breast Cancer* **2020**, *6*, 10. [CrossRef]
33. Li, B.T.; Shen, R.; Buonocore, D.; Olah, Z.T.; Ni, A.; Ginsberg, M.S.; Ulaner, G.A.; Offin, M.; Feldman, D.; Hembrough, T.; et al. Ado-trastuzumab emtansine for patients with her2-mutant lung cancers: Results from a phase ii basket trial. *J. Clin. Oncol.* **2018**, *36*, 2532–2537. [CrossRef]
34. Tsang, R.Y.; Sadeghi, S.; Finn, R.S. Lapatinib, a dual-targeted small molecule inhibitor of egfr and her2, in her2-amplified breast cancer: From bench to bedside. *Clin. Med. Insights Ther.* **2011**, *3*, 1–13. [CrossRef]
35. Yin, L.; Duan, J.J.; Bian, X.W.; Yu, S.C. Triple-negative breast cancer molecular subtyping and treatment progress. *Breast Cancer Res.* **2020**, *22*, 61. [CrossRef]
36. Jubair, S.A.; Alkhateeb, A.; Tabl, A.A.; Rueda, L.; Ngom, A. A novel approach to identify subtype-specific network biomarkers of breast cancer survivability. *Netw. Modeling Anal. Health Inform. Bioinform.* **2020**, *9*, 43. [CrossRef]
37. Iwata, T.N.; Ishii, C.; Ishida, S.; Ogitani, Y.; Wada, T.; Agatsuma, T. A HER2-targeting antibody-drug conjugate, trastuzumab deruxtecan (ds-8201a), enhances antitumor immunity in a mouse model. *Mol. Cancer* **2018**, *17*, 1494–1503. [CrossRef] [PubMed]
38. Enhertu (Trastuzumab Deruxtecan) Approved in the US for HER2-Positive Unresectable or Metastatic Breast Cancer Following Two or More Prior Anti-HER2 Based Regimens. Available online: <https://www.astrazeneca.com/media-centre/press-releases/2019/enhertu-trastuzumab-deruxtecan-approved-in-the-us-for-her2-positive-unresectable-or-metastatic-breast-cancer-following-2-or-more-prior-anti-her2-based-regimens.html> (accessed on 4 November 2020).
39. FDA Approves Alpelisib for Metastatic Breast Cancer. Available online: <https://www.fda.gov/drugs/resources-information-approved-drugs/fda-approves-alpelisib-metastatic-breast-cancer> (accessed on 4 November 2020).
40. Andre, F.; Ciruelos, E.; Rubovszky, G.; Campone, M.; Loibl, S.; Rugo, H.S.; Iwata, H.; Conte, P.; Mayer, I.A.; Kaufman, B.; et al. Alpelisib for pik3ca-mutated, hormone receptor-positive advanced breast cancer. *N. Engl. J. Med.* **2019**, *380*, 1929–1940. [CrossRef] [PubMed]
41. A Study of Tucatinib, vs. Placebo in Combination with Capecitabine & Trastuzumab in Patients with Advanced her2+ Breast Cancer (her2climb). Available online: <https://www.Clinicaltrials.Gov/ct2/show/nct02614794> (accessed on 4 November 2020).
42. Jordan, M.A.; Wilson, L. Microtubules as a target for anticancer drugs. *Nat. Reviews Cancer* **2004**, *4*, 253–265. [CrossRef]
43. Van Vuuren, R.J.; Visagie, M.H.; Theron, A.E.; Joubert, A.M. Antimitotic drugs in the treatment of cancer. *Cancer Chemother. Pharm.* **2015**, *76*, 1101–1112. [CrossRef]
44. FDA Grants Accelerated Approval to Sacituzumab Govitecan-Hziy for Metastatic Triple Negative Breast Cancer. Available online: <https://www.Fda.Gov/drugs/drug-approvals-and-databases/fda-grants-accelerated-approval-sacituzumab-govitecan-hziy-metastatic-triple-negative-breast-cancer> (accessed on 4 November 2020).

45. Safety and Efficacy of Sgn-Liv1a Plus Pembrolizumab for Patients with Locally-Advanced or Metastatic Triple-Negative Breast Cancer. Available online: <https://www.Clinicaltrials.gov/ct2/show/nct03310957> (accessed on 4 November 2020).
46. Potter, B.V.L. Sulfation pathways: Steroid sulphatase inhibition via aryl sulphamates: Clinical progress, mechanism and future prospects. *J. Mol. Endocrinol.* **2018**, *61*, T233–T252. [CrossRef]
47. Synnott, N.C.; Murray, A.; McGowan, P.M.; Kiely, M.; Kiely, P.A.; O'Donovan, N.; O'Connor, D.P.; Gallagher, W.M.; Crown, J.; Duffy, M.J. Mutant p53: A novel target for the treatment of patients with triple-negative breast cancer? *Int. J. Cancer* **2017**, *140*, 234–246. [CrossRef] [PubMed]
48. Pettit, G.R.; Singh, S.B.; Boyd, M.R.; Hamel, E.; Pettit, R.K.; Schmidt, J.M.; Hogan, F. Antineoplastic agents. 291. Isolation and synthesis of combretastatins A-4, A-5, and A-6(1A). *J. Med. Chem.* **1995**, *38*, 1666–1672. [CrossRef] [PubMed]
49. Perez-Perez, M.J.; Priego, E.M.; Bueno, O.; Martins, M.S.; Canela, M.D.; Liekens, S. Blocking blood flow to solid tumors by destabilizing tubulin: An approach to targeting tumor growth. *J. Med. Chem.* **2016**, *59*, 8685–8711. [CrossRef] [PubMed]
50. Su, M.; Huang, J.; Liu, S.; Xiao, Y.; Qin, X.; Liu, J.; Pi, C.; Luo, T.; Li, J.; Chen, X.; et al. The anti-angiogenic effect and novel mechanisms of action of combretastatin A-4. *Sci. Rep.* **2016**, *6*, 28139. [CrossRef]
51. Lu, Y.; Chen, J.; Xiao, M.; Li, W.; Miller, D.D. An overview of tubulin inhibitors that interact with the colchicine binding site. *Pharm. Res.* **2012**, *29*, 2943–2971. [CrossRef]
52. McLoughlin, E.C.; O'Boyle, N.M. Colchicine-binding site inhibitors from chemistry to clinic: A review. *Pharmaceuticals* **2020**, *13*, 8. [CrossRef]
53. Greene, L.M.; Meegan, M.J.; Zisterer, D.M. Combretastatins: More than just vascular targeting agents? *J. Pharmacol. Exp. Ther.* **2015**, *355*, 212–227. [CrossRef]
54. Gaspari, R.; Prota, A.E.; Bargsten, K.; Cavalli, A.; Steinmetz, M.O. Structural basis of cis- and trans-combretastatin binding to tubulin. *Chem* **2017**, *2*, 102–113. [CrossRef]
55. Pettit, G.R.; Toki, B.E.; Herald, D.L.; Boyd, M.R.; Hamel, E.; Pettit, R.K.; Chapuis, J.C. Antineoplastic agents. 410. Asymmetric hydroxylation of trans-combretastatin a-4. *J. Med. Chem.* **1999**, *42*, 1459–1465. [CrossRef]
56. Malebari, A.M.; Fayne, D.; Nathwani, S.M.; O'Connell, F.; Noorani, S.; Twamley, B.; O'Boyle, N.M.; O'Sullivan, J.; Zisterer, D.M.; Meegan, M.J. Beta-lactams with antiproliferative and antiapoptotic activity in breast and chemoresistant colon cancer cells. *Eur. J. Med. Chem.* **2020**, *189*, 112050. [CrossRef] [PubMed]
57. Odlo, K.; Hentzen, J.; dit Chabert, J.F.; Ducki, S.; Gani, O.A.; Sylte, I.; Skrede, M.; Florenes, V.A.; Hansen, T.V. 1,5-disubstituted 1,2,3-triazoles as cis-restricted analogues of combretastatin A-4: Synthesis, molecular modeling and evaluation as cytotoxic agents and inhibitors of tubulin. *Bioorganic Med. Chem.* **2008**, *16*, 4829–4838. [CrossRef] [PubMed]
58. Mustafa, M.; Anwar, S.; Elgamal, F.; Ahmed, E.R.; Aly, O.M. Potent combretastatin A-4 analogs containing 1,2,4-triazole: Synthesis, antiproliferative, anti-tubulin activity, and docking study. *Eur. J. Med. Chem.* **2019**, *183*, 111697. [CrossRef] [PubMed]
59. Romagnoli, R.; Baraldi, P.G.; Prencipe, F.; Oliva, P.; Baraldi, S.; Tabrizi, M.A.; Lopez-Cara, L.C.; Ferla, S.; Brancale, A.; Hamel, E.; et al. Design and synthesis of potent in vitro and in vivo anticancer agents based on 1-(3',4',5'-trimethoxyphenyl)-2-aryl-1h-imidazole. *Sci. Rep.* **2016**, *6*, 26602. [CrossRef]
60. Li, W.; Xu, F.; Shuai, W.; Sun, H.; Yao, H.; Ma, C.; Xu, S.; Yao, H.; Zhu, Z.; Yang, D.H.; et al. Discovery of novel quinoline-chalcone derivatives as potent antitumor agents with microtubule polymerization inhibitory activity. *J. Med. Chem.* **2019**, *62*, 993–1013. [CrossRef]
61. He, J.; Zhang, M.; Tang, L.; Liu, J.; Zhong, J.; Wang, W.; Xu, J.P.; Wang, H.T.; Li, X.F.; Zhou, Z.Z. Synthesis, biological evaluation, and molecular docking of arylpyridines as antiproliferative agent targeting tubulin. *ACS Med. Chem. Lett.* **2020**, *11*, 1611–1619. [CrossRef] [PubMed]
62. Messaoudi, S.; Treguier, B.; Hamze, A.; Provot, O.; Peyrat, J.F.; De Losada, J.R.; Liu, J.M.; Bignon, J.; Wdziedzak-Bakala, J.; Thoret, S.; et al. Isocombretastatins a versus combretastatins a: The forgotten isoca-4 isomer as a highly promising cytotoxic and antitubulin agent. *J. Med. Chem.* **2009**, *52*, 4538–4542. [CrossRef]
63. La Regina, G.; Bai, R.; Rensen, W.M.; Di Cesare, E.; Coluccia, A.; Piscitelli, F.; Famigliani, V.; Reggio, A.; Nalli, M.; Pelliccia, S.; et al. Toward highly potent cancer agents by modulating the c-2 group of the arylthioindole class of tubulin polymerization inhibitors. *J. Med. Chem.* **2013**, *56*, 123–149. [CrossRef] [PubMed]
64. Kumar, G.B.; Nayak, V.L.; Sayeed, I.B.; Reddy, V.S.; Shaik, A.B.; Mahesh, R.; Baig, M.F.; Shareef, M.A.; Ravikumar, A.; Kamal, A. Design, synthesis of phenstatin/isocombretastatin-oxindole conjugates as antimetabolic agents. *Bioorganic Med. Chem.* **2016**, *24*, 1729–1740. [CrossRef] [PubMed]
65. Naret, T.; Khelifi, I.; Provot, O.; Bignon, J.; Levaique, H.; Dubois, J.; Souce, M.; Kasselouri, A.; Deroussent, A.; Paci, A.; et al. 1,1-diheterocyclic ethylenes derived from quinaldine and carbazole as new tubulin-polymerization inhibitors: Synthesis, metabolism, and biological evaluation. *J. Med. Chem.* **2019**, *62*, 1902–1916. [CrossRef]
66. Pettit, G.R.; Toki, B.; Herald, D.L.; Verdier-Pinard, P.; Boyd, M.R.; Hamel, E.; Pettit, R.K. Antineoplastic agents. 379. Synthesis of phenstatin phosphate. *J. Med. Chem.* **1998**, *41*, 1688–1695. [CrossRef] [PubMed]
67. Ghinet, A.; Rigo, B.; Henichart, J.P.; Le Broc-Ryckewaert, D.; Pommery, J.; Pommery, N.; Thuru, X.; Quesnel, B.; Gautret, P. Synthesis and biological evaluation of phenstatin metabolites. *Bioorganic Med. Chem.* **2011**, *19*, 6042–6054. [CrossRef]
68. Cascioferro, S.; Attanzio, A.; Di Sarno, V.; Musella, S.; Tesoriere, L.; Cirrincione, G.; Diana, P.; Parrino, B. New 1,2,4-oxadiazole nortopsentin derivatives with cytotoxic activity. *Mar. Drugs* **2019**, *17*, 35. [CrossRef] [PubMed]

69. Carbone, D.; Parrino, B.; Cascioferro, S.; Pecoraro, C.; Giovannetti, E.; Di Sarno, V.; Musella, S.; Auriemma, G.; Cirrincione, G.; Diana, P. 1,2,4-oxadiazole topentin analogs with antiproliferative activity against pancreatic cancer cells, targeting GSK3b kinase. *ChemMedChem* **2021**, *16*, 537–554. [CrossRef]
70. Cascioferro, S.; Petri, G.L.; Parrino, B.; Carbone, D.; Funel, N.; Bergonzini, C.; Mantini, G.; Dekker, H.; Geerke, D.; Peters, G.J.; et al. Imidazo[2,1-b][1,3,4]thiadiazoles with antiproliferative activity against primary and gemcitabine-resistant pancreatic cancer cells. *Eur. J. Med. Chem.* **2020**, *189*, 112088. [CrossRef] [PubMed]
71. Chang, C.Y.; Chuang, H.Y.; Lee, H.Y.; Yeh, T.K.; Kuo, C.C.; Chang, C.Y.; Chang, J.Y.; Liou, J.P. Antimitotic and vascular disrupting agents: 2-hydroxy-3,4,5-trimethoxybenzophenones. *Eur. J. Med. Chem.* **2014**, *77*, 306–314. [CrossRef] [PubMed]
72. Brancale, A.; Silvestri, R. Indole, a core nucleus for potent inhibitors of tubulin polymerization. *Med. Res. Rev.* **2007**, *27*, 209–238. [CrossRef] [PubMed]
73. Hadimani, M.B.; Macdonough, M.T.; Ghatak, A.; Strecker, T.E.; Lopez, R.; Sriram, M.; Nguyen, B.L.; Hall, J.J.; Kessler, R.J.; Shirali, A.R.; et al. Synthesis of a 2-aryl-3-aryl indole salt (Oxi8007) resembling combretastatin A-4 with application as a vascular disrupting agent. *J. Nat. Prod.* **2013**, *76*, 1668–1678. [CrossRef] [PubMed]
74. Tung, Y.S.; Coumar, M.S.; Wu, Y.S.; Shiao, H.Y.; Chang, J.Y.; Liou, J.P.; Shukla, P.; Chang, C.W.; Chang, C.Y.; Kuo, C.C.; et al. Scaffold-hopping strategy: Synthesis and biological evaluation of 5,6-fused bicyclic heteroaromatics to identify orally bioavailable anticancer agents. *J. Med. Chem.* **2011**, *54*, 3076–3080. [CrossRef]
75. Chen, J.; Ahn, S.; Wang, J.; Lu, Y.; Dalton, J.T.; Miller, D.D.; Li, W. Discovery of novel 2-aryl-4-benzoyl-imidazole (ABI-III) analogues targeting tubulin polymerization as antiproliferative agents. *J. Med. Chem.* **2012**, *55*, 7285–7289. [CrossRef] [PubMed]
76. Wang, Q.; Arnst, K.E.; Wang, Y.; Kumar, G.; Ma, D.; White, S.W.; Miller, D.D.; Li, W.; Li, W. Structure-guided design, synthesis, and biological evaluation of (2-(1H-indol-3-yl)-1H-imidazol-4-yl)(3,4,5-trimethoxyphenyl) methanone (ABI-231) analogues targeting the colchicine binding site in tubulin. *J. Med. Chem.* **2019**, *62*, 6734–6750. [CrossRef]
77. Bai, Z.; Gao, M.; Zhang, H.; Guan, Q.; Xu, J.; Li, Y.; Qi, H.; Li, Z.; Zuo, D.; Zhang, W.; et al. BZML, a novel colchicine binding site inhibitor, overcomes multidrug resistance in a549/taxol cells by inhibiting P-gp function and inducing mitotic catastrophe. *Cancer Lett.* **2017**, *402*, 81–92. [CrossRef] [PubMed]
78. O'Boyle, N.M.; Pollock, J.K.; Carr, M.; Knox, A.J.; Nathwani, S.M.; Wang, S.; Caboni, L.; Zisterer, D.M.; Meegan, M.J. Beta-lactam estrogen receptor antagonists and a dual-targeting estrogen receptor/tubulin ligand. *J. Med. Chem.* **2014**, *57*, 9370–9382. [CrossRef] [PubMed]
79. Knox, A.J.; Price, T.; Pawlak, M.; Golfis, G.; Flood, C.T.; Fayne, D.; Williams, D.C.; Meegan, M.J.; Lloyd, D.G. Integration of ligand and structure-based virtual screening for the identification of the first dual targeting agent for heat shock protein 90 (Hsp90) and tubulin. *J. Med. Chem.* **2009**, *52*, 2177–2180. [CrossRef]
80. Zhong, B.; Chennamaneni, S.; Lama, R.; Yi, X.; Geldenhuys, W.J.; Pink, J.J.; Dowlati, A.; Xu, Y.; Zhou, A.; Su, B. Synthesis and anticancer mechanism investigation of dual Hsp27 and tubulin inhibitors. *J. Med. Chem.* **2013**, *56*, 5306–5320. [CrossRef]
81. Lv, W.; Liu, J.; Skaar, T.C.; Flockhart, D.A.; Cushman, M. Design and synthesis of norendoxifen analogues with dual aromatase inhibitory and estrogen receptor modulatory activities. *J. Med. Chem.* **2015**, *58*, 2623–2648. [CrossRef] [PubMed]
82. Lv, W.; Liu, J.; Lu, D.; Flockhart, D.A.; Cushman, M. Synthesis of mixed (*E,Z*)-, (*E*)-, and (*Z*)-norendoxifen with dual aromatase inhibitory and estrogen receptor modulatory activities. *J. Med. Chem.* **2013**, *56*, 4611–4618. [CrossRef] [PubMed]
83. Lu, W.J.; Desta, Z.; Flockhart, D.A. Tamoxifen metabolites as active inhibitors of aromatase in the treatment of breast cancer. *Breast Cancer Res. Treat.* **2012**, *131*, 473–481. [CrossRef] [PubMed]
84. Woo, L.W.; Bubert, C.; Purohit, A.; Potter, B.V. Hybrid dual aromatase-steroid sulfatase inhibitors with exquisite picomolar inhibitory activity. *ACS Med. Chem. Lett.* **2011**, *2*, 243–247. [CrossRef] [PubMed]
85. Dohle, W.; Jourdan, F.L.; Menchon, G.; Prota, A.E.; Foster, P.A.; Mannion, P.; Hamel, E.; Thomas, M.P.; Kasprzyk, P.G.; Ferrandis, E.; et al. Quinazolinone-based anticancer agents: Synthesis, antiproliferative, antitubulin activity, and tubulin co-crystal structure. *J. Med. Chem.* **2018**, *61*, 1031–1044. [CrossRef]
86. Dohle, W.; Prota, A.E.; Menchon, G.; Hamel, E.; Steinmetz, M.O.; Potter, B.V.L. Tetrahydroisoquinoline sulfamates as potent microtubule disruptors: Synthesis, antiproliferative and antitubulin activity of dichlorobenzyl-based derivatives, and a tubulin cocrystal structure. *ACS Omega* **2019**, *4*, 755–764. [CrossRef]
87. Gangjee, A.; Pavana, R.K.; Ihnat, M.A.; Thorpe, J.E.; Disch, B.C.; Bastian, A.; Bailey-Downs, L.C.; Hamel, E.; Bai, R. Discovery of antitubulin agents with antiangiogenic activity as single entities with multitarget chemotherapy potential. *ACS Med. Chem. Lett.* **2014**, *5*, 480–484. [CrossRef]
88. Doiron, J.; Soultan, A.H.; Richard, R.; Toure, M.M.; Picot, N.; Richard, R.; Cuperlovic-Culf, M.; Robichaud, G.A.; Touaibia, M. Synthesis and structure-activity relationship of 1- and 2-substituted-1,2,3-triazole letrozole-based analogues as aromatase inhibitors. *Eur. J. Med. Chem.* **2011**, *46*, 4010–4024. [CrossRef]
89. Wood, P.M.; Woo, L.W.; Labrosse, J.R.; Trusselle, M.N.; Abbate, S.; Longhi, G.; Castiglioni, E.; Lebon, F.; Purohit, A.; Reed, M.J.; et al. Chiral aromatase and dual aromatase-steroid sulfatase inhibitors from the letrozole template: Synthesis, absolute configuration, and in vitro activity. *J. Med. Chem.* **2008**, *51*, 4226–4238. [CrossRef]
90. Negi, A.S.; Gautam, Y.; Alam, S.; Chanda, D.; Luqman, S.; Sarkar, J.; Khan, F.; Konwar, R. Natural antitubulin agents: Importance of 3,4,5-trimethoxyphenyl fragment. *Bioorganic Med. Chem.* **2015**, *23*, 373–389. [CrossRef]

91. Misawa, T.; Aoyama, H.; Furuyama, T.; Dodo, K.; Sagawa, M.; Miyachi, H.; Kizaki, M.; Hashimoto, Y. Structural development of benzhydrol-type 1'-acetoxychavicol acetate (aca) analogs as human leukemia cell-growth inhibitors based on quantitative structure-activity relationship (QSAR) analysis. *Chem. Pharm. Bull.* **2008**, *56*, 1490–1495. [CrossRef] [PubMed]
92. Wang, J.B.; Bei, F.L.; Li, R.Y.; Yang, X.J.; Wang, X. Synthesis, characterization and single crystal structure of 4,4'-(1H-1,2,4-triazol-1-methylene)-bisbenzotrile. *Chin. J. Org. Chem.* **2004**, *24*, 550.
93. Plobeck, N.; Delorme, D.; Wei, Z.Y.; Yang, H.; Zhou, F.; Schwarz, P.; Gawell, L.; Gagnon, H.; Pelcman, B.; Schmidt, R.; et al. New diarylmethylpiperazines as potent and selective nonpeptidic delta opioid receptor agonists with increased in vitro metabolic stability. *J. Med. Chem.* **2000**, *43*, 3878–3894. [CrossRef]
94. Tang, Y.; Dong, Y.; Vennerstrom, J.L. The reaction of carbonyldiimidazole with alcohols to form carbamates and N-alkylimidazoles. *Synthesis* **2004**, *15*, 2540–2544. [CrossRef]
95. Ohta, S.; Kawasaki, I.; Uemura, T.; Yamashita, M.; Yoshioka, T.; Yamaguchi, S. Alkylation and acylation of the 1,2,3-triazole ring. *Chem. Pharm. Bull.* **1997**, *45*, 1140–1145. [CrossRef]
96. Belskaya, N.P.; Subbotina, J.; Lesogorova, S. *Synthesis of 2H-1,2,3-Triazoles*; Springer: Berlin/Heidelberg, Germany, 2014.
97. Martins, P.; Jesus, J.; Santos, S.; Raposo, L.R.; Roma-Rodrigues, C.; Baptista, P.V.; Fernandes, A.R. Heterocyclic anticancer compounds: Recent advances and the paradigm shift towards the use of nanomedicine's tool box. *Molecules* **2015**, *20*, 16852–16891. [CrossRef]
98. Vitaku, E.; Smith, D.T.; Njardarson, J.T. Analysis of the structural diversity, substitution patterns, and frequency of nitrogen heterocycles among U.S. FDA approved pharmaceuticals. *J. Med. Chem.* **2014**, *57*, 10257–10274. [CrossRef]
99. Sakai, N.; Hori, H.; Yoshida, Y.; Konakahara, T.; Ogiwara, Y. Copper(I)-catalyzed coupling reaction of aryl boronic acids with N,O-acetals and N,N-aminals under atmosphere leading to alpha-aryl glycine derivatives and diarylmethylamine derivatives. *Tetrahedron* **2015**, *71*, 4722–4729. [CrossRef]
100. LeGall, E.; Troupel, M.; Nedelec, J. One-step three-component coupling of aromatic organozinc reagents, secondary amines, and aromatic aldehydes into functionalized diarylmethylamines. *Tetrahedron* **2006**, *62*, 9953–9965. [CrossRef]
101. Sengmany, S.L.; LeGall, E.; LeJean, C.; Troupel, M.; Nedelec, J. Straightforward three-component synthesis of diarylmethylpiperazines and 1,2-diarylethylpiperazines. *Tetrahedron* **2007**, *63*, 3672–3681. [CrossRef]
102. Malebari, A.M.; Greene, L.M.; Nathwani, S.M.; Fayne, D.; O'Boyle, N.M.; Wang, S.; Twamley, B.; Zisterer, D.M.; Meegan, M.J. Beta-lactam analogues of combretastatin A-4 prevent metabolic inactivation by glucuronidation in chemoresistant HT-29 colon cancer cells. *Eur. J. Med. Chem.* **2017**, *130*, 261–285. [CrossRef]
103. Cushman, M.; Nagarathnam, D.; Gopal, D.; He, H.M.; Lin, C.M.; Hamel, E. Synthesis and evaluation of analogues of (z)-1-(4-methoxyphenyl)-2-(3,4,5-trimethoxyphenyl)ethene as potential cytotoxic and antimetabolic agents. *J. Med. Chem.* **1992**, *35*, 2293–2306. [CrossRef] [PubMed]
104. Barbosa, E.G.; Bega, L.A.; Beatriz, A.; Sarkar, T.; Hamel, E.; do Amaral, M.S.; de Lima, D.P. A diaryl sulfide, sulfoxide, and sulfone bearing structural similarities to combretastatin a-4. *Eur. J. Med. Chem.* **2009**, *44*, 2685–2688. [CrossRef] [PubMed]
105. Kamal, A.; Kumar, G.B.; Vishnuvardhan, M.V.; Shaik, A.B.; Reddy, V.S.; Mahesh, R.; Sayeeda, I.B.; Kapure, J.S. Synthesis of phenstatin/isocombretastatin-chalcone conjugates as potent tubulin polymerization inhibitors and mitochondrial apoptotic inducers. *Org. Biomol. Chem.* **2015**, *13*, 3963–3981. [CrossRef]
106. Alvarez, R.; Alvarez, C.; Mollinedo, F.; Sierra, B.G.; Medarde, M.; Pelaez, R. Isocombretastatins A: 1,1-diarylethenes as potent inhibitors of tubulin polymerization and cytotoxic compounds. *Bioorganic Med. Chem.* **2009**, *17*, 6422–6431. [CrossRef]
107. National Cancer Institute. *DCTD Division of Cancer Treatment and Diagnostics, DTP Development Therapeutics Programme*; National Cancer Institute: Bethesda, MD, USA; Available online: <https://dtp.cancer.gov/organization/btb/default.htm> (accessed on 20 February 2020).
108. Qu, Y.; Han, B.; Yu, Y.; Yao, W.; Bose, S.; Karlan, B.Y.; Giuliano, A.E.; Cui, X. Evaluation of MCF10a as a reliable model for normal human mammary epithelial cells. *PLoS ONE* **2015**, *10*, e0131285. [CrossRef]
109. Visconti, R.; Grieco, D. Fighting tubulin-targeting anticancer drug toxicity and resistance. *Endocr. Relat. Cancer* **2017**, *24*, T107–T117. [CrossRef] [PubMed]
110. Mc Gee, M.M. Targeting the mitotic catastrophe signaling pathway in cancer. *Mediat. Inflamm.* **2015**, *2015*, 146282. [CrossRef] [PubMed]
111. Vitale, I.; Antoccia, A.; Cenciarelli, C.; Crateri, P.; Meschini, S.; Arancia, G.; Pisano, C.; Tanzarella, C. Combretastatin CA-4 and combretastatin derivative induce mitotic catastrophe dependent on spindle checkpoint and caspase-3 activation in non-small cell lung cancer cells. *Apoptosis Int. J. Program. Cell Death* **2007**, *12*, 155–166. [CrossRef]
112. O'Boyle, N.M.; Ana, G.; Kelly, P.M.; Nathwani, S.M.; Noorani, S.; Fayne, D.; Bright, S.A.; Twamley, B.; Zisterer, D.M.; Meegan, M.J. Synthesis and evaluation of antiproliferative microtubule-destabilising combretastatin A-4 piperazine conjugates. *Org. Biomol. Chem.* **2019**, *17*, 6184–6200. [CrossRef]
113. Satoh, M.S.; Lindahl, T. Role of poly(ADP-ribose) formation in DNA repair. *Nature* **1992**, *356*, 356–358. [CrossRef] [PubMed]
114. Tsujimoto, Y. Role of BCL-2 family proteins in apoptosis: Apoptosomes or mitochondria? *Genes Cells* **1998**, *3*, 697–707. [CrossRef]
115. Michels, J.; Johnson, P.W.; Packham, G. Mcl-1. *Int. J. Biochem. Cell Biol.* **2005**, *37*, 267–271. [CrossRef] [PubMed]
116. Davar, D.; Beumer, J.H.; Hamieh, L.; Tawbi, H. Role of PARP inhibitors in cancer biology and therapy. *Curr. Med. Chem.* **2012**, *19*, 3907–3921. [CrossRef]

117. Stresser, D.M.; Turner, S.D.; McNamara, J.; Stocker, P.; Miller, V.P.; Crespi, C.L.; Patten, C.J. A high-throughput screen to identify inhibitors of aromatase (CYP19). *Anal. Biochem.* **2000**, *284*, 427–430. [CrossRef]
118. Maiti, A.; Cuendet, M.; Croy, V.L.; Endringer, D.C.; Pezzuto, J.M.; Cushman, M. Synthesis and biological evaluation of (+/-)-abyssinone II and its analogues as aromatase inhibitors for chemoprevention of breast cancer. *J. Med. Chem.* **2007**, *50*, 2799–2806. [CrossRef]
119. Endringer, D.C.; Guimaraes, K.G.; Kondratyuk, T.P.; Pezzuto, J.M.; Braga, F.C. Selective inhibition of aromatase by a dihydroisocoumarin from xyris pterygoblephara. *J. Nat. Prod.* **2008**, *71*, 1082–1084. [CrossRef]
120. Yu, C.; Shin, Y.G.; Kosmeder, J.W.; Pezzuto, J.M.; van Breemen, R.B. Liquid chromatography/tandem mass spectrometric determination of inhibition of human cytochrome p450 isozymes by resveratrol and resveratrol-3-sulfate. *Rapid Commun. Mass Spectrom.* **2003**, *17*, 307–313. [CrossRef] [PubMed]
121. Ravelli, R.B.; Gigant, B.; Curmi, P.A.; Jourdain, I.; Lachkar, S.; Sobel, A.; Knossow, M. Insight into tubulin regulation from a complex with colchicine and a stathmin-like domain. *Nature* **2004**, *428*, 198–202. [CrossRef] [PubMed]
122. Tafi, A.; Anastassopoulou, J.; Theophanides, T.; Botta, M.; Corelli, F.; Massa, S.; Artico, M.; Costi, R.; Di Santo, R.; Ragno, R. Molecular modeling of azole antifungal agents active against *Candida albicans*. 1. A comparative molecular field analysis study. *J. Med. Chem.* **1996**, *39*, 1227–1235. [CrossRef]
123. Bruker AXS Inc. *Bruker APEX v2014*; Bruker AXS Inc.: Madison, WI, USA, 2014.
124. SADABS. Area Detector Absorption Correction Program, Sheldrick, G.M. University of Göttingen, Germany. 2014. Available online: <https://journals.iucr.org/e/services/stdswrefs.html>; (accessed on 20 February 2021).
125. Sheldrick, G.M. Shelxt-integrated space-group and crystal-structure determination. *Acta Cryst. A Found. Adv.* **2015**, *71*, 3–8. [CrossRef] [PubMed]
126. Sheldrick, G.M. Crystal structure refinement with Shelxl. *Acta Cryst. C Struct. Chem.* **2015**, *71*, 3–8. [CrossRef] [PubMed]
127. Dolomanov, O.V.; Bourhis, L.J.; Gildea, R.J.; Howard, J.A.K.; Puschmann, H. Olex2: A complete structure solution, refinement and analysis program. *J. Appl. Crystallogr.* **2009**, *42*, 339–341. [CrossRef]
128. Cytoskeleton. Available online: <https://www.Cytoskeleton.Com/tubulin-resources> (accessed on 1 December 2020).
129. Chemical Computing Group Inc. *Molecular Operating Environment (MOE), 2015.10*; Chemical Computing Group Inc.: Montreal, QC, Canada, 2015.
130. Kendall, A.; Dowsett, M. Novel concepts for the chemoprevention of breast cancer through aromatase inhibition. *Endocr. Relat. Cancer* **2006**, *13*, 827–837. [CrossRef] [PubMed]



## Article

# Synthesis and Cytotoxic Activity of Combretastatin A-4 and 2,3-Diphenyl-2H-indazole Hybrids

Jaime Pérez-Villanueva <sup>1,\*</sup>, Félix Matadamas-Martínez <sup>1,2</sup>, Lilián Yépez-Mulia <sup>3,\*</sup>, Vadim Pérez-Koldenkova <sup>4</sup>, Martha Leyte-Lugo <sup>5</sup>, Karen Rodríguez-Villar <sup>6</sup>, Francisco Cortés-Benítez <sup>1</sup>, Ana Perla Macías-Jiménez <sup>1</sup>, Ignacio González-Sánchez <sup>5</sup>, Ariana Romero-Velásquez <sup>7</sup>, Juan Francisco Palacios-Espinosa <sup>1</sup> and Olivia Soria-Arteche <sup>1</sup>

**Citation:** Pérez-Villanueva, J.; Matadamas-Martínez, F.; Yépez-Mulia, L.; Pérez-Koldenkova, V.; Leyte-Lugo, M.; Rodríguez-Villar, K.; Cortés-Benítez, F.; Macías-Jiménez, A.P.; González-Sánchez, I.; Romero-Velásquez, A.; et al. Synthesis and Cytotoxic Activity of Combretastatin A-4 and 2,3-Diphenyl-2H-indazole Hybrids. *Pharmaceuticals* **2021**, *14*, 815. <https://doi.org/10.3390/ph14080815>

Academic Editors: Mary J. Meegan and Niamh M. O'Boyle

Received: 11 May 2021

Accepted: 13 August 2021

Published: 19 August 2021

**Publisher's Note:** MDPI stays neutral with regard to jurisdictional claims in published maps and institutional affiliations.



**Copyright:** © 2021 by the authors. Licensee MDPI, Basel, Switzerland. This article is an open access article distributed under the terms and conditions of the Creative Commons Attribution (CC BY) license (<https://creativecommons.org/licenses/by/4.0/>).

- <sup>1</sup> Departamento de Sistemas Biológicos, División de Ciencias Biológicas y de la Salud, Universidad Autónoma Metropolitana-Xochimilco (UAM-X), Ciudad de México 04960, Mexico; felixmatadamas@yahoo.com.mx (F.M.-M.); jcortesb@correo.xoc.uam.mx (F.C.-B.); anmacp61@gmail.com (A.P.M.-J.); jpalacios@correo.xoc.uam.mx (J.F.P.-E.); soriao@correo.xoc.uam.mx (O.S.-A.)
  - <sup>2</sup> Maestría y Doctorado en Ciencias Farmacéuticas, División de Ciencias Biológicas y de la Salud, Universidad Autónoma Metropolitana-Xochimilco (UAM-X), Ciudad de México 04960, Mexico
  - <sup>3</sup> Unidad de Investigación Médica en Enfermedades Infecciosas y Parasitarias, UMAE Hospital de Pediatría, Centro Médico Siglo XXI, Instituto Mexicano del Seguro Social, Ciudad de México 06720, Mexico
  - <sup>4</sup> Laboratorio Nacional de Microscopía Avanzada, Centro Médico Nacional Siglo XXI, Instituto Mexicano del Seguro Social, Ciudad de México 06720, Mexico; vadim.perez@imss.gob.mx
  - <sup>5</sup> Catedrático CONACYT Comisionado a Departamento de Sistemas Biológicos, División de Ciencias Biológicas y de la Salud, Universidad Autónoma Metropolitana-Xochimilco (UAM-X), Ciudad de México 04960, Mexico; mleyte@correo.xoc.uam.mx (M.L.-L.); ignacio.gonzalez.s@gmail.com (I.G.-S.)
  - <sup>6</sup> Doctorado en Ciencias Biológicas y de la Salud, Universidad Autónoma Metropolitana (UAM), Ciudad de México 04960, Mexico; qkarenrodv@hotmail.com
  - <sup>7</sup> Maestría en Ciencias Biológicas, Universidad Nacional Autónoma de México (UNAM), Ciudad de México 04510, Mexico; ariromerov@gmail.com
- \* Correspondence: jpwillanueva@correo.xoc.uam.mx (J.P.-V.); lilianyepes@yahoo.com (L.Y.-M.); Tel.: +52-5-54-83-72-59 (J.P.-V.); Fax: +52-5-55-94-79-29 (J.P.-V.)

**Abstract:** Cancer is the second leading cause of death, after cardiovascular diseases. Different strategies have been developed to treat cancer; however, chemotherapy with cytotoxic agents is still the most widely used treatment approach. Nevertheless, drug resistance to available chemotherapeutic agents is still a serious problem, and the development of new active compounds remains a constant need. Taking advantage of the molecular hybridization approach, in the present work we designed, synthesized, and tested the cytotoxic activity of two hybrid compounds and seven derivatives based on the structure of combretastatin A-4 and 2,3-diphenyl-2H-indazole. Practical modifications of reported synthetic protocols for 2-phenyl-2H-indazole and 2,3-diphenyl-2H-indazole derivatives under microwave irradiation were implemented. The cytotoxicity assays showed that our designed hybrid compounds possess strong activity, especially compound **5**, which resulted even better than the reference drug cisplatin against HeLa and SK-LU-1 cells (IC<sub>50</sub> of 0.16 and 6.63 μM, respectively), and it had similar potency to the reference drug imatinib against K562 cells. Additionally, in silico and in vitro studies strongly suggest tubulin as the molecular target for hybrid compound **5**.

**Keywords:** cancer; combretastatin A-4; cytotoxic activity; hybrid compounds; indazole

## 1. Introduction

Cancer is “a group of diseases characterized by uncontrollable growth and spread of abnormal cells, which can then invade adjoining parts of the body and spread to other organs” [1,2]. Globally, after cardiovascular diseases, cancer is the second leading cause of death [2]. Different strategies have been developed to treat cancer; however, chemotherapy



with cytotoxic agents is still the most widely used treatment approach. Nevertheless, drug resistance to available chemotherapeutic agents is still a serious problem, and the development of new active compounds remains a constant need [3].

The indazole nucleus is considered an important heterocyclic moiety in medicinal chemistry, since several derivatives harboring this scaffold have shown anticancer, hypoglycemic, antiprotozoal, anti-inflammatory, antimicrobial, anti-HIV, and antihypertensive activities [4–7]. Furthermore, some drugs containing the indazole nucleus have been approved as anticancer agents (e.g., pazopanib, axitinib, and niraparib) [6]. Previous studies focused on the search of antiprotozoal compounds showed that 2,3-diphenyl-2*H*-indazole (**4**) exhibits cytotoxic activity against HeLa cells ( $IC_{50} = 125 \mu M$ ) [8]. Although the cytotoxic activity of this compound is weak, it reveals itself as a new scaffold of interest to develop new cytotoxic agents with the appropriate substituents. Hence, taking advantage of the molecular hybridization approach, in the present work we designed, synthesized, and tested the cytotoxic activity of two hybrid compounds (**5** and **6**) inspired on 2,3-diphenyl-2*H*-indazole and the natural product Combretastatin A-4 (**CA-4**, Figure 1). **CA-4**, isolated from the bushwillow tree *Combretum caffrum*, is a well-known cytotoxic stilbenoid that acts as a tubulin polymerization inhibitor by binding to the colchicine site [9]. The hybridization of both molecules, 2,3-diphenyl-2*H*-indazole and **CA-4**, was pursued to increase the cytotoxic effect by combination of two biologically active structures [8–10]. Additionally, the stabilization of the cis-diphenyl pattern, that can isomerize into the trans isomer in **CA-4** (less active), could be achieved by replacing the ethylene bridge in **CA-4** by the indazole moiety [9,10]. To learn more about the structural requirements of hybrid compounds to exhibit cytotoxic activity, structurally simplified derivatives (**1–3** and **7–9**) and the unsubstituted reference compound **4** are also synthesized and their cytotoxic activity tested. In addition, the effect of the best cytotoxic compound is characterized and its effect on tubulin is studied by *in silico* and *in vitro* assays.

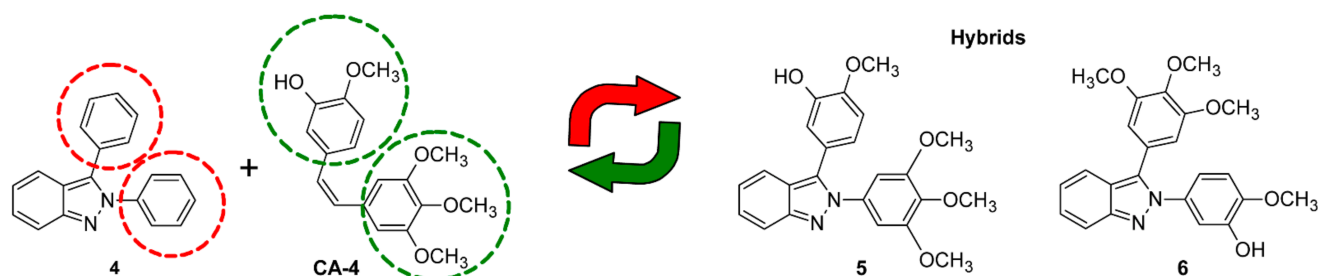


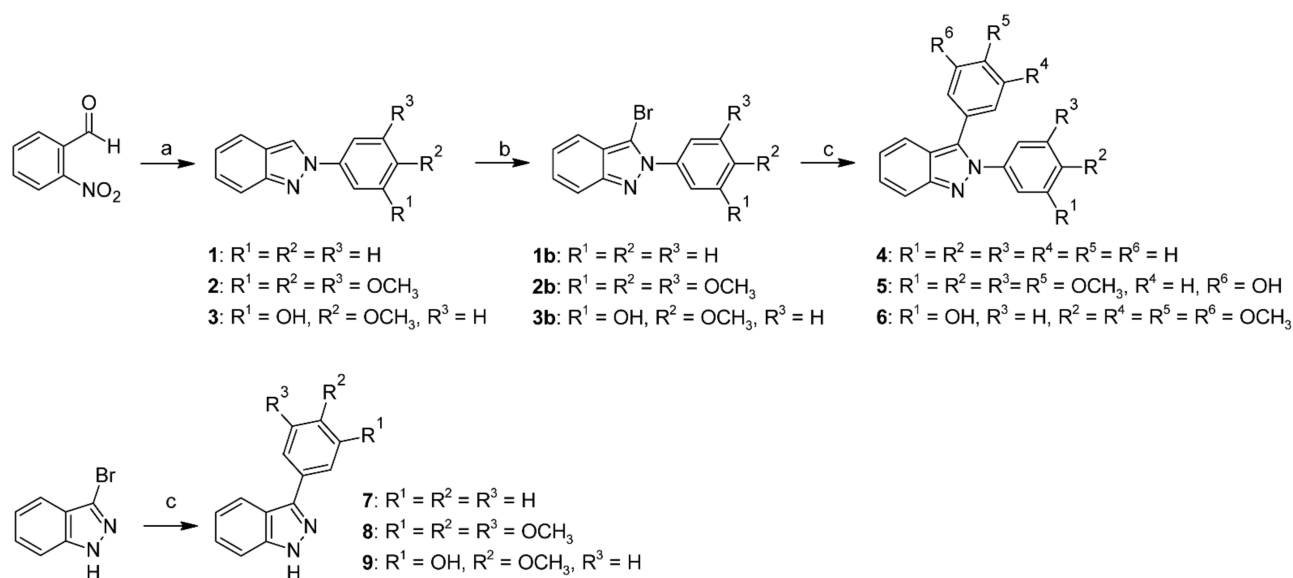
Figure 1. Molecular design of hybrid compounds.

## 2. Results and Discussion

### 2.1. Chemistry

The hybrid compounds and their derivatives (**1–9**) were synthesized as illustrated in Scheme 1. Compounds **1–3** were obtained by a slight modification of Cadogan's method, where the commercially available 2-nitrobenzaldehyde was heated with aniline or the appropriate substituted aniline under microwave irradiation to afford the corresponding Schiff base, which was then treated with triethyl phosphite to give the 2-phenyl-2*H*-indazole derivatives **1–3** [11]. Compounds **1–3** were selectively brominated at the three-position employing a previously described method using bromine in acetic acid [12]. The 2,3-diphenyl-2*H*-indazole (**4**) and derivatives (**5** and **6**) were synthesized by a palladium-catalyzed coupling reaction, employing a slight modification under microwave irradiation of the previously reported conventional method under reflux [13]. It is worth mentioning that the microwave irradiation method gave the best yields and improved the reaction times for compounds **4–6** as compared to the same examples employing the original report (see Table S1 in the supporting information). Finally, employing the commercially available 3-bromo-1*H*-indazole as starting material, 3-phenyl-1*H*-indazole derivatives **7–9**

were synthesized using this same microwave-assisted method. Compounds **5** and **9** were obtained by using the commercially available 3-acetoxy-4-methoxyphenylboronic acid pinacol ester; nonetheless, the 3-acetoxy group was hydrolyzed in situ under the basic reaction conditions to directly obtain the desired compounds (**5** and **9**). All synthesized compounds were characterized by  $^1\text{H}$  NMR and  $^{13}\text{C}$  NMR spectroscopy. The data on previously reported structures were consistent with literature reports (**1**, **2**, **4** and **7**). It is important to note that hybrids **5** and **6**, and derivatives **3**, **8**, and **9**, resulted in new structures, which were also characterized by mass spectrometry; particularly, the most active compound **5** was also characterized by high resolution mass spectrometry. The nuclear magnetic resonance and mass spectra of these compounds can be found in the Supporting Information (Figures S1–S29).



**Scheme 1.** Synthesis of indazole derivatives **1–9**. Reagents and conditions: (a) 1. Aniline or substituted aniline, EtOH; 2.  $\text{P}(\text{OEt})_3$ ,  $150\text{ }^\circ\text{C}$ ; (b)  $\text{Br}_2$ , AcOH; (c) appropriate phenylboronic acid or phenylboronic acid pinacol ester, 1-propanol,  $\text{Pd}(\text{OAc})_2$ ,  $(\text{C}_6\text{H}_5)_3\text{P}$ ,  $\text{Na}_2\text{CO}_3$ ,  $\text{H}_2\text{O}$ .

## 2.2. Cytotoxicity Assays

**CA-4** and several **CA-4** derivatives have been shown to have cytotoxic potency and anti-proliferative activity in a variety of human cancer cells, such as non-small cell lung cancer [14], ovarian cancer [15], and human leukemia cells [16,17], among others [18]. Therefore, in this study, three cancer cell lines—HeLa (human cervix), SK-LU-1 (human non-small cell lung), and K562 (human chronic myelogenous leukemia)—were selected. It is worth mentioning that the cell lines selected are representative of some high incidence cancer types [2]. The antiproliferative activity of all compounds (**1–9**) was initially tested at 50 micromolar after 48 h of exposition using the MTT assay on HeLa cells. Briefly, hybrids **5** and **6** possessed the best cytotoxic effect at 50  $\mu\text{M}$  (Table S2). This result suggests that the entire 2,3-diphenyl-2H-indazole scaffold is important for the cytotoxic effect. The simplified structures based on 2-phenyl-2H-indazole (**1–3**) and 3-phenyl-1H-indazole derivatives (**7–9**) at the same concentration resulted in higher viability values. Thus, we decided to determine  $\text{IC}_{50}$  values for compounds **5** and **6** on HeLa, SK-LU-1, and K562 cells. Compound **4** was included as unsubstituted reference, whereas cisplatin and imatinib were included as reference drugs, Table 1. The results of  $\text{IC}_{50}$  showed the major effect for substituted hybrids (**5** and **6**) on HeLa, SK-LU-1, and K562 cells as compared with the unsubstituted compound **4**. Compound **5** displayed higher cytotoxic effect than **6** against the three cell lines: particularly, with an  $\text{IC}_{50}$  value of 0.16  $\mu\text{M}$  against HeLa cells, making compound **5** 241-fold more active than **6**. Compound **5** was 116 times more active

against HeLa cells and slightly more active against SK-LU-1 cells (two-fold) than the reference drug cisplatin, which is employed for cervical and lung cancer therapy [19]. Additionally, compound **5** showed against K562 cells, similar in vitro activity to imatinib, a drug used for the therapy of chronic myelogenous leukemia [20]. Cytotoxicity values for **CA-4** has been extensively reported on HeLa cells after 48 h by MTT assay. In ChEMBL database [21], 18 reference values were found with  $IC_{50}$  ranging from 0.003 to 14.830  $\mu$ M, with a median value of 0.011  $\mu$ M, which indicates that **CA-4** is still 15-fold more cytotoxic than compound **5** (0.16  $\mu$ M). Whereas no reports were found for **CA-4** on SK-LU-1 cells, two reference values were found on K562 cells under the same assay conditions (0.0048 and 0.046  $\mu$ M) [21]. Therefore, the cytotoxic activity for compound **5** is still lower as compared with previous **CA-4** reports, but it showed higher activity than cisplatin and imatinib, the reference drugs included in this study (Table 1). On the other hand, some studies suggest that antioxidants may lead to interferences with the MTT assay [22,23]; hence, the antioxidant activity of compounds **4–6**, was studied employing the DPPH and ABTS models. Results can be found at the supporting information (Table S3). Compounds were inactive on DPPH test, whereas very poor effect was found on ABTS test for compounds **5** and **6**, with  $IC_{50}$  values of 216 and 262  $\mu$ M, respectively. Therefore, the intrinsic reductive potential of the compounds tested is not involved in the determination of  $IC_{50}$  values on MTT assays. In addition, the purity of the compounds **4**, **5**, and **6** was determined by quantitative NMR to ensure that the observed  $IC_{50}$  values were caused by the pure compounds (purity > 95%, Table S4).

**Table 1.** Cytotoxicity ( $IC_{50}$  [ $\mu$ M]  $\pm$  SE) for compounds **5** and **6** and reference compounds **4**, cisplatin, and imatinib on different cancer cell lines.

Compound	HeLa	SK-LU-1	K562
<b>4</b>	125.8 $\pm$ 14.8 <sup>1</sup>	96.43 $\pm$ 8.65	> 120
<b>5</b>	0.16 $\pm$ 0.01	6.63 $\pm$ 0.52	1.68 $\pm$ 0.27
<b>6</b>	38.6 $\pm$ 7.51	25.21 $\pm$ 9.06	18.59 $\pm$ 1.56
Cisplatin	18.5 $\pm$ 3.0	12.0 $\pm$ 2.5	-
Imatinib	-	-	2.37 $\pm$ 0.12

<sup>1</sup> Reference [8].

Bright-field microscopy reveals the presence of spherical cells on HeLa cultures treated with hybrid compounds **5** and **6** after 48 h (Figure S30 in supporting information) as compared with the typically observed epithelial polygonal morphology. This result and the reported effect of **CA-4** on microtubule assemblage, allowed us to consider microtubules as a possible target of the synthesized hybrids. Hence, in silico and in vitro studies were also performed.

### 2.3. Molecular Docking

To investigate the potential binding mode of hybrids **5** and **6** and their derivatives (**1–4** and **7–9**) to the colchicine binding site of beta-tubulin, we performed docking simulations using AutoDock 4.2 and the X-Ray structure of Tubulin-cis-**CA-4** Complex (PDB: 5LYJ) [24,25]. For comparison, **CA-4** and colchicine were also docked. The comparison of co-crystallized and docked **CA-4** structures superimposes with Root Mean Square Deviation (RMSD) of 0.835 Å, validating our method. As expected, **CA-4** and colchicine fit at the binding site with  $\Delta G$  values of  $-7.45$  and  $-8.24$  kcal/mol, respectively. Interestingly, we found an improved docking score for indazole inhibitors **4** ( $-8.92$  kcal/mol), **5** ( $-9.90$  kcal/mol), and **6** ( $-9.60$  kcal/mol) suggesting their higher affinity. It is worth to emphasize the score found for the 2-phenyl-2*H*-indazole derivatives **1–3** ( $-7.06$ ,  $-6.73$ , and  $-6.49$  kcal/mol respectively) and the 3-phenyl-1*H*-indazole derivatives **7–9** ( $-5.81$ ,  $-6.79$ , and  $-6.50$  kcal/mol respectively) suggesting a lower affinity. Moreover, the 3,4,5-trimethoxyphenyl at N2 or C3 for **5** and **6**, respectively, is oriented in same way as found in colchicine and **CA-4** (Figure 2). Furthermore, this moiety produces hydrophobic interac-

tions with Ala250, Ala316 and  $\pi$ - $\sigma$  interactions with Leu255. Unlike CA-4, the 3-hydroxy-4-methoxy substituted ring at C3 or N2 for 5 and 6, respectively, is positioned to form an H-bond with the side chain of Asn101 (distance = 2.0 Å and 2.1 Å for compounds 5 and 6, respectively), hydrophobic interactions with Lys254 as well as  $\pi$ -interactions with Thr179. Conversely, the indazole core of both analogs is oriented into a cavity and is further stabilized by hydrophobic interactions with residues Val181, Ala316, and Lys352. Surprisingly, compound 5 produced an extra  $\pi$ -sulfur contact with Met259. Thus, this compound fits better into the colchicine binding site of tubulin, providing slightly better binding energy than obtained for compound 6.

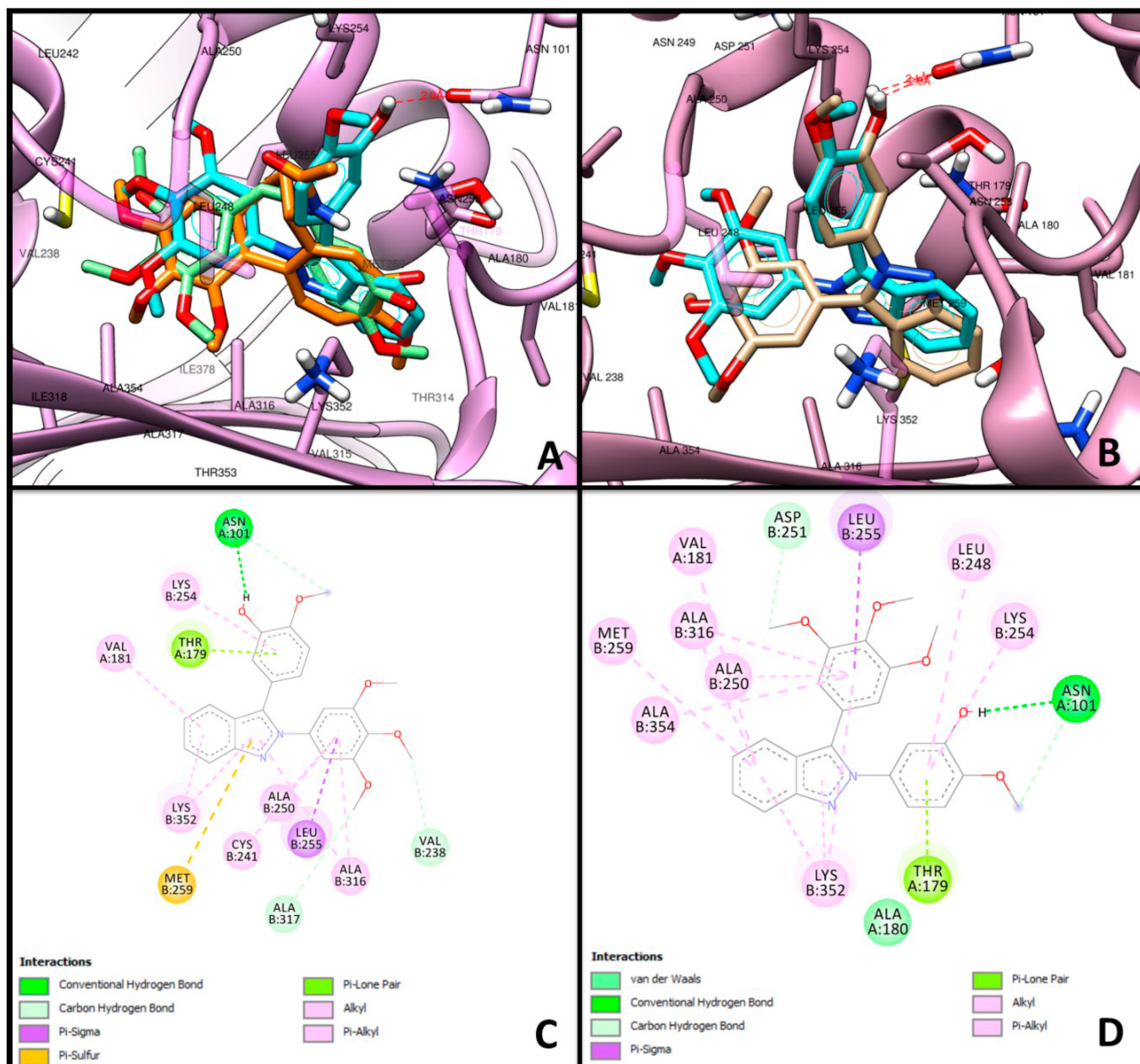


**Figure 2.** Molecular coupling of compounds 5 and 6 at the colchicine site on beta-tubulin. (A) Binding mode of colchicine (orange), CA-4 (green) and compound 5 (cyan) docked into the colchicine binding site cavity (lilac) (PDB: 5LYJ). (B) Binding mode of compound 5 (cyan) and 6 (khaki) docked into the colchicine binding site cavity. 2D diagram of docked compounds 5 (C) and 6 (D) into the colchicine binding site cavity showing their interaction with the binding site residues.

#### 2.4. In Vitro Tubulin Polymerization Assays

To learn more about the effect of compounds **5** and **6** on tubulin polymerization, we conducted a polymerization assay [26–28]. Figure 3 shows the drug-dependent effect on tubulin polymerization, in presence of paclitaxel (PTX), CA-4 and hybrid compounds **5** and **6** or vehicle. The polymerization  $V_{max}$  value was enhanced 2.7 times in the presence of the stabilizing agent PTX, with respect to vehicle (84 vs. 31 mOD/min). On the other hand, the microtubule destabilizing drug, CA-4, reduced 3.4 times the  $V_{max}$  value as compared to vehicle (9 vs. 31 mOD/min). Compounds **5** and **6** decreased the polymerization  $V_{max}$ , 3.8 and 1.3 times, respectively, in comparison to vehicle (8 and 24 vs. 31 mOD/min). These results suggest that hybrid compound **5** is a potential inhibitor of tubulin polymerization that displays an effect similar to that of CA-4 at 10  $\mu$ M.

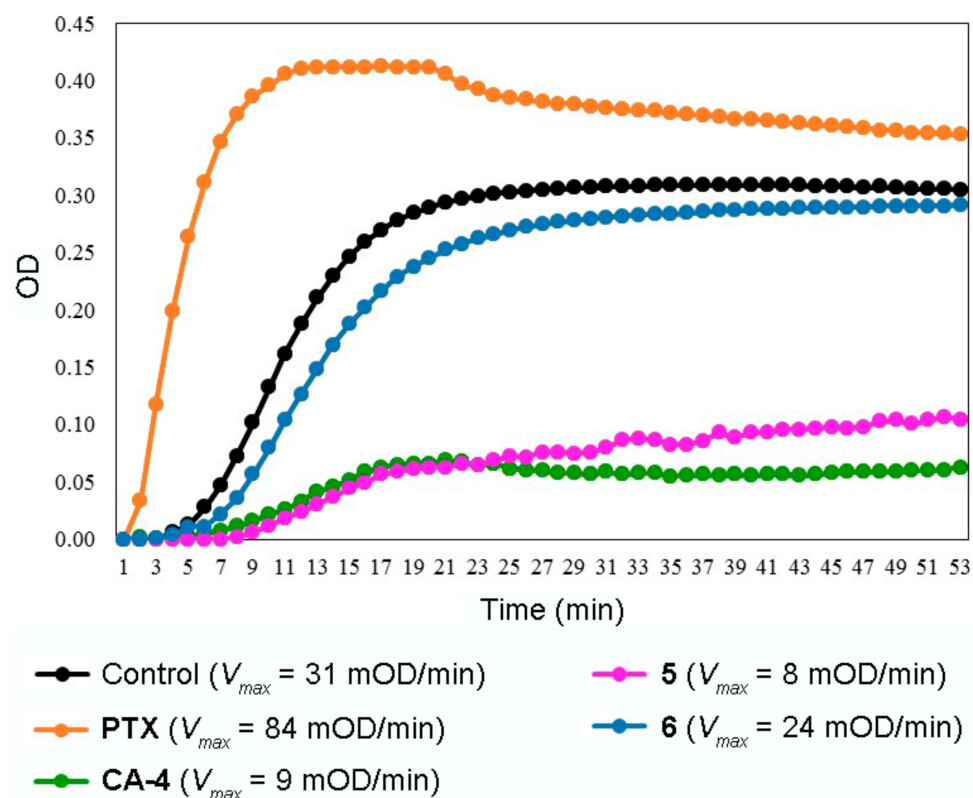


**Figure 3.** Effect of hybrid compounds **5** and **6** on tubulin polymerization. Polymerization reactions were carried out by incubation at 37 °C and followed by absorbance readings at 340 nm for 53 min at 37 °C. CA-4 and PTX were used as positive controls. All compounds were used at a final concentration of 10  $\mu$ M.

#### 2.5. Indirect Immunofluorescence (IFI)

The effect of compounds **5**, PTX and CA-4 on HeLa cells tubulin network was examined by IFI (Figure 4). The well-organized tubulin network can be observed on untreated HeLa cells. In the case of PTX, a microtubule stabilizing agent, it led to an asymmetrical cell shape, and collapse of the tubulin network with the appearance of microtubule arrays and tubulin bundles. Compound **5** induced a loss of organized microtubule structure; tubulin staining was diffuse and disorganized with aggregated staining in parts. In addition, morphological changes such as round-shaped cells, formation of protuberances in the cytoplasm, nucleus size increase, and multinucleation were observed, all of them indicative features of mitotic catastrophe [29]. Meanwhile, treatment with CA-4, a destabilizing agent, resulted in small round-shaped cells with a disrupted microtubule cytoskeleton; multiple punctuate signals of beta tubulin were visible in the cytoplasm while nuclear damage characterized by multilobular deformed nuclei and micronuclei was evident.

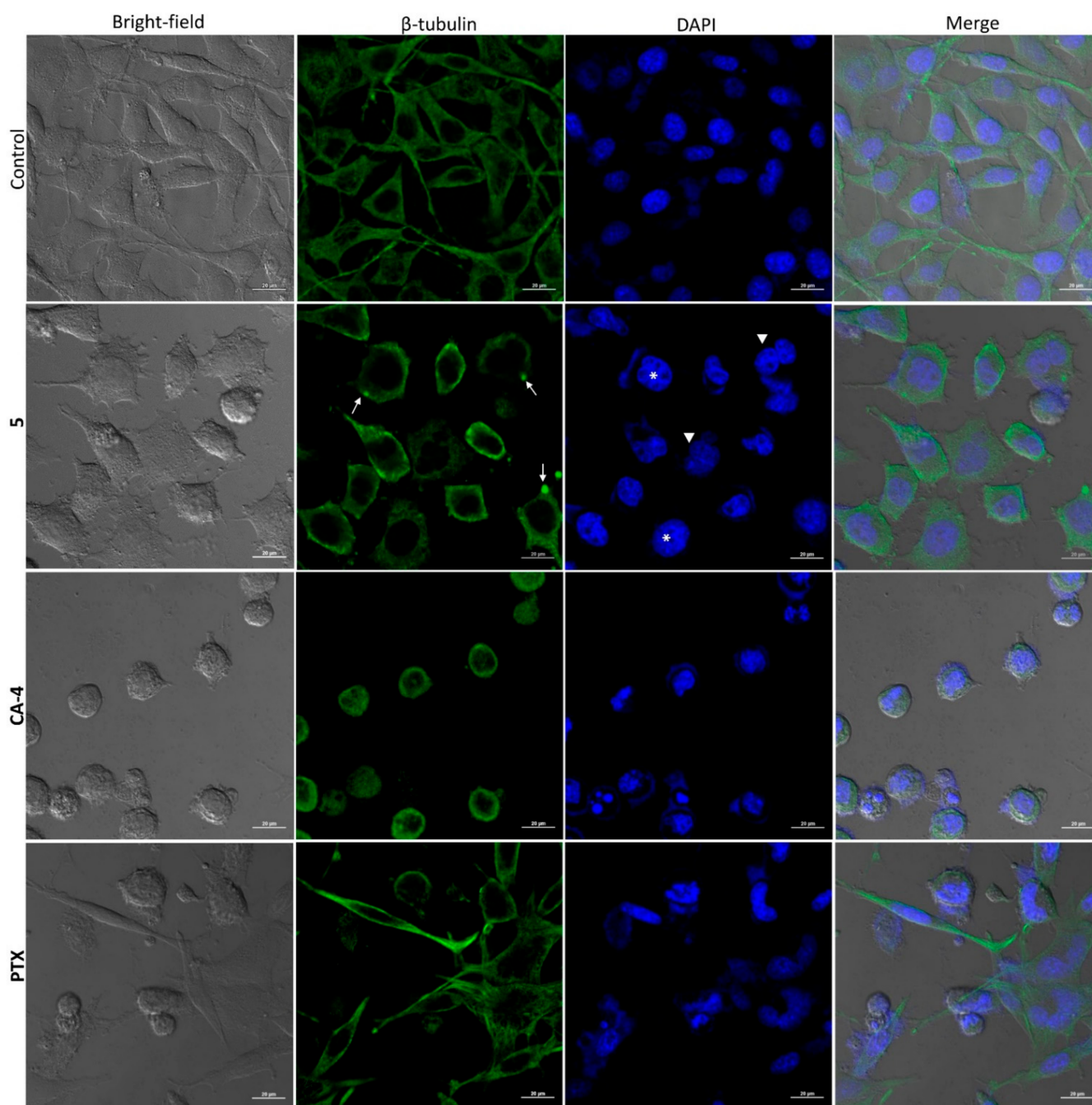


**Figure 4.** Effect of compound **5**, **PTX**, and **CA-4** on HeLa cells tubulin network analyzed by indirect immunofluorescence. Cells were treated with DMSO at 0.01% (Control), compound **5** (0.16  $\mu\text{M}$ ), **CA-4** (1.49  $\mu\text{M}$ ) and **PTX** (0.08  $\mu\text{M}$ ) for 24 h. Cell samples were incubated with anti-beta-tubulin antibody at 1:1000 dilution and anti-mouse IgG-FITC diluted 1:1000 as secondary antibody. The nuclear DNA was stained with 4,6-diamidino-2-phenylindole (DAPI). Beta-tubulin is stained in green, DNA in blue. First column: Bright-field images, second column: Beta-tubulin array, stained with FITC, third column: DAPI stain, fourth column: Merge. Samples were visualized by confocal microscopy. Arrow: Tubulin aggregates; Arrowhead: Multinucleation; Asterisk: Macronuclei. Scale bar: 20  $\mu\text{m}$ .

It is known that the interference of microtubule dynamics by **CA-4** and some derivatives consequently disrupts mitotic progression and induce cytostasis and ultimately leads to apoptosis and cell death [30–32]. Therefore, the effect of compound **5** on the cell cycle of HeLa cells was analyzed by flow cytometry. Data showed that, in fact, HeLa cells were arrested in  $G_2/M$  phase by compound **5** (52.5%), sharing this feature with **CA-4** (42.5%) (Figure 5). In addition, it was also shown that compound **5** triggers the apoptosis

of HeLa cells (Figure S31 in supplementary information). Our data agrees with the mechanism of action of different microtubule depolymerizing agents such as nocodazole [33], colchicine [34], and CA-4 and its derivatives [31,35] that induce the program cell death.

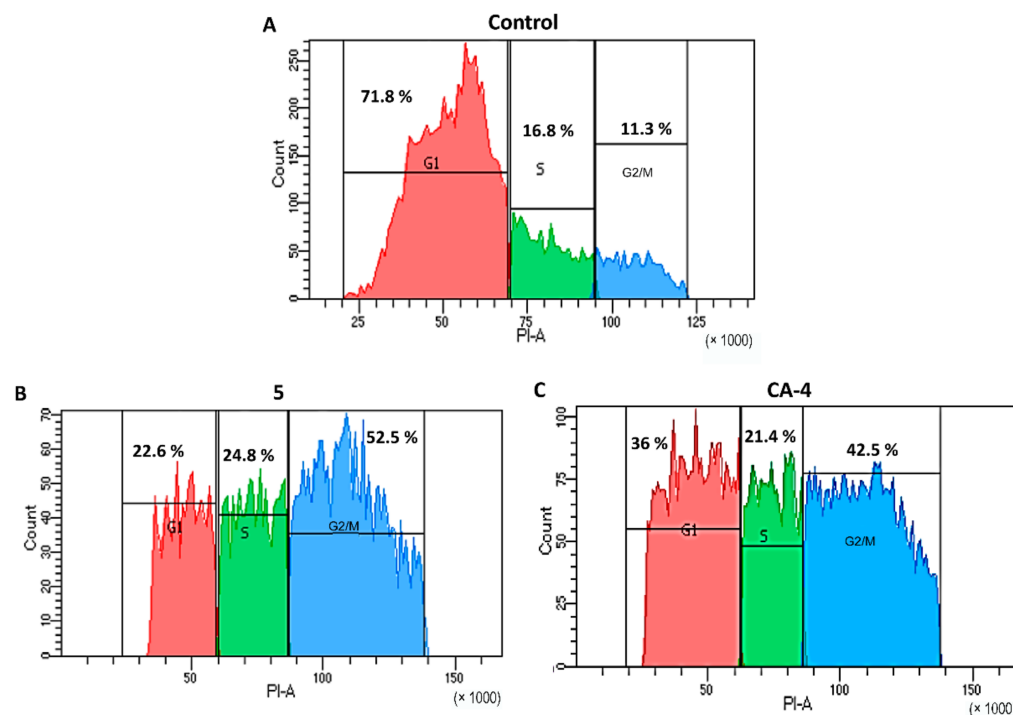


**Figure 5.** Analysis of cell cycle progression of HeLa cells by flow cytometry: (A) Control cells, (B) treated with compound 5, (C) treated with CA-4. HeLa cells were treated with compound 5 (0.16  $\mu$ M) and CA-4 (1.49  $\mu$ M) for 48 h.

## 2.6. Effect of Compound 5, PTX, and CA-4 on Soluble and Polymerized Tubulin

IFI assays showed that compound 5 induced alterations in the microtubule network. Then, to identify the mechanism by which compound 5 affects the stability of microtubules, soluble and polymerized tubulin protein obtained from treated HeLa cells were analyzed by Western blotting. PTX and CA-4 were included as microtubule stabilizing and destabilizing agents, respectively, and DMSO as a negative control. In control and treated samples, bands of 50 kDa corresponding to beta-tubulin were detected (Figure 6A). Densitometric analysis showed that in cells treated with CA-4 or compound 5, the fraction of soluble tubulin increased in comparison to the control condition or PTX treatment. On the contrary, in cells treated with PTX, an increase of polymerized tubulin was evident. The ratio of soluble to polymerized tubulin fractions was determined for each compound and changes in the tubulin polymerization state following drug treatment were evidenced (Figure 6B). PTX showed a lower ratio of soluble-to-polymerized tubulin compared to control due to its stabilizing effect of the polymerized state of tubulin proteins. Meanwhile, CA-4 and compound 5 displayed a higher soluble-to-polymerized tubulin ratio in comparison to control or PTX. This suggests that compound 5 exhibits an inhibitory activity of tubulin polymerization similar to that of CA-4. This inhibitory activity was indeed observed in the tubulin polymerization assay.

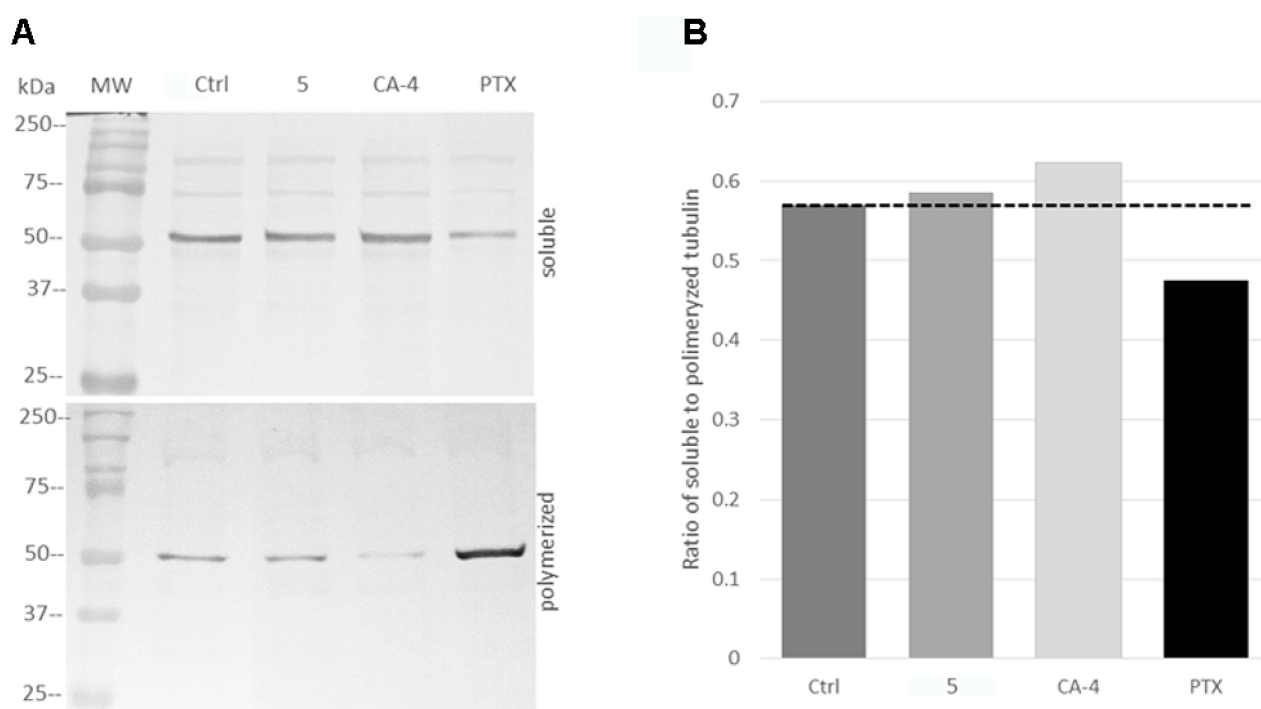


**Figure 6.** (A) Western blot analysis of soluble and polymerized tubulin fractions of cells without treatment (Ctrl) and cells treated with compound **5** (0.16  $\mu\text{M}$ ), **CA-4** (1.49  $\mu\text{M}$ ), and **PTX** (0.08  $\mu\text{M}$ ). (B) Ratio of soluble-to-polymerized tubulin of the data A. MW = molecular weight.

### 3. Materials and Methods

#### 3.1. Chemistry

All chemicals were obtained from Sigma-Aldrich (Sigma-Aldrich, Toluca, MEX, Mexico). Reactions were monitored by TLC on 0.2 mm percolated silica gel 60 F254 plates (Merck, Darmstadt, Germany) and visualized by irradiation with a UV lamp (Cole-Parmer, Vernon Hills, IL, USA). Silica gel 60 (70–230 mesh) was used for column chromatography (Macherey-Nagel, Düren, Germany). Melting points were determined in open capillary tubes with a Büchi M-565 melting point apparatus (Büchi, Flawil, Switzerland) and are uncorrected. Microwave-assisted reactions were carried out in a Monowave 300 monomodal reactor equipped with a hydraulic pressure sensing device and an infrared temperature-sensor (Anton-Paar, Graz, Austria).  $^1\text{H}$  NMR and  $^{13}\text{C}$  NMR were measured with an Agilent DD2 spectrometer (Agilent, Santa Clara, CA, USA), operating at 600 and 151 MHz for  $^1\text{H}$  and  $^{13}\text{C}$ , respectively. Chemical shifts are given in parts per million relatives to tetramethylsilane ( $\text{Me}_4\text{Si}$ ,  $\delta = 0$ );  $J$  values are given in Hz. Splitting patterns are expressed as follow: s, singlet; d, doublet; t, triplet; q, quartet; dd, doublet of doublet; td, triplet of doublet; ddd, doublet doublet of doublet; dq, doublet of quartets; m, multiplet; bs, broad singlet. The purity of compounds **4**, **5**, and **6** was determined by quantitative NMR spectroscopy (qNMR) using sodium 2,2-dimethyl-2-silapentane-5-sulfonate (DSS) as internal standard (Cambridge Isotope Laboratories, Inc., Tewksbury, MA, USA). High resolution mass spectra were recorded on a Bruker ESI/APCI-TOF, MicroTOF-II-Focus spectrometer (Bruker, Billerica, MA, USA) by electrospray ionization (ESI); whereas low resolution Mass spectra were recorded on a Waters Xevo TQ-MS spectrometer (Waters, Milford, MA, USA) by electron impact (EI).

##### 3.1.1. General Procedure for the Synthesis of 2-Phenyl-2H-indazole Derivatives

2-Phenyl-2H-indazole derivatives were synthesized employing a slight modification of the Cadogan method [11]. A 10 mL microwave vial was charged with 2-nitrobenzaldehyde (0.5 g, 3.308 mmol), aniline or the appropriate substituted aniline (3.308 mmol, 1 eq) and



anhydrous ethanol (3 mL). The mixture was heated at 160 °C under microwave irradiation for 10 min. The mixture was transferred to a round bottom flask and distilled under vacuum. The evaporation residue was treated with triethyl phosphite (10 mmol) and heated at 150 °C (0.5–2 h) until the starting material was totally consumed. Then, the phosphite excess was oxidized with 20 mL of 5% hydrogen peroxide solution. The product was extracted with ethyl acetate (20 mL × 3) and the combined organic phase was finally washed with brine (20 mL) and dried with anhydrous sodium sulfate. The organic solution was refluxed for 10 min with activated carbon (200 mg), and filtered and concentrated under vacuum distillation. The evaporation residue was purified using column chromatography with silica and hexane-ethyl acetate (85:15) as a mobile phase, the combined fractions containing the product were concentrated to 10–20 mL under reduced pressure and cooled to induce crystallization. The solid was finally filtered and washed with cold hexane to give the product.

#### 2-Phenyl-2*H*-indazole (1)

White solid, 56% yield, mp: 81–82 °C (lit: 81–82 °C) [11]. The spectroscopic data matched previously reported data [36]: <sup>1</sup>H NMR (600 MHz, CDCl<sub>3</sub>) δ 8.40 (d, *J* = 0.9 Hz, 1H), 7.91–7.88 (m, 2H), 7.79 (dd, *J* = 8.8, 0.9 Hz, 1H), 7.70 (dt, *J* = 8.5, 1.0 Hz, 1H), 7.54–7.50 (m, 2H), 7.41–7.37 (m, 1H), 7.32 (ddd, *J* = 8.8, 6.6, 1.0 Hz, 1H), 7.11 (ddd, *J* = 8.4, 6.6, 0.7 Hz, 1H); <sup>13</sup>C NMR (151 MHz, CDCl<sub>3</sub>) δ (ppm): 149.78, 140.52, 129.54, 127.88, 126.81, 122.76, 122.44, 120.99, 120.39, 120.37, 117.94.

#### 2-(3,4,5-Trimethoxyphenyl)-2*H*-indazole (2)

Pale yellow solid, 61% yield, mp: 94–95 (lit: 82–84 °C) [37]. The spectroscopic data matched previously reported data [37]: <sup>1</sup>H NMR (600 MHz, CDCl<sub>3</sub>) δ 8.36 (d, *J* = 0.8 Hz, 1H), 7.78 (dt, *J* = 9.6, 0.8 Hz, 1H), 7.70 (dt, *J* = 8.3, 1.0 Hz, 1H), 7.33 (ddd, *J* = 8.8, 6.6, 1.0 Hz, 1H), 7.14–7.10 (m, 3H), 3.97 (s, 6H), 3.90 (s, 3H). <sup>13</sup>C NMR (151 MHz, CDCl<sub>3</sub>) δ 153.78, 149.62, 137.83, 136.55, 126.82, 122.67, 122.45, 120.64, 120.26, 117.79, 98.93, 61.04, 56.39.

#### 5-(2*H*-Indazol-2-yl)-2-methoxyphenol (3)

White solid, 33% yield, mp: 143–144 °C. <sup>1</sup>H NMR (600 MHz, CDCl<sub>3</sub>) δ 8.29 (d, *J* = 0.8 Hz, 1H), 7.80–7.76 (m, 1H), 7.71–7.67 (m, 1H), 7.46 (d, *J* = 2.6 Hz, 1H), 7.39 (dd, *J* = 8.7, 2.6 Hz, 1H), 7.31 (ddd, *J* = 8.7, 6.6, 1.0 Hz, 1H), 7.10 (ddd, *J* = 8.4, 6.5, 0.7 Hz, 1H), 6.94 (d, *J* = 8.6 Hz, 1H), 6.06 (s, 1H), 3.93 (s, 3H); <sup>13</sup>C NMR (151 MHz, CDCl<sub>3</sub>) δ 149.53, 146.46, 146.33, 134.60, 126.60, 122.64, 122.25, 120.47, 120.27, 117.77, 112.72, 110.92, 108.17, 56.21; MS (HR-ESI) for C<sub>14</sub>H<sub>13</sub>N<sub>2</sub>O<sub>2</sub> [M + H]<sup>+</sup>, calcd: *m/z* 241.0972, found: *m/z* 241.0970.

#### 3.1.2. General Procedure for the Synthesis of 3-Bromo-2-phenyl-2*H*-indazole Derivatives

2-Phenyl-2*H*-indazole (2 mmol), or the appropriate substituted derivative (2–3), was dissolved in acetic acid (10 mL) at room temperature. The formed solution was treated, drop to drop gradually during a period of 1 h at room temperature, with a second solution of bromine 2.1 mmol in 10 mL of acetic acid. The resulting solution was stirred overnight at room temperature. The mixture was treated with 2 mL of water and then quenched under 100 mL of iced water. The solid formed was filtered under vacuum and dried. The product was used crude for to the next reaction [12].

#### 3-Bromo-2-phenyl-2*H*-indazole (1b)

White solid, 86% yield, a sample was recrystallized from ethanol/water to give mp: 77–79 (lit: 75.5–77 °C) [12]. <sup>1</sup>H NMR (600 MHz, CDCl<sub>3</sub>) δ 7.74 (dt, *J* = 8.8, 0.8 Hz, 1H), 7.70–7.66 (m, 2H), 7.59 (dt, *J* = 8.5, 1.0 Hz, 1H), 7.57–7.50 (m, 3H), 7.37 (ddd, *J* = 8.7, 6.6, 1.1 Hz, 1H), 7.18 (ddd, *J* = 8.4, 6.6, 0.7 Hz, 1H); <sup>13</sup>C NMR (151 MHz, CDCl<sub>3</sub>) δ 149.20, 139.26, 129.23, 129.04, 127.58, 126.17, 122.97, 122.89, 119.68, 118.19, 106.13.

**3-Bromo-2-(3,4,5-trimethoxyphenyl)-2H-indazole (2b)**

White solid, 91% yield, mp: 115–117.  $^1\text{H}$  NMR (600 MHz,  $\text{CDCl}_3$ )  $\delta$  7.73 (dt,  $J = 8.7$ , 0.8 Hz, 1H), 7.58 (dt,  $J = 8.4$ , 1.0 Hz, 1H), 7.37 (ddd,  $J = 8.8$ , 6.6, 1.1 Hz, 1H), 7.19 (ddd,  $J = 8.4$ , 6.6, 0.7 Hz, 1H), 6.89 (s, 2H), 3.93 (s, 3H), 3.92 (s, 6H);  $^{13}\text{C}$  NMR (151 MHz,  $\text{CDCl}_3$ )  $\delta$  153.24, 149.02, 138.70, 134.73, 127.64, 123.02, 122.80, 119.61, 118.06, 106.22, 103.93, 61.01, 56.35.

**3-Bromo-2-(3,4,5-trimethoxyphenyl)-2H-indazole (3b)**

White solid, 98% yield, mp: 118–121.  $^1\text{H}$  NMR (600 MHz,  $\text{CDCl}_3$ )  $\delta$  7.72 (d,  $J = 8.8$  Hz, 1H), 7.57 (dt,  $J = 8.4$ , 0.9 Hz, 1H), 7.35 (ddd,  $J = 8.7$ , 6.6, 1.0 Hz, 1H), 7.23 (d,  $J = 2.5$  Hz, 1H), 7.18–7.13 (m, 2H), 6.97 (d,  $J = 8.6$  Hz, 1H), 6.08 (s, 1H), 3.97 (s, 3H);  $^{13}\text{C}$  NMR (151 MHz,  $\text{CDCl}_3$ )  $\delta$  148.90, 147.34, 145.76, 132.66, 127.46, 122.81, 122.64, 119.61, 118.03, 112.99, 110.26, 106.46, 56.16.

**3.1.3. General Procedure for Palladium-Catalyzed Coupling Reactions**

A 10 mL microwave vial was charged with the properly substituted 3-bromo-2-phenyl-2H-indazole or 3-bromo-1H-indazole (0.6 mmol), the appropriate phenylboronic acid or phenylboronic acid pinacol ester (0.63 mmol), palladium (II) acetate (0.006 mmol, 1%), triphenylphosphine (0.018 mmol, 3%), sodium carbonate (1.2 mmol), water (0.6 mL), and *n*-propanol (3 mL). The mixture was heated at 150 °C under microwave irradiation for 20 min. The reaction was poured into 15 mL of water and extracted thrice with 15 mL of ethyl acetate. The organic phase was washed with brine (15 mL), dried with anhydrous sodium sulfate, and concentrated under vacuum. The evaporation residue was purified by column chromatography using hexane-ethyl acetate, 90:10 for compound 4 and 75:25 for compounds 5 and 6.

**2,3-Diphenyl-2H-indazole (4)**

White solid, 72% yield; mp: 107–108 °C (lit: 102–103 °C) [38]. The spectroscopic data matched previously reported data [8,38]:  $^1\text{H}$  NMR (600 MHz,  $\text{CDCl}_3$ )  $\delta$  7.82–7.79 (m, 1H), 7.73–7.70 (m, 1H), 7.45–7.42 (m, 2H), 7.41–7.34 (m, 9H), 7.14 (ddd,  $J = 8.4$ , 6.6, 0.8 Hz, 1H);  $^{13}\text{C}$  NMR (151 MHz,  $\text{CDCl}_3$ )  $\delta$  148.99, 140.24, 135.41, 129.91, 129.69, 128.97, 128.76, 128.30, 128.25, 126.98, 126.02, 122.50, 121.74, 120.52, 117.76; Purity (qNMR, % *w/w*) 98.01  $\pm$  2.10.

**2-Methoxy-5-(2-(3,4,5-trimethoxyphenyl)-2H-indazol-3-yl)phenol (5)**

White solid, 84% yield; mp: 160–162 °C;  $^1\text{H}$  NMR (600 MHz,  $\text{CDCl}_3$ )  $\delta$  7.77 (dt,  $J = 8.8$ , 0.9 Hz, 1H), 7.69 (dt,  $J = 8.5$ , 1.0 Hz, 1H), 7.35 (ddd,  $J = 8.7$ , 6.6, 0.9 Hz, 1H), 7.12 (ddd,  $J = 8.5$ , 6.6, 0.8 Hz, 1H), 7.03 (d,  $J = 2.1$  Hz, 1H), 6.88 (d,  $J = 8.4$  Hz, 1H), 6.84 (dd,  $J = 8.3$ , 2.0 Hz, 1H), 6.68 (s, 2H), 5.84 (s, 1H), 3.92 (s, 3H), 3.87 (s, 3H), 3.72 (s, 6H);  $^{13}\text{C}$  NMR (151 MHz,  $\text{CDCl}_3$ )  $\delta$  153.09, 148.68, 146.72, 145.78, 137.82, 135.82, 135.23, 127.00, 123.07, 122.24, 121.89, 121.60, 120.58, 117.46, 115.69, 110.78, 103.61, 60.98, 56.13, 55.98; MS (HR-ESI) for  $\text{C}_{23}\text{H}_{23}\text{N}_2\text{O}_5$  [M + H]<sup>+</sup>, calcd: *m/z* 407.1601, found: *m/z* 407.1595; Purity (qNMR, % *w/w*) 98.46  $\pm$  1.7.

**2-Methoxy-5-(3-(3,4,5-trimethoxyphenyl)-2H-indazol-2-yl)phenol (6)**

White solid, 68% yield, mp: 192–194 °C;  $^1\text{H}$  NMR (600 MHz,  $\text{CDCl}_3$ )  $\delta$  7.78 (dt,  $J = 8.8$ , 0.9 Hz, 1H), 7.74 (dt,  $J = 8.5$ , 1.0 Hz, 1H), 7.36 (ddd,  $J = 8.7$ , 6.6, 1.0 Hz, 1H), 7.15 (ddd,  $J = 8.4$ , 6.5, 0.7 Hz, 1H), 7.10 (d,  $J = 2.4$  Hz, 1H), 6.90 (dd,  $J = 8.6$ , 2.5 Hz, 1H), 6.83 (d,  $J = 8.6$  Hz, 1H), 6.58 (s, 2H), 5.97 (s, 1H), 3.92 (s, 3H), 3.90 (s, 3H), 3.73 (s, 6H);  $^{13}\text{C}$  NMR (151 MHz,  $\text{CDCl}_3$ )  $\delta$  153.34, 148.65, 146.71, 145.87, 138.11, 135.36, 133.90, 126.86, 125.15, 122.41, 121.25, 120.39, 117.93, 117.76, 112.95, 110.28, 106.95, 60.98, 56.20, 56.14; MS (EI) *m/z* 407.25 ([M + H]<sup>+</sup>, 100%); Purity (qNMR, % *w/w*) 96.65  $\pm$  1.43.

**3-Phenyl-1H-indazole (7)**

Light yellow solid, 80% yield, mp: 105–107 °C (lit: 106–107) [39]. The spectroscopic data matched previously reported data [40]:  $^1\text{H}$  NMR (600 MHz,  $\text{CDCl}_3$ )  $\delta$  11.44 (s, 1H), 8.05–7.99 (m, 3H), 7.56–7.51 (m, 2H), 7.47–7.42 (m, 1H), 7.37–7.33 (m, 1H), 7.29–7.25 (m,

1H), 7.23–7.19 (m, 1H); <sup>13</sup>C NMR (151 MHz, CDCl<sub>3</sub>) δ 145.74, 141.68, 133.56, 128.93, 128.17, 127.72, 126.78, 121.34, 121.09, 120.96, 110.22.

### 3-(3,4,5-Trimethoxyphenyl)-1H-indazole (8)

Yellow oil, 94% yield; <sup>1</sup>H NMR (600 MHz, CDCl<sub>3</sub>) δ 11.04 (bs, 1H), 8.01 (dt, *J* = 8.2, 0.9 Hz, 1H), 7.43–7.38 (m, 2H), 7.26–7.23 (m, 1H), 7.22 (s, 2H), 3.94 (2s, *J* = 0.5 Hz, 9H); <sup>13</sup>C NMR (151 MHz, CDCl<sub>3</sub>) δ 153.67, 145.73, 141.74, 138.27, 129.12, 126.95, 121.49, 120.97, 120.86, 110.23, 104.87, 61.02, 56.26; MS (EI) *m/z* 285.20 ([*M* + *H*]<sup>+</sup>, 100%).

### 5-(1H-Indazol-3-yl)-2-methoxyphenol (9)

White solid, 85% yield, mp: 190–194 °C; <sup>1</sup>H NMR (600 MHz, DMSO-*d*<sub>6</sub>) δ 13.06 (s, 1H), 9.18 (s, 1H), 7.99 (d, *J* = 8.2 Hz, 1H), 7.56 (d, *J* = 8.4 Hz, 1H), 7.46 (d, *J* = 2.1 Hz, 1H), 7.41–7.36 (m, 2H), 7.18 (t, *J* = 7.7 Hz, 1H), 7.05 (d, *J* = 8.3 Hz, 1H), 3.83 (s, 3H); <sup>13</sup>C NMR (151 MHz, DMSO-*d*<sub>6</sub>) δ 147.44, 146.67, 143.12, 141.42, 126.64, 125.83, 120.57, 120.53, 119.87, 117.70, 113.91, 112.45, 110.37, 55.56; MS (EI) *m/z* 241.14 ([*M* + *H*]<sup>+</sup>, 100%).

## 3.2. Cytotoxicity Assays in Human Cells

HeLa (derived from human epithelial cervical cancer, ATCC 93021013), SK-LU-1 (derived from human non-small lung adenocarcinoma ATCC 93120835), and K562 (derived from a patient in the blast crisis stage of chronic myelogenous leukemia ATCC 93112521) cancer cell lines were chosen to test the cytotoxicity of all compounds. Cancer cell lines were kindly provided by Dr. Marco A. Cerbón, Laboratory of Molecular Endocrinology, Facultad de Química UNAM.

HeLa, SK-LU-1, and K562 cell lines were grown in DMEM (BioWest, Riverside, MO, USA) supplemented with 10% FBS (BioWest, Riverside, MO, USA) and maintained in standard culture conditions (37 °C, 95% humidity, and 5% CO<sub>2</sub>). Cells were grown to a density of 80% and then were harvested using sterile PBS/EDTA (pH 7.4) before starting every experiment. Cells were seeded in 96-well plates (7 × 10<sup>3</sup> cells/well in 200 μL of DMEM) and maintained 24 h in standard conditions. Afterwards, cells were exposed during 48 h to tested compounds dissolved in DMSO (J.T. Baker, Phillipsburg, NJ) at different concentrations and diluted in 50 μL of DMEM, to reach 250 μL in the well. After treatment, cellular viability was analyzed by MTT assay, the absorbance of formazan was determined using a microplate reader Epoch 2 (BioTek, Winooski, VT, USA) at 540 nm and the viability for each concentration was related to the vehicle (100%). The IC<sub>50</sub> was calculated from dose-response curve by non-linear fit using the Software OriginPro 7.0 (RockWare, Golden, CO, USA) [8,41,42].

## 3.3. Molecular Docking

Docking studies were performed using AutoDock 4.2, whereas the graphical interface AutoDockTools 1.7.1 suite was used to prepare and analyze the docking simulations [24]. The X-Ray structure of tubulin-cis-CA-4 complex was retrieved from Protein Data Bank (<http://www.rcsb.org/> (accessed on 2 February 2019)) entry 5LYJ [25,43,44]. First, chains A and B were selected and the solvent molecules as well as CA-4 were removed. The pdb structure was submitted for minimization using the YASARA web server (YASARA, Vienna, Austria) [45]. The minimized protein was then exported to AutoDockTools interface 1.7.1. Hydrogen atoms were added and Gasteiger-Marsilli charges were assigned to the atoms into the protein as well. The chemical structures of CA-4, colchicine and indazole were retrieved from ZINC database [46]. Ligands were built by systematic modifications of indazole and then energy-minimized by semiempirical PM6 method using Gaussian 09 software [47]. Docking simulations were performed using a grid box of size 50 Å × 50 Å × 50 Å with a spacing of 0.345 Å focused on the binding region of CA-4 (coordinates: *x* = 17.85, *y* = 65.75 and *z* = 42.59). The search was carried out with the Lamarckian Genetic Algorithm. A total of 50 GA runs with a maximal number of 25,000,000 evaluations, a mutation rate of 0.02 and an initial population of 150 conformers were covered. Docking

results were clustered using a root mean square (RMS) tolerance = 1. Finally, each ligand with the best cluster size and the lowest binding free energy was further selected for the analysis. The docking protocol was validated by comparison of docked **CA-4** and the co-crystallized **CA-4**. The ligand interactions were analyzed using AutoDockTools 1.7.1 interface along with BIOVIA Discovery Studio Visualizer 2016 [48]. Figures and 2D diagrams were produced with UCSF Chimera program [49], and BIOVIA Discovery Studio Visualizer 2016.

### 3.4. Tubulin Polymerization Assays

The in vitro tubulin polymerization assays were performed using the kit manufactured by Cytoskeleton, Inc., catalog number BK006P (Cytoskeleton, Denver, CO, USA). Assays were carried out following the instructions provided by the manufacturer [26–28]. Briefly, compounds **5**, **6**, and references (**PTX** and **CA-4**) were dissolved in DMSO and tested at 10  $\mu$ M. The tubulin polymerization assay was conducted at 37 °C, recording the change in absorbance every minute at 340 nm after test compound was added.

### 3.5. Indirect Immunofluorescence Assays

HeLa cells ( $4 \times 10^5$ ) were seeded on coverslips in 30 mm petri dishes and incubated in DMEM with 10% of fetal bovine serum (FBS) for 24 h with compound **5** (0.16  $\mu$ M). DMSO (0.01%) was included as negative control and **PTX** (0.08  $\mu$ M) and **CA-4** (1.49  $\mu$ M) as positive controls. After removal of the supernatant, the cells were fixed with 4% of paraformaldehyde in phosphate-buffered saline 1 $\times$  (PBS) pH 7.4 for 1 h at 4 °C and permeabilized with 0.5% Triton X-100-SDS for 10 min. Nonspecific binding was blocked with 3% bovine serum albumin (BSA) in PBS for 1 h at 37 °C. Afterwards, treated cells were incubated with a monoclonal antibody anti-beta-tubulin (Sigma-Aldrich, T0198) diluted 1:1000 in PBS for 1 h at room temperature and washed three times with PBS; subsequently incubation with secondary anti-mouse-FITC antibody (Millipore, AP308F) diluted 1:500 and 4',6'-diamidino-2-phenylindole (DAPI) at 0.5  $\mu$ g/mL was carried out for 1 h at room temperature in the dark. The cover slips were washed three times with PBS and mounted on glass slides with Vectashield (Vector Laboratories). Images were acquired on a Nikon Ti Eclipse inverted confocal microscope equipped with an A1 imaging system. Imaging was performed using a 20 $\times$  (dry, NA = 0.8) objective lens. Excitation was performed sequentially using the laser lines provided by the manufacturer (403 nm—DAPI, 488 nm—FITC, brightfield) and the appropriate emission filters.

### 3.6. Cell Cycle Analysis

Cell cycle progression was monitored by flow cytometry using propidium iodide (PI, Sigma, St. Louis, MO, USA). For this, HeLa cells were treated for 48 h with compound **5** (0.16  $\mu$ M) and **CA-4** (1.49  $\mu$ M). Afterwards, cells were collected by centrifugation, washed with PBS, and fixed with ice-cold 75% ethanol. The fixed cells were harvested by centrifugation at 1400 rpm for 5 min and resuspended in 500  $\mu$ L of PBS, and treated with RNase A (100  $\mu$ g/mL, 30 min, 37 °C). After incubation, the cells were stained with PI at 10  $\mu$ g/mL at 37 °C for 30 min.

### 3.7. Western Blot Analysis of Soluble and Polymerized Tubulin in HeLa cells

HeLa cells ( $1.65 \times 10^6$  cells) cultured in DMEM medium complemented with FBS (10%) were seeded in 60 mm petri dishes and treated with compound **5** at 0.16  $\mu$ M for 24 h at 37 °C. **PTX** (0.08  $\mu$ M) and **CA-4** (1.49  $\mu$ M) were included as positive controls and DMSO (0.01%) as negative control. Soluble and polymerized tubulin were obtained as previously recommended [50]. To collect soluble fraction, cells were permeabilized with 300  $\mu$ L lysis buffer (80 mM Pipes-KOH (pH 6.8), 1 mM MgCl<sub>2</sub>, 1mM EGTA, 0.2% Triton X-100, 10% glycerol, 0.1% protease inhibitor cocktail (Sigma-Aldrich)) for 3 min at 30 °C. Afterwards, the soluble tubulin contained in the supernatant was gently removed. Polymerized tubulin (insoluble fraction) was obtained in the pellet with 200  $\mu$ L of Laemmli's buffer

(180 mM, Tris-HCl (pH 6.8), 6% SDS, 15% glycerol, 7.5%  $\beta$ -mercaptoethanol and 0.01% of bromophenol blue) which was heated for 3 min at 95 °C. Protein concentration was determined by 2-D Quant kit (GE Healthcare). Fractions containing soluble and polymerized tubulin were run on SDS-12% polyacrylamide gel for 1 h 30 min at 100 V and transferred to a nitrocellulose membrane (Bio-Rad, Hercules, CA, USA). The membrane was blocked with 3% BSA in PBS overnight at 4 °C and further incubated with an anti-beta-tubulin monoclonal antibody (Sigma-Aldrich, T0198) at 1:1000 dilution for 1 h 30 min at 37 °C. After this, the membrane was washed 3 $\times$  with PBS and incubated with goat anti-mouse IgG-horseradish peroxidase conjugated as secondary antibody (Millipore, AP308P) (1:1000 dilution) for 1 h 30 min at 37 °C (Merck Millipore, Burlington, MA, USA). Bands were revealed with 4-chloro-1-naphthol. Images were captured with a photodocumenter (UVITEC, Cambridge, UK) and intensity of each band was analyzed with Quantity One 4.6 software (Bio-Rad, Hercules, CA, USA).

### 3.8. Antioxidant Evaluation

#### 3.8.1. DPPH Assay

In a 96-well plate, 200  $\mu$ L of an ethanolic solution of DPPH (0.208 mM) and 100  $\mu$ L of the compound solution at different concentrations (10, 50, 100, 200, and 300  $\mu$ M) were added. Ethanol was used as a negative control, while Trolox was used as positive control. The plates were incubated for 30 min in dark. Finally, the DPPH discoloration was measured by absorbance in a microplate reader Epoch 2 (BioTek, Winooski, VT, USA) at 515 nm. The IC<sub>50</sub> values were calculated from the dose–response curve by non-linear fit [51].

#### 3.8.2. ABTS Assay

The determinations were carried out employing a slight modification of the previously reported method [52]. Briefly, stock solutions of ABTS at 7 mM and potassium persulfate at 2.45 mM were mixed in equal proportions. The resulted solution was stored for 12 h at room temperature in dark. Then, in a 96-well plate, 20  $\mu$ L of the compound solution (at concentrations of 10, 50, 100, 200 and 300  $\mu$ M) and 180  $\mu$ L the reactive solution were added. Ethanol was used as a negative control, while Trolox was used as positive control. Plates were incubated for 10 min in dark. Then, the absorbance was measured in a microplate reader Epoch 2 (BioTek, Winooski, VT, USA) at 734 nm. The IC<sub>50</sub> values were calculated from the dose–response curve by non-linear fit [51].

## 4. Conclusions

Two hybrid compounds of **CA-4** and 2,3-diphenyl-2*H*-indazole (**5** and **6**) and seven related derivatives were synthesized with microwave assisted chemistry showing short reaction times and good yields. The seven derivative compounds were designed and synthesized to gain knowledge about the importance of different substituents on the cytotoxic activity. Biological evaluation revealed that hybrid compounds **5** and **6** have strong cytotoxic activity against HeLa, SK-LU-1, and K562 cancer cell lines. The 3,4,5-trimethoxyphenyl and 4-methoxy-3-hydroxyphenyl groups at positions 2 and 3 of the indazole nucleus were essential to the observed cytotoxic effect, at least on the three cell lines tested. Compound **5** possess the best cytotoxic effect on HeLa, SK-LU-1, and K562 cell lines as compared with **4** and **6**. Additionally, its cytotoxic effect is greater than the reference drug cisplatin against HeLa and SK-LU-1 cells and similar in potency than the reference drug imatinib against K562 cells. Molecular docking studies and in vitro tubulin polymerization assay strongly suggest tubulin as a molecular target for compound **5**; however, an additional action mechanism for compound **5** can be also involved. Taken altogether, data demonstrated that compound **5** is a potent agent that induces G<sub>2</sub>/M arrest via disrupting the microtubule network that deserves further research and, importantly, it provides information for exploring new **CA-4** analogues.

**Supplementary Materials:** The following are available online at <https://www.mdpi.com/article/10.3390/ph14080815/s1>, Table S1: Palladium-catalyzed arylation of 3-bromophenylindazoles and microwave assisted modification, Table S2: Cellular viability  $\pm$  SE on HeLa cell line upon treatment with compounds 1–9 at 50  $\mu$ M, Table S3: Antioxidant activity (IC<sub>50</sub> [ $\mu$ M]) of compounds 4–6 employing DPPH and ABTS assays, Table S4: Purity of compounds 4, 5, and 6 by qNMR used an internal standard (%purity, mean  $\pm$  standard deviation), Figures S1–S29: <sup>1</sup>H NMR; <sup>13</sup>C NMR, and MS spectra for synthesized compounds, Figure S30: Morphological changes of HeLa cells after 48 h of treatment, Figure S31: Quantitative apoptosis assay of HeLa using Annexin V-FITC/Ghost-Red.

**Author Contributions:** Conceptualization, J.P.-V., L.Y.-M.; funding acquisition, J.P.-V., L.Y.-M.; investigation, J.P.-V., F.M.-M., M.L.-L., K.R.-V., F.C.-B., A.P.M.-J., A.R.-V. and J.F.P.-E.; methodology, J.P.-V., F.M.-M., L.Y.-M., V.P.-K. and O.S.-A.; project administration, J.P.-V.; resources, J.P.-V. and O.S.-A.; supervision, J.P.-V., L.Y.-M., V.P.-K., F.C.-B., I.G.-S., J.F.P.-E. and O.S.-A.; writing—original draft, J.P.-V.; writing—review and editing, F.M.-M., L.Y.-M., V.P.-K., M.L.-L., K.R.-V., F.C.-B., J.F.P.-E. and O.S.-A. All authors have read and agreed to the published version of the manuscript.

**Funding:** This research was funded by Secretaría de Educación Pública (SEP), grant number UAM-X-CA-114 (apoyo al fortalecimiento de cuerpos académicos), Consejo Nacional de Ciencia y Tecnología, grant number 1238 (cátedras CONACyT) and 317036 (Fortalecimiento y Mantenimiento de Infraestructuras de Investigación de Uso Común y Capacitación Técnica CONACyT).

**Institutional Review Board Statement:** Not applicable.

**Informed Consent Statement:** Not applicable.

**Data Availability Statement:** Data is contained within the article and supplementary material.

**Acknowledgments:** F.M.-M. acknowledges CONACyT for the postdoctoral fellowship. The authors would like to express their sincere gratitude to Ernesto Sánchez Mendoza, Mónica A. Rincón, and Miguel Cortés Gines for the analytical support; and to Pharmometrica research center for the support with mass spectra determinations. The authors also acknowledge for the free access software and web servers employed in this work: The Scripps Research Institute for providing AutoDock Tools 1.7.1. and Autodock 4.2, the Resource for Biocomputing, Visualization, and Informatics (RBVI) for providing Chimera (Chimera is developed by the RBVI at the UCSF supported by NIGMS P41-GM103311), BIOVIA for providing Discovery Studio Visualizer 2016, and to YASARA Biosciences GmbH for providing the YASARA Energy Minimization server.

**Conflicts of Interest:** The authors declare no conflict of interest.

## References

1. National Cancer Institute. What Is Cancer? Available online: <https://training.seer.cancer.gov/disease/cancer/review.html> (accessed on 26 March 2021).
2. WHO (World Health Organization). Available online: <http://www.who.int/cancer/en/> (accessed on 7 November 2020).
3. Mansoori, B.; Mohammadi, A.; Davudian, S.; Shirjang, S.; Baradaran, B. The Different Mechanisms of Cancer Drug Resistance: A Brief Review. *Adv. Pharm. Bull.* **2017**, *7*, 339–348. [CrossRef] [PubMed]
4. Thangadurai, A.; Minu, M.; Wakode, S.; Agrawal, S.; Narasimhan, B. Indazole: A medicinally important heterocyclic moiety. *Med. Chem. Res.* **2011**, *21*, 1509–1523. [CrossRef]
5. Gaikwad, D.D.; Chapolikar, A.D.; Devkate, C.G.; Warad, K.D.; Tayade, A.P.; Pawar, R.P.; Domb, A.J. Synthesis of indazole motifs and their medicinal importance: An overview. *Eur. J. Med. Chem.* **2015**, *90*, 707–731. [CrossRef] [PubMed]
6. Dong, J.; Zhang, Q.; Wang, Z.; Huang, G.; Li, S. Recent Advances in the Development of Indazole-based Anticancer Agents. *ChemMedChem* **2018**, *13*, 1490–1507. [CrossRef] [PubMed]
7. Zhang, S.-G.; Liang, C.-G.; Zhang, W.-H. Recent Advances in Indazole-Containing Derivatives: Synthesis and Biological Perspectives. *Molecules* **2018**, *23*, 2783. [CrossRef]
8. Pérez-Villanueva, J.; Yépez-Mulía, L.; González-Sánchez, I.; Palacios-Espinosa, J.F.; Soria-Arteche, O.; Sainz-Espuñes, T.D.R.; Cerbón, M.A.; Rodríguez-Villar, K.; Rodríguez-Vicente, A.K.; Cortés-Gines, M.; et al. Synthesis and Biological Evaluation of 2H-Indazole Derivatives: Towards Antimicrobial and Anti-Inflammatory Dual Agents. *Molecules* **2017**, *22*, 1864. [CrossRef] [PubMed]
9. Lu, Y.; Chen, J.; Xiao, M.; Li, W.; Miller, D.D. An Overview of Tubulin Inhibitors That Interact with the Colchicine Binding Site. *Pharm. Res.* **2012**, *29*, 2943–2971. [CrossRef] [PubMed]
10. Tron, G.C.; Pirali, T.; Sorba, G.; Pagliai, F.; Busacca, A.S.; Genazzani, A. Medicinal Chemistry of Combretastatin A4: Present and Future Directions. *J. Med. Chem.* **2006**, *49*, 3033–3044. [CrossRef]
11. Cadogan, J.I.G.; Mackie, R.K. 2-Phenylindazole. *Org. Synth.* **1968**, *48*, 113.

12. Waalwijk, P.S.; Cohen-Fernandes, P.; Habraken, C.L. Indazole studies. 3. The bromination of 2-phenyl-2H-indazole. Formation and structure determination of mono-, di-, and tribromo-2-phenyl-2H-indazoles. *J. Org. Chem.* **1984**, *49*, 3401–3403. [CrossRef]
13. Huff, B.E.; Koenig, T.M.; Mitchell, D.; Staszak, M.A. Synthesis of unsymmetrical biaryls using a modified Suzuki cross-coupling: 4-Biphenylcarboxaldehyde. ([1,1'-Biphenyl]-4-carboxaldehyde). *Org. Synth.* **2004**, *10*, 102.
14. Wehbe, H.; Kearney, C.M.; Pinney, K.G. Combretastatin A-4 resistance in H460 human lung carcinoma demonstrates distinctive alterations in beta-tubulin isotype expression. *Anticancer. Res.* **2005**, *25*, 3865–3870. [PubMed]
15. Duan, Y.-T.; Man, R.-J.; Tang, D.-J.; Yao, Y.-F.; Tao, X.-X.; Yu, C.; Liang, X.-Y.; Makawana, J.A.; Zou, M.-J.; Wang, Z.-C.; et al. Design, Synthesis and Antitumor Activity of Novel link-bridge and B-Ring Modified Combretastatin A-4 (CA-4) Analogues as Potent Antitubulin Agents. *Sci. Rep.* **2016**, *6*, 25387. [CrossRef]
16. Ma, M.; Sun, L.; Lou, H.; Ji, M. Synthesis and biological evaluation of Combretastatin A-4 derivatives containing a 3'-O-substituted carbonic ether moiety as potential antitumor agents. *Chem. Central J.* **2013**, *7*, 179. [CrossRef]
17. Greene, L.M.; Nathwani, S.M.; Bright, S.A.; Fayne, D.; Croke, A.; Gagliardi, M.; McElligott, A.; O'Connor, L.; Carr, M.; Keely, N.O.; et al. The Vascular Targeting Agent Combretastatin-A4 and a Novel cis-Restricted  $\beta$ -Lactam Analogue, CA-432, Induce Apoptosis in Human Chronic Myeloid Leukemia Cells and Ex Vivo Patient Samples Including Those Displaying Multidrug Resistance. *J. Pharmacol. Exp. Ther.* **2010**, *335*, 302–313. [CrossRef] [PubMed]
18. Seddigi, Z.S.; Malik, M.S.; Saraswati, A.P.; Ahmed, S.A.; Babalghith, A.O.; Lamfon, H.A.; Kamal, A. Recent advances in combretastatin based derivatives and prodrugs as antimitotic agents. *MedChemComm* **2017**, *8*, 1592–1603. [CrossRef] [PubMed]
19. Dasari, S.; Tchounwou, P.B. Cisplatin in cancer therapy: Molecular mechanisms of action. *Eur. J. Pharmacol.* **2014**, *740*, 364–378. [CrossRef] [PubMed]
20. Moen, M.D.; McKeage, K.; Plosker, G.L.; Siddiqui, M.A. Imatinib: A review of its use in chronic myeloid leukaemia. *Drugs* **2007**, *67*, 299–320. [CrossRef]
21. Gaulton, A.; Bellis, L.; Bento, A.P.S.F.F.; Chambers, J.; Davies, M.; Hersey, A.; Light, Y.; McGlinchey, S.; Michalovich, D.; Al-Lazikani, B.; et al. ChEMBL: A large-scale bioactivity database for drug discovery. *Nucleic Acids Res.* **2011**, *40*, D1100–D1107. [CrossRef]
22. Bruggisser, R.; von Daeniken, K.; Jundt, G.; Schaffner, W.; Tullberg-Reinert, H. Interference of Plant Extracts, Phytoestrogens and Antioxidants with the MTT Tetrazolium Assay. *Planta Med.* **2002**, *68*, 445–448. [CrossRef]
23. Wang, P.; Henning, S.M.; Heber, D. Limitations of MTT and MTS-Based Assays for Measurement of Antiproliferative Activity of Green Tea Polyphenols. *PLoS ONE* **2010**, *5*, e10202. [CrossRef]
24. Morris, G.; Huey, R.; Lindstrom, W.; Sanner, M.F.; Belew, R.K.; Goodsell, D.S.; Olson, A.J. AutoDock4 and AutoDockTools4: Automated docking with selective receptor flexibility. *J. Comput. Chem.* **2009**, *30*, 2785–2791. [CrossRef]
25. Gaspari, R.; Protá, A.E.; Bargsten, K.; Cavalli, A.; Steinmetz, M.O. Structural Basis of cis- and trans-Combretastatin Binding to Tubulin. *Chem* **2017**, *2*, 102–113. [CrossRef]
26. Cytoskeleton Inc. Tubulin Polymerization Assay Using >99% Pure Tubulin, od Based—Porcine (BK006P). Manual: Tubulin Polymerization Assay Kit. Available online: <https://www.cytoskeleton.com/bk006p> (accessed on 26 March 2021).
27. Shelanski, M.L.; Gaskin, F.; Cantor, C.R. Microtubule Assembly in the Absence of Added Nucleotides. *Proc. Natl. Acad. Sci. USA* **1973**, *70*, 765–768. [CrossRef]
28. Lee, J.C.; Timasheff, S.N. In Vitro Reconstitution of Calf Brain Microtubules: Effects of Solution Variables. *Biochemistry* **1977**, *16*, 1754–1764. [CrossRef] [PubMed]
29. Romagnoli, R.; Baraldi, P.G.; Brancale, A.; Ricci, A.; Hamel, E.; Bortolozzi, R.; Basso, G.; Viola, G. Convergent synthesis and biological evaluation of 2-amino-4-(3',4',5'-trimethoxyphenyl)-5-aryl thiazoles as microtubule targeting agents. *J. Med. Chem.* **2011**, *54*, 5144–5153. [CrossRef] [PubMed]
30. Liang, W.; Lai, Y.; Zhu, M.; Huang, S.; Feng, W.; Gu, X. Combretastatin A4 Regulates Proliferation, Migration, Invasion, and Apoptosis of Thyroid Cancer Cells via PI3K/Akt Signaling Pathway. *Med. Sci. Monit.* **2016**, *22*, 4911–4917. [CrossRef] [PubMed]
31. Zhu, H.; Zhang, J.; Xue, N.; Hu, Y.; Yang, B.; He, Q. Novel combretastatin A-4 derivative XN0502 induces cell cycle arrest and apoptosis in A549 cells. *Investig. N. Drugs* **2010**, *28*, 493–501. [CrossRef] [PubMed]
32. Kanthou, C.; Greco, O.; Stratford, A.; Cook, I.; Knight, R.; Benzakour, O.; Tozer, G. The Tubulin-Binding Agent Combretastatin A-4-Phosphate Arrests Endothelial Cells in Mitosis and Induces Mitotic Cell Death. *Am. J. Pathol.* **2004**, *165*, 1401–1411. [CrossRef]
33. Zacharaki, P.; Stephanou, G.; Demopoulos, N.A. Comparison of the aneugenic properties of nocodazole, paclitaxel and griseofulvin in vitro. Centrosome defects and alterations in protein expression profiles. *J. Appl. Toxicol.* **2012**, *33*, 869–879. [CrossRef] [PubMed]
34. Sun, Y.; Lin, X.; Chang, H. Proliferation inhibition and apoptosis of breast cancer MCF-7 cells under the influence of colchicine. *J. BUON Off. J. Balk. Union Oncol.* **2016**, *21*, 570–575.
35. Ibrahim, T.S.; Hawwas, M.M.; Malebari, A.M.; Taher, E.S.; Omar, A.M.; Neamatallah, T.; Abdel-Samii, Z.K.; Safo, M.K.; Elshaier, Y.A.M.M. Discovery of novel quinoline-based analogues of combretastatin A-4 as tubulin polymerisation inhibitors with apoptosis inducing activity and potent anticancer effect. *J. Enzym. Inhib. Med. Chem.* **2021**, *36*, 802–818. [CrossRef] [PubMed]
36. Fang, Y.; Wu, C.; LaRock, R.C.; Shi, F. Synthesis of 2H-Indazoles by the [3 + 2] Dipolar Cycloaddition of Sydnone with Arynes. *J. Org. Chem.* **2011**, *76*, 8840–8851. [CrossRef]
37. Vidyacharan, S.; Sagar, A.; Chaitra, N.C.; Sharada, D.S. A facile synthesis of 2H-indazoles under neat conditions and further transformation into aza- $\gamma$ -carboline alkaloid analogues in a tandem one-pot fashion. *RSC Adv.* **2014**, *4*, 34232–34236. [CrossRef]

38. Ohnmacht, S.A.; Culshaw, A.J.; Greaney, M.F. Direct Arylations of 2H-Indazoles On Water. *Org. Lett.* **2009**, *12*, 224–226. [CrossRef]
39. Croce, P.D.; La Rosa, C. A Convenient synthesis of indazoles. *Synthesis* **1984**, *1984*, 982–983. [CrossRef]
40. Jin, T.; Yamamoto, Y. An Efficient, Facile, and General Synthesis of 1H-Indazoles by 1,3-Dipolar Cycloaddition of Arynes with Diazomethane Derivatives. *Angew. Chem. Int. Ed.* **2007**, *46*, 3323–3325. [CrossRef]
41. Quintero, A.; Pelcastre, A.; Solano, J.D. Antitumoral activity of new pyrimidine derivatives of sesquiterpene lactones. *J. Pharm. Sci.* **1999**, *2*, 108–112.
42. Loza-Mejía, M.A.; Olvera-Vázquez, S.; Maldonado-Hernández, K.; Guadarrama-Salgado, T.; González-Sánchez, I.; Rodríguez-Hernández, F.; Solano, J.D.; Rodríguez-Sotres, R.; Lira-Rocha, A. Synthesis, cytotoxic activity, DNA topoisomerase-II inhibition, molecular modeling and structure–activity relationship of 9-anilinothiazolo[5,4-b]quinoline derivatives. *Bioorg. Med. Chem.* **2009**, *17*, 3266–3277. [CrossRef]
43. Berman, H.; Henrick, K.; Nakamura, H. Announcing the worldwide Protein Data Bank. *Nat. Struct. Mol. Biol.* **2003**, *10*, 980. [CrossRef] [PubMed]
44. Berman, H.M.; Westbrook, J.D.; Feng, Z.; Gilliland, G.; Bhat, T.N.; Weissig, H.; Shindyalov, I.N.; Bourne, P.E. The Protein Data Bank. *Nucleic Acids Res.* **2000**, *28*, 235–242. [CrossRef] [PubMed]
45. Krieger, E.; Joo, K.; Lee, J.; Lee, J.; Raman, S.; Thompson, J.; Tyka, M.; Baker, D.; Karplus, K. Improving physical realism, stereochemistry, and side-chain accuracy in homology modeling: Four approaches that performed well in CASP8. *Proteins Struct. Funct. Bioinform.* **2009**, *77*, 114–122. [CrossRef] [PubMed]
46. Irwin, J.; Shoichet, B.K. ZINC—A Free Database of Commercially Available Compounds for Virtual Screening. *J. Chem. Inf. Model.* **2004**, *45*, 177–182. [CrossRef]
47. Frisch, M.J.T.G.W.; Schlegel, H.B.; Scuseria, G.E.; Robb, M.A.; Cheeseman, J.R.; Scalmani, G.; Barone, V.; Mennucci, B.; Petersson, G.A.; Nakatsuji, H.; et al. *Gaussian 09*; Revision E.01; Gaussian Inc.: Wallingford, CT, USA, 2009.
48. *Dassault Systèmes BIOVIA Discovery Studio*; Version 17.2.0.16349; Dassault Systemes: San Diego, CA, USA, 2016.
49. Pettersen, E.F.; Goddard, T.D.; Huang, C.C.; Couch, G.S.; Greenblatt, D.M.; Meng, E.C.; Ferrin, T.E. UCSF Chimera—A visualization system for exploratory research and analysis. *J. Comput. Chem.* **2004**, *25*, 1605–1612. [CrossRef] [PubMed]
50. Kamal, A.; Shaik, A.B.; Polepalli, S.; Reddy, V.S.; Kumar, G.B.; Gupta, S.; Krishna, K.V.S.R.; Nagabhushana, A.; Mishra, R.K.; Jain, N. Pyrazole–Oxadiazole conjugates: Synthesis, antiproliferative activity and inhibition of tubulin polymerization. *Org. Biomol. Chem.* **2014**, *12*, 7993–8007. [CrossRef]
51. Palacios-Espinosa, J.F.; Arroyo-García, O.; García-Valencia, G.; Linares, E.; Bye, R.; Romero, I. Evidence of the anti-*Helicobacter pylori*, gastroprotective and anti-inflammatory activities of *Cuphea aequipetala* infusion. *J. Ethnopharmacol.* **2014**, *151*, 990–998. [CrossRef] [PubMed]
52. Thaipong, K.; Boonprakob, U.; Crosby, K.; Cisneros-Zevallos, L.; Byrne, D.H. Comparison of ABTS, DPPH, FRAP, and ORAC assays for estimating antioxidant activity from guava fruit extracts. *J. Food Compos. Anal.* **2006**, *19*, 669–675. [CrossRef]







## Article

# Exploration of Benzenesulfonamide-Bearing Imidazole Derivatives Activity in Triple-Negative Breast Cancer and Melanoma 2D and 3D Cell Cultures

Benas Balandis <sup>1</sup>, Vytautas Mickevičius <sup>1,\*</sup> and Vilma Petrikaitė <sup>2,3</sup>

<sup>1</sup> Department of Organic Chemistry, Kaunas University of Technology, Radvilėnų pl. 19, LT-50254 Kaunas, Lithuania; benas.balandis@ktu.lt

<sup>2</sup> Laboratory of Drug Targets Histopathology, Institute of Cardiology, Lithuanian University of Health Sciences, Sukilėlių pr. 13, LT-50162 Kaunas, Lithuania; vilmapetrikaite@gmail.com

<sup>3</sup> Institute of Physiology and Pharmacology, Faculty of Medicine, Lithuanian University of Health Sciences, A. Mickevičiaus g. 9, LT-44307 Kaunas, Lithuania

\* Correspondence: vytautas.mickevicius@ktu.lt; Tel.: +370-69940928

**Abstract:** Heterocyclic compounds are one of the main groups of organic compounds possessing wide range of applications in various areas of science and their derivatives are present in many bioactive structures. They display a wide variety of biological activities. Recently, more and more attention has been focused to such heterocyclic compounds as azoles. In this work, we have synthesized a series of new imidazole derivatives incorporating a benzenesulfonamide moiety in their structure, which then were evaluated for their cytotoxicity against human triple-negative breast cancer MDA-MB-231 and human malignant melanoma IGR39 cell lines by MTT assay. Benzenesulfonamide-bearing imidazole derivatives containing 4-chloro and 3,4-dichlorosubstituents in benzene ring, and 2-ethylthio and 3-ethyl groups in imidazole ring have been determined as the most active compounds. Half-maximal effective concentration (EC<sub>50</sub>) of the most cytotoxic compound was 27.8 ± 2.8 μM against IGR39 cell line and 20.5 ± 3.6 μM against MDA-MB-231 cell line. Compounds reduced cell colony formation of both cell lines and inhibited the growth and viability of IGR39 cell spheroids more efficiently compared to triple-negative breast cancer spheroids.

**Keywords:** benzenesulfonamides; imidazoles; alkylated; anticancer activity; colony formation; tumor spheroids

**Citation:** Balandis, B.; Mickevičius, V.; Petrikaitė, V. Exploration of Benzenesulfonamide-Bearing Imidazole Derivatives Activity in Triple-Negative Breast Cancer and Melanoma 2D and 3D Cell Cultures. *Pharmaceuticals* **2021**, *14*, 1158. <https://doi.org/10.3390/ph14111158>

Academic Editors: Mary J. Meegan and Niamh M O'Boyle

Received: 26 October 2021

Accepted: 10 November 2021

Published: 13 November 2021

**Publisher's Note:** MDPI stays neutral with regard to jurisdictional claims in published maps and institutional affiliations.



**Copyright:** © 2021 by the authors. Licensee MDPI, Basel, Switzerland. This article is an open access article distributed under the terms and conditions of the Creative Commons Attribution (CC BY) license (<https://creativecommons.org/licenses/by/4.0/>).

## 1. Introduction

After huge breakthrough in pharmaceutical chemistry in early twentieth century, treating more and more previously incurable or difficult-to-treat diseases has become common practice in doctor's offices nowadays. Research and synthesis of various functionalized heterocycle compounds have contributed significantly to this progress. Heterocycles are one of the largest classical divisions in organic chemistry and they play important role in modern drug design due to their wide range of biological properties [1]. A lot of marketed drugs contains aromatic or saturated, fused or spirocyclic heterocyclic moieties. The heteroatoms can provide potential binding interactions to the target and the cyclic nature limits structural flexibility, thus reducing the entropic penalty of binding [2]. Imidazole derivatives showed a wide scope of applicability in medicinal chemistry in recent years. Molecules bearing an imidazole moiety have become a promising antifungal [3], antibacterial [4,5], anti-tuberculosis [6], and anti-inflammatory [7] agents. However, oncological diseases remain a major threat to the society due to their mutagenic and insidious nature [8,9]. Thus, there is an urgent need to develop new anticancer agents to combat these illnesses. Recently, imidazole derivatives gained a lot of interest in the development of lead molecules and drug candidates for cancer treatment [10–12]. For instance, newly designed trans-restricted analogues of resveratrol were synthesized in which the C–C double bond of the natural

derivative has been replaced by 1,4-diaryl-substituted imidazole analogues [13]. One of the resveratrol analogues (Figure 1) showed very high cytotoxic activity and potency against NCI-60 tumor cells. Furthermore, a study was conducted, in which phenylmethimazole was tested against triple negative breast cancer cells MDA-MB-231, Hs578T, MDA-MB-468 (Figure 1) [14]. This research showed that phenylmethimazole significantly inhibited interleukin 6 (IL-6) expression by MDA-MB-231 and other triple-negative breast cancer (TNBC) cell lines.

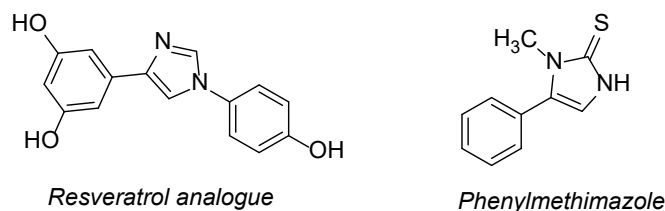


**Figure 1.** Imidazole molecules.

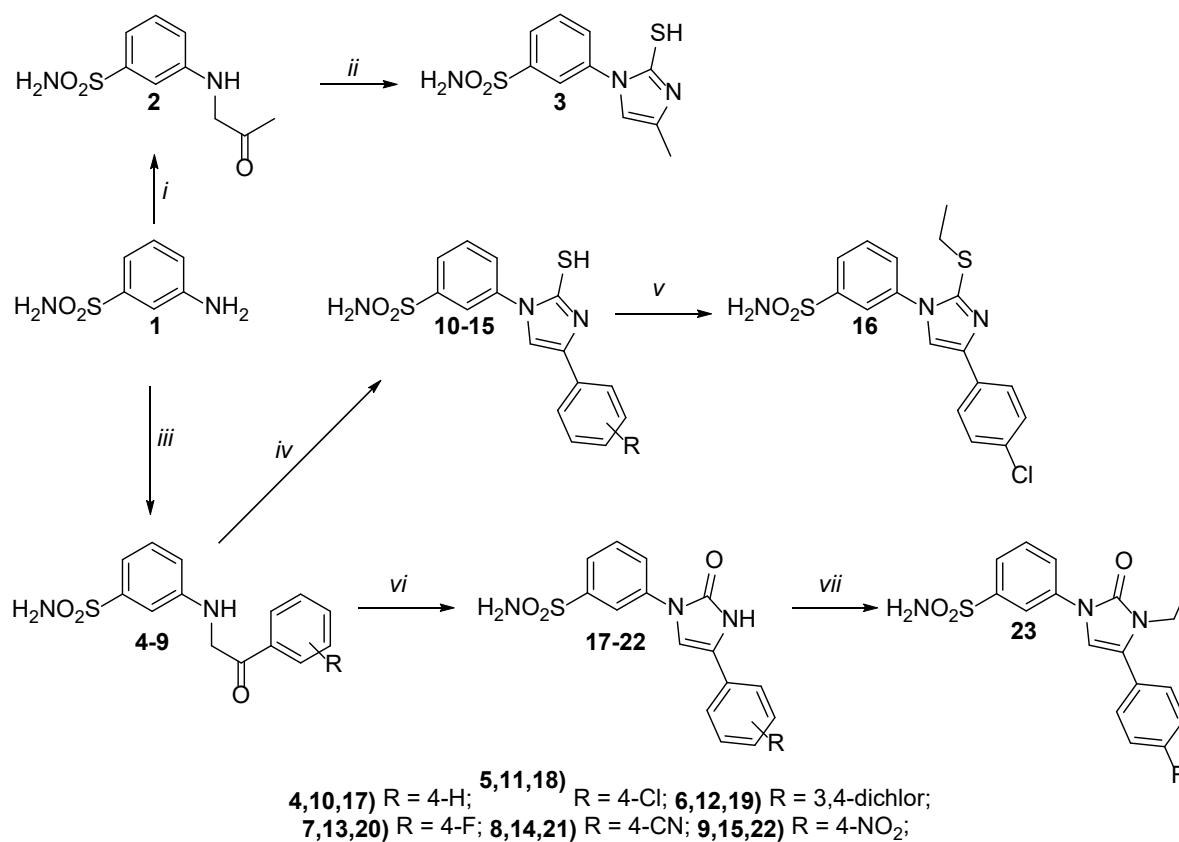
Therefore, based on recent studies, benzenesulfonamide-bearing imidazole derivatives were synthesized in this work. Two cancer cell lines, namely TNBC cell line MDA-MB-231 and human melanoma cell line IGR39 were selected to test cytotoxic activity and compound effect on cell colony-forming ability. Both cancer types are considered very aggressive and have a low survival prognosis. Resistance to drugs occurs quite often in the case of melanoma treatment with targeted therapeutics, due to BRAF mutations [15]. More than half of patients with TNBC at an early stage have a recurrence of the disease, and about 40% of them die within the first 5 years [16]. We decided to explore synthesized compounds in clonogenic assay, which shows a single cell ability to grow into a colony [17] and mimics the cell ability to survive and proliferate after chemotherapy. We also tested novel compound effect on cancer cell spheroid (three-dimensional cultures) growth, as this model much better represents the real spatial connections between cells found in real tumor, compared to monolayers cell cultures [18,19]. As a continuation of our interest in further search for the nitrogen-containing heterocyclic molecules possessing biological activity [20–22], we report the synthesis of a series of compounds bearing benzenesulfonamide and imidazole moieties, and evaluation of their anticancer activity.

## 2. Results and Discussion

### 2.1. Chemistry

The 3-((2-oxopropyl)amino)benzenesulfonamide (**2**) was prepared in the reaction of amine **1** with 1-chloropropanone in small amount of water at reflux (Scheme 1). The structures of **2** and all other compounds have been confirmed by the data of FT-IR,  $^1\text{H}$  and  $^{13}\text{C}$  NMR spectroscopy as well as elemental analysis data. Later, compound **2** has been cyclized to imidazolethiol **3** during the reaction with KSCN in glacial acetic acid in a presence of HCl as a catalyst. In a  $^1\text{H}$  NMR spectrum of compound **3**, the singlets assigned to the protons in the CH group at 8.20 ppm and in the SH group at 12.39 ppm have proven the presence of 1*H*-imidazolethiol moiety in the molecule. It is widely known that similar thiolamides can exist in their thione/thiol forms due to ongoing tautomerism [23]. However, the carbon attributed to the C-SH group resonated at 161.29 ppm in the  $^{13}\text{C}$  NMR spectrum, which shows, that in this case, compound **3** exists as thiol in DMSO- $d_6$  solution [24]. Moreover, in FT-IR spectrum, absorption at  $2664\text{ cm}^{-1}$  was attributed to S-H bond stretching, which shows that thiol form is also predominant in the crystal. Furthermore, 3-aminobenzenesulfonamide (**1**) was treated with various  $\alpha$ -haloketones in water/1,4-dioxane solution to obtain compounds **4–9**, which were later used as precursors for synthesis of corresponding imidazoles **10–15** in similar reaction conditions as were in product **3** synthesis (Scheme 1) [25]. We also found out, that these imidazole derivatives **10–15** (or the rest in this work) can be purified without using any organic solvents. For purification, these imidazole derivatives can be dissolved into 5% sodium hydroxide

aqueous solution instead. Then, after filtration, the acidification of the obtained solution with glacial acetic acid will provide purer forms of the desired products without any significant loss to the purified amount of it. We also wanted to modify some of the pharmacokinetic properties of 1*H*-imidazole derivatives **10–15** to see, how it would affect the cancer cells. We decided to perform S-alkylation of 1*H*-imidazole **11** to reach higher solubility in organic solvents and lipophilicity. As a result, in the first attempt, imidazole **11** was treated with ethyl iodide in DMF overnight to obtain compound **16**. In a <sup>1</sup>H NMR spectrum for **16**, the triplet assigned to the protons in the CH<sub>3</sub> group at 1.30 ppm and quartet assigned to the protons in the CH<sub>2</sub> group at 3.15 ppm have proved the presence of ethyl moiety in the molecule. Elemental analysis data of **16** confirmed that imidazole **16** did not form hydroiodide salt. Moreover, to increase reaction rate, we used triethylamine as a base catalyst, which shortened the reaction time to 3 h.



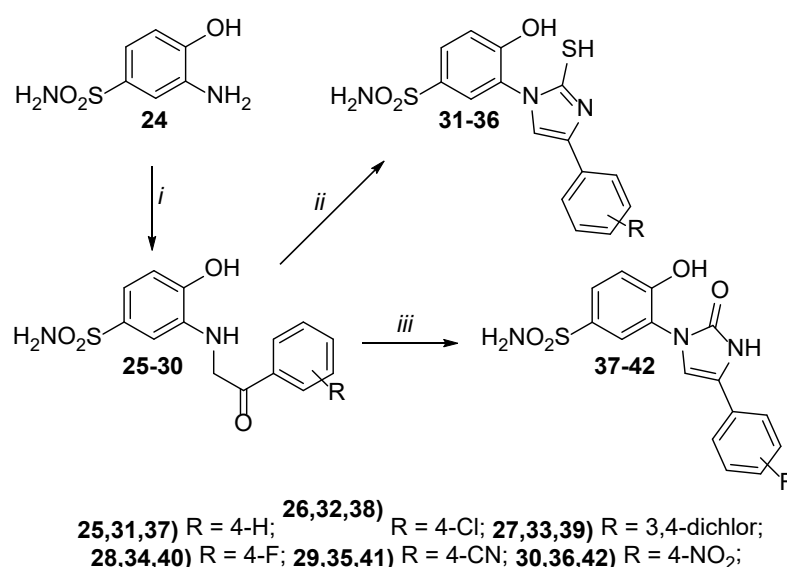
Reaction conditions: i) 1-chloropropanone, water, reflux, 4 h; ii) KSCN, HCl, glacial acetic acid, reflux, 4h; iii) corresponding  $\alpha$ -haloketone, water, 1,4-dioxane, reflux, 2h; iv) KSCN, HCl, glacial acetic acid, reflux, 4h; v) ethyl iodide, TEA, DMF, r.t, 3h; vi) urea, glacial acetic acid, reflux, 12h; vii) ethyl iodide, TEA, DMF, r.t, 10h;

**Scheme 1.** Synthesis of compounds 2–23.

Furthermore, compounds **4–9** were dissolved in glacial acetic acid and treated with urea to afford oxoimidazoles **17–22** (Scheme 1). For instance, in a <sup>1</sup>H NMR spectrum for **17**, the singlet was assigned to the proton of the NH group at 11.23 ppm. The resonances in <sup>13</sup>C NMR spectrum at 106.27 ppm and 152.34 were attributed to CH or C=O groups respectively, which have proven the presence of oxoimidazole moiety in the molecule. In addition, typical absorption of C=O bond stretching is also present in the FT-IR spectrum of compound **17** at 1703 cm<sup>-1</sup>. Similar results were also observed analyzing compounds **18–22** NMR spectra. Keto tautomer form was also justified after the reaction of imidazole **20** with ethyl iodide in DMF at room temperature. In the presence of triethylamine as base catalyst, after 10 h compound **23** was obtained. In a <sup>1</sup>H NMR spectrum for **23**, the triplet

at 1.30 ppm was assigned to the protons in the CH<sub>3</sub> group and quartet at 3.14 ppm was assigned to the protons in the CH<sub>2</sub> group to confirm that an alkylation of compound **20** was successful. However, in <sup>13</sup>C NMR spectrum, the carbon attributed to the N-CH<sub>2</sub> group resonated at 27.56 ppm. The chemical shift of this carbon atom was observed more towards the high field, than O-CH<sub>2</sub> groups carbon would have resonated [26]. This confirms that N-alkylation occurred during the alkylation of imidazole **23**.

3-Amino-4-hydroxybenzenesulfonamide (**24**) was used in reactions with α-haloketones in water/1,4-dioxane mixture to obtain precursors **25–30** for further synthesis of imidazoles **31–36** (Scheme 2). Compounds **25–30** were treated with potassium thiocyanate and HCl in glacial acetic acid to afford 2-mercaptimidazoles **31–36**. For instance, in <sup>1</sup>H NMR spectrum for **31**, the singlets at 10.89 ppm and 12.92 ppm were assigned to the protons in the OH at SH groups, respectively. In the <sup>13</sup>C NMR spectrum for **31**, carbon attributed to the C-SH group resonated at 163.65 ppm. Furthermore, 2-oxo-1*H*-imidazoles **37–42** were obtained during the corresponding reactions between compounds **25–30** and urea in glacial acetic acid (Scheme 2). In a <sup>1</sup>H NMR spectrum for **37**, the singlets were assigned to the protons in the OH group at 10.84 ppm and in the NH group at 11.11 ppm. Moreover, the resonances in <sup>13</sup>C NMR spectrum at 109.71 ppm and 154.82 was attributed to CH and C=O groups respectively, which have proven the presence of 2-oxoimidazole moiety in the molecule.



Reaction conditions: *i*) corresponding α-haloketone, water, 1,4-dioxane, reflux, 2h; *ii*) KSCN, HCl, glacial acetic acid, reflux, 4h; *iii*) urea, glacial acetic acid, reflux, 12h;

**Scheme 2.** Synthesis of compounds **25–42**.

## 2.2. Anticancer Activity

Tested imidazole derivatives showed different activity against human triple-negative breast cancer and human melanoma cell lines at 100 μM concentration (Figure 2). Almost half of compounds were more active against MDA-MB-231 cell line, and eight compounds showed higher cytotoxicity against IGR39 cell line. Other compounds possessed a similar activity against both types of cancer cells. More active compounds (**5**, **8**, **12**, **16**, **18**, **19**, **23**), that reduced cell viability below 50%, have been identified between non-hydroxylated compounds, especially with imidazolone fragment. 4-Hydroxybenzenesulfonamide derivatives with thioimidazole ring (compounds **31–36**) were practically inactive against both tested cell lines. It is worthy to notice, that the most active compounds in separate groups contained either 4-chloro (**5**, **18**, **26**, **38**) or 3,4-dichloro (**12**, **19**, **27**, **39**) substituents. The least active compounds were those containing cyano group in phenyl ring (the only active compound was **8**). Two compounds (**23** and **16**) contain 2-ethylthio and 3-ethyl substituents in

imidazole ring, which could contribute to their high anticancer activity, and the importance of this fragment in this position could be of great interest in the future research.

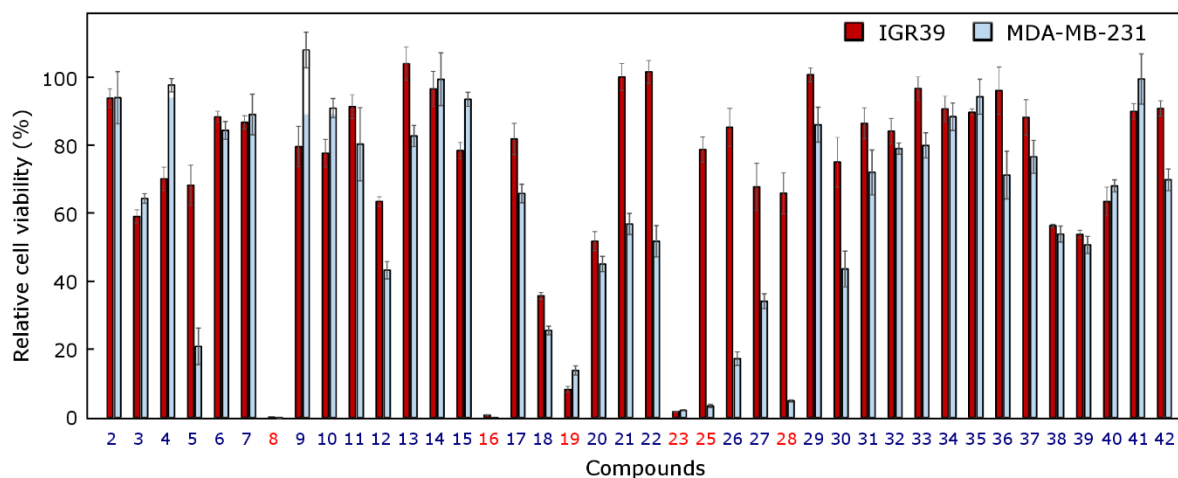


**Figure 2.** Effect of tested compounds on cancer cell viability at 100  $\mu\text{M}$  concentration after 72 h of incubation,  $n = 3$ . Experiments were repeated three times, calculating the mean and standard deviation. The number of the most active compounds selected for further experiments are shown in red.

The most active compounds were imidazole derivatives **8**, **16**, **19**, **23**, **25**, and **28**, which reduced cell viability of at least one cell line below 10%, and they were then tested more thoroughly both against human cancer cell lines and normal cells lines (fibroblasts (HF) and endothelial cells (EC)). The effective concentrations that reduce cell viability by 50% ( $\text{EC}_{50}$  values) have been established (Figure 3A).

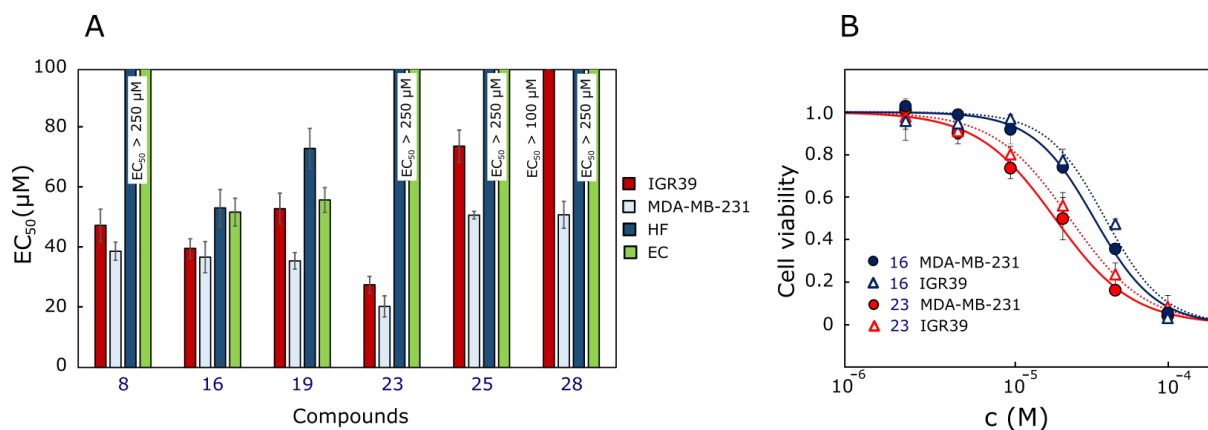


**Figure 3.** Effect of the most active compounds on cancer cell viability. (A).  $\text{EC}_{50}$  values of the most active compounds after 72 h of incubation by MTT assay. (B). Dose–response curves of compounds 16 and 23.  $n = 3$ . Experiments were repeated three times, calculating the mean and standard deviation.

Compound **23** was established to be the most active of tested compounds, its  $\text{EC}_{50}$  value was  $27.8 \pm 2.8 \mu\text{M}$  against IGR39 cell line and  $20.5 \pm 3.6 \mu\text{M}$  against MDA-MB-231 cell line. It was 1.4 times more active against IGR39 and 1.8 times more active against MDA-MB-231 cell lines, compared to the second most active compound **16** from this series (Figure 3B). Moreover, the selectivity of compound **23** against cancer cell lines compared to noncancerous cells was the highest between tested compounds. To compare with, IGR39 cell line was shown to be resistant to BRAF inhibitor dabrafenib, which is approved and used in clinics as a second line drug for malignant melanoma ( $\text{EC}_{50}$  value after 6 days of incubation was  $>50 \mu\text{M}$ ) [27]. Dabrafenib reduces melanoma cell line SK-MEL-24 viability

by MTT assay after 72 h of incubation at a concentration of 35.9  $\mu\text{M}$  [28]. In general, malignant melanoma is characterized as highly mutated and lethal type of cancer [29], and for years was treated with conventional relatively toxic drugs with limited effectiveness [30]. However, despite the targeted therapy that affects BRAF and MEK pathways, the failure of treatment, side effects, and the development of resistance shows that there is a need of novel therapeutic strategies [31]. IGR39 cell line is considered to be as one the most resistant to drugs melanoma cell lines [32] and there are limited data of agent activity in this cell line. Another cell line A375, which is more sensitive to drugs, responds to the treatment with dacarbazine better, but still after 48 h of incubation with it, half of cells remained viable when incubated with 25–50  $\mu\text{g}/\text{mL}$  of drug [33]. Meanwhile, targeted BRAF inhibitor vemurafenib achieves 50% of A375 cell viability reduction at 139 nM concentration but only at >10  $\mu\text{M}$  concentration reduces human melanoma cell line SK-MEL-2 viability by 50% [34].

Doxorubicin, which is considered as a chemotherapeutic agent against triple-negative breast cancer, reduces MDA-MB-231 cell viability below 50% at 5  $\mu\text{M}$  concentration [35], and strategies of combining this drug with the other compounds sensitizing cells to its treatment [36] or enhancing doxorubicin transport inside [37], are widely explored. This type of cancer has limited treatment option, and quite often includes such non-specific drugs as anthracyclines, taxanes, platinum derivatives, and fluorouracil [38]. As this type of cancer is very heterogenous and has limited possibilities for development of targeted agents, available more specific therapeutics show limited effectiveness. It is very invasive and resistant to many available drugs [16], thus search for the newer, more effective agents for this type of cancer is a long-term ongoing process.

Both types of cancer are characterized as recurrent, thus we decided to test the compound effect on single cell ability to survive and proliferate using clonogenic assay. The most active agents **8**, **16**, **19**, **23**, **25**, and **28** were tested for their effect on IGR39 and MDA-MB-231 cell colony formation at 50% of their established  $\text{EC}_{50}$  concentrations.

Almost all compounds showed greater activity on MDA-MB-231 cell colony growth (Figure 4). The most active compound **23**, which was the most cytotoxic in MTT assay, showed comparable activity with compounds **8** and **16** against both cell lines. In the presence of compound **23**, MDA-MB-231 cell colony area dropped down to  $27.1 \pm 6.6\%$ , compared to the control ( $p < 0.05$ ) (Figure 4). All three compounds produced almost twice more expressed effect on MDA-MB-231 than IGR39 cell line. Compounds **19** and **28** were active only on one of tested cell line.

As previously mentioned, the strategy of combinational therapy is being extensively studied and investigated whether this approach could reduce the resistance of cancer to available therapy. It has been established MERTK inhibitor UNC2025 reduces colony formation of BRAF mutant and BRAF wild-type cell lines at 300–500 nM concentration [39]. Combinations of dacarbazine and all-trans retinoic acid were shown to be more active against the B16F10 melanoma cell colony growth compared to dacarbazine alone [40]. Yuan et al. [28] determined that the combination of 3.2  $\mu\text{M}$  A100 and 0.8  $\mu\text{M}$  dabrafenib decreases cell growth of SK-MEL-24 more efficiently compared to single agent dabrafenib. However, this effect has not been found in the case of other tested melanoma cell lines A375 and WM115. It means, that the different response to the same drug and its combination exist between different cell lines, thus it would be worthy to study the effect of our synthesized derivatives in some other melanoma cell lines, too.

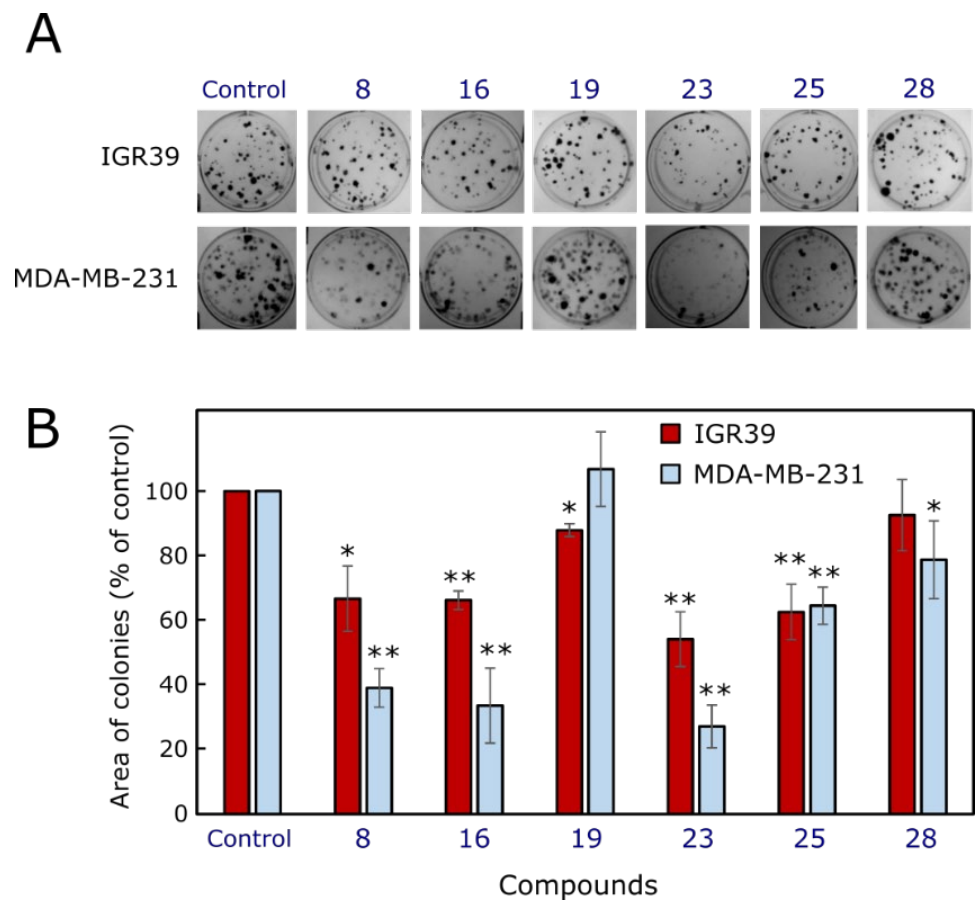


**Figure 4.** Effect of compounds on cell colony formation. (A) Photos of human melanoma IGR39 and human triple-negative breast cancer MDA-MB-231 colonies at the end of experiment. (B) Area of colonies at the end of experiment. Asterisks (\*) indicate  $p < 0.05$  and (\*\*) indicate  $p < 0.01$  compared to the control (untreated cells). Experiments were repeated three times, calculating the mean and standard deviation.

Many studies have been done on MDA-MB-231 cell colony formation in the presence of drugs used for triple-negative breast cancer treatment, novel compounds, or their combinations. Franco et al. [41] established that MDA-MB-231 cell colony formation is reduced more efficiently by 70 nM of doxorubicin compared to 70 nM of paclitaxel. Alkaloid aloperine derived from plants could inhibit MDA-MB-231 cell colony formation number up to ~40% compared to the control; however, at rather high concentration of 400  $\mu$ M [42]. By using clonogenic assay, it has been shown that the clinically used cholesterol level lowering drug pitavastatin at 90% from its  $EC_{50}$  value could reduce MDA-MB-231 cell colony formation up to 40% [43]. Combination of 5 nM eribulin (non-taxane microtubule dynamics inhibitor) and CDK2 inhibitor 300 nM CYC065 reduced the MDA-MB-231 cell colony growth after 4 days treatment [44]. In summary, the beneficial effect of different compounds and their combinations on MDA-MB-231 cell colony formation ability provides hopes in combating the triple-negative breast cancer recurrence after the treatment. Novel benzenesulfonamide-bearing imidazole derivatives could be also explored as sensitizers of cells to the conventional therapy.

Three-dimensional cell models are gaining more and more attention from cell biologists, especially in testing activity and mechanisms of novel substances due to their high resemblance to the real tumors [45,46]. It has been shown that such cell systems regain tissue-specific functions and are more predictive as in vivo models compared to cell monolayers [47]. Thus, the effects of novel benzenesulfonamide-bearing imidazole derivatives 8, 16, 19, 23, 25, and 28 on melanoma IGR39 and triple-negative breast cancer



MDA-MB-231 cell spheroid growth (Figure 5) were studied. As shown in Figure 5C, all tested compounds reduced IGR39 spheroid growth much more efficiently in comparison to the control group. Meanwhile, the effect of compounds on MDA-MB-231 spheroid growth was negligible. Compounds 8, 16, and 19 showed a similar inhibitory effect on IGR39 spheroid growth, however the most cytotoxic compound 23 was not the most active one in 3D cultures. Compounds 25 and 28 did not show activity in both types of spheroids, compared to control groups (Figure 5C).

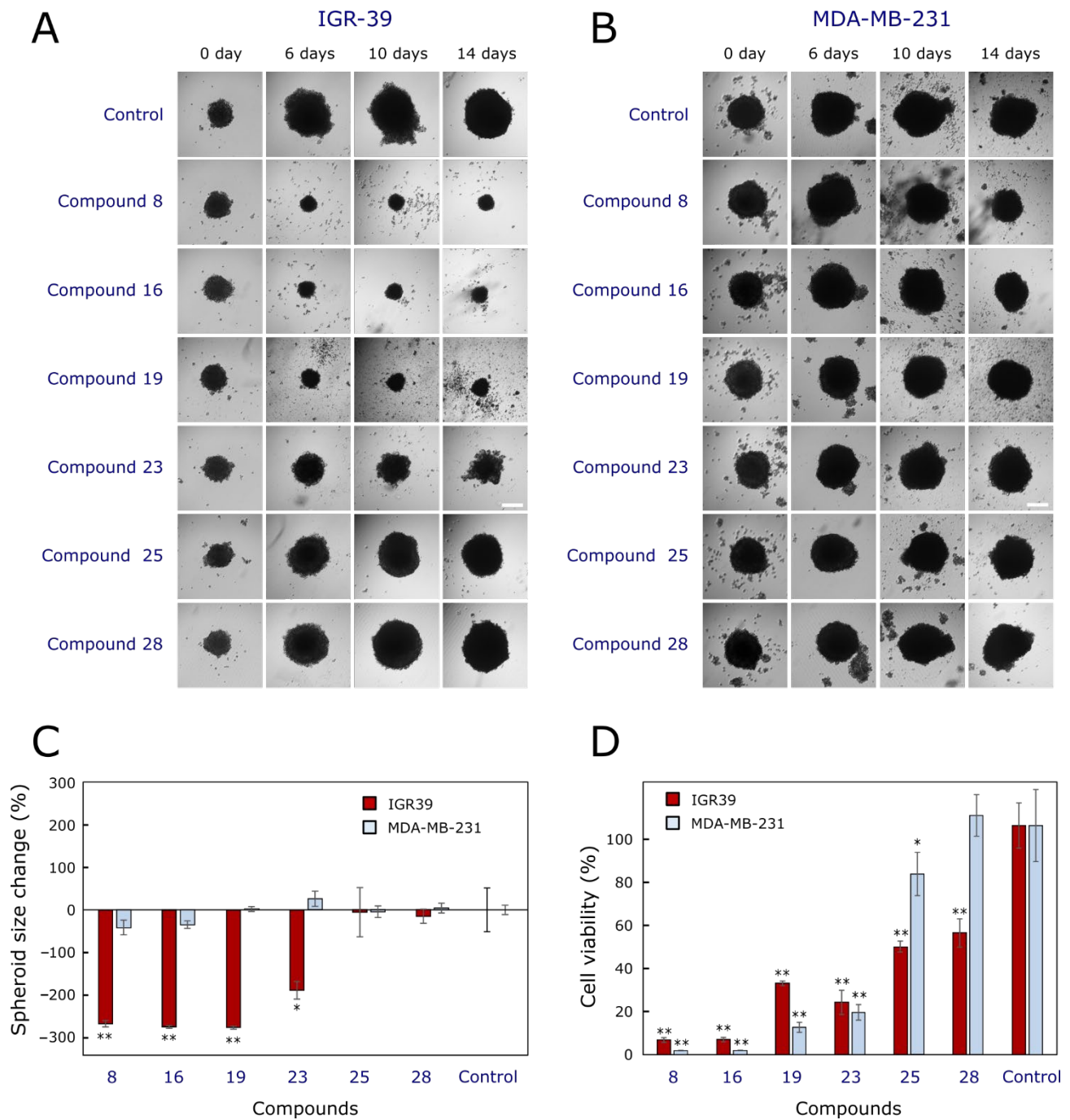


**Figure 5.** Effect of compounds on 3D cell cultures. (A) Photos of human melanoma IGR39 tumor spheroids at different periods of experiment. (B) Photos of human triple-negative breast cancer MDA-MB-231 tumor spheroids at different periods of experiment. (C) Spheroid size at the end of experiment. (D) Cell viability in MDA-MB-231 and IGR39 spheroids. Asterisks (\*) indicate  $p < 0.05$  and (\*\*) indicate  $p < 0.01$  compared to the control (untreated spheroids). Scale bars indicated 200  $\mu\text{m}$ . Each group contained 8–10 spheroids. Data are presented as means  $\pm$  standard deviations.

It is known that compounds' effect on spheroid growth does not necessarily correlate with their effect on cell viability [48]. We determined that the only compound **28** did not reduce cell viability in MDA-MB-231 spheroids (Figure 5D). Meanwhile, all other compounds diminished cell viability in both types of spheroids, and compound **28** also reduced viability of IGR39 3D cultures. Interestingly, differences between cell viability in spheroids were not so big as the size of spheroids. In addition, despite the size of IGR39 spheroids treated with compound **19** was the smallest one between all groups, the viability of these spheroids was higher compared to those incubated with compounds **8**, **16**, and **23**. This could be explained that cells inside the spheroids could become more hypoxic, denser and this could lead to a lower viability. Some spheroids, especially treated with compound **8** and **19**, at the end of experiment began to disintegrate (Figure 5A,B). It has been shown that cytostatic drug docetaxel affects external cells in melanoma spheroids formed from three types of cells: melanoma cells, keratinocytes, and fibroblasts [49]. In our case, spheroids were also formed from several types of cells: cancer cells and fibroblasts. We could only speculate that the compounds could have different effects both on different cells and different zones in spheroids, but it has yet to be established yet.

Hundsberger et al. [50] demonstrated that a huge differences could be detected between 2D and 3D cultures depending on cell line and different concentrations of the same compound. Huang et al. [51] established that triple-negative breast cancer spheroids exhibit an increased resistance to anticancer compounds due significantly up-regulated levels of EMT-associated proteins. Similarly, in our research we established higher resistance of MDA-MB-231 spheroids to the tested compounds in comparison with melanoma cell line, and the differences between 2D and 3D models were shown.

In summary, benzenesulfonamide-bearing imidazole derivatives **8**, **16**, and **23** have shown melanoma and triple-negative breast cancer cell colony formation and tumor spheroid growth inhibition activity and require further attention as possible anticancer agents from very aggressive and invasive types of tumours.

### 3. Materials and Methods

#### 3.1. Chemistry

Reagents were purchased from Sigma-Aldrich (St. Louis, MO, USA). The reaction course and purity of the synthesized compounds were monitored by TLC using aluminum plates pre-coated with silica gel 60 F<sub>254</sub> (MerckKGaA, Darmstadt, Germany). Melting points were determined on a MEL-TEMP (Electrothermal, Bibby Scientific Company, Burlington, NJ, USA) melting point apparatus and are uncorrected. IR spectra ( $\nu$ , cm<sup>-1</sup>) were recorded on a Perkin-Elmer Spectrum BX FT-IR spectrometer (PerkinElmer, Inc., Waltham, Massachusetts, United States) using KBr pellets. The <sup>1</sup>H and <sup>13</sup>C-NMR spectra were recorded in DMSO-d<sub>6</sub> on a Bruker Avance III (400 MHz, 101 MHz) spectrometer. Chemical shifts ( $\delta$ ) are reported in parts per million (ppm) calibrated from TMS (0 ppm) as an internal standard for <sup>1</sup>H NMR, and DMSO-d<sub>6</sub> (39.43 ppm) for <sup>13</sup>C NMR. Elemental analyses (C, H, N) were performed on an Elemental Analyzer CE-440 (Exeter Analytical, Inc., North Chelmsford, MA, USA). Compounds **2-23** and **25-42** synthesis methods, identification data and NMR spectra can be found in Supplementary Materials file. The peak shapes are denoted as follows: s, singlet; d, doublet; t, triplet; q, quartet; m, multiplet; br, broad.

#### 3.2. Cell Culturing

The human melanoma IGR39 and the human triple-negative breast cancer MDA-MB-231 cell lines, as well as the human endothelial cells (EC) CRL-1730 were obtained from the American Type Culture Collection (ATCC, Manassas, VA, USA). Human foreskin fibroblasts (HF) CRL-4001 were originally obtained from ATCC and kindly provided by Prof. Helder Santos (University of Helsinki, Finland). IGR39, MDA-MB-231, EC, and HF were cultured in Dulbecco's Modified Eagle's GlutaMAX medium (Gibco (Carlsbad, CA, USA)). Medium was supplemented with 10,000 U/mL penicillin, 10 mg/mL streptomycin

(Gibco), and 10% fetal bovine serum (Gibco). Cells were incubated at 37 °C in a humidified atmosphere containing 5% CO<sub>2</sub>. They were used until the passage of 20.

### 3.3. Cell Viability Assay

Cell viability was tested using 3-(4,5-dimethylthiazol-2-yl)-2,5-diphenyltetrazolium bromide (MTT; Sigma-Aldrich Co., St. Louis, MO, USA) assay, as described elsewhere [52]. Briefly, IGR39 and MDA-MB-231 cells were seeded in 96-well plates (Corning) in triplicate repeats at a volume of 100 µL (5 × 10<sup>3</sup> cells/well). After 24 h, the cells were treated with 100 µM of various concentrations of tested compounds. Only medium without cells was used as a positive control, and the medium with 0.5% DMSO (Sigma-Aldrich Co.) served as a negative control. After 72 h, the medium from cells was discarded and the fresh medium containing 0.5 mg/mL of MTT solution (Sigma-Aldrich Co.) was added. Cells were incubated for the next 4 h. Then the liquid was aspirated, and the colored formazan product was dissolved in 100 µL DMSO (Sigma-Aldrich Co.). The absorbance was measured at 570 and 630 nm using a multi-detection microplate reader. Compound effect on cell viability was calculated using a formula:

$$\text{Relative cell viability (\%)} = \frac{A - A_0}{A_{NC} - A_0}$$

where:

*A*—mean of absorbance of tested compound,

*A*<sub>0</sub>—mean of absorbance of blank (no cells, positive control),

*A*<sub>NC</sub>—mean of absorbance of negative control (only cells, no treatment).

For establishing EC<sub>50</sub> of the most active compounds, the same MTT procedure has been applied, only the compound serial dilutions from 50 µM to 1.56 µM have been made in a medium and added to the cells in triplicate repeats. EC<sub>50</sub> value that represent the concentration of a compound causing 50% reduction of cancer cell metabolic activity has been calculated using Hill equation.

### 3.4. Colony Formation Assay

Colony formation assay was applied to evaluate the inhibitory effect of the most active compounds on cell ability to survive, and proliferate by forming colonies, as described elsewhere [43]. Briefly, both, melanoma IGR39 and triple-negative breast cancer MDA-MB-231 cells were seeded into 12-well plates in triplicate repeats (2 × 10<sup>2</sup> cells/well) and grown in DMEM GlutaMAX supplemented with 10% FBS (ThermoFisher Scientific, Waltham, MA, USA) and 1% antibiotics (ThermoFisher Scientific, Waltham, MA, USA) at 37 °C in a humidified atmosphere containing 5% CO<sub>2</sub>. After 24 h, the fresh medium containing tested compound 8, 16, 19, 23, 25, and 28 at a concentration representing 50% of calculated EC<sub>50</sub> values were added to cells, followed by incubation at 37 °C in a humidified atmosphere containing 5% CO<sub>2</sub> for the next 10 days (for IGR39 cell line) and 12 days (for MDA-MB-231 cell line), replenishing the media with the compounds once a week. Cells treated with medium containing 0.5% DMSO served as a negative control. After incubation, the colonies were stained with 0.1% Crystal Violet (Sigma-Aldrich Co.) solution. To start with, the media from cells was removed and the cells were washed once with sterile PBS. Then, the cells were fixed in a 4% formaldehyde (Thermo Scientific) solution and washed with PBS two times to remove the fixative, and stained with Crystal Violet solution for 20 min. After the stain had been removed, the remaining stain residues were washed three times sterile water. Lastly, the plates were dried overnight, and imaged with SYNGENE G:BOX gel doc system (Synoptics Limited, Cambridge, UK), using GeneSys software version 1.5.5.0, followed by quantification Gene tools software version 4.3.8.

### 3.5. Compound Activity in Spheroids

Magnetic 3D Bioprinting method was used to form spheroids, as described elsewhere [43]. Briefly, melanoma IGR39, triple-negative breast cancer MDA-MB-231 cells and

human fibroblasts at 70% confluency in a 6-well plate were incubated with Nanoshuttle (Nano 3D Biosciences, Inc., Houston, TX, USA) for 8 h at 37 °C in a humidified atmosphere containing 5% CO<sub>2</sub>. Then, cells were trypsinized, centrifuged, and seeded into ultra-low attachment 96-well plate in a volume of 100 µL (1 × 10<sup>3</sup> IGR39 and 1 × 10<sup>3</sup> human fibroblasts/well, and 2 × 10<sup>3</sup> MDA-MB-231 and 2 × 10<sup>3</sup> human fibroblasts/well). The plate was placed on a magnetic drive (Nano 3D Biosciences, Inc., Houston, TX, USA) and incubated for 2 days at 37 °C in a humidified atmosphere containing 5% CO<sub>2</sub>. Then the fresh medium containing tested compound concentration representing 100% of calculated EC<sub>50</sub> values was added to the wells. The spheroids were captured every two days using the Olympus IX73 inverted microscope (OLYMPUS CORPORATION). The quantitative analysis of compound anticancer activity in spheroids was performed using ImageJ (National Institutes of Health) and Microsoft Office Excel 2016 software.

### 3.6. Statistical Analysis

All biological experiments were repeated at least three times, calculating the mean and standard deviation. The data was processed using Microsoft Office Excel 2016 software (Microsoft Corporation, Redmond, WA, USA). Statistical analysis was performed by using Student's t-test. The level of significance was set as  $p < 0.05$ .

## 4. Conclusions

In this study, the chemical transformations of benzenesulfonamides were carried out and a series of 1-substituted imidazoles with aliphatic, aromatic fragments were synthesized and evaluated for their anticancer activities in 2D and 3D models in vitro.

In the MTT assay, compounds were more effective against human triple-negative breast cancer MDA-MB-231 cell line, compared to malignant melanoma IGR39 cell line. Benzenesulfonamide-bearing imidazole derivatives containing 4-chloro and 3,4-dichlorosubstituents in benzene ring, and 2-ethylthio and 3-ethyl groups in imidazole ring have been determined as the most active compounds. These compounds reduced cell colony formation of both cell lines. Tested derivatives inhibited the growth and viability of IGR39 cell spheroids more efficiently compared to triple-negative breast cancer spheroids.

The obtained results suggest that benzenesulfonamide-bearing imidazole could be a suitable core for the anticancer compounds against such aggressive and invasive tumour types as malignant melanoma and triple-negative breast cancer.

**Supplementary Materials:** The following are available online at <https://www.mdpi.com/article/10.3390/ph14111158/s1>, Figure S1: <sup>1</sup>H NMR of compound **2** at 400 MHz (DMSO-*d*<sub>6</sub>), Figure S2: <sup>13</sup>C NMR of compound **2** at 101 MHz (DMSO-*d*<sub>6</sub>), Figure S3: <sup>1</sup>H NMR of compound **3** at 400 MHz (DMSO-*d*<sub>6</sub>), Figure S4: <sup>13</sup>C NMR of compound **3** at 101 MHz (DMSO-*d*<sub>6</sub>), Figure S5: <sup>1</sup>H NMR of compound **4** at 400 MHz (DMSO-*d*<sub>6</sub>), Figure S6: <sup>13</sup>C NMR of compound **4** at 101 MHz (DMSO-*d*<sub>6</sub>), Figure S7: <sup>1</sup>H NMR of compound **5** at 400 MHz (DMSO-*d*<sub>6</sub>), Figure S8: <sup>13</sup>C NMR of compound **5** at 101 MHz (DMSO-*d*<sub>6</sub>), Figure S9: <sup>1</sup>H NMR of compound **6** at 400 MHz (DMSO-*d*<sub>6</sub>), Figure S10: <sup>13</sup>C NMR of compound **6** at 101 MHz (DMSO-*d*<sub>6</sub>), Figure S11: <sup>1</sup>H NMR of compound **7** at 400 MHz (DMSO-*d*<sub>6</sub>), Figure S12: <sup>13</sup>C NMR of compound **7** at 101 MHz (DMSO-*d*<sub>6</sub>), Figure S13: <sup>1</sup>H NMR of compound **8** at 400 MHz (DMSO-*d*<sub>6</sub>), Figure S14: <sup>13</sup>C NMR of compound **8** at 101 MHz (DMSO-*d*<sub>6</sub>), Figure S15: <sup>1</sup>H NMR of compound **9** at 400 MHz (DMSO-*d*<sub>6</sub>), Figure S16: <sup>13</sup>C NMR of compound **9** at 101 MHz (DMSO-*d*<sub>6</sub>), Figure S17: <sup>1</sup>H NMR of compound **10** at 400 MHz (DMSO-*d*<sub>6</sub>), Figure S18: <sup>13</sup>C NMR of compound **10** at 101 MHz (DMSO-*d*<sub>6</sub>), Figure S19: <sup>1</sup>H NMR of compound **11** at 400 MHz (DMSO-*d*<sub>6</sub>), Figure S20: <sup>13</sup>C NMR of compound **11** at 101 MHz (DMSO-*d*<sub>6</sub>), Figure S21: <sup>1</sup>H NMR of compound **12** at 400 MHz (DMSO-*d*<sub>6</sub>), Figure S22: <sup>13</sup>C NMR of compound **12** at 101 MHz (DMSO-*d*<sub>6</sub>), Figure S23: <sup>1</sup>H NMR of compound **13** at 400 MHz (DMSO-*d*<sub>6</sub>), Figure S24: <sup>13</sup>C NMR of compound **13** at 101 MHz (DMSO-*d*<sub>6</sub>), Figure S25: <sup>1</sup>H NMR of compound **14** at 400 MHz (DMSO-*d*<sub>6</sub>), Figure S26: <sup>13</sup>C NMR of compound **14** at 101 MHz (DMSO-*d*<sub>6</sub>), Figure S27: <sup>1</sup>H NMR of compound **15** at 400 MHz (DMSO-*d*<sub>6</sub>), Figure S28: <sup>13</sup>C NMR of compound **15** at 101 MHz (DMSO-*d*<sub>6</sub>), Figure S29: <sup>1</sup>H NMR of compound **16** at 400 MHz (DMSO-*d*<sub>6</sub>), Figure S30: <sup>13</sup>C NMR of compound **16** at 101 MHz (DMSO-*d*<sub>6</sub>), Figure S31: <sup>1</sup>H NMR of compound **17** at 400 MHz (DMSO-*d*<sub>6</sub>), Figure S32: <sup>13</sup>C NMR of

compound 17 at 101 MHz (DMSO-*d*<sub>6</sub>), Figure S33: <sup>1</sup>H NMR of compound 18 at 400 MHz (DMSO-*d*<sub>6</sub>), Figure S34: <sup>13</sup>C NMR of compound 18 at 101 MHz (DMSO-*d*<sub>6</sub>), Figure S35: <sup>1</sup>H NMR of compound 19 at 400 MHz (DMSO-*d*<sub>6</sub>), Figure S36: <sup>13</sup>C NMR of compound 19 at 101 MHz (DMSO-*d*<sub>6</sub>), Figure S37: <sup>1</sup>H NMR of compound 20 at 400 MHz (DMSO-*d*<sub>6</sub>), Figure S38: <sup>13</sup>C NMR of compound 20 at 101 MHz (DMSO-*d*<sub>6</sub>), Figure S39: <sup>1</sup>H NMR of compound 21 at 400 MHz (DMSO-*d*<sub>6</sub>), Figure S40: <sup>13</sup>C NMR of compound 21 at 101 MHz (DMSO-*d*<sub>6</sub>), Figure S41: <sup>1</sup>H NMR of compound 22 at 400 MHz (DMSO-*d*<sub>6</sub>), Figure S42: <sup>13</sup>C NMR of compound 22 at 101 MHz (DMSO-*d*<sub>6</sub>), Figure S43: <sup>1</sup>H NMR of compound 23 at 400 MHz (DMSO-*d*<sub>6</sub>), Figure S44: <sup>13</sup>C NMR of compound 23 at 101 MHz (DMSO-*d*<sub>6</sub>), Figure S45: <sup>1</sup>H NMR of compound 25 at 400 MHz (DMSO-*d*<sub>6</sub>), Figure S46: <sup>13</sup>C NMR of compound 25 at 101 MHz (DMSO-*d*<sub>6</sub>), Figure S47: <sup>1</sup>H NMR of compound 26 at 400 MHz (DMSO-*d*<sub>6</sub>), Figure S48: <sup>13</sup>C NMR of compound 26 at 101 MHz (DMSO-*d*<sub>6</sub>), Figure S49: <sup>1</sup>H NMR of compound 27 at 400 MHz (DMSO-*d*<sub>6</sub>), Figure S50: <sup>13</sup>C NMR of compound 27 at 101 MHz (DMSO-*d*<sub>6</sub>), Figure S51: <sup>1</sup>H NMR of compound 28 at 400 MHz (DMSO-*d*<sub>6</sub>), Figure S52: <sup>13</sup>C NMR of compound 28 at 101 MHz (DMSO-*d*<sub>6</sub>), Figure S53: <sup>1</sup>H NMR of compound 29 at 400 MHz (DMSO-*d*<sub>6</sub>), Figure S54: <sup>13</sup>C NMR of compound 29 at 101 MHz (DMSO-*d*<sub>6</sub>), Figure S55: <sup>1</sup>H NMR of compound 30 at 400 MHz (DMSO-*d*<sub>6</sub>), Figure S56: <sup>13</sup>C NMR of compound 30 at 101 MHz (DMSO-*d*<sub>6</sub>), Figure S57: <sup>1</sup>H NMR of compound 31 at 400 MHz (DMSO-*d*<sub>6</sub>), Figure S58: <sup>13</sup>C NMR of compound 31 at 101 MHz (DMSO-*d*<sub>6</sub>), Figure S59: <sup>1</sup>H NMR of compound 32 at 400 MHz (DMSO-*d*<sub>6</sub>), Figure S60: <sup>13</sup>C NMR of compound 32 at 101 MHz (DMSO-*d*<sub>6</sub>), Figure S61: <sup>1</sup>H NMR of compound 33 at 400 MHz (DMSO-*d*<sub>6</sub>), Figure S62: <sup>13</sup>C NMR of compound 33 at 101 MHz (DMSO-*d*<sub>6</sub>), Figure S63: <sup>1</sup>H NMR of compound 34 at 400 MHz (DMSO-*d*<sub>6</sub>), Figure S64: <sup>13</sup>C NMR of compound 34 at 101 MHz (DMSO-*d*<sub>6</sub>), Figure S65: <sup>1</sup>H NMR of compound 35 at 400 MHz (DMSO-*d*<sub>6</sub>), Figure S66: <sup>13</sup>C NMR of compound 35 at 101 MHz (DMSO-*d*<sub>6</sub>), Figure S67: <sup>1</sup>H NMR of compound 36 at 400 MHz (DMSO-*d*<sub>6</sub>), Figure S68: <sup>13</sup>C NMR of compound 36 at 101 MHz (DMSO-*d*<sub>6</sub>), Figure S69: <sup>1</sup>H NMR of compound 37 at 400 MHz (DMSO-*d*<sub>6</sub>), Figure S70: <sup>13</sup>C NMR of compound 37 at 101 MHz (DMSO-*d*<sub>6</sub>), Figure S71: <sup>1</sup>H NMR of compound 38 at 400 MHz (DMSO-*d*<sub>6</sub>), Figure S72: <sup>13</sup>C NMR of compound 38 at 101 MHz (DMSO-*d*<sub>6</sub>), Figure S73: <sup>1</sup>H NMR of compound 39 at 400 MHz (DMSO-*d*<sub>6</sub>), Figure S74: <sup>13</sup>C NMR of compound 39 at 101 MHz (DMSO-*d*<sub>6</sub>), Figure S75: <sup>1</sup>H NMR of compound 40 at 400 MHz (DMSO-*d*<sub>6</sub>), Figure S76: <sup>13</sup>C NMR of compound 40 at 101 MHz (DMSO-*d*<sub>6</sub>), Figure S77: <sup>1</sup>H NMR of compound 41 at 400 MHz (DMSO-*d*<sub>6</sub>), Figure S78: <sup>13</sup>C NMR of compound 41 at 101 MHz (DMSO-*d*<sub>6</sub>), Figure S79: <sup>1</sup>H NMR of compound 42 at 400 MHz (DMSO-*d*<sub>6</sub>), Figure S80: <sup>13</sup>C NMR of compound 42 at 101 MHz (DMSO-*d*<sub>6</sub>).

**Author Contributions:** Conceptualization, V.M. and V.P.; methodology, V.M. and V.P.; synthesis, B.B.; investigation, B.B. and V.P.; writing—original draft preparation, B.B. and V.P.; writing—review and editing, V.M. and V.P.; supervision, V.M. and V.P. All authors have read and agreed to the published version of the manuscript.

**Funding:** This research received no external funding.

**Institutional Review Board Statement:** Not applicable.

**Informed Consent Statement:** Not applicable.

**Data Availability Statement:** Data is contained within the article or Supplementary Materials.

**Conflicts of Interest:** The authors declare no conflict of interest.

## References

1. Gomtsyan, A. Heterocycles in Drugs and Drug Discovery. *Chem. Heterocycl. Comp.* **2012**, *48*, 7–10. [CrossRef]
2. King, T.A.; Stewart, H.L.; Mortensen, K.T.; North, A.J.P.; Sore, H.F.; Spring, D.R. Cycloaddition Strategies for the Synthesis of Diverse Heterocyclic Spirocycles for Fragment-Based Drug Discovery: Cycloaddition Strategies for the Synthesis of Diverse Heterocyclic Spirocycles for Fragment-Based Drug Discovery. *Eur. J. Org. Chem.* **2019**, *2019*, 5219–5229. [CrossRef]
3. Amine Khodja, I.; Boulebd, H.; Bensouici, C.; Belfaitah, A. Design, Synthesis, Biological Evaluation, Molecular Docking, DFT Calculations and in Silico ADME Analysis of (Benz)Imidazole-Hydrazone Derivatives as Promising Antioxidant, Antifungal, and Anti-Acetylcholinesterase Agents. *J. Mol. Struct.* **2020**, *1218*, 128527. [CrossRef]
4. Hu, Y.; Shen, Y.; Wu, X.; Tu, X.; Wang, G.-X. Synthesis and Biological Evaluation of Coumarin Derivatives Containing Imidazole Skeleton as Potential Antibacterial Agents. *Eur. J. Med. Chem.* **2018**, *143*, 958–969. [CrossRef]
5. Khabnadideh, S.; Rezaei, Z.; Khalafi-Nezhad, A.; Bahrinajafi, R.; Mohamadi, R.; Farrokhrooz, A.A. Synthesis of N-Alkylated Derivatives of Imidazole as Antibacterial Agents. *Bioorg. Med. Chem. Lett.* **2003**, *13*, 2863–2865. [CrossRef]

6. Moura, K.C.G.; Carneiro, P.F.; Maria do Carmo, F.R.; da Silva, J.A.; Malta, V.R.S.; de Simone, C.A.; Dias, G.G.; Jardim, G.A.M.; Cantos, J.; Coelho, T.S.; et al. 1,3-Azoles from Ortho-Naphthoquinones: Synthesis of Aryl Substituted Imidazoles and Oxazoles and Their Potent Activity against Mycobacterium Tuberculosis. *Bioorg. Med. Chem.* **2012**, *20*, 6482–6488. [CrossRef]
7. Dos Santos Nascimento, M.V.P.; Mattar Munhoz, A.C.; De Campos Facchin, B.M.; Fratoni, E.; Rossa, T.A.; Mandolesi Sá, M.; Campa, C.C.; Ciralo, E.; Hirsch, E.; Dalmarco, E.M. New Pre-Clinical Evidence of Anti-Inflammatory Effect and Safety of a Substituted Fluorophenyl Imidazole. *Biomed. Pharmacother.* **2019**, *111*, 1399–1407. [CrossRef] [PubMed]
8. Zhang, J.; Yan, Z.; Wang, Y.; Wang, Y.; Guo, X.; Jing, J.; Dong, X.; Dong, S.; Liu, X.; Yu, X.; et al. Cancer-Associated 53BP1 Mutations Induce DNA Damage Repair Defects. *Cancer Lett.* **2021**, *501*, 43–54. [CrossRef]
9. Stirparo, G.G.; Smith, A.; Guo, G. Cancer-Related Mutations Are Not Enriched in Naive Human Pluripotent Stem Cells. *Cell Stem Cell* **2021**, *28*, 164–169.e2. [CrossRef] [PubMed]
10. Hu, M.-H.; Lin, X.-T.; Liu, B.; Tan, J.-H. Dimeric Aryl-Substituted Imidazoles May Inhibit ALT Cancer by Targeting the Multimeric G-Quadruplex in Telomere. *Eur. J. Med. Chem.* **2020**, *186*, 111891. [CrossRef] [PubMed]
11. Hassan, A.Y.; El-Sebaey, S.A.; El Deeb, M.A.; Elzoghbi, M.S. Potential Antiviral and Anticancer Effect of Imidazoles and Bridgehead Imidazoles Generated by HPV-Induced Cervical Carcinomas via Reactivating the P53/ PRb Pathway and Inhibition of CA IX. *J. Mol. Struct.* **2021**, *1230*, 129865. [CrossRef]
12. Ali, E.M.H.; Abdel-Maksoud, M.S.; Ammar, U.M.; Mersal, K.I.; Ho Yoo, K.; Jooryeong, P.; Oh, C.-H. Design, Synthesis, and Biological Evaluation of Novel Imidazole Derivatives Possessing Terminal Sulphonamides as Potential BRAFV600E Inhibitors. *Bioorg. Chem.* **2021**, *106*, 104508. [CrossRef] [PubMed]
13. Bellina, F.; Guazzelli, N.; Lessi, M.; Manzini, C. Imidazole Analogues of Resveratrol: Synthesis and Cancer Cell Growth Evaluation. *Tetrahedron* **2015**, *71*, 2298–2305. [CrossRef]
14. Noori, M.S.; O'Brien, J.D.; Champa, Z.J.; Deosarkar, S.P.; Lanier, O.L.; Qi, C.; Burdick, M.M.; Schwartz, F.L.; Bergmeier, S.C.; McCall, K.D.; et al. Phenylmethimazole and a Thiazole Derivative of Phenylmethimazole Inhibit IL-6 Expression by Triple Negative Breast Cancer Cells. *Eur. J. Pharmacol.* **2017**, *803*, 130–137. [CrossRef]
15. Sullivan, R.J.; Flaherty, K.T. Resistance to BRAF-Targeted Therapy in Melanoma. *Eur. J. Cancer* **2013**, *49*, 1297–1304. [CrossRef]
16. Januškevičienė, I.; Petrikaitė, V. Heterogeneity of Breast Cancer: The Importance of Interaction between Different Tumor Cell Populations. *Life Sci.* **2019**, *239*, 117009. [CrossRef] [PubMed]
17. Helmbach, H.; Rossmann, E.; Kern, M.A.; Schadendorf, D. Drug-Resistance in Human Melanoma. *Int. J. Cancer* **2001**, *93*, 617–622. [CrossRef]
18. Nunes, A.S.; Barros, A.S.; Costa, E.C.; Moreira, A.F.; Correia, I.J. 3D Tumor Spheroids as in Vitro Models to Mimic in Vivo Human Solid Tumors Resistance to Therapeutic Drugs. *Biotechnol. Bioeng.* **2019**, *116*, 206–226. [CrossRef] [PubMed]
19. Huang, B.-W.; Gao, J.-Q. Application of 3D Cultured Multicellular Spheroid Tumor Models in Tumor-Targeted Drug Delivery System Research. *J. Control. Release* **2018**, *270*, 246–259. [CrossRef] [PubMed]
20. Balandis, B.; Ivanauskaitė, G.; Smirnovienė, J.; Kantminienė, K.; Matulis, D.; Mickevičius, V.; Zubrienė, A. Synthesis and Structure–Affinity Relationship of Chlorinated Pyrrolidinone-Bearing Benzenesulfonamides as Human Carbonic Anhydrase Inhibitors. *Bioorg. Chem.* **2020**, *97*, 103658. [CrossRef]
21. Vaškevičienė, I.; Paketurytė, V.; Zubrienė, A.; Kantminienė, K.; Mickevičius, V.; Matulis, D. N -Sulfamoylphenyl- and N -Sulfamoylphenyl- N -Thiazolyl-β-Alanines and Their Derivatives as Inhibitors of Human Carbonic Anhydrases. *Bioorg. Chem.* **2017**, *75*, 16–29. [CrossRef]
22. Balandis, B.; Anusevičius, K.; Šiugždaitė, J.; Kantminienė, K.; Mickevičius, V. Synthesis and Antibacterial Activity of 3-Substituted 1-(2-Methyl-5-Nitrophenyl)-5-Oxopyrrolidine Derivatives. *Res. Chem. Intermed.* **2019**, *45*, 5499–5517. [CrossRef]
23. Po, H.N.; Shariff, Z.; Masse, J.A.; Freeman, F.; Keindl-yu, M.C. Thermodynamic And Electrochemical Properties of Imidazole-2-Thiols (Imidazole-2(3 H)-Thiones). *Phosphorus Sulfur Silicon Relat. Elem.* **1991**, *63*, 1–12. [CrossRef]
24. Gupta, G.K.; Saini, V.; Khare, R.; Kumar, V. 1,4-Diaryl-2-Mercaptoimidazoles Derivatives as a Novel Class of Antimicrobial Agents: Design, Synthesis, and Computational Studies. *Med. Chem. Res.* **2014**, *23*, 4209–4220. [CrossRef]
25. Congiu, C.; Onnis, V.; Balboni, G.; Supuran, C.T. Synthesis and Carbonic Anhydrase I, II, IX and XII Inhibition Studies of 4-N,N-Disubstituted Sulfanilamides Incorporating 4,4,4-Trifluoro-3-Oxo-but-1-Enyl, Phenacylthiourea and Imidazol-2(3H)-One/Thione Moieties. *Bioorg. Med. Chem. Lett.* **2014**, *24*, 1776–1779. [CrossRef] [PubMed]
26. Aly, A.A.; Hopf, H.; Ernst, L.; Dix, I.; Jones, P.G. New Cycloadditions of (E)-N,α-Dimethyl-α-(4-[2.2]Paracyclophanyl)Nitron. *Eur. J. Org. Chem.* **2006**, *2006*, 3001–3006. [CrossRef]
27. Vizoso, M.; Ferreira, H.J.; Lopez-Serra, P.; Carmona, F.J.; Martínez-Cardús, A.; Girotti, M.R.; Villanueva, A.; Guil, S.; Moutinho, C.; Liz, J.; et al. Epigenetic Activation of a Cryptic TBC1D16 Transcript Enhances Melanoma Progression by Targeting EGFR. *Nat. Med.* **2015**, *21*, 741–750. [CrossRef]
28. Yuan, L.; Mishra, R.; Patel, H.; Abdulsalam, S.; Greis, K.D.; Kadekar, A.L.; Merino, E.J.; Garrett, J.T. Utilization of Reactive Oxygen Species Targeted Therapy to Prolong the Efficacy of BRAF Inhibitors in Melanoma. *J. Cancer* **2018**, *9*, 4665–4676. [CrossRef]
29. Akbani, R.; Akdemir, K.C.; Aksoy, B.A.; Albert, M.; Ally, A.; Amin, S.B.; Arachchi, H.; Arora, A.; Auman, J.T.; Ayala, B.; et al. Genomic Classification of Cutaneous Melanoma. *Cell* **2015**, *161*, 1681–1696. [CrossRef] [PubMed]
30. Cerezo, M.; Lehraiki, A.; Millet, A.; Rouaud, F.; Plaisant, M.; Jaune, E.; Botton, T.; Ronco, C.; Abbe, P.; Amdouni, H.; et al. Compounds Triggering ER Stress Exert Anti-Melanoma Effects and Overcome BRAF Inhibitor Resistance. *Cancer Cell* **2016**, *29*, 805–819. [CrossRef] [PubMed]

31. Kozar, I.; Margue, C.; Rothengatter, S.; Haan, C.; Kreis, S. Many Ways to Resistance: How Melanoma Cells Evade Targeted Therapies. *Biochim. Biophys. Acta Rev. Cancer* **2019**, *1871*, 313–322. [CrossRef] [PubMed]
32. Konieczkowski, D.J.; Johannessen, C.M.; Abudayyeh, O.; Kim, J.W.; Cooper, Z.A.; Piris, A.; Frederick, D.T.; Barzily-Rokni, M.; Straussman, R.; Haq, R.; et al. A Melanoma Cell State Distinction Influences Sensitivity to MAPK Pathway Inhibitors. *Cancer Discov.* **2014**, *4*, 816–827. [CrossRef]
33. Bedia, C.; Casas, J.; Andrieu-Abadie, N.; Fabriàs, G.; Levade, T. Acid Ceramidase Expression Modulates the Sensitivity of A375 Melanoma Cells to Dacarbazine. *J. Biol. Chem.* **2011**, *286*, 28200–28209. [CrossRef] [PubMed]
34. Parmenter, T.J.; Kleinschmidt, M.; Kinross, K.M.; Bond, S.T.; Li, J.; Kaadige, M.R.; Rao, A.; Sheppard, K.E.; Hugo, W.; Pupo, G.M.; et al. Response of BRAF Mutant Melanoma to BRAF Inhibition Is Mediated by a Network of Transcriptional Regulators of Glycolysis. *Cancer Discov.* **2014**, *4*, 423–433. [CrossRef]
35. Wen, S.; Su, S.; Liou, B.; Lin, C.; Lee, K. Sulbactam-Enhanced Cytotoxicity of Doxorubicin in Breast Cancer Cells. *Cancer Cell Int.* **2018**, *18*, 1–18. [CrossRef]
36. Lee, K.-S.; Lee, M.-G.; Kwon, Y.-S.; Nam, K.-S. Arctigenin Enhances the Cytotoxic Effect of Doxorubicin in MDA-MB-231 Breast Cancer Cells. *Int. J. Mol. Sci.* **2020**, *21*, 2997. [CrossRef] [PubMed]
37. Paškevičiūtė, M.; Petrikaitė, V. Application of Carbonic Anhydrase Inhibitors to Increase the Penetration of Doxorubicin and Its Liposomal Formulation into 2D and 3D Triple Negative Breast Cancer Cell Cultures. *Am. J. Cancer Res.* **2020**, *10*, 1761–1769.
38. Yin, L.; Duan, J.-J.; Bian, X.-W.; Yu, S.-C. Triple-Negative Breast Cancer Molecular Subtyping and Treatment Progress. *Breast Cancer Res.* **2020**, *22*, 61. [CrossRef] [PubMed]
39. Sinik, L.; Minson, K.A.; Tentler, J.J.; Carrico, J.; Bagby, S.M.; Robinson, W.A.; Kami, R.; Burstyn-Cohen, T.; Eckhardt, S.G.; Wang, X.; et al. Inhibition of MERTK Promotes Suppression of Tumor Growth in BRAF Mutant and BRAF Wild-Type Melanoma. *Mol. Cancer* **2019**, *18*, 278–288. [CrossRef]
40. Li, C.; Han, X. Co-Delivery of Dacarbazine and All-Trans Retinoic Acid (ATRA) Using Lipid Nanoformulations for Synergistic Antitumor Efficacy Against Malignant Melanoma. *Nanoscale Res. Lett.* **2020**, *15*, 1–10. [CrossRef] [PubMed]
41. Franco, M.S.; Roque, M.C.; Oliveira, M.C. Short and Long-Term Effects of the Exposure of Breast Cancer Cell Lines to Different Ratios of Free or Co-Encapsulated Liposomal Paclitaxel and Doxorubicin. *Pharmaceutics* **2019**, *11*, 178. [CrossRef] [PubMed]
42. Tian, D.; Li, Y.; Li, X.; Tian, Z. Aloperine Inhibits Proliferation, Migration and Invasion and Induces Apoptosis by Blocking the Ras Signaling Pathway in Human Breast Cancer Cells. *Mol. Med. Rep.* **2018**, *18*, 3699–3710. [CrossRef] [PubMed]
43. Bytautaite, M.; Petrikaite, V. Comparative Study of Lipophilic Statin Activity in 2D and 3D in Vitro Models of Human Breast Cancer Cell Lines MDA-MB-231 and MCF-7. *Onco Targ.* **2020**, *13*, 13201–13209. [CrossRef] [PubMed]
44. Rao, S.S.; Stoehr, J.; Dokic, D.; Wan, L.; Decker, J.T.; Konopka, K.; Thomas, A.L.; Wu, J.; Kaklamani, V.G.; Shea, L.D.; et al. Synergistic Effect of Eribulin and CDK Inhibition for the Treatment of Triple Negative Breast Cancer. *Oncotarget* **2017**, *8*, 83925–83939. [CrossRef] [PubMed]
45. Friedrich, J.; Seidel, C.; Ebner, R.; Kunz-Schughart, L.A. Spheroid-Based Drug Screen: Considerations and Practical Approach. *Nat. Protoc.* **2009**, *4*, 309–324. [CrossRef]
46. Kunz-Schughart, L.A. Multicellular Tumor Spheroids: Intermediates between Monolayer Culture and in Vivo Tumor. *Cell Biol. Int.* **1999**, *23*, 157–161. [CrossRef] [PubMed]
47. Edmondson, R.; Broglie, J.J.; Adcock, A.F.; Yang, L. Three-Dimensional Cell Culture Systems and Their Applications in Drug Discovery and Cell-Based Biosensors. *Assay Drug Dev. Technol.* **2014**, *12*, 207–218. [CrossRef]
48. Schumacher, U.; Nehmann, N.; Adam, E.; Mukthar, D.; Slotki, I.N.; Horny, H.-P.; Flens, M.J.; Schlegelberger, B.; Steinemann, D. MDR-1-Overexpression in HT 29 Colon Cancer Cells Grown in SCID Mice. *Acta Histochem.* **2012**, *114*, 594–602. [CrossRef]
49. Klicks, J.; Mañlo, C.; Kluth, A.; Rudolf, R.; Hafner, M. A Novel Spheroid-Based Co-Culture Model Mimics Loss of Keratinocyte Differentiation, Melanoma Cell Invasion, and Drug-Induced Selection of ABCB5-Expressing Cells. *BMC Cancer* **2019**, *19*, 402. [CrossRef]
50. Hundesberger, H.; Stierschneider, A.; Sarne, V.; Ripper, D.; Schimon, J.; Weitzenböck, H.P.; Schild, D.; Jacobi, N.; Eger, A.; Atzler, J.; et al. Concentration-Dependent Pro- and Antitumor Activities of Quercetin in Human Melanoma Spheroids: Comparative Analysis of 2D and 3D Cell Culture Models. *Molecules* **2021**, *26*, 717. [CrossRef]
51. Huang, Z.; Yu, P.; Tang, J. Characterization of Triple-Negative Breast Cancer MDA-MB-231 Cell Spheroid Model. *Onco Targets* **2020**, *13*, 5395–5405. [CrossRef] [PubMed]
52. Grigalius, I.; Petrikaite, V. Relationship between Antioxidant and Anticancer Activity of Trihydroxyflavones. *Molecules* **2017**, *22*, 2169. [CrossRef] [PubMed]



## Article

# Investigation of the Mechanisms of Cytotoxic Activity of 1,3-Disubstituted Thiourea Derivatives

Paulina Strzyga-Łach , Alicja Chrzanowska, Katarzyna Podsadni and Anna Bielenica \*

Chair and Department of Biochemistry, Medical University of Warsaw, 02-097 Warszawa, Poland; pstrzyga@wum.edu.pl (P.S.-Ł.); achrzanowska@wum.edu.pl (A.C.); kpodsadni@wum.edu.pl (K.P.)

\* Correspondence: abielenica@wum.edu.pl; Tel.: +(48)-022-572-06-93; Fax: +(48)-022-572-06-79

**Abstract:** Substituted thiourea derivatives possess confirmed cytotoxic activity towards cancer but also normal cells. To develop new selective antitumor agents, a series of 3-(trifluoromethyl)phenylthiourea analogs were synthesized, and their cytotoxicity was evaluated in vitro against the cell line panel. Compounds **1–5**, **8**, and **9** were highly cytotoxic against human colon (SW480, SW620) and prostate (PC3) cancer cells, and leukemia K-562 cell lines ( $IC_{50} \leq 10 \mu M$ ), with favorable selectivity over normal HaCaT cells. The derivatives exerted better growth inhibitory profiles towards selected tumor cells than the reference cisplatin. Compounds incorporating 3,4-dichloro- (**2**) and 4-CF<sub>3</sub>-phenyl (**8**) substituents displayed the highest activity ( $IC_{50}$  from 1.5 to 8.9  $\mu M$ ). The mechanisms of cytotoxic action of the most effective thioureas **1–3**, **8**, and **9** were studied, including the trypan blue exclusion test of cell viability, interleukin-6, and apoptosis assessments. Compounds reduced all cancerous cell numbers (especially SW480 and SW620) by 20–93%. Derivatives **2** and **8** diminished the viability of SW620 cells by 45–58%. Thioureas **1**, **2**, and **8** exerted strong pro-apoptotic activity. Compound **2** induced late apoptosis in both colon cancer cell lines (95–99%) and in K-562 cells (73%). All derivatives acted as inhibitors of IL-6 levels in both SW480 and SW620 cells, decreasing its secretion by 23–63%.

**Keywords:** thiourea; cytotoxic activity; apoptosis; interleukin-6; trypan blue assay

**Citation:** Strzyga-Łach, P.; Chrzanowska, A.; Podsadni, K.; Bielenica, A. Investigation of the Mechanisms of Cytotoxic Activity of 1,3-Disubstituted Thiourea Derivatives. *Pharmaceuticals* **2021**, *14*, 1097. <https://doi.org/10.3390/ph14111097>

Academic Editors: Mary J. Meegan and Niamh M O'Boyle

Received: 28 September 2021

Accepted: 26 October 2021

Published: 28 October 2021

**Publisher's Note:** MDPI stays neutral with regard to jurisdictional claims in published maps and institutional affiliations.



**Copyright:** © 2021 by the authors. Licensee MDPI, Basel, Switzerland. This article is an open access article distributed under the terms and conditions of the Creative Commons Attribution (CC BY) license (<https://creativecommons.org/licenses/by/4.0/>).

## 1. Introduction

Cancer is now considered as the second cause of death after cardiovascular disorders. It is estimated that the number of newly diagnosed tumor cases will increase to 15 million episodes every year [1]. Currently, the most common method used for the treatment of cancer is chemotherapy. However, powerful chemotherapeutics also have an adverse impact on non-cancerous cells, slowing their growth and/or inducing apoptosis. Thus, the main challenge for the pharmaceutical industry is to synthesize new anticancer agents that are more effective and selective but less toxic for normal cells.

One of the most suitable strategies in the field of drug development is the combination of two bioactive nuclei. The (thio)urea branch is an element of several medicines with anticancer profiles, such as sorafenib, multikinase-inhibitory diarylthiourea derivative, or tenovin-1, the benzylthiourea, which acts as a reversible inhibitor of class III HDAC sirtuins (Figure 1). On the other hand, it was reported that (hetero)aryl terminal fragments of thiourea moiety, enriched with electron-negative substituents, could provide biological responses, not only cytotoxic [2–4], but also antibacterial [2–8], antiviral [2,9–12], antimycobacterial [5,13], antioxidant [14], and anti-inflammatory [6] properties, as well as central nervous system activation [15–18].



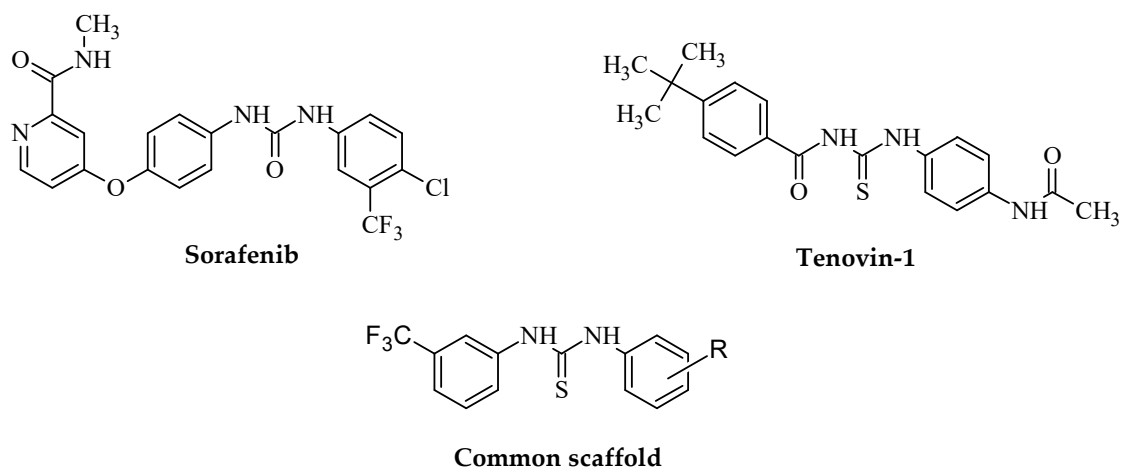


**Figure 1.** Anticancer agents derived from diaryl(thio)urea and the common scaffold of the designed target 3-(trifluoromethyl)phenylthioureas.

Large numbers of 1,3-disubstituted derivatives of urea and thiourea have been reported to possess antiproliferative properties against various solid and leukemia tumor cell lines, simultaneously resulting in low side effects. The most effective agents were found in a group of derivatives with electron-withdrawing substituents introduced to the terminal phenyl rings. In recent years, some trifluoromethyl- and trifluoromethoxyphenyl(thio)ureas bearing the thiochroman ring have been synthesized, which exerted an ovarian cancer cell inhibitory effect [19]. Several biphenyl thiourea derivatives, which incorporated  $\text{CF}_3$ , nitro, and halogen groups on the pendent aryl rings, were described as inhibitors of lung cancer cell A549 growth, with blocking of K-Ras protein as the identified mechanism [20]. It was reported that 2-bromo-5-(trifluoromethoxy)phenylthiourea, the derivative of quinazoline, suppressed proliferation and migration of human cervical HeLa cells via inhibition of the Wnt/ $\beta$ -catenin signaling pathway [21]. Representative 7-trifluoromethyl-quinolinyl-piperazine compounds based on the thiourea scaffold showed improved anti-breast cancer action [22]. In their presence, the membrane integrity of the cytoplasm, mitochondria, and lysosomes of cancer cells were compromised. Series of 4-thiazolidinone-phenylaminopyrimidine hybrids bearing *ortho*-chloro and *para*- $\text{CF}_3$  substituents displayed anticancer activity on chronic myeloid leukemia cells, inducing programmed cell death by inhibition of Abl kinase [23]. Within a group of 1,2,4-triazole-linked (thio)urea conjugates synthesized by Tokala et al., the 4-cyanophenyl derivative with bis(trifluoromethyl)phenyl moiety expressed the highest apoptosis-inducing activity against the breast cancer cell line [24]. The representative diarylurea endowed with both  $\text{CF}_3/\text{OCF}_3$  substituents has recently been developed as an inhibitor of the most lethal and aggressive subtype of breast cancer [25]. Selective kinase inhibitory agents towards hepatocellular carcinoma cells were found among a series of conformationally restricted fluorinated ureas, analogues of sorafenib [26].

Within the thiourea derivatives, halogenated phenyl-containing heterocyclic thioureas play important roles as anticancer agents against solid tumors, such as derivatives of 1,3,4-thiadiazine [27], dihydroquinoline [28], pyridine [29], piperidine [30], quinazoline [31,32], or thiazole [33]. Their mechanisms of action include inhibition of vascular endothelial growth factor receptor 2 [27], epidermal growth factor receptor kinase [31,32], or acetylcholinesterase [33]. Similarly, the presence of the nitrophenyl moiety at the thiourea branch is identified to impart promising cytotoxic activity towards various solid tumors, including lung, colorectal [34], prostate, and breast [35] carcinoma, acting via mitogen kinase enzyme (MK-2) inhibition [34].

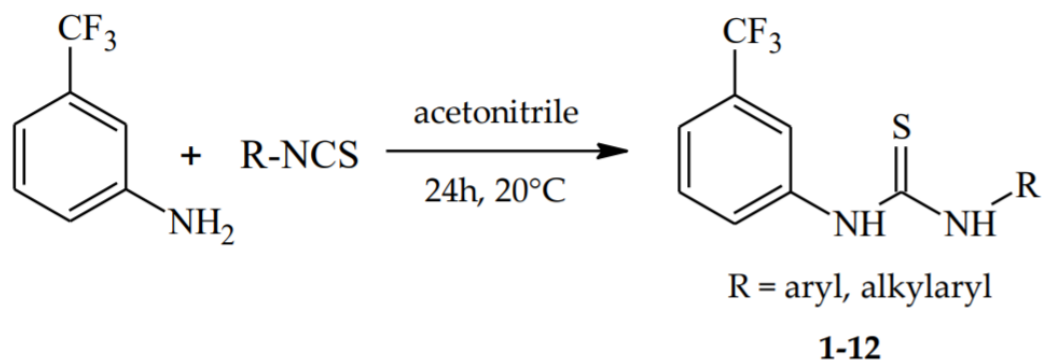
The 3-(Trifluoromethyl)phenylthiourea moiety is a versatile scaffold in medicinal chemistry, also used previously by our team for the design of new compounds with variable and improved pharmacological profiles, mainly antimicrobial [2,8], antiviral [2,12], and CNS-activating [15] compounds. Herein, we focus on possible mechanisms of the cytotoxic properties of a series

of 3-(trifluoromethyl)phenylthiourea analogs, incorporating differential electron-withdrawing terminal groups.

## 2. Results and Discussion

### 2.1. Chemistry

The final 1,3-disubstituted thioureas **1–12** were synthesized in a single-step reaction of 3-(trifluoromethyl)aniline with various isothiocyanates, belonging to a group of dihalogenophenyl (**1–4**), halogenomethylphenyl (**5, 6**), alkylphenyl (**12**), or monophenyl-substituted (**7–11**) derivatives (Scheme 1). The presented selection of the phenyl ring terminal groups allowed an investigation of the impact of the substitution isomerism, as well as the influence of the electron-withdrawing elements attached to the benzene ring on the biological properties within the tested thiourea series. The synthesis of compounds **1, 2, 9, 10**, and **12** was described previously. The structures of the newly synthesized derivatives (**3–8, 11**) were characterized by both  $^1\text{H}$  and  $^{13}\text{C}$  NMR spectroscopy and HRMS analysis.



**Scheme 1.** Synthetic procedure for 3-(trifluoromethyl)phenylthiourea derivatives **1–12**.

### 2.2. Biological Studies

#### 2.2.1. Cytotoxic Activity

As a first step in assessing their cytotoxic properties, all thioureas of the series were assayed against four human carcinoma cell lines, such as SW480 (primary colon cancer), SW620 (metastatic colon cancer), PC3 (metastatic prostate cancer), and K-562 (chronic myelogenous leukemia), as well as against the normal cell line HaCaT (immortalized human keratinocytes). Table 1 lists the compound concentrations that produced 50% of growth inhibition ( $\text{IC}_{50}$ ,  $\mu\text{M}$ ), generated by the MTT method [36], in comparison with two commonly used chemotherapeutic agents, doxorubicin and cisplatin.

Dihalogenophenyl derivatives (**1–4**), followed by *para*-substituted thioureas (**8, 9**) were the most active among the series towards all tumor cell lines. They were particularly potent against SW620 cells, which appeared to be the most susceptible among the studied pathological cells. The lowest  $\text{IC}_{50}$  was achieved by 3,4-dichlorophenylthiourea (**2**) and equaled  $1.5 \pm 0.72 \mu\text{M}$ . Its isomer **3**, and also derivatives of 4-(trifluoromethyl)phenylthiourea (**8**) and 4-chlorophenylthiourea (**9**), inhibited the growth of metastatic colon cancer cells at concentrations ranging from  $5.8 \pm 0.76$  to  $7.6 \pm 1.75 \mu\text{M}$ . The 3-chloro-4-fluorophenylthiourea (**1**) filled up the group of the most outstanding cytotoxic agents towards the SW620 cell line ( $\text{IC}_{50} = 9.4 \pm 1.85 \mu\text{M}$ ). Moderate anticancer potency at the level of  $14.0$ – $18.7 \mu\text{M}$  was observed for derivatives **4, 10**, and **11**. Importantly, the strongest inhibitors of the growth of these cells (**1–4, 8, 9**) were also described by high selectivity indexes (SIs), ranging from 4.6 (compound **1**) to 16.5 (compound **2**). In addition, when compared to cisplatin, substances **2, 3**, and **9** were found to be more effective, considering both their  $\text{IC}_{50}$  values and selectivity factors. The potency of compound **2** was up to 4.5 times stronger and its SI and 18 times higher than the reference metalodrug.

**Table 1.** Cytotoxic activity (IC<sub>50</sub>, μM) of hte studied compounds estimated by the MTT assay <sup>a</sup>.

Compound	R	Cancer Cells						Normal Cells		
		SW480 <sup>d</sup>		SW620 <sup>e</sup>		PC3 <sup>f</sup>		K562 <sup>g</sup>		HaCaT <sup>h</sup>
		IC <sub>50</sub> <sup>b</sup>	SI <sup>c</sup>	IC <sub>50</sub>	SI	IC <sub>50</sub>	SI	IC <sub>50</sub>	SI	IC <sub>50</sub>
1	3-Cl,4-F-Ph	12.7 ± 1.53	3.4	9.4 ± 1.85	4.6	53.6 ± 2.94	0.8	6.8 ± 1.57	6.4	43.6 ± 4.22
2	3-Cl,4-Cl-Ph	9.0 ± 1.42	2.7	1.5 ± 0.72	16.5	31.7 ± 2.07	0.8	6.3 ± 1.28	3.9	24.7 ± 0.05
3	2-Cl,4-Cl-Ph	30.1 ± 3.11	1.7	5.8 ± 0.76	9.0	13.7 ± 7.04	3.8	54.3 ± 1.86	1.0	52.1 ± 0.95
4	2-Cl,3-Cl-Ph	22.5 ± 0.10	0.6	14.0 ± 1.73	1.0	10.5 ± 2.52	1.3	35.9 ± 0.07	0.4	13.9 ± 1.70
5	2-CH <sub>3</sub> ,3-Cl-Ph	7.3 ± 0.89	7.6	23.2 ± 4.07	2.4	51.8 ± 3.19	1.1	52.5 ± 2.14	1.1	55.6 ± 1.74
6	2-CH <sub>3</sub> ,5-Cl-Ph	15.6 ± 4.10	0.9	22.1 ± 4.36	0.7	65.9 ± 10.50	0.2	40.3 ± 3.88	0.4	14.5 ± 1.08
7	2-CF <sub>3</sub> -Ph	>100	0.7	30.1 ± 9.74	2.2	17.1 ± 0.57	3.8	76.5 ± 4.57	0.9	65.7 ± 3.83
8	4-CF <sub>3</sub> -Ph	8.9 ± 1.14	4.6	7.6 ± 1.75	5.4	6.9 ± 1.64	6.0	54.8 ± 0.24	0.8	41.3 ± 0.17
9	4-Cl-Ph	38.1 ± 4.38	1.9	6.7 ± 1.74	10.7	22.6 ± 1.25	3.2	10.2 ± 0.35	7.4	71.5 ± 3.08
10	4-CN-Ph	20.6 ± 3.59	2.4	18.7 ± 5.92	2.7	66.2 ± 4.47	0.8	12.9 ± 4.33	3.9	50.1 ± 4.89
11	4-Br-Ph	41.5 ± 4.46	0.4	16.2 ± 4.08	1.1	76.6 ± 4.70	0.2	74.2 ± 6.82	0.2	17.2 ± 0.64
12	-CH <sub>2</sub> CH <sub>2</sub> -Ph	25.3 ± 8.53	2.2	38.2 ± 3.10	1.5	26.7 ± 3.95	2.1	23.8 ± 0.45	2.3	55.4 ± 1.08
Doxorubicin <sup>i</sup>	-	0.8 ± 0.10	0.4	0.3 ± 0.08	1.0	0.3 ± 0.12	1.0	0.2 ± 0.10	1.5	0.3 ± 0.11
Cisplatin <sup>j</sup>	-	10.4 ± 0.90	0.6	6.7 ± 1.10	0.9	13.2 ± 2.10	0.5	8.2 ± 4.08	0.8	6.3 ± 0.70

<sup>a</sup> Data are expressed as mean SD, <sup>b</sup> IC<sub>50</sub> (μM)—the concentration of the compound that corresponds to 50% growth inhibition of the cell line (as compared to the control) after cells were cultured for 72 h with the individual compound. <sup>c</sup> The SI (Selectivity Index) was calculated using the formula: SI = IC<sub>50</sub> for the normal cell line/IC<sub>50</sub> cancer cell line. <sup>d</sup> Human primary colon cancer (SW480), <sup>e</sup> Human metastatic colon cancer (SW620), <sup>f</sup> Human metastatic prostate cancer (PC3), <sup>g</sup> Human chronic myelogenous leukemia (K562), <sup>h</sup> Human immortal keratinocyte cell line from adult human skin (HaCaT). <sup>i,j</sup> The reference compounds.

The disubstituted chlorine-containing derivatives **2** and **5**, as well as 4-(trifluoromethyl)-phenyl compound (**8**), applied at concentrations of 7.3–9.0 μM were able to effectively inhibit primary SW480 cell lines, while also being more potent than cisplatin. Additionally, within all compounds, the thiourea **5** was highly selective against SW480 cells vs. the other pathological lines tested. On the other hand, the selectivity of both thioureas towards HaCaT cells was advantageous, extending between 2.7 and 7.6. Moreover, the values of IC<sub>50</sub> of their close structural analogs, **1** and **6**, ranged from 12.7 ± 1.53 to 15.6 ± 4.10 μM.

A significant cytotoxic effect on the erythroleukemic K-562 cell lines was observed for dihalogenophenylthioureas **1** and **2**, as well as for the monosubstituted derivative **9**, with all of them containing at least one chlorine atom attached to the terminal ring. Analogs **1** and **2** were 20–30% more effective and several-fold more selective than the reference drug cisplatin. The antiproliferative potency of the *para*-substituted derivatives **9** and **10** was estimated at IC<sub>50</sub> of 10.2–12.9 μM.

Prostate cancer cells belonged in the group that were the least vulnerable to the presence of thiourea compounds; however, three halogenated analogs still exerted higher than (compounds **4**, **8**) or comparable (derivative **3**) activity to cisplatin. Their concentrations corresponding to 50% growth inhibition of the PC3 line varied from 6.9 ± 1.64 to 13.7 ± 7.04 μM, and their selectivity indexes were also favorable (1.3–6.0). The most potent 4-(trifluoromethyl)phenylthiourea (**8**) was also strongly effective against both colon cancer lines but not K-562 cells.

The cytotoxic action of the 2-phenylethylthiourea derivative **12** against cancer cells differed from 23.8 ± 0.45 to 38.2 ± 3.10 μM, depending on the tumor line tested, and it was the only inefficient compound of the designed series. It is worth mentioning that generally the lower the IC<sub>50</sub> values assigned, the higher the SI found. The most promising drug candidates (**1–4**, **8**, **9**) were weakly cytotoxic towards normal HaCaT cell lines. While none of the tested compounds were as potent as ciprofloxacin, the most effective of them expressed a better cytotoxic profile than cisplatin, and possessed higher selectivity indexes in comparison with both referential chemotherapeutics.

A wide selection of the character, location, and number of phenyl ring substituents of the thiourea branch allowed investigation of the influence of the structure of the studied compounds on their antitumor activity. According to our studies, the terminal benzene moiety functionalities were arranged with their increasing impact on cytotoxicity as follows: 4-bromo- (**11**) < 2-(trifluoromethyl)- (**7**) < 2-methyl-5-chloro- (**6**) < 4-cyano- (**10**) < 2-methyl-3-chloro- (**5**) < 2,3-dichloro- (**4**) << 2,4-dichloro- (**3**) < 4-chloro- (**9**) < 3-chloro-4-fluoro- (**1**) < 4-(trifluoromethyl)- (**8**) < 3,4-dichloro- (**2**). As shown, the most pronounced cytotoxic effect was associated with an incorporation of two halogen atoms in the benzene ring, whereby chlorine (**2**, **3**) or fluorine (**1**) were in the *para*- position. Considering the active monosubstituted derivatives, this position of the phenyl moiety was favored by the trifluoromethyl group (**8**) or chlorine (**9**). The replacement chlorine with fluorine is less beneficial in the case of disubstituted derivatives (**2** → **1**) and heavily unfavorable in a group of monosubstituted thioureas (**9** → **11**). Similarly, the noticeable decrease in bioactivity was observed when the electron-donating methyl group was introduced instead of the second halogen (**5**, **6**). Furthermore, from the closest mutual arrangement of both methyl and chlorine groups with the highest activity, the thiourea **5** is more effective against SW480 and selective towards HaCaT cells than its isomer **6**. Considering other isomers of the substituent position, the most cytotoxic profile was exerted by compound **2** with the 3,4-dichlorophenyl fragment. The change of substituent locations to carbons 2,4 or 2,3 (derivatives **3** and **4**, respectively) led to a gradual reduction in their biological potency. By analogy, the replacement of the *ortho*-substituted CF<sub>3</sub> group (**7**) for the *para* (**8**) position was much more fruitful. While an exchange of this voluminous substituent for chlorine (**8** → **9**) still gave a strongly active analog, switching it into the cyano (**10**) or bromo (**11**) group considerably diminished the antitumor effect. Finally, the introduction of the unsubstituted alkylphenyl group (**12**) to the thiourea branch dramatically decreased the compound's bioactivity.

The most potent derivatives (**1–3**, **8**, **9**) were selected for further investigations of their mechanisms of cytotoxic action.

### 2.2.2. Antiproliferative Activity

In order to estimate the tumor and normal cell population density and their viability after treatment with compounds **1–3**, **8**, and **9**, the trypan blue dye exclusion assay was performed. The live cell number of all cancerous cells incubated for 72 h with the studied thioureas was considerably lower in comparison with the controls (Table 2; Figure S1A). The highest reduction in cell amount was denoted for both colon SW480 and SW620 cells treated with the dichlorophenyl derivative **2**, and it accounted for 93%. This compound also considerably reduced the PC3 and K-562 cell number by 69% and 66%, respectively. Similarly, a noticeable decline in both colon cancer cell populations was observed after treatment with the *ortho*-substituted compound **8**. The number of live cells equaled 12% and 18%, respectively, as compared to controls. This thiourea also led to a reduction of PC3 cells of 38%, and leukemia K-562 cell lines of 27%. The number of SW620 and PC3 cells decreased by 72% and 63% in the presence of *para*-substituted compound **9**. However, the reducing influence of this thiourea on the number of other cancerous cells was at the level of 21–32%. It is worth noting that the amount of PC3 cells also diminished to 24% compared to the control after long-term exposure to the IC<sub>50</sub> concentration of dihalogenophenyl derivative **1**. A significant effect on the other studied pathological cells was also noticed and accounted for 32–46%. Furthermore, the derivative **3** reduced the amount of live cancer cells by 32–59%, of which its decreasing impact on colon cancer cells was the greatest. The obtained results show that thioureas **1–3**, **8**, and **9** exerted a cytostatic effect on cancer cells, suppressing their growth and proliferation.

**Table 2.** Trypan blue assay. The effect of compounds **1**, **2**, **3**, **8**, and **9** on the live cell number and viability (%) in SW480, SW620, PC3, K-562, and HaCaT cells. Cells were incubated for 72 h with the tested compounds used in their IC<sub>50</sub> concentrations, then cells were harvested, stained with trypan blue, and analyzed using a cell counter. Data are expressed as the mean ± SD.- “control without compound”, <sup>a</sup> Human primary colon cancer (SW480), <sup>b</sup> Human metastatic colon cancer (SW620), <sup>c</sup> Human metastatic prostate cancer (PC3), <sup>d</sup> Human chronic myelogenous leukemia (K562), <sup>e</sup> Human immortal keratinocyte cell line from adult human skin (HaCaT).

		Compound	Cell Number × 10 <sup>5</sup>	Viability (%)
Cancer cell line	SW480 <sup>a</sup>	-	3.6 ± 0.20	93 ± 1.35
		<b>1</b>	2.0 ± 0.30	69 ± 1.30
		<b>2</b>	0.3 ± 0.35	45 ± 2.40
		<b>3</b>	1.5 ± 0.10	90 ± 1.30
		<b>8</b>	0.4 ± 0.15	90 ± 2.30
		<b>9</b>	2.5 ± 0.12	72 ± 2.25
	SW620 <sup>b</sup>	-	5.7 ± 0.10	96 ± 3.30
		<b>1</b>	1.3 ± 0.25	79 ± 1.30
		<b>2</b>	0.4 ± 0.22	42 ± 1.30
		<b>3</b>	2.4 ± 0.20	93 ± 2.33
		<b>8</b>	1.0 ± 0.20	55 ± 1.11
		<b>9</b>	1.6 ± 0.11	84 ± 3.08
	PC3 <sup>c</sup>	-	3.4 ± 0.25	97 ± 2.30
		<b>1</b>	2.3 ± 0.15	93 ± 1.50
		<b>2</b>	2.4 ± 0.16	93 ± 1.40
		<b>3</b>	1.8 ± 0.18	58 ± 1.20
		<b>8</b>	2.1 ± 0.12	82 ± 1.10
		<b>9</b>	1.2 ± 0.15	73 ± 1.99
	K-562 <sup>d</sup>	-	4.4 ± 0.15	98 ± 1.30
		<b>1</b>	1.8 ± 0.24	93 ± 2.05
<b>2</b>		1.0 ± 0.21	55 ± 1.03	
<b>3</b>		3.0 ± 0.27	85 ± 1.20	
<b>8</b>		3.2 ± 0.14	88 ± 1.10	
<b>9</b>		3.5 ± 0.22	90 ± 2.40	
Normal cell line	HaCaT <sup>e</sup>	-	9.2 ± 0.25	98 ± 1.30
		<b>1</b>	6.5 ± 0.15	97 ± 1.33
		<b>2</b>	1.6 ± 0.31	84 ± 1.03
		<b>3</b>	7.8 ± 0.14	96 ± 3.01
		<b>8</b>	4.9 ± 0.28	98 ± 1.02
		<b>9</b>	8.6 ± 0.12	98 ± 1.50

In addition, after thiourea treatment, the viability of the majority of pathological cell lines was diminished, which proved not only the cytostatic, but also the cytotoxic influence of the selected derivatives (Table 2; Figure S1B). This effect was clearly observed in both SW480 and SW620 cells for thioureas **1**, **2**, and **9**. The largest decrease of cell viability was found for the compound **2** (by 48% and 58%, respectively), while substances **2** and **9** were efficient in 16–24%. Additionally, the derivative **8** reduced the viability of SW620 cells by 45%. Derivatives **2**, **3**, and **9** decreased the survival of PC3 cells by 15–39%, as compared to the control, and the most evident cytotoxic activity in these cells was observed for **3**. The K-562 cell line was the least sensitive to incubation with the evaluated compounds. Its viability was diminished by 10–15% after 72 h of contact with thioureas **2**, **3**, and **8**. Importantly, the various concentrations of the target compounds did not affect normal HaCaT cells' viability.

### 2.2.3. Apoptotic Activity

To estimate the mechanism of anticancer activity of the selected compounds **1–3**, **8**, and **9**, their effect on both early and late apoptosis was evaluated by flow cytometry analysis. As shown in Figures 2–4, the studied derivatives applied in their IC<sub>50</sub> concentrations induced considerably late apoptosis or necrosis in cancerous cells compared to controls. The

apoptosis-activating effect was the strongest in the SW480, SW620, and K-562 cell lines, and the most noticeable activity was observed for the thiourea **2**, followed by its analogs **1** and **8**. Dichlorophenyl derivative **2** and fluorinated thiourea **8** showed a very high percentage of SW480 cells in late apoptosis (95%  $\pm$  1.5% and 97%  $\pm$  1.2%, respectively). Other tested substances also significantly influenced primary colon cancer cells, causing 24%  $\pm$  0.4% (compound **9**) to 60%  $\pm$  1.8% (compound **1**) of SW480 cells to be in late apoptosis. The derivative **2** was similarly the most potent activator of apoptosis in metastatic SW620 cells (99%  $\pm$  0.5%), in comparison with the thiourea **1** (57%  $\pm$  1.2%). The pro-apoptotic impact of derivatives **3**, **8**, and **9** in these cells was not so spectacular and did not exceed 26%. On the other hand, thiourea-derived compounds **1** and **2** considerably affected the level of late apoptosis in leukemia K-562 cells, and gave comparable results (74%  $\pm$  3.8% and 73%  $\pm$  2.0%, respectively). Additionally, visible late apoptosis-inducing properties in these cell lines were denoted for the compound **9** (47%  $\pm$  3.0%), which was twice as strong towards the colon tumor cells mentioned above. The apoptotic properties of analogs **3** and **8** in K-562 cells varied from 30%  $\pm$  1.6% to 33%  $\pm$  2.3%. In contrary, treatment of PC3 cells with thiourea derivatives did not increase their apoptosis, except for the compound **8** (25%  $\pm$  1.5%). The analysis performed in HaCaT cells, incubated with the studied substances **1**, **8**, and **9**, revealed the low level of cells in late apoptosis, counted from 11% to 14%. Whereas the apoptosis-generating influence of derivatives **2** and **3** on normal keratinocytes was higher (29% and 23%), their selectivity measured by MTT methods is favorable. The obtained results are in agreement with the IC<sub>50</sub> values assigned to pathological cancer cell lines.

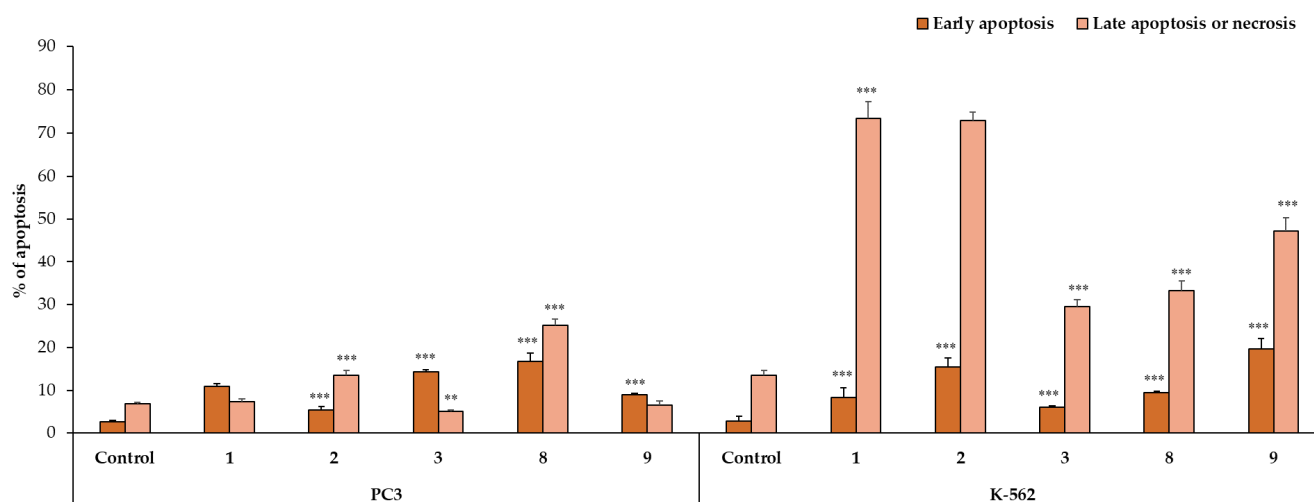


**Figure 2.** The effect of compounds **1–3**, **8**, and **9** on early and late apoptosis in SW480, SW620, and HaCaT cells. Cells were incubated for 72 h with the tested compounds used in their IC<sub>50</sub> concentrations, then cells were harvested, stained with Annexin V-FITC and PI, and analyzed using flow cytometry. Data are expressed as % of cells in the early stage of apoptosis, and as % of cells in the late stage of apoptosis or necrosis. Data are expressed as the mean  $\pm$  SD. \*\*\*  $p \leq 0.001$ , \*\*  $p \leq 0.01$ , as compared to the control.

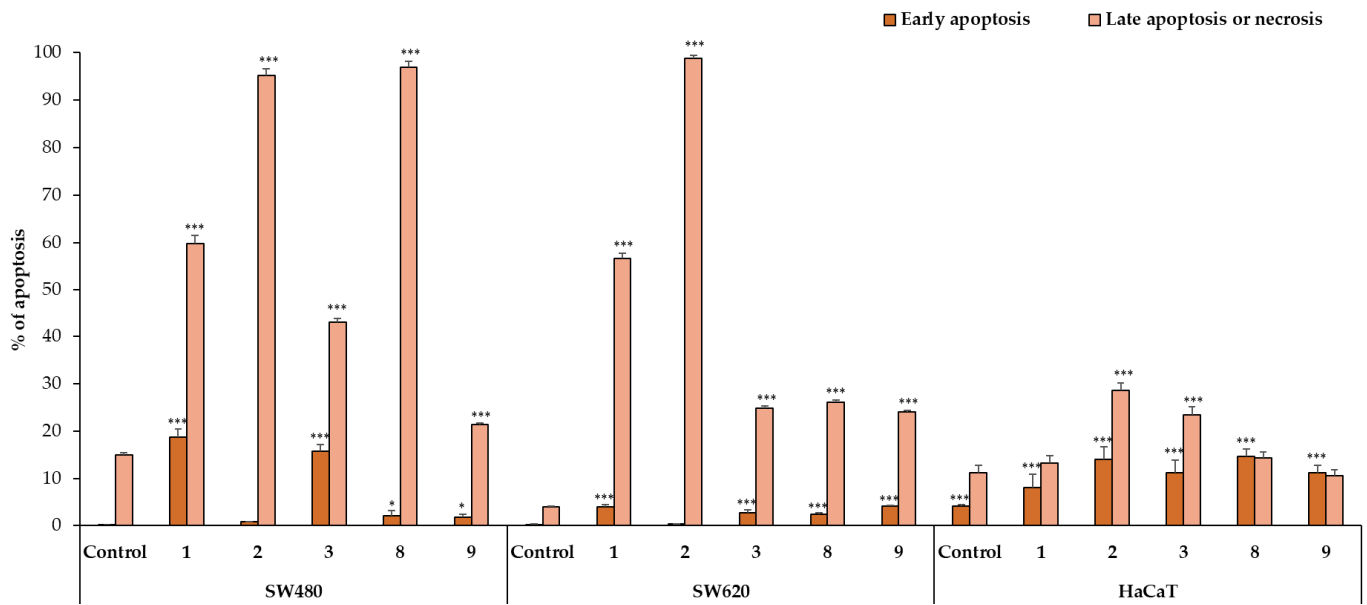


**Figure 3.** The effect of compounds 1–3, 8, and 9 on early and late apoptosis in PC3 and K-562 cells. Cells were incubated for 72 h with the tested compounds used in their IC<sub>50</sub> concentrations, then cells were harvested, stained with Annexin V-FITC and PI, and analyzed using flow cytometry. Data are expressed as % of cells in the early stage of apoptosis, and as % of cells in the late stage of apoptosis. Data are expressed as the means ± SD. \*\*\*  $p \leq 0.001$ , \*  $p \leq 0.05$ , as compared to the control.

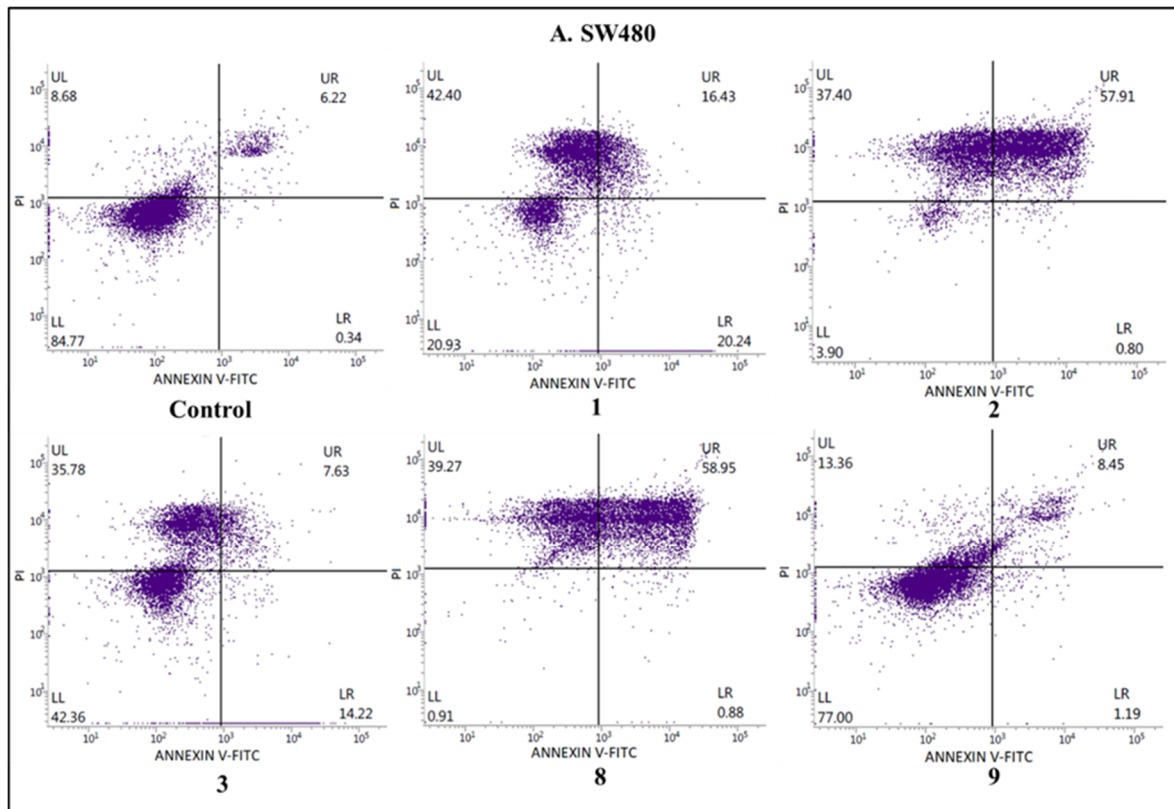


**Figure 4.** Cont.

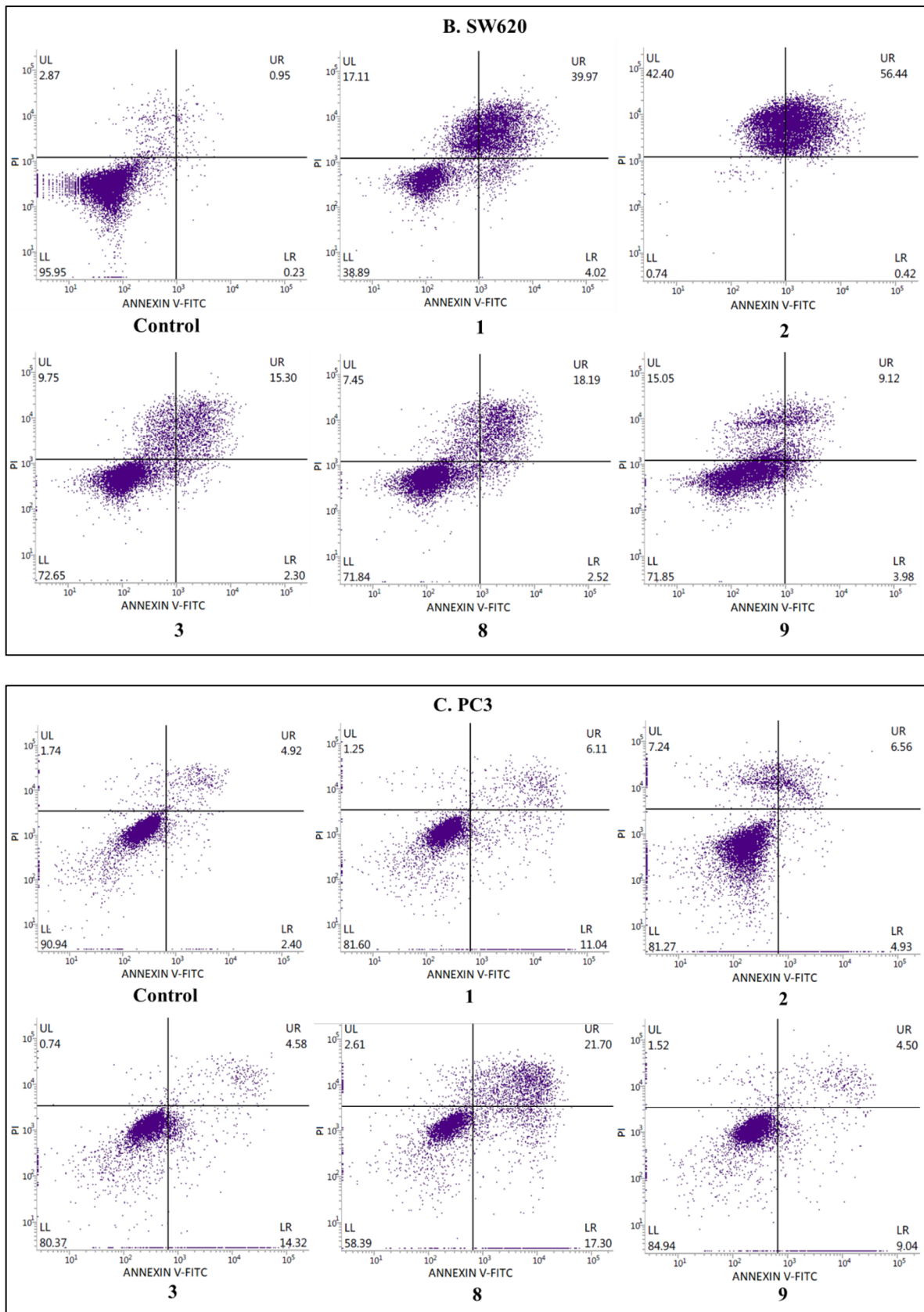
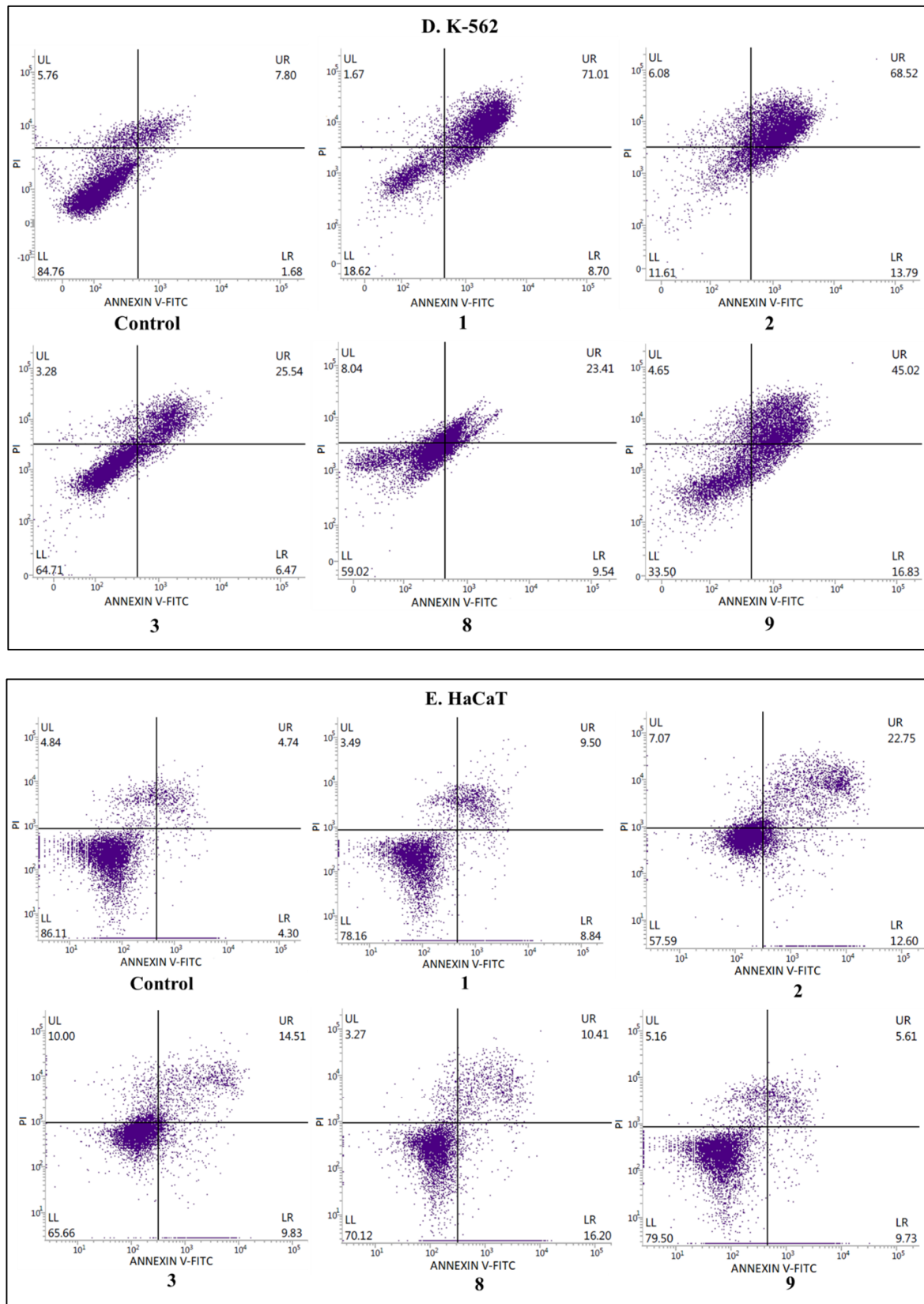


Figure 4. Cont.





**Figure 4.** The effects of compounds 1, 2, 3, 8, and 9 on early and late apoptosis or necrosis in (A) SW480, (B) SW620, (C) PC3, (D) K-562, and (E) HaCaT cells detected with Annexin V-FITC/PI by flow cytometry. Cells were incubated for 72 h with the tested compounds. Dot plot diagrams show representative experiments. The lower left (LL) quadrant represents viable cells and the lower right (LR) quadrant early apoptotic cells. The upper right (UR) quadrant contains late-stage apoptotic cells, and the upper left (UL) quadrant necrotic cells.

#### 2.2.4. Inhibition of IL-6 Release

Interleukin-6 (IL-6) is a cytokine that stimulates the inflammatory and auto-immune processes in many diseases, including pancreatic, prostate, and colon cancers. As its level is higher in advanced and metastatic cancer, IL-6 is also involved in tumor development and progression [37].

Because of the low secretion of IL-6 by leukemic cells compared to solid tumors, and in addition to the lack of IL-6 receptors in K-562 cells [38], studies of the effect of derivatives **1–3**, **8**, and **9** on the inhibition of IL-6 release were carried out on primary and secondary solid tumor cells (SW480, SW620, and PC3). The results are given in Table 3 and Figure S2. A remarkable inhibition of the IL-6 level was denoted for both colon cancer cell lines. Compound **2**, identified as the strongest inhibitor, reduced the interleukin level by 54% (in SW480 cells) and 63% (SW620 cells). A significant effect was also observed in these cells for its structural isomer **3** (39% and 23% of inhibition, respectively). Additionally, compound **3** considerably affected the IL-6 level produced by PC3 cells, and reduced it by 33%. Similarly, the treatment with derivative **1** was effective for both colon cancer cells. In its presence, IL-6 release decreased by 28–36%, as compared to controls. For monosubstituted derivatives **8** and **9**, the observed IL-6-reducing influence was weaker. They both inhibited IL-6 secretion in SW480 and SW620 cell lines by 25–32%. In contrast to compound **9**, thiourea **8** additionally diminished the cytokine level in PC3 cells by 26%.

**Table 3.** Effects of compounds **1–3**, **8**, and **9** on IL-6 levels, measured by the ELISA test. Data are expressed as the mean  $\pm$  SD from <sup>a</sup> Human primary colon cancer (SW480), <sup>b</sup> Human metastatic colon cancer (SW620), <sup>c</sup> Human metastatic prostate cancer (PC3), <sup>d</sup> Human immortal keratinocyte cell line from adult human skin (HaCaT).

		Compound	IL-6 Concentration (pg/mL)
Cancer cell line	SW480 <sup>a</sup>	Control	7.8 $\pm$ 0.03
		<b>1</b>	5.7 $\pm$ 0.01
		<b>2</b>	3.6 $\pm$ 0.02
		<b>3</b>	4.8 $\pm$ 0.04
		<b>8</b>	5.3 $\pm$ 0.01
		<b>9</b>	5.5 $\pm$ 0.02
	SW620 <sup>b</sup>	Control	7.7 $\pm$ 0.05
		<b>1</b>	4.9 $\pm$ 0.01
		<b>2</b>	2.8 $\pm$ 0.03
		<b>3</b>	5.9 $\pm$ 0.03
		<b>8</b>	5.8 $\pm$ 0.06
		<b>9</b>	5.2 $\pm$ 0.03
	PC3 <sup>c</sup>	Control	10.9 $\pm$ 0.07
		<b>1</b>	9.6 $\pm$ 0.02
		<b>2</b>	9.1 $\pm$ 0.04
<b>3</b>		7.3 $\pm$ 0.06	
<b>8</b>		8.1 $\pm$ 0.08	
<b>9</b>		9.9 $\pm$ 0.03	
Normal cell line	HaCaT <sup>d</sup>	Control	9.7 $\pm$ 0.03
		<b>1</b>	8.7 $\pm$ 0.03
		<b>2</b>	9.1 $\pm$ 0.03
		<b>3</b>	8.9 $\pm$ 0.01
		<b>8</b>	9.1 $\pm$ 0.06
		<b>9</b>	9.0 $\pm$ 0.01

### 3. Materials and Methods

#### 3.1. Chemistry

##### 3.1.1. General Procedure

(Trifluoromethyl)aniline was supplied by Alfa Aesar (Stock No. A15910). Isothiocyanates were purchased from Alfa Aesar or Sigma Aldrich. Acetonitrile, chloroform, and

methanol were supplied by POCh (Polskie Odczynniki Chemiczne). All chemicals were of analytical grade and were used without any further purification. Prior to usage, acetonitrile was kept in crown cap bottles over anhydrous phosphorus pentoxide (Carl Roth, Karlsruhe, Germany). The NMR spectra were recorded on a Bruker AVANCE DMX400 spectrometer, operating at 300 ( $^1\text{H}$  NMR) and 75.5 MHz ( $^{13}\text{C}$  NMR). The spectra were measured in DMSO and are given as  $\delta$  values (in ppm) relative to TMS. Mass spectral ESI measurements were carried out on an LCT Micromass TOF HiRes apparatus. Flash chromatography was performed on Merck silica gel 60 (200–400 mesh) using chloroform:methanol mixture. Analytical TLC was carried out on silica gel F254 (Merck, Darmstadt, Germany) plates (0.25 mm thickness).

#### General Procedure for the Preparation of N-aryl-[3-(trifluoromethyl)phenyl]thiourea Derivatives (1–12)

A solution of commercially available 3-(trifluoromethyl)aniline (0.0031 mol, 0.50 g) in anhydrous acetonitrile (5 mL) was treated with appropriate isothiocyanate (0.0031 mol) and the mixture was stirred at room temperature for 24 h. Then, solvent was removed on a rotary evaporator. The residue was purified by column chromatography (chloroform:methanol; 9.5:0.5 vol.) to yield derivatives 1–12.

1-(3-chloro-4-fluorophenyl)-3-[3-(trifluoromethyl)phenyl]thiourea (1) was synthesized as described previously [39].

1-(3,4-dichlorophenyl)-3-[3-(trifluoromethyl)phenyl]thiourea (2) was synthesized as described previously [39].

1-(2,4-dichlorophenyl)-3-[3-(trifluoromethyl)phenyl]thiourea (3) Yield 70%, cream powder, m.p. 155–157 °C.  $^1\text{H}$  NMR (300 MHz, DMSO)  $\delta$  (ppm): 10.22 (s, 1H, NH), 9.73 (s, 1H, NH), 8.00 (s, 1H, Ar-H), 7.80–7.77 (d, 1H,  $J = 9.0$  Hz, Ar-H), 7.71–7.70 (d, 1H,  $J = 3.0$  Hz, Ar-H), 7.62–7.55 (m, 2H, Ar-H), 7.50–7.43 (m, 2H, Ar-H).  $^{13}\text{C}$  NMR (75.5 MHz, DMSO)  $\delta$  (ppm): 180.62, 140.11, 135.34, 131.49, 131.30, 131.07, 129.62, 129.06 (q,  $J_{\text{C-F}} = 31.7$  Hz), 129.06, 128.43, 127.48, 124.03 (q,  $J_{\text{C-F}} = 272.6$  Hz), 120.97 (q,  $J_{\text{C-F}} = 3.8$  Hz), 119.91 (q,  $J_{\text{C-F}} = 3.8$  Hz). HRMS (ESI) calc. for  $\text{C}_{14}\text{H}_8\text{N}_2\text{F}_3\text{SCl}_2$   $[\text{M} - \text{H}]^-$ : 362.9726, found: 362.9737.

1-(2,3-dichlorophenyl)-3-[3-(trifluoromethyl)phenyl]thiourea (4) Yield 65%, white powder, m.p. 140–142 °C.  $^1\text{H}$  NMR (300 MHz, DMSO)  $\delta$  (ppm): 10.24 (s, 1H, NH), 9.83 (s, 1H, NH), 7.99 (s, 1H, Ar-H), 7.80–7.77 (d, 1H,  $J = 9.0$  Hz, Ar-H), 7.61–7.53 (m, 3H, Ar-H), 7.50–7.47 (m, 1H, Ar-H), 7.41–7.35 (m, 1H, Ar-H).  $^{13}\text{C}$  NMR (75.5 MHz, DMSO)  $\delta$  (ppm): 180.63, 140.13, 138.17, 131.90, 129.62, 129.32, 129.05 (q,  $J_{\text{C-F}} = 31.7$  Hz), 128.63, 128.35, 127.88, 127.47, 124.03 (q,  $J_{\text{C-F}} = 272.6$  Hz), 120.98 (q,  $J_{\text{C-F}} = 3.8$  Hz), 119.93 (q,  $J_{\text{C-F}} = 4.5$  Hz). HRMS (ESI) calc. for  $\text{C}_{14}\text{H}_8\text{N}_2\text{F}_3\text{SCl}_2$   $[\text{M} - \text{H}]^-$ : 362.9726, found: 362.9737.

1-(3-chloro-2-methylphenyl)-3-[3-(trifluoromethyl)phenyl]thiourea (5) Yield 65%, white powder, m.p. 163–165 °C.  $^1\text{H}$  NMR (300 MHz, DMSO)  $\delta$  (ppm): 9.95 (s, 1H, NH), 9.77 (s, 1H, NH), 7.94 (m, 1H, Ar-H), 7.79–7.75 (m, 1H, Ar-H), 7.61–7.44 (m, 2H, Ar-H), 7.41–7.34 (m, 1H, Ar-H), 7.26–7.23 (m, 2H, Ar-H), 2.27 (s, 3H,  $\text{CH}_3$ ).  $^{13}\text{C}$  NMR (75.5 MHz, DMSO)  $\delta$  (ppm): 180.80, 140.43, 139.07, 133.85, 133.50, 129.44, 129.36 (q,  $J_{\text{C-F}} = 31.7$  Hz), 128.73, 127.51, 127.23, 127.10, 124.07 (q,  $J_{\text{C-F}} = 272.6$  Hz), 120.72 (q,  $J_{\text{C-F}} = 3.8$  Hz), 119.98 (q,  $J_{\text{C-F}} = 4.5$  Hz), 15.27. HRMS (ESI) calc. for  $\text{C}_{15}\text{H}_{11}\text{N}_2\text{F}_3\text{SCl}$   $[\text{M} - \text{H}]^-$ : 343.0315, found: 343.0284.

1-(5-chloro-2-methylphenyl)-3-[3-(trifluoromethyl)phenyl]thiourea (6) Yield 63%, cream powder, m.p. 146–148 °C.  $^1\text{H}$  NMR (300 MHz, DMSO)  $\delta$  (ppm): 10.03 (s, 1H, NH), 9.64 (s, 1H, NH), 7.96–7.93 (m, 1H, Ar-H), 7.79–7.74 (m, 1H, Ar-H), 7.59–7.54 (t, 1H,  $J = 7.5$  Hz, Ar-H), 7.50–7.45 (m, 1H, Ar-H), 7.39–7.38 (d, 1H,  $J = 3.0$  Hz, Ar-H), 7.31–7.28 (m, 1H, Ar-H), 7.26–7.20 (m, 1H, Ar-H), 2.23 (s, 3H,  $\text{CH}_3$ ).  $^{13}\text{C}$  NMR (75.5 MHz, DMSO)  $\delta$  (ppm): 180.55, 140.34, 138.83, 133.84, 131.85, 129.85, 129.51, 128.99 (q,  $J_{\text{C-F}} = 31.7$  Hz), 127.52, 126.43, 125.86, 124.10 (q,  $J_{\text{C-F}} = 271.8$  Hz), 120.75 (q,  $J_{\text{C-F}} = 4.5$  Hz), 119.95 (q,  $J_{\text{C-F}} = 3.8$  Hz), 17.29. HRMS (ESI) calc. for  $\text{C}_{15}\text{H}_{11}\text{N}_2\text{F}_3\text{SCl}$   $[\text{M} - \text{H}]^-$ : 343.0315, found: 343.0284.

1-[2-(trifluoromethyl)phenyl]-3-[3-(trifluoromethyl)phenyl]thiourea (7) Yield 72%, white powder, m.p. 173–175 °C.  $^1\text{H}$  NMR (300 MHz, DMSO)  $\delta$  (ppm): 10.18 (s, 1H, NH), 9.60 (s, 1H, NH), 8.05 (s, 1H, Ar-H), 7.78–7.68 (m, 3H, Ar-H), 7.60–7.47 (m, 4H, Ar-H).  $^{13}\text{C}$  NMR (75.5 MHz, DMSO)  $\delta$  (ppm): 181.51, 140.17, 136.79, 132.81, 132.33, 129.62, 129.05

(q,  $J_{C-F}$  = 31.7 Hz), 128.42, 127.52, 127.26, 126.25 (q,  $J_{C-F}$  = 4.5 Hz), 125.85, 125.38, 120.91 (q,  $J_{C-F}$  = 3.8 Hz), 119.74 (q,  $J_{C-F}$  = 3.8 Hz). HRMS (ESI) calc. for  $C_{15}H_9N_2F_6S$   $[M - H]^-$ : 363.0368, found: 363.0391.

1-[3-(trifluoromethyl)phenyl]-3-[4-(trifluoromethyl)phenyl]thiourea (**8**) Yield 76%, white powder, m.p. 134–136 °C.  $^1H$  NMR (300 MHz, DMSO)  $\delta$  (ppm): 10.36–10.34 (m, 1H, NH), 10.26–10.23 (m, 1H, NH), 7.96–7.93 (m, 1H, Ar-H), 7.79–7.68 (m, 5H, Ar-H), 7.61–7.55 (t, 1H,  $J$  = 9.0 Hz, Ar-H), 7.50–7.47 (m, 1H, Ar-H).  $^{13}C$  NMR (75.5 MHz, DMSO)  $\delta$  (ppm): 179.90, 143.02, 140.14, 129.64, 129.32, 128.48, 127.43, 126.13, 125.73 (q,  $J_{C-F}$  = 3.8 Hz), 124.26, 124.27 (q,  $J_{C-F}$  = 32.5 Hz), 123.06, 122.38, 120.94 (q,  $J_{C-F}$  = 3.8 Hz), 119.91 (q,  $J_{C-F}$  = 3.9 Hz). HRMS (ESI) calc. for  $C_{15}H_9N_2F_6S$   $[M - H]^-$ : 363.0368, found: 363.0391.

1-(4-chlorophenyl)-3-[3-(trifluoromethyl)phenyl]thiourea (**9**) was synthesized as described previously [2].

1-(4-cyanophenyl)-3-[3-(trifluoromethyl)-phenyl]thiourea (**10**) was synthesized as described previously [2].

1-(4-bromophenyl)-3-[3-(trifluoromethyl)phenyl]thiourea (**11**) Yield 75%, white powder, m.p. 182–184 °C.  $^1H$  NMR (300 MHz, DMSO)  $\delta$  (ppm): 10.09–10.08 (d, 2H,  $J$  = 3.0 Hz, NH), 7.94 (s, 1H, Ar-H), 7.77–7.74 (d, 1H,  $J$  = 9.0 Hz, Ar-H), 7.59–7.52 (m, 3H, Ar-H), 7.48–7.44 (m, 3H, Ar-H).  $^{13}C$  NMR (75.5 MHz, DMSO)  $\delta$  (ppm): 179.82, 140.31, 138.52, 131.39, 129.52, 128.6 (q,  $J_{C-F}$  = 31.0 Hz), 128.38, 127.36, 125.72, 124.06 (q,  $J_{C-F}$  = 272.6 Hz), 120.73 (q,  $J_{C-F}$  = 3.8 Hz), 119.85 (q,  $J_{C-F}$  = 4.5 Hz), 118.64, 116.81. HRMS (ESI) calc. for  $C_{14}H_9N_2F_3SBr$   $[M - H]^-$ : 372.9620, found: 372.9622.

1-(2-phenylethyl)-3-[3-(trifluoromethyl)-phenyl]thiourea (**12**) was synthesized as described previously [2].

### 3.2. Biological Studies

#### 3.2.1. Cell Culture

The human primary (SW480), metastatic (SW620) colon cancer, metastatic prostate cancer (PC3), chronic myelogenous leukemia (K-562), and human immortal keratinocyte (HaCaT) cell lines were purchased from the American Type Culture Collection (ATCC, Rockville, MD, USA). The cells were cultured in medium according to protocols (MEM for SW480 and SW620, RPMI 1640 for PC3 and K-562, and DMEM for HaCaT cells), supplemented with 10% FBS, penicillin (100 U/mL) and streptomycin (100  $\mu$ g/mL), and cultured in a 37 °C/5% CO<sub>2</sub> humidified incubator. The cells were cultured until appropriate confluence was achieved (80–90%). Next, they were harvested by treatment with 0.25% trypsin (Gibco Life Technologies, Waltham, MA, USA) excluding the non-adherent K-562 cell line and used for studies.

#### 3.2.2. MTT Assay

To determine the IC<sub>50</sub> of the thiourea compounds **1–12**, cells were seeded in 96-well plates ( $1 \times 10^4$  cells per well) and treated for 72 h with different concentrations of compounds. Cells without the studied compounds in medium were used as a control.

The cell viability was assessed by determination of MTT salt [3-(4,5-dimethylthiazol-2-yl)-2,5-diphenyltetrazoliumbromide] conversion by mitochondrial dehydrogenase. The MTT assay was performed as previously described [37]. Alternatively, non-adherent leukemic cells were centrifuged in a microplate centrifuge ( $400 \times g$ , 5 min) during the collection stages. Experiments were repeated three times. Cell viability was presented as a percent of MTT reduction in the treated cells versus the control cells. The number of viable cells cultured without the studied compounds was assumed as 100%. A decreased relative MTT level indicated decreased cell viability. Thiourea compounds with the highest cytotoxic potential assessed by MTT determination (with the lowest IC<sub>50</sub>) were chosen for subsequent assessments of cytotoxicity mechanisms.

### 3.2.3. Trypan Blue Assay

Cells ( $1 \times 10^5$  cells per well) were seeded in 12-well plates and after 72 h of incubation with  $IC_{50}$  concentrations of the studied compounds **1–3**, **8**, and **9**, they were washed twice with PBS (phosphate-buffered saline) and harvested. The live cell count was assessed by the trypan blue exclusion dye assay using an automated cell counter (Countess™ Invitrogen, Waltham, MA, USA). Untreated cells were used as the control.

### 3.2.4. Annexin V Binding Assay

The cells were cultured and harvested under the conditions described in Section 3.2.1. Then, they were seeded in six-well plates ( $2 \times 10^5$  cells per well), and treated with the selected thioureas **1–3**, **8**, and **9** at their  $IC_{50}$  concentration for 72 h. The effect of these compounds on the process of early and late apoptosis and necrosis was determined as described previously [37] by dual staining with Annexin V:FITC and propidium iodide, according to the manufacturer's protocol (Becton Dickinson). The cells that were Annexin V:FITC positive and PI negative were identified as early apoptotic, and Annexin V:FITC and PI positive as late apoptotic or necrotic.

### 3.2.5. IL-6 Level Assay

The IL-6 concentration in all studied cancer cells and normal HaCaT cell lines was measured by an ELISA kit (Diaclon SAS Besancon CEDEX, Besançon, France). Cells were seeded in 12-well plates ( $1 \times 10^5$  cells per well) and treated with the  $IC_{50}$  concentration of the studied compounds **1–3**, **8**, and **9** for 72 h. IL-6 in cell culture supernatant was measured using the enzyme-linked immunosorbent assay in accordance with the manufacturer's protocol.

### 3.2.6. Statistical Analyses

Statistical analyses were performed using GraphPad Prism 9 software (GraphPad Software). The results were expressed as mean  $\pm$  SD from at least three independent experiments. The statistical significance of differences between means was established by ANOVA with Dunnett's multiple comparison post hoc test. P values below 0.05 were considered statistically significant.

## 4. Conclusions

In summary, we herein report a high-throughput synthesis of 3-(trifluoromethyl)aniline with various isothiocyanates. The effect of all the synthesized compounds' inhibition of the growth of human tumor cell lines, such as SW480 (primary colon cancer), SW620 (metastatic colon cancer), PC3 (metastatic prostate cancer), and K-562 (chronic myelogenous leukemia), was evaluated. Dihalogenophenyl (**1–4**) and *para*-substituted thioureas (**8**, **9**) were highly cytotoxic against the mentioned pathological cell cultures ( $IC_{50} \leq 10 \mu\text{M}$ ), with selectivity over normal HaCaT cells. Compounds **2**, **3**, and **9** were more effective and selective than the reference cisplatin. The mechanisms of the *in vitro* cytotoxic activity of the most bioactive compounds **1–3**, **8**, and **9** were studied. All of them were cytostatic and reduced the cancer cells' number, being safe for normal keratinocytes. Cytotoxic thioureas **1**, **2**, and **9** considerably diminished the viability of both SW480 and SW620 cells. Derivatives **1**, **2**, and **8** exerted the strongest apoptosis-activating effect in SW480, SW620, and K-562 cell lines. Among them, compound **2** showed the highest percentage of colon cancer cells in late apoptosis. The tested derivatives revealed anti-IL-6 activity and significantly decreased the levels of the proinflammatory cytokine produced by both colon carcinoma cells.

The structural modifications of the thiourea terminal moieties indicated the dihalogenophenyl derivative **2**, followed by its isomer **3** and *para*-substituted analog **8**, as the most effective in cancer treatment. This work constitutes an evaluation of the potential and mechanisms of cytotoxic action of thiourea-derived compounds, which will be developed.

**Supplementary Materials:** The following are available online at <https://www.mdpi.com/article/10.3390/ph14111097/s1>, Figure S1. (A) Trypan blue assay. The effect of compounds **1**, **2**, **3**, **8** and **9** on cell number in SW480, SW620, PC3, K-562 and HaCaT cells. (B) Trypan blue assay. The effect of compounds **1**, **2**, **3**, **8** and **9** on viability in SW480, SW620, PC3, K-562 and HaCaT cells. Figure S2. Effects of compounds **1–3**, **8** and **9** on IL-6 levels, measured by ELISA test.  $^1\text{H}$  and  $^{13}\text{C}$  NMR spectra of synthesized compounds **3–8**, **11**. Table S1. High Resolution Mass Spectra (HRMS) of compounds **4**, **6**, **7**, **11**.

**Author Contributions:** Conceptualization, A.B. and A.C.; software, P.S.-Ł.; validation, A.C.; investigation, P.S.-Ł. and K.P.; writing—original draft preparation, A.B.; writing—review and editing, A.C.; visualization, P.S.-Ł. and A.B.; supervision, A.B. All authors have read and agreed to the published version of the manuscript.

**Funding:** This research received no external funding.

**Institutional Review Board Statement:** Not applicable.

**Informed Consent Statement:** Not applicable.

**Data Availability Statement:** Data is contained within the article or supplementary material.

**Conflicts of Interest:** The authors declare no conflict of interest.

## References

1. Frankish, H. 15 Million New Cancer Cases per Year by 2020, Says Who. *Lancet* **2003**, *361*, 1278. [CrossRef]
2. Bielenica, A.; Stefańska, J.; Stępień, K.; Napiórkowska, A.; Augustynowicz-Kopeć, E.; Sanna, G.; Madeddu, S.; Boi, S.; Giliberti, G.; Wrzosek, M.; et al. Synthesis, Cytotoxicity and Antimicrobial Activity of Thiourea Derivatives Incorporating 3-(Trifluoromethyl)phenyl Moiety. *Eur. J. Med. Chem.* **2015**, *101*, 111–125. [CrossRef] [PubMed]
3. Bielenica, A.; Sanna, G.; Madeddu, S.; Giliberti, G.; Stefańska, J.; Koziół, A.; Savchenko, O.; Strzyga-Łach, P.; Chrzanowska, A.; Kubiak-Tomaszewska, G.; et al. Disubstituted 4-Chloro-3-Nitrophenylthiourea Derivatives: Antimicrobial and Cytotoxic Studies. *Molecules* **2018**, *23*, 2428. [CrossRef] [PubMed]
4. Maalik, A.; Rahim, H.; Saleem, M.; Fatima, N.; Rauf, A.; Wadood, A.; Malik, M.I.; Ahmed, A.; Rafique, H.; Zafar, M.N.; et al. Synthesis, Antimicrobial, Antioxidant, Cytotoxic, Antiurease and Molecular Docking Studies of N-(3-Trifluoromethyl)Benzoyl-N'-Aryl Thiourea Derivatives. *Bioorg. Chem.* **2019**, *88*, 102946. [CrossRef]
5. Bielenica, A.; Stępień, K.; Napiórkowska, A.; Augustynowicz-Kopeć, E.; Krukowski, S.; Włodarczyk, M.; Struga, M. Synthesis and Antimicrobial Activity of 4-Chloro-3-Nitrophenylthiourea Derivatives Targeting Bacterial Type II Topoisomerases. *Chem. Biol. Drug Des.* **2016**, *87*, 905–917. [CrossRef]
6. Mazzotta, S.; Cebrero-Canguero, T.; Frattaruolo, L.; Vega-Holm, M.; Carretero-Ledesma, M.; Sánchez-Céspedes, J.; Cappello, A.R.; Aiello, F.; Pachón, J.; Vega-Pérez, J.M.; et al. Exploration of Piperazine-Derived Thioureas as Antibacterial and Anti-Inflammatory Agents. In Vitro Evaluation against Clinical Isolates of Colistin-Resistant *Acinetobacter Baumannii*. *Bioorg. Med. Chem. Lett.* **2020**, *30*, 127411. [CrossRef]
7. Ameryckx, A.; Pochet, L.; Wang, G.; Yildiz, E.; Saadi, B.E.; Wouters, J.; Van Bambeke, F.; Frédérick, R. Pharmacomodulations of the Benzoyl-Thiosemicarbazide Scaffold Reveal Antimicrobial Agents Targeting D-Alanyl-D-Alanine Ligase in Bacterio. *Eur. J. Med. Chem.* **2020**, *200*, 112444. [CrossRef]
8. Bielenica, A.; Drzewiecka-Antonik, A.; Rejmak, P.; Stefańska, J.; Koliński, M.; Kmiecik, S.; Lesyng, B.; Włodarczyk, M.; Pietrzyk, P.; Struga, M. Synthesis, Structural and Antimicrobial Studies of Type II Topoisomerase-Targeted Copper(II) Complexes of 1,3-Disubstituted Thiourea Ligands. *J. Inorg. Biochem.* **2018**, *182*, 61–70. [CrossRef]
9. Bielenica, A.; Sanna, G.; Madeddu, S.; Struga, M.; Józwiak, M.; Koziół, A.E.; Sawchenko, A.; Materek, I.B.; Serra, A.; Giliberti, G. New Thiourea and 1,3-Thiazolidin-4-one Derivatives Effective on the HIV-1 Virus. *Chem. Biol. Drug Des.* **2017**, *90*, 883–891. [CrossRef]
10. Nagalakshamma, V.; Venkataswamy, M.; Pasala, C.; Umamaheswari, A.; Thyagaraju, K.; Nagaraju, C.; Chalapathi, P.V. Design, Synthesis, Anti-Tobacco Mosaic Viral Aand Molecule Docking Simulations of Urea/Thiourea Derivatives of 2-(Piperazine-1-Yl)-Pyrimidine and 1-(4-Fluoro/4-Chloro Phenyl)-Piperazine and 1-(4-ChloroPhenyl)-Piperazine—A Study. *Bioorg. Chem.* **2020**, *102*, 104084. [CrossRef]
11. Khachatoorian, R.; Micewicz, E.D.; Micewicz, A.; French, S.W.; Ruchala, P. Optimization of 1,3-Disubstituted Urea-Based Inhibitors of Zika Virus Infection. *Bioorg. Med. Chem. Lett.* **2019**, *29*, 126626. [CrossRef]
12. Bielenica, A.; Szulczyk, D.; Olejarz, W.; Madeddu, S.; Giliberti, G.; Materek, I.B.; Koziół, A.E.; Struga, M.  $^1\text{H}$ -Tetrazol-5-Amine and 1,3-Thiazolidin-4-one Derivatives Containing 3-(Trifluoromethyl)Phenyl Scaffold: Synthesis, Cytotoxic and Anti-Hiv Studies. *Biomed. Pharmacother.* **2017**, *94*, 804–812. [CrossRef]
13. Doğan, Ş.D.; Gündüz, M.G.; Doğan, H.; Krishna, V.S.; Lherbet, C.; Sriram, D. Design and Synthesis of Thiourea-Based Derivatives as Mycobacterium Tuberculosis Growth and Enoyl Acyl Carrier Protein Reductase (InhA) Inhibitors. *Eur. J. Med. Chem.* **2020**, *199*, 112402. [CrossRef]

14. Kollu, U.; Avula, V.K.; Vallela, S.; Pasupuleti, V.R.; Zyryanov, G.V.; Neelam, Y.S.; Chamarthi, N.R. Synthesis, Antioxidant Activity and Bioinformatics Studies of L-3-Hydroxytyrosine Templated N-Alkyl/ Aryl Substituted Urea/Thioureas. *Bioorg. Chem.* **2021**, *111*, 104837. [CrossRef]
15. Bielenica, A.; Kędzierska, E.; Koliński, M.; Kmiecik, S.; Koliński, A.; Fiorino, F.; Severino, B.; Magli, E.; Corvino, A.; Rossi, I.; et al. 5-HT<sub>2</sub> receptor affinity, docking Studies and Pharmacological Evaluation of a Series of 1,3-Disubstituted Thiourea Derivatives. *Eur. J. Med. Chem.* **2016**, *116*, 173–186. [CrossRef]
16. Kaymakçioğlu, B.K.; Rollas, S.; Körçegez, E.; Arıcıoğlu, F. Synthesis and Biological Evaluation of New N-Substituted-N'-(3,5-Di/1,3,5-Trimethylpyrazole-4-yl)Thiourea/Urea Derivatives. *Eur. J. Pharm. Sci.* **2005**, *26*, 97–103. [CrossRef]
17. Stefanska, J.; Szulczyk, D.; Koziol, A.E.; Mirosław, B.; Kedzierska, E.; Fidecka, S.; Busonera, B.; Sanna, G.; Giliberti, G.; La Colla, P.; et al. Disubstituted Thiourea Derivatives and Their Activity on CNS: Synthesis and Biological Evaluation. *Eur. J. Med. Chem.* **2012**, *55*, 205–213. [CrossRef]
18. Bielenica, A.; Kedzierska, E.; Fidecka, S.; Maluszynska, H.; Mirosław, B.; Koziol, A.E.; Stefanska, J.; Madeddu, S.; Giliberti, G.; Sanna, G.; et al. Synthesis, Antimicrobial and Pharmacological Evaluation of Thiourea Derivatives of 4H-1,2,4-Triazole. *Lett. Drug Discov. Dev.* **2015**, *12*, 263–276. [CrossRef]
19. Nammalwar, B.; Bunce, R.A.; Berlin, K.D.; Benbrook, D.M.; Toal, C. Synthesis and Biological Evaluation of Sheta2 (NSC-721689) Analogs against the Ovarian Cancer Cell Line a2780. *Eur. J. Med. Chem.* **2019**, *170*, 16–27. [CrossRef]
20. Zhang, Y.; Meng, X.; Tang, H.; Cheng, M.; Yang, F.; Xu, W. Design, Synthesis, and Biological Evaluation of Novel Substituted Thiourea Derivatives as Potential Anticancer Agents for NSCLC by Blocking k-Ras Protein-Effectors Interactions. *J. Enzyme Inhib. Med. Chem.* **2019**, *35*, 344–353. [CrossRef]
21. Dai, B.; Yang, T.; Shi, X.; Ma, N.; Kang, Y.; Zhang, J.; Zhang, Y. HMQ-T-F5 (1-(4-(2-Aminoquinazolin-7-yl)Phenyl)-3-(2-Bromo-5-(Trifluoromethoxy)Phenyl) Thiourea) Suppress Proliferation and Migration of Human Cervical HeLa Cells *via* Inhibiting Wnt/ $\beta$ -Catenin Signaling Pathway. *Phytomedicine* **2018**, *51*, 48–57. [CrossRef] [PubMed]
22. Viswas, R.S.; Pundir, S.; Lee, H. Design and Synthesis of 4-Piperazinyl Quinoline Derived Urea/Thioureas for Anti-Breast Cancer Activity by a Hybrid Pharmacophore Approach. *J. Enzyme Inhib. Med. Chem.* **2019**, *34*, 620–630. [CrossRef] [PubMed]
23. Türe, A.; Ergül, M.; Ergül, M.; Altun, A.; Küçükgül, İ. Design, Synthesis, and Anticancer Activity of Novel 4-Thiazolidinone-Phenylaminopyrimidine Hybrids. *Mol. Divers.* **2020**, *25*, 1025–1050. [CrossRef] [PubMed]
24. Tokala, R.; Bale, S.; Janrao, I.P.; Vennela, A.; Kumar, N.P.; Senwar, K.R.; Godugu, C.; Shankaraiah, N. Synthesis of 1,2,4-Triazole-Linked Urea/Thiourea Conjugates as Cytotoxic and Apoptosis Inducing Agents. *Bioorg. Med. Chem. Lett.* **2018**, *28*, 1919–1924. [CrossRef]
25. Johnson, J.; Rychahou, P.; Sviripa, V.M.; Weiss, H.L.; Liu, C.; Watt, D.S.; Evers, B.M. Induction of AMPK Activation By N,N'-Diarylurea FND-4b Decreases Growth and Increases Apoptosis in Triple Negative and Estrogen-Receptor Positive Breast Cancers. *PLoS ONE* **2019**, *14*, e0209392. [CrossRef]
26. Sbenati, R.M.; Zaraei, S.-O.; El-Gamal, M.I.; Anbar, H.S.; Tarazi, H.; Zoghbor, M.M.; Mohamood, N.A.; Khakpour, M.M.; Zaher, D.M.; Omar, H.A.; et al. Design, Synthesis, Biological Evaluation, and Modeling Studies of Novel Conformationally-Restricted Analogues of Sorafenib as Selective Kinase-Inhibitory Antiproliferative Agents against Hepatocellular Carcinoma Cells. *Eur. J. Med. Chem.* **2021**, *210*, 113081. [CrossRef]
27. Ragab, F.A.F.; Abdel-Aziz, S.A.; Kamel, M.; Ouf, A.M.; Allam, H.A. Design, Synthesis and Biological Evaluation of Some New 1,3,4-Thiadiazine-Thiourea Derivatives as Potential Antitumor Agents against Non-Small Cell Lung Cancer Cells. *Bioorg. Chem.* **2019**, *93*, 103323. [CrossRef]
28. Farooqi, S.I.; Arshad, N.; Perveen, F.; Channar, P.A.; Saeed, A.; Javed, A. Corrigendum to “Aroylthiourea Derivatives of Ciprofloxacin Drug as DNA Binder: Theoretical, Spectroscopic and Electrochemical Studies along with Cytotoxicity Assessment”. *Arch. Biochem. Biophys.* **2020**, *686*, 108268. [CrossRef]
29. Elseginy, S.A.; Hamdy, R.; Menon, V.; Almehtdi, A.M.; El-Awady, R.; Soliman, S.S.M. Design, Synthesis, and Computational Validation of Novel Compounds Selectively Targeting Her2-Expressing Breast Cancer. *Bioorg. Med. Chem. Lett.* **2020**, *30*, 127658. [CrossRef]
30. Ghorab, M.M.; Alsaid, M.S.; El-Gaby, M.S.A.; Safwat, N.A.; Elaasser, M.M.; Soliman, A.M. Biological Evaluation of Some New N-(2,6-Dimethoxy-pyrimidinyl) Thioureido Benzenesulfonamide Derivatives as Potential Antimicrobial and Anticancer Agents. *Eur. J. Med. Chem.* **2016**, *124*, 299–310. [CrossRef]
31. Mowafy, S.; Galanis, A.; Doctor, Z.M.; Paranal, R.M.; Lasheen, D.S.; Farag, N.A.; Jänne, P.A.; Abouzid, K.A.M. Toward Discovery of Mutant EGFR Inhibitors; Design, Synthesis and in Vitro Biological Evaluation of Potent 4-Arylamino-6-Ureido and Thioureido-Quinazoline Derivatives. *Bioorg. Med. Chem.* **2016**, *24*, 3501–3512. [CrossRef]
32. Hamed, M.M.; Darwish, S.S.; Herrmann, J.; Abadi, A.H.; Engel, M. First Bispecific Inhibitors of the Epidermal Growth Factor Receptor Kinase and the Nf-Kb Activity as Novel Anticancer Agents. *J. Med. Chem.* **2017**, *60*, 2853–2868. [CrossRef]
33. Turan-Zitouni, G.; Altıntop, M.D.; Özdemir, A.; Kaplancıklı, Z.A.; Çiftçi, G.A.; Temel, H.E. Synthesis and Evaluation of Bis-Thiazole Derivatives as New Anticancer Agents. *Eur. J. Med. Chem.* **2016**, *107*, 288–294. [CrossRef]
34. Ghorab, M.M.; Alsaid, M.S.; Al-Dosary, M.S.; Nissan, Y.M.; Attia, S.M. Design, Synthesis and Anticancer Activity of Some Novel Thioureido-Benzenesulfonamides Incorporated Biologically Active Moieties. *Chem. Cent. J.* **2016**, *10*, 19. [CrossRef]
35. Liu, S.; Louie, M.C.; Rajagopalan, V.; Zhou, G.; Ponce, E.; Nguyen, T.; Green, L. Synthesis and Evaluation of the Diarylthiourea Analogs as Novel Anti-Cancer Agents. *Bioorg. Med. Chem. Lett.* **2015**, *25*, 1301–1305. [CrossRef]

36. Sylvester, P.W. Optimization of the tetrazolium dye (MTT) colorimetric assay for cellular growth and viability. *Methods Mol. Biol.* **2011**, *716*, 157–168. [CrossRef]
37. Chrzanowska, A.; Roszkowski, P.; Bielenica, A.; Olejarz, W.; Stepień, K.; Struga, M. Anticancer and Antimicrobial Effects of Novel Ciprofloxacin Fatty Acids Conjugates. *Eur. J. Med. Chem.* **2020**, *185*, 111810. [CrossRef]
38. Navarro, S.; Mitjavila, M.T.; Katz, A.; Doly, J.; Vainchenker, W. Expression of interleukin 6 and its specific receptor by untreated and PMA-stimulated human erythroid and megakaryocytic cell lines. *Exp. Hematol.* **1991**, *19*, 11–17.
39. Heinz, L.J.; Panetta, J.A.; Phillips, M.L.; Reel, J.K.; Shadle, J.K.; Simon, R.L.; Whitesitt, C.A. Inhibitors of amyloid beta-protein production. U.S. Patent 5814646 A1, 29 September 1998.







Review

# An Update on the Anticancer Activity of Xanthone Derivatives: A Review

Yehezkiel Steven Kurniawan <sup>1</sup>, Krisfian Tata Aneka Priyanga <sup>1</sup>, Jumina <sup>1,\*</sup>, Harno Dwi Pranowo <sup>1</sup>, Eti Nurwening Sholikhah <sup>2</sup>, Abdul Karim Zulkarnain <sup>3</sup>, Hana Anisa Fatimi <sup>3</sup> and Jeffry Julianus <sup>4</sup>

<sup>1</sup> Department of Chemistry, Faculty of Mathematics and Natural Science, Universitas Gadjah Mada, Yogyakarta 55281, Indonesia; yehezkiel.steven.k@mail.ugm.ac.id (Y.S.K.); krisfian.tata.a@mail.ugm.ac.id (K.T.A.P.); harnodp@ugm.ac.id (H.D.P.)

<sup>2</sup> Department of Pharmacology and Therapy, Faculty of Medicine, Public Health and Nursing, Universitas Gadjah Mada, Yogyakarta 55281, Indonesia; etinurweningsholikhah@ugm.ac.id

<sup>3</sup> Department of Pharmaceutical Technology, Faculty of Pharmacy, Universitas Gadjah Mada, Yogyakarta 55281, Indonesia; akarimzk@ugm.ac.id (A.K.Z.); hana.anisa.fatimi@mail.ugm.ac.id (H.A.F.)

<sup>4</sup> Department of Pharmaceutical Chemistry, Faculty of Pharmacy, Universitas Sanata Dharma, Yogyakarta 55282, Indonesia; jeffry@usd.ac.id

\* Correspondence: jumina@ugm.ac.id; Tel.: +62-274-545188

**Abstract:** The annual number of cancer deaths continues increasing every day; thus, it is urgent to search for and find active, selective, and efficient anticancer drugs as soon as possible. Among the available anticancer drugs, almost all of them contain heterocyclic moiety in their chemical structure. Xanthone is a heterocyclic compound with a dibenzo- $\gamma$ -pyrone framework and well-known to have “privileged structures” for anticancer activities against several cancer cell lines. The wide anticancer activity of xanthones is produced by caspase activation, RNA binding, DNA cross-linking, as well as P-gp, kinase, aromatase, and topoisomerase inhibition. This anticancer activity depends on the type, number, and position of the attached functional groups in the xanthone skeleton. This review discusses the recent advances in the anticancer activity of xanthone derivatives, both from natural products isolation and synthesis methods, as the anticancer agent through in vitro, in vivo, and clinical assays.

**Keywords:** xanthone; cancer; in vitro; in vivo; isolation; synthesis; heterocyclic compound

**Citation:** Kurniawan, Y.S.; Priyanga, K.T.A.; Jumina; Pranowo, H.D.; Sholikhah, E.N.; Zulkarnain, A.K.; Fatimi, H.A.; Julianus, J. An Update on the Anticancer Activity of Xanthone Derivatives: A Review. *Pharmaceuticals* **2021**, *14*, 1144. <https://doi.org/10.3390/ph14111144>

Academic Editors: Mary J. Meegan and Niamh M. O’Boyle

Received: 19 October 2021  
Accepted: 9 November 2021  
Published: 11 November 2021

**Publisher’s Note:** MDPI stays neutral with regard to jurisdictional claims in published maps and institutional affiliations.



**Copyright:** © 2021 by the authors. Licensee MDPI, Basel, Switzerland. This article is an open access article distributed under the terms and conditions of the Creative Commons Attribution (CC BY) license (<https://creativecommons.org/licenses/by/4.0/>).

## 1. Introduction

Cancer is one of the most fatal diseases in the world. Cancer mainly occurs due to gene mutations, and the condition is worsened by other carcinogenic agents. Both gene mutations and carcinogenic agents then influence and change the cell functions and metabolism, and thereby, the replication and spread of cancer cells are uncontrolled. The cancer cells grow and multiply rapidly, thus crowding the other normal cells [1]. In some cases, the cancer cells also attack and consume the normal cells, since cancer cells require large amounts of biomaterials for cell division. Because of that, drastic weight loss with lumps on the cancer cell locations is commonly found in cancer patients [2]. In 2020, world cancer cases were reported to be 15 million. It was found that the number of men patients (51%) is slightly higher than the number of women patients (49%). Lung, prostate, and colorectal cancers contribute to 46% of cancer cases in men, while lung, breast, and colorectal cancers contribute to 50% of cancer cases in women [3]. In 2021, it is estimated that around 1.9 million new cancer cases are found in the United States, with around 0.6 million deaths. This means that one in three patients with cancer in the United States do not survive, which is terrifying. The number of cancer and mortality cases has kept increasing, and it is expected that world cancer cases will increase to 23.6 million in 2030 [4].

The research on anticancer drug design and development is an urgent need, because people are suffering and the number of death cases is unstoppable until active, selective,

and efficient anticancer drugs are found [5–7]. Cancer treatment is one of the most challenging research subjects in the medicinal and pharmacological fields [8,9]. Research into new anticancer drugs from natural sources and synthetic methods is still being conducted. To date, more than 85% of recent bioactive compounds have consisted of heterocyclic structures [10,11]. Among the heterocyclic compounds, hundreds of xanthone derivatives have been isolated, synthesized, and evaluated as anticancer agents [12–18]. The latest review article on the anticancer activity of xanthone derivatives was reported by Na in 2009 [19]. From that report, unfortunately, an updated review on the anticancer activity of xanthone derivative has not been available yet, as of today. This review, to a certain extent, provides a brief update on the research and development of xanthone derivatives, both from natural products isolation and synthesis methods, such as the anticancer agent through in vitro, in vivo, and clinical assays.

## 2. Xanthone Derivatives as Anticancer Agents

### 2.1. Xanthone Derivatives

The name of xanthone was coined by J.C. Roberts in 1961. The word “xanthone” comes from the word for the color yellow, “xanthos” (ξανθός, Greek), since the xanthone compounds are commonly obtained as yellow solids. The first reported xanthone derivative was gentisin, which was isolated from the roots of *Gentiana lutea* in 1821. Xanthone with an IUPAC name of 9*H*-xanthen-9-one is a heterocyclic compound with a dibenzo- $\gamma$ -pyrone framework, with a basic molecular formula of  $C_{13}H_8O_2$  [20]. The general structure of xanthone and its atom numbering is shown in Figure 1.

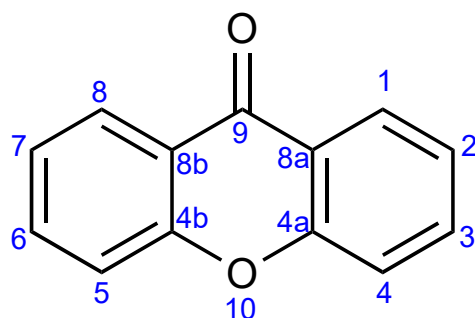


**Figure 1.** General structure of xanthone.

Xanthone is well-known to have “privileged structures” because this simple tricyclic compound exhibits wide biological activities [21,22]. The wide biological activities of xanthone derivatives are caused by their ability to bind with multiple protein receptors. It was reported that xanthone derivatives also exhibit antimicrobial, antidiabetic, antioxidant, antiviral, anti-Alzheimer, anti-inflammatory, and anti-tyrosinase activities. Updates on these biological activities of xanthone derivatives have been available recently [23–29]. On the other hand, the latest update on the anticancer activity of xanthenes was reported in 2009 [19]. The anticancer activity of xanthone derivatives depends on the type, number, and position of the attached functional groups in the xanthone framework. It was reported that xanthone derivatives are able to bind with multiple protein receptors such as cyclooxygenase, protein kinase, and topoisomerase, demonstrating their anticancer activity [22]. These binding properties are also serving in self-monitoring drug application for cancer therapy. In this case, xanthone derivatives act as anticancer agents, as well as sensor agent for selective imaging of cytoplasm of cancer cells through fluorescence spectroscopy [30].

Briefly, xanthone derivatives can be classified into six groups according to their substituents: simple oxygenated xanthone, glycosylated xanthone, prenylated xanthone, xanthone dimers, xanthonolignoid, and miscellaneous xanthone. The simple oxygenated xanthone can be further divided into six subgroups depending on the number of oxygen atoms: mono-oxygenated, di-oxygenated, tri-oxygenated, tetra-oxygenated, penta-oxygenated, and hexa-oxygenated xanthenes. The examples of xanthone derivative in each subgroup

of oxygenated-xanthone are shown in Figure 2. On the other hand, glycosylated xanthone can be divided into two subgroups: O-glycosides and C-glycosides. In O-glycosides, the glycosidic bond is formed between anomeric carbon atom of sugar ring and oxygen atom of hydroxyl group present in xanthone skeleton. In C-glycosides, xanthone is connected with glycosyl moiety through the C-C bond [31]. The common example of O-glycoside xanthone is rutinoylxanthone, while the example of C-glycoside xanthone is mangiferin, as shown in Figure 2.

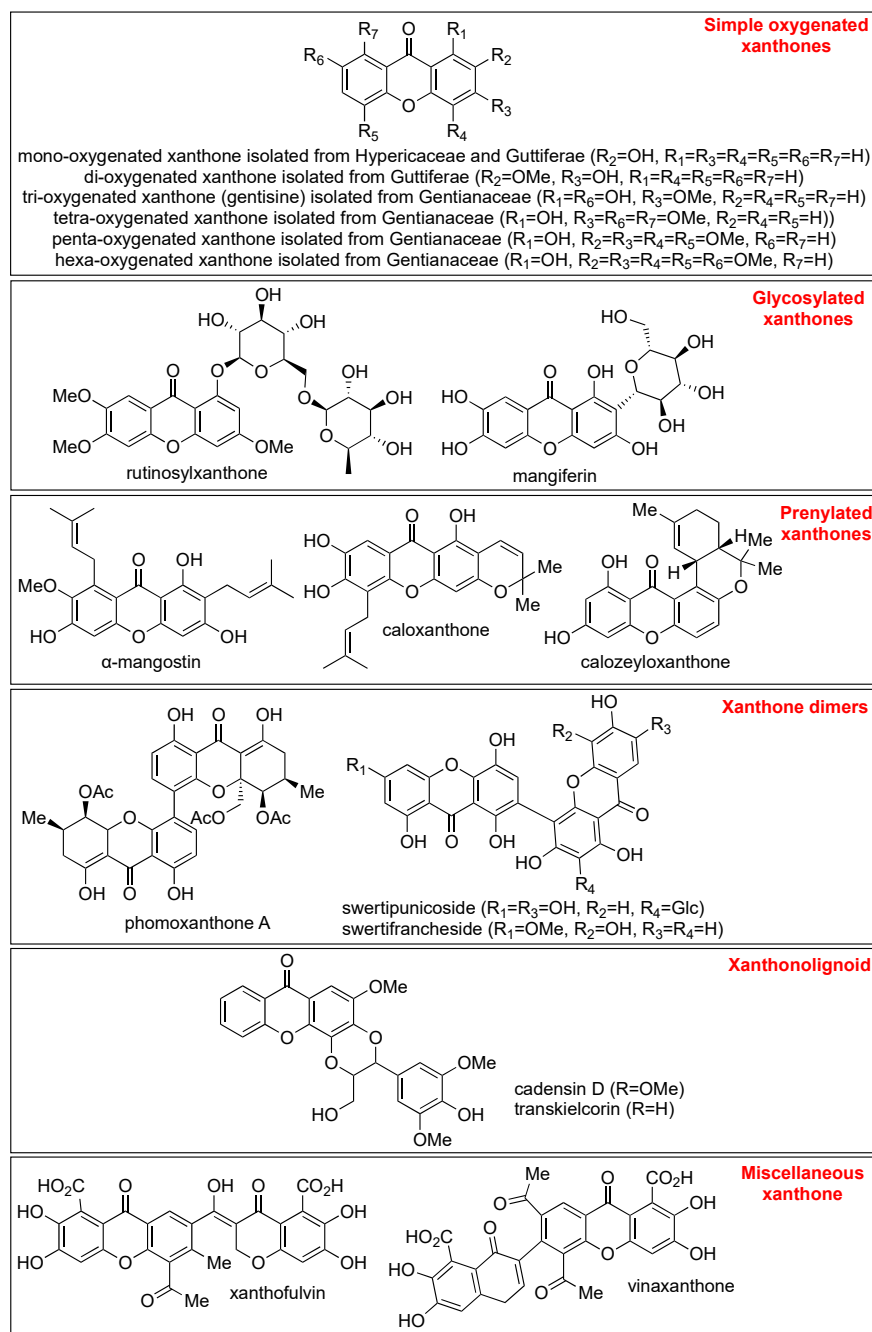


**Figure 2.** Classification of xanthone derivatives with some examples for each group.

The prenylated xanthone group is characterized by the presence of prenyl and geranyl substituents [32]. The prenylated xanthone group contains the largest number of natural xanthone derivatives, such as  $\alpha$ -mangostin, caloxanthone, and calozeilyxanthone, as shown in Figure 2. Prenyl substituents are being reported as a pivotal functional group for the anticancer activity of xanthone [33]. As an example, Castanheiro et al. reported that the introduction of the prenyl group to the 1-hydroxyxanthone dramatically increased its anticancer activity against the MCF-7 cell line [34]. On the other hand, xanthone dimers or bisxanthenes are quite rare, and only around 12 xanthone dimers have been reported so far. The first isolated xanthone dimer was swertipunicoside obtained from the whole plant of *Swertia punicea* in 2002. Swertipunicoside, swertifrancheside, and phomoxanthone A are the examples of xanthone dimers [35], and their chemical structures are shown in Figure 2.

The group of xanthonolignoids is characterized by a connection between xanthone and lignin (coniferyl alcohol) frameworks. The isolated xanthonolignoids have been reported from Guttiferae, such as candesin D and transkielcorin. The number of xanthonolignoids is also limited. Figure 2 shows the chemical structure of candesin D and transkielcorin. On the other hand, miscellaneous xanthenes are defined for all xanthone derivatives which could not be classified into the other groups, such as xanthofulvin and vinaxanthone, and their chemical structures are shown in Figure 2. Thioxanthenes and azaxanthenes are also categorized as miscellaneous xanthenes. Klein–Junior et al. reported that around 303 simple oxygenated xanthenes, 137 glycosylated xanthenes, 737 prenylated xanthenes, 7 xanthone dimers, 8 xanthonolignoids, and 33 miscellaneous xanthenes have been isolated within 2012–2019 [36].

## 2.2. Characteristics on Chemical Identification of Xanthone Derivatives

For chemical elucidation purposes, infrared (IR), ultraviolet (UV), mass (MS), and nuclear magnetic resonance (NMR) spectra are required to determine the correct structure of xanthone derivatives [37]. In fact, the IR and UV spectra of xanthone do not serve as accurate tools for structure elucidation. The IR spectrum only recognizes the functional group of xanthenes (Table 1); consequently, the position and neighbor conditions of each functional group are not understood well [22]. The UV spectrum of xanthone reflects the absorption characteristics of xanthenes chromophore in the ultraviolet region (200–400 nm). The most found chromophore in the xanthone structure is conjugated aromatic and carbonyl moieties; thus, non-chromophore substituents of xanthone are hardly observed. The molecular weight of xanthone can be determined from its MS spectrum. The unsaturation degree of xanthone, as well as halogen substituents, are mostly determined from the MS spectrum. The core structure of the xanthone has one pyran structure, two aromatic rings, and one C=O double bond; thus, the xanthone core itself has an unsaturation degree of 10. The halogen substituent can be indicated by its isotopic effect on the MS spectra. Chloro- and bromo-substituted xanthenes commonly give two molecular ion fragments with  $m/z$  of  $[M]^+$  and  $[M + 2]^+$  in 3:1 and 1:1 ratios, respectively. In contrast, elucidation of fluoro- and iodo-substituted xanthenes from their MS spectrum is difficult, as both halogen atoms are only found as a single isotope. Therefore, fluoro- and bromo-substituents in xanthenes can be observed using the  $^{19}\text{F}$ -NMR and  $^{127}\text{I}$ -NMR techniques, respectively [38].

NMR elucidation is very useful to determine the more detailed structure of xanthone derivatives. The aromatic protons of xanthone are generally found in the chemical shift of 6–9 ppm, depending on the protons' environment (Table 1). Furthermore, information on the protons' multiplicity and coupling constant is useful to determine the substituents in the xanthone framework [39]. The nature and position of xanthone substituents can also be evaluated from the  $^{13}\text{C}$ -NMR spectrum. For the bare structure of xanthone (Figure 1), the xanthone gives 7 carbon signals, as shown in Table 1. The presence of an additional functional group shifts the chemical shift of carbon signals to lower/higher value depending on the nature and location of the functional group [39]. A combination of  $^1\text{H}$ - and  $^{13}\text{C}$ -NMR of xanthone derivative is also useful for detailed elucidation of xanthone structure. A brief summary on the structure elucidation of xanthenes using spectroscopy techniques is shown

in Table 1. Other techniques including circular dichroism and X-ray crystallography are very helpful in the final assessment of structure elucidation of xanthone derivatives [39–41].

**Table 1.** A brief summary on the structure elucidation of xanthenes using spectroscopy techniques.

Xanthone Structure	IR (cm <sup>-1</sup> )	UV (nm)	<sup>1</sup> H-NMR (ppm)	<sup>13</sup> C-NMR (ppm)
Csp <sup>2</sup> -H	3000–3100	-	6–9	-
C=O	1650–1720	-	-	176
C=C aromatic	1450–1600	200–400	-	126 (C-1) 124 (C-2) 135 (C-3) 118 (C-4) 156 (C-4a) 121 (C-8a)
C-O-C ether	1000–1200	-	-	-
O-H	3300–3500	-	9–10 (C-2 or C-7) 9–11 (C-4 or C-5) 10–11 (C-3 or C-6) 12–14 (C-1 or C-8)	-

### 2.3. Isolation of Xanthone Derivatives

As of today, thousands of natural xanthone derivatives have been isolated from Amaranthaceae, Anacardiaceae, Annonaceae, Asteraceae, Clusiaceae, Eriocaulaceae, Fabaceae, Filicineae, Gentianaceae, Guttiferae, Hypericaceae, Moraceae, Leguminosae, Loganiaceae, and Polygalaceae families [42–52]. Within 2012–2019, as many as 1225 xanthone derivatives have been isolated from natural sources. Among these families, Clusiaceae and Gentianaceae are the most productive plants to give hundreds of xanthone derivatives. From 2012–2019, 48% and 16% of isolated xanthone derivatives have been obtained only from Clusiaceae and Gentianaceae, respectively. The rest of the isolated xanthone derivatives mainly came from Hypericaceae (11%), Moraceae (8%), and Polygalaceae (6%) [34]. These herbs have been used as traditional medicine in several countries, such as China, Thailand, India, and Indonesia. As an example, the whole extract of *Swertia chirata* (Gentianaceae) has been used as an antimalarial drug. The radix extract of *Cudrania cochin* (Moraceae) has been used for hepatitis and rheumatic treatment. Additionally, crude extract of *Monnina obtusifolia* (Polygalaceae) has been used as an anticancer and antimicrobial agent as an indigenous medicine [21].

*Garcinia mangostana* (Clusiaceae) is a tropical plant that is widely abundant in the Southeast Asia region, such as in Indonesia, Thailand, and Vietnam. One mangosteen plant produces almost 3000 fruits annually. The mangosteen fruit is usually harvested in a spherical form with thin purple peels. The mangosteen fruit is famous as the “queen of fruit” or “superfruit”, due to its multi-biological purposes such as anticancer, anti-inflammatory, antihypertensive, antidiabetic, and antituberculosis activities [37]. In Indonesia, mangosteen fruit has been employed for the traditional treatment of diabetes, hypertension, and cancer. Meanwhile, mangosteen fruit has been utilized for the traditional treatment of fatigue, diarrhea, skin infection, and urinary disorders in Vietnam and Thailand. The mangosteen fruit contains carbohydrates (15%), protein (0.5%), fat (0.4%), and fiber (5.0%) [37]. It was reported that the mangosteen fruit consists of some secondary metabolites, such as xanthenes, anthocyanins, flavonoids, phenolics, and organic acids [53]. Remarkably, more than sixty xanthone derivatives have been identified from the pericarp of the mangosteen fruit. The major xanthenes isolated from the pericarp of mangosteen fruit are  $\alpha$ -mangostin,  $\beta$ -mangostin,  $\gamma$ -mangostin, mangostinone, mangostanol, desoxymorellin, gambogic acid, gartanin, 8-deoxygartanin, garcinone B, garcinone C, garcinone D, and garcinone E. Their chemical structures are shown in Figure 3.

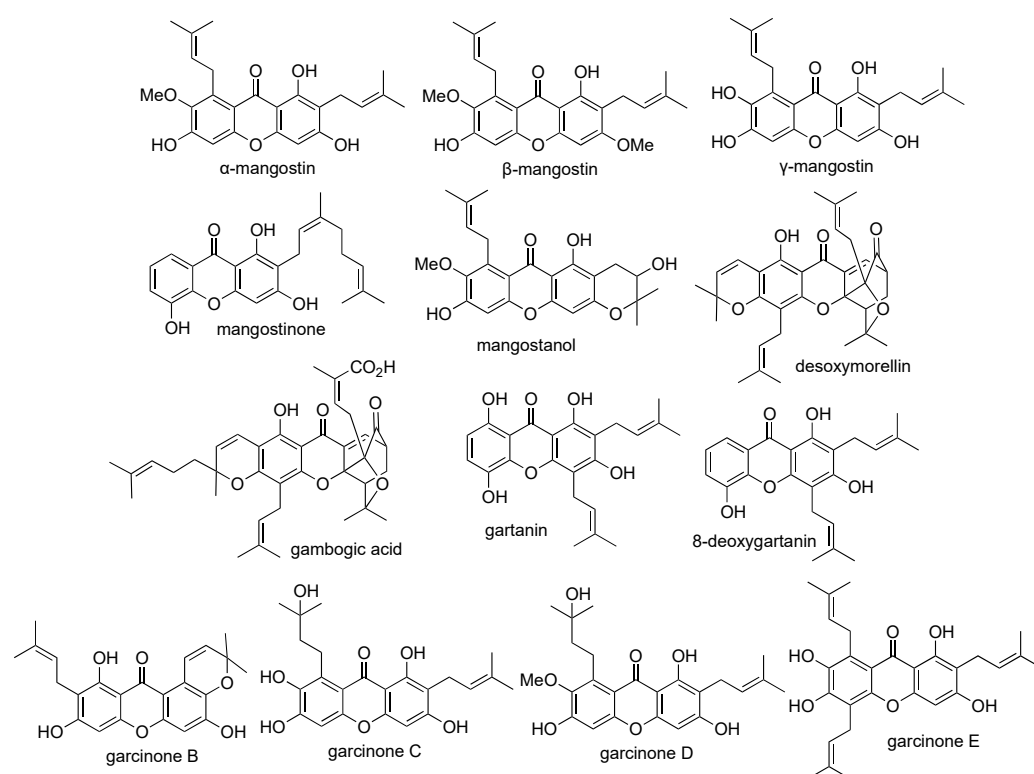


**Figure 3.** The chemical structure of major xanthenes isolated from the pericarp of mangosteen fruit.

The natural xanthone derivatives are mainly generated from acetate polymalonic and mixed shikimic acetate pathways. Birch et al. studied the acetate polymalonic pathway in the biosynthesis of ravelenin from *Helminthosporium ravenelii* using carbon-isotopes labeling [54] (Figure 4a). Eight acyl groups were connected with each other to form 1,3,5,7,9,11,13,15-octaketonic intermediate. Then, the octaketonic intermediate was cyclized to form benzoquinone and benzophenone intermediates. The benzophenone intermediate was further transformed to produce ravelenin. The second pathway (mixed shikimic acetate pathway) was reported by Fujita and Inoue in 1980 for mangiferin biosynthesis in *Anemarrhena asphodeloides* (Figure 4b) [55]. In general, one aromatic ring of xanthone was generated from the shikimic acid pathway, with another aromatic ring coming from the acetate-malonate polyketide pathway. This mixed pathway is responsible for the existence of almost all simple oxygenated and prenylated xanthone derivatives in nature. It was reported that mangiferin was produced from caffeic acid and two acetate units. Glycosidation reaction of mangiferin was found to occur on the benzophenone intermediate. Similarly, the prenylation reaction also happened on the benzophenone intermediate, and not directly on the caffeic acid one. Then, the benzophenone intermediate underwent the ring-closing reaction to form the xanthone as the final product [56].

Besides isolation from the terrestrial ecosystem, xanthone isolations from the marine ecosystem have been also reported [57]. The marine ecosystem covers almost 70% of the earth surface, which is equivalent to 95% of the biosphere. Therefore, recent research is focused on the exploration of marine natural products, since the marine natural products may not be found in the terrestrial ecosystem. More than 25,000 marine natural products have been isolated and elucidated, together with hundreds of new marine natural products which have been discovered as of today [38]. Marine fungi have been reported as the most abundant source for xanthone derivatives [58].

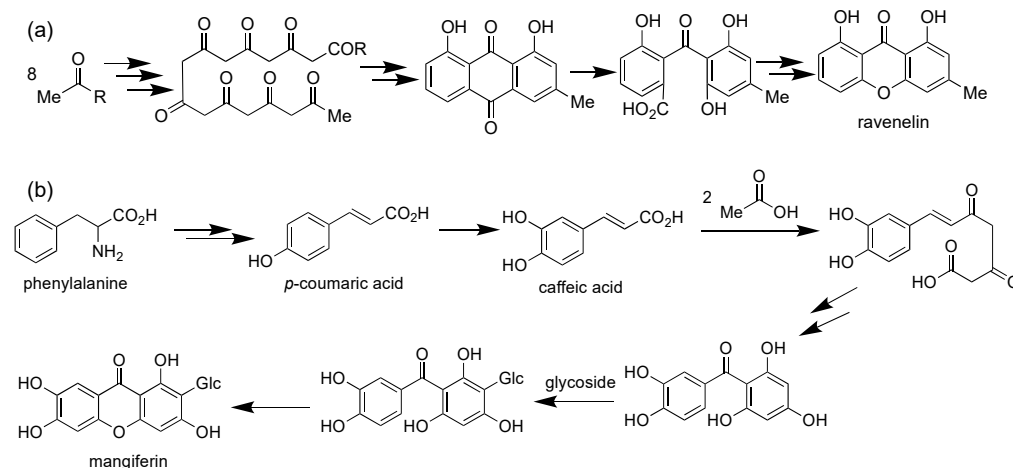


**Figure 4.** Brief biosynthesis pathway of xanthone derivatives through (a) acetate polymalonic pathway (biosynthesis of ravenelin), and (b) mixed shikimic acetate pathway (biosynthesis of mangiferin).

Several research studies on the isolation of xanthone derivatives from both terrestrial and marine ecosystems are selectively highlighted in this review article based on their anticancer activity report. An anticancer agent can be divided into four classes based on its half-maximal inhibitory concentration ( $IC_{50}$ ) value, i.e., strong ( $IC_{50} < 5 \mu M$ ), moderate ( $IC_{50} 5\text{--}10 \mu M$ ), weak ( $IC_{50} 10\text{--}50 \mu M$ ), and non-active ( $IC_{50} > 50 \mu M$ ) [59]. In 2002, Malmstrom et al. reported the isolation of shamixanthone, tajixanthone and varixanthone from the fungus *Emericella vaericolor*; however, these compounds show no cytotoxic activity against HT29, A549, and P388 cell lines at  $1 \mu g/mL$  concentration [60]. In 2008, Shao et al. successfully isolated three xanthone derivatives, named as 8-methoxycarbonyl-1-hydroxy-9-oxo-9H-xanthen-3-carboxylic acid, dimethyl 8-methoxy-9-oxo-9H-xanthen-1,6-dicarboxylate, and methyl 8-hydroxy-6-methyl-9-oxo-9H-xanthen-1-carboxylate from fungus *Penicillium* sp. strain ZZF 32#. The crude extracts of these isolated xanthenes exhibit cytotoxic activity against KB and KBv200 cell lines with  $IC_{50}$  values of 1.50 and 2.50  $\mu g/mL$ , respectively [61].

In 2010, Lee et al. isolated sterigmatocystin and dihydrosterigmatocystin from the fungus *Aspergillus versicolor*. Both compounds exhibited cytotoxic activity against HCT-15, SK-OV-3, A549, XF-498, and SK-MEL-2 cell lines. It was found that sterigmatocystin gave higher toxicity than dihydrosterigmatocystin in an  $IC_{50}$  range of 3.76–14.2  $\mu M$  for these cell lines. Furthermore, sterigmatocystin also gave higher anticancer activity than dihydrosterigmatocystin against Bel-7402 and NCI-H460 cell lines. The structural difference between sterigmatocystin and dihydrosterigmatocystin was the presence of allyl group at the C-5 position of xanthone, demonstrating that the allyl group was critical for anticancer activity [62]. In the same year, Huang et al. successfully isolated two xanthenes, named 1,7-dihydroxy-2-methoxy-3-(3-methylbut-2-enyl)-9H-xanthen-9-one and 1-hydroxy-4,7-dimethoxy-6-(3-oxobutyl)-9H-xanthen-9-one, from the fungus *Avicennia marina*. These isolated compounds exhibited moderate cytotoxic activity against KB and KBv200 cell lines. The 1,7-dihydroxy-2-methoxy-3-(3-methylbut-2-enyl)-9H-xanthen-9-one gave  $IC_{50}$  value of 20.0 and 30.0  $\mu M$ , while 1-hydroxy-4,7-dimethoxy-6-(3-oxobutyl)-9H-xanthen-9-one gave  $IC_{50}$  value of 35.0 and 41.0  $\mu M$  against KB and KBv200 cancer cell lines, respectively [63].



In 2011, Xu et al. reported the isolation of paeciloxanthone from the fungus *Paecilomyces* sp. This compound exhibited moderate to strong anticancer activity against HepG2 and AChE (acetylcholine esterase) with  $IC_{50}$  values of 3.33 and 6.94  $\mu\text{M}$ , respectively. They also reported the successful isolation of secalonic acid D from the fungus *Penicillium oxalicum* and *Paecilomyces* sp. strain ZSU44. The secalonic acid D compound exhibited remarkable anticancer activity against K562 and HL60 leukemia cancer cell lines with  $IC_{50}$  values of 0.43 and 0.38  $\mu\text{M}$ , respectively. Furthermore, secalonic acid D was able to inhibit human topoisomerase I enzyme, with an  $IC_{50}$  value of 0.16  $\mu\text{M}$  and minimum inhibitory concentration (MIC) value of 0.40  $\mu\text{M}$ . From a further bioassay, it was found that secalonic acid D influenced the GSK-3 $\beta$ / $\beta$ -catenin/c-Myc pathway, thereby arresting the cancer cell cycle and inhibiting the proliferation of cancer cells [64]. In 2016, Tang et al. reported the isolation of 10 new xanthone derivatives from the leaf of *Garcinia oligantha*. These isolated xanthenes belong to dihydroxanthone and tetrahydroxanthone groups. These compounds exhibited moderate to strong anticancer activity against A549, HepG2, HT-29, PC-3, and HL-7702, with  $IC_{50}$  values of 3.90–5.50, 4.50–10.0, 4.10–6.40, 3.20–4.60, and 6.40–10.0  $\mu\text{M}$ , respectively [65].

In 2017, a novel prenylated xanthone was isolated from the pericarp of *Garcinia mangostana* by Yang et al. This novel xanthone gave moderate to strong anticancer activity against U-87, SGC-7901, PC-3, H490, A549, CNE-1, and CNE-2 cancer cell lines, with  $IC_{50}$  values of 6.39, 8.09, 6.21, 7.84, 4.84, 3.35, and 4.01  $\mu\text{M}$ , respectively. The mechanism of action of this novel prenylated xanthone occurred through apoptosis induction on the cancer cells [66]. In 2018, Wei et al. reported the isolation of ananixanthone from the stem bark of *Calophyllum teysmanni*. Furthermore, the isolated ananixanthone was modified through esterification and alkylation reactions to give monoacetate-, diacetate-, 5-methoxy-, and 5-O-benzyl-derivatives. These ananixanthone derivatives exhibited anticancer activity against LS174T, SNU-1, and K562 cancer cell lines, with  $IC_{50}$  values in the range of 2.96–50.0  $\mu\text{g}/\text{mL}$ . It was reported that methoxy substituents on 5-methoxyananixanthone had higher anticancer activity (14.7  $\mu\text{M}$ ) than original hydroxy substituents in the parent compound (19.8  $\mu\text{M}$ ). Meanwhile, the diacetate-ananixanthone derivatives gave lower anticancer activity (50.7–119  $\mu\text{M}$ ) than the parent compound (7.82–23.7  $\mu\text{M}$ ) [67]. In 2019, Kaennakam et al. reported the isolation of two new xanthenes, i.e., schomburgones A and B from the bark of *Garcinia schomburgkiana*. Unfortunately, these compounds are non-active against HepG2, MCF-7, HT-29, HeLa S-3, and KB cancer cells, with  $IC_{50}$  values of 45.05–69.22  $\mu\text{M}$  [68].

In 2019, Zamakshshari et al. successfully isolated ananixanthone and caloxanthone B from the stem bark of *Calophyllum* species. The first isolation of caloxanthone B from *Calophyllum* species was recorded from this research. Both ananixanthone and caloxanthone B compounds gave moderate and strong anticancer activity against the K562 cell line, with  $IC_{50}$  values of 7.21 and 3.00  $\mu\text{M}$ , respectively. The anticancer activity of both compounds may be generated from the protein kinases inhibition [69]. In 2021, Oanh et al. reported another new xanthone derivative isolated from propolis of the stingless bee *Lisotrigona furoa*, with weak anticancer activity against SK-LU-1, HepG2, and KB cancer cells in an  $IC_{50}$  range of 12.63–34.23  $\mu\text{g}/\text{mL}$  [70]. In the same year, Wang et al. reported two new xanthone derivatives: oxisterigmatocystins J and K from fungus *Penicillium* sp. strain DWS10-P-6. Both oxisterigmatocystins exhibited weak anticancer activity against PC-3, MDA-MB-231, and HL-60 cancer cell lines in the  $IC_{50}$  range of 12.0–50.0  $\mu\text{M}$  [71]. The chemical structures of the aforementioned xanthenes are shown in Figure 5, while the summary of the anticancer activity of isolated xanthone derivatives is listed in Table 2.

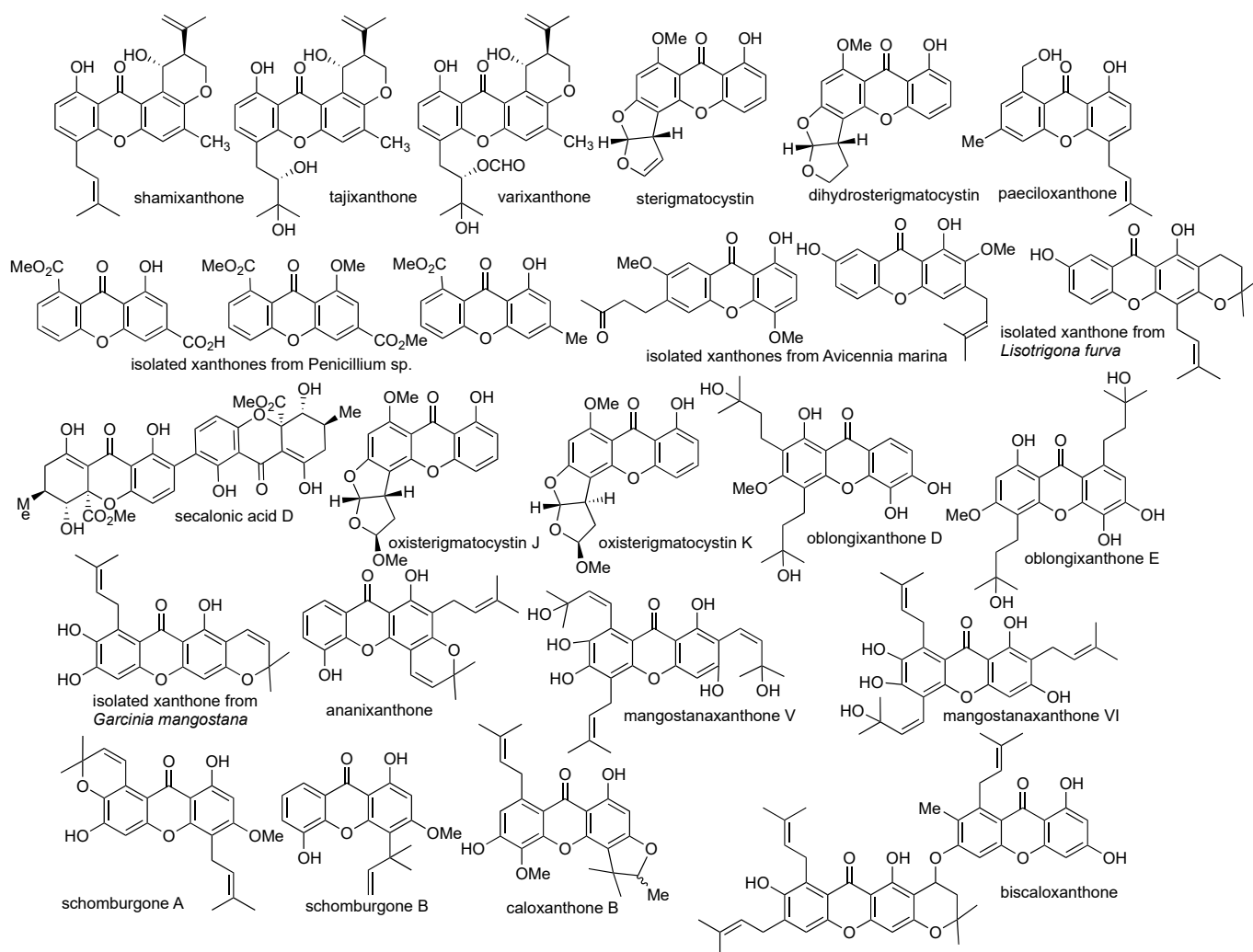


**Figure 5.** The chemical structure of isolated xanthone derivatives from natural sources.

The greatest obstacle to the anticancer activity evaluation of isolated xanthenes is the very low isolation yield, since xanthenes exist as the secondary metabolites in natural sources. To obtain a higher amount of isolated xanthone, the plant parts are cultured and incubated in a certain malt-agar media with tryptone, glucose, and phosphate buffer media, to maintain the pH value. Next, the xanthone derivatives are commonly isolated through a solid-phase extraction using aqueous acetone in 4:1 *v/v* as the maceration solvent. Afterwards, the aqueous solvent is subjected to a liquid–liquid extraction with ethyl acetate. Both extracts are then evaporated under vacuum for a further partition process with petroleum ether and/or methanol [38].

After the crude extracts have been obtained, the desired xanthenes were purified using column chromatography with gradient elution, using a mixture of solvents as the mobile phase. Sephadex LH-20<sup>®</sup>, RP-C18, and silica gel columns are widely used as stationary phase for this purification purpose. In general, xanthone glycosides are isolated using cyanosilane-silica gel and methanol-water-acetonitrile as the solid and mobile phases, respectively. Meanwhile, xanthone aglycones are generally isolated using RP-C18 and phosphoric acid-water-acetonitrile as the solid and mobile phases, respectively. Preparative silica gel chromatography is commonly used for rapid and simple purification of xanthenes, however, it gives a less purity than column chromatography [37].

**Table 2.** Summary of the anticancer activity of isolated xanthone derivatives.

Xanthone Derivative	Source	IC <sub>50</sub> (Cancer Cells)	Ref.
Crude extract of xanthenes	Fungus <i>Penicillium</i> sp. strain ZZF 32#.	1.50 µg/mL (KB) 2.50 µg/mL (KBv200)	[61]
Sterigmatocystin	Fungus <i>Aspergillus versicolor</i>	3.76 µM (SK-MEL-2)	[62]
1,7-Dihydroxy-2-methoxy-3-(3-methylbut-2-enyl)-9H-xanthen-9-one	Fungus <i>Avicennia marina</i>	20 µM (KB) 30 µM (KBv200)	[63]
1-Hydroxy-4,7-dimethoxy-6-(3-oxobutyl)-9H-xanthen-9-one		35 µM (KB) 41 µM (KBv200)	
Secalonic acid D	Fungus <i>Penicillium oxalicum</i>	0.43 µM (K562) 0.38 µM (HL60)	[64]
Dihydroxanthone	Leaf of <i>Garcinia oligantha</i>	3.90 µM (A549) 3.20 µM (PC-3)	[65]
Tetrahydroxanthone		5.50 µM (A549) 4.60 µM (PC-3)	
Prenylated xanthone	Pericarp of <i>Garcinia mangostana</i>	3.35 µM (CNE-1) 4.01 µM (CNE-2)	[66]
5-methoxyananixanthone	Stem bark of <i>Calophyllum teysmanni</i>	14.7 µM (K562)	[67]
schomburgones A	Bark of <i>Garcinia schomburgkiana</i>	45.05 µM (HepG2) 52.21 µM (HeLa S-3)	[68]
Ananixanthone	Stem bark of <i>Calophyllum</i> species	7.21 µM (K562)	[69]
Caloxanthone B		3.00 µM (K562)	
Isolated xanthone	Propolis of the stingless bee <i>Lisotrigona furva</i>	12.63 µg/mL (HepG2) 14.36 µg/mL (SK-LU-1)	[70]
Oxisterigmatocystins J	Fungus <i>Penicillium</i> sp. strain DWS10-P-6	15.14 µM (HL-60)	[71]
Oxisterigmatocystins K		21.62 µM (MDA-MB-231)	
		12.06 µM (HL-60)	

#### 2.4. Synthesis of Xanthone Derivatives

As the isolation of xanthone derivatives is complicated and time consuming, the synthesis of xanthone derivatives has been extensively studied. The oldest synthetic route was reported by Kostanecki in 1829. In this synthesis route, the mixture of *ortho*-hydroxybenzoic acid and polyphenol compounds in an equimolar amount was heated in the presence of acetic anhydride or zinc(II) chloride (ZnCl<sub>2</sub>) as the dehydrating agent [72]. Later in 1955, Grover et al. employed a mixture of ZnCl<sub>2</sub> and phosphorus oxychloride (POCl<sub>3</sub>) as the dehydrating agent at lower temperature, giving a higher yield than the Michael-Kostanecki route. However, the limitation of the Grover route is its incapacity to produce xanthone derivatives from resorcinol and pyrogallol. This inability is caused by the reaction stopping at the benzophenone intermediate [73].

The Grover Shah and Shah (GSS) method is another traditional method to synthesize xanthone derivatives through the cyclodehydration of 2,2'-dihydroxybenzophenone or cycloacylation of 2-aryloxybenzoic acid synthetic route. The mixture of ZnCl<sub>2</sub> and POCl<sub>3</sub> is commonly used as the cyclization agent in the GSS method. When the salicylic acid derivative is used as the starting material, then the synthetic route occurs through Friedel-Crafts acylation to form the 2,2'-dihydroxybenzophenone intermediate. The 2,2'-dihydroxybenzophenone intermediate is thus cyclized through a dehydration process to form the xanthone skeleton [74]. On the other hand, when *ortho*-halogen substituted benzoic acid is used as the starting material, then the synthetic route occurs through Ullman condensation to form the 2-aryloxybenzoic acid intermediate. The 2-aryloxybenzoic acid

intermediate is thus cyclized through an electrophilic cycloacylation process to form the xanthone skeleton [75].

It was reported that the yield of the GSS synthetic route through benzophenone intermediate is slightly higher than the aryloxybenzoic acid intermediate. The average yield for synthetic xanthone through the GSS-benzophenone route is 60–90%. To improve the synthesis yield, other cyclization reagents have been evaluated, such as a mixture of phosphorus pentoxide ( $P_2O_5$ ) and methanesulfonic acid ( $MeSO_3H$ ), trifluoromethanesulfonic acid ( $F_3CSO_3H$ ), trifluoroacetic acid anhydride ( $F_3CCO_2COCF_3$ ), stannic chloride ( $SnCl_4$ ), triphenylphosphine ( $PPh_3$ ) in carbon tetrachloride ( $CCl_4$ ), and others. So far, a mixture of  $P_2O_5$  and  $MeSO_3H$ , named as Eaton's reagent, gave a remarkable yield (80–95%) for xanthone derivatives. Employing Eaton's reagent leads to a direct cyclization process of xanthone derivatives with no detectable benzophenone intermediate [74].

Other synthetic methods to obtain a higher yield of xanthenes in fewer synthetic steps have been evaluated. Cyclization using  $F_3CSO_3H$  for diaryl ether is useful to prepare benzoxanthone and/or xanthone dimers in a single-step reaction. Friedel–Crafts acylation followed by the cyclization of 2,2'-dialkoxybenzophenone has been reported as a successful synthesis route of di-oxygenated xanthone. The Robinson–Nishikawa route employs resorcinol and cyanobenzene derivatives to form ketimine intermediate. Afterwards, strong base such as NaOH was employed to hydrolyze the imine functional group and form the ether bond between two aromatic rings. The Tanase synthetic route utilizes salicylaldehyde and phloroglucinol to form the pyran ring. Then, benzylic carbon was further oxidized by chromium(VI) oxide to obtain the xanthone structure. Potassium permanganate on manganese(IV) dioxide or ruthenium(IV) complex can be also used to replace toxic chromium(VI) oxide in the green chemistry approach. The Ullman synthetic route is a successful method to prepare euxanthone from *ortho*-chlorobenzoic acid and phenolic derivatives. The 5,6-dimethylxanthone-4-acetic acid (DMXAA) was successfully synthesized from 3,4-dimethylbenzoic acid in 22% yield using the Ullman synthetic route [76].

Synthesis of xanthenes using 4-picoline or 4-dimethylaminopyridine organocatalyst has been reported from its chromone and acetylene derivatives. This reaction happened through the Diels–Alder cyclization process [77]. Other Diels–Alder approaches are [4+2] cycloaddition of vinylchromone and Fries rearrangement of phenoxyisobenzofuran-1,3-dione with Lewis acid catalyst. The esterification of benzoic acid with phenolic derivative gave diaryl ester as a useful intermediate for the synthesis of xanthone skeleton. The diaryl ester can be further transformed to benzophenone intermediate through Fries rearrangement. On the other hand, the diaryl ester can be converted into diaryl ether intermediate through the Smiles rearrangement. Meanwhile, the direct transformation of diaryl ester to xanthone can be done through the pyrolysis reaction, losing water molecules as the side product. Meanwhile, the Friedländer synthesis is a common route in the synthesis of xanthone glycosides. This reaction occurs between the amino- and carbaldehyde-substituted chromones with ketonic glycosides under alkaline conditions [78]. A brief synthesis scheme of the xanthone derivative is shown in Figure 6.

Further improvement in the synthesis of xanthone derivatives recently focused on heterogeneous catalysis and microwave-assisted organic synthesis (MAOS). Heterogeneous catalysis is desirable in the green chemistry approach for our sustainable future, as the heterogeneous catalyst material demonstrates a faster synthesis process, a higher product yield, and a milder reaction condition. Moreover, heterogeneous catalyst material can be recovered for further reusability purposes [79]. On the other hand, the MAOS technique has been widely employed in the synthesis of xanthone derivatives, as the required reaction time is significantly shortened, together with dramatic improvement in the product yield and selectivity [80]. The MAOS synthesis of xanthone derivatives from salicylic acid with resorcinol, pyrogallol, cresol, and phloroglucinol gave the corresponding xanthone derivatives in 72–98% yield within 5 min reaction time [81]. Palladium-catalyzed acylation reaction can be used for the formation of xanthone skeleton from salicylaldehyde

and dihalotoluene in 41–81% yield [82]. The *tert*-butylammonium hydroxide (TBAOH) as the base has been employed in water-based reaction under MAOS technique to give a quantitative yield of 2-methylxanthone within 4 min [80]. In 2020, metal-free synthesis of benzo[*c*]xanthone from 1,3-diarylketone was reported by Liang et al., employing 1,8-diazabicyclo[5.4.0]undec-7-ene (DBU) as the base in dimethylsulfoxide (DMSO) solution. The attraction of H- $\alpha$  with DBU leads to the cyclization reaction to form the  $\gamma$ -pyrone scaffold within 30 min in 78–93% yield [83]. Another recent approach to synthesize xanthone derivatives was reported by Steingruber et al., employing salicylaldehyde and dibromobenzene derivatives using palladium nanoparticles. High yield (up to 88% yield), as well as high regioselectivity reaction, were achieved within 30 min reaction time in which the nanopalladium catalyst can be used up to four consecutive cycles without losing its activity [84]. Figure 7 shows the recent examples of the synthesis of xanthone derivatives using MAOS technique.

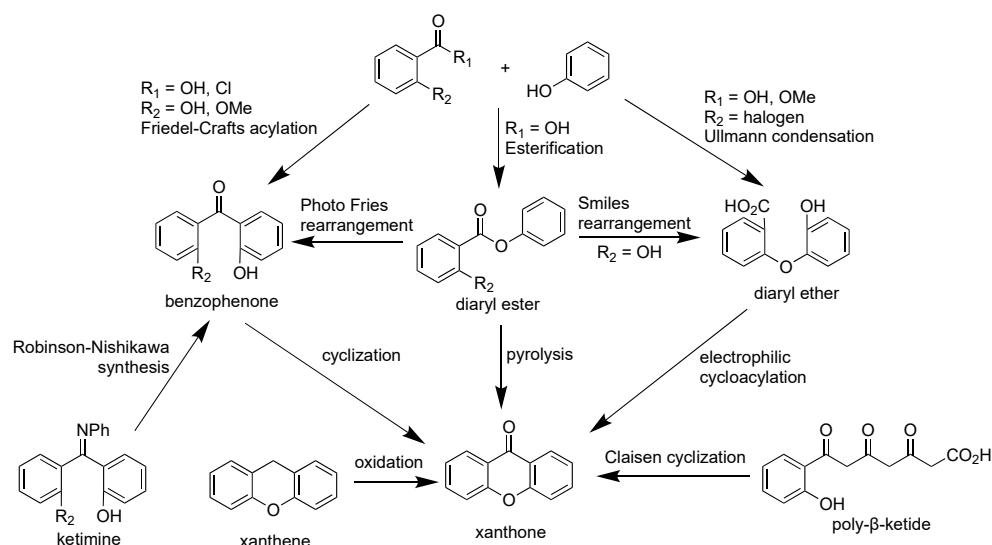


**Figure 6.** Brief synthetic scheme of xanthone derivatives.

Multicomponent reaction in a one-pot synthesis of xanthone derivatives has been attracting researchers' attention due to the simple and convenient process [85]. In this multicomponent reaction, all the reagents are mixed in a reaction system, sometimes without any usage of solvent, and the final product is the highly substituted xanthone derivative. One-pot synthesis of xanthone was reported by Zhao et al., involving Michael addition, cyclization, 1,2-addition, and elimination reactions in a consecutive process [86]. The coupling reaction between methyl salicylate and diaryliodonium triflate salt yielded xanthone derivative in 72% yield, however, the reaction took 12 h to reach the equilibrium state [75]. In 2019, multicomponent synthesis of xanthone dimer was reported from isocyanide, dienophile, and 3-carbonylchromone in 79% yield through [4+2] cycloaddition [87]. Recently, in 2021, one-pot synthesis of xanthone was reported through carbonylative Suzuki coupling reaction by Loureiro et al. This synthetic route utilized three reagents: *ortho*-iodophenol, organoboron, and carbon monoxide, with Pincer palladium as complex as the catalyst material. The reaction yield was quantitative (~100%), however, the reaction was time-consuming (15 h) [88]. Figure 8 shows the recent examples of the multireagent synthesis of xanthone derivatives. More detailed information on the synthesis of xanthone derivatives is available in the published review article by Resende et al. in 2020 [89].

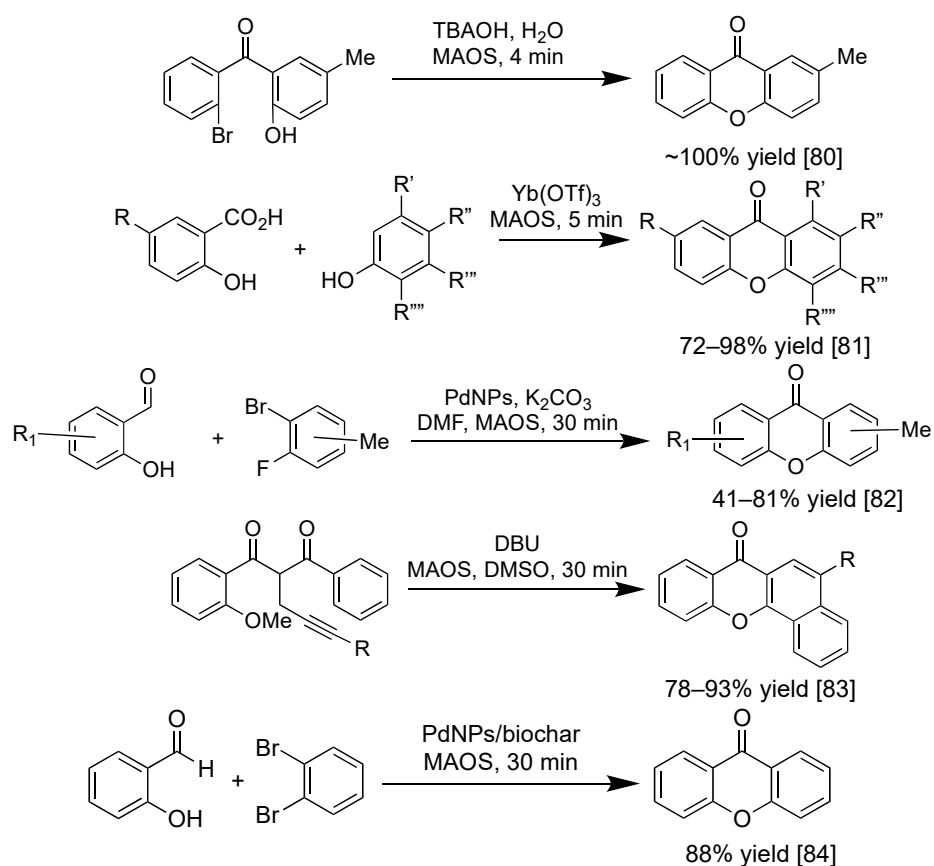


Figure 7. Recent examples of the synthesis of xanthone derivatives using MAOS technique.

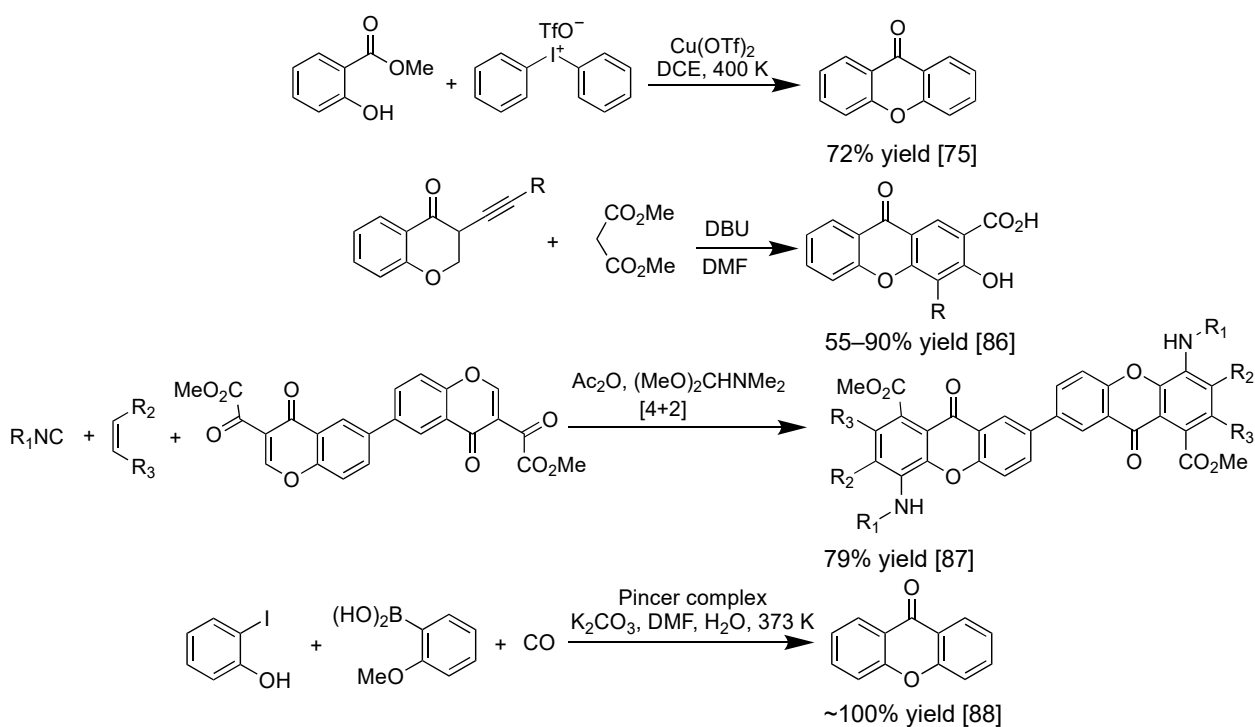


Figure 8. Recent examples of the multireagent synthesis of xanthone derivatives.

The functional groups' interconversion of xanthone derivative is shown in Figure 9. In general, methylation, formylation, nitration, and halogenation reactions of the xanthone

aromatic rings can be directly performed. Afterward, the other functional groups can be converted through reduction, oxidation, nucleophilic substitution, esterification, amidation, diazotization, and carbon–carbon coupling reactions. As prenylated xanthenes serve as the ideal platform for large biological activities, researchers sometimes do semi-synthesis experiments by introducing a prenyl functional group in the naturally available xanthenes. Alkylation of hydroxyxanthone using prenyl bromide with potassium carbonate as the base is the most used protocol to obtain prenylated xanthenes. However, the selectivity of this approach is unsatisfying, as the direct alkylation to the aromatic rings of xanthone is inevitable. Thus, this method is only useful for the functionalization of completely substituted xanthenes. It means that a selective prenylation of a certain hydroxyl group in the polyhydroxyxanthone is also hardly obtained. For a direct prenylation of the aromatic rings of xanthone, 2-methylbut-3-en-2-ol and boron trifluoride are useful reagents for a selective prenylation reaction. The 1,3-dihydroxy-4-prenylxanthone has been successfully obtained from 1,3-dihydroxyxanthone by using this route. Another approach to obtain prenylated xanthone is through a Claisen rearrangement of prenoxyxanthone. The hydroxyxanthone at first is prenylated using prenylbromide and potassium iodide to obtain the prenoxyxanthone as the intermediate, and then the prenoxyxanthone was heated in the presence of Lewis acid catalyst to obtain the prenylated xanthone. However, it should be kept in mind that further cyclization between hydroxy and prenyl groups sometimes directly occurred to give the dihydrobenzofuran derivative of xanthone [74]. Total synthesis of xanthone derivatives has been reported due to the trace isolation yield of certain xanthenes from natural sources. The total synthesis of termicalcolanone A,  $\alpha$ -mangostin, and mangiferin has been reported recently [90–93].

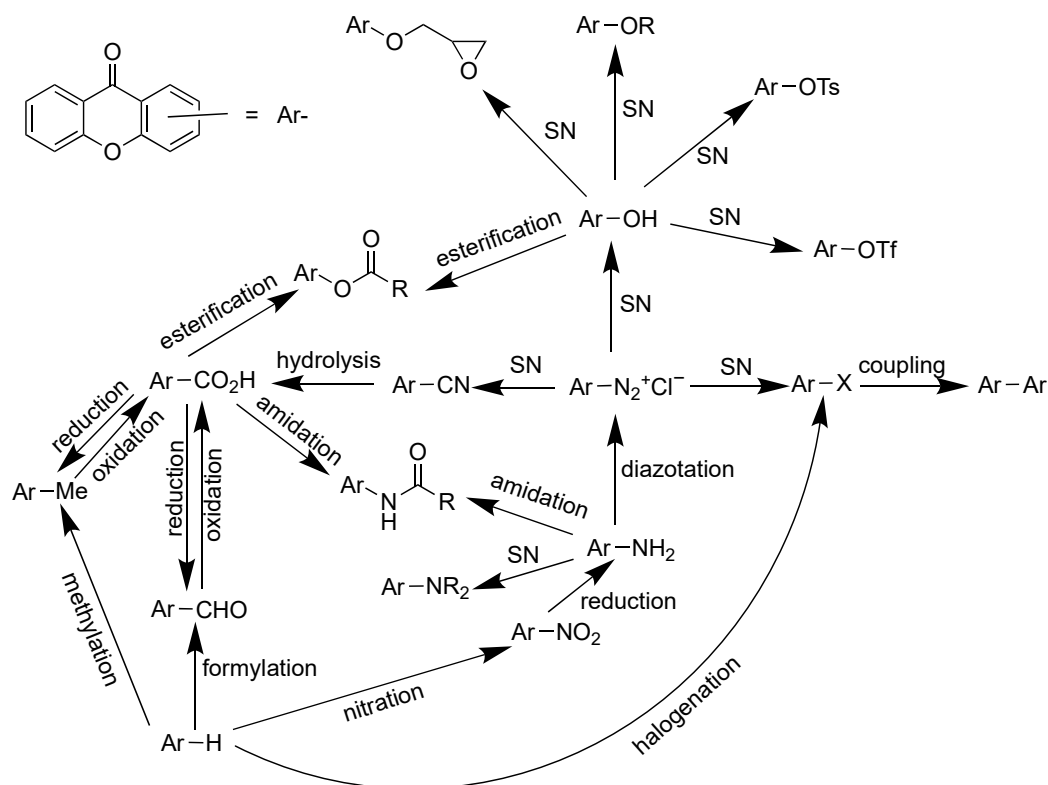


Figure 9. The functional groups' interconversion of xanthone derivatives.

### 2.5. In Vitro Anticancer Assay of Xanthone Derivatives

Figure 10 shows the commonly evaluated cancer cells through in vitro assay, such as breast, hepatoma, cervix, colorectal, ovarian, lung, gastric, leukemia, skin, epidermoid nasopharynx, prostate, neuron, brain glioblastoma, and other cancer cells, including murine, pancreatic, and renal cancer cells. Each cancer cell has its own characteristics. As an

example, NCI-H187 is a small lung cancer cell, while NCI-H460 is a non-small lung cancer cell. As another example, K562 represents sensitive leukemia cancer cells, while K562/R represents drug-resistant leukemia cancer cells. On the other hand, cytotoxic assay for normal cells usually employs H9C2, HEMC, HL-7702, and Vero cell lines [5].

The xanthone derivatives act as anticancer agents through several mechanisms of action. First, activation of caspase proteins induces the apoptosis of cancer cells. Second, inhibition of protein kinases leads to the proliferation of cancer cells. Third, inhibition of aromatase enzyme leads to the inhibition of breast cancer cells' growth [19]. Fourth, prostaglandin PG-E2 inhibition is another mechanism for the anticancer activity of xanthone derivatives. The PG-E2 is a lipid biomolecule that is involved in the inflammation, angiogenesis, apoptosis, and proliferation of cancer cells [94–97]. Fifth, topoisomerase inhibition is critical to stop the DNA replication process in cancer cells [98]. Sixth, the inhibition of P-glycoprotein (P-gp) is critical for the multidrug resistance of the cancer cells, since P-gp protein protects the cancer cells by preventing xenobiotics transport into the membrane cells [99,100]. Seventh, RNA bindings and DNA cross-links could significantly suppress the replication of cancer cells [101]. In this section, a brief update on the anticancer assay of xanthone derivatives based on the structure of xanthone derivatives will be described in the following order: simple oxygenated xanthenes, glycosylated xanthenes, prenylated xanthenes, and thioxanthenes. The chemical structures of the evaluated xanthenes are shown in Figure 11.

Simple oxygenated xanthenes are widely explored as anticancer agents. The 1,3-dihydroxyxanthone is well known for its remarkable anticancer activity against cancer cell lines. In 2007, Woo et al. introduced 2-epoxypropyl group on the 1,3-dihydroxyxanthone to improve its inhibitory activity against topoisomerase I and II proteins. Compound **1a** was inactive against MCF-7 and HeLa cells with IC<sub>50</sub> values of 68.4 and 68.7 μM, respectively. Meanwhile, an additional 2-epoxypropyl group at C-1 position (compound **1b**) drastically improved the IC<sub>50</sub> values to 3.28 and 23.3 μM against MCF-7 and HeLa cells, respectively [102]. It was also reported that xanthone derivatives with halohydrin, methoxy, and amino substituents at C-3 and C-5 positions were also active for topoisomerase inhibition [103,104]. Furthermore, it was reported that DNA crosslinking occurred on the targeted cancer cells after the treatment with the epoxy-xanthenes.

In 2008, Varache-Lembège et al. synthesized several xanthone derivatives and evaluated their anticancer activity. Among the prepared xanthenes, compound **2** gave a potential anticancer activity against KB and MCF-7 cell lines through the antiproliferative mechanism. The presence of nitrogen atoms in the heterocyclic rings was found to enhance the anticancer activity of these xanthone derivatives. However, no clear structure–activity relationship was observed with the difference of hydrazonomethyl moiety position. The acetylated group also enhanced the anticancer activity, as the intracellular enzyme could hydrolyze back to dihydroxyxanthone. They found that compound **2a–c** exhibited strong inhibition activity with the IC<sub>50</sub> values of 2.40, 0.90, and 1.05 μM against KB cells, while these compounds gave IC<sub>50</sub> values of 1.3, 0.8, and 0.9 μM against MCF-7 cancer cell line, respectively. These values were much lower compared to the doxorubicin with IC<sub>50</sub> values of 25.0 and 25.7 μM toward KB and MCF-7, respectively [105]. On the other hand, the anticancer activity of synthetic aminoalkoxylated benzo[b]xanthenes was evaluated against HepG2, Bel-7402, HeLa, MGC-803, and CNE cell lines. Compound **3** gave the most potent anticancer activity, with IC<sub>50</sub> values of 3.51, 1.64, 1.59, 0.85, and 0.47 μM against HepG2, Bel-7402, HeLa, MGC-803, and CNE cell lines, respectively. The presence of the dimethylamino group at C-3 position on the benzo[b]xanthone structure seemed to be critical for the anticancer activity against these cell lines [106]. It was reported that aminoalkanol-xanthenes could generate the overexpression of manganese superoxide dismutase, thus decreasing reactive oxygen species (ROS)-mediated cell senescence. The aminoalkanol-xanthenes also lead mitochondrial dysfunction and cellular apoptosis on the evaluated cancer cell lines [107].



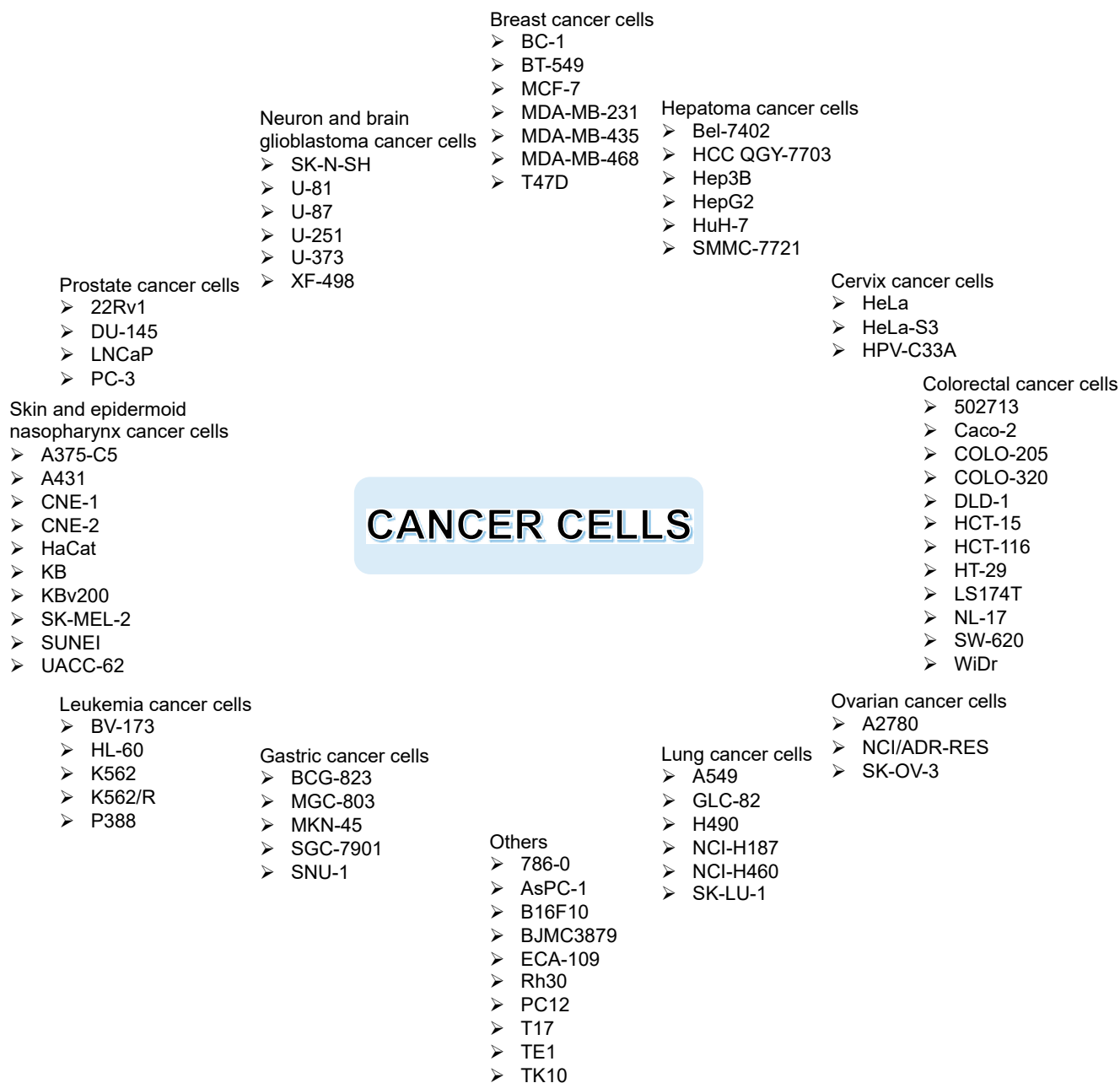


**Figure 10.** Commonly targeted cancer cells for evaluation through in vitro assay.

In 2014, Yang et al. examined the anticancer activity of several synthetic compounds based on 1,3-dihydroxyxanthone against CNE, MGC-803, Bel-7402, and A549 cell lines. It was reported that mono- and dioxygen functional groups were pivotal for the inhibitory activity against protein kinases. The presence of the aminoalkoxy group showed the increment of anticancer activity, while the introduction of the bromoalkoxyl group did not improve the anticancer activity. When the terminal amino group was quaternary ammonium salt, the anticancer activity of xanthone became weaker, due to poor cytomembrane penetration. The different terminal amino substituents had different effects in the increment of anticancer activity with the order: diethylamino > dimethylamino > pyrrolidine > piperidine > morpholino. Compound **4** exhibited the best anticancer activity, as measured by inhibitory activity (3.57–20.1  $\mu\text{M}$ ) against the aforementioned cancer cells. For a specific MGC-803 cancer cell, compound **4** exhibited a time- and dose-dependent proliferation inhibition. For a concentration greater than 1.0  $\mu\text{M}$ , MGC-803 cells viability decreased

significantly, due to lower mitochondrial membrane potential and intracellular calcium leading to the apoptosis mechanism [108].

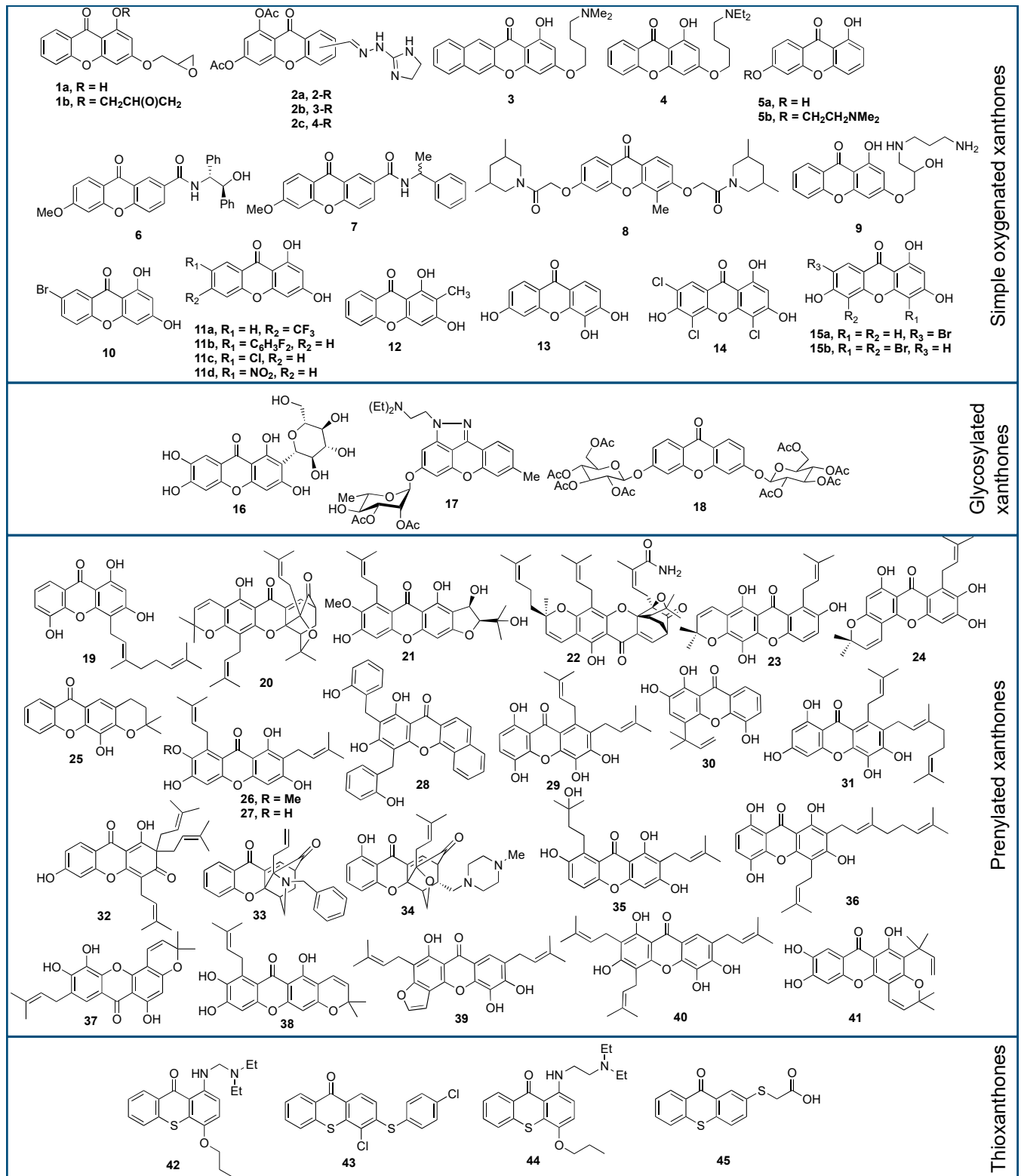


Figure 11. Evaluated xanthone derivatives as the anticancer agents through in vitro assay.

In 2014, Shen et al. synthesized several xanthenes through the modification of the free hydroxyl group of xanthone with dimethylamine group. The inhibitory activity of these

xanthenes was tested against ECA109, SGC-7901, and GLC-82 cell lines. It was found that the presence of aminoalkyl moiety was critical to its anticancer activity, as well as DNA binding. Moreover, the addition of dimethylamino side-chain resulted in the enhancement of anticancer activity. Compound **5a** gave the IC<sub>50</sub> value of 25.7, 33.2, and >50.0 μM against ECA109, SGC7901, and GLC-82 cell lines, respectively. Meanwhile, compound **5b** with aminoalkyl moiety gave lower IC<sub>50</sub> values of 9.56, 13.3, and 16.1 μM against the same cancer cell lines, respectively. The presence of polar aminoalkyl moiety in compound **5b** gave a higher hydrophilicity; thus, this compound could easily penetrate the cancer cell membrane, leading to anticancer activity enhancement. Additionally, the aminoalkyl moiety having a higher pKa value is easily protonated which generate a cationic charge in order to bind with the DNA through its phosphate groups. This phenomenon blocked the DNA replication which is related to the inhibitory activity against the evaluated cancer cell lines [109]. In the same year, Fernandes et al. prepared a chiral xanthone derivative and evaluated its anticancer activity against A375-C5, MCF-7, and NCI-H460 cell lines. Compound **6** was the most potent anticancer agent against the A375-C5, MCF-7, and NCI-H460 cell lines, with IC<sub>50</sub> values of 32.2, 22.6, and 14.1 μM, respectively. They found that the effect of the growth inhibitory activity of the xanthone compound was not only affected by the nature and position of the substituent but also the enantioselective effect. The presence of aryl group on the stereogenic center of xanthone was found to enhance the inhibitory activity against cancer cell lines [110]. On the other hand, it was reported that (*R*)-isomer of compound **7** gave lower IC<sub>50</sub> value (IC<sub>50</sub> = 24.0 μM) than the (*S*)-isomer (IC<sub>50</sub> = 112 μM) against MCF-7 cancer cell line. This phenomenon was caused by a more stable complex conformation between the (*R*)-isomer with the DNA through crosslinking reactions than the (*S*)-isomer one [111].

In 2016, Liu et al. synthesized xanthone derivatives bearing 3,6-disubstituted aminocarboxymethoxy moiety and evaluated them as the anticancer agent. Among the evaluated xanthenes, compound **8** exhibited the highest anticancer activity with the IC<sub>50</sub> value of 6.18, 8.06, 4.76, 4.59, and 6.09 μM against PC-3, MDA-MB-231, AsPC-1, A549, and HCT-116 cell lines, respectively. Compound **8** promoted cell cycle arrest, induced cell apoptosis, and provided antiproliferative effect on cancer cell viability. The presence of the 4-methyl group was critical in the xanthone structure, as it exhibited a higher potent anticancer activity. In contrast, the presence of oxygen atoms on the side chain of xanthone reduced the growth inhibitory activity against these cancer cell lines. This effect may be generated from the possibility of hydrogen bonds formation with other biological macromolecules outside the active site of the protein target. Additionally, the steric effect of the substituent at the side chain may also contribute to a lower inhibitory activity [112]. A similar result was reported by Dai et al. whereas the substituted phenyl moiety decreased the anticancer activity of xanthone derivatives due to steric effect [113].

Minniti et al. in 2017 investigated the anticancer activity of synthetic xanthone derivatives with various polyamine moieties, including spermine, spermidine, butanediamine, and propanediamine at C-3 position. It was reported that the presence of the secondary amine group in the side chain significantly affected the topoisomerase II-drug interaction. Compound **9** was found to give the most potent inhibition of the catalytic activity of topoisomerase II $\alpha$ , as evaluated using DNA relaxation assay. Compound **9** inhibited DNA relaxation with the IC<sub>50</sub> of 1.00 μM. Specifically, compound **9** acts at the DNA cleavage/ligation active side and compound **9** is able to inhibit the ability of DNA to stimulate the rate of ATP hydrolysis. Furthermore, the presence of primary and secondary amine side-chains is more important, rather than the number of primary amines in the chain, or their distance from the primary amine [114].

In 2017, Liu et al. examined the anticancer activity of synthetic xanthenes against MCF-7, MDA-MB-231, HepG2, K562, and COLO-320 cell lines. Among the synthesized xanthenes, compound **10** showed the highest anticancer activity against MDA-MB-231 cell line, with an IC<sub>50</sub> value of 0.46 μM. The inhibitory activity of compound **10** against MDA-MB-231 cell line was found to be much stronger compared to DMXAA (IC<sub>50</sub> = 48.0 μM).

Additionally, compound **10** also showed potent inhibitory activity against MCF-7, HepG2, K562, and COLO-320 cell lines, with  $IC_{50}$  values of 3.40, 9.20, 13.4, and 10.5  $\mu\text{M}$ , respectively. The inhibitory effect was found as the result of induced apoptosis of the evaluated cancer cell lines. The effect of the electron-withdrawing group introduced to the opposite aromatic ring of 1,3-dihydroxyxanthone derivatives increased the anticancer activity, while the electron-donating group showed the opposite effect. Remarkably, the xanthone derivatives showed an enhanced inhibitory activity when combined with DMXAA. This synergistic effect demonstrated a good approach for the design and development of more potent anticancer drugs [115].

In 2018, Zhou et al. synthesized several xanthone derivatives and evaluated their anticancer activity against A549 and SMMC-7721 cancer cell lines. Compounds **11a–b** with fluoro substituents were active against A549 cells, whereas compounds **11c–d** were inactive against this cancer cell line. The anticancer activity of compound **11a** ( $IC_{50} = 29.9 \mu\text{M}$ ) and compound **11b** ( $IC_{50} = 24.9 \mu\text{M}$ ) was stronger than cisplatin ( $IC_{50} = 32.4 \mu\text{M}$ ) as the positive control. In contrast, the anticancer activity of non-fluorinated xanthenes ( $IC_{50} = 6.14\text{--}14.0 \mu\text{M}$ ) was stronger than that of fluorinated ones ( $IC_{50} = 27.2\text{--}37.4 \mu\text{M}$ ) against SMMC-7721 cell line. The anticancer activity of non-fluorinated xanthenes **11c–d** ( $IC_{50} = 6.14\text{--}14.0 \mu\text{M}$ ) was also stronger than cisplatin ( $IC_{50} = 26.3 \mu\text{M}$ ) [116].

Recently, Pedro et al. synthesized oxygenated xanthenes and evaluated their anticancer activity against MCF-7, TK-10, and UACC-62 cell lines. Additional oxygenated groups in the xanthone core gave a significant effect on the anticancer activity enhancement. Among several synthesized xanthone derivatives, compound **12** was reported as the best anticancer agent against MCF-7, TK-10, and UACC-62 cells with the  $IC_{50}$  values of 21.9, 34.3, and 20.0  $\mu\text{M}$ , respectively. In addition, the compound **12** is considered to be safe for the anticancer application as no cytotoxic to the human lymphocytes (cell viability > 70%) is observed. The nature of substituents in oxygenated xanthone structure had a significant effect on its anticancer activity. For example, the 1,2-dihydroxyxanthone exhibited a weaker anticancer activity than 2-hydroxy-1-methoxyxanthone. Therefore, the suitable functional group should be considered to be a critical parameter in the design of oxygenated xanthone derivative, with high potential for anticancer activity [117].

Our research group has been working on anticancer research employing xanthone derivatives since 2010. Several hydroxyxanthone derivatives including 2-hydroxyxanthone, 3-hydroxyxanthone, 1,3-dihydroxyxanthone, 1,6-dihydroxyxanthone, 3,4-dihydroxyxanthone, 3,6-dihydroxyxanthone, 1,3,6-trihydroxyxanthone, 1,5,6-trihydroxyxanthone, 3,4,6-trihydroxyxanthone, and 1,3,8-trihydroxyxanthone have been synthesized in 2010–2021 [118–126]. Among them, 3,4,6-trihydroxyxanthone (**13**) was one of the most active anticancer agents. The anticancer activity of compound **13** against WiDr cells gave an  $IC_{50}$  value of 37.8  $\mu\text{M}$ . Furthermore, compound **13** was not toxic against Vero cell lines ( $IC_{50} = 2510 \mu\text{M}$ ), giving a selectivity index (SI) of 66.4, which was higher than doxorubicin (49.4) [127]. From the quantitative real time-polymerase chain reaction, compound **13** suppressed the mRNA cyclooxygenase-2 (COX-2) expression by 37%, with no inhibitory expression against vascular endothelial growth factor receptors. Therefore, it was concluded that compound **13** inhibited the COX-2 enzyme and started chronic inflammation in the cancer cells. A molecular docking study showed that compound **13** interacted with Tyr355 and Arg120 amino acid residues of COX-2 enzymes, yielding a binding energy of  $-77.0 \text{ kcal/mol}$  [128].

Anticancer activity of chlorinated-hydroxyxanthenes has been evaluated against HepG2 and P388 cell lines. Chlorinated-hydroxyxanthenes, i.e., 4-chloro-1,3-dihydroxyxanthone, 4,5,7-trichloro-1,3,6-trihydroxyxanthone and 4-chloro-3,6-dihydroxyxanthone are inactive against HepG2 cells with  $IC_{50}$  values of 206–666  $\mu\text{M}$ . These  $IC_{50}$  values are lower than hydroxyl derivatives (786–828  $\mu\text{M}$ ) against the same HepG2 cancer cell line. Furthermore, the SI value of chlorinated-hydroxyxanthenes was higher (5.31–22.0) than hydroxyxanthenes (2.58–10.60) against HepG2 cells. On the other hand, 4-chloro-1,3-dihydroxyxanthone also gave a lower  $IC_{50}$  (12.5  $\mu\text{M}$ ) than 1,3-dihydroxyxanthone (68.0  $\mu\text{M}$ ) against the P388 cancer cell line. The 4,5,7-trichloro-1,3,6-trihydroxyxanthone gave a lower

IC<sub>50</sub> (5.21 μM) than 1,3,6-trihydroxyxanthone (23.5 μM) against P388 cells. Meanwhile, the 4-chloro-3,6-dihydroxyxanthone gave a lower IC<sub>50</sub> (0.69 μM) than 3,6-dihydroxyxanthone (10.4 μM) against P388 cancer cells. The SI value of chlorinated-hydroxyxanthenes were much higher (87.6–9200) than hydroxyxanthenes (31.2–844) against P388 cell line. From the molecular docking study, it was found that chlorinated-hydroxyxanthenes were able to inhibit the c-KIT protein through hydrogen bond interactions with Asp810, Cys809, Ile789, His790, and Leu644 [124].

The 4,5,7-trichloro-1,3,6-trihydroxyxanthone (**14**) gave no anticancer activity against HeLa (IC<sub>50</sub> = 251 μM), T47D (IC<sub>50</sub> = 1398 μM), and HepG2 (IC<sub>50</sub> = 262 μM) cancer cell lines. In contrast, compound **14** gave moderate anticancer activity against P388 (IC<sub>50</sub> = 5.21 μM) cancer cells. Furthermore, the IC<sub>50</sub> value of compound **14** (IC<sub>50</sub> = 15.9 μM) was lower than doxorubicin (IC<sub>50</sub> = 25.4 μM) against Raji lymphoma cell line. The toxicity of compound **14** for Vero cell lines was reported to be in IC<sub>50</sub> of 256 μM, yielding an SI value of 16.1. From the molecular docking study, compound **14** gave strong binding energy against Raf-1 (−79.4 kcal/mol) and c-Jun-N-terminal protein kinase (c-JNK) (−75.4 kcal/mol) proteins. Compound **14** formed hydrogen bonds with Cys424, Lys431, Ser427, and Gly426. The number of the hydrogen bond interactions (4) of compound **14** with Raf-1 protein was much higher than for the native ligand (1 hydrogen bond with Cys424). Compound **14** generated additional hydrogen bonds with Met111, Glu109, and Ser34 (two hydrogen bonds) on the active site of c-JNK protein. The number of hydrogen bond interactions (4) of compound **14** with c-JNK protein was also higher than the native ligand (2 hydrogen bonds with Met111 and Glu109) [124].

The synergistic effect between compound **14** and doxorubicin against Raji lymphoma cell line has also been studied. It is well-known that drug resistance can be overcome through drug combination as the mechanism of action of two/more drug compounds, which may be different from in their individual usage. Furthermore, a synergistic effect of two/more drugs could lower the dose and thus suppress the side effects to the human body [127]. Combination of both compounds gave the combination index value in a range of 0.06–0.29, indicating a good synergistic anticancer effect. It was reported that compound **14** inhibited Raf-1 protein and activated c-JNK protein. Inhibition of Raf-1 protein led to a higher sensitivity of cancer cells to doxorubicin. On the other hand, the activation of c-JNK protein led to the translocation of pro-apoptotic protein Bax to cytoplasm and stimulated the apoptosis mechanism of cancer cells [128].

Two new brominated-hydroxyxanthenes, i.e., compounds **15a** and **15b**, have also been prepared from 2,4-dihydroxybenzoic acid. The compound **15a** was synthesized through bromination reaction of 2,4-dihydroxybenzoic acid first, and then followed by a cyclization reaction with phloroglucinol. On the other hand, compound **15b** was obtained from a bromination reaction of 1,3,6-trihydroxyxanthone. Both compounds gave moderate anticancer activity against P388 cell line, with IC<sub>50</sub> and SI values of 6.34–10.7 μM and 43.2–74.4, respectively. The molecular docking study revealed that the anticancer activity of brominated-hydroxyxanthenes was generated by hydrogen bonding interactions with His790, Cys809, Leu644, Ile789, and Asp810 on the active site of c-KIT protein [129].

Glycosylated xanthenes have also been evaluated as anticancer agents. Mangiferin (**16**), a famous glycosylated xanthone, was reported for its anticancer activity against colorectal cancer cells through the inhibition of *bcr/abl* gene expression, thus inducing cellular apoptosis. In 2013, Li et al. isolated mangiferin from mangosteen fruit, and evaluated its anticancer activity against MDA-MB-231 and BT-549 cell lines. Mangiferin exhibited poor anticancer activity against MDA-MB-231 and BT-549 cells, giving the IC<sub>50</sub> of 299 and 274 μM, respectively. Mangiferin gave a lower expression of matrix metalloproteinase-7 (MMP-7), MMP-9, beta-catenin, and vimentin, and simultaneously gave a higher expression of E-cadherin, thus leading to the antiproliferative phenomenon [130]. On the other hand, mangiferin also acts through influencing cell cycle arrest, activating the caspase-3 protein, and inhibiting the nuclear factor kappa B (NF-κB) pathway [131]. A synergistic

cancer treatment employing mangiferin with doxorubicin and oxaliplatin has also been reported to enhance the anticancer activity of mangiferin [132].

In 2015, Song et al. synthesized several xanthone derivatives bearing rhamnopyranoside moiety, and evaluated their anticancer activity against several cancer cell lines. It was found that the presence of sugar moiety was crucial for anticancer activity. Compound **17** exhibited moderate to strong anticancer activity against HL-60, MDA-MB-231, MDA-MB-468, HCT-116, PC3, Rh30, A549, BEL-7402, MKN45, A431, 786-O, and KB cell lines, with IC<sub>50</sub> values of 2.20, 4.30, 3.47, 2.20, 3.99, 2.37, 1.05, 2.43, 6.29, 2.59, 4.70, and 0.55 μM, respectively. Specific to KB cancer cells, compound **17** could inhibit cell growth by inducing apoptosis, both in extrinsic and intrinsic pathways, and arresting cell cycle progression at the G2/M phase. It was reported that xanthone-O-glycosides at C-3 and C-6 positions were inactive against NCI-H460, MCF-7, and A375-C5 cell lines. However, acylation of all of the hydroxy groups of this xanthone-O-glycosides drastically enhanced the anticancer activity against NCI-H460 and MCF-7 cell lines, with IC<sub>50</sub> values of 0.19 and 0.46 μM, respectively. This result demonstrated that the acetyl group on the pyranosyl ring was critical for the anticancer activity [133].

In 2019, Alves et al. evaluated the anticancer activity of synthetic xanthone compounds, with acetyl groups against A375-C5, MCF-7, NCI-H460, U-251, U-373, and U-87 cancer cell lines. Compound **18** showed the most potent growth inhibitory activity against these cancer cells. Compound **18** gave IC<sub>50</sub> values of 135, 0.46, 0.19, 0.55, 0.42, and 0.42 μM against A375-C5, MCF-7, NCI-H460, U-251, U-373, and U-87 cell lines, respectively. The presence of acetyl groups in compound **18** was found to increase its anticancer activity. However, the presence of acetyl groups led to poor water solubility, which can be overcome by encapsulating compound **18** in a drug delivery system [12].

Prenylated xanthenes are the most evaluated xanthenes, due to their promising application as the anticancer agent. In general, prenylated xanthenes exhibited higher anticancer activities than the other classes. Early in 1992, Sordat-Diserens et al. reported that compound **19** isolated from the root bark of *Garcinia livingstonei* gave the IC<sub>50</sub> value of 1.58 μM against WiDr cancer cells, which was twice as low as 5-fluorouracil (IC<sub>50</sub> = 3.08 μM) [134]. The anticancer activity of psorospermin has also been reported. Initially, psorospermin was isolated from the radix of *Psorospermum febrifugum* in Africa in 1980. This compound exhibited in vitro and in vivo anticancer activity against wild type and drug-resistant leukemia cells. Furthermore, good anticancer activity of psorospermin against breast and colorectal cancer cells has also been reported. The psorospermin acts as the anticancer agent through DNA intercalation between base pairs at positions 11 and 12, as well as guanine alkylation on the topoisomerase II protein with its epoxydihydrofuran moiety. The DNA alkylation on the active site of topoisomerase II protein leads to inactivation on the DNA replication of cancer cells [135]. Another anticancer agent based on natural xanthone derivatives is desoxymorellin (**20**) isolated from the dry latex of *Garcinia hanburyi*. It was reported that desoxymorellin gave IC<sub>50</sub> values of 0.74, 0.77, and 1.15 μM against HeLa, K562, and K562/R cell lines, respectively, through the apoptosis induction mechanism [136,137].

In 2006, Laphookhieo et al. isolated a prenylated xanthone from the roots of *Cratoxylum cochinchinense* and evaluated its anticancer activity against NCI-H187. This compound showed a potential cytotoxic effect against NCI-H187 cancer cell line with an IC<sub>50</sub> value of 1.45 μM. Remarkably, it showed no cytotoxic activity against KB and BC-549 cell lines, which indicated excellent selectivity against NCI-H187 cancer cells. It was proposed that the presence of geranyl moiety in the isolated compound corresponded to its strong anticancer activity [138]. In the same year, Suksamrarn et al. reported the isolation of a new prenylated type xanthone, mangostenone C (**21**), from the early ripe fruit of *Garcinia mangostana*. The anticancer activity of mangostenone C was evaluated against KB, BC-1, and NCI-H187 cells, giving IC<sub>50</sub> values of 6.11, 7.70, and 8.11 μM, respectively. The anticancer activity of mangostenone C against NCI-H187 was still weaker, but comparable to α-mangostin (5.07 μM) and gartanin (IC<sub>50</sub> = 2.72 μM). This finding means that the tetraoxygen framework exhibits stronger anticancer activity [139].

Gambogic acid is one of the most famous natural xanthenes as an anticancer agent [140,141]. Gambogic acid shows strong anticancer activity against BGC-823, KB, A549, NCI-H460, HepG2, HT-29, MCF-7, DU-145, HL-60, P388, K562/S, and K562/R cell lines in the range  $IC_{50}$  of 0.38–4.45  $\mu\text{M}$  [136,142–146]. Furthermore, gambogic acid is very valuable for the treatment of cholangiocarcinoma liver cancer, since no effective anticancer drug is available as of today for this disease [56]. Gambogic acid exhibited anticancer activity for several cancer cells due to many mechanisms of action. The main mechanism of action is apoptosis induction on cancer cells. The apoptosis induction from gambogic acid was generated from several inhibition pathways against NF- $\kappa$ B signaling, c-JNK phosphorylation, G0/G1 phase cell cycle arrest, and Bcl-2 mRNA expression. It was reported that gambogic acid also activated Bax mRNA expression and p53, interacted to transferrin receptor 1 (TfR-1) protein, decreased mitochondria membrane potential, accumulated reactive oxygen species, and depolymerized the microtubules [147–152]. These pathways led to a strong apoptosis induction signal on the cancer cells. In 2007, Jang et al. isolated gambogic amide (**22**) as the main component in gamboge, an orange-brownish resin exuded from the plant of *Garcinia hanburryi*, which is often used as traditional medicine for cancer treatment. The anticancer activity of gambogic amide was found to be related to the apoptotic activity against T17 cells with an  $IC_{50}$  of 5.00 nM. The T17 cell line was derived from the basal forebrain of SN56 cell; therefore, T17 cells were defined as TrkA stably transfected SN56 cells. The gambogic amide could selectively bind to TrkA, triggering its tyrosine phosphorylation, and preventing neuronal cell death. These phenomena yielded an agonist effect to nerve growth factor (NGF) thus giving potent neurotrophic activity. Moreover, gambogic amide could block apoptotic machinery independent of the Trk receptor, which led to its ability to trigger programmed cell death for the cancer cell lines [153].

Two new xanthenes isolated from *Terminalia calcicicola* named as termicalcicolanones A (**23**) and B (**24**) have been reported in 2007. Termicalcicolanones A and B showed weak to moderate anticancer activity against A2780 cells, with  $IC_{50}$  values of 40.6 and 8.10  $\mu\text{M}$ , respectively [154]. With a similar structure, the positions of hydroxyl and pyranosyl moieties on termicalcicolanone significantly influence anticancer activity [155]. A combination of pyranoxanthone and paclitaxel has also been reported to enhance their anticancer activity [156]. In 2010, Palmeira et al. synthesized xanthone derivatives by modifying the dihydroxyxanthone through prenylation and ring closure reactions. The synthesized compounds were evaluated as the anticancer agents against K-562, HL-60, and BV-173 cell lines. They found that compound **25** gave the most promising inhibitory activity on the K-562 cell viability, with an  $IC_{50}$  value of 20.0  $\mu\text{M}$ . Additionally, compound **25** gave a moderate inhibitory activity against HL-60 and BV-173, with an  $IC_{50}$  value of 7.00 and 14.0  $\mu\text{M}$ , respectively. The inhibitory mechanism was suggested to come from the antiproliferative and apoptotic effects on the evaluated cancer cell lines [157].

In 2011, Johnson et al. evaluated the anticancer activity of pure  $\alpha$ -mangostin (**26**) against LNCaP, 22Rv1, DU 145, and PC-3 cancer cell lines, with  $IC_{50}$  values of 5.90, 6.90, 22.5, and 12.7  $\mu\text{M}$ , respectively. The  $\alpha$ -mangostin could induce cancer cell apoptosis at a concentration equal to or higher than 15  $\mu\text{M}$ . Meanwhile,  $\alpha$ -mangostin can promote G0/G1 cell cycle arrest at a lower concentration (<15  $\mu\text{M}$ ) [158]. Other research groups reported that  $\alpha$ -mangostin also showed moderate anticancer activities against T47D, MDA-MB-231, PC12, DLD-1, and HL-60 cell lines, with  $IC_{50}$  values of 2.44–28.5  $\mu\text{M}$  [159–164]. The main mechanisms of action for  $\alpha$ -mangostin as the anticancer agent were antiproliferation, apoptosis induction, and dysfunction of mitochondria [161,165]. Furthermore, the other mechanisms of action for  $\alpha$ -mangostin were observed through influencing the G0/G1 phase cell cycle arrest and inhibition of tau-phosphorylation, p38 mitogen-activated protein kinase (MAPK), human epidermal growth factor receptor 2/phosphatidylinositol-3-kinase/Akt (HER2/PI3K/Akt), and extracellular signal-regulated protein kinase 1/2 (ERK1/2) signaling pathways [34,166]. A synergistic effect between  $\alpha$ -mangostin and cisplatin has been reported for cervix cancer cells treatment [167]. The introduction of prenyl group at C-1 position dramatically increased the anticancer activity of  $\alpha$ -mangostin against the MCF-7 cell line [34]. Azevedo et al. explained that 2,2-dimethyl-3,4-dihydropyran moi-

ety was critical for the anticancer activity against HL-60, A375-C5, NCI-H460, and MCF-7 cells [168]. On the other hand, the hydroxyl groups at C-3 and C-6 positions were also critical for the anticancer activity of  $\alpha$ -mangostin against B16F10, MDA-MB-231, AsPC-1, SW-620, and NCI-H460 cell lines [169].

In 2012, Chang and Yang isolated another natural xanthone,  $\gamma$ -mangostin (**27**), from the hull of mangosteen fruit. The  $\gamma$ -mangostin was one of the major xanthone components in the mangosteen fruit. The  $\gamma$ -mangostin was evaluated as the anticancer agent against HT-29 cells. Unfortunately,  $\gamma$ -mangostin was non-active against HT-29 cells ( $IC_{50} = 68.5 \mu M$ ). This inhibitory activity occurred through the induced apoptosis mechanism [170]. Cheng et al. synthesized benzoxanthones and evaluated their anticancer activity against A549, MDA-MB-435, and HCT-116 cell lines. Compound **28** showed the most potent anticancer activity, with  $IC_{50}$  values of 14.3, 15.8, and  $5.17 \mu M$  for A549, MDA-MB-435, and HCT-116, respectively. The inhibitory activity of compound **28** as an anticancer agent relies on topoisomerase I protein inhibition, which led to the DNA relaxation of cancer cells [171].

In 2012, Niu et al. isolated a bioactive compound-based xanthone derivative from the stem bark of *Garcinia bracteata* and evaluated its anticancer activity against HL-60. The extraction, partition, and purification of the stem bark of *Garcinia bracteata* yielded up to 31 xanthone derivatives. Among them, three compounds: compound **29**, globuxanthone (**30**), and garciniaxanthone E (**31**) exhibited strong anticancer activity against HL-60 cell line, with  $IC_{50}$  values of 2.80, 3.40, and  $3.10 \mu M$ , respectively. Compound **29** and garciniaxanthone E had prenyl moiety at their structure which corresponded to a stronger anticancer activity against HL-60 cells, indicating that the prenyl groups play an important role in the growth inhibitory activity. The number of prenyl groups was also suggested to significantly increase the inhibitory activity of xanthone. However, the addition of prenyl groups at the side-chain as in garciniaxanthone E did not significantly affect its activity compared to compound **29**. Garciniaxanthone E was also reported for its anticancer activity against breast, lung, liver, gastric, colorectal, and leukemia cancer cell lines through the activation of caspase proteins and inhibition of PG-E2 pathways [172].

Lim et al., 2012 synthesized several xanthone derivatives owing to the prenyl group, and evaluated their anticancer activity against HeLa and MDA-MB-231 cell lines. Among the synthesized compounds, compound **32** showed the most promising anticancer activity. Compound **32** gave  $IC_{50}$  values of 8.90 and  $4.50 \mu M$  against HeLa and MDA-MB-231 cell lines, respectively. The anticancer activity of compound **32** was twice as strong as doxorubicin and cisplatin as the positive standards. The presence of nonplanar geminal-diprenylated rings was suggested to enhance its inhibitory activity against the cancer cell lines [173]. In the same year, Zhang et al. synthesized several xanthone derivatives which belong to the aza-caged *Garcinia* analogues. The synthesized compounds were evaluated as anticancer agents against HepG2, A549, and U-251 cell lines. Among them, compound **33** showed the highest anticancer activity, with  $IC_{50}$  values of 2.62, 2.10, and  $16.4 \mu M$  against HepG2, A549, and U-251 cell lines, respectively. Moreover, compound **33** also showed inhibitory activity against serine/threonine protein kinase, nuclear factor kappa-B kinase subunit gamma ( $IKK-\beta$ ), with an  $IC_{50}$  value of  $8.02 \mu M$ . The introduction of hydrophobic moiety in the aza-caged xanthone structure leads to a stronger anticancer activity. Moreover, it was reported that the presence of substituent group with larger volume was preferred in the anticancer activity enhancement, due to preferable interaction with the putative receptors. Compound **33** exhibited the anticancer activity through the apoptosis induction mechanism [174].

In 2013, Zhang et al. synthesized a natural xanthone derived from *Garcinia* species and evaluated its anticancer activity against HepG2 and A549 cell lines. Compound **34** was considered to give strong anticancer activity against HepG2 and A549 cell lines with  $IC_{50}$  values of 3.25 and  $3.60 \mu M$ , respectively. Furthermore, compound **34** was also found to have good bioavailability, and it was orally active, as tested through an in vivo assay. Compound **34** was capable of giving the inhibition rate of 58% against tumor growth (hepatoma solidity/Heps) at 100 mg/kg daily oral dose for 4 days, which was much better



compared to the natural product with a similar structure, gambogic acid. However, a further clinical evaluation has not been reported yet [175].

In 2015, several isolated xanthenes from the branches of *Garcinia achachairu* were investigated as the anticancer agents against nasopharynx cancer cells (CNE-1, CNE-2, and SUNE1). A new prenylated xanthone (**35**) showed a remarkable anticancer activity with the IC<sub>50</sub> of 1.43, 0.73, and 2.23 μM against CNE-1, CNE-2, and SUNE1 cell lines, respectively. On the other hand, the anticancer activity of compound **36** was evaluated against U-251, MCF-7, NCI/ADR-RES, 786-0, NCI-H460, PC-3, HT-29, and HaCat cell lines, giving IC<sub>50</sub> values of 11.2, 34.0, 8.61, 19.6, 56.2, 10.5, 58.1, and 30.6 μM, respectively, which was comparable to doxorubicin [176]. The mechanism of anticancer activity of both compounds was suggested through the antiproliferative effect on the evaluated cancer cell lines [177]. In 2016, Li et al. isolated xanthone derivatives from the leaves of *Garcinia paucinervis* plant, which yielded a new compound, paucinervin I (**37**). Paucinervin I showed strong anticancer activity against HL-60 cell line with the IC<sub>50</sub> value of 1.30 μM. The anticancer activity of paucinervin I was stronger than 5-fluorouracil (IC<sub>50</sub> = 2.37 μM). The presence of angular pyranoxanthone skeleton in paucinervin I compound seemed to play a pivotal role in its antiproliferative activity [178]. In 2017, Yang et al. isolated a new prenylated xanthone derivative, 7-O-demethyl mangostanin (**38**), from the pericarp of mangosteen fruits, and studied its anticancer activity against CNE-1, CNE-2, A549, H490, PC-3, SGC-7901, and U-87 cancer cell lines. The 7-O-demethyl mangostanin gave IC<sub>50</sub> values of 3.35, 4.01, 4.84, 7.84, 6.21, 8.09, and 6.39 μM against CNE-1, CNE-2, A549, H490, PC-3, SGC-7901, and U-87 cancer cell lines, respectively. The 7-O-demethyl mangostanin gave a stronger anticancer activity when compared to the Hirsutanol A as the positive control (IC<sub>50</sub> = 6.30–15.0 μM). The mechanism of action of 7-O-demethyl mangostanin was generated by the induction of the late and early-stage apoptosis of cancer cells [67].

In 2018, Jia et al. isolated xanthone derivatives from the stem of *Garcinia paucinervis* and evaluated their anticancer activity against HL-60, PC-3, and Caco-2 cell lines. The isolation process yielded two new xanthenes, (-)-paucinervin O (**39**) and paucinervin P (**40**). Compound **39** showed strong anticancer activity, with IC<sub>50</sub> values of 0.87 and 2.06 μM against HL-60 and Caco-2 cells, respectively. Compound **39** owing a furan ring was found to be more active against three cancer cell lines compared to the compounds with a dihydrofuran ring. On the other hand, compound **40** gave a strong anticancer activity, with IC<sub>50</sub> value of 4.66 μM against PC-3 cells [179]. In 2019, Liu et al. synthesized several xanthone derivatives and evaluated their potential anticancer activity against hepatoma cancer cells, i.e., HepG2, Hep3B, SMMC-7721, and HuH-7. They found that the presence of the 3-methyl-2-butenyl group was crucial for the enhancement of anticancer activity specifically against HepG2 cells. Additionally, when 3-methyl-2-butenyl and 1,3-dihydroxy moieties formed a cyclic conjugate system, a much stronger anticancer activity was observed against all evaluated cancer cells. Among them, compound **41** was found to give the strongest anticancer activity, with IC<sub>50</sub> values of 18.6, 36.5, 52.8, and 69.6 μM against HepG2, Hep3B, SMMC-7721, and HuH-7, respectively. The mechanism of its anticancer activity was reported through interactions with caspase 3, caspase 9, and poly(adenosine diphosphate-ribose) polymerase (PARP) proteins, which participate in programmed cell death [18].

Since a limited number of isolated and synthesized xanthone dimers and xantholignoids are found, both groups are rarely investigated as anticancer agents. On the other hand, thioxanthone is a xanthone derivative in which the oxygen atom of the pyran ring is replaced by a sulfur atom [180,181]. In 2012, Palmeira et al. reported the synthesis and anticancer activity of 1-substituted 4-propoxythioxanthone against K562 cancer cells. It was reported that compound **42** with the (*N,N*-diethylamino)ethylamino functional group at C-1 position was the most active anticancer agent. Compound **42** gave IC<sub>50</sub> value of 1.90 μM, which was much lower than doxorubicin (12.0 μM) [157]. In 2015, Chen et al. synthesized 3-substituted-4-chloro-thioxanthenes and evaluated their anticancer activity for several cell lines. These thioxanthone analogues were prepared by Ullmann condensa-

tion and Friedel–Crafts intramolecular reactions. It was known that the functional group attachment at C-3 of thioxanthone enhanced its anticancer activity. Among the prepared thioxanthone derivatives, compound **43** showed the most promising anticancer activity. Compound **43** gave moderate to strong anticancer activity, with IC<sub>50</sub> values of 7.90 and 3.90 μM for MCF-7 and MDA-MB-468 cells, respectively. Compound **43** showed no significant toxicity effect toward H9C2 cells (>25.0 μM), demonstrating that it could be applied as a potential candidate for an anticancer lead compound [182].

In 2016, Barbosa et al. examined the anticancer activity of synthetic thioxanthone derivatives against MCF-7, NCI-H460, and A375-C5 cell lines. Compound **44** showed the most potent anticancer activity, with an IC<sub>50</sub> value of 6.10, 6.00, and 3.60 μM against MCF-7, NCI-H460, and A375-C5 cells, respectively. The anticancer activity was caused through the induced apoptosis mechanism. The modification of compound **44** to its hydrochloride salt form was found to enhance its solubility and bioavailability [183]. In 2020, Ataci et al. synthesized compound **45** and tested its cytotoxic anticancer activity against HT-29 cells. Compound **45** showed no anticancer activity (IC<sub>50</sub> > 165 μM) against HT-29 cell lines. In contrast, UV light irradiation stimulated compound **45** to enhance its cytotoxic activity (IC<sub>50</sub> = 65.5 μM). Moreover, compound **45** exhibited higher activity compared to the common chemotherapeutic agents, such as 5-fluorouracil (IC<sub>50</sub> = 222 μM) and cisplatin (IC<sub>50</sub> = 66.4 μM). Under UV light irradiation, compound **45** released CO<sub>2</sub> and produced alkyl radicals, thus increasing its anticancer activity. Therefore, compound **45** has potential for its application as a theragnostic agent toward specific targeted cancer treatment [184]. The summary of the in vitro anticancer activity of xanthone derivatives is listed in Table 3. Meanwhile, the summary of the most promising anticancer agents based on xanthone derivatives in this review article is shown in Figure 12.

**Table 3.** Summary of the in vitro anticancer activity assay of reported xanthone derivatives.

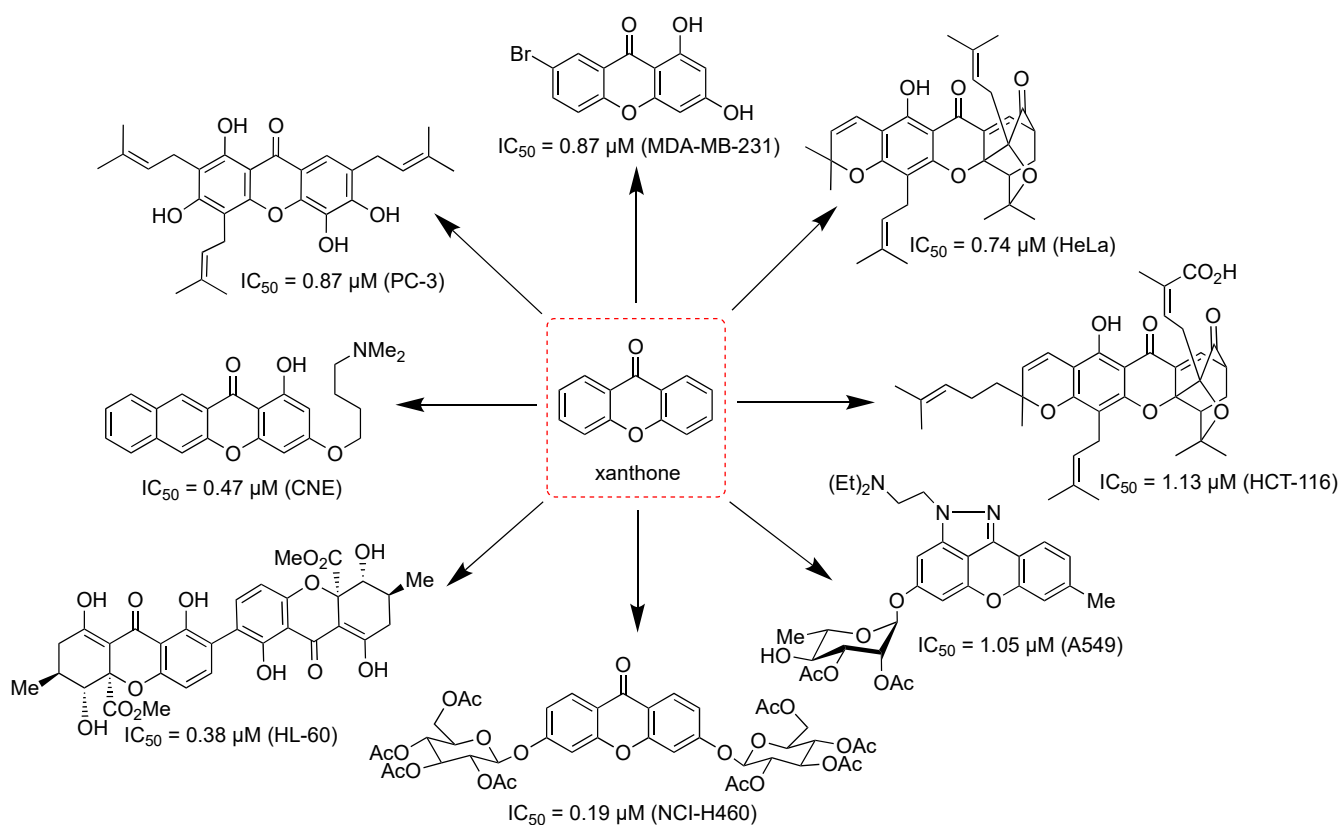
Xanthone Derivative	Source	IC <sub>50</sub> (μM) (Cancer Cells)	Main Mechanism	Ref.
<b>1a</b>	Synthesis	68.4 (MCF-7)	Topoisomerase inhibition, DNA crosslinking	[102]
<b>1b</b>		3.28 (MCF-7)		
<b>2a</b>	Synthesis	1.3 (MCF-7)	-	[105]
<b>2b</b>		0.8 (MCF-7)		
<b>2c</b>		1.05 (KB)		
<b>3</b>	Synthesis	0.47 (CNE)	Mitochondrial dysfunction	[106]
<b>4</b>	Synthesis	3.57 (MGC-803)	Mitochondrial dysfunction	[108]
<b>5a</b>	Synthesis	25.7 (ECA109)	DNA binding	[109]
<b>5b</b>		9.56 (ECA109)		
<b>6</b>	Synthesis	22.6 (MCF-7)	DNA crosslinking	[110]
(R)- <b>7</b>	Synthesis	24.0 (MCF-7)	DNA crosslinking	[111]
(S)- <b>7</b>		112 (MCF-7)		
<b>8</b>	Synthesis	4.59 (A549)	Promoting cell cycle arrest	[112]
<b>9</b>	Synthesis	1.00 (-)	Topoisomerase IIα inhibition	[114]
<b>10</b>	Synthesis	0.46 (MDA-MB-231)	Apoptosis induction	[115]
<b>11a</b>	Synthesis	27.16 (SMMC-7721)	-	[116]
<b>11b</b>		24.9 (A549)		
<b>11c</b>		6.14 (SMMC-7721)		
<b>11d</b>		14.02 (SMMC-7721)		
<b>12</b>	Synthesis	20.0 (UACC-62)	-	[117]

Table 3. Cont.

Xanthone Derivative	Source	IC <sub>50</sub> (μM) (Cancer Cells)	Main Mechanism	Ref.
13	Synthesis	37.8 (WiDr)	Suppressing mRNA COX-2 expression	[127]
14	Synthesis	5.21 (P388)	Raf-1 and c-JNK inhibition	[124]
15a	Synthesis	6.34 (P388)	c-KIT inhibition	[129]
15b		10.7 (P388)		
16	Isolation	274 (BT-549)	bcr/abl gene expression inhibition	[130]
17	Synthesis	0.19 (NCI-H460)	Promoting cell cycle arrest	[133]
18	Synthesis	0.19 (NCI-H460)	-	[12]
19	Isolation	1.58 (WiDr)	-	[134]
20	Isolation	0.74 (HeLa)	Apoptosis induction	[136]
21	Isolation	6.11 (KB)	-	[140]
22	Isolation	0.005 (T17)	Apoptosis induction	[153]
23	Isolation	40.6 (A2780)	-	[154]
24		8.10 (A2780)		
25	Synthesis	7.00 (HL-60)	Apoptosis induction	[157]
26	Isolation	5.90 (LNCaP)	Apoptosis induction	[158]
27	Isolation	68.5 (HT-29)	Apoptosis induction	[170]
28	Synthesis	5.17 (HTC116)	Topoisomerase inhibition	[171]
29	Isolation	2.80 (HL-60)	Caspase activation and PG-E2 inhibition	[172]
30		3.40 (HL-60)		
31		3.10 (HL-60)		
32	Synthesis	4.50 (MDA-MB-231)	-	[173]
33	Synthesis	2.10 (A549)	Protein kinase inhibition	[174]
34	Synthesis	3.25 (HepG2)	-	[175]
35	Isolation	0.73 (CNE-2)	Antiproliferative induction	[176]
36		8.61 (NCI/ADR-RES)		
37	Isolation	1.30 (HL-60)	Antiproliferative induction	[178]
38	Isolation	3.35 (CNE-1)	Apoptosis induction	[67]
39	Isolation	0.87 (HL-60)	-	[179]
40		4.66 (PC-3)		
41	Synthesis	18.6 (HepG2)	Caspase activation	[18]
42	Synthesis	1.90 (K562)	-	[157]
43	Synthesis	3.90 (MDA-MB-468)	-	[182]
44	Synthesis	3.60 (A375-C5)	Apoptosis induction	[183]
45	Synthesis	>165 (HT-29)	-	[184]

A molecular docking study of xanthone and thioxanthone derivatives against platelet-derived growth factor response (PDGFR) and epidermal growth factor receptor (EGFR) protein kinases has been evaluated in our previous study. It was found that hydroxyxanthones with halogen substituents gave stronger binding energies (−6.87 to −7.25 kcal/mol) than erlotinib (−6.58 kcal/mol) against EGFR protein. However, they gave weaker binding energies (−7.92 to −8.57 kcal/mol) than imatinib (−13.4 kcal/mol) against PDGFR protein. A similar hydrogen bond of Met769 with erlotinib was also found on the hydroxyxanthones

with halogen substituents. Furthermore, the hydroxyxanthenes with halogen substituents gave an additional hydrogen bond with Thr766; consequently, they gave stronger binding energy than imatinib against EGFR protein. Meanwhile, a similar hydrogen bond with Cys673 of imatinib was also found on the hydroxyxanthenes with halogen substituents. However, the hydrogen bond between imatinib with Asp810 was not found in the hydroxyxanthenes with halogen substituents; thus, it may be the reason why they gave weaker binding energy than imatinib against PDGFR protein [185]. On the other hand, the molecular docking study of xanthyl chalcone derivatives has also been conducted against KIT tyrosine kinases. The inhibition of KIT protein kinases led to inhibiting cell growth and proliferation of signal transduction on small cell lung cancer, gastrointestinal stromal, and myeloid leukemia cancer cells. The xanthyl xanthone derivatives gave stronger binding energies ( $-8.79$  to  $-10.9$  kcal/mol) as well as lower inhibition constants (10–364 nM) than sunitinib ( $-8.25$  kcal/mol; 890 nM), due to the presence of hydrogen bonds with Lys593 and Cys673 amino acid residues [186].



**Figure 12.** Summary of the most promising anticancer agents based on xanthone derivatives in this review.

Rational design on the structure and anticancer activity of xanthone derivatives has been reported; however, a comprehensive and holistic point of view is still very limited. For example, it was reported that the hydroxyl group at C-1 position of xanthone was critical for the anticancer activity against MCF-7 [117]. The 1-hydroxyxanthone derivative was 6 times more active in the anticancer activity than xanthone with the absence of 1-hydroxyl substituent. On the other hand, it was reported that 1,3-diacetyl groups gave stronger anticancer activity against MCF-7 cells [105]. The introduction of the prenyl group to the 1-hydroxyxanthone was also able to dramatically increase its anticancer activity against MCF-7 cell line [34]. Azevedo et al. stated that diethylamino at C-8 position together with 2,2-dimethyl-3,4-dihydropyran moiety were critical for the anticancer activity of xanthone against MCF-7 cells. On the other hand, the presence of electron-withdrawing group on 1,3-dihydroxyxanthone enhanced anticancer activity [187]. These results are confusing,

since each researcher reported based on a limited number of anticancer activities of the isolated and/or synthesized xanthone derivatives.

Quantitative structure–activity relationship (QSAR) is a computational approach to rationalize the relationship between the chemical structure of drugs with their biological activity [188]. A QSAR study on the anticancer activity of 33 haloxanthenes against HepG2 and MCF-7 cells was performed in our previous study. Haloxanthenes gave anticancer activity against both cancer cells, due to the activation of c-JNK protein through hydrogen bond interactions with Met111 and Gln109, as well as halogen interactions with Met108 and Asp112. From the QSAR analysis, it was found that  $IC_{50}$  of haloxanthenes against HepG2 cancer cells can be predicted through  $\log(IC_{50}) = -1.198(qC7) + 9.274(qC8b) - 1.887(qC8) - 23.35(qO \text{ carbonyl}) - 6.034$  ( $R^2 = 0.94$ ), where  $qX$  represented the charge of atom X. On the other hand, it was found that  $IC_{50}$  of haloxanthenes against MCF-7 cancer cells can be predicted through  $\log(IC_{50}) = 100(LUMO) + 0.36(DM) - 3.02(qC6) - 1.71(qC4) - 7.98(qC1) + 7.85$  ( $R^2 = 0.89$ ), whereas LUMO and DM represent the lowest unoccupied molecular orbital and dipole moment, respectively [189]. A QSAR study of xanthone derivatives as topoisomerase II $\alpha$  inhibitors was reported by Alam and Khan in 2014. It was found that  $IC_{50}$  of xanthenes as topoisomerase II $\alpha$  inhibitors can be predicted through  $pIC_{50} = 2.19(DE) + 0.22(n(OH)) - 0.54(LogP) - 0.469(SIB) + 0.018(SSA) + 2.57$  ( $R^2 = 0.84$ ), whereas DE,  $n(OH)$ , LogP, SIB, and SSA represent dielectric energy, the group count of hydroxyl substituents, logarithm of the partition coefficient between *n*-octanol and water, shape index basic (order 3), and solvent-accessible surface area, respectively [190].

A more comprehensive QSAR study on the anticancer activity of xanthone derivatives was investigated by Alam and Khan in 2018 [191]. They evaluated the anticancer activity of more than one hundred xanthone derivatives from *Garcinia* species and built QSAR mathematic models. They reported that the  $IC_{50}$  value of xanthone derivatives against A549 cancer cell line can be predicted through  $\log(IC_{50}) = -39.0090(x1) - 0.8078(x2) - 1.0827(x3) - 0.0483(x4) + 0.5053(x5) - 0.0560$  ( $R^2 = 0.87$ ), whereas  $x1$  is a parameter of electronegativity contribution,  $x2$  is the atom type count descriptor class,  $x3$  is the number of carbon atoms connected with four single bonds,  $x4$  is the number of C=C bonds, and  $x5$  is the electrotopological state of methyl group. Meanwhile, the  $IC_{50}$  value of xanthone derivatives against HepG2 cancer cell line can be predicted through  $\log IC_{50} = -0.6407(y1) - 0.0336(y2) - 0.1278(y3) + 0.2226(y4) + 0.5877(y5) + 0.5940$  ( $R^2 = 0.87$ ), whereas  $y1$  is electrotopological state of carbon atoms,  $y2$  is the number of double bonds,  $y3$  is the number of hydrogen bond acceptor atoms,  $y4$  is electrotopological state of methine group, and  $y5$  is the number of oxygen atoms. On the other hand, the  $IC_{50}$  value of xanthone derivatives against U251 cancer cell line can be predicted through  $\log IC_{50} (\mu M) = 0.0948(z1) + 0.5217(z2) + 0.3687(z3) + 1.1313$  ( $R^2 = 0.86$ ), whereas  $z1$  is the electrotopological state of nitrogen atoms,  $z2$  is the number of oxygen atoms, and  $z3$  is the topological state of carbon atoms. However, a more comprehensive QSAR study involving all reported xanthone derivatives against a certain cancer cell is not available yet, as of today. Therefore, computational studies on this research are still open to be investigated by researchers in the future.

## 2.6. In Vivo and Clinical Anticancer Assays of Xanthone Derivatives

The xanthone derivatives showed promising in vitro anticancer activity; thus, further investigation through in vivo and then clinical assays is required [168]. The in vivo test of  $\alpha$ -mangostin revealed the potential usage of  $\alpha$ -mangostin as chemotherapeutic and chemopreventive agents, since it could suppress tumor formation in nude mice induced 22Rv1 cell lines. Oral administration of  $\alpha$ -mangostin was able to reduce the growth of 22Rv1 cells by more than 5 times compared to the negative control (without any oral administration of  $\alpha$ -mangostin), due to the activation of the caspase-3 protein [158]. It was also reported that oral  $\alpha$ -mangostin consumption reduced growth by 50–70% and reduced 40% of the mass of NL-17 cancer cells in the mice by suppressing the cell proliferation and activation of apoptotic mechanisms [192]. A similar result for the oral administration

of  $\alpha$ -mangostin was also reported to be effective for COLO-205 and HCT-116 cells [193]. Meanwhile, intraperitoneal injection of  $\alpha$ -mangostin on the mice inhibited 50% of the growth of GBM8401 due to the increment of adenosine monophosphate-activated protein kinase (AMPK) protein thus triggering the autophagy of cancer cells [194]. On the other hand,  $\gamma$ -mangostin was reported for its ability for HT-29 cells through mitochondrial collapse and apoptosis pathways [170]. An in vivo investigation on mice through oral administration of  $\gamma$ -mangostin was conducted. After 1.5 h, the  $\gamma$ -mangostin compound was mostly found in the blood plasma of mice [130].

It was reported that panaxanthone (a mixture of  $\alpha$ -mangostin and  $\gamma$ -mangostin in 6:1 wt/wt) inhibited the DNA replication and induced the G1 phase cell cycle arrest of cancer cells [195]. Subcutaneous injection of panaxanthone significantly inhibited the metastatic growth of BJMC3879 cancer cells in the mice. The inhibitory activity was related to the activation of caspase-3 and caspase-9 proteins, with a loss of cytochrome c from the mitochondria causing the collapse of the mitochondria membrane potential of cancer cells [196]. On the other hand, subcutaneous injection xanthone extract from *Garcinia mangostana* fruit rinds containing 81% of  $\alpha$ -mangostin and 16% of  $\gamma$ -mangostin significantly reduced the tumor volume of HCT-116 on mice. The inhibitory activity was related to the induction of apoptosis and inhibition of cancer cells migration, invasion, and clonogenicity [197].

A clinical study for mangosteen juice (containing 3.90 g/L of  $\alpha$ -mangostin) to the human group (20 people) was conducted [198]. It was found that maximum  $\alpha$ -mangostin concentration was up to 3.10  $\mu\text{g/L}$ , while the time to maximum plasma concentration ( $T_{\text{max}}$ ) was found to be at 1 h, with a decrement to 65% after 4 h. A similar result was reported in China for maximum  $\alpha$ -mangostin concentration (4.20  $\mu\text{g/L}$ ) and  $T_{\text{max}}$  (1 h) value in the human group (20 people) [199]. In 2012, Chitchumroonchokchai and coworkers reported the clinical study of mangosteen juice (containing 1.22 g/L of  $\alpha$ -mangostin) to the human group (10 people) with a high-fat breakfast. It was found that the maximum  $\alpha$ -mangostin concentration was up to 0.45  $\mu\text{g/L}$ , while the  $T_{\text{max}}$  value was found to be at 2–4 h on average [200]. Faster distribution of  $\alpha$ -mangostin can be achieved through intravenous administration. It was reported that, after intravenous injection, the  $\alpha$ -mangostin was metabolized to form in its hydrogenated, oxidized, glucuronidated, and methylated forms [201].

Detailed anticancer investigation on DMXAA has also been reported. The DMXAA leads to vascular collapse and tumor necrosis through tumor necrosis factor- $\alpha$  induction. Synergistic anticancer activity with chemotherapy agents such as doxorubicin, imatinib, erlotinib, and sunitinib, as well as with the cancer radiotherapy technique has been reported. DMXAA exhibited low toxicity to the normal cells with suitable pharmacokinetic parameters. Furthermore, the clinical trials of DMXAA as the anticancer agent have been evaluated in New Zealand and the United Kingdom. The phase I clinical trial of DMXAA to 63 patients gave no drug-related myelosuppression. The DMXAA was well tolerated up to 4900  $\text{mg/m}^2$  dose. At a higher dose, the DMXAA gave the side effects of visual disturbance, tremors, confusion, slurred speech, and anxiety [202]. Unfortunately, the DMXAA only gives strict species-specificity to the mouse stimulator of interferon genes (STING), with no significant activity against human STING in phase III clinical trial. Researchers are doing their best to modify the chemical structure of DMXAA, to obtain more active anticancer agents such as in alkylated-, alkoxyated-, fluorinated-, hydrazonated-, cyclic-, and heterocyclic substituted-derivatives [203]. However, no significant improvement in anticancer activity has been achieved yet.

As an isostere of xanthone, thioxanthenes have similar structures and physicochemical properties to xanthone derivatives [204]. Nowadays, dozens of thioxanthone derivatives are under investigation for a possible application as anticancer agents [99,205]. Hycanthone and lucanthone are anticancer drug candidates based on thioxanthone structure [206]. Their anticancer activity was related to the topoisomerase inhibition and DNA intercalation mechanisms. However, their clinical trials were stopped due to their mutagenic effect.

Other potential anticancer agents based on thioxanthenes are SR233377 and SSR271425. However, their clinical trials were also withdrawn due to their cardiotoxic effect [207–209]. The chemical structures of DMXAA, hycanthone, lucanthone, SR233377, and SSR271425 are shown in Figure 13.

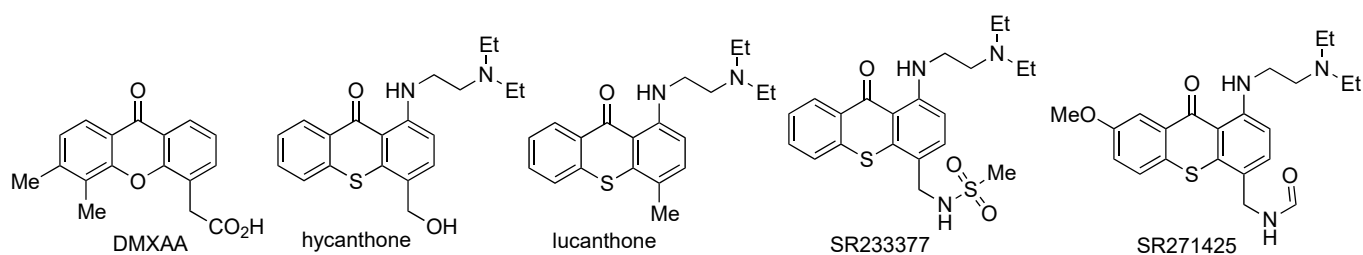


**Figure 13.** Evaluated xanthone derivatives as the anticancer agents through in vitro assay.

The most serious drawbacks for the utilization of xanthone derivatives as the anticancer agent are their poor solubility in water and their reactivity to be transformed into phase 2 conjugates form. Therefore, further technologies are critical to overcome these limitations [210,211]. It was reported that the coating of gambogic acid in the form of nanoparticles core shell dramatically increased its anticancer activity against HepG2 and A549 cancer cells due to the intracellular drug delivery process [212]. To overcome the poor solubility of thioxanthone, Yilmaz et al. prepared polymeric thioxanthone materials and evaluated their anticancer activity against A549 cells in the radiotherapy process. Radiotherapy is sometimes used to enhance the activity of anticancer agents through ionizing radiation. It was reported that ionizing radiation acts as a sensitizer to enhance the inhibition of cancer cells proliferation. The thioxanthone derivative was connected to polyvinyl alcohol and polyethylene glycol materials through covalent bonds. Two types of polymer materials were prepared: thioxanthone-polyethylene glycol through C-N amide bond, and thioxanthone-polyvinyl alcohol through C-O acetal bond. The thioxanthone-polyvinyl alcohol did not decrease the A549 cell viability percentage at 0.03 mg/mL. In contrast, thioxanthone-polyethylene glycol decreased the A549 cell viability percentage to 70% at the same concentration. It means that thioxanthone-polyethylene glycol gave a higher anticancer activity against A549 cancer cells than thioxanthone-polyvinyl alcohol. Radiating the thioxanthone-polyethylene glycol material with 2.5 Gy exposure drastically decreased the A549 cell viability percentage to 30%. This research offers an option for the usage of low solubility xanthone and/or thioxanthone derivatives for in vivo and clinical uses [213]. In contrast to the reports on the clinical study of  $\alpha$ -mangostin and DMXAA that are available now, the reports on both in vivo and clinical study of other xanthone derivatives are very limited. Therefore, extensive efforts are still needed for the development of the anticancer drug for our better health and future.

### 3. Conclusions and Future Direction

This review highlights the potential anticancer of xanthone derivatives, contributing to the design and develop of new drugs. Both isolated and synthesized xanthone derivatives have been proven to have promising anticancer activities against breast, hepatoma, cervix, colorectal, ovarian, lung, gastric, leukemia, skin, epidermoid nasopharynx, prostate, neuron, brain glioblastoma, and other cancer cells through in vitro assay. However, their further evaluation as anticancer agents through in vivo and clinical assays is still limited as of today. Furthermore, a comprehensive QSAR study for the better design of anticancer drugs based on the xanthone structure has not yet been established. These research gaps require extensive collaborations and contributions from researchers around the world to further develop active, selective, and efficient anticancer drugs based on xanthone derivatives.

**Author Contributions:** Conceptualization, J. and Y.S.K.; Writing—original draft preparation, Y.S.K., K.T.A.P. and J.; writing—review and editing, J., H.D.P., E.N.S., A.K.Z., H.A.F. and J.J. All authors have read and agreed to the published version of the manuscript.

**Funding:** The financial support from KEMENDIKBUD-RISTEK The Republic of Indonesia through the World Class Research grant 2021–2023 with contract number 4492/UN1/DITLIT/DIT-LIT/PT/2021 is greatly acknowledged.

**Institutional Review Board Statement:** Not applicable.

**Informed Consent Statement:** Not applicable.

**Data Availability Statement:** Data sharing not applicable.

**Conflicts of Interest:** The authors declare no conflict of interest.

## References

- Hassanpour, S.H.; Dehghani, M. Review of cancer from perspective of molecular. *J. Cancer Res. Pract.* **2017**, *4*, 127–129. [CrossRef]
- Kotecha, R.; Takami, A.; Espinoza, J.L. Dietary phytochemicals and cancer chemoprevention: A review of the clinical evidence. *Oncotarget* **2016**, *7*, 52517–52529. [CrossRef]
- Siegel, R.L.; Miller, K.D.; Jemal, A. Cancer statistics, 2020. *CA Cancer J. Clin.* **2020**, *70*, 7–30. [CrossRef]
- Siegel, R.L.; Miller, K.D.; Jemal, A. Cancer statistics, 2021. *CA Cancer J. Clin.* **2021**, *71*, 7–33. [CrossRef]
- Blackadar, C.B. Historical review of the causes of cancer. *World J. Clin. Oncol.* **2016**, *7*, 54–86. [CrossRef] [PubMed]
- Carugo, A.; Draetta, G.F. Academic discovery of anticancer drugs: Historic and future perspectives. *Annu. Rev. Cancer Biol.* **2019**, *3*, 385–408. [CrossRef]
- Olgen, S. Overview on anticancer drug design and development. *Curr. Med. Chem.* **2018**, *25*, 1704–1719. [CrossRef]
- Buyel, J.F. Plants as sources of natural and recombinant anti-cancer agents. *Biotech. Adv.* **2018**, *36*, 506–520. [CrossRef] [PubMed]
- Falzone, L.; Salomone, S.; Libra, M. Evolution of cancer pharmacological treatments at the turn of the third millenium. *Front. Pharmacol.* **2018**, *9*, 1300. [CrossRef]
- Resende, D.I.S.P.; Pereira-Terra, P.; Moreira, J.; Freitas-Silva, J.; Lemos, A.; Gales, L.; Pinto, E.; De Sousa, M.E.; Da Costa, P.M.; Pinto, M.M.M. Synthesis of a small library of nature-inspired xanthenes and study of their antimicrobial activity. *Molecules* **2020**, *25*, 2405. [CrossRef] [PubMed]
- Ren, Y.; de Blanco, E.J.C.; Fuchs, J.R.; Soejarto, D.D.; Burdette, J.E.; Swanson, S.M.; Kinghorn, A.D. Potential anticancer agents characterized from selected tropical plants. *J. Nat. Prod.* **2019**, *82*, 657–679. [CrossRef]
- Alves, A.; Correia-da-Silva, M.; Nunes, C.; Campos, J.; Sousa, E.; Silva, P.M.A.; Bousbaa, H.; Rodrigues, F.; Ferreira, D.; Costa, P.C.; et al. Discovery of a new xanthone against glioma: Synthesis and development of (pro)liposome formulations. *Molecules* **2019**, *24*, 409. [CrossRef] [PubMed]
- Chukaew, A.; Saithong, S.; Chusri, S.; Limsuwan, S.; Watanapokasin, R.; Voravuthikunchai, S.P.; Chakthong, S. Cytotoxic xanthenes from the roots of *Mesua ferrea* L. *Phytochemistry* **2019**, *157*, 64–70. [CrossRef]
- Lemos, A.; Gomes, A.S.; Loureiro, J.B.; Brandao, P.; Palmeira, A.; Pinto, M.M.M.; Saraiva, L.; Sousa, M.E. Synthesis, biological evaluation, and in silico studies of novel aminated xanthenes as potential p53-activating agents. *Molecules* **2019**, *24*, 1975. [CrossRef]
- Raksat, A.; Maneerat, W.; Andersen, R.J.; Pyne, S.G.; Laphookhieo, S. A tocotrienol quinone dimer and xanthenes from the leaf extract of *Garcinia nigrolineata*. *Fitoterapia* **2019**, *136*, 104175. [CrossRef] [PubMed]
- Zhang, B.J.; Fu, W.-W.; Wu, R.; Yang, J.-L.; Yao, C.-Y.; Yan, B.-X.; Tan, H.-S.; Zheng, C.-W.; Song, Z.-J.; Xu, H.-X. Bioactive scalemic caged xanthenes from the leaves of *Garcinia bracteata*. *Bioorg. Chem.* **2019**, *82*, 274–283. [CrossRef] [PubMed]
- Zhang, H.; Zheng, D.; Ding, Z.J.; Lao, Y.Z.; Tan, H.S.; Xu, H.X. UPLC-PDA-QTOFMS-guided isolation of prenylated xanthenes and benzoylphloroglucinols from the leaves of *Garcinia oblongifolia* and their migration-inhibitory activity. *Sci. Rep.* **2016**, *6*, 35789. [CrossRef] [PubMed]
- Liu, J.; Bao, H.; Wang, H.; Luo, Q.; Zuo, J.; Liu, Z.; Qiu, S.; Sun, X.; Liu, X. Synthesis of xanthone derivatives and anti-hepatocellular carcinoma potency evaluation: Induced apoptosis. *RSC Adv.* **2019**, *9*, 40781–40791. [CrossRef]
- Na, Y. Recent cancer drug development with xanthone structures. *J. Pharm. Pharmacol.* **2009**, *61*, 707–712. [CrossRef] [PubMed]
- Roberts, J.C. Naturally occurring xanthenes. *Chem. Rev.* **1961**, *61*, 591–605. [CrossRef]
- Pinto, M.M.M.; Palmeira, A.; Fernandes, C.; Resende, D.I.S.P.; Sousa, E.; Cidade, H.; Tiritan, M.E.; da Silva, M.C.; Cravo, S. From natural products to new synthetic small molecules: A journey through the world of xanthenes. *Molecules* **2021**, *26*, 431. [CrossRef] [PubMed]
- Shagufta, S.; Ahmad, I. Recent insight into the biological activities of synthetic xanthone derivatives. *Eur. J. Med. Chem.* **2016**, *116*, 267–280. [CrossRef] [PubMed]
- Araújo, J.; Fernandes, C.; Pinto, M.; Tiritan, M.E. Chiral derivatives of xanthenes with antimicrobial activity. *Molecules* **2019**, *24*, 314. [CrossRef]



24. Santos, C.M.M.; Freitas, M.; Fernandes, E. A comprehensive review on xanthone derivatives as  $\alpha$ -glucosidase inhibitor. *Eur. J. Med. Chem.* **2018**, *157*, 1460–1479. [CrossRef]
25. Salman, Z.; Yu-Qing, J.; Bin, L.; Cai-Yun, P.; Iqbal, C.M.; Atta-ur, R.; Wei, W. Antioxidant nature adds further therapeutic value: An updated review on natural xanthenes and their glycosides. *Digit. Chin. Med.* **2019**, *2*, 166–192. [CrossRef]
26. Cruz, M.I.; Cidade, H.; Pinto, M. Dual/multitargeted xanthone derivatives for Alzheimer's disease: Where do we stand? *Future Med. Chem.* **2017**, *9*, 1611–1630. [CrossRef]
27. Gunter, N.V.; Teh, S.S.; Lim, Y.M.; Mah, S.H. Natural xanthenes and skin inflammatory disease: Multitargeting mechanisms of action and potential application. *Front. Pharmacol.* **2020**, *11*, 594202. [CrossRef]
28. Feng, Z.; Lu, X.; Gan, L.; Zhang, Q.; Lin, L. Xanthenes, a promising anti-inflammatory scaffold: Structure, activity, and drug likeness analysis. *Molecules* **2020**, *25*, 598. [CrossRef]
29. Rosa, G.P.; Palmeira, A.; Resende, D.I.S.P.; Almeida, I.F.; Kane-Pagès, A.; Barreto, M.C.; Sousa, E.; Pinto, M.M.M. Xanthenes for melanogenesis inhibition: Molecular docking and QSAR studies to understand their anti-tyrosinase activity. *Bioorg. Med. Chem.* **2021**, *29*, 115873. [CrossRef]
30. Yu, F.-C.; Lin, X.-R.; Liu, Z.-C.; Zhang, J.-H.; Liu, F.-F.; Wu, W.; Ma, Y.-L.; Qu, W.-W.; Yan, S.-J.; Lin, J. Beyond the antagonism: Self-labeled xanthone inhibitors as modeled “two-in-one” drugs in cancer therapy. *ACS Omega* **2017**, *2*, 873–889. [CrossRef]
31. Huang, Q.; Wang, Y.; Wu, H.; Yuan, M.; Zheng, C.; Xu, H. Xanthone glucosides: Isolation, bioactivity and synthesis. *Molecules* **2021**, *26*, 5575. [CrossRef]
32. Zhang, B.J.; Fu, W.-W.; Wu, R.; Yang, J.-L.; Yao, C.-Y.; Yan, B.-X.; Tan, H.-S.; Zheng, C.-W.; Song, Z.-J.; Xu, H.-X. Cytotoxic prenylated xanthenes from the leaves of *Garcinia bracteata*. *Planta Med.* **2019**, *85*, 444–452. [CrossRef]
33. Markowicz, J.; Uram, L.; Sobich, J.; Mangiardi, L.; Maj, P.; Rode, W. Antitumor and anti-nematode activities of  $\alpha$ -mangostin. *Eur. J. Pharmacol.* **2019**, *863*, 172678. [CrossRef] [PubMed]
34. Castanheiro, R.A.P.; Silva, A.M.S.; Campos, N.A.N.; Nascimento, M.S.J.; Pinto, M.M.M. Antitumor activity of some prenylated xanthenes. *Pharmaceuticals* **2009**, *2*, 33–43. [CrossRef]
35. Bedi, P.; Gupta, R.; Pramanik, T. Synthesis and biological properties of pharmaceutically important xanthenes and benzoxanthone analogs: A brief review. *Asian J. Pharm. Clin. Res.* **2018**, *11*, 12–20. [CrossRef]
36. Klein-Junior, L.C.; Campos, A.; Niero, R.; Correa, R.; Heyden, Y.V.; Filho, V.C. Xanthenes and cancer: From natural sources to mechanisms of action. *Chem. Biodivers.* **2020**, *17*, e1900499. [CrossRef]
37. Ibrahim, M.Y.; Hashim, N.M.; Mariod, A.A.; Mohan, S.; Abdulla, M.A.; Abdelwahab, S.I.; Arbab, I.A.  $\alpha$ -Mangostin from *Garcinia mangostana* Linn: An updated review of its pharmacological properties. *Arab. J. Chem.* **2016**, *9*, 317–329. [CrossRef]
38. Pinto, M.M.M.; Castanheiro, R.A.P.; Kijjoa, A. Xanthenes from marine-derived microorganism: Isolation, structure elucidation, and biological activities. In *Encyclopedia of Analytical Chemistry: Applications, Theory and Instrumentation*; Meyers, R.A., Ed.; John Wiley & Sons: Hoboken, NJ, USA, 2014; pp. 12–17. [CrossRef]
39. Arends, P.; Helboe, P. Xanthone studies. IV. Hydroxyl proton chemical shifts in the structural investigation of xanthenes. *Acta Chem. Scand.* **1972**, *26*, 4180–4182. [CrossRef]
40. Ohtani, I.; Kusumi, T.; Kashman, Y.; Kakisawa, H. High-field FT NMR application of Mosher's method. the absolute configurations of marine terpenoids. *J. Am. Chem. Soc.* **1991**, *113*, 4092–4096. [CrossRef]
41. Fernandes, C.; Carraro, M.L.; Ribeiro, J.; Araujo, J.; Tiritan, M.E.; Pinto, M.M.M. Synthetic chiral derivatives of xanthenes: Biological activities and enantioselectivity studies. *Molecules* **2019**, *24*, 791. [CrossRef]
42. Sukandar, E.R.; Kaennakam, S.; Rassamee, K.; Ersam, T.; Siripong, P.; Tip-pyang, S. Tetrandraxanthenes A–I, prenylated and geranylated xanthenes from the stem bark of *Garcinia tetrandra*. *J. Nat. Prod.* **2019**, *82*, 1312–1318. [CrossRef]
43. Sukandar, E.R.; Kaennakam, S.; Rassamee, K.; Siripong, P.; Fatmawati, S.; Ersam, T.; Tip-pyang, S. Xanthenes and biphenyls from the stems of *Garcinia cylindrocarpa* and their cytotoxicity. *Fitoterapia* **2018**, *130*, 112–117. [CrossRef]
44. Yang, H.X.; Li, W.; Li, Q.; Ai, H.-L.; Li, Z.-H.; Huang, R.; Feng, T.; Liu, J.-K. Piperidine alkaloids and xanthone from the roots of *Caulophyllum robustum* Maxim. *Fitoterapia* **2019**, *132*, 22–25. [CrossRef]
45. Meechai, I.I.; Phupong, W.; Chunglok, W.; Meepowpan, P. Dihydroosajaxanthone: A new natural xanthone from the branches of *Garcinia schomburgkiana* Pierre. *Iran J. Pharm. Res.* **2018**, *17*, 1347–1352.
46. He, K.; Fan, L.-L.; Wu, T.-T.; Du, J. A new xanthone glycoside from *Pyrrosia shearerii*. *Nat. Prod. Res.* **2019**, *33*, 2982–2987. [CrossRef] [PubMed]
47. Ishaque, M.; Bibi, Y.; Qayyum, A.; Iriti, M. Isolation and structural confirmation of xanthone isomers from *Dryopteris ramosa* (Hope) C. Chr. and their in vitro antioxidant mechanism. *Arab. J. Sci. Eng.* **2021**, *46*, 5327–5337. [CrossRef]
48. Tanjung, M.; Tjahjandarie, T.S.; Saputri, R.D.; Kurnia, B.D.; Rachman, M.F.; Syah, Y.M. Calotetrapterins A-C, three new pyranoxanthenes and their cytotoxicity from the stem bark of *Calophyllum tetrapterum* Miq. *Nat. Prod. Res.* **2021**, *35*, 407–412. [CrossRef] [PubMed]
49. Tanaka, N.; Kashiwada, Y. Characteristic metabolites of Hypericum plants: Their chemical structures and biological activities. *J. Nat. Med.* **2021**, *75*, 423–433. [CrossRef] [PubMed]
50. Umoh, Y.F.; Thomas, P.S.; Essien, E.E.; Okokon, J.E.; Leo, M.D.; Ajibesin, K.K.; Flamini, G.; Eseyin, O.A. Isolation and characterization of bioactive xanthenes from *Hippocratea africana* (Willd.)Loes.ex Engl. (Celastraceae). *J. Ethnopharmacol.* **2021**, *280*, 114031. [CrossRef] [PubMed]

51. Jo, Y.H.; Kim, S.B.; Ahn, J.H.; Turk, A.; Kown, E.-B.; Kim, M.-O.; Hwang, B.Y.; Lee, M.K. Xanthenes from the stems of *Cudrania tricuspidata* and their inhibitory effects on pancreatic lipase and fat accumulation. *Bioorg. Chem.* **2019**, *92*, 103234. [CrossRef]
52. Tang, Y.X.; Fu, W.-W.; Xi, Z.-C.; Yang, J.-L.; Zheng, C.-W.; Lu, Y.; Shen, Z.-W.; Xu, H.-X. Xanthone derivatives from the leaves of *Garcinia oligantha*. *Eur. J. Med. Chem.* **2019**, *181*, 111536. [CrossRef]
53. Kurniawan, Y.S.; Fahmi, M.R.G.; Yuliati, L. Isolation and optical properties of natural pigments from purple mangosteen peels. *IOP Conf. Ser.* **2020**, *833*, 012018. [CrossRef]
54. Birch, A.J.; Baldas, J.; Hlubucek, J.R.; Simpson, T.J.; Westerman, P.W. Biosynthesis of the fungal xanthone ravenelin. *J. Chem. Soc. Perkin Trans. I* **1976**, *8*, 898–904. [CrossRef]
55. Fujita, M.; Inoue, T. New hypocholesterolemic abietamide derivatives. structure-activity relationship. *Chem. Pharm. Bull.* **1980**, *28*, 453–458. [CrossRef]
56. Anantachoke, N.; Tuchinda, P.; Kuhakarn, C.; Pohmakotr, M.; Reutrakul, V. Prenylated caged xanthenes: Chemistry and biology. *Pharm. Biol.* **2012**, *50*, 78–91. [CrossRef] [PubMed]
57. Kumla, D.; Dethoup, T.; Gales, L.; Pereira, J.A.; Freitas-Silva, J.; Costa, P.M.; Silva, A.M.S.; Pinto, M.M.M.; Kijjoa, A. Erubescensoic Acid, a new polyketide and a xanthonopyrone SPF-3059-26 from the culture of the marine sponge-associated fungus *penicillium erubescens* KUFA 0220 and Antibacterial activity evaluation of some of its constituents. *Molecules* **2019**, *24*, 208. [CrossRef]
58. Loureiro, D.R.P.; Soares, J.X.; Costa, J.C.; Magalhães, Á.F.; Azevedo, C.M.G.; Pinto, M.M.M.; Afonso, C.M.M. Structures, activities and drug-likeness of anti-infective xanthone derivatives isolated from the marine environment: A review. *Molecules* **2019**, *24*, 243. [CrossRef]
59. Fouche, G.; Cragg, G.M.; Pillay, P.; Kolesnikova, N.; Maharaj, V.J.; Senabe, J. In vitro anticancer screening of South African plants. *J. Ethnopharmacol.* **2008**, *119*, 455–461. [CrossRef] [PubMed]
60. Malmström, J.; Christophersen, C.; Barrero, A.F.; Oltra, J.E.; Justicia, J.; Rosales, A. Bioactive metabolites from a marine-derived strain of the fungus *Emericella variegata*. *J. Nat. Prod.* **2002**, *65*, 364–367. [CrossRef]
61. Shao, C.; Wang, C.; Wei, M.; Gu, Y.; She, Z.; Lin, Y. Structure elucidation of two new xanthone derivatives from the marine fungus *Penicillium* sp. (ZZF 32#) from South China Sea. *Magn. Reson. Chem.* **2008**, *46*, 1066–1069. [CrossRef]
62. Lee, Y.M.; Li, H.; Hong, J.; Cho, H.Y.; Bae, K.S.; Kim, M.A.; Kim, D.-K.; Jung, J.H. Bioactive metabolites from the sponge-derived fungus *Aspergillus versicolor*. *Arch. Pharm. Res.* **2010**, *33*, 231–235. [CrossRef]
63. Huang, Z.; Yang, R.; Guo, Z.; She, Z.; Lin, Y. A new xanthone derivative from mangrove endophytic fungus No. ZSU-H16. *Chem. Nat. Compd.* **2010**, *46*, 348–351. [CrossRef]
64. Xu, J. Biomolecules produced by mangrove-associated microbes. *Curr. Med. Chem.* **2011**, *18*, 5224–5266. [CrossRef]
65. Tang, Y.X.; Fu, W.W.; Wu, R.; Tan, H.S.; Shen, Z.W.; Xu, H.X. Bioassay-guided isolation of prenylated xanthone derivatives from the leaves of *Garcinia oligantha*. *J. Nat. Prod.* **2016**, *79*, 1752–1761. [CrossRef]
66. Yang, R.; Li, P.; Li, N.; Zhang, Q.; Bai, X.; Wang, L.; Xiao, Y.; Sun, L.; Yang, Q.; Yan, J. Xanthenes from the pericarp of *Garcinia mangostana*. *Molecules* **2017**, *22*, 683. [CrossRef] [PubMed]
67. Wei, L.K.; Zamakshshari, N.H.; Ee, G.C.L.; Mah, S.H.; Nor, S.M.M. Isolation and structural modifications of ananixanthone from *Calophyllum teysmannii* and their cytotoxic activities. *Nat. Prod. Res.* **2018**, *32*, 2147–2151. [CrossRef]
68. Kaennakam, S.; Mudsing, K.; Rassamee, K.; Siripong, P.; Tip-pyang, S. Two new xanthenes and cytotoxicity from the bark of *Garcinia schomburgkiana*. *J. Nat. Med.* **2019**, *73*, 257–261. [CrossRef]
69. Zamakshshari, N.H.; Ee, G.C.L.; Ismail, I.S.; Ibrahim, Z.; Mah, S.H. Cytotoxic xanthenes isolated from *Calophyllum depressinervosum* and *Calophyllum buxifolium* with antioxidant and cytotoxic activities. *Food Chem. Toxicol.* **2019**, *133*, 110800. [CrossRef] [PubMed]
70. Oanh, V.T.K.; Thoa, H.T.; Hang, N.T.M.; Phuong, D.T.L.; Lien, N.T.P.; Popova, M.; Trusheva, B.; Bankova, V.; Le, T.N. New dihydrochromene and xanthone derivatives from *Lisotrigona furva* propolis. *Fitoterapia* **2021**, *149*, 104821. [CrossRef]
71. Wang, Y.J.; Ma, N.; Liu, C.-Y.; Feng, Y.-X.; Zhang, F.-X.; Li, C.; Pei, Y.-H. Xanthenes and anthraquinones from the soil fungus *Penicillium* sp. DWS10-P-6. *RSC Adv.* **2021**, *11*, 3162–3167. [CrossRef]
72. Kostanecki, S.V.; Nessler, B. Synthesen von oxyxanthenen. *Ber. Dtsch. Chem. Ges.* **1891**, *24*, 1894–1897. [CrossRef]
73. Grover, P.K.; Shah, G.D.; Shah, R.C. Xanthenes. Part IV. A new synthesis of hydroxyxanthenes and hydroxybenzophenones. *J. Chem. Soc.* **1955**, 3982–3985. [CrossRef]
74. Sousa, M.E.; Pinto, M.M.M. Synthesis of xanthenes: An overview. *Curr. Med. Chem.* **2005**, *12*, 2447–2479. [CrossRef]
75. Liu, G.; Wu, C.; Chen, B.; He, R.; Chen, C. Concise synthesis of xanthenes by the tandem etherification: Acylation of diaryliodonium salts with salicylates. *Chin. Chem. Lett.* **2018**, *29*, 985–988. [CrossRef]
76. Atwell, G.J.; Yang, S.; Denny, W.A. An improved synthesis of 5,6-dimethylxanthenone-4-acetic acid (DMXAA). *Eur. J. Med. Chem.* **2002**, *37*, 825–828. [CrossRef]
77. Otrubova, K.; Fitzgerald, A.E.; Mani, N.S. A novel entry to xanthenes by an intramolecular Diels-Alder reaction involving 2-(1,2-dichlorovinyl)oxyaryldienones. *Tetrahedron* **2018**, *74*, 5715–5724. [CrossRef]
78. Nagarajan, S.; Arjun, P.; Raaman, N.; Das, T.M. Regioselective facile one-pot Friedländer synthesis of sugar-based heterocyclic biomolecules. *Carbohydr. Res.* **2010**, *345*, 1988–1997. [CrossRef] [PubMed]
79. Kurniawan, Y.S.; Priyanga, K.T.A.; Krisbiantoro, P.A.; Imawan, A.C. Green chemistry influences in organic synthesis: A Review. *J. Multidiscipl. Appl. Nat. Sci.* **2021**, *1*, 1–12. [CrossRef]

80. Zhang, X.J.; Yang, L.; Wu, Y.J.; Du, J.Y.; Mao, Y.L.; Wang, X.; Luan, S.J.; Lei, Y.H.; Li, X.; Sun, H.P.; et al. Microwave-assisted transition-metal-free intramolecular Ullmann-type *O*-arylation in water for the synthesis of xanthenes and azaxanthenes. *Tetrahedron Lett.* **2014**, *55*, 4883–4887. [CrossRef]
81. Genovese, S.; Fiorito, S.; Specchiulli, M.C.; Taddeo, V.A.; Epifano, F. Microwave-assisted synthesis of xanthenes promoted by ytterbium triflate. *Tetrahedron Lett.* **2015**, *56*, 847–850. [CrossRef]
82. Shen, C.R.; Wu, X.F. Selective preparation of xanthenes from 2-bromofluorobenzenes and salicylaldehydes via palladium-catalyzed acylation-SNAr approach. *Synlett* **2016**, *27*, 1269–1273. [CrossRef]
83. Liang, Y.E.; Barve, B.D.; Kuo, Y.-H.; Fang, H.-W.; Kuo, T.-S.; Li, W.-T. Metal-free, DBU-mediated, microwave assisted synthesis of benzo[*c*]xanthenes by tandem reactions of alkynyl-1,3-diketones. *Adv. Synth. Catal.* **2021**, *363*, 505–511. [CrossRef]
84. Steingruber, H.S.; Mendioroz, P.; Diez, A.S.; Gerbino, D.C. A green nanopalladium-supported catalyst for the microwave-assisted direct synthesis of xanthenes. *Synthesis* **2020**, *52*, 619–628. [CrossRef]
85. Fu, Y.; Fan, B.; Chen, H.; Huang, H.; Hu, Y. Promiscuous enzyme-catalyzed cascade reaction: Synthesis of xanthone derivatives. *Bioorg. Chem.* **2018**, *80*, 555–559. [CrossRef]
86. Zhao, L.Z.; Xie, F.C.; Cheng, G. A base-promoted tandem reaction of 3-(1-alkynyl)chromones with 1,3-dicarbonyl compounds: An efficient approach to functional xanthenes. *Ang. Chem. Int.* **2009**, *48*, 6520–6523. [CrossRef] [PubMed]
87. Bornadiego, A.; Diaz, J.; Marcos, C.F. Expedious multicomponent synthesis of xanthone dimers. *Proceedings* **2019**, *9*, 13. [CrossRef]
88. Loureiro, D.R.P.; Soares, J.X.; Maia, A.; Silva, A.M.N.; Rangel, M.; Azevedo, C.M.G.; Hansen, S.V.; Ulven, T.; Pinto, M.M.M.; Reis, S.; et al. One-pot synthesis of xanthone by carbonylative Suzuki coupling reaction. *ChemistrySelect* **2021**, *6*, 4511–4514. [CrossRef]
89. Resende, D.I.S.P.; Duraes, F.; Maia, M.; Sousa, E.; Pinto, M.M.M. Recent advances in the synthesis of xanthenes and azaxanthenes. *Org. Chem. Front.* **2020**, *7*, 3027–3066. [CrossRef]
90. Loureiro, D.R.P.; Magalhães, Á.F.; Soares, J.X.; Pinto, J.; Azevedo, C.M.G.; Vieira, S.; Henriques, A.; Ferreira, H.; Neves, N.; Bousbaa, H.; et al. Yicathins B and C and analogues: Total synthesis, lipophilicity and biological activities. *ChemMedChem* **2020**, *15*, 749–755. [CrossRef]
91. Xu, D.; Nie, Y.; Liang, X.; Ji, L.; Hu, S.; You, Q.; Wang, F.; Ye, H.; Wang, J. A concise and efficient total synthesis of  $\alpha$ -mangostin and  $\beta$ -mangostin from *Garcinia mangostana*. *Nat. Prod. Commun.* **2013**, *8*, 1101–1103. [CrossRef]
92. Wei, X.; Liang, D.; Wang, Q.; Meng, X.; Li, Z. Total synthesis of mangiferin, homomangiferin, and neomangiferin. *Org. Biomol. Chem.* **2016**, *14*, 8821–8831. [CrossRef] [PubMed]
93. Ito, S.; Kitamura, T.; Arulmozhiraja, S.; Manabe, K.; Tokiwa, H.; Suzuki, Y. Total synthesis of Termicalcicolanone A via organocatalysis and regioselective Claisen rearrangement. *Org. Lett.* **2019**, *21*, 2777–2781. [CrossRef]
94. Finetti, F.; Travelli, C.; Ercoli, J.; Colombo, G.; Buoso, E.; Trabalzini, L. Prostaglandin E2 and cancer: Insight into tumor progression and immunity. *Biology* **2020**, *9*, 434. [CrossRef] [PubMed]
95. Sun, R.R.; Miao, F.-P.; Zhang, J.; Wang, G.; Yin, X.-L.; Ji, N.-Y. Three new xanthone derivatives from an algicolous isolate of *Aspergillus wentii*. *Magn. Reson. Chem.* **2013**, *51*, 65–68. [CrossRef]
96. Park, A.; Lee, Y.; Kim, M.S.; Kang, Y.J.; Park, Y.J.; Jung, H.; Kim, T.D.; Lee, H.G.; Choi, I.; Yoon, S.R. Prostaglandin E2 secreted by thyroid cancer cells contributes to immune escape through the suppression of natural killer (NK) cell cytotoxicity and NK cell differentiation. *Front. Immunol.* **2018**, *9*, 1859. [CrossRef]
97. Su, X.; Li, Q. Prostaglandin EP2 receptor: Novel therapeutic target for human cancers. *Int. J. Mol. Med.* **2018**, *42*, 1203–1214. [CrossRef]
98. Forterre, P.; Gribaldo, S.; Gabelle, D.; Serre, M.C. Origin and evolution of DNA topoisomerases. *Biochimie* **2007**, *89*, 427–446. [CrossRef] [PubMed]
99. Silva, V.; Gil-Martins, E.; Silva, B.; Rocha-Pereira, C.; Sousa, M.E.; Remião, F.; Silva, R. Xanthenes as P-glycoprotein modulators and their impact on drug bioavailability. *Expert Opin. Drug Metab. Toxicol.* **2021**, *17*, 441–482. [CrossRef] [PubMed]
100. Kim, Y.; Chen, J. Molecular structure of human P-glycoprotein in the ATP-bound, outward-facing conformation. *Science* **2018**, *359*, 915–919. [CrossRef]
101. Koulgi, S.; Jani, V.; Uppuladinne, V.N.; Sonavane, U.; Joshi, R. Natural plant products as potential inhibitors of RNA dependent RNA polymerase of severe acute respiratory syndrome coronavirus-2. *PLoS ONE* **2021**, *16*, e0251801. [CrossRef]
102. Woo, S.; Jung, J.; Lee, C.; Kwon, Y.; Na, Y. Synthesis of new xanthone analogues and their biological activity test—cytotoxicity, topoisomerase II inhibition, and DNA cross-linking study. *Bioorg. Med. Chem. Lett.* **2007**, *17*, 1163–1166. [CrossRef] [PubMed]
103. Woo, S.; Kang, D.; Nam, J.M.; Lee, C.S.; Ha, E.-M.; Lee, E.-S.; Kwon, Y.; Na, Y. Synthesis and pharmacological evaluation of new methyloxiranylmethoxyxanthone analogues. *Eur. J. Med. Chem.* **2010**, *45*, 4221–4228. [CrossRef] [PubMed]
104. Jun, K.Y.; Lee, E.-Y.; Jung, M.-J.; Lee, O.-H.; Lee, E.-S.; Choo, H.-Y.P.; Na, Y.; Kwon, Y. Synthesis, biological evaluation, and molecular docking study of 3-(3'-heteroatom substituted-2'-hydroxy-1'-propyloxy)xanthone analogues as novel topoisomerase IIa catalytic inhibitor. *Eur. J. Med. Chem.* **2011**, *46*, 1964–1971. [CrossRef]
105. Varache-Lembège, M.; Moreau, S.; Larrouture, S.; Montaudon, D.; Robert, J.; Nuhlich, A. Synthesis and antiproliferative activity of aryl- and heteroaryl-hydrazones derived from xanthone carbaldehydes. *Eur. J. Med. Chem.* **2008**, *43*, 1336–1343. [CrossRef]
106. Luo, L.; Qin, J.K.; Dai, Z.-K.; Gao, S.-H. Synthesis and biological evaluation of novel benzo[*b*]xanthone derivatives as potential antitumor agents. *J. Serb Chem. Soc.* **2013**, *78*, 1301–1308. [CrossRef]

107. Sypniewski, D.; Szkaradek, N.; Loch, T.; Waszkielewicz, A.M.; Gunia-Krzyzak, A.; Matczynska, D.; Soltysik, D.; Marona, H.; Bednarek, I. Contribution of reactive oxygen species to the anticancer activity of aminoalkanol derivatives of xanthone. *Investig. New Drugs* **2018**, *36*, 355–369. [CrossRef] [PubMed]
108. Yang, Z.M.; Huang, J.; Qin, J.-K.; Dai, Z.-K.; Lan, W.-L.; Su, G.-F.; Tang, H.; Yang, F. Design, synthesis and biological evaluation of novel 1-hydroxyl-3-aminoalkoxy xanthone derivatives as potent anticancer agents. *Eur. J. Med. Chem.* **2014**, *85*, 487–497. [CrossRef]
109. Shen, R.; Wang, W.; Yang, G. DNA binding property and antitumor evaluation of xanthone with dimethylamine side chain. *J. Fluoresc.* **2014**, *24*, 959–966. [CrossRef] [PubMed]
110. Fernandes, C.; Masawang, K.; Tiritan, M.E.; Sousa, E.; de Lima, V.; Afonso, C.; Bousbaa, H.; Sudprasert, W.; Petro, M.; Pinto, M.M. New chiral derivatives of xanthenes: Synthesis and investigation of enantioselectivity as inhibitors of growth of human tumor cell lines. *Bioorg. Med. Chem.* **2014**, *22*, 1049–1062. [CrossRef]
111. Carraro, M.L.; Marques, S.; Silva, A.S.; Freitas, B.; Silva, P.M.A.; Pedrosa, J.; De Marco, P.; Bousbaa, H.; Fernandes, C.; Tiritan, M.E.; et al. Synthesis of new chiral derivatives of xanthenes with enantioselective effect on tumor cell growth and DNA crosslinking. *ChemistrySelect* **2020**, *5*, 10285–10291. [CrossRef]
112. Liu, C.; Zhang, M.; Zhang, Z.; Zhang, S.B.; Yang, S.; Zhang, A.; Yin, L.; Swarts, S.; Vidyasagar, S.; Zhang, L.; et al. Synthesis and anticancer potential of novel xanthone derivatives with 3,6-substituted chains. *Bioorg. Med. Chem.* **2016**, *24*, 4263–4271. [CrossRef] [PubMed]
113. Dai, M.; Yuan, X.; Kang, J.; Zhu, Z.-J.; Yue, R.-C.; Hu, Y.; Chen, B.-Y.; Zhang, W.-D.; Liu, R.-H.; Sun, Q.-Y. Synthesis and biological evaluation of phenyl substituted polyoxygenated xanthone derivatives as anti-hepatoma agents. *Eur. J. Med. Chem.* **2013**, *69*, 159–166. [CrossRef] [PubMed]
114. Minniti, E.; Byl, J.A.W.; Riccardi, L.; Sissi, C.; Rosini, M.; Vivo, M.D.; Minarini, A.; Osheroff, N. Novel xanthone-polyamine conjugates as catalytic inhibitors of human topoisomerase II $\alpha$ . *Bioorg. Med. Chem. Lett.* **2017**, *27*, 4687–4693. [CrossRef]
115. Liu, J.; Zhang, J.; Wang, H.; Liu, Z.; Zhang, C.; Jiang, Z.; Chen, H. Synthesis of xanthone derivatives and studies on the inhibition against cancer cells growth and synergistic combinations of them. *Eur. J. Med. Chem.* **2017**, *133*, 50–61. [CrossRef] [PubMed]
116. Zhou, B.-D.; Zeng, L.-L.; Tong, Y.-G.; Fang, J.-Y.; Ruan, Z.-P.; Zeng, X.-Y.; Fang, Y.-Y.; Xu, G.-F.; Hu, D.-B. Synthesis and antitumor, antityrosinase, and antioxidant activities of xanthone. *J. Asian Nat. Prod. Res.* **2018**, *20*, 467–476. [CrossRef]
117. Pedro, M.; Cerqueira, F.; Sousa, M.E.; Nascimento, M.S.J.; Pinto, M. Xanthenes as inhibitors of growth of human cancer cell lines and their effects on the proliferation of human lymphocytes in vitro. *Bioorg. Med. Chem.* **2002**, *10*, 3725–3730. [CrossRef]
118. Amanatie, A.; Jumina, J.; Mustofa, M.; Hanafi, M.; Armunanto, R. QSAR study of xanthone derivatives as antiplasmodial agents. *Indones. J. Chem.* **2010**, *10*, 357–362. [CrossRef]
119. Amanatie, A.; Jumina, J.; Mustofa, M.; Hanafi, M.; Kadidae, L.O.; Sahidin, I. Synthesis of 2-hydroxyxanthone from xanthone as a basic material for new antimalarial drugs. *Asian J. Pharm. Clin. Res.* **2017**, *10*, 242–246. [CrossRef]
120. Fitriastuti, D.; Jumina, J.; Priatmoko, P. Heme polymerization inhibition activity (HPIA) assay of synthesized xanthone derivative as antimalarial compound. *AIP Conf. Proc.* **2017**, *1823*, 020120. [CrossRef]
121. Fitriastuti, D.; Jumina, J.; Priatmoko, P. Synthesis and characterization of 2,3,4-trihydroxy-5-methyl xanthone as antimalarial compound. *EKSAKTA J. Sci. Data Anal.* **2016**, *16*, 94–102. [CrossRef]
122. Miladiyah, I.; Tahir, I.; Jumina, J.; Mubarika, S.; Mustofa, M. Quantitative structure-activity relationship analysis of xanthone derivatives as cytotoxic agents in liver cancer cell line HepG2. *Molekul* **2016**, *11*, 143–157. [CrossRef]
123. Yuanita, E.; Pranowo, H.D.; Jumina, J.; Mustofa, M. Design of hydroxy xanthenes derivatives as anticancer using quantitative structure-activity relationship. *Asian J. Pharm. Clin. Res.* **2016**, *9*, 180–185.
124. Yuanita, E.; Pranowo, H.D.; Mustofa, M.; Swasono, R.T.; Syahri, J.; Jumina, J. Synthesis, characterization and molecular docking of chloro-substituted hydroxyxanthone derivatives. *Chem. J. Mold.* **2019**, *14*, 68–76. [CrossRef]
125. Yuanita, E.; Pranowo, H.D.; Siswanta, D.; Swasono, R.T.; Mustofa, M.; Zulkarnain, A.K.; Syahri, J.; Jumina, J. One-pot synthesis, antioxidant activity and toxicity evaluation of some hydroxyxanthenes. *Chem. Chem. Technol.* **2018**, *12*, 290–295. [CrossRef]
126. Zakiah, M.; Syarif, R.A.; Mustofa, M.; Jumina, J.; Fatmasari, N.; Sholikhah, E.N. In vitro antiplasmodial, heme polymerization, and cytotoxicity of hydroxyxanthone derivatives. *J. Trop. Med.* **2021**, *2021*, 8866681. [CrossRef]
127. Miladiyah, I.; Jumina, J.; Haryana, S.M.; Mustofa, M. Biological activity, quantitative structure-activity relationship analysis, and molecular docking of xanthone derivatives as anticancer drugs. *Drug Des. Dev. Ther.* **2018**, *12*, 149–158. [CrossRef]
128. Miladiyah, I.; Yuanita, E.; Nuryadi, S.; Jumina, J.; Haryana, S.M.; Mustofa, M. Synergistic effect of 1,3,6-trihydroxy-4,5,7-trichloroxanthone in combination with doxorubicin on b-cell lymphoma cells and its mechanism of action through molecular docking. *Curr. Ther. Res.* **2020**, *92*, 100576. [CrossRef]
129. Yuanita, E.; Ulfa, M.; Sudirman, S.; Sumarlan, I.; Sudarma, I.M.; Dharmayani, N.K.T.; Syahri, J.; Jumina, J. Synthesis, cytotoxic evaluation and molecular docking of bromo-substituted 1,3,6-trihydroxyxanthone as protein tyrosine kinase inhibitor. *Malays. J. Chem.* **2021**, *23*, 24–32.
130. Li, H.; Huang, J.; Yang, B.; Xiang, T.; Yin, X.; Peng, W.; Cheng, W.; Wan, J.; Luo, F.; Li, H.; et al. Mangiferin exerts antitumor activity in breast cancer cells by regulating matrix metalloproteinases, epithelial to mesenchymal transition, and  $\beta$ -catenin signaling pathway. *Toxicol. Appl. Pharmacol.* **2013**, *272*, 180–190. [CrossRef]
131. Gold-Smith, F.; Fernandez, A.; Bishop, K. Mangiferin and cancer: Mechanisms of action. *Nutrients* **2016**, *8*, 396. [CrossRef] [PubMed]

132. Selles, D.J.N.; Daglia, M.; Rastrelli, L. The potential role of mangiferin in cancer treatment through its immunomodulatory, anti-angiogenic, apoptotic, and gene regulatory effects. *Biofactors* **2016**, *42*, 475–491. [CrossRef] [PubMed]
133. Song, G.; Li, S.-M.; Si, H.-Z.; Li, Y.-B.; Li, Y.-S.; Fan, J.-H.; Liang, Q.-Q.; He, H.-B.; Ye, H.-M.; Cui, Z.-N. Synthesis and bioactivity of novel xanthone and thioxanthone l-rhamnopyranosides. *RSC Adv.* **2015**, *5*, 36092–36103. [CrossRef]
134. Sordat-Diserens, I.; Hamburger, M.; Rogers, C.; Hostettmann, K. Dimeric xanthones from *Garcinia livingstonei*. *Phytochemistry* **1992**, *31*, 3589–3593. [CrossRef]
135. Heald, R.A.; Dexheimer, T.S.; Vankayalapati, H.; Siddiqui-Jain, A.; Szabo, L.Z.; Gleason-Guzman, M.C.; Hurley, L.H. Conformationally restricted analogues of psorospermin: Design, synthesis, and bioactivity of natural-product-related bisfuranoxanthones. *J. Med. Chem.* **2005**, *48*, 2993–3004. [CrossRef] [PubMed]
136. Han, Q.; Yang, L.; Liu, Y.; Wang, Y.; Qiao, C.; Song, J.; Xu, L.; Yang, D.; Chen, S.; Xu, H. Gambogic acid and epigambogic acid, C-2 epimers with novel anticancer effects from *Garcinia hanburyi*. *Planta Med.* **2006**, *72*, 281–284. [CrossRef]
137. Asano, J.; Chiba, K.; Tada, M.; Yoshii, T. Cytotoxic xanthones from *Garcinia hanburyi*. *Phytochemistry* **1996**, *41*, 815–820. [CrossRef]
138. Laphookhieo, S.; Syers, J.K.; Kiattansakul, R.; Chantrapromma, K. Cytotoxic and antimalarial prenylated xanthones from *Cratoxylum cochinchinense*. *Chem. Pharm. Bull.* **2006**, *54*, 745–747. [CrossRef]
139. Suksamrarn, S.; Komutiban, O.; Ratananukul, P.; Chimnoi, N.; Lartpornmatulee, N.; Suksamrarn, A. Cytotoxic prenylated xanthones from the young fruit of *Garcinia mangostana*. *Chem. Pharm. Bull.* **2006**, *54*, 301–305. [CrossRef] [PubMed]
140. Li, I.V.; Wang, Q.; Wang, X.; Li, G.; Shen, S.; Wei, X. Gambogic acid exhibits anti-metastatic activity on malignant melanoma mainly through inhibition of PI3K/Akt and ERK signaling pathways. *Eur. J. Pharmacol.* **2019**, *864*, 172719. [CrossRef]
141. Wan, L.; Zhang, Q.; Wang, S.; Gao, Y.; Chen, X.; Zhao, Y.; Qian, X. Gambogic acid impairs tumor angiogenesis by targeting YAP/STAT3 signaling axis. *Phytother. Res.* **2019**, *33*, 1579–1591. [CrossRef]
142. Zhao, L.; Guo, Q.L.; You, Q.D.; Wu, Z.Q.; Gu, H.Y. Gambogic acid induces apoptosis and regulates expressions of bax and bcl-2 protein in human gastric carcinoma MGC-803 cells. *Biol. Pharm. Bull.* **2004**, *27*, 998–1003. [CrossRef]
143. Tao, S.J.; Guan, S.H.; Wang, W.; Lu, Z.Q.; Chen, G.T.; Sha, N.; Yue, Q.X.; Liu, X.; Guo, D.A. Cytotoxic polyprenylated xanthones from the resin of *Garcinia hanburyi*. *J. Nat. Prod.* **2009**, *72*, 117–124. [CrossRef]
144. Wang, J.; Liu, W.; Zhao, Q.; Qi, Q.; Lu, N.; Yang, Y.; Nei, F.F.; Rong, J.J.; You, Q.D.; Guo, Q.L. Synergistic effect of 5-fluorouracil with gambogic acid on BGC-823 human gastric carcinoma. *Toxicology* **2009**, *256*, 135–140. [CrossRef]
145. Yen, C.T.; Goto, K.N.; Hwang, T.-L.; Natschke, S.L.M.; Bastow, K.F.; Wu, Y.-C.; Lee, K.-H. Design and synthesis of gambogic acid analogs as potent cytotoxic and anti-inflammatory agents. *Bioorg. Med. Chem. Lett.* **2012**, *22*, 4018–4022. [CrossRef]
146. Khaing, E.I.; Saenpunya, T.; Kerdklai, P.; Pangpongma, S.; Vongvijit, S.; Phaechamud, T.; Intaraphairot, T. Combination effects of gambogic acid on imatinib mesylate cytotoxicity in colon cancer cells. *Key Eng. Mater.* **2020**, *859*, 27–33. [CrossRef]
147. Hahnvajanawong, C.; Boonyanugomol, W.; Nasomyon, T.; Loilome, W.; Namwat, N.; Anantachoke, N.; Tassaneeyakul, W.; Sripa, B.; Namwat, W.; Reutrakul, V. Apoptotic activity of caged xanthones from *Garcinia hanburyi* in cholangiocarcinoma cell lines. *World J. Gastroenterol.* **2010**, *16*, 2235–2243. [CrossRef]
148. Kasibhatla, S.; Jessen, K.A.; Maliartchouk, S.; Wang, J.Y.; English, N.M.; Drewe, J.; Qiu, L.; Archer, S.P.; Ponce, A.E.; Sirisoma, N.; et al. A role for transferrin receptor in triggering apoptosis when targeted with gambogic acid. *Proc. Natl. Acad. Sci. USA* **2005**, *102*, 12095–12100. [CrossRef] [PubMed]
149. Pandey, M.K.; Sung, B.; Ahn, K.S.; Kunnumakkara, A.B.; Chaturvedi, M.M.; Aggarwal, B.B. Gambogic acid, a novel ligand for transferrin receptor, potentiates TNF-induced apoptosis through modulation of the nuclear factor-kappaB signaling pathway. *Blood* **2007**, *110*, 3517–3525. [CrossRef]
150. Zhang, Q.G.; Li, C.P.; Chen, J.H.; Ouyang, J. Apoptosis-inducing effect of gambogic acid on K562 cells and its mechanism. *Zhongguo Shi Yan Xue Ye Xue Za Zhi* **2009**, *17*, 1443–1447. [PubMed]
151. Nie, F.; Zhang, X.; Qi, Q.; Yang, L.; Yang, Y.; Liu, W.; Lu, N.; Wu, Z.; You, Q.; Guo, Q. Reactive oxygen species accumulation contributes to gambogic acid-induced apoptosis in human hepatoma SMMC-7721 cells. *Toxicology* **2019**, *260*, 60–67. [CrossRef]
152. Tang, Q.; Lu, M.; Zhou, H.; Chen, D.; Liu, L. Gambogic acid inhibits the growth of ovarian cancer tumors by regulating p65 activity. *Oncol. Lett.* **2017**, *13*, 384–388. [CrossRef] [PubMed]
153. Jang, S.W.; Okada, M.; Sayeed, I.; Xiao, G.; Stein, D.; Jin, P.; Ye, K. Gambogic amide, a selective agonist for TrkA receptor that possesses robust neurotrophic activity, prevents neuronal cell death. *Proc. Natl. Acad. Sci. USA* **2007**, *104*, 16329–16334. [CrossRef]
154. Cao, S.; Brodie, P.J.; Miller, J.S.; Randrianaivo, R.; Ratovoson, F.; Birkinshaw, C.; Andriantsiferana, R.; Rasamison, V.E.; Kingston, D.G.I. Antiproliferative xanthones of *Terminalia calcicole* from the Madagascar rain forest. *J. Nat. Prod.* **2007**, *70*, 679–681. [CrossRef] [PubMed]
155. Kumar, D.; Sharma, P.; Singh, H.; Nepali, K.; Gupta, G.K.; Jain, S.K.; Ntie-Kang, F. The value of pyrans as anticancer scaffolds in medicinal chemistry. *RSC Adv.* **2017**, *7*, 36977. [CrossRef]
156. França, F.; Silva, P.M.A.; Soares, J.X.; Henriques, A.C.; Loureiro, D.R.P.; Azevedo, C.M.G.; Afonso, C.M.M.; Bousbaa, H. A pyranoxanthone as a potent antimetabolic and sensitizer of cancer cells to low doses of paclitaxel. *Molecules* **2020**, *25*, 5845. [CrossRef]
157. Palmeira, A.; Vasconcelos, M.H.; Paiva, A.; Fernandes, M.X.; Pinto, M.; Sousa, E. Dual inhibitors of P-glycoprotein and tumor cell growth: (re)discovering thioxanthones. *Biochem. Pharmacol.* **2012**, *83*, 57–68. [CrossRef]

158. Johnson, J.J.; Petiwala, S.M.; Syed, D.N.; Rasmussen, J.T.; Adhami, V.M.; Siddiqui, I.A.; Kohl, A.M.; Mukhtar, H.  $\alpha$ -Mangostin, a xanthone from mangosteen fruit, promotes cell cycle arrest in prostate cancer and decreases xenograft tumor growth. *Carcinogenesis* **2011**, *33*, 413–419. [CrossRef]
159. Kritsanawong, S.; Innajak, S.; Imoto, M.; Watanapokasin, R. Antiproliferative and apoptosis induction of  $\alpha$ -mangostin in T47D breast cancer cells. *Int. J. Oncol.* **2016**, *48*, 2155–2165. [CrossRef]
160. Moongkarndi, P.; Kosem, N.; Kaslungka, S.; Luanratana, O.; Pongpan, N.; Neungton, N. Antiproliferation, antioxidation and induction of apoptosis by *Garcinia mangostana* (mangosteen) on SKBR3 human breast cancer cell line. *J. Ethnopharmacol.* **2004**, *90*, 161–166. [CrossRef]
161. Matsumoto, K.; Akao, Y.; Yi, H.; Ohguchi, K.; Ito, T.; Tanaka, T.; Kobayashi, E.; Iinuma, M.; Nozawa, Y. Preferential target is mitochondria in  $\alpha$ -mangostin-induced apoptosis in human leukemia HL60 cells. *Bioorg. Med. Chem.* **2004**, *12*, 5799–5806. [CrossRef]
162. Matsumoto, K.; Akao, Y.; Ohguchi, K.; Ito, T.; Tanaka, T.; Iinuma, M.; Nozawa, Y. Xanthenes induce cell-cycle arrest and apoptosis in human colon cancer DLD-1 cells. *Bioorg. Med. Chem.* **2005**, *13*, 6064–6069. [CrossRef] [PubMed]
163. Ibrahim, M.Y.; Hashim, N.M.; Mohan, S.; Abdulla, M.A.; Abdelwahab, S.I.; Kamalidehghan, B.; Ghaderian, M.; Dehghan, F.; Ali, L.Z.; Karimian, H.; et al. Involvement of Nf-kB and HSP-70 signaling pathways in the apoptosis of MDA-MB-231 cells induced by a prenylated xanthone compound,  $\alpha$ -mangostin from *Cratoxylum arborescens*. *Drug Des. Dev. Ther.* **2014**, *8*, 2193–2211. [CrossRef]
164. Quang, T.H.; Ngan, N.T.T.; Yoon, C.-S.; Cho, K.-H.; Kang, D.G.; Lee, H.S.; Kim, Y.-C.; Oh, H. Protein tyrosine phosphatase 1B inhibitors from the root of *Cudrania tricuspidata*. *Molecules* **2015**, *20*, 11173–11183. [CrossRef]
165. Zhang, K.J.; Gu, Q.L.; Yang, K.; Ming, X.J.; Wang, J.X. Anticarcinogenic effects of  $\alpha$ -mangostin: A review. *Planta Med.* **2017**, *83*, 188–202. [CrossRef]
166. Khan, P.; Queen, A.; Smita, T.M.; Khan, N.S.; Hafeez, Z.B.; Hassan, M.I.; Ali, S. Identification of  $\alpha$ -mangostin as a potential inhibitor of microtubule affinity regulating kinase 4. *J. Nat. Prod.* **2019**, *82*, 2252–2261. [CrossRef]
167. Pérez-Rojas, J.M.; González-Macías, R.; González-Cortes, J.; Jurado, R.; Pedraza-Chaverri, J.; García-López, P. Synergic effect of  $\alpha$ -mangostin on the cytotoxicity of cisplatin in a cervical cancer model. *Oxid. Med. Cell. Longev.* **2016**, *2016*, 7981397. [CrossRef] [PubMed]
168. Azevedo, C.M.G.; Afonso, C.M.M.; Sousa, D.; Lima, R.T.; Helena Vasconcelos, M.; Pedro, M.; Barbosa, J.; Corrêa, A.G.; Reis, S.; Pinto, M.M.M. Multidimensional optimization of promising antitumor xanthone derivatives. *Bioorg. Med. Chem.* **2013**, *21*, 2941–2959. [CrossRef] [PubMed]
169. Fei, X.; Jo, M.; Lee, B.; Han, S.-B.; Lee, K.; Jung, J.-K.; Seo, S.-Y.; Kwak, Y.-S. Synthesis of xanthone derivatives based on  $\alpha$ -mangostin and their biological evaluation for anticancer agents. *Bioorg. Med. Chem. Lett.* **2014**, *24*, 2062–2065. [CrossRef]
170. Chang, H.F.; Yang, L.-L. Gamma-mangostin, a micronutrient of mangosteen fruit, induces apoptosis in human colon cancer cells. *Molecules* **2012**, *17*, 8010–8021. [CrossRef]
171. Cheng, P.; Zhu, L.; Guo, W.; Liu, W.; Yao, J.; Dong, G.; Zhang, Y.; Zhuang, C.; Sheng, C.; Miao, Z.; et al. Synthesis of novel benzoxanthone analogues as non-camptothecin topoisomerase I inhibitors. *J. Enzym. Inhib. Med. Chem.* **2011**, *27*, 437–442. [CrossRef]
172. Niu, S.L.; Li, Z.-L.; Ji, F.; Liu, G.-Y.; Zhao, N.; Liu, X.-Q.; Jing, Y.-K.; Hua, H.-M. Xanthenes from the stem bark of *Garcinia bracteata* with growth inhibitory effects against HL-60 cells. *Phytochemistry* **2012**, *77*, 280–286. [CrossRef] [PubMed]
173. Lim, C.K.; Tho, L.-Y.; Lim, Y.M.; Syed, A.A.S.; Weber, J.F.F. Synthesis of 1,3,6-trioxygenated prenylated xanthone derivatives as potential antitumor agents. *Lett. Org. Chem.* **2012**, *9*, 549–555. [CrossRef]
174. Zhang, X.; Li, X.; Sun, H.; Jiang, Z.; Tao, L.; Gao, Y.; Guo, Q.; You, Q. Synthesis and evaluation of novel aza-caged *Garcinia* xanthenes. *Org. Biomol. Chem.* **2012**, *10*, 3288. [CrossRef]
175. Zhang, X.; Li, X.; Sun, H.; Wang, X.; Zhao, L.; Gao, Y.; Liu, X.; Zhang, S.; Wang, Y.; Yang, Y.; et al. *Garcinia* xanthenes as orally active antitumor agents. *J. Med. Chem.* **2013**, *56*, 276–292. [CrossRef] [PubMed]
176. Xu, Z.; Huang, L.; Chen, X.-H.; Zhu, X.-F.; Qian, X.-J.; Feng, G.-K.; Lan, W.-J.; Li, H.-J. Cytotoxic prenylated xanthenes from the pericarps of *Garcinia mangostana*. *Molecules* **2014**, *19*, 1820–1827. [CrossRef]
177. Mariano, L.N.B.; Vendramini-Costa, D.B.; Ruiz, A.L.T.G.; de Carvalho, J.E.; Corrêa, R.; Filho, V.C.; Monache, F.D.; Niero, R. In vitro antiproliferative activity of uncommon xanthenes from branches of *Garcinia achachairu*. *Pharm. Biol.* **2015**, *54*, 1697–1704. [CrossRef] [PubMed]
178. Li, D.H.; Li, C.-X.; Jia, C.-C.; Sun, Y.-T.; Xue, C.-M.; Bai, J.; Hua, H.-M.; Liu, X.-Q.; Li, Z.-L. Xanthenes from *Garcinia paucinervis* with in vitro anti-proliferative activity against HL-60 cells. *Arch. Pharm. Res.* **2015**, *39*, 172–177. [CrossRef]
179. Jia, C.; Xue, J.; Gong, C.; Li, X.; Li, D.; Li, Z.; Hua, H. Chiral resolution and anticancer effect of xanthenes from *Garcinia paucinervis*. *Fitoterapia* **2018**, *127*, 220–225. [CrossRef]
180. Paiva, A.M.; Pinto, M.M.; Sousa, E. A century of thioxanthenes: Through synthesis and biological applications. *Curr. Med. Chem.* **2013**, *20*, 2438–2457. [CrossRef]
181. Almeida, J.R.; Palmeira, A.; Campos, A.; Cunha, I.; Freitas, M.; Felpeto, A.B.; Turkina, M.V.; Vasconcelos, V.; Pinto, M.; Correia-Dasilva, M.; et al. Structure-antifouling activity relationship and molecular targets of bio-inspired (thio)xanthenes. *Biomolecules* **2020**, *10*, 1126. [CrossRef]
182. Chen, C.L.; Chen, T.-C.; Lee, C.-C.; Shih, L.-C.; Lin, C.-Y.; Hsieh, Y.-Y.; Ali, A.A.A.; Huang, H.-S. Synthesis and evaluation of new 3-substituted-4-chloro-thioxanthone derivatives as potent anti-breast cancer agents. *Arab. J. Chem.* **2015**, *12*, 3503–3516. [CrossRef]

183. Barbosa, J.; Lima, R.; Sousa, D.; Gomes, A.; Palmeira, A.; Seca, H.; Choosang, K.; Pakkong, P.; Bousbaa, H.; Pinto, M.M.; et al. Screening a small library of xanthenes for antitumor activity and identification of a hit compound which induces apoptosis. *Molecules* **2016**, *21*, 81. [CrossRef]
184. Ataci, N.; Kazancioglu, E.O.; Kalindemirtas, F.D.; Kuruca, S.E.; Arsu, N. The interaction of light-activatable 2-thioxanthone thioacetic acid with ct-DNA and its cytotoxic activity: Novel theranostic agent. *Spectrochim. Acta A Mol. Biomol. Spectrosc.* **2020**, *239*, 118491. [CrossRef]
185. Hermawan, F.; Jumina, J.; Pranowo, H.D. Design of thioxanthone derivatives as potential tyrosine kinase inhibitor: A molecular docking study. *Rasayan J. Chem.* **2020**, *13*, 2626–2632. [CrossRef]
186. Iresha, M.R.; Jumina, J.; Pranowo, H.D. Molecular docking study of xanthyl chalcone derivatives as potential inhibitor agents against KIT tyrosine kinase and KIT kinase domain mutant D816H. *J. Appl. Pharm. Sci.* **2020**, *10*, 18–26. [CrossRef]
187. Azevedo, C.M.G.; Afonso, C.M.M.; Soares, J.X.; Reis, S.; Sousa, D.; Lima, R.T.; Vasconcelos, M.H.; Pedro, M.; Barbosa, J.; Gales, L.; et al. Pyranoxanthenes: Synthesis, growth inhibitory activity on human tumor cell lines and determination of their lipophilicity in two membrane models. *Eur. J. Med. Chem.* **2013**, *69*, 798–816. [CrossRef]
188. Chantarasriwong, C.; Milcarek, A.T.; Morales, T.H.; Settle, A.L.; Rezende, C.O., Jr.; Althufairi, B.D.; Theodoraki, M.A.; Alpaugh, M.L.; Theodorakis, E.A. Synthesis, structure-activity relationship and in vitro pharmacodynamics of A-ring modified caged xanthenes in a preclinical model of inflammatory breast cancer. *Eur. J. Med. Chem.* **2019**, *168*, 405–413. [CrossRef] [PubMed]
189. Sugara, T.H.; Jumina, J.; Sholikhah, E.N.; Pranowo, H.D. QSAR and molecular docking approaches for development of haloxanthenes as the anticancer agent against MCF-7 and HepG2. *Rasayan J. Chem.* **2021**, *14*, 1927–1937. [CrossRef]
190. Alam, S.; Khan, F. QSAR and docking studies on xanthone derivatives for anticancer activity targeting DNA topoisomerase II $\alpha$ . *Drug Des. Dev. Ther.* **2014**, *8*, 183–195. [CrossRef]
191. Alam, S.; Khan, F. Virtual screening, docking, ADMET and system pharmacology studies on Garcinia caged xanthone derivatives for anticancer activity. *Sci. Rep.* **2018**, *8*, 5524. [CrossRef]
192. Kosem, N.; Ichikawa, K.; Utsumi, H.; Moongkarndi, P. In vivo toxicity and antitumor activity of mangosteen extract. *J. Nat. Med.* **2013**, *67*, 255–263. [CrossRef]
193. Nabandith, V.; Suzui, M.; Morioka, T.; Kaneshiro, T.; Kinjo, T.; Matsumoto, K.; Akao, Y.; Iinuma, M.; Yoshimi, N. Inhibitory effects of crude  $\alpha$ -mangostin, a xanthone derivative, on two different categories of colon preneoplastic lesions induced by 1,2-dimethylhydrazine in the rat. *Asian Pac. J. Cancer Prev.* **2004**, *5*, 433–438. [PubMed]
194. Chao, A.C.; Hsu, Y.L.; Liu, C.K.; Kuo, P.L.  $\alpha$ -Mangostin, a dietary xanthone, induces autophagic cell death by activating the AMP-activated protein kinase pathway in glioblastoma cells. *J. Agric. Food Chem.* **2011**, *59*, 2086–2096. [CrossRef] [PubMed]
195. Doi, H.; Shibata, M.A.; Shibata, E.; Morimoto, J.; Akao, Y.; Iinuma, M.; Tanigawa, N.; Otsuki, Y. Panaxanthone isolated from pericarp of *Garcinia mangostana* L. suppresses tumor growth and metastasis of a mouse model of mammary cancer. *Anticancer Res.* **2009**, *29*, 2485–2495. [PubMed]
196. Shibata, M.; Iinuma, M.; Morimoto, J.; Kurose, H.; Akamatsu, K.; Okuno, Y.; Akao, Y.; Otsuki, Y.  $\alpha$ -Mangostin extracted from the pericarp of the mangosteen (*Garcinia mangostana* Linn.) reduces tumor growth and lymph node metastasis in an immunocompetent xenograft model of metastatic mammary cancer carrying a p53 mutation. *BMC Med.* **2011**, *9*, 69. [CrossRef]
197. Aisha, A.F.A.; Abu-Salah, K.M.; Ismail, Z.; Majid, A.M.S.A. In vitro and in vivo anti-colon cancer effects of *Garcinia mangostana* xanthenes extract. *BMC Complement. Altern. Med.* **2012**, *12*, 104. [CrossRef]
198. Kondo, M.; Zhang, L.; Ji, H.; Kou, Y.; Ou, B. Bioavailability and antioxidant effects of a xanthone-rich mangosteen (*Garcinia mangostana*) product in humans. *J. Agric. Food Chem.* **2009**, *57*, 8788–8792. [CrossRef]
199. Xie, G.; Sintara, M.; Chang, T.; Ou, B. Functional beverage of *Garcinia mangostana* (mangosteen) enhances plasma antioxidant capacity in healthy adults. *Food Sci. Nutr.* **2015**, *3*, 32–38. [CrossRef]
200. Chitchumroonchokchai, C.; Riedl, K.M.; Suksumrarn, S.; Clinton, S.K.; Kinghorn, D.A.; Failla, M.L. Bioavailability of xanthenes from mangosteen juice in healthy adults. *J. Nutr.* **2012**, *142*, 675–680. [CrossRef]
201. Han, S.Y.; You, B.H.; Kim, Y.C.; Chin, Y.-W.; Choi, Y.H. Dose-independent ADME properties and tentative identification of metabolites of  $\alpha$ -mangostin from *Garcinia mangostana* in mice by automated microsampling and UPLC-MS/MS methods. *PLoS ONE* **2015**, *10*, e0131587. [CrossRef]
202. Jameson, M.B.; Thompson, P.I.; Baguley, B.C.; Evans, B.D.; Harvey, V.J.; Porter, D.J.; McCrystal, M.R.; Small, M.; Bellenger, K.; Gumbrell, L.; et al. Clinical aspects of a phase I trial of 5,6-dimethylxanthenone-4-acetic acid (DMXAA), a novel antivascular agent. *Br. J. Cancer* **2003**, *88*, 1844–1850. [CrossRef] [PubMed]
203. Gobbi, S.; Belluti, F.; Rampa, A.; Bisi, A. Flavonoid-inspired vascular disrupting agents: Exploring flavone-8-acetic acid and derivatives in the new century. *Molecules* **2021**, *26*, 4228. [CrossRef] [PubMed]
204. Lima, R.T.; Sousa, D.; Gomes, A.S.; Mendes, N.; Matthiesen, R.; Pedro, M.; Marques, F.; Pinto, M.M.; Sousa, E.; Vasconcelos, M.H. The antitumor activity of a lead thioxanthone is associated with alterations in cholesterol localization. *Molecules* **2018**, *23*, 3301. [CrossRef]
205. Lopes, A.; Martins, E.; Silva, R.; Pinto, M.M.M.; Remião, F.; Sousa, E.; Fernandes, C. Chiral thioxanthenes as modulators of P-glycoprotein: Synthesis and enantioselectivity studies. *Molecules* **2018**, *23*, 626. [CrossRef]
206. Naidu, M.D.; Agarwal, R.; Pena, L.A.; Cunha, L.; Mezei, M.; Shen, M.; Wilson, D.M., III; Liu, Y.; Sanchez, Z.; Chaudhary, P.; et al. Lucanthone and its derivative hycanthone inhibit apurinic endonuclease-1 (APE1) by direct protein binding. *PLoS ONE* **2011**, *6*, e23679. [CrossRef] [PubMed]

207. Soria, J.C.; Dieras, V.; Girre, V.; Yovine, A.; Mialaret, K.; Armand, J.-P. QTc Monitoring during a phase I study: Experience with SR271425. *Am. J. Clin. Oncol.* **2007**, *30*, 106–112. [CrossRef]
208. Goncalves, P.H.; High, F.; Juniewicz, P.; Shackleton, G.; Li, J.; Boerner, S.; LoRusso, P.M. Phase I dose-escalation study of the thioxanthone SR271425 administered intravenously once every 3 weeks in patients with advanced malignancies. *Investig. New Drugs* **2008**, *26*, 347–354. [CrossRef]
209. LoRusso, P.M.; Foster, B.J.; Wozniak, A.; Heilbrun, L.K.; McCormick, J.I.; Ruble, P.E.; Graham, M.A.; Purvis, J.; Rake, J.; Drozd, M.; et al. Phase I pharmacokinetic study of the novel antitumor agent SR233377. *Clin. Cancer Res.* **2000**, *6*, 3088–3094.
210. Santos, A.; Soares, J.X.; Cravo, S.; Tiritan, M.E.; Reis, S.; Afonso, C.; Fernandes, C.; Pinto, M.M.M. Lipophilicity assessment in drug discovery: Experimental and theoretical methods applied to xanthone derivatives. *J. Chromatogr. B Anal. Technol. Biomed. Life Sci.* **2018**, *1072*, 182–192. [CrossRef] [PubMed]
211. Teixeira, M.; Pedro, M.; Nascimento, M.S.J.; Pinto, M.M.M.; Barbosa, C.M. Development and characterization of PLGA nanoparticles containing 1,3-dihydroxy-2-methylxanthone with improved antitumor activity on a human breast cancer cell line. *Pharm. Dev. Technol.* **2019**, *24*, 1104–1114. [CrossRef]
212. Liu, F.; Huang, X.; Han, L.; Sang, M.; Hu, L.; Liu, B.; Duan, B.; Jiang, P.; Wang, X.; Qiao, Z.; et al. Improved drugability of gambogic acid using core-shell nanoparticles. *Biomater. Sci.* **2019**, *7*, 1028–1042. [CrossRef] [PubMed]
213. Yilmaz, G.; Guler, E.; Barlas, F.B.; Timur, S.; Yagci, Y. Polymeric thioxanthenes as potential anticancer and radiotherapy agents. *Macromol. Rapid Commun.* **2016**, *37*, 1046–1051. [CrossRef] [PubMed]







## Article

# Inflammation as a Possible Trigger for Mitoxantrone-Induced Cardiotoxicity: An In Vivo Study in Adult and Infant Mice

Ana Reis-Mendes <sup>1,\*</sup>, José Luís Soares-Sousa <sup>1</sup>, Ana Isabel Padrão <sup>2</sup>, Margarida Duarte-Araújo <sup>3,4</sup>, José Alberto Duarte <sup>2,5</sup>, Vítor Seabra <sup>5</sup>, Salomé Gonçalves-Monteiro <sup>6,7</sup>, Fernando Remião <sup>1</sup>, Félix Carvalho <sup>1</sup>, Emília Sousa <sup>8,9</sup>, Maria Lourdes Bastos <sup>1</sup> and Vera Marisa Costa <sup>1,\*</sup>

- <sup>1</sup> UCIBIO, REQUIMTE, Laboratory of Toxicology, Department of Biological Sciences, Faculty of Pharmacy, University of Porto, 4050-313 Porto, Portugal; joseldsousa@gmail.com (J.L.D.-S.); remiao@ff.up.pt (F.R.); felixdc@ff.up.pt (F.C.); mlbastos@ff.up.pt (M.L.B.)
- <sup>2</sup> Research Center in Physical Activity, Health and Leisure (CIAFEL), Laboratory for Integrative and Translational Research in Population Health (ITR), Faculty of Sport, University of Porto, 4200-450 Porto, Portugal; apadrao@fade.up.pt (A.I.P.); jarduarte@fade.up.pt (J.A.D.)
- <sup>3</sup> LAQV/REQUIMTE, University of Porto, 4050-313 Porto, Portugal; mdcma@icbas.up.pt
- <sup>4</sup> Department of Immune-Physiology and Pharmacology, Institute of Biomedical Sciences Abel Salazar, University of Porto, 4050-313 Porto, Portugal
- <sup>5</sup> IINFACTS—Institute of Research and Advanced Training in Health Sciences and Technologies, University Institute of Health Sciences (IUCS), CESPU, 4585-116 Paredes, Portugal; vitor.seabra@iucs.cespu.pt
- <sup>6</sup> LAQV/REQUIMTE, Laboratory of Pharmacology, Department of Drug Sciences, Faculty of Pharmacy, University of Porto, 4050-313 Porto, Portugal; salomemonteiro8180@gmail.com
- <sup>7</sup> MOREHealth, Outcomes Research Lab, Portuguese Institute of Oncology at Porto Francisco Gentil (IPO Porto), 4200-072 Porto, Portugal
- <sup>8</sup> Laboratory of Organic and Pharmaceutical Chemistry, Chemistry Department, Faculty of Pharmacy, University of Porto, 4050-313 Porto, Portugal; esousa@ff.up.pt
- <sup>9</sup> CIMAR—Interdisciplinary Centre of Marine and Environmental Research, 4450-208 Porto, Portugal
- \* Correspondence: afreis.mendes@gmail.com (A.R.-M.); veramcosta@ff.up.pt (V.M.C.); Tel.: +351-220-428-599 (A.R.-M.); +351-220-428-599 (V.M.C.)

**Citation:** Reis-Mendes, A.; Soares-Sousa, J.L.; Padrão, A.I.; Duarte-Araújo, M.; Duarte, J.A.; Seabra, V.; Gonçalves-Monteiro, S.; Remião, F.; Carvalho, F.; Sousa, E.; et al. Inflammation as a Possible Trigger for Mitoxantrone-Induced Cardiotoxicity: An In Vivo Study in Adult and Infant Mice.

*Pharmaceuticals* **2021**, *14*, 510.  
<https://doi.org/10.3390/ph14060510>

Academic Editors: Mary J. Meegan and Niamh O'Boyle

Received: 12 April 2021  
Accepted: 21 May 2021  
Published: 26 May 2021

**Publisher's Note:** MDPI stays neutral with regard to jurisdictional claims in published maps and institutional affiliations.



**Copyright:** © 2021 by the authors. Licensee MDPI, Basel, Switzerland. This article is an open access article distributed under the terms and conditions of the Creative Commons Attribution (CC BY) license (<https://creativecommons.org/licenses/by/4.0/>).

**Abstract:** Mitoxantrone (MTX) is a pharmaceutical drug used in the treatment of several cancers and refractory multiple sclerosis (MS). Despite its therapeutic value, adverse effects may be severe, namely the frequently reported cardiotoxicity, whose mechanisms need further research. This work aimed to assess if inflammation or oxidative stress-related pathways participate in the cardiotoxicity of MTX, using the mouse as an animal model, at two different age periods (infant or adult mice) using two therapeutic relevant cumulative doses. Histopathology findings showed that MTX caused higher cardiac toxicity in adults. In MTX-treated adults, at the highest dose, noradrenaline cardiac levels decreased, whereas at the lowest cumulative dose, protein carbonylation increased and the expression of nuclear factor kappa B (NF- $\kappa$ B) p65 subunit and of M1 macrophage marker increased. Moreover, MTX-treated adult mice had enhanced expression of NF- $\kappa$ B p52 and tumour necrosis factor (TNF- $\alpha$ ), while decreasing interleukin-6 (IL-6). Moreover, while catalase expression significantly increased in both adult and infant mice treated with the lowest MTX cumulative dose, the expression of glyceraldehyde-3-phosphate dehydrogenase (GAPDH) and glutathione peroxidase only significantly increased in infant animals. Nevertheless, the ratio of GAPDH to ATP synthase subunit beta decreased in adult animals. In conclusion, clinically relevant doses of MTX caused dissimilar responses in adult and infant mice, being that inflammation may be an important trigger to MTX-induced cardiotoxicity.

**Keywords:** mitoxantrone; cardiotoxicity; inflammation; oxidative stress; age; cumulative dose

## 1. Introduction

Mitoxantrone (MTX) is a well-established anticancer agent used in metastatic breast cancer, acute myeloid leukaemia, non-Hodgkin's lymphoma, acute lymphoblastic leukaemia

in children, metastatic hormone-refractory prostate cancer, as well as in aggressive or refractory multiple sclerosis (MS) [1]. MTX inhibits DNA and RNA synthesis through DNA intercalation and topoisomerase-II inhibition [2]. MTX is used in MS because of its powerful immunosuppressive and immunomodulatory properties, abrogating T helper cell activity, enhancing T suppressor cell function, inhibiting B lymphocyte function, and macrophage proliferation. MTX also inhibits the synthesis of pro-inflammatory cytokines, namely interferon  $\gamma$  (IFN- $\gamma$ ), tumour necrosis factor (TNF- $\alpha$ ), interleukin-2 (IL-2), and overall antibody production [3,4].

Despite its clinical efficacy, MTX's high lipophilicity facilitates its distribution to healthy tissues and organs, namely to the heart, where it accumulates [5], which may lead to deleterious effects in this organ. In fact, MTX-induced cardiotoxicity is one of its most severe side effects and this can hamper its therapeutic use. MTX-induced cardiac side effects increase with the total cumulative dose, so MTX recommended maximum lifetime cumulative dose has been established at 140 mg/m<sup>2</sup> for cancer treatment [6] and 100 mg/m<sup>2</sup> in MS treatment. Nevertheless, MTX cardiotoxicity has been described in lower cumulative doses [7]. In a study by Rivera and collaborators, cardiotoxicity was observed in patients who received cumulative doses of  $\leq 75$  mg/m<sup>2</sup>. Actually, 19.1% of the 97 patients enrolled have developed cardiotoxicity, with 6.19% of those receiving  $\leq 35$  mg/m<sup>2</sup>, 19.6% receiving 36–75 mg/m<sup>2</sup>, 34.0% receiving 76–105 mg/m<sup>2</sup>, and only 40.2% of the patients received  $>105$  mg/m<sup>2</sup> of MTX [8]. Clinical signs of MTX-inflicted cardiotoxicity include decreased left ventricular ejection fraction, heart failure (HF), and/or dilated cardiomyopathy [6].

Myocardial inflammation has emerged as a pathophysiologic process that contributes to cardiac hypertrophy, fibrosis, and dysfunction [9–11]. In that context, activation and nuclear translocation of the nuclear factor kappa B (NF- $\kappa$ B) may play an important role in the regulation of cardiac inflammatory signalling pathways, being a major contributor to myocardial dysfunction and remodelling as seen in HF [12,13]. On the other hand, oxidative stress can activate NF- $\kappa$ B pathways with consequent cytokine production stimulation [14,15]. Cytokines contribute to the initiation and modulation of critical responses within the overloaded myocardium, leading to myocyte growth, apoptotic myocyte death, and reactive fibrosis [16,17]. Interestingly, one of the cytokines involved, TNF- $\alpha$ , exerts antioxidant and antiapoptotic effects in the myocardium at physiological levels [18,19], but when levels increase, it stimulates myocyte apoptosis [20], cardiac hypertrophy, and fibrosis [21]. Another cytokine involved in cardiac homeostasis is interleukin-6 (IL-6), which possesses univocal antiapoptotic properties, protecting cardiac myocytes during acute damage [22]. However, if IL-6 levels remain chronically elevated, it promotes a sustained inflammatory response, contributing to cardiac hypertrophy [23]. It is also a strong marker of diastolic dysfunction, ejection fraction, risk, and severity of HF [23]. Despite the MTX's immunomodulatory effect on MS, to the best of our knowledge, its role on inflammatory cardiac pathways has not been traced yet.

Noteworthy, an important factor that influences the development of MTX cardiotoxicity is patients' age. Available studies demonstrate that the very young and the elderly are more prone to develop cardiotoxicity after MTX-treatment [8,24], but the effect on adults also has an important social and economic impact, especially in a moment where life expectancy is increasing. Several studies have also shown that MTX is able to trigger cardiotoxicity in small children ( $<4$  years) [25–27]. These effects can last and affect their life expectancy and quality of life [28–31]. This factor must be put into perspective nowadays, as prior to the 1970s, the 5-year survival of childhood cancer was lower than 50% [32], while now it is reaching 85% [33]. Therefore, the number of children who survive cancer is drastically increasing, being that chemotherapy side effects, such as cardiotoxicity, will have a long-term impact. Nevertheless, the reasons for age susceptibility towards MTX-inflicted cardiotoxicity have been poorly investigated [34].

This study aimed to evaluate MTX-induced cardiotoxicity in two groups of animals of different age periods (infant and adults) and two cumulative doses. The highest cumulative

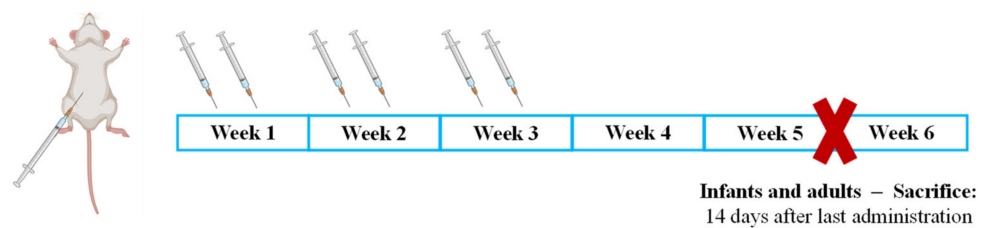
dose was used as a starting point to assess the mechanisms of cardiotoxicity induced by MTX. The lowest cumulative dose caused less animal suffering but allowed for the assessment of MTX interference towards inflammation or oxidative stress pathways, and to determine early markers of heart damage that allows the study of subtle and even non-clinically undisclosed cardiotoxic mechanisms.

## 2. Results

In experiment 1, both adults and infants received a 7.0 mg/kg cumulative dose and were sacrificed 14 days after the last administration (Figure 1). The results obtained in experiment 1 together with previously published data [34] indicate that infants are more resilient to MTX side effects, as will be shown in this section. As suffering was apparent in most of the animals that received the highest dose, in experiment 2, the dose was decreased (6.0 mg/kg) (Figure 1), and two different approaches were taken:

- Infant mice were sacrificed 17 days after the last administration to determine if, with increased lag time, infants would present signs of cardiac damage or still maintained higher cardiac resilience;
- Adults were sacrificed earlier, namely after 7 days to determine early markers of heart damage that may reveal subtle cardiotoxic mechanisms before unacceptable damage occurred.

### Experiment 1 - Cumulative dose 7.0 mg/kg



### Experiment 2 - Cumulative dose 6.0 mg/kg

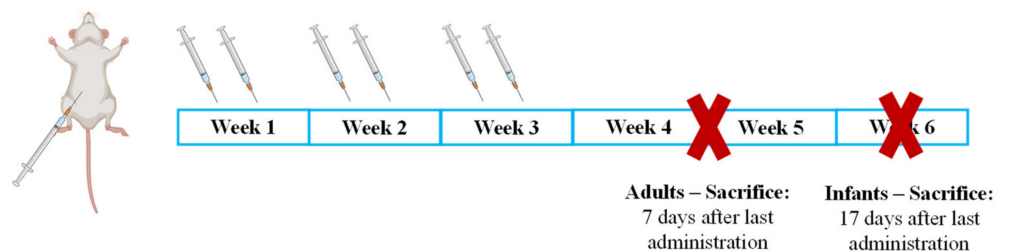


**Figure 1.** Schematic representation of the distribution of the animals by cumulative dose, as well as the timeline of administration of MTX and sacrifice.

### 2.1. MTX Caused Significant Effects on Body Weight and Food/Water Consumption

In the infant population, 7.0 mg/kg MTX-treated animals had significantly less body weight gain when compared to controls after the 17th day (Figure S1A). The 7.0 mg/kg MTX-treated adult mice had a lower average body weight than the control group after reaching the maximum cumulative dose. In detail, statistically significant differences in body weight occurred after the 21st day, and loss of weight occurred on the 24th day (Figure S1B).

The amount of food and water intake was based on each animal's body weight, since the animals were maintained in a social environment and therefore in a group. Regarding water consumption, overall, the 7.0 mg/kg MTX-treated infants (Figure S1C) and adults (Figure S1D) had lower consumption than controls during all the experimental periods. Food consumption was significantly decreased in the case of the 7.0 mg/kg MTX-treated infant group (Figure S1E), after the 14th day. Adults that received the cumulative dose of

7.0 mg/kg had statistically significant higher food consumption in the week following the last MTX administration, compared with the control group (Figure S1F).

In the infant population, animals had initially significant differences in the body weight gain between the 6.0 mg/kg MTX-treated and the control groups (Figure S2A). These initial differences were due to the random distribution, for each cage, of the mice belonging to different litters (Figure S2A). On the other hand, in the 6.0 mg/kg MTX-treated adult population, a statistically significant body weight decrease was observed in the last days of the experiment (Figure S2B).

Concerning water intake, a decrease in MTX-treated infant population intake was observed throughout the experiment, reaching statistical significance by the end of the protocol, when compared with the control group (Figure S2C). Regarding the adults treated with a MTX cumulative dose of 6.0 mg/kg, a statistically significant decrease in water intake was observed in the last days of the experiment (Figure S2D). Similar to what happened in water intake, food consumption in the 6.0 mg/kg MTX-treated infant mice decreased, being statistically significant in the last days of the protocol, when compared with the control group (Figure S2E). We found that a significant decrease between the food consumption of the MTX 6.0 mg/kg-treated adults and the control group was observed towards the end of the experiment (Figure S2F).

#### *2.2. Plasma Levels of Total-CK and AST/ALT Ratio Were Increased in the 7.0 mg/kg MTX-Treated Adult Mice*

In the 7.0 mg/kg MTX-treated infant group, no statistically significant differences were observed in the aminotransferase's levels, when compared to control mice (Table S2). Concerning the adult mice, a tendency for increased aspartate aminotransferase (AST)/alanine aminotransferase (ALT) ratio of the 7.0 mg/kg MTX-treated group, compared with the control, was observed ( $p = 0.06$ ). In the 6.0 mg/kg MTX-treated infants, ALT levels were elevated while the AST/ALT ratio was found to be decreased when compared with the control group. Concerning the 6.0 mg/kg-treated adult mice, there were no significant changes in plasma aminotransferases (Table S3).

In the infant mice, plasma creatine kinase–MB (CK–MB) levels were significantly higher in the 7.0 mg/kg MTX-treated mice when compared with the respective controls (Table S2), while no statistically significant changes were observed in the plasma total creatine kinase (total-CK) levels. In adult mice, plasma total-CK levels were significantly higher in the 7.0 mg/kg MTX-treated mice, compared to respective controls (Table S2), but no meaningful changes were found in their plasma CK–MB values compared to controls. No significant differences in CK–MB and total-CK levels were found between control and the 6.0 mg/kg MTX-treated adult animals (Table S3). Unfortunately, in the 6.0 mg/kg-treated infant mice, total-CK and CK–MB levels were not determined due to an insufficient amount of plasma.

#### *2.3. The Ratio of Heart/Body Weight Decreased in Adults after the Highest Dose of MTX*

Heart to body weight ratio was significantly decreased in the 7.0 mg/kg MTX group (Table S2). In the 6.0 mg/kg MTX-treated adult population, no significant differences were observed in heart weight/body weight ratio (Table S3). In addition, no statistically significant differences were observed in heart/body weight ratio between MTX-treated infant mice and the control group, in both doses (Tables S2 and S3).

#### *2.4. Histological Damage Occurred in Cardiac Tissue after MTX-Treatment, Adult Population Being More Susceptible to Cardiac Damage*

The qualitative histologic examination of the heart of MTX-treated mice and controls was done using the haematoxylin and eosin staining. Major qualitative and representative structural alterations are depicted in Figures 2 and 3. Meanwhile, the results of the semi-quantitative analysis are presented in Table 1. Lesions in the cardiac tissue caused by MTX were characterized by cellular degeneration, interstitial inflammatory cell infiltration, and necrotic zones. In experiment 1, the heart of both infant and adult control mice showed a

preserved heart tissue structure (Figure 2A,C). In the 7.0 mg/kg MTX-treated infant group, cardiac tissue showed interstitial inflammatory cell infiltration, signs of vacuolization, as well as necrotic zones but to a lower extent when compared with adults. In the 7.0 mg/kg MTX-treated adult mice, the presence of cellular oedema, cytoplasmic vacuolization of cardiomyocytes, interstitial inflammatory cell infiltration, as well as some necrotic zones were evident (Figure 2D).

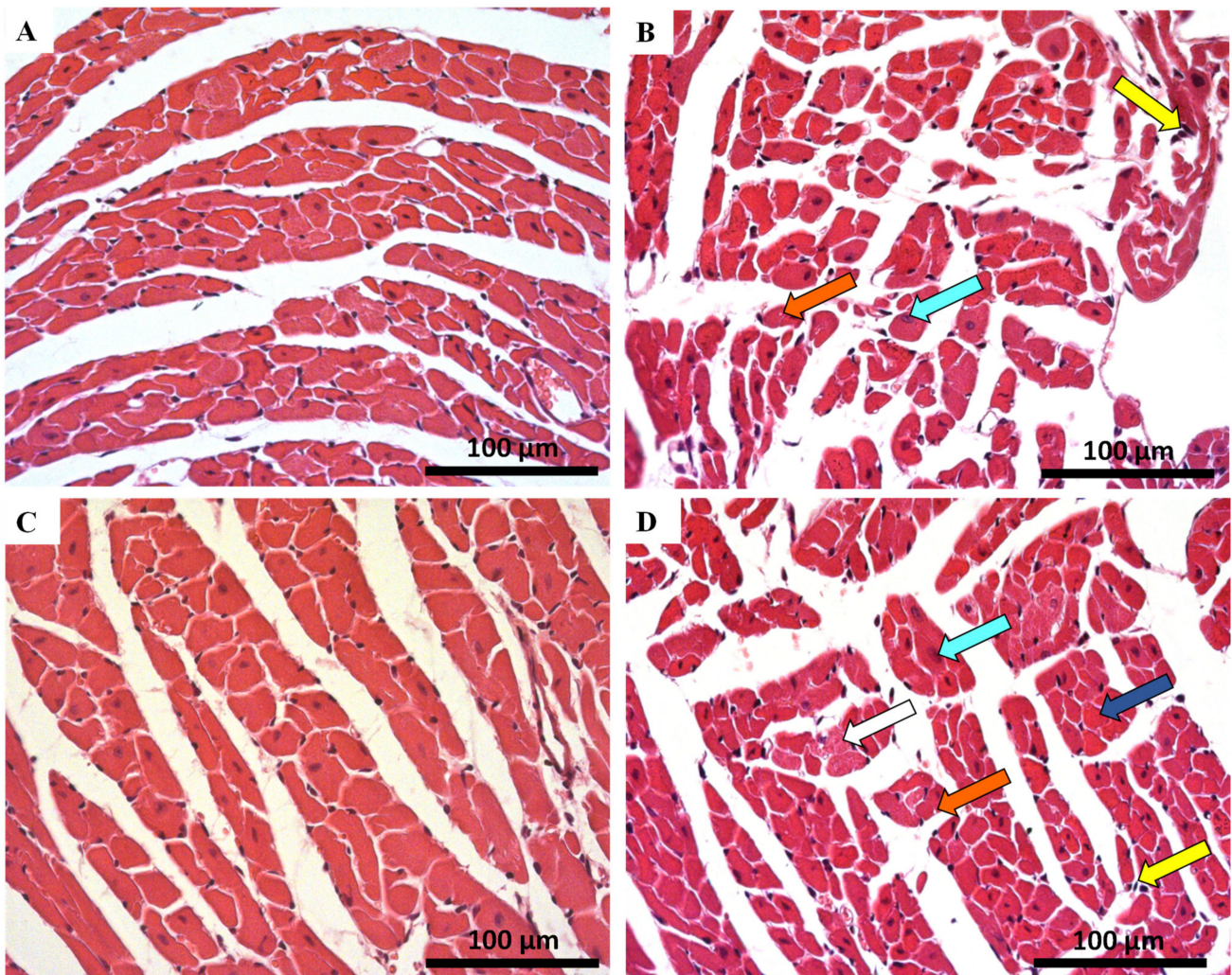


**Figure 2.** Cardiac histopathology evaluation done by light microscopy from MTX-treated adult and infant animals and respective controls, as assessed by haematoxylin and eosin staining (experiment 1, mice were euthanized 14 days after the last administration) (A–D). Light micrograph from: (A) infant mice controls in experiment 1, showing normal morphology and structure; (B) infant mice given a cumulative dose of 7.0 mg/kg MTX; (C) adult mice in experiment 1 showed normal morphology and structure; (D) adult mice given a cumulative dose of 7.0 mg/kg MTX. Presence of vacuolization (orange arrow), inflammatory infiltration (yellow arrow), as well as large and uncondensed nucleus (cyan arrow). Cellular oedema (white arrow) and necrotic zones (blue arrow) are evident only in adult mice. Scale bar = 100 µm,  $n = 3$ . Images taken at 40× amplification.

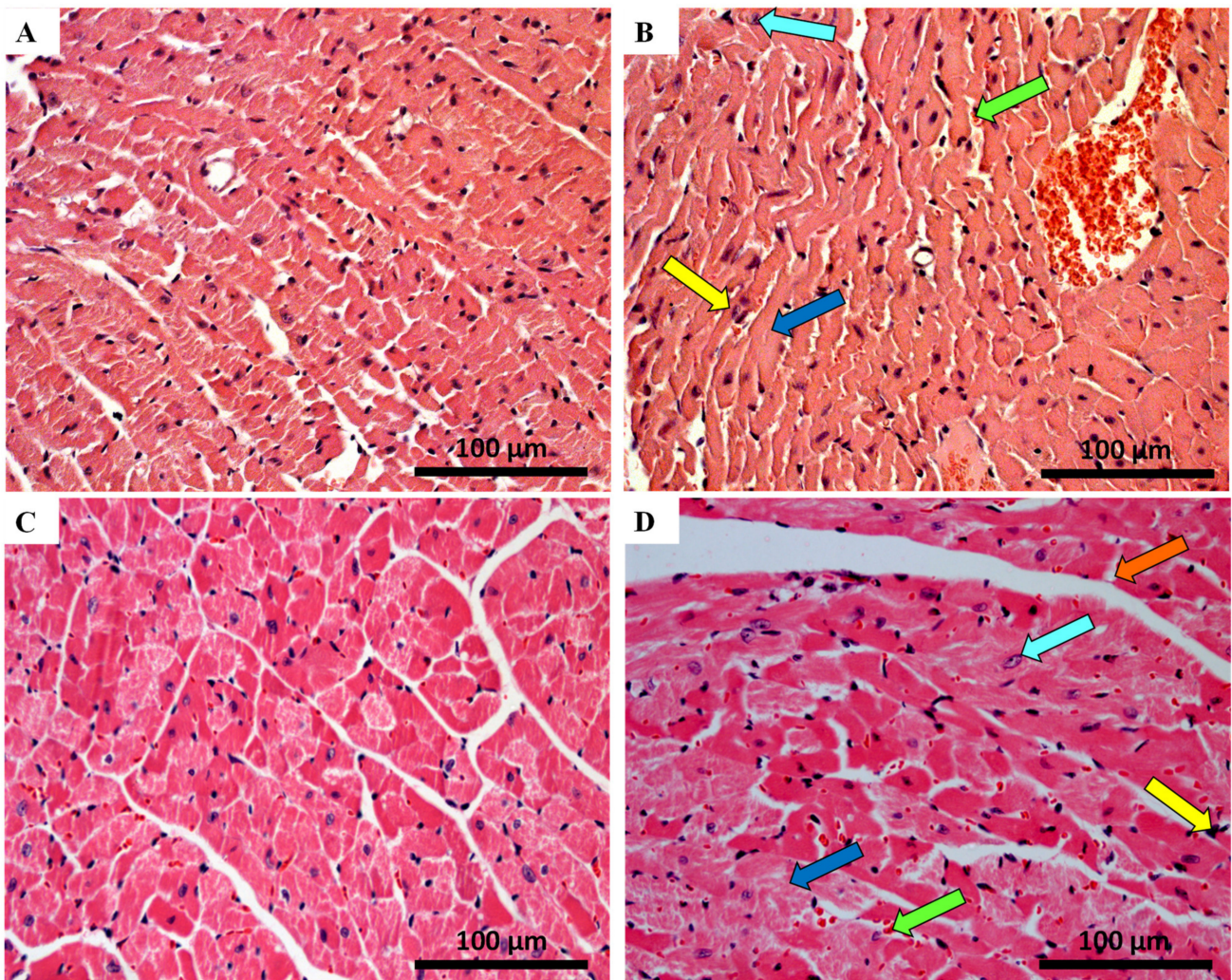


**Figure 3.** Cardiac histopathology evaluation done by light microscopy from MTX-treated adult and infant animals and respective, as assessed by haematoxylin and eosin staining controls (experiment 2, adult and infant mice were euthanized 7 or 17 days after the last administration, respectively) (A–D). Light micrograph from: (A) infant mice controls in experiment 2, showing normal morphology and structure; (B) infant mice given a cumulative dose of 6.0 mg/kg MTX; (C) adult mice in experiment 2 showed normal morphology and structure; (D) adult mice given a cumulative dose of 6.0 mg/kg MTX. Presence of vacuolization (orange arrow), inflammatory infiltration (yellow arrow), vascular congestion (green arrow), necrotic zones (blue arrow), as well as large and uncondensed nucleus (cyan arrow) is evident. Scale bar = 100 µm,  $n = 3$ . Images taken at 40× amplification.

In experiment 2, control groups did not present any changes in the tissue structure, as expected (Figure 3A,C). The 6.0 mg/kg MTX-treated infant group showed signs of vascular congestion, with enlarged blood vessels, necrotic zones, inflammatory infiltrations, vacuolization, with a large and uncondensed nucleus (Figure 3B). In MTX-treated adults, the presence of cytoplasmic vacuolization of cardiomyocytes, vascular congestion, interstitial inflammatory cell infiltration, as well as some necrotic zones was evident (Figure 3D, Table 1). The lesions were most notorious in the endocardium. Signs of obstruction in some small calibre arteries were observed in the 6.0 mg/kg MTX-treated adult mice (data not shown). All groups showed myocardium with preserved structure (score = 0), therefore data regarding tissue disorganization were omitted from Table 1 (data not shown).

**Table 1.** Semi-quantitative analysis of morphological parameters (cellular degeneration, necrosis, inflammatory activity, and tissue disorganization) in the heart of 7.0 mg/kg and 6.0 mg/kg MTX-treated and controls groups, in adult and infant animals.

Hematoxylin-eosin staining				
	INFANT		ADULT	
	Control	MTX 7.0 mg/kg	Control	MTX 7.0 mg/kg
<b>Cellular Degeneration</b>	0.50 ± 0.54	0.82 ± 0.63 **	0.64 ± 0.63	1.42 ± 0.71 ****
<b>Necrosis</b>	0.00 ± 0.00	0.04 ± 0.20	0.00 ± 0.00	0.23 ± 0.43 ***
<b>Inflammatory Activity</b>	0.22 ± 0.42	0.85 ± 0.52 ****	0.30 ± 0.46	1.02 ± 0.49 ****
	Control	MTX 6.0 mg/kg	Control	MTX 6.0 mg/kg
<b>Cellular Degeneration</b>	0.07 ± 0.25	0.47 ± 0.51 ***	0.02 ± 0.13	1.00 ± 0.00 ****
<b>Necrosis</b>	0.00 ± 0.00	0.27 ± 0.45 **	0.00 ± 0.00	1.02 ± 0.14 ****
<b>Inflammatory Activity</b>	0.08 ± 0.27	0.50 ± 0.51 ***	0.05 ± 0.22	1.65 ± 0.49 ****

Results of haematoxylin–eosin staining, given in scores, are presented as mean ± SD and were obtained from 3 animals from each treatment group, with exception of the control in 7.0 mg/kg MTX-treated infant group of haematoxylin–eosin staining ( $n = 2$ ). Statistical comparisons were made using the Mann-Whitney test: \*\*  $p < 0.01$ , \*\*\*  $p < 0.001$ , \*\*\*\*  $p < 0.0001$ , MTX vs. control.

### 2.5. Myocardial Fibrosis Was Significantly Increased in MTX-Treated Adult Mice at Both Doses

Myocardial fibrosis, which is a hallmark of cardiac hypertrophy, was assessed by the Sirius red technique. Results are presented in Figure 4 and Table 2. No significant differences were observed among the infant groups regarding the percentage of collagen/muscle area of the heart. In contrast, the MTX-treated adults had significant increases in the percentage of collagen/muscle area, at both doses.

**Table 2.** Semi-quantitative analysis of fibrosis in the heart of the 7.0 mg/kg and 6.0 mg/kg MTX-treated and respective controls groups, in adult and infant animals.

Sirius Red Staining				
	INFANT		ADULT	
	Control	MTX 7.0 mg/kg	Control	MTX 7.0 mg/kg
<b>% area ratio of collagen/skeletal muscle</b>	0.14 ± 0.07	0.17 ± 0.05	0.14 ± 0.02	0.24 ± 0.06 ****
	Control	MTX 6.0 mg/kg	Control	MTX 6.0 mg/kg
<b>% area ratio of collagen/skeletal muscle</b>	0.10 ± 0.03	0.15 ± 0.03	0.10 ± 0.02	0.16 ± 0.05 **

Results of Sirius red staining, given in area of collagen/skeletal muscle, are presented as mean ± SD and were obtained from 3 animals from each treatment group. Statistical comparisons were made using the Mann-Whitney test: \*\*  $p < 0.01$ , \*\*\*\*  $p < 0.0001$ , MTX vs. control.



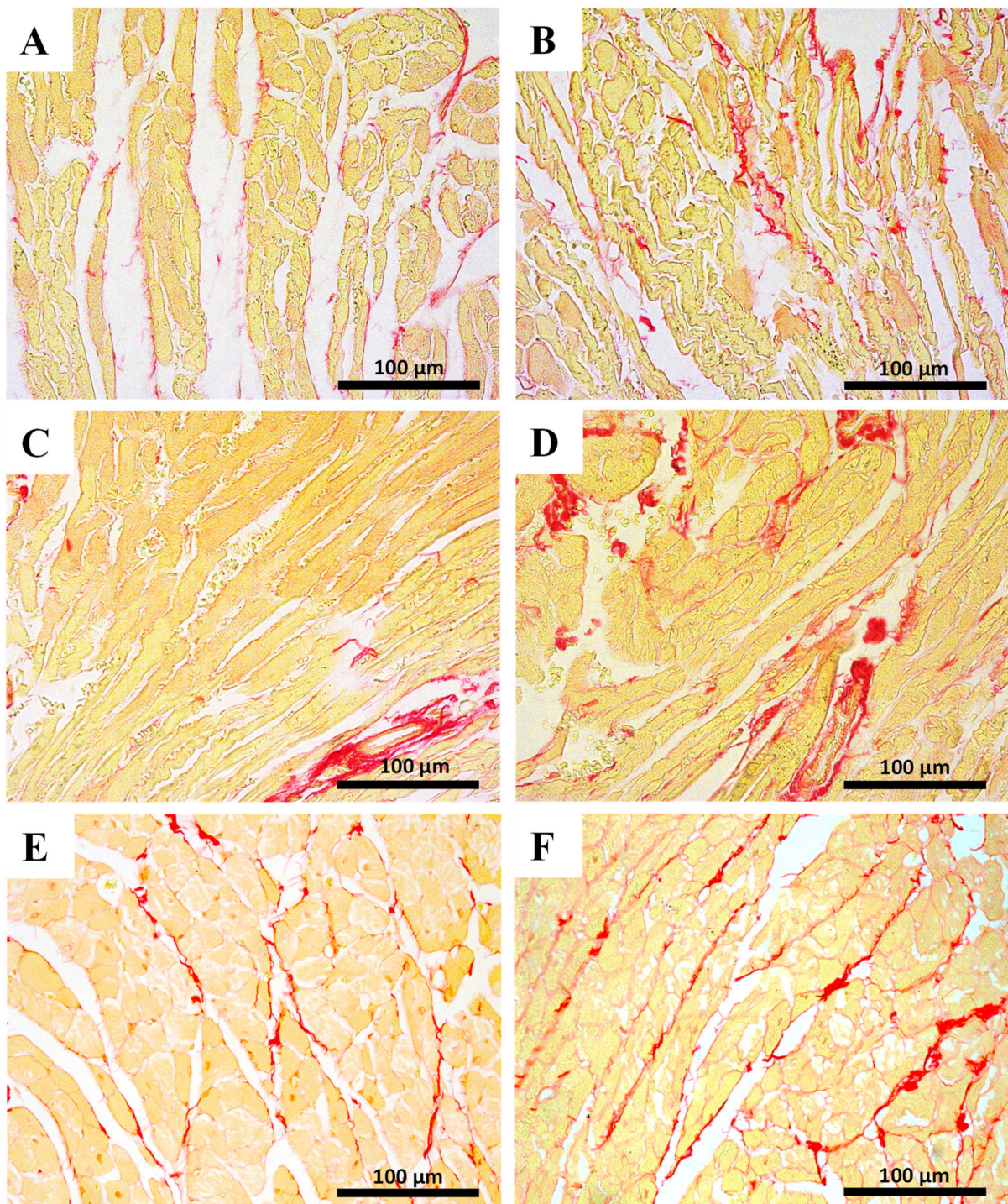


**Figure 4.** Sirius red cardiac staining assessed by light microscopy from MTX-treated adult and infant animals and respective controls (A–F). Light micrograph from (A) the control infant mice (experiment 1, mice were euthanized 14 days after the last administration); (B) infant mice injected with a cumulative dose of 7.0 mg/kg MTX; (C) control adult mice; (D) adult mice injected with a cumulative dose of 7.0 mg/kg MTX showing higher fibrosis. (E) Control adults (experiment 2, mice were euthanized 7 days after the last administration); (F) adult mice after receiving a cumulative dose of 6.0 mg/kg MTX. Scale bar = 100 µm,  $n = 3$ . Images taken at 40× amplification.

### 2.6. The Highest Cumulative Dose of MTX Increased Cardiac Total Glutathione in Infants, While Decreasing Noradrenaline Cardiac Levels in Adults

The 7.0 mg/kg MTX-treated infant group presented significantly higher cardiac values of total glutathione (tGSH) than the control group (Table 3). No differences were found in oxidized glutathione (GSSG) and reduced glutathione (GSH)/GSSG ratio of the infant population treated with MTX when compared to controls. No statistically significant changes in the cardiac levels of tGSH, GSSG, and GSH/GSSG ratio were found in 7.0 mg/kg MTX-treated adult mice. In the 6.0 mg/kg MTX-treated infant and adult mice, no differences were found between groups (data not shown). Moreover, no statistically significant changes were found in the marker of lipid peroxidation, malondialdehyde (MDA), between groups in experiment 1.

**Table 3.** Biochemical cardiac parameters of the 7.0 mg/kg MTX-treated and control mice.

	INFANT		ADULT	
	Control	MTX 7.0 mg/kg	Control	MTX 7.0 mg/kg
tGSH (nmol/mg protein)	7.72 ± 1.18	9.41 ± 1.63 *	8.01 ± 0.77	8.57 ± 2.33
GSSG (nmol/mg protein)	0.62 ± 0.19	0.77 ± 0.15	0.60 ± 0.10	0.60 ± 0.34
GSH/GSSG ratio	11.94 ± 5.23	10.62 ± 2.01	11.84 ± 3.52	15.40 ± 8.63
MDA (nmol/g protein)	27.23 ± 9.23	28.42 ± 7.32	30.65 ± 7.59	34.83 ± 12.44
ATP (nmol/mg protein)	3.94 ± 1.97	3.77 ± 1.42	3.92 ± 1.34	3.23 ± 1.39
Creatine (nmol/mg protein)	74.77 ± 16.25	78.94 ± 11.09	82.17 ± 13.24	84.13 ± 25.30
Phosphocreatine (nmol/mg protein)	41.06 ± 9.71	43.08 ± 6.68	37.25 ± 8.11	49.10 ± 14.36 ( <i>p</i> = 0.06)
Noradrenaline (nmol/g protein)	8.26 ± 5.18	9.03 ± 4.63	9.79 ± 1.99	4.64 ± 5.16 *

Results, in nmol/mg protein or nmol/g protein, are presented as mean ± SD and were obtained from 7 to 8 animals from each treatment group. Statistical analyses were made using the t-test for all adult groups, with the exception of total glutathione (tGSH) and reduced glutathione/oxidized glutathione ratio (GSH/GSSG), where the Mann–Whitney test was done. For the infant data, the Mann–Whitney test was used. \* *p* < 0.05, MTX 7.0 mg/kg vs. control.

In experiment 1, to understand if MTX had any impact on the cellular energetics on the two populations (infant and adult), intracellular adenosine 5'-triphosphate (ATP) and phosphocreatine levels were measured (Table 3). In the 7.0 mg/kg MTX condition in both populations, no significant differences in ATP levels were observed. Furthermore, no significant differences were seen in phosphocreatine and creatine levels in the MTX-treated infant group, when compared to control mice. However, in the adult population, there is a tendency for increased phosphocreatine levels in the MTX-treated group, compared with the control group (*p* = 0.06).

In experiment 2, no significant changes in ATP levels were observed in 6.0 mg/kg-treated mice of both ages (data not shown).

For experiment 1, levels of noradrenaline are depicted in Table 3. Noradrenaline cardiac levels were significantly lower in MTX-treated adults when compared to controls. No meaningful differences were seen between control and infant MTX-treated mice at 7.0 mg/kg.

### 2.7. The Expression of GAPDH Increased in the 6.0 mg/kg MTX-Treated Infant Mice

After major and general data were gathered, the animals treated with a lower cumulative dose (6.0 mg/kg) were subjected to other determinations as to assess early markers of damage in adults, or to determine the underlying reasons that make infants more resilient to MTX-cardiac effects after a longer washout time.

In order to assess the impact of MTX treatment on cardiac metabolism, the expression of metabolic enzymes was evaluated by Western blotting (Figure 5). No changes were observed on the levels of ATP synthase subunit beta while the expression of the glycolytic enzyme, glyceraldehyde-3-phosphate dehydrogenase (GAPDH), was significantly higher in MTX-treated infant mice, compared with control mice (Figure 5A,B). No changes were

observed in the ratio of GAPDH to ATP synthase subunit beta in MTX-treated infant mice, when compared with control mice (Figure 5C). No changes were seen in the levels of ATP synthase subunit beta nor in the levels of GAPDH in MTX-treated adult mice, when compared with control mice (Figure 5D,E). Nevertheless, significant differences were observed in the ratio of GAPDH to ATP synthase subunit beta between MTX-treated adult mice and the control group (Figure 5F).

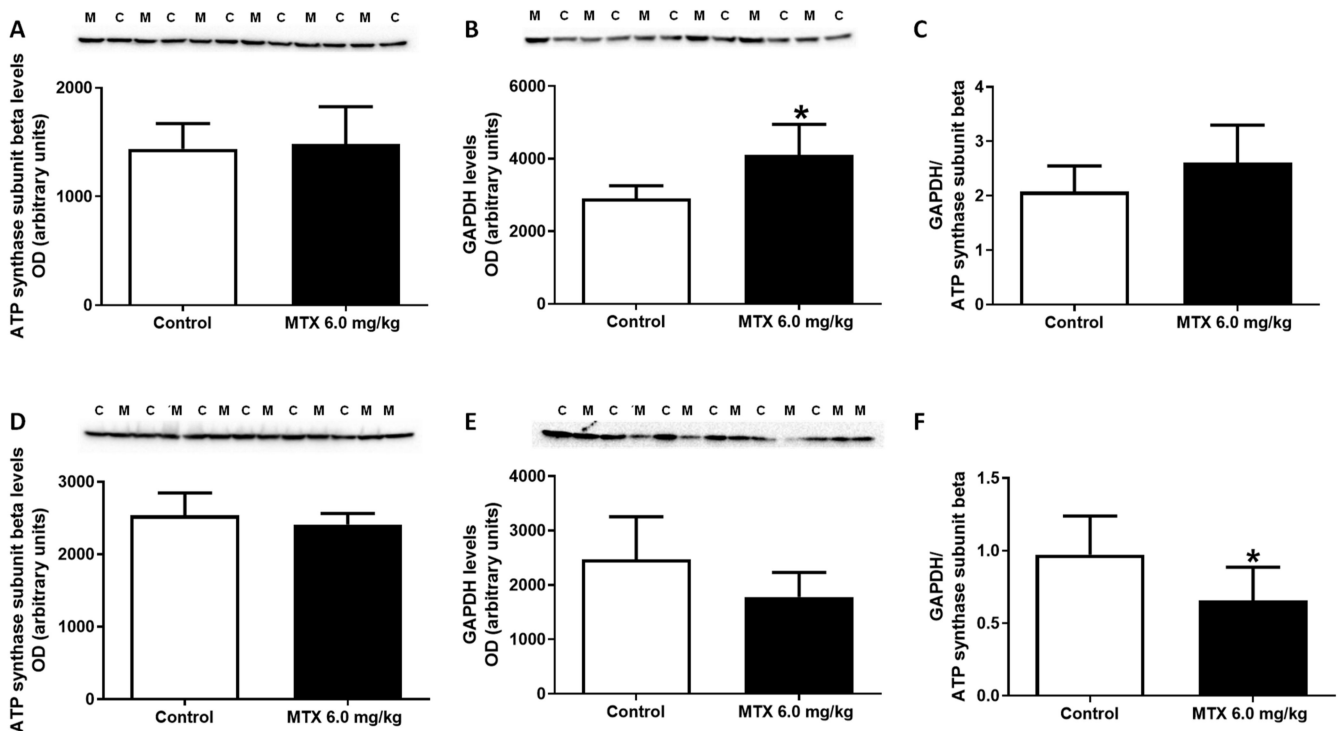


**Figure 5.** ATP synthase subunit beta (52 kDa), glyceraldehyde-3-phosphate dehydrogenase (GAPDH) (37 kDa) expression, and ratio GAPDH to ATP synthase subunit beta evaluated by Western blotting, from (A–C) infant MTX-treated (M), and control mice (C), and (D–F) adult mice exposed to a cumulative dose of 6.0 mg/kg MTX (M), and control (C) adult mice (experiment 2, infant and adult mice were euthanized 17 or 7 days after the last administration, respectively). Values are expressed as mean  $\pm$  SD and were obtained from 6 (infant) and 6–7 (adult) animals from each treatment group. Statistical comparisons were made using the t-test: \*  $p < 0.05$ , MTX 6.0 mg/kg vs. control. OD: optic density. Protein loading was confirmed by the Ponceau S staining (Figures S3 and S4).

### 2.8. At the Lower Cumulative Dose, Protein Carbonylation Increased in Adult Mice

The protein carbonylation in the cardiac lysates increased in the 6.0 mg/kg MTX-treated adult mice, compared to control mice (Figure 6B). No differences were found in the MTX-treated infant mice (Figure 6A).

### 2.9. MTX Increased Catalase Expression Both in Adults and Infants, While in Infants' Glutathione Peroxidase Expression Increased

As shown in Figure 7C, levels of glutathione peroxidase were increased in MTX-treated infant mice, when compared with control mice, while in adults no statistically significant differences were observed (Figure 7F). Neither in adults nor infants, superoxide dismutase/manganese-dependent superoxide dismutase (SOD2/MnSOD) had any significant changes after MTX administration (Figure 7A,D). On the contrary, the levels of catalase were increased in both MTX-treated adult and infant mice, when compared with control mice (Figure 7B,E).

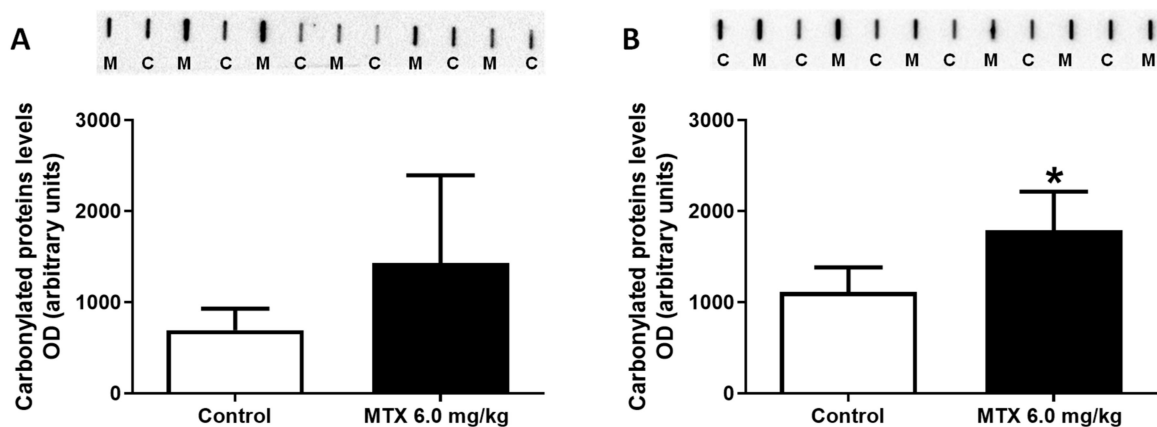


**Figure 6.** Protein carbonylation cardiac content evaluated by slot blot in (A) infant mice and (B) adult mice exposed to a cumulative dose of 6.0 mg/kg MTX (experiment 2, infant and adult mice were euthanized 17 or 7 days after the last administration, respectively). Values are expressed as mean  $\pm$  SD and were obtained from six animals from each treatment group. Statistical comparisons were made using the t-test: \*  $p < 0.05$ , MTX 6.0 mg/kg vs. control. OD: optic density, M: mitoxantrone, C: control.

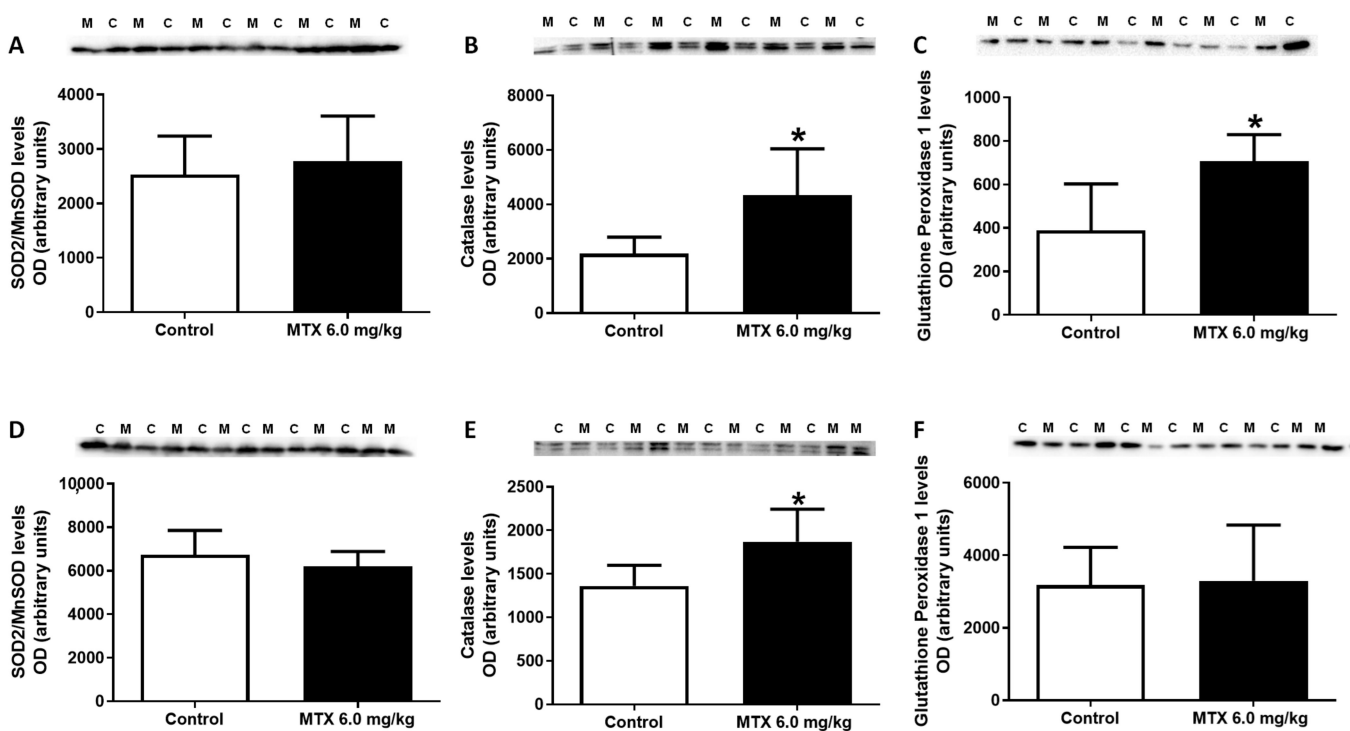


**Figure 7.** Superoxide dismutase 2/ manganese-dependent superoxide dismutase (SOD2/MnSOD) (26.6 kDa), catalase (60 kDa) and glutathione peroxidase (22 kDa) expression evaluated by Western blotting, from (A–C) infant MTX-treated (M) and control (C) mice, and (D–F) adult mice exposed to a cumulative dose of 6.0 mg/kg MTX (M) and their respective controls (C) (experiment 2, infant and adult mice were euthanized 17 or 7 days after the last administration, respectively). Values are expressed as mean  $\pm$  SD and were obtained from 6 (infant) and 6–7 (adult) animals from each treatment group. Statistical comparisons were made using the t-test: \*  $p < 0.05$ , MTX 6.0 mg/kg vs. control. OD: optic density. Protein loading was confirmed by the Ponceau S staining (Figures S3 and S4).

### 2.10. The Heart of MTX-Treated Adult Mice Showed a Higher Density of Infiltrating M1 Macrophages

The immunohistochemistry evaluation in the heart of pro-inflammatory M1 macrophages, using CD68+ immunostaining, and anti-inflammatory M2 macrophage, using CD206 immunostaining, is shown in Figure 8 and Table 4. Data analysis indicated that the number of CD68 positive cells had a significant increase ( $p < 0.001$ ) after MTX exposure in adult mice (Table 4). Conversely, no meaningful differences were observed in the M2 subset of the adult population treated with MTX when compared with controls. In the 6.0 mg/kg MTX-treated infant group, no differences were observed in the M1 and M2 macrophages when compared with controls (photomicrographs not shown).

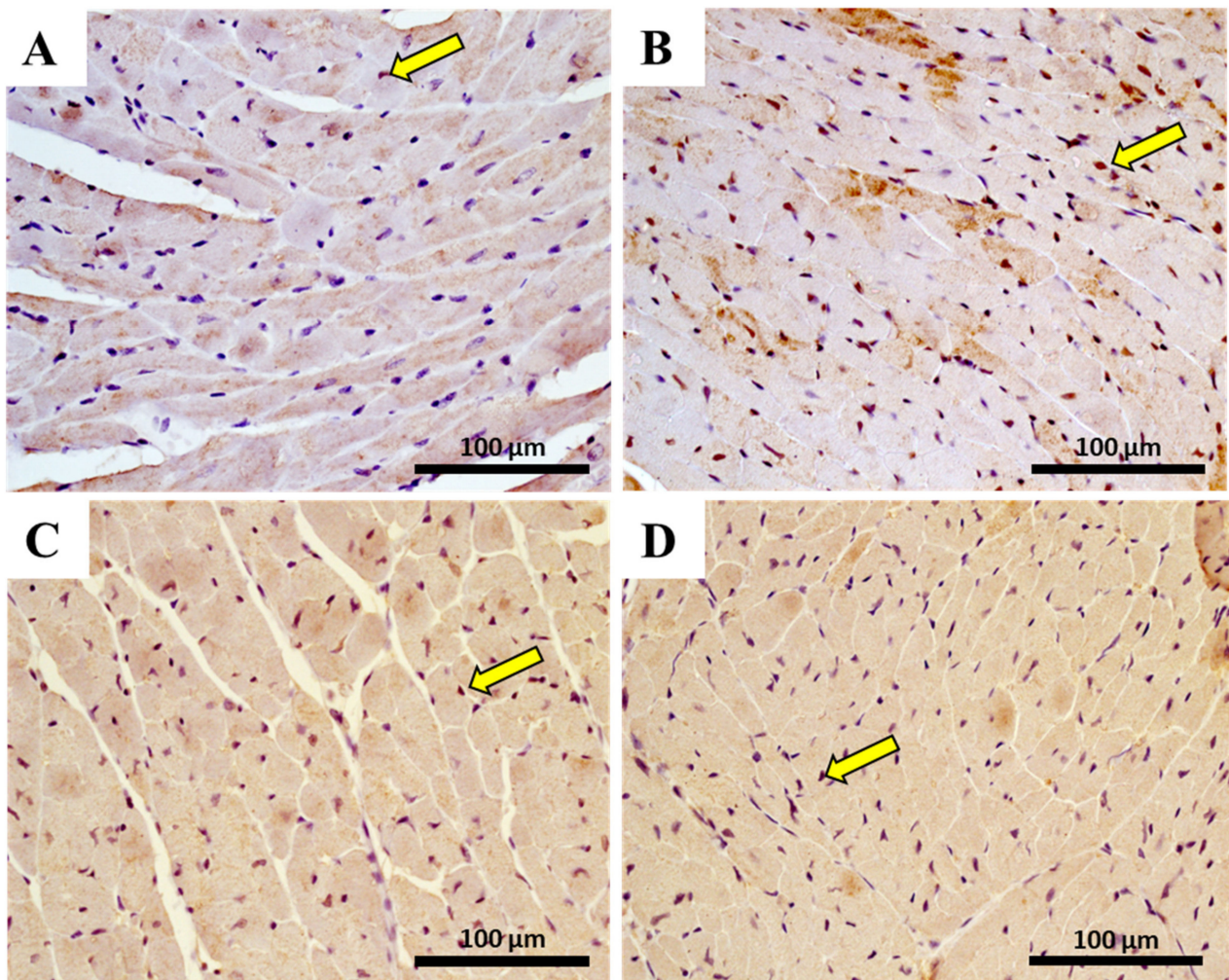


**Figure 8.** Representative photomicrographs of heart immunohistochemistry from 6.0 mg/kg MTX-treated adult and respective controls (experiment 2, mice euthanized 7 days after the last administration), by a marker (CD68+) for macrophages M1 (A,B) and by a marker for (CD206) macrophage M2 (C,D) detection, and indicated by yellow arrows. Light micrograph (A,C) from the control of M1 (A) and M2 staining (C); light micrograph (B,D) from adult mice given a cumulative dose of 6.0 mg/kg MTX and performed staining for M1 (B) or M2 (D). Scale bar = 100 µm,  $n = 3$ . Images taken at 40× amplification.

**Table 4.** Number of cells staining positive for activated macrophages marked as M1 and macrophage marked as M2 in the heart of MTX-treated and control groups, in adult and infant animals.

Immunohistochemistry	INFANT		ADULT	
	Control	MTX 6.0 mg/kg	Control	MTX 6.0 mg/kg
M1 macrophage	4.28 ± 3.03	9.33 ± 7.70	12.83 ± 15.37	68.11 ± 22.77 ****
M2 macrophage	66.61 ± 43.40	62.56 ± 24.92	113.70 ± 23.10	96.56 ± 28.33

Results were expressed as mean ± SD. The value of macrophages was obtained from three animals from each treatment group. Statistical comparisons were made using the t-test for M2 macrophage evaluation in the adult group and the Mann–Whitney test for all infant group and M1 macrophage of adult group: \*\*\*\*  $p < 0.0001$ , MTX 6.0 mg/kg vs. control. Three animals per treatment, and for each animal, six photos of different areas of cardiac tissue were evaluated and quantified using ImageJ software version 1.52a.

#### 2.11. In Adults, the Lower Cumulative Dose of MTX Significantly Increased the Expression of NF- $\kappa$ B p65

Cardiac immunohistochemistry analysis was performed in order to assess the activation of the inflammatory transcriptional factor, NF- $\kappa$ B, namely the fraction p65. The immunohistochemistry data of NF- $\kappa$ B is shown in Figure 9 and Table 5. Immunohistochemical staining of NF- $\kappa$ B p65 in the control group showed low cytoplasmic expression (Figure 9A). However, the 6.0 mg/kg MTX-treated adult group showed positive cytoplasmic and nuclear expression. In addition, in MTX-treated animals, the endothelium of the blood vessels showed a high expression of p65, which was evident from the intense brown staining (Figure 9B). When performing a semiquantitative analysis, a statistically significant increase ( $p < 0.01$ ) in the mean number of the NF- $\kappa$ B immunopositive cells in the MTX adult group was observed when compared with the control group (Table 5).

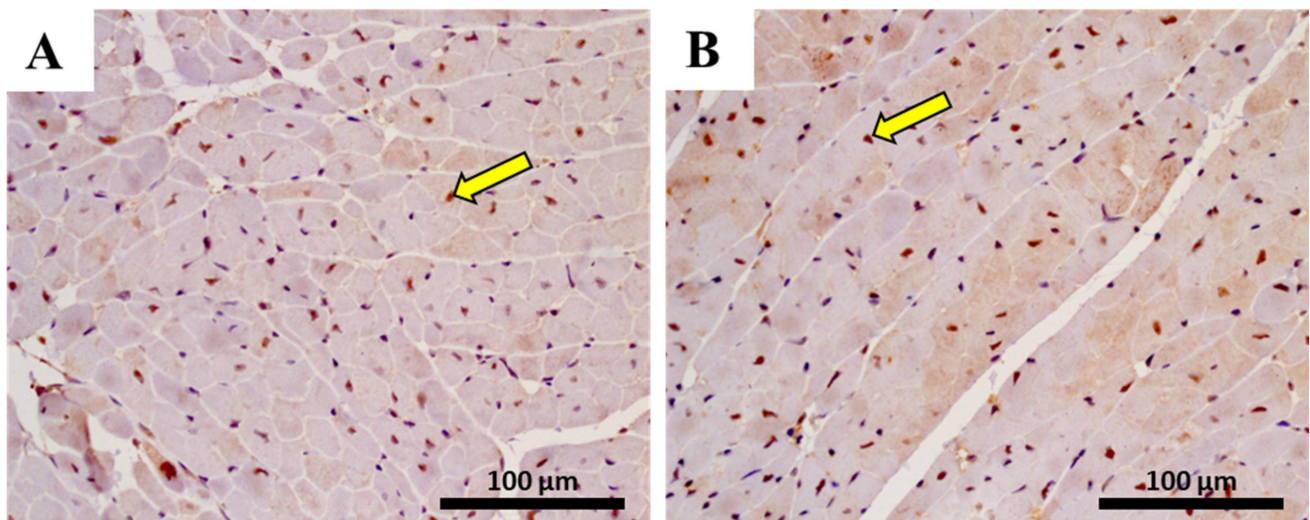


**Figure 9.** Representative photomicrographs of immunohistochemistry determination of NF- $\kappa$ B p65 in the cardiomyocytes-like cells from 6.0 mg/kg MTX-treated adult and respective controls (experiment 2, mice euthanized 7 days after the last administration) (A,B). Light micrograph (A) from the controls; and (B) from adult mice given a cumulative dose of 6.0 mg/kg MTX. Scale bar = 100  $\mu$ m,  $n = 3$ . Images taken at 40 $\times$  amplification.

Conversely, no meaningful differences were observed in the infant population treated with MTX when compared with controls (photomicrographs not shown).

Subsequently, Western blot analysis showed that, in the cardiac total homogenates, MTX led to a tendency for increased expression of NF- $\kappa$ B p65 levels ( $p = 0.08$ ) (Figure 10D), while no differences were observed in the infant mice (Figure 10B). Furthermore, MTX-treated adult mice had enhanced expression of NF- $\kappa$ B p52 (Figure 10C), while MTX-treated

infant mice showed a tendency for increased NF- $\kappa$ B p52 levels ( $p = 0.07$ ) in comparison with the control group (Figure 10A).

**Table 5.** Number of cells staining positive for activated NF- $\kappa$ B in the heart of MTX-treated and control groups, in adult and infant animals.

Immunohistochemistry	INFANT		ADULT	
	Control	MTX 6.0 mg/kg	Control	MTX 6.0 mg/kg
NF- $\kappa$ B p65 cells	28.00 $\pm$ 12.35	26.00 $\pm$ 8.62	56.28 $\pm$ 15.69	75.17 $\pm$ 17.05 **

Results were expressed in number of cells positive to NF- $\kappa$ B p65 and as mean  $\pm$  SD. Results were obtained from three animals from each treatment group. Statistical comparisons were made using the t-test for adult group and the Mann–Whitney test for infant group: \*\*  $p < 0.01$ , MTX 6.0 mg/kg vs. control. Three animals per treatment, and for each animal, six photos of different areas of cardiac tissue were evaluated and quantified using ImageJ software version 1.52a.

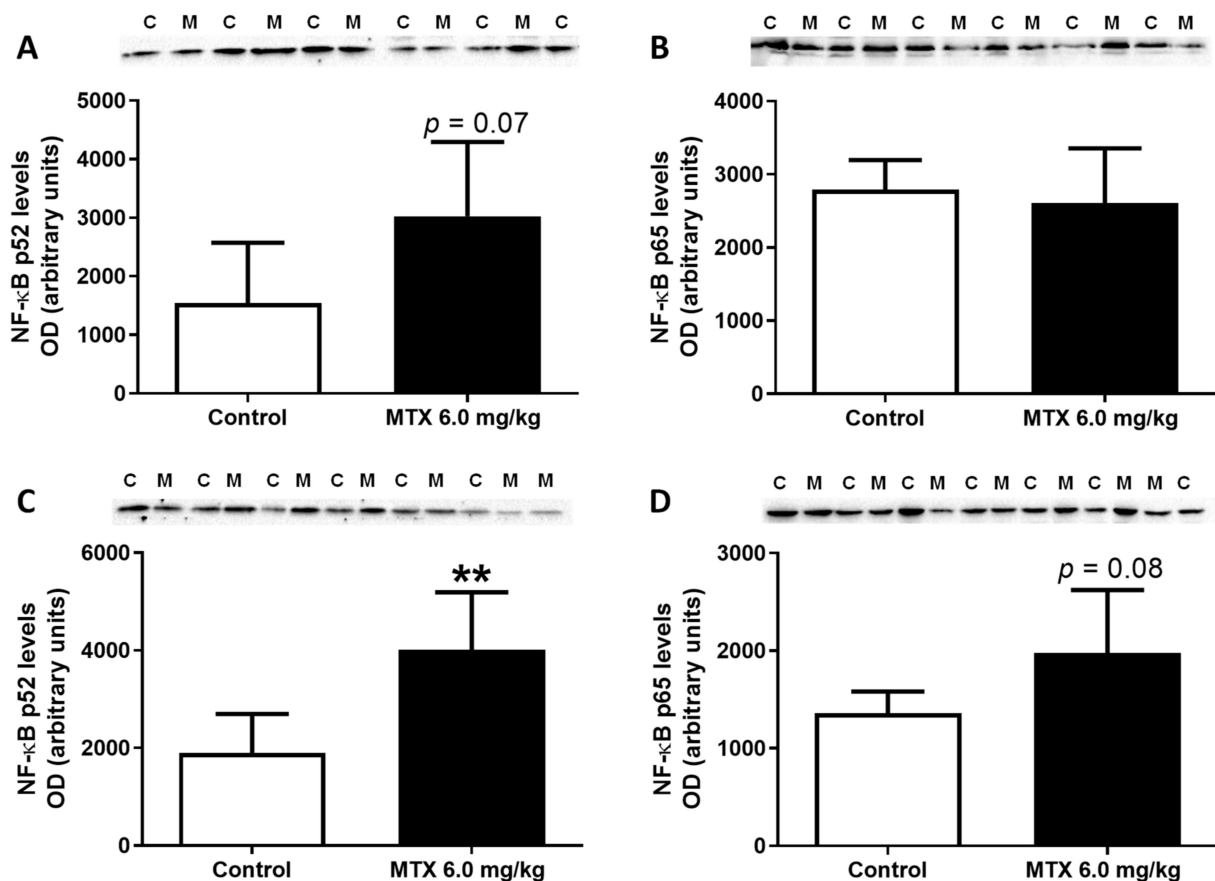


**Figure 10.** Nuclear kappa B nuclear transcription factor (NF- $\kappa$ B) p52 (50 kDa) and NF- $\kappa$ B p65 (60 kDa) expression evaluated by Western blotting, from (A,B) infant MTX-treated (M) and control (C) mice, and (C,D) adult mice exposed to a cumulative dose of 6.0 mg/kg MTX (M) and respective controls (C) (experiment 2, infant and adult mice were euthanized 17 or 7 days after the last administration, respectively). Values are expressed as mean  $\pm$  SD and were obtained from 5–6 (infant) and 6–7 (adult) animals from each treatment group. Statistical comparisons were made using the t-test: \*\*  $p < 0.01$ , MTX 6.0 mg/kg vs. control. OD: optic density. Protein loading was confirmed by the Ponceau S staining (Figures S3 and S4).

### 2.12. MTX Increased TNF- $\alpha$ Cardiac Expression while it Decreased IL-6

TNF- $\alpha$  was evaluated and MTX-treated adult mice had a significant increase in its expression in comparison with the control group (Figure 11D), while MTX-treated infant mice showed a tendency for increased TNF- $\alpha$  levels ( $p = 0.09$ ) in comparison with the control group (Figure 11A).

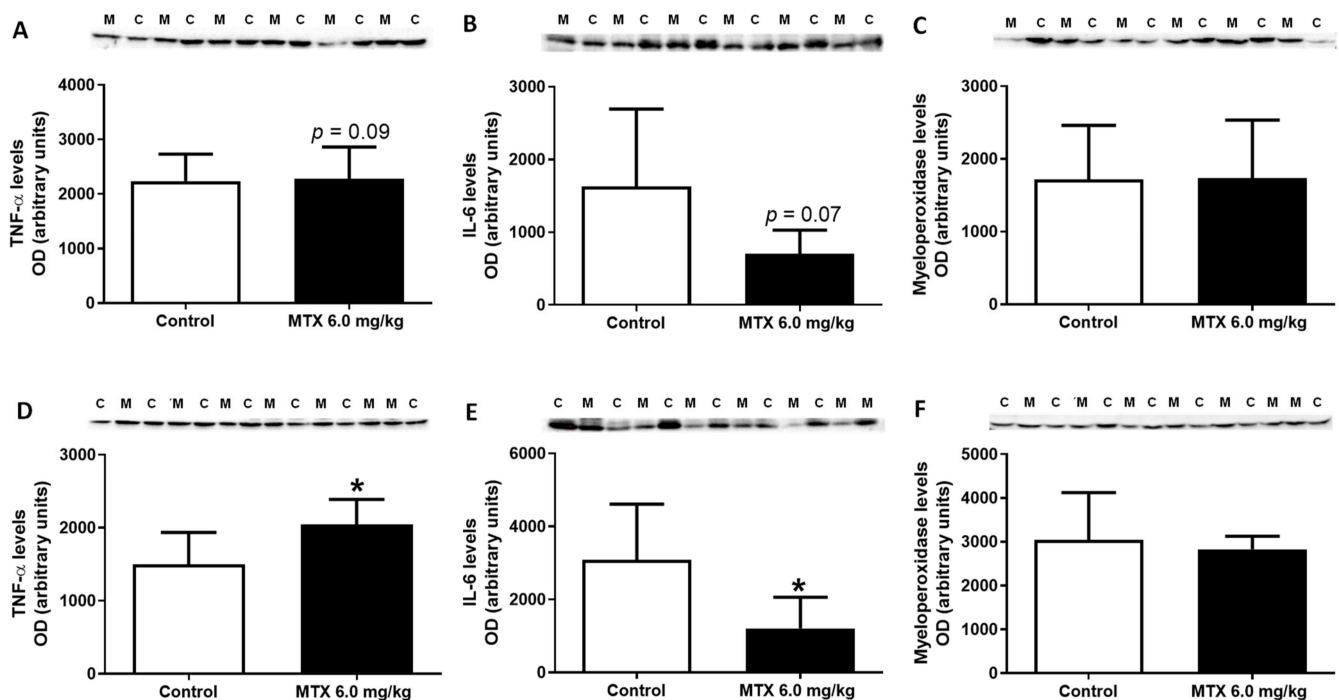


**Figure 11.** Tumour necrosis factor- $\alpha$  (TNF- $\alpha$ ) (25 kDa), interleukin-6 (IL-6) (24 kDa), myeloperoxidase (48 kDa) expression evaluated by western blotting, from (A–C) infant MTX-treated (M) and control (C) mice, and (D–F) adult mice exposed to a cumulative dose of 6.0 mg/kg MTX (M) and respective controls (C) (experiment 2, infant and adult mice euthanized 17 or 7 days after the last administration, respectively). Values are expressed as mean  $\pm$  SD and were obtained from 6 (infant) and 6–7 (adult) animals from each treatment group. Statistical comparisons were made using the t-test: \*  $p < 0.05$ , MTX 6.0 mg/kg vs. control. OD: optic density. Protein loading was confirmed by the Ponceau S staining (Figures S3 and S4).

Conversely, MTX significantly decreased IL-6 levels in the heart of MTX-treated adult mice (Figure 11E), while the MTX-treated infant mice only showed a tendency for decreased IL-6 levels ( $p = 0.07$ ) in comparison with the respective control group (Figure 11B).

Finally, data showed that MTX did not alter the expression of myeloperoxidase in both populations (Figure 11C,F).

### 3. Discussion

The major findings of this work were: (1) MTX treatment affected animals' body weight and food/water consumption; (2) histopathological examination showed that all MTX-treated groups had cardiac injury, being more severe in adults, and only adults had a significant increase in fibrotic tissue, in both MTX doses; (3) infants showed some adaptation features after MTX, namely the highest cumulative dose of MTX led to increased tGSH levels, while the expression of GAPDH and glutathione peroxidase only increased in 6.0 mg/kg MTX-treated infant animals; (4) the lower cumulative dose (6.0 mg/kg) elicited an increase in catalase expression, in both adult and infant mice; (5) in adults, noradrenaline cardiac levels decreased after 7.0 mg/kg MTX, whilst at the lower cumulative dose, protein carbonylation and the expression of NF- $\kappa$ B p65 and p52 subunits, and M1 macrophage marker increased; (6) TNF- $\alpha$  and IL-6 were differentially expressed within the myocardium in response to administration of MTX 6.0 mg/kg.

In experiment 1, the 7.0 mg/kg MTX-treated adult group had significantly less body weight compared to controls, whereas changes in body weight in the infant population were only seen after the 17th day. In fact, in experiment 2, the lowest dose of 6.0 mg/kg of MTX also caused a statistically significant body weight decrease in the adult population after the 21st day. We observed that, in general, food and water intake decreased in the following days after MTX-administration. Several studies reported a loss of body weight in mice after MTX administration [34–37]. Signs of diarrhoea after the last administration



of MTX in adults were seen, but not in infants, and therefore this fact can contribute to the weight decrease. In humans, MTX induces gastrointestinal alterations, such as nausea, vomiting, diarrhoea, and mucositis [6].

Plasma AST, ALT, total-CK, and CK-MB levels were measured in animals of both experiments. In experiment 1, no significant differences in the aminotransferase levels (AST and ALT) were found. However, a tendency for an increase was observed in the AST/ALT ratio of the 7.0 mg/kg MTX-treated adult population. An increased AST/ALT ratio has been proposed as a marker for the assessment of heart damage [38]. Dores-Sousa et al. also showed that animals sacrificed 24 h after the last MTX administration (9.0 mg/kg cumulative dose given in six administrations) had no significant differences in the aminotransferase levels in any of the MTX-treated groups [34]; nevertheless, three weeks after the last administration, AST/ALT ratio increased in the remaining infant mice, suggesting heart damage [34]. In experiment 2, only the 6.0 mg/kg-treated infant population had elevated ALT levels, while the AST/ALT ratio was found to be significantly decreased. Other authors reported increased ALT levels in rats treated with a cumulative dose of 7.5 mg/kg of MTX [39]. Therefore, the classic markers of heart damage were not a good correlation to the damage seen in this lower dose, either in earlier time point in adults or later time point in infants.

Regarding total-CK and CK-MB, in experiment 1, the 7.0 mg/kg cumulative MTX dose induced a significant elevation in plasma CK-MB in infant mice, which may be indicative of recent cardiac damage. In another study, mice treated with MTX [three doses of 2.5 mg/kg MTX (intraperitoneal (IP))], had increased serum levels of CK-MB [40]. In addition, the total-CK values of the 7.0 mg/kg MTX-treated adults were significantly higher than controls, which suggests that the overall muscle activity apparently is changed by MTX. No significant differences were seen in the 6.0 mg/kg MTX mice. Conversely, the heart weight/body weight ratio decreased in MTX-treated adult mice at a cumulative dose of 6.0 mg/kg. On the contrary, an increase in cardiac weight in rats 28 days after administering three doses of 2.5 mg/kg MTX was reported [37], suggesting different adaptation stages.

MTX treatment resulted in cardiac tissue damage manifested by histopathological changes. The histological examination of both right and left ventricles of the 7.0 mg/kg MTX-treated heart revealed cellular oedema, necrotic zones, signs of vacuolization, interstitial inflammatory cell infiltration, all signs of cellular degeneration. In the 6.0 mg/kg MTX-treated mice, signs of vascular congestion were observed, with enlarged blood vessels, inflammatory infiltrations in the interstitial spaces of the cardiomyocytes, and proliferation of connective tissue, large and uncondensed nucleus, the presence of cytoplasmic vacuolization, as well as some necrosis. Signs of obstruction in some small calibre arteries were observed in the 6.0 mg/kg MTX-treated adult mice. These changes were more evident in the sub-endocardial region when compared with the sub-pericardial one. According to the published literature, MTX produces degenerative cardiomyopathy evidenced by micro- and macro-vacuolization, intercellular oedema, atrophy, inflammatory infiltrates, aberrant mitochondria, myolysis of cardiomyocytes, and interstitial fibrosis in rodents [34,37,41,42], and humans [43]. These features were also observed herein, thus highlighting the relevance of our model. In the semi-quantitative histological analysis, the changes in heart tissue in infant mice occurred at a lower extent than in adults, in both cumulative doses. While one would expect that cardiac plasma toxicity markers would be increased in both studied populations, since histological damage was observed, that did not occur in the majority of the determinations. Whether the clearance of those markers from plasma, because of earlier damage or if the biomarkers are not sensitive enough for the damage endured, is not clear at this point.

The sympathetic and adrenal systems are key for cardiac function, and noradrenaline is the main neurotransmitter/hormone responsible for the rapid adjustment of the heart to the body's needs. In infant mice, the cardiac levels of noradrenaline did not suffer any significant changes, while adults treated with 7.0 mg/kg MTX had lower levels of nora-

drenaline than controls. In a previous work by the group, a cumulative dose of 9.0 mg/kg of MTX also caused a statistically significant decrease in cardiac noradrenaline levels in adults, suggesting that MTX causes noradrenergic dysfunction in adult animals [34], while not affecting infants. Age-associated changes in the autonomic nervous system are linked to increased cardiac sympathetic tone with decreased parasympathetic input, dampened cardiovagal baroreceptor sensitivity, and reduced clearance of plasma noradrenaline [44], which seems to be exacerbated by MTX.

Another crucial aspect of cardiac homeostasis relates to the hearts' energetic balance. The primary source of energy in the heart is phosphocreatine, which maintains local ATP pools and stabilizes cellular membranes due to electrostatic interactions with phospholipids [45]. Phosphocreatine has the ability to stabilize membranes and protect cells from damage [46]. In experiment 1, in the adult population treated with 7.0 mg/kg of MTX, a tendency existed for increased phosphocreatine levels, while no significant changes of creatine and phosphocreatine levels in infant mice were seen. The increased phosphocreatine seen in the MTX-treated adults may be an attempt to protect the cells or to stimulate protein synthesis [46]. It is clear that the phosphocreatine system is important to promote de novo synthesis of ATP, by means of CK action [47]. However, no changes in cardiac ATP were verified in the heart of both MTX-treated mice compared to controls. Similar results were reported by others, namely with a cumulative dose of 9.0 mg/kg, when animals were sacrificed 24 h after the last administration [34] or at a 7.5 mg/kg cumulative dose and sacrificed 2 days after the last administration [37]. Nevertheless, in the work of Rossato et al., when rats were administered with the cumulative dose of 7.5 mg/kg MTX but sacrificed 28 days after the last administration, a significant depletion of cardiac ATP levels took place, suggesting that ATP depletion is a late event [37], possibly because response/adaptation towards insult is probably overcome at that stage. The heart consumes large amounts of energy in the form of ATP that is continuously replenished by oxidative phosphorylation in mitochondria and, to a lesser extent, by glycolysis. Despite unchanged ATP synthase subunit beta levels, the expression of the glycolytic enzyme GAPDH was significantly higher in the MTX-treated infant mice (6.0 mg/kg), while glycolytic ratio (GAPDH/ATP synthase subunit beta) changes were seen in adults sacrificed earlier, suggesting that although the infant mice are more resilient to the highest dose, later on (17 days) a metabolic shift to glucose oxidation occurs, which may be a determinant sign of damage. A shift from the oxidation of fatty acids to increased oxidation of glucose, along with the inhibition of OXPHOS activity, has been described for another topoisomerase IIb inhibitor, doxorubicin, being these key features of heart damage [48]. Recently, our group has shown through a proteomic study in mitochondrial enriched fractions that MTX also causes downregulation of the fatty oxidation metabolic process [49].

Although MTX has been considered with a low ability to induce oxidative stress, several studies have been focused on those markers when MTX heart damage is being researched [34,37,50]. While in adults given a 7.0 mg/kg cumulative dose of MTX, no significant changes in the cardiac levels of the tGSH, GSSG, and GSH/GSSG ratio were found, in the infants that took the same cumulative dose, cardiac tGSH levels increased significantly. Dores-Sousa et al. had similar results when 9.0 mg/kg of MTX was administered to infant mice that presented the highest values of tGSH three weeks after the last administration. The authors suggested that there was an adaptation response of that population related to an up-regulation of  $\gamma$ -glutamylcysteine synthetase ( $\gamma$ -GCS) activity in the younger population [34]. In that sense, a recent work of the group showed that cardiac HL-1 cells exposed to MTX also had higher levels of tGSH, and that this increase was abrogated by the  $\gamma$ -GCS inhibitor, buthionine sulfoximine. On the other hand, in the 6.0 mg/kg MTX-treated infant and adult animals, in experiment 2, no differences in tGSH and GSSG values or ratios were observed; similarly, other authors also reported no statistically significant changes in the cardiac GSH levels in animals treated with an acute dose of 15.0 mg/kg of MTX, 4 days after administration [50], or with a cumulative dose of 7.5 mg/kg of MTX, 28 days after administration [37], thus advocating that the

cumulative dose and most likely the possibility of adaptation of the infant population may be determinant for de novo GSH synthesis. The levels of MDA, a marker of lipid peroxidation, were evaluated in the cumulative dose of 7.0 mg/kg in infant and adult mice, and no statistically significant changes were observed. Our data corroborate that, although MTX clearly induces cardiac damage, it has a low capacity to induce oxidative stress and lipid peroxidation. In fact, in our work, MTX (6.0 mg/kg) did not alter the expression of SOD2/MnSOD but significantly increased the levels of catalase in the heart of both adult and infant mice. Since catalase plays an important role in breaking down H<sub>2</sub>O<sub>2</sub> and maintaining cellular redox homeostasis, this increase may be due to the adaptation of the cells to damage caused by MTX. In fact, in low mitochondrial oxygen consumption, an increase of H<sub>2</sub>O<sub>2</sub> production occurred in skeletal muscle, which was accompanied by fatty acids  $\beta$ -oxidation. Nevertheless, catalase transfection and overexpression led to the normalization of energetic pathways [51]. Furthermore, and regarding glutathione peroxidase, its expression increased significantly in the heart of infant mice, 17 days after the last administration, suggesting that the heart is adjusting to MTX and that could give infant mice more protection concerning the MTX-induced oxidative injuries. That protection can be seen as infants had less histological damage than adults did.

The general conviction is that in *in vivo* models, MTX does not increase lipid peroxidation, serum lipids, or significantly alter the redox status of the heart, indicating that oxidative stress does not play a major role in MTX-induced cardiac damage [37,41,52]. Even so, a recent work by our group showed that MTX might increase protein oxidative damage [53]. Herein, protein carbonylation increased significantly in the heart of adult mice (6.0 mg/kg) exposed to MTX, suggesting that MTX is able to cause permanent changes in proteins. Protein carbonylation may lead to protein partial or total function inactivation, with a wide range of downstream functional consequences, subsequent cellular dysfunction, and tissue damage [54]. A previous work also showed that adult mice treated with a 9.0 mg/kg cumulative dose of MTX had increased heart protein carbonylation, 24 h after the last administration, while in infants those changes were not seen in the heart [34]. Once again, infants seemed more protected towards MTX-inflicted damage. Whether that happens because they are able to activate antioxidant defences, as seen earlier, or they have higher intrinsic proteasome activity, needs to be further looked at.

Despite the low impact of MTX at 6.0 mg/kg dose on oxidative stress markers, cardiac immunohistochemical analysis revealed that MTX significantly increased the expression of NF- $\kappa$ B p65 subunit. Subsequently, a Western blot analysis indicated that the MTX-treated adult mice showed a tendency for increased expression of NF- $\kappa$ B p65 levels ( $p = 0.08$ ), the canonical NF- $\kappa$ B pathway, and significantly enhanced the expression of NF- $\kappa$ B p52 levels, the noncanonical pathway of this transcription factor. Activation of the canonical NF- $\kappa$ B pathway provides rapid responses (within minutes) [55]. In contrast, the noncanonical pathway is comparatively slower (activated within hours) and can be sustained for longer periods [55]. NF- $\kappa$ B plays an important role in regulating inflammatory response and its activation alters the phenotype of macrophages [56]. In this study, the MTX-treated adult mice showed a higher density of infiltrating M1 macrophages. Macrophages have an important role in the innate immune system and have been described to be relevant cells within the cardiovascular system [57,58]. The increase of cardiac macrophages in adult mice can suggest that upon MTX-induced lesions, an immunologic response is induced, resulting in infiltration of inflammatory cells. M1 macrophages are involved in pro-inflammatory responses and following activation, they produce pro-inflammatory cytokines such as IL-1, IL-6, IL-12, and TNF- $\alpha$ , and chemokines [56]. Notably, MTX administration significantly altered the expression of pro-inflammatory cytokines, increasing TNF- $\alpha$  and decreasing IL-6 in mice cardiac tissue, reaching statistical significance in adult mice. The 26S proteasome activity has a role in substantially augmenting the generation of pro-inflammatory cytokines, although immunoproteasome activity differs with aging [59]. Whether differences in the activity of proteasome on different ages implicate differential results seen in protein carbonylation and in cytokine levels needs to be determined in more

detail. Nonetheless, the pro-inflammatory cytokines such as TNF- $\alpha$  and IL-6, are responsible for the development and progression of cardiovascular diseases [60]. TNF- $\alpha$  has been implicated in patients with newly diagnosed HF, where increased levels are associated with ventricular hypertrophy, ventricular dilatation, interstitial infiltrates, interstitial fibrosis, rare myocyte apoptosis, a diminished ejection fraction, attenuation of  $\beta_1$ -adrenergic responsiveness, and expression of atrial natriuretic factor in the left ventricle [21]. IL-6 is involved in inflammation but reveals additional cardiovascular properties through the regulation of cardiomyocyte hypertrophy and apoptosis [61]. Under stressful conditions, namely excessive hemodynamic stimulation and mechanical stress, cytokines promote and sustain an unbalanced status within the myocardium, with enhanced production of TNF- $\alpha$  accompanied by a simultaneous reduction of IL-6 levels and insulin-like growth factor (IGF)-1, that may critically contribute to the development of the HF phenotype [62]. Doxorubicin is an anthracycline often used in cancer that shares similar clinical cardiotoxicity with MTX. It has been shown that doxorubicin caused a significant increase in the production of pro-inflammatory interleukins (IL-8, IL-6, and IL-1 $\beta$ ) in vitro, showing the possible importance of inflammation on doxorubicin-induced cardiotoxicity [63]. Moreover, nanoemulsions loaded with anti-inflammatory nutraceuticals inhibited the secretion of inflammatory cytokines IL-6, IL-8, IL-1 $\beta$ , and TNF- $\alpha$  from cardiac cells incubated with doxorubicin, suggesting that anti-inflammatory drugs activated molecular mechanisms of cardioprotection during doxorubicin treatment [64]. Nevertheless, the inflammatory pathways are also affected by immune checkpoint inhibitors, nivolumab and ipilimumab, that caused changes in NLRP3 inflammasome, MyD88 complex NF- $\kappa$ B/p65 expression, and in several interleukins in co-cultures of lymphocytes with tumor or with cardiac cells. Those changes in several inflammatory signals were also seen in the heart after ipilimumab in an in vivo model [65]. While in peripheral blood mononuclear cells of secondary progressive MS patients, MTX was reported to not seemly influence the production of inflammatory mediators, IL-6, IL-12p40, IL-10, and TGF- $\beta$  [66], our data shows other results in the heart. Our data may in fact reveal other pathways of MTX-induced cardiotoxicity.

#### 4. Materials and Methods

$\beta$ -Nicotinamide adenine dinucleotide 2'-phosphate reduced (NADPH) tetrasodium salt hydrate was acquired from PanReac AppliChem ITW Reagents (Barcelona, Spain). Ethylenediaminetetraacetic acid (EDTA), perchloric acid (HClO<sub>4</sub>), sodium hydroxide (NaOH), magnesium chloride (MgCl<sub>2</sub>), sodium carbonate (Na<sub>2</sub>CO<sub>3</sub>), disodium phosphate (Na<sub>2</sub>HPO<sub>4</sub>), copper (II) sulphate (CuSO<sub>4</sub>), potassium bicarbonate (KHCO<sub>3</sub>), potassium dihydrogen phosphate (KH<sub>2</sub>PO<sub>4</sub>), magnesium sulphate (MgSO<sub>4</sub>), potassium chloride (KCl), Histosec paraffin pastilles, and FolinCiocalteu reagent, mouse monoclonal dinitrophenyl (DNP)-KLH (MAB2223) were purchased from Merck (Darmstadt, Germany). Bio-Rad DC protein assay kit was purchased from Bio-Rad Laboratories (Hercules, CA, USA). Phosphate buffered saline solution (PBS) was purchased from Biochrom (Berlin, Germany), sodium chloride (NaCl), and sodium dodecyl sulphate (SDS) from VWR (Leuven, Belgium), potassium sodium tartrate from Fluka (Buchs SG, Switzerland), methanol, DPX mounting media, and xylene from Thermo Fisher Scientific (Loughborough, UK). Harris haematoxylin was purchased from Harris Surgipath (Richmond, IL, USA), eosin 1% aqueous from Biostain (Traralgon, Australia), and Isoflurane (Isoflo<sup>®</sup>) was obtained from Abbott Animal Health (North Chicago, IL, USA). ABX Pentra reagents were purchased from HORIBA (Kyoto, Japan). Enhanced chemiluminescence (ECL) reagents, and 0.45  $\mu$ m Amersham Protran nitrocellulose blotting membrane were purchased from GE Healthcare Bio-Sciences (Pittsburgh, PA, USA). Mouse monoclonal anti-ATP synthase subunit beta (ab14730), rabbit polyclonal anti-GAPDH(ab9485), rabbit polyclonal anti-IL-6 (ab83339), rabbit polyclonal anti-NF- $\kappa$ B p65 (ab16502), mouse monoclonal anti-NF- $\kappa$ B p100/p52 (ab71108), rabbit polyclonal anti-TNF- $\alpha$  (ab66579), rabbit polyclonal anti-SOD2/MnSOD (ab13534), rabbit polyclonal anti-catalase (ab16731), rabbit polyclonal anti-glutathione peroxidase 1 (ab22604), rabbit polyclonal anti-myeloperoxidase (ab139748), rabbit poly-

clonal anti-mannose receptor (M2 macrophage, ab64693), rabbit polyclonal anti-CD68 (M1 macrophage, ab125212), goat anti-rabbit IgG-horseradish peroxidase (ab97051) and rabbit anti-mouse IgG-horseradish peroxidase (ab6728) from Abcam (Cambridge, UK). 3,3'-Diaminobenzidine (DAB), HIGHDEF<sup>®</sup> DAB chromogen/substrate set was purchased from Enzo Life Sciences (Miraflores, Portugal). Water was purified with a Milli-Q Plus ultrapure water purification system (Millipore, Bedford, Massachusetts, USA). All the other reagents used were purchased from Sigma Aldrich (St. Louis, MO, USA).

#### 4.1. Animals

Male CD-1 mice (*Mus Musculus*) were acclimated for a week before experiments began and were accompanied by experienced veterinarians during all experimental procedures. Temperature ( $22 \pm 2$  °C) and humidity ( $50 \pm 10\%$ ) were maintained at appropriate intervals, during 12-hour light–dark cycles. The animals were kept in groups of 3 per cage, with environmental enrichment always present. The mice were maintained on a rodent diet (with 4RF21 GLP certificate diet from Mucedola, Settimo Milanese, Italy) and with autoclaved water given ad libitum according to the guidelines defined by the European Council Directive (2010/63/EU) transposed into Portuguese legislation (Decreto-Lei no. 113/2013). Considering the animals' welfare, a "scoring system" was created (Table S1) to evaluate and minimize their suffering and stress. All experiments with animals were handled with the approval of the local animal welfare body (ICBAS-UP ORBEA) and the Portuguese national authority for animal health (DGAV, processes no. 0421/000/000/2013 and 0421/000/000/2016).

#### 4.2. Experimental Protocol

Male CD-1 mice have been considered a good model to mimic the effects of MTX therapy in two different life stages [34]. Herein, infant and adult mice were used: the mice in the infant group weighed 10–12 g and were 3–4 weeks old, while mice in the adult group weighed 38–56 g and were 8–12 weeks old. According to the literature, infant mice had not entered puberty (equivalent to children), since in this stage of development 1 human year corresponds to 56.77 mice days [67,68], meaning that at the beginning of the administrations, the age of infant mice corresponded to roughly 135–180 human days. On the other hand, the mice at 8 to 12 weeks old clearly reached the young adulthood phase [67,68], since adult mice reach sexual maturity on average at 10 weeks, while in humans, this stage corresponds to an average age of 20 years [67,68].

#### 4.3. Administration Schedule

Since MTX is given in cycles and throughout multiple administrations in humans, the experiments herein enclosed aimed to mimic human MTX-therapy, and drug administration was interrupted by free-drug periods [34]. Furthermore, allometric scaling was used to ensure that the cumulative dose of MTX administered did not exceed the maximum MTX recommended in humans [69,70], as to maintain clinical relevance. Two cumulative doses were given: 6.0 mg/kg MTX and 7.0 mg/kg MTX. In infants (to convert dose in mg/kg to dose in mg/m<sup>2</sup>, we multiply by Km factor 25), it corresponded in human equivalent to 33.5 mg/m<sup>2</sup> and 39.1 mg/m<sup>2</sup>, respectively [69,70]. In adult mice (Km factor 37), the cumulative doses of 6.0 mg/kg MTX and 7.0 mg/kg MTX had a human equivalent of 36.3 mg/m<sup>2</sup> and 42.3 mg/m<sup>2</sup>, respectively [69,70]. These calculations were estimated from the general body weight of infant (8.0 kg) and adult (70.0 kg) human population [69,70] at the ages calculated previously.

The mice received IP administrations of MTX, in the afternoon period, to decrease MTX-induced lethality attributed to the daily circadian rhythm [35]. In humans, MTX is administered intravenously, but in mice, the IP route affords the same cardiac effects of MTX [34], while avoiding the high risk of extravasation of the endovenous route that can lead to tissue necrosis [71]. The doses were delivered through 6 IP injections (two per week), alternating between the left and right side of the abdomen in order to avoid extra injury

and pain. MTX dihydrochloride was dissolved in sterile 0.9% saline solution. Control mice were injected with saline solution (0.9% NaCl) in the same volume and conditions as MTX-treated mice. During the experimental period, food and water intake, body weight, and animal welfare were assessed daily.

#### 4.4. Blood Collection and Plasma Biomarkers

Animals were anesthetized through the inhalation of 5% isoflurane and then sacrificed by exsanguination when fully sedated. After euthanasia, the animal's abdominal cavity was exposed, and blood was collected in the inferior vena cava into EDTA-containing tubes. Blood was then centrifuged (920 g, 10 min, 4 °C), and the obtained plasma was stored at −20 °C for the determination of AST, ALT, CK-MB, and total-CK. Plasma biomarkers were determined through enzymatic assays in the apparatus ABX Pentra 400 with ABX Pentra reagents (Japan), according to the manufacturer's instructions.

#### 4.5. Tissue Collection

Hearts were removed, weighed, and processed as follows: (1) segments of heart that covered both the left and right ventricle were placed in 4% paraformaldehyde, pH 7.2–7.4, and used for histological and immunohistochemistry analysis; (2) cardiac sections of the same segments were placed in complete RIPA buffer (50 mM Tris-HCl, 150 mM NaCl, 1% Triton X-100 (*v/v*), 0.5% sodium deoxycholate (*w/v*), and 0.1% SDS (*w/v*), pH 8.0, supplemented with 0.25 mM phenylmethanesulfonyl fluoride (PMSF), 1 mM sodium metavanadate (Na<sub>3</sub>VO<sub>4</sub>), 10 mM sodium fluoride (NaF), 1 mM DL-dithiothreitol (DTT) and 0.5% (*v/v*) complete protease inhibitor cocktail and stored at −80 °C for immunoblotting analysis; and (3) the remaining heart was homogenized with an Ultra-Turrax<sup>®</sup> homogenizer in ice-cold 0.1 M phosphate-buffered solution, pH 7.4. The homogenate was aliquoted for other determinations (namely protein determination by the Lowry method [72]) or placed to a final concentration of 5% HClO<sub>4</sub> [for ATP, tGSH, GSH, and GSSG, catecholamines, and lipid peroxidation]. All steps were performed on ice.

#### 4.6. Histological Analysis of Heart Tissue

All histological procedures were conducted according to previously published procedures [34]. Sections were subjected to haematoxylin and eosin for routine histological evaluation and Sirius red for fibrous tissue. The slides were examined and photographed with a Carl Zeiss Imager A1 light microscope equipped with an AxioCam MRc 5 digital camera (Oberkochen, Germany). Histopathological evidence of tissue damage was calculated according to its severity and incidence in every slide, as previously published [34]. Sections stained with Sirius red were used to assess collagen deposition, which was evaluated using ImageJ software (version 1.52a, <http://imagej.nih.gov/ij>, Wayne Rasband, NIH, Bethesda, MD, USA). The results of collagen content are expressed as a percentage of collagen fibres, as previously detailed [34].

#### 4.7. Determination of Cardiac Noradrenaline Levels

In experiment 1, cardiac noradrenaline levels were determined, as described before [34]. For a more ascertain identification of the chromatographic peaks in heart samples, two independent procedures were used: comparison of retention time with pure standards and spiking the samples with standards of noradrenaline.

#### 4.8. Measurement of ATP Levels

ATP levels were determined by a bioluminescent assay based on the luciferin-luciferase reaction, as previously described [34,73]. The results were expressed as nmol of ATP per mg of protein (nmol ATP/mg protein).

#### 4.9. Determination of Cardiac Creatine and Phosphocreatine Levels

In experiment 1, cardiac creatine and phosphocreatine levels were evaluated, as described [34]. The phosphocreatine levels were calculated setting the difference between total creatine and free creatine.

#### 4.10. Measurement of tGSH, GSH, and GSSG

tGSH and GSSG levels were evaluated by the DTNB-GSSG reductase recycling assay, as previously described [34,74]. The levels of GSH were calculated by the formula:  $GSH = tGSH - 2 \times GSSG$ . The results of tGSH, GSH, and GSSG were normalized to the total protein content and were expressed as nmol of GSH or GSSG per mg of protein (nmol GSH/mg protein or nmol GSSG/mg protein).

#### 4.11. Assessment of Lipid Peroxidation

Lipid peroxidation was measured by assessing MDA values and comparing them with a standard curve of MDA after reaction with thiobarbituric acid (TBA). The analysis of MDA-equivalent content in standards and samples was performed by high-performance liquid chromatography, as previously described [34].

#### 4.12. Protein Carbonylation by Slot Blot Analysis

Heart sections were lysed in RIPA buffer (supplemented with PMSF, DTT, NaF,  $Na_3VO_4$ , and a cocktail of protease inhibitors) through sonication and were kept at  $-80\text{ }^\circ\text{C}$  until analysis. Samples containing 20  $\mu\text{g}$  of protein (as assessed by the Bio-Rad DC Protein assay) were then processed as previously described [75]. Immunoreactive bands were detected, and digital images were acquired using the ChemiDoc Imaging System version 2.3.0.07 (Bio-Rad, Hercules, CA, USA). The obtained images were analysed with Image Lab software version 6.0.1 (Bio-Rad, Hercules, CA, USA).

#### 4.13. Western Blotting Analysis

Heart tissue was lysed in a lysis buffer (RIPA supplemented with PMSF, DTT, NaF,  $Na_3VO_4$ , and a cocktail of protease inhibitors). The amount of total protein was quantified using the Bio-Rad DC Protein assay, and then the total protein (20  $\mu\text{g}$  from each sample) was fractionated by electrophoresis on a 12.5% SDS-PAGE. Gels were blotted onto a nitrocellulose membrane (Amersham Protran, GE Healthcare, Germany) in a transfer buffer (25 mM Tris, 192 mM glycine, pH 8.3, and 20% methanol) for 2 h (200 mA). Then, nonspecific binding was blocked with 5% (*w/v*) dry non-fat milk in TBS-T (100 mM Tris, 1.5 mM NaCl, pH 8.0 and 0.5% Tween 20). Membranes were incubated with primary antibody diluted 1:1000 (mouse anti-ATP synthase subunit beta, rabbit anti-GAPDH, mouse anti-NF- $\kappa\text{B}$  p100/p52, rabbit anti-NF- $\kappa\text{B}$  p65, rabbit anti-SOD2/MnSOD, rabbit anti-glutathione peroxidase 1) or 1:500 (rabbit anti-IL-6, rabbit anti-TNF- $\alpha$ , rabbit anti-catalase, and rabbit anti-myeloperoxidase) in 5% *w/v* non-fat dry milk in TBS-T, for 2 h at room temperature or overnight, washed and incubated with secondary horseradish peroxidase-conjugated anti-rabbit (1:10,000) or anti-mouse (1:5000). Immunoreactive bands were detected by enhanced chemiluminescence ECL (Amersham Pharmacia Biotech) according to the manufacturer's indications. The immunoreactive bands were detected using the ChemiDoc Imaging System version 2.3.0.07 (Bio-Rad, Hercules, CA, USA). The obtained images were analysed with Image Lab software version 6.0.1 (Bio-Rad, Hercules, CA, USA). Protein loading was confirmed by the Ponceau S staining.

#### 4.14. Immunohistochemistry

The detection of NF- $\kappa\text{B}$  subunit p65 and M1 and M2 macrophage markers was performed by immunohistochemistry in a protocol already described [76], where we made minor modifications. After heart tissue was deparaffinized, antigens were unmasked by the pressure cooker antigen-retrieval procedure: slides were immersed in 10 mM citrate buffer, pH 6.0, at  $100\text{ }^\circ\text{C}$  and were placed in a pressure cooker for 10 min and then cooled

for 20–30 min. Following the blocking step, each slide was incubated with anti-NF- $\kappa$ B p65 polyclonal rabbit antibody (1:50), or anti-mannose receptor polyclonal rabbit antibody (M2 macrophage) (1:50), or anti-CD68 polyclonal rabbit antibody (M1 macrophage) (1:50) in PBS containing 0.05% Tween 20 (*v/v*) (PBS-T) overnight (4 °C). After washing four times (5 min each) with PBS, the sections were incubated for 2 h, at 37 °C with a goat anti-rabbit IgG-horseradish peroxidase secondary antibody (1:100) in PBS-T. The sections were then washed four times (5 min) under gentle stirring and incubated with DAB reagent for 1 min. After washing, the slides were counterstained with a solution of haematoxylin-water (1:11) for 3 min and once again washed. Finally, slides were mounted in DPX medium with coverslips and routine procedures followed. Negative controls were performed as described, with the omission of the primary antibody incubation step. All preparations were analysed in a Carl Zeiss Imager A1 light microscope and images were recorded with a coupled AxioCam MRc5 digital camera (Oberkochen, Germany). The semi-quantitative analysis of IHC images was made using ImageJ software (version 1.52a, <http://imagej.nih.gov/ij>, Wayne Rasband, NIH, Bethesda, MD, USA).

#### 4.15. Statistical Analysis

Results are expressed as mean  $\pm$  standard deviation (SD). Statistical analyses of animal weight, food, and water intake data were carried out by the two-way analysis of variance (two-way ANOVA) followed by the Sidak post hoc test. When two groups and one time point were analysed, the outliers were identified using the ROUT method ( $Q = 1\%$ ) first and then statistical analysis was performed by the Student's *t*-test when the distribution was normal or by the Mann–Whitney test when the distribution was not normal. Statistical significance was considered when *p* values  $<0.05$ . To perform the statistical analysis, the GraphPad Prism 8.0 software program (San Diego, CA, USA) was used.

## 5. Conclusions

Inflammation plays a key role in the development and progression of cardiovascular diseases. To the best of our knowledge, this is the first time that inflammatory signals were shown to play an important role on MTX-induced cardiotoxicity. Overall, our work demonstrates inflammation in cardiac tissue even when no major changes were observed in the redox status and the ATP cardiac levels in mice exposed to lower doses of MTX. Moreover, MTX administration caused dissimilar responses in adult and infant mice, which may be linked to the highest antioxidant adaptation of infant or repair ability. Nonetheless, more research is warranted to investigate the involvement of inflammation on MTX-induced cardiotoxicity or if targeting specific mechanisms of the immune system will be advantageous to reverse cardiotoxicity of this anticancer drug.

**Supplementary Materials:** The following are available online at <https://www.mdpi.com/article/10.3390/ph14060510/s1>, Figure S1. [A, B] Body weight in [A] infant and [B] adult mice exposed to a cumulative dose of 7.0 mg/kg MTX. [C and D] Water consumption of [C] infant and [D] adult mice exposed to a cumulative dose of 7.0 mg/kg MTX. [E, F] Food consumption of [E] infant and [F] adult mice exposed to a cumulative dose of 7.0 mg/kg MTX. Results are presented in grams (g) of food intake/day/weight of animal, mL of water intake/day/weight of animal, or g of body weight, and as mean  $\pm$  standard deviation (SD), from 8 per group. Statistical comparisons were made using two-way ANOVA followed by the Sidak's post hoc test (\*  $p < 0.05$ , \*\*  $p < 0.01$ , \*\*\*  $p < 0.001$ , and \*\*\*\*  $p < 0.0001$ , MTX 7.0 mg/kg vs. control). Figure S2. [A and B] Body weight in [A] infant and [B] adult mice exposed to a cumulative dose of 6.0 mg/kg MTX. [C and D] Water consumption of [C] infant and [D] adult mice exposed to a cumulative dose of 6.0 mg/kg MTX. [E and F] Food consumption of [E] infant and [F] adult mice exposed to a cumulative dose of 6.0 mg/kg MTX. Results are presented in grams (g) of food intake/day/weight of animal, mL of water intake/day/weight of animal, or g of body weight, and as mean  $\pm$  SD, from 6 per infant group and 17 per adult group. Statistical comparisons were made using two-way ANOVA followed by the Sidak's post hoc test \*  $p < 0.05$ , \*\*  $p < 0.01$ , \*\*\*  $p < 0.001$ , and \*\*\*\*  $p < 0.0001$ , MTX 6.0 mg/kg vs. control). Figure S3. Loading control of Ponceau S staining of [A] ATP synthase subunit beta (52 kDa) and glyceraldehyde-3-phosphate



dehydrogenase (GAPDH) (37 kDa), [B] Superoxide dismutase 2/manganese-dependent superoxide dismutase (SOD2/MnSOD) (26.6 kDa) and Nuclear kappa B nuclear transcription factor (NF-κB) p65 (60 kDa), [C] catalase (60 kDa) and [D] glutathione peroxidase (22 kDa), [E] Tumour necrosis factor-α (TNF- α) (25 kDa), [F] interleukin-6 (IL-6) (24 kDa), [G] myeloperoxidase (48 kDa), [H] NF-κB p52 (50 kDa) from infant mice exposed to a cumulative dose of 6.0 mg/kg MTX or control animals. Figure S4. Loading control of Ponceau S staining of [A] ATP synthase subunit beta (52 kDa), glyceraldehyde-3-phosphate dehydrogenase (GAPDH) (37 kDa) and interleukin-6 (IL-6) (24 kDa), [B] catalase (60 kDa) and glutathione peroxidase (22 kDa), [C] Tumour necrosis factor-α (TNF-α) (25 kDa), [D] myeloperoxidase (48 kDa), [E] Superoxide dismutase 2/manganese-dependent superoxide dismutase (SOD2/MnSOD) (26.6 kDa) and Nuclear kappa B nuclear transcription factor (NF-κB) p52 (50 kDa) and [F] NF-κB p65 (60 kDa) from adult mice exposed to a cumulative dose of 6.0 mg/kg MTX or control animals. Table S1. General distress scoring sheet implemented for the evaluation of the general welfare of mice during all the experiment. Table S2. Plasma biomarkers and heart weight/body weight ratio after MTX (7.0 mg/kg cumulative dose). Table S3. Plasma biomarkers and heart weight/body weight ratio after MTX (6.0 mg/kg cumulative dose).

**Author Contributions:** Conceptualization, A.R.-M. and V.M.C.; formal analysis, A.R.-M. and V.M.C.; investigation, A.R.-M., J.L.D.-S., A.I.P.; J.A.D.; methodology (in vivo), A.R.-M., J.L.D.-S., V.S., M.D.-A., S.G.-M., V.M.C.; writing—original draft preparation, A.R.-M., and V.M.C.; writing review and editing, A.R.-M., J.L.D.-S., A.I.P., M.D.-A., J.A.D., V.S., S.G.-M., F.R., F.C., E.S., M.L.B., V.M.C.; supervision, E.S., M.L.B. and V.M.C.; project administration, V.M.C.; funding acquisition, A.R.-M., V.M.C. All authors have read and agreed to the published version of the manuscript.

**Funding:** This work is funded by national funds through FCT—Fundação para a Ciência e a Tecnologia, I.P., under the Norma Transitória—DL57/2016/CP1334/CT0006. A.R.-M. and V.M.C. acknowledge Fundação da Ciência e Tecnologia (FCT) for their grants (SFRH/BD/129359/2017 and SFRH/BPD/110001/2015, respectively). This work was supported by FEDER funds through the Operational Programme for Competitiveness Factors—COMPETE and by national funds by the Fundação para a Ciência e Tecnologia (FCT) within the project “PTDC/DTP-FTO/1489/2014—POCI01-0145-FEDER-016537”. The work was also supported by UID/MULTI/04378/2019, UIDB/04423/2020, UID/DTP/00617/2020, UIDB/04423/2020, UIDP/04423/2020 (Group of Natural Products and Medicinal Chemistry) with funding from FCT/MCTES through national funds.

**Institutional Review Board Statement:** The study was conducted according to the guidelines of the Declaration of Helsinki, and approved by the Ethics Committee of the local animal welfare body (ICBAS-UP ORBEA) and the Portuguese national authority for animal health (DGAV, processes no. 0421/000/000/2013 and 0421/000/000/2016).

**Informed Consent Statement:** Not applicable.

**Data Availability Statement:** The data presented in this study are available on request from the corresponding author.

**Acknowledgments:** We greatly acknowledge Laura Pereira for her assistance in the plasma and haematological determinations and Celeste Resende for her assistance in histological procedures.

**Conflicts of Interest:** The authors declare no conflict of interest.

## References

1. Reis-Mendes, A.F.; Sousa, E.; de Lourdes Bastos, M.; Costa, V.M. The Role of the Metabolism of Anticancer Drugs in Their Induced-Cardiotoxicity. *Curr. Drug Metab.* **2015**, *17*, 75–90. [CrossRef]
2. Doroshow, J.H. Topoisomerase II inhibitors. In *Cancer Chemotherapy and Biotherapy: Principles and Practice*; Chabner, B.A., Long, D.L., Eds.; Lippincott Williams and Wilkins: Philadelphia, PA, USA, 2011; pp. 356–391.
3. Fox, E.J. Mechanism of action of mitoxantrone. *Neurology* **2004**, *63*, S15–S18. [CrossRef]
4. Scott, L.J.; Figgitt, D.P. Mitoxantrone: A review of its use in multiple sclerosis. *CNS Drugs* **2004**, *18*, 379–396. [CrossRef] [PubMed]
5. Costa, V.M.; Carvalho, F.; Duarte, J.A.; de Lourdes Bastos, M.; Remião, F. The heart as a target for xenobiotic toxicity: The cardiac susceptibility to oxidative stress. *Chem. Res. Toxicol.* **2013**, *26*, 1285–1311. [CrossRef] [PubMed]
6. Seiter, K. Toxicity of the topoisomerase II inhibitors. *Expert Opin. Drug Saf.* **2005**, *4*, 219–234. [CrossRef] [PubMed]
7. Fleischer, V.; Salmen, A.; Kollar, S.; Weyer, V.; Siffrin, V.; Chan, A.; Zipp, F.; Luessi, F. Cardiotoxicity of mitoxantrone treatment in a german cohort of 639 multiple sclerosis patients. *J. Clin. Neurol.* **2014**, *10*, 289–295. [CrossRef]

8. Rivera, V.M.; Jeffery, D.R.; Weinstock-Guttman, B.; Bock, D.; Dangond, F. Results from the 5-year, phase IV RENEW (Registry to Evaluate Novantrone Effects in Worsening Multiple Sclerosis) study. *BMC Neurol.* **2013**, *13*, 80. [CrossRef]
9. Frieler, R.A.; Mortensen, M.R. Immune cell and other noncardiomyocyte regulation of cardiac hypertrophy and remodeling. *Circulation* **2015**, *131*, 1019–1030. [CrossRef] [PubMed]
10. Mann, D.L. Innate immunity and the failing heart: The cytokine hypothesis revisited. *Circ. Res.* **2015**, *116*, 1254–1268. [CrossRef]
11. Prabhu, S.D.; Frangogiannis, N.G. The Biological Basis for Cardiac Repair after Myocardial Infarction: From Inflammation to Fibrosis. *Circ. Res.* **2016**, *119*, 91–112. [CrossRef]
12. Zhou, B.; Rao, L.; Peng, Y.; Wang, Y.; Li, Y.; Gao, L.; Chen, Y.; Xue, H.; Song, Y.; Liao, M.; et al. Functional polymorphism of the NFkB1 gene promoter is related to the risk of dilated cardiomyopathy. *BMC Med. Genet.* **2009**, *10*, 47. [CrossRef] [PubMed]
13. Santos, D.G.; Resende, M.F.; Mill, J.G.; Mansur, A.J.; Krieger, J.E.; Pereira, A.C. Nuclear Factor (NF) kappaB polymorphism is associated with heart function in patients with heart failure. *BMC Med. Genet.* **2010**, *11*, 89. [CrossRef] [PubMed]
14. Tsutsui, H.; Kinugawa, S.; Matsushima, S. Oxidative stress and heart failure. *Am. J. Physiol. Heart Circ. Physiol.* **2011**, *301*, H2181–H2190. [CrossRef] [PubMed]
15. Voigt, A.; Rahnefeld, A.; Kloetzel, P.M.; Krüger, E. Cytokine-induced oxidative stress in cardiac inflammation and heart failure—how the ubiquitin proteasome system targets this vicious cycle. *Front. Physiol.* **2013**, *4*, 42. [CrossRef]
16. Nakamura, M.; Sadoshima, J. Mechanisms of physiological and pathological cardiac hypertrophy. *Nat. Rev. Cardiol.* **2018**, *15*, 387–407. [CrossRef]
17. Travers, J.G.; Kamal, F.A.; Robbins, J.; Yutzey, K.E.; Blaxall, B.C. Cardiac Fibrosis: The Fibroblast Awakens. *Circ. Res.* **2016**, *118*, 1021–1040. [CrossRef]
18. Kurrelmeyer, K.M.; Michael, L.H.; Baumgarten, G.; Taffet, G.E.; Peschon, J.J.; Sivasubramanian, N.; Entman, M.L.; Mann, D.L. Endogenous tumor necrosis factor protects the adult cardiac myocyte against ischemic-induced apoptosis in a murine model of acute myocardial infarction. *Proc. Natl. Acad. Sci. USA* **2000**, *97*, 5456–5461. [CrossRef]
19. Nakano, M.; Knowlton, A.A.; Dibbs, Z.; Mann, D.L. Tumor necrosis factor-alpha confers resistance to hypoxic injury in the adult mammalian cardiac myocyte. *Circulation* **1998**, *97*, 1392–1400. [CrossRef]
20. Krown, K.A.; Page, M.T.; Nguyen, C.; Zechner, D.; Gutierrez, V.; Comstock, K.L.; Glembotski, C.C.; Quintana, P.J.; Sabbadini, R.A. Tumor necrosis factor alpha-induced apoptosis in cardiac myocytes. Involvement of the sphingolipid signaling cascade in cardiac cell death. *J. Clin. Investig.* **1996**, *98*, 2854–2865. [CrossRef]
21. Kubota, T.; McTiernan, C.F.; Frye, C.S.; Slawson, S.E.; Lemster, B.H.; Koretsky, A.P.; Demetris, A.J.; Feldman, A.M. Dilated cardiomyopathy in transgenic mice with cardiac-specific overexpression of tumor necrosis factor-alpha. *Circ. Res.* **1997**, *81*, 627–635. [CrossRef]
22. Craig, R.; Larkin, A.; Mingo, A.M.; Thuerauf, D.J.; Andrews, C.; McDonough, P.M.; Glembotski, C. C p38 MAPK and NF-kappa B collaborate to induce interleukin-6 gene expression and release. Evidence for a cytoprotective autocrine signaling pathway in a cardiac myocyte model system. *J. Biol. Chem.* **2000**, *275*, 23814–23824. [CrossRef]
23. Terrell, A.M.; Crisostomo, P.R.; Wairiuko, G.M.; Wang, M.; Morrell, E.D.; Meldrum, D.R. Jak/STAT/SOCS signaling circuits and associated cytokine-mediated inflammation and hypertrophy in the heart. *Shock* **2006**, *26*, 226–234. [CrossRef]
24. Rigacci, L.; Carpaneto, A.; Alterini, R.; Carrai, V.; Bernardi, F.; Bellesi, G.; Longo, G.; Bosi, A.; Rossi Ferrini, P. Treatment of large cell lymphoma in elderly patients with a mitoxantrone, cyclophosphamide, etoposide, and prednisone regimen: Long-term follow-up results. *Cancer* **2003**, *97*, 97–104. [CrossRef]
25. Tan, R.M.; Quah, T.C.; Aung, L.; Liang, S.; Kirk, R.C.; Yeoh, A.E. Improved outcome in childhood acute myeloid leukemia in Singapore with the MRC AML 10 protocol. *Pediatr. Blood Cancer* **2007**, *48*, 262–267. [CrossRef]
26. Pratt, C.B.; Vietti, T.J.; Etcubanas, E.; Sexauer, C.; Krance, R.A.; Mahoney, D.H.; Patterson, R.B. Novantrone for childhood malignant solid tumors. A pediatric oncology group phase II study. *Investig. New Drugs* **1986**, *4*, 43–48. [CrossRef] [PubMed]
27. Dahl, G.V.; Lacayo, N.J.; Brophy, N.; Dunussi-Joannopoulos, K.; Weinstein, H.J.; Chang, M.; Sikic, B.I.; Arcenci, R.J. Mitoxantrone, etoposide, and cyclosporine therapy in pediatric patients with recurrent or refractory acute myeloid leukemia. *J. Clin. Oncol.* **2000**, *18*, 1867–1875. [CrossRef]
28. Van der Pal, H.J.; van Dalen, E.C.; Hauptmann, M.; Kok, W.E.; Caron, H.N.; van den Bos, C.; Oldenburger, F.; Koning, C.C.; van Leeuwen, F.E.; Kremer, L.C. Cardiac function in 5-year survivors of childhood cancer: A long-term follow-up study. *Arch. Intern. Med.* **2010**, *170*, 1247–1255. [CrossRef] [PubMed]
29. Armstrong, G.T.; Oeffinger, K.C.; Chen, Y.; Kawashima, T.; Yasui, Y.; Leisenring, W.; Stovall, M.; Chow, E.J.; Sklar, C.A.; Mulrooney, D.A.; et al. Modifiable risk factors and major cardiac events among adult survivors of childhood cancer. *J. Clin. Oncol.* **2013**, *31*, 3673–3680. [CrossRef] [PubMed]
30. Mulrooney, D.A.; Armstrong, G.T.; Huang, S.; Ness, K.K.; Ehrhardt, M.J.; Joshi, V.M.; Plana, J.C.; Soliman, E.Z.; Green, D.M.; Srivastava, D.; et al. Cardiac Outcomes in Adult Survivors of Childhood Cancer Exposed to Cardiotoxic Therapy: A Cross-sectional Study. *Ann. Intern. Med.* **2016**, *164*, 93–101. [CrossRef] [PubMed]
31. Wise, J. Adult survivors of childhood cancer are at high risk of cardiac abnormalities, study finds. *BMJ* **2016**, *352*, h7026. [CrossRef]
32. Scully, R.; Lipshultz, S.E. Cardiovascular toxicity of antitumor drugs: Dimension of the problem in children. In *Cardiotoxicity of Non-Cardiovascular Drugs*; Minotti, G., Ed.; John Wiley & Sons, Ltd.: New York, NY, USA, 2010; pp. 97–126.

33. Howlader, N.N.A.; Krapcho, M.; Miller, D.; Brest, A.; Yu, M.; Ruhl, J.; Tatalovich, Z.; Mariotto, A.; Lewis, D.R.; Chen, H.S.; et al. (Eds.) *SEER Cancer Statistics Review 1975–2017*; National Cancer Institute: Bethesda, MD, USA, 2019. Available online: [https://seer.cancer.gov/csr/1975\\_2017/](https://seer.cancer.gov/csr/1975_2017/) (accessed on 9 April 2020).
34. Dores-Sousa, J.L.; Duarte, J.A.; Seabra, V.; de Lourdes Bastos, M.; Carvalho, F.; Costa, V.M. The age factor for mitoxantrone's cardiotoxicity: Multiple doses render the adult mouse heart more susceptible to injury. *Toxicology* **2015**, *329*, 106–119. [CrossRef] [PubMed]
35. Levi, F.; Tampellini, M.; Metzger, G.; Bizi, E.; Lemaigre, G.; Hallek, M. Circadian changes in mitoxantrone toxicity in mice: Relationship with plasma pharmacokinetics. *Int. J. Cancer* **1994**, *59*, 543–547. [CrossRef] [PubMed]
36. Subramaniam, V.; Chuang, G.; Xia, H.; Burn, B.; Bradley, J.; Maderdrut, J.L.; Coy, D.H.; Varner, K.J. Pituitary adenylate cyclase-activating polypeptide (PACAP) protects against mitoxantrone-induced cardiac injury in mice. *Peptides* **2017**, *95*, 25–32. [CrossRef] [PubMed]
37. Rossato, L.G.; Costa, V.M.; Dallegrave, E.; Arbo, M.; Silva, R.; Ferreira, R.; Amado, F.; Dinis-Oliveira, R.J.; Duarte, J.A.; de Lourdes Bastos, M.; et al. Mitochondrial cumulative damage induced by mitoxantrone: Late onset cardiac energetic impairment. *Cardiovasc. Toxicol.* **2014**, *14*, 30–40. [CrossRef] [PubMed]
38. Rej, R. Aminotransferases in disease. *Clin. Lab. Med.* **1989**, *9*, 667–687. [CrossRef]
39. Rossato, L.G.; Costa, V.M.; Dallegrave, E.; Arbo, M.; Dinis-Oliveira, R.J.; Santos-Silva, A.; Duarte, J.A.; de Lourdes Bastos, M.; Palmeira, C.; Remião, F. Cumulative mitoxantrone-induced haematological and hepatic adverse effects in a subchronic in vivo study. *Basic Clin. Pharmacol. Toxicol.* **2014**, *114*, 254–262. [CrossRef]
40. Anghel, N.; Cotoraci, C.; Ivan, A.; Suci, M.; Herman, H.; Balta, C.; Nicolescu, L.; Olariu, T.; Galajda, Z.; Ardelean, A.; et al. Chrysin attenuates cardiomyocyte apoptosis and loss of intermediate filaments in a mouse model of mitoxantrone cardiotoxicity. *Histol. Histopathol.* **2015**, *30*, 1465–1475.
41. Alderton, P.M.; Gross, J.; Green, M.D. Comparative study of doxorubicin, mitoxantrone, and epirubicin in combination with ICRF-187 (ADR-529) in a chronic cardiotoxicity animal model. *Cancer Res.* **1992**, *52*, 194–201.
42. Cavalletti, E.; Crippa, L.; Mainardi, P.; Oggioni, N.; Cavagnoli, R.; Bellini, O.; Sala, F. Pixantrone (BBR 2778) has reduced cardiotoxic potential in mice pretreated with doxorubicin: Comparative studies against doxorubicin and mitoxantrone. *Investig. New Drugs* **2007**, *25*, 187–195. [CrossRef]
43. Unverferth, D.V.; Unverferth, B.J.; Balcerzak, S.P.; Bashore, T.A.; Neidhart, J.A. Cardiac evaluation of mitoxantrone. *Cancer Treat. Rep.* **1983**, *67*, 343–350.
44. Santulli, G.; Iaccarino, G. Adrenergic signaling in heart failure and cardiovascular aging. *Maturitas* **2016**, *93*, 65–72. [CrossRef]
45. Strumia, E.; Pelliccia, F.; D'Ambrosio, G. Creatine phosphate: Pharmacological and clinical perspectives. *Adv. Ther.* **2012**, *29*, 99–123. [CrossRef]
46. Clark, J.F. Creatine and phosphocreatine: A review of their use in exercise and sport. *J. Athl. Train.* **1997**, *32*, 45–51.
47. Bertero, E.; Maack, C. Metabolic remodelling in heart failure. *Nat. Rev. Cardiol.* **2018**, *15*, 457–470. [CrossRef] [PubMed]
48. Carvalho, R.A.; Sousa, R.P.; Cadete, V.J.; Lopaschuk, G.D.; Palmeira, C.M.; Bjork, J.A.; Wallace, K.B. Metabolic remodeling associated with subchronic doxorubicin cardiomyopathy. *Toxicology* **2010**, *270*, 92–98. [CrossRef] [PubMed]
49. Brandão, S.; Reis-Mendes, A.; Domingues, P.; Alberto Duarte, J.; Lourdes Bastos, M.; Carvalho, F.; Ferreira, R.; Costa, V.M. Exploring the effects of the anticancer drugs doxorubicin and mitoxantrone on cardiac mitochondrial proteome using a murine model. *Toxicology* **2021**. Submitted.
50. Lores Arnaiz, S.; Llesuy, S. Oxidative stress in mouse heart by antitumoral drugs: A comparative study of doxorubicin and mitoxantrone. *Toxicology* **1993**, *77*, 31–38. [CrossRef]
51. Barbosa, M.R.; Sampaio, I.H.; Teodoro, B.G.; Sousa, T.A.; Zoppi, C.C.; Queiroz, A.L.; Passos, M.A.; Alberici, L.C.; Teixeira, F.R.; Manfiolli, A.O.; et al. Hydrogen peroxide production regulates the mitochondrial function in insulin resistant muscle cells: Effect of catalase overexpression. *Biochim. Biophys. Acta* **2013**, *1832*, 1591–1604. [CrossRef]
52. Koutinos, G.; Stathopoulos, G.P.; Dontas, I.; Perrea-Kotsarelis, D.; Couris, E.; Karayannacos, P.E.; Deliconstantinos, G. The effect of doxorubicin and its analogue mitoxantrone on cardiac muscle and on serum lipids: An experimental study. *Anticancer Res.* **2002**, *22*, 815–820.
53. Costa, V.M.; Capela, J.P.; Sousa, J.R.; Eleutério, R.P.; Rodrigues, P.R.S.; Dores-Sousa, J.L.; Carvalho, R.A.; de Lourdes Bastos, M.; Duarte, J.A.; Remião, F.; et al. Mitoxantrone impairs proteasome activity and prompts early energetic and proteomic changes in HL-1 cardiomyocytes at clinically relevant concentrations. *Arch. Toxicol.* **2020**, *94*, 4067–4084. [CrossRef] [PubMed]
54. Aldini, G.; Dalle-Donne, I.; Facino, R.M.; Milzani, A.; Carini, M. Intervention strategies to inhibit protein carbonylation by lipoxidation-derived reactive carbonyls. *Med. Res. Rev.* **2007**, *27*, 817–868. [CrossRef] [PubMed]
55. Evans, S.; Tzeng, H.P.; Veis, D.J.; Matkovich, S.; Weinheimer, C.; Kovacs, A.; Barger, P.M.; Mann, D.L. TNF receptor-activated factor 2 mediates cardiac protection through noncanonical NF- $\kappa$ B signaling. *JCI Insight* **2018**, *3*, e98278. [CrossRef] [PubMed]
56. Yunna, C.; Mengru, H.; Lei, W.; Weidong, C. Macrophage M1/M2 polarization. *Eur. J. Pharmacol.* **2020**, *877*, 173090. [CrossRef]
57. Moore, K.J.; Sheedy, F.; Fisher, E.A. Macrophages in atherosclerosis: A dynamic balance. *Nat. Rev. Immunol.* **2013**, *13*, 709–721. [CrossRef] [PubMed]
58. Van Dijk, R.A.; Rijs, K.; Wezel, A.; Hamming, J.F.; Kolodgie, F.D.; Virmani, R.; Schaapherder, A.F.; Lindeman, J.H. Systematic Evaluation of the Cellular Innate Immune Response during the Process of Human Atherosclerosis. *J. Am. Heart Assoc.* **2016**, *5*, e002860. [CrossRef]

59. Ponnappan, S.; Ponnappan, U. Aging and immune function: Molecular mechanisms to interventions. *Antioxid. Redox Signal.* **2011**, *14*, 1551–1585. [CrossRef]
60. Khaper, N.; Bryan, S.; Dhingra, S.; Singal, R.; Bajaj, A.; Pathak, C.M.; Singal, P.K. Targeting the vicious inflammation-oxidative stress cycle for the management of heart failure. *Antioxid. Redox Signal.* **2010**, *13*, 1033–1049. [CrossRef] [PubMed]
61. Wollert, K.C.; Drexler, H. The role of interleukin-6 in the failing heart. *Heart Fail. Rev.* **2001**, *6*, 95–103. [CrossRef] [PubMed]
62. Palmieri, E.A.; Benincasa, G.; Di Rella, F.; Casaburi, C.; Monti, M.G.; De Simone, G.; Chiariotti, L.; Palombini, L.; Bruni, C.B.; Saccà, L.; et al. Differential expression of TNF-alpha, IL-6, and IGF-1 by graded mechanical stress in normal rat myocardium. *Am. J. Physiol. Heart Circ. Physiol.* **2002**, *282*, H926–H934. [CrossRef] [PubMed]
63. Quagliariello, V.; Coppola, C.; Mita, D.G.; Piscopo, G.; Iaffaioli, R.V.; Botti, G.; Maurea, N. Low doses of Bisphenol A have pro-inflammatory and pro-oxidant effects, stimulate lipid peroxidation and increase the cardiotoxicity of Doxorubicin in cardiomyoblasts. *Environ. Toxicol. Pharmacol.* **2019**, *69*, 1–8. [CrossRef]
64. Quagliariello, V.; Vecchione, R.; Coppola, C.; Di Cicco, C.; De Capua, A.; Piscopo, G.; Paciello, R.; Narciso, V.; Formisano, C.; Tagliatalata-Scafati, O.; et al. Cardioprotective Effects of Nanoemulsions Loaded with Anti-Inflammatory Nutraceuticals against Doxorubicin-Induced Cardiotoxicity. *Nutrients* **2018**, *10*, 1304. [CrossRef] [PubMed]
65. Quagliariello, V.; Passariello, M.; Rea, D.; Barbieri, A.; Iovine, M.; Bonelli, A.; Caronna, A.; Botti, G.; De Lorenzo, C.; Maurea, N. Evidences of CTLA-4 and PD-1 Blocking Agents-Induced Cardiotoxicity in Cellular and Preclinical Models. *J. Pers. Med.* **2020**, *10*, 179. [CrossRef]
66. Angelucci, F.; Batocchi, A.P.; Caggiula, M.; Frisullo, G.; Patanella, K.; Sancricca, C.; Nociti, V.; Tonali, P.A.; Mirabella, M. In vivo effects of mitoxantrone on the production of pro- and anti-inflammatory cytokines by peripheral blood mononuclear cells of secondary progressive multiple sclerosis patients. *Neuroimmunomodulation* **2006**, *13*, 76–81. [CrossRef]
67. Dutta, S.; Sengupta, P. Men and mice: Relating their ages. *Life Sci.* **2016**, *152*, 244–248. [CrossRef] [PubMed]
68. Wang, S.; Lai, X.; Deng, Y.; Song, Y. Correlation between mouse age and human age in anti-tumor research: Significance and method establishment. *Life Sci.* **2020**, *242*, 117242. [CrossRef] [PubMed]
69. Curry, S.H.; DeCory, H.H.; Gabrielsson, J. Phase I: The first opportunity for extrapolation from animal data to human exposure. In *Principles and Practice of Pharmaceutical Medicine*; Edwards, L.D., Fox, A.W., Stonier, P.D., Eds.; Wiley-Blackwell: Hoboken, NJ, USA, 2010; pp. 84–106.
70. Reagan-Shaw, S.; Nihal, M.; Ahmad, N. Dose translation from animal to human studies revisited. *FASEB J.* **2008**, *22*, 659–661. [CrossRef] [PubMed]
71. Al Shoyaib, A.; Archie, S.R.; Karamyan, V.T. Intraperitoneal Route of Drug Administration: Should it Be Used in Experimental Animal Studies? *Pharm. Res.* **2019**, *37*, 12. [CrossRef] [PubMed]
72. Lowry, O.H.; Rosebrough, N.J.; Farr, A.L.; Randall, R.J. Protein measurement with the Folin phenol reagent. *J. Biol. Chem.* **1951**, *193*, 265–275. [CrossRef]
73. DeLuca, M.; McElroy, W.D. Kinetics of the firefly luciferase catalyzed reactions. *Biochemistry* **1974**, *13*, 921–925. [CrossRef]
74. Carvalho, M.; Milhazes, N.; Remiao, F.; Borges, F.; Fernandes, E.; Amado, F.; Monks, T.J.; Carvalho, F.; de Lourdes Bastos, M. Hepatotoxicity of 3,4-methylenedioxyamphetamine and alpha-methyl dopamine in isolated rat hepatocytes: Formation of glutathione conjugates. *Arch. Toxicol.* **2004**, *78*, 16–24. [PubMed]
75. Padrão, A.I.; Oliveira, P.; Vitorino, R.; Colaço, B.; Pires, M.J.; Márquez, M.; Castellanos, E.; Neuparth, M.J.; Teixeira, C.; Costa, C.; et al. Bladder cancer-induced skeletal muscle wasting: Disclosing the role of mitochondria plasticity. *Int. J. Biochem. Cell Biol.* **2013**, *45*, 1399–1409. [CrossRef] [PubMed]
76. Garcia, J.; Costa, V.M.; Carvalho, A.T.; Silvestre, R.; Duarte, J.A.; Dourado, D.F.; Arbo, M.D.; Baltazar, T.; Dinis-Oliveira, R.J.; Baptista, P.; et al. A breakthrough on Amanita phalloides poisoning: An effective antidotal effect by polymyxin B. *Arch. Toxicol.* **2015**, *89*, 2305–2323. [CrossRef] [PubMed]





## Article

# Morin-5'-Sulfonic Acid Sodium Salt (NaMSA) Attenuates Cyclophosphamide-Induced Histological Changes in Genitourinary Tract in Rats—Short Report

Anna Merwid-Łąd <sup>1,\*</sup> , Dorota Książczyńska <sup>1</sup>, Agnieszka Hałoń <sup>2</sup>, Danuta Szkudlarek <sup>3</sup>, Małgorzata Trocha <sup>1</sup>, Marta Szandruk-Bender <sup>1</sup> , Agnieszka Matuszewska <sup>1</sup> , Beata Nowak <sup>1</sup> , Tomasz Sozański <sup>1</sup>, Anna Kuźniar <sup>4</sup> and Adam Szelaż <sup>1</sup>

- <sup>1</sup> Department of Pharmacology, Wrocław Medical University, ul. Mikulicza-Radeckiego 2, 50-345 Wrocław, Poland; dorota.ksiadzynska@umed.wroc.pl (D.K.); malgorzata.trocha@umed.wroc.pl (M.T.); marta.szandruk@umed.wroc.pl (M.S.-B.); agnieszka.matuszewska@umed.wroc.pl (A.M.); beata.nowak@umed.wroc.pl (B.N.); tomasz.sozanski@umed.wroc.pl (T.S.); adam.szelaż@umed.wroc.pl (A.S.)
- <sup>2</sup> Department of Pathomorphology and Oncological Cytology, Wrocław Medical University, ul. Borowska 213, 50-556 Wrocław, Poland; agnieszka.halon@umed.wroc.pl
- <sup>3</sup> Department of Pathomorphology, Wrocław Medical University, ul. Marcinkowkiego 1, 50-368 Wrocław, Poland; danuta.szkudlarek@umed.wroc.pl
- <sup>4</sup> Department of Inorganic and Analytical Chemistry, Rzeszów University of Technology, al. Powstańców Warszawy 6, 35-959 Rzeszów, Poland; akuzniar@prz.edu.pl
- \* Correspondence: anna.merwid-lad@umed.wroc.pl; Tel.: +48-71-784-1442

**Citation:** Merwid-Łąd, A.; Książczyńska, D.; Hałoń, A.; Szkudlarek, D.; Trocha, M.; Szandruk-Bender, M.; Matuszewska, A.; Nowak, B.; Sozański, T.; Kuźniar, A.; et al. Morin-5'-Sulfonic Acid Sodium Salt (NaMSA) Attenuates Cyclophosphamide-Induced Histological Changes in Genitourinary Tract in Rats—Short Report. *Pharmaceuticals* **2021**, *14*, 192. <https://doi.org/10.3390/ph14030192>

Academic Editor: Mary Meegan

Received: 1 February 2021

Accepted: 23 February 2021

Published: 26 February 2021

**Publisher's Note:** MDPI stays neutral with regard to jurisdictional claims in published maps and institutional affiliations.



**Copyright:** © 2021 by the authors. Licensee MDPI, Basel, Switzerland. This article is an open access article distributed under the terms and conditions of the Creative Commons Attribution (CC BY) license (<https://creativecommons.org/licenses/by/4.0/>).

**Abstract:** Cyclophosphamide (CPX) exerts toxicity in the urogenital system. The current study was designed to evaluate the effect of morin-5'-sulfonic acid sodium salt (NaMSA) on CPX-induced urogenital toxicity in rats. NaMSA (100 mg/kg/daily) and CPX (15 mg/kg/daily) alone or in combination and 0.9% NaCl (as a control) were given intragastrically for 10 days. Testes and epididymes from male and urinary bladders from male and female rats were evaluated histologically. In testes and epididymes, morphological changes and relative decrease in sperm count were assessed. In urinary bladders edema, hemorrhage and urothelium erosions were described by 0–2 points scoring system. Reproductive score (RS—in total 6 points) and urinary bladder score (BS—in total 6 points) were thereafter calculated. In CPX-receiving group RS (2.7) and BS (3.3) were significantly higher than in the control (0.5 and 0.25 for RS and BS, respectively). Co-administration of NaMSA reversed most of the morphological changes, which was reflected by lower RS and BS score (0.5 and 1.2 for RS and BS, respectively). The preliminary findings suggest that NaMSA may attenuate CPX-induced histological changes in rat urogenital tract.

**Keywords:** NaMSA; cyclophosphamide; histopathology; testis; urinary bladder

## 1. Introduction

The male reproductive system is very sensitive to noxious factors and permanent or transient infertility is a great clinical problem, especially in younger patients. There are still not too many possibilities to counteract these drug-induced complications. Among many reasons of decreased fertility or even infertility such as anatomical pathologies, diabetes, obesity, smoking, cancers, radiation or environmental toxins, adverse effects of many anticancer agents are very important [1–3].

Cyclophosphamide (CPX) is a conventional anticancer drug belonging to the alkylating agents [4]. Despite introduction in clinical practice, many targeted treatment options as immunosuppressant or anticancer drugs [5], it is estimated that still every year many patients develop and are diagnosed with cancers, which are the indication for CPX administration [6].

Cyclophosphamide exerts significant adverse effects in the urinary tract and affects the male reproductive system, causing disorders of spermatogenesis with oligo- and azoospermia, testicular atrophy in men taking this drug and sometimes infertility, which may be irreversible. Lesions caused by CPX in the urinary tract are also well described and are observed after both short- or long-term treatment. In human hemorrhagic cystitis, pyelonephritis and hematuria are common complications [7]. With the mechanism of the urinary tract, especially the urinary bladder, injury is multifactorial and involves first of all the reaction of CPX metabolite (acrolein) with urothelium with subsequent inflammatory cascade. In the prevention of urinary toxicity, mainly life-threatening hemorrhagic cystitis, there are a few possibilities with good hydration, systemic administration of mesna (whose efficacy in this indication is recently discussed and doubtful), local irrigation of the urinary bladder with various substances or sometimes even surgical, invasive procedures [4,6]. Much less is known about the prevention of chronic injury of kidneys or the reproductive system. Therefore, there is still a great need to search for compounds that may decrease CPX-induced tissue toxicity instead or as adjuvant to standard prevention schedules and in this way, decrease mortality due to complications of anticancer therapy and increase patients' quality of life. Plant-derived substances and their chemically modified derivatives are in the interest of scientists in a variety of medical indications. Many different compounds have been until now tested in experimental studies for reduction of cyclophosphamide-induced urogenital toxicity, especially in male rats using models of acute or chronic cyclophosphamide administration [8–10].

Morin-5'-sulfonic acid sodium salt (NaMSA) is a derivative of natural flavonoid morin, but as a sodium salt exerts much better water-solubility. We have described in our previous papers that NaMSA reversed some CPX-induced changes in oxidative stress parameters in liver and kidney in rat models of 10 days CPX administration at a daily dose of 15 mg/kg [11] and attenuated pathological changes in intestine morphology [12]. Generation of oxidative radicals may be one of the factors responsible for damages observed in male gonads and in the urinary tract [10,13–15]. In this paper, we describe preliminary results of the influence of NaMSA administration on CPX-induced toxicity in male rat gonads based on the histopathological evaluation of testes and epididymes and the effect of NaMSA on histological toxicity in the urinary bladders of both sexes.

## 2. Results

### 2.1. Tested and Epididymes Evaluation

Results of the testes, epididymes and sperm score, and urinary bladder score are presented in Figures 1 and 2. Intragastric CPX administration for 10 days in a daily dose of 15 mg/kg caused significant increase in testes and epididymes histological lesions described as irregular and diminished seminiferous tubules of a mild or severe grade along with various levels of decreased sperm count within the lumen of seminiferous tubules. Co-treatment with NaMSA in a daily dose of 100 mg/kg reversed those change, which was reflected by decreased testes and epididymes score. Representative histological changes for tested groups in testes and epididymes are presented in Figures 3 and 4, respectively.

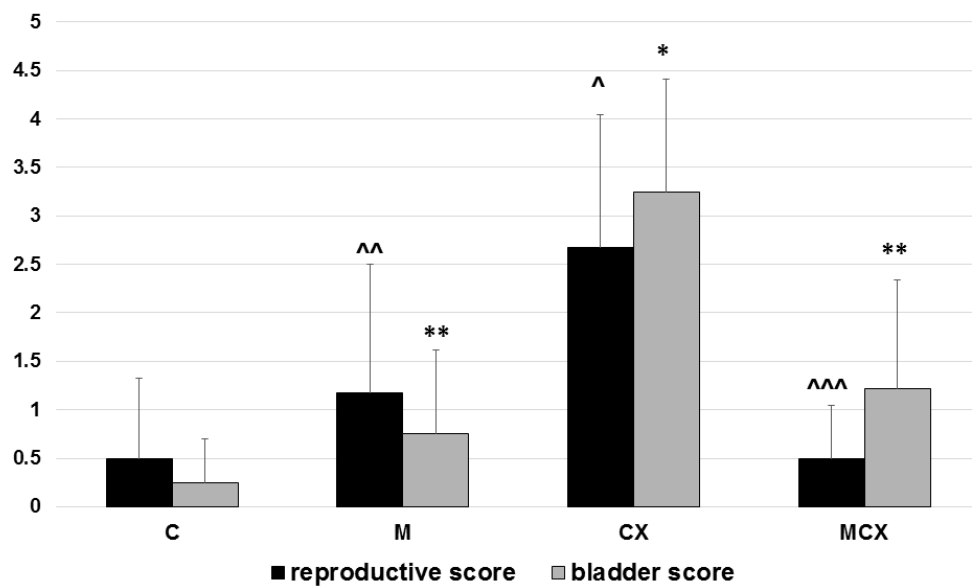


**Figure 1.** Total reproductive score (testes, epididymes and sperm, 0–6 points) and total urinary bladder score (hemorrhage, edema, erosions, 0–6 points). Scoring system described in the Material and Methods section. Bladder score: \*  $p < 0.001$ , CX vs. C; \*\*  $p < 0.001$ , M vs. CX and MCX vs. CX. Reproductive score: ^  $p < 0.01$ , CX vs. C; ^^  $p < 0.05$ , M vs. CX and ^^  $p < 0.01$ , MCX vs. CX. Data presented as mean values and SD.

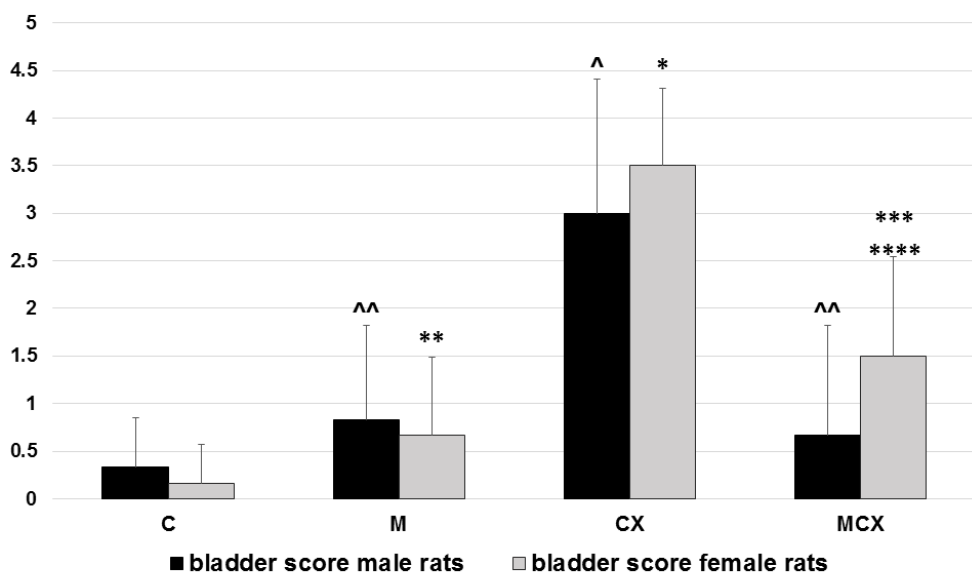


**Figure 2.** Total urinary bladder score (hemorrhage, edema, erosions, 0–6 points) in male and female rats. Scoring system described in the Material and Methods section. Male rats: ^  $p < 0.001$ , CX vs. C; ^^  $p < 0.01$ , M vs. CX and MCX vs. CX. female rats: \*  $p < 0.001$ , CX vs. C; \*\*  $p < 0.001$ , M vs. CX; \*\*\*  $p < 0.01$ , MCX vs. CX; \*\*\*\*  $p < 0.05$ , MCX vs. C. Data presented as mean values.



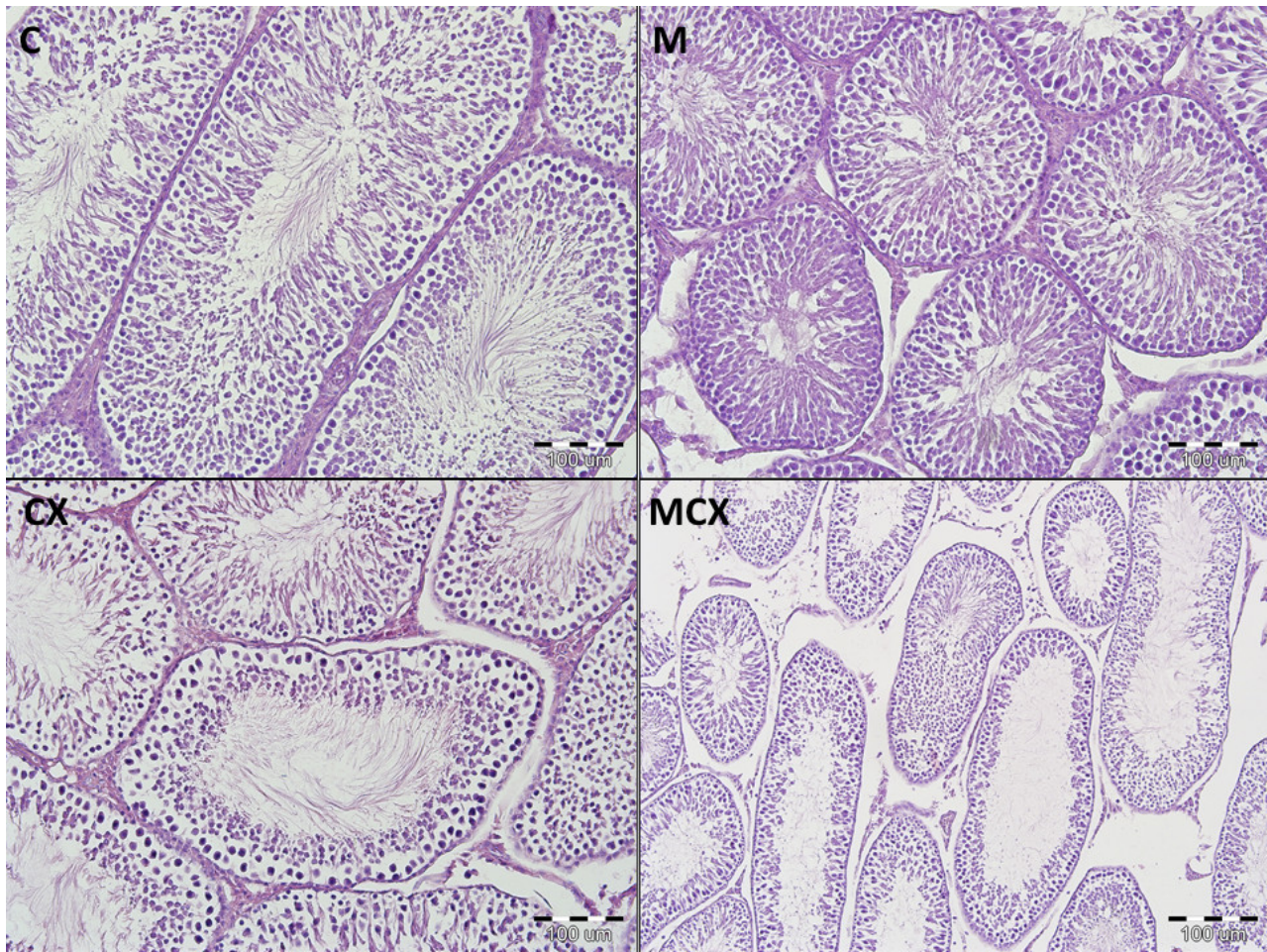


**Figure 3.** Histological cross-sections of testes (HE staining, magnification 200×). C—control group—appearance of normal testis with orderly maturation of germ cells from the base to the center of the lumen: numerous spermatogonia (along the basement membrane), primary and secondary spermatocytes, spermatids, and spermatozoa; M— Morin-5'-sulfonic acid sodium salt (NaMSA) receiving group—appearance of normal testis: the seminiferous tubules with numerous germ cells; CX—cyclophosphamide receiving group—changes grade 2—the seminiferous tubules with loss of germ cells, there is an orderly maturation of germ cells from the base to the center of the lumen, but the number of spermatogonia (along the basement membrane), primary and secondary spermatocytes, spermatids, and spermatozoa is decreased; MCX—group receiving cyclophosphamide and NaMSA—changes grade 1—the seminiferous tubules with discrete germ cells loss, there is an orderly maturation of germ cells from the base to the center of the lumen, but the number of spermatogonia (along the basement membrane), primary and secondary spermatocytes, spermatids, and spermatozoa is slightly reduced.

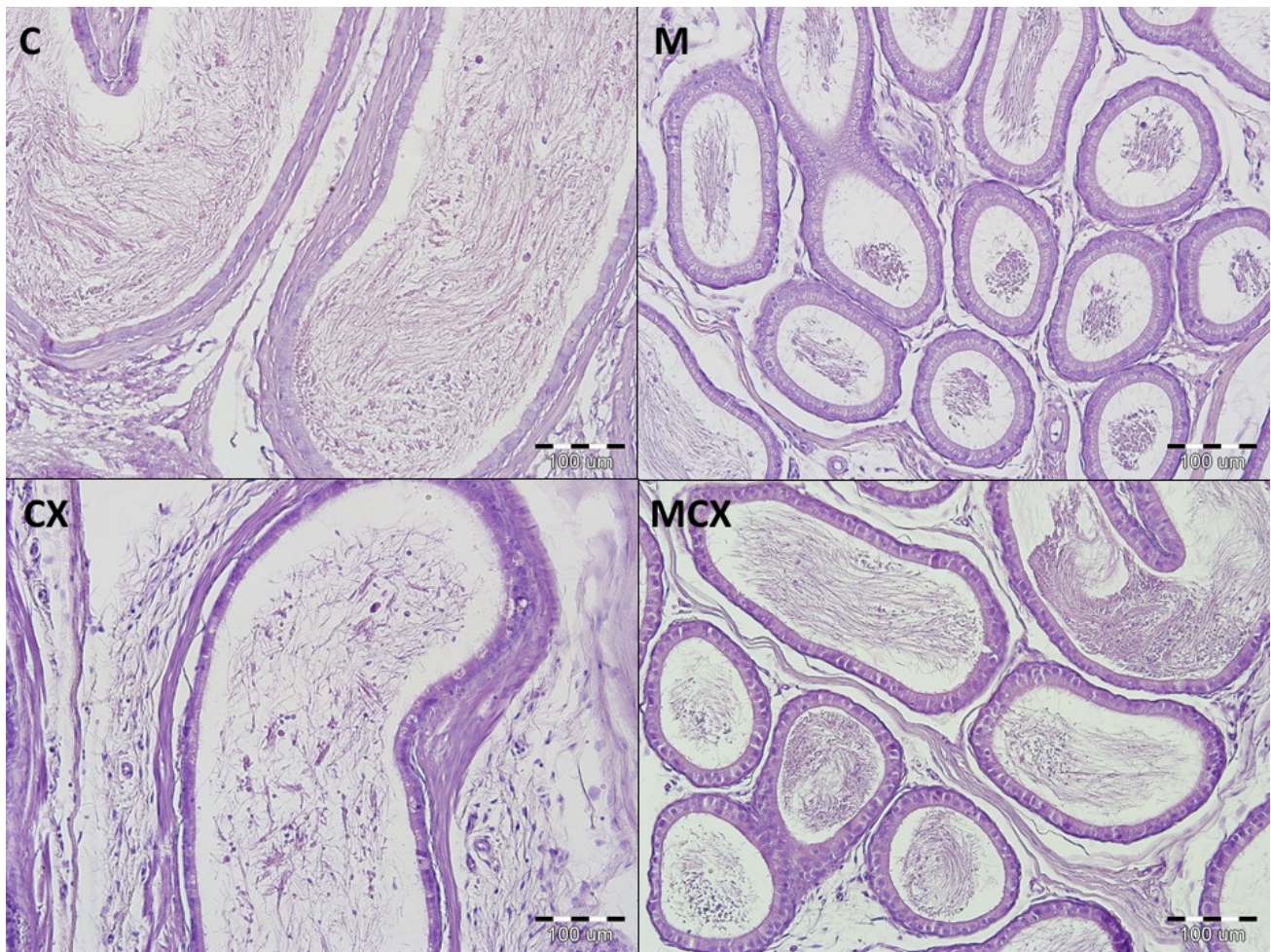


**Figure 4.** Histological cross-sections of epididymes (HE staining, magnification 200×). C—control group—no pathological changes, tubules have thick muscular coat, the lining is composed of tall, ciliated columnar cells, without atypia; M—NaMSA receiving group—no pathological changes, tubules have thick muscular coat, the lining is composed of tall, ciliated columnar cells, without atypia; CX—cyclophosphamide receiving group—changes grade 1—tubules have thick muscular coat, the lining is composed of tall, ciliated columnar cells, with some discrete changes; MCX—group receiving cyclophosphamide and NaMSA—no pathological changes, tubules have thick muscular coat, the lining is composed of tall, ciliated columnar cells, without atypia.

## 2.2. Urinary Bladder Evaluation

Hemorrhage, edema, and ulcerations/erosions in the urinary bladders were assessed and pathological changes were also the most significant in the CPX-receiving group. Similarly, treatment for 10 days with NaMSA reversed significantly CPX-induced changes reflected by decreased urinary bladder scoring system shown in Figure 1.

Additionally, in urinary bladders, analysis of bladder score was performed separately for male and female rats and results as shown in Figure 2. In male rats, the most significant pathologies were found in the CPX-receiving group and the addition of NaMSA fully reversed these changes. In female rats, abnormalities caused by CPX were only partly reversed by NaMSA co-administration. Representative histological changes for tested groups for urinary bladders are presented in Figure 5.

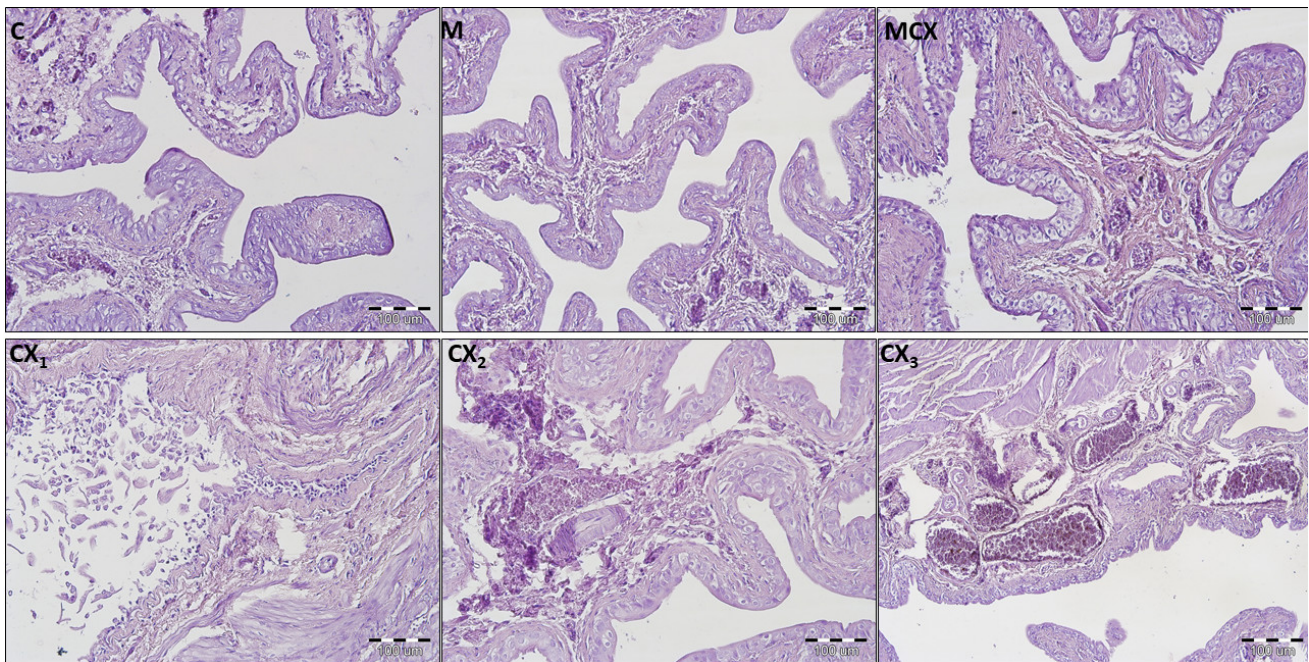


**Figure 5.** Histological cross-sections of urinary bladders (HE staining, magnification 200×). C—control group—no pathological changes; M—group receiving NaMSA—edema and discrete hyperemia of submucosa, there are normal 5–7 layers of transitional epithelium without atypia and some slightly dilated blood vessels; MCX—group receiving cyclophosphamide and NaMSA—edema of submucosa, there are normal 5–7 layers of transitional epithelium without atypia and some slightly dilated blood vessels; CX—group receiving cyclophosphamide—selected characteristic abnormalities; CX1—erosion of normal transitional epithelium without inflammation; CX2—edema and discrete hyperemia of submucosa, there are normal 5–7 layers of transitional epithelium without atypia and some slightly dilated blood vessels; CX3—high degree hyperemia of submucosa, there are normal 5–7 layers of transitional epithelium without atypia and some significantly dilated blood vessels.

### 3. Discussion

Cyclophosphamide belongs to the conventional anticancer agents but still is used as an important treatment option for many solid tumors or hematological malignancies, e.g., breast cancer or Hodgkin lymphoma. The drug is also a part of conditioning for a bone marrow transplantation or an alternative immunosuppressant in drug-resistant nephrotic syndrome in children or in systemic lupus erythematosus. Besides myelotoxicity typical for many anticancer drugs, cyclophosphamide causes significant adverse effects in the urinary tract and affects the male reproductive system with oligo- and azoospermia, testicular atrophy and sometimes irreversible infertility [7]. Hemorrhagic cystitis is a potentially life-threatening complication [16] and the recommended prevention with mesna administration with forced saline diuresis is still one of the most often chosen options, but not sufficient in all patients [17]. Therefore, there is a great need to search for new substances to increase efficacy of prevention of CPX-induced toxicities. Natural compounds, especially flavonoids, or their chemically modified derivatives are in the interest of many researches due to their potential anti-inflammatory and antioxidant activities. Morin-5'-sulfonic acid sodium salt (NaMSA) is a water-soluble derivative of naturally-occurred morin. Morin was found in many fruits and vegetables, e.g., *Psidium guajava*, *Acridocarpus orientalis*, *Moringa oleifera*, *Satureja hortensis*, all parts of almonds or in seaweed. Natural morin and NaMSA was found to scavenge free radicals and protect from damage caused by oxygen free radicals [18–21]. Among others, generation of free radicals is one of the postulated CPX-induced toxicity in various tissues [22]. We have previously found that NaMSA reversed CPX-induced decrease in superoxide dismutase activity and GSH level in rat kidneys [11] and protected from CPX-caused abnormalities in the gastrointestinal tract, revealed in a histological examination [12]. In this paper, we describe morphological

changes in rat testes, epididymes, and urinary bladder after administration of CPX in a daily dose of 15 mg/kg for 10 days. CPX-induced changes in urogenital tract in animals are well described in various experimental models of CPX toxicity. The model of single intraperitoneal injection of CPX in a dose of 200 mg/kg is often used with the studied compound administered before or after the CPX injection to induce acute hemorrhagic cystitis or testicular toxicity [10,23,24], but other regimens of CPX administration are also applied, e.g., daily intraperitoneal injection of 100 mg/kg CPX dose for 3 days [25]. We chose 10 days intragastric administration of CPX in a low daily dose of 15 mg/kg with concomitant administration of NaMSA (100 mg/kg) as the potentially protective agent. This resembles more immunosuppressive rather than anticancer scheme, however, in our model we also found significant abnormalities in histological examination in testes, epididymes, and urinary bladders. In testes and epididymes, irregular and diminished seminiferous tubules were described as focal or diffuse. In urinary bladders edema, hemorrhage and urothelial erosions with desquamation of urothelium were found. Changes in the urinary bladders were less pronounced than described by other scientists in acute models of hemorrhagic cystitis induced by intraperitoneal injections of high-dose CPX. In this kind of CPX-induced bladder toxicity urothelial necrosis, vesical edema, increased urothelium thickness, erosion, ulceration, severe hemorrhage, inflammation, leukocyte infiltration, or even fibrosis were noticed [10,25,26].

Flavonoids were, and still are, an emerging topic for scientists due to many potential actions as free radicals scavenging, antitumor, or anti-inflammatory effects. Among various flavonoids, morin is of interest because it may heal injured cells [18]. Some environmental toxins such as titanium dioxide nanoparticles or mercuric chloride (HgCl<sub>2</sub>) upregulate expression of Bax and caspase-3 genes expression and downregulate Bcl-2. Morin or NaMSA may attenuate those changes which, next to the antioxidant activity of both substances, may protect from membrane damage resulting in decreased cell death and apoptosis [18,27].

Little is known about the protective effects of morin or its water-soluble derivative—morin-5'-sulfonic acid sodium salt—on damages caused by cyclophosphamide. Testicular toxicity is also an adverse effect of some other anticancer agents, e.g., procarbazine. Olaynka et al. [28] found that morin significantly restored the procarbazine-induced abnormal sperm parameters (count, motility, percentage of normal sperm). Some studies claim that morin protects testicular tissue from morphological injuries and pathology of sperm count and viability induced by titanium dioxide nanoparticles [27,29]. Pretreatment with morin significantly decreases expression of proinflammatory cytokines such as IL-1, TNF-alpha, NF-kappaB, and histological damage in rat kidney in doxorubicin-induced toxicity [30]. In vitro morin protects from apoptosis of renal proximal tubular cells (HK-2 cell line) caused by endoplasmic reticulum stress [31]. Recent studies also suggest that morin may increase anticancer activity of some conventional anticancer agents, e.g., fludarabine, inhibiting low molecular weight protein tyrosine phosphatase (LMW-PTP) [32], and may inhibit proliferation, migration, and invasion of EJ cells of bladder cancer via many different intracellular mechanisms [33].

To our best knowledge, little is known about the action of morin or its derivative such as NaMSA on damages caused by cyclophosphamide or other toxins in urinary bladder. Based on our preliminary findings, it may be suggested that NaMSA exerts some protective effects in the urinary bladder in rats receiving CPX in low daily doses. The exact mechanism of this activity requires further, detailed studies, also in the well-established acute model of CPX bladder toxicity. The NaMSA effect in urinary bladders seems to be more pronounced in male than female rats, but it also must be confirmed in the future. A study of Bon et al. [34] examined differences in CPX-induced bladder inflammation in male and female rats after administration of a single 100 mg/kg intraperitoneal dose. In general, they did not observe sex differences in bladder inflammation after CPX. Neither the time of day nor estrous cycle gave significantly different effects on the degree of cystitis but bladder inflammation in female rats was the most severe in rats in estrous stage when

CPX was administered in the morning. Terado et al. [35] administered intraperitoneally CPX to ovariectomized or castrated rats and described typical histological changes in bladders in a form of submucosal edema, urothelial damage, hemorrhage, and leukocyte infiltration. Observed pathologies were more severe in ovariectomized females than in the CPX-administered sham-operated females, on the other hand, in male rats castration did not influence the severity of pathological changes in urinary bladder when compared to the sham-operated group. Treatment of ovariectomized females with estrogen ameliorated histological changes induced by CPX administration [35]. It was also found that estrogen administration decreases the severity of inflammation in the bladder in mice model of acute or chronic CPX-induced cystitis [36]. Early clinical data from very few series of cases also suggested some additional benefits in patients treated with conjugated estrogen who received CPX treatment, especially in decreasing hematuria. The mechanism of estrogen's action in controlling the CPX-induced hematuria is still unclear, but some data suggest the action on cellular and cytokine immune response during inflammation, enhanced healing of damaged tissue, and/or improved endothelial cell function [37–39]. In our study, the females were not ovariectomized and we did not check the reproductive phase, so to make conclusions about differences in NaMSA action in bladders in male and females detailed studies are necessary. The degree of pathological changes in bladders of males and females, expressed in 0–6-point scoring system, was not significantly different.

#### 4. Materials and Methods

##### 4.1. Animals

An experiment was performed after the approval of the Local Ethics Committee for Animal Experiments in Wrocław at the Hirszfild Institute of Immunology and Experimental Therapy of Polish Academy of Sciences and all experiments were performed in accordance with relevant named guidelines and regulations. There were 48 male and female Wistar rats, obtained from the Animal Research Center at Wrocław Medical University (Wrocław, Poland), with average weight of  $203.5 \text{ g} \pm 17.6 \text{ g}$ , housed in standard laboratory conditions (12 h:12 h light-dark cycle, 21–23 °C, free access to standard rat chow and water) arranged in four experimental groups of 12 animals each (6 males and 6 females).

##### 4.2. Design of the Experiment

The groups were as follows: C, M, CX, and MCX, receiving 0.9% saline solution only (Polpharma S.A., Starogard Gdański, Poland), NaMSA alone (100 mg/kg/day), cyclophosphamide alone (15 mg/kg/day, Sigma, Steinheim, Germany), and CPX (15 mg/kg/day) with NaMSA (100 mg/kg/day), respectively. CPX and NaMSA were administered intragastrically by the tube, after reconstitution in normal saline in 4 mL/kg volume for 10 days. Normal saline in group C was given in the equivalent volume. CPX was given at 9 a.m., whereas NaMSA was administered at 2 p.m. as it was described in earlier publications to minimize chemical interaction in the gastrointestinal tract [11,40,41]. Morin-5'-sulfonic acid sodium salt was synthesized at the Department of Inorganic and Analytical Chemistry, Rzeszow University of Technology, Poland, according to the methods described previously [42–44]. On the 11th day of the study rats were euthanized by dislocation of cervical vertebrae in deep peritoneal barbiturate anesthesia.

##### 4.3. Histological Assessment

Testes and epididymes from male and urinary bladders from male and female rats were isolated, 4% buffered formalin fixed, paraffin-embedded and cut with a microtome into 5 µm thick slices and stained with hematoxylin-eosin for histological examination performed by two independent practiced two pathomorphologists. In testes and epididymes changes in spermatogenic epithelium and in seminiferous tubules epithelium were described as irregular and diminished seminiferous tubules with minimal, low grade (<25%) focal changes (1 point) or with moderate, high grade (≥25%) diffuse changes (2 points). Decreased amount of sperm within the lumen of seminiferous tubules was assessed ac-

according to the control group and described as minimal (1 point) or moderate (2 points). Every specimen was described by points (0–6), 0 points were given when no pathological changes were found in testes, epididymes and sperm count. Microscopic evaluation of urinary bladders assessed hemorrhage, edema, and urothelium loss. Each pathology was scored separately from 0 to 2 points. Scoring system of hemorrhage was as follows: 0 point—none, 1 point—mild, 2 points—severe and edema was scored as: 0 point—none, 1 point—flattening with submucosal edema, 2 points—severe. Erosions in urothelium were scored: 0 points—none, 1 point—minimal lesions, single cells loss, exfoliation of superficial epithelial cells, 2 points—significant mucosal erosion.

#### 4.4. Statistical Analysis

Means  $\pm$  standard deviation (SD) were used to describe experimental data. Statistical analysis of the effects of the drug on the studied parameters was performed using analysis of variance (ANOVA). After checking the equality of variances by Brown-Forsythe test, specific comparisons between studies groups were done with post-hoc NIR test. Hypotheses were considered positively verified if  $p < 0.05$ . Statistical analysis was performed using STATISTICA 13 PL (StatSoft, Kraków, Poland).

## 5. Conclusions

In conclusion, our preliminary findings suggest that NaMSA may prevent from morphological changes induced by CPX administration in the male reproductive system and in bladders of both sexes, especially in male rats, but this requires further research in other experimental models of CPX administration focused on detailed, potential mechanisms of such action.

**Author Contributions:** Conceptualization, A.M.-L.; methodology, A.M.-L.; formal analysis, A.M.-L.; investigation, A.M.-L., A.H., D.S. and M.T.; resources, A.S.; writing—original draft preparation, A.M.-L., M.T. and M.S.-B.; writing—review and editing, A.M.-L.; D.K., A.M., B.N., T.S. and A.S.; supervision, A.S.; project administration, A.M.-L.; funding acquisition, A.S.; synthesis of the original compound NaMSA, A.K. All authors have read and agreed to the published version of the manuscript.

**Funding:** This research received no external funding.

**Institutional Review Board Statement:** Animal experiment was performed after the approval of the Local Ethics Committee for Animal Experiments in Wrocław at Hirsfeld Institute of Immunology and Experimental Therapy of Polish Academy of Sciences (approval code 36/08) and all experiments were performed in accordance with relevant named guidelines and regulations.

**Informed Consent Statement:** Not applicable.

**Data Availability Statement:** The data underlying this article will be shared on request to the corresponding author.

**Conflicts of Interest:** The authors declare no conflict of interest.

## References

- Allen, C.M.; Lopes, F.; Mitchell, R.T.; Spears, N. How does chemotherapy treatment damage the prepubertal testis? *Reproduction* **2018**, *156*, R209–R233. [CrossRef]
- Zhu, B.; Zheng, Y.F.; Zhang, Y.Y.; Cao, Y.S.; Zhang, L.; Li, X.G.; Liu, T.; Jiao, Z.Z.; Wang, Q.; Zhao, Z.G. Protective effect of L-carnitine in cyclophosphamide-induced germ cell apoptosis. *J. Zhejiang Univ. Sci. B* **2015**, *16*, 780–787. [CrossRef] [PubMed]
- Ghaleno, L.R.; Alizadeh, A.; Drevet, J.R.; Shahverdi, A.; Valojerdi, M.R. Oxidation of sperm dna and male infertility. *Antioxidants* **2021**, *10*, 97. [CrossRef] [PubMed]
- Yilmaz, N.; Emmungil, H.; Gucenmez, S.; Ozen, G.; Yildiz, F.; Balkarli, A.; Kimyon, G.; Coskun, B.N.; Dogan, I.; Pamuk, O.N.; et al. Incidence of cyclophosphamide-induced urotoxicity and protective effect of mesna in rheumatic diseases. *J. Rheumatol.* **2015**, *42*, 1661–1666. [CrossRef]
- Demlova, R.; Valík, D.; Obermannova, R.; Zdražilová-Dubská, L. The safety of therapeutic monoclonal antibodies: Implications for cancer therapy including immuno-checkpoint inhibitors. *Physiol. Res.* **2016**, *65*, S455–S462. [CrossRef] [PubMed]
- Matz, E.L.; Hsieh, M.H. Review of Advances in Uroprotective Agents for Cyclophosphamide- and Ifosfamide-induced Hemorrhagic Cystitis. *Urology* **2017**, *100*, 16–19. [CrossRef]

7. Cyclophosphamide Cadiasun—Summary of Product Characteristics. 2021. Available online: <https://mri.cts-mrp.eu/hu> (accessed on 31 January 2021).
8. Arena, A.C.; Jorge, B.C.; Silva, M.C.; de Barros, A.L.; Fernandes, A.A.H.; Nóbrega, R.H.; Martinez, E.R.M.; Cardoso, C.A.L.; Anselmo-Franci, J.A.; Muzzi, R.M. Acrocomia aculeata oil: Beneficial effects on cyclophosphamide-induced reproductive toxicity in male rats. *Andrologia* **2018**, *50*, 1–11. [CrossRef]
9. Potnuri, A.G.; Allakonda, L.; Lahkar, M. Crocin attenuates cyclophosphamide induced testicular toxicity by preserving glutathione redox system. *Biomed. Pharmacother.* **2018**, *101*, 174–180. [CrossRef]
10. Wu, K.C.; Lin, W.Y.; Sung, Y.T.; Wu, W.Y.; Cheng, Y.H.; Chen, T.S.; Chiang, B.J.; Chien, C.T. Glycine tomentella hayata extract and its ingredient daidzin ameliorate cyclophosphamide-induced hemorrhagic cystitis and oxidative stress through the action of antioxidation, anti-fibrosis, and anti-inflammation. *Chin. J. Physiol.* **2019**, *62*, 188–195. [CrossRef]
11. Merwid-Łąd, A.; Trocha, M.; Chlebda, E.; Sozański, T.; Magdalan, J.; Książczyńska, D.; Kopacz, M.; Kuźniar, A.; Nowak, D.; Pieśniewska, M.; et al. Effects of morin-5'-sulfonic acid sodium salt (NaMSA) on cyclophosphamide-induced changes in oxido-redox state in rat liver and kidney. *Hum. Exp. Toxicol.* **2012**, *31*, 812–819. [CrossRef]
12. Merwid-Łąd, A.; Książczyńska, D.; Hałoń, A.; Chlebda-Sieragowska, E.; Trocha, M.; Szandruk, M.; Sozański, T.; Magdalan, J.; Kopacz, M.; Kuźniar, A.; et al. Impact of morin-5'-sulfonic acid sodium salt on cyclophosphamide-induced gastrointestinal toxicity in rats. *Pharmacol. Rep.* **2015**, *67*, 1259–1263. [CrossRef]
13. Salimnejad, R.; Spermehani Rad, J.; Mohammad Nejad, D.; Roshangar, L. Effect of ghrelin on total antioxidant capacity, lipid peroxidation, sperm parameters and fertility in mice against oxidative damage caused by cyclophosphamide. *Andrologia* **2018**, *50*, 1–7. [CrossRef]
14. Onaolapo, A.Y.; Oladipo, B.P.; Onaolapo, O.J. Cyclophosphamide-induced male subfertility in mice: An assessment of the potential benefits of Maca supplement. *Andrologia* **2018**, *50*, e12911. [CrossRef]
15. Zhang, X.; Gao, S.; Tanaka, M.; Zhang, Z.; Huang, Y.; Mitsui, T.; Kamiyama, M.; Koizumi, S.; Fan, J.; Takeda, M.; et al. Carbenoxolone inhibits TRPV4 channel-initiated oxidative urothelial injury and ameliorates cyclophosphamide-induced bladder dysfunction. *J. Cell. Mol. Med.* **2017**, *21*, 1791–1802. [CrossRef]
16. Kaplan, J.R.; Wolf, J.S. Efficacy and Survival Associated With Cystoscopy and Clot Evacuation for Radiation or Cyclophosphamide Induced Hemorrhagic Cystitis. *J. Urol.* **2009**, *181*, 641–646. [CrossRef]
17. Moy, B.; Linder, B.J.; Chao, N.J.; Gounder, M.M. Hemorrhagic cystitis in cancer patients. *UpToDate* **2018**, *11*, 1–29.
18. Venkatesan, R.S.; Sadiq, A.M.M. Effect of morin-5'-sulfonic acid sodium salt on the expression of apoptosis related proteins caspase 3, Bax and Bcl 2 due to the mercury induced oxidative stress in albino rats. *Biomed. Pharmacother.* **2017**, *85*, 202–208. [CrossRef]
19. Emre, İ.; Kurşat, M.; Yilmaz, Ö.; Erecevit, P. Chemical compositions, radical scavenging capacities and antimicrobial activities in seeds of *Satureja hortensis* L. and *Mentha spicata* L. subsp. *spicata* from Turkey. *Braz. J. Biol.* **2020**, *81*, 144–153. [CrossRef]
20. Caicedo-Lopez, L.H.; Cuellar-Nuñez, M.L.; Luzardo-Ocampo, I.; Campos-Vega, R.; Lóarca-Piña, G. Colonic metabolites from digested *Moringa oleifera* leaves induced HT-29 cell death via apoptosis, necrosis, and autophagy. *Int. J. Food Sci. Nutr.* **2020**, 1–14. [CrossRef]
21. Caselli, A.; Cirri, P.; Santi, A.; Paoli, P. Morin: A Promising Natural Drug. *Curr. Med. Chem.* **2016**, *23*, 774–791. [CrossRef] [PubMed]
22. Abraham, P.; Isaac, B.; Ramamoorthy, H.; Natarajan, K. Oral Glutamine Attenuates Cyclophosphamide-Induced Oxidative Stress in the Bladder but Does Not Prevent Hemorrhagic Cystitis in Rats. *J. Med. Toxicol.* **2011**, *7*, 118–124. [CrossRef]
23. Kaya, C.; Baseskioglu, A.B.; Yigitaslan, S.; Ozatik, F.Y.; Ozatik, O.; Uslu, S. The therapeutic potential of amifostine on cyclophosphamide-induced testicular dysfunction in rats: An experimental study. *Int. J. Reprod. Biomed.* **2019**, *17*, 245–252. [CrossRef]
24. Caglayan, C. The effects of naringin on different cyclophosphamide-induced organ toxicities in rats: Investigation of changes in some metabolic enzyme activities. *Environ. Sci. Pollut. Res.* **2019**, *26*, 26664–26673. [CrossRef] [PubMed]
25. Sucic, M.; Luetic, K.; Jandric, I.; Drmic, D.; Sever, A.Z.; Vuletic, L.B.; Halle, Z.B.; Strinic, D.; Kokot, A.; Seiwert, R.S.; et al. Therapy of the rat hemorrhagic cystitis induced by cyclophosphamide. Stable gastric pentadecapeptide BPC 157, L-arginine, L-NAME. *Eur. J. Pharmacol.* **2019**, *861*. [CrossRef] [PubMed]
26. Wróbel, A.; Serefko, A.; Bańcerowska-Górska, M.; Szopa, A.; Dudka, J.; Poleszak, E. Intravesical administration of blebbistatin prevents cyclophosphamide-induced toxicity of the urinary bladder in female Wistar rats. *NeuroUrol. Urodyn.* **2019**, 1044–1052. [CrossRef] [PubMed]
27. Shahin, N.N.; Mohamed, M.M. Nano-sized titanium dioxide toxicity in rat prostate and testis: Possible ameliorative effect of morin. *Toxicol. Appl. Pharmacol.* **2017**, *334*, 129–141. [CrossRef]
28. Olayinka, E.T.; Ore, A.; Adeyemo, O.A.; Ola, O.S. The role of flavonoid antioxidant, morin in improving procarbazine-induced oxidative stress on testicular function in rat. *Porto Biomed. J.* **2019**, *4*, e28. [CrossRef] [PubMed]
29. Hussein, M.M.A.; Gad, E.; Ahmed, M.M.; Arisha, A.H.; Mahdy, H.F.; Swelum, A.A.A.; Tukur, H.A.; Saadeldin, I.M. Amelioration of titanium dioxide nanoparticle reprotoxicity by the antioxidants morin and rutin. *Environ. Sci. Pollut. Res.* **2019**, *26*, 29074–29084. [CrossRef] [PubMed]
30. Kuzu, M.; Yıldırım, S.; Kandemir, F.M.; Küçükler, S.; Çağlayan, C.; Türk, E.; Dörtbudak, M.B. Protective effect of morin on doxorubicin-induced hepatorenal toxicity in rats. *Chem. Biol. Interact.* **2019**, *308*, 89–100. [CrossRef]

31. Mo, J.S.; Choi, D.; Han, Y.R.; Kim, N.; Jeong, H.S. Morin has protective potential against ER stress induced apoptosis in renal proximal tubular HK-2 cells. *Biomed. Pharmacother.* **2019**, *112*. [CrossRef]
32. Capitani, N.; Lori, G.; Paoli, P.; Patrussi, L.; Troilo, A.; Baldari, C.T.; Raugei, G.; D'Elia, M.M. LMW-PTP targeting potentiates the effects of drugs used in chronic lymphocytic leukemia therapy. *Cancer Cell Int.* **2019**, *19*, 1–9. [CrossRef]
33. Shin, S.S.; Won, S.Y.; Noh, D.H.; Hwang, B.; Kim, W.J.; Moon, S.K. Morin Inhibits Proliferation, Migration, and Invasion of Bladder Cancer EJ Cells via Modulation of Signaling Pathways, Cell Cycle Regulators, and Transcription Factor-Mediated MMP-9 Expression. *Drug Dev. Res.* **2017**, *78*, 81–90. [CrossRef]
34. Bon, K.; Lantéri-Minet, M.; Menétrey, D.; Berkley, K.J. Sex, time-of-day and estrous variations in behavioral and bladder histological consequences of cyclophosphamide-induced cystitis in rats. *Pain* **1997**, *73*, 423–429. [CrossRef]
35. Terado, M.; Nomura, M.; Mineta, K.; Nishii, H.; Fujimoto, N.; Sasaguri, T.; Sasaguri, Y.; Matsumoto, T. Involvement of estrogen in the pathogenesis of cyclophosphamide-induced cystitis in rats. *Endocrine* **2005**, *26*, 55–63. [CrossRef]
36. Martinez-Ferrer, M.; Iturregui, J.M.; Uwamariya, C.; Starkman, J.; Sharif-Afshar, A.R.; Suzuki, K.; Visedsindh, W.; Matusik, R.J.; Dmochowski, R.R.; Bhowmick, N.A. Role of nicotinic and estrogen signaling during experimental acute and chronic bladder inflammation. *Am. J. Pathol.* **2008**, *172*, 59–67. [CrossRef]
37. Liu, Y.K.; Harty, J.I.; Steinbock, G.S.; Holt, H.A.; Goldstein, D.H.; Amin, M. Treatment of radiation or cyclophosphamide induced hemorrhagic cystitis using conjugated estrogen. *J. Urol.* **1990**, *144*, 41–43. [CrossRef]
38. Ordemann, R.; Naumann, R.; Geissler, G.; Bornhauser, M.; Schuler, U.; Ehninger, G. Encouraging results in the treatment of haemorrhagic cystitis with estrogen-report of 10 cases and review of the literature. *Bone Marrow Transplant.* **2000**, *25*, 981–985. [CrossRef]
39. Kopterides, P.; Theodorakopoulou, M.; Mentzelopoulos, S.; Armaganidis, A. Cyclophosphamide-induced hemorrhagic cystitis successfully treated with conjugated estrogens. *Am. J. Hematol.* **2005**, *80*, 166–167. [CrossRef]
40. Magdalan, J.; Szeląg, A.; Kopacz, M.; Kuźniar, A.; Nowak, D.; Kowalski, P.; Pieśniewska, M. Morin–5′–Sulfonic Acid Sodium Salt as an Antidote in the Treatment of Acute Chromium Poisoning in Rats. *Adv. Clin. Exp. Med.* **2006**, *15*, 767–776.
41. Magdalan, J.; Szeląg, A.; Kopacz, M.; Kuźniar, A.; Nowak, D.; Kowalski, P.; Pieśniewska, M. Quercetin–5′–Sulfonic Acid Sodium Salt and Morin–5′–Sulfonic Acid Sodium Salt as Antidotes in the Treatment of Acute Inorganic Mercury Poisoning—Experimental Studies. *Adv. Clin. Exp. Med.* **2006**, *15*, 581–587.
42. Kopacz, M. Sulfonic derivatives of morin. *Pol. J. Chem.* **1981**, *55*, 225–229.
43. Kopacz, M. Quercetin- and Morinsulfonates as Analytical Reagents. *J. Anal. Chem.* **2003**, *58*, 225–229. [CrossRef]
44. Kuźniar, A.; Kopacz, M.; Nowak, D. Characterization and spectroscopic study of new complexes of Cd(II), Hg(II) and Pb(II) with the sodium salt of morin-5′-sulfonic acid. *J. Coord. Chem.* **2008**, *61*, 1005–1018. [CrossRef]







## Article

# Effect of a Low Dose of Carvedilol on Cyclophosphamide-Induced Urinary Toxicity in Rats—A Comparison with Mesna

Anna Merwid-Łąd <sup>1,\*</sup>, Piotr Ziółkowski <sup>2</sup>, Marta Szandruk-Bender <sup>1,\*</sup>, Agnieszka Matuszewska <sup>1</sup>, Adam Szelaǵ <sup>1</sup> and Małgorzata Trocha <sup>1</sup>

<sup>1</sup> Department of Pharmacology, Wrocław Medical University, J. Mikulicza-Radeckiego 2, 50-345 Wrocław, Poland; agnieszka.matuszewska@umw.edu.pl (A.M.); adam.szelaǵ@umw.edu.pl (A.S.); malgorzata.trocha@umw.edu.pl (M.T.)

<sup>2</sup> Department of Pathology, Wrocław Medical University, K. Marcinkowskiego 1, 50-368 Wrocław, Poland; piotr.ziolkowski@umw.edu.pl

\* Correspondence: anna.merwid-lad@umw.edu.pl (A.M.-L.); marta.szandruk@umw.edu.pl (M.S.-B.); Tel.: +48-717-841-442 (A.M.-L.); +48-717-841-438 (M.S.-B.)

**Abstract:** One of the major side effects of cyclophosphamide (CPX)—an alkylating anticancer drug that is still clinically used—is urotoxicity with hemorrhagic cystitis. The present study was designed to evaluate the ability of carvedilol to protect rats from cyclophosphamide-induced urotoxicity. Rats were injected intraperitoneally (*i.p.*) with CPX (200 mg/kg) and administered carvedilol (2 mg/kg) intragastrically a day before, at the day and a day after a single *i.p.* injection of CPX, with or without mesna (40, 80, and 80 mg/kg *i.p.* 20 min before, 4 h and 8 h after CPX administration, respectively). Pretreatment with carvedilol partly prevented the CPX-induced increase in urinary bladder and kidney index, and completely protects from CPX-evoked alterations in serum potassium and creatinine level, but did not prevent histological alterations in the urinary bladder and hematuria. However, carvedilol administration resulted in significant restoration of kidney glutathione (GSH) level and a decrease in kidney interleukin 1 $\beta$  (IL-1 $\beta$ ) and plasma asymmetric dimethylarginine (ADMA) concentrations. Not only did mesna improve kidney function, but it also completely reversed histological abnormalities in bladders and prevented hematuria. In most cases, no significant interaction of carvedilol with mesna was observed, although the effect of both drugs together was better than mesna given alone regarding plasma ADMA level and kidney IL-1 $\beta$  concentration. In conclusion, carvedilol did not counteract the injury caused in the urinary bladders but restored kidney function, presumably via its antioxidant and anti-inflammatory properties.

**Citation:** Merwid-Łąd, A.; Ziółkowski, P.; Szandruk-Bender, M.; Matuszewska, A.; Szelaǵ, A.; Trocha, M. Effect of a Low Dose of Carvedilol on Cyclophosphamide-Induced Urinary Toxicity in Rats—A Comparison with Mesna. *Pharmaceuticals* **2021**, *14*, 1237. <https://doi.org/10.3390/ph14121237>

Academic Editors: Mary J. Meegan and Niamh M O'Boyle

Received: 30 October 2021

Accepted: 25 November 2021

Published: 29 November 2021

**Publisher's Note:** MDPI stays neutral with regard to jurisdictional claims in published maps and institutional affiliations.



**Copyright:** © 2021 by the authors. Licensee MDPI, Basel, Switzerland. This article is an open access article distributed under the terms and conditions of the Creative Commons Attribution (CC BY) license (<https://creativecommons.org/licenses/by/4.0/>).

**Keywords:** cyclophosphamide; carvedilol; urinary bladder; kidney; oxidative stress; toxicity

## 1. Introduction

Many drugs, excreted with the kidneys, are later accumulated in urine in high amounts and may interact with urothelium for a long time, especially in the urinary bladder during the night. Urothelium, lining the urinary tract from the kidney to the urethra, is a high-resistance barrier preventing the diffusion of a variety of substances excreted by kidneys to the tissues. This specific structure is, therefore, exposed to high concentrations of endogenous waste products as well as some xenobiotics, including drugs. Additionally, the urothelium is exposed to mechanical stretch due to the physiology of the urination process [1]. Despite the high resistance of urothelium to noxious stimuli, they may irritate the urinary tract, and trigger alterations in the urothelium, nonbacterial inflammatory response (cystitis) leading finally to various injuries, e.g., edema, erosions, ulcerations, or even hematuria. Although damages in the urinary tract are the best described for systemic cyclophosphamide (CPX) administration, some other anticancer agents may interact with

urothelium, causing chemical cystitis as it was found in the case of thiotepa, mitomycin C, doxorubicin, or epirubicin, especially when they are given intravesically for urinary bladder cancer treatment [2,3].

Despite many new, targeted biologic therapies in the treatment of malignancies or autoimmune diseases [4], conventional drugs, such as cyclophosphamide, are still in clinical use. Cyclophosphamide is a DNA-alkylating agent registered, among others, in the treatment of acute and chronic leukemias, Hodgkin's and non-Hodgkin's lymphomas, breast and lung cancers in adults as well as sarcomas in children. It may be also used in some life-threatening autoimmune diseases [2]. There are many possible adverse effects of CPX, very problematic for the patients, and sometimes even fatal in the outcome, and among these are the disorders of the urinary tract with very common cystitis or less common hemorrhagic cystitis with micro- or macroscopic hematuria. Pyelitis, injury of renal tubules, and increased serum creatinine levels with kidney failure are also described. Toxicity in the urinary tract may be seen after both long- and short-term treatment. Ulcerations, necrosis, fibrosis, contracture, or sometimes secondary cancers are also possible complications in the urinary bladder [2,5].

The mechanism of CPX-induced injury in the urinary tract is multifactorial and triggered mainly by the interaction of acrolein, a toxic CPX metabolite, with urothelium that induces the inflammatory response. Up-regulation of nuclear factor kappa B (NF- $\kappa$ B) is important in causing such cytokines to release as tumor necrosis factor-alpha (TNF- $\alpha$ ), interleukin 1 $\beta$  (IL-1 $\beta$ ), or IL-6. Additionally, the generation of reactive oxygen species (ROS), overexpression of cyclooxygenase-2 (COX-2) and inducible nitric oxide synthase (iNOS), involvement of bradykinin, substance P, and platelet-activating factor (PAF) is important or suggested in this pathological pathway. This leads to the destruction of the urothelium, erosions, ulcerations, pain, and bladder overactivity with the possible role of activation of alpha-1 adrenergic receptors [6–9]. In addition to the well-described toxicity of CPX in urinary bladders, kidneys are also often affected. Changes in renal function, urine amount, and composition or kidney morphology were noticed [10,11].

For the prevention of CPX-induced hemorrhagic cystitis and reduction in urinary toxicity, bladder irrigation or forced diuresis with prior hydration with or without intravenous administration of mesna (sodium 2-mercapto-ethanesulphonate) are commonly used. The postulated mechanism of mesna, a sulfhydryl compound, is that it binds the methyl group of acrolein which leads to the formation of thioether, which is non-toxic, and does not trigger the inflammatory process [12,13]. Recently, the efficacy of mesna in clinical practice has been widely discussed and some trials, as well as the literature overview, indicate great differences in the conclusions drawn [14–16]. Therefore, there is still a great need to look for new compounds, which may prevent CPX-induced cystitis decreasing the risk of severe hemorrhagic outcomes and additionally may prevent kidney injury.

Carvedilol is a highly lipophilic, third-generation nonselective beta-adrenergic antagonist, additionally acting as an antagonist of alpha-1 receptors with a ratio of beta to alpha blockade of about 10:1. It is also one of the beta adrenergic drugs described as biased agonists promoting  $\beta$ -arrestin-mediated ERK phosphorylation, which finally suggests inhibition of neoplastic transformation and carcinogenesis [17,18].

It is postulated that carvedilol, and its metabolites, are potent antioxidants and scavengers of ROS [19,20]. It is worth mentioning that carvedilol may decrease levels of proinflammatory cytokines, e.g., IL-1 $\beta$ , TNF- $\alpha$  and inhibits COX-2, matrix metalloproteinase 2 (MMP-2), or NF- $\kappa$ B expression in various inflammatory models [21–23].

Many studies focused on the preventive potential of carvedilol in anthracycline-induced cardiotoxicity in humans and in a variety of in vitro or animal models [20,24,25], but it was also found that carvedilol may prevent, e.g., from cisplatin-induced kidney injury [26] or testicular and sperm damages [27], may exert nephroprotective action in the model of cyclosporine-induced nephrotoxicity [28] or may prevent from gastric mucosa injury after administration of acetylsalicylic acid [29]. In addition to the postulated protec-

tion in different models of tissue damages, carvedilol seems to modulate MDR1-mediated resistance to anticancer agents [30].

Based on these premises, our study aimed to evaluate the potential of carvedilol in acute, cyclophosphamide-induced urinary tract toxicity.

## 2. Results

### 2.1. Body Weight Changes and Organ Weight

After the adaptation period, on day 1 of the main experiment, the mean body weight in all experimental groups was comparable and no significant differences between groups were noticed (CON— $317.5 \pm 25.3$  g, CPX— $324.2 \pm 22.7$  g, CPX-M— $316.7 \pm 8.9$  g, CPX-C— $304.2 \pm 10.8$ , CPX-MC— $315.8 \pm 12.4$  g). For an explanation of the groups' abbreviations, please see the Materials and Methods section. In all groups receiving cyclophosphamide intraperitoneally in a single dose of 200 mg/kg, a significant decrease in body weight in comparison to the control group was found with the largest body weight loss in the group receiving only CPX. Administration of mesna (200 mg/kg in divided doses), alone or with carvedilol (2 mg/kg, for 3 days), partly prevented the body weight decrease (significant differences vs. CON and CPX group). The action was the least pronounced in the CPX-C group (Figure 1A).

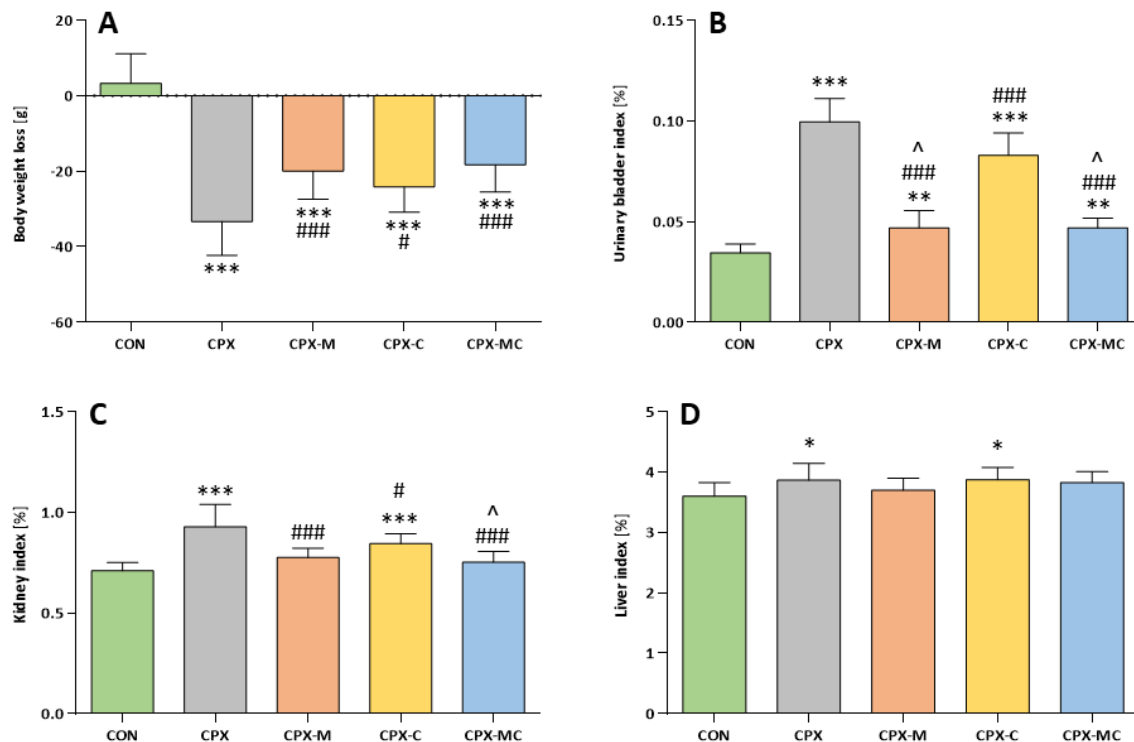


**Figure 1.** Body weight loss (A), urinary bladder index (B), kidney index (C), and liver index (D) calculated as percentages of the total body weight. Data are presented as means  $\pm$  SD. A detailed description of experimental groups is presented in Figure 1 and the Materials and Methods section. \*  $p < 0.05$ , \*\*  $p < 0.01$ , \*\*\*  $p < 0.001$  vs. CON group; #  $p < 0.05$ , ###  $p < 0.001$  vs. CPX group; ^  $p < 0.05$  vs. CPX-C group.

The urinary bladder, kidney, and liver indexes are presented in Figure 1B–D, respectively. The urinary bladder index was the highest in the group receiving CPX, in which it was over 3 times greater than in the control group, and the difference between that and the control was significant. Administration of carvedilol alone partly prevented the increase in bladder index (significant difference compared to the CPX and CON groups), but still it was almost 2.5 times greater than in the control group. The most pronounced prevention was found for groups receiving mesna. The bladder index increase in both cases was about 1.4 times greater than in the control group, but still it was significantly greater than in

CON. However, the difference compared to the CPX group was also significant in the CPX-M and CPX-MC groups. The action of mesna was greater than carvedilol because significant differences were found between CPX-M vs. CPX-C and CPX-MC vs. CPX-C groups. There was no difference between the CPX-M and CPX-MC groups. In the CPX group, the kidney index was the highest and was significantly different from the CON group. Administration of carvedilol only partly prevented an increase in the kidney weight increase. The difference was still significant to the CON, but was also significant to the CPX group. Only groups receiving mesna (CPX-M and CPX-MC) significantly prevented the kidney index increase after CPX and the statistical differences between those and the CPX-receiving group were significant, but insignificant with the control group. The liver index was the highest in the CPX and CPX-C groups and was significantly different from the control group. The addition of mesna completely prevented the increase in the liver index (CPX-M vs. CON and CPX-MC vs. CON,  $p = NS$  in both cases).

## 2.2. Serum Potassium and Creatinine Levels

The highest serum potassium level on day 4 of the study was measured for the CPX group and was significantly different from CON. Administration of mesna alone only partly prevented the increase in serum potassium level (CPX-M vs. CON and CPX-M vs. CPX,  $p < 0.05$  in both comparisons). Carvedilol given alone or in combination with mesna fully prevented the increase in the potassium level in serum and the differences between these two groups and the control group were insignificant, but there were significant differences with the CPX group. In the group receiving CPX, the serum creatinine level was the highest and was significantly different from the control group (1.76 times greater than in the CON). All studied substances fully prevented the serum creatinine level increase and the differences between these groups and CON were insignificant, but significantly different from the CPX group. The action of carvedilol, mesna, and the combination of the treatment was comparable, and no significant differences were noticed between these groups ( $p = NS$  in all comparisons). The mean values and SD for both parameters are presented in Figure 2A,B.

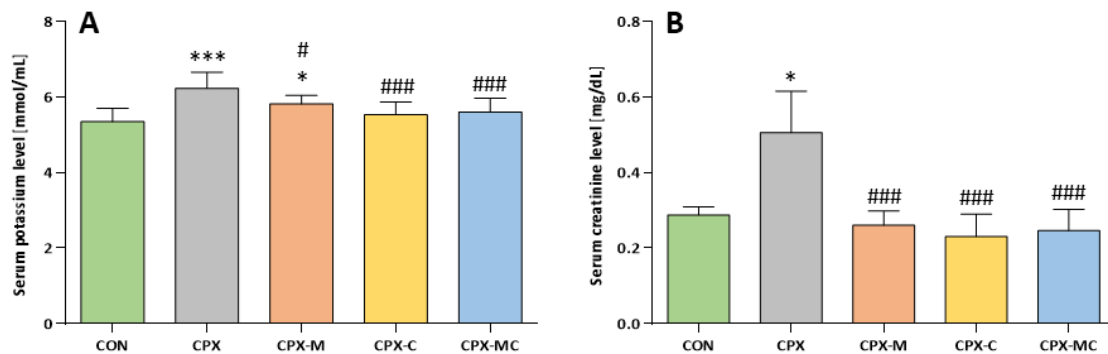


**Figure 2.** Serum potassium (A) and creatinine (B) levels on day 4 of the study. Data are presented as means  $\pm$  SD. A detailed description of experimental groups is presented in Figure 1 and the Materials and Methods section. \*  $p < 0.05$ , \*\*\*  $p < 0.001$  vs. CON group; #  $p < 0.05$ , ###  $p < 0.001$  vs. CPX group.

## 2.3. Hematuria, Urinary Bladder and Kidney Histology, Urinary Bladder and Kidney Scores

Before the intraperitoneal injection of CPX on the dipstick test, no hematuria was noticed in any of the studied groups. Significant hematuria was noticed in the CPX and CPX-C groups in comparison to the control group at 4 h, 8 h, 24 h, and 48 h after the injection of CPX. Intraperitoneal administration of mesna, in an equivalent dose to that of CPX, fully prevented the CPX-induced hematuria (significant difference compared to CPX, but insignificant to CON). The changes in hematuria in time in all experimental groups are presented in Figure 3. Representative images of dipstick tests of hematuria and

macroscopic changes in urinary bladders (just after resection) are presented in Figure 4A,B, respectively.

**Table 1.** Statistical comparisons of hematuria measured semi-quantitatively on the dipstick test between studied groups. Mean values of hematuria in the studied time points with corresponding SD are presented in Figure 4. A detailed description of experimental groups is presented in Figure 1 and in the Materials and Methods section. \*  $p < 0.05$ , \*\*\*  $p < 0.001$  vs. CON group; ##  $p < 0.01$ , ###  $p < 0.001$  vs. CPX group; ^  $p < 0.05$ , ^^  $p < 0.01$ , ^^  $p < 0.001$  vs. CPX-C group.

	5 min before <i>i.p.</i> CPX or Normal Saline Injection	4 h after <i>i.p.</i> CPX or Normal Saline Injection	8 h after <i>i.p.</i> CPX or Normal Saline Injection	24 h after <i>i.p.</i> CPX or Normal Saline Injection	48 h after <i>i.p.</i> CPX or Normal Saline Injection
CON	0.0 ± 0.0	0.0 ± 0.0	0.0 ± 0.0	0.0 ± 0.0	0.0 ± 0.0
CPX	0.0 ± 0.0	2.58 ± 0.67 ***	3.92 ± 0.29 ***	4.00 ± 0.0 ***	4.00 ± 0.0 ***
CPX-M	0.0 ± 0.0	0.17 ± 0.25 ###	0.13 ± 0.31 ###,^^	0.58 ± 0.63 ###,^	1.04 ± 1.03 ###
CPX-C	0.0 ± 0.0	1.29 ± 1.16 *	3.75 ± 0.62 ***	3.33 ± 0.65 ***	2.92 ± 0.29 ***
CPX-MC	0.0 ± 0.0	0.17 ± 0.39 ###	0.29 ± 0.45 ##,^^	0.42 ± 0.51 ###,^^	0.17 ± 0.39 ###,^^

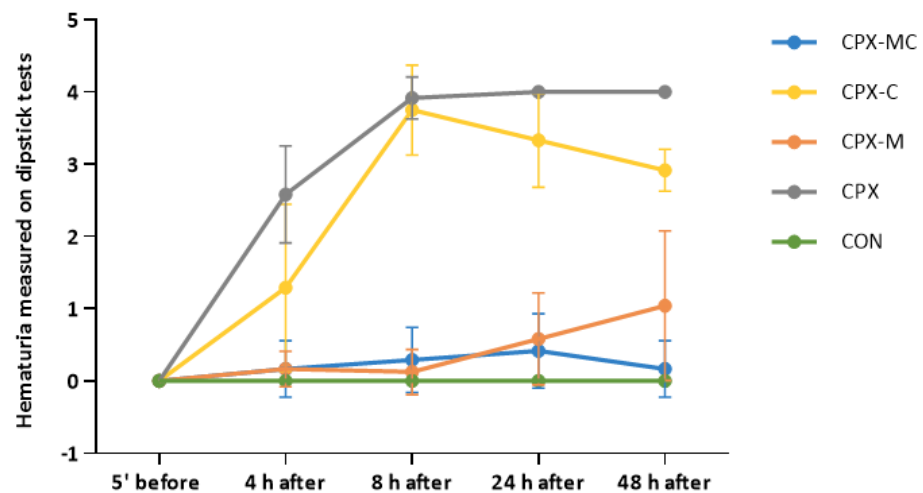


**Figure 3.** Hematuria measured semi-quantitatively on the dipstick test 5 min before, 4 h, 8 h, 24 h, and 48 h after injection of CPX in the studied groups or normal saline in the control group. Hematuria was evaluated from 0 to 4+ (0 means no hematuria detected and 4+ means macroscopically detectable hematuria). Data are presented as means ± SD. A detailed description of experimental groups is presented in Figure 1 and the Materials and Methods section, and detailed statistical comparisons are presented in Table 1.

In the microscopic evaluation of urinary bladders, in almost all studied specimens focal or diffuse urothelium reduction were found; therefore, these changes were not involved in the scoring system as they were nonspecific to any of the performed experimental procedure. The most pronounced changes in a form of inflammatory infiltrations, edema, hemorrhage, or erosions were found in the group receiving only CPX. Additionally, ulceration of urothelium was found in one case. Considering the scoring system of histological changes in urinary bladders, the highest score was calculated for the CPX group and was significantly different from the control group. Carvedilol did not prevent histological injury in urinary bladders and the score value in the CPX-C group was not significantly different from the CPX group, but was significantly different from the CON group. Administration of mesna alone or in combination with carvedilol fully prevented the histological injury and reversed the CPX-induced changes. A significant difference between groups receiving mesna was found in comparison to the CPX-C group. The representative images from urinary bladder histological evaluation are presented in Figure 4C. The mean values with the corresponding SD for urinary bladder score are presented in Figure 5A.

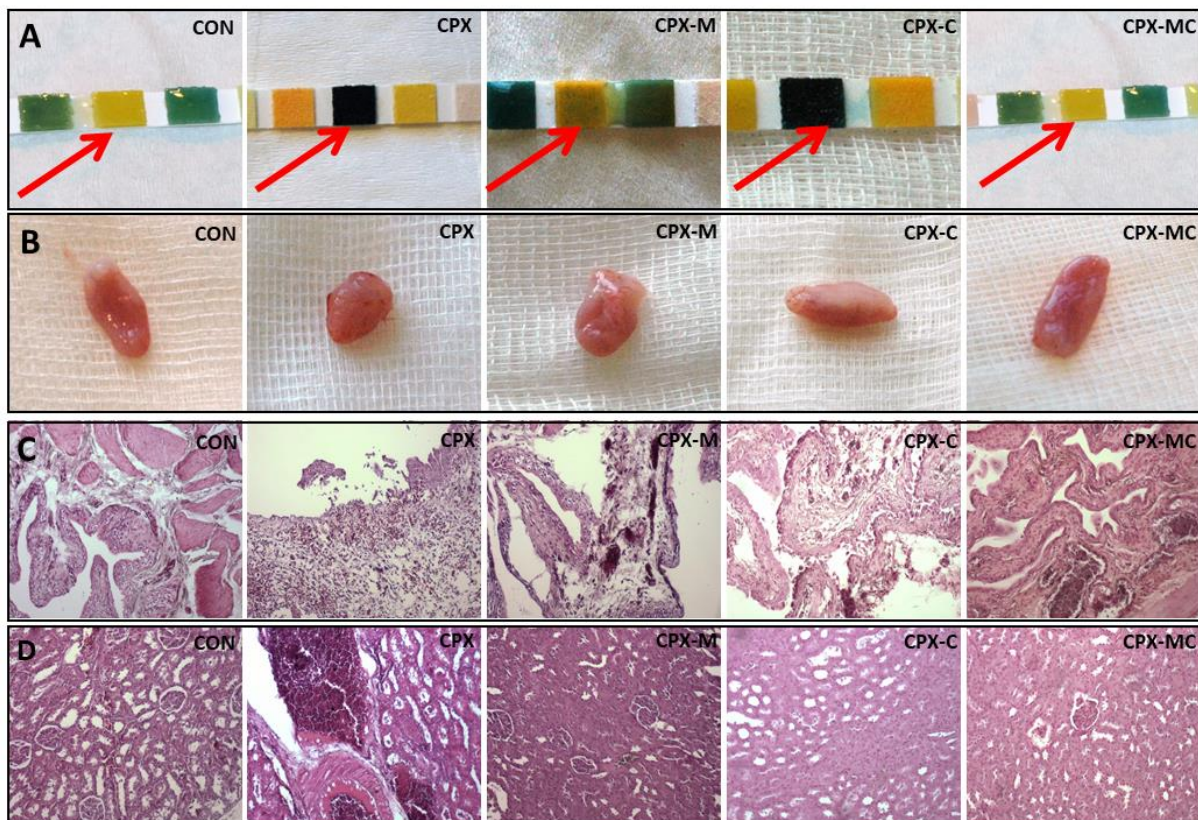


**Figure 4.** Representative results of dipstick tests for hematuria (A), macroscopic images of urinary bladders (B), microscopic images of urinary bladders (C), and microscopic images of kidneys (D). Histological images of bladders and kidneys (hematoxylin-eosin staining, 100× magnification). On dipstick tests (A) red arrows show the area of hematuria detection. In CON and CPX-MC groups no reaction is observed (yellow area), in CPX and CPX-C groups severe hematuria is noticed (the whole area is dark green), and in CPX-M group 1+ reaction is noticed (some green spots on the yellow area). Macroscopic images of urinary bladders (B) show no signs of edema in CON, CPX-M, and CPX-MC groups; urinary bladders from CPX and CPX-C groups are significantly swollen. Microscopic images of urinary bladders (C) reveal normal urothelium with normal lamina muscularis mucosae (CON group); inflammatory infiltrations, hemorrhages, and ulcerations (CPX group); hyperemia and thinning of the urothelium (CPX-M group); hyperemia, erosions, and thinning of the urothelium (CPX-C group); hyperemia with thinning of the urothelium (CPX-MC group). Microscopic images of the kidney (D) reveal hyperemia (CON group); large hemorrhages in the renal tissue (CPX group); swelling of tubules (CPX-M and CPX-MC groups), and atrophy of glomeruli (CPX-C group).

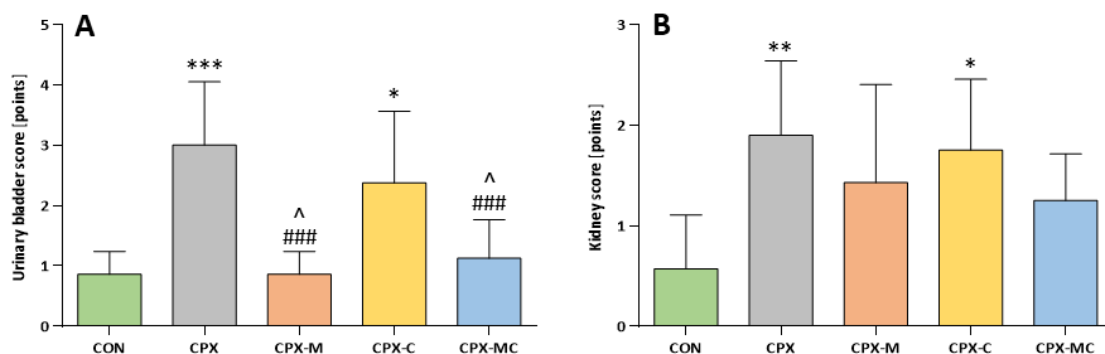


**Figure 5.** Urinary bladder score (A) and kidney score (B) based on histological injuries evaluation. The scoring system is presented in the Materials and Methods section. A detailed description of experimental groups is presented in Figure 1 and the Materials and Methods section. \*  $p < 0.05$ , \*\*  $p < 0.01$ , \*\*\*  $p < 0.001$  vs. CON group; ###  $p < 0.001$  vs. CPX group; ^  $p < 0.05$ .

The histological changes in the kidney were less specific and in almost all studied specimens parenchymatous offuscation and hyperemia were described, and similarly to the bladder scoring system, these two parameters are not involved as they are not dependent on experimental procedures. The most pronounced pathologies were described in the CPX-receiving group, where dilated urinary spaces, interstitial hemorrhages, and glomerular atrophy were found in almost all examined samples. Considering the scoring system CPX caused significant injury when compared to the control group ( $p < 0.01$  vs. CON). Administration of mesna (alone or with carvedilol) partly reversed the pathological changes expressed in scoring (in both cases the differences between mesna-receiving groups to CON and CPX groups were insignificant). Carvedilol alone did not exert any effect on CPX-induced damages ( $p < 0.05$  vs. CON, and  $p = \text{NS}$  vs. CPX group). However, these two groups (CPX-C and CPX) differ in such a way that in the group receiving CPX, interstitial hemorrhages were found in half of the specimens, whereas in the CPX-C group, interstitial hemorrhage was noticed only in one case. From all groups receiving studied substances, the least pronounced injuries were described in the group receiving both mesna and carvedilol, where no cases of interstitial hemorrhage were found. The representative images from kidney histological evaluation are presented in Figure 4D. The mean values with the corresponding SD for kidney score are presented in Figure 5B.

#### 2.4. Oxidative Stress Parameters in Urinary Bladder, Kidney and Liver and Kidney IL-1 $\beta$ Level

After the single intraperitoneal injection of CPX at a dose of 200 mg/kg, the malondialdehyde (MDA) level was significantly increased in all studied tissues (urinary bladder, kidney, and liver). Administration of mesna alone (group CPX-M) completely prevented the CPX-induced increase in MDA level in urinary bladder and kidney ( $p = \text{NS}$  vs. CON,  $p < 0.001$  vs. CPX, in both tissues) and partly reversed the CPX action in the liver ( $p = \text{NS}$  vs. CON and CPX). In none of the examined tissues was administration of carvedilol able to reverse the increased level of MDA caused by CPX (significant difference compared to the control group). The drug combination (group CPX-MC) only prevented the CPX-induced changes in MDA level in the urinary bladder and liver ( $p = \text{NS}$  vs. CON and CPX) but exerted no effect in the kidney ( $p < 0.01$  vs. CON,  $p = \text{NS}$  vs. CPX). The mean values with the corresponding SD for urinary bladder, kidney, and liver MDA levels are presented in Figure 6A–C, respectively.

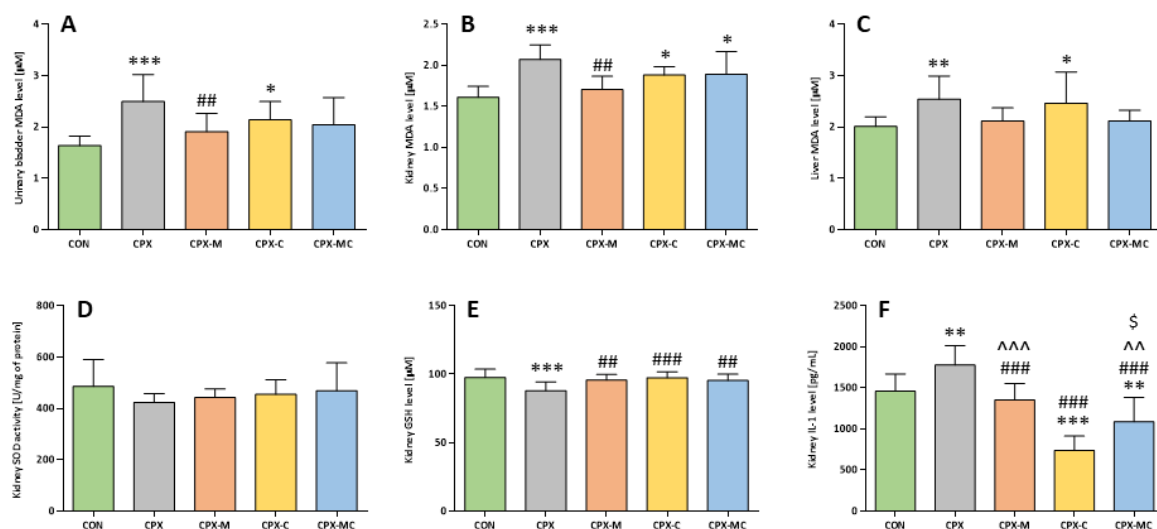


**Figure 6.** Malondialdehyde (MDA) levels in urinary bladder (A), kidney (B) and liver (C) homogenates, superoxide dismutase (SOD) activity (D), glutathione (GSH) level (E), and interleukin 1 $\beta$  (IL-1 $\beta$ ) level (F) in kidney homogenates. Data are presented as means  $\pm$  SD. A detailed description of experimental groups is presented in Figure 1 and in the Materials and Methods section. \*  $p < 0.05$ , \*\*  $p < 0.01$ , \*\*\*  $p < 0.001$  vs. CON group; ##  $p < 0.01$ , ###  $p < 0.001$  vs. CPX group; ~  $p < 0.01$ , ^  $p < 0.001$  vs. CPX-C group and \$  $p < 0.05$  vs. CPX-M.



CPX caused a significant decrease in glutathione (GSH) concentration in kidney homogenates ( $p < 0.001$  vs. CON) and both studied substances (mesna and carvedilol, alone or in combination) reversed this action, increasing the GSH concentrations (CPX-M vs. CPX and CPX-MC vs. CPX,  $p < 0.001$  in both cases, and CPX-C vs. CPX,  $p < 0.01$ ). It was also noticed that injection of CPX decreased superoxide dismutase (SOD) activity and the value was the lowest in this group from all experimental groups, but the difference between that and the control group was not significant. In the kidney, the tendency to increase SOD activity in comparison to the CPX group was observed in the case of all groups receiving studied compounds, but there were only insignificant differences regarding the CON and the CPX group. The mean values with corresponding SD for kidney GSH levels and SOD activity are presented in Figure 6D,E, respectively.

In the kidney, CPX significantly increased the level of IL-1 $\beta$  in comparison to the control group. Administration of mesna alone failed to reverse this action, but administration of carvedilol not only prevented a CPX-induced increase in IL-1 $\beta$  level (CPX-C vs. CPX and CPX-MC vs. CPX,  $p < 0.001$ ), but additionally, significantly decreased the level of this cytokine in kidney homogenates in comparison to the control group, because the IL-1 $\beta$  levels were lowest in groups receiving carvedilol, especially alone (CPX-C vs. CON,  $p < 0.001$  and CPX-MC vs. CON,  $p < 0.01$ ). The differences between the CPX-C group and both groups receiving mesna (CPX-M and CPX-MC) were also significant. The mean values with corresponding SD for kidney IL-1 $\beta$  levels are presented in Figure 6F.

### 2.5. Asymmetric Dimethylarginine (ADMA) and Dimethylarginine Dimethylaminotransferase (DDAH) Assessment

Administration of CPX significantly increases the plasma ADMA level. All studied substances (mesna and carvedilol given alone or together) completely prevented the CPX-induced ADMA increase ( $p = \text{NS}$  vs. CON in all treated groups and significant differences between the others and the CPX group). Additionally, the ADMA level is the lowest in the CPX-MC group, significantly lower not only compared to the CPX group but also compared to the CPX-M group (CPX-MC vs. CPX-M,  $p < 0.05$ ). No statistically significant differences in liver DDAH activity in comparison to the control group were noticed. However, the highest liver DDAH activity was measured in the CPX-M group, but it was still insignificant. Serum ADMA level and liver DDAH activity are presented in Figure 7A,B, respectively.

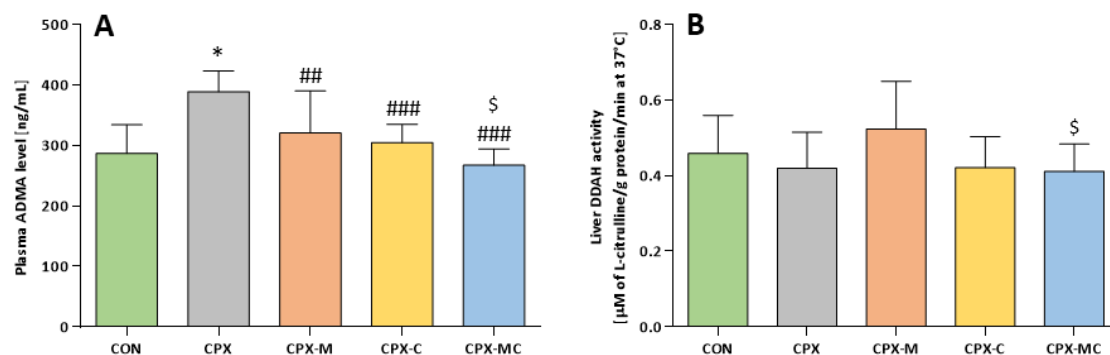


**Figure 7.** Plasma ADMA level (A) and DDAH activity (B) in liver homogenates. Data are presented as means  $\pm$  SD. A detailed description of experimental groups is presented in Figure 1 and in the Materials and Methods section. \*  $p < 0.05$  vs. CON; ##  $p < 0.01$ , ###  $p < 0.001$  vs. CPX group; \$  $p < 0.05$  vs. CPX-M.

### 3. Discussion

Based on many earlier experimental data, Ribeiro et al. [7] proposed a four-stage model of hemorrhagic cystitis induced by cyclophosphamide, similar to the model of mucositis (Figure 8). It involves the interaction of acrolein (the toxic metabolite of CPX) accumulated in the bladder with urothelium and urothelial damage, followed by up-regulation of a variety of transcription factors and proinflammatory cytokines (mainly TNF- $\alpha$  and IL-1 $\beta$ ) release from recruited macrophages. Large amounts of cytokines, ROS generation, and

overexpression of iNOS as well as COX-2 lead to the overproduction of nitric oxide (NO) and peroxynitrite. In the phase of clinical symptoms, erosions and ulcerations in the urothelium are present, which results in pain and bladder dysfunction. The last phase is the healing phase, involving fibroblasts and locally released growth factors [7,31–33].

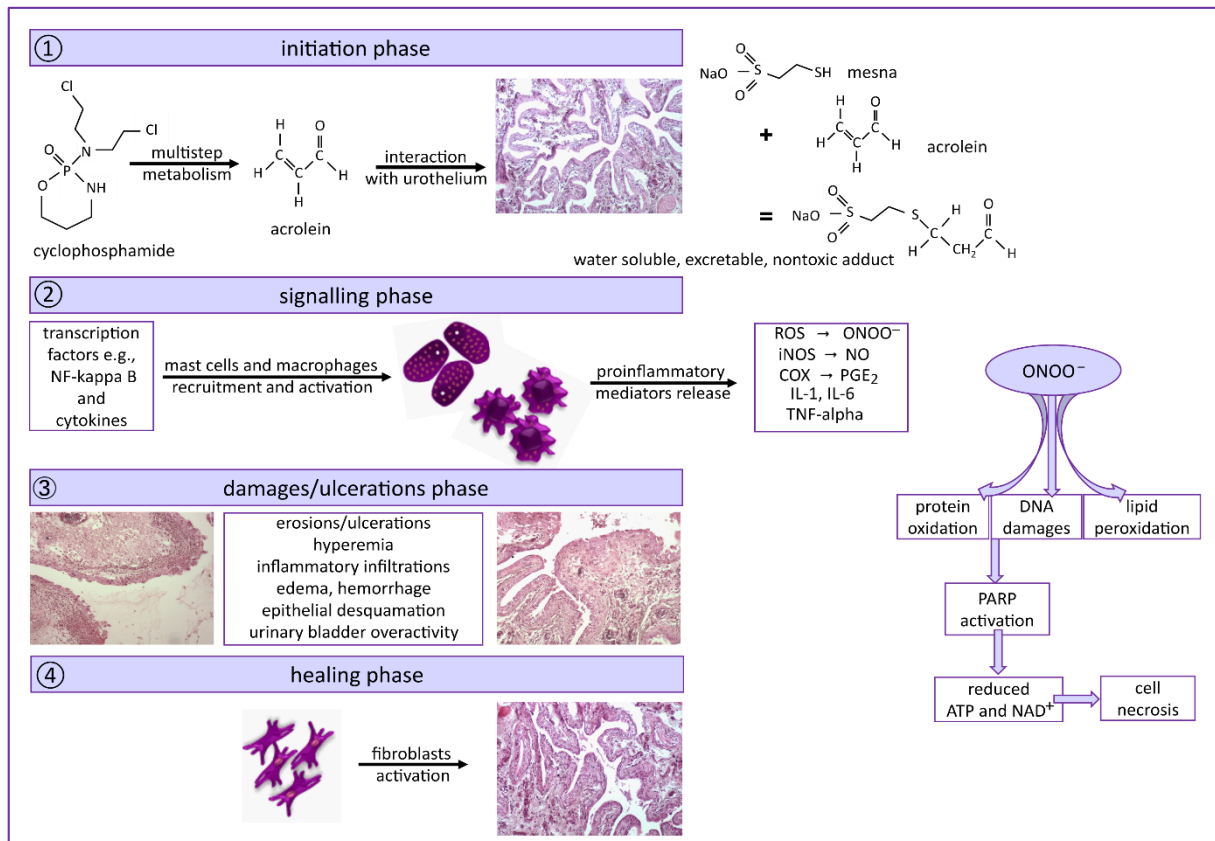


**Figure 8.** The proposed mechanism of urinary bladder toxicity induced by cyclophosphamide, based on [7,31–33]. ROS—reactive oxygen species, ONOO<sup>−</sup>—peroxynitrite, iNOS—inducible nitric oxide synthase, NO—nitric oxide, COX—cyclooxygenase, PGE<sub>2</sub>—prostaglandin E<sub>2</sub>, IL-1—interleukin 1, IL-6—interleukin 6, TNF- $\alpha$ —tumor necrosis factor-alpha, NF- $\kappa$ B—nuclear factor kappa B, PARP—poly (ADP-ribose) polymerase, ATP—adenosine triphosphate, NAD<sup>+</sup>—an oxidized form of nicotinamide adenine dinucleotide. Images magnification 100 $\times$ .

Acrolein is not solely the product of cyclophosphamide liver metabolism, but is also formed endogenously during oxidative stress-mediated lipid peroxidation, myeloperoxidase-mediated oxidation of amino acids, or may be of the environmental origin as a pollutant in tobacco smoke or from other sources [34–36]. Acrolein is a very reactive molecule physiologically rapidly neutralized. Conjugation with glutathione is the most important pathway, counting for about 60–70% of acrolein metabolism [37]. It is postulated that acrolein may be involved in endothelial dysfunction [34,38], may interfere with NO production, and may increase oxidative stress [39]. Another aspect of acrolein toxicity is found in the reproductive system, where acrolein induces apoptosis in male germ cells, Sertoli cells, or Leydig cells [35,36,40].

In clinical practice, mesna and/or hydration with or without diuretics are commonly used to prevent dose-dependent cyclophosphamide-induced urinary toxicity such as micro- and macrohematuria or hemorrhagic cystitis [5,14,41], which may be observed even in up to 75% of patients receiving very high intravenous doses of cyclophosphamide [12,14,42]. The recommended total dose of mesna in humans is, in most cases, 60% (*w/w*) of the CPX dose given in three divided doses (15–30 min before, 4 h and 8 h after the oxazaphosphorine), but may be increased up to 160% of the CPX dose in four divided doses or even up

to 320% of the daily post-transplant cyclophosphamide dose [5,41,43]. However, the efficacy of mesna use is currently being discussed, especially considering the CPX-induced urinary complications in the treatment of chronic diseases [15,16]. Additionally, mesna may cause some skin and systemic hypersensitivity-like-reactions, but it is sometimes difficult to distinguish these from the adverse effects of the basic anticancer protocol [41,44]. Therefore, there is still a great need to search for new compounds which may be active in alleviating CPX-induced cystitis. The first idea was to search among other drugs with thiol groups, such as amifostine or N-acetylcysteine. Amifostine is registered for the prevention of cisplatin-induced nephrotoxicity [45], and some studies suggest that it may be also effective in CPX-induced bladder toxicity [42]. N-acetylcysteine is used in the treatment of paracetamol overdose [46], but the newest study of Dobrek et al. [11,47] revealed protective action of N-acetylcysteine in a model of acute and chronic CPX-induced bladder and kidney toxicity. N-acetylcysteine was found to protect not only against CPX-induced urinary toxicity but was effective in CPX-induced cardiotoxicity [48].

Due to the very complex mechanism of CPX-induced urinary toxicity, research focuses on substances inhibiting, e.g., the inflammation cascade or overactivation of oxidative stress. Introducing new natural or synthetic compounds to clinical practice takes a long time of pre-clinical and clinical tests. Searching for new applications among already registered drugs with known toxicity and pharmacokinetic is a promising way to shorten this time [49]. In experimental studies, such attempts were made, for example, with ambroxol [50], pantoprazole [51], or ketamine [52]. Carvedilol has been known since the 1980s [53] and is currently used in the treatment of essential hypertension, chronic stable angina pectoris, or heart failure [54]. For the last almost 40 years in the history of carvedilol clinical administration, many new properties of this drug, other than only beta non-selective and selective alpha-1 adrenergic blockade were described [19,54]. These features open new possibilities for the use of carvedilol in indications other than cardiovascular. Carvedilol is a potent antioxidant, metabolized to metabolites with 30–100 times greater [19,30] antioxidant activity than a parent compound. It has both ROS-scavenging properties and ROS-suppressing effects. The carbazole group in the carvedilol structure is responsible for antioxidant activity, and high lipophilicity enables the access of the drug to the intramembrane sites which are targets for lipid peroxidation [55]. Carvedilol is unique, having anti-inflammatory, antiapoptotic, antifibrotic or anticancer activity [17,30,49,56,57]. Well described is carvedilol prevention from heart injury caused by anthracyclines [20,56]. Many papers describe the alleviation by carvedilol kidney injury caused by ischemia/reperfusion (I/R) [58,59], cisplatin [26,60], or azithromycin [23]. Some works outline the protective action of carvedilol in other organs, such as the pancreas of diabetic animals [61,62]. The postulated mechanisms of carvedilol action are different and cover not only the antioxidant activity but also decrease in TNF- $\alpha$  and other proinflammatory or fibrogenic cytokines (e.g., IL-1 $\beta$ , IL-6, IL-18, TGF- $\beta$ 1), increase in anti-inflammatory cytokines (e.g., IL-10), decrease expression of MMP-2 and MMP-9, COX-2, iNOS or caspase-3 [23,25,29,57,62,63].

In the present study, we have chosen a low dose of carvedilol (2 mg/kg) given once daily by gastric tube for 3 days. The low dose was selected based on the earlier published papers confirming that an intraperitoneal dose of 2 mg/kg given in 12 h intervals is effective in the prevention of I/R kidney injury in rats where carvedilol restored antioxidants levels (SOD, GSH, catalase) and decreased MDA level in kidney tissue altered by I/R procedure. Moreover, doses from 1 to 3 mg/kg exerted the least pronounced hemodynamic effect, whereas higher doses did not give additional protection in the I/R model but produced a decrease in systolic blood pressure and heart rate [64]. The same oral dose of carvedilol was examined by Hayashi et al. [58,59] in a similar model of kidney I/R with benefits for serum creatinine and kidney SOD activity. What is more, Watanabe et al. [65] described better protection of 2 mg/kg dose of carvedilol over 20 mg/kg dose in a rat model of dilated cardiomyopathy. These findings prompted us to choose just this dose, administered intragastrically for three consecutive days, in the model of CPX-induced urinary toxicity. The efficacy of 2 mg/kg dose of carvedilol was also confirmed in the model of acute septic

kidney injury [66] where, among others, a reduction in kidney MDA and an increase in GSH levels were found, as well as improvement in serum creatinine without an impact on baseline blood pressure.

In our study, the model of a single intraperitoneal injection of 200 mg/kg of CPX was used to induce hemorrhagic cystitis and kidney injury as it is described in some other papers [42,47,48,67–69]. In our experiment, CPX caused a significant decrease in total body weight with a significant increase in urinary bladder index. Ozatica et al. [68] had similar results after the same dose of CPX. However, in some other papers only increased bladder index was noticed without decrease in total body weight of rats after injection of 200 mg/kg of CPX [69]. These differences may be due to the fact that Elrashidy et al. [69] sacrificed animals 24 h after CPX administration; in our work it was 48 h, whereas in the work of Ozatic et al., it was 7 days. Nevertheless, a significant decrease in total body weight after CPX observed in our experiment reveals important general toxicity of CPX. Increased bladder index indicates tissue swelling, which was also found macroscopically. Murali et al. [70] noticed a decrease in body weight and increase in bladder weight after 4, 24, and 48 h after injection of CPX in a mice model of urotoxicity, and this action was also significantly reversed by mesna and data were consistent with the macroscopic evaluation of bladders. The addition of mesna in our experiment partly prevented CPX-induced changes in both parameters. This is consistent with other published data, in which mesna administration reversed the CPX-induced bladder edema [69,71]. Furthermore, in our study, mesna alone or combined with carvedilol completely reversed the hematuria measured semi-quantitatively on a dipstick test, but carvedilol alone has no hematuria-preventive action. Administration of carvedilol partly reversed both decrease in body weight and bladder index increase. We did not observe any synergism of mesna and carvedilol, but the mean bladder index was the lowest in both groups receiving mesna and significantly lower not only in the CPX group, but also in the CPX-C group. As expected, CPX caused a significant increase in bladder MDA level, which is consistent with other studies [9,51]. What is surprising is that, despite many reports about the antioxidant activity of carvedilol in, e.g., doxorubicin-induced cardiotoxicity [25] or in mice model of diabetes [62], we did not observe a decrease in bladder MDA concentration. The differences may result from given doses; 2 mg/kg for 3 days in our model and much greater doses of 15–20 mg/kg for 14 days in a study by Amirshahrokhi et al. and even 30 mg/kg for 6 weeks in a study by Alanazi et al. However, as mentioned earlier, some authors noted the MDA decrease after only two intraperitoneal doses of 2 mg/kg of carvedilol [64]. The model used in our experiment was most of all designed to evoke acute cystitis, which was confirmed in histological evaluation of bladders. In the CPX group edema, inflammatory infiltrations, erosions, ulcerations, and hemorrhage were noticed. Similarly, mucosal erosions, ulceration, submucosal edema, hemorrhagic foci, and leukocyte infiltration were described by other authors in the same model CPX injection [67–69] or our previous paper after the 10-day-long CPX administration at a dose of 15 mg/kg daily [72]. Only treatment with mesna completely reversed the histological injury caused by CPX and this action was not only significant in comparison to the CPX, but also to the CPX-C group. This was confirmed by a significant decrease in hematuria and histological bladder score. Mesna reversed the CPX-evoked damages in many other models of bladder injury [51,69]. Carvedilol given alone did not exert any protection from CPX-induced cystitis either in bladder score and histologically described changes or in reducing the hematuria. It is difficult to compare our results to other authors' findings, since in the available for us databases we did not find any paper describing the action of beta adrenergic drugs on urothelium affected by cyclophosphamide.

CPX, in contrast to ifosfamide, is not uptaken by kidney proximal tubules and the nephrotoxic action of CPX is rather due to the generation of ROS and peroxynitrite, activation of inflammatory pathways, cell membrane disruption, mitochondrial dysfunction and DNA or protein adducts formation by acrolein [73]. In the study we performed, cyclophosphamide caused a significant increase in kidney index which indicates that the

edema of the renal tissue, and similar changes were described by Dobrek et al. [11] in a rat model or by Jiang et al. [74] in a mice model of chronic CPX administration. In the CPX group, we noticed a significant increase in serum potassium and creatinine levels which was reported by many other authors after CPX injection to rats [10,75,76] or mice [77–79] in both acute and chronic models of CPX administration. Mesna alone only partly decreased the potassium level, but carvedilol alone or in combination with mesna completely reversed the CPX-induced alteration in serum potassium. In the case of creatinine, both mesna and carvedilol, given alone or in combination, prevented a CPX-induced increase. Carvedilol was shown to prevent an increase in creatinine level in other experimental models, e.g., I/R kidney damage [58,59] or acute septic injury [66], and our study confirmed this preventive activity in the model of acute cyclophosphamide administration. The action of mesna is not surprising, and a nephroprotective effect was described with similarly acting N-acetylcysteine [11,47]. Cyclophosphamide caused alterations in oxidative stress and inflammatory parameters evaluated in our study. We found a significant increase in kidney IL-1 $\beta$  level, MDA concentration with a significant decrease in kidney GSH level and an insignificant decrease in kidney SOD activity. Mesna was potent in reversing all these abnormalities in kidney tissue and very similar results were obtained by Elrashidy et al. [69] in the urinary bladder, by Ghareeb et al. [79] in the kidney, or by Hagar et al. [80] in the pancreas. The antioxidant properties of mesna are comparable to ascorbic acid, a very well-known antioxidant, and were also confirmed in *in vitro* studies [81]. Increasing GSH concentration is of great value; as mentioned earlier, GSH is the most important pathway to detoxifying acrolein [37]. What is surprising is that despite the well documented antioxidant action of carvedilol in various models of tissue injury [25,57,62,64], in our study we did not notice the impact of carvedilol on CPX-evoked increase in kidney MDA level; we found only a significant restoration of renal GSH. We cannot exclude that a longer treatment with a low dose of carvedilol is necessary for the full antioxidant effect to be revealed. Interleukin 1 $\beta$  is an important proinflammatory cytokine and its level is increased after CPX administration in serum [75,76], urinary bladder [69,82], kidney [75,83], and many other tissues [84]. Carvedilol is potent in decreasing IL-1 $\beta$  concentration or mRNA expression in the model of brain I/R injury [85], experimental myocardial infarction [63], drug-induced cardiotoxicity [23,57], diabetes [62], or even in the rat model of periodontitis [22]. Despite so many published papers, we did not find anything about the action of carvedilol on CPX-induced increase in kidney IL-1 $\beta$  concentration or expression. In one very recently published study by Wanas et al. [83], nebivolol, another third-generation beta adrenolytic, decreased the IL-1 $\beta$  level in rat kidneys. Renal toxicity of cyclophosphamide was confirmed by us in histological evaluation. In the CPX group, we found interstitial hemorrhages, dilated urinary spaces, and glomerular atrophy to be the most pronounced pathology. Additionally, in groups receiving CPX, different levels of the swelling tubules were noticed. Similarly, other authors described swelling of proximal convoluted tubules, inflammatory cells infiltration, tubular and glomeruli atrophy, tubular degeneration, and dilatation in Bowman's capsules [76–79,83]. In contrast to our study, Dobrek et al. [47] did not reveal any significant pathology in the rat kidneys after the same intraperitoneal dose of CPX. The main difference was time of observation after CPX dose; 24 h in the previously mentioned study and 48 h in our experiment. In humans, the plasma half-life of CPX is from 4 to 8 h, which means that up to 40 h may be needed to eliminate a single dose. The plasma half-life of the active metabolites of CPX is not defined [2]. In our study, the exposure of kidneys to CPX was longer than in a study of Dobrek et al. [47]. As expected, mesna significantly reversed the CPX-induced changes, which was confirmed in the kidney score. In contrast to nebivolol [83], carvedilol did not attenuate significantly histological changes caused by CPX in kidneys, except for decreasing incidents of interstitial hemorrhages. It seems, however, that the presence of kidney pathologies does not 100% correlate with kidney function, as carvedilol alleviates CPX-induced changes in serum potassium and creatinine concentrations, which can be interpreted as improvement of kidney function. Dobrek et al. [11] noted that N-acetylcysteine improved CPX-induced alterations in kidney

function, although it did not significantly improve histopathological abnormalities. Inflammatory cells infiltration or hemorrhages in tissues after administration of CPX are not only characteristic for urinary bladder or kidney but are also present in other tissues, e.g., in the heart [84].

Liver toxicity was not the primary goal of our study, but we found significantly increased liver index in the CPX group, which was reversed only by mesna, but not by carvedilol alone. Cyclophosphamide may cause abnormal hepatic function and very rarely hepatitis and hepatomegaly [2]. A lot of research focused on finding natural, endogenous, or synthetic compounds that may decrease CPX-induced liver toxicity interfering with different mechanisms of injury [86–88]. We revealed only the protective action of mesna in reversing CPX-induced liver index increase and on liver MDA concentration. Carvedilol failed to prevent changes caused by CPX in the liver and in the case of MDA level, the explanation may be the same as in the case of bladder MDA level, which was discussed earlier. The protective action of mesna on CPX-induced increase in the liver index or MDA level may be explained by the aforementioned acrolein-binding properties. Acrolein was found to exert toxic action on the liver, affecting, among others, mitochondria of hepatocytes [89]. Al-Jawad et al. [90] confirmed the hepatoprotective effect of N-acetylcysteine in a carbon tetrachloride (CCl<sub>4</sub>) model of liver injury. Despite some reports about the hepatoprotection of carvedilol in other animal models of liver damage, such as CCl<sub>4</sub>-induced fibrosis [91] or I/R injury [92], our preliminary data did not confirm it, but a broader panel of studied parameters is necessary in order to make conclusions.

The protein arginine methyltransferase (PRMT) enzymes catalyze the formation of ADMA [93]. ADMA is an inhibitor of all nitric oxide synthases isoforms, including eNOS resulting in decreased NO production [94]. Increased level of ADMA is considered as the determinant of endothelial dysfunction and a risk factor of cardiovascular disorders [95]. Additionally, ADMA increases the NFκB expression causing the enhanced synthesis of proinflammatory cytokines [96]. Generated ADMA is metabolized predominantly (in about 80%) by DDAH to citrulline and dimethylamine or excreted with the urine (in less than 20%) [94,96]. DDAH is expressed in kidneys and many other tissues, e.g., the liver [97,98]. Still, little is known about the impact of cyclophosphamide administration on plasma ADMA level. In our previous work, we found that intragastrical administration of 15 mg/kg daily dose of CPX for 10 days caused significant decrease in serum ADMA level with a significant increase in liver DDAH activity [99]. This was, however, a very different model of CPX administration than we used in the current study, in which a single dose of 200 mg/kg of CPX was administered intraperitoneally. In this study, we noticed a significant increase in plasma ADMA level without impact on DDAH liver activity. Similar results of plasma ADMA concentration were reported by Mansour et al. [48] in rats injected intraperitoneally with 200 mg/kg CPX dose. Because ADMA is only in a small amount excreted with kidneys, DDAH metabolism is one of the most important ways to decrease ADMA plasma levels [94,96]. In our study, we did not notice a significant decrease in DDAH activity in the liver; however, it was the lowest in the CPX-receiving group out of all the studied groups. Probably the reason for increased ADMA level in the CPX group is something other than inhibition of liver DDAH activity. DDAH is present in kidneys in the renal proximal tubules [96,98,100], so unaffected kidney function is important for ADMA clearance in both, metabolism, and excretion [100]. It was shown in some clinical studies that impaired kidney function is associated with increased plasma ADMA levels [101–103]. It cannot be excluded that an increase in ADMA is caused by decreased kidney DDAH activity, which was not evaluated in the present study. However, Betz et al. [104] did not find the altered renal expression of DDAH or PRMTs in the acute rat model of ischemia/reperfusion kidney injury, but it was different from our model of injury. On the other hand, Wang et al. found decreased DDAH2 expression with increased PRMT1 expression in kidneys of Zucker diabetic fatty rats [105] or two-kidney, one-clip (2K1C) rat model of kidney injury [106] accompanied with increased ADMA plasma and kidney levels. We cannot completely rule out that the acutely impaired kidney function may, at

least partly, be responsible for the effect observed in our study. This requires further confirmation with a renal expression of PRMT and/or DDAH. Data concerning the action of carvedilol on plasma ADMA level are still rather scant and contradictory. Alfieri et al. [107] noticed the significant difference in plasma ADMA concentration after carvedilol in patients with heart failure, but only in the group responding to carvedilol treatment. On the contrary, in a group of patients with interdialytic hypertension, carvedilol was found to improve endothelial cell function but did not change plasma ADMA levels [108]. Data from animal experimental models on the impact of carvedilol on ADMA levels are even more limited. More information is found for another beta adrenergic with vasodilating properties: nebivolol. In the 2K1C rat model of kidney injury, nebivolol reversed increased plasma and kidney ADMA levels, additionally increasing DDAH2 and decreasing PRMT1 kidney expression [106]. Very similar results were obtained in the kidney injury in Zucker diabetic fatty rats [105]. Nebivolol also decreased serum ADMA levels in the cyclosporine-injured kidneys [109]. In our study, intragastrical administration of carvedilol completely reversed the CPX-induced increase in plasma ADMA levels, without changing the activity of liver DDAH. Nebivolol and carvedilol have some common properties, e.g., both dilate blood vessels, release NO and have antioxidant effects [110], which may explain the action of carvedilol on ADMA plasma concentration observed in the current study. Additionally, in our experiment, carvedilol improved kidney function, which was reflected in the prevention of CPX-induced increase in serum potassium and creatine concentrations and the exertion of some antioxidant and anti-inflammatory activity, preserving kidney GSH levels and decreasing IL-1 $\beta$  concentration in kidney homogenates. It is certain that further studies on the exact mechanism and kidney DDAH/PRMT expression or intrarenal ADMA level in CPX-induced nephrotoxicity are required. To the best of our knowledge, nothing was published about the effect of mesna on the ADMA/DDAH pathway. Some experimental data highlight the protective action of N-acetylcysteine [48]. The activity of N-acetylcysteine in reducing ADMA serum and kidney levels and in restoring kidney DDAH levels/activity was found in a mice model of renal I/R injury [111]. Administration of N-acetylcysteine to the hemodialyzed patients also decreased serum ADMA [112]. However, the closest to our research model is the model of CPX-induced cardiotoxicity in rats used by Mansour et al., in which administration of 200 mg/kg of N-acetylcysteine completely prevented the increase in serum ADMA caused by a single injection of CPX [48]. Mesna, as with N-acetylcysteine, contains -SH groups and is an antioxidant [81]. In our experiment, administration of 200 mg/kg of mesna in divided doses reduced the CPX-induced plasma ADMA level. When mesna was given in combination with carvedilol, the mean value of ADMA in the CPX-MC group was the lowest out of all the studied groups and was significantly lower than in the CPX-M group. Mesna did not significantly influence the liver DDAH activity, but, as it was stated earlier, to draw more accurate conclusions, the kidney expression of DDAH and PRMT in the CPX-induced model of tissue injury should be further investigated.

Carvedilol exerts many properties that can be important in protecting against CPX-induced urotoxicity. Despite the complex mechanism, we did not find significant protection against CPX-evoked cystitis or potentiation of mesna action. It cannot be excluded that direct neutralization of acrolein than antioxidant activity of carvedilol is more important for the prevention of cystitis. Despite a detailed review of the literature available to us, we did not find any paper describing the action of carvedilol in CPX-induced cystitis or nephrotoxicity, so it is difficult to compare our results with other studies. Some reports confirm that carvedilol prevents toxicity induced by other anticancer agents, especially in the doxorubicin- or daunorubicin-induced cardiotoxicity [25,56], cisplatin-induced nephrotoxicity [26,60], testicular damage [27], or aspirin-induced gastrototoxicity [29]. In this context, our results seem to be novel, but a little bit surprising and contrary to expectation, and more detailed studies should be provided, especially in the field of carvedilol potential as a nephroprotective agent.

## 4. Materials and Methods

### 4.1. Chemicals

Cyclophosphamide *subst.* (Sigma, Steinheim, Germany), mesna *subst.* (Sigma, Steinheim, Germany), carvedilol *subst.* (Sigma, Steinheim, Germany), 0.9% NaCl solution, ampules 10 mL (Polpharma S.A. Starogard Gdański, Poland), pentobarbital sodium 133.3 mg/mL + pentobarbital 26.7 mg/mL, bottles 100 mL (Morbital<sup>®</sup>, Biowet, Puławy, Poland).

### 4.2. Animals

Male Wistar rats with an average weight of 315.67 g ± 17.98 g were purchased from the Animal Research Center at Wrocław Medical University (Wrocław, Poland) and after 2 weeks of adaptation period, they were randomly divided into five experimental groups (12 animals/per group). Rats were housed two per cage in standard laboratory conditions of 21–23 °C, 12 h:12 h light:dark cycle, free access to standard rodent feed (Agropol, Motycz, Poland), and water ad libitum. The experiment was approved by the Local Ethics Committee for Animal Experiments in Wrocław (No. 13/2012).

### 4.3. Experiment Design

Hemorrhagic cystitis in rats was induced by a single intraperitoneal (*i.p.*) injection of 200 mg/kg of CPX. Mesna, as a reference treatment, was given *i.p.* 20 min before, 4 h and 8 h after CPX administration at a total dose of 200 mg/kg divided in 20%, 40%, and 40% doses, respectively, which was equal to 40 mg/kg, 80 mg/kg, and 80 mg/kg for separate injections. CPX and mesna were dissolved in normal saline and administered in a 5 mL/kg volume. Normal saline solution given intraperitoneally in the same volume and schedule served as a control. Carvedilol was given intragastrically (*i.g.*) by gastric tube (FST, Foster City, CA, USA) once daily at a dose of 2 mg/kg, dissolved in 4 mL/kg normal saline solution, a day before, on the day, and a day after CPX administration. Animals in the control group were given normal saline solution *i.g.* at the same volume and schedule. Animals were sacrificed by cervical dislocation in barbiturate anesthesia 48 h after the CPX administration. Before the CPX injection and after 4 h, 8 h, 24 h, and 48 h, urine samples were taken for assessment of hematuria. Blood samples from the tail vein were collected 24 h before CPX injection and 48 h after. Urinary bladders, kidneys, and livers were separated, weighed, and collected for further histological evaluation and preparation of tissue homogenates. The general organization of the experiment and the nomenclature of the experimental groups is summarized in Figure 9.

### 4.4. Body Weight and Organ Weight

Body weight (BW) was checked and recorded (in grams) once daily in the morning from day 1 to day 4 of the study. After the animals were sacrificed, the urinary bladders, kidneys, and livers were collected and weighed. The urinary bladder, kidney, and liver weights were expressed as the percentage of the total body weight (urinary bladder index, kidney index, and liver index) from day 4 and calculated according to the formula:

$$\text{Tissue index} = \frac{\text{organ weight (g)}}{\text{total body weight (g)}} \times 100\%$$

### 4.5. Serum Potassium and Creatinine Levels

Forty-eight hours after the CPX administration, blood samples were collected from the tail vein for serum potassium and creatinine measurements. The measurements in serum were made after centrifugation in the certified commercial laboratory just after the samples were collected.



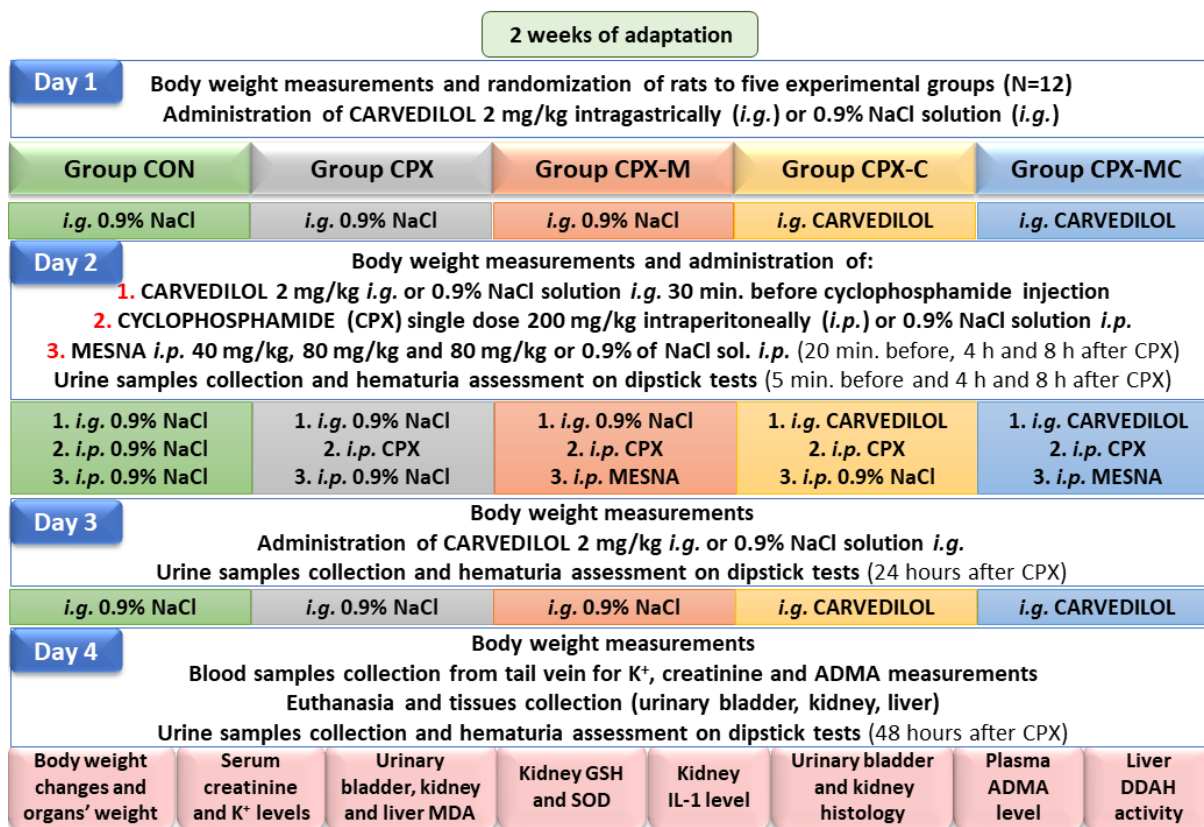


Figure 9. The general organization of the experiment.

#### 4.6. Hematuria

Urine samples for hematuria evaluation were collected directly on the Siemens Multi-stix 10SG test (Siemens Healthcare, Erlanger, Germany) by a gentle massage of suprapubic area 5 min before CPX or normal saline injection, and 4 h, 8 h, 24 h, and 48 h after CPX or normal saline injection. The magnitude of hematuria was assessed semi-quantitatively (from 1+ to 4+) using the scale on the dipstick, modified in this way, so that 4+ were given when macroscopic hematuria was noticed.

#### 4.7. Oxidative Stress Parameters in Urinary Bladder, Kidney and Liver and Kidney IL-1 $\beta$ Level

Part of the urinary bladder, kidney and liver tissues were homogenized on ice, with lysis buffer (140 mM NaCl, 10 mM EDTA, 10% glycerol, 1% NP40, 20 mM Tris base, pH 7.5) and thereafter centrifuged at 14,000 rpm for 25 min at 4 °C using homogenizer Pro250 (Pro Scientific Inc., Oxford, CT, USA). MDA, GSH, SOD, and IL-1 $\beta$  were assayed in supernatants. MDA concentrations were assessed in the urinary bladder, kidney, and liver tissues, whereas GSH concentrations and SOD activity were determined in kidney tissue using the kit and following the instructions of the manufacturers on the MARCEL S350 PRO spectrophotometer (Marcel S.A., Sp. z o.o., Zielonka, Poland). MDA and GSH were assayed using BIOXYTECH-MDA-586 kit and BIOXYTECH GSH-400, respectively (OxisResearch, Portland, OR, USA), and their concentrations were expressed in  $\mu$ M. The activity of SOD was evaluated using the Ransod kit (Randox Laboratories, Crumlin, UK) following the manufacturer's instruction, and activity was expressed as U/mg of protein. Total protein concentration in supernatants was measured in a certified laboratory using the Dimension RxL-Max (Siemens Healthineers Nederland B.V., Den Haag). In brief, in an alkaline solution, cuprum interacts with peptide bond in protein; the amount of measured Cu(II) complex is proportional to protein concentration.

Interleukin 1 $\beta$  in kidney tissue was assessed by Rat IL-1 $\beta$  ELISA kit (DIACLONE SAS, Besançon, France) according to the manufacturer's instructions on Epoch ELISA Reader (BioTek Instruments, Winooski, VT, USA) and the results were expressed in pg/mL.

#### 4.8. ADMA and DDAH Assessment

On the last day of the study, the blood samples from the tail vein were collected and plasma ADMA level was evaluated using E91301Ge ELISA Kit (USCN, Life Science Inc., Houston, TX, USA) according to the manufacturer's instruction and the results were expressed in ng/mL. Plasma ADMA concentrations were assessed on Epoch ELISA Reader (BioTek Instruments, Winooski, VT, USA).

DDAH activity was determined in liver tissue homogenates using the colorimetric method on spectrophotometer MARCEL S350 PRO (Marcel Sp. z o.o., Zielonka, Poland) according to the method described earlier [99] and expressed as  $\mu$ M of L-citrulline formation/g protein/min at 37 °C. The micromethod of Tain and Baylis [113] based on the rate of L-citrulline production was adopted to the macromethod. Shortly, homogenates of liver tissue were mixed with phosphate buffer (pH = 6.5). The samples were incubated at 37 °C for 45 min after the addition of 1 mM ADMA. The samples were centrifuged after the reaction had been stopped with 4% sulfosalicylic acid. Later, the oxime reagent (diacetyl monoxime (0.08% *w/v*) in 5% acetic acid) mixed with antipyrine/H<sub>2</sub>SO<sub>4</sub> (antipyrine (0.5% *w/v*) in 50% sulfuric acid) reagent was added. Next, samples were once more incubated at 60 °C for 110 min and later cooled in an ice bath for 10 min. Serial dilutions of L-citrulline were used as standard. L-citrulline formation was measured at 466 nm. Values were subtracted from respective blanks (without ADMA).

#### 4.9. Histological Evaluation

Part of the urinary bladders and one kidney were fixed in 4% buffered formalin and later prepared for histological evaluation by embedding in paraffin, cutting into 4  $\mu$ m slices, and staining with hematoxylin and eosin. Samples were coded and assessed blindly by an experienced pathologist using a microscope Olympus BX41 (Olympus Corporation, Tokyo, Japan) with Fujitsu computer system (Fujitsu, Tokyo, Japan). In the kidney, the following features were determined for the scoring system: the presence of interstitial hemorrhages, glomerular atrophy, and dilation of urinary spaces. For each pathology, 0 points were given if it was absent or 1 point was given if it was present in a studied sample (total 3 points). In samples of urinary bladders, inflammatory infiltration, hyperemia, edema, ulcerations, erosions, and hemorrhages were determined for the scoring system. For each observed pathology, 0 points were given when absent and 1 point was given if present in the evaluated sample (total 6 points). From representative samples, the images are taken in 100 $\times$  magnification.

#### 4.10. Statistical Analysis

To express experimental data on all figures, means  $\pm$  standard deviations (SD) were used. Statistical analysis of the effects of the substances on the studied parameters was carried out with the analysis of variance (ANOVA). The equality of variances was checked by the Brown–Forsythe test and specific comparisons between studied groups were later performed with Tukey's post hoc test. In the case of inequality of variance (creatinine, hematuria, and histological urinary bladder score), the Kruskal–Wallis test was used as a post hoc test. Hypotheses were positively verified if  $p < 0.05$ . Statistical analysis was performed using TIBCO STATISTICA 13.3 PL (StatSoft, Kraków, Poland). Figures 2–4 and Figures 6–8 were performed using GraphPad Prism version 8.0 (GraphPad Software, San Diego, CA, USA).

## 5. Conclusions

Administration of CPX caused many damages to the urinary bladder and kidneys. The best protection against CPX-induced injury was found to be mesna, which improved most

of the studied parameters. Carvedilol failed to counteract the injury caused in the urinary bladders, but restored kidney function as expressed in serum potassium and creatinine levels, and exerted antioxidant and anti-inflammatory action. Additionally, carvedilol and mesna alone or given together prevented CPX-induced plasma ADMA elevation. It cannot be excluded that protective action of carvedilol may be better expressed after longer administration, e.g., 21–28 days, similarly to the duration of breaks between cycles of chemotherapy. The results of our study, along with the data published by other researchers, support the hypothesis of possible nephroprotection exerted by the third generation of beta adrenergic drugs.

**Author Contributions:** Conceptualization, A.M.-L.; methodology, A.M.-L.; formal analysis, A.M.-L. and M.S.-B.; investigation, A.M.-L., P.Z.; resources, A.S., P.Z.; writing—original draft preparation, A.M.-L., A.M.; writing—review and editing, A.M.-L., M.S.-B., A.S., A.M., P.Z., M.T.; visualization, A.M.-L., M.S.-B.; supervision, A.S.; project administration, A.M.-L.; funding acquisition, A.S., M.T. All authors have read and agreed to the published version of the manuscript.

**Funding:** This research was funded by Wrocław Medical University statutory means ST-555.

**Institutional Review Board Statement:** The study was approved by the Local Ethics Committee for Animal Experiments in Wrocław at Hirszfeld Institute of Immunology and Experimental Therapy of the Polish Academy of Sciences (No. 13/2012). All experimental procedures were performed following relevant regulations and guidelines.

**Informed Consent Statement:** Not applicable.

**Data Availability Statement:** The data is contained in the article.

**Acknowledgments:** The authors are grateful to Joanna Kwiatkowska for support with the experiments' conduction.

**Conflicts of Interest:** The authors declare no conflict of interest.

## Abbreviations

ADMA	Asymmetric dimethylarginine
ATP	Adenosine triphosphate
CAT	Catalase
CCl <sub>4</sub>	Carbon tetrachloride
CPX	Cyclophosphamide
COX	Cyclooxygenase
DDAH	Dimethylarginine dimethylaminotransferase
eNOS	Endothelial nitric oxide synthase
GSH	Glutathione
IL	Interleukin
iNOS	Inducible nitric oxide synthase
I/R	Ischemia reperfusion
MDA	Malondialdehyde
MDR	Multidrug resistance
MMP	Matrix metalloproteinases
NAD <sup>+</sup>	Oxidized form of nicotinamide adenine dinucleotide
NF-κB	Nuclear factor kappa B
NO	Nitric oxide
NS	Not significant
ONOO <sup>-</sup>	Peroxynitrite
PAF	Platelet-activating factor
PARP	Poly (ADP-ribose) polymerase
PGE <sub>2</sub>	Prostaglandin

PRMT	Protein arginine methyltransferase
ROS	Reactive oxygen species
SD	Standard deviation
SOD	Superoxide dismutase
TGF- $\beta$ 1	Transforming growth factor beta 1
TNF- $\alpha$	Tumor necrosis factor alpha

## References

- Dalghi, M.G.; Montalbetti, N.; Carattino, M.D.; Apodaca, G. The Urothelium: Life in a Liquid Environment. *Physiol. Rev.* **2020**, *100*, 1621–1705. [CrossRef]
- Cyclophosphamide 1000 mg Powder for Solution for Injection or Infusion—Summary of Product Characteristics (SmPC)—(emc). Available online: <https://www.medicines.org.uk/emc/product/3525> (accessed on 27 October 2021).
- López-Beltrán, A.; Luque, R.J.; Mazzucchelli, R.; Scarpelli, M.; Montironi, R. Changes produced in the urothelium by traditional and newer therapeutic procedures for bladder cancer. *J. Clin. Pathol.* **2002**, *55*, 641–647. [CrossRef]
- Demlova, R.; Valík, D.; Obermannova, R.; Zdrzilova-Dubská, L. The Safety of Therapeutic Monoclonal Antibodies: Implications for Cancer Therapy Including Immuno-Checkpoint Inhibitors. *Physiol. Res.* **2016**, *65*, S455–S462. [CrossRef]
- Linder, B.J.; Nelson, J.C.; Gounder, M.M. Chemotherapy and radiation-related hemorrhagic cystitis in cancer patients—UpToDate. Available online: [https://www.uptodate.com/contents/chemotherapy-and-radiation-related-hemorrhagic-cystitis-in-cancer-patients?search=chemotherapy-and-radiation-related-hemorrhagic-cystitis-in-cancer-patients&source=search\\_result&selectedTitle=1~{}](https://www.uptodate.com/contents/chemotherapy-and-radiation-related-hemorrhagic-cystitis-in-cancer-patients?search=chemotherapy-and-radiation-related-hemorrhagic-cystitis-in-cancer-patients&source=search_result&selectedTitle=1~{}) (accessed on 27 October 2021).
- Chopra, B.; Barrick, S.R.; Meyers, S.; Beckel, J.; Zeidel, M.L.; Ford, A.P.D.W.; De Groat, W.C.; Birder, L.A. Expression and function of bradykinin B1 and B2 receptors in normal and inflamed rat urinary bladder urothelium. *J. Physiol.* **2005**, *562*, 859–871. [CrossRef]
- Ribeiro, R.A.; Lima-Junior, R.C.; Leite, C.A.V.; Mota, J.M.S.; Macedo, F.Y.; Lima, M.V.; Brito, G.A. Chemotherapy-induced hemorrhagic cystitis: Pathogenesis, pharmacological approaches and new insights. *J. Exp. Integr. Med.* **2012**, *2*, 95–112. [CrossRef]
- Ko, I.G.; Moon, B.M.; Kim, S.E.; Jin, J.J.; Hwang, L.; Ji, E.S.; Kim, C.J.; Kim, T.H.; Choi, H.H.; Chung, K.J. Effects of Combination Treatment of Alpha 1-Adrenergic Receptor Antagonists on Voiding Dysfunction: Study on Target Organs in Overactive Bladder Rats. *Int. Neurourol. J.* **2016**, *20*, S150–S158. [CrossRef]
- Wróbel, A.; Zapała, Ł.; Kluz, T.; Rogowski, A.; Misiek, M.; Juszcak, K.; Sieńko, J.; Gold, D.; Stangel-Wójcikiewicz, K.; Poleszak, E.; et al. The Potential of Asiatic Acid in the Reversion of Cyclophosphamide-Induced Hemorrhagic Cystitis in Rats. *Int. J. Mol. Sci.* **2021**, *22*, 5853. [CrossRef]
- Dobrek, Ł.; Skowron, B.; Baranowska, A.; Płoszaj, K.; Badziul, D.; Thor, P. The influence of oxazaphosphorine agents on kidney function in rats. *Medicina* **2017**, *53*, 179–189. [CrossRef]
- Dobrek, Ł.; Nalik-Iwaniak, K.; Fic, K.; Arent, Z. The Effect of Acetylcysteine on Renal Function in Experimental Models of Cyclophosphamide and Ifosfamide-Induced Cystitis. *Curr. Urol.* **2020**, *14*, 150–162. [CrossRef]
- Dorairajan, L.N.; Manikandan, R.; Kumar, S. Hemorrhagic cystitis: A challenge to the urologist. *Indian J. Urol.* **2010**, *26*, 159–166. [CrossRef]
- Matz, E.L.; Hsieh, M.H. Review of Advances in Uroprotective Agents for Cyclophosphamide- and Ifosfamide-induced Hemorrhagic Cystitis. *Urology* **2017**, *100*, 16–19. [CrossRef]
- Robinson, D.; Schulz, G.; Langley, R.; Donze, K.; Winchester, K.; Rodgers, C. Evidence-Based Practice Recommendations for Hydration in Children and Adolescents With Cancer Receiving Intravenous Cyclophosphamide. *J. Pediatr. Oncol. Nurs.* **2014**, *31*, 191–199. [CrossRef]
- Yilmaz, N.; Emmungil, H.; Gucenmez, S.; Ozen, G.; Yildiz, F.; Balkarli, A.; Kimyon, G.; Coskun, B.N.; Dogan, I.; Pamuk, O.N.; et al. Incidence of Cyclophosphamide-induced Urotoxicity and Protective Effect of Mesna in Rheumatic Diseases. *J. Rheumatol.* **2015**, *42*, 1661–1666. [CrossRef]
- Almalag, H.M.; Alasmari, S.S.; Alrayes, M.H.; A Binhameed, M.; A Alsudairi, R.; Alosaimi, M.M.; A Alnasser, G.; A Abuzaid, R.; Khalil, N.; Abouzaid, H.H.; et al. Incidence of hemorrhagic cystitis after cyclophosphamide therapy with or without mesna: A cohort study and comprehensive literature review. *J. Oncol. Pharm. Pr.* **2021**, *27*, 340–349. [CrossRef]
- Cleveland, K.H.; Yeung, S.; Huang, K.M.; Liang, S.; Andresen, B.T.; Huang, Y. Phosphoproteome profiling provides insight into the mechanism of action for carvedilol-mediated cancer prevention. *Mol. Carcinog.* **2018**, *57*, 997–1007. [CrossRef]
- Ma, Z.; Liu, X.; Zhang, Q.; Yu, Z.; Gao, D. Carvedilol suppresses malignant proliferation of mammary epithelial cells through inhibition of the ROS-mediated PI3K/AKT signaling pathway. *Oncol. Rep.* **2018**, *41*, 811–818. [CrossRef]
- Book, W.M. Carvedilol: A Nonselective  $\beta$  Blocking Agent With Antioxidant Properties. *Congest. Heart Fail.* **2002**, *8*, 173–190. [CrossRef]
- Jhorawat, R.; Kumari, S.; Varma, S.C.; Rohit, M.K.; Narula, N.; Suri, V.; Malhotra, P.; Jain, S.K. Preventive role of carvedilol in adriamycin-induced cardiomyopathy. *Indian J. Med. Res.* **2016**, *144*, 725–729. [CrossRef]
- Lin, P.-Y.; Shen, H.-C.; Chen, C.-J.; Wu, S.-E.; Kao, H.-L.; Huang, J.-H.; Wang, D.L.; Chen, S.-C. The inhibition in tumor necrosis factor- $\alpha$ -induced attenuation in endothelial thrombomodulin expression by carvedilol is mediated by nuclear factor- $\kappa$ B and reactive oxygen species. *J. Thromb. Thrombolysis* **2009**, *29*, 52–59. [CrossRef]

22. Júnior, R.F.D.A.; Souza, T.O.; De Medeiros, C.A.X.; De Souza, L.B.; Freitas, M.D.L.; De Lucena, H.F.; Alves, M.D.S.C.F.; De Araújo, A.A. Carvedilol Decrease IL-1 $\beta$  and TNF- $\alpha$ , Inhibits MMP-2, MMP-9, COX-2, and RANKL Expression, and Up-Regulates OPG in a Rat Model of Periodontitis. *PLoS ONE* **2013**, *8*, e66391. [CrossRef]
23. El-Shitany, N.A.; El-Desoky, K. Protective Effects of Carvedilol and Vitamin C against Azithromycin-Induced Cardiotoxicity in Rats via Decreasing ROS, IL1- $\beta$ , and TNF- $\alpha$  Production and Inhibiting NF- $\kappa$ B and Caspase-3 Expression. *Oxidative Med. Cell. Longev.* **2016**, *2016*, 1–13. [CrossRef]
24. Wu, T.; Li, H.; Lan, Q.; Zhao, Z.; Cao, Y.; Zhou, P.; Wan, S.; Zhang, J.; Jiang, H.; Zhang, Q.; et al. Protective effects of S-carvedilol on doxorubicin-induced damages to human umbilical vein endothelial cells and rats. *J. Appl. Toxicol.* **2019**, *39*, 1233–1244. [CrossRef]
25. Alanazi, A.M.; Fadda, L.; Alhusaini, A.; Ahmad, R.; Hasan, I.H.; Mahmoud, A.M. Liposomal Resveratrol and/or Carvedilol Attenuate Doxorubicin-Induced Cardiotoxicity by Modulating Inflammation, Oxidative Stress and S100A1 in Rats. *Antioxidants* **2020**, *9*, 159. [CrossRef]
26. Rodrigues, M.A.C.; Gobe, G.; Santos, N.A.G.; Santos, A.C. Carvedilol protects against apoptotic cell death induced by cisplatin in renal tubular epithelial cells. *J. Toxicol. Environ. Health Part A* **2012**, *75*, 981–990. [CrossRef]
27. Eid, A.H.; Abdelkader, N.F.; El-Raouf, O.M.A.; Fawzy, H.M.; El-Denshary, E.-E.-D.S. Carvedilol alleviates testicular and spermatological damage induced by cisplatin in rats via modulation of oxidative stress and inflammation. *Arch. Pharmacol. Res.* **2016**, *39*, 1693–1702. [CrossRef]
28. Padi, S.S.; Chopra, K. Salvage of cyclosporine A-induced oxidative stress and renal dysfunction by carvedilol. *Nephron* **2002**, *92*, 685–692. [CrossRef]
29. Ahmed, I.; Elkablawy, M.A.; El-Agamy, D.S.; A Bazarbay, A.; Ahmed, N. Carvedilol safeguards against aspirin-induced gastric damage in rats. *Hum. Exp. Toxicol.* **2020**, *39*, 1257–1267. [CrossRef]
30. Takara, K.; Sakaeda, T.; Okumura, K. Carvedilol: A new candidate for reversal of MDR1/P-glycoprotein-mediated multidrug resistance. *Anti-Cancer Drugs* **2004**, *15*, 303–309. [CrossRef]
31. Sloderbach, A.; Górska, A.; Sikorska, M.; Misiura, K.; Hladoń, B. Classical oxazaphosphorines – metabolism and therapeutic properties—New implications. *Postępy Hig. Med. Dosw.* **2013**, *67*, 1235–1253. [CrossRef]
32. Dobrek, Ł.; Thor, P.J. Bladder urotoxicity pathophysiology induced by the oxazaphosphorine alkylating agents and its chemoprevention. *Postępy Hig. Med. Dosw.* **2012**, *66*, 592–602. [CrossRef]
33. Sherif, I. Uroprotective mechanisms of natural products against cyclophosphamide-induced urinary bladder toxicity: A comprehensive review. *Acta Sci. Pol. Technol. Aliment.* **2015**, *19*, 333–346. [CrossRef]
34. Tamamizu-Kato, S.; Wong, J.Y.; Jairam, V.; Uchida, K.; Raussens, V.; Kato, H.; Ruyschaert, J.-M.; Narayanaswami, V. Modification by Acrolein, a Component of Tobacco Smoke and Age-Related Oxidative Stress, Mediates Functional Impairment of Human Apolipoprotein E. *Biochem.* **2007**, *46*, 8392–8400. [CrossRef]
35. Gu, Y.-P.; Yang, X.-M.; Luo, P.; Li, Y.-Q.; Tao, Y.-X.; Duan, Z.-H.; Xiao, W.; Zhang, D.-Y.; Liu, H.-Z. Inhibition of acrolein-induced autophagy and apoptosis by a glycosaminoglycan from *Sepia esculenta* ink in mouse Leydig cells. *Carbohydr. Polym.* **2017**, *163*, 270–279. [CrossRef]
36. Yildizbayrak, N.; Orta-Yilmaz, B.; Aydin, Y.; Erkan, M. Acrolein exerts a genotoxic effect in the Leydig cells by stimulating DNA damage-induced apoptosis. *Environ. Sci. Pollut. Res.* **2020**, *27*, 15869–15877. [CrossRef]
37. DeJarnett, N.; Conklin, D.J.; Riggs, D.W.; Myers, J.A.; O'Toole, T.E.; Hamzeh, I.; Wagner, S.; Chugh, A.; Ramos, K.S.; Srivastava, S.; et al. Acrolein Exposure Is Associated with Increased Cardiovascular Disease Risk. *J. Am. Heart Assoc.* **2014**, *3*. [CrossRef]
38. O'Toole, T.E.; Abplanalp, W.; Li, X.; Cooper, N.; Conklin, D.J.; Haberzettl, P.; Bhatnagar, A. Acrolein Decreases Endothelial Cell Migration and Insulin Sensitivity Through Induction of I $\kappa$ B. *Toxicol. Sci.* **2014**, *140*, 271–282. [CrossRef]
39. Horinouchi, T.; Mazaki, Y.; Terada, K.; Miwa, S. Cigarette Smoke Extract and Its Cytotoxic Factor Acrolein Inhibit Nitric Oxide Production in Human Vascular Endothelial Cells. *Biol. Pharm. Bull.* **2020**, *43*, 1804–1809. [CrossRef]
40. Liu, F.; Li, X.-L.; Lin, T.; He, D.-W.; Wei, G.-H.; Liu, J.-H.; Li, L.-S. The cyclophosphamide metabolite, acrolein, induces cytoskeletal changes and oxidative stress in Sertoli cells. *Mol. Biol. Rep.* **2011**, *39*, 493–500. [CrossRef]
41. Mesna Injection—Summary of Product Characteristics (SmPC)—(emc). Available online: <https://www.medicines.org.uk/emc/product/1838/smpc> (accessed on 27 October 2021).
42. Kanat, O.; Kurt, E.; Yalcinkaya, U.; Evrensel, T.; Manavoglu, O. Comparison of uroprotective efficacy of mesna and amifostine in Cyclophosphamide-induced hemorrhagic cystitis in rats. *Indian J. Cancer* **2006**, *43*, 12–15. [CrossRef]
43. Mac, S.; Ngo, D.; Yang, D.; Chen, J.; Ali, H.; Arslan, S.; Dadwal, S.; Salhotra, A.; Cao, T.; Karras, N.; et al. Use of high-dose mesna and hyperhydration leads to lower incidence of hemorrhagic cystitis after posttransplant cyclophosphamide-based allogeneic transplantation. *Bone Marrow Transplant.* **2021**, *56*, 2464–2470. [CrossRef]
44. Khaw, S.L.; Downie, P.A.; Waters, K.D.; Ashley, D.M.; Heath, J.A. Adverse hypersensitivity reactions to mesna as adjunctive therapy for cyclophosphamide. *Pediatr. Blood Cancer* **2007**, *49*, 341–343. [CrossRef] [PubMed]
45. ETHYOL®(amifostine) for Injection RX only—Summary of Product Characteristics (SmPC). Available online: [https://www.accessdata.fda.gov/drugsatfda\\_docs/label/1999/20221s12lbl.pdf](https://www.accessdata.fda.gov/drugsatfda_docs/label/1999/20221s12lbl.pdf) (accessed on 27 October 2021).
46. Acetylcysteine 200mg/ml Injection—Summary of Product Characteristics (SmPC)—(emc). Available online: <https://www.medicines.org.uk/emc/product/3447/smpc> (accessed on 27 October 2021).

47. Dobrek, L.; Nalik-Iwaniak, K.; Kopanska, M.; Arent, Z.; Thor, P.J. Evaluation of selected protein biomarkers of renal function in rats with an experimental model of acute cyclophosphamide-induced cystitis treated with N-acetylcysteine. *J. Physiol. Pharmacol.* **2019**, *70*, 787–799.
48. Mansour, H.H.; El Kiki, S.M.; Hasan, H. Protective effect of N-acetylcysteine on cyclophosphamide-induced cardiotoxicity in rats. *Environ. Toxicol. Pharmacol.* **2015**, *40*, 417–422. [CrossRef] [PubMed]
49. Pasquier, E.; Street, J.; Pouchy, C.; Carre, M.; Gifford, A.; Murray, J.; Norris, M.D.; Trahair, T.; Andre, N.; Kavallaris, M.  $\beta$ -blockers increase response to chemotherapy via direct antitumour and anti-angiogenic mechanisms in neuroblastoma. *Br. J. Cancer* **2013**, *108*, 2485–2494. [CrossRef] [PubMed]
50. Barut, E.N.; Engin, S.; Barut, B.; Kaya, C.; Kerimoglu, G.; Ozel, A.; Kadioglu, M. Uroprotective effect of ambroxol in cyclophosphamide-induced cystitis in mice. *Int. Urol. Nephrol.* **2019**, *51*, 803–810. [CrossRef] [PubMed]
51. Engin, S.; Barut, E.N.; Barut, B.; Duman, M.K.; Kaya, C.; Kerimoglu, G.; Ozel, A. Uroprotective effect of pantoprazole against cyclophosphamide-induced cystitis in mice. *Support. Care Cancer* **2019**, *27*, 4273–4281. [CrossRef]
52. Ozguven, A.A.; Yilmaz, O.; Taneli, F.; Ulman, C.; Vatanserver, S.; Onag, A. Protective effect of ketamine against hemorrhagic cystitis in rats receiving ifosfamide. *Indian J. Pharmacol.* **2014**, *46*, 147–151. [CrossRef]
53. Eggertsen, R.; Andrén, L.; Sivertsson, R.; Hansson, L. Acute haemodynamic effects of carvedilol (BM 14190), a new combined beta-adrenoceptor blocker and precapillary vasodilating agent, in hypertensive patients. *Eur. J. Clin. Pharmacol.* **1984**, *27*, 19–22. [CrossRef]
54. Carvedilol 25 mg Film-coated Tablets–Summary of Product Characteristics (SmPC)–(emc). Available online: <https://www.medicines.org.uk/emc/product/2547/smpc> (accessed on 27 October 2021).
55. Dandona, P.; Ghanim, H.; Brooks, D.P. Antioxidant activity of carvedilol in cardiovascular disease. *J. Hypertens.* **2007**, *25*, 731–741. [CrossRef]
56. Arozal, W.; Sari, F.R.; Watanabe, K.; Arumugam, S.; Veeraveedu, P.T.; Ma, M.; Thandavarayan, R.A.; Sukumaran, V.; Lakshmanan, A.P.; Kobayashi, Y.; et al. Carvedilol-Afforded Protection against Daunorubicin-Induced Cardiomyopathic Rats In Vivo: Effects on Cardiac Fibrosis and Hypertrophy. *ISRN Pharmacol.* **2011**, *2011*, 1–8. [CrossRef]
57. Zhang, Q.-L.; Yang, J.-J.; Zhang, H.-S. Carvedilol (CAR) combined with carnosic acid (CAA) attenuates doxorubicin-induced cardiotoxicity by suppressing excessive oxidative stress, inflammation, apoptosis and autophagy. *Biomed. Pharmacother.* **2019**, *109*, 71–83. [CrossRef] [PubMed]
58. Hayashi, T.; Saitou, Y.; Nose, K.; Nishioka, T.; Ishii, T.; Uemura, H. Efficacy of Carvedilol for Ischemia/Reperfusion-Induced Oxidative Renal Injury in Rats. *Transplant. Proc.* **2008**, *40*, 2139–2141. [CrossRef] [PubMed]
59. Hayashi, T.; De Velasco, M.A.; Saitou, Y.; Nose, K.; Nishioka, T.; Ishii, T.; Uemura, H. Carvedilol protects tubular epithelial cells from ischemia-reperfusion injury by inhibiting oxidative stress. *Int. J. Urol.* **2010**, *17*, 989–995. [CrossRef] [PubMed]
60. Guo, D.; Yang, H.; Li, Q.; Bae, H.J.; Obianom, O.; Zeng, S.; Su, T.; Polli, J.E.; Shu, Y. Selective Inhibition on Organic Cation Transporters by Carvedilol Protects Mice from Cisplatin-Induced Nephrotoxicity. *Pharm. Res.* **2018**, *35*, 204. [CrossRef]
61. Diogo, C.V.; Deus, C.M.; Lebedzinska-Arciszewska, M.; Wojtala, A.; Wieckowski, M.R.; Oliveira, P.J. Carvedilol and antioxidant proteins in a type I diabetes animal model. *Eur. J. Clin. Invest.* **2017**, *47*, 19–29. [CrossRef]
62. Amirshahrokhi, K.; Zohouri, A. Carvedilol prevents pancreatic  $\beta$ -cell damage and the development of type 1 diabetes in mice by the inhibition of proinflammatory cytokines, NF- $\kappa$ B, COX-2, iNOS and oxidative stress. *Cytokine* **2021**, *138*, 155394. [CrossRef]
63. Li, B.; Liao, Y.-H.; Cheng, X.; Ge, H.; Guo, H.; Wang, M. Effects of carvedilol on cardiac cytokines expression and remodeling in rat with acute myocardial infarction. *Int. J. Cardiol.* **2006**, *111*, 247–255. [CrossRef]
64. Singh, D.; Chander, V.; Chopra, K. Carvedilol attenuates ischemia-reperfusion-induced oxidative renal injury in rats. *Fundam. Clin. Pharmacol.* **2004**, *18*, 627–634. [CrossRef]
65. Watanabe, K.; Ohta, Y.; Nakazawa, M.; Higuchi, H.; Hasegawa, G.; Naito, M.; Fuse, K.; Ito, M.; Hirono, S.; Tanabe, N.; et al. Low dose carvedilol inhibits progression of heart failure in rats with dilated cardiomyopathy. *Br. J. Pharmacol.* **2000**, *130*, 1489–1495. [CrossRef]
66. Kawy, H.A. Low-dose carvedilol protects against acute septic renal injury in rats during the early and late phases. *Can. J. Physiol. Pharmacol.* **2015**, *93*, 443–450. [CrossRef]
67. Moraes, J.P.; Pereira, D.S.; Matos, A.S.; Santana, D.G.; Santos, C.A.; Estevam, C.S.; Fakhouri, R.; Junior, W.D.L.; Camargo, E.A. The Ethanol Extract of the Inner Bark of *Caesalpinia pyramidalis*(Tul.) Reduces Urinary Bladder Damage during Cyclophosphamide-Induced Cystitis in Rats. *Sci. World J.* **2013**, *2013*, 1–8. [CrossRef]
68. Özatik, F.Y.; Özatik, O.; Tekşen, Y.; Yiğitaslan, S.; Ari, N.S. Protective and therapeutic effect of Hydrogen sulfide on hemorrhagic cystitis and testis dysfunction induced with Cyclophosphamide. *Turk. J. Med. Sci.* **2021**, *51*, 1530–1542. [CrossRef]
69. Elrashidy, R.A.; Hasan, R.A. Modulation of autophagy and transient receptor potential vanilloid 4 channels by montelukast in a rat model of hemorrhagic cystitis. *Life Sci.* **2021**, *278*, 119507. [CrossRef]
70. Murali, V.P.; Kuttan, G. *Curculigo orchioides* Gaertn Effectively Ameliorates the Uro- and Nephrotoxicities Induced by Cyclophosphamide Administration in Experimental Animals. *Integr. Cancer Ther.* **2016**, *15*, 205–215. [CrossRef] [PubMed]
71. Mahmoudi, N.; Eftekhazadeh, S.; Golmohammadi, M.; Khorramirouz, R.; Hashemi, J.; Kashani, Z.; Alijani, M.; Hamidieh, A.A.; Kajbafzadeh, A.-M. Alleviation of Cyclophosphamide-induced Hemorrhagic Cystitis by Dietary Pomegranate: A Comparative Experimental Study With Mesna. *J. Pediatr. Hematol.* **2018**, *40*, 609–615. [CrossRef] [PubMed]

72. Merwid-Łąd, A.; Książczyńska, D.; Hałoń, A.; Szkudlarek, D.; Trocha, M.; Szandruk-Bender, M.; Matuszewska, A.; Nowak, B.; Sozański, T.; Kuźniar, A.; et al. Morin-5'-Sulfonic Acid Sodium Salt (NaMSA) Attenuates Cyclophosphamide-Induced Histological Changes in Genitourinary Tract in Rats—Short Report. *Pharmaceuticals* **2021**, *14*, 192. [CrossRef]
73. Moghe, A.; Ghare, S.; Lamoreau, B.; Mohammad, M.; Barve, S.; McClain, C.; Joshi-Barve, S. Molecular Mechanisms of Acrolein Toxicity: Relevance to Human Disease. *Toxicol. Sci.* **2015**, *143*, 242–255. [CrossRef] [PubMed]
74. Jiang, S.; Zhang, Z.; Huang, F.; Yang, Z.; Yu, F.; Tang, Y.; Ding, G. Protective Effect of Low Molecular Weight Peptides from *Solenocera crassicornis* Head against Cyclophosphamide-Induced Nephrotoxicity in Mice via the Keap1/Nrf2 Pathway. *Antioxidants* **2020**, *9*, 745. [CrossRef]
75. Liu, Q.; Lin, X.; Li, H.; Yuan, J.; Peng, Y.; Dong, L.; Dai, S. Paeoniflorin ameliorates renal function in cyclophosphamide-induced mice via AMPK suppressed inflammation and apoptosis. *Biomed. Pharmacother.* **2016**, *84*, 1899–1905. [CrossRef]
76. Galal, S.M.; Mansour, H.H.; ElKhoely, A.A. Diallyl sulfide alleviates cyclophosphamide-induced nephropathic encephalopathy in rats. *Toxicol. Mech. Methods* **2019**, *30*, 208–218. [CrossRef]
77. Hamzeh, M.; Amiri, F.T.; Beklar, S.Y.; Hosseinimehr, S.J. Nephroprotective effect of cerium oxide nanoparticles on cyclophosphamide-induced nephrotoxicity via anti-apoptotic and antioxidant properties in BALB/c mice. *Marmara Pharm. J.* **2018**, *22*, 180–189. [CrossRef]
78. Sharma, S.; Sharma, P.; Kulurkar, P.; Singh, D.; Kumar, D.; Patial, V. Iridoid glycosides fraction from *Picrorhiza kurroa* attenuates cyclophosphamide-induced renal toxicity and peripheral neuropathy via PPAR- $\gamma$  mediated inhibition of inflammation and apoptosis. *Phytomedicine* **2017**, *36*, 108–117. [CrossRef] [PubMed]
79. Ghareeb, M.A.; Sobeh, M.; El-Maadawy, W.H.; Mohammed, H.S.; Khalil, H.; Botros, S.; Wink, M. Chemical Profiling of Polyphenolics in *Eucalyptus globulus* and Evaluation of Its Hepato-Renal Protective Potential Against Cyclophosphamide Induced Toxicity in Mice. *Antioxidants* **2019**, *8*, 415. [CrossRef] [PubMed]
80. Hagar, H.H.; Almubrik, S.A.; Attia, N.M.; AlJasser, S.N. Mesna Alleviates Cerulein-Induced Acute Pancreatitis by Inhibiting the Inflammatory Response and Oxidative Stress in Experimental Rats. *Dig. Dis. Sci.* **2020**, *65*, 1–9. [CrossRef] [PubMed]
81. Kim, J.H.; Oh, C.-T.; Kwon, T.-R.; Bak, D.-H.; Kim, H.; Park, W.-S.; Kim, B.J. Inhibition of melanogenesis by sodium 2-mercaptoethanesulfonate. *Korean J. Physiol. Pharmacol.* **2020**, *24*, 149–156. [CrossRef]
82. Wróbel, A.; Serefko, A.; Bańczerowska-Górska, M.; Szopa, A.; Dudka, J.; Poleszak, E. Intravesical administration of blebbistatin prevents cyclophosphamide-induced toxicity of the urinary bladder in female Wistar rats. *Neurol. Urodyn.* **2019**, *38*, 1044–1052. [CrossRef]
83. Wanas, H.; El-Shabrawy, M.; Mishriki, A.; Attia, H.; Emam, M.; Aboulhoda, B.E. Nebivolol protects against cyclophosphamide-induced nephrotoxicity through modulation of oxidative stress, inflammation, and apoptosis. *Clin. Exp. Pharmacol. Physiol.* **2021**, *48*, 811–819. [CrossRef]
84. Refaie, M.M.M.; Shehata, S.; El-Hussieny, M.; Abdelraheem, W.M.; Bayoumi, A.M.A. Role of ATP-Sensitive Potassium Channel (KATP) and eNOS in Mediating the Protective Effect of Nicorandil in Cyclophosphamide-Induced Cardiotoxicity. *Cardiovasc. Toxicol.* **2019**, *20*, 71–81. [CrossRef]
85. Savitz, S.I.; Erhardt, J.A.; Anthony, J.V.; Gupta, G.; Li, X.; Barone, F.C.; Rosenbaum, D.M. The Novel  $\beta$ -Blocker, Carvedilol, Provides Neuroprotection in Transient Focal Stroke. *Br. J. Pharmacol.* **2000**, *20*, 1197–1204. [CrossRef]
86. Amiri, F.T.; Hamzeh, M.; Hosseinimehr, S.J.; Khalatbary, A.R.; Mohammadi, H.R.; Dashti, A. Atorvastatin mitigates cyclophosphamide-induced hepatotoxicity via suppression of oxidative stress and apoptosis in rat model. *Res. Pharm. Sci.* **2018**, *13*, 440–449. [CrossRef]
87. Abdelghfar, E.A.; El-Nashar, H.A.S.; Al-Mohammadi, A.G.A.; Eldahshan, O.A. Orange fruit (*Citrus sinensis*) peel extract attenuates chemotherapy-induced toxicity in male rats. *Food Funct.* **2021**, *12*, 9443–9455. [CrossRef] [PubMed]
88. Khordad, E.; Alipour, F.; Pourabbas, M.; Mansouri, S.; Salimnejad, R. Hepatoprotective Impact of Ghrelin against Cyclophosphamide-Induced Toxicity in the Male Mice. *Drug Res.* **2021**, *71*, 407–412. [CrossRef] [PubMed]
89. Shafie, B.; Pourahmad, J.; Rezaei, M. N-acetylcysteine is more effective than ellagic acid in preventing acrolein induced dysfunction in mitochondria isolated from rat liver. *J. Food Biochem.* **2021**, *45*, e13775. [CrossRef] [PubMed]
90. Al-Jawad, F.H.; Al-Attar, Z.; Abbood, M.S. The Protective Effect of Nitroglycerin, N-Acetyl Cysteine and Metoprolol in CCL4 Induced Animal Model of Acute Liver Injury. *Open Access Maced. J. Med. Sci.* **2019**, *7*, 1739–1743. [CrossRef]
91. El-Wakeel, S.A.; Rahmo, R.M.; El-Abhar, H.S. Anti-fibrotic impact of Carvedilol in a CCL-4 model of liver fibrosis via serum microRNA-200a/SMAD7 enhancement to bridle TGF- $\beta$ 1/EMT track. *Sci. Rep.* **2018**, *8*, 14327. [CrossRef]
92. El Sayed, N.F.; Abdallah, D.M.; Awad, A.S.; Ahmed, K.A.; El-Abhar, H.S. Novel peripheral role of Nurr-1/GDNF/AKT trajectory in carvedilol and/or morin hydrate hepatoprotective effect in a model of hepatic ischemia/reperfusion. *Life Sci.* **2021**, *273*, 119235. [CrossRef] [PubMed]
93. Tsikas, D. Urinary Dimethylamine (DMA) and Its Precursor Asymmetric Dimethylarginine (ADMA) in Clinical Medicine, in the Context of Nitric Oxide (NO) and Beyond. *J. Clin. Med.* **2020**, *9*, 1843. [CrossRef]
94. Hulin, J.-A.; Gubareva, E.A.; Jarzebska, N.; Rodionov, R.N.; Mangoni, A.A.; Tommasi, S. Inhibition of Dimethylarginine Dimethylaminohydrolase (DDAH) Enzymes as an Emerging Therapeutic Strategy to Target Angiogenesis and Vasculogenic Mimicry in Cancer. *Front. Oncol.* **2020**, *9*, 1455. [CrossRef]
95. Dowsett, L.; Higgins, E.; Alanazi, S.; Alshuwayer, N.A.; Leiper, F.C.; Leiper, J. ADMA: A Key Player in the Relationship between Vascular Dysfunction and Inflammation in Atherosclerosis. *J. Clin. Med.* **2020**, *9*, 3026. [CrossRef]

96. Oliva-Damaso, E.; Oliva-Damaso, N.; Rodriguez-Esparragon, F.; Payan, J.; Baamonde-Laborda, E.; Gonzalez-Cabrera, F.; Santana-Estupiñan, R.; Rodriguez-Perez, J.C. Asymmetric (ADMA) and Symmetric (SDMA) Dimethylarginines in Chronic Kidney Disease: A Clinical Approach. *Int. J. Mol. Sci.* **2019**, *20*, 3668. [CrossRef]
97. Palm, F.; Onozato, M.L.; Luo, Z.; Wilcox, C.S. Dimethylarginine dimethylaminohydrolase (DDAH): Expression, regulation, and function in the cardiovascular and renal systems. *Am. J. Physiol. Heart Circ. Physiol.* **2007**, *293*, H3227–H3245. [CrossRef] [PubMed]
98. Wojtaszek, E.; Oldakowska-Jedynak, U.; Kwiatkowska, M.; Glogowski, T.; Malyszko, J. Uremic Toxins, Oxidative Stress, Atherosclerosis in Chronic Kidney Disease, and Kidney Transplantation. *Oxidative Med. Cell. Longev.* **2021**, *2021*, 1–15. [CrossRef] [PubMed]
99. Merwid-Ład, A.; Trocha, M.; Chlebda-Sieragowska, E.; Sozański, T.; Magdalan, J.; Książczyńska, D.; Szuba, A.; Kopacz, M.; Kuźniar, A.; Nowak, D.; et al. Effect of cyclophosphamide and morin-5'-sulfonic acid sodium salt, alone or in combination, on ADMA/DDAH pathway in rats. *Pharmacol. Rep.* **2013**, *65*, 201–207. [CrossRef]
100. Jayachandran, I.; Sundararajan, S.; Paramasivam, P.; Venkatesan, B.; Subramanian, S.C.; Balasubramanyam, M.; Mohan, V.; Manickam, N. Association of circulatory asymmetric dimethylarginine (ADMA) with diabetic nephropathy in Asian Indians and its causative role in renal cell injury. *Clin. Biochem.* **2017**, *50*, 835–842. [CrossRef]
101. Grassi, G.; Seravalle, G.; Ghiadoni, L.; Tripepi, G.; Bruno, R.M.; Mancina, G.; Zoccali, C. Sympathetic Nerve Traffic and Asymmetric Dimethylarginine in Chronic Kidney Disease. *Clin. J. Am. Soc. Nephrol.* **2011**, *6*, 2620–2627. [CrossRef] [PubMed]
102. Lu, T.-M.; Hsu, C.-P.; Chang, C.-F.; Lin, C.-C.; Lee, T.-S.; Lin, S.-J.; Chan, W.-L. Asymmetric dimethylarginine predicts the risk of contrast-induced acute kidney injury in patients undergoing cardiac catheterization. *Atheroscler.* **2016**, *254*, 161–166. [CrossRef]
103. Zhang, L.; Zhang, K.; Dong, W.; Li, R.; Huang, R.; Zhang, H.; Shi, W.; Liu, S.; Li, Z.; Chen, Y.; et al. Raised Plasma Levels of Asymmetric Dimethylarginine Are Associated with Pathological Type and Predict the Therapeutic Effect in Lupus Nephritis Patients Treated with Cyclophosphamide. *Kidney Dis.* **2020**, *6*, 355–363. [CrossRef]
104. Betz, B.; Möller-Ehrlich, K.; Kress, T.; Kniepert, J.; Schwedhelm, E.; Böger, R.H.; Wanner, C.; Sauvant, C.; Schneider, R. Increased symmetrical dimethylarginine in ischemic acute kidney injury as a causative factor of renal L-arginine deficiency. *Transl. Res.* **2013**, *162*, 67–76. [CrossRef]
105. Wang, Y.; An, W.; Zhang, F.; Niu, M.; Liu, Y.; Shi, R. Nebivolol ameliorated kidney damage in Zucker diabetic fatty rats by regulation of oxidative stress/NO pathway: Comparison with captopril. *Clin. Exp. Pharmacol. Physiol.* **2018**, *45*, 1135–1148. [CrossRef]
106. Wang, Y.; Niu, M.; Yin, S.; Zhang, F.; Shi, R. Nephroprotective effects of nebivolol in 2K1C rats through regulation of the kidney ROS-ADMA-NO pathway. *Pharmacol. Rep.* **2018**, *70*, 917–929. [CrossRef]
107. Alfieri, A.B.; Briceno, L.; Fragasso, G.; Spoladore, R.; Palloshi, A.; Bassanelli, G.; Montano, C.; Arioli, F.; Cuko, A.; Ruotolo, G.; et al. Differential Long-term Effects of Carvedilol on Proinflammatory and Antiinflammatory Cytokines, Asymmetric Dimethylarginine, and Left Ventricular Function in Patients With Heart Failure. *J. Cardiovasc. Pharmacol.* **2008**, *52*, 49–54. [CrossRef] [PubMed]
108. Inrig, J.K.; Van Buren, P.; Kim, C.; Vongpatanasin, W.; Povsic, T.J.; Toto, R. Probing the Mechanisms of Intradialytic Hypertension: A Pilot Study Targeting Endothelial Cell Dysfunction. *Clin. J. Am. Soc. Nephrol.* **2012**, *7*, 1300–1309. [CrossRef] [PubMed]
109. Hewedy, W.A.; Mostafa, D.K. Nebivolol suppresses asymmetric dimethylarginine and attenuates cyclosporine-induced nephrotoxicity and endothelial dysfunction in rats. *Pharmacol. Rep.* **2016**, *68*, 1319–1325. [CrossRef] [PubMed]
110. Szajerski, P.; Zielonka, J.; Sikora, A.; Adamus, J.; Marcinek, A.; Gebicki, J.; Kozlovski, V.I.; Drelicharz, Ł.; Chłopicki, S. Radical scavenging and NO-releasing properties of selected  $\alpha$ -adrenoreceptor antagonists. *Free. Radic. Res.* **2006**, *40*, 741–752. [CrossRef] [PubMed]
111. Nakayama, Y.; Ueda, S.; Yamagishi, S.-I.; Obara, N.; Taguchi, K.; Ando, R.; Kaida, Y.; Iwatani, R.; Kaifu, K.; Yokoro, M.; et al. Asymmetric dimethylarginine accumulates in the kidney during ischemia/reperfusion injury. *Kidney Int.* **2014**, *85*, 570–578. [CrossRef]
112. Giannikouris, I. The effect of N-acetylcysteine on oxidative serum biomarkers of hemodialysis patients. *Hippokratia* **2016**, *19*, 131–135.
113. Tain, Y.-L.; Baylis, C. Determination of dimethylarginine dimethylaminohydrolase activity in the kidney. *Kidney Int.* **2007**, *72*, 886–889. [CrossRef]







## Article

# Acquired Drug Resistance Enhances Imidazoquinoline Efflux by P-Glycoprotein

Anunay J. Pulukuri<sup>1</sup>, Anthony J. Burt<sup>1,2</sup>, Larissa K. Opp<sup>1</sup>, Colin M. McDowell<sup>3</sup>, Maryam Davaritouchae<sup>1,4,5</sup>, Amy E. Nielsen<sup>1</sup> and Rock J. Mancini<sup>1,5,\*</sup>

- <sup>1</sup> Department of Chemistry, Washington State University, Pullman, WA 99164, USA; anunay.pulukuri@wsu.edu (A.J.P.); ajburt@sdsu.edu (A.J.B.); larissa.opp@wsu.edu (L.K.O.); maryam.davaritouchae@cornell.edu (M.D.); amy.nielsen@wsu.edu (A.E.N.)
- <sup>2</sup> Department of Chemistry & Biochemistry, San Diego State University, San Diego, CA 92182, USA
- <sup>3</sup> School of Molecular Biosciences, Washington State University, Pullman, WA 99164, USA; colin.mcdowell@wsu.edu
- <sup>4</sup> Department of Food Science, Cornell University, Ithaca, NY 14853, USA
- <sup>5</sup> The Gene & Linda Voiland School of Chemical Engineering and Bioengineering, Washington State University, Pullman, WA 99164, USA
- \* Correspondence: Rmancini@wsu.edu

**Abstract:** Multidrug-Resistant (MDR) cancers attenuate chemotherapeutic efficacy through drug efflux, a process that transports drugs from within a cell to the extracellular space via ABC (ATP-Binding Cassette) transporters, including P-glycoprotein 1 (P-gp or ABCB1/MDR1). Conversely, Toll-Like Receptor (TLR) agonist immunotherapies modulate activity of tumor-infiltrating immune cells in local proximity to cancer cells and could, therefore, benefit from the enhanced drug efflux in MDR cancers. However, the effect of acquired drug resistance on TLR agonist efflux is largely unknown. We begin to address this by investigating P-gp mediated efflux of TLR 7/8 agonists. First, we used functionalized liposomes to determine that imidazoquinoline TLR agonists Imiquimod, Resiquimod, and Gardiquimod are substrates for P-gp. Interestingly, the least potent imidazoquinoline (Imiquimod) was the best P-gp substrate. Next, we compared imidazoquinoline efflux in MDR cancer cell lines with enhanced P-gp expression relative to parent cancer cell lines. Using P-gp competitive substrates and inhibitors, we observed that imidazoquinoline efflux occurs through P-gp and, for Imiquimod, is enhanced as a consequence of acquired drug resistance. This suggests that enhancing efflux susceptibility could be an important consideration in the rational design of next generation immunotherapies that modulate activity of tumor-infiltrating immune cells.

**Keywords:** Imiquimod; drug efflux; multidrug resistance; immunotherapy; Toll-Like Receptor

**Citation:** Pulukuri, A.J.; Burt, A.J.; Opp, L.K.; McDowell, C.M.; Davaritouchae, M.; Nielsen, A.E.; Mancini, R.J. Acquired Drug Resistance Enhances Imidazoquinoline Efflux by P-Glycoprotein. *Pharmaceuticals* **2021**, *14*, 1292. <https://doi.org/10.3390/ph14121292>

Academic Editors: Mary J. Meegan, Niamh M O'Boyle and Jean Jacques Vanden Eynde

Received: 7 November 2021

Accepted: 7 December 2021

Published: 10 December 2021

**Publisher's Note:** MDPI stays neutral with regard to jurisdictional claims in published maps and institutional affiliations.



**Copyright:** © 2021 by the authors. Licensee MDPI, Basel, Switzerland. This article is an open access article distributed under the terms and conditions of the Creative Commons Attribution (CC BY) license (<https://creativecommons.org/licenses/by/4.0/>).

## 1. Introduction

Multidrug-Resistant (MDR) cancers are implicated in over 90% of metastatic cancer deaths, including melanomas, breast cancer, and prostate cancer [1]. A general trend among MDR cancers is enhanced drug efflux, a term describing the expression of transport proteins that traffic drugs from within a cell to the extracellular space, thereby lowering intracellular drug concentration [2]. In MDR cancers, drug efflux is facilitated by the ABC (ATP-Binding cassette) superfamily which consists of at least 48 distinct transport proteins [3,4]. Of these, P-glycoprotein (P-gp or ABCB1/MDR1) was the first discovered [5,6] and is the most well-studied [7,8]. P-gp is particularly promiscuous, transporting structurally diverse compounds with minimal correlation other than a weak association with hydrophobicity [9–13]. Entire classes of chemotherapeutics, such as taxanes or anthracyclines, are substrates for P-gp-mediated drug efflux [14,15], which makes defeating this mechanism of chemoresistance particularly challenging [16]. However, this same promiscuity could be useful for enhancing extracellular concentrations of small molecule immunomodulator drugs that target bystander cells in the tumor microenvironment, such as tumor-infiltrating lymphocyte

(TIL) and tumor-associated macrophage (TAM) populations. As such, we were interested in examining the effect of MDR on the ability of small molecule immunomodulators to undergo drug efflux.

From the first empirical whole-organism Toll-Like Receptor (TLR) agonists in the late 1800s [17,18], a range of proinflammatory immunotherapeutics have emerged with mechanisms of action fundamentally orthogonal to P-gp-mediated drug resistance. Within this drug class, imidazoquinoline TLR 7/8 agonists promote TIL and TAM reprogramming along tumor-suppressing axes [19], resulting in a myriad of immune-mediated anti-cancer effects [20–25] in both mono [26] and combination [27] therapies. To achieve these effects, while also limiting systemic inflammatory toxicity, imidazoquinolines are typically administered locally, via topical application or intratumoral injection. This has led our group [28–30] and others [31–34] to develop prodrug delivery strategies that liberate imidazoquinolines, either within the tumor microenvironment, or within cancer cells themselves, by intracellular immunostimulant accumulation followed by drug efflux. Although these strategies have the potential to facilitate delivery of imidazoquinolines to TILs and TAMs, the results also point to drug efflux as a potential rate-limiting step in immune cell activation for imidazoquinolines liberated within cancer cells. This suggests that MDR cancer cells with enhanced transport protein expression could be more susceptible to small-molecule immunotherapeutics. However, the effect of acquired MDR on imidazoquinoline immunotherapeutic efflux has never been explored, apart from a recent study that exclusively examines Resiquimod trafficking [35]. As such, we hypothesized that identifying a pathway for imidazoquinoline efflux and establishing the effects of acquired MDR on efflux would inform the design of the next generation of small-molecule immunotherapeutic prodrugs.

Herein, we demonstrate that imidazoquinolines are highly variable as substrates for P-gp efflux, both in a membrane vesicle model, as well as in vitro across a range of MDR cancer cells (Figure 1). Overall, we find that efflux is significantly enhanced by the MDR phenotype depending on both the type of cancer and the substituent variation regarding N1 and C2 locations on the imidazoquinoline structure itself.

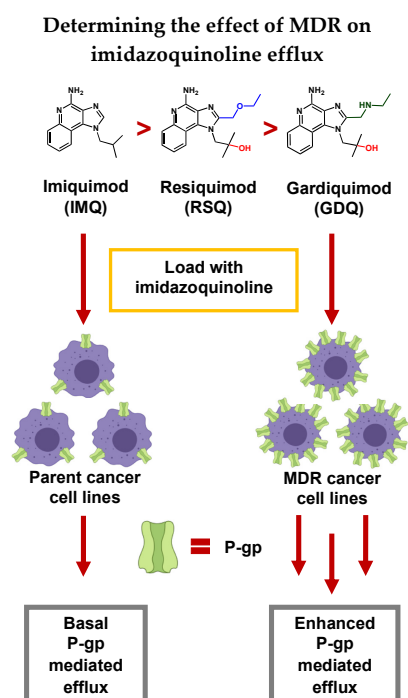


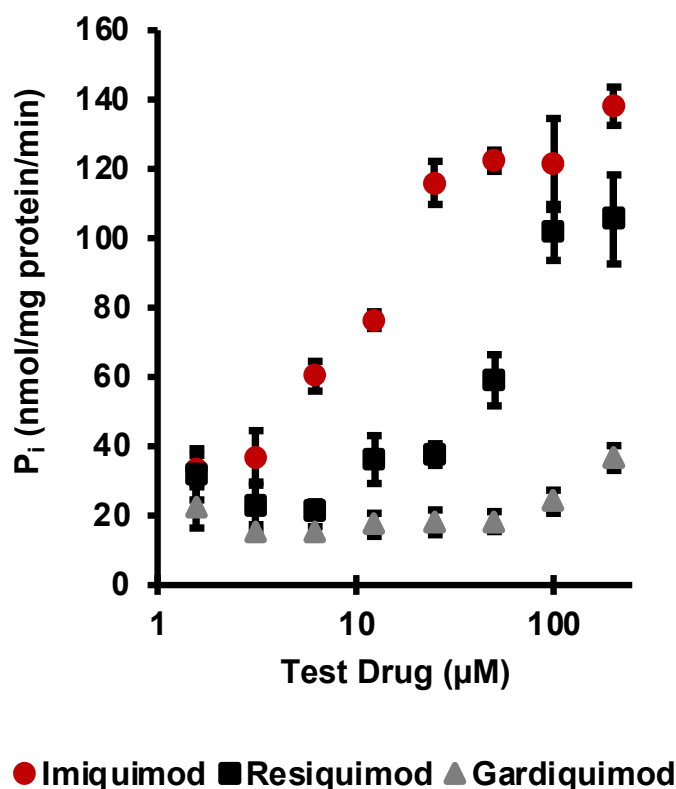
**Figure 1.** In this study we establish that Imiquimod (IMQ), Resiquimod (RSQ), and Gardiquimod (GDQ) are substrates of P-gp, and compare P-gp-mediated efflux between Multidrug-Resistant (MDR) cancer cell lines relative to parent cell lines. We also conclude that some efflux likely occurs through other transport proteins as well as passive transport into the extracellular space.

## 2. Results

### 2.1. Imiquimod, Resiquimod, and Gardiquimod Are Substrates of P-gp

To determine if imidazoquinolines are substrates of P-gp, an ATPase assay using purified membrane vesicles expressing P-gp was performed (Figure 2). All three imidazoquinolines were tested at the same concentrations, from 1.56 to 200  $\mu\text{M}$ . Concentration dependent activation of P-gp ATP (quantified as liberated  $\text{P}_i$ ) was detectable down to 6.25  $\mu\text{M}$  for IMQ. RSQ also stimulated P-gp at higher concentrations, whereas GDQ was a poor substrate by comparison, only liberating  $\text{P}_i$  above baseline at the highest concentrations tested. That said, each imidazoquinoline did liberate  $\text{P}_i$  in the activation test, confirming that all are P-gp substrates, albeit to varying degrees. Based upon this result, we calculated imidazoquinoline P-gp substrate affinity as (Table 1): IMQ ( $K_D = 7.66 \mu\text{M}$ ) > RSQ ( $K_D = 24.37 \mu\text{M}$ ) > GDQ (N.D.). These results were further confirmed using SwissADME, which predicted each imidazoquinoline to be a substrate for P-gp [36]. None of the three imidazoquinolines significantly inhibited maximal vanadate-sensitive ATPase activity when tested as inhibitors, an important point because P-gp-mediated drug efflux occurs through multiple mechanisms (Figure S3) [37].

### Imidazoquinolines are substrates of membrane vesicle P-gp



**● Imiquimod ■ Resiquimod ▲ Gardiquimod**  
**Figure 2.** ATPase assay with IMQ, RSQ, and GDQ. In the activation test, IMQ, RSQ, and GDQ all stimulated vanadate-sensitive ATPase activity above baseline, confirming that the imidazoquinolines are substrates of P-gp. Error bars are standard deviation from the mean of experiments repeated in duplicate.

### 2.2. MDR Cancer Cell Lines Enhance P-gp Expression

MDR cancer cell lines were derived from parent cancer cell lines by introducing 1 nM Doxorubicin (Dox) in the growth media and doubling the concentration at each passage until cell populations capable of stable proliferation in 1  $\mu\text{M}$  Dox were obtained (Figure 3A; Supplementary Material for MDR progression). This process is established to

provide epigenetic pressure that increases expression of P-gp [38]. Western blot (Figure 3B) confirmed that MDR-derived cell lines expressed more P-gp than their parent cancer cell line counterparts with the amount of P-gp quantified in each of the MDR-derived cell lines (Figure S7). P-gp localization on cellular membranes was confirmed by fluorescence microscopy using an Anti-P-gp-Alexa Fluor 488 antibody conjugate (Figure 3C). The 4T1 cell lines were not used in the immunofluorescence assay due to spectral overlap between the antibody and GFP expression linked to the Luc2 gene.

**Table 1.** cLogP and  $K_D$  values of imidazoquinolines. cLogP was calculated using ChemDraw 19.1 Software—PerkinElmer.  $K_D$  was estimated (sum of squares) from the membrane vesicle P-gp assay.

Imidazoquinoline	cLogP	$K_D$ ( $\mu$ M)
Imiquimod	1.428	7.66
Resiquimod	0.036	24.37
Gardiquimod	−0.254	N.D.

### 2.3. Imiquimod Competes with Rhodamine 123 Efflux in MDR-Derived Cancer Cell Lines

To determine whether the imidazoquinolines compete with known P-gp substrates, competitive efflux studies were performed with Rhodamine 123 (Rh123) under active transport conditions (37 °C) in both parent and MDR cancer cell lines. P-gp-mediated Rh123 efflux was confirmed by increased Rh123 retention, quantified by Mean Fluorescence Intensity (MFI), upon co-incubation with P-gp substrate Verapamil (VER) [39,40] and Tariquidar (TQR), a third-generation inhibitor of P-gp [41] (Figure S1). Significant increases in Rh123 retention were also observed in the MDR cell lines, particularly AT3B-1, TC2-MDR, and B16-MDR cells dually loaded with Rh123 and IMQ, compared to Rh123 alone (Figures 4A and S5). No significant increase in Rh123 retention was observed with RSQ and GDQ, which could be indicative of either their lowered affinity for P-gp or decreased intracellular loading concentration relative to IMQ, which we subsequently determined by HPLC. None of the imidazoquinolines affected Rh123 retention for the 4T1-MDR or any parent cancer cell lines (Figure 4A). Additionally, there was no increase in fluorescence upon co-incubation with VER or TQR in the parent cell lines. These results were consistent with enhanced P-gp expression in the MDR cell lines promoting Rh123 and IMQ efflux. Interestingly, significant increases in MFI were observed in the presence of IMQ, in contrast to other studies reporting imidazoquinolines such as RSQ do not affect efflux [35]. From our competitive efflux experiments, we concluded that, with the exception of inconclusive results in 4T1-MDR cells, IMQ competes with Rh123 in the MDR cancer cell lines for P-gp-mediated efflux.

### 2.4. Imiquimod Increases Rhodamine 123 Uptake under Passive Diffusion Conditions

Although active transport efflux experiments confirmed that IMQ competes with Rh123 in most of the MDR cancer cell lines, but not in parent cancer cell lines, this trend was not observed with RSQ or GDQ. In order to determine if changing the loading conditions would impact the results observed in the competitive efflux experiments, uptake studies with Rh123 were performed under passive diffusion conditions (4 °C) where P-gp is inactive [42]. No significant increases in Rh123 accumulation were observed in most of the cell lines tested with RSQ and GDQ relative to Rh123 alone except for minimal differential accumulation with RSQ in B16-MDR cells (Figures 4B and S6). VER exhibited the same trend as IMQ, as did TQR, though to a lesser extent (Figure S2). Similar to the competitive efflux experiments, this trend was only observed in the same MDR-cell lines, suggesting that IMQ leads to more Rh123 uptake in the MDR-derived cell lines compared to their parent counterparts under passive diffusion conditions.

### MDR-derived cancer cells overexpress P-gp

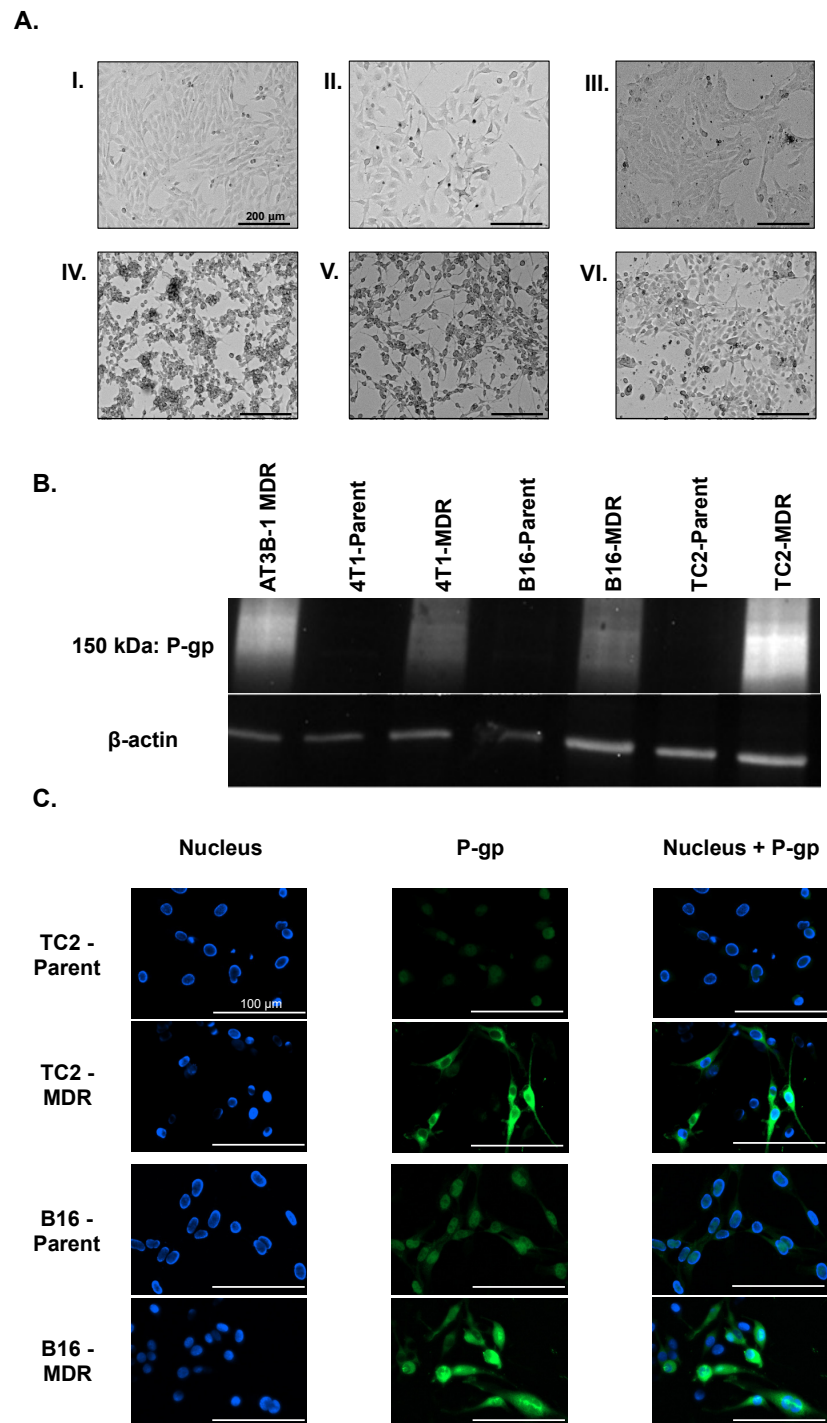


**Figure 3.** (A) MDR cancer cells were derived from parent cancer cell lines by incrementally increasing the Dox concentration in growth media. (I) TRAMP-C2 (TC2) prostate parent cancer cell line. (II) B16-F10 (B16) melanoma parent cancer cell line. (III) 4T1-Luc2 (4T1) breast parent cancer cell line. (IV) TC2-MDR cancer cell line. (V) B16-MDR cancer cell line. (VI) 4T1-MDR cancer cell line. Scale: 200  $\mu$ m (B) Western blot shows the increased expression of P-gp in MDR cancer cells compared to parent cancer cell lines. (C) TC2-Parent, TC2-MDR, B16-Parent, and B16-MDR stained with Anti-P-gp-Alexa Fluor 488 antibody conjugate reveals the increased expression of P-gp in MDR-derived cancer cell lines, as well as membrane localization of P-gp.

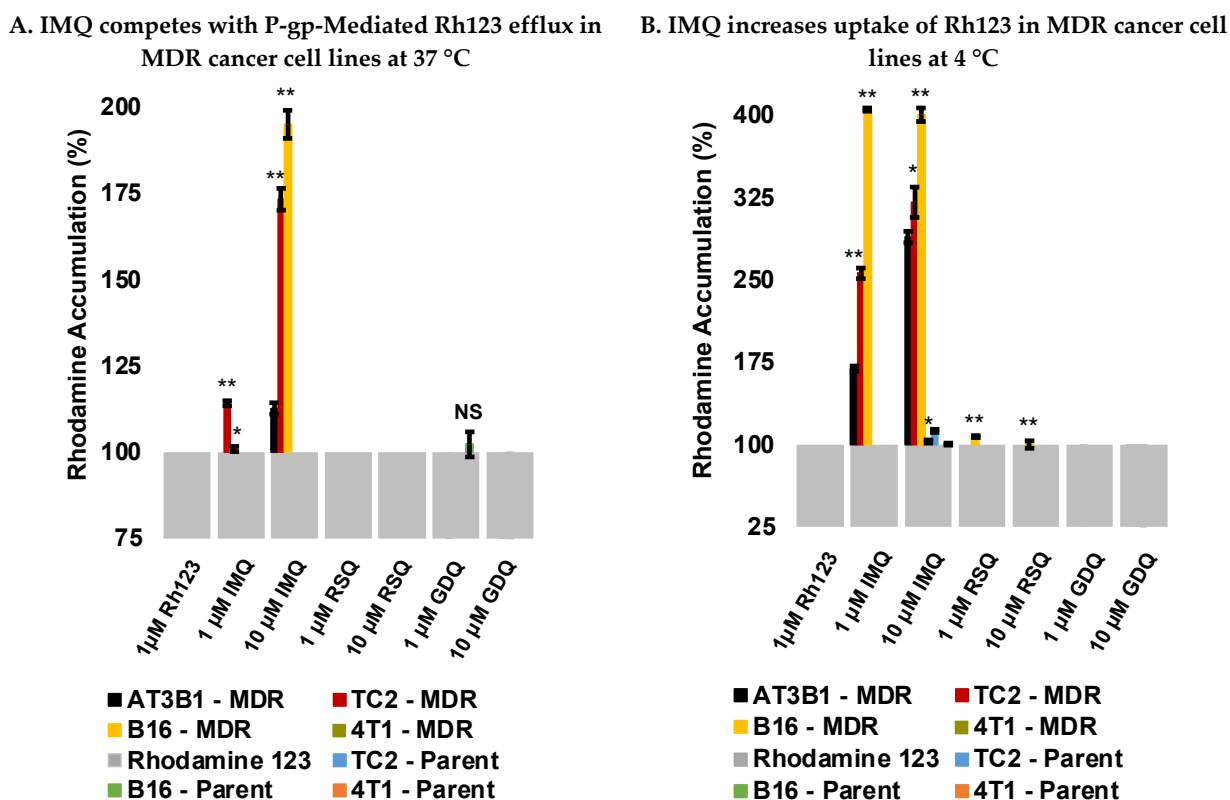


**Figure 4.** (A) Competitive experiments performed at 37 °C with P-gp substrate Rh123. IMQ leads to an increase in Rh123 accumulation in MDR-derived cancer cells under active transport conditions. Data representative of triplicate experiments. (B) Uptake experiments performed at 4 °C with P-gp substrate, Rhodamine 123. IMQ leads to an increase in Rh123 accumulation in MDR-derived cancer cells under passive diffusion conditions. Data representative of triplicate experiments. *p*-values were calculated between parent vs. MDR cancer cell type with \* *p* < 0.01, \*\* *p* < 0.001 and NS: Not significant.

### 2.5. Resiquimod and Gardiquimod Are Not Passively Taken up by MDR Cancer Cells

To examine the effect of MDR on uptake, cell lysate was examined for imidazoquinolines following loading under passive conditions (4 °C). Cancer cells loaded with imidazoquinolines (100  $\mu$ M) were lysed and lysate imidazoquinoline content was quantified by HPLC. Results of this experiment indicated that RSQ and GDQ were not significantly taken up by TC2-MDR, B16-MDR, or AT3B-1-MDR cells; however, IMQ showed efficient uptake under identical loading conditions (Figure 5). TC2-MDR cells had the highest intracellular IMQ (20.75  $\mu$ M) among the MDR lines derived in-house. In comparison, all imidazoquinolines were taken up by the parent cancer cell lines. Here, the TC2-Parent (16.58  $\mu$ M) had the highest IMQ uptake, followed by the 4T1-Parent (11.06  $\mu$ M) and B16-Parent (5.72  $\mu$ M) cell lines. RSQ was only detectable in parent cancer cell lines: TC2-Parent (25.84  $\mu$ M), B16-Parent (11.65  $\mu$ M), and 4T1-Parent (1.34  $\mu$ M). Likewise, GDQ was only detected in parent cancer cell lines, with B16-Parent having the highest uptake (16.42  $\mu$ M). Interestingly, detectable amounts of IMQ (16.31  $\mu$ M), RSQ (4.47  $\mu$ M), and GDQ (10.13  $\mu$ M) are taken up by the 4T1-MDR-derived cancer cell line; however, significant competition for P-gp-mediated efflux was not observed with Rh123 for RSQ and GDQ. Furthermore, we also observed that MDR cell lines take up more IMQ compared to the parent cancer cells. Finally, because imidazoquinolines are also known to directly induce apoptosis in a variety of cancers, independent of immunogenic effects [43], we also confirmed that the tested concentrations/incubation times were not cytotoxic to the cancer cells via resazurin cell viability assay (Figure S4).

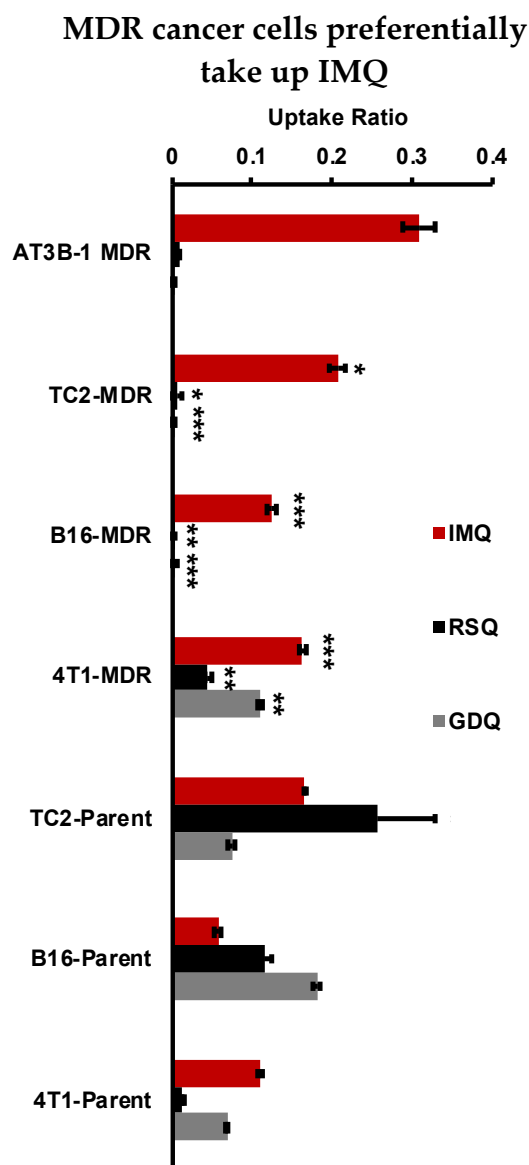


**Figure 5.** Uptake experiments performed by loading IMQ, RSQ, or GDQ (100  $\mu$ M) under passive diffusion conditions in parent and MDR-derived cancer cell lines followed by analysis of imidazoquinoline in cell lysate by HPLC. Cellular uptake ratio was calculated by dividing the peak area of substrate in lysate by the peak area calibrated for 100  $\mu$ M imidazoquinoline using standard solutions. Data representative of experiments performed in triplicate. *p*-values were calculated between parent vs. MDR cancer cell lines with \* *p* < 0.05, \*\* *p* < 0.01, and \*\*\* *p* < 0.001.

### 3. Discussion

Multidrug resistance is a major challenge for traditional chemotherapy, and attributed to many different mechanisms, including increased DNA damage repair, reduced apoptosis, aberrant drug metabolism, and enhanced drug efflux [44,45]. The cancer cell types chosen for this study were B16-F10 (B16) melanoma, TRAMP-C2 (TC2) prostate, and 4T1-Luc2 (4T1) breast cancer. These cell lines were primarily chosen based on their ability to acquire drug resistance [46–48], as well as the established efficacy of TLR 7/8 agonists in corresponding *in vivo* models [26,49–51]. As a positive control we chose AT3B-1 prostate cancer cells, as opposed to Caco-2 or MDCK-II lines routinely used for measuring efflux of small molecules [52], because AT3B-1 cells possessed the previously well-characterized Dox-derived MDR phenotype [53] and have subsequently been used in studies involving membrane transport through P-gp [54].



The imidazoquinoline immunostimulants chosen for this study were: Imiquimod (IMQ), Resiquimod (RSQ), and Gardiquimod (GDQ). We chose these particular imidazoquinolines for their extensive use in cancer immunotherapy. In particular, the TLR 7 agonist IMQ is FDA-approved for treatment of basal skin cell carcinoma and known to confer anti-cancer immunogenicity [55]. RSQ, a more potent TLR 7/8 dual agonist, features nanomolar potency [56], and is capable of activating TLR 8 in humans which is expressed by myeloid-derived dendritic cells [57,58], an advantage when compared to IMQ. GDQ, a TLR 7 agonist, is more potent than IMQ, and likewise exhibits enhanced antitumor effects [59].

Previously, our own work implied that IMQ [29] and RSQ [30] undergo drug efflux from a range of cancer cell lines. However, specific routes of efflux were only indirectly investigated. In the present study, we directly confirmed that IMQ, RSQ, and GDQ are substrates of P-gp, with variable affinity, using an ATPase membrane transport study (Figure 2). We also concluded that the less potent TLR 7 agonist IMQ is a better substrate for P-gp efflux than RSQ or GDQ in both membrane vesicles and MDR cancer cells.

Next, we created MDR cancer cells which overexpressed P-gp by growing the non-MDR Parent cell lines in increasing concentrations of Dox from 1 nM to 1  $\mu$ M. Each of the cancer cell lines reached the 1  $\mu$ M Dox threshold at different times. The TC2-MDR version took 3 months, the B16-MDR took 7 months, and the 4T1-MDR cells took over 8 months (see Supplementary Materials for timeline). Via brightfield microscopy (Figure 3A), we observed that cell morphology changed to elongated structures at increased Dox concentration, perhaps suggestive of the epithelial to mesenchymal transition that can occur upon chronic exposure to chemotherapeutics [60]. Regardless, our MDR cancer cell lines increased P-gp expression compared to parent cell lines, as quantified by Western blot (Figures 3B and S7) with visually confirmed membrane localization via fluorescence microscopy (Figure 3C).

With both imidazoquinoline P-gp substrate specificity and P-gp expression in MDR cancer cell lines confirmed, we next investigated imidazoquinoline efflux in our parent and MDR cell lines. Here, IMQ competed with Rh123 for efflux in most of the MDR-cancer cell lines, a trend not observed in the parent cancer cell lines (Figures 4A and S5). This result directly correlated with P-gp expression in the MDR-derived cancer cell lines and is consistent with our previous report that IMQ competes with Rh123 for efflux in AT3B-1 cells [29]. Alternatively, the baseline MFIs (loading with Rh123 alone) of MDR-derived cancer cells were lower than the parent cancer cell lines, as is expected with enhanced efflux potential from acquired drug resistance (Figure S5) [61]. This means a smaller absolute fluorescence could appear as a larger signal when reported as a percent of baseline accumulation. That said, it is possible that poor uptake of RSQ and GDQ in MDR cancer cell lines could be responsible for the lack of competition observed in the efflux experiments (Figures 4 and S6). We also observed enhanced uptake of IMQ in MDR cells compared to parent cell lines, both with and without Rh123. This could be explained by a variety of mechanisms. For example, drug-resistant cells could have altered membrane permeability beyond transport protein expression. Another possibility is that P-gp may influence substrate influx as well [62].

Based upon these results, we conclude that P-gp efflux susceptibility, which correlates to hydrophobicity/ $c\text{LogP}$ , should be considered, alongside potency, when choosing the optimal TLR agonist for delivery to MDR cancers.  $c\text{LogP}$  can influence P-gp efflux and does not negatively impact passive permeability unless the values fall well outside drug-like ranges ( $c\text{LogP} < 1$  or  $c\text{LogP} \geq 7$ ) [15]. IMQ falls within this range; however, RSQ and GDQ fall outside this range which could explain both the lack of uptake of RSQ and GDQ as well as their minimal competition for efflux.

It is important to note that even though expression of P-gp was increased in the 4T1-MDR cell line, relative to the non-MDR parent line, we did not observe imidazoquinoline competition with Rh123. Interestingly, we did observe an increase in Luc2 gene in the MDR-derived cell line, directly correlating to the acquisition of drug resistance

(Figures S5 and S6). While this study demonstrates that imidazoquinolines, particularly IMQ, are substrates for P-gp mediated efflux, it is also likely that imidazoquinolines could serve as substrates for some of the many other ABC transporters, which may have led to no change in Rh123 accumulation, especially in the 4T1-MDR cell line. It is also possible that Dox-derived MDR provokes compensatory expression of other ABC transporters or other ABC-independent efflux mechanisms as well. Although some generalizable differences in substrate scopes do exist between transport proteins implicated in drug efflux, there is also significant overlap, particularly with proteins associated with MDR that further complicate both development and analysis of efflux [63–65].

#### 4. Materials and Methods

##### 4.1. Materials

The B16-F10 melanoma cell line was purchased from the American Type Culture Collection (ATCC, Manassas, VA, USA). As per manufacturer instructions, the B16-F10 cell line (ATCC, Manassas, VA, USA, CRL-6475, mouse melanoma) was grown in complete culture media composed of DMEM (VWR, Radnor, PA, USA, 6777-406) with 4.5 g L<sup>-1</sup> glucose, 2 mM L-glutamine, 100 U mL<sup>-1</sup> PenStrep (Caisson Labs, Smithfield, VA, USA, PSL01), and supplemented with 10% Premium Grade HI-FBS (VWR, Radnor, PA, USA, 97068-091). Media was changed every 3–4 days. Cells were passaged upon reaching 80% confluence. Trypsin solution (Sigma Aldrich, St. Louis, MO, USA, T-4049) was used per manufacturer instructions to release cells before passaging which involved changing media, counting, and seeding 3 × 10<sup>5</sup> cells in 35 mL of new complete media in a new T-175 culture flask (VWR, Radnor, PA, USA, 10861-650).

The TRAMP-C2 prostate cell line was purchased from ATCC. As per manufacturer instructions, the TRAMP C2 cell line (ATCC, Manassas, VA, USA, CRL-2731, mouse transgenic adenocarcinoma) was grown in complete culture media composed of DMEM with 4.5 g L<sup>-1</sup> glucose, 2 mM L-glutamine, 100 U mL<sup>-1</sup> PenStrep, and supplemented with 1 µg mL<sup>-1</sup> Insulin (Sigma-Aldrich, St. Louis, MO, USA, I0516), 2 nM (+)-Dehydroisoandrosterone (VWR, Radnor, PA, USA, 200008-124), 5% HI-FBS, and 5% Nu-Serum IV (Corning, Corning, NY, USA, 355504). Media was changed every 3–4 days. Cells were passaged upon reaching 80% confluence. Trypsin solution (Sigma Aldrich, St. Louis, MO, USA, T-4049) was used per manufacturer instructions to release cells before passaging which involved changing media, counting, and seeding 3 × 10<sup>5</sup> cells in 35 mL of new complete media in a new T-175 culture flask (VWR, Radnor, PA, USA, 10861-650).

4T1-Luc2 breast cancer cell line was gifted from Darrell Irvine's lab (Massachusetts Institute of Technology, Cambridge, MA, USA). The 4T1-Luc2 cell line (ATCC, Manassas, VA, USA, CRL-2539-LUC2, mouse mammary gland carcinoma) was grown in complete culture media composed of DMEM with 4.5 g L<sup>-1</sup> glucose, 2 mM L-glutamine, 100 U mL<sup>-1</sup> PenStrep, and supplemented with 10% HI-FBS. Media was changed every 3–4 days. Cells were passaged upon reaching 80% confluence. Trypsin solution (Sigma Aldrich, St. Louis, MO, USA, T-4049) was used per manufacturer instructions to release cells before passaging which involved changing media, counting, and seeding 3 × 10<sup>5</sup> cells in 35 mL of new complete media in a new T-175 culture flask (VWR, Radnor, PA, USA, 10861-650).

AT3B-1 prostate cancer cells were chosen for their well-characterized P-gp expression as a result of epigenetic pressure caused by exposure to the Doxorubicin [53]. The AT3B-1 cell line was purchased from ATCC. The AT3B-1 cell line (ATCC, Manassas, VA, USA, CRL-2375, rat MDR prostate carcinoma) was grown in complete culture media composed of DMEM with 4.5 g L<sup>-1</sup> glucose, 2 mM L-glutamine, 100 U mL<sup>-1</sup> PenStrep, supplemented with 10% HI-FBS and 1 µM Doxorubicin (TCI America, Portland, OR, USA, D4193100MG). Media was changed every 3–4 days. Cells were passaged upon reaching 80% confluence. Trypsin solution (Sigma Aldrich, St. Louis, MO, USA, T-4049) was used per manufacturer instructions to release cells before passaging which involved changing media, counting, and seeding 3 × 10<sup>5</sup> cells in 35 mL of new complete media in a new T-175 culture flask (VWR, Radnor, PA, USA, 10861-650).

The B16-F10 Melanoma (B16), TRAMP C-2 prostate (TC2), and 4T1-Luc2 breast (4T1) parent cancer cell lines were seeded at  $3 \times 10^5$  cells in T-175 culture flasks separate from the parent cancer cell lines. These cells were cultured in complete cell media which contained Doxorubicin (Dox). The original media was composed of: DMEM with  $4.5 \text{ g L}^{-1}$  glucose, 2 mM L-glutamine,  $100 \text{ U mL}^{-1}$  PenStrep, 10% HI-FBS and 1 nM Dox. The media was changed every 3–4 days until the cells reached 80% confluence. Trypsin solution (Sigma Aldrich, St. Louis, MO, USA, T-4049) was used per manufacturer instructions to release cells before passaging which involved changing media, counting, and seeding  $3 \times 10^5$  cells in 35 mL of new complete media in a new T-175 culture flask (VWR, Radnor, PA, USA, 10861-650). Dox concentration was doubled only after stable proliferation, which for some cell lines took multiple passages, before reaching a final concentration of  $1 \mu\text{M}$  (Figure 2).

#### 4.2. ATPase Assay

Colorimetric measurement of imidazoquinoline interaction with P-gp was determined using a PREDEASY ATPase Assay Kit (SOLVO Biotechnology, Sigma-Aldrich, St. Louis, MO, USA) in 96-well plate format following the manufacturer's protocol. Stock solutions of developer and blocker were diluted using Ultrapure DNase/Rnase Free Distilled Water (Invitrogen, Waltham, MA, USA, 10977015). Briefly, across individual wells, Imiquimod (IMQ) (eNovation Chemicals, Green Brook, NJ, USA, SY017571), Resiquimod (RSQ) (Accel Pharmtech, East Brunswick, NJ, USA, XP2356), Gardiquimod (GDQ) (synthesized in-house; see Supplementary Materials) were added at 8 different concentrations (1–200  $\mu\text{M}$ ) to membrane vesicles expressing hMDR1. Each well contained 4  $\mu\text{g}$  membrane protein, and 1  $\mu\text{L}$  of imidazoquinoline was added to arrive at the final concentrations noted. The plate was pre-incubated (37 °C, 10 min) before 10  $\mu\text{L}$  of MgATP solution was added to start the reaction. The plate was incubated (37 °C, 10 min) before the ATPase reaction was quenched using 100  $\mu\text{L}$  of Developer Solution at room temperature. After 2 min, 100  $\mu\text{L}$  of Blocker solution was added to each well at room temperature before incubation (37 °C, 30 min). Following incubation, the absorbance was measured using a microplate reader at 610 nm. Absorbance values were used to calculate liberated  $\text{P}_i$  (Figure 2) and  $K_D$ .

#### 4.3. Western Blot

Cell lysates were extracted using Triton X-100 lysing buffer, and lysate was quantified using Pierce BCA Protein Assay Kit (ThermoFisher Scientific, Waltham, MA, USA, 23225). For each cell lysate, 20  $\mu\text{g}$  of protein was run on a 4–15% SDS gel (Bio-Rad, Hercules, CA, USA, 4561083DC) and electrotransferred onto a PVDF membrane. The membrane was washed with TBS and blocked overnight with 3% BSA in TBST. The membrane was incubated with primary Rabbit anti-P-gp antibody (Abcam, Waltham, MA, USA, ab170904) for 2 h, washed  $2 \times$  for 10 min with TBST, and incubated with a secondary Goat anti-Rabbit IgG HandL (Abcam, Waltham, MA, USA, ab97051) antibody for 1 h. Rabbit anti- $\beta$ -actin antibody (Abcam, Waltham, MA, USA, ab8227) along with the MDR AT3B-1 cell line were used as controls (Figure 3B). As per manufacturer's instructions, the primary antibody detects the predominant protein band migrating in the region of 180–200 kDa and typically will demonstrate a smear on the membrane in the region of 150–300 kDa due to the glycosylation profile of the protein [66].

#### 4.4. Immunofluorescence Assay

Cancer cells (parent and MDR-derived) were plated on glass coverslips (neuVITRO, Vancouver, WA, USA, GG-25-1.5-pdl) in a 6-well plate and allowed to reach 70% confluency. The cells were fixed using 4% formaldehyde for 15 min at room temperature. After three washes with 1 mL PBS, the cells were blocked (10% HI-FBS in PBS) for 1 h at 37 °C. Cells were incubated with Mouse anti-P-gp antibody conjugated to Alexa Fluor 488 (Santa Cruz Biotechnology, Dallas, TX, USA, sc55510 AF488) overnight in the dark at 4 °C before incubation with Mouse IgG Fc binding protein conjugated to CruzFluor 488 (Santa Cruz Biotechnology, Dallas, TX, USA, sc533653) in the dark at room temperature

for 1 h. Finally, coverslips were washed in PBS and mounted with Vectashield antifade mounting medium with DAPI (Vector Labs, Burlingame, CA, USA, H-2000-10) diluted in Vectashield antifade mounting media (Vector Labs, Burlingame, CA, USA, H-1900-10) to  $0.1 \mu\text{g mL}^{-1}$ . Fluorescent images ( $40\times$ ) were acquired on a Lionheart FX (BioTek Instruments) microscope (Figure 3C).

#### 4.5. Competitive Efflux Studies with Rhodamine 123

Cancer cells (parent and MDR-derived) were passaged, and  $1 \times 10^6$  cells were used for each compound tested with Rhodamine 123 (Rh123) (Cayman Chemical, Ann Arbor, MI, USA, 16672). Cells were suspended in DMEM, supplemented with 10% HI-FBS, and  $1 \mu\text{M}$  Rh123; and incubated ( $37^\circ\text{C}$ , 30 min). Following incubation with Rh123, 1 or  $10 \mu\text{M}$  of imidazoquinoline (IMQ, RSQ, GDQ), and/or P-gp inhibitor of Verapamil (VER) (Cayman Chemical, Ann Arbor, MI, USA, 14288), or Tariquidar (TQR) (Sigma-Aldrich, St. Louis, MO, USA, SML 1790) were added to the cells and incubated for another 30 min at  $37^\circ\text{C}$ . After incubation, samples were centrifuged (300 RCF, 5 min) and the supernatant discarded. Cells were fixed with 4% formaldehyde for 15 min at room temperature. The samples were centrifuged (300 RCF, 5 min) and suspended in 1 mL cold FACS buffer. Finally, the Mean Fluorescence Intensity (MFI) of Rh123 in the samples was measured via flow cytometry (BD Accuri C6 Plus). Results are representative of triplicate experiments and normalized to MFI for  $1 \mu\text{M}$  Rh123 (Figure 4A and Figure S5; see Supplementary Materials for histograms).

#### 4.6. Uptake Studies with Rhodamine 123

Cancer cells (parent and MDR-derived) were passaged, and  $1 \times 10^6$  cells were used for each compound being tested with Rh123. Cancer cells were suspended in DMEM, supplemented with 10% HI-FBS, and  $1 \mu\text{M}$  Rh123. The cells were incubated ( $4^\circ\text{C}$ , 30 min) followed by adding IMQ, RSQ, GDQ, VER, or TQR ( $1$  or  $10 \mu\text{M}$ ) and incubating further for 30 min at  $4^\circ\text{C}$ . Next, samples were centrifuged (300 RCF, 5 min) and the supernatant discarded. Cells were fixed with 4% formaldehyde for 15 min at room temperature. The samples were centrifuged again (300 RCF, 5 min), suspended in 1 mL ice cold FACS buffer, and analyzed in triplicate for Rh123 MFI via flow cytometry. Samples were normalized to uptake of  $1 \mu\text{M}$  Rh123 as indicated in (Figure 4B and Figure S6; see Supplementary Materials for histograms).

#### 4.7. Cellular Uptake Studies

Cancer cells (parent and MDR-derived) were passaged, and  $5 \times 10^6$  cells were used for each experiment. Cells were suspended in 1 mL DMEM, supplemented with 10% HI-FBS, with  $100 \mu\text{M}$  of IMQ, RSQ, or GDQ, and incubated at  $4^\circ\text{C}$  for 30 min. Samples were then centrifuged (300 RCF, 5 min) and washed 2 times with 1 mL cold PBS. The samples were re-suspended in lysing buffer: For IMQ and RSQ, lysing buffer consisted of 40% HPLC Grade acetonitrile (ACN) in HPLC Grade water ( $\text{H}_2\text{O}$ ) with 0.1% Trifluoroacetic acid (TFA) and 1% *v/v* Triton X-100. Due to solubility differences, GDQ lysing buffer consisted of HPLC Grade water with 0.1% TFA and 1% *v/v* Triton X-100. Cells were lysed on ice for 20 min. Following the lysing step, samples were centrifuged (12500 RCF, 10 min) with the supernatant collected and filtered using a  $0.2 \mu\text{m}$  PTFE filter. Filtered samples were analyzed by HPLC (Thermo Dionex UltiMate 3000 running Chromeleon software (V6.80 SR14) with a C18 analytical column (Phenomenex XB-C18  $100\text{\AA}$ ,  $250 \times 4.6 \text{ mm}$ ,  $5 \mu\text{m}$ ) at a flow rate of  $1 \text{ mL/min}$ , A:  $\text{H}_2\text{O}$  with 0.1% TFA, B: ACN with 0.1% TFA, with UV detection at 254 nm. For IMQ and RSQ an isocratic method (40% B) was used. For GDQ, a gradient method (10% B for 5 min, 10 to 95% B over 14 min, 95% B for 10 min) was used. For each of the imidazoquinolines, 9-point calibration curves were derived using standards with concentrations ranging from 500 nM to  $250 \mu\text{M}$ . The calibration curves were used to fit using linear regression for each imidazoquinoline: IMQ ( $y = 0.039x$ ;  $R^2 = 0.9976$ ), RSQ ( $y = 0.0447x$ ;  $R^2 = 0.9994$ ), and GDQ ( $y = 0.0271x$ ;  $R^2 = 0.9996$ ). All samples were analyzed

in triplicate. Cellular uptake ratio was obtained by dividing the peak area of substrate in lysate by the peak area calibrated for 100  $\mu$ M imidazoquinoline (Figure 5).

#### 4.8. Cytotoxicity Assay

Resazurin Cell Viability Assay kit (Abcam, Waltham, MA, USA, ab129732) was used to determine if the concentrations of IMQ, RSQ, and GDQ used in experiments were cytotoxic to the cancer cell lines under experimental conditions. To begin, cancer cells were plated in complete cell media (DMEM, 10% HI-FBS) in 96-well plates, with two rows per plate of each density/well tested: 2000 cells/well, 25,000 cells/well, 50,000 cells/well, and 100,000 cells/well. Cells were treated with 20  $\mu$ L of 1 mM solutions of IMQ, RSQ, and GDQ, to give a final concentration per well of 100  $\mu$ M for each compound. Plates were incubated at 37  $^{\circ}$ C for 1 h. After incubation, 10  $\mu$ L of resazurin stain was added to wells in alternating rows on the plate, such that for each density and compound tested in triplicate there was a corresponding blank without stain added. Plates were incubated further with absorbance measured at 570 nm and 600 nm at 1, 2, 3, 4, and 24 h intervals. The absorbance measurements at 600 nm, which correlated to the absorbance of resazurin, were subtracted from those taken at 570 nm, correlating to the resorufin absorbance. After this, values were normalized to cell viability of the negative control. Experiments were performed in triplicate and the 3 h time-point for  $5 \times 10^5$  cells is shown (Figure S4).

## 5. Conclusions

In conclusion, this study demonstrates the imidazoquinolines IMQ, RSQ, and GDQ are substrates for P-gp and begins to elucidate differences in their trafficking in cancer cells as a consequence of acquired drug resistance. Using Dox to derive MDR-versions of B16, TC2, and 4T1 cells resulted in enhanced P-gp expression and IMQ efflux. Additionally, using competitive experiments with Rh123, we demonstrate that IMQ competes with Rh123 P-gp efflux in the MDR phenotypes. Ultimately, this work contributes to the development of new cancer immunotherapies, particularly imidazoquinoline prodrugs, which could be enhanced by means of drug efflux following intracellular liberation of active drug. We believe this work that begins to examine imidazoquinoline trafficking will prove useful in the future rational design of immunotherapeutics with enhanced susceptibility to P-gp efflux that enable increased bioavailability, in MDR cancers.

## 6. Patents

A.J.B., A.E.N., and R.J.M. are inventors on WSU's patent 11,117,918; A.E.N. and R.J.M. are owners of Astante Therapeutics Inc. both of which use concepts related to those in this work.

**Supplementary Materials:** The following are available online at <https://www.mdpi.com/article/10.3390/ph14121292/s1>, Figure S1: Verapamil (VER) and Tariquidar (TQR) compete with Rhodamine 123 (Rh123) in all cancer cells, leading to more accumulation in MDR cancer cell lines at 37  $^{\circ}$ C, Figure S2: Verapamil (VER) and Tariquidar (TQR) lead to an increased uptake of Rhodamine 123 (Rh123) in MDR-derived cancer cells at 4  $^{\circ}$ C, Figure S3: Imidazoquinolines do not inhibit maximal vanadate sensitive ATPase activity, Figure S4: Imidazoquinolines are not cytotoxic to cancer cells at high concentrations, Figure S5: Mean Fluorescence Intensities of competitive experiments with Rhodamine 123 at 37  $^{\circ}$ C, Figure S6: Mean Fluorescence Intensities of uptake experiments with Rhodamine 123 at 4  $^{\circ}$ C, Figure S7: Amount of P-gp present in the MDR cancer cells as per the Western blot. Additionally,  $K_D$  calculations and values of imidazoquinolines, flow cytometry histograms, microscope images of the progression of parent to MDR-derived cancer cell lines, and synthetic procedure and characterization of GDQ [67–70] can also be found in the supporting information.

**Author Contributions:** A.J.P. derived MDR cell lines, conducted uptake and competitive efflux experiments, and performed the immunofluorescence assays. A.J.B. synthesized GDQ and assisted with uptake experiments. L.K.O. performed the Western blot and assisted with cell culture and immunofluorescence. C.M.M. conducted the ATPase assay. M.D. assisted with preliminary uptake experiments. A.E.N. conducted the imidazoquinoline cytotoxicity assays. R.J.M. conceived of the

project and directed the work. All authors contributed to preparation of the manuscript. All authors have read and agreed to the published version of the manuscript.

**Funding:** Research reported in this publication was supported by the National Cancer Institute of the National Institutes of Health under Award Number 1R01CA234115. C.M. was supported by the National Institute of Health Biotechnology Training Grant T32 GM 008336. The content is solely the responsibility of the authors and does not necessarily represent the official views of the National Institutes of Health. NMR characterization of GDQ and synthetic intermediates was made possible through use of the Washington State University NMR Center with equipment supported by NIH RR0631401, RR12948, NSF CHE-9115282, and DBI-9604689, the Murdock Charitable Trust, and private donors Don and Marianna Matteson.

**Institutional Review Board Statement:** Not applicable.

**Informed Consent Statement:** Not applicable.

**Data Availability Statement:** Data is contained within the article or Supplementary Material.

**Acknowledgments:** The authors thank Katrina Mealey for expert advice with efflux experiments and Darrell Irvine for donating the 4T1-Luc2 cells. Figure 1 created with BioRender.com (accessed on 11 November 2021).

**Conflicts of Interest:** The authors declare no conflict of interest. The funders had no role in the design of the study; in the collection, analyses, or interpretation of data; in the writing of the manuscript, or in the decision to publish the results.

## References

- Longley, D.B.; Johnston, P.G. Molecular Mechanisms of Drug Resistance. *J. Pathol.* **2005**, *205*, 275–292. [CrossRef]
- Szakács, G.; Paterson, J.K.; Ludwig, J.A.; Booth-Genthe, C.; Gottesman, M.M. Targeting Multidrug Resistance in Cancer. *Nat. Rev. Drug Discov.* **2006**, *5*, 219–234. [CrossRef]
- Glavinas, H.; Krajcsi, P.; Cserepes, J.; Sarkadi, B. The Role of ABC Transporters in Drug Resistance, Metabolism and Toxicity. *Curr. Drug Deliv.* **2004**, *1*, 27–42. [CrossRef]
- Borst, P.; Elferink, R.O. Mammalian ABC Transporters in Health and Disease. *Annu. Rev. Biochem.* **2002**, *71*, 537–592. [CrossRef]
- Juliano, R.L.; Ling, V. A Surface Glycoprotein Modulating Drug Permeability in Chinese Hamster Ovary Cell Mutants. *Biochim. Biophys. Acta (BBA)-Biomembr.* **1976**, *455*, 152–162. [CrossRef]
- Riordan, J.R.; Ling, V. Purification of P-Glycoprotein from Plasma Membrane Vesicles of Chinese Hamster Ovary Cell Mutants with Reduced Colchicine Permeability. *J. Biol. Chem.* **1979**, *254*, 12701–12705. [CrossRef]
- Juranka, P.F.; Zastawny, R.L.; Ling, V. P-Glycoprotein: Multidrug-Resistance and a Superfamily of Membrane-Associated Transport Proteins. *FASEB J.* **1989**, *3*, 2583–2592. [CrossRef]
- Ferreira, R.J.; dos Santos, D.J.; Ferreira, M.-J.U. P-Glycoprotein and Membrane Roles in Multidrug Resistance. *Future Med. Chem.* **2015**, *7*, 929–946. [CrossRef]
- Ueda, K.; Cardarelli, C.; Gottesman, M.M.; Pastan, I. Expression of a Full-Length cDNA for the Human “MDR1” Gene Confers Resistance to Colchicine, Doxorubicin, and Vinblastine. *Proc. Natl. Acad. Sci. USA* **1987**, *84*, 3004–3008. [CrossRef]
- Gottesman, M.M. Mechanisms of Cancer Drug Resistance. *Annu. Rev. Med.* **2002**, *53*, 615–627. [CrossRef]
- Gatlik-Landwojtowicz, E.; Äänismaa, P.; Seelig, A. Quantification and Characterization of P-Glycoprotein–Substrate Interactions. *Biochemistry* **2006**, *45*, 3020–3032. [CrossRef] [PubMed]
- Ramachandra, M.; Ambudkar, S.V.; Chen, D.; Hrycyna, C.A.; Dey, S.; Gottesman, M.M.; Pastan, I. Human P-Glycoprotein Exhibits Reduced Affinity for Substrates during a Catalytic Transition State. *Biochemistry* **1998**, *37*, 5010–5019. [CrossRef]
- Pawagi, A.B.; Wang, J.; Silverman, M.; Reithmeier, R.A.F.; Deber, C.M. Transmembrane Aromatic Amino Acid Distribution in P-Glycoprotein. *J. Mol. Biol.* **1994**, *235*, 554–564. [CrossRef]
- Matsson, P.; Pedersen, J.M.; Norinder, U.; Bergström, C.A.S.; Artursson, P. Identification of Novel Specific and General Inhibitors of the Three Major Human ATP-Binding Cassette Transporters P-Gp, BCRP and MRP2 Among Registered Drugs. *Pharm. Res.* **2009**, *26*, 1816–1831. [CrossRef] [PubMed]
- Hitchcock, S.A. Structural Modifications That Alter the P-Glycoprotein Efflux Properties of Compounds. *J. Med. Chem.* **2012**, *55*, 4877–4895. [CrossRef] [PubMed]
- Gottesman, M.M.; Ling, V. The Molecular Basis of Multidrug Resistance in Cancer: The Early Years of P-Glycoprotein Research. *FEBS Lett.* **2006**, *580*, 998–1009. [CrossRef] [PubMed]
- Coley, W.B., II. Contribution to the Knowledge of Sarcoma. *Ann. Surg.* **1891**, *14*, 199–220. [CrossRef]
- Coley, W.B. The Treatment of Inoperable Sarcoma by Bacterial Toxins (the Mixed Toxins of the Streptococcus Erysipelas and the Bacillus Prodigiosus). *Proc. R. Soc. Med.* **1910**, *3*, 1–48. [CrossRef]
- Smits, E.L.J.M.; Ponsaerts, P.; Berneman, Z.N.; Van Tendeloo, V.F.I. The Use of TLR7 and TLR8 Ligands for the Enhancement of Cancer Immunotherapy. *Oncologist* **2008**, *13*, 859–875. [CrossRef] [PubMed]

20. Prins, R.M.; Craft, N.; Bruhn, K.W.; Khan-Farooqi, H.; Koya, R.C.; Stripecke, R.; Miller, J.F.; Liao, L.M. The TLR-7 Agonist, Imiquimod, Enhances Dendritic Cell Survival and Promotes Tumor Antigen-Specific T Cell Priming: Relation to Central Nervous System Antitumor Immunity. *J. Immunol.* **2006**, *176*, 157–164. [CrossRef]
21. Caron, G.; Duluc, D.; Frémaux, I.; Jeannin, P.; David, C.; Gascan, H.; Delneste, Y. Direct Stimulation of Human T Cells via TLR5 and TLR7/8: Flagellin and R-848 Up-Regulate Proliferation and IFN- $\gamma$  Production by Memory CD4<sup>+</sup> T Cells. *J. Immunol.* **2005**, *175*, 1551–1557. [CrossRef]
22. Huang, S.J.; Hijnen, D.; Murphy, G.F.; Kupper, T.S.; Calarese, A.W.; Mollet, I.G.; Schanbacher, C.F.; Miller, D.M.; Schmults, C.D.; Clark, R.A. Imiquimod Enhances IFN- $\gamma$  Production and Effector Function of T Cells Infiltrating Human Squamous Cell Carcinomas of the Skin. *J. Investig. Dermatol.* **2009**, *129*, 2676–2685. [CrossRef] [PubMed]
23. Hart, O.M.; Athie-Morales, V.; O'Connor, G.M.; Gardiner, C.M. TLR7/8-Mediated Activation of Human NK Cells Results in Accessory Cell-Dependent IFN- $\gamma$  Production. *J. Immunol.* **2005**, *175*, 1636–1642. [CrossRef] [PubMed]
24. Peng, G. Toll-Like Receptor 8-Mediated Reversal of CD4<sup>+</sup> Regulatory T Cell Function. *Science* **2005**, *309*, 1380–1384. [CrossRef]
25. Yin, T.; He, S.; Wang, Y. Toll-like Receptor 7/8 Agonist, R848, Exhibits Antitumoral Effects in a Breast Cancer Model. *Mol. Med. Rep.* **2015**, *12*, 3515–3520. [CrossRef] [PubMed]
26. Han, J.-H.; Lee, J.; Jeon, S.-J.; Choi, E.-S.; Cho, S.-D.; Kim, B.-Y.; Kim, D.-J.; Park, J.-H.; Park, J.-H. In Vitro and in Vivo Growth Inhibition of Prostate Cancer by the Small Molecule Imiquimod. *Int. J. Oncol.* **2013**, *42*, 2087–2093. [CrossRef]
27. Mullins, S.R.; Vasilakos, J.P.; Deschler, K.; Grigsby, I.; Gillis, P.; John, J.; Elder, M.J.; Swales, J.; Timosenko, E.; Cooper, Z.; et al. Intratumoral Immunotherapy with TLR7/8 Agonist MEDI9197 Modulates the Tumor Microenvironment Leading to Enhanced Activity When Combined with Other Immunotherapies. *J. Immunother. Cancer* **2019**, *7*, 244. [CrossRef]
28. Hantho, J.D.; Strayer, T.A.; Nielsen, A.E.; Mancini, R.J. An Enzyme-Directed Imidazoquinoline for Cancer Immunotherapy. *ChemMedChem* **2016**, *11*, 2496–2500. [CrossRef]
29. Burt, A.J.; Hantho, J.D.; Nielsen, A.E.; Mancini, R.J. An Enzyme-Directed Imidazoquinoline Activated by Drug Resistance. *Biochemistry* **2018**, *57*, 2184–2188. [CrossRef]
30. Ryan, A.T.; Pulukuri, A.J.; Davaritouchae, M.; Abbasi, A.; Hendricksen, A.T.; Opp, L.K.; Burt, A.J.; Nielsen, A.E.; Mancini, R.J. Comparing the Immunogenicity of Glycosidase-Directed Resiquimod Prodrugs Mediated by Cancer Cell Metabolism. *Acta Pharm. Sin.* **2020**, *41*, 995–1004. [CrossRef]
31. Li, H.; Van Herck, S.; Liu, Y.; Hao, Y.; Ding, X.; Nuhn, L.; Zhong, Z.; Combes, F.; Sanders, N.N.; Lienenklaus, S.; et al. Imidazoquinoline-Conjugated Degradable Coacervate Conjugate for Local Cancer Immunotherapy. *ACS Biomater. Sci. Eng.* **2020**, *6*, 4993–5000. [CrossRef] [PubMed]
32. Mottas, I.; Bekdemir, A.; Cereghetti, A.; Spagnuolo, L.; Yang, Y.-S.S.; Müller, M.; Irvine, D.J.; Stellacci, F.; Bourquin, C. Amphiphilic Nanoparticle Delivery Enhances the Anticancer Efficacy of a TLR7 Ligand via Local Immune Activation. *Biomaterials* **2019**, *190–191*, 111–120. [CrossRef] [PubMed]
33. Nuhn, L.; De Koker, S.; Van Lint, S.; Zhong, Z.; Catani, J.P.; Combes, F.; Deswarte, K.; Li, Y.; Lambrecht, B.N.; Lienenklaus, S.; et al. Nanoparticle-Conjugate TLR7/8 Agonist Localized Immunotherapy Provokes Safe Antitumoral Responses. *Adv. Mater.* **2018**, *30*, 1803397. [CrossRef]
34. Yoo, E.; Salyer, A.C.D.; Brush, M.J.H.; Li, Y.; Trautman, K.L.; Shukla, N.M.; De Beuckelaer, A.; Lienenklaus, S.; Deswarte, K.; Lambrecht, B.N.; et al. Hyaluronic Acid Conjugates of TLR7/8 Agonists for Targeted Delivery to Secondary Lymphoid Tissue. *Bioconjugate Chem.* **2018**, *29*, 2741–2754. [CrossRef]
35. Theile, D.; Wagner, L.; Haefeli, W.E.; Weiss, J. In Vitro Evidence Suggesting That the Toll-like Receptor 7 and 8 Agonist Resiquimod (R-848) Unlikely Affects Drug Levels of Co-Administered Compounds. *Eur. J. Pharm. Sci.* **2021**, *162*, 105826. [CrossRef]
36. Daina, A.; Michielin, O.; Zoete, V. SwissADME: A Free Web Tool to Evaluate Pharmacokinetics, Drug-Likeness and Medicinal Chemistry Friendliness of Small Molecules. *Sci. Rep.* **2017**, *7*, 42717. [CrossRef] [PubMed]
37. Aller, S.G.; Yu, J.; Ward, A.; Weng, Y.; Chittaboina, S.; Zhuo, R.; Harrell, P.M.; Trinh, Y.T.; Zhang, Q.; Urbatsch, I.L.; et al. Structure of P-Glycoprotein Reveals a Molecular Basis for Poly-Specific Drug Binding. *Science* **2009**, *323*, 1718–1722. [CrossRef]
38. Cox, J.; Weinman, S. Mechanisms of Doxorubicin Resistance in Hepatocellular Carcinoma. *Hepatic Oncol.* **2016**, *3*, 57–59. [CrossRef]
39. Ledwitch, K.V.; Gibbs, M.E.; Barnes, R.W.; Roberts, A.G. Cooperativity between Verapamil and ATP Bound to the Efflux Transporter P-Glycoprotein. *Biochem. Pharmacol.* **2016**, *118*, 96–108. [CrossRef]
40. Durie, B.G.M.; Dalton, W.S. Reversal of Drug-Resistance in Multiple Myeloma with Verapamil. *Br. J. Haematol.* **1988**, *68*, 203–206. [CrossRef]
41. Weidner, L.D.; Fung, K.L.; Kannan, P.; Moen, J.K.; Kumar, J.S.; Mulder, J.; Innis, R.B.; Gottesman, M.M.; Hall, M.D. Tariquidar Is an Inhibitor and Not a Substrate of Human and Mouse P-Glycoprotein. *Drug Metab. Dispos.* **2016**, *44*, 275–282. [CrossRef]
42. Urbatsch, I.L.; Sankaran, B.; Weber, J.; Senior, A.E. P-Glycoprotein Is Stably Inhibited by Vanadate-Induced Trapping of Nucleotide at a Single Catalytic Site. *J. Biol. Chem.* **1995**, *270*, 19383–19390. [CrossRef]
43. Schön, M.P.; Schön, M. Immune Modulation and Apoptosis Induction: Two Sides of the Antitumoral Activity of Imiquimod. *Apoptosis* **2004**, *9*, 291–298. [CrossRef] [PubMed]
44. Kachalaki, S.; Ebrahimi, M.; Mohamed Khosroshahi, L.; Mohammadinejad, S.; Baradaran, B. Cancer Chemoresistance; Biochemical and Molecular Aspects: A Brief Overview. *Eur. J. Pharm. Sci.* **2016**, *89*, 20–30. [CrossRef] [PubMed]
45. Salehan, M.R.; Morse, H.R. DNA Damage Repair and Tolerance: A Role in Chemotherapeutic Drug Resistance. *Br. J. Biomed. Sci.* **2013**, *70*, 31–40. [CrossRef]

46. Mariani, M.; Supino, R. Morphological Alterations Induced by Doxorubicin in B16 Melanoma Cells. *Cancer Lett.* **1990**, *51*, 209–212. [CrossRef]
47. Foster, B.A.; Gingrich, J.R.; Kwon, E.D.; Madias, C.; Greenberg, N.M. Characterization of Prostatic Epithelial Cell Lines Derived from Transgenic Adenocarcinoma of the Mouse Prostate (TRAMP) Model. *Cancer Res.* **1997**, *57*, 3325.
48. Bao, L.; Haque, A.; Jackson, K.; Hazari, S.; Moroz, K.; Jetly, R.; Dash, S. Increased Expression of P-Glycoprotein Is Associated with Doxorubicin Chemoresistance in the Metastatic 4T1 Breast Cancer Model. *Am. J. Pathol.* **2011**, *178*, 838–852. [CrossRef]
49. Lee, M.; Park, C.-S.; Lee, Y.-R.; Im, S.-A.; Song, S.; Lee, C.-K. Resiquimod, a TLR7/8 Agonist, Promotes Differentiation of Myeloid-Derived Suppressor Cells into Macrophages and Dendritic Cells. *Arch. Pharm. Res.* **2014**, *37*, 1234–1240. [CrossRef] [PubMed]
50. Krieg, A.M. Toll-like Receptor 9 (TLR9) Agonists in the Treatment of Cancer. *Oncogene* **2008**, *27*, 161–167. [CrossRef]
51. Singh, M.; Khong, H.; Dai, Z.; Huang, X.-F.; Wargo, J.A.; Cooper, Z.A.; Vasilakos, J.P.; Hwu, P.; Overwijk, W.W. Effective Innate and Adaptive Antimelanoma Immunity through Localized TLR7/8 Activation. *J. Immunol.* **2014**, *193*, 4722–4731. [CrossRef] [PubMed]
52. Youhanna, S.; Lauschke, V.M. The Past, Present and Future of Intestinal In Vitro Cell Systems for Drug Absorption Studies. *J. Pharm. Sci.* **2021**, *110*, 50–65. [CrossRef]
53. Replogle-Schwab, T.S.; Schwab, E.D.; Pienta, K.J. Development of Doxorubicin Resistant Rat Prostate Cancer Cell Lines. *Anticancer Res.* **1997**, *17*, 4535–4538. [PubMed]
54. Liang, J.F.; Yang, V.C. Synthesis of Doxorubicin–Peptide Conjugate with Multidrug Resistant–Tumor Cell Killing Activity. *Bioorganic Med. Chem. Lett.* **2005**, *15*, 5071–5075. [CrossRef] [PubMed]
55. Cho, J.H.; Lee, H.-J.; Ko, H.-J.; Yoon, B.-I.; Choe, J.; Kim, K.-C.; Hahn, T.-W.; Han, J.A.; Choi, S.S.; Jung, Y.M.; et al. The TLR7 Agonist Imiquimod Induces Anti-Cancer Effects via Autophagic Cell Death and Enhances Anti-Tumoral and Systemic Immunity during Radiotherapy for Melanoma. *Oncotarget* **2017**, *8*, 24932–24948. [CrossRef]
56. Jurk, M.; Heil, F.; Vollmer, J.; Schetter, C.; Krieg, A.M.; Wagner, H.; Lipford, G.; Bauer, S. Human TLR7 or TLR8 Independently Confer Responsiveness to the Antiviral Compound R-848. *Nat. Immunol.* **2002**, *3*, 499. [CrossRef] [PubMed]
57. Hornung, V.; Rothenfusser, S.; Britsch, S.; Krug, A.; Jahrsdörfer, B.; Giese, T.; Endres, S.; Hartmann, G. Quantitative Expression of Toll-Like Receptor 1–10 mRNA in Cellular Subsets of Human Peripheral Blood Mononuclear Cells and Sensitivity to CpG Oligodeoxynucleotides. *J. Immunol.* **2002**, *168*, 4531–4537. [CrossRef] [PubMed]
58. Crozat, K.; Vivier, E.; Dalod, M. Crosstalk between Components of the Innate Immune System: Promoting Anti-Microbial Defenses and Avoiding Immunopathologies. *Immunol. Rev.* **2009**, *227*, 129–149. [CrossRef]
59. Ma, F.; Zhang, J.; Zhang, J.; Zhang, C. The TLR7 Agonists Imiquimod and Gardiquimod Improve DC-Based Immunotherapy for Melanoma in Mice. *Cell Mol. Immunol.* **2010**, *7*, 381–388. [CrossRef]
60. Thiery, J.P.; Aclouque, H.; Huang, R.Y.J.; Nieto, M.A. Epithelial-Mesenchymal Transitions in Development and Disease. *Cell* **2009**, *139*, 871–890. [CrossRef] [PubMed]
61. Brouty-Boyé, D.; Kolonias, D.; Wu, C.J.; Savaraj, N.; Lampidis, T.J. Relationship of Multidrug Resistance to Rhodamine-123 Selectivity between Carcinoma and Normal Epithelial Cells: Taxol and Vinblastine Modulate Drug Efflux. *Cancer Res.* **1995**, *55*, 1633.
62. Vasiliou, V.; Vasiliou, K.; Nebert, D.W. Human ATP-Binding Cassette (ABC) Transporter Family. *Hum. Genom.* **2008**, *3*, 281. [CrossRef] [PubMed]
63. Johnson, Z.L.; Chen, J. Structural Basis of Substrate Recognition by the Multidrug Resistance Protein MRP1. *Cell* **2017**, *168*, 1075–1085.e9. [CrossRef] [PubMed]
64. Orlando, B.J.; Liao, M. ABCG2 Transports Anticancer Drugs via a Closed-to-Open Switch. *Nat. Commun.* **2020**, *11*, 2264. [CrossRef] [PubMed]
65. Rosenberg, M.F.; Bikadi, Z.; Hazai, E.; Starborg, T.; Kelley, L.; Chayen, N.E.; Ford, R.C.; Mao, Q. Three-Dimensional Structure of the Human Breast Cancer Resistance Protein (BCRP/ABCG2) in an Inward-Facing Conformation. *Acta Cryst. D Biol. Cryst.* **2015**, *71*, 1725–1735. [CrossRef]
66. Greer, D.A.; Ivey, S. Distinct N-Glycan Glycosylation of P-Glycoprotein Isolated from the Human Uterine Sarcoma Cell Line MES-SA/Dx5. *Biochim. Biophys. Acta (BBA)-Gen. Subj.* **2007**, *1770*, 1275–1282. [CrossRef] [PubMed]
67. Fujita, Y.; Hirai, K.; Nishida, K.; Taguchi, H. 6-(4-Amino-2-Butyl-Imidazoquinoly)-Norleucine: Toll-like Receptor 7 and 8 Agonist Amino Acid for Self-Adjuvanting Peptide Vaccine. *Amino Acids* **2016**, *48*, 1319–1329. [CrossRef] [PubMed]
68. Gerster, J.F.; Lindstrom, K.J.; Miller, R.L.; Tomai, M.A.; Birmachu, W.; Bomersine, S.N.; Gibson, S.J.; Imbertson, L.M.; Jacobson, J.R.; Knafla, R.T.; et al. Synthesis and Structure–Activity-Relationships of 1H-Imidazo[4,5-c]Quinolines That Induce Interferon Production. *J. Med. Chem.* **2005**, *48*, 3481–3491. [CrossRef] [PubMed]
69. Shukla, N.M.; Malladi, S.S.; Mutz, C.A.; Balakrishna, R.; David, S.A. Structure–Activity Relationships in Human Toll-Like Receptor 7-Active Imidazoquinoline Analogues. *J. Med. Chem.* **2010**, *53*, 4450–4465. [CrossRef] [PubMed]
70. Shukla, N.M.; Kimbrell, M.R.; Malladi, S.S.; David, S.A. Regioisomerism-Dependent TLR7 Agonism and Antagonism in an Imidazoquinoline. *Bioorg. Med. Chem. Lett.* **2009**, *19*, 2211–2214. [CrossRef] [PubMed]





MDPI  
St. Alban-Anlage 66  
4052 Basel  
Switzerland  
Tel. +41 61 683 77 34  
Fax +41 61 302 89 18  
[www.mdpi.com](http://www.mdpi.com)

*Pharmaceuticals* Editorial Office  
E-mail: [pharmaceuticals@mdpi.com](mailto:pharmaceuticals@mdpi.com)  
[www.mdpi.com/journal/pharmaceuticals](http://www.mdpi.com/journal/pharmaceuticals)





MDPI  
St. Alban-Anlage 66  
4052 Basel  
Switzerland

Tel: +41 61 683 77 34  
Fax: +41 61 302 89 18

[www.mdpi.com](http://www.mdpi.com)



ISBN 978-3-0365-4347-5